AD-A069 015 ADVISORY GROUP FOR AEROSPACE RESEARCH AND DEVELOPMENT--ETC F/G 17/2.1
MILLIMETER AND SUBMILLIMETER WAVE PROPAGATION AND CIRCUITS.(U)
FEB 79 E SPITZ, G CACHIER
UNCLASSIFIED AGARD-CP-245 NL

1 OF 6
AD
A069015

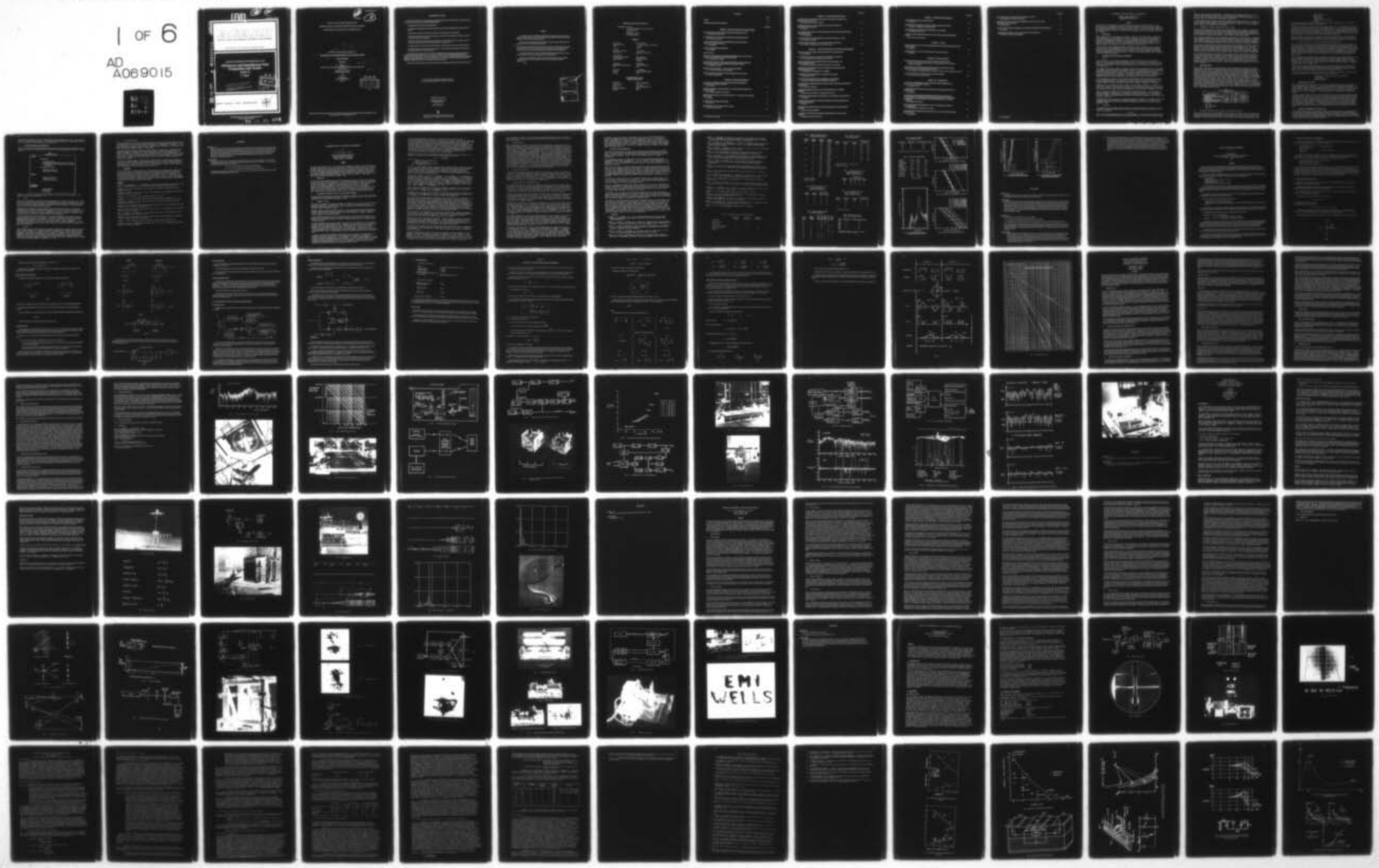

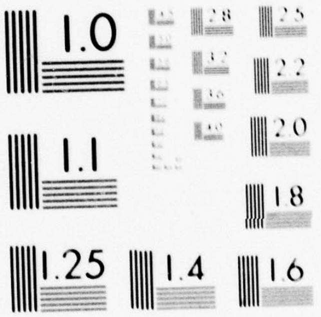
1.0
2.8
2.5
3.2
2.2
3.6
4.0
2.0
1.1
1.8
1.25
1.4
1.6

MICROCOPY RESOLUTION TEST CHART
NATIONAL BUREAU OF STANDARDS 1963-A

LEVEL

③

AGARD-CP-245

AD A069015

DDC FILE COPY

AGARD-CP-245

AGARD

ADVISORY GROUP FOR AEROSPACE RESEARCH & DEVELOPMENT

7 RUE ANCELLE 92200 NEUILLY SUR SEINE FRANCE

AGARD CONFERENCE PROCEEDINGS No. 245

Millimeter and Submillimeter Wave Propagation and Circuits

Edited by

E. Spitz

This document has been approved for public release and sale; its distribution is unlimited.

DDC
RECEIVED
MAY 29 1979
C

NORTH ATLANTIC TREATY ORGANIZATION

DISTRIBUTION AND AVAILABILITY
ON BACK COVER

79 05 24 038

AGARD-CP-245

(3)

NORTH ATLANTIC TREATY ORGANIZATION

ADVISORY GROUP FOR AEROSPACE RESEARCH AND DEVELOPMENT

(ORGANISATION DU TRAITE DE L'ATLANTIQUE NORD)

(14) AGARD-CP-245

(9)

AGARD Conference Proceedings No.245

(6)

MILLIMETER AND SUBMILLIMETER WAVE PROPAGATION AND CIRCUITS

Edited by

(10) E.Spitz
Directeur du Laboratoire Central de Recherche de Thomson-CSF
B.P. No.10
Domaine de Corbeville
91401, Orsay, France

(11) Feb 79

(12) 555 p.

and

G.Cachier
Thomson CFS/LCR
France

DDC
RECEIVED
MAY 29 1979
C

Papers and discussions presented at the 25th Meeting of the Electromagnetic Wave Propagation Panel
held in Munich, 4–8 September 1978.

400 043

THE MISSION OF AGARD

The mission of AGARD is to bring together the leading personalities of the NATO nations in the fields of science and technology relating to aerospace for the following purposes:

- Exchanging of scientific and technical information;
- Continuously stimulating advances in the aerospace sciences relevant to strengthening the common defence posture;
- Improving the co-operation among member nations in aerospace research and development;
- Providing scientific and technical advice and assistance to the North Atlantic Military Committee in the field of aerospace research and development;
- Rendering scientific and technical assistance, as requested, to other NATO bodies and to member nations in connection with research and development problems in the aerospace field;
- Providing assistance to member nations for the purpose of increasing their scientific and technical potential;
- Recommending effective ways for the member nations to use their research and development capabilities for the common benefit of the NATO community.

The highest authority within AGARD is the National Delegates Board consisting of officially appointed senior representatives from each member nation. The mission of AGARD is carried out through the Panels which are composed of experts appointed by the National Delegates, the Consultant and Exchange Programme and the Aerospace Applications Studies Programme. The results of AGARD work are reported to the member nations and the NATO Authorities through the AGARD series of publications of which this is one.

Participation in AGARD activities is by invitation only and is normally limited to citizens of the NATO nations.

The content of this publication has been reproduced
directly from material supplied by AGARD or the authors.

Published February 1979

Copyright © AGARD 1979
All Rights Reserved

ISBN 92-835-0231-0

Printed by Technical Editing and Reproduction Ltd
Harford House, 7–9 Charlotte St, London W1P 1HD

THEME

The millimeter and the submillimeter ranges belong to the upper part of the microwave spectrum, where they take most of their techniques and technologies. However, some of their applications are derived from optical techniques.

The progress in technology has been impressive in the past few years, mainly due to the development of active and passive solid state devices.

The purpose of the meeting will be to present a broad view of the state of the art in solid state sources and detectors, and in associated circuit techniques and technologies. Recent progress in power tubes, laser techniques and high power techniques will be dealt with.

The system aspects will be covered, including atmospheric propagation effects as well as specific problems in detection, telecommunications and visualisation.

There will be an opportunity to discuss what future developments of the technology would be desirable and could be expected to cover the needs, especially in military applications.

ACCESSION for
NTIS White Section ☑
DDC Buff Section ☐
UNANNOUNCED ☐
JUSTIFICATION
BY
DISTRIBUTION/AVAILABILITY CODES
SPECIAL
A

PROGRAM AND MEETING OFFICIALS

CHAIRMAN: Dr E.Spitz
Directeur du Laboratoire Central de Recherche de Thomson-CSF
B.P. No.10
Domaine de Corbeville
91401, Orsay, France

MEMBERS

Dr G.Cachier
Thomson CSF/LCR
France

Dr F.Fedi
Fondazione Ugo Bordoni
Roma, Italy

Dr K.Hambleton
Admiralty Surface Weapons Establishment
UK

Dr H.J.Kuno
Hughes Electron Dynamics Div.
USA

Dr M.Vogel
DFVLR
Germany

Prof. E.Constant
Université des Sciences et Techniques de Lille
France

Dr G.Gibbons
The Plessey Company Ltd
UK

Dr G.Hartmann
Max-Planck Institut
Germany

Dr R.P.Moore
Naval Weapons Center
USA

Dr L.R.Whicker
Naval Research Laboratory
USA

ELECTROMAGNETIC WAVE PROPAGATION PANEL

CHAIRMAN:

Dr H.J.Albrecht
FGAN
Wachtberg-Werthhoven
Germany

DEPUTY CHAIRMAN:

Dr J.Aarons
Air Force Geophysics Lab.
Bedford
USA

CONTENTS

Page

THEME iii

PROGRAM AND MEETING OFFICIALS iv

Reference

SESSION I – MILITARY SYSTEMS AND APPLICATIONS

THE POTENTIAL MILITARY APPLICATIONS OF MILLIMETER WAVES
by L.R.Whicker and D.C.Webb 1

ENVIRONMENTAL EFFECTS ON MILLIMETER RADAR PERFORMANCE
by F.B.Dyer and N.C.Currie 2

SLANT PASS ATTENUATIONS AT MILLIMETRE WAVELENGTHS FOR VERY LOW ELEVATION ANGLES*
by E.E.Altshuller 3

FAISCEAU HERTZIEN MILLIMETRIQUE
par J.P.Dehaene 4

Paper 5 Cancelled

REVIEW OF TWO DECADES OF EXPERIENCE BETWEEN 30 GHz AND 900 GHz IN THE DEVELOPMENT OF MODEL RADAR SYSTEMS
by L.A.Cram and S.C.Woolcock 6

MODEL SIMULATION OF TARGET CHARACTERISTICS AND ENGAGEMENT SITUATIONS EMPLOYING MILLIMETRE WAVE RADAR SYSTEMS
by W.Gabsdil and W.Jacobi 7

MICROWAVE HOLOGRAPHY: A DECADE OF DEVELOPMENT
by L.A.Cram, G.W.Newberry and K.O.Rossiter 8

DESIGN AND PERFORMANCE OF 90 GHz RADIOMETER FRONT-ENDS
by H.Barth and B.Rembold 9

SESSION II – SOLID STATE SOURCES

UN NOUVEAU COMPOSANT POUR LES SYSTEMES MILLIMETRIQUES: LE TRANSISTOR A EFFET DE CHAMP
par J.-L.Teszner 10

STABLE MILLIMETRE WAVE SOURCES BY AVALANCHE DIODE FREQUENCY MULTIPLICATION
by P.A.Rolland, G.Salmer and E.Constant 11

WIDE-BAND MECHANICALLY TUNABLE W-BAND (75–110 GHz) CW GUNN DIODE OSCILLATOR
by J.Ondria 12

PARAMETRIC AMPLIFIER PUMP DESIGN
by J.J.Purcell 13

HUGHES IMPATT DEVICE WORK ABOVE 100 GHz
by H.J.Kuno and T.T.Fong 14

---

* Not available at time of printing.

Reference

SESSION III – SUBMILLIMETRE RECEIVERS

DETERMINATION OF SCHOTTKY DIODE MIXER CONVERSION LOSSES IN THE SUBMM WAVELENGTH RANGE
by H.P.Röser, E.Sauter and G.V.Schultz 15

THE MOTTKY-DIODE: A NEW ELEMENT FOR LOW NOISE MIXERS AT MILLIMETER WAVELENGTHS
by N.J.Keen 16

ADVANCES IN GaAs SCHOTTKY DIODE SUBMILLIMETER HETERODYNE RECEIVERS AND RADIOMETERS
by P.E.Tannenwald 17

THE DEVELOPMENT OF SUBHARMONICALLY PUMPED MIXERS AT 230 GHz
by K.F.Künzi and H.Berger 18

SUBMILLIMETRIC RECEIVERS: LOCAL OSCILLATORS AND MIXERS
by J.J.Jimenez, P.Plainchamp, A.Comeron and A.Clairon 19

SESSION IV – NEW TECHNOLOGIES AND INTEGRATION TECHNIQUES

INTEGRATED-CIRCUIT MEDIA FOR MILLIMETER-WAVE APPLICATIONS
by B.E.Spielman 20

ADVANCED TECHNOLOGY FOR THE MM AND SUBMM WAVE REGION
by D.T.Hodges, M.McColl, A.H.Silver and T.S.Hartwick 21

ADVANCED DEVICES AND COMPONENTS FOR THE MILLIMETER AND SUBMILLIMETER SYSTEMS
by J.A.Calviello, J.J.Taub, D.I.Brietzer, E.H.Kraemer and J.L.Wallace 22

CONCEPTS AND TECHNIQUES IN THE UTILIZATION OF MILLIMETER AND SUBMILLIMETER WAVES
by J.H.Rainwater, R.W.McMillan and J.J.Gallagher 23

JOSEPHSON EFFECT MIXERS (Paper not available for Proceedings)
by R.Adde and G.Vernet 24

ADVANCES IN MILLIMETER WAVE COMPONENTS AND SYSTEMS
by B.Adelseck, H.Barth, H.Hofmann, H.Meinel and B.Rembold 25

VARACTOR TUNED MILLIMETER WAVE OSCILLATOR IN THE PRETUNED MODULE TECHNOLOGY
by G.Cachier and J.Stevance 26

MICROSTRIP COMPONENTS FOR LOW COST MILLIMETER WAVE MISSILE SEEKERS
by H.G.Oltman, D.M.Weems, G.M.Lindgren and F.D.Walton 27

HYBRID-OPEN MICROSTRIP MIC TECHNOLOGY AT MILLIMETER WAVELENGTHS
by T.H.Oxley 28

QUASI-PLANAR DIELECTRIC WAVEGUIDE APPROACH FOR MILLIMETER-WAVE INTEGRATED CIRCUITS
by T.Itoh 29

FEASIBILITY STUDIES OF INSULAR GUIDE MILLIMETRE WAVE INTEGRATED CIRCUITS
by M.J.Aylward and N.Williams 30

FEASIBILITY OF DESIGNING MILLIMETRE MICROSTRIP PLANAR ANTENNA ARRAYS
by P.S.Hall, C.Garratt and J.R.James 31

Reference

SESSION V – COMPONENTS AND CIRCUITS

MILLIMETRE PIN DIODE CONTROL DEVICES
by M.L.Nyss 32

MILLIMETER PULSE MODULATION WITH LUMPED ELEMENT CIRCUITRY
by E.Kpodzo, G.Begemann and K.Schuenemann 33

PHASE CONTROL ELEMENTS FOR MILLIMETER WAVE SYSTEMS
by R.W.Babitt and R.A.Stern 34

AN OSCILLATOR MULTIPLIER CIRCUIT FOR THE GENERATION OF MILLIMETER WAVES
by L.Szabo and K.Schünemann 35

SESSION VI – TUBES

RECENT PROGRESS AND FUTURE PERFORMANCES OF MILLIMETER BACKWARD-WAVE OSCILLATORS
by B.Epsztein 36

DEVELOPMENT OF A 5-WATT TRAVELLING WAVE TUBE FOR 60 GHz
by N.Pranter 37

SESSION VII – SPECIAL DEVICES

NEW HIGH POWER MICROWAVE SOURCES IN THE MILLIMETRIC RANGE
by J.Buzzi, H.Doucet, P.Drossart, B.Etlicher, P.Haldenwang, H.Lamain, X.Mauchant, J.P.Marque and C.Rouille 38

RELATIVISTIC ELECTRON BEAM INTERACTIONS FOR GENERATION OF HIGH POWER MILLIMETER AND SUBMILLIMETER WAVES
by V.L.Granatstein, P.Sprangle, R.Parker, K.R.Chu, A.T.Drobot, L.Seftor, M.Read and T.Coffey 39

ANALYSIS OF OPTICALLY PUMPED CW FIR LASER EFFICIENCY
by J.M.Lourtioz, R.Adde and J.Pontnau 40

SESSION VIII – PROPAGATION

A SURVEY OF ATMOSPHERIC PROPAGATION RESEARCH EXPERIMENTS ON SLANT PATHS IN THE BAND 15–40 GHz
by A.S.Vander Vorst 41

ATMOSPHERIC INFLUENCES ON THE MILLIMETER AND SUBMILLIMETER WAVE PROPAGATION
by K.E.Fischer 42

REALISATION D'EQUIPEMENTS EMISSION RECEPTION POUR SYSTEMES DE TRANSMISSION AUX LONGUEURS D'ONDES MILLIMETRIQUES ET APPLICATION A L'ETUDE DES CARACTERISTIQUES RADIOELECTRIQUES DANS LA REGION PARISIENNE
par J.R.Mahieu et R.Devinne 43

RAIN ATTENUATION MEASURMENTS AT 94 GHz: COMPARISON OF THEORY AND EXPERIMENT
by W.P.M.N.Keizer, J.Snieder and C.D. de Haan 44

MEASUREMENTS OF EFFECTIVE SEA REFLECTIVITY AND ATTENUATION DUE TO RAIN AT 81 GHz
by R.J.Sherwell 45

Reference

MEASUREMENT OF ATTENUATION DUE TO RAIN AT 74 GHz
by M.M.Kharadly, J.D.McNicol and J.B.Peters 46

MEASUREMENTS OF LOW-ANGLE TROPOSPHERIC FADING AT 4 AND 30 GHz
USING THE ATS-6 SATELLITE*
by K.McCormick 47

THE INFLUENCE OF THE ATMOSPHERE ON PASSIVE RADIOMETRIC MEASUREMENTS
by J.Preissner 48

ATMOSPHERIC SOUNDING USING MILLIMETER WAVE RADIOMETRY
by K.F.Künzi, D.Meier and A.Randegger 49

---

* Not to be published.

THE POTENTIAL MILITARY APPLICATIONS OF MILLIMETER WAVES

Lawrence R. Whicker, Denis C. Webb
Naval Research Laboratory
Washington, DC 20375, U.S.A.

SUMMARY

This paper reviews the propagation characteristics of millimeter waves, considering effects of rain, clouds and fog. The fundamental limitations of microwave, millimeter and optical systems are discussed and the strengths and weaknesses of each class of system are outlined. Based on these considerations, the most promising application areas for millimeter waves are outlined. Applications for radar, communication and electronic warfare are discussed. Additionally needed component research and development activities are considered.

1.0 INTRODUCTION

Within the past few years, there has been a resurgence of interest in millimeter waves. (SKOLNIK, M.I., 1970), (JOHNSTON, S.L., 1977), (WEISBERG, L.R., 1977), (STROM, L.D., 1977) This is partly attributable to advances in component technology but also reflects the changing priorities of military systems. There is increased emphasis on employing as well as detecting small platforms [(e.g., missiles and RPV's (Remotely Piloted Vehicles)] . The necessity of achieving high resolution as well as being able to penetrate fog and smoke leads to the use of millimeter waves either as the primary system or in complementary equipment to be integrated with present microwave or optical equipment.

This paper first reviews the propagation factors of millimeter waves. The effects of rain, clouds and fog are considered. The fundamental limitations of microwave, millimeter wave and optical systems are described. The strengths and weaknesses of each class are outlined. Based upon these considerations, promising application areas for millimeter waves are outlined. The areas of application are subdivided into radar, communication and electronic warfare. A final section addresses component needs to effectively meet future system requirements.

2.0 CHARACTERISTICS OF MILLIMETER WAVE PROPAGATION

2.1 Weather

A prime consideration in the design and performance of a millimeter wave system is the atmospheric attenuation under the range of anticipated weather conditions. In general the system employs one of two modes: 1) a low attenuation mode for maximum range or 2) an LPI (low probability of intercept) mode for short range secure operation. Figure 1 indicates propagation loss in clear weather and in various types of inclement weather.

For reasonably low values of propagation attenuation in the millimeter wavelength portion of the spectrum the system must operate within one of the atmospheric windows. As is indicated in Figure 1, these windows are centered at 94, 140, and 220 GHz respectively. All have a percentage bandwidth of roughly 20%. The "clear air" attenuation between 94 GHz and the far-infrared is dominated by water-vapor absorption. Under hot humid conditions the attenuation in the windows may increase by as much as a factor of five over the values noted in the figure. Attenuation in the infrared windows centered at 10 and 4 microns is comparable to that of the 94 GHz window and is lower than that of the 140 and 220 GHz windows.

For LPI applications a few dB/km is usually desired and frequencies near the absorption peak centered at 60 GHz are commonly employed. Since this peak is a result of absorption by the oxygen molecule it is relatively stable under changes in temperature and relative humidity. Furthermore, componentry is considerably simpler here than at the higher frequencies where comparable attenuation can be achieved.

Attenuation due to a moderately heavy rain, 10 mm/hr., is also indicated in Figure 1. In general it depends both on particle size and particle density but remains roughly constant from 94 GHz to the visible portion of the spectrum. Below 94 GHz the attenuation due to rain decreases monotonically. Backscatter from raindrops is not a significant problem at frequencies of 94 GHz and higher. (RAINWATER, J.H., 1977)

Figure 1 also shows attenuation due to a heavy fog and a moderately dense cloud. For both the loss at optical wavelengths is prohibitive but is not excessive at millimeter wavelengths and is negligible at microwave frequencies. Characteristics for commonly used smokes are similar, i.e., an attenuation of 100 dB/km is common at infrared wavelengths while there is no measurable attenuation in the millimeter wave portion of the spectrum.

An important point to note is that it is frequently impractical to compensate for the degradation of system performance caused by inclement weather by simply increasing transmitter power. For example, if the propagation attenuation is 5 dB/km, the power must be increased by a factor of ten for each additional kilometer of range.

2.2 Resolution

A prime motivation for employing millimeter wavelengths rather than microwaves is the need for a narrow beam without an excessively large antenna aperture. The diffraction limited angular resolution, Ω, is given by the expression:

$$\Omega = 1.2\lambda/D$$

where λ is the operating wavelength and D is the antenna diameter. Typical high resolution requirements are $\Omega = 10^{-2}$ to 10^{-3} radians for beam riders and tracking radars and $\Omega = 10^{-4}$ and 10^{-3} radians for target detection, identification and classification. The maximum allowable antenna diameter may be a meter or less for aircraft and ground vehicles and as little as a few tens of centimeters for missiles, satellites, RPV's and hand-held radar. There are a significant number of military applications where the resolution offered by conventional microwave systems is inadequate.

For many applications even millimeter waves provide marginal or sub-marginal resolution. For example, a 1.5 meter diameter antenna operating at 230 GHz provides an angular resolution of only 10^{-3} radians. For higher resolution, synthetic aperture radar techniques (TOMIYASU, K., 1978) can be used from moving platforms, otherwise optical techniques must be employed.

2.3 Comparison of Microwave, Millimeter and Optical Systems

As noted above millimeter waves are employed rather than microwaves either to realize a narrower beam in an aperture limited system or to achieve covertness through moderately high atmospheric attenuation. Other advantages of millimeter wave systems are the increased bandwidth capability hence greater information carrying potential and better immunity to countermeasures. Furthermore, components and circuitry are more compact, an important consideration in missile, RPV and man-pack applications.

Where the above considerations are not overriding, microwave systems are usually preferable. Propagation loss is significantly lower in all weather conditions and high power sources and circuitry are much more readily available. These factors lead to much greater range for microwave systems than for millimeter wave systems. Furthermore, most components are more difficult to fabricate at millimeter wavelengths because of the required dimensional accuracies, and are more expensive than their microwave counterparts.

In high resolution applications where millimeter waves have clear advantages over microwaves, millimeter wave systems must compete with the generally better developed thermal imaging systems. The latter possess a 2 to 3 order of magnitude smaller wavelength and by using the powerful focal plane array technology can achieve a considerably greater clear weather range than millimeter wave systems. However, since they are passive an auxiliary active system is required to derive range and velocity information. This may be either a laser or if the clutter problems are not severe may be a complete microwave radar.

The clear advantage millimeter wave systems have over optical systems is their ability to penetrate clouds, smoke, fog and haze. The frequency and predictability of one or more of these conditions often dictates that military systems be operable in them to prevent the enemy from concealing his movements. For example, in Western Europe in approximately one of three mornings during the fall and winter the visibility is reduced to less than 1 km by ground fog. Also, roughly two-thirds of the time the total cloud cover exceeds 50% in the North Atlantic. Effective surveillance and/or operation under these weather conditions mandates use of microwave or millimeter wave systems as primary systems or as backups to optical systems.

3.0 RADAR APPLICATIONS

From the time of World War II much funding has gone into the development and optimization of microwave radar systems. These systems have been designed for particular functions and missions operating at frequencies from UHF to 35 GHz. Generally the search radar function has been accomplished at frequencies below 4 GHz while functions requiring higher resolution, such as airborne ground mapping, have been realized at frequencies up to and above 10 GHz. Radars at 35 GHz, which are technically in the longer millimeter region, are identified generally with the microwave portion of the spectrum. At frequencies above 35 GHz where the high resolution and large bandwidth capabilities of millimeter wave systems might be exploited, considerably less work has been done. Instead, effort has been concentrated in the infrared and visible portion of the spectrum. Table I which is based on considerations stated earlier, lists some of the tradeoffs that must be considered in selecting a radar's operating frequency. As indicated in this chart both optical and microwave radar systems offer certain performance features superior to that promised by millimeter systems. For example, a microwave system is clearly better for a large volume search while an optical system in clear weather is better for an imaging radar. Thus, to find considerable and important applications, the millimeter systems must either complement microwave or optical systems or exhibit a combination of features which make them more effective than their microwave or optical counterparts. Several examples are given below.

TABLE I
RADAR SYSTEM COMPARISONS

RADAR CHARACTERISTIC	MICROWAVE	MILLIMETER WAVE	OPTICAL
TRACKING ACCURACY	✓	✓✓	✓✓✓
CLASSIFICATION/IDENTIFICATION	✓	✓✓	✓✓✓
COVERTNESS	✓	✓✓	✓✓✓
VOLUME SEARCH	✓✓✓	✓✓	✓
ADVERSE WEATHER PERFORMANCE	✓✓✓	✓✓	✓
PERFORMANCE IN SMOKE	✓✓✓	✓✓✓	✓

✓ POOR
✓✓ INTERMEDIATE
✓✓✓ GOOD

3.1 Millimeter Wave Radar Systems to Augment or Replace Optical Systems

The era of precision weapons has materialized with the invention of the lasers and its utilization with "smart" bombs. However, the poor performance of optical systems using lasers or FLIR's in a fog or smoke environment make millimeter systems attractive for this application either as a replacement for or as a complement to present optical systems. Other areas where lasers and IR systems may be replaced include:

- Target Designators
- Beam Riders
- Range Finders
- Passive Seekers
- Detection and Classification
- Imaging

All these applications have the common requirements that the range is relatively short, 1-5 km and the beamwidth is not prohibitively small, 1-10 milliradians.

Short range target detection, identification and classification in a smoke or fog environment both on land and at sea is an important application for millimeter imaging radars. For such a radar an antenna aperture of approximately 10 square meters is required. While such an antenna is too large to mount on a vehicle such as a tank, such a system could be mounted on an auxiliary vehicle. Received data would then be transmitted to other vehicles within the immediate area. With antennas of one meter diameter or smaller, ground vehicles may still be detected and tracked with millimeter waves. Classification of such vehicles may be possible by analysis of the radar returns including the glint characteristics.

Imaging with smaller antenna apertures is possible on moving objects such as RPV's by employing synthetic aperture techniques. Optimum center frequencies for such systems--94 GHz, 140 GHz or 220 GHz--must be determined from tradeoff studies which consider resolution vs. atmospheric attenuation and available power.

3.2 Millimeter Radar Systems to Augment or Replace Microwave Radar Systems

One important application for millimeter shipboard search and track radars is for the detection and tracking of low altitude cruise missiles. It is well known that when a radar tracks targets at elevation angles of the order of an antenna beamwidth or less, the ground reflections produce signals that can cause erroneous measurements of elevation angle resulting in poor tracking. Thus, there is need for the narrow-beam millimeter system. The millimeter system of short to intermediate range can be used to augment other shipboard radars. Recent developments of gyratron tubes (GODLOVE, T.F., GRANATSTEIN, V.L., 1977) give promise of providing suitable power sources at 35 and 94 GHz. This function can be accomplished, also, with an optical system. However, the all-weather capability of the millimeter wave system makes it the logical choice.

Another potentially important application for millimeter wave systems is the LPI radar mentioned previously. Microwave systems utilize frequency hopping and/or matched filtering to achieve security. Millimeter wave systems gain from their narrower beams and also could take advantage of the 60 GHz oxygen absorption line. Such systems could vary their frequency to adjust for weather conditions. The maximum absorption offered at 60 GHz would limit the range of such radars but minimize the danger of detection at distances larger than the operating range.

Other possible microwave-replacement applications include terrain following/terrain avoidance and fire control. The main advantage millimeter wavelengths offer in the former application is their greater security due to the smaller beamwidth and the greater atmospheric attenuation. Millimeter fire control radars would benefit from the increased angular, range and/or doppler resolution.

In still other millimeter radar applications the size and weight reduction of millimeter wave systems vs. their microwave counterpart is the most important feature. Examples are:

- High resolution radars for mini-RPV's and satellites
- Active fuses
- Active missile seekers
- Hand held radars

4.0 COMMUNICATIONS APPLICATIONS

Over the past several years there has been much discussion of the faults and virtues of millimeter wavelength communication links. (SKOLNIK, M.I., 1970) The broad bandwidth capabilities lead to large channel capacity; however, adverse weather conditions can lead to poorer performance than microwave links. In some commercial applications closed waveguide systems can be used. Such systems use the TE_{01} circular waveguide. Here the waveguide may be filled with gas and avoid the irregularities of propagation experienced within the earth's atmosphere. Closed systems appear to have limited military applications, however.

An area of greater potential utilization for military applications is low probability of intercept (LPI) communication links. (VIGNALI, J.A., 1970) As in the case of LPI radar, an LPI communication link would use a narrow beam antenna at frequencies near 60 GHz where the atmospheric attenuation limits the range of detectability. Above the earth's atmosphere a 60 GHz satellite-satellite link can operate with little attenuation. Such systems would be protected from detection or interference from the earth's surface. The other two areas of LPI communication links are for short range (1-5 kw) ship-to-ship communication and for battlefield communications. In these applications the ability of millimeter waves to penetrate fog or smoke is an essential feature. For battlefield applications where large numbers of terminals might be used by individual foot soldiers the terminals must be quite small and lightweight and offer low cost.

5.0 ELECTRONIC COUNTERMEASURE (ECM) APPLICATIONS

As millimeter wavelength radar and communication systems are developed to augment or replace optical and microwave systems, it becomes necessary to develop electronic countermeasures. Before countermeasures can be utilized, the unfriendly millimeter wavelength signal must be located and identified. Thus a first priority in ECM equipment is in surveillance receivers. Such receivers must exhibit good noise characteristics and must cover the various windows between 35 and 300 GHz. An additional band near 60 GHz is required for intercepting LPI radar and communications signals.

In addition to surveillance receivers, the ECM community needs broadband power sources to provide jamming power to defeat the potential threats. Such power must come from conventional microwave tubes or from new tubes using relativistic electron-beams such as the gyratron.

6.0 COMPONENT RESEARCH AND DEVELOPMENT NEEDS

In order to realize new millimeter wavelength radar, communication and ECM systems, substantial military support at the component or technology level is required. Areas requiring particular attention are listed in Table II.

TABLE II
COMPONENT R&D AREAS

SOURCES

(a) High Power

- Conventional Tubes
- Conventional Tubes with New Slow Wave Structures
- New Relativistic Beam Power Tubes Such as Gyratron Broadbanding

(b) Medium and Low Power

- IMPATT Power Combining
- High Frequency Operation

CIRCUITS

- Waveguide Broadbanding
- Integrated Circuits
- Quasi-Optical Techniques

SOLID STATE COMPONENTS

- Low Noise Mixers
- Phase Shifters
- JJ Detectors

This table is broken down into three categories--sources, circuits, and solid state components. Some comments on each of these areas follow.

6.1 Sources

High power in the millimeter wave region as in the microwave region is obtained from vacuum tubes. Certain types of tubes (coupled cavity tubes) have provided 100-200 watts of cw power at frequencies in the 30-94 GHz range. However, such tubes are expensive to fabricate and require the use of extremely high tolerance parts. Along with the continued development of conventional tubes, new approaches to forming slow wave structures for millimeter tubes need be investigated.

Applications such as shipboard low angle tracking radar require considerable power. New tubes using relativistic electron beams such as the gyratron promise to provide tens to hundreds of kilowatts of power at frequencies up to 300 GHz. (GODLOVE, T.F., GRANATSTEIN, V.L., 1977) Further work on such tubes is required to bring the technology to the point where they are deployable in systems. Broadbanding studies in particular need to be pursued to address EW and LPI system requirements.

For many millimeter wave military applications the high power capabilities of the tubes will not be required and solid state sources will be adequate. For short range imaging systems, missile seekers and target designators, typical power requirements are 1-10 watts. In excess of 1 watt cw power has been obtained at 94 GHz (STROM, L.D., 1977) by the use of power combining. Recently IMPATT diode oscillators have been reported that offer a cw power output of 50 mW at 202 GHz. (ISHIBASHI, T., OHMARI,M., 1976) Achieving high power with solid state diodes, especially at the lower millimeter wavelengths, is a high priority requirement

6.2 Circuits

In the circuits area, work is needed to improve the bandwidth capabilities of standard waveguide components such as couplers and magic tees. Component development in integrated circuit format is needed also for both cost and size reduction for anticipated high volume applications such as missile seekers and target designators. Several types of transmission lines are needed to be compatible with the various component configurations which may be employed throughout the millimeter wave spectrum. Conventional microstrip approaches are not attractive for frequencies of 94 GHz and higher and work is being concentrated on other formats, such as dielectric waveguide and suspended microstrip. Quasi-optical techniques appear to be useful for the higher millimeter frequencies. (GUSTINCIC, J.J., 1977)

6.3 Solid State Components

A common requirement for all military millimeter wave systems is the need for a high performance receiver. GaAs Schottky barrier diodes have been the most successful at millimeter wavelengths to date with a 5 dB noise figure reported for a 95 GHz sub-harmonically pumped mixer. (SCHNEIDER, M.V., CARLSON, E.R., 1977) Again, further work is needed to realize low cost, ruggedized receivers suitable for military applications. Additional emphasis on wideband versions is required also.

For extremely low noise operation cryogenic receiver technology is being studied. For example, a mixer employing a Josephson Junction as the nonlinear element exhibited a 55^{o}K noise temperature at 36 GHz. (TAUR, Y., CLAUSSEN, J.H., RICHARDS, P.L., 1974) These devices are likely to be competitive with Schottky barrier devices at the lower millimeter wavelengths; however, significant utilization in military applications is at least 5 to 10 years away because of the devices present limitations in dynamic range and the need for improved planar (non-point-contact) versions. Improved closed cycle refrigerator technology is also essential.

Electronically steerable beams at 94 GHz and higher frequencies are not currently practical because of limitations in control components. Innovative approaches are needed in phase shifters and modulators to overcome the severe cost and fabrication problems at these frequencies. Similar limitations exist for other commonly used solid state components, e.g., circulators, isolators, switches. Again realization of broadband components is an area which needs particular attention.

7.0 CONCLUSIONS

At this point in time, millimeter waves have found only limited use in military systems. This is true since most system needs could adequately be met with better developed microwave and optical systems. This paper has focussed on a range of applications where millimeter waves exhibit a combination of features which make their use attractive compared to other systems. It is felt that millimeter waves will find military application in many of the areas described in this paper. It is difficult at this time to predict which areas of application will be the most important. However, the increasing emphasis on high resolution, small size, high information capability and all weather performance points toward an important role for millimeter waves in future systems.

REFERENCES

GODLOVE, T.F., GRANATSTEIN, V.L., 1977, "Relativistic electron beam interactions for generation of high power at microwave frequencies," 1977 IEEE MTT-S International Microwave Symposium Digest, p.69.

GUSTINCIC, J.J., 1977, "A quasi-optical receiver design," 1977 IEEE MTT-S International Microwave Symposium Digest, p.99.

ISHIBASHI, T., OHMORI, M., 1976, "200 GHz 50 mw cw oscillators with silicon IMPATT diodes," IEEE Trans. Micro.Theory Tech., Vol.MTT-24, p.85.

JOHNSON, S.L., 1977, "Millimeter radar," Microwave Journal, Vol.20, p.18.

RAINWATER, J.H., 1977, "Weather affects mm-wave missile guidance systems," Microwaves, Vol.16, p.62.

SCHNEIDER, M.V., CARLSON, E.R., 1977, "Notch-front diodes for millimetre-wave integrated circuits," Electronics Letters; Vol.24, p.745.

SKOLNIK, M.I., 1970, "Millimeter and submillimeter wave applications," Proc.Symp.on Submillimeter waves," Polytechnic Press of Poly.Inst.of Brooklyn, NY, p.9.

STROM, L.D., 1977, "The unresolved problems and issues," (U), Proc.of Sixth DARPA/Tri-Service Millimeter Wave Conference, p.10 (SECRET).

TAUR, Y., CLAUSSEN, J.H., RICHARDS, P.L., 1974, "Josephson junctions as heterodyne detectors," IEEE Trans.on Micro.Theory Tech., Vol.MTT-22, p.1005.

TOMIYASU, K., 1978, "Tutorial review of synthetic-aperture radar (SAR) with applications to imaging of the ocean surface," Proc.of IEEE, Vol.66, p.563.

VIGNALI, J.A., 1970, "Millimeter waves and Naval airborne communications," NRL Report 7165.

WEISBERG, L.R., 1977, "Millimeter waves--the coming of age," (U), Proc.of Sixth DARPA/Tri-Service Millimeter Wave Conference, p.4 (SECRET).

DISCUSSION

R.P.Moore, US

What are the assumptions underlying the requirements for resolution required for tracking and target identification and did they take into account other signal characteristics that can be used for identification such as spectral content and thus reduce required resolution and thus antenna diameter required by several fold? Optical resolution criteria applied to mm-wave systems often lead to erroneous conclusions concerning system feasibility, and effectiveness also. Have the requirements taken into account doppler beam sharpness and other techniques used at lower frequencies to obtain better resolution?

Author's Reply

This paper is general in nature. The resolution requirements listed were based on the equation $\Omega = 1.2\lambda/D$. It is true that based on signal return characteristics somewhat smaller antenna sizes may be utilized. The characteristics of specific targets were not given. As indicated

$\Omega = 10^{-2}$ to 10^{-3} radians for beam riders and tracking radars.

$\Omega = 10^{-4}$ to 10^{-3} radians for target identification and classification.

Specific returns from targets would allow for the larger Ω and thus the smaller antenna, doppler information, glint, and other specific target returns may be utilized.

ENVIRONMENTAL EFFECTS ON MILLIMETER RADAR PERFORMANCE

by

F. B. Dyer and N. C. Currie

Radar and Instrumentation Laboratory
Engineering Experiment Station
Georgia Institute of Technology
Atlanta, Georgia 30332 USA

SUMMARY

This paper explores the effects of clutter and non-ideal atmospheric conditions on the performance of millimeter radar systems. A series of investigations of radar returns from land, sea, rain, and snow have been performed over the past several years which were designed to define the potential utility of millimeter waves to selected system applications. The data and supporting analyses include results for all of the commonly used radar operating frequencies between 9.5 GHz and 95 GHz. Average values were measured to develop frequency dependencies, and considerations were made of those factors such as polarization, amplitude distributions, and spectra which significantly impact the application of modern signal processing techniques to millimeter radar.

1. INTRODUCTION

The objective of any measurement program lies in the application of data to some real-world problem; the key to this aspect of the program lies in the analysis and presentation of results. Results might include presentation of such average quantities such as radar cross-section, radar cross-section per unit area, and attenuation coefficient. These parameters can be coupled with meteorological, temporal, or environmental parameters in the final presentations of results. Fluctuation characteristics such as amplitude distributions, frequency spectra, or correlation functions are also important for many applications; however, considerable care is needed in the interpretation of such data. Finally, there are data which are related to specific signal processing techniques, such as special polarization or frequency processing, which will require their own specific presentations.

2. ENVIRONMENTAL PARAMETERS AFFECTING MILLIMETER RADAR PERFORMANCE

Millimeter radar performance is affected by the environment in a number of ways including attenuation and backscatter from the atmosphere, backscatter from the background such as sea or land clutter, and attenuation due to natural cover such as snow or foliage.

2.1 Atmospheric Effects

Millimeter waves propagating through the atmosphere are affected by their interaction with atmospheric gases, particulate matter, and hydrometeors. These interactions occur through three primary mechanisms: absorption, scattering, and refraction. The effects of these interaction mechanisms on millimeter waves are summarized in Table I.

Absorption and scattering are the result of direct interaction between the millimeter waves and the atmosphere (gases, particulate matter, hydrometeors). The primary gases that affect millimeter waves are water vapor and oxygen. Gaseous absorption varies with millimeter wave frequency, atmospheric pressure, temperature, and absolute humidity.

The primary particulate matters that effect millimeter waves are dust, smog, and smoke particles. Because these particles have dielectric constants much smaller than the dielectric constant of water droplets, their attenuation cross section is small. Thus particulate matter has a negligible effect on millimeter waves.

The primary hydrometeors that affect millimeter waves are rain, cloud droplets, hail, fog, and snow. Of these, rain has the most significant effect. Suspended water droplets and rain cause absorption of millimeter waves that exceeds that caused by the combination of water vapor and oxygen (gaseous absorption in the non-resonant frequency region). Rain absorption is a function of rain rate, drop size, drop size distribution, temperature, frequency, and path length. Cloud droplets and fog attenuate millimeter waves in the same manner as rain, but the amount of attenuation is generally much less than that due to rain. Dry snow produces very small attenuation except at very heavy snow-fall rates.

In a clear, non-precipitating atmosphere, gaseous water vapor and oxygen are the major absorbers of millimeter waves. The attenuation functional dependencies are determined by the atmospheric parameters of temperature and pressure. In the atmosphere, the values of these parameters will depend on altitude and prevailing weather conditions. For oxygen, the pressure parameter depends not only on altitude, but also on the humidity at the altitude being considered. Figure 1 illustrates typical millimeter wave attenuation characteristics due to the combination of oxygen and water vapor for representative relative humidity values at standard sea level altitude.

In a precipitating atmosphere, liquid water is the major absorber of millimeter waves. A precipitating atmosphere comprises rain, fog, snow, and hail. Of these, rain has the most significant effect on millimeter waves. Over the past 30 years, many people working in both radar and meteorology have made calculations attempting to model rain and determine the properties of electromagnetic absorption and scattering by raindrops. Adjustments have been made in the models employed to account for such parameters as drop shape; the dielectric constant, which is a function of temperature and frequency; frequency of incident power; type of rain (drop size distributions; type and location of rain, such as thunderstorms, frontal systems, maritime or orographic environment); and polarization of incident power. One result of these investigations is a general relationship between the rain rate and the absorption and scattering properties. The usual presentation shows both the radar cross-section and attenuation to increase as the rain rate increases.

Absorption of millimeter waves by water droplets is proportional to the size of the droplets. The absorption cross-section of a water droplet is generally expressed as follows:

$$q_a = \frac{\lambda^2}{\pi} \beta^3 \, \mathrm{Im}\left(-\frac{m^2-1}{m^2+2}\right) \qquad (1)$$

where; $\beta = 2\pi r/\lambda$

λ = wavelength of the millimeter wave

r = radius of the droplet

m = complex index of refraction of water

Im ( ) = imaginary part of ( )

Equation 1 is valid to within 0.5 dB for droplets having a radius less than 0.06 times the wavelength (i.e., 0.49 mm for 35 GHz and 0.18 mm for 95 GHz). Droplets having a radius less than 0.1 mm are considered non-precipitating, and their absorption cross-section is more than 10 times their scattering cross-section at these frequencies. The absorption of millimeter waves by rain in a particular storm, therefore, depends on the nature of the storm itself and consequently on how the rainfall rates and drop sizes are distributed.

Extensive data (CURRIE, N. C., DYER, F. B. and HAYES, R. D., 1975; GODARD, S. L., 1970; SEMPLAK, R. A. and TURRIN, R. H., 1969; IPPOLITO, L. J., 1970; KERR, E., ed., 1951; RICHARD, V. W., 1976) have been generated concerning rain attenuation of millimeter waves and radar performance in rain. In general, a one way attenuation of 1 dB km^{-1} would reduce the radar range of a system from 10 nautical miles in clear air to approximately 5.4 nautical miles (LO, L. T., FANNIN, B. M. and STRAITON, A. W., 1975). Typical values of rain attenuation range from 4 dB km^{-1} at 35 GHz and 9.1 dB km^{-1} at 95 GHz for a 16 mm hr^{-1} (heavy) rainfall to 0.24 dB km^{-1} at 35 GHz and 0.95 dB km^{-1} at 95 GHz for 1 mm hr^{-1} (very light) rainfall (RICHARD, V. W. and KAMMERER, J. E., 1975).

Typical values of fog attenuation at 35 and 95 GHz, respectively, range from 0.11 and 0.47 dB km^{-1} at 0°C to 0.034 and 0.22 dB km^{-1} at 40°C for a fog with 0.1 gm m^{-3} liquid water (150 - 250 m optical visibility (LO, L. T., FANNIN, B. M. and STRAITON, A. W., 1975).

Attenuation in the millimeter windows by clouds of various types has been thoroughly treated by Lo et al (ALTSHULER, E. E. and EBEOGLU, D. B., 1976). They report average attenuation of 0.18 and 0.61 dB in stratocumulus and 0.2 and 0.34 dB in cumulus at 35 and 95 GHz, respectively.

Limited calculations and measurements of attenuation in falling snow indicate that attenuation by dry snow is much less than that of rain having an equivalent water content, except at the shortest wavelengths in the millimeter region. Attenuation by wet snow is more significant, particularly in the melting region, where water-coated snowflakes yield backscattering 5 to 10 dB greater than that of the rain below. Backscatter measurements by McCormick and Hendry (MCCORMICK, G. C. and HENDRY, A., 1975) indicate that the radar "bright band" at the melting level may be less distinct at 16.5 GHz than at lower microwave frequencies. The absorption and backscatter characteristics of the melting level have not been documented at higher frequencies. Absorption and scattering when hail is present is comparable to or larger than that due to rain alone. The magnitude depends strongly on the sizes and shapes of the hailstones and on the presence and thickness of a water coating.

Particulate matter in the atmosphere has little effect on millimeter waves. Dust, smog, and smoke particles have dielectric constants that are small compared to that of water droplets, hence they have negligible effect on millimeter-wave propagation. Ice crystals in clouds cause attenuation particularly near the melting level; however, few data have been reported.

Atmospheric scattering is associated with atmospheric absorption; both are caused by the interaction of electromagnetic waves with atmospheric matter (i.e., gases, hydrometeors, and particulate matter. Scattering and absorption both cause attenuation of an incident electromagnetic wave, but the mechanisms differ. Absorption is a quantum effect, but scattering can be explained in terms of the wave energy loss due to scattering is a function of wavelength and particle size.

Calculations on the backscattered radiation from fog and clouds reveal that the energy returned to the receiver as noise is more than two orders of magnitude smaller than from rain (LO, L. T., FANNIN, B. M. and STRAITON, A. W., 1975; LUKES, G. D., 1968). Hence, backscatter range reduction from fog and clouds can be ignored.

A study was conducted by EES and the Ballistic Research Laboratories, Aberdeen, Maryland to measure millimeter rain backscatter (CURRIE, N. C., DYER, F. B. and HAYES, R. D., 1975; RICHARD, V. W. and KAMMERER, J. E., 1975). Simultaneous measurements were made of rain backscatter at 10, 35, 70 and 95 GHz for vertical and circular polarizations. The basic results are indicated in Tables 2 and 3. As can be seen from the Tables, the polarization of the incident wave is important in terms of the degree of backscatter due to the differential scattering by nonspherical rain drops. The circularly polarized signals were seen to be 10 to 15 dB lower in backscatter magnitude as was the rain rate. In fact, variations of ± 5 dB were obtained in the data when plotted as a function of rain rate without considering drop size.

2.2 Background Effects

Radar performance can be limited by interference from the background near a target of interest in addition to atmospheric effects. The interfering area can include snow-covered ground, trees, grassy fields, and the sea surface. Measurements have been performed by EES to characterize the reflectivity of these types of background over the last several years and the results are summarized in Tables 2 through 5 (DYER, F. B., CURRIE, N. C. and APPLEGATE, M. S., 1977). Tables 2 and 3 give average values of σ° for land and sea backscatter respectively while Tables 4 and 5 give standard deviations for the land and sea data assuming log-normal distributions. (Clutter is generally log-normal for the small antenna spot sizes encountered at millimeter waves.) Table 4 shows that the average reflectivity (σ°) of trees, grass, and snow increases with decreasing wavelength and increasing depression angle. It also shows that crusted snow (that is, snow which has melted and refrozen) gives the highest return of the three types of clutter listed in the table at 8.6 mm and below while at longer wavelengths (3.2 cm) dry trees have the highest reflectivity. Table 5 shows that the trend of increasing reflectivity with decreasing wavelength also holds for sea clutter although the effect is not nearly as pronounced as for land clutter, and for higher sea states the reflectivity at 3 mm wavelength is less than that at 3 cm wavelength. The values for σ° do correlate strongly with wave height and to a lesser degree with wind speed. Tables 6 and 7 give typical values of standard deviations for various types of clutter. Briefly, for land clutter, the standard deviation increases with decreasing wavelength. For sea clutter, the standard deviation decreases with decreasing wavelength.

2.3 Ground-Cover Attenuation

In addition to backscattering energy which interferes with detection of a target, certain types of ground cover such as foliage or snow can attenuate millimeter wave energy so that a target is masked by this cover. Measurement programs were conducted to measure the attenuation properties of foliage and snow at millimeter wavelengths and the results are summarized in Tables 8 and 9. (CURRIE, N. C., DYER, F. B. and EWELL, G. W., 1976; CURRIE, N. C., DYER, F. B. AND MARTIN, E. E., 1976; CURRIE, N. C. AND MORTON, T. M., 1977). As can be seen from the figures, very little penetration would be achieved through either foliated trees or through snow at 35 GHz and above.

3. CLUTTER EFFECTS ON SYSTEM PARAMETER CHOICE

The ultimate weight and size of a radar will depend very strongly on the frequency of operation, as both component size and power consumption vary inversely with frequency (for a given upper bound of performance). The choice of operating frequency depends on a number of factors, including allowable antenna aperture, maximum range, weather performance, anticipated target-to-clutter ratios, and the anticipated processing gains which may be obtained with that choice. The key factor in system sizing considered here is the behavior of the target-to-clutter ratio as a function of frequency.

Although a limited quantity of comparative data is available in the literature on the cross-section of various man-made targets (HAYES, R. D. and DYER, F. B., 1973)a number of independent investigations have been made by EES of target returns at the various frequencies of interest here. The general tendency seen in such data is for the effective cross-sections of vehicles, buildings, and personnel to be approximately independent of frequency above 9 GHz. The assumption used below is that target cross-section is not frequency dependent.

Normally the initial question to be answered in any system study is the effect of frequency scaling on maximum detection range. The overall consideration includes, of course, any physical constraints of the platform, application, etc. It is necessary to establish an acceptable set of ground rules for such a comparison; however, the detailed treatment of such a comparison is beyond the scope of this paper. General considerations for guiding the comparison of frequency effects of system parameters can be found in several radar handbooks (SKOLNIK, M. I. (ed.) 1970; NATHANSON, E. E., 1969). Given a knowledge of available transmitter power, receiver noise figure, and losses as a function of frequency it is possible to make order-of-magnitude performance comparisons which will bound the anticipated system capability.

The frequency dependence of clutter on radar system performance can be illustrated by defining three radar systems differing only in frequency as shown by Table 10. Figures 2 through 4 show the equivalent average signal-to-clutter ratios as functions of range for land clutter, sea clutter, and rain clutter assuming a +10 dBsm constant target, a -10 dBsm constant target, and a 0 dBsm constant target respectively. (These target sizes are typical of those which would be encountered for each type of environment.) The target-to-clutter ratios indicated are independent of transmitted power (assuming that the signals are not in the noise) and are dependent only on aperture size, frequency, pulse length and reflectivity of the clutter (σ or η).

The problem of radar detection in clutter is further complicated by the statistical nature of the returns from targets and clutter. Investigations described in References HAYES, R. D. and DYER, F. B., 1973; DYER, F. B., GARY, M. J. and EWELL, G. W., 1974; HAYES, R. D., DYER, F. B. and CURRIE, N. C., 1976; and CURRIE, N. C., DYER, F. B. and HAYES, R. D., 1975 suggest that often experimental amplitude distributions behave as log-normal distributions with large standard deviation. Example sets of Receiver Operating Characteristic curves are shown in Figures 5 and 6. While these figures are idealized they serve to illustrate the impact on the detection problem which results when the extension is made from a non-fluctuating target in receiver (Rayleigh) noise to the case of log-normally distributed clutter and targets.

For example, consider the difference in performance due only to the clutter background which is implied in the comparison of Figures 5 and 6. For a false alarm rate of 10^{-6}, the required signal-to-background clutter is similar to those discussed above. Figure 6 also illustrates the greatly reduced possibility of achieving very high probabilities of detection when returns from both target and background are log-normally distributed. If a probability of detection of 80% is required with a false-alarm probability of 10^{-6}, a clutter background of trees (for example), and a moderately fluctuating target, then a target cross section of 20 dBsm or more will be required for the example radars illustrated in Table 10.

4. CONCLUSIONS AND RECOMMENDATIONS

It should be concluded from these discussions that operation in the millimeter wave region offers a number of potential advantages, principally small size and weight, but at the same time, systems analysis is complicated by the relatively small and inconsistent data base which exists for systems operating at these frequencies. This is in spite of the systematic efforts of a number of investigators.

A few comprehensive surveys of available data on reflectivity at millimeter wavelengths have appeared--for example, HAYES, R. D. and DYER, F. B., 1973. In addition, some additional data appear in SKOLNIK, M. I. (ed.), 1970; NATHANSON, E. E., 1969; and LONG, M. W., 1975. Unfortunately, examination of these data indicates that the amount of variety of data decreases strongly as frequency increases above 10 GHz.

Much of the data available at frequencies above 10 GHz suffers from being taken under widely varying conditions, using systems having widely varying parameters, thus making meaningful comparisons of the results difficult. Perhaps the most obvious deficiencies in the data involve the lack of measurements taken using coherent systems or short pulse (less than 20 ns) systems, and the lack of exploration of polarization and frequency as variable parameters. Much of the data which are available are presented as averaged, highly processed information; considerably more useful are more "dynamic" or less processed information such as amplitude distributions, power density spectra, or temporal correlation functions.

The data base for ground clutter needs to be expanded to include: trees at grazing incidence, tree lines and fields, roads, buildings, rivers, and lakes. Some significant variable parameters will include the amount of surface water, wind speed, foliage content, bistatic angle (where appropriate), and specific geometries of the target and the antenna axis.

Similarly, the atmospheric propagation path requires additional data to fully describe backscatter, attenuation, and refraction for paths containing fog, clouds, snow, rain, and ice. Some of the more important parameters for these measurements will include characterization over the entire path length of relative (or absolute) humidity, drop-size distribution, water content, and location of water (i.e., whether water coated ice, ice in fog or ice in cloud).

In particular, recent rain attenuation and backscatter measurements have pointed out the need to attempt simultaneous measurements at 70, 95, 140 and 230 GHz in order to resolve some serious modeling questions, particularly the Mie scattering problem. Of particular interest during these measurements would be detailed characterization of drop-size distributions, dielectric properties of the individual drops, and relative humidity--all throughout the transmission path.

The problem of target characterization, particularly of motorized vehicles, is as significant, and no less difficult, as the problem of characterizing the environment. Particularly for the active radar case, the geometrical sensitivity of the backscattering from the target makes a three-dimensional description of the reflectivity desirable. The influence of surface coatings such as snow, ice, or water on the target return requires detailed attention to the dielectric properties of the coating, surface roughness, and possible influence on specular reflection properties. Possibly the exploitation of polarization or frequency properties of reflectivity would prove useful; however, no valid data base exists in the millimeter region. Bistatic behavior of targets and clutter is also a matter which should receive attention since little or no definitive work has been done on this aspect of the reflectivity problem, especially at the millimeter wavelengths.

5. REFERENCES

ALTSHULER, E. E. and EBEOGLU, D. B., 1976, "Second DoD Workshop on Millimeter Wave Terminal Guidance Systems (Adverse Weather Effects)," RADC-TR-76-9, Rome Air Development Center, Griffiss AFB, New York.

CURRIE, N. C., DYER, F. B. and EWELL, G. W., October 1976, "Characteristics of Snow at Millimeter Wavelengths," Proceedings of the IEEE AP-S International Symposium, Amherst, Massachusetts. 13.

CURRIE, N. C., DYER, F. B. and HAYES, R. D., 1975, "Analysis of Radar Rain Return at Frequencies of 9.375, 35, 70 and 95 GHz," Final Technical Report on Contract DAAA25-73-C-0256, Georgia Institute of Technology, February, AD A007254.

CURRIE, N. C., DYER, F. B. and HAYES, R. D., 1975,"Some Properties of Radar Return at 9.375, 35, 70 and 95 GHz," IEEE International Radar Conference, Arlington, Virginia.

CURRIE, N. C., DYER, F. B. and MARTIN, E. E.,October 1976, "Millimeter Foliage Penetration Measurements," Proceedings of the IEEE AP-S International Symposium, Amherst, Massachusetts.

CURRIE, N. C. and MORTON, T. M. January 1977, "Comparison of Winter/Summer Microwave Foliage Penetration Measurements," Engineering Experiment Station, Georgia Institute of Technology, Atlanta, Georgia, Final Report on Task 2 of MIT/LL P. O. No. CK-1069.

DYER, F. B., CURRIE, N. C. and APPLEGATE, M. S., October 1977, "Radar Backscatter From Land, Sea, Rain, and Snow at Millimeter Wavelengths," Digest of the 1977 IEEE International Radar Conference, London, England.

DYER, F. B., GARY, M. J. and EWELL, G. W., 1974, "Radar Sea Clutter at 9.5, 16.5, 35, and 95 GHz," IEEE AP-S International Symposium, Atlanta, Georgia.

GODARD, S. L., July 1970, "Propagation of Centimeter and Millimeter Wavelengths Through Precipitation," IEEE Transactions on Antennas and Propagation, Vol. AP-18, No. 4.

HAYES, R. D. and DYER, F. B., 1973, "Land Clutter Characteristics for Computer Modeling of Fire Control Radar Systems," Engineering Experiment Station, Georgia Institute of Technolougy, Atlanta, Georgia, Technical Report No. 1 on Contract DAAA 25-73-C-0256.

HAYES, R. D., DYER, F. B. and CURRIE, N. C., 1976, "Backscatter From Ground Vegetation at Frequencies Between 10 GHz and 100 GHz," IEEE AP-S International Syposium, Amherst, Massachusetts.

IPPOLITO, L. J., July 1970, "Millimeter Wave Propagation Measurements from the Applications Technology Satellite (ATS-V)," IEEE Transactions on Antennas and Propagation, Vol. AP-18, No. 4.

KERR, P. E., (ed.) Propagation of Short Radio Waves, MIT Radiation Lab Series, 13, New York: McGraw-Hill, 1951.

LO, L. T., FANNIN, B. M. and STRAITON, A. W., November 1975, "Attenuation of 8.6 and 3.2 mm Radio Waves by Clouds," IEEE Transactions on Antennas and Propagation, Vol. AP-23, No. 6.

LONG, M. W., 1975, Radar Reflectivity of Land and Sea, D. C. Heath and Company, Lexington, Massachusetts.

LUKES, G. D., May 1968, "Penetrability of Haze, Fog, Clouds and Precipitation by Radiant Energy Over the Spectral Range 0.1 Micron to 10 Centimeters," The Cneter for Naval Analyses, Study No. 61.

MCCORMICK, G. C. and HENDRY, A. 1975, "Principles for the Radar Determination of the Polarization Properties of Precipitation," Radio Science, Vol. 10, pp. 421 - 434.

NATHANSON, F. E., 1969, Radar Design Principles, McGraw-Hill Book Co., New York.

RICHARD, V. W., June 1976, "Millimeter Wave Radar Applications to Weapons Systems," Ballistic Research Laboratories, Memorandum Report No. 2631.

RICHARD, V. W. and KAMMERER, J. E., October 1975, "Rain Backscatter Measurements and Theory at Millimeter Wavelengths," BRL Report No. 1838, AD B008173L.

SEMPLAK, R. A. and TURRIN, R. H., July-August 1969, "Some Measurements of Attenuation by Rainfall at 18.5 GHz," The Bell System Technical Journal, Vol. 48, Pt. 2.

SKOLNIK, M. I. (ed.), 1970, Radar Handbook, McGraw-Hill Book Co., New York.

TABLE 1. ATMOSPHERIC EFFECTS ON MILLIMETER-WAVES

	Atmospheric Absorption	Interaction Scattering	Mechanism Refraction
Attenuation	x	x	
Depolarization	x	x	
Backscatter		x	
Amplitude Scintillation	x	x	x
Phase Scintillation	x	x	x
Ducting			x

TABLE 2. SUMMARY OF AVERAGE RAIN ATTENUATION AND BACKSCATTER SHARACTERISTICS

Wavelength (mm)	Rain Rate (mm/hr)	Attenuation (dB/km)	Backscatter (m^2/m^3)
32*	1	0.01	1.3×10^{-8}
	5	0.05	2×10^{-7}
	10	0.13	6.2×10^{-7}
	20	0.30	2×10^{-6}
8.6*	1	0.27	1.0×10^{-6}
	5	1.33	1.9×10^{-5}
	10	2.64	6.4×10^{-5}
	20	5.22	2.0×10^{-4}
3.2*	1	1.60	1.5×10^{-5}
	5	4.48	9×10^{-5}
	10	6.98	1.9×10^{-4}
	20	10.88	4.0×10^{-4}
32**	1	0.01	1.1×10^{-9}
	5	0.05	9×10^{-9}
	10	0.13	5×10^{-8}
	20	0.30	1.6×10^{-7}
8.6**	1	0.27	3.5×10^{-8}
	5	1.33	8.5×10^{-7}
	10	2.64	3.5×10^{-6}
	20	5.22	1.3×10^{-5}
3.2**	1	1.60	2.2×10^{-6}
	5	4.48	1.3×10^{-5}
	10	6.98	2.7×10^{-5}
	20	10.88	6×10^{-6}

*Vertical polarization

**Circular polarization

TABLE 3 - TYPICAL STANDARD DEVIATION VALUES FOR RAIN RETURN EXPRESSED IN dB ASSUMING LOG NORMAL DISTRIBUTION

Wavelength (mm)	Rain Rate (mm/hr)	Standard Deviation (dB)	
		Vertical	Circular
32	5	7.5	8.0
	20	8.0	8.5
8.6	5	3.0	2.7
	20	3.2	2.5
3.2	5	3.2	3.0
	20	3.0	2.9

TABLE 4 - SUMMARY OF AVERAGE LAND CLUTTER REFLECTIVITY CHARACTERISTICS

Wavelength (mm)	Depression Angle Degrees	Radar Cross-Section per Unit Area (dB)				
		Wet Trees	Dry Trees	Dry Grass	Wet Snow	Crusted Snow
32	2	-	-32	-36	-45	-
8.6	2	-	-22	-28	-	-
3.2	2	-	-22	-	-	-
32	8	-	-28	-	-35	-
8.6	8	-	-22	-	-20	-10
3.2	8	-	-17	-	-	-
32	15	-	-	-	-30	-
8.6	15	-	-	-	-18	- 8
3.2	15	-	-	-	<-10	<-10
8.6	30	-15	-19	-	-	-
3.2	30	-11	- 8	-	-	-
8.6	45	-14	-18	-	-	-
3.2	45	- 7	- 5	-	-	-

TABLE 5 - SUMMARY OF AVERAGE SEA BACKSCATTER CHARACTERISTICS

Wavelength (mm)	Wave Height** (ft)	Wind Speed (mph)	Average Cross-Section per Unit Area (dB)	
			H	V
32	0.6	0	<-70.0	<-73.0
	1.0	0	-69.5	-60.2
	1.6	12	-47.0	-42.0
	3.7	11	-42.8	-36.5
8.6	0.6	0	-63.7	-59.8
	1.0	0	-41.8	-43.6
	1.6	12	-44.1	-37.3
	3.7	11	-	-
3.2	-	4	-38.0	-43.0
	-	7	-35.0	-43.0
	-	12	-35.0	-38.0

*Data were acquired at a 1.4° depression angle.

**Significant wave height.

TABLE 6 - TYPICAL STANDARD DEVIATION VALUES FOR LAND CLUTTER EXPRESSED IN dB ASSUMING LOG NORMAL DISTRIBUTIONS

Wavelength (mm)	Standard Deviation (dB)			
	Dry Trees	Dry Grass	Wet Snow	Crusted Snow
32	4.0	1.5	-	-
8.6	4.4	1.7	1.0	1.0
3.2	6.0	2.0	1.5	1.5

TABLE 7 - TYPICAL STANDARD DEVIATION VALUES FOR SEA CLUTTER EXPRESSED IN dB ASSUMING LOG NORMAL DISTRIBUTIONS

Wavelength (mm)	Wave Height* (ft)	Wind Speed (mph)	Standard Deviation (dB)	
			H	V
32	0.8	0	9.0	5.2
	1.6	12	7.7	4.4
	3.7	11	5.7	5.4
8.6	0.8	0	7.2	4.2
	1.6	12	5.7	4.3

*Significant wave height.

TABLE 8 - MEASURED DECIDUOUS FOLIAGE ATTENUATION FOR MILLIMETER WAVE ENERGY

Season	Frequency (GHz)	One-Way Attenuation α* (dB/m)
Summer	10	2.9
Winter	10	1.4
Summer	16	3.8
Winter	16	1.6
Summer	35	8.0
Summer	95	15.0

*Foliage depth was defined as the sum of the diameters of the branches in the path of the signal.

TABLE 9 - ONE-WAY SNOW ATTENUATION
FOR MILLIMETER WAVE ENERGY

Snow Condition	Frequency (GHz)	One-Way Attenuation α** (dB/m)
Wet	35	200
Dry	35	50
Wet	95	>300
Dry	95	250

**Dry snow was crusted; wet snow was packed into a snow bank.

TABLE 10. EXAMPLE SETS OF RADAR PARAMETERS

Frequency, f	9.4 GHz	35 GHz	94 GHz
Wavelength, λ	3.2 cm	8.6 mm	3.2 mm
Antenna Diameter	50 cm	50 cm	50 cm
Antenna Gain	27.4 dB	33.1 dB	37.4 dB
Beamwidth	4.1°	1.1°	0.4°
Transmitted Power	100 kW	60 kW	6 kW
Pulse Length	50 nsec	50 nsec	50 nsec
Noise Figure $\overline{NF}_o$	8 dB	8 dB	10 dB
Loss (T/R), L	2 dB	4 dB	6 dB
Polarization	HH	HH	HH
Beam Area (σ°)	0.379R	0.101R	0.037R
Beam Volume (η)	$0.23R^2$	$0.00167R^2$	$0.00022R^2$

R is the slant range.

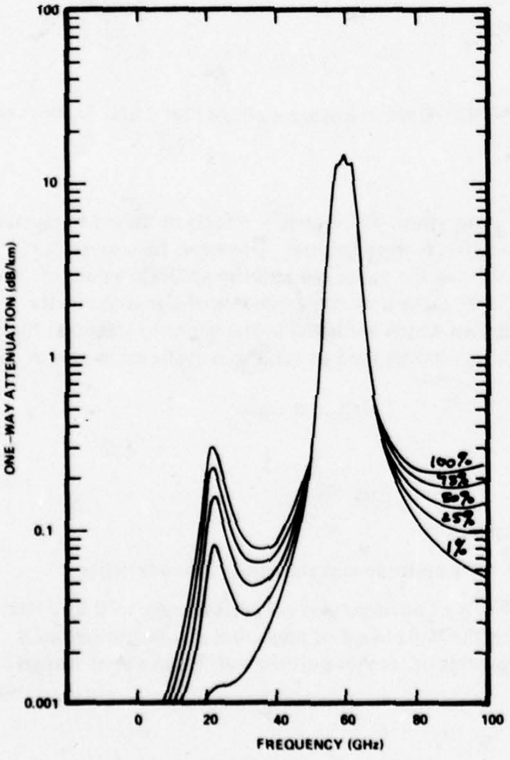

Figure 1. Total Atmospheric Attenuation Due to Both Water and Oxygen for Several Different Relative Humidities.

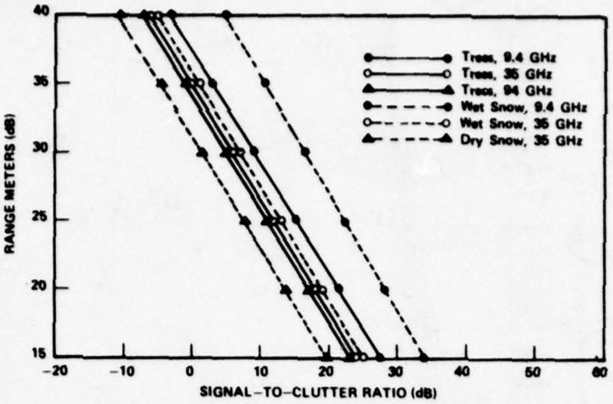

Figure 2. Signal-to-Clutter Ratio for Land Clutter Assuming a +10 dBsm Target.

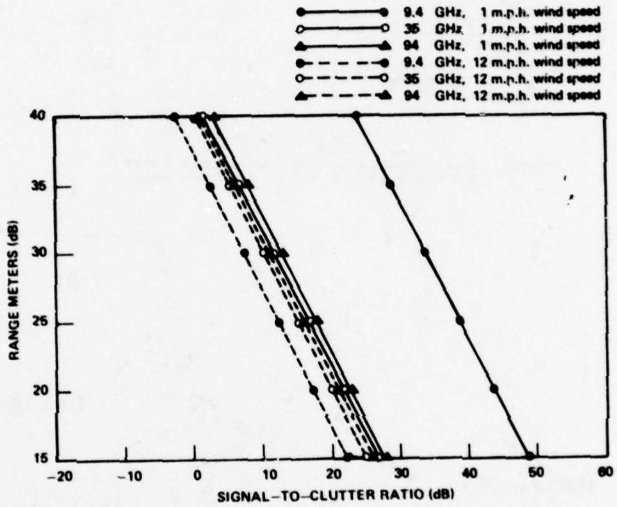

Figure 3. Signal-to-Clutter Ratio for Sea Clutter Assuming a -10 dBsm Target.

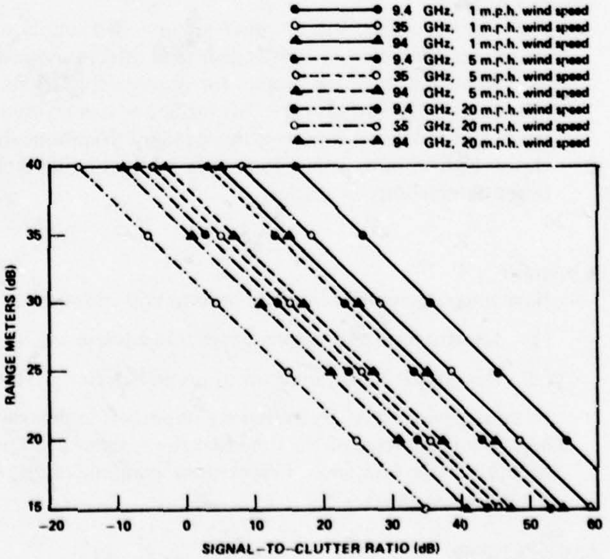

Figure 4. Signal-to-Clutter Ratio for Rain Assuming a 0 dBsm Target.

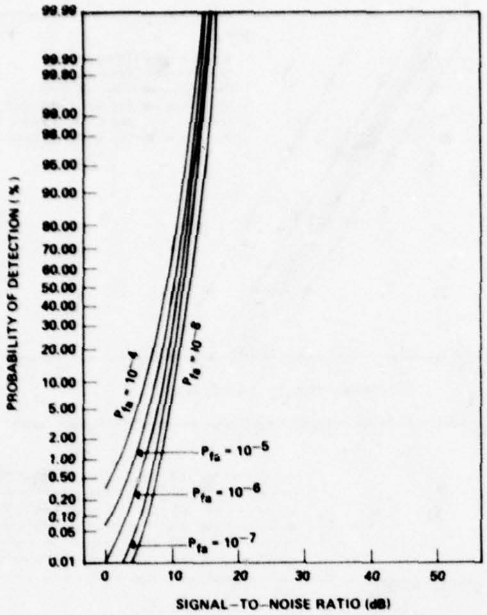

Figure 5. Receiver Operating Curves for a Nonfluctuating Target in a Noise (Rayleigh) Background, Single Pulse Detection.

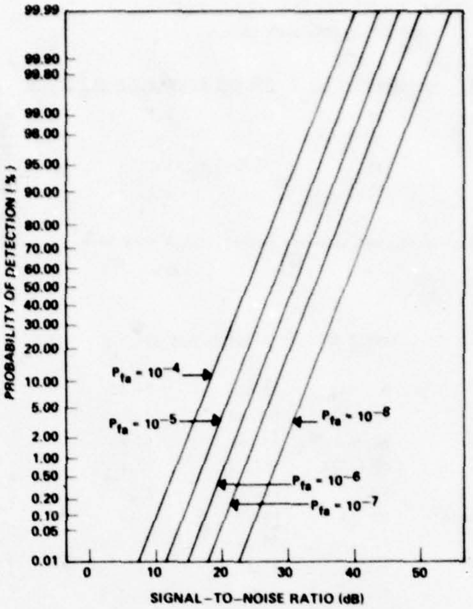

Figure 6. Receiver Operating Curves for a Log-Normal Target and Log-Normal Clutter with Standard Deviations of 4.34 and 6.5 dB Respectively, Single Pulse Detection.

DISCUSSION

E.P.Baars, FRG

Given signal-to-clutter ratios over a range of 30 to 10.000 m as straight lines in log-log scaling (Figs 3 and 4), how are the dimensions of the clutter cell calculated for near field returns?

Author's Reply

The target-to-clutter values shown are intended simply to allow comparison of frequency effects on target-to-clutter ratios. As such, factors such as near field effects and propagation effects were ignored. However, the curves can be used to obtain "ballpark" values for system applications. The tables in the paper contain the accurate values of $\sigma°$ obtained for the various types of clutter and can be used to calculate more accurate estimates of signal-to-clutter ratios. To be of use, however, the standard deviations should be used which are listed in the paper to calculate the clutter distributions. Also, some type of fluctuating target model should be used to achieve realistic estimates of target detectability in clutter.

R.P.Moore, US

Have measurements been made or have you considered:

(1) the structure and inhomogenities in adverse weather atmosphere

(2) the geographical variations of ground clutter affecting both its amplitude and statistical characteristics.

Both of these factors are extremely important in determining effects of environment on performance as they determine the percentage of the time that the systems can operate and the percentage of areas that can be covered as a function of performance. Calculations assuming uniform atmospheres or, as you pointed out, mean values can give descriptive answers.

Author's Reply

(1) The inhomogenity of the atmosphere is known to be a problem. However, we have not been funded to look into the problem. However, during an experiment to measure rain backscatter at mm wavelengths in 1974 (Reference B in the paper) rain drop size distributions were recorded and analyzed for short intervals. It was determined that the drop size distributions varied widely over short time intervals (at least for the type of rain encountered which were mainly localized thunderstorms) and that the reflectivity depended as strongly on the dropsize distribution as on the rain rate.

(2) We are aware of the possible effects on clutter reflectivity characteristics of different geographies. For this reason, present and future measurement programs in which we are participating or expect to participate in include measurement of the reflectivity of snow, land and the sea at several sites both in CONUS and in Europe. Also, attempts are being made to characterize the environment at each site so that reflectivity differences can be explained. These efforts need to be expanded to include other scenarios not included in the present program plans. An example of our interest in this problem is presented in References 5 and 6 in which we define a new approach to the characterisation of foliage path thickness for the purpose of providing a more uniform way of comparing results for foliage penetration measurements obtained in different regions of the world.

FAISCEAU HERTZIEN MILLIMETRIQUE

par

Jean Pierre Dehaene
Ingénieur à la Division Faisceau Hertzien de la Thomson CSF
55, rue Greffulhe – 92301 Levallois Perret
France

RESUME

Dans le domaine des ondes millimétriques, l'évolution des performances des composants de base tels que les générateurs à l'état solide, offre un nouvel éventail de possibilités aux liaisons hertziennes. Cette présentation a pour objet de décrire un faisceau hertzien fonctionnant dans la bande 36–38 GHz ainsi que la raison des choix techniques et technologiques qui ont permis d'y aboutir.

La motivation première dans l'élaboration d'un matériel est son ou ses applications possibles. Ces dernières pour un faisceau hertzien millimétrique, sont liées aux caractéristiques propres à la longueur d'onde:

- bande disponible
- courte portée (influence de la pluie) 5 à 10 Km
- directivité des faisceaux
- faible encombrement (notamment des aériens)

Ces caractéristiques nous ont orientés vers la conception d'un faisceau hertzien mobile de courte portée, analogique et numérique. Les applications dans le domaine militaire s'entendent du déport d'un multiplex radar en ce qui concerne la version analogique à la transmission d'un multiplex 2 ou 8 Mbit/s (voies ou vidéophone) sur une base, dans une zone urbaine.

Les impératifs économiques nous ont amenés à mettre en oeuvre des techniques de transmission assurant un bon compromis avec les performances techniques recherchées.

Deux choix principaux ont orienté la conception du faisceau:

- utilisation de sources GUNN à génération directe
- modulation directe de fréquence à l'émission de la source GUNN par l'intermédiaire d'un varactor couplé à sa cavité.

Le premier choix est essentiellement d'ordre économique. Il a pour conséquence un accroissement de l'occupation spectrale lié aux dérives des oscillateurs (température partiellement stabilisée), rendu possible par la bande disponible.

La modulation directe de fréquence de la source émission répond aux exigences:

· *économique* ——→ simplicité
→ compatibilité analogique/numérique
· techniques → performance en transmission numérique

La modulation de fréquence dans la version numérique est utilisée par un codage particulier comme méthode pour réaliser l'équivalent d'une modulation à saut de phase avec mise en forme spectrale. Ce procédé baptisé FM/WALSH permet en réception une démodulation cohérente de phase identique à celle d'un PSK 20, simplifiée du fait de la présence dans le spectre émis de la porteuse de référence. Les performances sont donc celles d'un CPSK 20.

Une maquette dans une version numérique à 8 Mbit/s a fait l'objet d'une expérimentation de transmission durant une année dans la région parisienne (relevé de champ et pluviométrie).

Une prototype de faisceau hertzien mobile accordable dans la bande 36–38 GHz est actuellement en cours de réalisation pour une version analogique et numérique avec en particulier le développement de source GUNN (100 mW de 36 à 38 GHz par accord mécanique) et d'antenne (CASSEGRAIN 40 dB).

I. CHOIX D'UN SYSTEME DE TRANSMISSION –

Le choix des caractéristiques d'un système de transmission résulte habituellement d'un compromis entre le coût du matériel et les performances attendues. On distingue principalement

- type de signaux à transmettre
- agilité en fréquence } mode d'exploitation
- bilan de liaison – portée
- bande occupée
- directivité } performances techniques

Les applications potentielles d'un faisceau hertzien en ondes millimétriques (liaisons urbaines, déport de base ....) nous ont orientés vers la conception d'un faisceau simple, mobile, satisfaisant aux exigences économiques de ce type d'applications. En ce qui concerne les performances attendues, nos objectifs principaux étaient:

- transmission analogique (vidéo) et numérique (2 Mbit/s)
- agilité en fréquence (36 – 38 GHz)
- performance du modem (cas numérique)

Notre choix s'est fixé sur un système de modulation directe à l'émission utilisant des sources GUNN, non pilotées par quartz qui allient à la fois la simplicité (coût faible) et la performance du point de vue puissance disponible à l'émission et agilité en fréquence. Pour répondre à la compatibilité numérique-analogique, la modulation de fréquence a été choisie. Elle est de plus aisée à réaliser (varactor couplé à une cavité GUNN) d'où simplicité de l'équipement. En ce qui concerne la performance en transmission numérique, le procédé FM/WALSH II utilisant à l'émission la modulation de fréquence rend la performance du modem comparable à celle d'une modulation PSK 20.

II. MODULATION FM/WALSH I ET II –

Ce procédé consiste à utiliser une modulation de fréquence comme méthode pour réaliser une modulation d'amplitude sur deux porteuses en quadrature.

La modulation d'amplitude sur deux porteuses en quadrature englobe en effet la plupart des systèmes de modulation numérique utilisés (2 phases 4 phases, multiniveaux ....).

La modulation de fréquence, comme nous allons le voir permet d'y aboutir, ceci par un choix judicieux des "formes" de symbole précédant le modulateur.

Considérons une porteuse modulée en phase ou en fréquence

$$s(t) = \cos(\omega_0 . t + \varphi(t)),$$

ω_0 , pulsation de la fréquence porteuse;
$\varphi(t)$, phase modulée par les signaux d'entrée

$$s(t) = \cos(\omega_0 . t) \cos \varphi(t) - \sin(\omega_0 . t) \sin \varphi(t).$$

On peut donc considérer que l'on a réalisé une modulation sur deux porteuses en quadrature par les trains $\cos \varphi(t)$, $-\sin \varphi(t)$ corrélés de manière à ce que la résultante soit à enveloppe constante.

Ceci peut également s'interpréter par la projection du vecteur de FRESNEL $\vec{OM}$ sur les deux axes $\vec{X}$ $\vec{Y}$ (fig. 1).

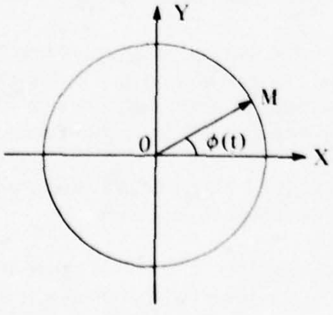

Figure 1

Supposons que l'on effectue un saut de fréquence Δf à l'instant $t = 0$:

$$\varphi(t) = 2\pi \int_0^t \Delta f \, dt + \varphi_0 .$$

La phase varie donc linéairement et les deux composantes de modulation sur les deux axes en quadrature sont composées d'arches de sinusoïde.

MODULATION FM WALSH I ET II –

Considérons les deux types de symboles ci-dessous, attaquant un modulateur de fréquence:

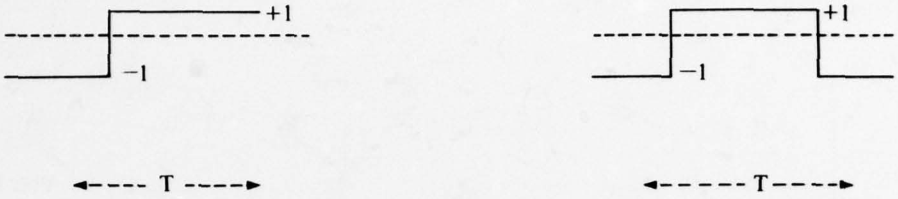

"WALSH I"

"WALSH II"

Figure 2

représentant le "1" logique de la source d'information, obtenus après codage (les "O" étant de signes opposés) (fig. 2)

La dénomination WALSH vient de ce que la forme de ces symboles est indentique aux fonctions périodiques WALSH.

Ces signaux attaquent le modulateur de fréquence avec des excursions telles que les variations de phases satisfassent à:

$$\varphi(t) \leqq \frac{\pi}{2}$$

Nous allons effectuer la décomposition précédente sur les deux axes

INTERPRETATION –

Pour les signaux de type WALSH I, la forme de signal de la voie Y est constituée d'une demi sinusoïde dont le signe dépend du signal binaire de la source d'information. On a donc équivalence à une modulation deux phases où la mise en forme par filtrage serait telle que les signaux obtenus aient une forme sinusoïdale (fig. 3)

Sur la voie X, on a au contraire un signal périodique (sinusoïde redressée) ne dépendant pas de l'information (fig. 3).

On a donc réalisé une modulation d'amplitude sur deux porteuses en quadrature:

- l'une de ces porteuses véhicule l'information proprement dite sous la forme d'une modulation de type biphase à "mise en forme sinusoïdale";
- l'autre au contraire véhicule une information périodique comprenant une valeur moyenne générant une raie à la fréquence porteuse et des raies aux fréquences du rythme et de ses harmoniques.

Dans le cas des signaux de type WALSH II, l'interprétation est identique mais conduit à une modulation par des signaux de type biphase "à forme sinusoïdale" sur la voie Y et une information périodique sur la voie X générant de la même façon une raie à la fréquence porteuse et aux harmoniques du rythme double.

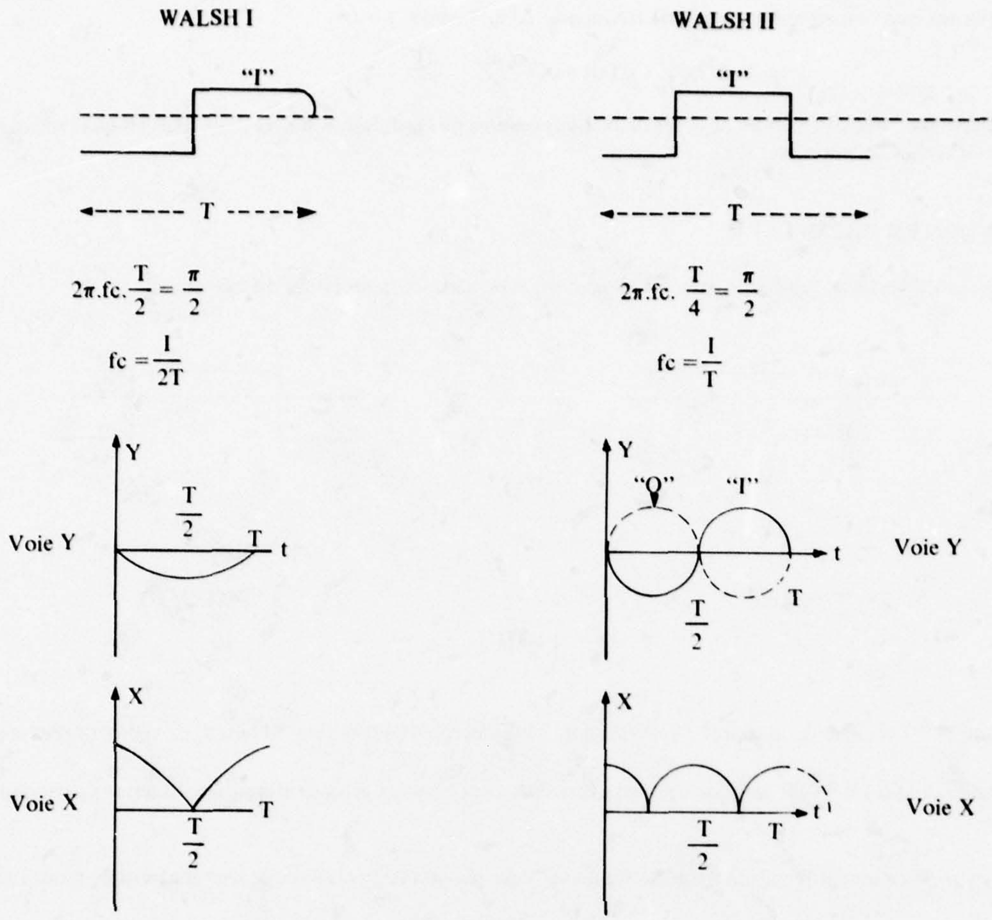
WALSH I
WALSH II
"I"
"I"
T
T
$2\pi.fc.\frac{T}{2} = \frac{\pi}{2}$
$fc = \frac{1}{2T}$
$2\pi.fc.\frac{T}{4} = \frac{\pi}{2}$
$fc = \frac{1}{T}$
Y
$\frac{T}{2}$
T
t
Voie Y
Y
"Q"
"I"
t
Voie Y
$\frac{T}{2}$
T
X
Voie X
T
$\frac{T}{2}$
X
t
$\frac{T}{2}$
T
Voie X

Figure 3

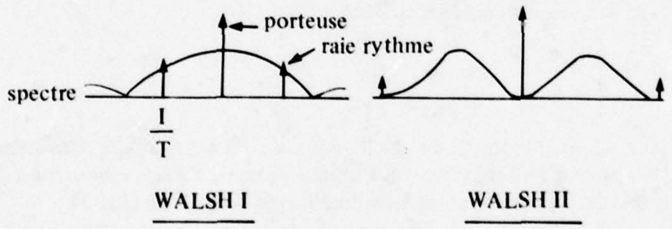
porteuse
raie rythme
spectre
$\frac{1}{T}$
WALSH I
WALSH II

Figure 4

La démodulation d'une porteuse ainsi modulée peut s'effectuer de façon cohérente. Il suffit de récupérer la fréquence porteuse contenue dans le spectre à l'aide d'une boucle de phase lock pour démoduler la voie Y supportant l'information (figures 4 et 5).

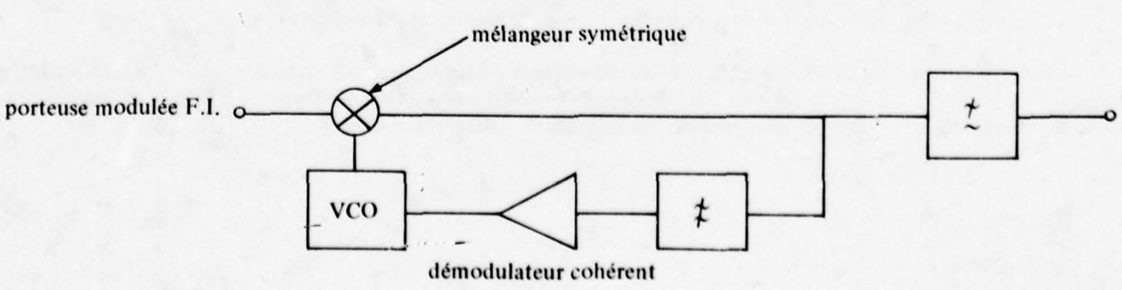
mélangeur symétrique
porteuse modulée F.I.
VCO
démodulateur cohérent

Figure 5

BILAN de LIAISON –

La voie Y emportant l'information proprement dite a une énergie inférieure de 3 dB à celle que l'on aurait en modulation à saut de phase.

La moitié de la puissance est donc consacrée à l'information de porteuse et de rythme.

Cette perte apparente sur le bilan est en fait compensée par la technique mise en oeuvre pour réaliser la modulation dans notre application.

OCCUPATION SPECTRALE –

Le problème de l'occupation spectrale se pose lorsque l'on veut établir un plan de fréquence pour la transmission de canaux dans des bandes de fréquences voisines. Dans le cas d'une modulation directe à l'émission notamment en onde millimétrique, il est difficile, voire impossible de réaliser un filtre limitant le spectre émis pour de faibles débits d'information. C'est donc le spectre obtenu après modulation et plus particulièrement sa décroissance lointaine qui détermine le niveau d'interférence, donc le rapprochement possible des canaux.

Ce problème important est examiné dans l'annexe jointe.

Dans le cas d'une modulation à saut de phase, le spectre décroit en $1/f^2$. Pour les deux types de modulation décrits, la décroissance est en $1/f^4$. Il apparait également dans l'annexe qu'un choix différent des signaux permettrait d'obtenir une décroissance en $1/f^6$.

III. DESCRIPTION DU FAISCEAU HERTZIEN MILLIMETRIQUE –

Description gęnerale

La figure donne le synoptique général d'un émetteur-récepteur dans sa version numérique (équipements analogiques en pointillé)

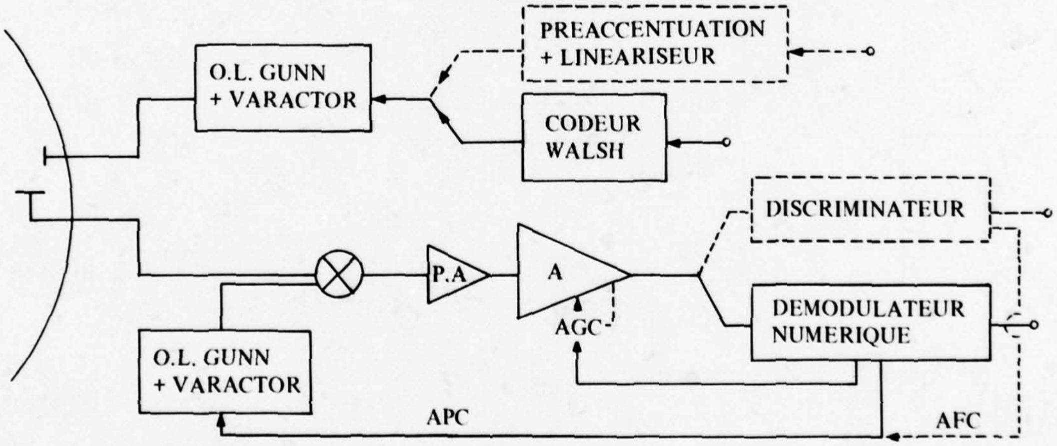

L'antenne de type CASSEGRAIN est équipée de deux polarisations linéaires à 45° (l'une émission, l'autre réception). Cette disposion permet de rendre physiquement identiques les branchements émission-réception des extrêmités d'une liaison bilatérale.

L'émission est essentiellement constituée d'un oscillateur GUNN direct, modulable en fréquence par un varactor couplé à sa cavité. Le signal modulant est constitué du train numérique codé dans la version numérique ou du signal analogique préaccentué dans la version analogique. Les oscillateurs GUNN sont thermostatés pour assurer une stabilité suffisante des fréquences. En réception, l'onde reçue est directement convertie à 70 MHz, fréquence intermédiaire de démodulation, sans suppression de fréquence image. Le signal reçu est ensuite démodulé par discriminateur pour la version analogique ou par démodulateur cohérent dans la version numérique.

Une fonction AFC est effectuée en réception pour assurer un centrage permanent de la fréquence intermédiaire, ceci par commande de l'O.L émission, commandable en fréquence. L'information de commande est fournie par le discriminateur pour la version analogique. Dans la version numérique, cette fonction est en fait un asservissement en phase sur une référence en fréquence intermédiaire.

MODEM NUMERIQUE –

La modulation utilise le procédé FM/WALSH II. Le modulateur est donc constitué de l'O.L. GUNN modulable en fréquence, précédé d'un codeur chargé de générer les symboles que nous avons vu précédemment.

Ce codeur est simple puisqu'il consiste à additionner modulo 2, le rythme retardé d'un quart de symbole avec le message NRZ de la source d'information.

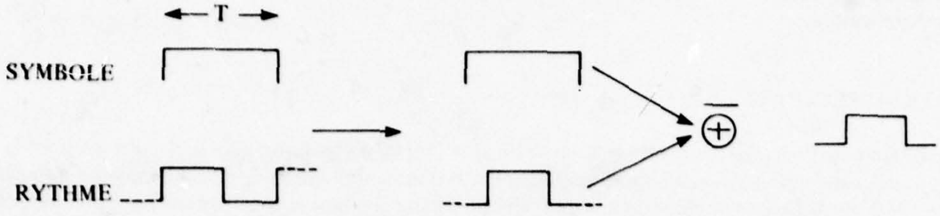

L'excursion de fréquence est ajustée pour que les variations crête de phase soient voisines de $\pi/2$.

On peut noter d'autre part que le signal attaquant le modulateur de fréquence ne nécessite pas le passage du continu. (Le code n'a pas de densité à la fréquence 0).

Le démodulateur est de type cohérent 4Φ. On récupère par filtrage dans une boucle de phase, la raie porteuse générée dans le spectre émis. Cette opération est en fait réalisée par asservissement de l'O.L. de réception sur référence fixe en fréquence intermédiaire pour assurer un centrage permanent de la fréquence intermédiaire. L'O.L.R. joue alors le rôle de VCO.

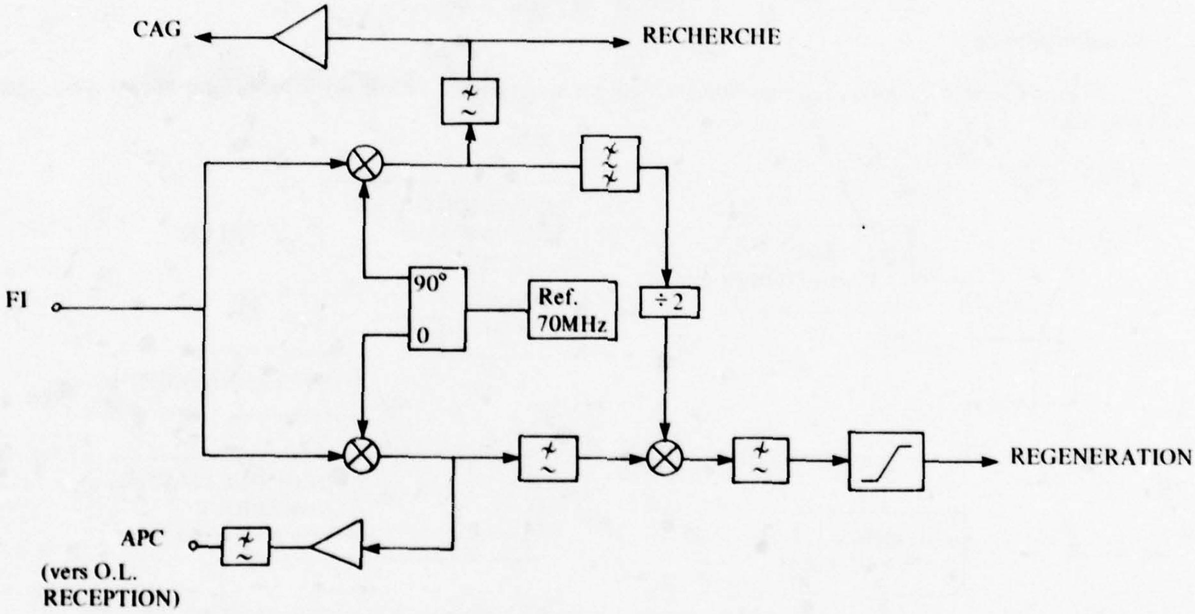

Du fait de la quadrature de phase entre la raie porteuse et le support de l'information, l'information apparait directement en sortie du comparateur de phase (mélangeur en anneau) utilisée dans la boucle de récupération porteuse.

Le message à ce niveau est de type biphase. Il est transformé en message NRZ par démodulation cohérente avec le rythme. En effet, un message biphase est une modulation cohérente d'un signal NRZ par son propre rythme.

Ce rythme est récupéré par démodulation de la voie en quadrature (spectre de raies). On dispose en réalité du rythme double qui après filtrage est divisé par 2. L'ambiguité de π introduite sur cette seconde démodulation est levée par un codage-décodage transitionnel effectué à l'émission et à la réception.

La détection de la voie en quadrature permet d'autre part d'extraire l'information continue de niveau reçu, utilisée pour la commande de CAG. Cette fonction est utile dans la mesure ou la détection de CAG normale opère à large bande, donc risque d'être sensible au bruit total reçu. Cette composante est également utilisée pour déclancher éventuellement une recherche en cas de décrochage.

Les équipements sont disposés dans un coffret intégré à l'antenne et monté sur trépied.

IV. PERFORMANCES –

– *Principales caractéristiques* –

– bande	36–38 GHz : accord mécanique continu
– gain des aériens	> 40 dB
– Puissance émission	100 mW
– facteur de bruit	< 14 dB
seuil du démodulateur numérique à 10^{-4} (taux d'erreur)	$\left(\frac{C}{N}\right)$bande NYQUIST 16 dB

– *Bilan de liaison à 2 Mbits/s* –

Affaiblissement espace libre 5 Km à 38 GHz	138 dB
$\left(\frac{C}{N_0}\right)$ temps clair	122 dB
$\left(\frac{C}{N}\right)$2 MHz	59 dB
Marge au seuil par temps clair	43 dB

Compte tenu d'un découplage de 40 dB aux accès émission réception; et d'une protection d'interférence de 30 dB (C/I) l'éloignement des fréquences émission réception doit être tel que l'affaiblissement du spectre soit de 132 dB pour la modulation WALSH II R. (soit f = 112 X débit de transmission).

CONCLUSION

Nous avons cherché à montrer, au cours de cette présentation comment on pouvait adapter les caractéristiques d'un système de transmission, compte tenu de l'état de l'art de la technologie, aux exigences technico économiques.

Les caractéristiques de transmission en ondes millimétriques (faibles dimensions, directivité des aériens courte portée) font du faisceau hertzien millimétrique un équipement bien adapté aux liaisons type urbaines et déports de base.

Nous tenons à remercier le Ministère des Armées Françaises qui, par ses représentants du STTA, a permis l'étude et la réalisation d'un équipement faisceau hertzien millimétrique.

ANNEXE

SPECTRES A L'INFINI EN MODULATIONS NUMERIQUES

L'objet de cette annexe est d'examiner un critère simple permettant d'évaluer le spectre loin de la porteuse d'une classe importante de modulations numériques.

La plupart des systèmes de modulation numérique utilisés peuvent se ramener à une modulation d'amplitude sur deux porteuses en quadrature. Cette représentation engloble également le cas des modulateurs de fréquence.

Nous supposerons donc que chacune de ces deux porteuses en quadrature est modulée en amplitude, à porteuse supprimée, par un signal de la forme:

$$s(t) = \sum_{-N}^{+N} f_i(t - n \cdot T)$$

$s(t)$ représente le signal constitué de $2N$ symboles émis aux temps $t = nT$ et dont la forme est caractérisée par l'indice i.

Nous supposerons d'autre part que:

$$f_i(t) = a_i \cdot f(t)$$

c'est à dire tous les symboles ont la même "forme" à une homothétie près sur leur amplitude (a_i).

Le calcul du spectre de la porteuse ainsi modulée en amplitude se ramène au calcul du spectre du signal modulant qui peut s'exprimer sous la forme[2]: lorsque $N \dashrightarrow \infty$

$$\boxed{\begin{aligned} W(f) = {} & T\left|\frac{S(f)}{T}\right|^2 \left(\Sigma p_i a_i^2 - (\Sigma p_i a_i)^2\right) \\ & + \left|\frac{S(f)}{T}\right|^2 (\Sigma p_i a_i)^2 \sum_{-\infty}^{+\infty} \delta\left(f - \frac{k}{T}\right) \end{aligned}}$$

p_i = probabilité à priori d'appararition du symbole (i),
$S(f)$ = transformé de Fourier de $f(t)$.

Le second nombre de cette expression fait apparaitre deux termes:

- le premier donne un spectre continu ne dépendant que de $\left|\frac{S(f)}{T}\right|^2$
- le second est un spectre de raies $\left(\frac{k}{T}\right)$ dont l'enveloppe dépend de $\left|\frac{S(f)}{T}\right|^2$. Ce dernier est nul si le signal est à valeur moyenne nulle $(\Sigma p_i a_i = 0)$.

Cas particulier: 2 symboles symétriques: $a_i = \pm 1$, $p_i = \frac{1}{2}$

$$\Longrightarrow W(f) = T\left|\frac{S(f)}{f}\right|^2.$$

Ce cas recouvre les modulations 2 et 4 phases.

La connaissance du spectre se ramène donc à l'évaluation de la transformée de Fourier de la forme du symboles, $S(f)$. Nous allons montrer en utilisant la transformation de Laplace de $f(t)$ qu'il n'est pas nécessaire re d'effectuer le calcul de $S(f)$ pour connaitre le spectre loin de la porteuse mais que la connaissance des discontinuités pouvant apparaitre en dérivant $f(t)$ suffit pour l'evaluation de ce spectre.

Rappelons pour cela certains résultats sur la transformation de Laplace soit $f(t)$, une fonction dérivable jusqu'à l'ordre $n - 1$ et possédant des dérivées continues jusqu'à l'ordre $n - 1$.

Si d'autre part la dérivée à l'ordre $nf^{(n)}(t)$ possède un certain nombre de discontinuités aux instants $t = t_k$ d'amplitude B_k (B_k désignant le saut de $t_k - \epsilon$ à $t_k + \epsilon$) en particulier:

$$f(0^+) = f^1(0^+) = \ldots\ldots = f^{n-1}(0^+) = 0$$

$$\Longrightarrow L(f^{*(n)}(t)) = p^n F(p) - \sum_0^\infty B_k e^{-pt_k}$$

*caractérise $f^{(n)}(t)$ obtenu en supprimant ses discontinuités.

Appliquant le théorème sur les valeurs limites:

$$\lim_{t\to 0} L\,(f^{*(n)}(t)) = \lim_{p\to\infty} p\left|p^n F(p) - \sum_0^\infty B_k e^{-pt_k}\right|$$

$$= 0$$

$$\Longrightarrow \boxed{\begin{array}{l} F(p) \dashrightarrow \dfrac{\sum_0^\infty B_k e^{-pt_k}}{p^{n+1}} \\ p \dashrightarrow \infty \end{array}} \quad t_k$$

$B_0 = f^{(n)}(0^+)$ représente l'éventuelle discontinuité à l'instant 0 de la dérivée à l'ordre n.

Dans cette relation nous pouvons en déduire que s'il faut dériver à l'ordre n le symbole $f(t)$ pour voir apparaître les premières discontinuités, le spectre $W(f)$ proportionnel à $|S(f)|^2$ aura une décroissance en:

$$\frac{1}{f^{2n+2}}.$$

Exemple:

Considérons les trois formes de symboles (nulles hors de [0 T])

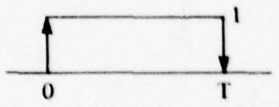

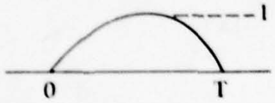

$\sin \pi \dfrac{t}{T}$

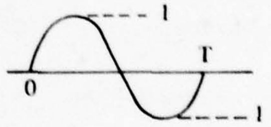

$\sin 2\pi \dfrac{t}{T}$

Apparition des discontinuités pour

n = 0	n = 1	n = 1
===> dérivation	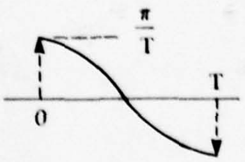	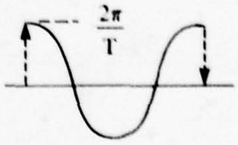
$B_0 = 1$	$B_0 = \dfrac{\pi}{T}$	$B_0 = \dfrac{2\pi}{T}$
$B_T = -1$	$B_T = \dfrac{\pi}{T}$	$B_T = \dfrac{-2\pi}{T}$
$F(p) \dashrightarrow \dfrac{1 - e^{-pT}}{p}$	$F(p) \dashrightarrow \dfrac{1 + e^{-pT}}{p^2} \cdot \dfrac{\pi}{T}$	$F(p) \dashrightarrow \dfrac{1 - e^{-pT}}{p^2} \cdot \dfrac{2\pi}{T}$

$$|S(f)| \dashrightarrow \left|\frac{\sin \pi f T}{\pi f}\right| \quad \Longrightarrow W(f) \dashrightarrow T\left|\frac{\sin \pi f T}{\pi f T}\right|^2$$

$$S(f) \dashrightarrow \left|\frac{\cos \pi f T}{2\pi T f^2}\right| \quad W(f) \dashrightarrow T\left|\frac{\cos \pi f T}{2\pi T^2 f^2}\right|^2$$

$$|S(f)| \frac{\sin \pi f T}{\pi T f^2} \quad W(f) \dashrightarrow T\left|\frac{\sin \pi f T}{\pi f^2 T^2}\right|^2$$

Cette méthode simple permet une évaluation rapide du spectre loin de la porteuse avec un minimum de calcul. Elle est particulièrement interessante dans le cas où l'intégration par le calcul direct de la transformation de Fourier ne permet pas l'expression sous la forme d'une formule analytique exploitable.

APPLICATION AUX MODULATIONS FM/WALSH (n)

Rappelons que ce type de modulation consiste à moduler en fréquence un oscillateur par des signaux de "forme Walsh (n)" avec des excursions de fréquence telles que les variations extrêmes de phase restent comprises entre $\pm\pi/2$. La décomposition sur deux voies en quadrature permet d'obtenir des formes d'ondes modulantes constituées de tronçons de sinusoïdes (figure 1 pour Walsh I et II).

Si l'on considére les procédés FM/Walsh I et II (figure 1) la modulation est équivalente respectivement à une modulation d'amplitude à porteuse supprimée par des signaux de type NRZ et Biphase à "forme sinusoïdale".

Le spectre se déduit des résultats précédents et a une décroissance en $1/f^4$.

On peut se poser alors le problème de savoir s'il est possible de construire un signal modulant tel que le spectre obtenu ait une décroissance plus rapide, en $1/f^6$.

Utilisons les résultats précédents:

Si l'on considère le procédé FM/Walsh I, le spectre à l'infini est dû aux discontinuités apparaissant aux instants $t = 0$ et $t = T$ sur la dérivée première.

Essayons de les émiminer en remplaçant le signal modulant:

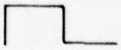

par

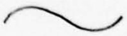

soit une excursion $\Delta f = \Delta f_c \sin \frac{2\pi t}{T} [0\ T]$

$\Longrightarrow$ une variation de phase:

$$\phi = 2\pi \int_p^t \Delta f(t) dt = 2 \Delta f_c T \sin^2\left(\frac{\pi t}{T}\right)$$

En limitant les excursions crêtes à $\frac{\pi}{2} \Longrightarrow \Delta f_c = \frac{\pi}{4T}$

$$\phi = \frac{\pi}{2} \sin^2\left(\frac{\pi t}{T}\right) [0\ T].$$

Le signal obtenu sur la voie Y (figure 1) supposant l'information à la forme:

$$y = \sin\left(\frac{\pi}{2} \sin^2 \frac{\pi t}{T}\right) [0\ T].$$

Les discontinuités apparaissent alors sur y''

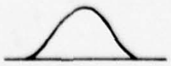

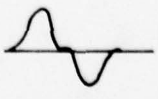

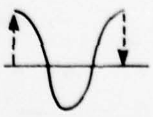

$$|F(p)| \dashrightarrow \frac{1}{|p^3|} \frac{\pi^3}{T^2} |1 - e^{-pT}|$$

$$\Longrightarrow W(f) \underset{f \to \infty}{\dashrightarrow} T \left| \frac{\sin \pi f T}{4T^3 f^3} \right|^2$$

Nous obtenons donc un spectre décroissant à l'infini en $1/f^6$.

Par analogie, on peut construire une modulation comparable au FM/Walsh II dont le spectre décroit en $1/f^6$.

Il faut remarquer que l'augmentation de l'ordre d'apparition des discontinuités sur les dérivées du signal a pour effet de diminuer les largeurs d'impulsion, donc d'augmenter l'occupation du spectre au voisinage de la fréquence centrale.

La figure 2 nous donne les allures spectrales pour les modulations Walsh I et II normales (R) et modifiées (S).

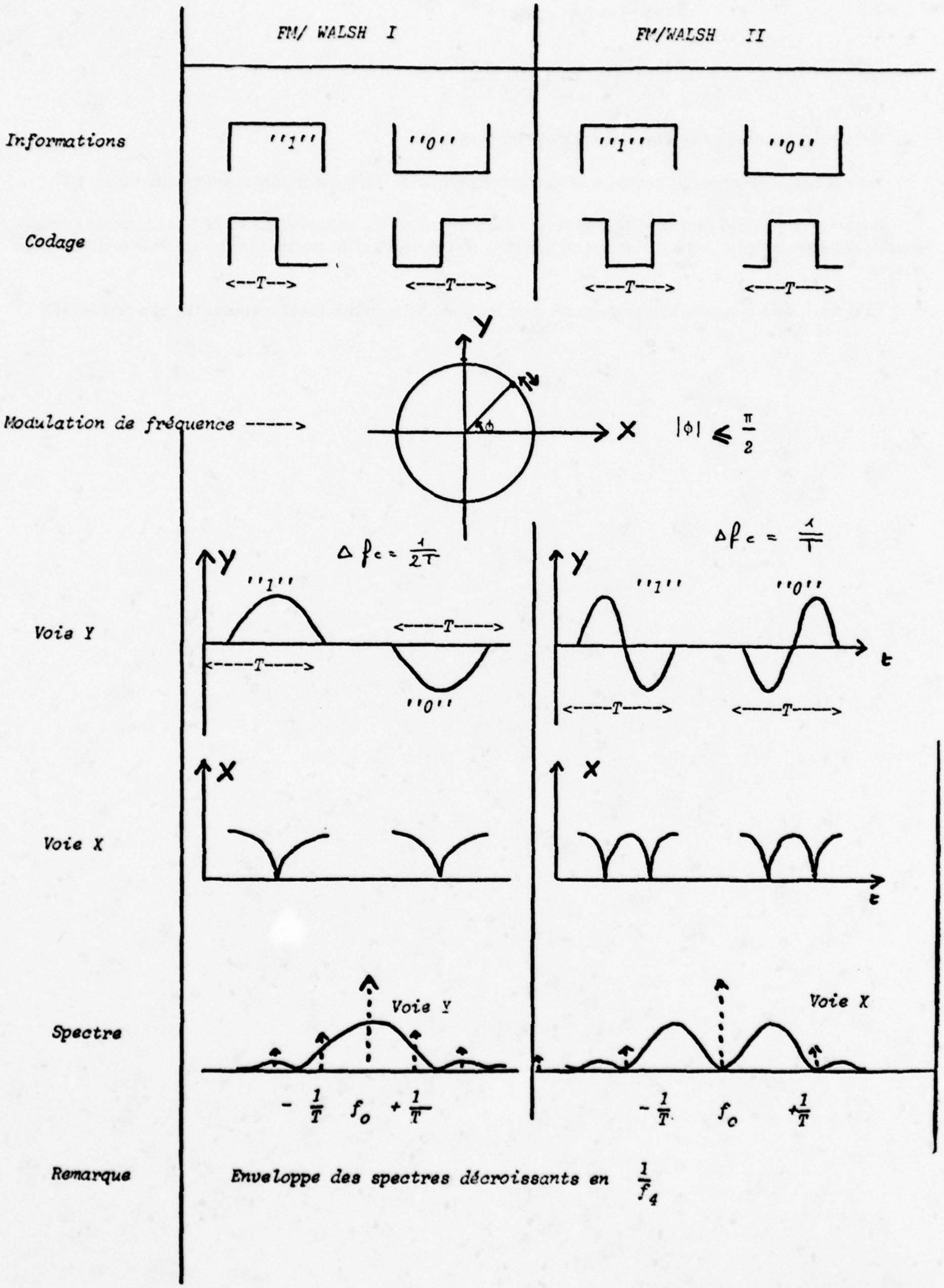
FM/ WALSH I
FM/WALSH II
Informations
"1"
"0"
Codage
<--T-->
<---T--->
Modulation de fréquence ----->
Y
X
ϕ
$|\phi| \leq \frac{\pi}{2}$
$\Delta f_c = \frac{1}{2T}$
$\Delta f_c = \frac{1}{T}$
Voie Y
Voie X
t
<----T---->
Spectre
Voie Y
Voie X
$-\frac{1}{T}$
f_0
$+\frac{1}{T}$
Remarque
Enveloppe des spectres décroissants en $\frac{1}{f_4}$

Figure 1

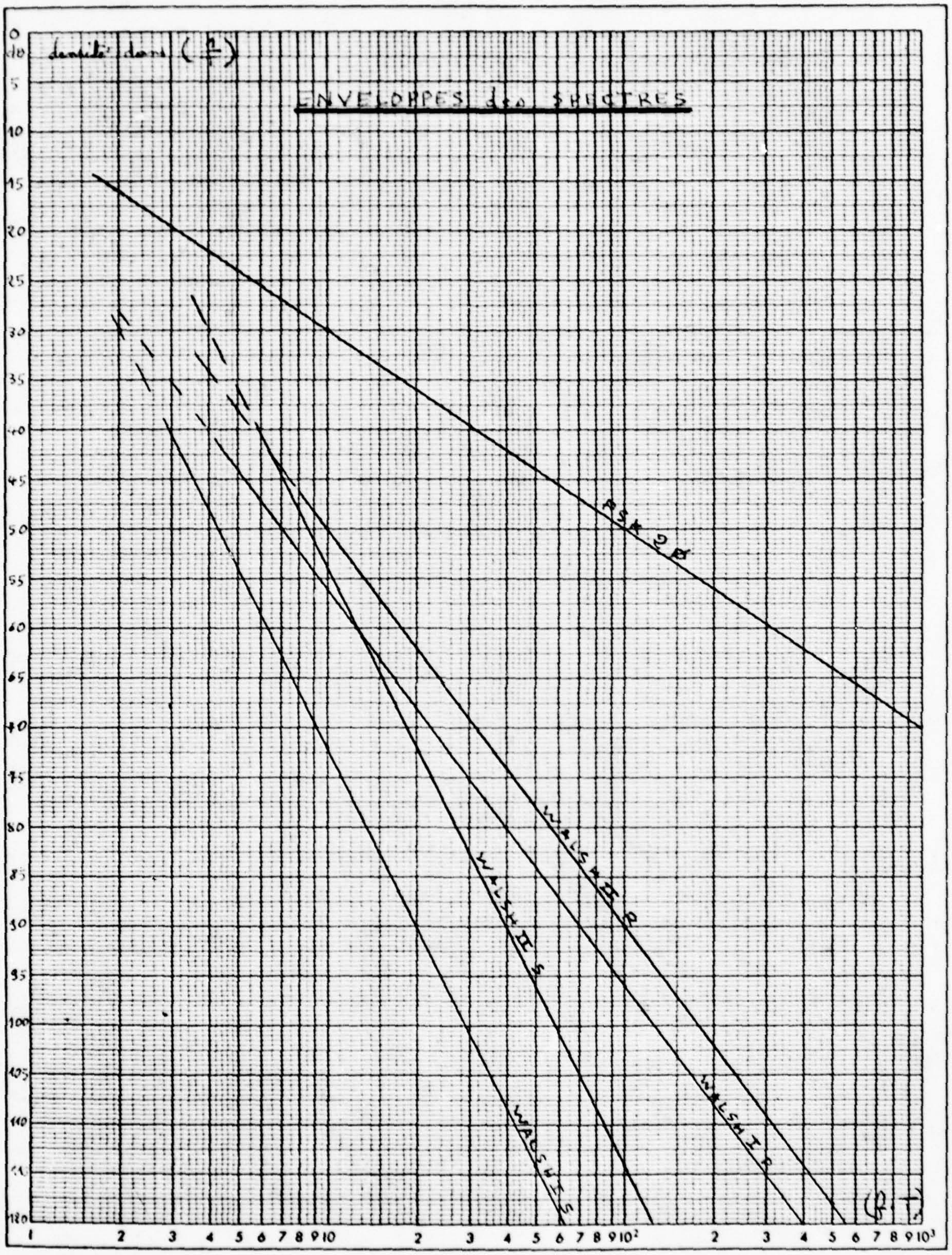

Fig. 2 Enveloppes des spectres

REVIEW OF TWO DECADES OF EXPERIENCE BETWEEN 30 GHz AND 900 GHz IN THE DEVELOPMENT OF MODEL RADAR SYSTEMS

L.A. Cram and S.C. Woolcock
EMI Electronics Limited
Wells, Somerset, England

SUMMARY

This paper discusses the purposes, principles and methods of radar scale modelling and describes the several different types of measuring radar which are in use for investigating different aspects of radar scattering. Interesting variations arise in these radars when adapted for use at sub-millimetre wavelengths where optical methods are used in component and system design. In any facility for collecting copious and diverse data, a foolproof organization is required to ensure that any erroneous data are recognized and rejected. The organization of data collection, and the processing and use of the data, are a major aspect of the work. The methods by which these data are simplified without loss of important reflection characteristics is discussed and examples of the results are presented. Finally some indication is given of likely trends in future developments of the measuring radar equipment.

1. INTRODUCTION

A facility for modelling radar systems to obtain detailed data on scattering characteristics of radar targets has been in continual use in the United Kingdom for the last two decades (Cram, L.A., Woolcock, S.C., Johnson, R.H., 1973; Cram, L.A., Staveley, J.R., 1977). Throughout this period it has been under constant development to extend the scope of measurements and to increase the range of radio frequencies available. This modelling activity has provided continuing stimulus to the advance of technologies and to component development in the region from 30 GHz to 2 THz. The centre for this work is the U.K. National Radio Modelling Facility and it is run by EMI Electronics Limited for the MOD and the RSRE. The balanced development of this facility is the outcome of the total involvement of EMI Electronics Limited in all aspects of the work. Our interest commenced with a need to design, test and assess new operational radar systems and it quickly became evident that the target reflection characteristics required for such assessments could only be obtained in sufficient detail by modelling methods.

In order to perform modelling at scaled wavelengths, we have had to develop millimetre radars for use as reliable measuring instruments. During the last decade we have also been working with sub-millimetre radars. Often no suitable sources or detectors at the required frequency have been available and research has been required before appropriate components could be developed. The aim has always been the practical one of obtaining, in the most economical way, target scattering information needed in order to assess the behaviour of a full-scale radar in operational conditions. Consequently, considerable emphasis has been given, first to stability and reliability in the measuring equipment, and, second, to rapid and economical processing of the data.

Initial measurements were made in 1958 with a non-coherent pulsed radar at 35 GHz. The facility has by now been extended to cover frequencies over three decades from 800 MHz to 890 GHz by means of more than 30 different specialized radars. At any one time seven of these radars may be operating without mutual interference. Models of many different types of target have now been made at a wide range of scaling factors.

2. RADAR TARGET REFLECTION CHARACTERISTICS

Any target which reflects radar power imparts several characteristics to the received signal which may be of considerable significance to the operation of the radar. Signal strength is an obvious feature and, if this is inadequate over the radar integration period, the radar may fail to detect the target. The target aspect may not be constant over that period however and, as shown in figure 1, the signal strength from a typical aircraft target varies rapidly with aspect angle and may change by 30 - 40 dB with very small angular changes. Furthermore, even if the signal is detected, the modulation of signal strength as the aspect of the target changes may have an important effect on the operation of the radar, and the frequency and depth of this modulation would then be of significance.

The target will also impart doppler frequency and radar polarisation characteristics to the signal and some radars may be sensitive not only to these but also to their modulations with respect to time. The directional data derived by a radar can be in error because of the glinting characteristics of the target, and the radar signal can even appear to come from a point outside the envelope of the target. If we are properly to assess the performance of a given radar, we must have quantitative knowledge of all such target characteristics.

The determination and use of radar scattering characteristics was the subject of Agard lecture series No. 59 (L.A. Cram, 1973). This series considered three methods of determining the data: full-scale trials, calculation, and scale modelling. While each method was found to be useful, it is only through scale modelling that sufficient data can be obtained efficiently and economically in order to permit the adequate assessment of modern radars.

3. METHODS OF RADAR SCALE MODELLING

The properties of electromagnetic waves are such that, if all the linear dimensions are scaled down in the same proportion S, then the fields will be of the same form. The radar backscatter has dimensions of area and hence, in the modelled system, the backscatter is reduced by S^2. Radar modelling makes use of these scaling properties; an accurate scale model of the target being made and viewed by a radar whose wavelength has been scaled and whose modulation parameters have also been appropriately scaled by the same factor as the target. Most man-made targets are made of conductive metals or of substantially lossless dielectrics and these will be respectively represented in the model by lossless metal and dielectric materials of the same dielectric constant. However, if the target does contain lossy materials in its outer structure, i.e. either resistive conductors or dielectrics with loss, then these have to be represented in the model by more highly conducting materials. This is because electrical resistance has length dimensions and must be scaled down with the same scaling factor S.

All the scattering effects, including interference effects, polarisation effects and travelling wave phenomena are correctly represented by such scale modelling.

Target Model Details

Experience has shown the need for attention to detail in the model target. Any orifices and the cavities behind them are particularly important, as are those internal corners which cause multiple reflections. As an example, the internal parts of a jet engine may be more important than the external parts of the aircraft which it propels. Likewise any airscoops, landing lights, flaps etc. are very significant. Signals 40 dB, or even 50 dB down on peak reflections may still appreciably affect the performance and design of a radar. Also the important detail of the backscatter signal is usually dependent more on the multiple small features than on the gross features of the shape.

Model Support

It is normally convenient and economic to perform the work with model targets of sizes between 0.5 m and 5.0 m. For aircraft targets, this implies scale factors between 1 : 4 and 1 : 20. For ship targets, a scale factor of order 1 : 100 or 1 : 200 may be needed. The model construction is, in any case, designed to minimize the weight of the model so that the supporting means may be thinner and less reflecting. A typical aircraft model supported on dielectric strings is shown in figure 2. This is a model HS 125 Executive Jet aircraft at 1 : 8 scale. The suspension system shown here incorporates motorized pulleys for changing the aspect of the model to the radar and with this suspension system the target can be rotated continuously about a vertical axis after pitch and roll have been set. Furthermore the effect of reflections from the thin dielectric strings is minimized by ensuring that they are not viewed at normal incidence.

Other suspension methods are in use. When high positional stability is required, for example, as it is for modelling work above 300 GHz, then a tapered column is used to support the model from beneath.

Clutter Rejection

In any case, the target support is too frail to withstand wind and weather and therefore the measurements are conducted inside a building. The interfering effects of scatter from the walls, floor and roof of the building are normally avoided by making the model radar a pulsed radar and using range gating to reject signals except from the target's range. Sometimes, however, directionality in the radar aerials for transmission and reception is also required to minimize unwanted clutter. The model radar pulse is usually made at least three times the model target length, thereby ensuring a period when returns from all parts of the target coexist. As a result, the central part of the received signal is equivalent to that from a radar of longer pulse length (or even c.w.) and this central portion is extracted by gating in the receiver. If the full-scale radar should use a pulse which is shorter than three times the target length, then this pulse length is correctly modelled in the model radar. Clutter rejection by pulse range gating in the radar model is very satisfactory and permits the operation of several radars in the one building without mutual interference, so long as p.r.f. interleaving is used also.

4. MODEL RADAR FREQUENCIES

Most full-scale radars operate between 3 GHz and 10 GHz although the range of frequencies used extends at least from 400 MHz to 94 GHz and possibly beyond. Consequently, with scaling factors of order 1 : 4 to 1 : 20, the main requirement *for model radars lies between, say, 10 GHz and 200 GHz with greatest emphasis in the middle of this range (30 - 80 GHz).* However, in some cases with small objects, it is useful to work with life-size targets, while in other cases greater scaling factors are needed. As a result, the overall range of frequencies used now extends from 800 MHz to 890 GHz. Precise and stable measurement radars are now available across this frequency band as is indicated in the chart of figure 3. This chart shows how a suitable scaling factor may be chosen for the target model together with a choice of model radar frequency so as to facilitate the modelling of any full-scale radar against a particular target.

5. RADAR MODELLING FACILITY

The first measurements with the facility were made in 1958 using a 35 GHz radar with 30 ns pulses. Scale model targets at scales 1 : 100 and 1 : 4 were used and sensitivities were adequate to measure 10^{-6} m^2 echoing area anywhere in a 5 m cube. This initial work was aimed at plotting the direct backscatter amplitude as a function of target aspect. For this type of measurement the target is hung from dielectric strings as in figure 2 and is then rotated about a vertical axis as radar measurements are being made. The radar sightline is slightly elevated so as to avoid any orthogonal reflection from the suspension strings. Calibration is done by measuring the reflection from an accurately made metal sphere which can be substituted for the target.

The facility has been expanded in terms not only of frequency coverage, as was indicated in figure 3, but also of the type of measurement which can be made. The initial work was with a non-coherent radar receiver, and work with such radars is still of interest. Additionally, however, we have model radars operating with coherent receivers and some have the facility for providing either or both types of output (coherent and non-coherent).

Model radars have also been made, and are in use, to indicate target direction and thus to determine the angular glint or error in the perceived target direction. One method of achieving this uses a coherent radar which measures the phase of the received signal as well as its amplitude, and such a system is particularly valuable for analysis of the reflecting elements in a target structure.

During the last decade there has been a growing appreciation of the importance of polarisation of the reflected signal and many of the measurement radars now incorporate facilities for transmitting and receiving either type of linear or circular polarisation. In some cases two types can be received coincidentally. More recently, a system has been developed for determining depolarisation of the received signal from a target illuminated with plane polarisation.

Coherent model radars can, of course, be used to measure doppler modulation on a signal, and this may arise either from gross movement of the target with respect to the radar, or from elements within the target which are not stationary. Some model radars have been specialized for such measurements.

With so many different types of data required, it has been necessary to establish a number of different, separate facilities within the one building. There are nine different radar facilities which operate with seven different target support equipments. Thus seven different types of measurements can be conducted at any one time. In some of these systems the radar is stationary while the target is either rotated or moved in range with respect to the radar. In other systems, the target is stationary during measurement and it is the radar which moves, either linearly past, or on an arc around, the target. Bistatic radars can be modelled, if desired, with the bistatic angle as an experimental variable. Some systems permit the recording of alternative polarisations (or of both simultaneously) with coherent and/or non-coherent reception. One system is specialized for measurements in which a water surface, subject to a controlled amount of disturbance, is at least a part of the target scene. The photograph of the facility shown as figure 4, and the diagrammatic representation of it presented in figure 5, give some indication of the scope now covered by the measurement facility.

A wide variety of target models is now available for use with this facility. These are to scales ranging from 1 : 1 to 1 : 200 and are of diverse types including fixed and variable wing aircraft, helicopters, drones, missiles, shells, mortar bombs, as well as land and sea vehicles. In some cases, models have been made at more than one scaling factor, but usually one scale suffices for each target, and the choice of a model radar frequency from those available is adequate to provide all the flexibility of measurement required.

Probably far more important than the installation itself is the wide range of experience with, and understanding of, radar reflection properties and problems that has been acquired. This applies in particular to the processing of the data so that they are first of all checked and interpreted, and then reduced to a compact form for customer use. These aspects will be dealt with later, but first we will discuss the model radar systems in somewhat greater detail.

6. MODEL RADARS

A diagrammatic representation of the radio modelling measurement system is given in figure 6 . All of the microwave and millimetre wave measuring systems incorporate range gating and use a transmitter pulse length of about 10 ns to 50 ns so as to envelop the target model completely. These pulses have sharp rise and fall times of order 1 - 3 ns and consequently a wide bandwidth intermediate frequency receiver is used. The i.f. is usually in F-band (3 -4 GHz).

7. NON-COHERENT RECEIVER

A typical non-coherent pulsed radar with range gating is shown in figure 7 . The transmitter source can be a magnetron, at frequencies up to 80 GHz but, increasingly, Impatt or Gunn devices are being employed. Between 140 GHz and 280 GHz a pulsed extended-interaction oscillator (EIO) or carcinotron is used. A reflex klystron, or solid state source, provides the local oscillator signal.

Schottky mixer diodes which have been specially developed by EMI are used in radar systems up to 280 GHz. Examples of such diodes are illustrated in figure 8 with an indication of their performance with frequency.

In past years 4 GHz travelling wave tubes were used for i.f. amplification. Range gating was achieved by pulsing the first anode of one of the tubes. Currently a solid state i.f. amplifier is used and range gating is accomplished by means of a diode gate operating at i.f. However, the non-coherent receiver uses a switch in the video circuitry. In order to ensure fidelity, the detector is operated at constant level by preceding it with a voltage controlled diode attenuator incorporated in an a.g.c. loop. This diode attenuator has a logarithmic law and its control voltage is used as the receiver output. Thus echoing area on a decibel scale can be obtained over a range of about 40 dB.

8. COHERENT RECEIVER

A system with coherent reception is shown diagrammatically in figure 9.

To obtain a coherent reference, a fraction of the transmitter power is delayed to correspond in time with the received pulse from reflection at the target. Both the reference and the received target signals are mixed down to the first i.f. using separate mixers driven by the same local oscillator. The two mixer outputs, both in F-band (3 - 4 GHz), are separately amplified before being mixed together in a balanced detector. Its output pulses are amplitude modulated by the doppler frequencies from the target. Analogue signals are derived using box-car and filtering circuitry. A digital phase shifter is present in the reference signal path before the final mixer, to achieve an effective doppler side-step of frequency such that all doppler components appear at the receiver output as positive frequencies. Values of instantaneous amplitude, a, and phase, Ø, can be derived by processing the doppler information in an on-line computer. A $\frac{\pi}{2}$ phase shift can also be injected into the reference channel periodically and thus the in-phase and quadrature components are generated in time multiplex and may be separated. Such a radar will faithfully reproduce doppler signals caused by target motion relative to the radar so permitting a and Ø measurements to be made.

It is often informative to perform a Fourier analysis upon the complex amplitude, $a\,(\theta)\,\exp\left[j\;\emptyset\;(\theta)\right]$, considered as a function of angle, θ. The resulting angular spectrum can, for example, be used in the determination of the angular location ('cross-range') and magnitude of the constituent reflecting sources. Alternatively if the target is a model aircraft, its engine can be rotated and, following frequency analysis, the spectral content of the resulting doppler sidebands can be examined.

Figure 10 shows a coherent radar in use with water waves as the target. This is an 80 GHz radar and uses a magnetron as a pulsed source.

9. DIRECTION FINDING RECEIVER

Interference between radar waves reflected from different parts of a target can lead to perturbation in the associated phase fronts. These can result in angular glint errors in the directional indication given by the radar. An early form of a model radar operating at 80 GHz had a two-port aerial system. The apertures were very tiny and were positioned side by side. A servo arrangement was used to align and maintain the aerial system normal to the phase front as the target aspect was changed. Currently, a phase/amplitude measuring radar is used, such as that described in Section 8, above. Angular glint is then derived from the rate of change of phase with target aspect, in an on-line computer. Pulsed radars designed in this latter way are available up to and including 280 GHz.

Beyond 280 GHz, we have employed optical technology and developed a laser source for use at submillimetre wavelengths.

10. SUBMILLIMETRE MODELLING

A homodyne coherent c.w. radar, operating at 890 GHz, has been in continuous use over the past five years. It is based on an HCN laser which we have developed into a reliable, stable 30 mW source. The system can be used for determining angular glint or for identification of echo sources on targets, using the angular spectral analysis technique. The radar is illustrated in figure 11. The HCN laser, which is excited by gas-discharge, is shown in the foreground. The radar system is shown in diagrammatic form in figure 12. Power is extracted from both ends of the laser using coupling holes in the confocal mirrors forming the laser optical cavity. Most of the power is radiated from the end pointing at the target and this is phase modulated ($0/\pi$) at 500 Hz, using a toothed dielectric wheel. The unmodulated signal from the back end of the laser is used as reference in the radar receiver. The balanced mixer uses indium antimonide photo-conductors which require to be cooled in liquid helium to a temperature of 4.2 K. In the helium dewar, these are placed back to back and each is illuminated by the reference signal through its respective window. Diffraction gratings and mirrors are used to divide and direct the reference signal along the two separate paths. The received backscatter signal from the target is directed onto one mixer only, using a lens receiver aerial. The difference between the mixer output voltages is coupled out using a transformer and, in order to minimize noise contributions, this transformer also is included in the dewar. The selected signal component at 500 Hz is amplified and then translated to base-band using a phase-detector and a 500 Hz reference derived from the $0/\pi$ phase-modulator drive. Quadrature detection of the coherent return is achieved using a $0/\frac{\pi}{2}$ phase-modulator in the receiver path immediately before the mixer. Time multiplexed in-phase and quadrature components are therefore provided by the receiver. An output bandwidth of 1 Hz is used in each channel and a signal-to-noise ratio of 30 dB is obtained from a target having a 1 sq.cm echoing area when aerials of 3 deg beamwidth are used. A typical angular glint record is shown in figure 13.

11. ORGANIZATION AND VALIDATION OF DATA

With seven data collection sites within the facility, each collecting a large quantity of data, it is imperative that information is expressed digitally for on-line and off-line computer processing. A mini-computer is provided at each site and figure 14 indicates how it is used to provide suitable monitor displays so that the experiment operator can confirm the validity of the experiment and of its data. The computer is also used to monitor target and radar settings and to add measurement conditions in the form of a header block, thus facilitating subsequent additional processing of the data in an off-line general purpose computer.

12. PROCESSING AND USE OF DATA

For some purposes, it may be necessary for all of the data collected to be used in an analysis of the performance of an operational radar system. However, for many assessments, the quantity of raw data is embarrassingly great and suitable summaries have to be devised and computed. Sometimes these summaries consist merely of mean, median and standard deviation values of, say, the echoing area or the angular glint error within a given aspect angle region around the target. Often a much fuller summary is needed.

For many years (Woolcock, S. C., 1973), angular spectral analysis techniques have been used at EMI for interpreting backscatter data. Information from an azimuthal scan around a target with a coherent radar is processed using the appropriate weighting and 'window aperture' to obtain an angular spectrum. An angular spectrum gives the cross-range location of the elementary reflectors within a target, and also their intensities. Further, by moving the window through the data recorded as a function of target aspect, the polar diagram of these sources can be determined. Figure 15 shows an angular spectrum for an aircraft viewed near 10 deg from head-on. A very succinct representation of a complex target can be derived from such information, and it is often more efficient to store such a 'multi-source' model and compute the signal amplitude and glint at any aspect, than to store the initial data. Figure 16 compares measured and computer backscatter data, the computation having been carried out using the geometry of the measurements. It is possible, using the mathematical model, to compute the radar signal characteristics for other target-to-radar ranges than that which was modelled. Thus time-varying backscatter signals can be obtained. For study of coherent radars in a computer, multi-source models of the 'skin' doppler backscatter would be derived as above and then a mathematical representation of doppler components from turbines, compressors and propellors would be added.

13. FUTURE DEVELOPMENTS

The radar modelling facility has been in full time use and also continually under development for the last 20 years. It is likely that such developments will continue. Exploitation of the frequency band between 200 GHz and 2 THz is clearly needed. This will require source development and also mixer developments. Submillimetre lasers excited by photons at 10.6 μm have already been made with several different active gases and have produced usable outputs at more than 30 frequencies in the band quoted. Figure 17 shows a laboratory submillimetre source which can be tuned to many different frequencies between 0.4 THz and 2.0 THz. The bandwidths of some of the transitions give promise that pulsed sources of such wavelengths can be made with pulse lengths suitable for range gating in a model range.

The distinctive expertise which this facility has nurtured, and the detailed understanding of radar scattering problems which has been acquired, are a special strength within NATO. A service is offered to all NATO countries in radar analysis and scattering problems.

This service has been used for many years by some of the more progressive companies in the U.S.A. and it is anticipated that companies in other NATO countries will appreciate the technical advantage which this conveys and will increase their own interest in using the facility here described. Such increased use will not only benefit NATO radar development but will also highlight other desirable extensions to the service offered by the facility.

14. ACKNOWLEDGEMENTS

We wish to acknowledge the continued support of the MOD and of the RSRE in this work.

15. REFERENCES

Cram L.A., Woolcock S.C., and Johnson R.H., 1973
'Radio Scale Modelling in support of Radar System Design and Assessment of Performance'
IEE Conference Publication No. 105
'Radar - Present and Future' London pp 422-430.

Cram L.A., and Staveley J.R., 1977
'Recent Developments in Scale Modelling of Radar Reflections by Radar and Sonar Methods'
IEE Conference Publication No. 155
'Radar 77' London pp 473-477.

Cram L.A., 1973 AGARD Lecture Series No. 59
'Determination and Use of Radar Scattering Characteristics'.

Woolcock S.C., 1973 Lecture 3(b) of AGARD Lecture Series No. 59
'Use of Radio Modelling Data'.

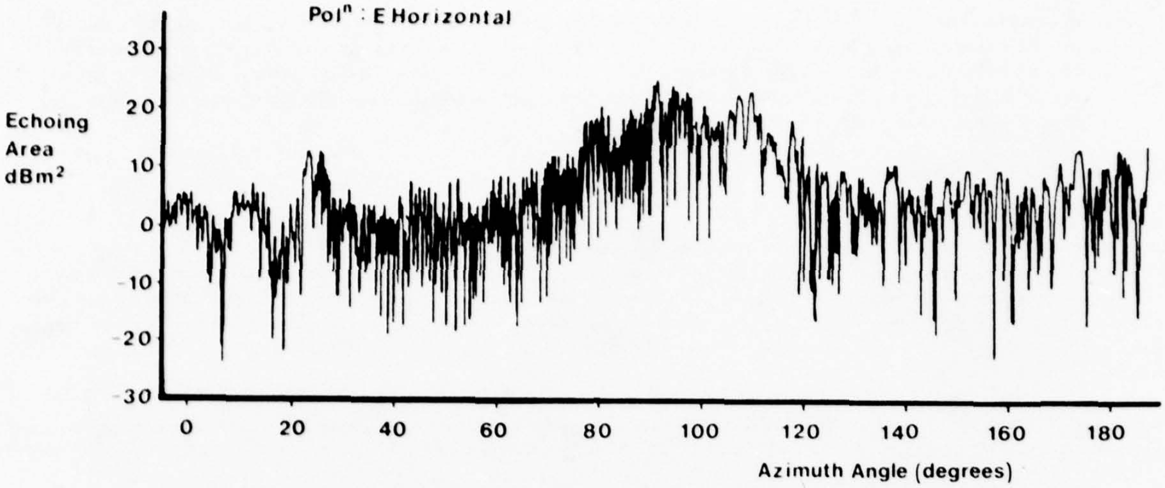

Fig. 1 - Typical Echoing Area of HS 125 at 3 GHz

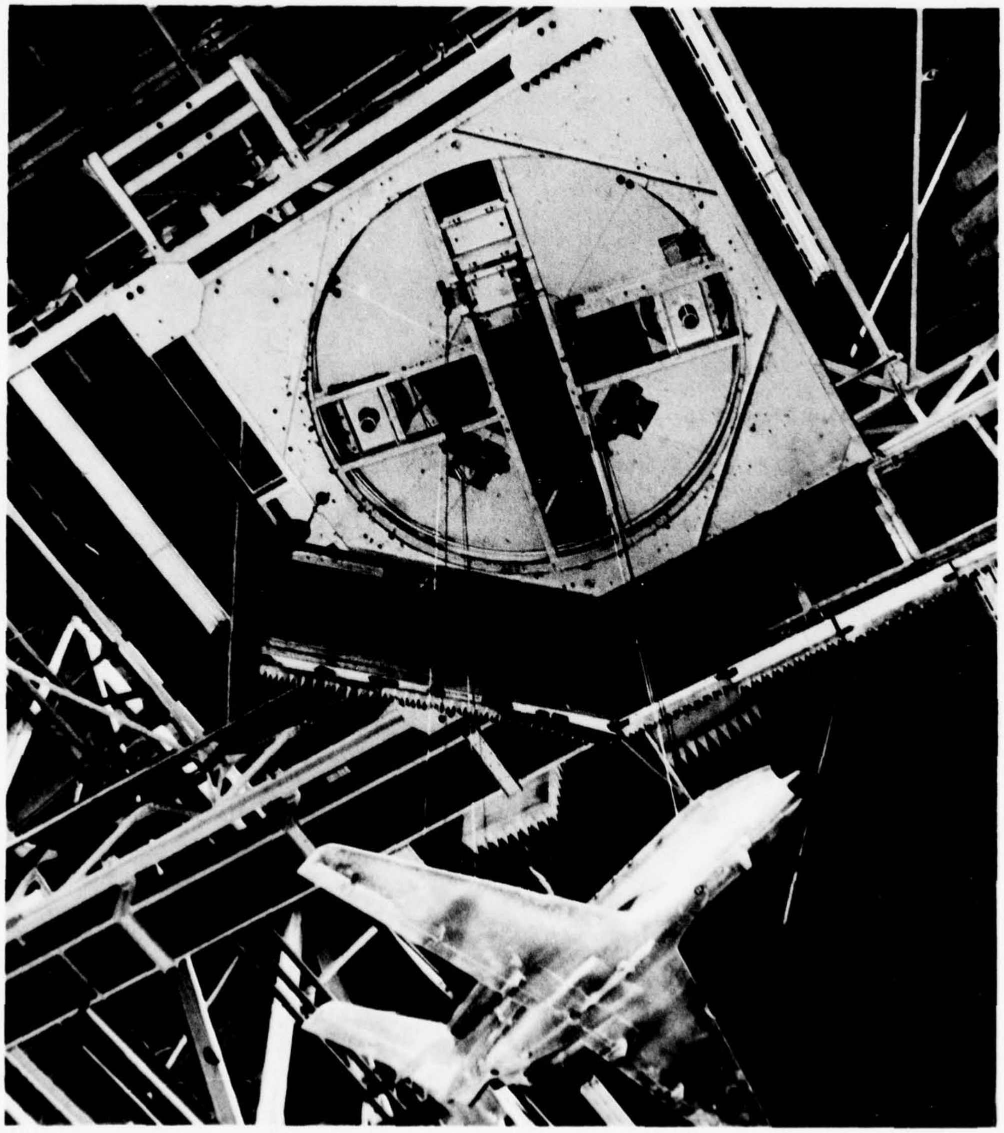

Fig. 2 - Gantry with HS 125 Model Suspended

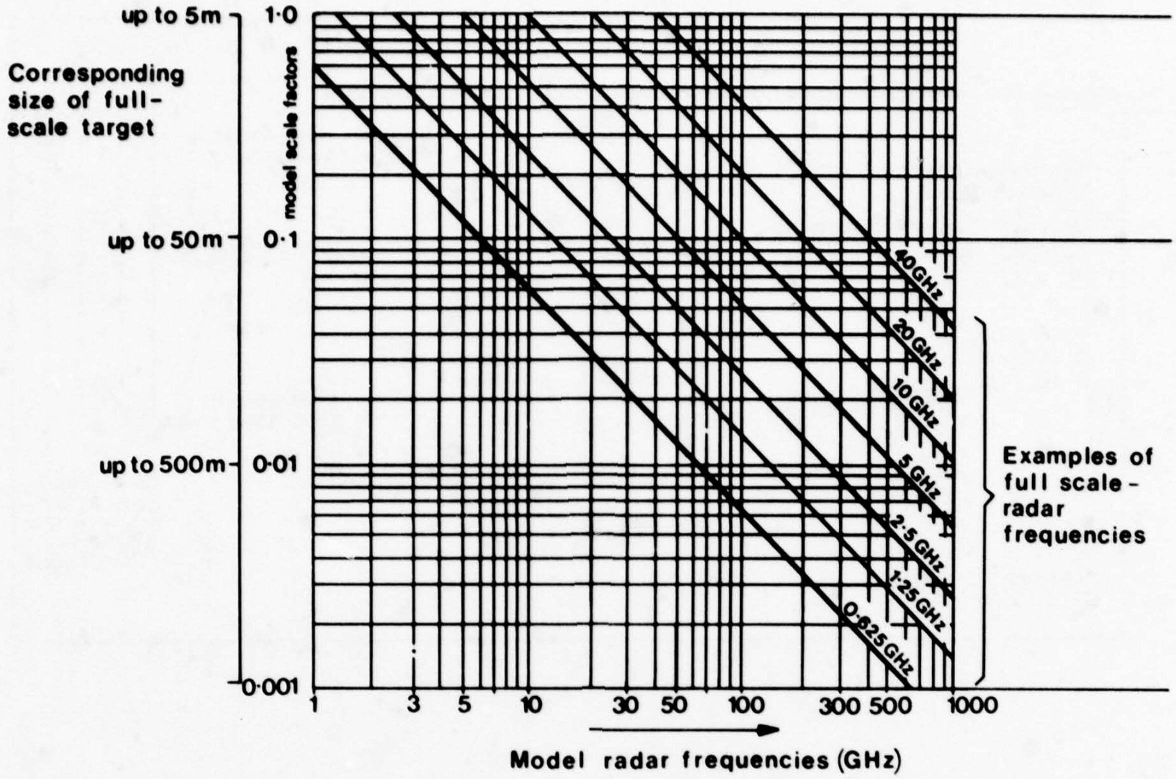

Fig. 3 - Chart of Radar Modelling Facilities

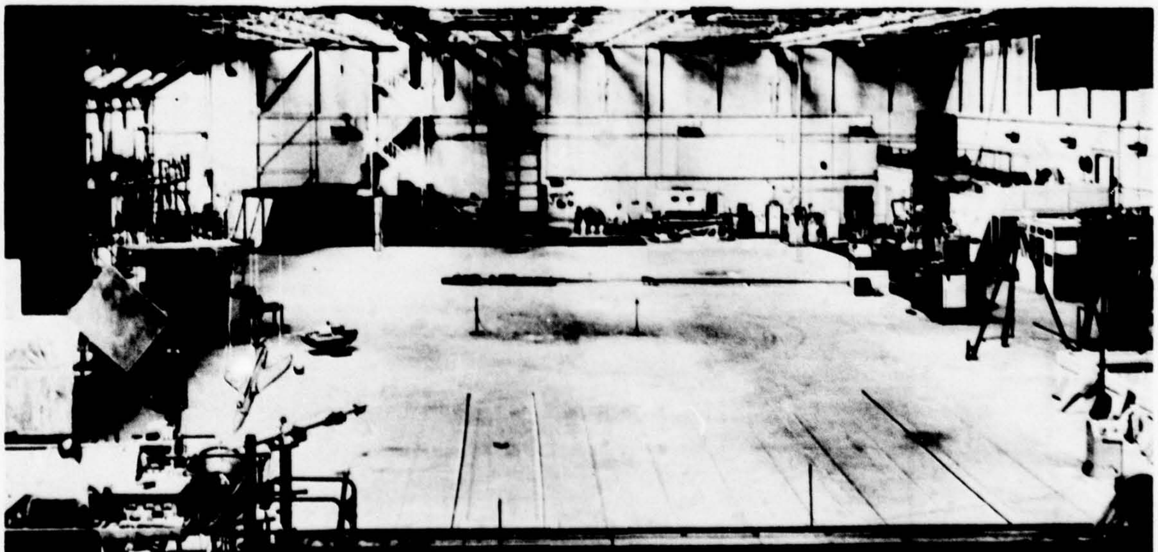

Fig. 4 - General View of Radar Modelling Facility

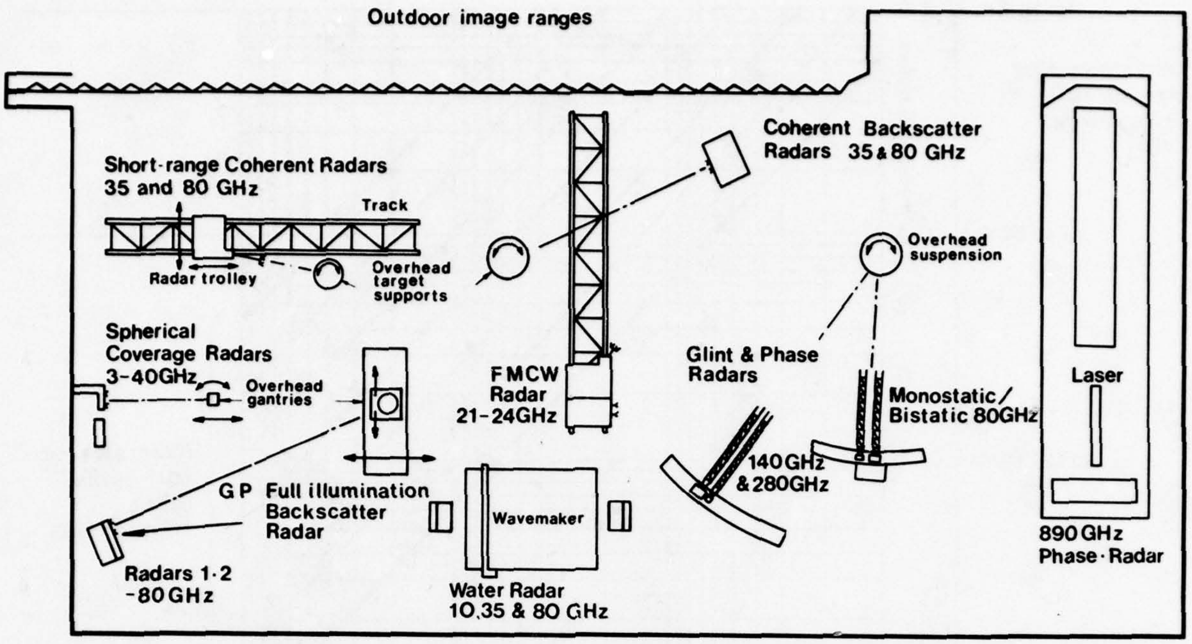
Outdoor image ranges
Short-range Coherent Radars
35 and 80 GHz
Track
Radar trolley
Overhead
target
supports
Coherent Backscatter
Radars 35 & 80 GHz
Overhead
suspension
Spherical
Coverage Radars
3-40GHz
Overhead
gantries
FMCW
Radar
21-24GHz
Glint & Phase
Radars
Monostatic/
Bistatic 80GHz
Laser
140GHz
& 280GHz
GP Full illumination
Backscatter
Radar
Wavemaker
Radars 1·2
-80GHz
Water Radar
10,35 & 80 GHz
890 GHz
Phase·Radar

Fig. 5 - Plan of Radar Modelling Facilities

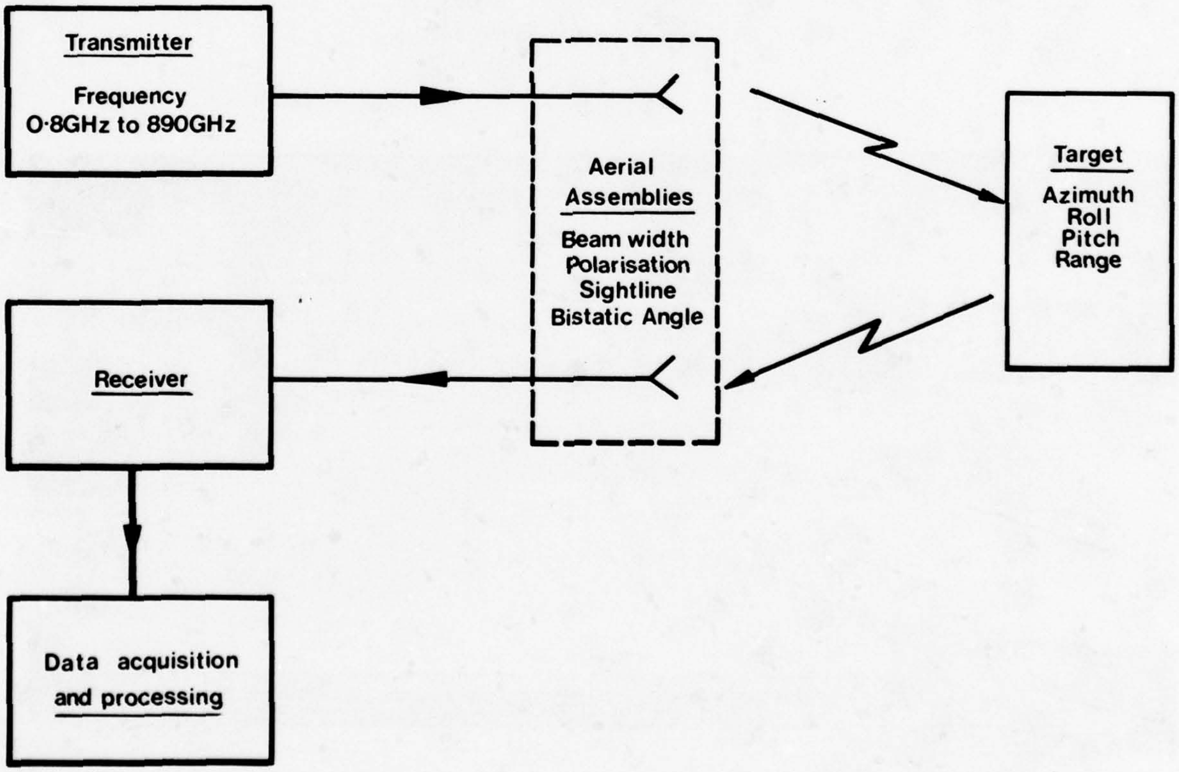
Transmitter
Frequency
0·8GHz to 890GHz
Aerial
Assemblies
Beam width
Polarisation
Sightline
Bistatic Angle
Target
Azimuth
Roll
Pitch
Range
Receiver
Data acquisition
and processing

Fig. 6 - Radar Modelling Measurement System

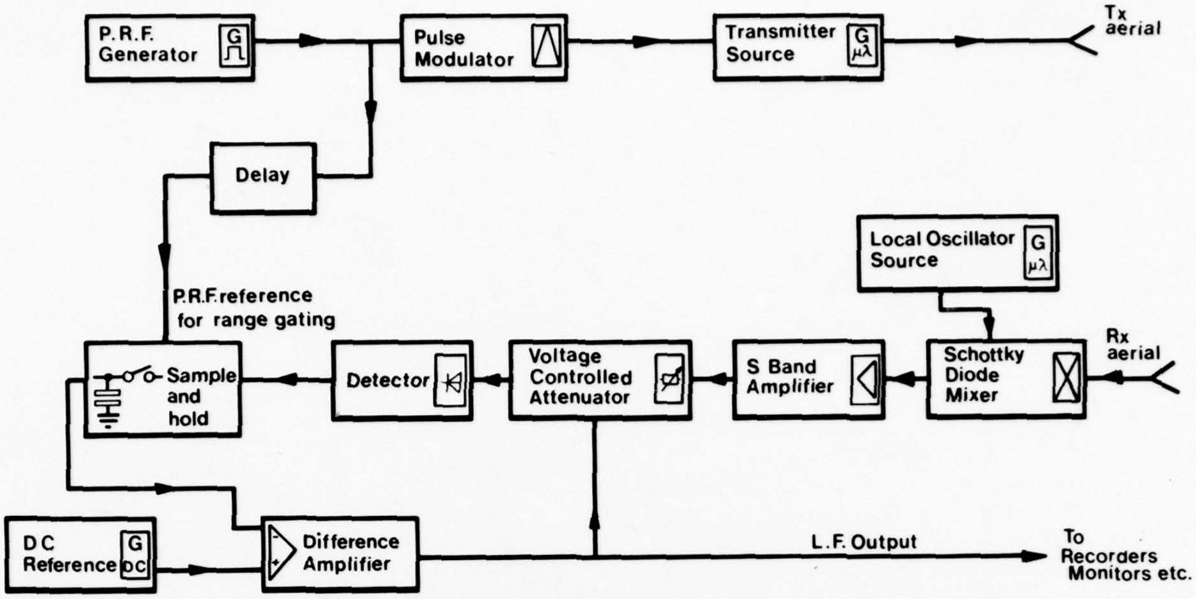
P.R.F. Generator
G
Pulse Modulator
Transmitter Source
G
μλ
Tx aerial
Delay
Local Oscillator Source
G
μλ
P.R.F. reference for range gating
Rx aerial
Sample and hold
Detector
Voltage Controlled Attenuator
S Band Amplifier
Schottky Diode Mixer
DC Reference
G
DC
Difference Amplifier
L.F. Output
To Recorders Monitors etc.

Fig. 7 - Measurement Radar with Non-Coherent Receiver

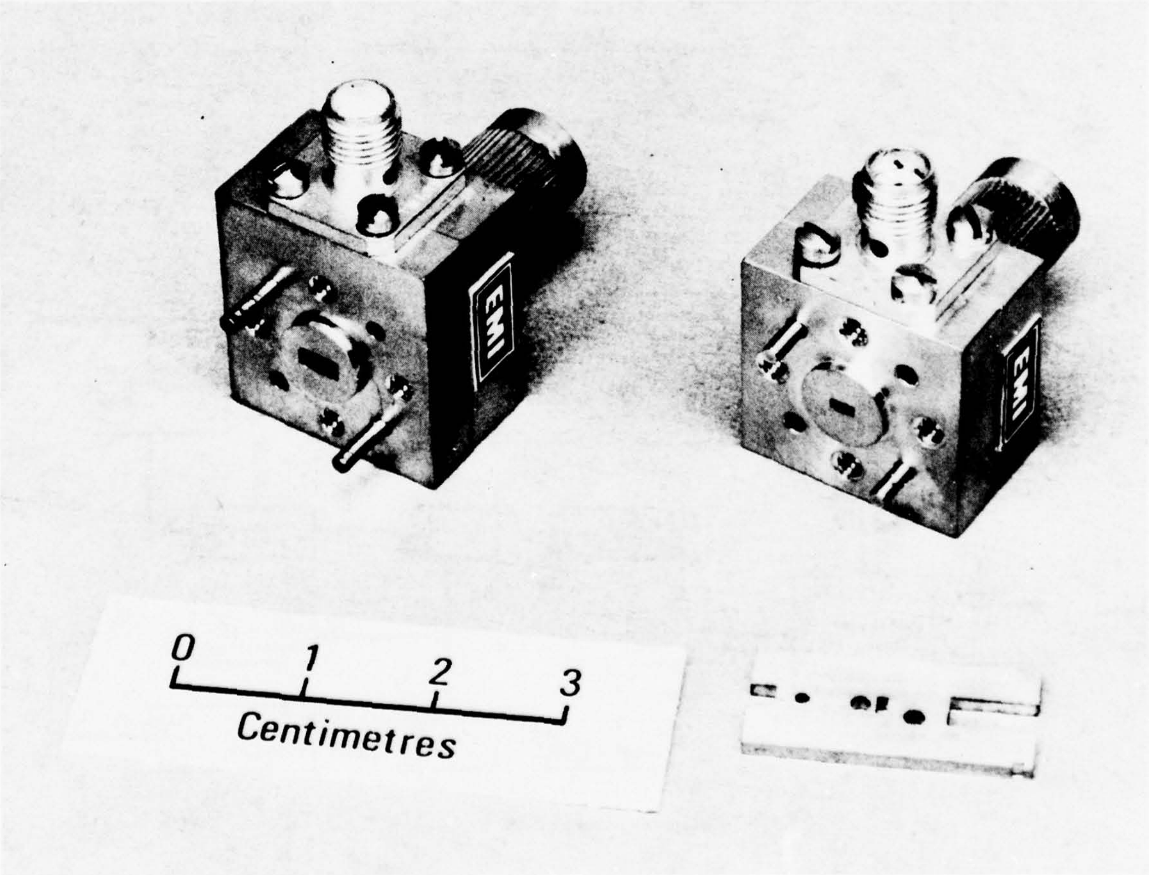
EMI
EMI
0
1
2
3
Centimetres

Fig. 8a - Examples of Schottky Millimetric Mixers 50-75 GHz (WR5) and 90-140 GHz (WR8)

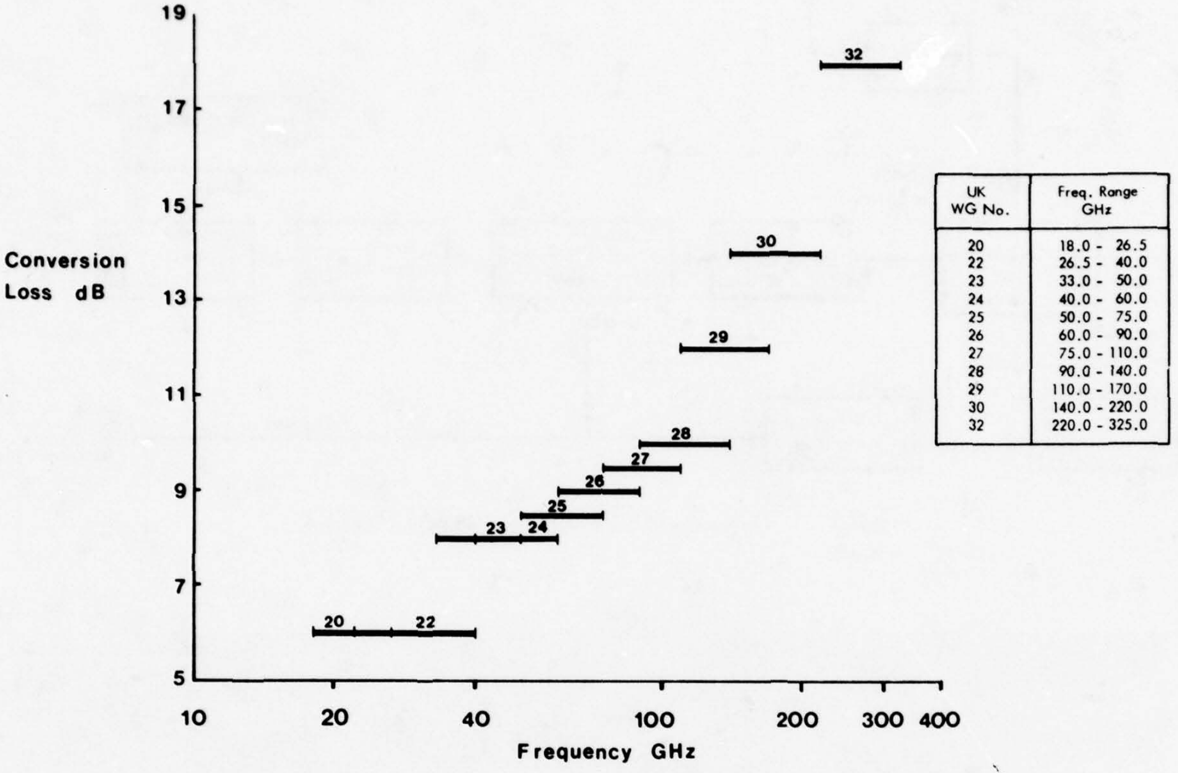

UK WG No.	Freq. Range GHz
20	18.0 - 26.5
22	26.5 - 40.0
23	33.0 - 50.0
24	40.0 - 60.0
25	50.0 - 75.0
26	60.0 - 90.0
27	75.0 - 110.0
28	90.0 - 140.0
29	110.0 - 170.0
30	140.0 - 220.0
32	220.0 - 325.0

Fig. 8b - Achieved Conversion Losses for Range of Millimetric Mixers

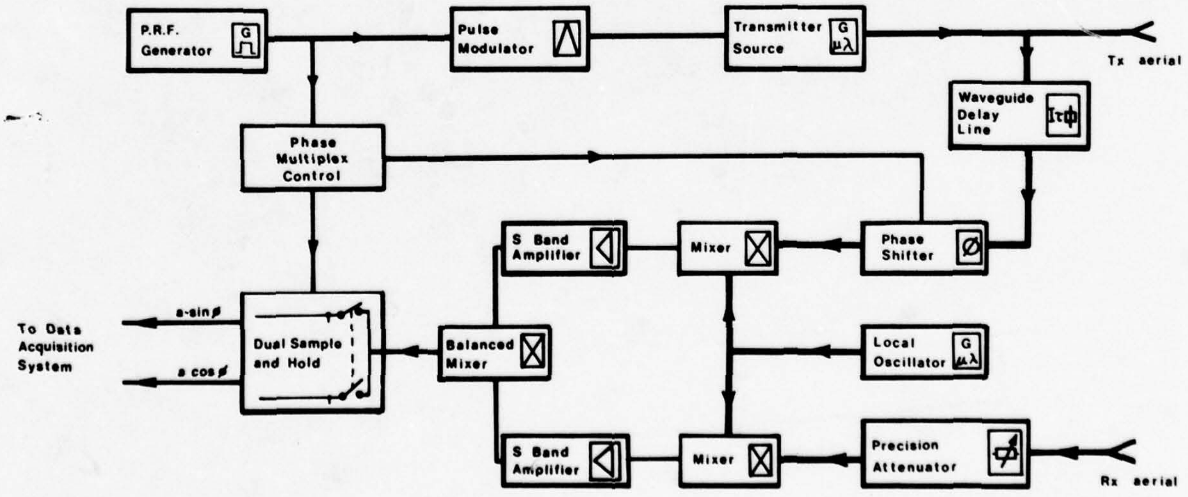
P.R.F. Generator
G
Pulse Modulator
Transmitter Source
G
μλ
Tx aerial
Waveguide Delay Line
Phase Multiplex Control
S Band Amplifier
Mixer
Phase Shifter
To Data Acquisition System
a-sinø
a cosø
Dual Sample and Hold
Balanced Mixer
Local Oscillator
G
μλ
S Band Amplifier
Mixer
Precision Attenuator
Rx aerial

Fig. 9 - Measurement Radar with Coherent Receiver

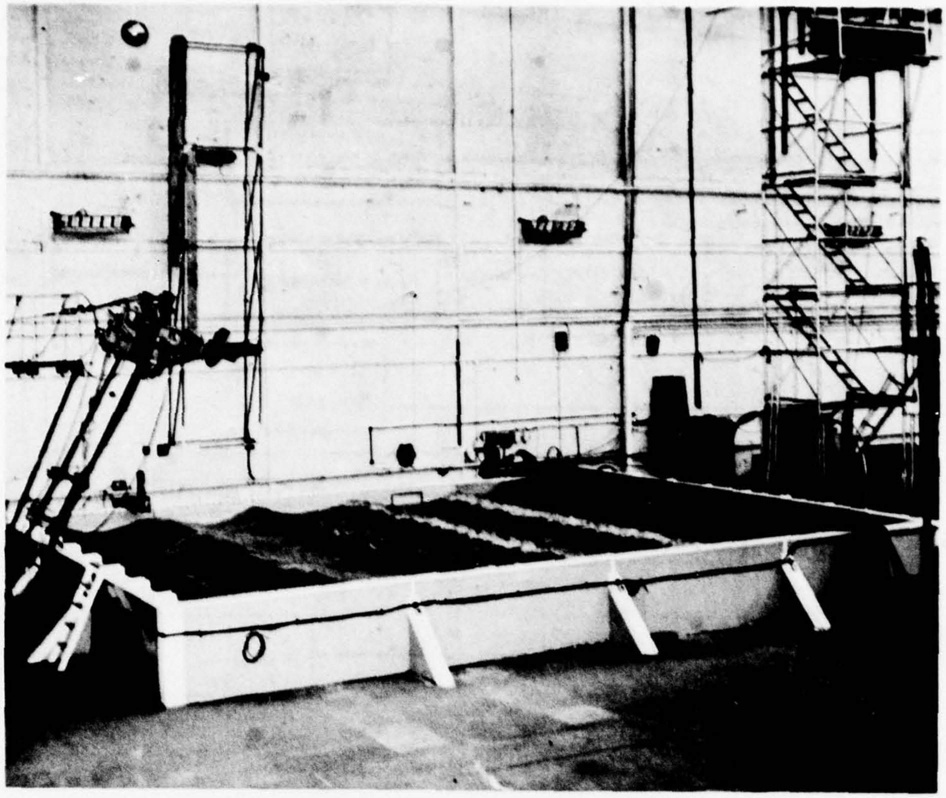

Fig. 10 - Water Reflectivity Measurement Facility

Fig. 11 - 890 GHz Radar Facility

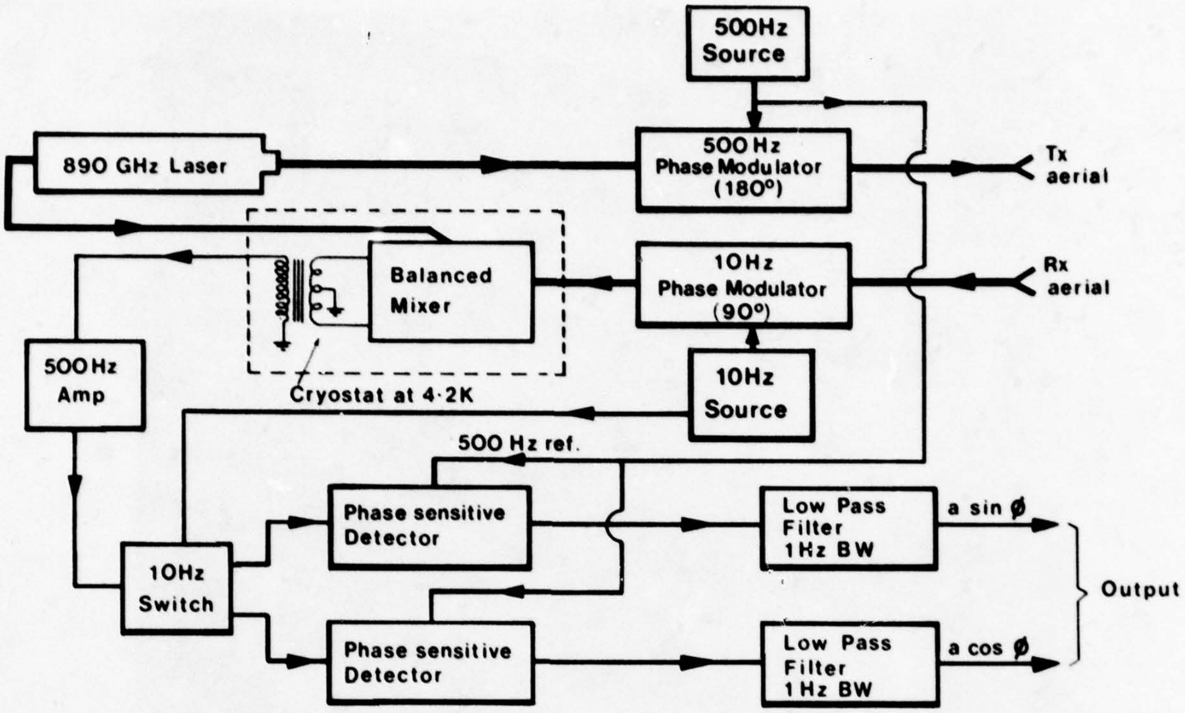
500Hz Source
890 GHz Laser
500 Hz Phase Modulator (180°)
Tx aerial
Balanced Mixer
10 Hz Phase Modulator (90°)
Rx aerial
500 Hz Amp
Cryostat at 4·2K
10Hz Source
500 Hz ref.
Phase sensitive Detector
Low Pass Filter 1 Hz BW
a sin Ø
10Hz Switch
Output
Phase sensitive Detector
Low Pass Filter 1 Hz BW
a cos Ø

Fig. 12 - 890 GHz Radar System

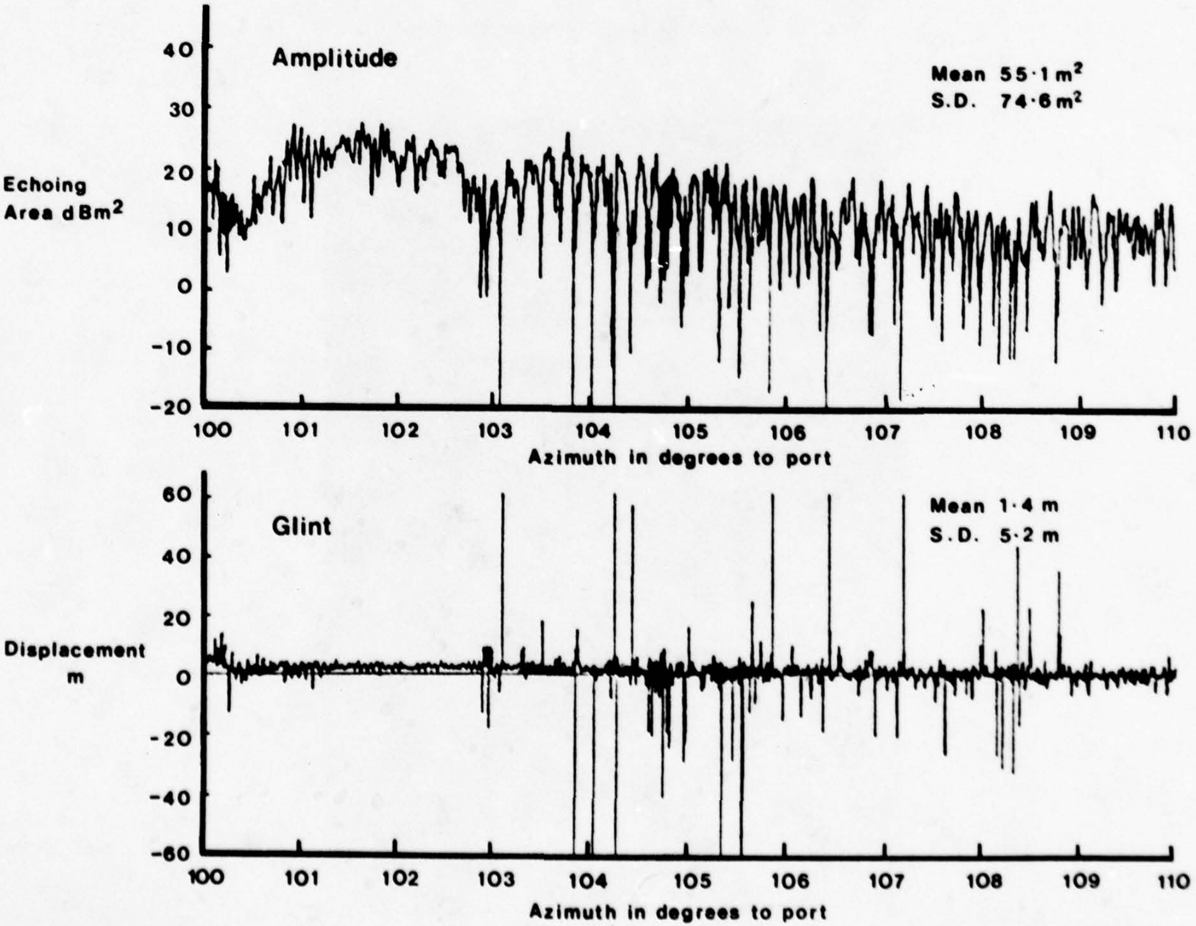

Fig. 13 - Typical Amplitude and Glint Plots from Radar Modelling

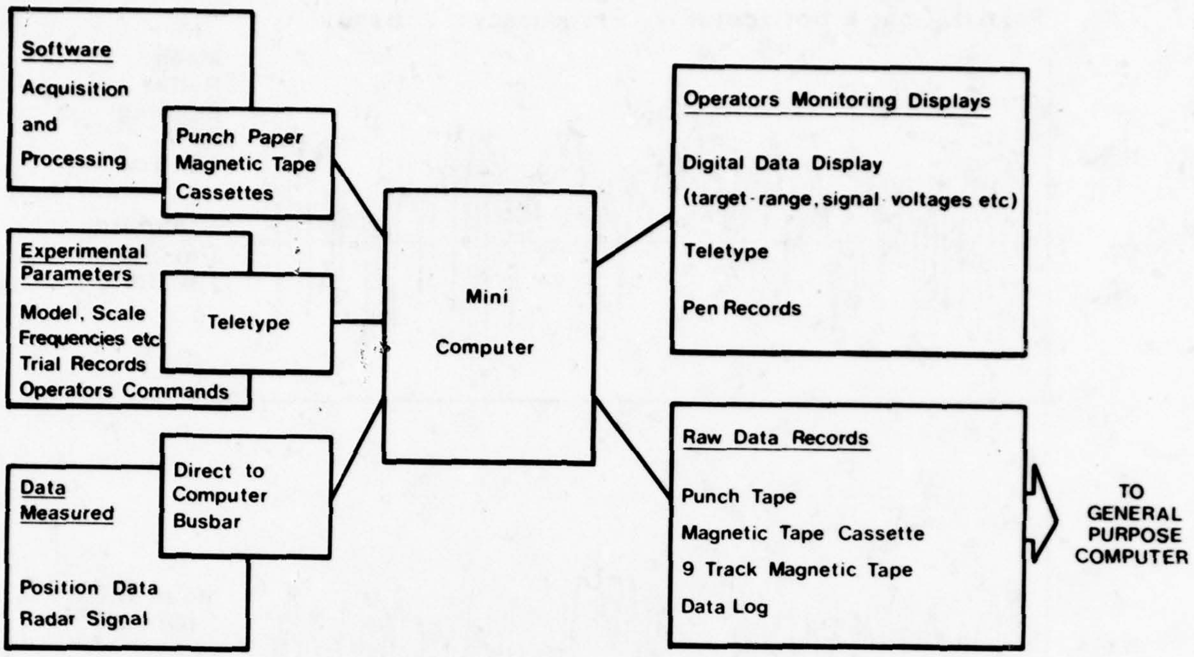
Software
Acquisition
and
Processing
Punch Paper
Magnetic Tape
Cassettes
Experimental Parameters
Model, Scale
Frequencies etc
Trial Records
Operators Commands
Teletype
Data Measured
Direct to
Computer
Busbar
Position Data
Radar Signal
Mini
Computer
Operators Monitoring Displays
Digital Data Display
(target-range, signal voltages etc)
Teletype
Pen Records
Raw Data Records
Punch Tape
Magnetic Tape Cassette
9 Track Magnetic Tape
Data Log
TO
GENERAL
PURPOSE
COMPUTER

Fig. 14 - Data Collection and Validation

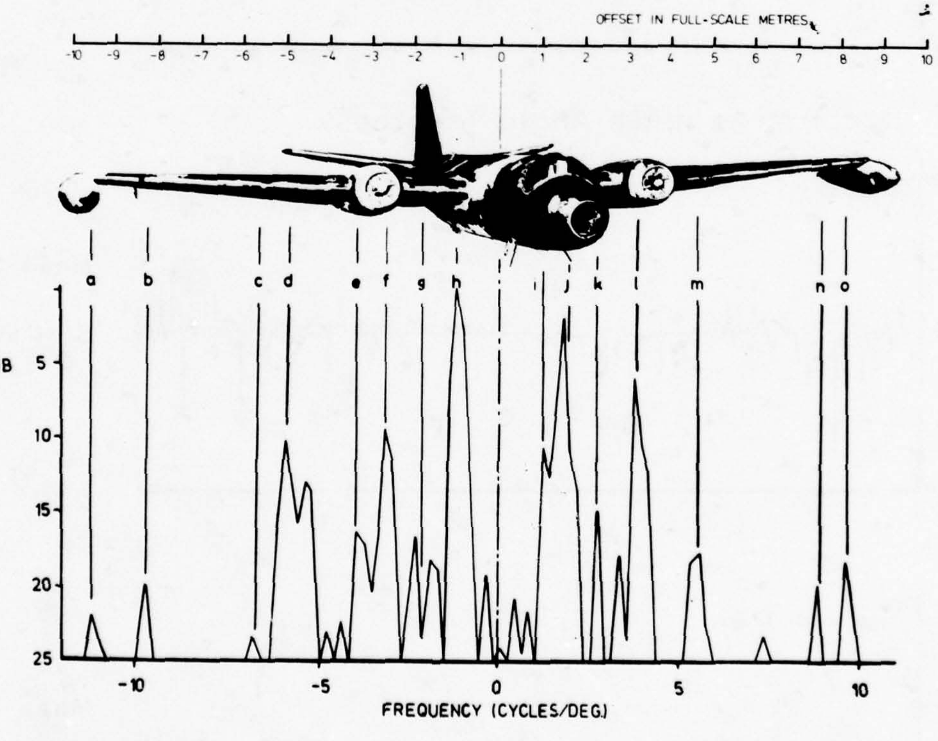

a-Stbd. wing tank
b-Stbd. wing aerial
c-Stbd. inner aerial
d-Stbd. outer wing edge
e-Stbd. engine outer lip
f-Stbd. engine

g-Tail
h-Corner reflector - Stbd. inner wing + Fuselage
i-Cockpit
j-Nose

k-Corner reflector - Port engine + Inner wing
l- Port engine
m-Port wing control surface (?)
n-Port outer aerial
o-Port wing tank

Radar wavelength - 3cm equivalent
Azimuth window - between 7deg. and 17deg. to stbd.

Fig. 15 - Identification of Sources by Angular Spectrum Analysis

Polarization: E Horizontal **Frequency: X Band**

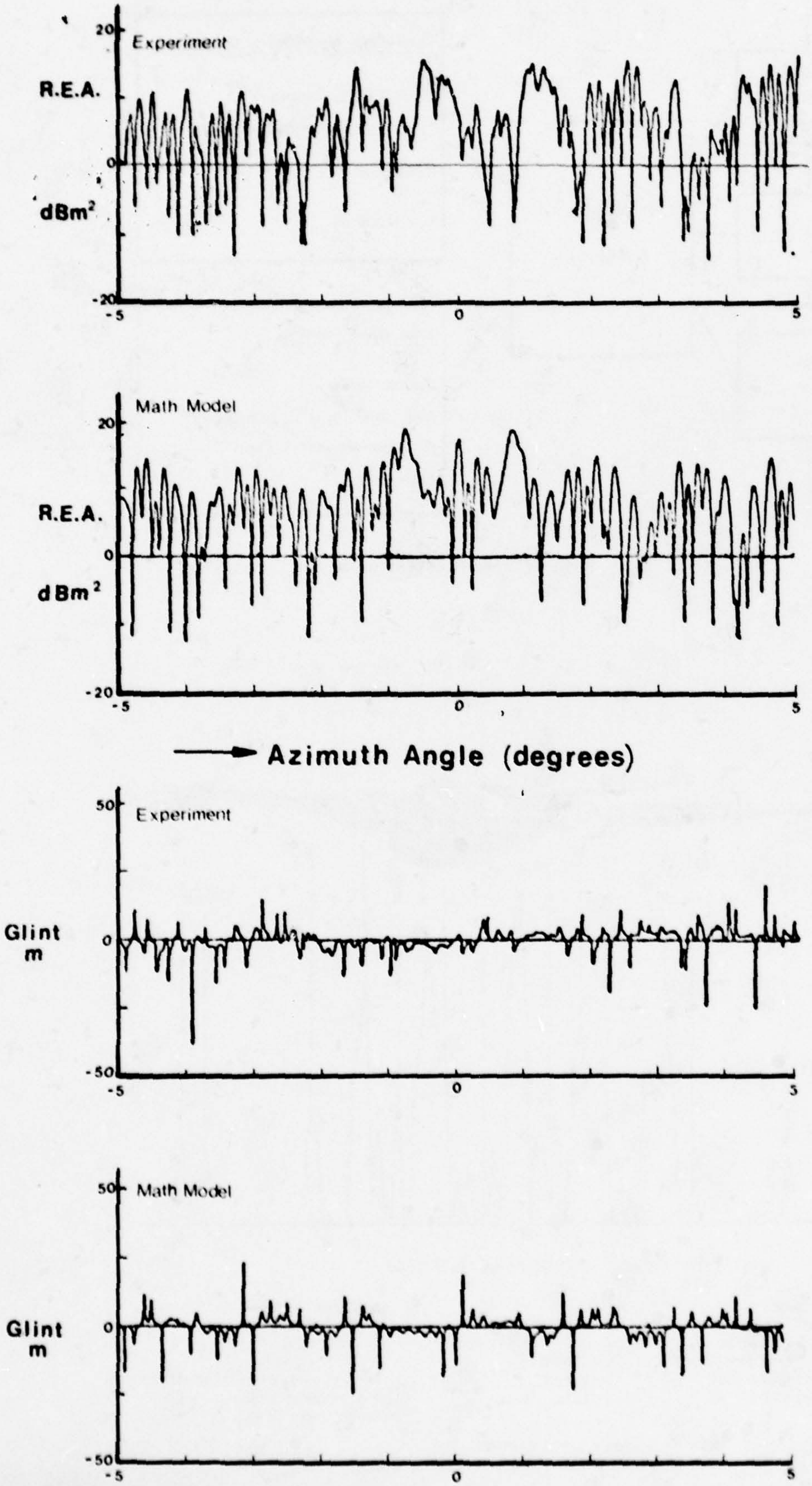

Mean Radar Echoing Area : 7·6 m²

Standard Deviation : 8·3 m²

Mean R.E.A. : 10·4 m²

St. Dev'n. : 12·4 m²

Mean : 0m

St. Dev'n. : 3·9 m

Mean :- 0·2m

St. Dev'n. : 3·5 m

Fig. 16 - Multisource Mathematical Model Compared with Experimental Plots

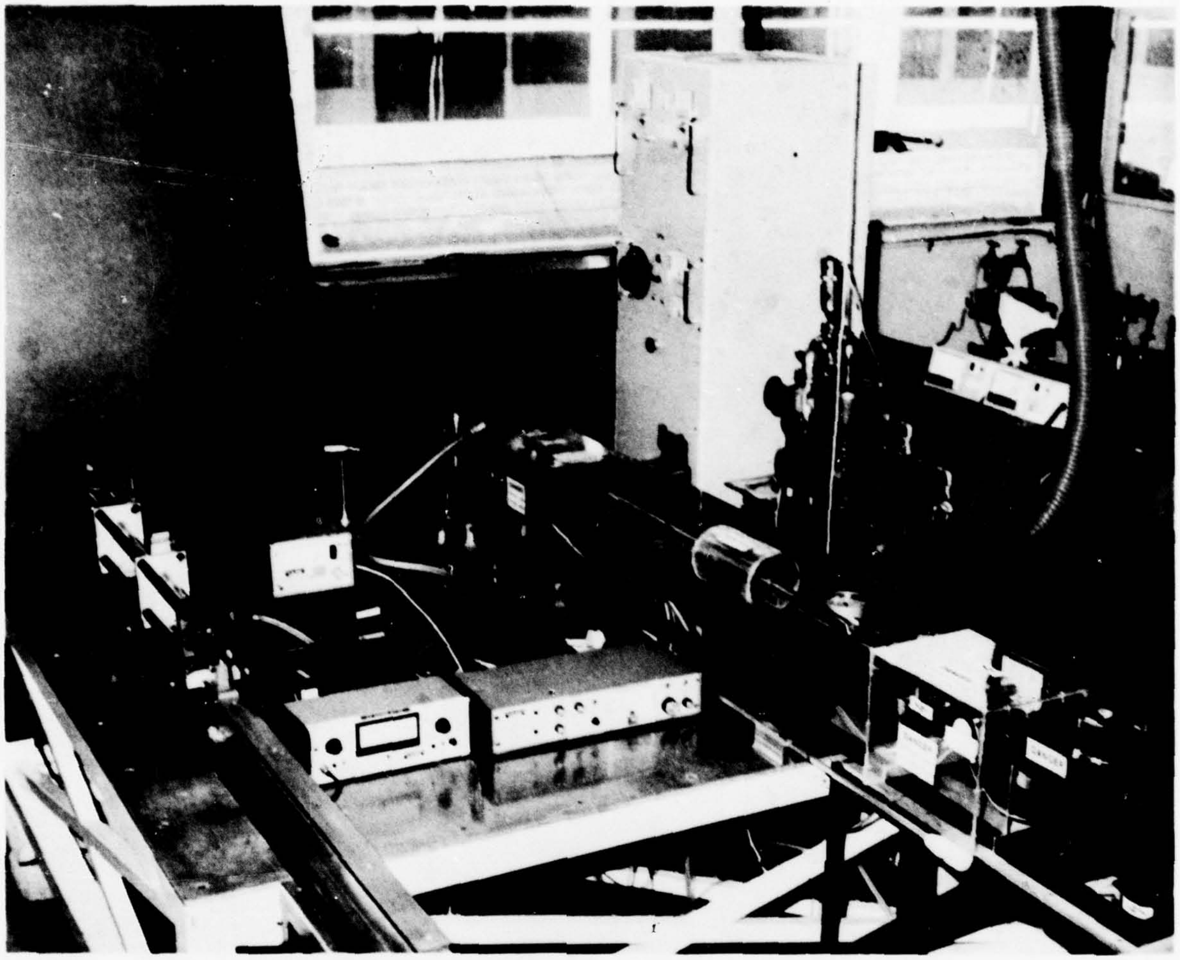

Fig. 17 - Experimental 2 THz Source

DISCUSSION

Hans Brand, FRG

Can you please give some comment on the 500-Hz phase shifter used for the 890-GHz laser transmitter?

Author's Reply

This was simply a toothed wheel of dielectric material of a suitable thickness to give $n\lambda/2$ delay in comparison with the air path (where n is a convenient small number, say three).

Model Simulation
# of Target Characteristics
and Engagement Situations Employing
Millimetre Wave Radar Systems

by

W. Gabsdil
W. Jacobi
AEG-TELEFUNKEN ULM
Elisabethenstr. 3
7900 Ulm / Donau
Germany

1 Introduction

In the development of radar proximity fuzes - which is done at AEG-TELEFUNKEN since about 1960 - one has on principle to deal with a radar system where the received signal is used to measure the encounter geometry between fuze and target and to determine from this the optimum detonation point.

This measurement is carried out in the extreme near-field of the target - normally aircraft - thus the distance between target and sensor is about maximum one order of magnitude greater than the target dimension while the radar operating wavelength is about a hundredth off.

Thus the normally used radar equation is no longer valid, the radar does not see a single fluctuating point target, but a number of reflection points whose amplitudes and locations are changing during the engagement, summing up or interfering to form a really complex signal.

On the other hand, these signals are needed first to optimize the system as well as to determine the effectiveness of the entire system and this has to be done for the whole set of possible encounter geometries.

On principle there are three solutions to this problem

- theoretical computation
- use of original targets in real flight tests
- use of down-scaled model measurements.

The first solution, the theoretical computation of these signals, leads to extreme difficulties although the different possible approaches - wire grid model, plate model and physical optics - are already approximations.

It is, nevertheless, worth to note that a very simple geometric optics-model leads in some special cases to satisfactory results. In this model, the complex target is represented by a few - typically 3 to 10 - point sources but the amplitudes and exact locations of these point sources have to be determined in general first by measurements.

The use of original targets in real flight tests is a possible solution. Figure 1 shows such a flight test where the radar fuze is on top of the mast and the marks on the left side are used for measuring the flight geometry.

Despite of the fact that such experiments may be dangerous, especially for small misdistances, they are of course very expensive and extremely difficult to control. Therefore they can at the most be used as limited, selected basic data but not as the required comprehensive data set for all interesting encounter geometries.

Therefore only the third solution, model measurement, remains valid and has in fact given a satisfactory solution for our problem.

2 Model Simulation

The possibility to use down-scaled model simulation is given by the linearity of Maxwell's equations. If one excludes non-linear media as ferromagnetics or ionized media with magnetic fields, the valid transformation equations are given in Figure 2. Here the index "O" stands for "original" and "m" for "model", respectively.

There are two basic scale factors

a) one of which governs the basic electromagnetic properties as well as target dimension

b) while the other one takes into account the scaling of time dependent properties.

Since the interesting targets are metallic ones and provided that the conductivity of model metallisation is high enough - the received target signal is only dependent on the ratio of target dimension to radar wavelength. Furthermore, the signal amplitude is independent of the relative engagement velocity which only determines the frequency speed of the doppler signal. The original signal can then be easily obtained by time transformation using different recording and reproducing scale factors.

3 Experimental set-up

In our model simulations at AEG-TELEFUNKEN in Ulm, we use radar systems with frequencies up to 90 GHz, usually with emphasis at 33 GHz and 86 GHz, corresponding to scaling factors of about 10 - 30. The radar sensors used are normal CW systems with the block diagram shown in Figure 3.

The transmitted signal provided by a gun oscillator at the lower and an impatt-oscillator at the higher frequency is fed via an antenna duplexer to the antenna. The received signal is mixed with a part of the transmitter signal supplied via a coupler or directly via the reverse circulator path. The resulting video signal is then amplified and recorded.

The RF output power of these radars is of about 100 mW at the lower frequencies down to 20 mW at the higher frequencies. The antennas used in the model simulation should show the same gain and beamwidth as the original ones, a requirement which may lead to problems which will be discussed later.

The next Figure 4 shows our simulation facility. The whole measuring set-up is housed in an anechoic chamber with the dimensions 15 by 4 meters. The target model, here a MIG 21 (a Fishbed), is mounted on top of a plastic rod which itself is mounted on a movable platform. This platform is driven on rails past the fixed radar at a constant speed of about 0.5 m/s.

Platform and rails are under microwave absorber plates which are tilted to avoid multipath problems. This measurement method, fixed radar and moving target, is in contrast to methods used in similar facilities in the UK and France where the radar is moved.

Therefore some comments why we proceed in this manner:

When moving our CW radars which do not have range resolution and low antenna gains the chamber walls, even when covered with best absorber material, would give high radar returns at target doppler frequencies. In our set-up only the moved platform and the target mounting can introduce error signals but this can be overcome by proper construction and the use of absorber material.

The recording set-up is shown in Figure 5. Instead of recording the measured signals with analog tape recorders we now use a 32 k, 8 bit transient recorder for intermediate storage. This has the advantage that the recording as well as the reproducing of the signal can be done at any desired speed.

For immediate inspection a display is used and last not least the signals are recorded in digital form on normal commercial tape cassettes.

Further data processing including fuze logics are up to now introduced off-range but we are just integrating a small computer in the system which, as we hope, will at least do a part of this on-line.

4 Results

Figure 6 shows - as an example - the measured signal for a sphere with a radius of 10 centimeters which is normally used for calibration purposes.

The four traces show the signal recorded with for different gain factors at the top distance marks are shown. The decrease of the doppler frequency when approaching the point of nearest distance as well as the jump in phase at this point is easily seen.

The next Figure 7 shows the signal of the real aircraft target, here a FIAT G 91, in a nearly head-on geometry. This picture shows clearly the "interference packets", typical for these complex targets as well as a general feature, that is decreasing frequency with decreasing distance, valid for the point target.

This fact is in detail shown in Figure 8 and Figure 9 where for this signal the power spectral densities are given for different time intervals. Time interval a) shows the small peak given by the relative target velocity while interval c) shows the broad low frequency spectrum when the sensor is near the part of closest approach.

5 Modelling problems

The models of aircraft, missiles and helicopters are made of wood which is then silver sprayed sufficiently to give about 5 skin depth at the corresponding model frequency. For the higher scale factors we also use commercial plastic model kits with good results. These models have the advantage of being light that means giving no mounting problems as well as become very cheap ones in contrast to the wood modules.

The choice of a scale factor as high as possible has the advantage that this leads to small dimensions of the targets as well as to small dimensions of the whole measuring set-up. Especially from a practical commercial point of view the last point is a very important one. Also the corresponding higher frequencies lead, for given relative velocities, to higher doppler frequencies. This means in general higher signal to noise ratio by avoiding frequency noise problems such as 50 Hz power lines, amplifier drift and so on as well as lower requirement on spectral purity of the RF oscillator.

Nevertheless there are some practical limits for the scale factor. First the lower sensor sensitivities at the higher frequencies at least for a given cost level. Also target dimension may reach a level where the modelling of the target details will be a problem.

Therefore we feel that scale factors in the order of 10 to 30 will be an optimum choice.

A special problem arises from the fact that at least in our case, in the original systems, the antennas are smaller than the wavelength. Therefore it is normally not possible to scale down these antennas and therefore new antenna design at the model frequency is necessary.

The next Figure 10 shows, for example, a low gain 90 GHz antenna which was developed in our central millimeter laboratory by Dr. Rembold an his staff.

6 Conclusion

Millimeter wave systems have been very successfully used for model simulation measurements to determine the near-field characteristics of complex targets.

These data are used for system optimisation, for the proof of system effectivity and are also used now for quality control in the production of the systems.

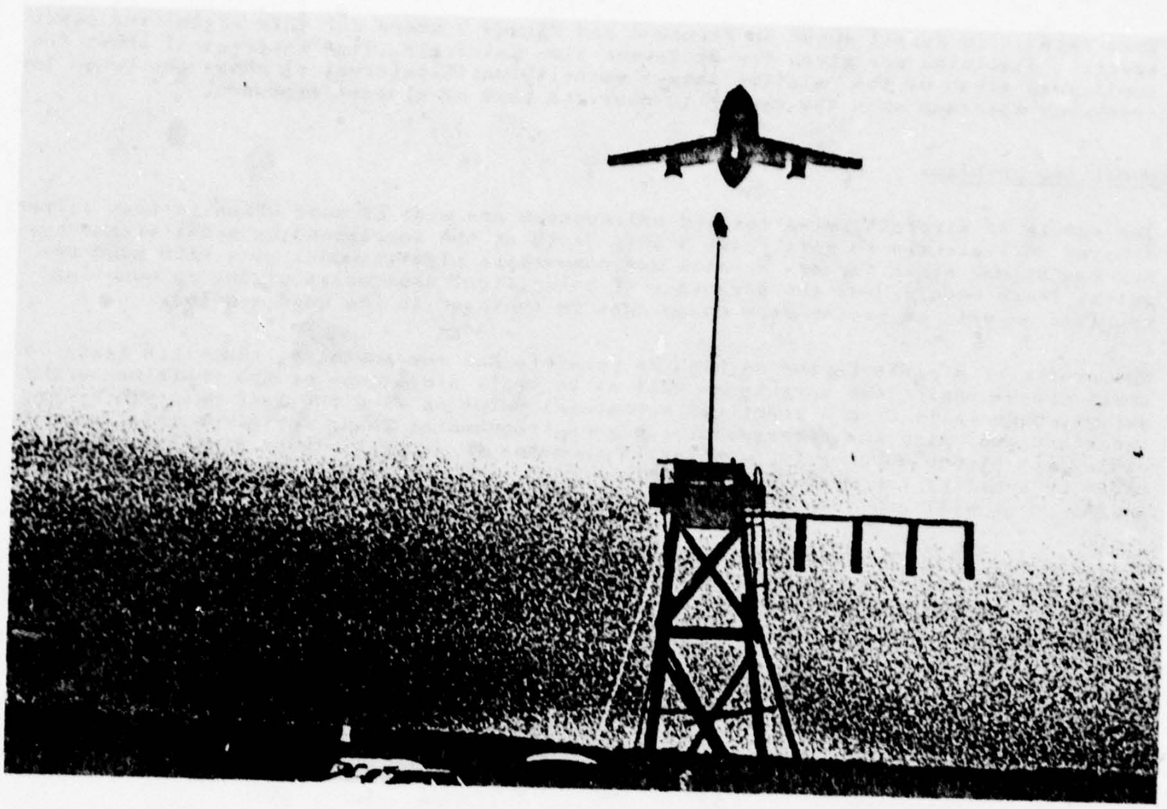

Fig.1 Fly-over trials

Length	$l_m = \frac{1}{q} l_o$
Frequency	$f_m = q f_o$
Conductivity	$\sigma_m = q \sigma_o$
Cross Section	$\sigma_{Rm} = \frac{1}{q^2} \sigma_{Ro}$
Antenna gain	$g_m = g_o$
Velocity	$v_m = \frac{1}{k} v_o$
Doppler frequency	$f_{Dm} = \frac{q}{k} f_{Do}$
Reprod. factor	$p = \frac{k}{q}$

Fig.2 Scaling of parameters

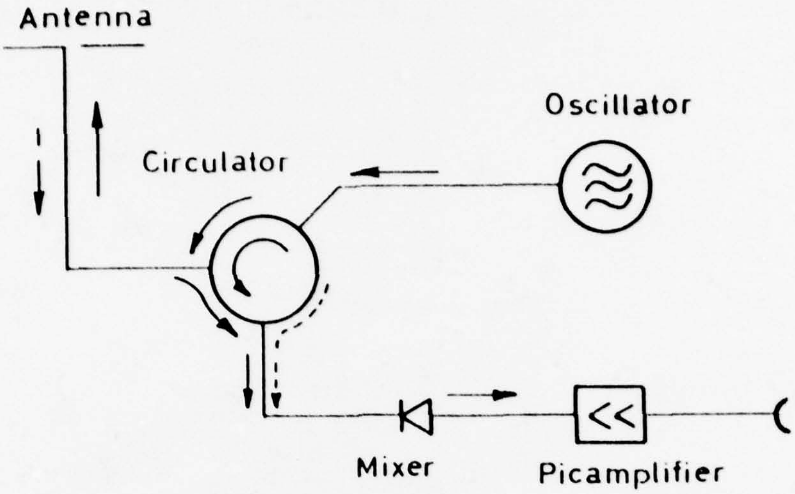
Antenna
Oscillator
Circulator
Mixer
Picamplifier

Fig.3 Blockdiagram of radar sensors

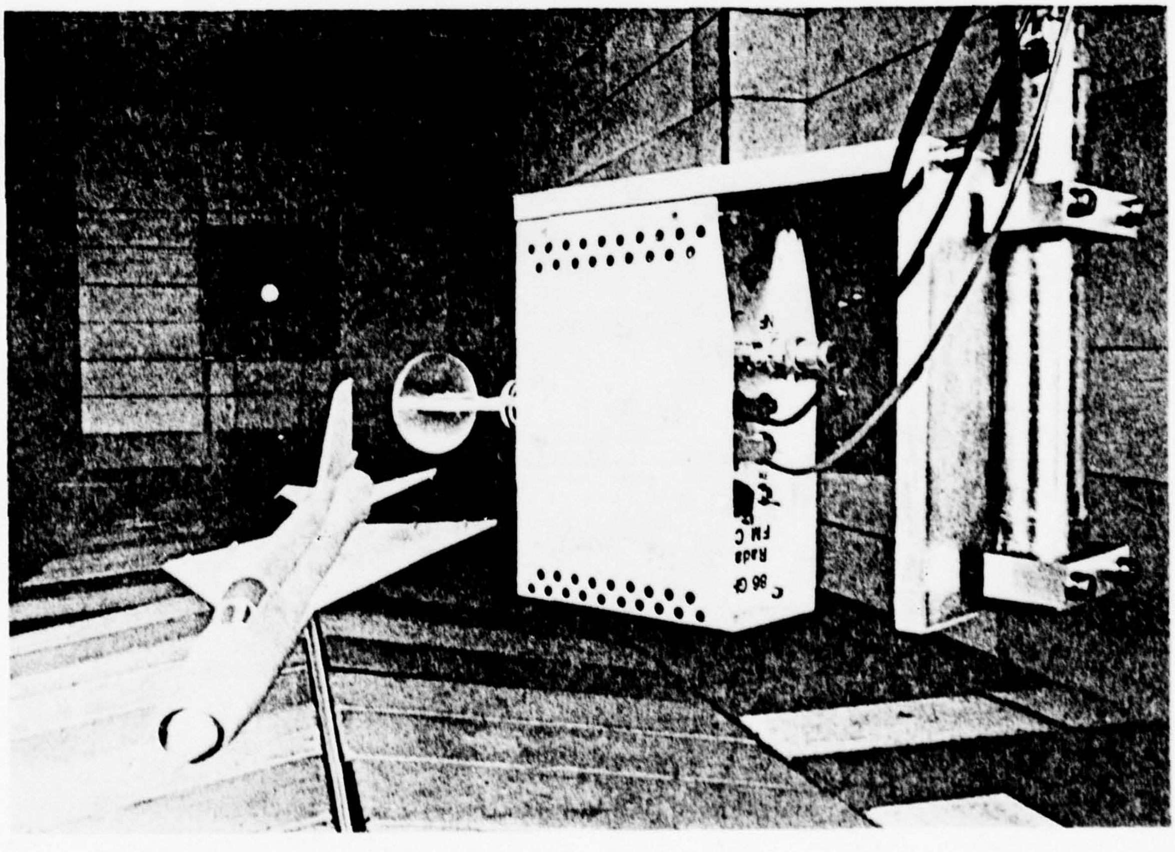
C 86 G
Rada
FM C

Fig.4 Simulation facility

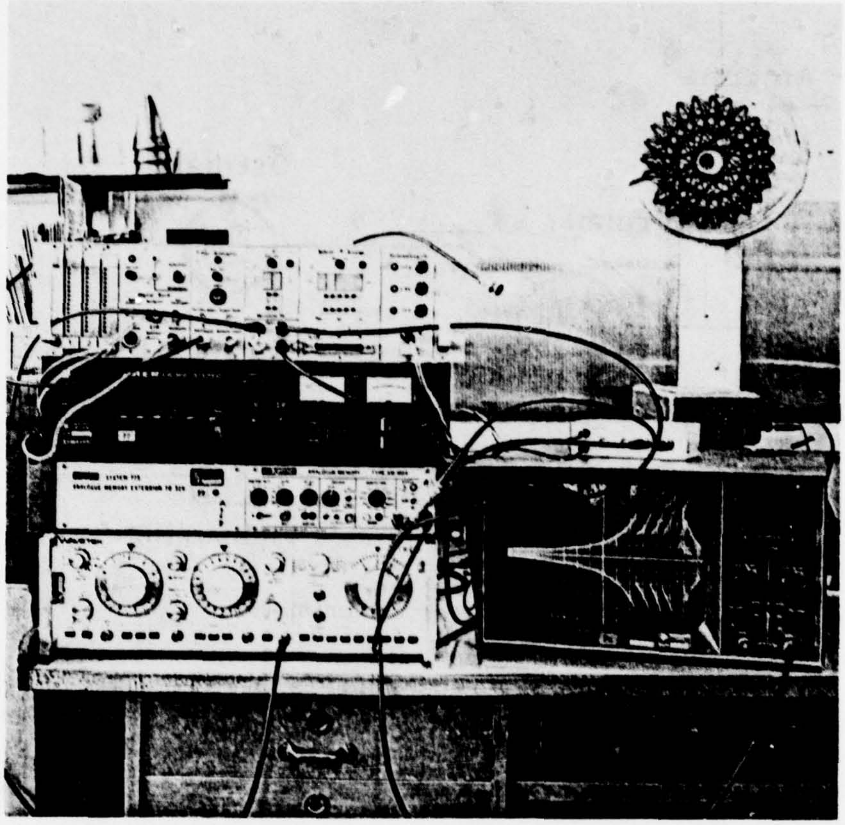

Fig.5 Recording set-up

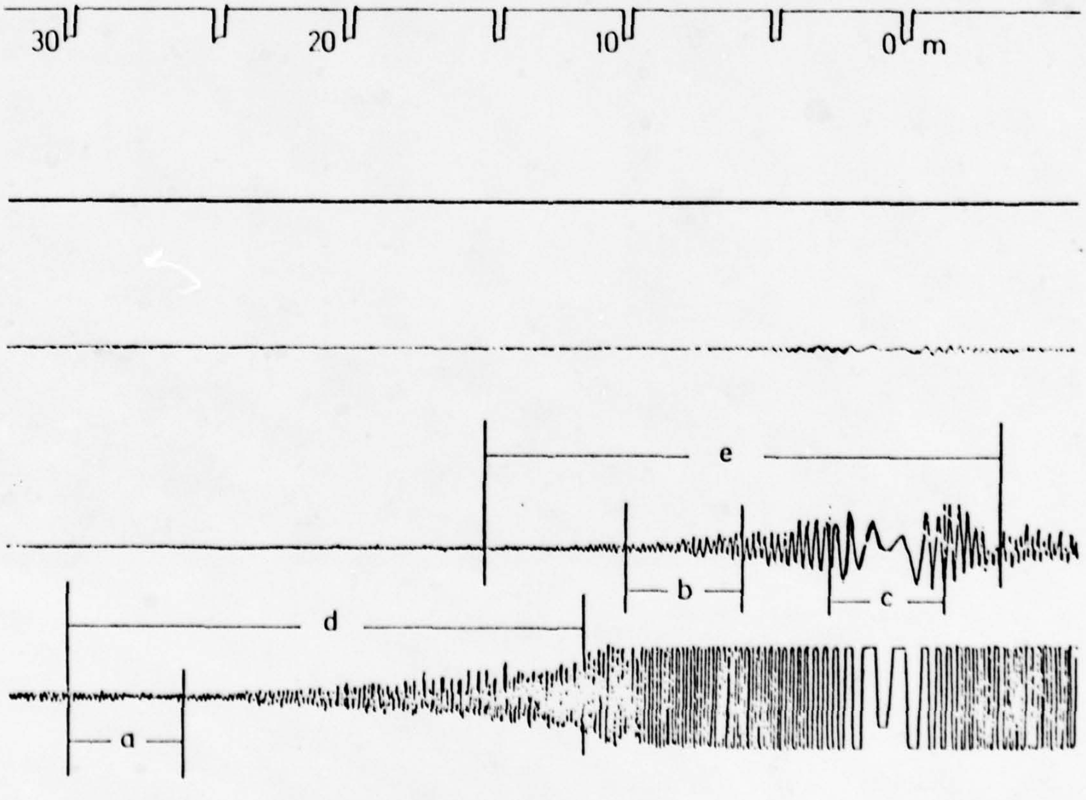

Fig.6 Signal of a sphere

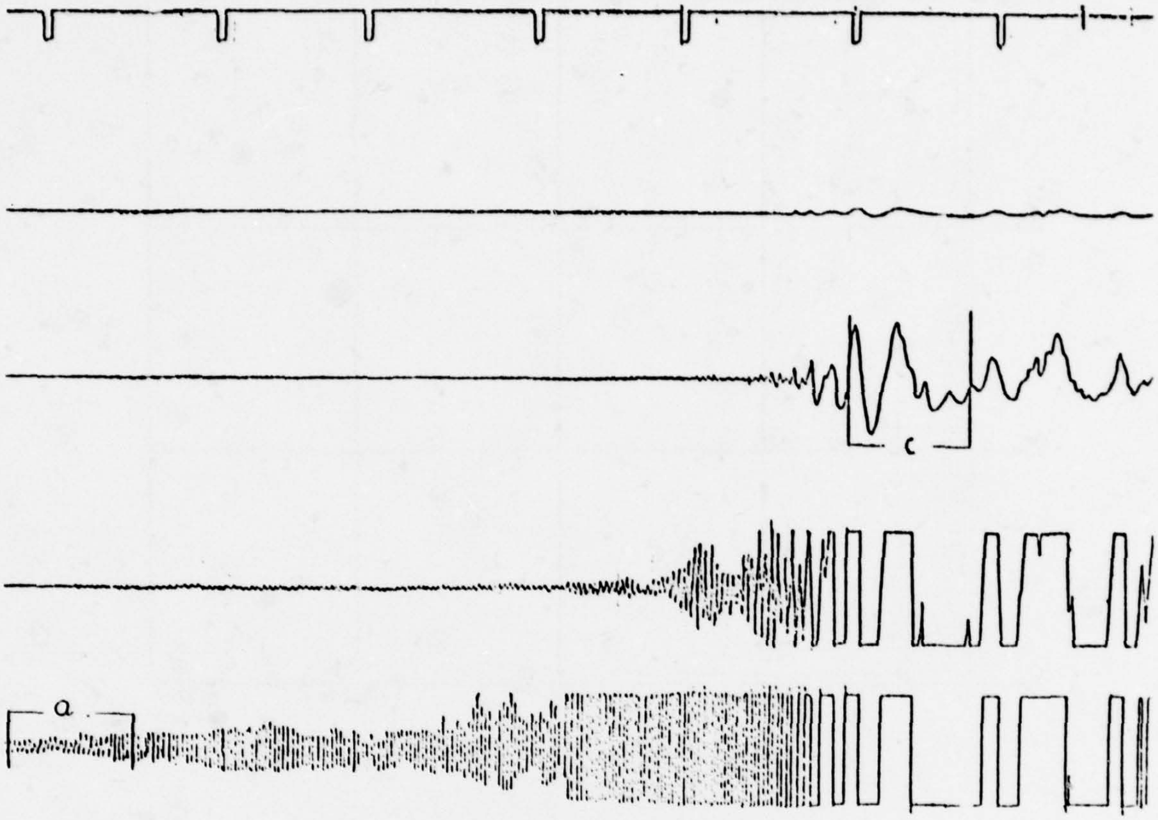

Fig.7 Signal of an aircraft

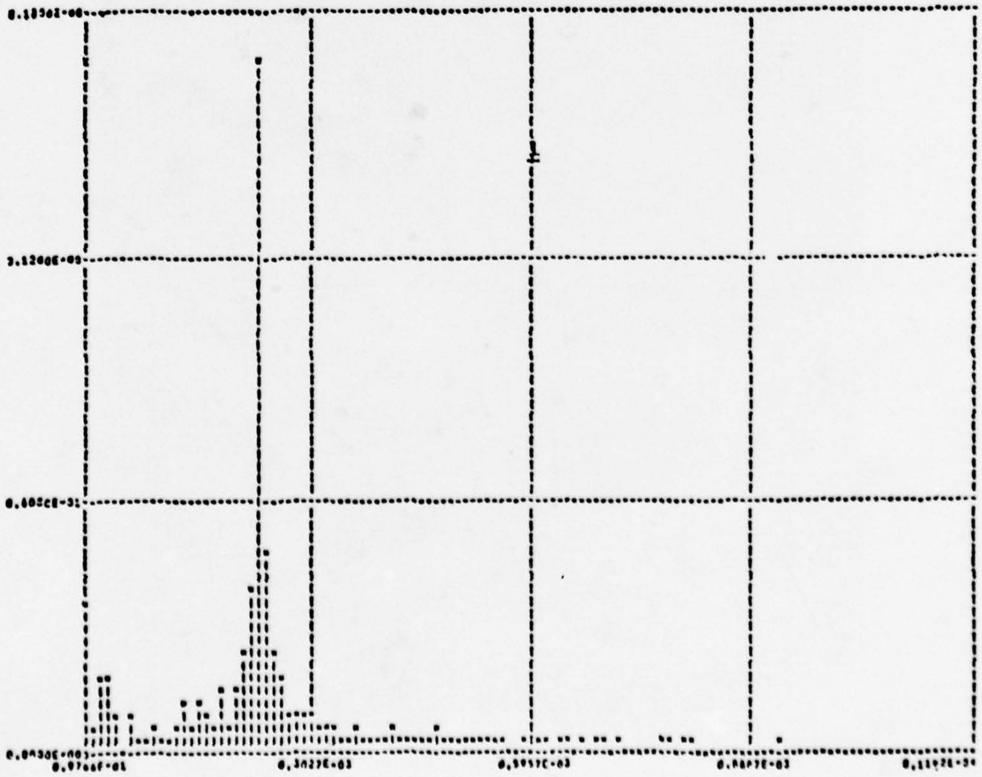

Fig.8 Spectrum of Figure 7. Time interval a

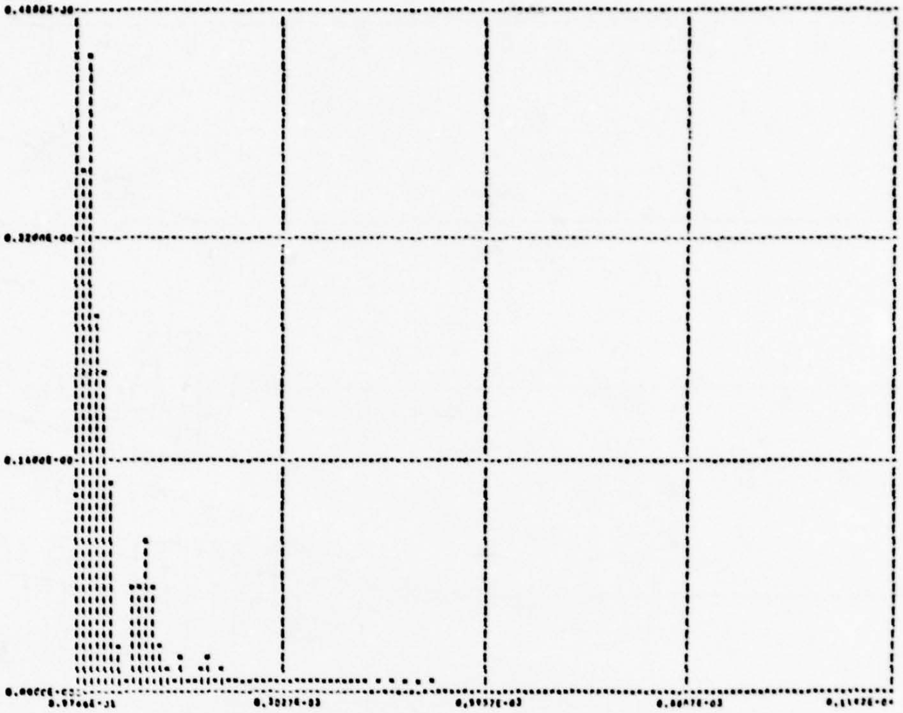

Fig.9 Spectrum of Figure 7. Time interval c

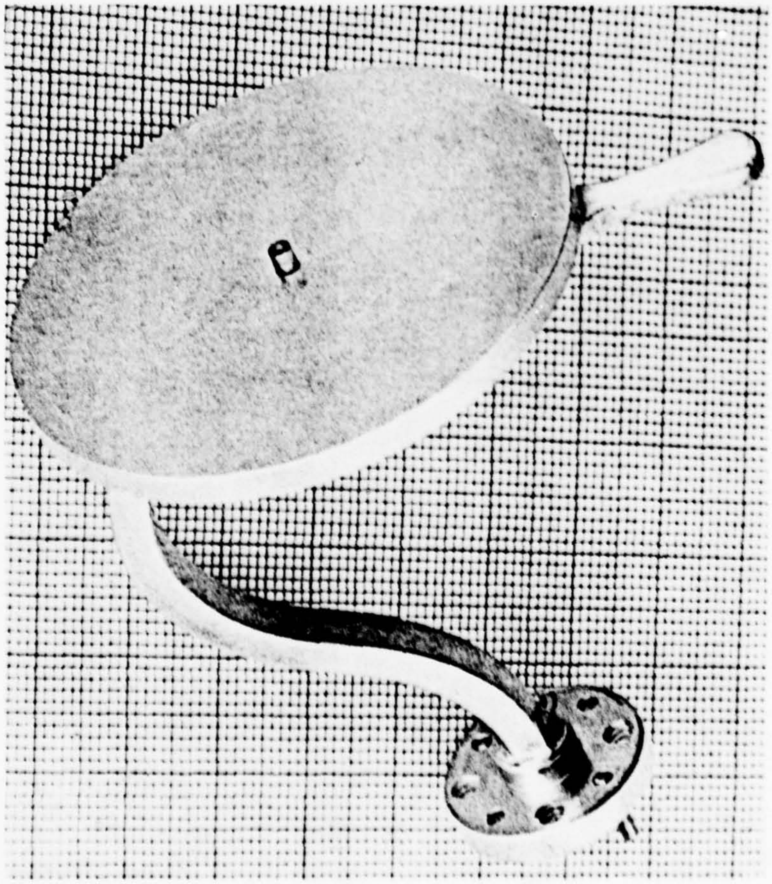

Fig.10 86 GHz low gain antenna

DISCUSSION

M.Carter, UK

How good is the Radar absorptive material used in the anechoic chamber.

Author's Reply

Approximately 5–10%.

MICROWAVE HOLOGRAPHY : A DECADE OF DEVELOPMENT

L.A. Cram, G.W. Newbery, K.O. Rossiter
EMI Electronics Limited
Wells, Somerset, England

SUMMARY

The advent of the laser as a source of coherent radiation within the optical spectrum regenerated interest in the techniques of wavefront reconstruction or holography first proposed by Gabor in 1948. Sources of coherent microwave radiation had, of course, been available for many years when, in the mid-1960's, it was appreciated by Dooley (1965) and independently at EMI Electronics Limited, Wells, that similar holographic techniques could be employed to investigate reflections from targets irradiated with microwaves. This paper traces some of the work on microwave holography that has been carried out at Wells in the subsequent years. The equipments devised to operate at various frequencies ranging from 10 GHz to 140 GHz are described and typical results achieved are presented. Reference is made to some of the components developed for use in the equipments.

1. INTRODUCTION

1.1 Basic Holography

To assist in the appreciation of the holographic systems described below, it is pertinent to review briefly the basic principles of wavefront reconstruction. Two plane waves, of the same optical wavelength, λ, and with wave normals k_1 and k_2, are shown schematically in figure 1(a). Their propagation directions are inclined at an angle θ and the manner in which they will beat together along a typical line AB is indicated. If a photographic plate, situated in the plane containing the line AB and perpendicular to k_1, is exposed to the incident radiation, it will, after development, display a sinusoidal spatial variation in transmittance with an interval of $d = \lambda/\sin\theta$ in the direction of the line AB as indicated in figure 1(b). Hence the pattern recorded on the photographic plate will be similar in appearance to a conventional diffraction grating and, when it is illuminated by collimated light, i.e. a plane wave, corresponding to the original wave in the direction k_1, two diffracted waves are generated as shown in figure 1(c). One of these waves is identical to the second wave, k_2, used in the production of the interference pattern or grating, i.e. the original wave has been reconstructed from the grating.

The process may be likened to the "freezing" of a signal, which has been produced by amplitude modulating a carrier (wave k_1) with a sinusoidal time function (wave k_2) and subsequently unfreezing the signal by mixing it with an identical carrier to reconstitute the original time function in conjunction with a conjugate or negative frequency sideband. In a conventional diffraction grating, created by ruling many parallel lines, the transmittance varies in a binary manner as indicated in figure 1(d). A variation of this form may, of course, be synthesised by the superposition of many harmonically related components of the type shown in figure 1(b) and, as is well known, when the conventional grating is illuminated, multiple orders of diffracted waves are generated corresponding to the various harmonics present.

It becomes apparent that any combination of waves superimposed on and mixed with a reference wave may be used to generate a complex diffraction grating or hologram and that the original combination of waves may be recovered when the hologram is illuminated appropriately.

Optical holograms can be recorded using the arrangement shown schematically in figure 2. Here the complex wave structure reflected by the object is mixed with the reference wave which appears to emanate from a point source. The reflected waves become frozen in the hologram and they may subsequently be reconstructed to provide a true, three-dimensional, virtual image of the original object.

A conjugate set of waves is also generated and these waves can be used to provide a conjugate image. The true image may be made real either by employing a simple lens system or by modifying the wave front used to illuminate the hologram.

1.2 Microwave Analogy

In microwave holography we generate an interference pattern in an analogous fashion by allowing microwave radiation reflected by objects within the field of view to mix with a suitable reference wave or signal. The hologram may, in principle, be constructed by fabricating a replica of the interference pattern, using radar absorbent material, so that, when this is illuminated by a wave at the original microwave frequency, the original wavefront structure is reconstructed.

The hologram is then acting as a microwave aerial; the resolution of the images will depend on the beamwidth of the aerial and, hence, on the size of the original holographic aperture measured in wavelengths. Microwave holograms are, therefore, typically recorded over an area 1 m square.

An alternative and more practical use for the data recorded in a microwave hologram is to provide an image at optical wavelengths. This effectively extends the spectrum at which we can visualise images to the microwave wavelengths. It is achieved by making a photographic version of the hologram at much reduced scale and using this with a coherent light source to generate an optical image.

Another method of obtaining a visible image would be to use digital rather than optical processing, computing the image structure from the holographic data. Digital processing becomes increasingly attractive as digital equipment continues to improve in speed and compactness but the inherent simplicity and rapidity of optical processing still offer many advantages for experimental work.

1.3 Effects of Scaling

If optical images are to be reconstructed from microwave holograms, the hologram should ideally be scaled down in size from the original record in the ratio of the optical to the microwave wavelengths. This ratio is typically of the order of 1:10 000 (0.6 µm to 6 mm) so that the original 1 m dimension of the holographic aperture becomes 100 µm, i.e. too small for convenient handling on a normal optical bench. Some compromise is required and, in practice, a scaling factor in the region of 1:200 is commonly used, leading to a scaling error of the order of 50:1. The effects of such a scaling error are significant but they may be compensated and do not detract from the utility of the images.

A simple, non-rigorous approach may be adopted to appreciate the main consequences of any scaling error present. Let us assume that the ratio of the wavelength of the microwave radiation, used for recording the hologram, to that of the coherent light, to be used for the reconstruction, is ρ. Then, if the height of the microwave hologram is ρH, the height of a corresponding, perfectly scaled, optical version would be H. An object of height ρh at a distance ρR from the recording would lead to a perfectly scaled image of height h, at a distance R from the ideal optical hologram, as in figure 3(a). Now let the optical hologram used in practice be larger in size than the ideal by a linear factor s, so that s is the scaling error referred to previously and the height of the practical hologram then becomes sH, as in figure 3(b). *Since the distances between the fringes constituting the hologram have also been increased by this linear factor s, the* angular diffraction, which is determined by the fringe separation, will be decreased at each point on the hologram. From the usual diffraction grating theory, we can predict that any original diffraction angle θ will be reduced to α, where $\sin\alpha = \frac{\sin\theta}{s}$. In most cases, θ and, hence, α are both sufficiently small that we may put $\alpha \doteqdot \theta/s \doteqdot h/sR$. The lines A_1B_1 and O_1B_1 which are separated by the angle θ in figure 3(a), may be loosely considered as rays which become A_2B_2 and O_2B_2 separated by the angle α in figure 3(b). Since the ray A_2B_2 remains perpendicular to the hologram, the two rays intersect to give an enlarged image, of height sh, at Q_2B_2 where $O_2Q_2 \doteqdot sh/\alpha \doteqdot s^2R$. It is apparent that the lateral and longitudinal image scaling differ in magnitude and that they are in the ratio of the scaling error s.

If we assume that the angular resolution of the original hologram is λ/H, the linear resolution across the image is $\lambda R/H$ which, when expressed as a fraction of the image height, becomes $\lambda R/hH$. For the enlarged hologram, the angular resolution is λ/sH and the lateral resolution at the image is $\lambda/sH \cdot s^2R = s\lambda R/H$. Hence, the fractional resolution at the image remains equal to $\lambda R/hH$, independent of s, and it is seen that the scaling error does not affect the resolution of the image.

The principal effect of the scaling error is, therefore, to introduce distortion due to the discrepancy in the lateral and longitudinal magnifications but this discrepancy is, of course, similar to that normally encountered when using a simple lens *system to achieve image magnification. An appreciation of such lens-like properties of holograms, is often extremely* useful.

1.4 Display of Images

Consider an object of height 1 m at a range of 5 m, then, using the scaling factor and scaling error introduced in section 1.3, the optical image will be of height 5 mm and at a distance of 1.25 m from the hologram. The small size of the image and the small diffraction angles inherent in the formation of the image render direct viewing by the human eye difficult and, possibly, hazardous with a laser. It is more convenient, therefore, to generate a real image directly on the face of a vidicon in a CCTV camera as shown in figure 4. By varying the distance between the vidicon and the hologram, it is possible to interrogate the image field rapidly, displaying on a monitor successive two dimensional slices of the three-dimensional image. An arrangement of this form can, of course, be calibrated to obviate the effects of any image distortion introduced by the differences in lateral and longitudinal magnification.

1.5 Intensity of Reflections

Since the intensity distribution over the optical image corresponds to the strength of the reflections of the microwave *radiation from objects within the original field of view, the image may be inspected to determine the relative echoing* areas of such objects. A convenient null method of achieving this involves the insertion of suitable neutral density filters in the path of the laser beam illuminating the hologram. An A-scope display of the vidicon output is used to interrogate the image detail and the attenuation in the laser beam is varied until the signal from the image attains a predetermined level.

2. 70 GHz SYSTEM

The first microwave, holographic recording apparatus constructed at Wells in 1966 operated at 70 GHz. The choice of frequency was dictated by a desire to achieve acceptable resolution with a relatively small pilot experiment employing components that were readily available at that time. The general experimental arrangement is shown schematically in figure 5 and it will be seen that the method adopted to form the interference pattern bore a close resemblance to the techniques in use for optical holography. A view of the apparatus, as seen from the location of the object to be imaged, is shown in figure 6.

The c.w. signal generated by the klystron was chopped at 500 kHz and 90% of it was then radiated from the horn on the right of the illustration to illuminate the region occupied by a suitably reflecting object. The remainder of the signal *was used to provide a reference wave which diverged from a second horn acting as a point source situated adjacent to the* desired field of view. An open-ended length of waveguide was employed as a small aperture aerial or probe to sample the interference pattern formed by the mixture of the reference wave with the radiation reflected from the object. The probe executed a raster of 500 lines to cover an area 500 mm square and, after detection, the beat signal was amplified at 500 kHz, with a bandwidth of 1 kHz, before it was fed to a phase sensitive detector which had an output bandwidth of 10 Hz. This bandwidth was adequate to accommodate all the frequencies present in the holographic fringe amplitude information when the probe scan velocity was limited to 200 mm/s. The output of a suitably masked Ferranti light source, type CL40, which can be seen mounted alongside the probe aerial, was modulated by the beat signal so that a photographic record could be obtained on Kodak Ortho Type 3 film using the camera standing behind the scanning frame. The experiment was carried out in a darkened room and the camera shutter was held open during the total period of the recording which lasted for approximately 20 minutes. The hologram obtained in this manner measured approximately 50 mm square and it was subsequently further reduced onto a Kodak MR plate so that it then occupied an area only 5 mm square, corresponding to a total linear scaling factor of 1:100. When the light from an HeNe laser was used for reconstruction, the ratio of reconstructing to recording wavelengths was 1:6 800, leading to a residual scaling error in this case of 68:1.

Holograms were made of a variety of objects including one in the form of the letters EMI. The letters were each 250 mm high and assembled from round-headed bolts attached to metal strips at intervals of approximately 25 mm. The distance of the letters from the scanning frame was slightly less than that of the reference source. When a hologram, made using this object, was illuminated by coherent light focussed on a point at a suitable distance beyond the hologram, true and conjugate real images were formed respectively in front of and behind the image of the reference source.

The images could be interrogated with a vidicon and the two-dimensional images obtained by siting the vidicon to bring either the true or conjugate image into focus are shown in figures 7(a) and 7(b). The conjugate image is, of course, inverted and when, as in figure 7(b), it is in focus, the true image is clearly out of focus. Thus this early work demonstrated the three-dimensional imagery of radio holograms.

An alternative method of reconstruction was also investigated using a simple electric flashlamp bulb as the source of illumination. At a distance of 2 m, the bulb provided a sufficiently small source that, when it was viewed through a red gelatine filter with the hologram held some 50 mm from the eye, true and conjugate virtual images were readily visible in the region of the source. By small changes in the relative positions of the eye, the hologram and the source, adequate parallax could be achieved to appreciate the separation in range between the true and conjugate images.

The results achieved at 70 GHz were sufficient to encourage further work, but in view of a desire to obtain greater sensitivity, it was decided to construct the next equipment to operate at a lower frequency.

3. 10 GHz SYSTEM

Sources with high power outputs and sensitive mixers with low noise figures are more easily obtained at the lower microwave frequencies but the use of a lower frequency leads to a reduction in the resolution that can be achieved with a given size of recording aperture. It was decided, therefore, to choose an operating frequency of 10 GHz and to increase the aperture size. During the initial experimental period at 10 GHz several innovations were introduced and the most significant of these was the replacement of the radiated reference wave, as used in the 70 GHz system described above, by a small fraction of the transmitter power coupled directly into the local oscillator port of a conventional mixer. Since a constant phase difference then existed between the phase of the reference signal and that of the transmitted signal, the injected reference simulated a plane reference wave incident on the recording aperture from a direction perpendicular to the aperture. The use of a simulated reference signal bestowed two immediate benefits: there was no longer a need to introduce hardware into the field of view to provide the reference source and the increased level of the reference signal available at the mixer led to greater system sensitivity.

It is apparent from the reciprocity theorem that, for a bistatic system, similar interference patterns would be recorded if either the transmitter or receiver aerial were scanned with the other held stationary and, in practice, it was more convenient to let the transmitter aerial be scanned. In either case, however, it was necessary to provide some form of flexible microwave linkage in the equipment between the transmitter and receiver aerials and low-loss, rotating joints were specially designed and constructed at Wells for use with rigid co-axial cable to carry the 10 GHz signal to the scanning aerial.

To reduce the loss in resolution consequent on selecting to work at 10 GHz, the size of the recording aperture was increased to 1 m square and it was scanned in a raster pattern with the vertical spacing between the horizontal scanning lines adjustable from 0.25 mm to 5 mm. A light-tight box was built to surround both the scanning frame and the camera lens and one side of the box consisted of a thin sheet of optically opaque polythene to allow the passage of the microwave radiation. It was then no longer necessary to operate the equipment in a blacked-out room.

The microwave source was a klystron providing a peak power of 80 mW and its output was amplitude modulated by a 500 kHz square wave. The received signal, after mixing with the injected reference, was amplified at 500 kHz by a narrow band amplifier prior to further mixing with a sample of the 500 kHz modulation in a phase sensitive detector. The low frequency output was used to modulate the intensity of a suitably masked, fluorescent indicator tube, Mullard type DM160, which was mounted alongside the scanning aerial. The intensity modulation was recorded on Polaroid 46L film and the holographic fringes could be seen clearly on the film when the hologram occupied an area approximately 10 mm square. This size of hologram corresponded to a scaling factor of 1:100 compared with the factor of 1:50000 required for perfect scaling when the light from a HeNe laser was used for reconstructing the images. The residual scaling error was therefore 500:1 but it was found that, with experience, satisfactory images could be displayed on a television monitor despite the large scaling error.

Attempts were made at that time to modify the recording technique so that the microwave interference patterns might be recorded directly in a manner analogous to that in which a photographic plate records optical holograms. The methods investigated relied on recording localised changes in temperature due to the absorption of the incident microwave energy.

If such temperature changes are large enough, they may be used to modify locally the speed of development of Polaroid colour film which has previously been uniformly exposed to light. Alternatively, liquid crystals might be used to display the temperature variations. Although this latter technique was found to be adequate, to indicate the near field polar diagram of a small aerial, neither technique was sufficiently sensitive to record holograms at the microwave power levels available.

Other methods of recording the output signal from the scanning frame were investigated including the use of a Mufax recorder, a brightness-modulated cathode ray tube and a cathodo-chromic device. Each of these methods had the advantage that the light-tight box could be dispensed with so that the total holographic recording equipment could be more compact. Synchronisation of each recording device with the scanning aerial was achieved either by means of a train of pulses generated by the aerial motion along a scan line or from positional information derived from potentiometers coupled to the aerial drive mechanism.

The Mufax recorder was a modified weather chart recorder, the input signal to which produced a colouration on sensitized paper sandwiched between a knife edge and a helix. As the helix rotated, in response to the synchronising pulse train, the point of intersection between the helix and the knife edge traversed the paper. The hologram recorded in this fashion was approximately 200 mm square and it was subsequently reduced photographically to provide a transparency, 10 mm square, which was used for the reconstruction process.

When using the cathode ray tube, the focussed spot was scanned over the phosphor in synchronism with the scanning aerial and the intensity of the spot was modulated by the holographic signal. Pulse duration modulation was used to overcome any non-linearity in the brightness characteristic of the phosphor. The hologram was recorded at the required size by taking a time exposure photograph of the raster.

Each of the recording methods described above involved the use of photographic processing to produce the hologram, an obvious obstacle to the achievement of a real-time system, and a novel cathodo-chromic tube was devised at Wells to overcome this obstacle. The device was basically a high resolution cathode ray tube in which a single polished crystal of a cathodo-chromic material, such as KBr, approximately 15 mm in diameter and 2 mm thick, replaced the phosphor of a conventional tube. An optically flat window was inserted into the side wall of the tube and a small plane mirror, inclined at 45 deg to the axis of the tube, was mounted on the anode, see figure 8. The electron beam passed through a hole in the centre of the mirror before striking the crystal, which was normally transparent, and the electron bombardment of the crystal created colour centres which absorbed light of the wavelength generated by a HeNe laser. Since the colouration took place on an atomic scale and was confined to the region close to the surface of the crystal, the resolution that could be achieved was determined principally by the electron optics.

When the electron beam was scanned in synchronism with the scanning aerial and the intensity of the beam was modulated by the receiver output, a reduced version of the hologram, approximately 10 mm square, was drawn in the crystal. The hologram was illuminated by coherent light which passed through the side window and was reflected by the mirror inside the tube. The reconstructed image was observed using a vidicon in the manner described previously and the resolution of the image could be seen to improve during the recording process as the extent of the recorded hologram increased.

The significance of using a sample of the transmitted signal as a local oscillator signal to simulate a reference wave has been described previously. Since it corresponded to a reference source on boresight, it appeared in and obscured the centre of the field of view when the holographic image was reconstructed. The obscuration could be removed by simulating the presence of an inclined reference wave over the recording aperture by the introduction of a uniform spatial rate of change of phase of the reference signal with respect to the transmitted signal. It was possible to take advantage of the scaling error to use a sufficiently high rate of change of phase on recording, that the entire image field, which was of reduced angular extent due to incorrect scaling, was completely removed from the region of the undiffracted reference beam when the image was reconstructed.

Initially, the offset reference wave was created by incrementing the phase of the reference signal by 90 deg at the start of each of the 240 scanning lines which were spaced 4 mm apart. This corresponded to a spatial frequency 62.5 cycles/m, almost twice the maximum of 33.3 cycles/m which would arise, at 10 GHz from signals arriving from a direction perpendicular to boresight. Hence, after mixing but before reduction, the spatial frequencies corresponding to objects in the field of view occupied the band from 29.2 to 95.8 cycles/m, well displaced from the zero frequency which corresponded to the undiffracted portion of the beam on reconstruction. The schematic arrangement of a typical equipment employing an inclined reference wave is shown in figure 9.

An example of the results is given in figure 10, which is a photograph of a reconstructed image. The corresponding hologram was recorded with the equipment positioned close to the laboratory window and viewing a scene consisting of sky and buildings at various angles. It brings out very clearly the advantage of displacing the image of the field; the spot at the top, corresponding to the undiffracted beam, is well separated from the circular image of the field. The reconstructed images of various objects are formed at different ranges, with the result that, in a single photograph only some can be in sharp focus.

A subsequent system used a larger scanned area, 2 m square, to record holograms of targets predominantly in a direction perpendicular to the scanned area. The low spatial frequencies induced in the hologram by the targets in this case permitted the separation between the lines constituting the raster to be increased, but this, of course, reduced the apparent angular offset of the reference beam simulated by 90 deg increments in the reference phase between the lines. It was desirable then to increment the phase shift as the aerial moved along each scan line and, in this case, the phase shift was controlled by a pulse train similar to that used to drive the Mufax recorder described above.

Initially the phase shift between lines was accomplished manually using a combination of a 90 deg and a 180 deg phase shifter. This arrangement was soon superseded by a ferrite phase shifter in which phase changes of 0 deg, 90 deg, 180 deg and 270 deg were introduced by passing the appropriate magnetising current through a solenoid wound around a slotted waveguide containing a suitable ferrite, see figure 11. A uniselector was actuated automatically at the end of each scan line to cycle the current through its four preselected values in turn.

The speed of operation of the ferrite phase shifter was limited, however, and it became inadequate when the requirement arose to increment the phase shift as the aerial travelled along each scan line. Consequently, the ferrite phase shifter was replaced by a pair of PIN diode phase shifters: one providing 90 deg shift and the other 180 deg. Each device comprised a circulator with one port connected to a length of short-circuited stripline. In one case, the PIN diode was positioned in the stripline at $\lambda/8$ from the short circuit so that the effective path length of the stripline could be varied by $\lambda/4$ to give a 90 deg phase change when current was switched into the diode. In the other device the diode was placed at $\lambda/4$ from the short circuit to give 180 deg phase change. These phase shifters proved to be very reliable and they could be switched rapidly.

The theoretical maximum angular resolution that can be obtained using a 1 m square scanned area at 10 GHz corresponds to approximately 30 mrad within the original field of view. In practice a resolution angle of the order of 45 mrad was measured and the loss in resolution could be attributed to the amplitude taper of the illumination present over the hologram during the reconstruction of the image. This amplitude taper was introduced to reduce the sidelobe level associated with each reconstructed image point and, hence, to increase the dynamic range of the images that could be reconstructed simultaneously.

The introduction of the equipment with the larger, 2 m square, scanned area provided an increase in resolution. This equipment had also a greatly improved scanning mechanism; the vertical motion was achieved by means of two vertical lead screws and the horizontal motion was carried out using a rack and pinion in association with the horizontal drive motor situated on the carriage bearing the transmitter aerial. With an equipment of this size, it was not practicable to photograph a modulated lamp directly as in the case of the smaller scanned areas. Instead, the holograms were recorded using the Mufax, c.r.t. or cathodo-chromic tube methods.

4. 35 GHz SYSTEM

An alternative to increasing the size of the scanned area from 1 m to 2 m square, in order to achieve higher resolution, was to increase the microwave frequency. The system developed at 10 GHz had proved its reliability and it was considered desirable to retain the system concepts as far as possible in any new equipment. Component availability, however, then dictated that the frequency should not exceed 35 GHz.

Initial investigations soon showed that it would not be feasible to employ a ferrite phase-shifter, principally due to the potentially high insertion loss of such a device at 35 GHz. PIN diode switches mounted in conventional waveguide were available, however, and it was possible to construct a suitable phase-shifter using circulators and short-circuited guide in a fashion analogous to that used at 10 GHz. The feed to the transmitter aerial, which was scanned in a raster relative to the rest of the equipment, was fabricated from lengths of rigid waveguide coupled by rotating joints which were specially designed to minimise the phase and amplitude modulation of the signal within the linkage.

The 35 GHz equipment was used in conjunction with the mechanical frame which had previously been used at 10 GHz to scan over an area 1 m square. The separation between the scan lines was reduced to 2 mm, a total of 500 lines over 1 m, leading to a spatial frequency of the reference signal equal to 125 cycles/m when the reference phase was incremented by 90 deg between scan lines. This simulated a plane reference wave incident from a direction perpendicular to boresight. In practice, small horn aerials with 3 dB beamwidths of approximately ± 15 deg were used to enhance the system sensitivity so that the effective field of view was limited and did not suffer from any intrusion of the undiffracted beam when the holographic image was reconstructed.

In order to accommodate the larger number of fringes present on the 35 GHz holograms, the area of the Polaroid 46L film used to record each hologram was increased to 20 mm square. The maximum fringe density on the recording was then equivalent to 8 line pairs per mm, well within the resolution capability of the film. Each hologram was subsequently reduced, on Kodak MR plates, until it occupied an area 2 mm square. The scaling factor was then 1:500 compared with the factor of 1:14 000 which would have been required for correct scaling. The residual scaling error was thus 28:1.

The theoretical maximum angular resolution that could be achieved with these holograms was equivalent to 8.5 mrad within the original, full scale field of view but, due to the amplitude taper of the illumination over the hologram during the reconstruction process, this figure was, in practice, degraded to 14 mrad. Nevertheless, it was possible to recognise the gross outline of a vehicle at a range of some 20 m and to identify specific reflectors on the body of the vehicle, see figure 12.

5. 140 GHz SYSTEM

One of the characteristics that was very apparent from the images reconstructed from the 35 GHz holograms was the absence of a uniform background return from most targets at this frequency; each image was more obviously composed of a set of discrete high-lights. Many more surface areas are rough to 2 mm than to 8 mm radiation so that more scattering will occur at the shorter wavelength. Hence, the microwave frequency has now been raised to 140 GHz to provide more background and to assist in the identification of more complex images.

The change to the higher frequency precipitated a significant modification of the holographic system. The considerable reduction in the weight of the microwave components permitted the whole of the microwave assembly to be mounted on the carriage which traverses the scanned area in a raster fashion. Mounting the microwave head in this compact fashion has minimised the waveguide losses and has also removed the requirement for any quasi-flexible r.f. linkage which would have been difficult to fabricate satisfactorily at 140 GHz.

The system now operates in a monostatic rather than a bistatic manner and, since both the path length from the transmitter aerial to any object in the field of view and the return path length back to the receiver aerial vary during the course of the scanning, the spatial frequencies of the fringes recorded on the hologram are increased. A similar fringe density would be evident if a bistatic system were to be used at a frequency in the region of 280 GHz. Hence the effective angular resolution of the system is increased and this increase is consistent with the utilisation of the whole scanned area by both aerials.

The first 140 GHz system, which is shown in schematic form in figure 13, comprised a klystron source, 10 dB coupler, variable attenuator, balanced mixer and transmitting and receiving aerials. The layout of the microwave components, the klystron protection circuits and the pre-amplifier is shown in figure 14. Unfortunately, no suitable phase shifter was available for incorporation into the system to permit the simulation of an offset reference wave of the type used at 10 GHz and 35 GHz. Consequently, the aerials are arranged to illuminate and interrogate a field of view offset at 45 deg to the direction perpendicular to the scanned area and the horizontal dimension of the aperture has been increased to maintain the same angular resolution capability in both the horizontal and vertical directions. The aerials, which were specially electroformed, each have a one way 1.5 dB beamwidth of ± 10 deg.

The 140 GHz source is an EMI-Varian Ltd. klystron, Type VRT 2121A, which has an output power rating of 100 mW. The remaining microwave components, including the aerials, were fabricated at Wells. The directional coupler is a Type MC2028, the level set attenuator is a Type MC90. The balanced mixer, Type MC1129, is fitted with waveguide wafers, Type MC1929, which incorporate low noise gallium arsenide Schottky barrier diodes.

The balanced mixer was selected initially to minimise the adverse effects of any amplitude modulated noise generated by the klystron. In practice, it was found that, with the present homodyne system, the low frequency noise from the Schottky barrier diodes imposed the more severe restriction on system sensitivity, and a single ended mixer has now been adopted. Since there is no longer the requirement to provide a balanced pair of diodes, the diode selection can now be based on the criteria of low noise temperature ratio and high conversion efficiency leading to improved system sensitivity.

The scanning mechanism, which transports the microwave unit in a raster over a vertical plane approximately 1 m high and 1.5 m wide, is considerably more robust than those used previously at the lower frequencies. It is designed to ensure that the horizontal scan lines are straight to within 0.2 mm and that the microwave unit does not deviate by more than 0.05 mm from the prescribed vertical scanning plane. Increments of 1, 2, 4, 8 or 16 mm between the scan lines can be selected.

The signal from the mixer, after suitable amplification, is used to modulate the output intensity of a light emitting diode mounted alongside the microwave unit. Variations in the intensity of the l.e.d. are recorded on Polaroid 46L film as on the previous equipments and a telescopic tube, with the l.e.d. at one end and the stationary camera at the other, is used to provide the requisite light-tight enclosure between them.

When first recorded, the holograms occupy an area of 50 mm by 75 mm on the film and a grey scale comprising ten discrete intensity levels is recorded simultaneously in the form of a step wedge alongside the hologram. This step wedge is used to verify the transfer characteristics between the l.e.d. and the film and to monitor the subsequent photographic processing when the holograms are reduced to an area of 5 mm by 7.5 mm on Kodak HR plates. The total scaling factor used is then approximately 1:200 compared with the ratio of effective wavelengths which is in the region 1:1 800 when due allowance is made for the monostatic operation of the equipment. The residual scaling error is then only 9:1, much lower than that pertaining to the previous equipment.

Reconstruction of the holographic images is usually achieved by means of a HeNe laser in conjunction with a television camera and monitor as described previously but, in some cases, it is possible to observe a virtual image by eye provided adequate safety precautions are observed.

Figure 15(b) shows a typical reconstructed image. The original vehicle is shown in figure 15(a). The Land Rover was situated at a range of 13 m and it was inclined at 10 deg to the broadside aspect so that the tail gate was just visible, at an oblique angle. The outline of the vehicle is clearly visible in the reconstructed image. The wheel arches are well defined due, it is believed, to the scattering of radiation by the rough surfaces beneath the wheel arches. The wheels, themselves, do not form recognisable images but characteristic returns are obtained from the wheel-hubs. The strongest return is obtained from the rear of the driver's cab which, due to the curvature of the surface, provided a strong specular reflection at all positions of the r.f. platform. The canvas canopy does not provide a significant echo but reflecting objects under it can be seen. For example an image of the spare wheel, which is carried upright behind the driver's cab, can be detected and echoes from two of the three hoops which support the canopy can also be seen. The gap between the nearside door and the body of the vehicle appears as a vertical line of small reflectors. The wing mirrors, door hinges, door handle, ventilator grille and the irregular surface of the tail gate all give characteristic echoes.

The second reconstruction, figure 16, was obtained from a 140 GHz hologram of letters approximately 200 mm high at a range of approximately 3 m. The object was placed in front of a non-reflecting background and was cut from material with a metallic surface coating. The reconstruction shows a considerable improvement in image quality compared with the early results shown in figure 7.

6. FUTURE POSSIBILITIES

Microwave holographic imaging methods of many kinds have been investigated and much experience has been acquired. The expected performance can be achieved and gives recognisable images of man-made objects. Developments will be directed towards real time systems with fast scanning and immediate visual reproduction and also towards systems with better resolution and extended dynamic range. In special applications, digital processing methods may well be exploited to give increased dynamic range. As component technology at millimetre and submillimetre wavelengths improves, the extension of microwave holography to even shorter wavelengths will be possible and this will lead to further improvements in resolution. A real time millimetric holographic system giving an immediate visual image with good resolution can certainly be envisaged during the next decade as a development with both civil and military potential.

7. ACKNOWLEDGEMENTS

We wish to acknowledge the support of MOD and of the RSRE in this work.

8. REFERENCE

DOOLEY, R.P., 1965, "X-Band Holography" Proc IEEE Vol. 53 pp 1733-35.

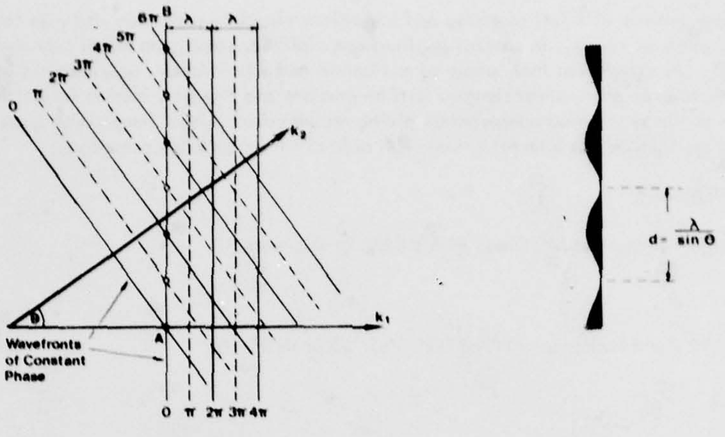
6π
B
λ
λ
5π
4π
3π
2π
π
0
k₂
θ
Wavefronts
of Constant
Phase
A
k₁
0 π 2π 3π 4π
d = λ / sin θ

1(a) Interference of two Plane Waves

1(b) Beat Pattern: *sinusoidal density*

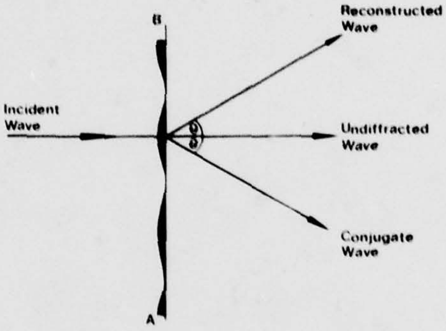
B
Reconstructed
Wave
Incident
Wave
θ
θ
Undiffracted
Wave
Conjugate
Wave
A

1(c) Reconstruction of Plane Wave

1(d) Conventional (Ruled) Grating

Fig. 1 Wavefront Reconstruction

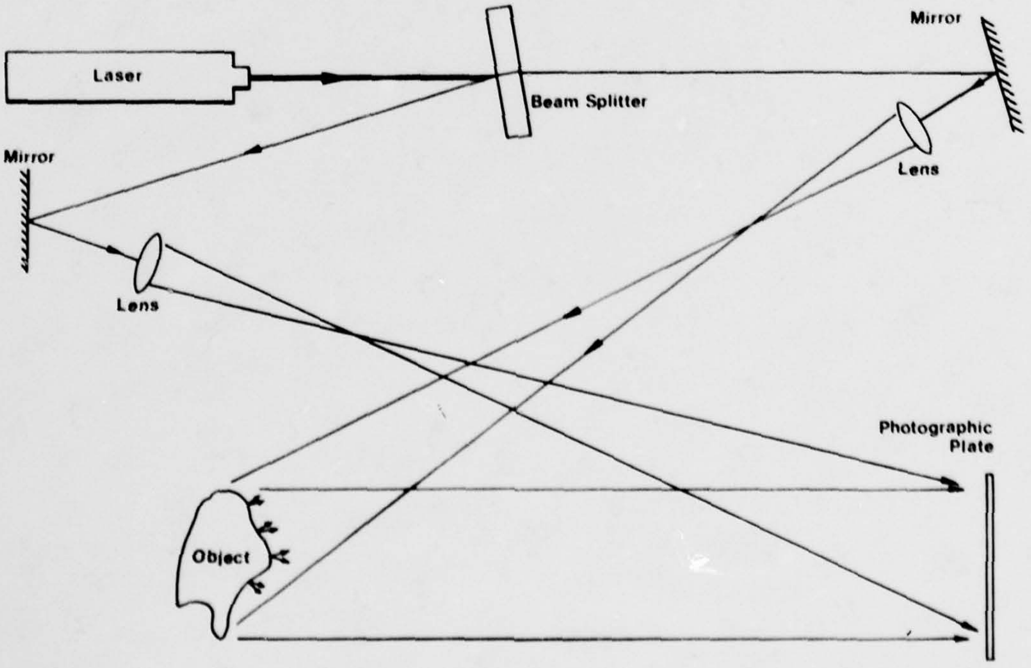
Mirror
Laser
Beam Splitter
Mirror
Lens
Lens
Photographic
Plate
Object

Fig. 2 Recording an Optical Hologram

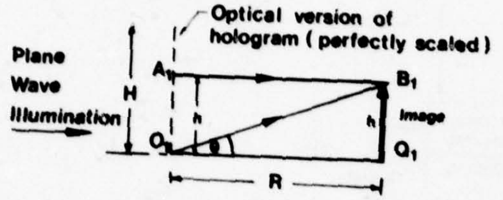
Optical version of
hologram (perfectly scaled)
Plane
Wave
Illumination
H
A1
B1
h
Image
h
O1
θ
Q1
R

3(a) Reconstruction with no scaling error

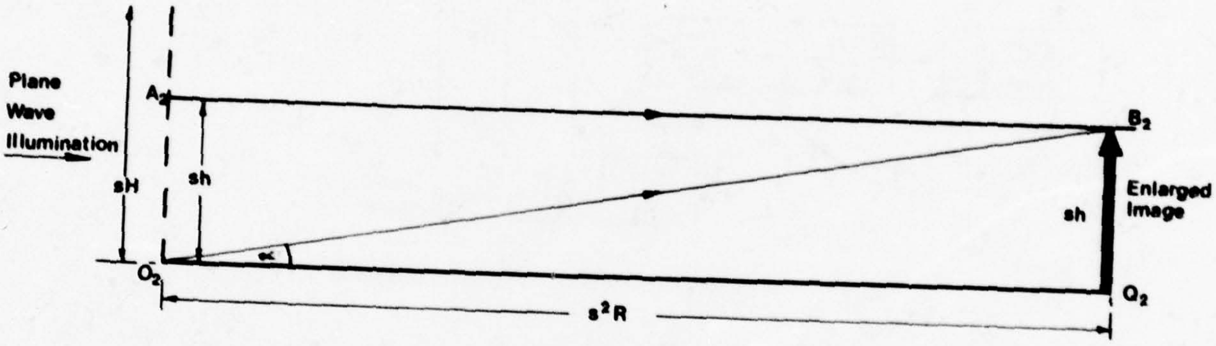
Plane
Wave
Illumination
A2
B2
sH
sh
Enlarged
Image
sh
α
O2
Q2
s²R

3 (b) Reconstruction with scaling error = s

Fig. 3 Effect of Scaling Error

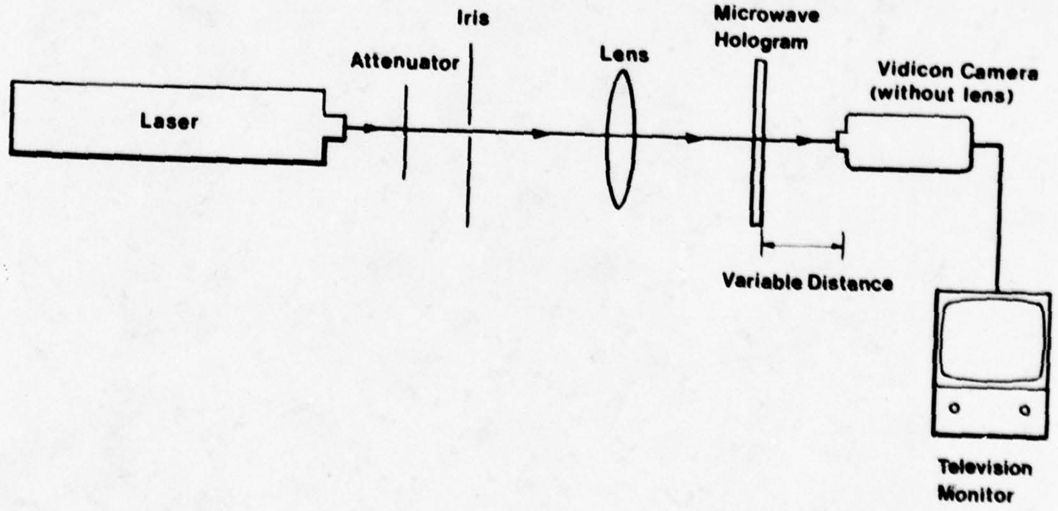
Iris
Attenuator
Lens
Microwave
Hologram
Vidicon Camera
(without lens)
Laser
Variable Distance
Television
Monitor

Fig. 4 Reconstruction of Image from a Microwave Hologram

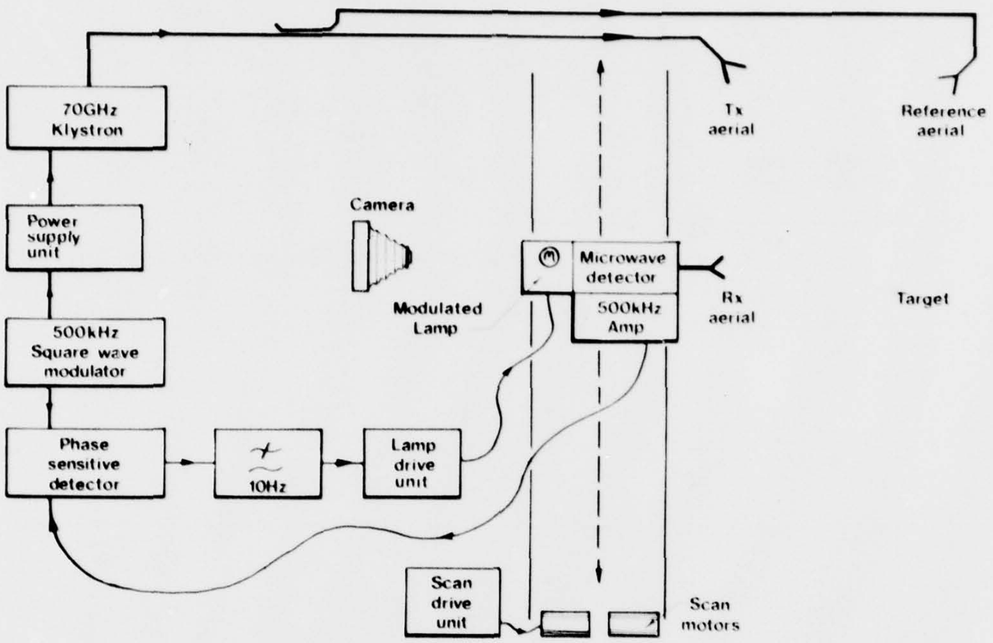
70GHz Klystron
Power supply unit
500kHz Square wave modulator
Phase sensitive detector
10Hz
Lamp drive unit
Camera
Modulated Lamp
Microwave detector
500kHz Amp
Tx aerial
Reference aerial
Rx aerial
Target
Scan drive unit
Scan motors

Fig. 5 Arrangement of 70 GHz Holographic Equipment

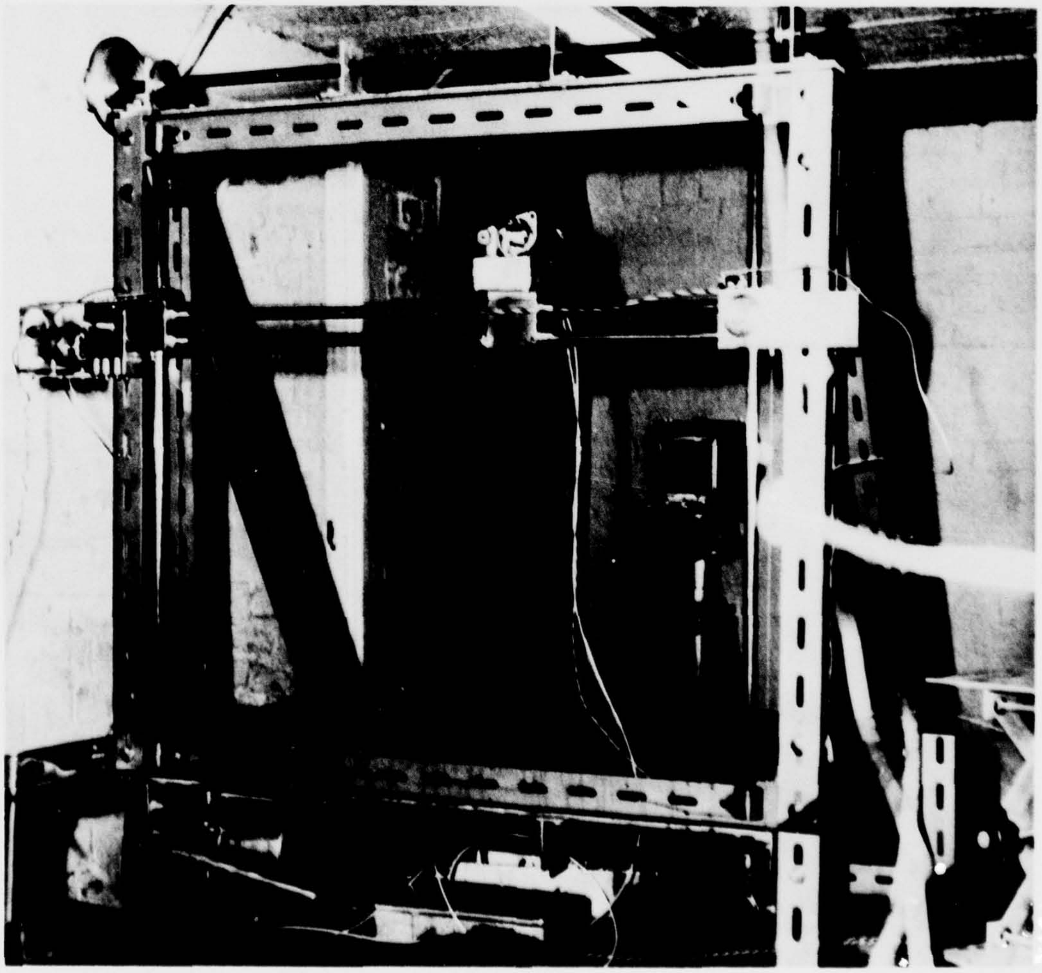

Fig. 6 General View of 70 GHz Equipment

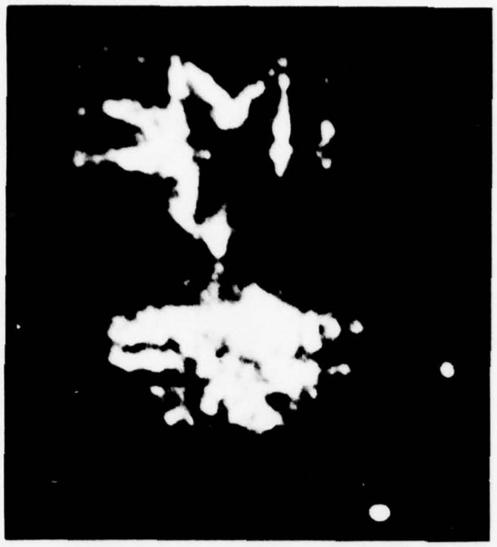

Fig. 7a True Image in Focus

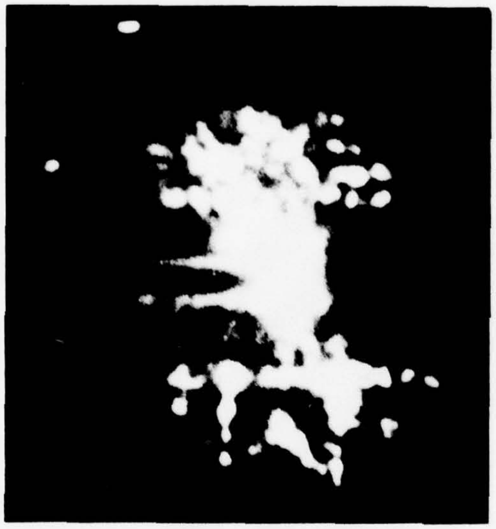

Fig. 7b Conjugate Image in Focus

Fig. 7 Reconstruction from 70 GHz Hologram

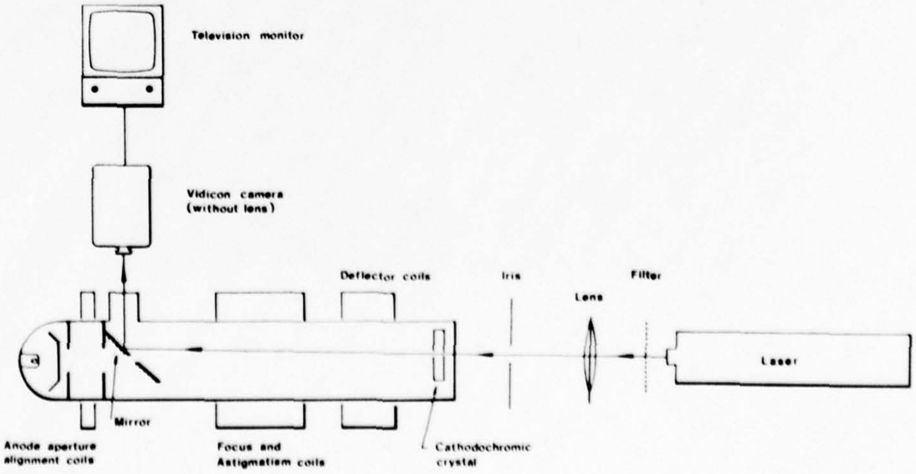
Television monitor
Vidicon camera (without lens)
Deflector coils
Iris
Filter
Lens
Laser
Mirror
Anode aperture alignment coils
Focus and Astigmatism coils
Cathodochromic crystal

Fig. 8 Reconstruction of Holographic Image using a Cathodochromic Tube

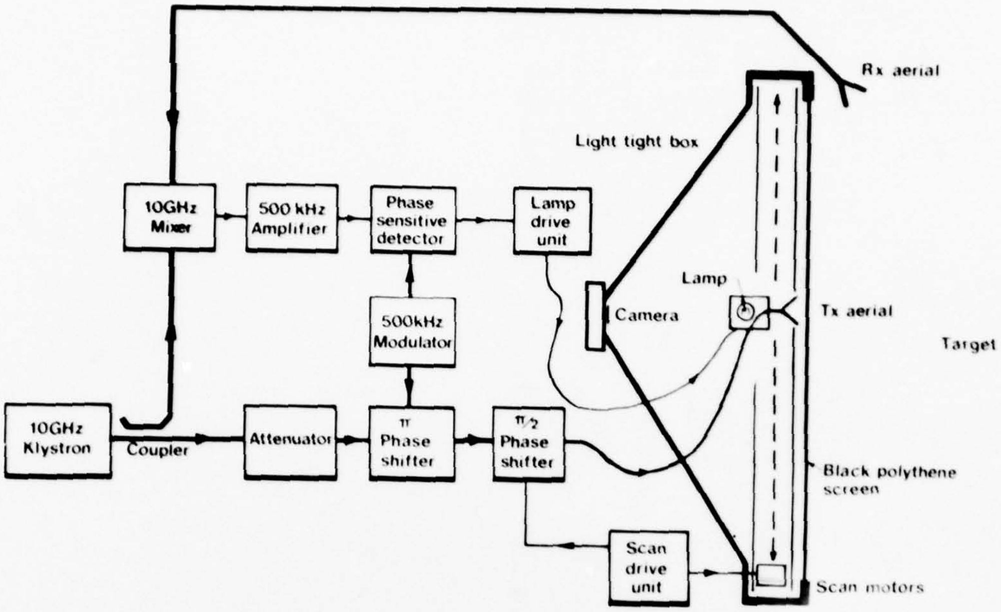
Rx aerial
Light tight box
10GHz Mixer
500 kHz Amplifier
Phase sensitive detector
Lamp drive unit
Lamp
Camera
Tx aerial
Target
500kHz Modulator
10GHz Klystron
Coupler
Attenuator
π Phase shifter
π/2 Phase shifter
Black polythene screen
Scan drive unit
Scan motors

Fig. 9 Typical 10 GHz Holographic Equipment

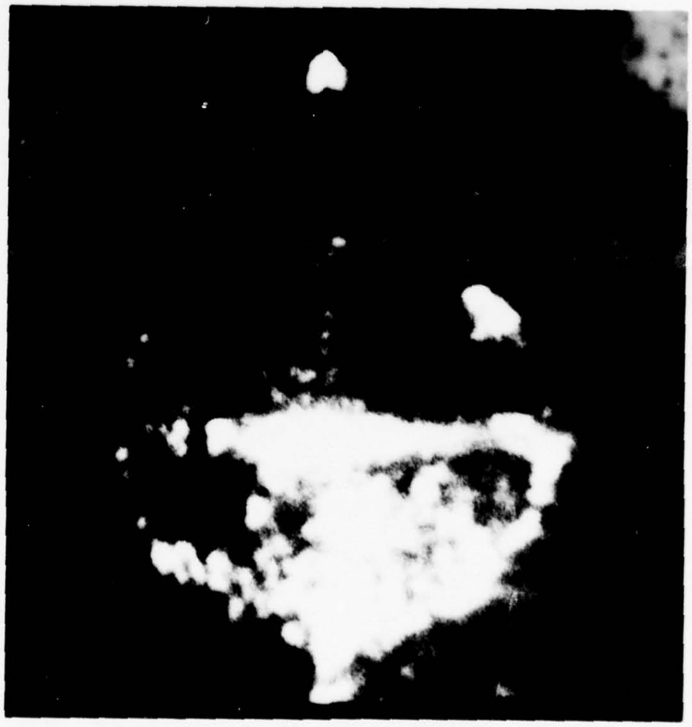

Fig. 10 View through Laboratory Window at 10 GHz

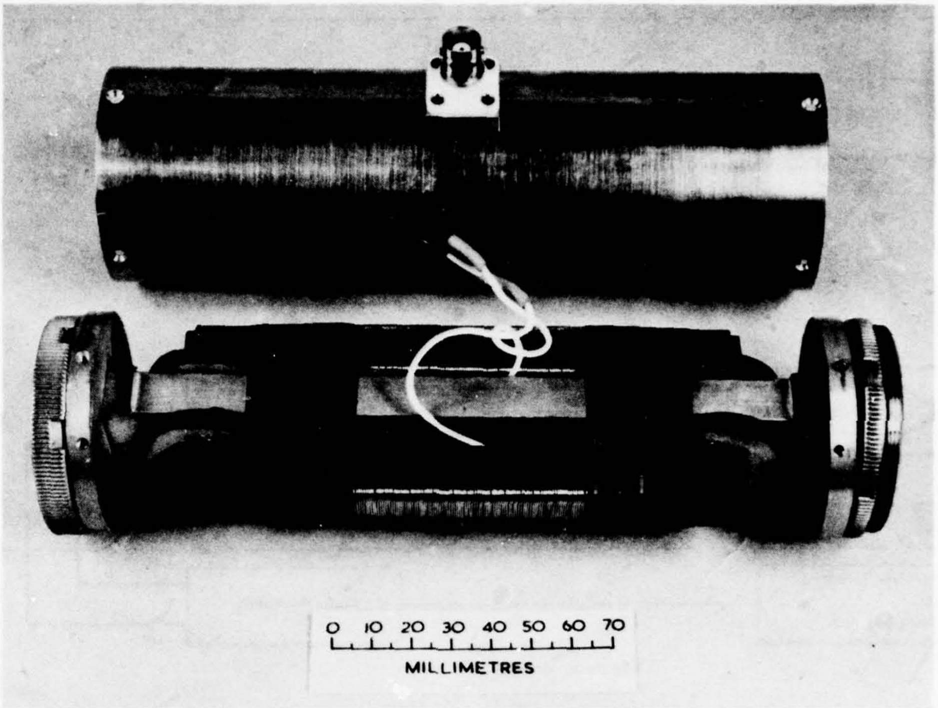
0 10 20 30 40 50 60 70
MILLIMETRES

Fig. 11 10 GHz Ferrite Phase Shifter

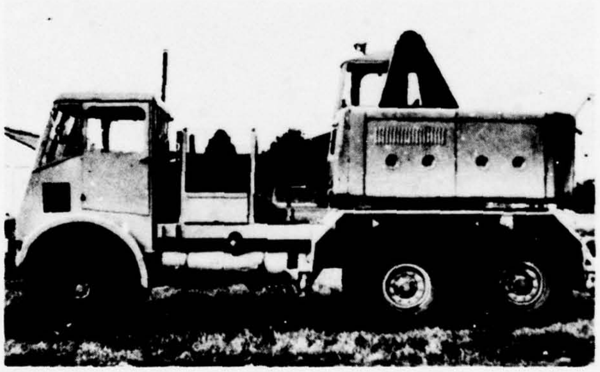

Fig. 12a Target Vehicle

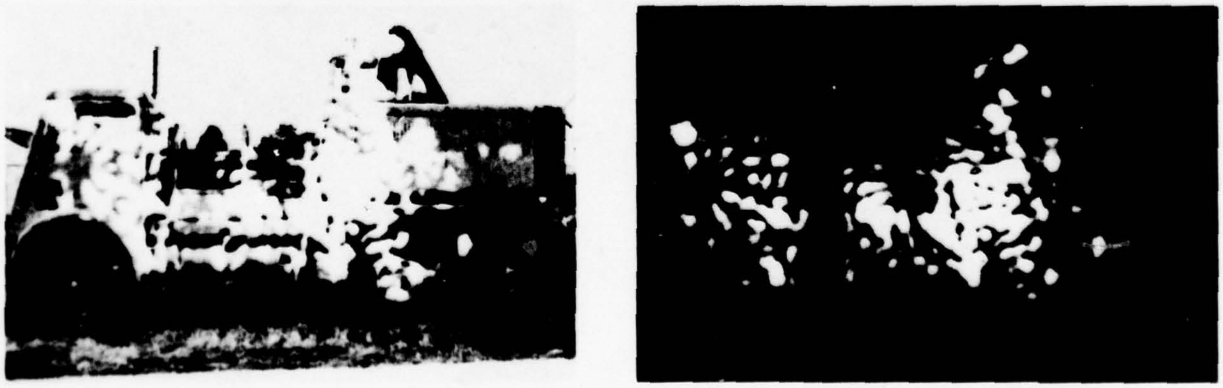

Fig. 12b Superimposed Holographic and Optical Images

Fig. 12c 35 GHz Holographic Image

Fig. 12 Apposition of Optical and 35 GHz Holographic Images

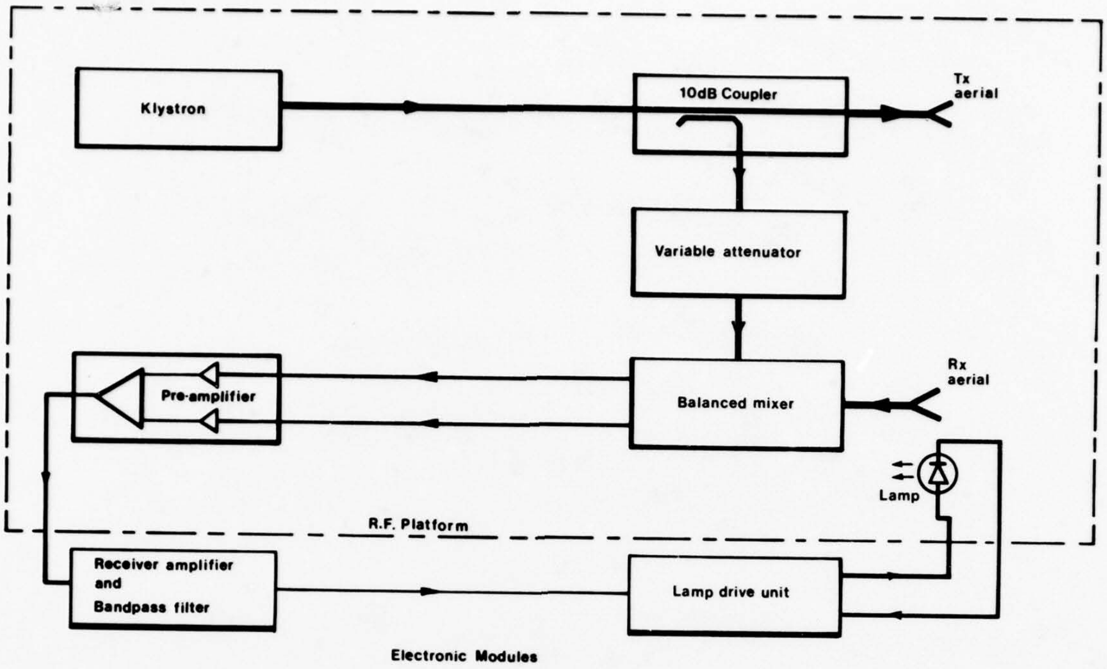
Klystron
10dB Coupler
Tx aerial
Variable attenuator
Pre-amplifier
Balanced mixer
Rx aerial
Lamp
R.F. Platform
Receiver amplifier and Bandpass filter
Lamp drive unit
Electronic Modules

Fig. 13 140 GHz Monostatic System

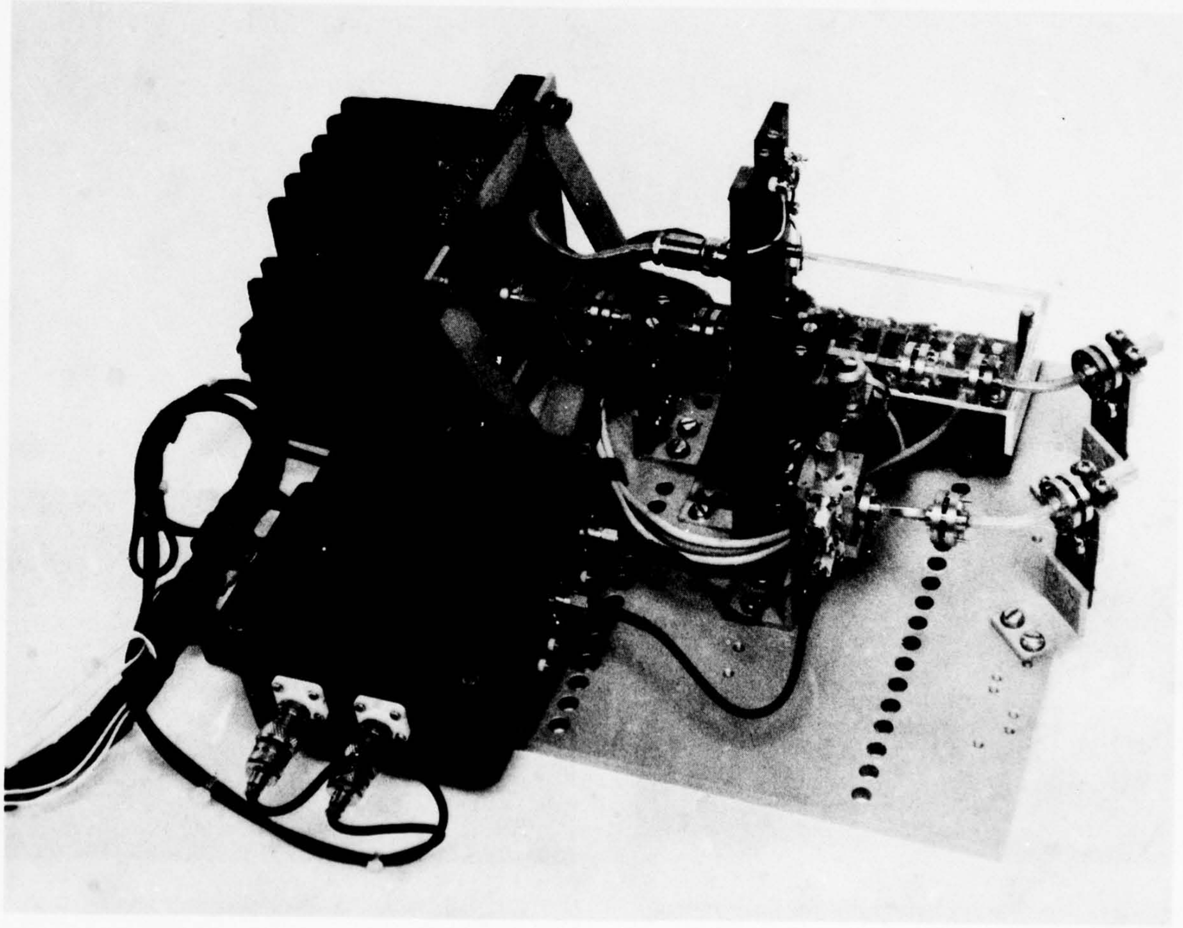

Fig. 14 140 GHz Microwave Head

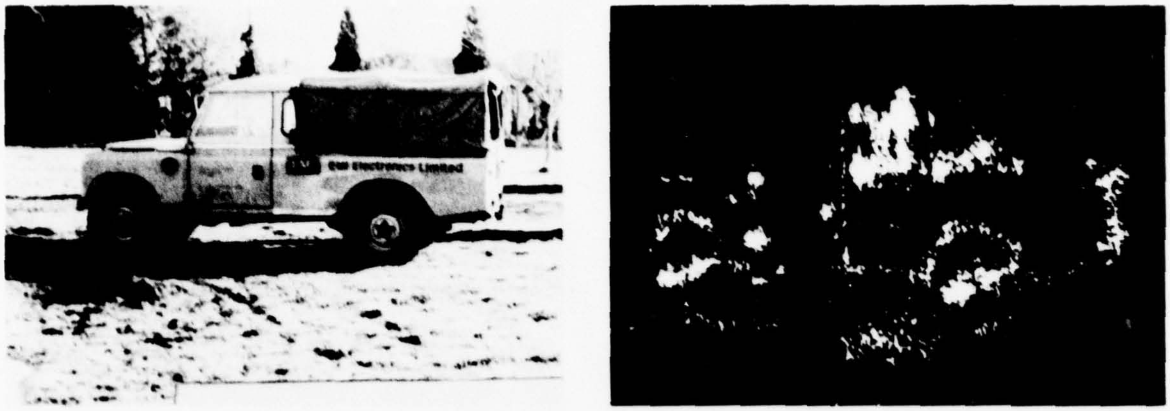
EMI Electronics Limited

Fig. 15 Corresponding Optical and 140 GHz Holographic Images of Landrover

Fig. 16 Reconstruction from a 140 GHz Hologram

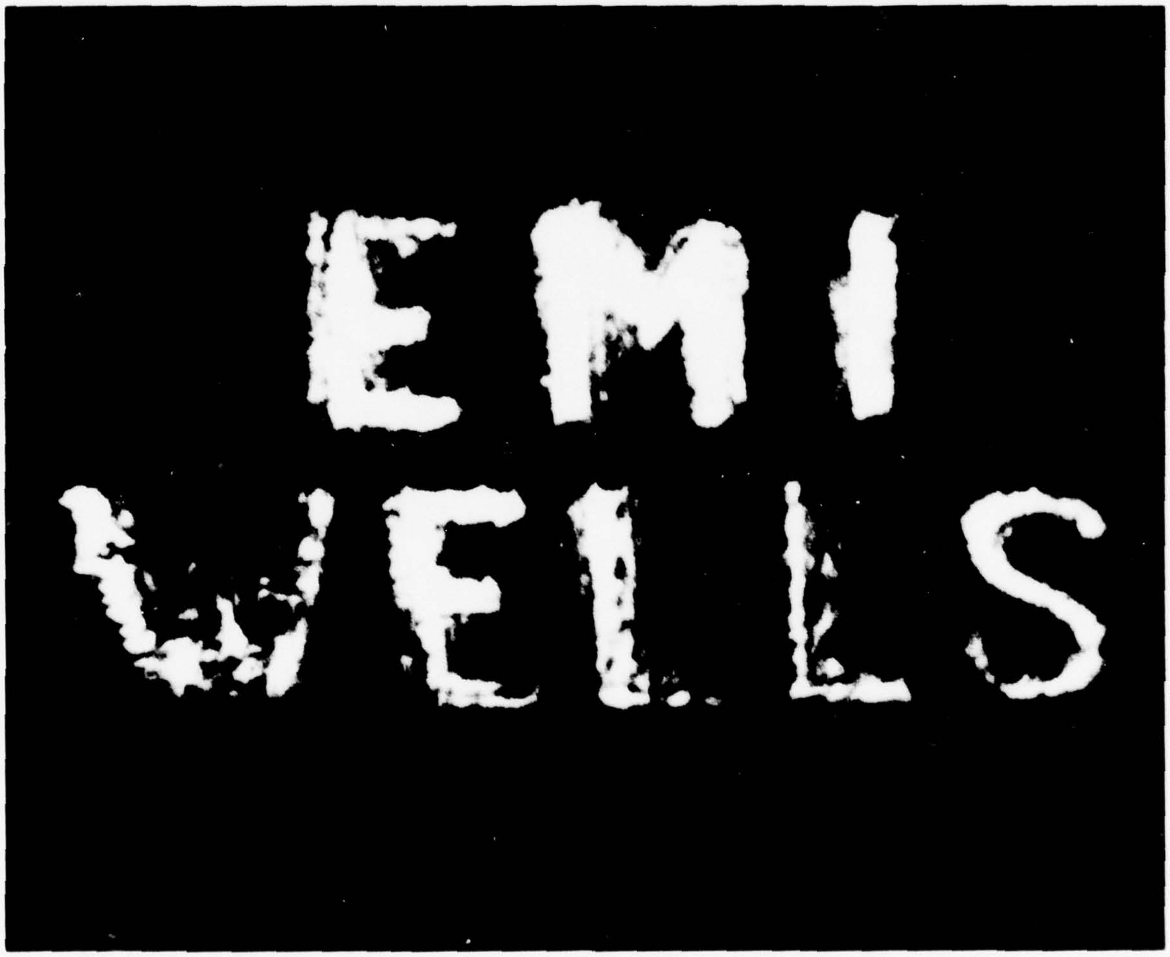

Fig. 16 Reconstruction from a 140 GHz Hologram

DISCUSSION

H.Brand, FRG

What is the recording time for one picture?

Is it possible to get this at real time e.g. less than 20 ms?

Author's Reply

No attempt was made, for the experiments described, to reduce the recording time, which was about 15 minutes (say 1 Ks). The use of rotary scanning rather than reciprocal scanning and the use of multiple receivers and/or transmitters could reduce scanning time as also could suitable "arraythining" techniques. Reductions to the order of 1–10 secs might be envisaged but only for very restricted applications could anything faster be achieved at present, bearing in mind the S/N requirements.

DESIGN AND PERFORMANCE OF 90 GHZ RADIOMETER FRONT ENDS

H. Barth, B. Rembold
AEG-TELEFUNKEN
Geschäftsbereich Hochfrequenztechnik
7900 Ulm/Do.
Federal Republic of Germany

SUMMARY

This paper describes the results of prototype radiometer frontends at 90 GHz using encapsulated whiskerdiodes. The diodes are embedded in a commonly used reduced hight waveguide, but in addition a special fixture allows to move the diodes up and down in respect to the waveguide or to turn it. This leads to a very simple matching procedure. The mixers are easy to balance. LO-power is achieved using a 45 GHz-Gunn-oscillator followed by a varactor-doubler. The unit has an efficiency of 14 % delivering an output power of about 10 mW at 90 GHz. Including isolator losses (0.6 dB) and IF-noise figure (2.5 dB) the dsb noise figure of the entire front end is about 9 dB, whereas the single mixers dsb noise figure is less than 4 dB.

1. INTRODUCTION

This paper describes design and performance of 90 GHz-font ends developed at AEG-TELEFUNKEN. Because of the purpose to realise front ends exhibiting high reliability with good electrical values, the devices incorporate encapsulated whisker diodes, which today still exhibit better mechanical stability. This is important especially regarding military applications.

Problems incorporated in the design of mm-wave-components are not only electrical but even more mechanical ones. Taking into account the excellent tooling-capabilities concerning milling, drilling, soldering, and lathing at AEG-TELEFUNKEN these devices were designed under this conditiones. In fig. 1 the principal block diagram of the devices is shown: Passing the circulator the signal is applied at the H-port of a folded Magic Tee and is down converted by means of two mixers mounted on backside. The LO-power enters the Magic Tee over the E-port. As well known these balanced devices provide a good LO-noise surpression in such a way, that the IF-currents are added, whereas the LO-noise contribution vanishes at the IF-amplifier input. But in contrast to common used lumped IF-hybrid transformers the shown diode configuration needs only a simple IF-junction which delivers less attenuation and more bandwith. In addition the high IF-output resistance which after optimising amounts to 150Ω can be reduced to about 75Ω by connecting mixer's IF-output in parallel.

2. COMPONENTS

2.1 Mixer Device

Fig. 2 gives a look at the mixer's block mount cross-section. The diode is soldered on a coin-silver post, centered and fixed by a collet, which consists of gold plated brass. The advantage of this diode-pick-up is that the diode can easily be matched by turning it or by vertical displacement of diode's position. This allowes to optimise the diode's coupling factor as well as the series inductance. The optimisation procedure demands, of course, a carefully tuning of the backshort. The built up technology needs several steps to get good results: At first the diode's caps as well as the choke's front planes must be covered with a thin layer of solder. After that, the tuning parameters, e.g. the positions of the diode and of the backshort are optimised in respect of conversion loss, noise figure, and balance. The so tuned unit now can be fixed by heating up. Small mismatches caused by this solder procedure can be compensated by change of the short position.

Some words should be said concerning the backshort, which is wellknown in principle, but differs from others in a small detail, fig. 2: The backshort has a second eye spaced half a wavelength from the first. This second eye has a little bit higher diameter compared with the waveguide height. The compression of this eye leads to a controlled bend-up of the first to achieve a good ohmic contact. The material used is fine rolled silver beeing strong enough to compensate some roughness, which may occure at the milled inner waveguide walls. The tapered waveguide itself, the choke section and the collet funnel are tooled in two separate pieces of coin silver press-fitted together in a block of brass. This construction was chosen by reason of the impossibility of gold plating the inner surface. The collet funnel formed by drilling and finished by printing in a special tool has a surface hard enough to allowe a repeated clamping procedure.

To achieve a reproducible positioning of diode and backshort, a suited tuning support has been developed.

In order to achieve an excellent mechanical stability with good electrical values, the choke has to be designed very carefully. The structure centered by a teflon support shell consists of two quarterwave long silver rolls which are stringed and soldered on a thin hardened steel needle. The isolation of the choke is better than 30 dB at 90 GHz.

2.2 Design Aspects for the Local Oscillator

Local oscillators for radiometer receivers at 90 GHz today consists either of a clystron, a 90 GHz-Gunn-oscillator, or of a 45 GHz Gunn-oscillator followed by a varactor doubler. Impatt-oscillators are used rather seldom for this purpose because of their higher inherent noise measure.

The radiometer front ends discussed here are equipped with a varactor doubler. This alternative exhibits a simpler set up compared with a clystron and is less expensive and seems to be more reliable than a 90 GHz Fundamental Mode Gunn Oscillator.

In fig. 3 the used local oscillator is shown. Varactor- and Gunn-mount are built up using reduced height waveguide technique. The cut-off-frequency of the varactor's waveguide is choosen in such a way, that the total varactor mount length amounts to a half wavelength at 45 GHz and to three half wavelength at 90 GHz. To achieve a well matched operation between Gunnelement and varactor diode a tuned combination of iris and WR 19 spacer is used, which together is responsible for decoupling both components at 90 GHz. The oscillator power at 45 GHz is reflected at the input of the WR 10 waveguide. The coaxial RF-band-stop filter of the varactor mount is valid for 45 GHz as well as for 90 GHz.

Some data should be listed up.

45 GHz oscillator typical power:	70 mW
efficiency of the Gunn-element:	1.5 %
varactor output power at 90 GHz:	10 mW
varactor efficiency:	14 %

This unit can be tuned over a frequency range of ± 500 MHz by a sapphire screw.

The application of the receiver for radiometer systems demands a high LO-decoupling of the signal input part. As well known an unbalanced diode mismatch of the LO leads to unwanted LO-leakage which may be responsible for false signals caused by the Dicke-switch or by doppler effects.

To eleminate this LO-leakage a circulator terminated by a sliding load was taken instead of a common used isolator having only 30 dB of isolation. This termination is realised using the small mismatch of a stepped absorber, which has a return loss being similar to the isolation of the circulator. The phase can be tuned by shifting the absorber (sliding load). The decoupling which easily can be reproduced in this way is better than 45 dB. Including 15 dB isolation of the Magic Tee the total LO-decoupling amounts to 60 dB. Thus the front end has a LO-emission of less than -50 dBm at 10 dBm LO-power.

3. ELECTRICAL PERFORMANCE

Fig. 4 gives a look at the front end without IF-amplifier. At the right the circulator with the sliding load can be seen.

The balanced mixer is situated on left hand side and the LO connected with the Folded Tee is placed in the middle.

The electrical data of the selfbiased mixer are:

RF - VSWR (89-91 GHz):	1.45:1
IF - VSWR (0.1-1 GHz):	1.50:1
Conversion Loss (89-91 GHz):	6.5 dB
Broadband DSB-Noise-Figure:	4 dB

The performance of the total front end presented in this paper is:

RF-Frequency-Range	89-91 GHz
DSB-Noise-Figure	9 dB
Input Matching	18 dB
RF/IF-Gain	54 dB
IF-Bandwith	0.1-1.0 GHz
Ripple	± 0,8 dB

The RF/IF-Transmission is shown in fig. 5. The bandlimits are given by the IF-amplifier.

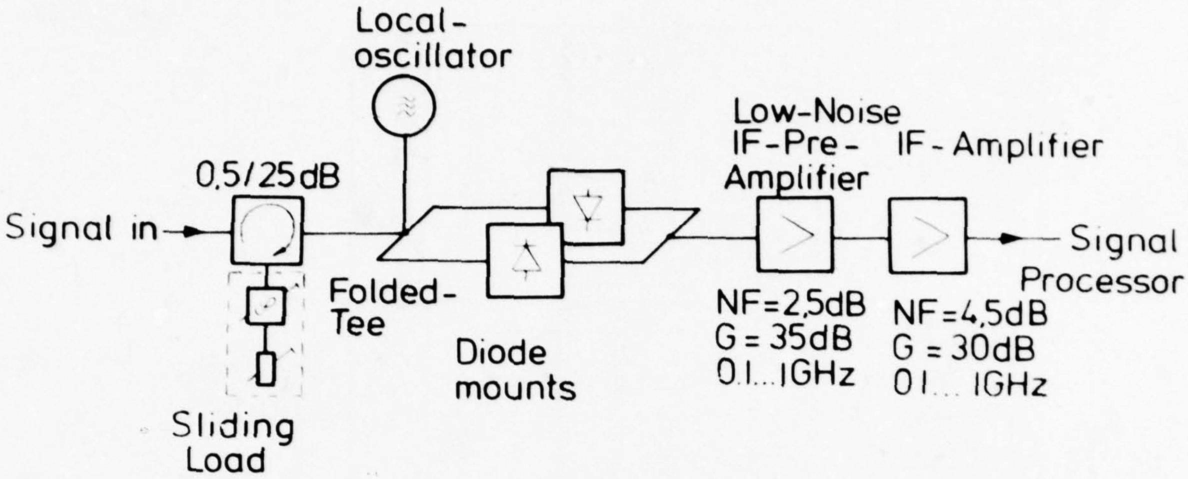
Local-
oscillator
0,5/25dB
Signal in
Folded-
Tee
Diode
mounts
Sliding
Load
Low-Noise
IF-Pre-
Amplifier
IF-Amplifier
NF=2,5dB
G = 35dB
0.1...1GHz
NF=4,5dB
G = 30dB
0.1... 1GHz
Signal
Processor

Fig.1 Radiometer front end

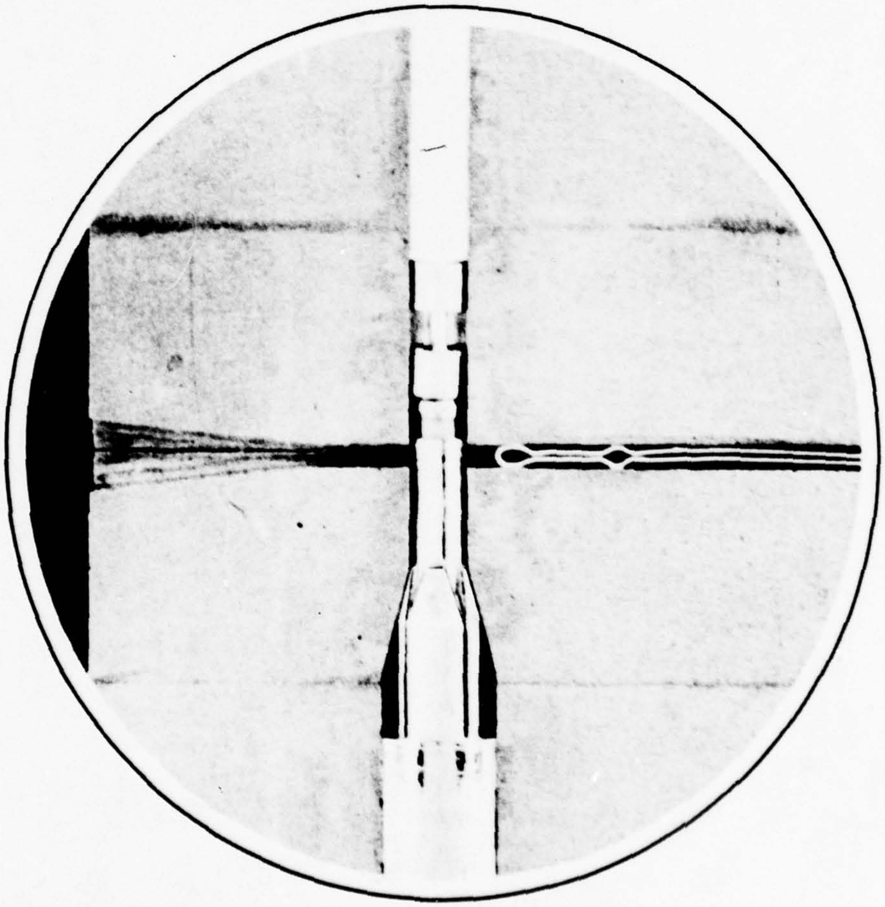

Fig.2 Diode-mount

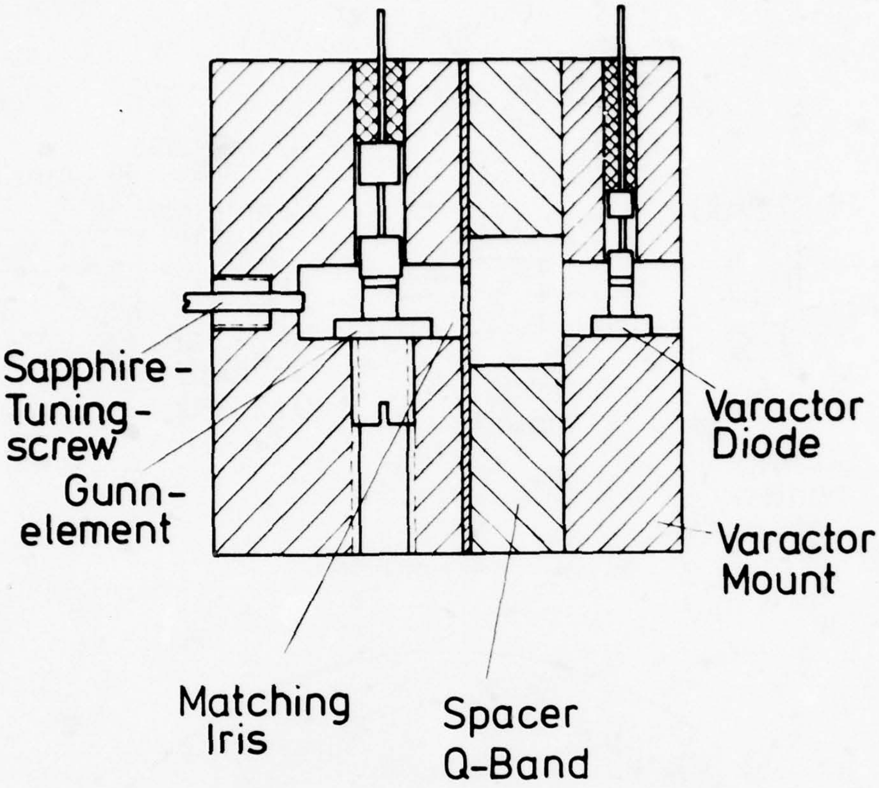
Sapphire-
Tuning-
screw
Gunn-
element
Varactor
Diode
Varactor
Mount
Matching
Iris
Spacer
Q-Band

Fig.3 45-90 GHz doubler

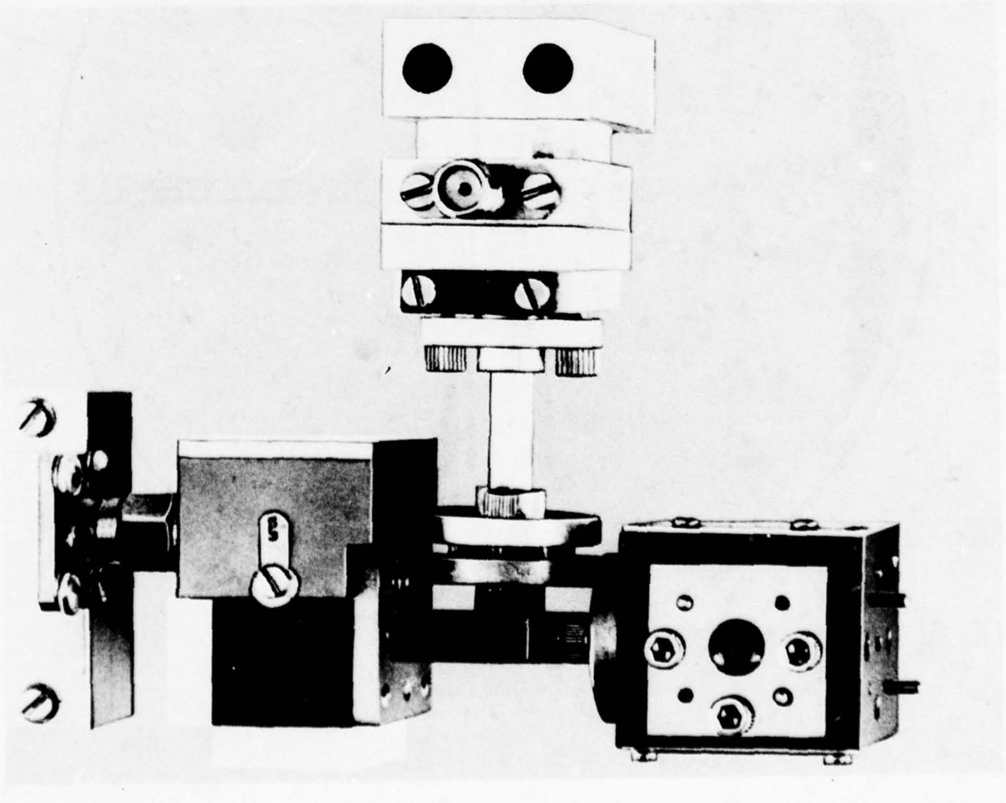

Fig.4 Radiometer front end

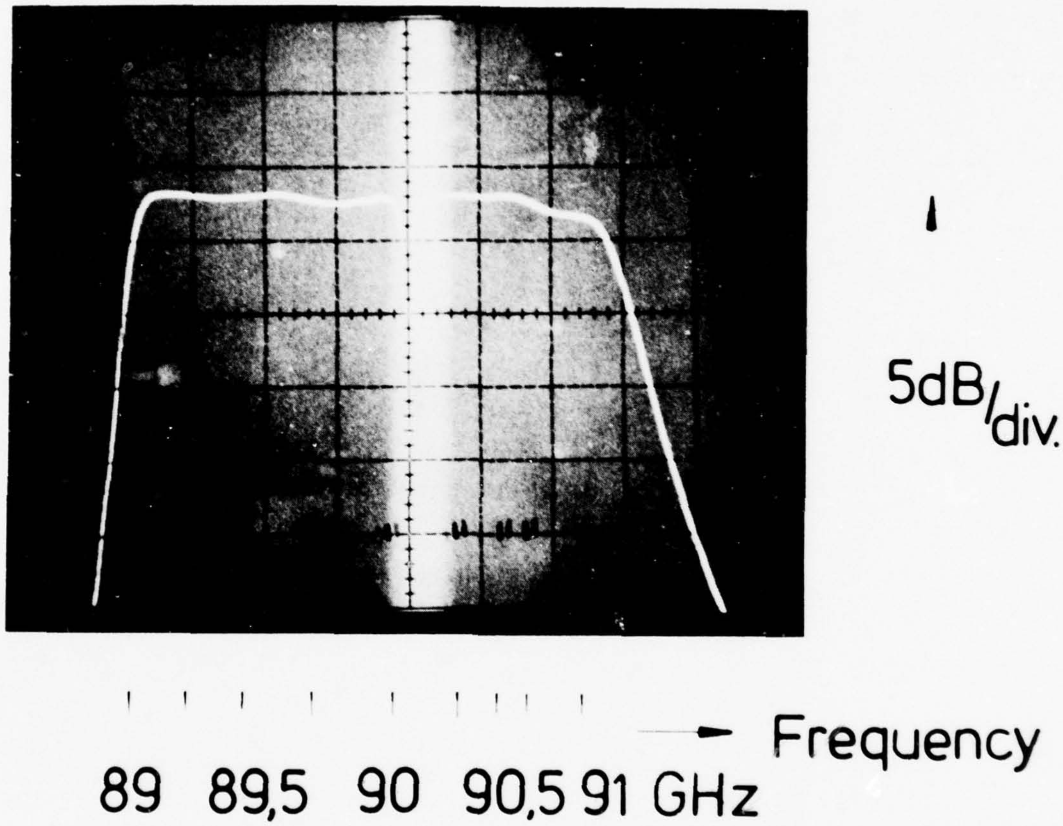

Fig.5 RF/IF-Transmission

Un nouveau composant pour les systèmes millimétriques : le transistor à effet de champ

J-L. TESZNER
Direction des Recherches, Etudes et Techniques - FRANCE

I.- Introduction.-

Le développement des systèmes opérant dans les gammes de fréquence millimétriques a connu des hauts et des bas pendant les deux dernières décennies. Après l'espoir du développement des applications de type télécommunications civiles aujourd'hui disparu avec l'avènement des fibres optiques, il semble qu'aujourd'hui les applications militaires soient clairement définies et représentent un intérêt suffisant pour motiver le développement de systèmes militaires au dessus de 35 GHz, à 94 GHz et 140 GHz en particulier voire 220 GHz (1). Dans un tel contexte, la nécessité de composants fonctionnant en millimétrique apparaît évidente. Or il se trouve que, jusqu'à présent, seules des diodes sont capables d'être utilisées dans cette gamme de fréquences pour réaliser des sources ou des amplificateurs. Les désavantages intrinsèques des diodes vis-à-vis des transistors étant bien connus, il semble donc important de considérer si les transistors à effet de champ (TEC) ne pourront pas dans un avenir proche être utilisé à leur tour au dessus de 35 GHz et ce d'autant plus que l'on assiste aujourd'hui à un développement extraordinaire des TEC en bande I et J. L'objet du présent article est de discuter d'une telle possibilité en considérant à partir des limites actuelles des TEC les méthodes qu'il faudra utiliser tant au niveau de la technologie qu'au niveau du matériau pour réaliser un tel objectif.

II.- Etat de l'art des TEC As Ga.-

Considérons tout d'abord les résultats actuels des TEC. L'examen des performances obtenues en laboratoire des TEC faible bruit (Fig. 1) amène les commentaires suivants :

- les TEC faible bruit ne fonctionnent pas encore au dessus de 35 GHz. Les résultats les plus performants se situent à 18 GHz. Encore faut-il mentionner des résultats extrêmement récents de TEC fonctionnant à 30 GHz (2) et à 26 GHz (3). Ces premiers résultats semblent être annonciateurs de la montée en fréquence des TEC.
- les performances obtenues en bandes I et J le sont à partir de méthodes de réalisation de la couche active extrêmement variées : épitaxie phase vapeur classique, organo-métalliques, implantation ionique, jets moléculaires et même épitaxie phase liquide. Il semble donc nécessaire de disposer d'un arsenal important au niveau technologique pour pouvoir demeurer dans la course.
- le matériau utilisé est essentiellement l'Arseniure de Gallium. Cependant quelques résultats commencent à sortir en Phosphure d'Indium, résultats malgré tout modestes, et en Ga In As qui semblent pour le ternaire être particulièrement remarquables.

Si l'on considère maintenant les résultats des TEC commercialisés (Fig. 2) on constate si l'on regarde les indications des catalogues un écart important. Cet écart est en fait plus considérable qu'il n'y parait au premier abord ainsi que l'a souligné le représentant de Farinon à la Conférence EMC 1978. La courbe donnée par le Dr Chang indique un décalage encore plus marqué qui témoigne de la difficulté d'industrialisation de tels composants. Cette remarque est d'autant plus valable que le TEC est plus complexe à réaliser. Ainsi pour les TEC à longueur de grille 0,5/u seul le NEC 388 est arrivé sur le marché il y a quelque temps déjà (vers 1975). Ce n'est qu'en 1978 que d'autres compagnies sont en mesure de le commercialiser. Cette lente maturation de composants technologiquement complexes est une des clés du problème posé.

Considérons enfin les performances des TEC de puissance (Fig. 3). L'écart entre les résultats commerciaux et les résultats de laboratoire est encore plus net. Cela n'est guère surprenant si l'on songe à l'extrême complexité du composant. Les résultats obtenus par RCA au dessus de 20 GHz ne doivent pas induire en erreur. L'élément moteur de la montée en fréquence des TEC sera le transistor faible bruit. Handicapé par des problèmes d'interconnexions et d'adaptation d'impédance, le TEC de puissance suivra le développement du TEC faible bruit avec un décalage en fréquence maximum de fonctionnement qui ne pourra que s'accentuer. L'analyse du problème posé sera donc consacrée au TEC faible bruit fonctionnant en amplificateur, les résultats et possibilités en oscillateur étant brièvement commentées à la fin.

III.- Les limitations actuelles du TEC faible bruit.-

Si l'on se réfère aux articles de base de Pucel (4) et de Liechti (5), le schéma du TEC et l'origine physique des différents éléments qui le constituent est donnée par la figure 4. Les formules définissant les fréquences maximales d'oscillations fu et ft fréquence de transition pour laquelle le gain en courant devient égal à l'unité sont les suivantes :

F_u fréquence maximum d'oscillation

$$F_u \# \frac{F_t}{\sqrt{r_1 + F_t \tau_3}}$$

F_t fréquence pour laquelle le gain en courant est égal à 1

$$F_t \# \frac{1}{2\pi} \frac{g_m}{C_{gs}}$$

r_1 rapport resistance entrée/sortie

$$r_1 = \frac{R_g + R_i + R_s}{R_{ds}}$$

τ_3 constante de temps égale à 2 $R_g C_{dg}$.

Ces fréquences sont définies en fonction des éléments du circuit du TEC. On peut voir que la montée en fréquence pour les TEC fonctionnant en oscillateur est identique à celle des TEC fonctionnant en amplificateur . Il suffit d'introduire une réaction entre la sortie et l'entrée du TEC de manière à créer un circuit oscillant.

L'augmentation de la fréquence d'oscillation passe par l'augmentation de la fréquence f_t mais aussi par la diminution de r_1 et τ_3. La diminution de r_1 et τ_3 impliquent à leur tour une diminution de Rg, Rs et Cdg donc des éléments parasites du TEC. Considérons tout d'abord l'optimisation de f_t : elle passe par l'augmentation de la transconductance gm et par la diminution de Cgs. L'élément critique est dans ce cas la longueur de grille. Pour des longueurs de grille de 0.5/um ou supérieures, la diminution de L augmente correlativement g_m tout en diminuant Cgs. Pour des longueurs de grille inférieures à 0,5/um, la diminution de L entraînerait une variation de f_t en 1/2. Ces résultats indiqués par Hover et Bechtel en 1973 (6) sont aujourd'hui infirmés par les théories actuelles développées sur les grilles courtes comme on le verra par la suite. La limite à la réduction de grille est atteinte lorsque L $\sim$ D épaisseur du canal. A ce moment le pincement du canal ne peut plus se faire dans de bonnes conditions et g_m se dégrade rapidement comme l'indiquent les premiers résultats de Plessey sur les TEC 0.2 /um. Il faut donc réduire corrélativement l'épaisseur du canal ce qui implique des épaisseurs de couche active de 0.1/um à transition abrupte vers le substrat et par conséquent la maîtrise de l'épitaxie. Ceci n'est pas simple en As Ga, l'entreprise devient autrement périlleuse pour de nouveaux matériaux. Cependant si l'on réduit l'épaisseur il faut augmenter le dopage pour maintenir une densité de courant élevée et une valeur de g_m suffisante. On est limité à ce moment là par le phénomène d'avalanche. Il semble que 2.10^{17} soit une valeur raisonnable qu'il ne soit guère possible de dépasser.

En résumé, il semble qu'un transistor As Ga présentant une longueur de grille de 0.2/um une épaisseur de couche active de 0.1/um et un dopage de 2.10^{17} puisse présenter une amélioration certaine en fréquence et par conséquent fonctionner en millimétrique.

Encore faut-il que les résistances, capacités et selfs parasites soient réduites d'autant ce qui n'est certainement pas chose facile. Considérons trois exemples de ces parasites.

- la résistance R_s résistance d'accès qui englobe la résistance de contact du contact source. Lorsqu'on réduit l'épaisseur du canal cette résistance va naturellement augmenter. Deux possibilités s'offrent alors : soit trouver une structure technologique plus complexe permettant de pallier cet inconvénient, soit trouver de nouveaux matériaux permettant d'avoir une mobilité à bas champ + élevée (à noter déja que l'As Ga est supérieur au Silicium et... au Phosphure d'Indium sur ce point)
- la capacité de grille fait en fait intervenir non seulement la capacité de la couche désertée sous la grille mais aussi la capacité du contact de grille qu'il est nécessaire de réaliser pour pouvoir mettre un fil. Cooke a montré de manière détaillée (7) les conséquences de cette capacité de contact (Figure 5). Pour que cette capacité dont la surface est nettement supérieure à celle de la grille (facteur 70) puisse être minimisée il faut naturellement que la couche sous le contact soit extrêmement résistive d'où la nécessité de maîtriser la réalisation de couches tampons très faiblement dopées ce qui pose certainement un problème difficile à résoudre aujourd'hui si l'on considère de nouveaux matériaux pour la couche active. Cette capacité de contact jouera un rôle de plus en plus important quand on réduira la surface intrinsèque de la grille. De plus en liaison avec le fil de contact qui constitue une self elle constitue un filtre passe bas extrêmement efficace (Figure 6). Autant dire que si l'on veut monter en fréquence, il faudra diminuer au maximum le rôle de ces capacité et self parasites.
- 3ème exemple : la résistance de grille : la diminution de la longueur de grille d'un facteur 2 entraîne l'augmentation de cette résistance d'un facteur 2. Pour conserver des valeurs acceptables à Rg il faut donc épaissir le contact. L'entreprise devient alors critique puisqu'il s'agit non seulement de réaliser des traits de 0.2/um construits à ± 10% sur des largeurs de 50 à 100 /um mais aussi présentant un rapport épaisseur/largeur >> 1. Réaliser un TEC présentant cette compléxité technologique implique l'utilisation de procédés de "lift off" associés à la duplication par rayons X.

L'on peut se demander alors si devant une telle compléxité technologique, le risque d'entreprendre vaut la peine d'être pris. De nouveaux matériaux ne pourraient-ils pas faire l'affaire ? Il me semble que, étant donnée l'avance technologique des TEC à l'Arseniure de Gallium et étant donné l'effet de synergie actuelle des études sur les TEC As Ga, de nouveaux matériaux devront rivaliser avec les TEC As Ga les plus performants et la maîtrise de la technologie 0.2/um sera un point de passage obligé. Avant donc de considérer l'utilisation de nouveaux matériaux, il semble important d'expliciter le fonctionnement du TEC 0.2/um qui est en lui même un nouveau composant.

IV.- Fonctionnement du TEC 0.2/um.-

Dans un tel transistor, les électrons transitant sous la grille d'une longueur de 0.2/um se trouvent dans un état non stationnaire et le fonctionnement du TEC risque d'être modifié par suite de la survitesse des électrons. Ce phénomène mis en évidence par Maloney et Frey (8, 9) est le suivant :

- en état non stationnaire les électrons soumis à une brusque variation de champ électrique, dépassent la vitesse d'équilibre pendant un bref instant ($\sim$ 1/us). Cette survitesse affecte considérablement le fonctionnement des transistors à canal court.

Le phénomène de survitesse est particulièrement intéressant dans les matériaux tels que Ga As et In P qui présentent des vallées satellites. Dans ce cas avant que les électrons ne transitent dans les vallées supérieures une énergie suffisante doit pouvoir leur être communiquée. Si l'on considère que cette énergie est d'origine cinétique elle ne sera acquise qu'en un temps donné fonction de la mobilité à bas champ. Si les porteurs transitent suffisamment rapidement sous la grille, ils n'auront pas le temps de transiter vers les vallées satellites. Pendant le temps de transit les électrons demeureront donc dans la vallée centrale où ils acquerront une vitesse élevée dans le champ élevé du canal (Figure 7).

Les courbes de Maloney et Frey donnent la vitesse instantanée des porteurs plongés dans un champ électrique élevé. On constate que les porteurs acquièrent sur une distance inférieure à 0.5/um des survitesses considérables (Figure 8) la fraction d'électrons passant dans la vallée satellite étant aussi indiquée pour un champ critique respectivement de 5KV/cm pour Ga As et 15KV/cm pour In P. On constate alors que pour des grilles courtes de 0.2/um le temps de transit sous la grille étant de l'ordre de la picoseconde, les électrons conservent la mobilité à bas champ et que les matériaux les plus intéressants dans ce contexte sont les matériaux présentant la mobilité à bas champ la plus élevée.

Les calculs de l'équipe de l'Université de Lille présentés à EMC 78 (10), précisent l'importance de cette survitesse pour les TEC à grille courte (Figure 9). Cette courbe indique la réponse des porteurs dans l'Arseniure de Gallium soumis à un échelon électrique. Les courbes V et E fonction de X montrent la répartition en champ et en vitesse dans le cas d'une grille de 1/um et d'une grille de 0.2/um. On voit très nettement l'importance des effets non stationnaires dans le cas d'une grille de 0.2/um. Pour la grille de 1/um il n'y a pas de survitesse notable sauf à l'extrémité de la grille côté drain lorsque le champ électrique croît rapidement. Par contre pour la structure 0.2/um les effets non stationnaires sont tels que la vitesse moyenne est doublée pendant tout le transit sous la grille*

On constate donc que la réduction de la longueur de grille induit un effet double sur la fréquence de transition, d'une part par la réduction de la longueur d'un facteur 2, d'autre part par une multiplication de la vitesse des porteurs par un facteur 2 qui se répercute directement au niveau de la transconductance (Figure 10).

Le résultat global serait donc un gain d'un facteur 4 sur f_t si les éléments parasites n'étaient pas augmentés d'une part et si la capacité de grille pouvait tendre vers zéro. Il est évident que les effets de bord amènent la valeur de Cgs à tendre vers une asymptote (11) et les variations de Cgs et g_m sont indiquées sur la Figure 11 ainsi que l'évolution de F_T sur la Figure 12 (10). Ces résultats rejoignent ceux de Plessey (12) et montrent qu'il est donc vraisemblable de penser qu'à plus ou moins long terme les TEC As Ga faible bruit à grille courte fonctionneront en millimétrique avec des gains appréciables (> 5 db). D'ici 1980 il est donc raisonnable de penser que des TEC fonctionneront aux alentours de 40 GHz avec des gains supérieurs à 6 db et des facteurs de bruit de l'ordre de 4 db.

V.- L'utilisation de nouveaux matériaux pour les TEC millimétriques.-

Dans un tel contexte quelles peuvent être les chances de développement de nouveaux matériaux pour les transistors à effet de champ ? La réponse est claire. Ils ne pourront se développer qu'à deux conditions :

- permettre de dépasser largement les performances obtenues avec l'Arseniure de Gallium
- avoir eu un développement préalable suffisant indépendamment des applications TEC.

Si l'on considère le premier point la comparaison est toujours difficile à faire et le nouveau matériau partira avec un handicap considérable, celui de la maturité technologique. Cet obstacle risque donc d'être insurmontable s'il n'y a pas eu de développement préalable dans d'autres domaines tels que l'optoélectronique.

Examinons maintenant les différents candidats possibles.

1. Le phosphure d'Indium In P.-

Le phosphure d'Indium a été considéré comme un matériau intéressant en hyperfréquences dès le début des années 70 par Hilsum et ceci plus particulièrement pour les diodes à transfert d'électrons. Rappelons à ce sujet que Gunn avait mis en évidence les oscillations dues au transfert d'électrons entre vallée centrale et vallées satellites dans l'Arseniure de Gallium et... le phosphure d'Indium en 1963. L'intérêt pour les TEC n'est venu que plus tard et les justifications semblent assez limitées. Le bilan présenté par Kennedy à Bruxelles (13) ne permet pas de conclure réellement en faveur de l'In P pour les TEC dans le cadre de la montée en fréquence. L'In P a une mobilité à bas champ nettement plus faible que Ga As (3 000 $cm^2 V^{-1} sec^{-1}$ contre 4 500 $cm^2 V^{-1} sec^{-1}$ pour un même dopage de $10^{17} cm^{-3}$) ce qui le désavantage, d'une part pour des résistances parasites d'accès, d'autre part dans le cas des TEC grille courte. En effet dans le cadre des phénomènes de survitesse le raisonnement simple précédemment indiqué montre que l'arseniure de Gallium est un matériau plus intéressant que le phosphure d'Indium, ce résultat étant confirmé par les calculs de Hill, Robson et Majerfeld (14) montrant qu'en dessous de 0.4/u de grille Ga As devient préférable. De toute façon, il semble bien que les résultats en In P ne puissent être que marginalement supérieurs à ceux obtenus en Ga As à supposer qu'ils le soient réellement un jour ! Car les considérations technologiques apportent encore des arguments en défaveur de l'In P.

* Ce résultat est valable en toute rigueur pour une tension de grille nulle. A tension de grille non nulle il sera nécessaire d'homogénéiser le champ électrique sous la grille par une modification soit du profil de dopage soit de la structure de grille.

En effet la réalisation d'une grille Schottky sur In P est un problème extrêmement difficile étant donnée la barrière de potentiel extrêmement faible (0.3 eV contre 0.8 eV pour Ga As). Les solutions de rechange proposées récemment (15) compliquent immanquablement la réalisation technologique et par conséquent limitent ses chances de déboucher industriellement.

Les résultats à ce jour sont relativement peu nombreux. Mis à part les résultats d'Hewlett Packard en 1975 présentés par Barrera et Archer (15), seuls à ma connaissance ont été publiés les résultats de Plessey par K Gray à Bruxelles (16) et les résultats de Varian à la conférence sur Ga As et les composés III V de Saint Louis (17). Les résultats de Hewlett Packard étaient médiocres mais on pouvait à cette époque incriminer la médiocre qualité du substrat qui était insuffisamment isolant. Les résultats de Plessey et de Varian en 1978 sont plus encourageants mais insuffisants pour provoquer un réel intérêt. A 8 GHz pour une grille de 1.3 μ les résultats de Plessey sont les suivants :

	In P sans couche tampon	Ga As avec couche tampon
Facteur de bruit	3.3 db	3.3 - 5 db
Gain associé	10 db	8.5 - 9 db

Quant aux résultats de Varian indiqués sur la figure 1 ils se placent à un niveau nettement inférieur aux performances actuelles des TEC Ga As à la même figure.

Il semble donc aujourd'hui que l'intérêt majeur des études sur les TEC In P a été l'obtention de matériau semi-isolant de bonne qualité qui manquait il y a quelques années. Or ce maillon, le substrat In P semi-isolant, était un point de passage obligé vers l'utilisation des ternaires et quaternaires III V, maillon qui n'était pas pris en compte dans le cadre du développement des diodes électroluminescentes et des diodes lasers III V...

2. Les composés III V ternaires et quaternaires.-

Les études et recherches sur ces matériaux en vue d'applications hyperfréquences ont été récemment stimulées par la publication Littlejohn et al (18). Les résultats théoriques présentés, en particulier les courbes σ (E), montrent les avantages relatifs des ternaires et quaternaires par rapport à Ga As et In P (Fig. 13). Ces courbes montrent l'intérêt du ternaire $Ga_{0.5}\,In_{0.5}\,As$ et du quaternaire $Ga_{0.27}\,In_{0.73}\,P_{0.4}\,As_{0.6}$ par rapport à Ga As et In P. Le tableau suivant, extrait du même article, résume les caractéristiques des quatre matériaux déduites par Littlejohn et al de calculs de Monte Carlo :

	Ga As	In P	$Ga_{0.5}In_{0.5}As$		$Ga_{0.27}In_{0.73}P_{0.4}As_{0.6}$	
			désordonné	ordonné	désordonné	ordonné
μ_D cm^2 V^{-1} sec^{-1} à 100 V/cm	4600	3100	7900	9700	7000	7800
Vmax cm sec^{-1}	$2{,}010^7$	$2{,}3.10^7$	$2{,}3.10^7$	$2{,}8.10^7$	$2{,}8.10^7$	$3{,}1.10^7$
E max (KV cm^{-1})	5,2	11,5	4,2	3,7	5,0	4,0
$\frac{V\ pic}{V\ vallée}$ vallée (à 16 Kv cm^{-1})	2,1	1,3	3,6	4,0	3,1	3,6
μ_{ND}^* cm^2 V^{-1} sec^{-1}	2300	1100	3200	4800	3600	3700

* μ_{ND} mobilité différentielle négative maximum.

Ces résultats théoriques indiqueraient donc que $Ga_{0.5}\,In_{0.5}\,As$ et $Ga_{0.27}\,In_{0.73}\,P_{0.4}\,As_{0.6}$ seraient des matériaux permettant des performances nettement supérieures dans le cas des transistors à effet de champ à grille courte et que par conséquent des TEC utilisant de tels matériaux fonctionneraient au dela de 50 GHz jusqu'à des fréquences proches de 100 GHz !

Jusqu'à présent les résultats obtenus sur les ternaires et les quaternaires concernent, naturellement, davantage le matériau en lui-même que les TEC réalisés à partir de ce matériau. Si l'on considère tout d'abord le matériau ternaire, les recherches ont porté sur le matériau $Ga_{0.5}\,In_{0.5}\,As$ mais aussi sur le matériau $Ga_{0.8}\,In_{0.2}\,As$. Dans le premier cas ce matériau s'adapte directement au réseau cristallin du phosphure d'Indium et par conséquent l'In P est un excellent substrat pour réaliser à partir de ce substrat une épitaxie du matériau ternaire. Les résultats de Takeda et al (19) publiés au début de cette année sont encourageants. Les couches actives sont réalisées directement sur un substrat In P dopé Chrome ($\rho > 10^5\ \Omega$cm) orienté $(111)_B$ par épitaxie en phase liquide. La concentration de porteurs dans la couche active est de $2{,}3.10^{16}$ pour une mobilité de 8 240 cm^2 V^{-1} sec^{-1}. Il faut noter cependant que la quantité de dislocations est importante dans la couche active ($\sim 10^5$ cm^{-2} dans le meilleur des cas). Cette quantité de dislocations reflète en fait la qualité du substrat qui apparaît donc être un substrat de qualité médiocre tant par le niveau de dislocations que par sa faible résistivité. Il semble de toute façon nécessaire de réaliser une couche tampon non intentionnellement dopée entre le substrat et la couche active. La complexité d'une telle étude n'échappera à personne si l'on se rappelle l'ampleur des efforts consacrés à la maîtrise de la couche tampon de Ga As sur un substrat semi-isolant Ga As ! Il faut mentionner enfin que dans un article très récent (20), Varian consacre des résultats remarquables sur ce type de matériau : pour un dopage 10^{17} cm^{-3} une mobilité de 8 000 cm^2 V^{-1} sec^{-1} mais ne donne guère de détails sur le mode de réalisation.

Les recherches sur $Ga_{0.8}\,In_{0.2}$ ont été essentiellement faites jusqu'à présent par Varian avec le soutien de l'Office of Naval Research en particulier. La méthode de croissance décrite par Hyder (21) en 1976 est une méthode de croissance en phase vapeur bien adaptée à la réalisation de couches tampons permettant une adaptation cristallographique graduelle entre le substrat Ga As semi-isolant et la couche active de $Ga_{0.8}$ $In_{0.2}$ As. La couche tampon est rendue isolante par l'introduction dans le réacteur de Cr O_2 Cl_2 qui permet d'obtenir ainsi des résistivités de l'ordre de 2.10^8 Ω cm. Les couches d'adaptation ont typiquement une épaisseur de 3/u et la mobilité des couches actives ainsi réalisées est supérieure à 5 000 cm^2 V^{-1} sec^{-1} pour un dopage de $10^{17} cm^{-3}$. Les résultats obtenus en 1977 par Varian (22) mettent en évidence la dégradation de la valeur de la vitesse de saturation à mesure que l'on se rapproche de l'interface cristallographique, dégradation plus rapide que pour l'arseniure de gallium. Ce résultat indique donc clairement que la qualité de l'interface couche active - couche tampon n'est pas encore satisfaisant et qu'il conviendrait probablement de différencier l'interface électrique de l'interface cristallographique. Ceci étant, les résultats actuels sont d'ores et déjà très encourageants en bande I. Les valeurs données par M. Yoder (23) à Bruxelles montrent que Varian a réalisé des TEC $Ga_{0.9}$ $In_{0.1}$ As de longueur de grille 0.8/u avec un facteur de bruit de 2.3 db et un gain associé de 13 db à 8 GHz sous polarisation de grille nulle ce qui indique que de nombreux états d'interface se trouvent entre la couche tampon et la couche active et que la mobilité sous la grille est nettement plus élevée que près de la couche tampon. A titre de comparaison un TEC As Ga ayant la même définition donnerait 4 db de facteur de bruit à 8 GHz sous polarisation nulle.

Si l'on considère enfin les résultats sur $Ga_{0.27}$ $In_{0.73}$ $P_{0.4}$ $As_{0.6}$ on ne dispose pour confirmer ou infirmer les résultats théoriques de Littlejohn que des résultats publiés récemment par Varian (20). Les couches ont été réalisées en épitaxie phase liquide (à noter qu'il s'agit là d'un transfert direct de connaissances provenant des recherches en optoélectronique et notamment en photocathodes...). Les couches ont été réalisées sur substrat In P semi-isolant orienté (100) dopé Chrome ou dopé Fer. Les couches tampons présentent une concentration de porteurs de 2.10^{16} cm^{-3} ce qui semble excessif et la mobilité dans la couche active n'est que de 7 450 cm^2 V^{-1} sec^{-1} à 77°K pour le matériau quaternaire présentant une largeur de bande interdite de 0,9eV. Les résultats sur un transistor de longueur de grille 5/u indiquent un gain maximum de 5 db à 10 GHz pour un matériau ayant une largeur de bande interdite de 1,2eV. Ces résultats au niveau des TEC ne peuvent être considérés comme significatifs. Il n'en demeure pas moins que les caractéristiques du matériau obtenu sont loin d'être celles déduites par Littlejohn de son modèle. Il est probable que le matériau réalisé aujourd'hui est loin d'être optimisé mais il semble aussi que le modèle présenté par Littlejohn et al ait besoin de sérieuses retouches en particulier sur le problème de la diffusion induite par la structure désordonnée du matériau.

Il semble donc aujourd'hui que les résultats les plus encourageants soient ceux obtenus sur le ternaire $Ga_{0.47}$ $In_{0.53}$ As sur substrat semi-isolant In P. Malheureusement ce matériau présente comme In P une barrière de Schottky trop faible ($\sim$ 0.3eV) et par conséquent les courants de fuite au niveau de la grille risquent d'être importants. L'évolution de la barrière de surface en fonction de la teneur en indium du matériau Ga_{1-x} In_x As a été donnée dès 1973 par Kajiyama et al (24). On voit donc que par contraste avec $Ga_{0.8}$ $In_{0.2}$ As pour lequel le potentiel de surface demeure acceptable, la valeur obtenue pour $Ga_{0.47}$ $In_{0.53}$ As est inacceptable pour un fonctionnement correct des TEC. Il en serait de même pour $Ga_{0.27}$ $In_{0.73}$ $As_{0.6}$ $P_{0.4}$ pour lequel $\emptyset s$ serait égal à 0.4eV. Une grille de type Schottky est donc à proscrire. Heureusement d'autres solutions existent potentiellement qui tirent parti de la souplesse introduite par l'existence d'un ou deux paramètres complémentaires à savoir composition relative Ga/In et éventuellement P/As. De telles solutions conduiront immanquablement à compliquer la structure donc à accroître les difficultés technologiques de réalisation de TEC à partir de matériaux III V ternaires et quaternaires.

VI.- Considérations sur les TEC de puissance et les TEC montés en oscillateur.-

Ainsi que je l'ai mentionné dans l'introduction le développement des TEC de puissance fonctionnant en millimétrique se fera plus difficilement par suite des problèmes posés par les interconnexions et les adaptations d'impédance. L'interconnexion au niveau des TEC de puissance pose des problèmes de topologie particulièrement complexe puisqu'il s'agit d'associer en parallèle un grand nombre de TEC élémentaires afin d'obtenir le développement de grille maximum tout en maintenant un niveau acceptable de résistances, capacités et selfs parasites. La tendance actuelle est de tirer parti des trois dimensions au lieu de se limiter à un espace plan pour prendre les contacts sur les trois électrodes. Le contact de source est pris soit à travers des piliers qui permettent de relier la source au dissipateur thermique (25-26) soit par une structure flip-chip utilisée par RCA et MSC. Quant au problème d'adaptation d'impédance, il ne pourra être résolu que par l'amélioration du facteur de mérite à savoir l'augmentation de la puissance délivrée par millimètre de grille. Enfin si l'on considère le phénomène de survitesse discuté précédemment, il risque fort de ne pas se produire ou tout au moins d'être fortement diminué. En effet par suite de l'importance des tensions appliquées au bornes, le champ électrique sous la grille sera plus élevé et par conséquent si l'on se réfère aux courbes de Maloney et Frey (Fig. 8) l'effet de survitesse sera plus faible, les électrons transitant plus rapidement vers les vallées satellites. De plus lorsque V_{DS} est élevé, l'extension latérale de la zone de désertion sous la grille se déplace vers le drain et contrôle le temps de transit des électrons. En effet par suite de l'importance du champ atteint, la vitesse de saturation est atteinte et le phénomène de survitesse négligeable (27). En conclusion l'ensemble de ces données fait que la montée en fréquence des transistors de puissance se fera beaucoup plus lentement que dans le cas des transistors faible bruit et que, par conséquent, il est difficile aujourd'hui de prévoir à quelle date il sera possible de disposer d'un transistor délivrant une puissance de l'ordre du Watt à 50 GHz.

Considérons enfin le TEC monté en oscillateur. Si l'on considère la fréquence maximum d'oscillation telle que définie dans la première partie :

$$fu = \frac{f_T}{\sqrt{2 \quad r_1 + \tau_3 f_T}}$$

on peut dire que la montée en fréquence d'un TEC fonctionnant en amplificateur va de pair, intrinsèquement, avec la montée en fréquence d'un TEC fonctionnant en oscillateur. Il suffit de placer un TEC dans un circuit présentant une réaction de la sortie sur l'entrée afin d'obtenir des oscillations entretenues. Deux configurations sont possibles :

1. grille électrode commune : une inductance placée entre la grille et la masse permet alors de créer la réaction désirée. L'ajustement de la longueur de fil de grille permet de régler la fréquence.

2. source électrode commune : la capacité entre la grille et la source est alors l'élément de réaction.

L'augmentation du développement de grille permet alors d'augmenter la puissance de sortie et la diminution de la longueur de grille permet la montée en fréquence, les limitations décrites dans le cas des TEC en amplification demeurant valables.

Si l'on considère maintenant les résultats, ils sont encourageants mais faut-il encore le souligner, l'élément moteur étant le TEC faible bruit en amplificateur, les résultats sur le TEC monté en oscillateur sont plus récents et nettement en retrait. Citons les résultats obtenus par Texas Instruments qui sont particulièrement intéressants (28).

FREQUENCE GHz	P_s mW	RENDEMENT %	LONGUEUR DE GRILLE μm	LARGEUR DE GRILLE μm	STRUCTURE
8,2	132	36	2	600	source : électrode commune
8,6	300	15	1	1 200	grille : électrode commune
9,0	500	26,8	1	2 400	"
10,0	50	45	0,5	300	"
11,5	210	17,5	1	1 200	"
15,2	150	9	1	3 600	"
22,7	10	8,6	0,5	300	"
25,2	6,5	4,7	0,5	300	"

Signalons enfin qu'au niveau commercial il semble que MSC aujourd'hui présente le TEC le plus performant : 1 W de puissance délivrée en oscillation à 12 GHz.

VII.- Conclusion.-

Au terme de cet exposé sur la montée en fréquence des TEC, il me semble évident que l'on puisse dire sans risque de se tromper, que les TEC faible bruit ont largement la possibilité de fonctionner en millimétrique d'une part par la réduction de la longueur de grille et la réduction concomitante des résistances et capacités parasites, d'autre part par l'utilisation de nouveaux matériaux III V ternaires et quaternaires. Déjà au cours de l'année 1978 des premiers résultats en bande K ont été signalés et il est probable que l'effet de synergie actuel fera que ce développement ira en s'amplifiant. Dès 1980 il est probable que des TEC grille courte fonctionnant aux alentours de 50 GHz avec un gain supérieur ou égal à 5 db mais ce n'est que dans le courant de la prochaine décennie que l'on verra réellement apparaître sur le marché des TEC à base de matériaux III V ternaires et quaternaires. L'introduction d'hétérojonctions dans le domaine des composants hyperfréquences risque de provoquer à terme un bouleversement total de la situation actuelle, les hétérostructures présentant un nombre considérable d'avantages potentiels qui dépassent le cadre des transistors à effet de champ. Citons en particulier la possibilité de réaliser des diodes à avalanche en hétérostructure. L'introduction d'un degré de liberté complémentaire devrait permettre d'améliorer considérablement le rendement et même la puissance de sortie des diodes. En effet la réalisation d'hétéroépitaxies permettrait de réaliser une zone d'avalanche dans un matériau à faible largeur de bande interdite où le champ d'avalanche est plus faible et de réaliser la zone de transit dans un matériau ayant une mobilité à bas champ élevée. Les essais réalisés aux Etats-Unis et en France (29-30) sur des structures Ge-AsGa se sont révélés infructueux par suite de la difficulté d'obtention de couches hétéroépitaxiées de bonne qualité mais l'utilisation de structures telles que $Ga_{0,47}\ In_{0,53}\ As/InP$ devrait à cet égard se révéler beaucoup plus fructueuse. Quant aus diodes de type Gunn, les calculs théoriques de Littlejohn et al sembleraient indiquer un intérêt potentiel des matériaux III V ternaires et quaternaires. Les premiers essais (31) ont jusqu'ici seulement mis en évidence la possibilité d'obtenir dans ces matériaux des oscillations de transfert d'électrons.

Il apparaît donc que les hétéroépitaxies pour les composants hyperfréquences sont promises à un développement important. Si l'on condidère que cet effort sur les matériaux doit aller de pair avec un accroissement de la complexité technologique par suite de la diminution des dimensions des composants, l'on peut se demander si la prochaine décennie ne verra pas une forte diminution du nombre de sociétés actives dans le domaine car le coût des investissements risque fort de se révéler trop important pour nombre de petites sociétés qui ont jusqu'ici réussi avec succès à damer le pion aux plus grands laboratoires industriels.

Souhaitons en conclusion que malgré tout cette diversité puisse se maintenir car la situation actuelle est source d'esprit de compétition et est donc, bel et bien, à l'origine de l'essor actuel.

- REFERENCES -

1. L. Whicker "The Potential of mm waves for Military Applications" Agard meeting on millimetre and submillimetre wave propagation and circuits Münich 4-8 Sept. 1978.

2. C.S. Krumm, H.T. Suyenatsu et B.L. Walsh "30 GHz FET Amplifier" 1978 IEEE MTT Symposium Ottawa pp 383 - 385.

3. Chiung T. Li, Philip T. Chen, Patrick H. Wang "A K -Band Ion-Implanted GaAs FET "European Microwave Conference Proceedings Paris Sept. 1978 pp 396 - 400.

4. R.A. Pucel, H.A. Haus et H. Statz "Signal and noise properties of Gallium arsenide microwave field Effect transistors "Advance in electronics and Electron Physics" Vol 38 1975.

5. C.A. Liechti "Microwave Field Effect Transistors 1976" IEEE MTT Vol 24 N° 6 Juin 1976 pp 279 - 300.

6. P. Hover et G. Bechtel "Current saturation and small signal characteristics of GaAs FET" IEEE Trans. El. Devices Vol ED 20 Mars 1973 pp 213 - 220.

7. H.F. Cooke "Microwave Field Effect Transistors in 1978" Microwave Journal Avril 1978 pp 43 - 48.

8. JJ. Maloney et J. Frey "Frequency Limits of GaAs and InP FET at 300°K and 77°K with typical Active Layer doping"
IEEE Trans. Devices ED 23 Mai 1976 p 519.

9. T.J. Maloney et J. Frey "Transient and Steady State Electron Transport Properties of GaAs and InP" J. Appl. Phys Fevrier 1977 Vol 48 n° 2 pp 781 - 787.

10. B. Carnez, A. Cappy, A. Kaszinski at G. Salmer "Desk computer simulation of FET.s including non stationary electron dynamics" European Microwave Conference Proceedings Paris Sept. 1978 pp 410 - 414.

11. R.A. Pucel, H.A. Haus et H. Statz "Signal and noise properties of Gallium arsenide microwave field effect transistors "Advance in Electronics and Electron Physics Vol 38 1975 .

12. J.Turner "The versatile FET expands its horizons" Microwave System News Fevrier 1978 pp 71 - 74.

13. J. Kennedy, H. Lessoff et D.L. Lile "InP An Assessment of US Activities" Proceedings of the Symposium on microwave components for the frequency range above 6 GHz Bruxelles Janvier 1978 pp 115 - 182.

14. G. Hill, P.N. Robson, A. Majerfeld "Effects of ionised impurity scattering on the electron transit time in GaAs and InP FETs" Electronics letters 14 Avril 1977 Vol 13 n° 8 pp 235 - 236.

15. O. Weda at A. Majerfeld "Low Leakage nearly ideal Schottky barriers to n-InP Electronics Letters 2 mars 1978 Vol 14 n°5 pp 125 - 126.

15^b. J.S. Barrera and R.J. Archer "InP Schottky Gate Field Effect Transistors" IEEE Trans. El. Devices ED 22 Nov. 1975 pp 1023 - 1030.

16. K. Gray and P.W. Braddock "Recent Progress in InP Microwave Active Devices" Symposium on microwave components for f above 6 GHz Bruxelles 1978 pp 183 - 192.

17. H. Morkoc, S. Hyder et J. Andrews "InP Mesfets prepared by VPE" 7th Int. Symposium on GaAs and Related Compounds 24 - 27 Septembre 1978 St. Louis.

18. M.A. Littlejohn, J.R. Hauser et T.H. Glisson "Velocity field characteristics of Ga_{1-x} In_x P_{1-y} As_y quaternary alloys" Appl. Phys. Lett. Vol 30 n° 5 1er Mars 1977 pp 242 - 244.

19. Y. Takeda, A. Sasaki, Y. Inamura et T. Takagi "Properties of Liquid Phase Epitaxial In_{1-x} Ga_x As ($x \neq 0.5$) on InP substrate" J. Electrochemical Soc. Janvier 1978 pp 130 - 135.

20. H. Morkoc, J.T. Andrews. Y.M. Houng, R. Sankaran, S.G. Bandy, G.A. Antypas "Microwave In_x Ga_{1-x} As_y P_{1-y}/InP FET" Electronis Letters 6 juillet 1978 Vol 74 N° 14 pp 448 - 449.

21. S.B. Hyder "Thin Film Epitaxial Growth of In_x Ga_{1-x} As on GaAs" J. Electrochemical Soc. Octobre 1976 pp 1503 - 1508.

22. R.L. Bell and S.G. Bandy "Investigation of InGaAs FETs" ONR Final Report Nov. 1976 - Feb. 1977.

23. M.N. Yoder "Solid State Microwave and Millimeter Wave Device Advances in the U.S." Symposium on Microwave Components for f above 6 GHz Bruxelles Janvier 1978 pp 268 - 298.

24. K. Kajiyama, Y. Mizoshima et S. Sakata "Schottky barrier height of n In_x Ga_{1-x} As diodes" Appl. Phys. Lett. Vol 23 N° 8 15 octobre 1975 pp 458 - 459.

25. L.A. d'Asaro, J.V. di Lorenzo et H. Fukui "Improved Performances of GaAs Microwave FET with Low inductance via-connections through the substrate" IEEE Trans. El. Devices Oct. 78 Vol ED 25 Nr10 pp 1218 - 1221.

26. P. Baudet, M. Binet, D. Boccon-Gibod et L. Hollan "Self Aligned GaAs Power Mesfet's for X. Band" EMC 1978 pp 391 - 395.

27. H. Yamasaki et D.K. Mclain "Velocity Overshoot effect on the FET devices" Cornell Workshop Août 1977.

28. H.Q. Tserng, H.M. Macksey et V. Sokolov "Performance of GaAs MESFET oscillators in the frequency range 8-25 GHz". Electronics Letters 3 Février 1977 Vol 13 n° 3 pp 85 - 86.

29. B.B. Wollins "New Impatt R and D drives up efficiency ; processing key to improved specs" Microwaves Décembre 1977 pp 9 - 18.

30. D. Delagebeaudeuf, Bui, M. Lecroesl et M. Colombier. "Heteroepitaxie de Germanium sur arseniure de gallium" Marché DRME 76.34.395.

31. R.E. Hayes et R.M. Raymond "Observation of the transferred electron effect on Ga_x In_{1-x} As_y P_{1-y}" Appl. Phys. Lett. Vol 31 n° 4 15 avril 1977 pp 300 - 301.

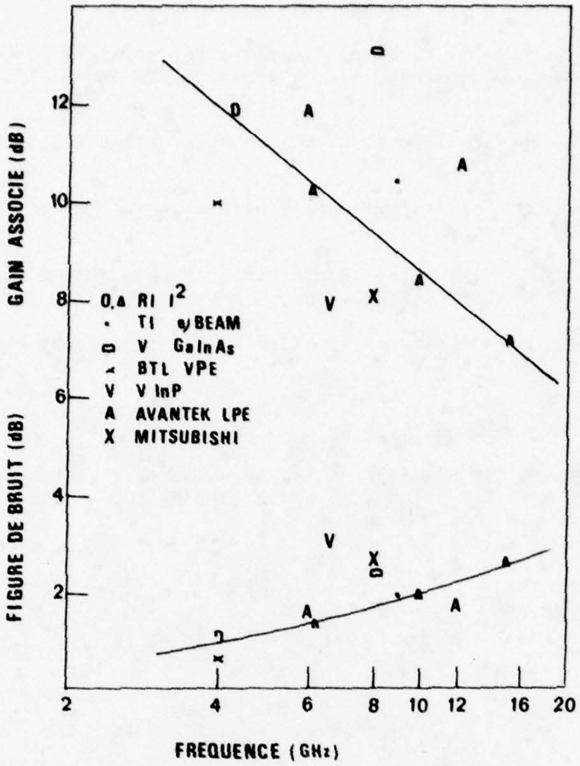

Fig. 1 Performances actuelles en laboratoire des TEC faible bruit

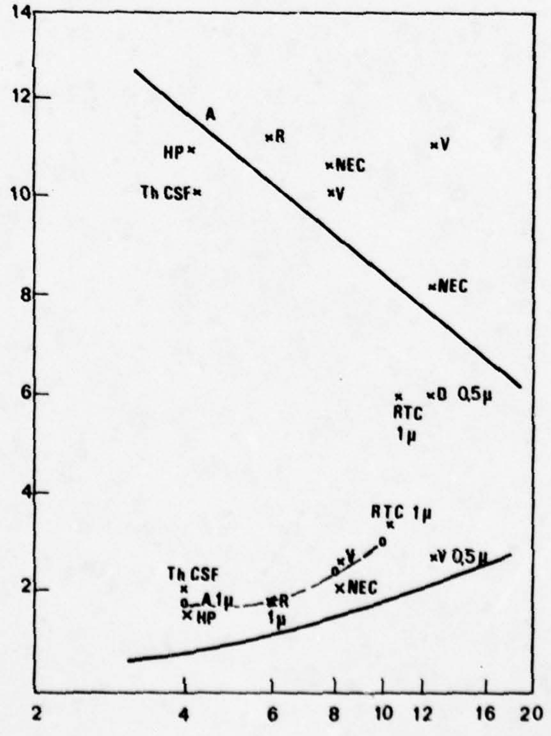

o · Figure de Bruit Disponible (EMC 78)

Fig. 2 Performances actuelles commerciales des TEC faible bruit

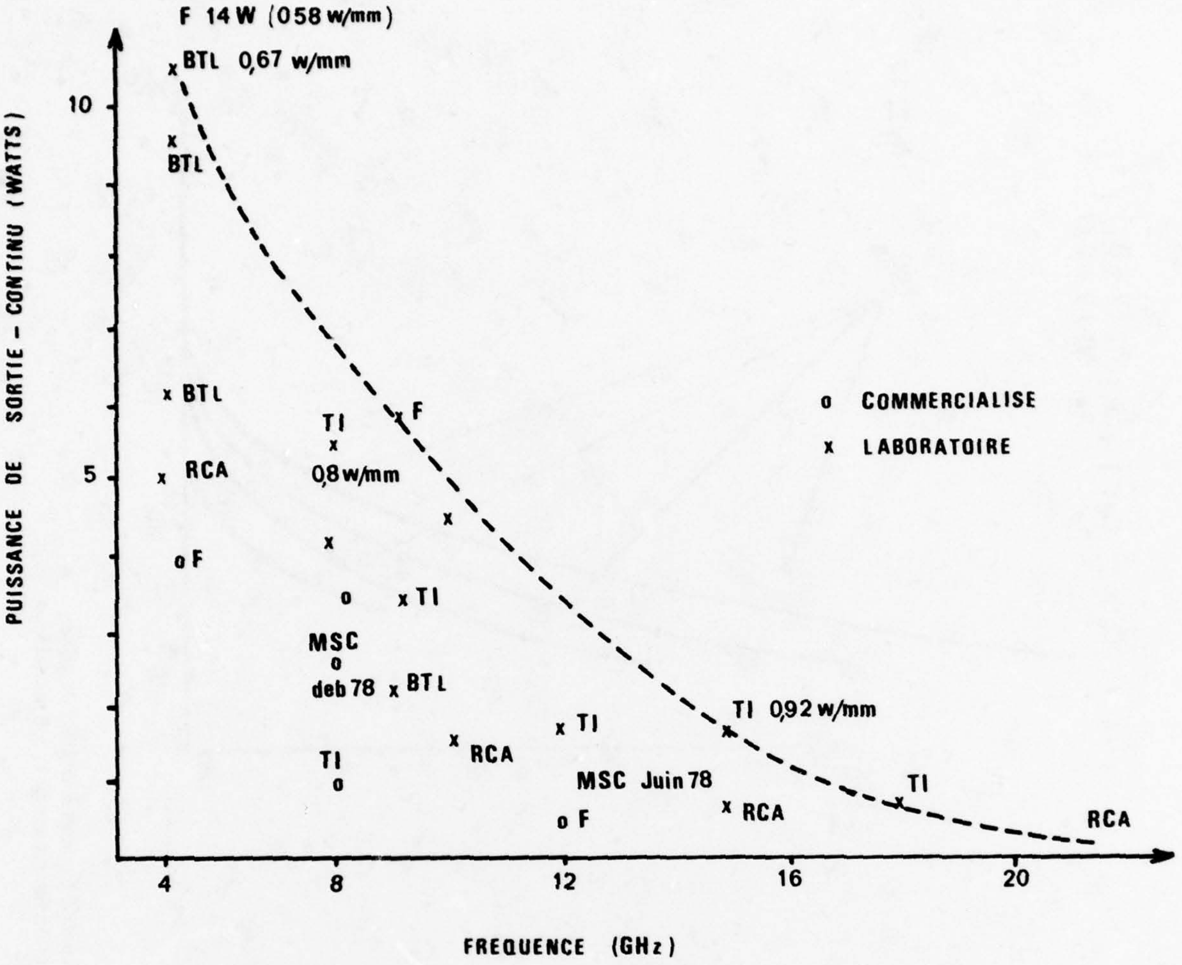

Fig.3 Performances actuelles des TEC de puissance

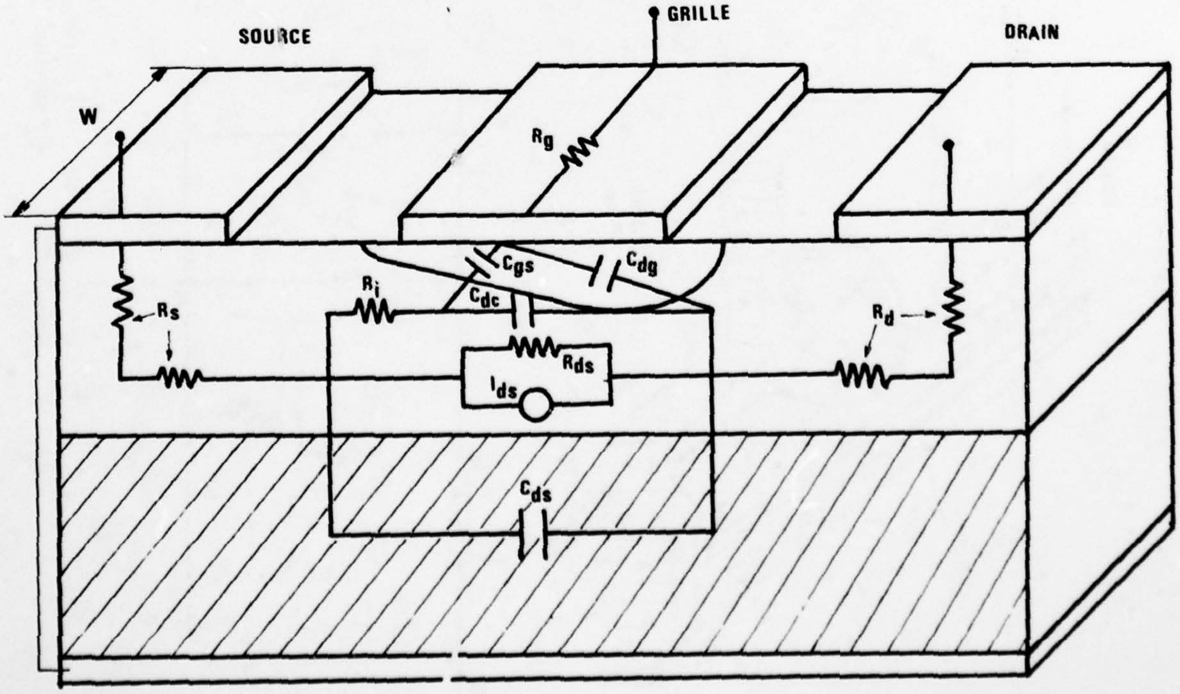
SOURCE
GRILLE
DRAIN
W
R_g
R_s
R_i
C_{gs}
C_{dg}
C_{dc}
R_{ds}
I_{ds}
R_d
C_{ds}

Fig.4 Schéma équivalent du TEC intrinsèque

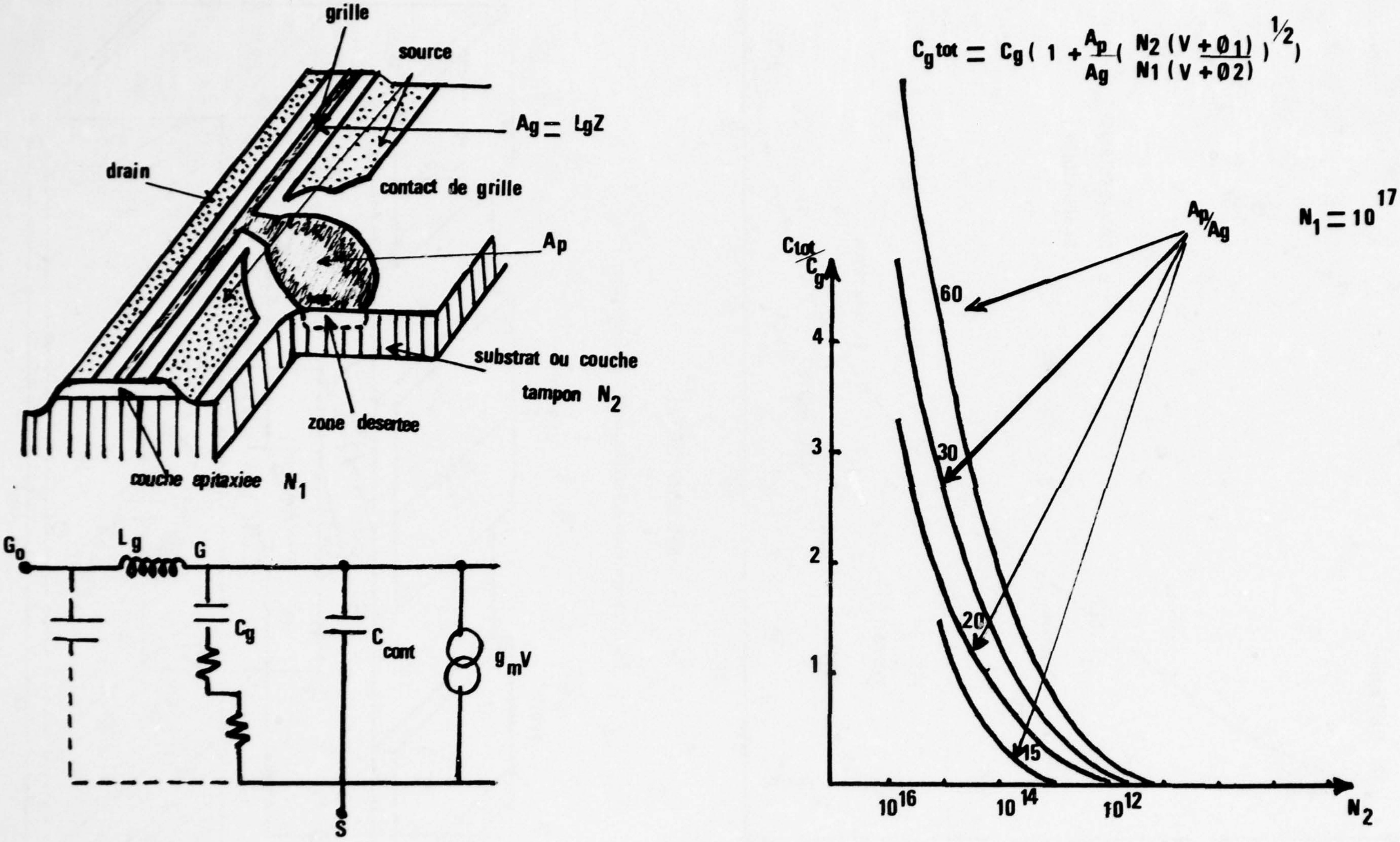
grille
source
drain
Ag = LgZ
contact de grille
Ap
substrat ou couche tampon N2
zone desertee
couche epitaxiee N1
Go
Lg
G
Cg
Ccont
gmV
S
Cgtot = Cg (1 + Ap/Ag (N2 (V + Ø1) / N1 (V + Ø2))^1/2)
Ap/Ag
N1 = 10^17
Ctot/Cg
4
3
2
1
60
30
20
15
10^16
10^14
10^12
N2

Fig.5 Définition de la capacité C_X sous le contact de grille.
Importance de C_X en fonction du dopage de la couche active

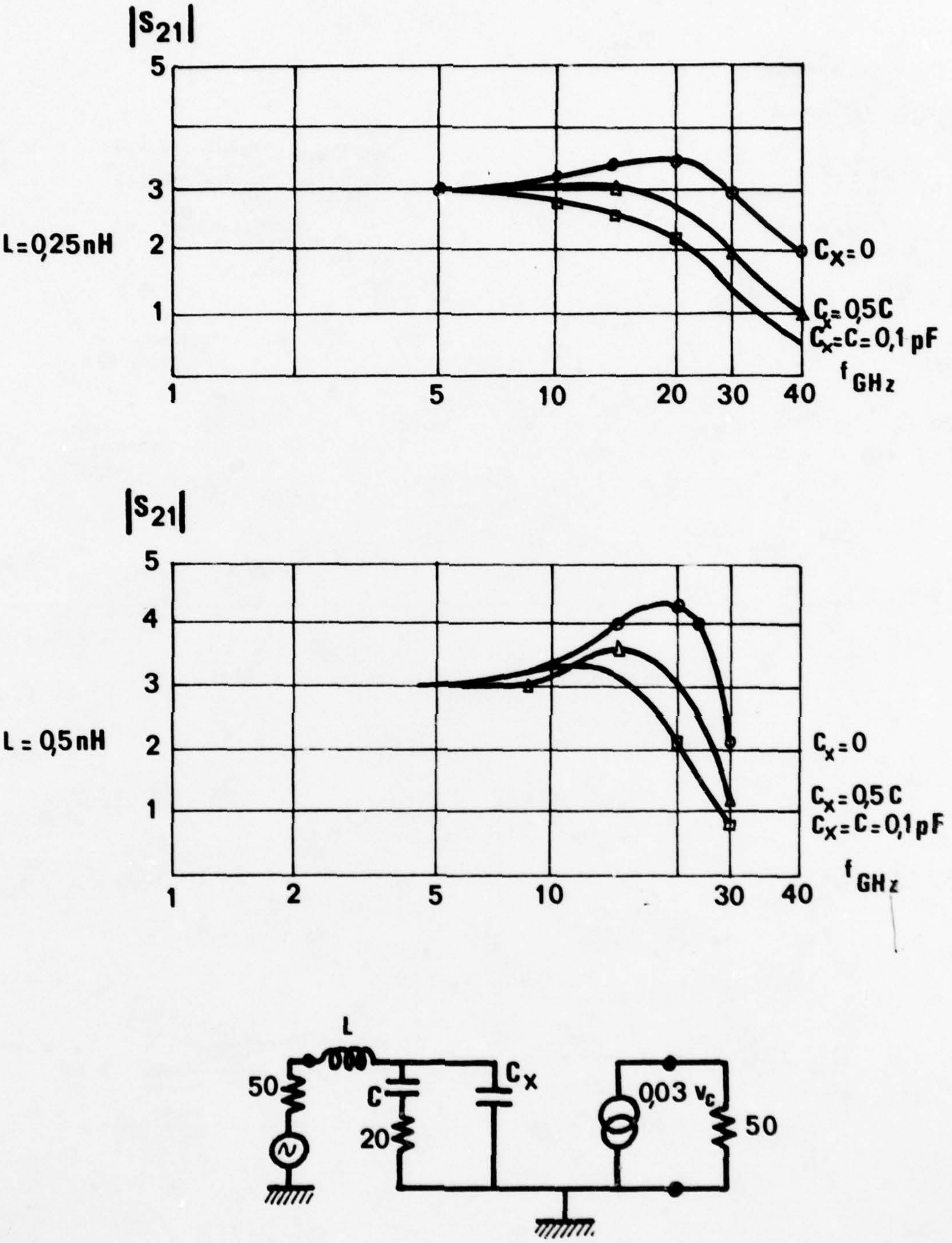

Fig.6 Evolution de/S_{21}/et/S_{12}/en fonction de la fréquence pour une valeur de self de fil de grille donnée et différentes valeurs de la capacité C_X

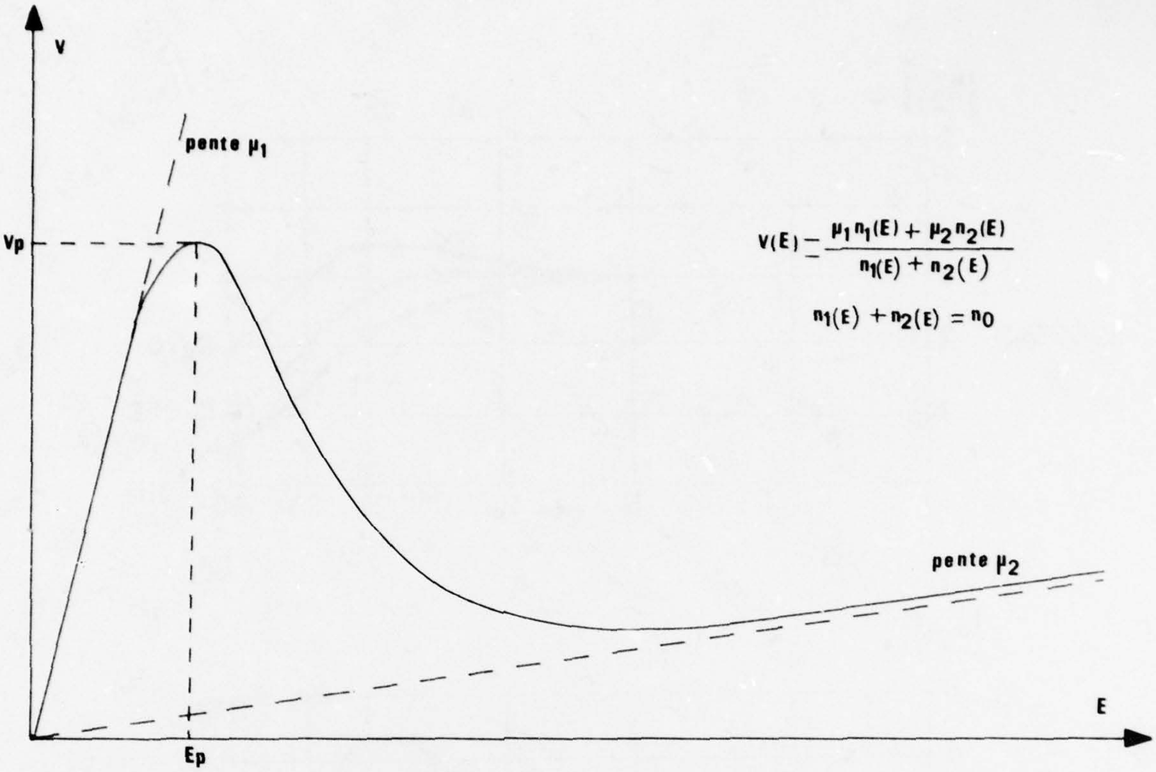

$$V(E) = \frac{\mu_1 n_1(E) + \mu_2 n_2(E)}{n_1(E) + n_2(E)}$$

$$n_1(E) + n_2(E) = n_0$$

Fig.7 Courbe V (E) de matériau III V présentant une mobilité différentielle négative

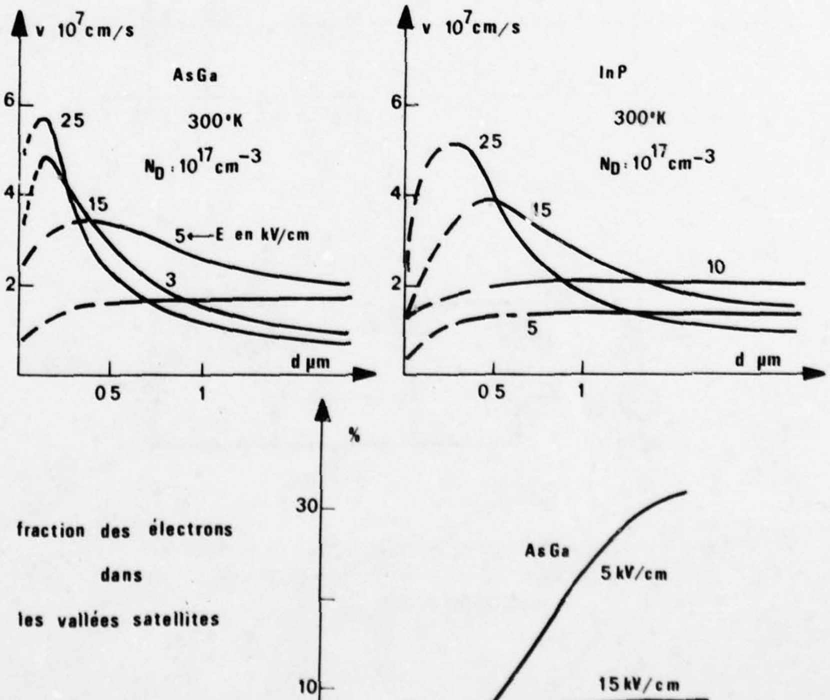

Fig.8 Phénomène de survitesse dans l'InP et le GaAs

AD-A069 015 ADVISORY GROUP FOR AEROSPACE RESEARCH AND DEVELOPMENT--ETC F/G 17/2.1
MILLIMETER AND SUBMILLIMETER WAVE PROPAGATION AND CIRCUITS.(U)
FEB 79 E SPITZ, G CACHIER
UNCLASSIFIED AGARD-CP-245 NL

2 OF 6
AD
A069015

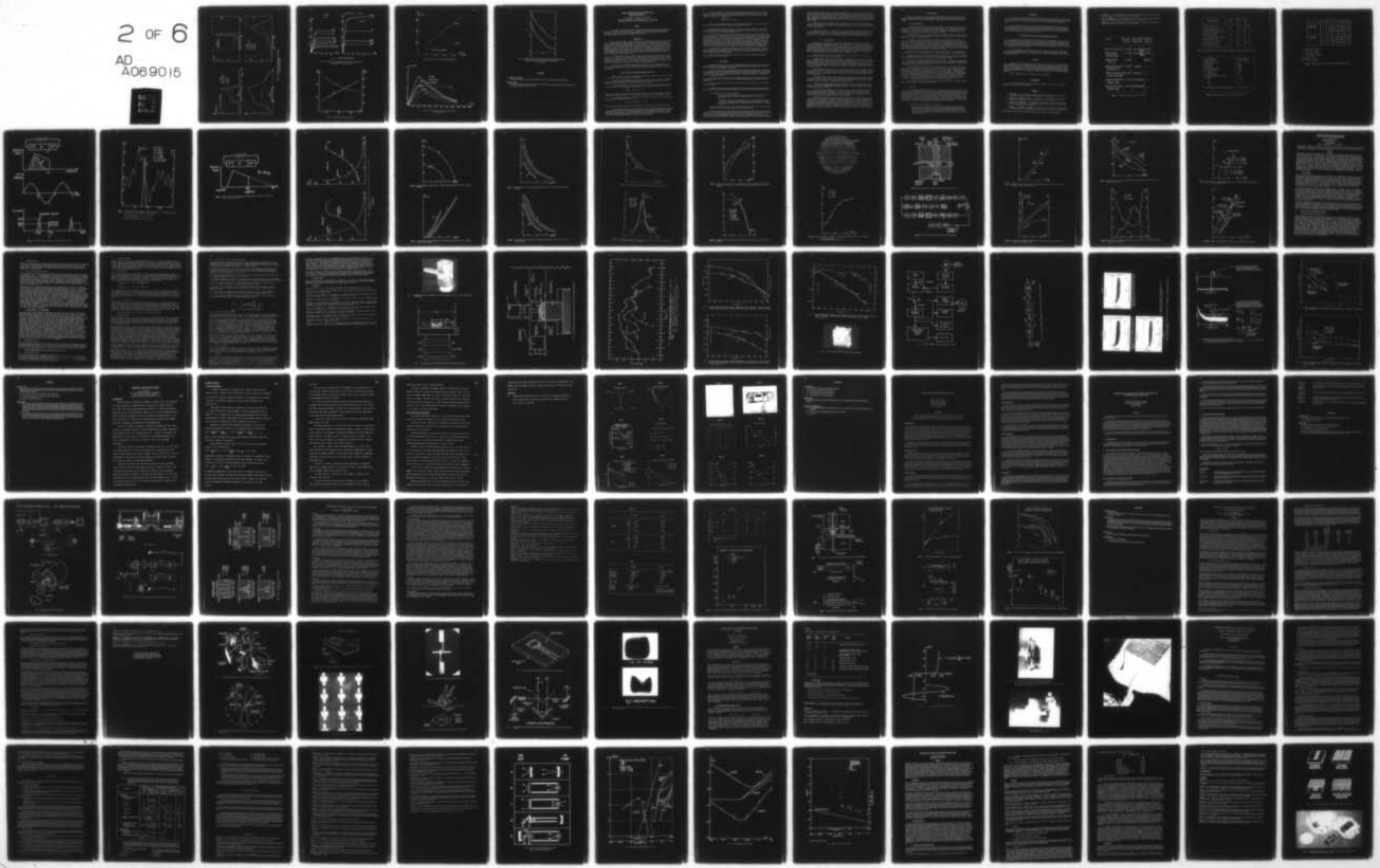

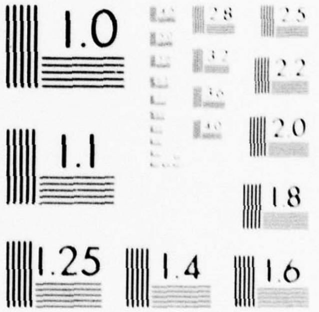
1.0
2.8
2.5
3.2
2.2
3.6
4.0
2.0
1.1
1.8
1.25
1.4
1.6

MICROCOPY RESOLUTION TEST CHART
NATIONAL BUREAU OF STANDARDS-1963-A

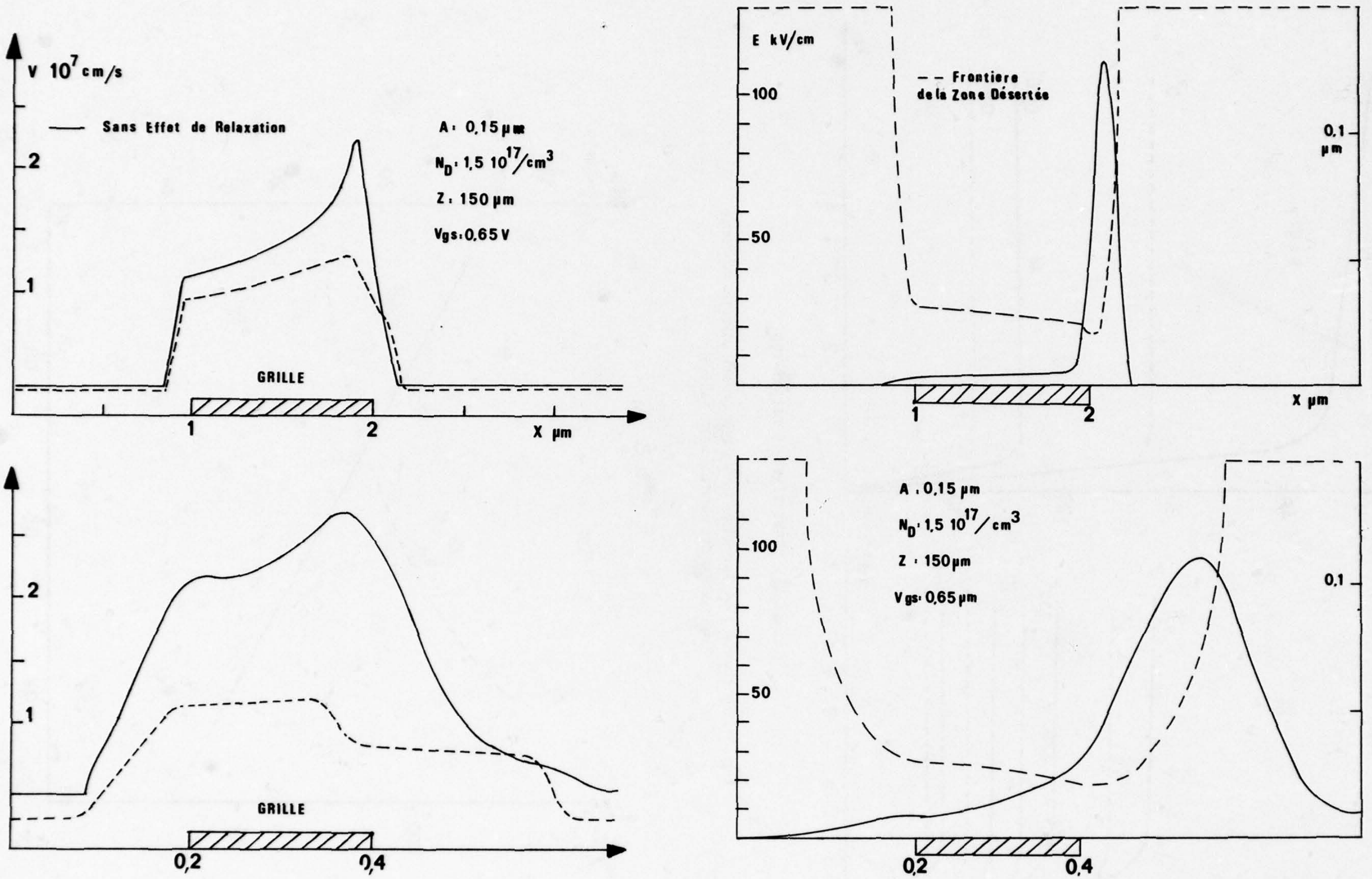

Fig.9 Distribution du champ électrique et de la vitesse des porteurs sous la grille

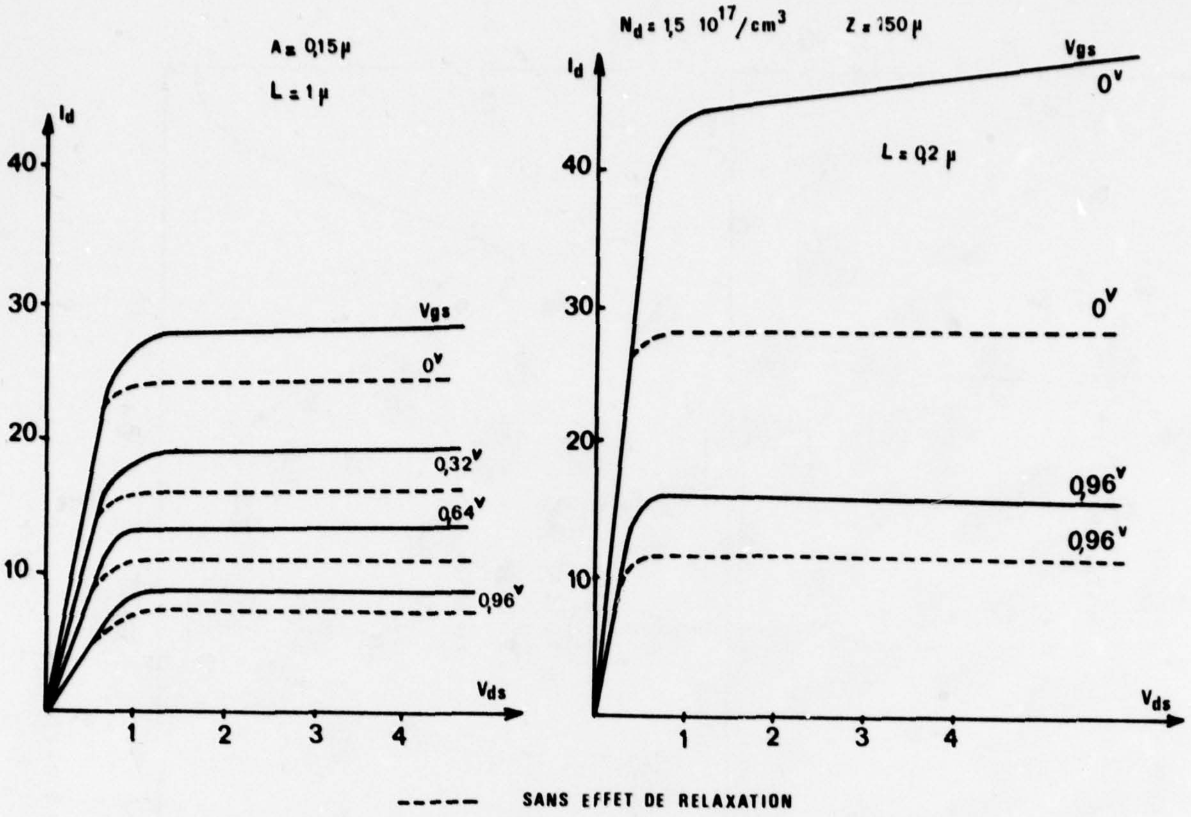

Fig.10 Courbes I_D (V_{DS}) fonction de Vg avec ou sans effet de survitesse (relaxation des porteurs entre vallées)

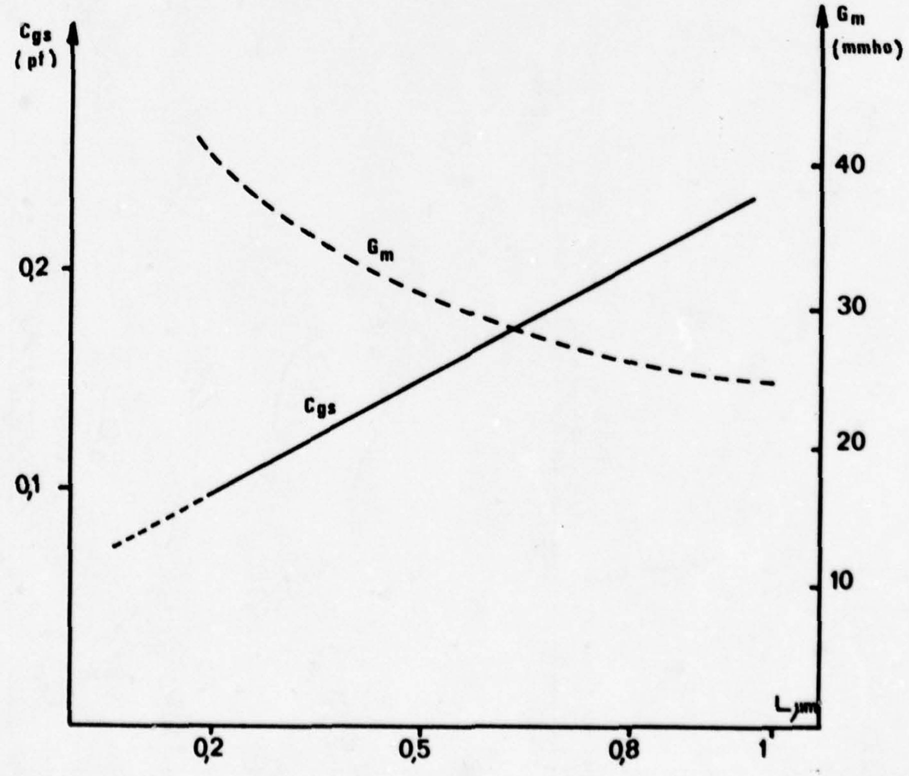

Fig.11 Courbes Gm et Cgs en fonction de $1/_L$

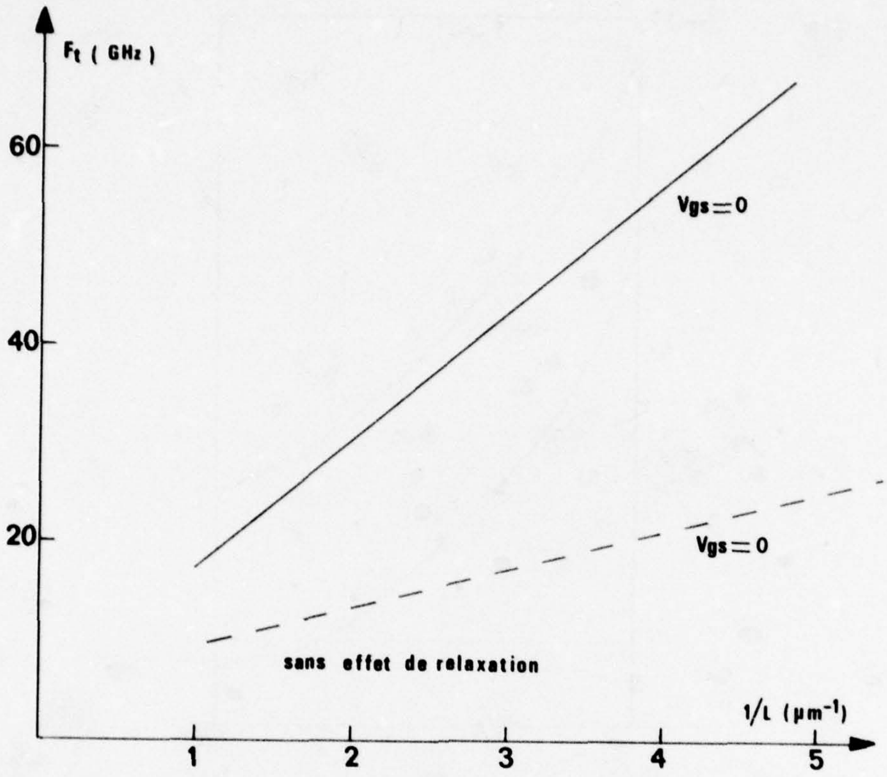

Fig.12 Courbe F_T $(1/_L)$ avec ou sans effet de survitesse

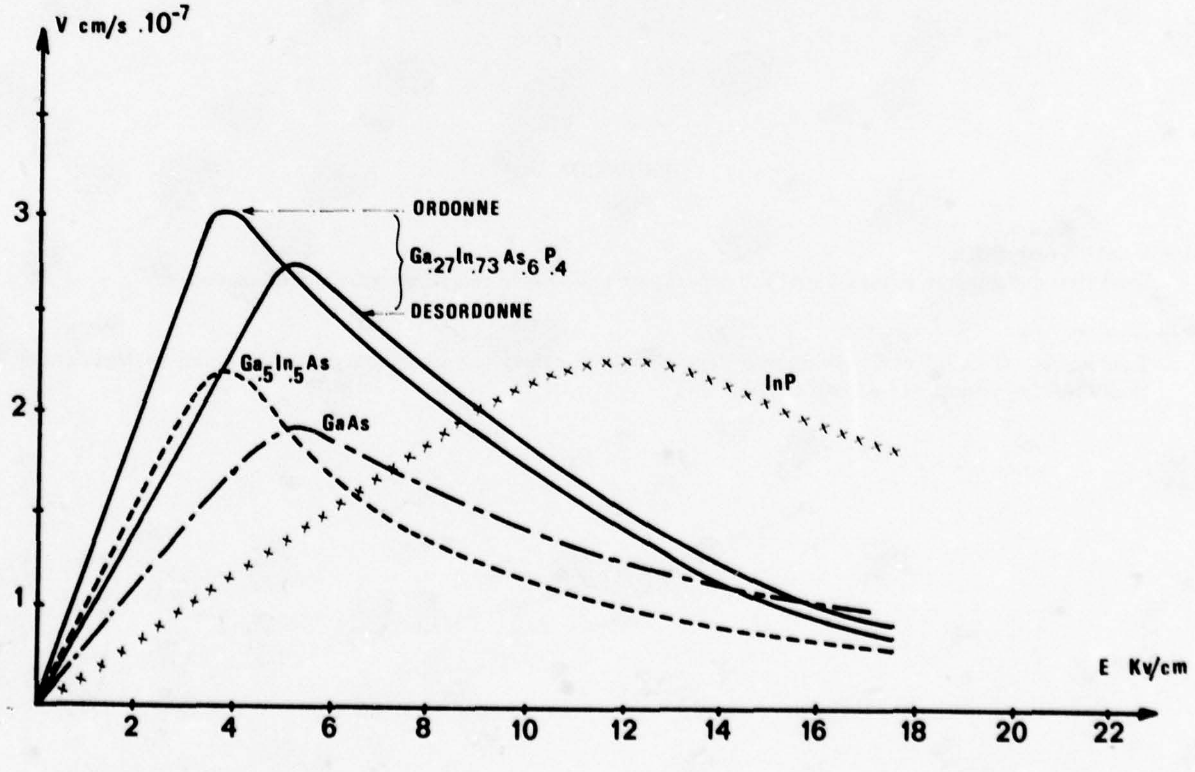

Fig.13 Courbes V (E) pour InP, GaAs, $Ga_xIn_{1-x}As$ et $Ga_xIn_{1-x}AsyP_{1-y}$

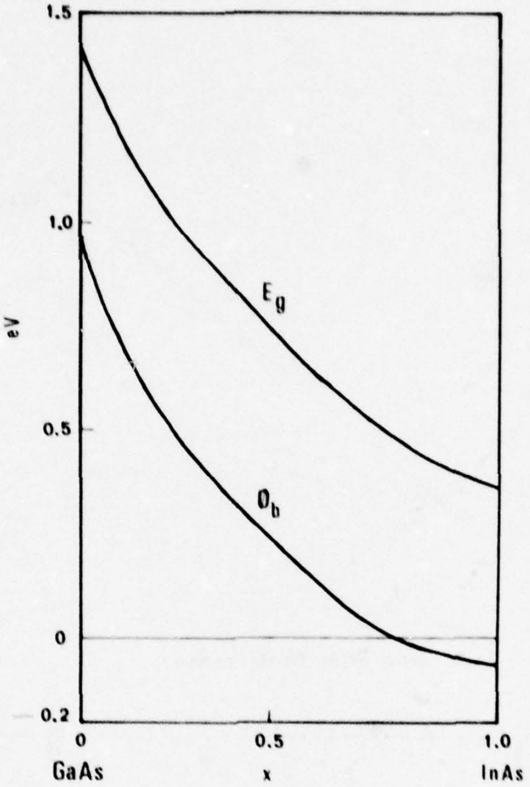

Fig.14 Evolution de la barrière de potentiel à la surface et de la largeur de bande interdite en fonction de la concentration en Indium dans $Ga_{1-x}In_x As$

DISCUSSION

A.S. Vander Vorst, Belgium

Quel effet de température y a-t-il sur l'InP par rapport au GaAs, en ce qui concerne le refroidissement?

Reponse d'Auteur

Les courbes v (E) d'InP et GaAs sont sensiblement modifiées mais il ne me semble pas qu'il y ait un intérêt essentiel pour l'InP par rapport au GaAs sur ce point.

STABLE MILLIMETRE WAVE SOURCES BY AVALANCHE DIODE FREQUENCY MULTIPLICATION

P.A. ROLLAND, G. SALMER and E. CONSTANT

"CENTRE HYPERFREQUENCES & SEMICONDUCTEURS" L.A. au CNRS n°287
Université de LILLE I BP 36 59650 VILLENEUVE D'ASCQ France.

SUMMARY

In this paper the main characteristics of avalanche frequency multipliers are presented. Special attention is paid to the diode structure for operation from 25 to 100 GHz. The design philosophy of multiplier circuit is given. Datas on the noise behaviour of such multiplier are also presented. Then results obtained from a 7000 hours endurance test are given.

INTRODUCTION

Stable sources are needed in almost all millimeter wave systems. These sources can use either direct conversion devices in various resonnant structures or quartz controlled oscillators. Table I is a comparison of the quartz oscillator stability far from stable direct conversion devices. The important point to note is the extremely good stability, far superior to any of the direct conversion devices, exhibited by the quartz oscillator even without temperature control. There is, however, an upper limit on fundamental frequency at about 30 MHz, although crystals can be operated at harmonics up to 100-150 MHz. But frequency multiplication provides a quite useful means of readily achieving quartz stability. So, typical equipment uses a signal generated by a quartz oscillator, amplified and multiplied up to the desired frequency. SAW oscillators may provide a more convenient means of tapping the quartz stability reservoir, but the principle will remain the same.

At frequencies below 10 GHz, varactor and Step Recovery Diodes are widely used in frequency multipliers [1]. Unfortunately the harmonic-rich switching characteristics of the SRD is due to its thin active layer. Consequently, at high frequencies, the device area must be kept small in order to keep the capacitance at an acceptable level and this limits the extent to which the SRD can be scaled up in power. Besides, the use of varactor doublers or triplers leads to complex multistage circuits. In addition, both varactor and SRD conversion efficiency drops quickly at frequencies above 10 GHz.

On the other hand, avalanche diode frequency multipliers allow direct frequency multiplication, in a single harmonic stage, with high harmonic orders and high conversion efficiency up to the *millimeter wave range*. This kind of multipliers seems to be quite convenient for filling the Ka to E band gap [2][3][4].

I - BASIC PRINCIPLES OF AVALANCHE FREQUENCY MULTIPLIERS

Dynamic operating conditions of an avalanche diode frequency multiplier can be best understood by the following basic and phenomenological considerations :

The active zone of an avalanching P^+N junction can be divided into two parts : an avalanche zone where carrier generation by impact ionization occurs and a drift zone where impact ionization is negligible and where carriers drift at their saturated velocity. Figure 1.

Within some assumptions (small transit time effect and uniform field distribution) the total conduction current in the avalanche zone can be described by the generalized Read's equation : [5] [6]

$$\tau_i \frac{dI_{ca}}{dt} = I_{ca}\,(\bar{\alpha}\delta - 1) + I_s$$

where τ_i is the intrinsic response time of the avalanche process, $\bar{\alpha}$ an average ionization coefficient (averaged over electrons and holes), δ the length of the avalanche zone and I_s the saturation current.

If the saturation current is neglected, an easy integration of the Read's equation gives the general form of this conduction current :

$$I_{ca}(t) = \frac{I_\infty}{\tau_i} \exp \int_0^t [\bar{\alpha}\,\delta - 1]\, dt'$$

$\bar{\alpha}$ is a non linear function (exponential in most cases) of the electric field and thus of the voltage.

This relation shows a quite non linear behaviour of the avalanche zone, even under sinusoidal voltage operation . Figure 2 is an example of the conduction current waveform obtained from a computer simulation. It can be seen that this current wave form is close to sharp pulse. In addition the quick rise of the current peak, down to a few picoseconds ($\simeq$ 6 ps in the present case) allows us to expect high order and high frequency harmonics, up to the millimeter wave range.

A physical explanation of the avalanche zone behaviour can be obtained under the following assumption : if the amplitude V_a of the A.C. voltage imposed on the static voltage V_{ao}, is low enough to limit the expansion of the ionization coefficient to its first order voltage derivative, then the conduction current I_{ca} can be described by :

$$\frac{dI_{ca}(t)}{dt} = \frac{\bar{\alpha}'}{\tau_i} V_a(t) \quad I_{ca}(t)$$

This last relation obviously proves that the avalanche zone behaves as a non linear inductor, as opposed to the non linear capacitor effect found in varactor diodes [7].

Therefore, according to the "Manley Howe" power relations, the avalanche zone can operate as a parametric amplifier, an harmonic generator or a frequency up and down converter, with a conversion efficiency at the desired frequency approaching 100 %.

This current is then injected into the drift region of the diode. The current induced in the external circuit by this charge drifting through the drift region at a saturated drift velocity is shown at the bottom of Figure 1. It can be seen that the harmonic-rich characteristics of the injected current have been degraded by the transit time effect (Ramo-Schottky theorem). Therefore, for high order harmonic operation, it is better to aim for short transit time diodes, in order to approach the case of a sharp current pulse. Besides, to eliminate series resistance, it is desirable to have the P-N junction bounded by heavily doped P^+ and N^+ regions. So the diode is generally made as a $P^+N\ N^+$ structure. As we want very short transit times, the heavily doped regions (N^+ and P^+) must be sufficiently close to the junction, so that the depletion layer extends to this heavily doped regions for reverse voltages much less than the breakdown voltage. Such devices are said to be "Punched-Through" at breakdown.

This means that in an avalanche multiplication diode, the depletion layer width is constant so that the parasitic series resistance is much smaller than in varactor diodes. Besides this kind of diode is quite different from IMPATT ones, since the drift zone is nearly inexistant, which will in addition prevent from spurious oscillations.

Figure 3 shows the typical electric field profile of a frequency multiplication avalanche diode. This profile is close to PIN type.

II - DIODE DESIGN

The previous results have been derived from phenomenological considerations and have of course to be confirmed by a more quantitative analysis. A computer programm has been developed for that purpose [3] while extensive experiments were performed.

Figure 4 gives both the theoretical and experimental best results obtained from Silicon diodes as a function of their PTF in ATT and multiplication modes.The diodes considered were $P^+N\ N^+$ diodes with a constant N zone doping concentration ranging from 1,5 to 2 10^{16}at/cm^3 in multiplication mode and from 2 to 3 10^{16}at/cm^3 in ATT mode. Frequency decuplers from 3,5 to 35 GHz are opposed to IMPATT oscillators at the same output frequency.

It can be noted that the best results in multiplication mode are obtained with highly punched through diodes (PTF > 2). On the other hand, such a diode provides negligibly small output power in IMPATT mode.

Figure 5 shows the calculated output power capability versus frequency for a X 10 avalanche frequency multiplier.

Silicon and GaAs diodes were investigated. It can be seen that Silicon diodes are more powerfull than GaAs ones, while presenting an upper frequency limit about twice as high as that of GaAs devices.

This difference is due to material parameters :

- Silicon exhibit a higher degree of non linearity and the voltage derivative of the average ionization coefficient $\bar{\alpha}'$decreases for lower level in GaAs than in Si.
- The saturated velocity is lower in GaAs than in Si. So the depletion layer width is thinner for GaAs diode. Therefore the junction area must be smaller in order to keep the output impedance at an acceptable level. This results in a lower output power.

However, GaAs diode can exhibit greater conversion efficiencies than Si ones at low input level, since the second order voltage derivative $\bar{\alpha}''$ is much lower in GaAs.

The optimum electrical characteristics of avalanche frequency multiplication diodes are plotted in figures 6 to 8 as a function of the output frequency for a multiplication ratio of 10. The output frequency, indeed, is the main parameter when designing the diode for frequency multiplication.
The dashed area indicates the parameters-margin for fluctuations less than 10 % in the optimum performances. If the accuracy to be achieved in the N zone doping concentration is not very high, on the other

hand, the depletion layer width must be controlled more precisely in order to avoid transit time effects as shown in Figure 9. This is the most important technological point in multiplication diode fabrication. The N N^+ transition must be very abrupt in order to achieve high punch through factor. Besides, one point has to be cleared : the depletion layer width is roughly inversely proportional to the output frequency down to about 20 GHz. For output frequencies lower than 20 GHz, this law is no more valid and the N zone doping concentration must be kept near 10^{16}at/cm^3. This is necessary to prevent from burn out due to filament formation.

These characteristics have been given for a multiplication ratio of about 10. If now,for a precised output frequency,higher harmonic orders are wanted, it is desirable to choose the lowest value of N_D but the highest values of all the other parameters from Figures 5 to 7. This in order to avoid too difficult input matching.

These results show that, if the multiplication diodes are quite different from IMPATT ones, they are however no more difficult to make, and in any case,do not need a highly sophisticated technology. Typical electric characteristics of avalanche diodes used for frequency multiplication are listed in table II for three sets of Silicon devices corresponding to three different output frequencies.

III - CIRCUIT DESIGN

Maximum power conversion and efficiency can be obtained only be careful circuit design. For a given input power, if maximum output power is not required, the circuit design may be simple and usually does not employ deliberately introduced idler circuits. Figure 10 presents the calculated output power in multiplication by ten from 3,5 to 35 GHz as a function of the output circuit loading, in this simple case (without idler circuit). Maximum output power is obtained for small loading resistances. Besides the loading reactance tuning is somewhat critical and gets more so as the load resistance is smaller. Maximum conversion efficiencies of about 30 % can be expected in that case for medium output power (≃ 20 dBm) and multiplication factors of about 10, as shown in Figure 11.

However, if idler circuits are not introduced they do exist anyway and it is interesting to study their influence on the multiplier performances.

Computer simulations have shown that a capacitive tuning on one of the idler frequencies provides a great increase in the conversion efficiency. This is illustrated Figure 12, for a X 10 frequency multiplier between 3,5 and 35 GHz. It can be noted that this capacitive tuning is not critical at all and that no evenness effect appears when tuning on the second or third harmonic frequency. Tuning on one of these first idler frequencies improves the conversion efficiency which can reach values of about 60 %, while simultaneous tuning on the second and third harmonic frequencies increases the conversion efficiency up to 90 %.

On the other hand, inductive tuning on one of the idler frequencies has an unfavourable effect on the conversion efficiency. In addition, inductive tuning may develope a very high voltage component across the diode if its capacitance is tuned to resonance, especially at low idler frequencies. This may result in diode destruction under high power operation. So it is better to avoid inductive tuning on idler frequencies.

This important idler efffect was experimentally investigated with a X 20 frequency multiplier from 2 GHz to 18 GHz. The idler tuning on the second harmonic frequency was achieved by means of a wave guide cavity very tighly coupled to a coaxial line at the end of which the diode was located. Results are shown in Figure 13 and are in good agreement with theoretical ones.

A last effect related to idler tuning must be pointed out : such tunings increase the amplitude of the instantaneous **voltage across** the diodewhich results in an earlier conversion efficiency saturation, as shown Figure 20. This saturating effect can be used to provide an automatic level control if constant output power is desired.

To sum up, a great improvement in the conversion efficiency can be achieved by capacitive tuning on one of the first idler frequencies, but at the price of increased circuit complexity and earlier output power saturation. Note however that this idler tuning is not critical at all since it is not necessary to provide circuits resonant at the idler frequencies as in varactor multipliers. In addition this idler tuning increases the circuit reproductibility.

A typical multiplier circuit which has been widely used through out this study up to 90 GHz is described Figure 14. The diode terminates a matched low impedance coaxial line which passes through the broad wall of the waveguide in its center. The input power and D.C. bias current are fed by this coaxial line. The harmonic power generated by the diode is transmitted to the load by a coaxial to waveguide transition matched by a tapered ridge section. Output tuning is achived by varying the coaxial line length, while coupling between the coaxial line and the waveguide circuit can be controlled by an adjustable short circuit at one end of the waveguide and an EH tuner at the other. Idler tuning can be achieved by inserting an adjustable low pass filter and transformer structure in the input coaxial line.

IV - NOISE BEHAVIOUR

This is a very important point concerning avalanche multiplier. Indeed, the noise level at the output port of such a multiplier could be expected to be high if bearing in mind the poor noise behaviour of IMPATT devices. So we have experimentally investigated the AM and FM noise of these multipliers.

- F.M. noise measurement

In passing through the multiplier the frequency deviation of the primary quartz controlled oscillator will be multiplied N times, where N is the multiplication ratio. Indeed, like any frequency multiplier, the avalanche multiplier amplifies F.M. noise. The power in the output sidebands at the frequency $N\omega_o \pm \omega_n$ is N^2 times the power in the input noise sidebands at the frequency $\omega_o \pm \omega_n$. This corresponds to an amplification of 6 dB per octave of the F.M. noise.

But apart from this predictable F.M. noise sideband enhancement, there could be other mechanisms in the multiplier which could conceivably produce noise. The problem, then, is to measure the noise degradation over that of an ideal multiplier.

For measuring the additive phase noise contributed by the multiplier the test set up of Figure 15 was used. This method needs two identical multipliers. The common driver for the two multipliers was a quartz controlled oscillator. The two avalanche frequency multipliers were tuned for X 10 from 3,52 to 35,2 GHz operation, with a maximum output power of 20 dBm corresponding to a conversion efficiency of about 20 %. The output of the balanced phase detector was applied to low noise high gain video amplifier, and the rms output was read on a true rms voltmeter. The noise contributed by the measuring equipment was determined by allowing only the power in the local oscillator channel of the balanced mixer to flow and observing the reading on the rms meter at the output.

The noise contributed by the equipment was substracted from the total noise measured during the experiment. The net F.M. noise was more than 10 dB above the equipment noise for all measurements.

Reading point by point through the video frequency range of 500 Hz to 200 kHz gave a measurement of the additive rms phase noise as a function of frequency separation from the carrier. The phase noise was converted to F.M. noise by multiplying it by the measurement frequency.

The results of the measurements are shown in Figures 16 and 17. It can be seen from Figure 16 that avalanche multiplier exhibits a quasi constant additive phase noise independant of frequency separation from the carrier. In addition, this additive phase noise can be very low and of the same order as that contributed by Step Recovery Diodes.

Figure 16 shows the evolution of the rms frequency deviation, 10 kHz from the carrier as a function of the input power. At each point, circuit tuning and bias current were adjusted for maximum efficiency. The corresponding D.C. bias current curve is also shown in Figure 17. Under these conditions a change of 15 dB in the input power results only in a slight variation of the rms frequency deviation of less than 3 dB. On the other hand, for a given input drive level, if the diode is biased far from the optimum D.C. bias current value, the rms F.M. noise increases sharply. For example, the frequency deviation was measured to be $\Delta f_{rms} = 0{,}15$ 10 KHz from the carrier with $P_1 = 28$ dBm and $I_o = 115$ mA. If the current is decreased to 75 mA in the same conditions, the measured F.M. noise is $\Delta f_{rms} = 3$. It was observed that the minimum FM noise deviation occured for the couple (P_1, I_o) providing the maximum conversion efficiency, which is a quite interesting result.

These results show that with a proper circuit and biasing arrangement, an avalanche frequency multiplier can contribute a very low additive FM noise.

- A.M. noise

A.M. noise measurements were performed on a X 10 frequency multiplier from 3,3 GHz to 33 GHz. Typical results are shown in Figures 18 and 19. Figure 18 shows that the output carrier to noise ratio increases near the carrier. This is due to a major contribution of the primary source A.M. noise (dotted line). Besides these curves pointed out the fact that A.M. noise decreases when the multiplier is getting satured, for a given D.C. bias current. On the other hand, Figure 19 shows the evolution of the carrier to noise ratio versus the D.C. bias current for a constant input power of 1 Watt. The circuit was tuned for $P_{in} = 1$ W and $I_o = 120$ mA. As for F.M. noise, it can be noted that the minimum A.M. noise occurs when the conversion efficiency is maximum. Here again, it can be seen that A.M. noise increases sharply when the multiplier is operated far from its optimum operating conditions.

In conclusion of this noise study, we can say that :

- Avalanche frequency multiplier contributes a very low additive AM and FM noise if operated near its optimum conditions (strong interdependence of the two parameters, input power, D.C. bias current). The noise behaviour can be much worsten if the multiplier is tuned into far from these optimum operating conditions. However, the most important result to remember is that avalanche frequency multipliers can exhibit a quite good noise behaviour.

V - RELIABILITY

In order to make sure that avalanche diode frequency multiplier can provide a reliable stable source, we have achieved a 7000 hours endurance test*. The diode has been operated, throughout the test, in a X 16 multiplier and the operating conditions chosen for this 7000 hours test are detailed in table III.

The X 16 avalanche multiplier has gone successfully through this 7000 hours test. All the performance checks done during and after the test have not made it possible to point out any degradation nor fluctuation in any of the operating parameters. The good ageing of this frequency multiplier is illustrated in Figure 20 where the output power is plotted versus the input one for various bias currents, at the beginning of the test and at the end of it.

VI - INTEREST OF SUCH DEVICES FOR MILLIMETER WAVE APPLICATIONS

Frequency multipliers have power and efficiency as their main parameters. So on a cost and efficiency basis they will tend to have their input frequency in the 4-6 GHz region where the cost per watt is not too high. Typical application of avalanche multipliers would be then X 20 operation to fill the E band and X 30 operation to fill the 90-120 GHz band. Theoretical calculations have shown that a 10 % conversion efficiency is obtainable using X 20 avalanche frequency multiplier in the 100 GHz region with output power of the order of 100 mW.

First experimental results are shown in Figure 21. They illustrate the fact that avalanche multiplier may constitute an attractive alternative in the realization of millimeter stable sources. But like any other millimeter device they come up against the packaging problem which still limit their potential performance.

CONCLUSION

Avalanche frequency multipliers may be suitable for a wide range of millimetric applications where frequency stability is of paramount importance. They exhibit high power, high conversion efficiency and high multiplication ratio capabilities. In addition their noise level can be of the same order as that contributed bu Step Recovery Diode multipliers. Even disregarding the stability considerations, avalanche multipliers are competitive in power and efficiency with direct conversion devices, mainly Gunn and IMPATT diodes. So they may be considered for applications such as pumps for parametric amplifiers.

Table IV summarized what can be achieved using such multipliers.

ACKNOWLEDGMENT

The authors would like to thank J. MICHEL and B. KRAMER of the L.E.P. and J.V. BOUVET of THOMSON D.M.H. who have furnished the diodes.

REFERENCES

[1] BURCKHARDT, C.B., 1965, "Analysis of Varactor Frequency Multipliers for Arbitrary Capacitance Variation and Drive Level". Bell System Tech. J., 44, pp. 75-92.

[2] ROLLAND, P.A., SALMER, G., DERYCKE, A., and MICHEL, J., 1973, "Very-High-Rank Avalanche diode Frequency Multiplier". Proc. I.E.E.E. Vol. 61, n°12, pp. 1757-58.

[3] ROLLAND, P.A., VATERKOWSKI, J.L., CONSTANT, E., and SALMER, G., 1976, "New Modes of Operation for Avalanche Diodes : Frequency Multiplication and Upconversion". I.E.E.E. Trans. M.T.T., Vol. MTT 24, n° 11, pp. 768-775.

[4] ROLLAND, P.A., CONSTANT, E., DERYCKE, A , and MICHEL, J. 1974, "Multiplication de Fréquence par Diodes à Avalanche en Ondes Millimétriques", Acta Electronica, 17, 2, pp. 213-228.

---

*This work was supported by the European Space Agency under contract n° 2934/76/NL/AK(SC)

[5] GOEDBLOED,J.J., 1972, "Determination of the Intrinsic Response Time of Avalanche from Microwave Measurements", Solid State Electron, 15, pp. 635-642.

[6] HULIN, R., GOEDBLOED, J.J., 1972, "Influence of Carrier Diffusion on the Intrinsic response time of Semiconductor Avalanches", Appl. Phys. Lett., 21, pp 69-71.

[7] HINES, M.E., 1972, "Large-Signal Noise, Frequency Conversion and parametric instabilities in IMPATT-Diode Network". Proc. I.E.E.E., 60, pp. 1534-1548.

Source	Short term	Medium term	Long term
	1-10 secs	hours days	per year
Quartz sub standard	1 in 10^{11}	2 in 10^{9} per day	1 in 10^{8}
Quartz oscillator Temp. controlled	1 in 10^{10}	few in 10^{9} per day	1 in 10^{7}
Quartz oscillator AT– cut	1 in 10^{9}		few in 10^{7}
Direct conversion device in INVAR cavity	1 in 10^{6}	1 ppm/°C	–
Direct conversion device in compensated cavity	2-3 in 10^{6}	2-3ppm/°C	–
Direct conversion device in high Q cavity	1 in 10^{5}	15-30ppm/°C	–
Direct conversion device in low Q cavity	1 in 10^{4}	50-100ppm/°C	–

TABLE I Comparative stability of classical sources.

FREQUENCY RANGE	∿ 20 GHz	∿ 35 GHz	∿ 70 GHz
junction area (cm^2)	10^{-4}	$4\ 10^{-5}$	$1{,}5\ 10^{-5}$
doping concentration (cm^3)	10^{16}	$2\ 10^{16}$	$4\ 10^{16}$
depletion layer width (μm)	1	0,6	0,35
breakdown voltage	32^V	22^V	19^V
bias current density (A/cm^2)	$3\ 10^3$	$6\ 10^3$	10^4
maximum power output (W)	0,6	0,6	0,1
multiplication ratio	-7 dB	-8 dB	-10 dB
conversion efficiency	10	10	13

TABLE II Device parameters and performances of experimental Silicon multiplication diodes.

Input frequency	959 200 000 Hz
Output frequency	15 347 200 000 Hz
Multiplication ratio	16
Input power	20 dBm
Output power	13 dBm
Conversion efficiency	- 7 dB
D.C. bias current	20 mA
D.C. voltage	30 V
D.C. power supply	0.6 W
Unwanted harmonics rejection	
$= \frac{P_{15}}{P_{16}}$	- 12 dB
$= \frac{P_{17}}{P_{16}}$	- 28 dB
1 second short term frequency stability	better than 1 in 10^{10}

TABLE III Operating conditions chosen for this 7000 hours test.

	N	P_o	η	P_{out}	F_{out}
High Power Operation	10	1,8 W	- 8dB	[illegible]8dBm	35 GHz
	35	1,8 W	-13dB	24dBm	35 GHz
	13	1,4 W	-10dB	20dBm	72 GHz
Low Power Operation	24	1,5 W	- 7dB	15dBm	37 GHz
	60	1,6 W	-13dB	13dBm	36 GHz
	20	1,4 W	-13dB	14dBm	70 GHz

N : Multiplication ratio

P_o : D.C. power supply

η : Conversion efficiency

P_{out}: Output power

F_{out}: Output frequency

TABLE IV Example of what can be achieved using avalanche multipliers.

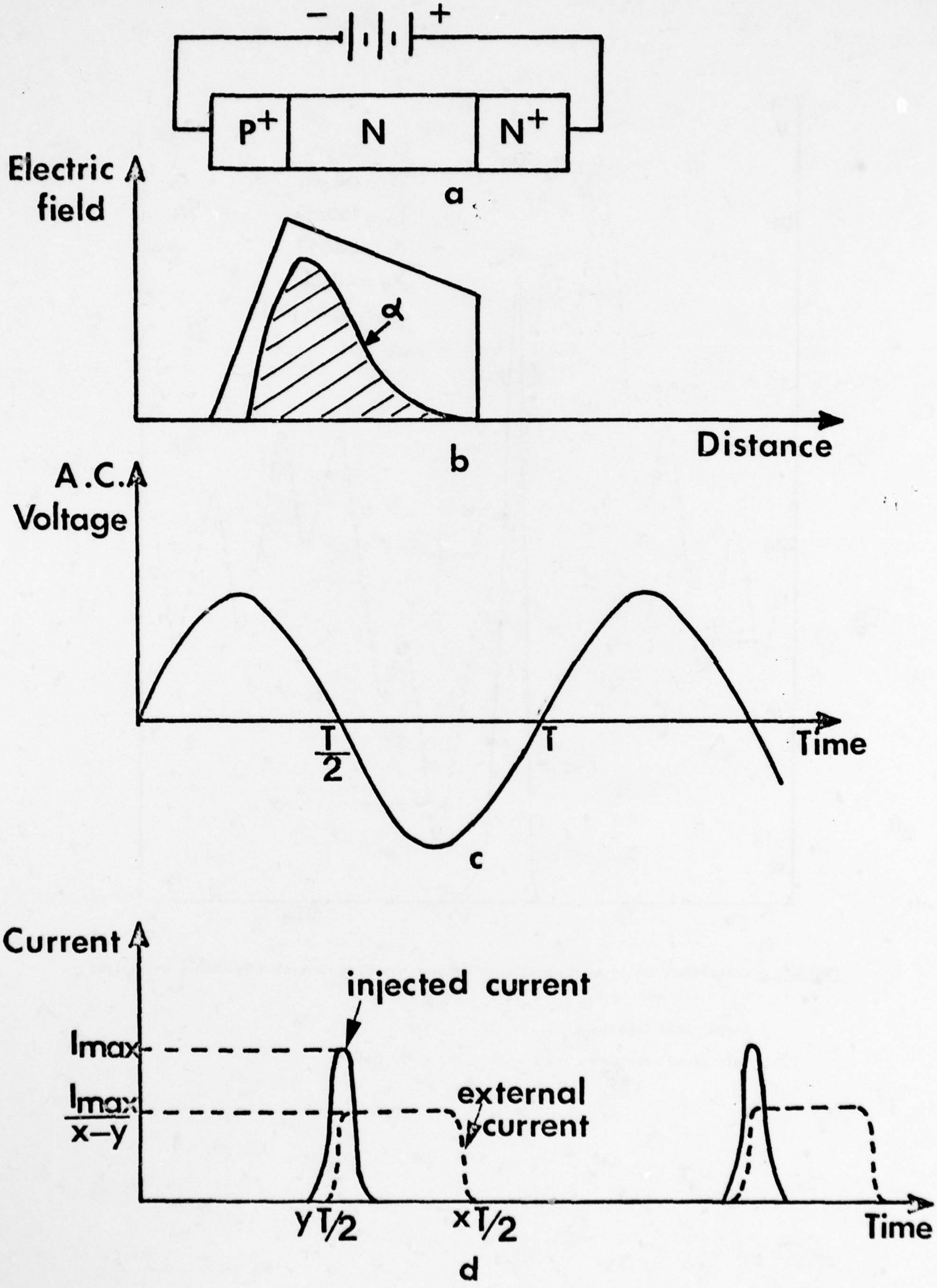
−
+
P+
N
N+
a
Electric field
α
Distance
b
A.C. Voltage
T/2
T
Time
c
Current
injected current
Imax
Imax/(x−y)
external current
yT/2
xT/2
Time
d

FIGURE 1 : Voltage and current waveforms in an avalanching P^+N junction.

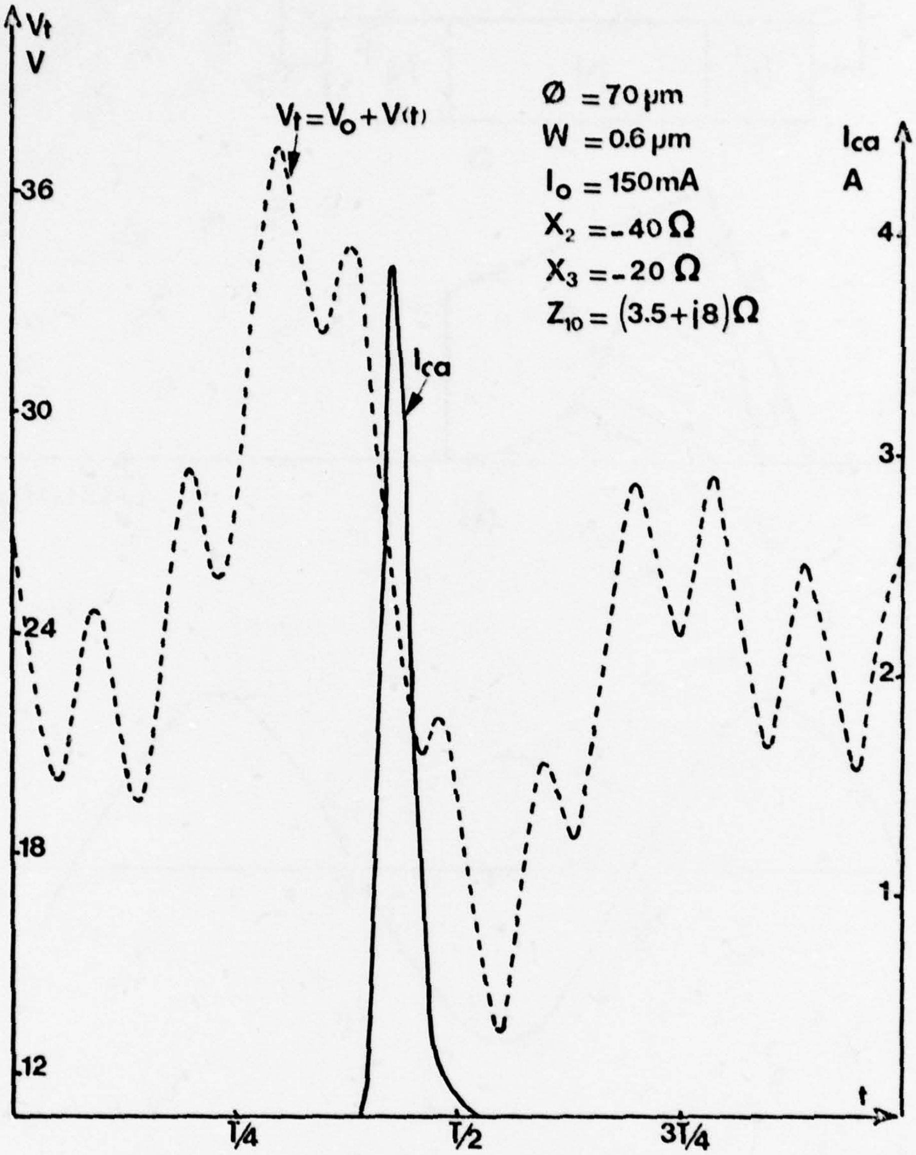

FIGURE 2 : Calculated voltage and conduction current waveform in a X 10 frequency multiplier

F_{in} = 3.5 GHz P_{in} = 400 mW I_o = 150 mA

output load impedance : Z_{10} = (3.5 + j 8)Ω

idler load reactances : X_2 = -40 Ω, X_3 = -20 Ω

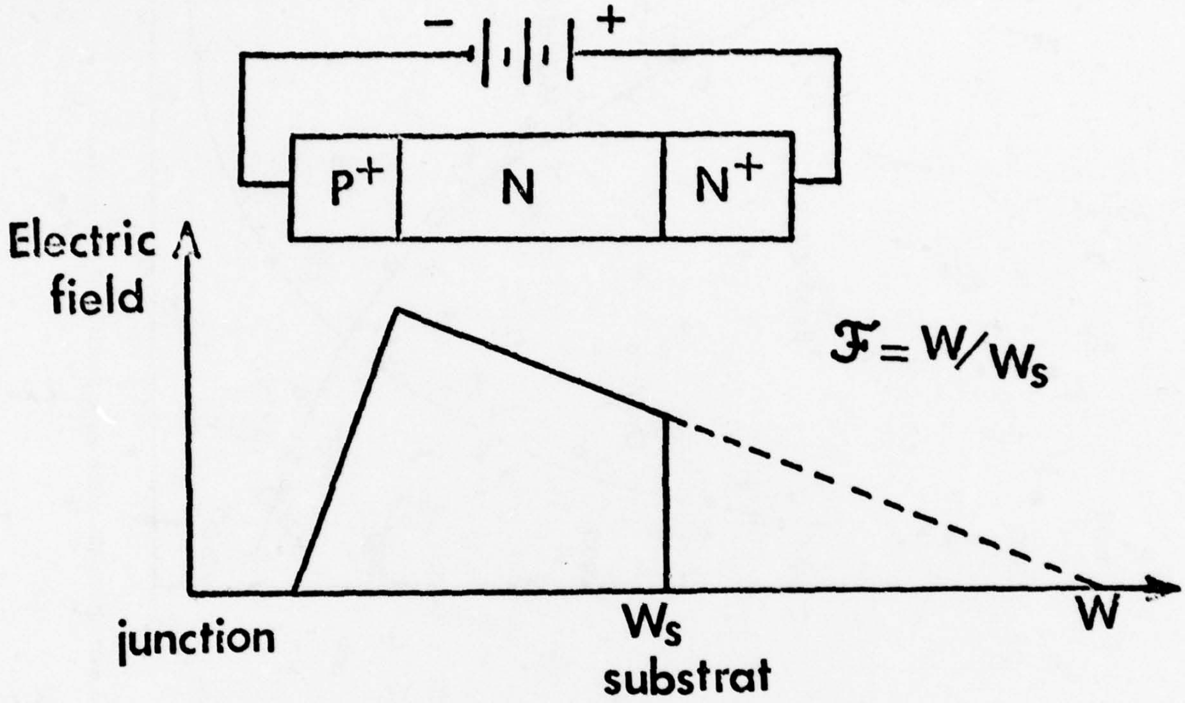
−
+
P+
N
N+
Electric field
$\mathcal{F} = W/W_s$
junction
W_s
substrat
W

FIGURE 3 : Typical electrical field profile of avalanche diode for frequency multiplication, with high punch through factor F.

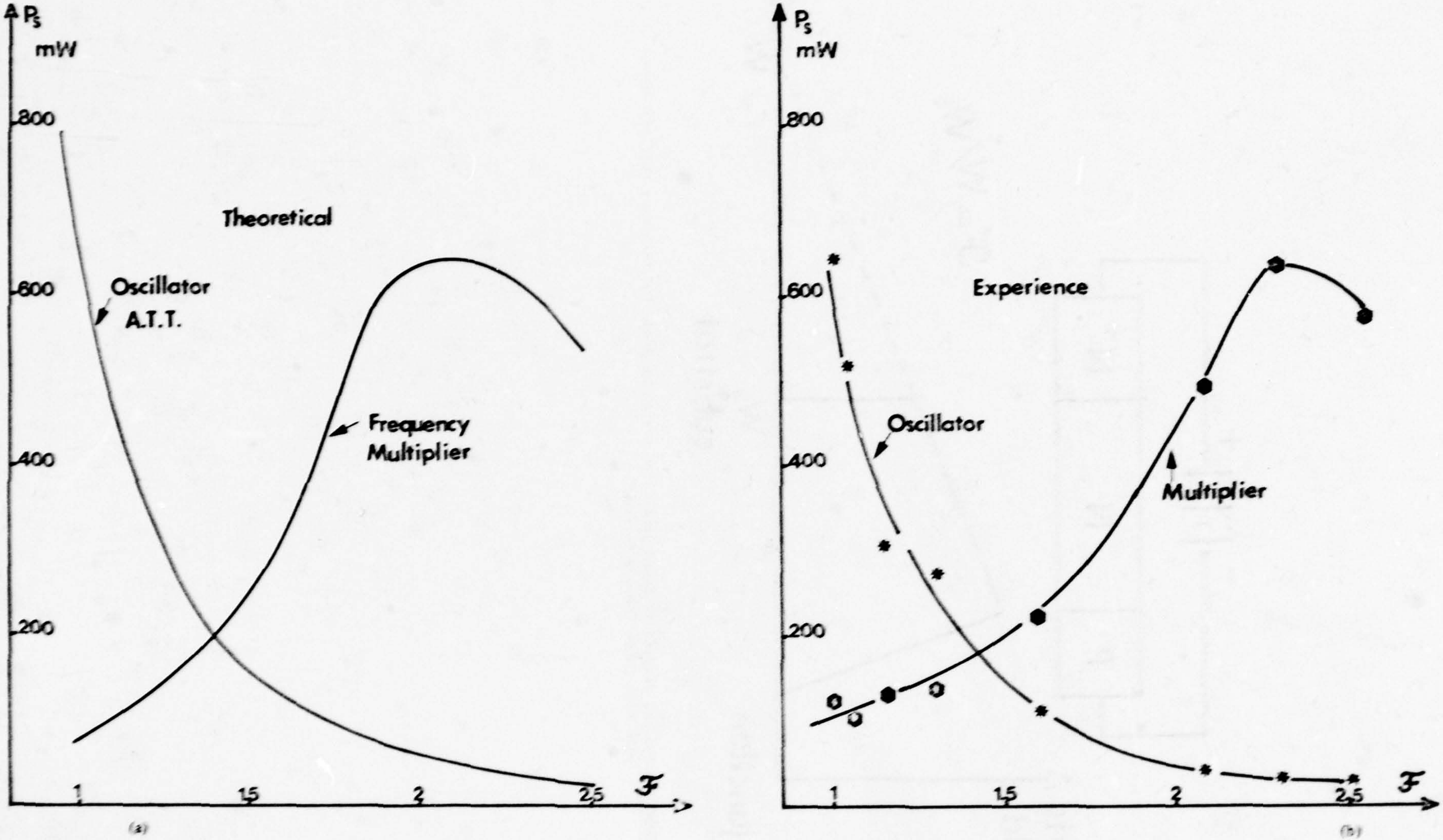

FIGURE 4 : Maximum output power in ATT and multiplication modes as a function of the punch-through factor F

a. theoretical
b. experimental

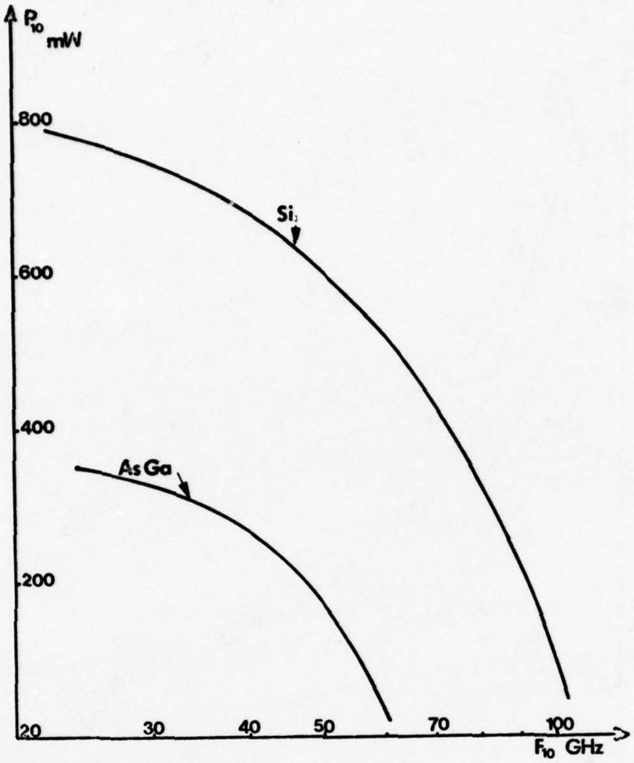

FIGURE 5 : Maximum theoretical output power in frequency multiplication by 10 versus the output frequency.

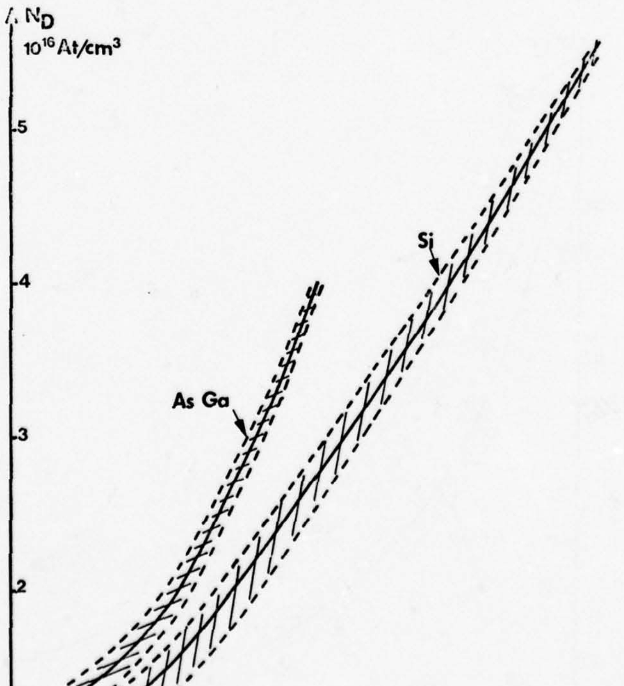

FIGURE 6 : Optimal N zone doping concentration in frequency multiplication by 10 as a function of the output frequency.

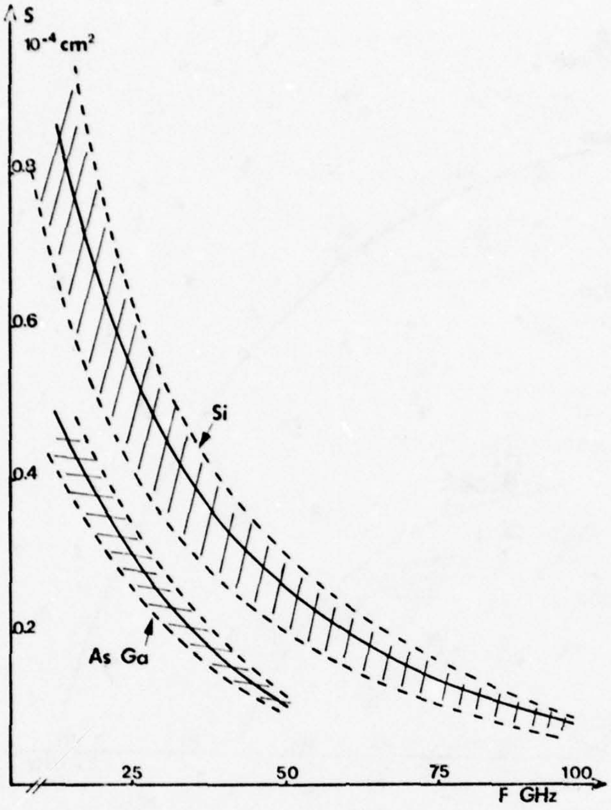

FIGURE 7 : Optimum junction area in frequency multiplication by ten as a function of the output frequency

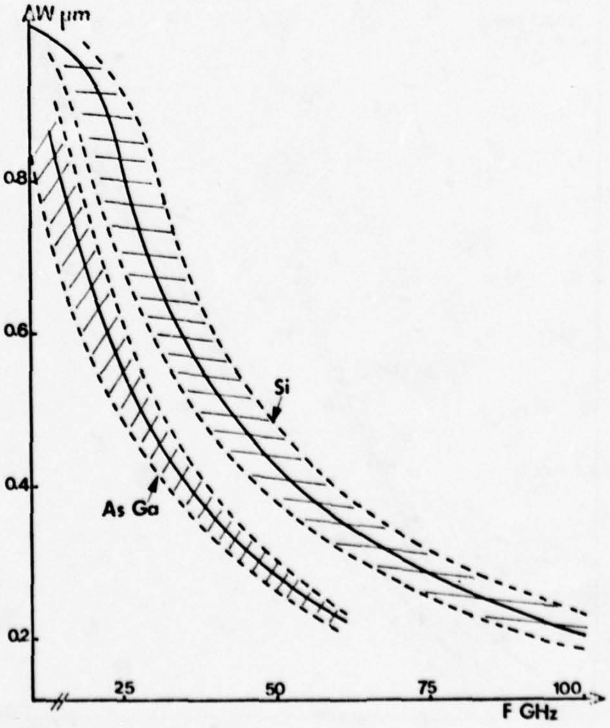

FIGURE 8 : Optimum depletion layer width in frequency multiplication by ten as a function of the output frequency.

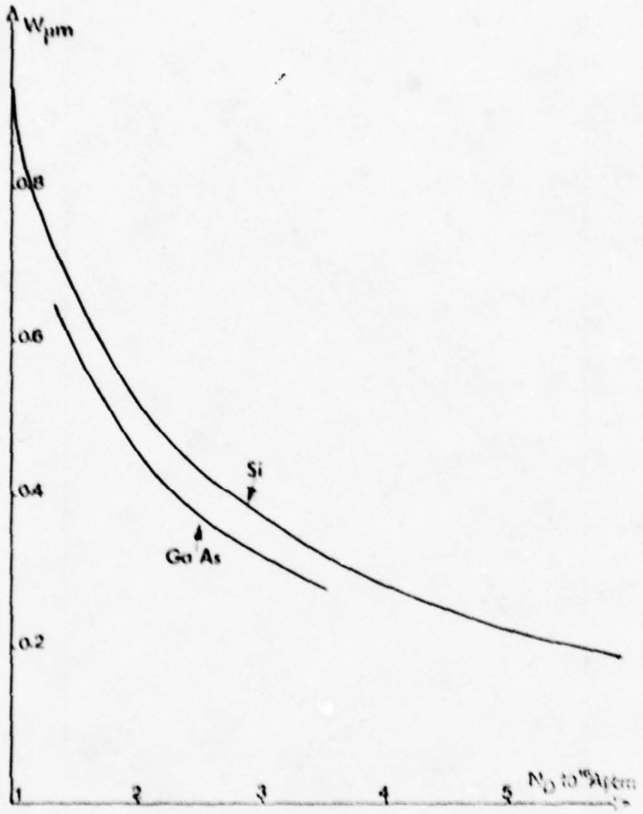

FIGURE 9 : Optimum depletion layer width versus the doping concentration.

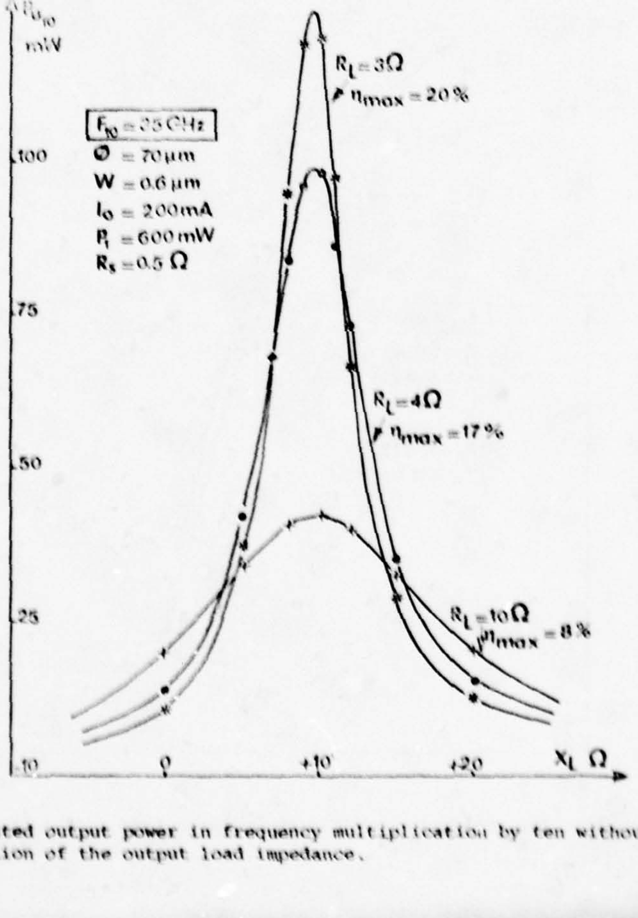

FIGURE 10: Calculated output power in frequency multiplication by ten without idler tuning as a function of the output load impedance.

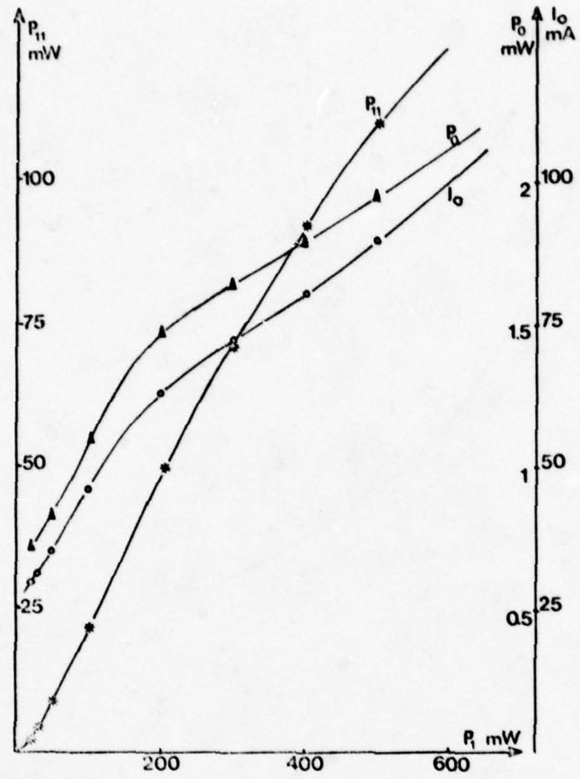

FIGURE 11: Measured output power P_{11}, D.C. bias current I_0, and D.C. power supply in multiplication by 11 as a function of the input power without deliberately introduced idler circuit.

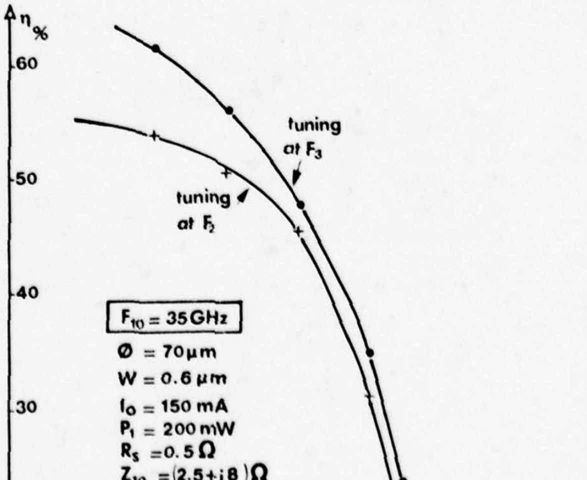

FIGURE 12: Improvement in the conversion efficiency by capacitive tuning on the first idler frequencies.

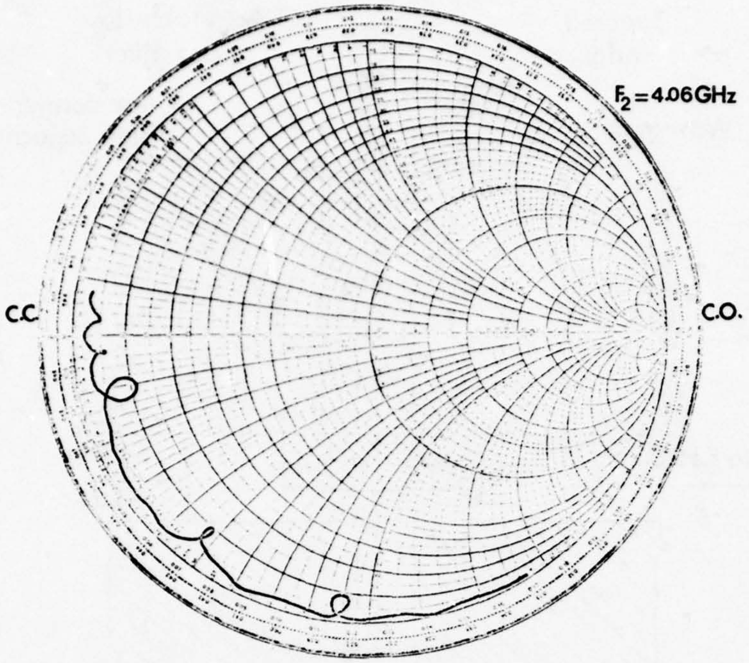

(a)

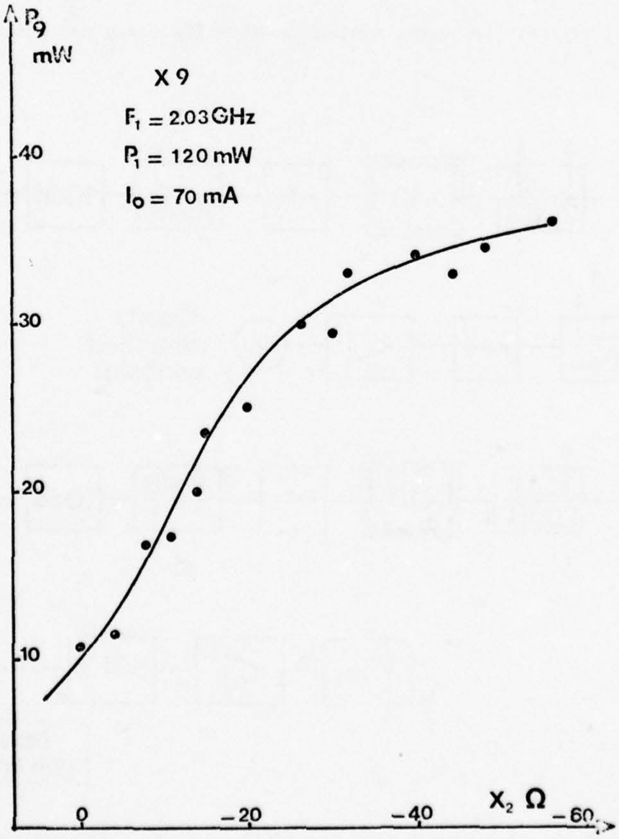

(b)

FIGURE 13: Measured influence of tuning on the second harmonic frequency for a X 9 multiplier :

a. idler load impedance
b. output power versus idler tuning.

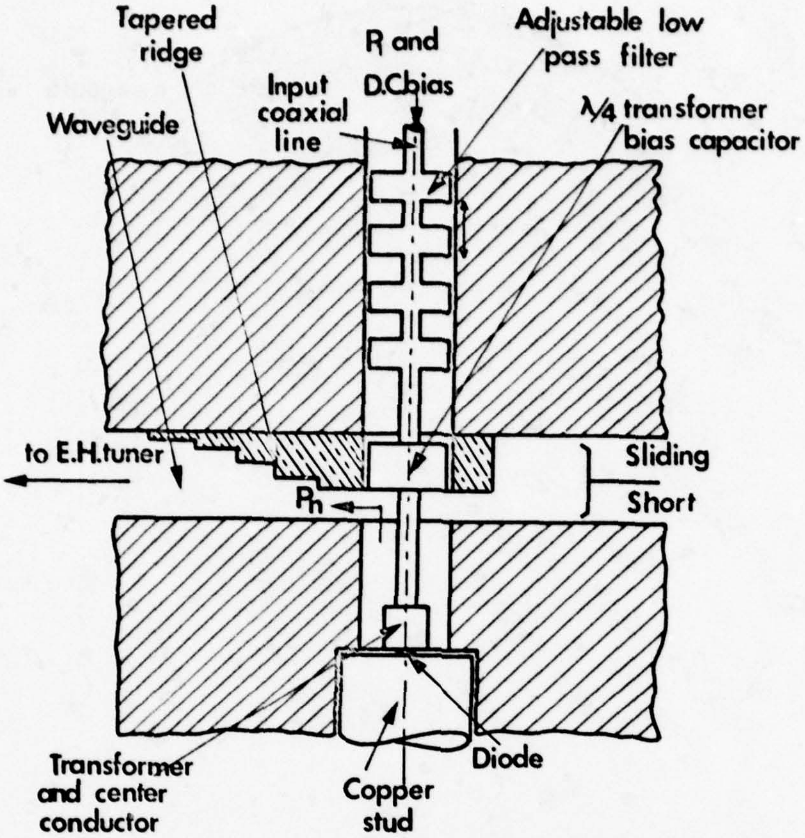
Tapered ridge
R and D.C bias
Adjustable low pass filter
Input coaxial line
Waveguide
λ/4 transformer bias capacitor
to E.H.tuner
Sliding
Short
Ph
Transformer and center conductor
Diode
Copper stud

FIGURE 14: Typical high order avalanche diode frequency multiplier circuit.

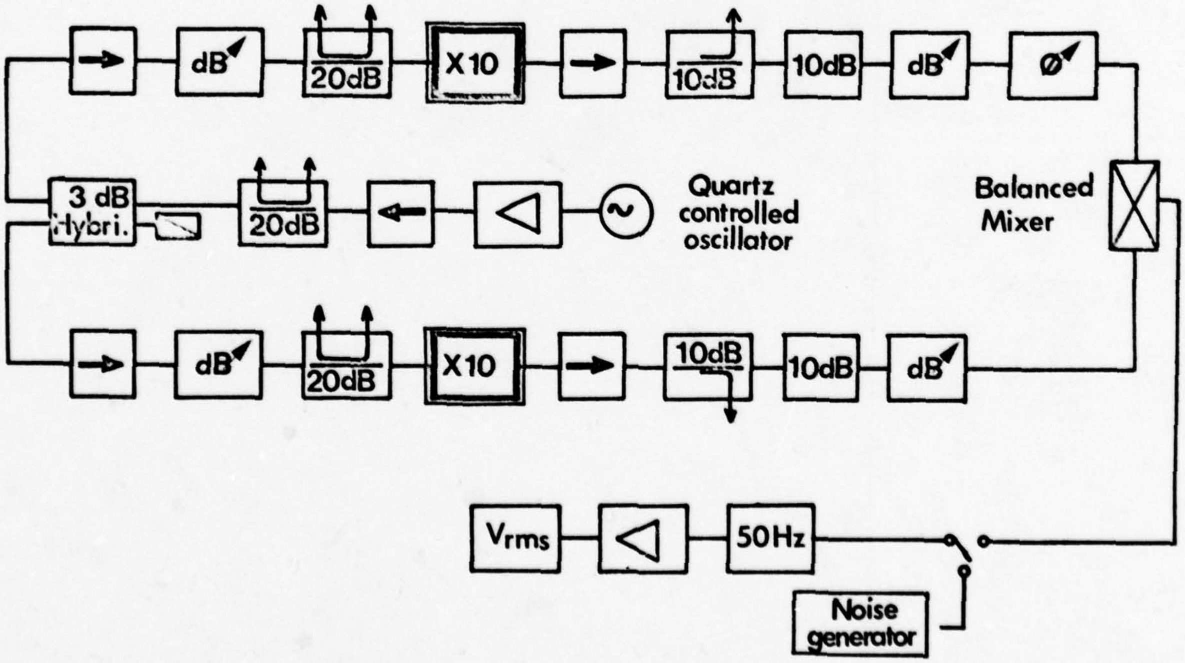
dB
20dB
X10
10dB
10dB
dB
Ø
3 dB Hybri.
20dB
Quartz controlled oscillator
Balanced Mixer
dB
20dB
X10
10dB
10dB
dB
Vrms
50Hz
Noise generator

FIGURE 15: Test set-up used for additive phase noise measurements

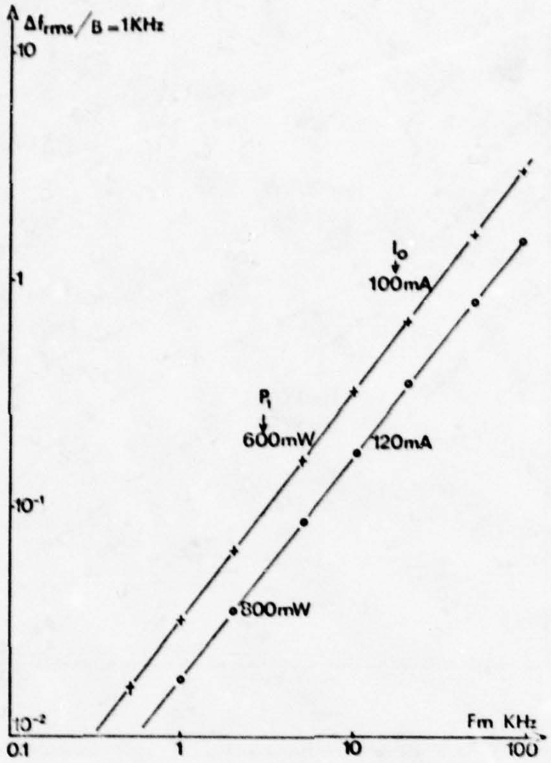

FIGURE 16: Additive FM noise contributed by a X 10 frequency multiplier as a function of the frequency separation from the carrier.

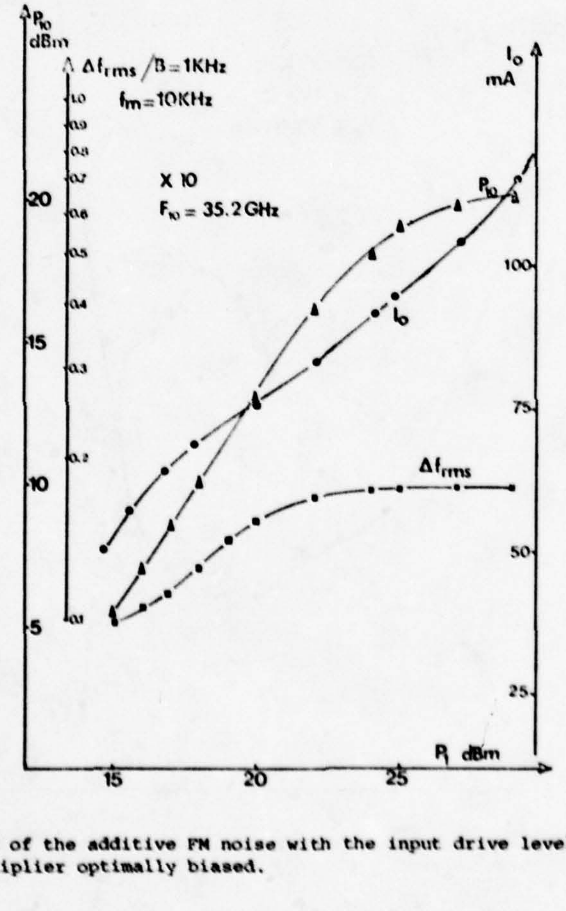

FIGURE 17: Evolution of the additive FM noise with the input drive level at the output of a X 10 multiplier optimally biased.

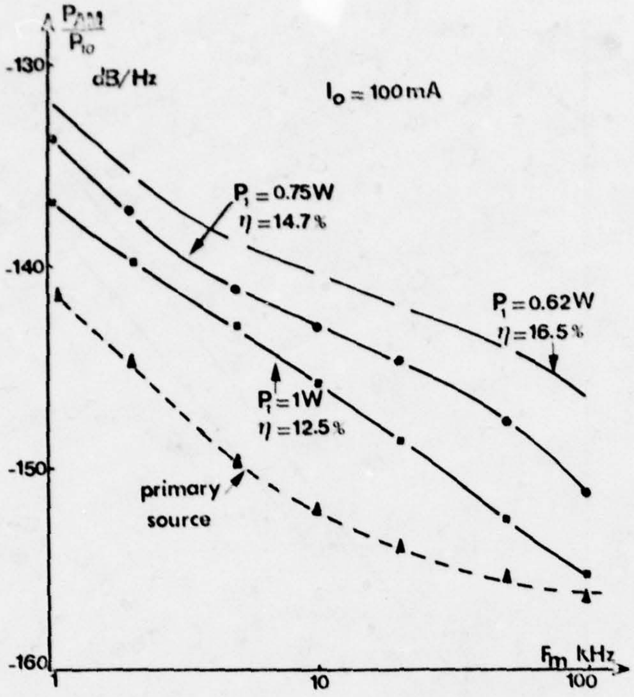

FIGURE 18: Output AM noise of a X 10 avalanche multiplier as a function of the frequency separation from the carrier.

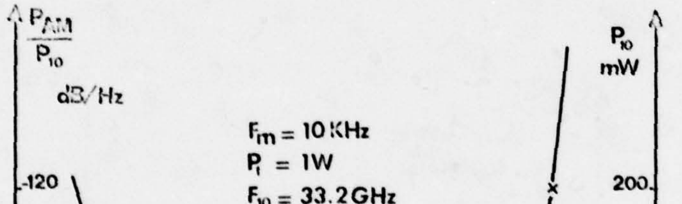

FIGURE 19: Evolution of the carrier to noise ratio at the output of a X 10 avalanche multiplier with the D.C. bias current.

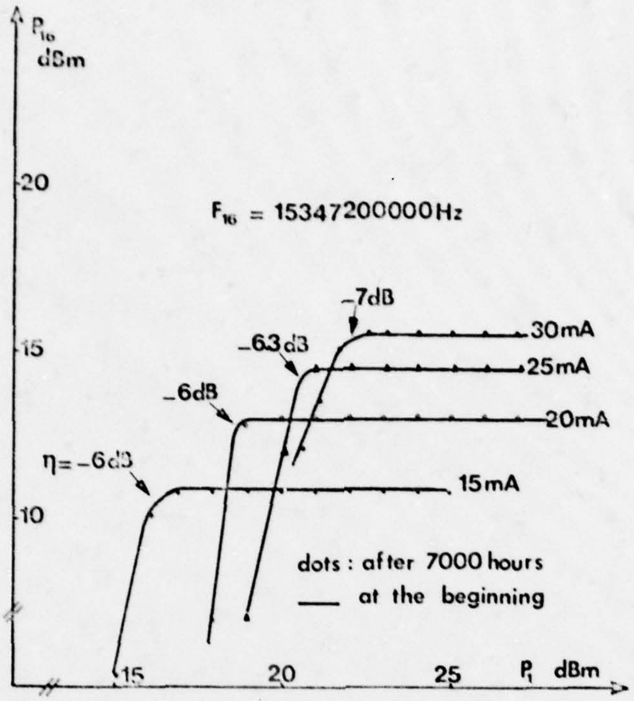

FIGURE 20: Evolution of the output characteristics of a X 16 avalanche frequency multiplier after a 7000 hours endurance test.

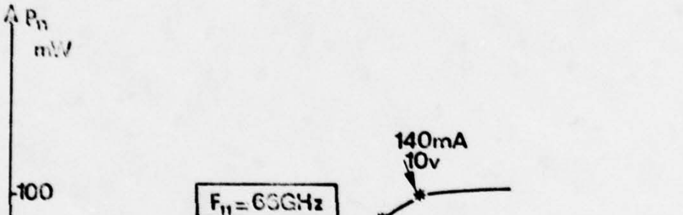

FIGURE 21: Typical output power versus input one for E band frequency multipliers.

WIDE-BAND MECHANICALLY TUNABLE W-BAND (75-110 GHz) CW GUNN DIODE OSCILLATOR

Dr. John Ondria*
Alpha Industries, Inc.
TRG Division
20 Sylvan Road
Woburn, Massachusetts, 01801, USA

*The author is Associate Professor of Electrical Engineering, Lehigh University, Bethlehem, Pennsylvania, 18015, USA. He is a consultant to TRG and has been employed there full-time during the summers of 1976, 1977, and 1978.

ABSTRACT

Experimental results are presented for a wide-band mechanically tunable CW Gunn diode oscillator in the 75 to 110 GHz range. A variable height radial mode resonator emersed in full height WR-10 (0.100 x 0.050") rectangular waveguide produced a continuous tuning range of almost 20 GHz. Corresponding output power of +10 dBm ± 1 dB was obtained when an adjustable waveguide short, located approximately $5/4\lambda g$ behind the diode, was simultaneously optimized at each frequency. Maximum power and frequency variations as function of temperature over the range $-40^{\circ}C$ to $+50^{\circ}C$ were $\Delta P/\Delta T \leq 0.133$ dB/°C and $\Delta f/\Delta T \leq 4.85$ MHz/°C respectively for a typical commercially available Gunn diode at 94 GHz. FM noise spectra for an oscillator tuned to 94 GHz is in agreement with recently published results (Tully, J. W.., 1978): typical measured noise deviation over the video range 0 to 2 kHz off the carrier frequency was less than 30 Hz rms, single sideband, referenced to a 1 Hz bandwidth at 1 kHz off carrier and exhibited a $1/f_m$ dependency in this region. The best CW results obtained thus far were an output power of +18.3 dBm at 94 GHz with 1.27% conversion efficiency.

1. INTRODUCTION

Experimental results are presented in this paper for a wide-band mechanically tunable CW Gunn diode oscillator operating at W-band (75-110 GHz) frequencies. Comparative data is included for Gunn devices operating in a similar circuit but fixed tuned in the vicinity of 94 GHz. Fundamental frequency Gunn (and IMPATT) diode oscillators can be built in waveguide, coaxial, stripline, or radial mode configurations. As the operating frequency increases, physical dimensions of both devices and circuits become inconveniently small. Previous work (Weller, K. P.., 1971 and Groves, I. S.., 1972) demonstrates that radial mode resonators are simple to design and have workable dimensions in the millimeter region; therefore, this geometry was selected.

In its most elementary form, a Gunn (or IMPATT) device is mounted in the broad dimension of either a standard or reduced height waveguide with dc bias applied thru an rf choke whose end section forms the radial hat resonator (Schwartz, G. A.., 1974). Although both hat diameter and its height above the waveguide floor determine the frequency of operation, the operating frequency for a given hat diameter can be tuned over a 20% bandwidth by varying hat height. Output power for any hat diameter and height is adjustable thru a waveguide short located approximately $\left[(2n+1)/4\right]\lambda g \pm 5\%$ behind the diode where n is an integer. Measured FM noise spectra close to the carrier frequency is dramatically affected by the short circuit position: stable, lowest noise output occurs when the oscillator is tuned to power peak.

Commercially available Gunn diodes in standard packages, such as the Alpha 296 configuration, and designed for U-band (45-55 GHz) operation, are used in these oscillators. In the sections which follow typical results are presented for devices purchased from various suppliers showing their output power versus frequency, power and frequency versus temperature characteristics, and FM noise deviation spectra measured over the video range 0 to 2 kHz off the carrier frequency in the vicinity of 94 GHz.

2. GUNN DIODE AND OSCILLATOR CIRCUIT

2.1 Fundamental Device Considerations

The fundamental frequency of Gunn diode oscillators is determined by both device and circuit constraints: (1) the circuit provides positive resistance equal to the diode's negative resistance at the frequency of resonance, (2) in the normal mode of operation, the transit-time length of the Gunn diode, $L = \bar{v}/f$ where $\bar{v}$ is average electron drift velocity and f is the oscillation frequency, must be chosen close to the frequency of operation. Since the average electron drift velocity in GaAs is approximately 1×10^5 m/sec, device transit-time lengths on the order of 1 μm are required for oscillators designed for the 100 GHz range. Present day technology limits GaAs Gunn diode useful upper frequency to about 70 GHz. Further, if the drift velocity is increased in an attempt to increase transit-time frequency, by reducing device bias voltage, the output power is drastically reduced. This occurs since peak-power voltage $V = \mathcal{E}L$, where $\mathcal{E}$ is the electric field satisfying the transit-time requirement, along with device threshold voltage, $V_T = 3.2$ kV/cm x length, are correspondingly reduced. Since rf voltage swings cannot go much below threshold their maximum excursions are only a few tenths of a volt and the corresponding output power is insignificant.

2.2 Diode Operation

GaAs Gunn diodes designed to operate in the 45 to 55 GHz region were successfully operated an octave or more above their intended frequency and produced nominally +7 to +10 dBm output power. The operating bias voltages, typically 4 to 5.5 Vdc, are substantially higher than values calculated from transit-time considerations which suggests they are operating in a hybrid mode.

2.3 Circuit Construction Details

A photograph of the prototype wide-band mechanically tunable W-band CW Gunn diode oscillator is shown in Fig. 1. The cross-section of a typical millimeter Gunn diode in standard threaded copper heat sink packages, having ceramic standoff ring and diode top cap diameter 0.030", is shown in Fig. 2. This device is mounted in a diode holder/frequency tuner and introduced into the broad wall (floor) of WR-10 waveguide. To ensure adequate heat conduction away from the diode junction, the beryllium copper diode holder/frequency tuner forms a large portion of the oscillator body. Smooth continuous frequency tuning is achieved using small pitch tuner threads. A cross-sectional view of the 94 GHz Gunn diode oscillator is shown in Fig. 3.

The bias circuit for Gunn diode oscillators is not especially critical as an impedance transformer but is a dominant element for IMPATT devices (Chao, C.., 1977). Bias voltage in this design is supplied thru the opposite waveguide broad wall by way of a standard single section, anodized aluminum rf choke. The choke end-section forms one face of a quarter wavelength quasi-radial mode resonator while the diodes' flange in cooperation with the corresponding broad wall (floor) of the waveguide form the other side. A sliding short placed behind the diode adjusts the coupling between the localized radial cavity and waveguide output. Since the frequency of operation is primarily established by the radial region very close to the diode, primary influence of the sliding short is impedance matching. At the point of optimum coupling, that is when the short is located approximately an odd number of quarter wavelengths $[(2n+1/4]\lambda g$ (Lee, T. P.., 1968) behind the diode, maximum power output coincident with minimum noise results. The diode package flange whose diameter is approximately 0.120" is introduced thru the waveguide floor by way of the diode flange passage, cf. Fig. 3. Frequency tuning is achieved by mechanically varying the diodes' position in the waveguide: inserting the diode further into the waveguide increases field fringing, effectively increasing the radial cavity dimensions which results in a lower oscillation frequency.

3. RF MEASUREMENTS AND PERFORMANCE

The output power versus frequency characteristics are shown in Fig. 4 for the W9400T-1 wide-band mechanically tunable CW Gunn diode oscillator. For the commercially available MA4349 Gunn diode, stabilized at +47°C, the bias voltage was set to $V_{op} = 3.83$ Vdc with $I_{op} = 1.2$A as the frequency was continuously varied. Corresponding output power of +10 dBm ± 1 dB was obtained for $77.5 \text{ GHz} \leq f_{op} \leq 95.5$ GHz. The adjustable waveguide short, located approximately $(5/4)\lambda g$ behind the diode, was simultaneously optimized at each frequency. Similar results were obtained for the NEC ND7H50 Gunn diode: output power over the 10 GHz range $83 \text{ GHz} \leq f_{op} \leq 93$ GHz was +11.2 dBm ±0.6 dB with the same bias choke/radial mode resonator used in conjunction with the MA4349 Gunn diode above. The tuning characteristic shown for an ALPHA G5726 Gunn diode from 86 GHz to 102 GHz was obtained using a smaller radial cavity hat. Power output was +9.5 dBm ±0.5 dB over the 11 GHz range $87 \text{ GHz} \leq f_{op} \leq 98$ GHz. Output power and frequency as function of temperature for the same MA4349 Gunn diode described above, are shown in Fig. 5 for the W9400T-1 tunable Gunn diode oscillator. Maximum power and frequency variations over the range -40°C to +50°C were $\Delta P/\Delta T \leq 0.133$ dB/°C and $\Delta f/\Delta T \leq 4.85$ MHz/°C respectively at 94 GHz. Similar results were obtained for the NEC ND7H50 Ser. No. 38 Gunn diode, cf. Fig. 6. The maximum variations were $\Delta P/\Delta T \leq 0.0625$ dB/°C and 5.5 MHz/°C respectively. The results, cf. Fig. 7, of a fixed tuned version of this oscillator, cf. Fig. 8, are given for the NEC ND7H50 Ser. No. 38, Gunn diode. Corresponding maximum power and frequency variations $\Delta P/\Delta T \leq 0.024$ dB/°C and $\Delta f/\Delta T \leq 4.29$ MHz/°C were obtained with the W9400F-0 fixed tuned oscillator initially set to 93.61 GHz at room temperature.

3.1 Additional Results

The operating characteristics given in Figs. 4 thru 7 are typical of those obtained using readily available Gunn devices. Of the more than 100 diodes measured in W9400T-1 approximately 80% produced similar results. The best Gunn diode oscillator CW results obtained thus far were an output power of +18.3 dBm with 1.27% conversion efficiency at 94 GHz.

4. FM NOISE MEASUREMENTS OF 94 GHz GUNN DIODE OSCILLATORS

4.1 General Discussion

FM Noise Measurements were performed on Alpha W9400 Gunn diode oscillators at 94 GHz. Noise spectra close to the carrier frequency (0-2 kHz) were measured using the standard heterodyne/IF discriminator technique, e.g. (Holman, R. H.., 1964). The measurements were conducted in a screened room with Gunn diode oscillator bias derived from a voltage regulator circuit driven by a 12 volt lead-acid battery.

4.2 Measuring System

A block diagram of the FM noise measuring system, cf. Fig. 9 consists of essentially two parts: (a) the IF calibration section and (b) the RF to IF conversion section. Basically, this technique relies on a low noise 94 GHz local oscillator which in this case is derived from a 109 MHz crystal oscillator - amplifier - harmonic multiplier chain. When heterodyned against the oscillator under test, which is offset in frequency by an amount equal to the IF (150 MHz), the resulting noise spectrum display after discrimination is essentially that of the 'noisy' oscillator under test.

4.2.1 Calibration

Discriminator calibration is done before and after each set of measurements is made in order to minimize inherent drift errors. To calibrate the system an audio oscillator tuned to 1 kHz (mid range for the baseband noise spectra measured) was used to modulate the Marconi signal generator to a modulation index of 2.405 which occurs at the first carrier null. By increasing the output level of the 1 kHz audio oscillator this condition is easily observed on the HP 8554B spectrum analyzer. At this point:

$$\text{Modulation Index} = m = 2.405 = \frac{\Delta f_{\text{peak deviation}}}{f_m}$$

$$\Delta f_{\text{peak deviation}} = 2.405\ f_m = 2.405\ \text{kHz}. \qquad (1)$$

After demodulation, in the 150 MHz discriminator, the 1 kHz line is amplified, passed thru the UA-6A video analyzer, and displayed on the vertical axis of an oscilloscope. The vertical position (and gain) controls on the spectrum analyzer and scope were set at 1.4 cm above the graticule center line. This voltage reference point corresponds to a peak deviation of 2.405 kHz and is used to convert the observed FM noise spectra into rms frequency deviation.

4.2.2 RF to IF Conversion

The low noise crystal controlled 94.00 GHz local oscillator, cf. block diagram Fig. 10, is attenuated and injected into an Alpha/TRG mixer (Model 9120) at a nominal drive level of 0 dBm. Simultaneously, the output signal and noise spectrum of the Gunn diode oscillator under test, tuned to 94 GHz ± 150 MHz, is introduced thru the mixer signal port. The down converted (150 MHz) spectrum at the mixer IF port is applied to the FM discriminator and photographs of the wave analyzer swept output display (0 to 2 kHz sweep range) taken. The calibration was rechecked to insure against possible system drift.

4.3 Noise Measurements and Calculation of rms FM Noise Deviation

4.3.1 Noise Measurements

Noise measurements close to the carrier must be performed in an electromagnetically shielded enclosure and the oscillator under test operated from a battery supply. All unnecessary equipment should be turned off during the measurement phase and where possible equipment should be battery powered. Measurements reported here were conducted in a screen room and the Gunn diode oscillator bias was derived from a voltage regulator circuit driven by a 12 volt lead acid battery.

The FM deviation of the Gunn diode oscillator under test appears as a noise power (spectral density) spectrum on the video analyzer/oscilloscope output display. FM noise measurements were made over the baseband (video) range extending out to 2 kHz off the carrier. A series of multiple exposures were made of each set of measurements (approximately 10) while carefully maintaining a null position on the zero centered microvoltmeter at the discriminator output. The correct null position is assured only if the down converted IF spectrum is exactly 150 MHz. Since the discriminator bandwidth is very narrow the center of its "S-curve", corresponding to the null, is obtained by simultaneously viewing the IF power spectrum on the HP 8554B analyzer while trimming the fine frequency adjust (micrometer) of the Gunn diode oscillator under test for the microvoltmeter null. The series of multiple exposures is necessary to aid in visual estimation of the relative peak level of the video noise spectral display: the multiple exposures, cf. Fig. 11, serve to average (integrate) the observed instantaneous oscilloscope fluctuations, thereby making them appear stationary.

The video measuring range of the low frequency wave analyzer was extended to its full range of 40 kHz during the course of the measurements. Since the noise spectra maintained the trend established at 2 kHz off carrier no attempt was made to photograph these results.

Photographs #1 and #3, cf. Fig. 11, are for the W9400T-1 wideband (77-97 GHz) mechanically tunable Gunn diode oscillator. Photograph #1 corresponds to the optimum tuning condition; namely, the oscillator was tuned to power peak and matched with the micrometer coupling (waveguide short) adjustment. The oscillator was then slightly detuned with the main frequency tuner, then "pulled" onto frequency with the coupling adjust micrometer, cf. Photograph #3, Fig. 11. This later condition corresponds to operation along the slope of the power-frequency locus and produces a noisier spectrum. Photograph #5, Fig. 11, is the FM noise power spectrum of the W9400 F-O (Fixed Tuned-Original) Gunn diode oscillator.

4.3.2 Calculations of rms FM Noise Deviation

Ordinarily, FM noise is described in terms of single sideband rms noise deviation, Δf_{rms}, and normalized to a one hertz bandwidth. Since the video analyzer displays, cf. Fig. 11, are power spectrums they must be converted. A sample calculation, cf. Fig. 12, illustrates the steps taken to generate the results, cf. Fig. 13, namely:

1) Adjust the calibration signal level to 1.4 cm (i.e. 14 dB) above the reference line (in this case the center line of the oscilloscope) when the 150 MHz reference signal is modulated to the first carrier null, cf. Section 4.2.1 above. This point corresponds to a peak deviation of 2.405 kHz, cf. Fig. 12a.

2) Display and photograph (using multiple exposures) the Gunn diode oscillator noise power spectrum as discussed in Section 4.3.1, cf. Fig. 11.

3) Estimate the peak level of the noise relative to the reference point. For this example it is 8 dB below the center line, i.e. 22 dB below the reference deviation point, cf. Fig. 12b.

4) The corresponding rms level is another 8 dB below the peak level (AN 150-4, 1974); therefore, the rms noise power is 30 dB below the reference level.

5) However, this noise power is the total power contained in two sidebands. Assuming equal noise power per sideband the single sideband rms noise power is 33 dB below the reference level.

6) The noise spectrum displayed was measured in a (video analyzer) noise bandwidth of 6.4 Hz, hence the noise relative to a 1 hertz bandwidth is less by another 8 dB.

7) Finally, for this example, the single sideband rms noise power level referenced to a 1 hertz bandwidth is 41 dB below the peak reference signal, i.e.

$$20 \log_{10} \left(\frac{\Delta f_{rms}}{\Delta f_{peak,\ ref.}} \right) \Bigg|_{1\ Hz\ BW} = -41\ dB, \qquad (2)$$

$$\Delta f_{rms} = 21.4\ Hz/1\ Hz\ BW/Single\ Sideband.$$

4.3.3 Measured FM Noise Results

Although the noise measuring technique used for these measurements is not as accurate as the phase bridge method (Ondria, J.., 1968), it is ideally suited for relative measurements and essential in selecting low noise Gunn diodes and constructing low noise sources.

The single sideband rms noise deviation, Δf_{rms}, normalized to a one hertz bandwidth for both the tunable W9400T-1 and fixed frequency W9400F-O Gunn diode oscillators are shown in Fig. 13 for frequencies 200 Hz to 2 kHz off carrier. These results were derived from Fig. 11 as described in Section 4.3.2 above. The general character of the noise in this region is $\kappa\ f_m^{-\alpha}$ in nature where f_m is video frequency (frequency off carrier) and $0.2<\alpha<1.2$ which is in agreement with the model for the noisy transferred electron oscillator (TEO) described recently (Gnerlich, H.., 1977). At video frequency $f_m = 1$ kHz the single sideband rms noise deviation was 27 Hz referred to a 1 hertz bandwidth for the W9400T-1 tunable Gunn diode oscillator when adjusted to power peak (+9.3 dBm) and 34 Hz when tuned off power peak. A fixed frequency W9400F-O Gunn diode oscillator tuned to power peak (+9.0 dBm) had corresponding $\Delta f_{rms} = 21$ Hz.

Measured Gunn diode oscillator FM noise deviation at 94 GHz, over the video range 1 kHz to 1,000 kHz off the carrier, reported recently, cf. Fig. 2 of (Tully, J. W.., 1978), is shown there for the Hughes Aircraft Company source. The corresponding value reported there is 60 Hz rms deviation referenced to a 1 hertz bandwidth at 1 kHz off the carrier frequency. For purposes of comparison this curve is superimposed on the results obtained here, cf. Fig. 13. The Alpha/TRG Gunn diode oscillator FM noise deviation are replotted on an expanded linear horizontal scale, cf. Fig. 14.

4.3.4. General Comments

For the results presented in this paper, no effort was made to select diodes for optimum output power or low noise. Further, these test oscillators are far from optimum regarding low noise performance. It is not unreasonable to anticipate a 3 to 5 dB improvement in noise performance using selected diodes and next generation oscillators.

5. SUMMARY

Experimental results presented in this paper demonstrate that wide mechanical tuning range can be achieved at millimeter frequencies using solid state devices. Specifically, almost 20 GHz of continuous tuning was obtained for a CW Gunn diode oscillator at W-band frequencies by emersing a quasi-radial mode cavity within full height WR-10 waveguide and gradually altering its effective volume. Cavity size is controlled in this design by displacement of the packaged Gunn diode and its flange relative to the waveguide. At the same time the top hat section of the resonator is moved in consonance with the diode.

Continuous adjustments to circuit impedance changes are easily achieved by way of a non-contacting sliding short in the waveguide section behind the diode. By simply changing radial cavity hat diameters another range of frequencies within the operating band can be selected. The Gunn diodes, designed to operate in the transit-time mode around 45 GHz, appear to be operating in a hybrid mode at W-band frequencies as evidenced by their correspondingly higher operating bias voltages. Although Gunn diodes designed for operation around 70 GHz have operated in the normal mode their output power is low, they are unreliable, and they are not readily available. U-band (40 GHz to 60 GHz) devices, on the other hand, are commercially available in considerable quantities.

FM noise measurements close to the carrier, made on sources incorporating these devices, is substantially better than comparable klystrons when the diodes are operated at power peak. Since no attempt was made thus far to optimize noise, considerable improvement is anticipated in next generation sources and by careful selection of mating diodes.

6. ACKNOWLEDGEMENT

The author would like to thank Messrs. J. Zimmer and E. T. Hitt, III of Raytheon Company, Wayland, Massachusetts for discussions and assistance concerning the FM noise measurements described in this paper and for the use of their test facilities.

7. REFERENCES

Application Note, 150-4, 1974, Spectrum Analysis Noise Measurements, Hewlett Packard.

Chao, C., et. al., December 1977, "Y-Band (170-260 GHz) Tunable CW IMPATT Diode Oscillators", IEEE MTT-25, No. 12, pp. 985-991.

Gnerlich, H. R. and Ondria, J., December 1977, "A New Look at Noise in Transferred Electron Oscillators", MTT-25, No. 12, 1977 Symposium Issue, pp. 977-981.

Groves, I. S., and Lewis, D. E., February 1972, "Resonant - Cap Structure for IMPATT Diodes", Electron. Lett., Vol. 8, No. 4, pp. 98-99.

Holman, R. H., and Paciorek, L. J., November 23-24, 1964, "Short-Term Stability Measurement Techniques and Results", IEEE-NASA Symposium on Short-Term Frequency Stability, NASA SP-80, Goddard Space Flight Center, Greenbelt, Maryland, pp. 237-252.

Lee, T. P., Standley, R. D., and Misawa, T., October 1968, "A 50-GHz Silicon IMPATT Diode Oscillator and Amplifier", IEEE Trans, ED-15, No. 10, pp. 741-747.

Ondria, J., September 1968, "A Microwave System for Measurement of AM and FM Noise Spectra", IEEE Trans. MTT-16, No. 9, Special Issue on Noise, pp. 767-781.

Schwartz, G. A., et. al., February 1974, "Performance of P-Type Epitaxial Silicon Millimeter-Wave IMPATT Diodes", IEEE Trans. ED-21, No. 2, pp. 165-177.

Tully, J. W., et. al., January 1978, "Noise Performance of a 94 GHz Gunn-Effect Local Oscillator", IEEE ED-25, No. 1, pp. 64-65.

Weller, K. P., et. al., August 1971, "Millimeter-Wave GaAs Avalanche Oscillator", Proc. 3rd Biennial Cornell Elec. Eng. Conf. High Frequency Generation and Amplification, pp. 191-198.

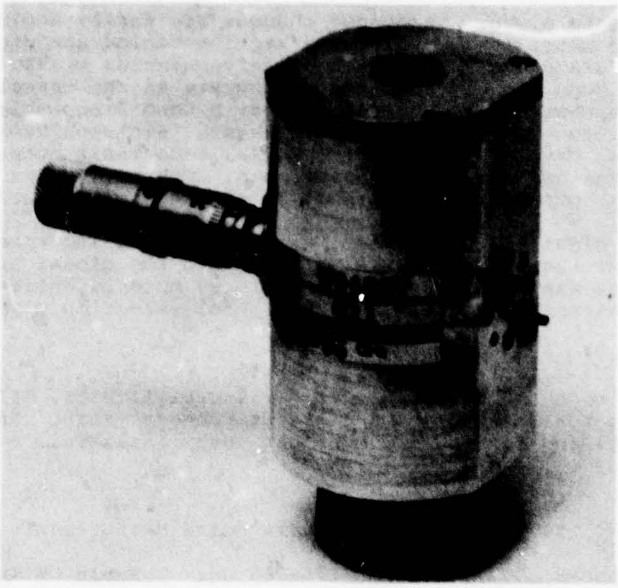

FIG. 1 PROTOTYPE WIDE-BAND MECHANICALLY TUNABLE W-BAND (75-110 GHz) CW GUNN DIODE OSCILLATOR

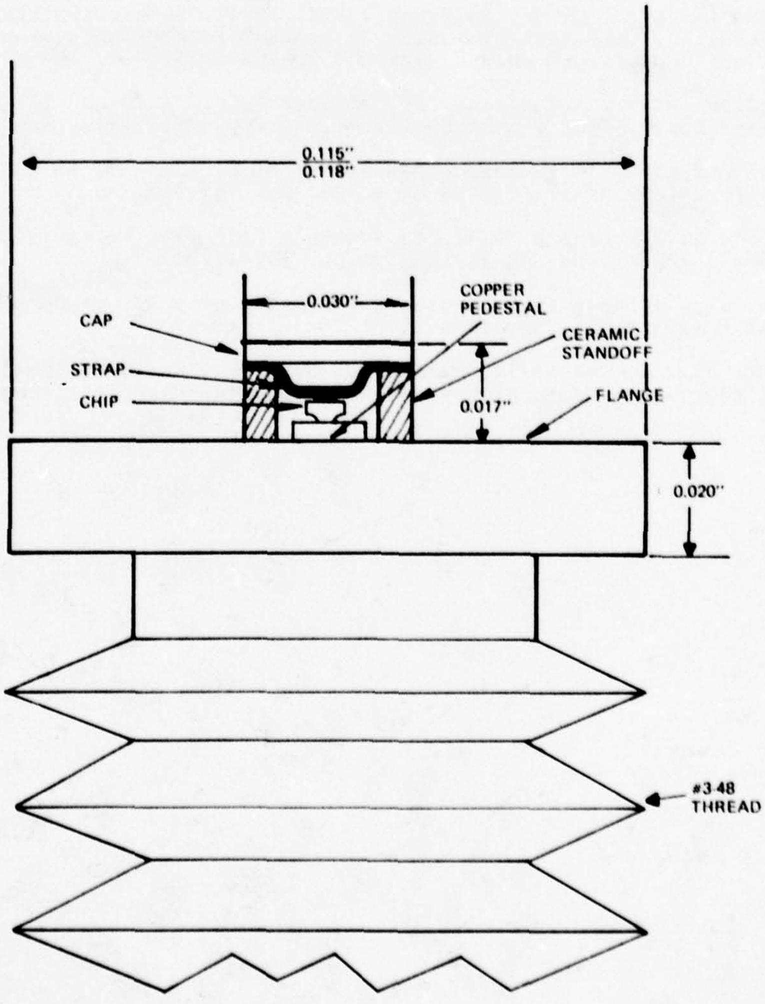
0.115"
0.118"
0.030"
CAP
STRAP
CHIP
COPPER PEDESTAL
CERAMIC STANDOFF
0.017"
FLANGE
0.020"
#3-48 THREAD

FIG. 2 CROSS SECTION OF A STANDARD PACKAGED MILLIMETER GUNN DIODE

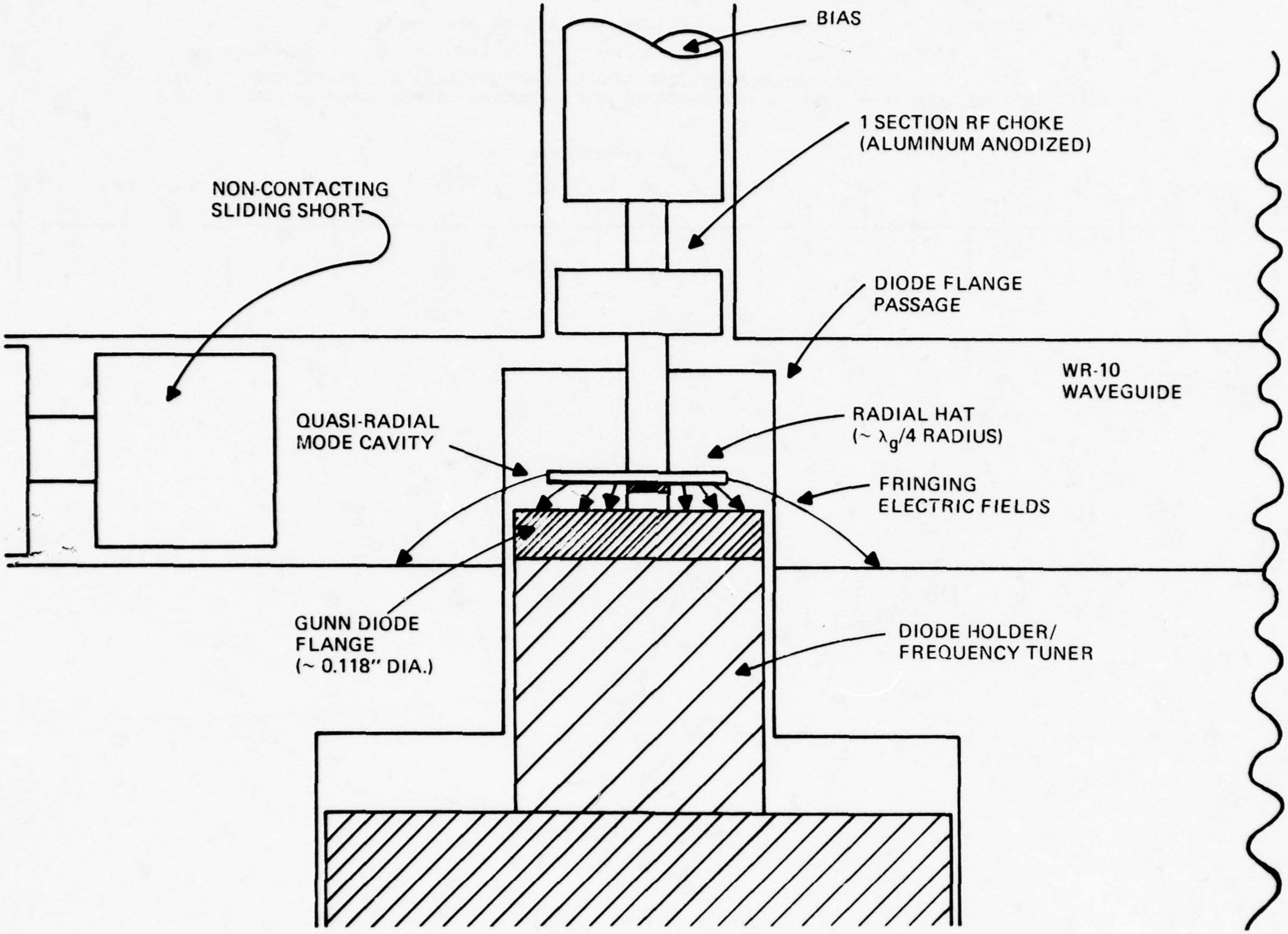
BIAS
1 SECTION RF CHOKE
(ALUMINUM ANODIZED)
NON-CONTACTING
SLIDING SHORT
DIODE FLANGE
PASSAGE
WR-10
WAVEGUIDE
QUASI-RADIAL
MODE CAVITY
RADIAL HAT
(~ $\lambda_g/4$ RADIUS)
FRINGING
ELECTRIC FIELDS
GUNN DIODE
FLANGE
(~ 0.118" DIA.)
DIODE HOLDER/
FREQUENCY TUNER

FIG. 3 CROSS SECTION OF GUNN DIODE QUASI-RADIAL CAVITY AND WAVEGUIDE CIRCUIT

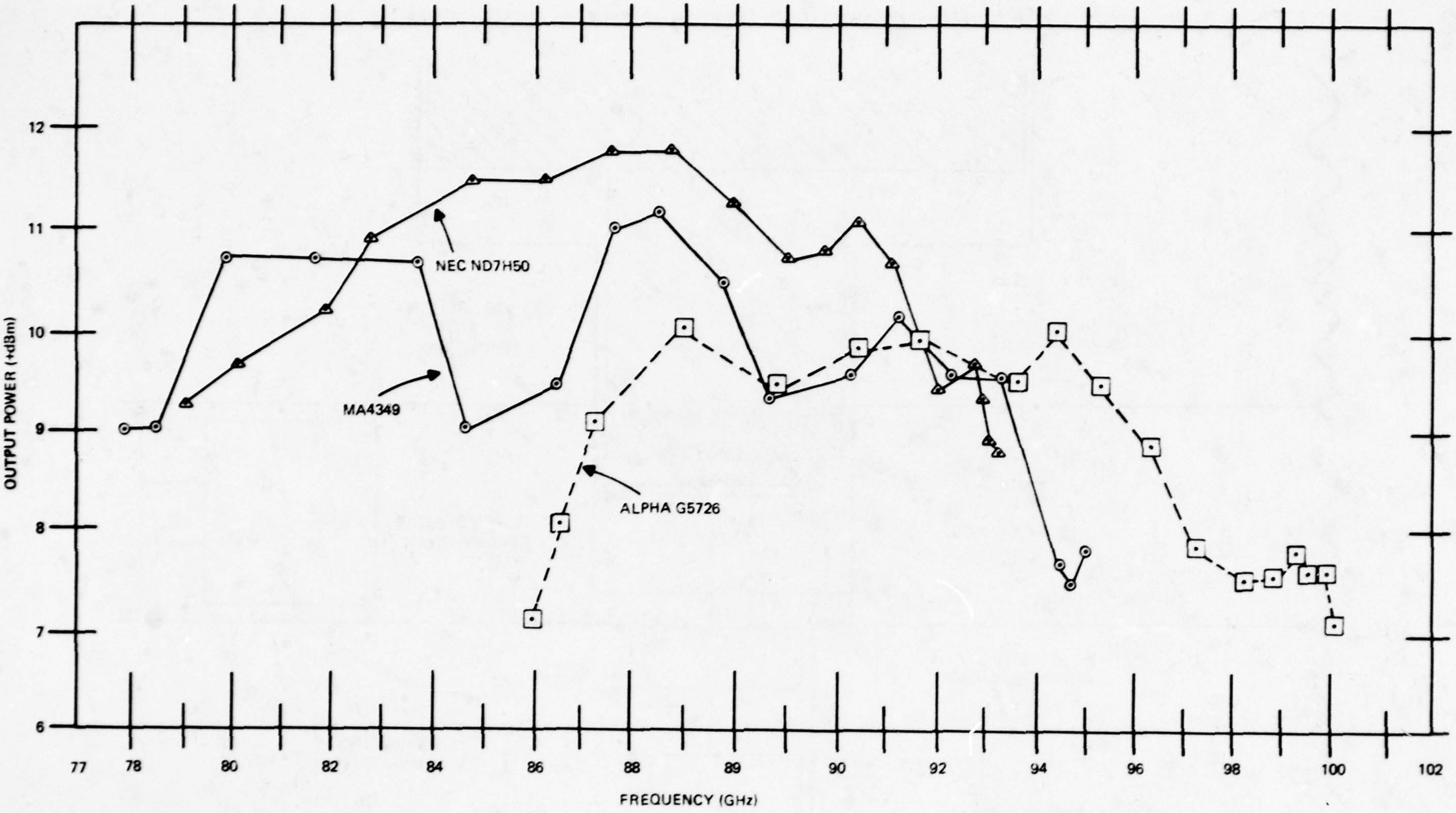

FIG. 4 OUTPUT POWER VERSUS FREQUENCY FOR MECHANICALLY TUNABLE W-9400T-1 CW GUNN DIODE OSCILLATOR FOR TYPICAL COMMERCIALLY AVAILABLE GUNN DIODES

LEGEND:
⊙ - MA4349, T_{op} = +47°C, V_{op} = 3.83Vdc, I_{op} = 1.2A
▲ - NEC ND7H50 SER. NO. 38, T_{op} = +48°C, V_{op} = 4.40Vdc, I_{op} = 1.1A
⊡ - ALPHA G5726, T_{op} = +32°C, V_{op} = 5.48Vdc, I_{op} = 0.38A

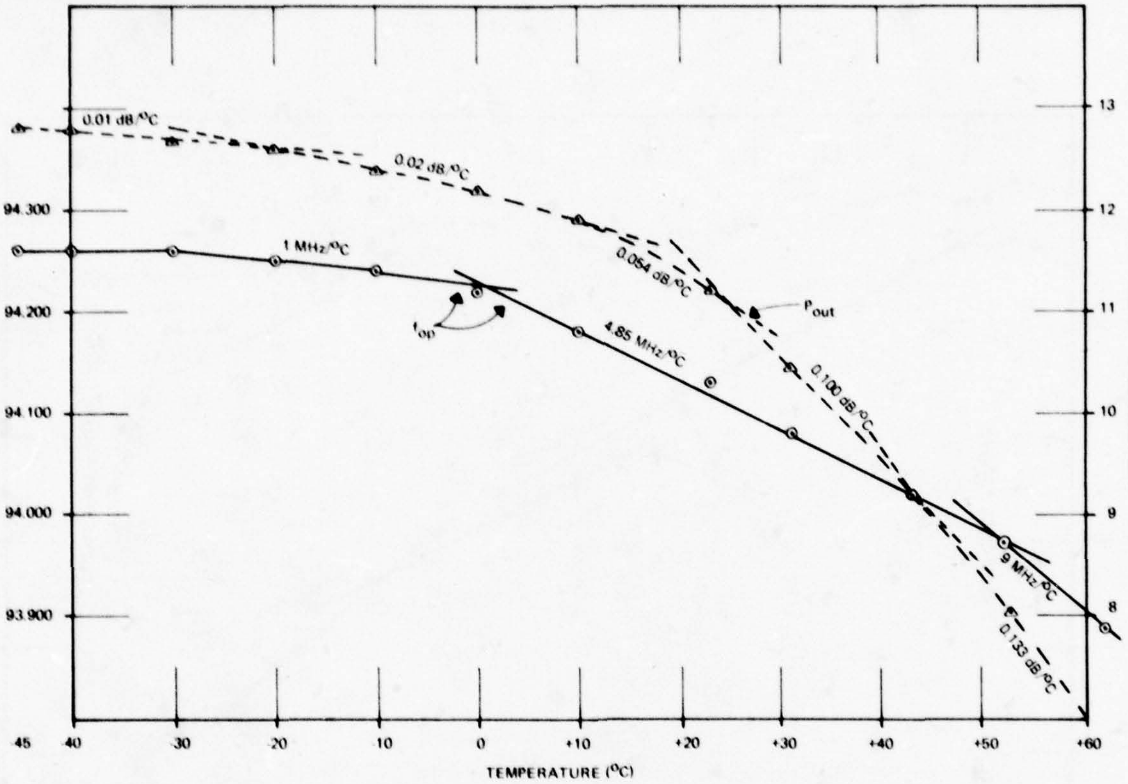

FIG. 5 OUTPUT POWER AND FREQUENCY VERSUS TEMPERATURE FOR MECHANICALLY TUNABLE W9400T-1 CW GUNN DIODE OSCILLATOR. MA4349 GUNN DIODE, V_{op} = +4.10Vdc, 1.16A $\le I_{op} \le$1.28A

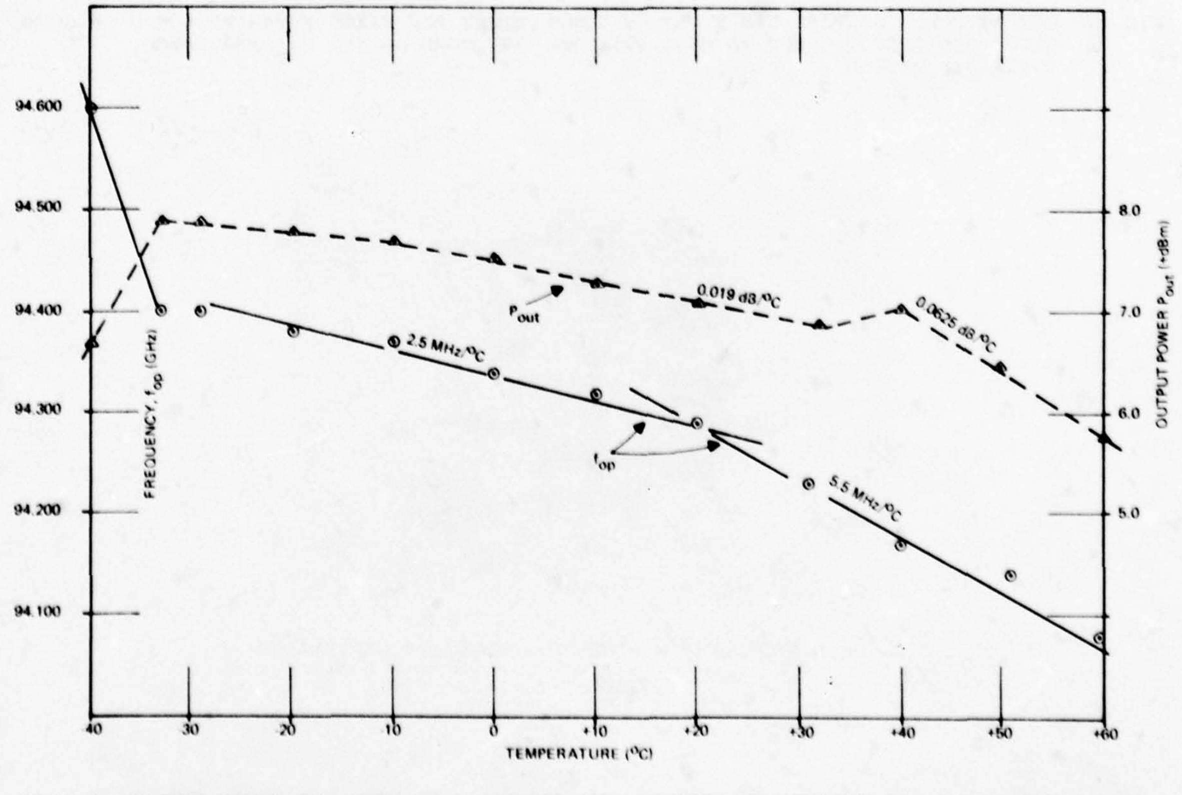

FIG. 6 OUTPUT POWER AND FREQUENCY VERSUS TEMPERATURE FOR MECHANICALLY TUNABLE W9400T-1 CW GUNN DIODE OSCILLATOR. NEC ND7H50, SER. NO. 38, GUNN DIODE, V_{op} = +4.4Vdc, $\le$0.99A $\le I_{op} \le$1.2A

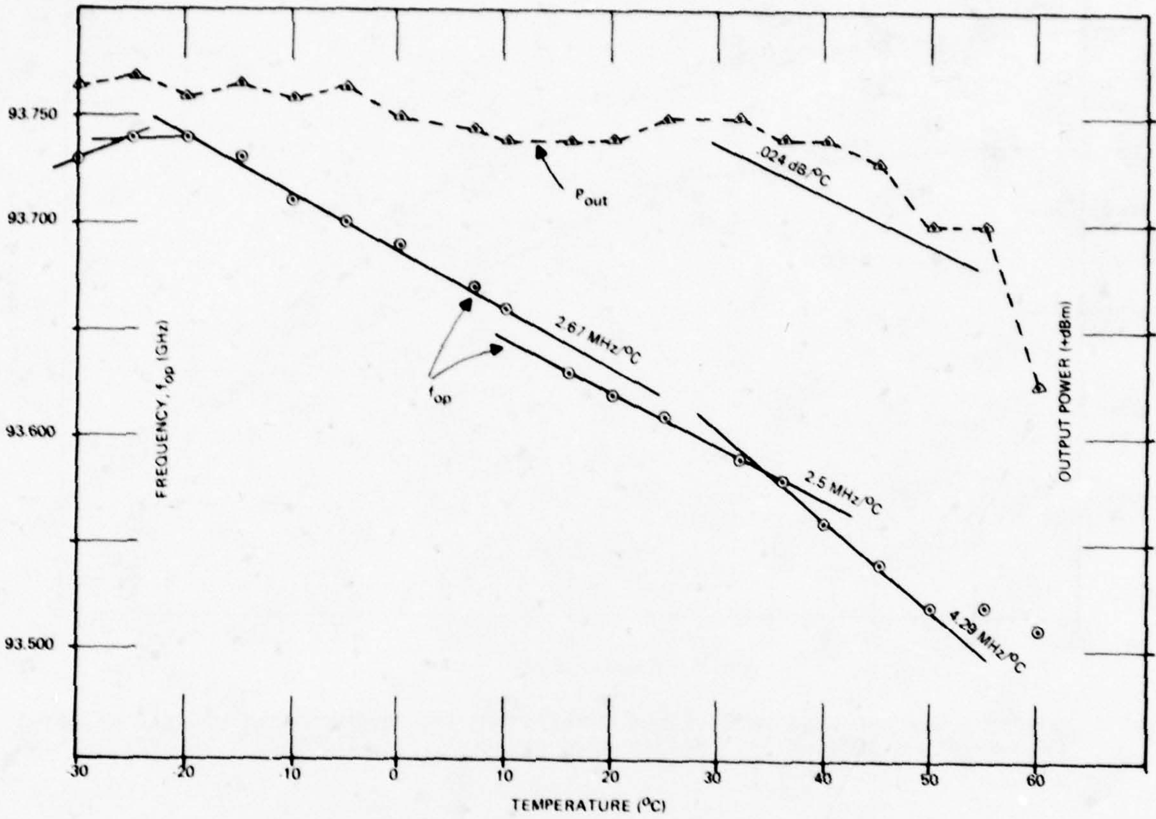

FIG. 7 OUTPUT POWER AND FREQUENCY VERSUS TEMPERATURE FOR FIXED TUNED W9400F-0 CW GUNN DIODE OSCILLATOR. NEC ND7H50, SER. NO. 38, GUNN DIODE, V_{op} = +4.30Vdc, 1.02A $\le I_{op} \le$ 1.15A

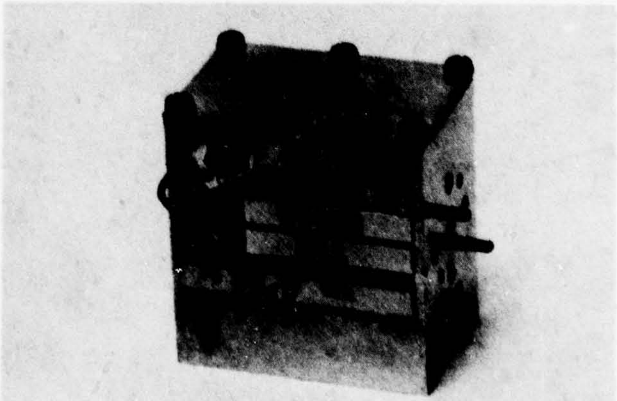

FIG. 8 FIXED TUNED W-BAND CW GUNN DIODE OSCILLATOR

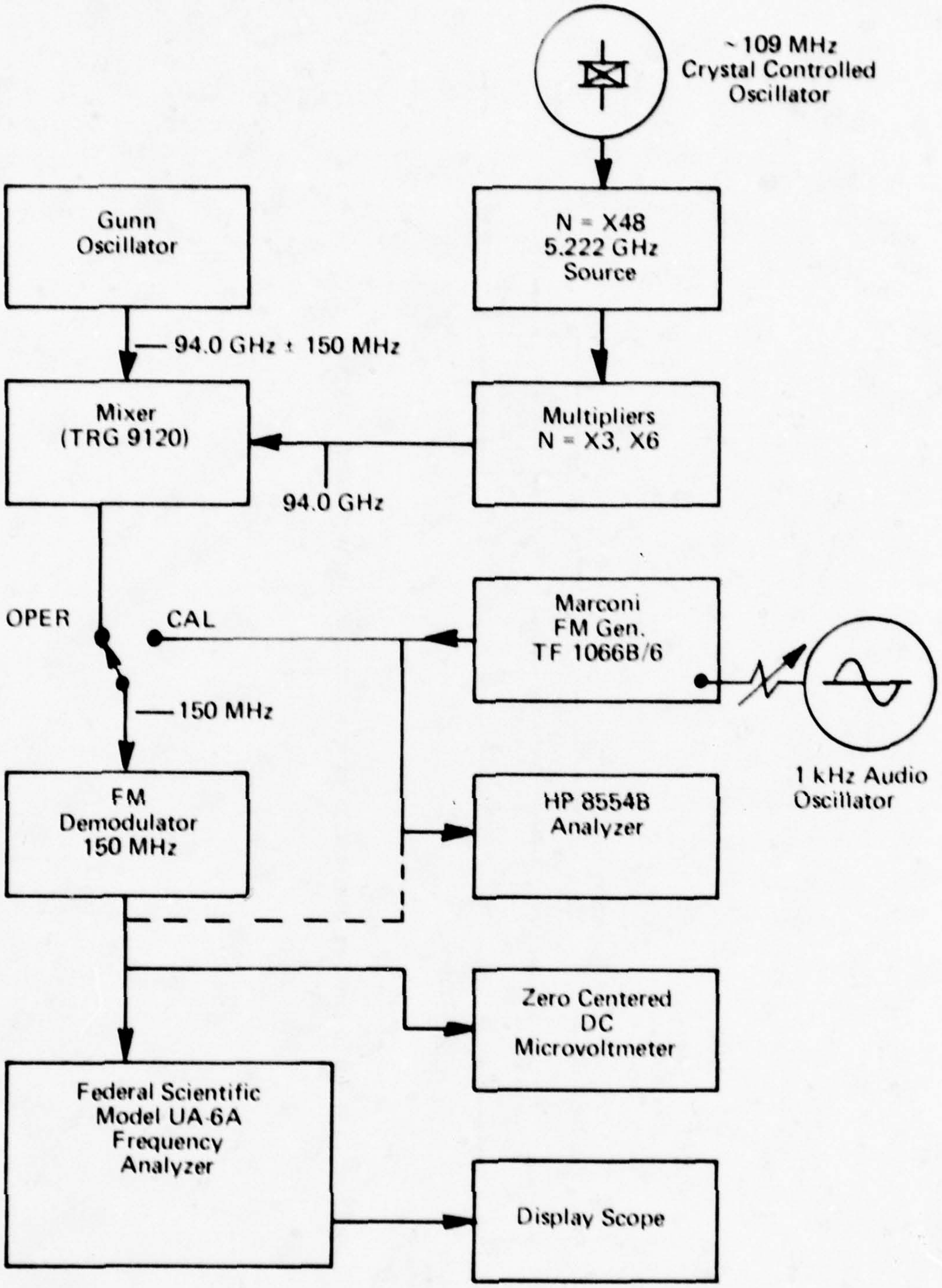
~109 MHz
Crystal Controlled
Oscillator
Gunn
Oscillator
N = X48
5.222 GHz
Source
94.0 GHz ± 150 MHz
Mixer
(TRG 9120)
Multipliers
N = X3, X6
94.0 GHz
OPER
CAL
Marconi
FM Gen.
TF 1066B/6
150 MHz
1 kHz Audio
Oscillator
FM
Demodulator
150 MHz
HP 8554B
Analyzer
Zero Centered
DC
Microvoltmeter
Federal Scientific
Model UA-6A
Frequency
Analyzer
Display Scope

FIG. 9 BLOCK DIAGRAM OF FM NOISE MEASURING SYSTEM

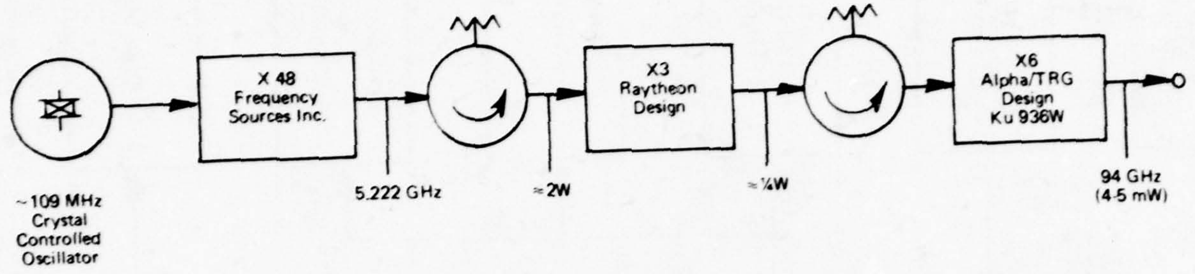
X 48
Frequency
Sources Inc.
X3
Raytheon
Design
X6
Alpha/TRG
Design
Ku 936W
~109 MHz
Crystal
Controlled
Oscillator
5.222 GHz
≈2W
≈¼W
94 GHz
(4·5 mW)

FIG. 10 LOW NOISE CRYSTAL CONTROLLED 94 GHz LOCAL OSCILLATOR BLOCK DIAGRAM

PHOTO 1

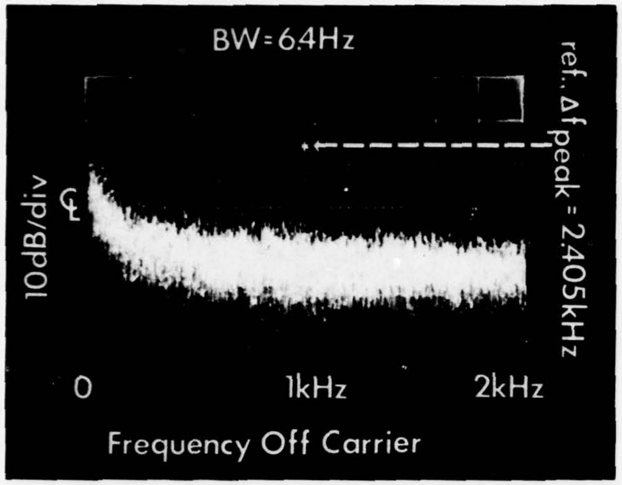

a) Mechanically tunable Gunn oscillator (77 - 97 GHz), Alpha/TRG W-9400 T-1, V_{op} = +4.63V, f_{op} = 94.15 GHz, P_{out} = +9.3 dBm.

PHOTO 3

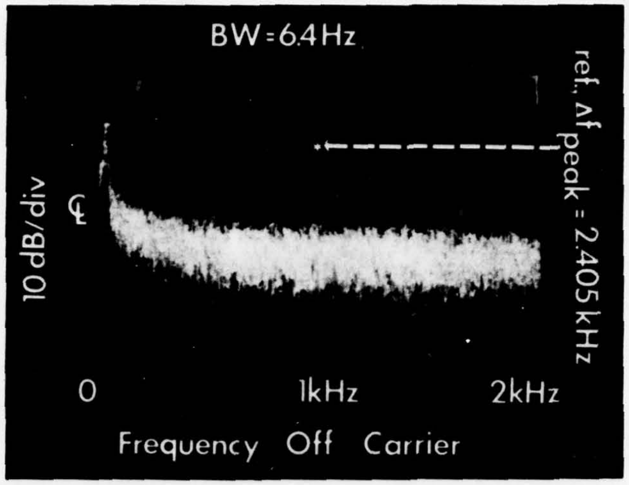

b) Same conditions as (a) but oscillator mechanically tuned off frequency and retuned (pulled) onto frequency with coupling adjust micrometer.

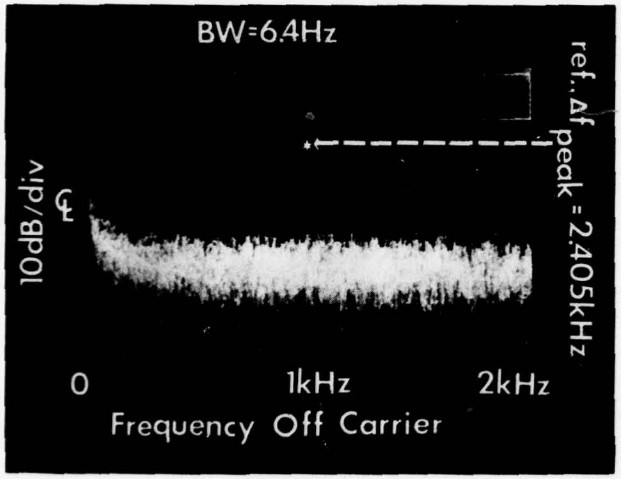

PHOTO 5

c) Fixed tuned Gunn oscillator, Alpha/TRG W-9400 F-0, V_{op} = +3.88V, f_{op} = 94.15 GHz, P_{out} = +9.0 dBm.

FIG. 11 FM NOISE POWER (SPECTRAL DENSITY) SPECTRUM (TWO SIDEBANDS) AT BASEBAND FREQUENCIES (0 TO 2 kHz OFF CARRIER)

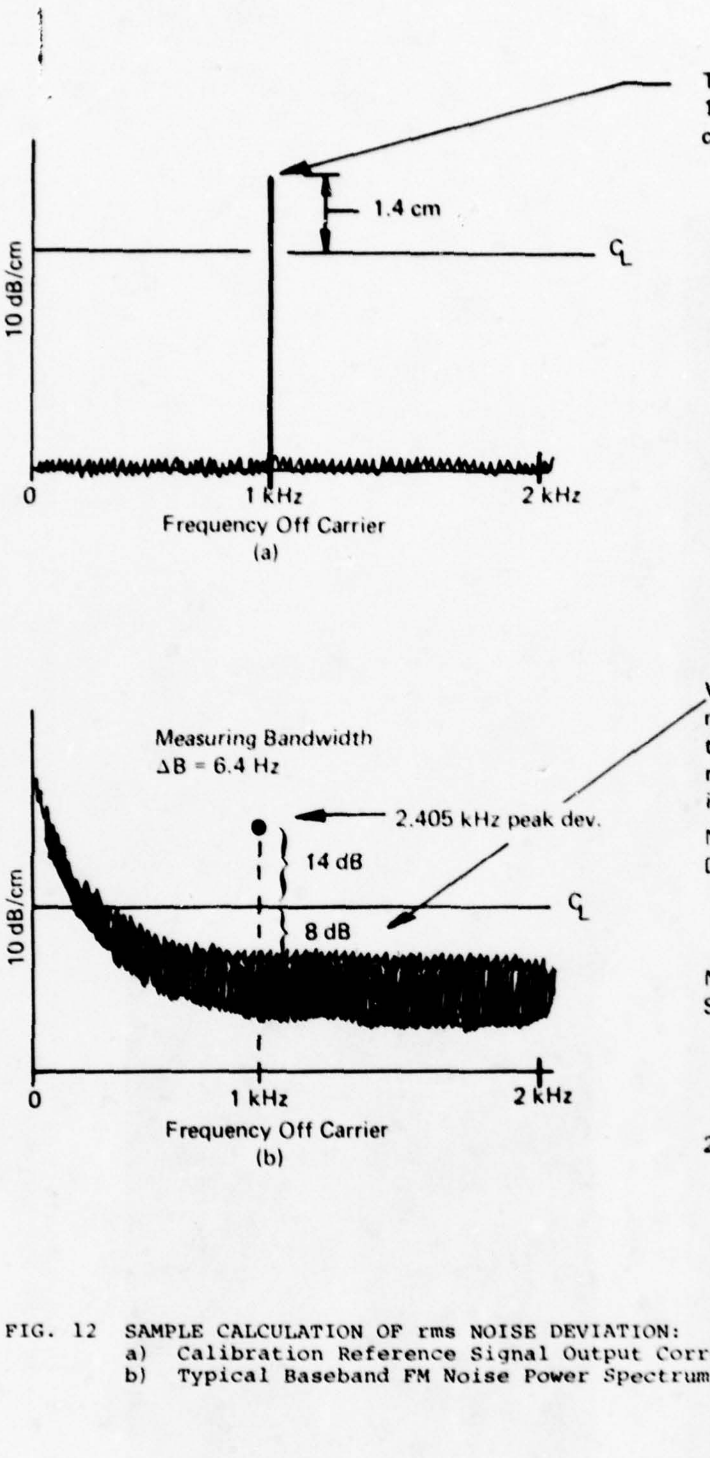

The reference signal level is adjusted to 1.4 cm (i.e. 14 dB) above the ℄. This corresponds to a peak deviation of 2.405 kHz.

Visual estimation of 8 dB. Hence the peak noise deviation is down 22 dB relative to the peak Ref. deviation and the corresponding rms deviation is 8 dB down from peak deviation, i.e.

$$\frac{\text{Noise DSB}}{\text{Ref. Level}} = -14-8-8 = -30\text{ dB}\Big/6.4\text{ Hz BW}$$

$$\frac{\text{Noise SSB}}{\text{Ref. Level}} = -33\text{ dB}\Big/6.4\text{ Hz BW} = -41\text{ dB}\Big/1\text{ Hz BW}$$

$$20\log_{10}\left(\frac{\Delta f_{rms}}{\Delta f_{peak,ref}}\right)\Bigg|_{1\text{ Hz BW}} = -41\text{ dB}$$

$$\Delta f_{peak,ref} = 2{,}405\text{ Hz}$$

$$\therefore\ \Delta f_{rms} = 21.4\text{ Hz}/1\text{ Hz BW}/\text{Single Sideband}$$

FIG. 12 SAMPLE CALCULATION OF rms NOISE DEVIATION:
a) Calibration Reference Signal Output Corresponding to the First Carrier Null.
b) Typical Baseband FM Noise Power Spectrum Display.

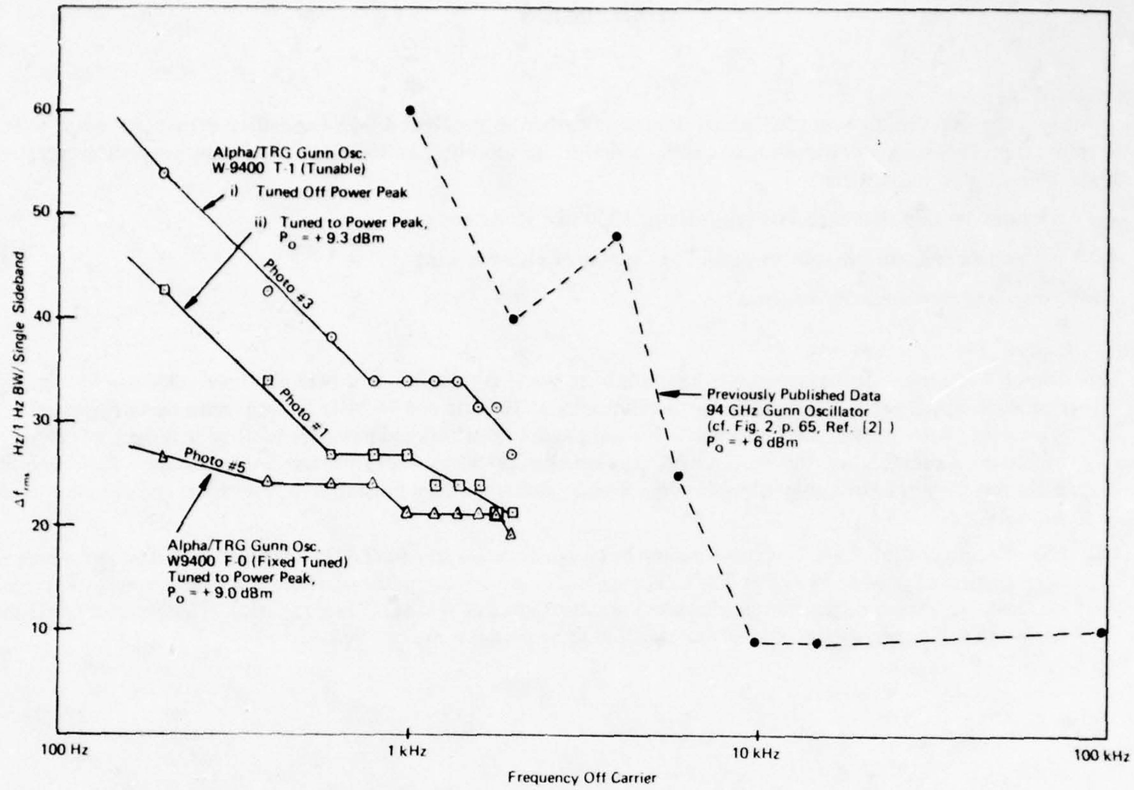

FIG. 13 GUNN OSCILLATOR SINGLE SIDEBAND FM NOISE DEVIATION VS. FREQUENCY OFF CARRIER f_{op} = 94.15 GHz

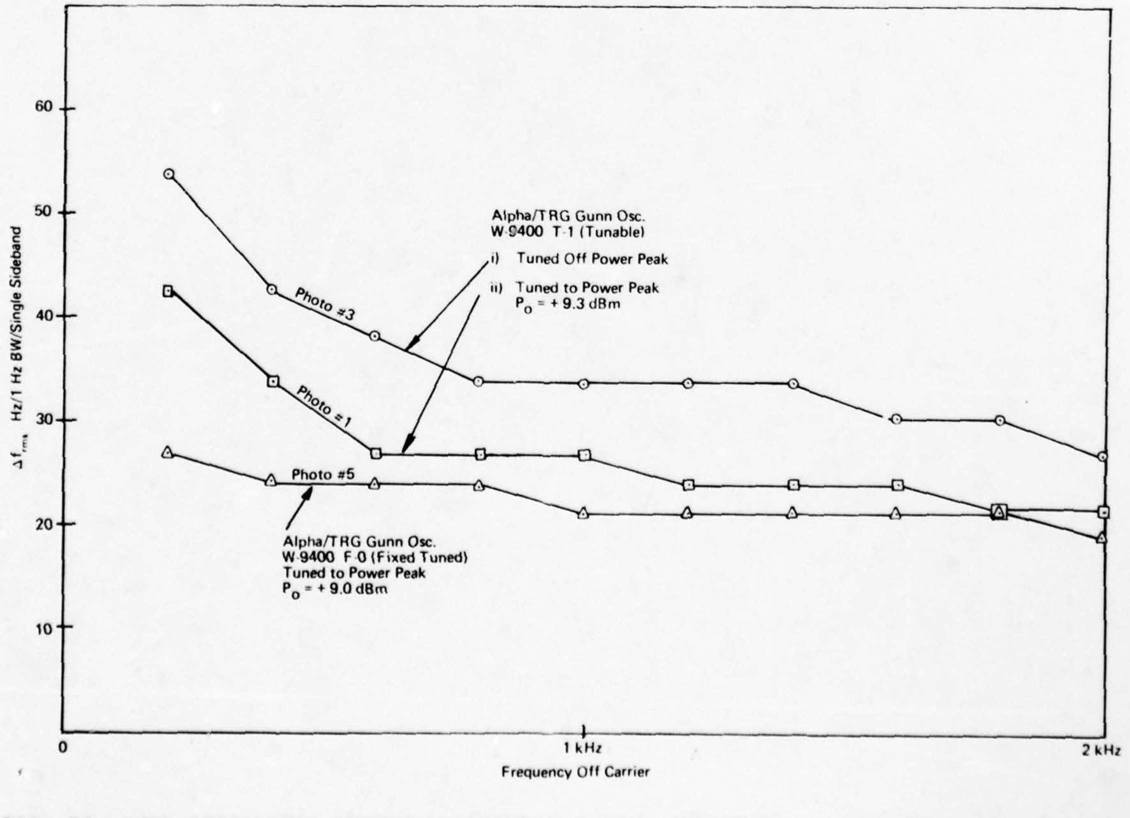

FIG. 14 GUNN OSCILLATOR SINGLE SIDEBAND FM NOISE DEVIATION VS. FREQUENCY OFF CARRIER f_{op} = 94.15 GHz

DISCUSSION

Nigel Keen, FRG

In view of the advances in Schottky barrier diodes, in particular the Mott diode, Gunn-diode/frequency-multiplier combinations become very interesting for local oscillators up to as high as 300 GMz. For many users, however, two conditions have to be satisfied:

(a) the noise level in the range 100's of MHz to 1000's of MHz; and

(b) the broad-band tunable sources should be capable of phase-locking.

Have you made measurements of these?

Author's Reply

(a) Direct, absolute noise measurements have not been made at this time, but used as a local oscillator in conjunction with a single ended mixer its noise performance at 30 MHz and 70 MHz IF frequencies is far superior to Klystrons. Also, used as a reference in a W-band phase bridge/reflectometer set resulted in a tightly focused oscilloscope presentation for Smith chart plots whereas kystron sources produce excessive beam dispersion and jitter resulting in a virtually useless display. This by inference is an indication of low noise performance of the gunn source.

(b) Phase locking of the 94 GHz tunable source has not attempted but similar 35 GHz and 70 GHz sources have been successfully phase locked at TRG. These sources are presently in operation in several systems. There is no reason to expect difficulties in phase locking this source at W-band (75–110 GHz). The necessary exterial hardware e.g. mixer, diodes, etc. is also available for accomplishing this task.

PARAMETRIC AMPLIFIER PUMP DESIGN

J.J. Purcell
Plessey Research (Caswell) Limited,
Allen Clark Research Centre,
Caswell, Towcester, Northants., U.K.

Fig.

Introduction

Miniaturized, all solid-state, parametric amplifers have been developed 1
for earth-to-satellite communications at frequencies as high as Ka-band (36-38 GHz) with typical operating characteristics of 100 MHz instantaneous bandwidth, gains of 18 dB and noise figures of 1.5 to 3 dB (AIL/NRL Raytheon/AFAL). Current developments are directed towards the demonstration of low noise performance at 94 GHz for such applications as coherent radar (LNR), space-object imaging, reconnaissance, and communications.

The use of cryogenic techniques to minimise the amplifier noise temperature is generally restricted to radio astronomy where expense, complexity, and reliability may be of secondary importance. However, in military communications or civil systems, refrigeration is usually precluded and low noise is obtained by 'electronic cooling', by the use of high pump frequencies.

Theoretical analyses of parametric amplifiers show that with high quality varactor diodes, the excess noise temperature is proportional to the ratio of idler frequency to signal frequency, with a minimum at γF_c, (Fig 2). 2
Development of GaAs varactor diode technology has enabled pump frequencies to be raised as high as 170 GHz (Hughes, AFAL).

Reference to current state-of-the-art results for Gunn and IMPATT sources (Fig 3) shows that Gunn pumps are limited to powers of about 80 mW 3
at 100 GHz using either GaAs or InP devices, whereas silicon avalanche diodes have produced cw powers of 700 mW at 94 GHz (Hughes). At lower pump frequencies of 40 to 50 GHz, however, both Gunn and IMPATT sources can produce adequate powers, and it is the purpose of this paper to compare their performance characteristics.

Paramp Stability

Fig.

(i) Gain Stability

A change in pump power or frequency has a direct effect upon the amplifier gain. Changes can be described as a lack of stability, or randomness, and drift caused by ambient variations. It is important that sources considered for parametric amplifiers should be well engineered and characterised.

Experimental values have been obtained to describe the sensitivity of a 13 dB, 500 MHz B.W., X-band paramp to changes in pump power and frequency(1). Of six amplifiers, the average gain/frequency sensitivity was approximately 0.1 dB per 2 MHz change in the 50 GHz pump frequency, and similarly, the gain to pump power ratio was measured as a factor 7.

Assuming an overall system stability requirement of G_T, then the permissible parameter variation can be estimated using the expression:- 4

$$\left(\Delta P + \frac{(\delta P)}{(\delta T)}\Delta T\right) \left.\frac{(\delta G)}{(\delta P)}\right._{F_o} + \left(\Delta F + \frac{(\delta F)}{(\delta T)}\Delta T\right) \left.\frac{(\delta G)}{(\delta F)}\right._{P_o} = G_T$$

where ΔP and ΔF represent the power and frequency stability and $\delta P/\delta T$, $\delta F/\delta T$ the temperature stability.

Substituting a realistic value of 0.5 dB for G_T, and the measured values of $\delta G/\delta P$ and $\delta G/\delta F$:-

$$\left(\Delta P + \frac{\delta P}{\delta T}\Delta T\right) \times 7 + \left(\Delta F + \frac{(\delta F)}{(\delta T)}\ \right)\ \Delta T)\ \frac{0.1}{2} \leq 0.5 \quad \text{(dB)}$$

Temperature stability is maintained either by heating to a temperature above ambient or controlling by Peltier devices below ambient. In either case, a stability of $\pm$ 0.5°C is readily obtained, and the expression becomes:-

$$\left(\Delta P + \frac{P}{T}\right) 7 + \left(\Delta F + \frac{(\delta F)}{(\delta T)}\right)\ 0.05 \leq 0.5 \text{ (dB)}$$

As boundary conditions, it can be seen that the frequency stability is to be better than 10 MHz (in 50 GHz) and the power stability better than 0.07 dB, placing tight constraints upon the source design. Indeed, the effectiveness of the paramp is largely determined by the quality of the pump source.

Fig.

(ii) Noise

The excess noise temperature of the amplifier is determined by noise
at the signal frequency, and by noise at the idler frequency down converted
by the paramp action. In Fig (5) is shown the f.m. noise spectrum of IMPATT 5
and GUNN pumps operating at 40 GHz.

It can be seen that comparable figures are obtained with both types of pump, with noise power decreasing at about 9 dB per octave. (A constant deviation F_{RMS} would produce a decrease of 6 dB per octave). The relatively large idler and signal bandwidths of most paramps render them insensitive to f.m. pump noise in most applications.

In Fig (6) is shown the a.m. noise power spectrum of IMPATT and GUNN 6
pumps, again at 40 GHz.

The noise power falls as $F^{-\frac{1}{2}}$ away from carrier; however, at frequencies greater than about 100 KHz, the IMPATT noise power is found to remain essentially constant. Measurements at R.S.R.E. (Baldock) have shown IMPATT a.m. noise levels of -160 dB/Hz as far as 8 GHz from carrier frequency. a.m. noise at the idler frequency is converted by the paramp action to degrade the amplifier noise figure at the signal frequency.

By including a simple 3-pole, 500 MHz bandwidth, 18 dB per octave, pass-band filter in the pump line, noise temperature degradation is eliminated with all IMPATT pumps (1). Under small-signal conditions, comparable performance has been obtained with a paramp using a Klystron, IMPATT, or Gunn Pump source.

In Fig (7) is shown a commercial 40 GHz GUNN pump in an aluminium 7
body with an integral isolator. In Fig (8) is shown a 55 GHz IMPATT pump 8
with an isolator (EMS) and the 3-pole filter.

The characteristic performance of these pumps in compared in the
following Table (Fig 9). 9

It may be seen that overall stability figures are very similar. The principal difference between the Gunn and IMPATT source is that the

Fig.

Gunn output power is not readily adjustable.

In order to maximise the dynamic range of the amplifier, the manufacturer requires to adjust the pump power over as much as 2 dB. In the case of an IMPATT pump, power is a direct function of diode bias level and control is simple. However, this range of power variation is not readily obtained from T.E.O's owing to the high frequency/voltage pushing factors. In practice, the T.E.O. manufacturer includes an adjustable lossy element, at the expense of overall efficiency.

Source Power and Efficiency

The paramp pump power requirement is not usually greater than 200 mW enabling both T.E.O. or IMPATT's to be considered below about 50 GHz.

Solid-state source reliability is primarily determined by the device operating temperature, and failure is associated with the metallurgical degradation of the contacts.

Operating M.T.B.F.'s of the order of 10^4 or 10^5 hours are predicted for devices maintained below 200°C, as shown by the accelerated life-test data in Fig (10). The inferior reliability of IMPATT diodes having chromium-palladium-gold metallisation is clearly shown. 10

Taking a figure of 200°C maximum temperature rise, and using observed efficiency values, a maximum output power against frequency curve can be plotted. In Fig (11) is shown the predicted Gunn source performance, predicting maximum frequencies of 50 GHz for 200 mW and 64 GHz for 100 mW output powers. The rapid fall-off with frequency is caused by a combination of low dc to r.f. conversion efficiencies and high thermal inpedances. 11

In Fig (12) is shown the corresponding data for double-drift silicon IMPATTs. The efficiency falls slowly with increasing frequency, and lower thermal impedances are achieved, enabling powers as high as 200 mW to be maintained to frequencies as high as 70 GHz, and 100 mW at 100 GHz. 12

Although intended only as a broad indication of their relative capabilities, it can be seen that, in general, Gunn pumps are best suited to frequencies below about 60 GHz for all but very low power requirements. The IMPATT sources produces 100 mW to frequencies as high as 100 GHz, with high reliability.

Reference

1. 'IMPATT Pump Sideband Noise and its Effect on Parametric Amplifier Noise Temperature', C.A. Tearle and K.R. Heath, IEEE MTT-23, 12, Dec. 1975, pp. 1036-1042.

FIG. 1

PARAMETRIC AMPLIFIER

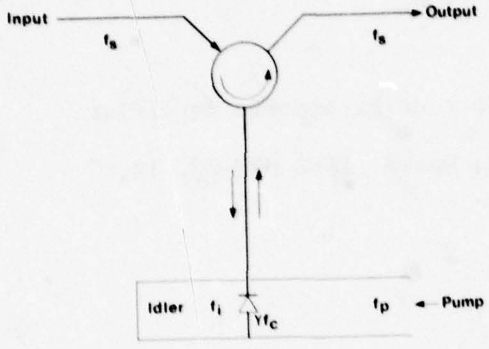

$f_p = f_i \pm f_s$

FIG. 2

PARAMP NOISE TEMPERATURE

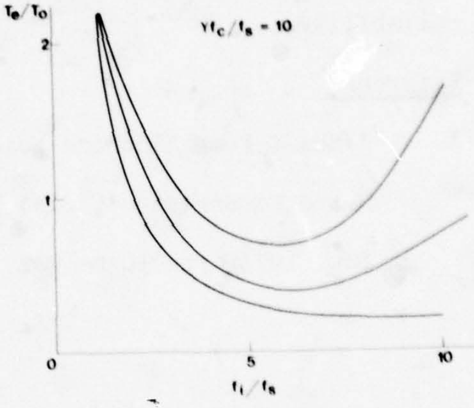

FIG. 3

LABORATORY CW POWER PERFORMANCE OF MICROWAVE DIODES VERSUS FREQUENCY

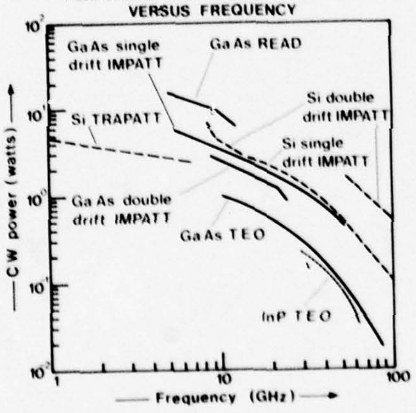

FIG. 4

PARAMP STABILITY

$$\left|\Delta P + \left(\frac{\delta P}{\delta T}\right)\Delta T\right| \left(\frac{\delta G}{\delta P}\right)_{F_0} + \left|\Delta F + \left(\frac{\delta F}{\delta T}\right)\Delta T\right| \left(\frac{\delta G}{\delta F}\right)_{P_0} = \Delta G_T$$

For

$\Delta G_T = 0{\cdot}5\ \text{dB}, \quad \Delta T = 1\,^\circ\text{C}$

$\left(\frac{\delta G}{\delta P}\right) = 7$ and $\left(\frac{\delta G}{\delta F}\right) = 0{\cdot}05\ \text{dB}/\text{MHz}$

$$\left|\Delta P + \left(\frac{\delta P}{\delta T}\right)\right| 7 + \left|\Delta F + \left(\frac{\delta F}{\delta T}\right)\right| 0{\cdot}05 \leq 0{\cdot}5\ \text{dB}$$

i.e.

$\Delta F < 10\ \text{MHz} \quad (0{\cdot}02\ \%)$

$\Delta P < 0{\cdot}07\ \text{dB} \quad (\sim 1{\cdot}6\ \%)$

FIG. 5

FM NOISE, SSB (dBc/Hz) @ 40 GHz

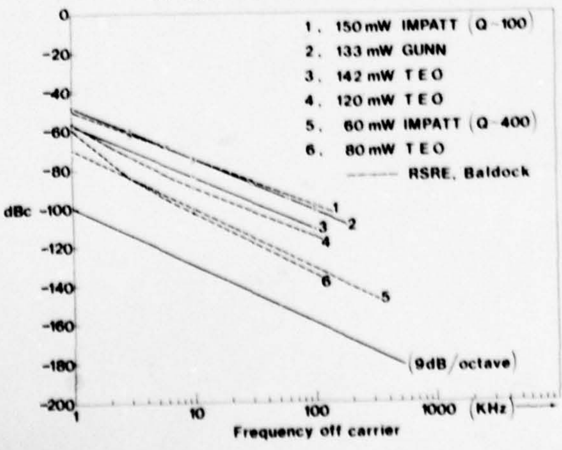

FIG. 6

AM NOISE N/C (dB/Hz) SSB @ 40 GHz

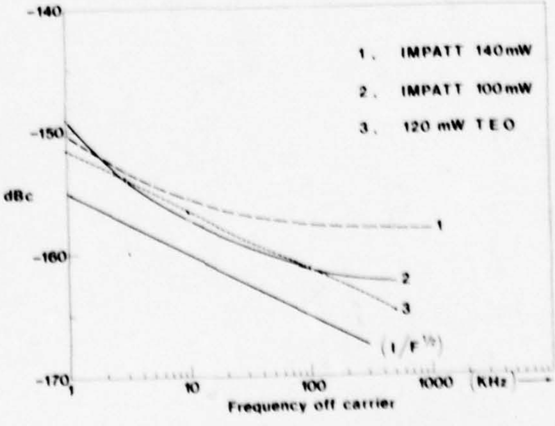

FIG. 7

FIG. 8

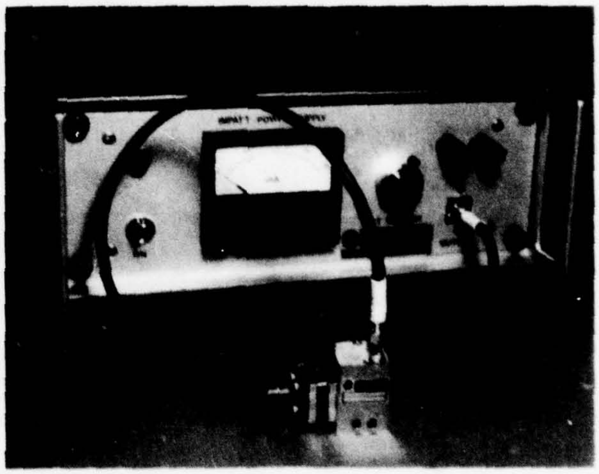

FIG. 9

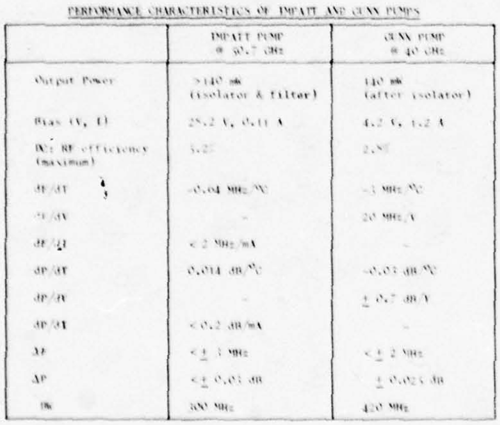

PERFORMANCE CHARACTERISTICS OF IMPATT AND GUNN PUMPS

	IMPATT PUMP @ 50.7 GHz	GUNN PUMP @ 40 GHz
Output Power	>140 mW (isolator & filter)	140 mW (after isolator)
Bias (V, I)	28.2 V, 0.11 A	4.2 V, 1.2 A
DC: RF efficiency (maximum)	5.2%	2.8%
df/dT	-0.04 MHz/°C	-3 MHz/°C
df/dV	-	20 MHz/V
df/dI	< 2 MHz/mA	-
dP/dT	0.014 dB/°C	-0.03 dB/°C
dP/dV	-	± 0.7 dB/V
dP/dI	< 0.2 dB/mA	-
Δf	< ± 3 MHz	< ± 2 MHz
ΔP	< ± 0.03 dB	± 0.025 dB
BW	300 MHz	420 MHz

FIG. 10

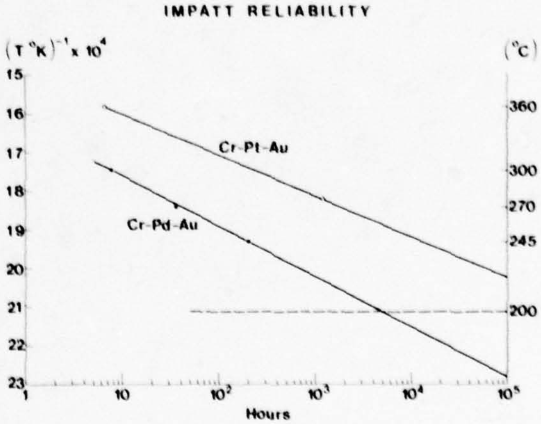

FIG. 11

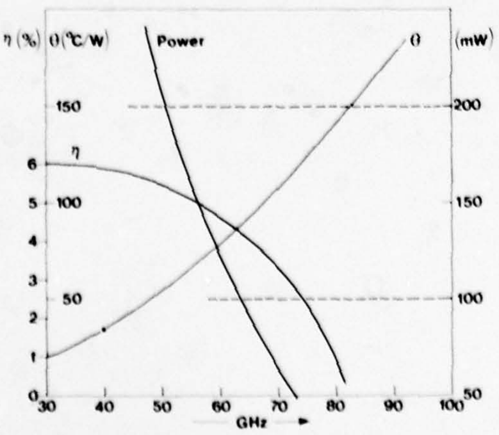

FIG. 12

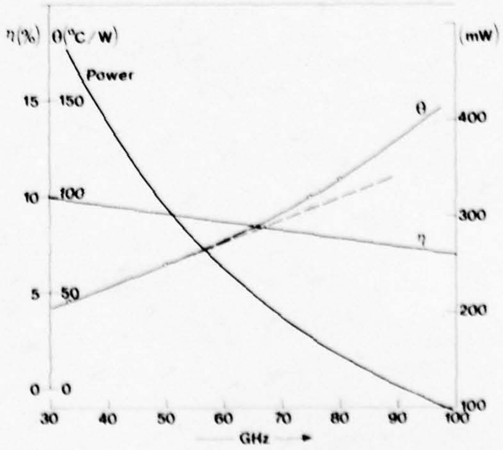

DISCUSSION

J.A.Calviello, US

Can you describe the quality of the varactors specifically

(a) what is the zero volt bias cut off frequency

(b) what technique did you use to measure Rs

(c) at what frequency was Rs characterized.

Author's Reply

We don't manufacture GaAs varactors at Plessey for these applications, although we do supply the epitaxial material.

Comment by A.Deadman, UK

(a) For GaAs diffused diodes Fco is typically 600 to 700 GHz. The latest Schottky banier diodes have Fco up to 1000 GHz.

(b) Rs is measured by a modified Deloach transmission technique.

(c) 5.6 GHz.

HUGHES IMPATT DEVICE WORK ABOVE 100 GHz

by

H.J.Kuno and T.T.Fong
Hughes Aircraft Company
Electron Dynamics Division
3100 West Lomita Boulevard
Torrance, California 90509
USA

SUMMARY

Recent progress in the IMPATT development above 100 GHz will be discussed. Both cw and pulsed oscillator results from 100 GHz to 240 GHz will be presented. The device processing, packaging and circuit techniques used in these developments will also be outlined.

INTRODUCTION

After a long, slow start, millimeter-wave systems development effort has recently been increasing at a rapid rate. Examples are tracking radars, missile seekers, radiometers, and short range communications. Millimeter-wave systems offer many advantages over both microwave systems and electro-optical systems. In comparison with microwave systems, millimeter-wave systems offer smaller size, lighter weight, improved accuracy, greater resolution, and smaller antenna size. Furthermore, in comparison with electro-optical or infrared systems, millimeter-wave systems provide greatly improved penetration through cloud, smoke, and dust. Most of the current activities for millimeter-wave systems are centered around 35 GHz and 94 GHz, where atmospheric attenuation is relatively low. Development activities in the 140 GHz range, which is the next low atmospheric attenuation window, are now underway. The exploratory work now extends to a frequency as high as 240 GHz.

Motivated by the systems requirements, the development of solid-state millimeter-wave components has increased at a significant rate in recent years. In this paper recent progress in IMPATT diode development above 100 GHz is presented. For the purpose of comparison, some lower frequency results are also quoted to calibrate the status of the high frequency work.

Oscillator Performance

Perhaps the most commonly available power sources are free running CW oscillators. IMPATT oscillators can provide CW power output of 2W at 35 GHz, 1W at 60 GHz, 700 mW at 94 GHz, 100 mW at 140 GHz, and 25 mW at 220 GHz. The recent improvement in output power from the millimeter-wave IMPATT oscillators are primarily due to the development of double-drift silicon IMPATT diodes with diamond heat sink package.

For many system applications high peak power pulsed oscillators are required. Significant progress has recently been achieved in the development of pulsed millimeter-wave sources. Peak output power levels of 18W at 35 GHz and 10W at 94 GHz can be achieved on a reproducible basis with double-drift IMPATT diodes. Peak powers of 1.5W and 500 mW were also achieved at 140 GHz and 225 GHz respectively. Although the power levels are still considerably below that of low frequency diodes, the power output is sufficient for experimental systems studies. We expect that significant improvement in diode performance will be realized in the next year or two at 140 GHz and 225 GHz.

Diode Development

The diodes used in the high frequency oscillators typically have an ion-implanted double-drift-region ($p^+ - p - n - n^+$) doping profile. The breakdown voltages range between 8V and 12V. At the high frequencies of operation the resistive losses in the diode substrate can become quite significant. For this reason the substrates of these diodes are reduced in thickness to a few microns.

Because of very high frequency of operation, the total active region of the IMPATT diode is only about 0.25 micron long. The realization of the desired doping profile and the elimination of the positive resistance associated with the unswept epitaxial region at the device operating level are difficult even with state-of-the-art technology. The accuracy required for determining the diode doping profile almost exceeds the resolution of the capacitance-voltage (C – V) method commonly used in profiling the diode. Most careful measurements are therefore required to characterize the doping profile. The measured epi doping profile is also used as a reference for ion implantation to form the compensated p region.

After epitaxial material growth and ion-implantation, a shallow boron diffusion is used to form the p^+ contact layer which is typically 0.15 μm thick. The silicon wafers are then metalized on both sides with Cr-Pt-Au metalization, followed by photolithography and etching of circular mesa diodes approximately 4 mils in diameter. The finished diode is subsequently bonded on a gold plated copper or diamond heat sinks by thermal compression bonding technique. The diode processing is completed by packaging the diode chips using special packaging techniques.

Package Development

In order to properly transform the relatively high circuit impedance to the low device impedance, package parasitics must have optimum values. In addition, one particular important design factor for any solid-state source is the efficient removal of heat due to the power dissipation in the diode. The operation of IMPATT diodes at these frequencies is largely thermally limited in output power and efficiency.

In order to develop a package configuration with optimum parasitics and good thermal properties, two approaches have been used. In the first approach, bias contact is made directly to the diode with a wire welded on the end of the bias pin thus eliminating the need for a quartz standoff and the associated package parasitics. Two versions of the wire configuration have been developed utilizing single- and double-welded wire contacts. The direct contact scheme results in low parasitics. Moreover, the spring action of the wire provides adequate compensation for the thermal expansion and contraction which occur as the device temperature is varied between the ambient and operating values. Unfortunately, this technique requires rigid mechanical tolerances.

In a second approach, the conventional quartz standoff package previously used successfully up to 170 GHz has been improved for operation at 220 GHz. A miniaturized version has been developed. Diodes with this type of package give consistently good RF performance with wide tunability. This feature indicates that the parasitics of this package configuration have reasonably optimized values.

Circuit Development

At frequencies higher than 140 GHz, several problems which are encountered commonly at lower millimeter-wave frequencies are amplified. First, the physical dimensions of the waveguide becomes inconveniently small. This feature makes the diode mounting and oscillator assembly difficult. In addition, because of the very short wavelength involved, the dimensions of the diode package become comparable to a wavelength. This fact makes impedance matching between the diode and the circuit more critically dependent on the package parameters which can limit the performance of the diode if not properly chosen. In order to overcome this performance limitation and to match the device and circuit impedances properly, the package design must be considered as an important part of the overall circuit design. This chip-level circuit design requires a new type of cavity to facilitate diode mounting and packaging.

The circuit used for the IMPATT oscillator is a reduced height waveguide cavity which consists of three major sections. A tapered waveguide section which transforms from full height to reduced height waveguide, a reduced height waveguide wafer section which contains the IMPATT diode and a mechanical tuning short section. The cavity design resembles Sharpless wafer-type circuits used for mixer diode applications. The wafer is sandwiched between the other two sections to form the complete waveguide cavity.

The wafer-mounted IMPATT diode modular cavity design permits variation of the circuit configuration at the chip level. The IMPATT diode is soldered to a heat sink slab which forms the lower wall of the waveguide slot. A bias pin is used to contact the diode which can be either packaged or unpackaged. The bias pin is inserted through a choke in the top of the wafer. In order to eliminate any low-frequency instabilities there are two sections of lossy material (Eccosorb) in the bias choke. This bias network design for eliminating instabilities is important for LO applications of the oscillator.

CONCLUSION

Solid-state device technology has advanced to the point where millimeter-wave sources are ready for system applications. Along with small size and light weight, solid state devices also offers high reliability. Extensive reliability studies of millimeter-wave devices have been made in the past several years so that systems can now be designed not only for performance but also for reliability. It appears that the key solid-state devices necessary for systems such as tracking radars and missile seekers are ready up to 100 GHz and that the frequency coverage is rapidly extending into 140 GHz and 220 GHz.

DETERMINATION OF SCHOTTKY DIODE MIXER CONVERSION LOSSES IN THE SUBMM WAVELENGTH RANGE

by

H.P.Röser, E.Sauter and G.V.Schultz
Max-Planck-Institut für Radioastronomie
Auf dem Hügel 69
53 Bonn, Germany

ABSTRACT

The HCN laser used as the local oscillator had an output power of 3.5 mW which was not sufficient to drive the diodes into saturation.

Optically pumped submm lasers have several submm laser lines with powers up to 30 mWatts suitable to drive a diode mixer to generate I.F. signals between 1 MHz and a few GHz. The sensitivity of the diode mixers which are used for heterodyne detection systems in the submm wavelength range was determined using HCN-lasers and optically pumped submm gas lasers between 41.7 μm and 1.217 μm. The difference frequency (I.F) signals are generated by mixing laser lines of two different submm lasers whose beams were combined by an optical diplexer. The beat signals are detected using a Schottky diode in an open structure mixer followed by a spectrum analyzer.

Using a quasi optical mixer and lasers as submm sources measurements have been made in order to determine the *conversion* loss L_0 of the diode and the mode structure of the submm laser system with metallic waveguides is discussed.

I. INTRODUCTION

The development of submm lasers and, recently, carcinotrons have advanced the interest in heterodyning techniques in the submm wavelength range. It may well turn out to be of great significance for different physical applications, especially for astronomical observations. (Hodges, D.T. 1973/Epsztein, B. 1978.)

II. THE HETERODYNE SYSTEM WITH TWO HCN LASERS

The first measurements were carried out at a frequency of 890 GHz using HCN-laser radiation ($\lambda = 337\ \mu m$) (Sauter, E.; Schultz, G.V. 1977/Kräutle, H.; Sauter, E.; Schultz, G.V. 1977). The HCN-laser, used as local oscillator (LO), has a maximum output power of 3.5 mW. The signal-laser beam and the LO beam are superimposed by a Mylar-foil, acting as a directional coupler. In an open-structure mixer (OSM) a whisker, having a length of several wavelengths, acts as a long-wire antenna for the submm radiation (Fig.1). The submm radiation is focussed by means of a TPX-lens into the main lobe of this long-wire antenna. Since the antenna pattern of a long-wire antenna is symmetrical about the wire axis, the antenna picks up only a very small part of the incident submm power. In order to reduce the coupling losses into the diode, the gain characteristics of the antenna were improved by combining the whisker with a corner reflector (Kräutle, H.; Sauter, E.; Schults, G.V. 1977). It has been found that a 90° corner reflector improves the coupling efficiency by 12 dB compared to a whisker without reflector (Fig.2) by changing the conical antenna pattern into a beam antenna pattern. The conversion loss L_0, which is the most important figure of merit for a submm mixer, is decreased by an optimized reflector and a GaAs Schottky diode to 21 dB in single side band operation mode (SSB). It should be mentioned that the conversion loss L_0 is not the internal loss of the diode itself, but includes especially the losses caused by poor coupling of the submm radiation to the diode and losses due to insufficient LO power.

III. THE OPTICALLY PUMPED SUBMM LASER

As HCN lasers have insufficient LO power to drive the diode into saturation we used CO_2-laser pumped submm lasers. The laser system consists of a 1.58 m long CO_2-pump laser with a 150 line/mm Au-coated and watercooled Aluminium grating. The laser has a CW output power of 30–40 W in all branches.

To achieve high output power also in the 9 μm P- and R-branches, it is necessary to change the partial pressure of He, N_2 and CO_2 depending on the branch and the laser transition.

The submm resonator has a length of 1.67 m and metallic waveguides of different diameters (6–60 mm) can be used (Fig.3). The output mirror located inside the waveguide tube to form a piston is used to tune the resonator. The submm radiation is coupled out through an optimized conical horn optimized for the wavelength of 534 μm having an opening angle of 12°.

Submm power greater than 30 mW has been achieved for different laser lines in HCOOH and CH_3OH in the wavelength range 41.7 μm – 1.217 mm. The output power was measured by a pyroelectric detector, a photon drag detector and a golay cell.

In order to stabilize the submm laser the submm laser power is fed back to the piezo control of the output coupling mirror of the CO_2-laser wobbled at a frequency of 80 Hz. A microphone, mounted in the gas resonator, gives a signal proportional to the absorbed CO_2 pump power. Hence the microphone signal can be used to improve the tuning and stabilization of the CO_2 laser frequency.

Using a brass tube as a waveguide we still find strong polarization for most of all submm laser lines (polarization > 90%).

IV. THE SUBMM HETERODYNE SYSTEM

Figure 4 shows the experimental arrangment of the new heterodyne system consisting of a local oscillator LO and a submm signal laser with an output power up to 10 mW described previously (Röser, H.P.; Schultz, G.V. 1977). Both laser beams are superimposed by a diplexer similar to the construction of Erickson (Erickson, N.R. 1977). The identity of the submm laser lines can also be determined by using the diplexer as an interferometer. The beat signals are detected by a GaAs Schottky diode in an open structure mixer followed by a spectrum analyzer (Sauter, E.; Schultz, G.V. 1977). The polarisation of the local oscillator is rotated to be perpendicular to the incident plane of the 50 μm thick Mylar beam splitter yielding a reflection coefficient of 50% at a wavelength of about 300 μm. Most of the measurements were carried out at the same frequencies for both submm lasers. With the quasi-optical mixer which was still optimized for the HCN laser radiation ($\lambda = 337\ \mu m$) we achieved a conversion loss $L_o = 17.8$ dB (SSB) for the HCOOH laser wavelength 393.62 μm (761.65 GHz) which was calculated by the ratio of the measured signal power P_s focussed on to the diode and the power P_{IF}.

With a powerful optically pumped submm laser different modes are excited (Röser, H.P.; Schultz, G.V. 1977). The spectrum analyzer trace shows in Figure 5 the beat signals of different modes of the powerful local oscillator lasing in HCOOH on 534.8 μm (560.7 GHz). Single mode operation of the local oscillator was verified by tuning the translatable mirror of the submm laser and the CO_2 laser.

Comparing our conversion loss $L_o = 17.8$ db (single side band) with the results of Fetterman (Fetterman, H.R. et al. 1978) $L_o = 12.3$ dB (double side band) it is necessary to consider that

$$L_o^{SSB} = 2\ L_o^{DSB}$$

under the assumption that upper and lower side band conversion losses are equal.

The submm laser heterodyne system is also useful to search for weak submm laser lines. Figure 6 shows the beat signals of the 393.62 μm HCOOH laser line and the new laser line in HCOOH optically pumped by R(18) 9 μm with a difference frequency of 56 MHz. The resolution of our interferometer was too small to determine the exact frequency of the new laser line.

Experiments are now under way to extend our mixing measurements up to 22 GHz using two submm lasers or a submm laser as LO and a black body as signal source (Fig.4).

REFERENCES

Epsztein, B.	*Recent Progress and Future Performance of MM-Wave BWO's.* AGARD Conference, MM and Submm Wave Propagation and Circuits, 1978.
Erickson, N.R.	*A Directional Filter Diplexer using Optical Techniques for Millimeter to Submm Wavelengths.* IEEE Vol. MTT-25 No.10, 1977.
Fetterman, H.R. et al.	*Far IR Heterodyne Radiometric Measurements with Quasi-Optical Schottky Diode Mixers.* Appl. Phys. Lett. 33(2), 1978.

Hodges, D.T. — *Waveguide Laser for the Far Infrared Pumped by a CO_2 Laser.* Appl. Phys. Lett. 23(2), 1973.

Kräutle, H.
Sauter, E.
Schultz, G.V. — *Antenna Characteristics of Whisker Diodes used as Submillimeter Receivers.* Infrared Physics Vol.17, No.6, 1977.

Röser, H.P.
Schultz, G.V. — *Development of an Optically Pumped Molecular Laser.* Infrared Physics, Vol.17, No.6, 1977.

Sauter, E.
Schultz, G.V. — *Comparison of Methods for Sensitivity Determination of Point-Contact Diodes at Submm Wavelength.* IEEE, Vol. MTT-25, No.6, 1977.

Yamanaka, M. — *Optically pumped Gas Lasers – A Wavelength Table of Laser Lines.* Review of Laser Engineering, Vol.3, No.4, 1976.

DISCUSSION

J.J.Jimenez, France

Do you think that this diode may be used in the submm range as the Schottky diode is?

There are some physical limitations?

Author's Reply

The fundamental differences between Mottky and Schottky diodes are:

(a) the disappearance of variable capacitance in the Mottky, and

(b) the extreme thinness of the Mottky epi-layer.

If variable C_j is important for frequency multiplication, then (a) is a limitation. If high power must (or will) be used, then (b) could be a disadvantage. However, in general my answer is "yes it may".

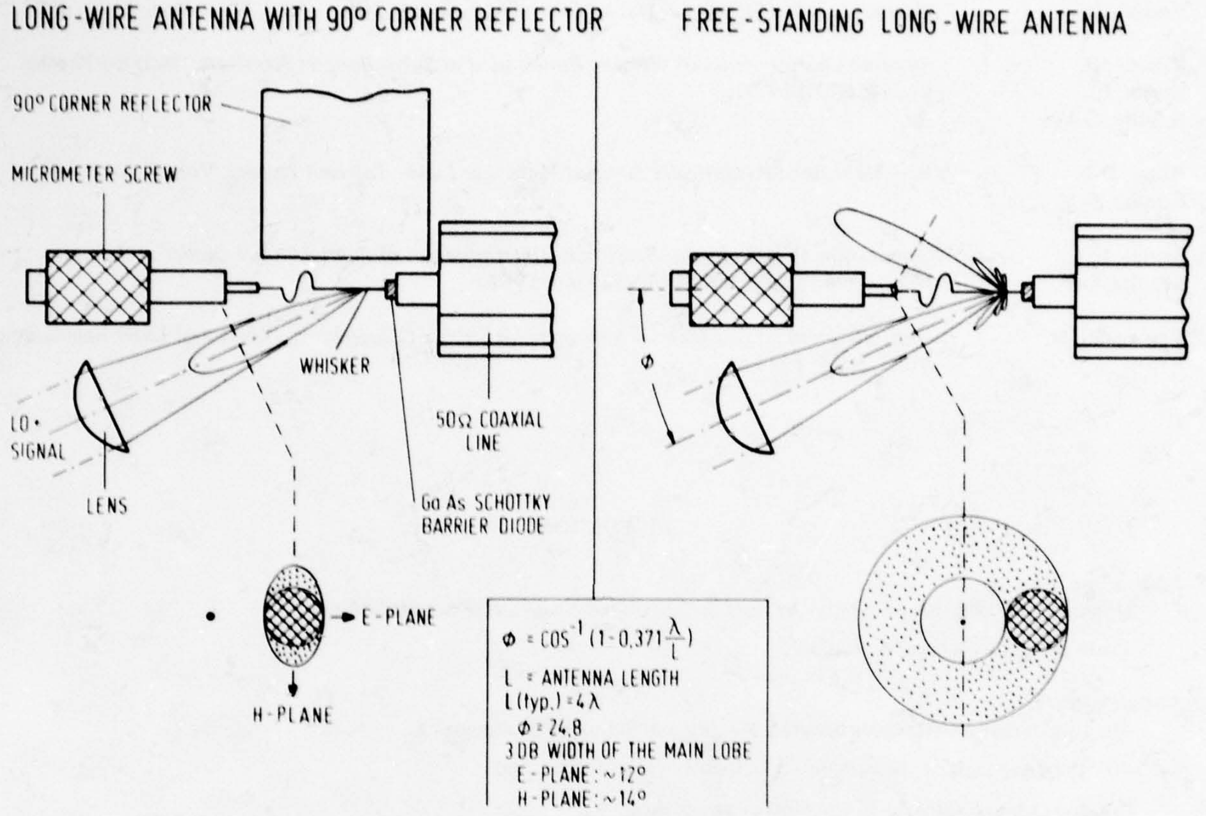
LONG-WIRE ANTENNA WITH 90° CORNER REFLECTOR
FREE-STANDING LONG-WIRE ANTENNA
90° CORNER REFLECTOR
MICROMETER SCREW
WHISKER
LO + SIGNAL
LENS
50Ω COAXIAL LINE
Ga As SCHOTTKY BARRIER DIODE
E-PLANE
H-PLANE
Φ
Φ = COS⁻¹ (1-0,371 λ/L)
L = ANTENNA LENGTH
L (typ.) = 4 λ
Φ = 24,8
3 DB WIDTH OF THE MAIN LOBE
E-PLANE: ~12°
H-PLANE: ~14°

Fig.1 Quasi-optical mixer

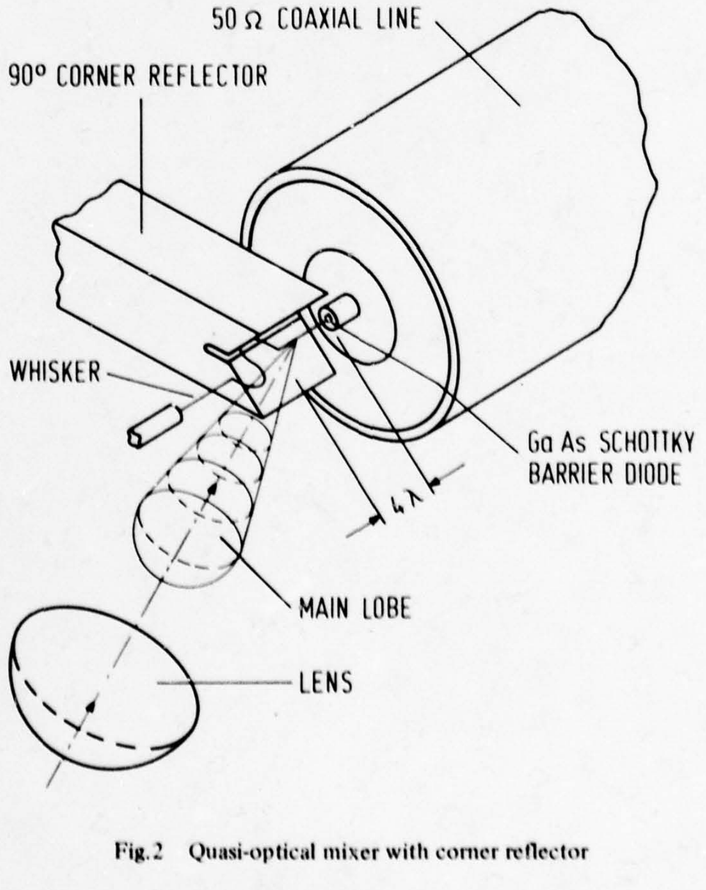
50 Ω COAXIAL LINE
90° CORNER REFLECTOR
WHISKER
Ga As SCHOTTKY BARRIER DIODE
4 λ
MAIN LOBE
LENS

Fig.2 Quasi-optical mixer with corner reflector

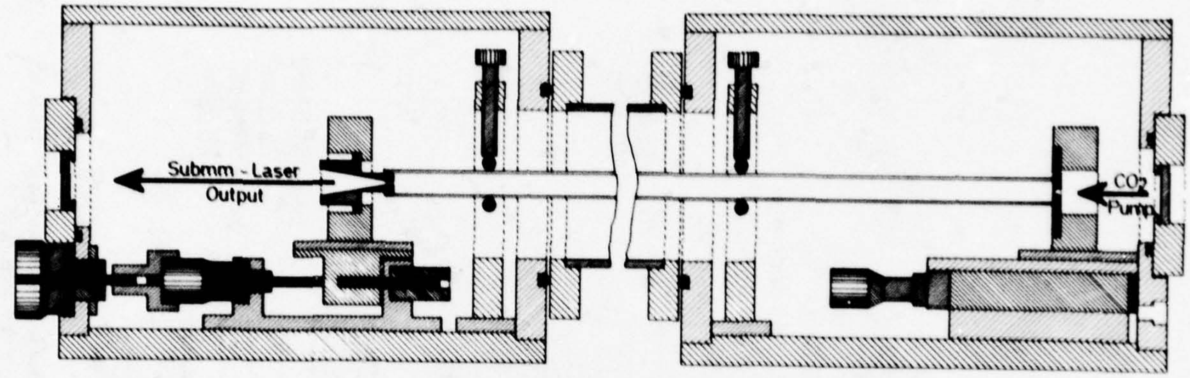
Submm - Laser
Output
CO₂
Pump

MAX-PLANCK-INSTITUT
FUR RADIOASTRONOMIE
BONN

Laserlength : 2.00m
Waveguide : Brass, Copper
Diameter ø : 6 - 60 mm
Mirrors : plane, concave

Fig.3 Submm laser

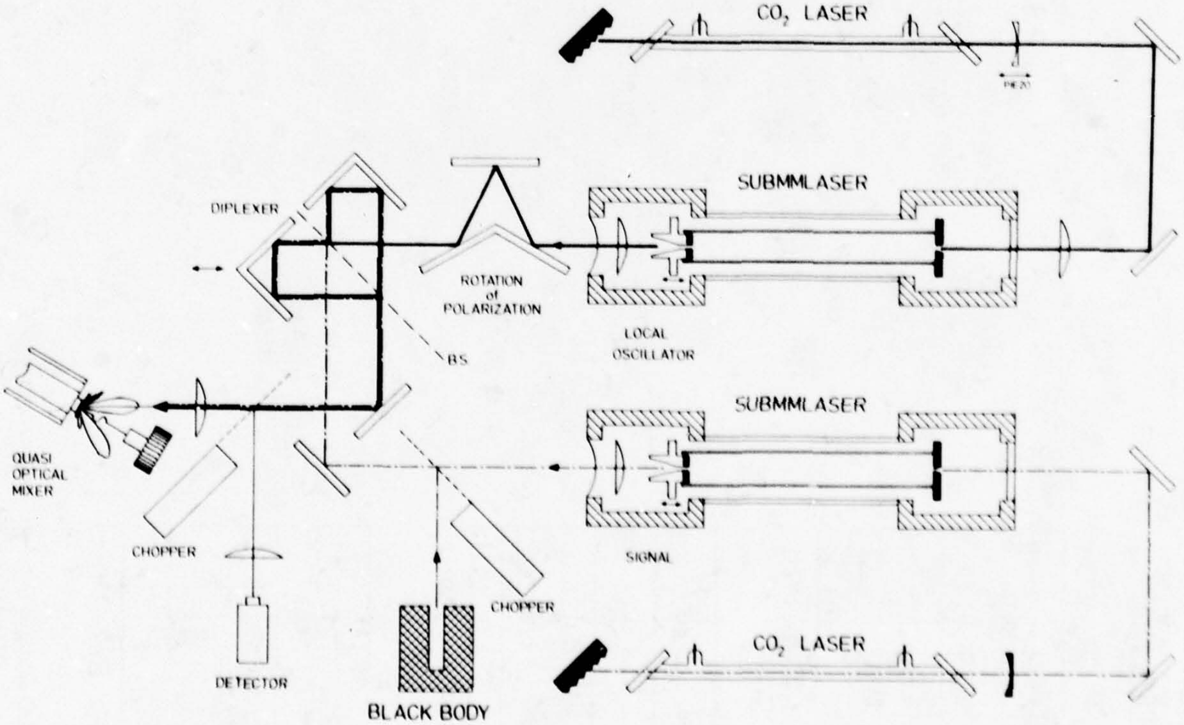
CO₂ LASER
PIEZO
SUBMMLASER
DIPLEXER
ROTATION of POLARIZATION
LOCAL OSCILLATOR
BS
SUBMMLASER
QUASI OPTICAL MIXER
CHOPPER
SIGNAL
CHOPPER
DETECTOR
BLACK BODY
CO₂ LASER

Fig.4 Submm heterodyne system with two optically pumped submm lasers and a black body

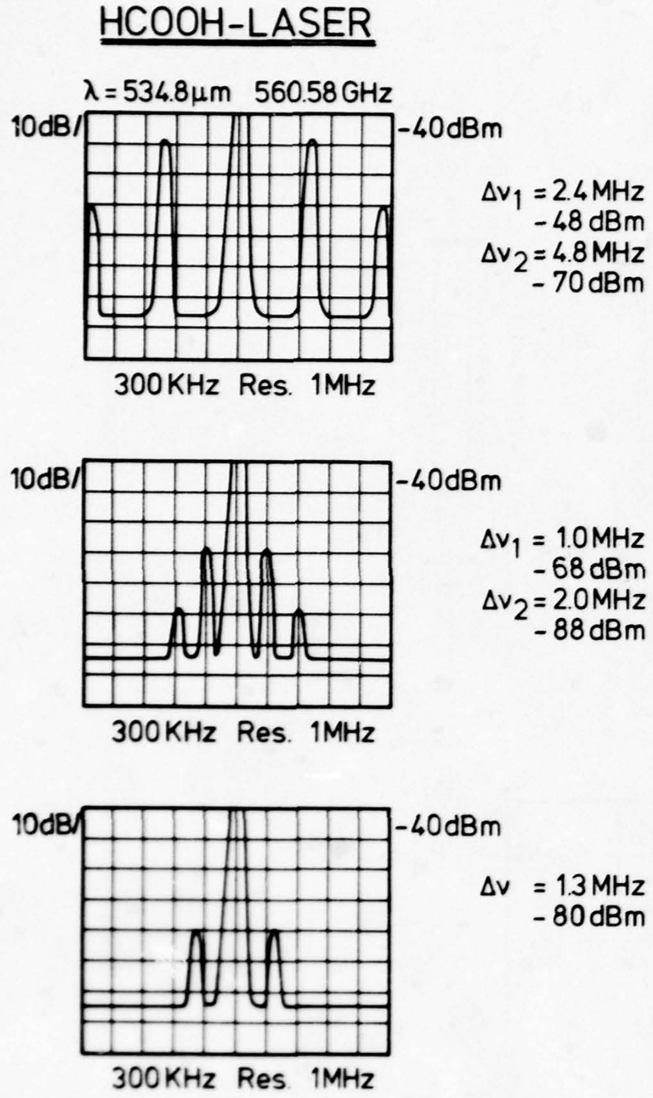

Fig.5 Spectrum analyzer trace with the beat signals of different modes

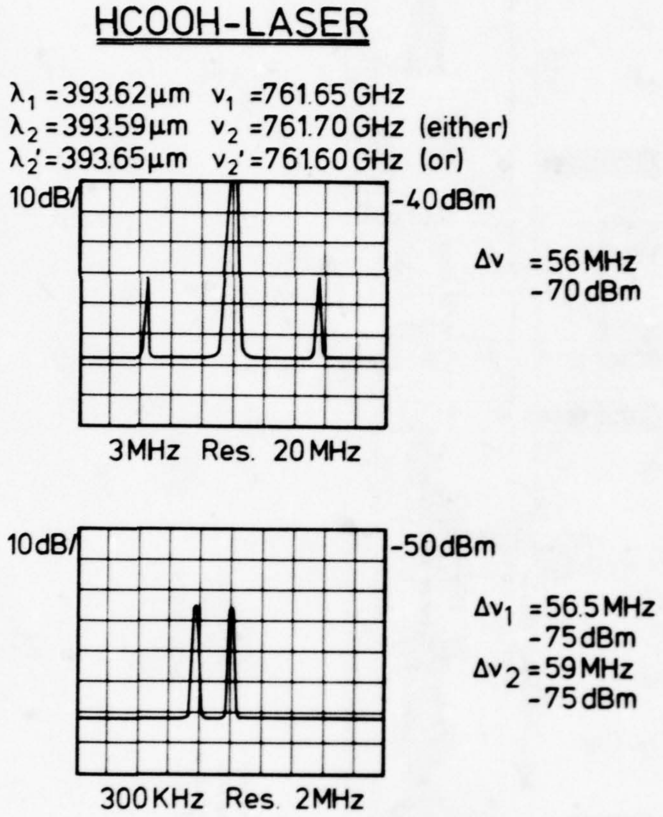

Fig.6 The spectrum analyzer trace shows the beat signals of 393.62 μm and a new laser line

The Mottky-Diode: A New Element for Low Noise Mixers at Millimeter Wavelengths

Nigel J. Keen
Max-Planck-Institut für Radioastronomie,
Bonn

Abstract

This paper reports measurements on a waveguide mixer at 115 GHz, employing a Schottky-barrier diode with an extremely thin epitaxial layer, so that it approximates a Mott-diode. The single-sideband mixer noise temperature was < 200 K when cooled to 20 K and pumped with only 150 microwatts of local oscillator power. Room temperature noise performance of the diode approximated that of the normal Schottky-barrier, except that the local oscillator power requirement was again significantly lower.

Initial measurements on this diode showed it to be robust and reliable, although somewhat more care was required when initially contacting the anode with the pointed whisker. An analysis of the noise performance indicates that further improvements should be attainable by modifications in diode design, and that classical models for mixer noise generation require modification.

Introduction

Schottky-barrier diodes have been employed for millimeter-wave mixers for some years. The first report of mixer operation at room and cryogenic temperatures was by Weinreb and Kerr (1973). Subsequently improved performance has been reported; the present status of room temperature mixers up to 350 GHz is summarized in Figure 1. All mixers represented in Figure 1 consist of a single diode in a reduced-height waveguide, contacted by a thin whisker; these mixers have consistently yielded the lowest noise across the frequency range 35 to 350 GHz.

Cooled mixers have been reported sporadically (Kerr, 1975; Vizard, 1977; Beaudin, Lazareff and Mahieu, 1977; Zimmermann and Haas, 1977), but a lower limit for single-sideband (SSB) mixer noise temperature was around 300 K at 115 GHz which did not represent a radical improvement compared to around 600 K at room temperature. It appeared that the Schottky-barrier diode would eventually have to give way to coherent bolometers, Josephson junctions or superconductor-semiconductor junctions, even though these contenders were in the very early stages of development.

The first report of Mott-barrier mixer operation was by McColl and Millea (1973) at a frequency of 110 GHz. More recently Schneider, Linke and Cho (1977) reported single sideband (SSB) mixer noise temperatures of 200 K at approximately 80 GHz. The results obtained by Schneider et al. stimulated interest not only amongst manufacturers and users of high-quality Schottky-barrier diodes, but indicated that some traditional noise generation models were both inaccurate and misleading. The results reported confirm not only the experimental results of Schneider et al., but also the validity of the noise models of Held (1977) and Keen (1977). In particular, further reductions in mixer temperature appear possible.

Measurements

The mixer is shown schematically in Figure 1 and is described by Haas (1978). The mixer was preceded by a feed-horn and tunable directional filter, the losses of which at 300 K and 20 K were carefully measured at signal (115 GHz) and image (107 GHz) frequencies; it was followed by a calibrated test receiver, similar to that reported by Weinreb and Kerr (1973). The mixer output was matched to 50 ohms so that only small residual i.f. mismatch-corrections were necessary. The doping-profile of the diode is shown in Figure 3 (b) and approximates the profile of a Mott-diode, except at large forward bias: hence the designation 'Mottky'-diode. The result of capacitance measurements are shown in Figure 4.

The results of mixer noise temperature measurements are shown in Table 1 together with other operating parameters. Diode parameters are shown in Table 2 with conventional Schottky parameters for comparison. It is seen that the cooled 'Mottky'-diode requires an order of magnitude less l.o. power than the conventional Schottky-diode, and even at room temperature a significant reduction in l.o. power is evident. The mixer input noise temperature for the cooled 'Mottky'-diode is 60 per cent of the value using a conventional Schottky-diode, whereas at room temperature the Schottky diode appears to be somewhat better.

Discussion

The Mottky-diode performance may be attributable to the different junction form, since the depletion layer is punched through to the highly-doped bulk material even for small positive bias voltages. It should however be noted that three other important factors can also contribute to the excellent performance:

(a) the epitaxial-layer (and also a 'buffer'-layer > 10 microns thick) are formed by molecular-beam epitaxy (Schneider 1978);
(b) the high-field regions at the perimeter of the Schottky contact are rounded off by anodising (Schneider et al, 1977);
(c) extreme care is taken to avoid interfacial impurities at the metal-semi-conductor junction.

The capacitance of the Mottky-diode was approximately double that of the Schottky-diode usually used at these frequencies, so that the constant capacitance scarcely appears to influence the diode performance in the mixer configuration used. More probably the capacitance variation in a Schottky diode masks the noise temperature improvement produced by the pumped barrier resistance. Since low conversion-loss operation occurs at much lower l.o. power levels, it is also possible that the Mottky-diode could be an efficient element for frequency multiplication. However, this depends on the effect of the constant barrier capacitance in short-circuiting the higher frequencies, and on the extent to which the non-linear capacitance contributes to harmonic generation.

The spreading resistance, as measured from the d.c. characteristics, increased from 6 ohms at 300 K to 13 ohms at 20 K. The reasons for this increase are not clear, but a plausible explanation might be the reduction of displacement current in the bulk GaAs at low temperatures due to reduced mobility. On the other hand the r.f. conduction currents travel over the surface of the diode (see Figure 5), so that the r.f. resistance at 20 K may not be correspondingly increased. Experiments with different diode forms and sizes should help answer these questions.

It is unlikely that carrier freeze-out plays a role in defining noise temperature, since the ionisation level of the donors (tin) is approximately 1 meV: this is illustrated in Figure 6.

Noise Considerations

The first extensive evaluation of Schottky-barrier diode mixers at room temperature and cryogenic temperatures was reported by Weinreb and Kerr (1973), and represented the synthesis of the work of many previous authors, as well as presenting important new experimental results. In particular, the advantage offered by cooling the diodes to 15 K (a reduction factor of about 2 in mixer noise) was very meagre in view of the technical complications required in cooling. Viola and Mattauch (1973) measured the output noise and d.c. characteristics of unpumped Schottky-barrier diodes with various epitaxial layer doping concentrations at temperatures between 4 K and 300 K, and showed the results to be consistent with the thermionic-field theory of Padovani and Stratton (1966). Coincidentally the epi-layer doping concentration usually used for millimeter-wave Schottky-barrier mixer diodes at this time was around 2×10^{17} cm^{-3}, which resulted in approximately a factor 2.5 reduction in unpumped diode output noise as ambient temperature was reduced from 300 K to 15 K. The near-equality of pumped and unpumped output noise temperatures at this time had two important effects: first, it appeared to verify the quasi-thermodynamic equilibrium (QTDE) noise models of Saleh (1971), Nemlikher and Strukov (1973), and others, who stipulated a lower output noise limit of $(1-2/L)\cdot\eta T_o/2$ for a pumped Schottky-barrier diode, where L = SSB conversion loss in a DSB mixer; second, further improvements in cooled mixer diode performance appeared only to be attainable by reducing diode ideality factor (η) at low temperatures.

Dragone (1968) had warned that "... T_{av} is not, in general, a function of the diode characteristics alone. In fact it depends on the particular characteristics of the network N', in which the diode is imbedded and on the value of the frequency W_1 at which T_{av} is defined unless $T(t)$ is constant". Held (1977) followed the warning of Dragone, and developed a very complete theory for the noise from a pumped Schottky-barrier mixer, although values of output mixer noise temperature $<(1-2/L)\cdot\eta T_o/2$ were only implicit in his model. Keen (1977) developed a somewhat simpler model, which demonstrated explicitly that such low output noise temperatures were possible, due to the interaction of the coherent components of diode shot noise across a pumped non-linear resistance alone: these results appeared to be verified experimentally on Schottky-barrier diodes, although the purely resistive model could only be rigorously applicable to a Schottky-barrier diode with constant capacity (i.e. a Mott-diode). The results reported here, and those of Schneider et al. appear to confirm the predictions of Keen's purely resistive diode-model, even to the extent of a noise-minimum at a local oscillator power of approximately 200 μW. Comparisons between experiment and the lossy-multiport model for a mixer (e.g. Kerr, 1978) indicate that the latter model cannot explain experimental results (see Table 3): at room temperature T_M' approaches $\eta T_o/2$, whereas at cryogenic temperatures T_M' has values between 0.7 and 1.4 times $(1-2/L)\cdot\eta T_o/2$.

There appears to be no obvious explanation for the considerable improvement of the Mottky-diode, compared to the conventional Schottky. One possibility is that hot-electron noise in the epitaxial layer (where the highest fields occur) cannot be adequately coupled into the diode, since the mean free path for impurity- and phonon-scattering at cryogenic temperatures is probably considerably longer than the thickness of the epitaxial layer. In addition the complete depletion of the epi-layer during almost the entire local-oscillator cycle could reduce high displacement currents in the epi-layer. Jaeger and Kassing (1977) have pointed out that the thermionic-field emission of Padovani and Stratton (1966) appears to break-down at low temperatures, and argue convincingly for the more complete theory of Pellegrini (1974). Unfortunately it is difficult to apply Pellegrini's complex theory directly to the problem of noise in a pumped Schottky-(or Mottky) diode: it appears that the next steps are up to the experimentalists!

Conclusions

Early noise models and experiments on conventional Schottky-diodes at millimeter-wavelengths indicated that little improvement in noise temperatures of resistive mixers could be expected. The performance of the Mottky-diode indicates the contrary, which could give new impulses to diode and mixer development. In particular the low local oscillator power requirement could permit the use of all-solid-state local oscillators to frequencies as high as 300 GHz. Some predictions of SSB system noise temperature improvements around 115 GHz are shown in Figure 7, for cryogenically cooled receivers.

The implications for noise-models should also not be overlooked, since the "resistive attenuator" model is severly perturbed by the experimental data on Mottky-diodes.

Acknowledgements

The author would like to express his appreciation to Martin Schneider for continuous support and advice during these measurements, to Robert Haas and Eduard Perchtold for calibrating the system and carrying out measurements, and to Anthony Kerr for helpful comments. Special thanks are also due to Dr.A.A.Penzias, for permission to use the diodes.

References

BEAUDIN, G., Lazareff, B. and Mahieu, J.R., 1977; "115 GHz low noise cryogenic receiver for radioastronomy", Proc. European Microwave Conference, Copenhagen, Sept. 1977, pp 432-437.

DRAGONE, C., 1968; "Analysis of thermal and shot noise in pumped resistive diodes" Bell Syst. Tech. J., 47 pp 1883-1902.

HAAS, R.W., 1978; "Improvements on a cryogenically cooled mixer for 80 - 120 GHz", in preparation.

HELD, D.N., 1977; "Analysis of room temperature millimeter-wave mixers using GaAs Schottky barrier diodes", Doctor's Thesis, Columbia University (Institute for Space Studies, NASA no. X-130-77-6).

JAGER, D. and Kassing, R., 1977; "Temperature anomalies of Schottky-barrier diodes on n-type silicon", J.Appl.Phys., 48, pp 4413-4414

KEEN, N.J., 1977; "Evidence for coherent noise in pumped Schottky diode mixers", Electronics Letters, 13, 10, pp 282-284

KERR, A.R., 1975; "Low-noise room temperature and cryogenic mixers for 80-120 GHz", IEEE Trans M.T.T. - 23, pp 781-787

McCOLL, M. and Millea, M.F., 1973; "Advantages of Mott barrier diodes", Proc. IEEE (Letters), 51, pp 499-500

NEMLIKHER, A.Y. and Strukov, I.A., 1973; "Noise characteristics of resistive-diode mixers using Schottky-barrier diodes", Radio Engineering and Electronic Physics, 19, pp 111-118

PELLEGRINI, B., 1974; "A detailed analysis of the metal-semiconductor contact", Solid-State Electronics, 17, pp 217-237

PADOVANI, F.A. and Stratton, R., 1966; "Field and thermionic-field emission in Schottky barriers", Solid-State Electronics, 9, pp 695-707

SALEH, A.A.M., 1971; "Theory of Resistive Mixers", Cambridge, Mass., M.I.T. Press

SCHNEIDER, M.V., 1978; private communication

SCHNEIDER, M.V., Linke, R.A. and Cho, A.Y., 1977; "Low-noise millimeter-wave mixer diodes prepared by molecular beam epitaxy (MBE)", Appl. Phys. Letters, 31, 3, pp 219-221

VIOLA, T.J. and Mattauch, R.J. "Unified theory of high-frequency noise in Schottky barriers", J.Appl. Phys., 44 pp 2805-2808

VIZARD, D., 1977; "Cryogenic characteristics of millimeter wavelengths Schottky barrier diodes", Proc European Microwave Conference, Copenhagen, Sept. 1977, pp 556-560

WEINREB, S. and Kerr, A.R., 1973; "Cryogenic cooling of mixers for millimeter and centimeter wavelengths", IEEE J. Solid-State Circuits, SC-8, pp 58-63

ZIMMERMANN, P. and Haas, R.W., 1977; "A broadband low noise mixer for 106-116 GHz", Nachrichtentechnische Zeitschrift, 30, pp 721-722

Table 1

		At 295 K	At 20 K
SCHOTTKY	L_{SSB}	= 6.2 dB	6.2 dB
	$T_{M.SSB}$	= 600	300 K
	I_D	= 1.5 mA	0.6 mA
	V_D	= 0 V	0.5 V
	P_{LO}	= 2.5 mW	1.0 mW
MOTTKY	L_{SSB}	= 6.6 dB	6.6 dB
	$T_{M.SSB}$	= 800 K	200 K
	I_D	= 1.4 mA	0.4 mA
	V_D	= 0.4 V	0.5 V
	P_{LO}	= 1mW	0.15 mW

Table 2

	SCHOTTKY	MOTTKY
Diode Size	2.5 micron diam.	5x1.3 micron ("bathtub")
Epi-Thickness	3000 Å	700 Å
Epi-Doping	2×10^{17} cm^{-3}	3×10^{16} cm^{-3}
R_S (at 300 K)	8 ohm	6 ohm
C_{J0}	8 fF	16 fF
η at 295 K	1.07	1.07
at 20 K	9.0	9.7
Chip Size	0.25 x 0.25 x 0.1 mm	0.25 x 0.25 x 0.1 mm
Epi-Dopant	Sulphur	Tin
V_B (10μ A)	∿8 Volt	10 Volt (12 Volt before anodising, but cutoff less abrupt)

Table 3

Diode	T_{PHYS}	T'_M	$\eta T_o/2$	L	T^*_M
Mottky	295 K	175 K	158 K	6.6 dB	89 K
Mottky (min. noise)	20	42	97	6.6	55
Mottky (min. conv. loss)	20	63	97	5.4	41
Schottky	295	150	158	6.0	79
Schottky	18	75	81	6.0	40

T'_M ≡ measured output noise of mixer alone

T^*_M ≡ $(1-2/L) \cdot \eta T_o/2$

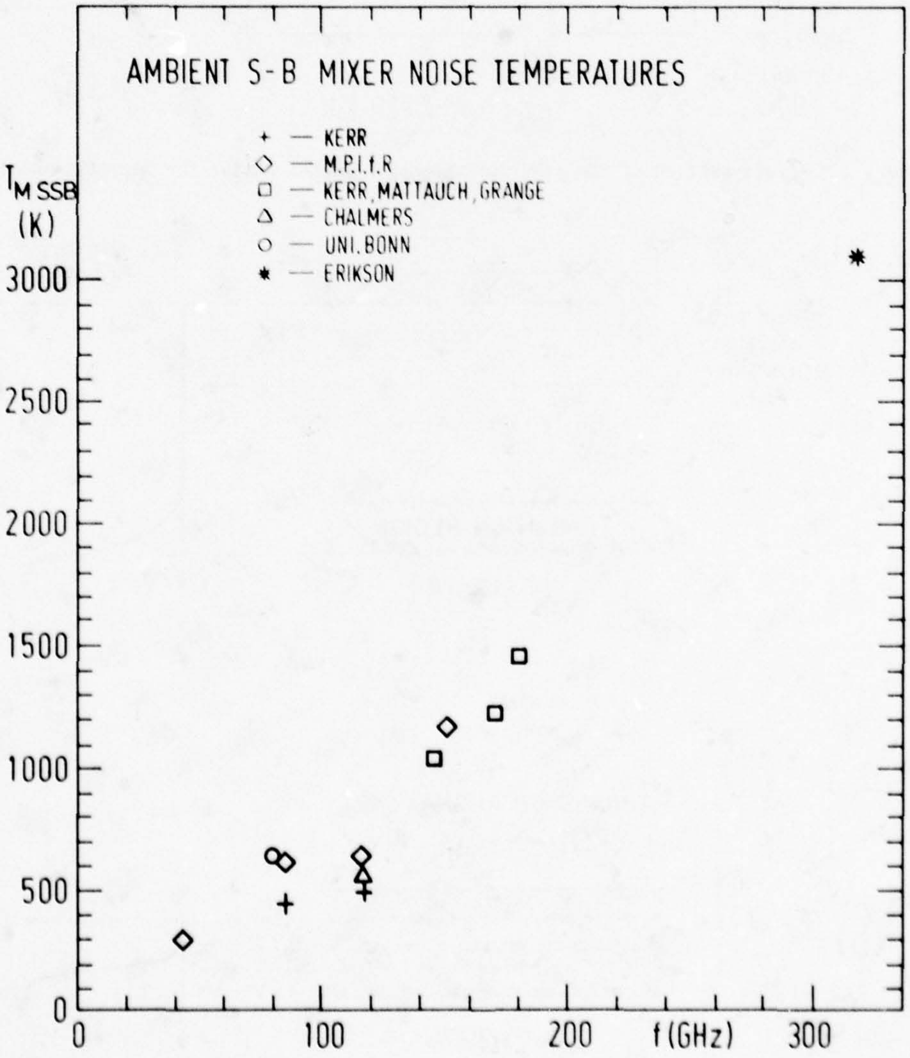

Figure 1 Comparison of room temperature mixer noise temperatures in the frequency range 35-350 GHz

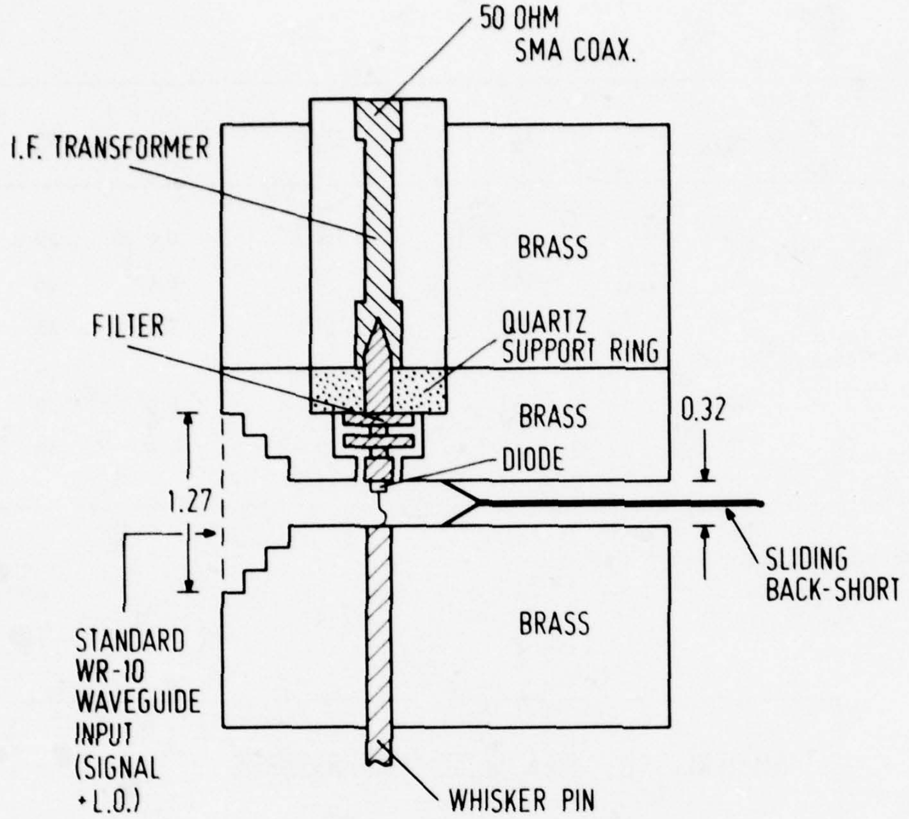
50 OHM
SMA COAX.
I.F. TRANSFORMER
BRASS
FILTER
QUARTZ
SUPPORT RING
BRASS
0.32
DIODE
1.27
SLIDING
BACK-SHORT
BRASS
STANDARD
WR-10
WAVEGUIDE
INPUT
(SIGNAL
+L.O.)
WHISKER PIN

Figure 2 Cross-section of the mixer of the Max-Planck-Institut für Radioastronomie

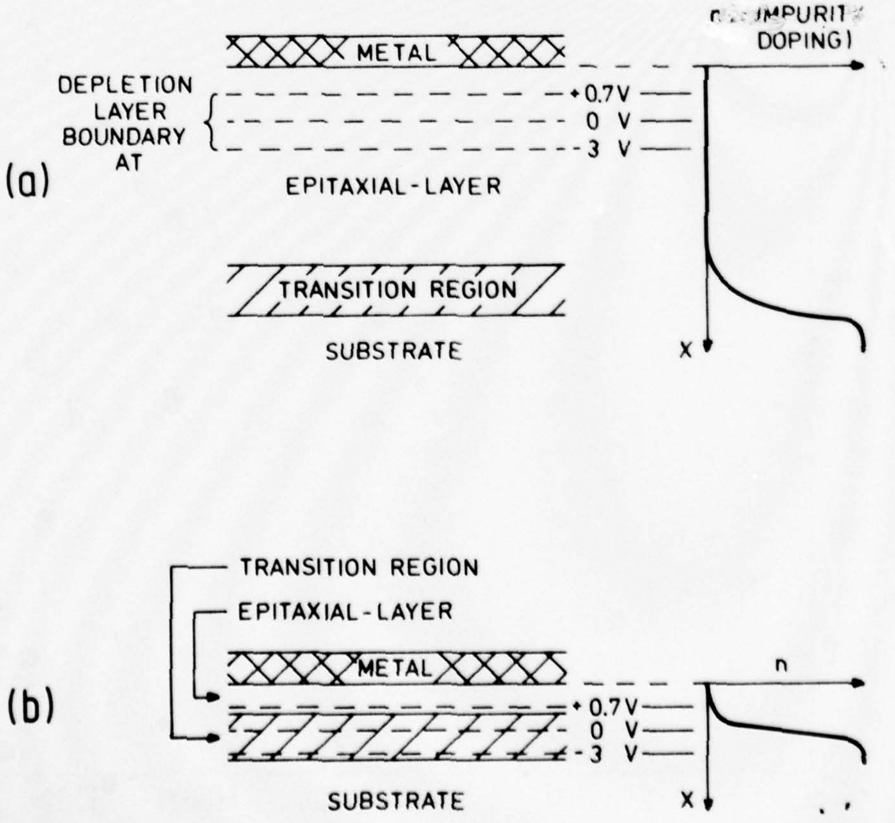
n (IMPURITY
DOPING)
METAL
DEPLETION
LAYER
BOUNDARY
AT
+0.7V
0 V
-3 V
(a)
EPITAXIAL-LAYER
TRANSITION REGION
SUBSTRATE
x
TRANSITION REGION
EPITAXIAL-LAYER
METAL
n
(b)
+0.7V
0 V
-3 V
SUBSTRATE
x

Figure 3 Doping profiles of Schottky- and Mottky-diodes

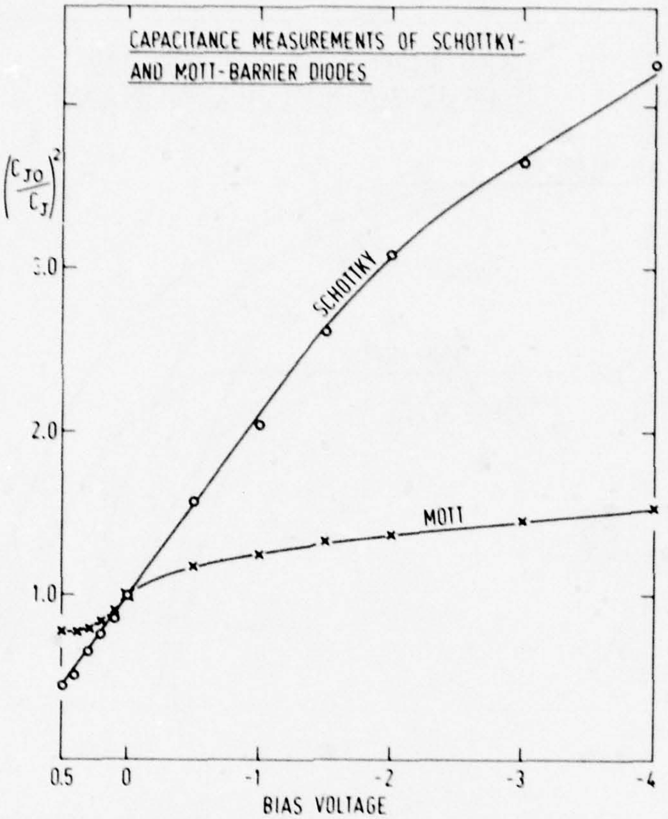

Figure 4 Capacitance measurements of Schottky- and Mottky-diodes

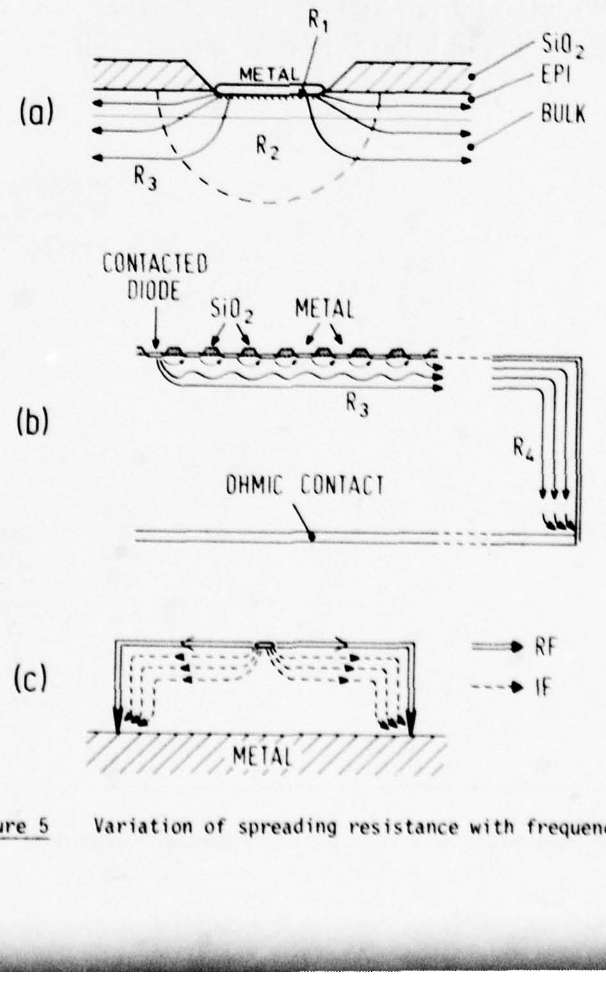
(a)
R_1
METAL
SiO_2
EPI
BULK
R_2
R_3
(b)
CONTACTED DIODE
SiO_2
METAL
R_3
R_4
OHMIC CONTACT
(c)
RF
IF
METAL

Figure 5 Variation of spreading resistance with frequency

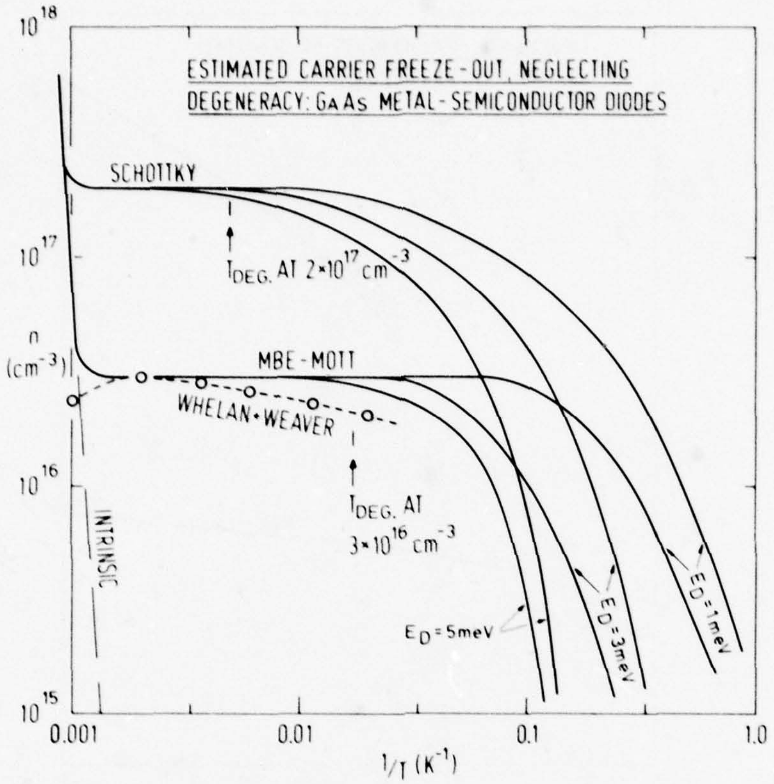

Figure 6 Predicted carrier concentration in epitaxial layers as a function of temperature

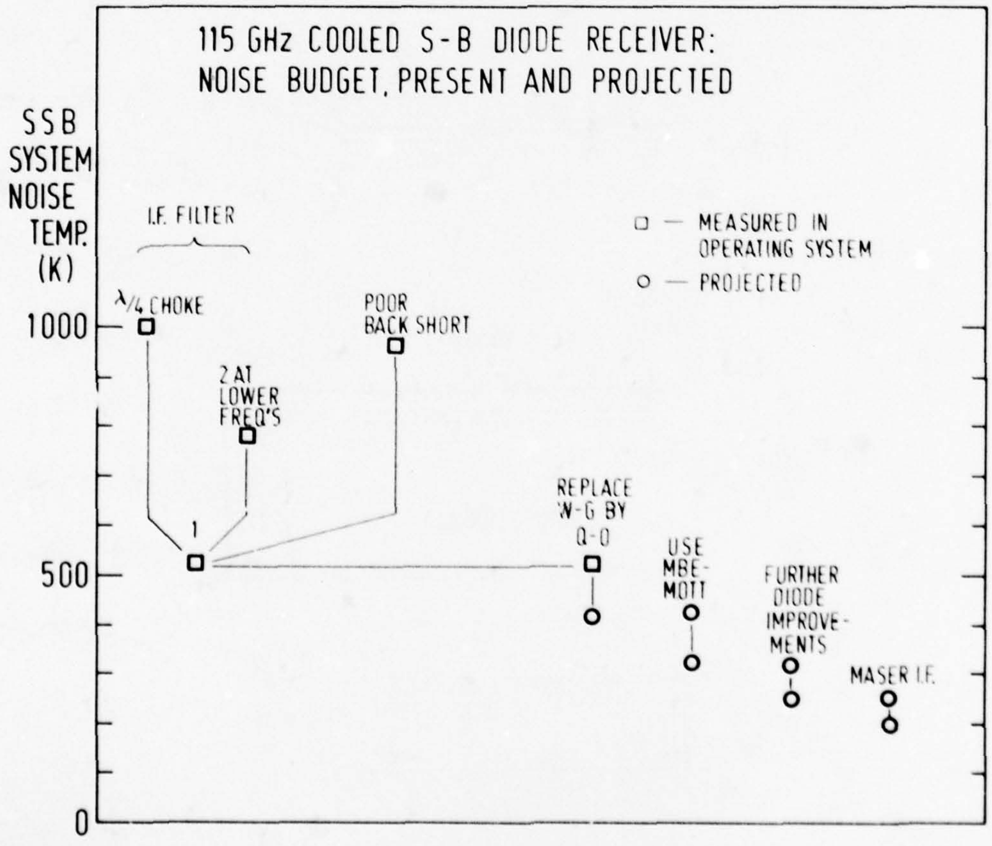

Figure 7 Predicted improvement in a cooled resistive-mixer system performance at around 115 GHz

DISCUSSION

David Ri Vizard, UK

Could you comment on whether any correlation was found between the d.c. reverse bias characteristics and the mixer noise performance?

Author's Reply

For a very good diode (e.g. Mottky), very little l.o. power is required so that reverse breakdowns of 6 volt or more are normally never obtained. Poor diodes have to be pumped harder, however, and could be pumped into breakdown: measurements of avalanche noise from 2.5 μm Schottky diodes (in our labs) show that high l.o. power could result in pulses of avalanche noise.

On the other hand, a sharp reverse breakdown is a sign of absence of microplasmas and high-field regions. These are essential preconditions for good low noise diodes.

G.Cachier, FR

Why is the temperature dependence different from the usual Schottky diodes.

Author's Reply

(1) The diode is in punchthrough.

(2) the speading resistance is smaller because the diode is very thin.

ADVANCES IN GaAs SCHOTTKY DIODE SUBMILLIMETER HETERODYNE RECEIVERS AND RADIOMETERS*

P. E. Tannenwald
Lincoln Laboratory, Massachusetts Institute of Technology
Lexington, Massachusetts 02173

SUMMARY

Radiometric sensitivity measurements have been made on a quasi-optical receiver in the spectral range 170 μm to 1 mm. Using GaAs Schottky mixer diodes in a corner reflector configuration, a total system noise temperature of 9,700 K (DSB), or an NEP of 1.3×10^{-19}W/Hz, has been obtained at 447 μm. This same quasi-optical mixer has also been used for the generation of tunable harmonic and side-band radiation suitable for submillimeter spectroscopic applications. Planar, surface-oriented GaAs Schottky diodes have been fabricated by means of photolithographic techniques in conjunction with ion implantation and proton bombardment. High-order harmonic mixing and direct heterodyne mixing with lasers up to 761 GHz have been achieved. These planar diodes can be fabricated into array configurations by means of an integrated circuit approach.

1. INTRODUCTION

Recent developments in radio astronomy, plasma physics, frequency standards and spectroscopy, atmospheric propagation, aeronomy, and in high-altitude aircraft and satellite-based surveillance have created a need for fast, sensitive far infrared detectors. Several groups have been studying the use of GaAs Schottky diode heterodyne receivers using either conventional waveguide (MC COLL, M., 1977) or quasi-optical approaches (GUISTINCIC, J. J., 1977). In general, the performance levels that have been achieved at frequencies above 300 GHz have not been comparable with those obtained at millimeter wavelengths. We report here the results of radiometric determinations of noise equivalent powers of a new quasi-optical system in the wavelength range of 1 mm to 170 μm. At a frequency of 671 GHz (447 μm) the highest sensitivity reported to date has been obtained (FETTERMAN, H. R., 1977)--namely, an NEP of 1.3×10^{-19}W/Hz, or an equivalent system noise temperature of 9,700°K (DSB). The quasi-optical Schottky diode mixer that was used in the heterodyne receiver has also been used to produce far IR laser sideband radiation of $\sim 10^{-7}$ watts tunable over 18 GHz, and to harmonically generate tunable submillimeter radiation up to 760 GHz. Application of this tunable source to spectroscopic problems has been demonstrated. These developments open up new possibilities for far infrared and submillimeter experiments which require extremely high sensitivities.

During the past year we have also developed the next generation of submillimeter detectors--planar, surface-oriented GaAs Schottky diodes fabricated by photolithographic techniques in conjunction with ion implantation and proton bombardment. In contrast to point-contact whisker diodes, here both terminals of the rectifying junction lie on the same surface of the GaAs wafer. This single-sided geometry lends itself naturally to an integrated circuit approach with the connection of matched stripline antennas and IF filter networks. These planar diodes have been successfully used as heterodyne mixers up to 779 GHz, including high-resolution detection of pulsed far IR radiation.

2. RADIOMETER/RECEIVER SYSTEM

The experimental system used in these measurements is essentially a Dicke type radiometer which mixes a laser local oscillator (LO) with radiation from a black body whose radiated power is solely a function of its temperature. Illustrated in Fig. 1, the system consists primarily of the following components: 1) corner-reflector diode mount, 2) ellipsoidal coupling mirror, 3) a quasi-optical diplexer, 4) laser local oscillator and 5) low temperature absorber. The GaAs Schottky diode mounted in the corner reflector was developed especially for high frequency applications and has been discussed elsewhere (CLIFTON, B. J., 1977). The diodes are typically 1 μm in diameter, have 1.5×10^{-15}F capacitance and a series resistance of 45 Ω.

A quasi-optical approach for the mixer was adopted because of the physical difficulties of embedding a diode in a fundamental waveguide at these frequencies. The approach taken, first proposed for the submillimeter by Sauter and Schultz (SAUTER, E., 1977), uses a long--typically four wavelengths--traveling wave-line source set in a corner reflector. The line source is an extended "whisker" point-contacted to the Schottky diode. Impedance and radiation characterisitics are determined by the length of the line source, the corner angle, and the separation between line source and corner.

In order to optimize a corner reflector mount we have carried out 100 times scale modeling experiments at 6 to 8 GHz. One design, similar to Kräutle (KRÄUTLE, H., 1977), which looked promising for actual submillimeter construction, is a 90° corner cube (i.e., 90° corner reflector with a ground plane) with a 4 λ antenna length spaced 1.2 λ from the corner. The beam pattern obtained from the modeling is shown in Fig. 2. The principal lobe is seen to be at an angle of 25° to the antenna, and has a roughly circular cross-section of beam width 14° x 15° (full width at 3 dB points).

The local oscillator and a corresponding mode from the black body (Eccosorb AN-72) at liquid nitrogen temperature were coupled to the mixer utilizing a diplexer. This diplexer was essentially a folded, double interferometer, similar in principle to that used by NRAO (GOLDSMITH, P. F., 1977) and Erickson (ERICKSON, N. R., 1977), but made specifically for the 0.4 or 0.9 mm wavelength region. The beam splitters are 3 mil mylar stretched over machined reflector mounts and gave roughly 50% transmission. An extremely short focal length, right angle, ellipsoidal mirror was used to match the transmitted signal and LO to the antenna pattern of the diode. With this system virtually all of the signal and better than 90% of the LO were transmitted to the detector.

The local oscillators consisted of optically pumped far infrared lasers for the submillimeter and a carcinotron for 1 mm. The laser LO was pumped by a free-running, stable CO_2 laser of about 50 W and had an output power of about 30 mW. This was found sufficient to saturate the mixer diode at all but the 170 μm line. The identity of each LO line was unambiguously determined by using the diplexer as an interferometer; tuning through approximately 10 interference maxima allowed a wavelength measurement to 0.5% accuracy.

---

*This work was supported by the Department of the Air Force, the U.S. Army Research Office, the National Science Foundation, and the Department of Energy.

3. RADIOMETRIC MEASUREMENTS

The results of our measurements are summarized in Table 1. Two separate corner reflectors were used to cover the wavelengths listed - one designed for 400 μm and a second one for 0.9 mm. For 170 μm neither the diode mount nor the diplexer was optimized, but a result is quoted to show that a black body heterodyne measurement was possible. The rectified IF signal was read on a digital voltmeter, and the difference in voltages between the hot (room temperature absorber or chopper) and cold absorber was synchronously detected. The amplifier had a measured noise temperature of 245 K (2.6 dB). A standard Y-method interpretation of the data then yielded the results shown in the table.

The conversion loss was both calculated from the expression $T_{sys} = T_{mixer} + L_c T_{IF}$ and measured directly by changing the temperature of the IF input resistor and comparing this with the signal produced by a known ΔT applied to the optical input of the radiometer. In general the diode noise temperature was near room temperature, and the LO added approximately 100 K excess noise. The diode noise temperatures were measured with an isolator inserted between the diode and the IF amplifiers to reduce the effects of changing impedances. Total system noise temperatures were measured without the isolator and are listed in the third column. The best values obtained are given, but variations from diode to diode and mount to mount were typically only about 1000 K.

Table I

λ (μm)	Frequency (GHz)	Total Systems Noise Temp. (DSB) (K)	Mixer Temp. (K)	Conversion Loss (dB)
887.0	338.2	8,200	4,000	9.3
447.1	670.5	9,700	5,900	11.6
432.6	692.9	13,100	6,900	11.9
419.6	716.2	13,000	6,800	11.9
393.6	761.6	14,500	7,600	12.3
170.6	1757.5	370,000*	--	--

*Diplexer not working at this wavelength

4. PLANAR, SURFACE-ORIENTED DIODES

Although the coupling of submillimeter radiation to a single Schottky mixer diode has been successfully solved with the quasi-optical approach of using a corner reflector, the discrete nature of the whisker contacting the diode chip precludes fabrication of arrays of detectors integrated directly into circuits. The objective of this phase of the work is to overcome this limitation by fabricating small, planar, surface-oriented Schottky diodes in which both terminals of the rectifying junction lie on the same surface of the GaAs wafer. This single-sided geometry lends itself naturally to an integrated circuit approach with the connection of matched stripline antennas and IF filter networks. In addition, the contacting of small devices becomes more feasible. Although devices with this topography have been fabricated previously (ALLEN, R. P. G., 1973; BALLAMY, W. C., 1976; WOOD, E. J., 1976), they have heretofore been restricted to frequencies below 100 GHz primarily because their relatively large device areas have led to higher capacitance and lower cutoff frequencies. Diodes with diameters as small as 2 μm have been fabricated in our effort, permitting operation at submillimeter wavelengths for the first time (MURPHY, R. A., 1977).

4.1. Device Construction

The geometry of the device is shown in Fig. 3. To fabricate this structure, two layers of GaAs are epitaxially grown on semi-insulating substrates in a hydrogen transport $AsCl_3$ vapor phase system. The first layer (n^+) is 3 μm thick and has an n-type concentration of $1 \times 10^{18} cm^{-3}$. The top layer (n) is 0.2 μm thick and has a concentration of $1\text{-}2 \times 10^{17} cm^{-3}$. Sulfur ($H_2S$) is used to dope both layers. Selective Se^+ ion implantation is then used to decrease the specific resistance of the Au-Ge alloyed ohmic contact. After the formation of the ohmic contact, the diode and ohmic contact areas are shielded by gold, and the wafer is proton bombarded, converting the n- and n^+-layers to high resistivity material in the bombarded regions. The e-beam deposited Ti/GaAs Schottky barrier is approximately 2 μm in diameter. Each device is contacted by means of a stripline overlay pattern. A photograph showing an array of these devices on a completed wafer is shown in Fig. 4.

The forward current-voltage (I-V) characteristic of a typical device is quite similar to those of whisker contact Pt/GaAs diodes, with the knee of the nonlinear region occurring at approximately 0.7V. The n-factors of these devices (describing the deviation from ideal Schottky-barrier behavior) range from 1.2 to 1.5.

4.2. Submillimeter Measurements

Figure 5 shows a device to which a planar radiating structure has been attached. The metal pattern was designed as a half-wavelength dipole at around 0.9 mm wavelength. The measured radiation pattern shows complex lobe structures apparently because of interference from other radiating elements. A typical radiation pattern obtained at 348 GHz is shown in Fig. 6. Our measurements indicate that modes are excited in the GaAs substrate, with the result that the whole GaAs slab acted as a radiating element. Even though some of the lobes are quite narrow, it is desirable to work with simpler and more controllable structures. Consequently we have begun to make measurements upon scale models of slot and coplanar antennas. One such design which has been modeled is shown in Fig. 7. The measurements have indicated that energy can be coupled quite efficiently to the nonlinear junction with these radiating structures. Submillimeter devices using such structures will be fabricated. Other antenna configurations are also under consideration.

Although no accurate quantitative measurements of the sensitivity of these devices have been made, they have been successfully used as detectors and mixers well into the submillimeter wavelength regime. It has become apparent in heterodyning with pulsed laser sources that in electrically noisy environments planar diodes show better survival and noise suppression characterisitics than conventional whisker-contacted diodes and in addition display remarkable physical ruggedness. High-order harmonic mixing has been obtained by coupling a 9.2879 GHz signal, introduced into the IF line, and a 862.196 GHz (393.6 μm) laser line of formic acid to a planar device. The IF response corresponded to mixing of the 82nd harmonic of the X-band signal with the laser and had a signal-to-noise ratio of better than 35 dB. This same system of harmonic mixing has been used to phase-lock our 1 mm carcinotron and is used routinely for that purpose.

4.3. Diode and Antenna Arrays

Because of their topography, these diodes can be fabricated in large numbers on a single wafer and thus provide the unique possibilities of array detection and submillimeter imaging. We plan to develop planar imaging arrays composed of planar antennas, surface-oriented mixer diodes, and low-noise FET amplifiers, all integrated on a single chip. Beam steering is also possible using phased-array techniques.

5. APPLICATIONS TO TUNABLE SUBMILLIMETER SPECTROSCOPY

5.1. Spectroscopy with a Black Body

Our current results suggest some immediate applications of this technology to far IR spectroscopy, and we have investigated a number of these. In one such experiment, not described in detail here, we have mixed the pulsed output of a D_2O laser operating at 385 μm (778, 870 MHz) with the cw output of a 394 μm (791, 607 MHz) formic acid laser in a Schottky diode mixer. The IF was at 17 GHz. In another experiment we have mixed two rotational cw lines of a formic acid laser at 393.6 and 405.6 μm; the resultant IF at 22.45 GHz was heterodyned again with the second harmonic of an X-band source fed into the IF port of the diode. These experiments demonstrate the wide-band capabilities of the mixer. We can thus expect to carry out tunable high-resolution spectroscopic measurements against a black body in the laboratory, as well as in a number of terrestrial and space applications using the sun as a remote source.

5.2. Generation of Tunable Far Infrared Radiation

Concurrent with the heterodyne detector effort in the far infrared/submillimeter region we are seeking sources of tunable radiation for applications to spectroscopy, to frequency standards and to remote sensing. The GaAs Schottky diode mixer which we have developed for our sensitive receiver and radiometer can be used as a source of tunable laser-sideband radiation and high-order microwave harmonics. Since the corner reflector configuration acts as an efficient receiver of radiation, it will act reciprocally as an efficient radiator. The resistive nonlinearity of the diode provides the mixing and harmonic generation mechanism.

In our initial experiments, radiated sidebands of a CH_3I submillimeter laser line at 447 μm were generated and detected using two corner-reflector diode mixers. One diode mixer was simultaneously illuminated by the far infrared laser and fed coaxially by microwave sources ranging from 2.5 to 18 GHz. A second diode mixer was then used as a high sensitivity heterodyne receiver to detect the radiated sidebands of the laser signal. Signals of about 10^{-7} watts, continuously tunable over 0.5 cm^{-1}, were observed. Extending this approach further, we investigated the use of these diode mixers as high-order harmonic signal generators. The experimental arrangement is shown in Fig. 8, with the microwave radiation between 17 and 37 GHz introduced via the IF connector line to the diode. Radiation generated as high as the 40th harmonic was then detected by a second diode mixer in our standard heterodyne receiver configuration. In one particular case, a 37 GHz GaAs Gunn oscillator was used to generate 761 GHz. This solid state source coupled with the rugged harmonic mixer provided a compact, stable, tunable source of about 5×10^{-11}W in the submillimeter. Because of the sensitivity of our heterodyne receiver, the observed S/N exceeded 35 dB on a spectrum analyzer having a 100 kHz bandwidth.

High resolution far infrared spectroscopic studies using both these source-detector systems are now underway. As a first demonstration, an absorption cell containing D_2O gas at low pressure was placed in one arm of the spectrometer, as shown in Fig. 8. 35.7 GHz radiation from a microwave source was used to drive the mixer diode, and the 17th harmonic generated (607.345 GHz), after passing through the absorption cell, was detected by the heterodyne receiver. The LO was supplied by an optically-pumped CH_3F laser operating at 604.295 GHz, giving an IF around 3 GHz. Tuning through the D_2O absorption line was accomplished by tuning the microwave source. Figure 9 shows the far infrared output with and without the gas. Because of residual pressure from condensed liquid in the absorption cell, the linewidth could not be reduced below the 20 MHz shown. The resolution of the spectrometer is about 100 kHz, being presently limited by the stability of the laser local oscillator. The design resolution of this system is 10 kHz (3×10^{-7} cm^{-1}) with continuous tunability of ≈1 cm^{-1}.

This preliminary work will now be continued with other gases that have absorptions near strong laser LO lines, and will be applied particularly to atomic fine structure resonance lines that have extremely narrow and stable transitions which can be used as references for far infrared frequency standards.

6. REFERENCES

ALLEN, R. P. G., and ANTELL, G. R., 1973, "Monolithic Mixers for 60-80 GHz", Proc. 1973 European Microwave Conf., Paper A. 15.3, Sept.

BALLAMY, W. C., and CHO, A. Y., 1976, "Planar Isolated GaAs Devices Produced by Molecular Beam Epitaxy", IEEE Trans. Electron Devices, Vol. ED-23, pp. 481-484, Apr.

CLIFTON, B. J., 1977, IEEE Trans. Microwave Theory Tech. 25, 457.

ERICKSON, N. R., 1977, IEEE Trans. Microwave Theory Tech. 25, 865.

FETTERMAN, H. R., TANNENWALD, P. E., CLIFTON, B. J., PARKER, C. D., FITZGERALD, W. D., and ERICKSON, N. R., 1977, "Far IR Heterodyne Radiometric Measurements with Quasi-Optical Schottky Diode Mixers", Appl. Phys. Lett. (to be published).

GOLDSMITH, P. F., 1977, private communication from the National Radio Astronomy Observatory.

GUSTINCIC, J. J., 1977, "Receiver Design Principles", Proc. Soc. Photo-Optical Instrumentation Engineers 105, April 18-21, Reston, VA (p. 40); and GUSTINCIC, J. J., DE GRAAUW, TH., HODGES, D. T., LUHMANN, N. C., Jr., "Extension of Schottky Diode Receiver into the Submillimeter Region", private communication.

KRÄUTLE, H., SAUTER, E., and SCHULTZ, G. V., 1977, Infrared Phys. 17, 477.

MC COLL, M., 1977, "Review of Submillimeter Wave Mixers", Proc. Soc. Photo-Optical Instrumentation Engineers 105, April 18-21, Reston, VA (p. 24).

MURPHY, R. A., BOZLER, C. O., PARKER, C. D., FETTERMAN, H. R., TANNENWALD, P. E., CLIFTON, B. J., DONNELLY, J. P., and LINDLEY, W. T., 1977, "Submillimeter Heterodyne Detection with Planar GaAs Schottky-Barrier Diodes", IEEE Trans. on Microwave Theory Tech. 25, 494.

SAUTER, E., and SCHULTZ, G. V., 1977, IEEE Trans. Microwave Theory Tech. 25, 468.

WOOD, E. J., and IMMORLICA, A. A., 1976, "Monolithic Microwave GaAs Mixer Diodes", Technical Digest, International Electron Devices Meeting, pp. 90-92, Dec.

The views and conclusions contained in this document are those of the contractor and should not be interpreted as necessarily representing the official policies, either expressed or implied, of the United States Government.

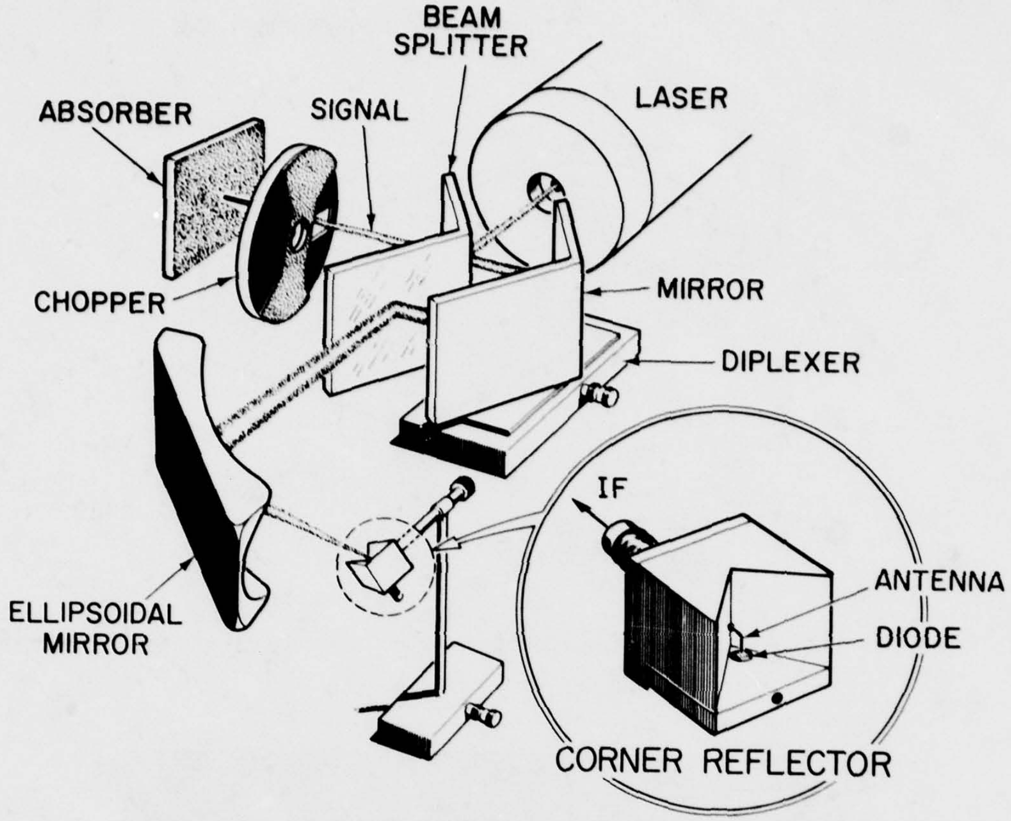
BEAM SPLITTER
LASER
ABSORBER
SIGNAL
CHOPPER
MIRROR
DIPLEXER
IF
ANTENNA
DIODE
ELLIPSOIDAL MIRROR
CORNER REFLECTOR

Fig. 1 Quasi-optical submillimeter receiver/radiometer operating between 170 μm and 1 mm.

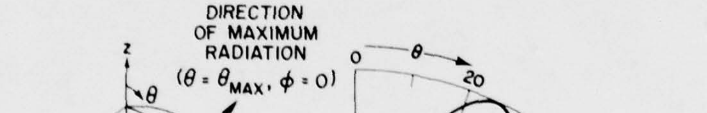

Fig. 2 Comparison of theoretical calculations with experimental data modeled at 7 GHz of corner-reflector antenna pattern.

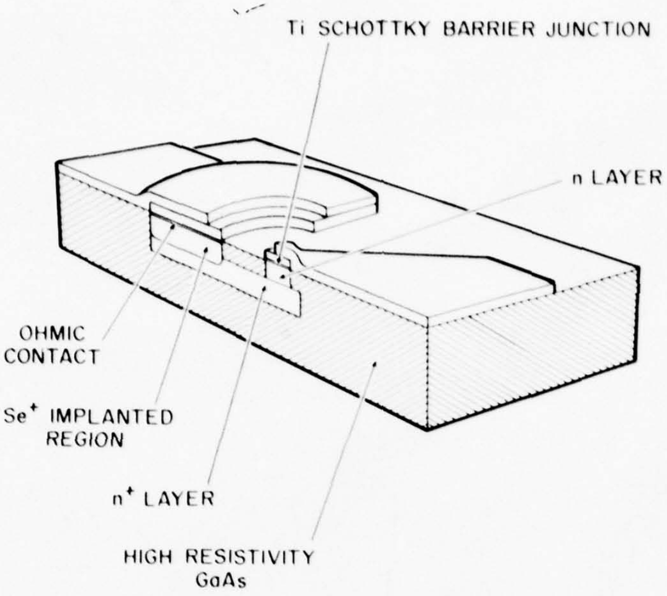
Ti SCHOTTKY BARRIER JUNCTION
n LAYER
OHMIC CONTACT
Se$^+$ IMPLANTED REGION
n$^+$ LAYER
HIGH RESISTIVITY GaAs

Fig. 3 Planar, surface-oriented diode as fabricated by growth of n-n$^+$ epitaxial layers on high-resistivity GaAs substrate.

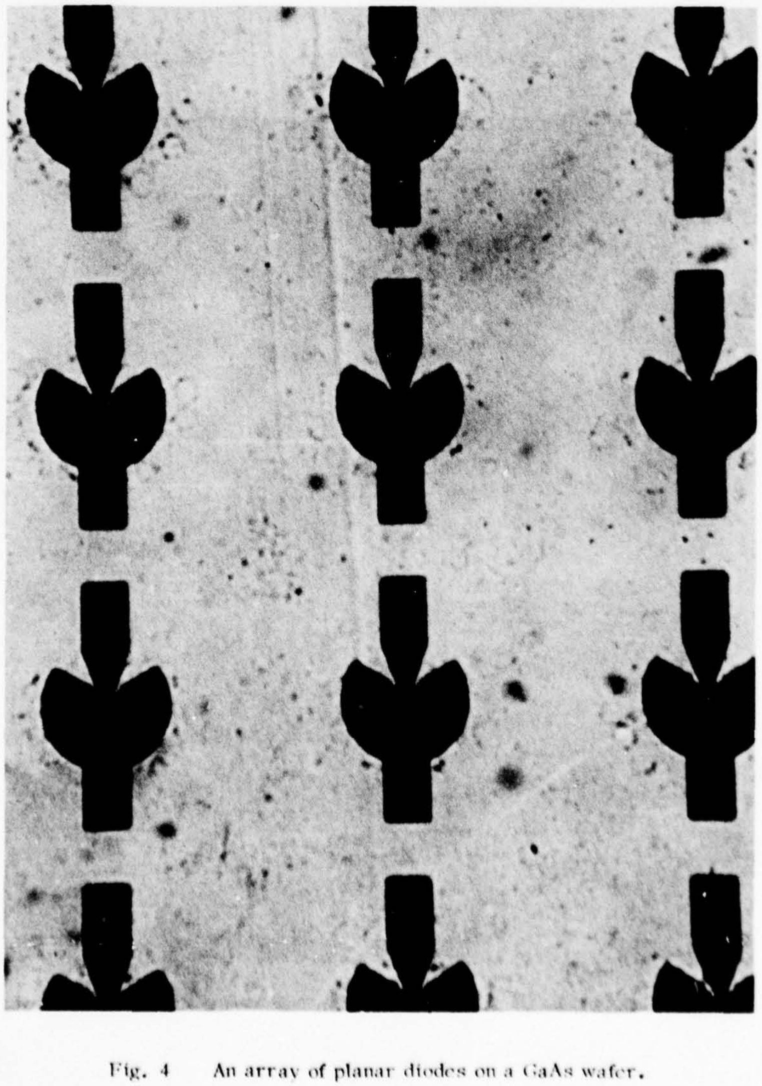

Fig. 4 An array of planar diodes on a GaAs wafer.

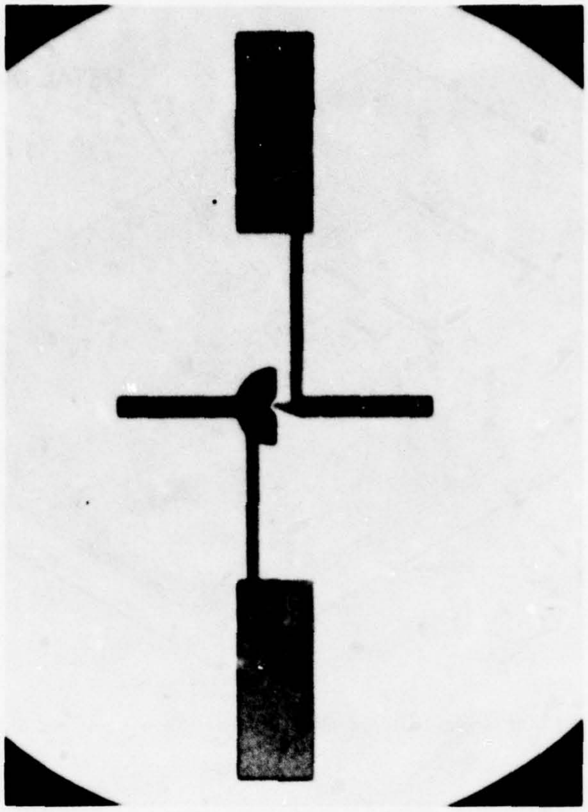

Fig. 5 Planar diode with attached half-wavelength dipole.

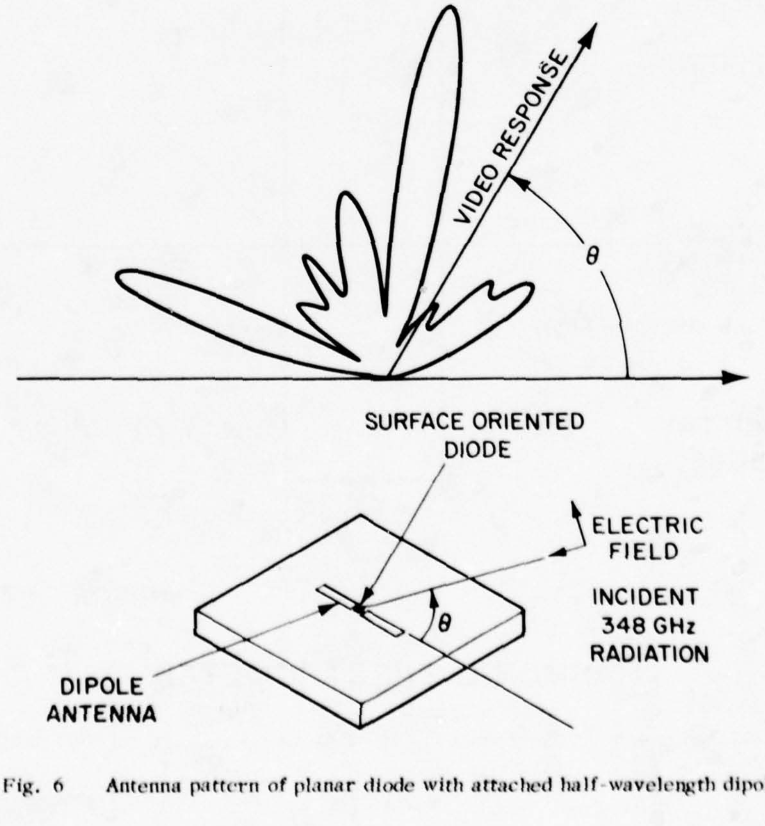
VIDEO RESPONSE
θ
SURFACE ORIENTED
DIODE
ELECTRIC
FIELD
INCIDENT
348 GHz
RADIATION
θ
DIPOLE
ANTENNA

Fig. 6 Antenna pattern of planar diode with attached half-wavelength dipole.

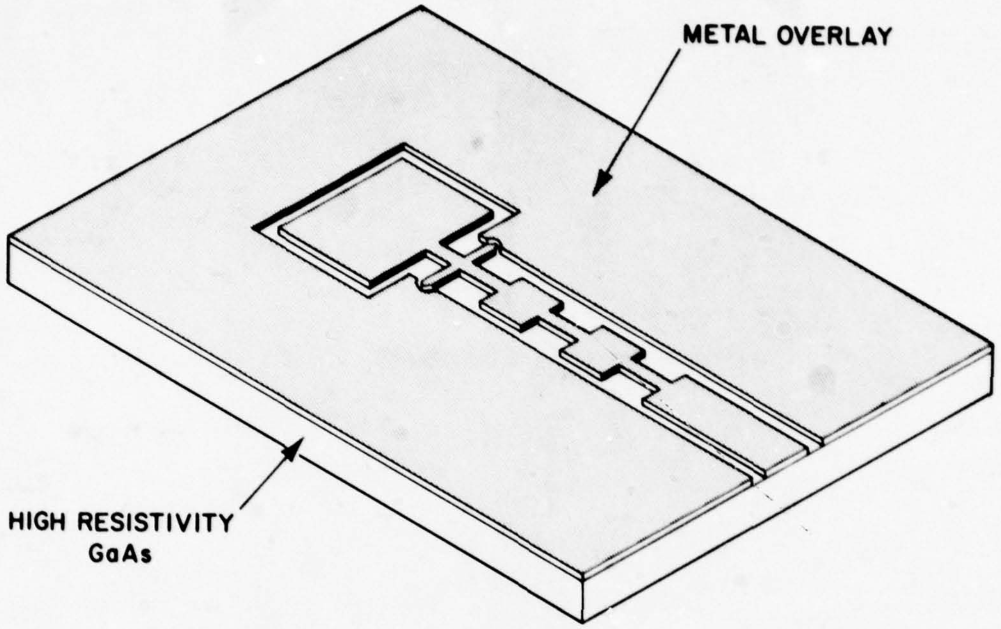
METAL OVERLAY
HIGH RESISTIVITY
GaAs

Fig. 7 Model of monolithically integrated planar mixer diode and slot antenna.

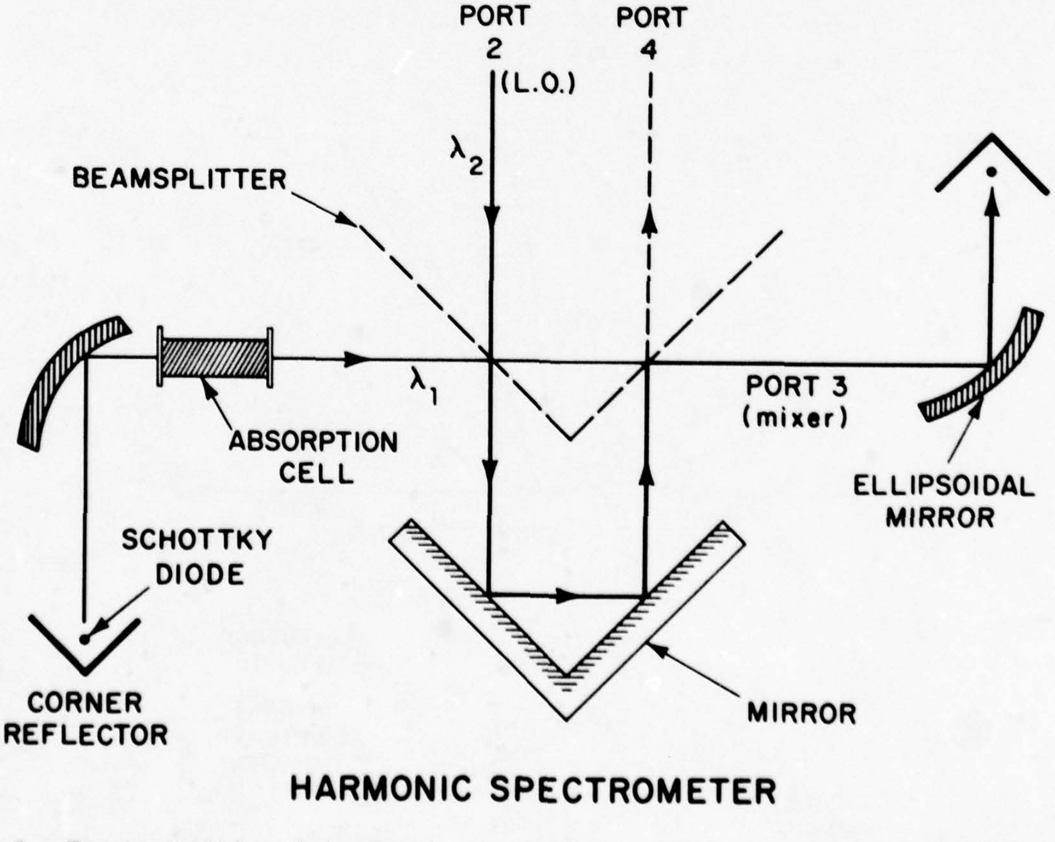
PORT
2
(L.O.)
PORT
4
λ_2
BEAMSPLITTER
λ_1
PORT 3
(mixer)
ABSORPTION
CELL
ELLIPSOIDAL
MIRROR
SCHOTTKY
DIODE
CORNER
REFLECTOR
MIRROR
HARMONIC SPECTROMETER

Fig. 8 Experimental high resolution spectrometer using quasi-optical diplexer and two Schottky diode corner reflectors.

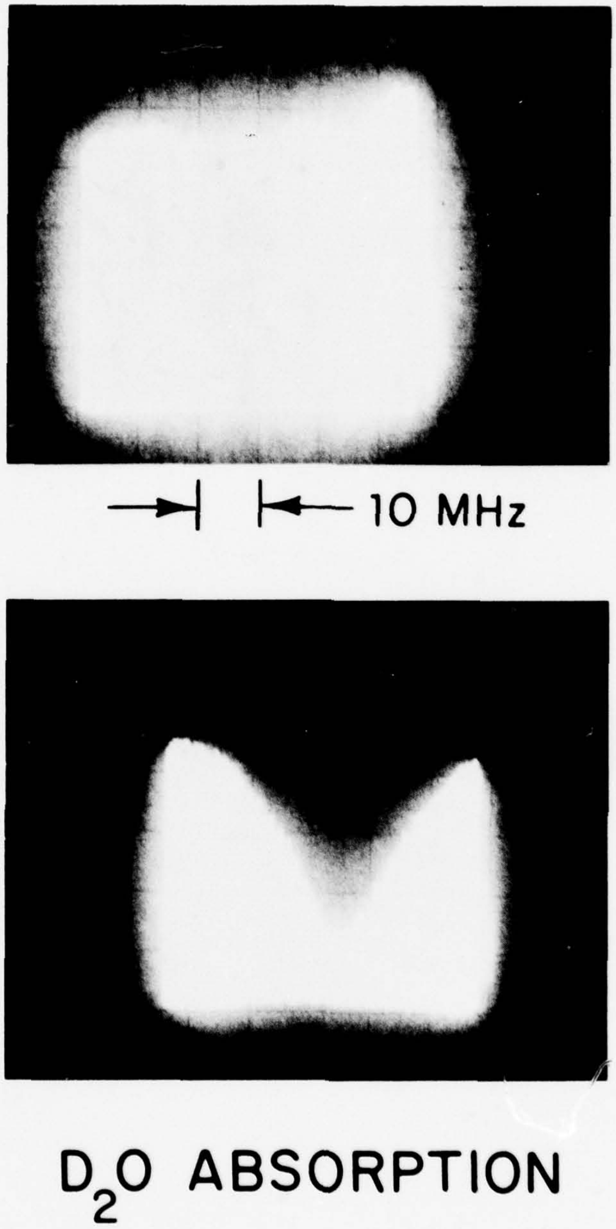

Fig. 9 Photographs of spectrum analyzer at 3 GHz showing the transmission of an absorption cell with (below) and without (above) D_2O gas.

THE DEVELOPMENT OF SUBHARMONICALLY PUMPED MIXERS
AT 230 GHz

K.F. Künzi, H. Berger
Institute of Applied Physics
University of Berne
Sidlerstrasse 5
CH-3012 Berne, Switzerland

SUMMARY

The millimeter wave portion of the spectrum is becoming increasingly more important for many different applications such as short range telecommunications, high resolution radars and radiometry, etc. At shorter millimeter waves local oscillators for mixers in receivers are expensive and difficult to operate. The subharmonically pumped mixer is an attractive technique useable into the submillimeter region. Subharmonic mixers operate with local oscillators at a submultiple of the signal frequency and provide AM-noise suppression of the local oscillator.

1. INTRODUCTION

Low-noise millimeter-wave receivers are becoming increasingly more important in many different areas, such as radio-astronomy, remote sensing, telecommunications, radars and plasma diagnostics. At millimeter-wave lengths Schottky-barrier mixers (down-converters) are the most frequently used receiver front ends with intermediate frequencies in the 1 to 10 GHz region. Receivers using masers, parametric amplifiers and others have been tested at various frequencies in the millimeter wave region, but are still in a very preliminary stage of development.

Most mm-wave mixers operate with a local oscillator (pump oscillator) frequency ω_p which is separated from the signal frequency ω_s by the intermediate frequency ω_{IF}.

$$\omega_p = \omega_s \pm \omega_{IF}.$$

At frequencies below 200 GHz such a mixer can easily be operated because reliable and not too expensive oscillators are available. For frequencies above 200 GHz oscillators become very expensive and difficult to operate requiring large high-voltage power supplies and liquid cooling, such as carcinotrons or extended interaction oscillators (EIO). To avoid this complication one can use harmonic mixing, by using the mixer diode for harmonic generation.

$$n \cdot \omega_p = \omega_s \pm \omega_{IF}. \qquad n = 2, 3, \ldots\ldots$$

However, these mixers tend to show larger mixer noise temperature due to the high pump power required and typically show conversion losses, in the case of the second order mixer (n=2), approximately 4 dB larger than for non-harmonic mixing. The reason for the higher conversion loss is fundamental mixing. This intermediate frequency is close to the local oscillator frequency and therefore difficult to suppress.

2. THE SUBHARMONICALLY PUMPED MIXER

In the subharmonically pumped mixer two diodes are mounted with opposite polarity. Figure 1 shows the I-V characteristics for such a diode pair. The theory of the subharmonically pumped mixers (for details see [1]) requires the frequency relation

$$n \cdot \omega_p = m \cdot \omega_s = \omega_{IF}. \qquad n+m = \text{odd}$$

therefore fundamental mixing (n=m=1) cannot exist. The lowest operating frequency is n=2, m=1. These mixers have been realized at frequencies up to 230 GHz. All these mixers have been built using suspended strip lines with appropriate filter-structures between signal, local oscillator and intermediate frequency ports. For optimizing the circuits, linearly scaled models at lower frequencies are used. Fig.2a shows the 10/5 GHz model of a 230/115 GHz mixer shown in Fig.2b. Fig.3 shows a SEM-picture of a contacted 230 GHz mixer diode mounted on a suspended quartz strip. Results of different subharmonic mixers are summarized in Table 1.

TABLE 1

Performance of subharmonically pumped mixers

Signal Frequency GHz	Pump Frequency GHz	Conversion Loss dB	Mixer Noise Temp. k	Comments
3.4 *)	1.7	3.2	-	Beam Lead Diodes Western Electric 197 A
3.4 *)	0.85	6.6	-	" "
10 *)	5	6	-	Beam Lead Diodes Airtech A-23744 (Capacitance of Diodes scaled from 230 GHz)
18	9	-	-	Used in Commercial Telefon links, Western Electric
50	25	3.3	-	Beam Lead Diodes AEI 1308
98	49	8.0	1600	Beam Lead Diodes AEI 1308
98	49	7.4	390	"Notch-Front" Diodes [2]
(230	115	8.9	2200)	"Notch-Front" Diodes, preliminary results [3])
(230	115	12	3500)	"Notch-Front" Diodes, preliminary results [4])

*) scaled models

3. CONCLUSIONS

Subharmonically pumped mixers appear very attractive for the short millimeter and submillimeter wave region. The best results obtained with this type of receiver are comparable with conventional single ended diode mixers. The advantages of subharmonically pumped mixers are:

- Local oscillator at a submultiple of the signal frequency;
- AM-noise suppression of local oscillator;
- Large local oscillator to signal port isolation;
- Simple signal port design, no need for local oscillator injection.

Acknowledgement: The authors would like to acknowledge the collaboration with M.V. Schneider, Bell Laboratories, Holmdel, N.J., U.S.A.

REFERENCES

[1] M.V. SCHNEIDER, W.W. SNELL, Jr., "Harmonically Pumped Stripline Down-Converter", MTT-23, No.3, March 1975.

[2] M.V. SCHNEIDER, E.R. CARLSON, "Notch-Front Diodes for Millimeter-Wave Integrated Circuits", Electronics Letters, Vol.13, No.24, November 1977.

[3] E. CARLSON, reported at MTT-Workshop, Ottawa, June 1978.

[4] R. DECKER, reported at MTT-Workshop, Ottawa, June 1978.

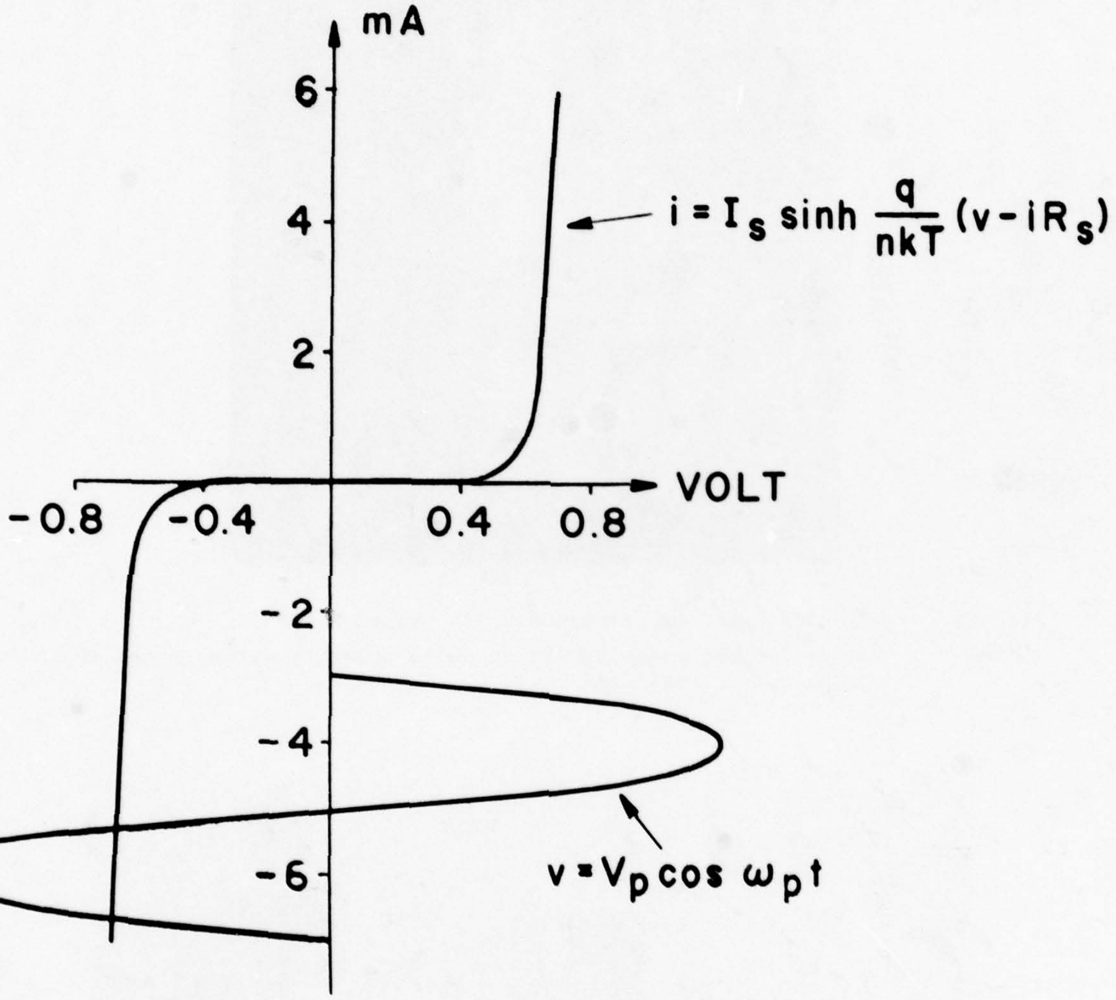

Fig. 1 : I-V characteristics of diode pair

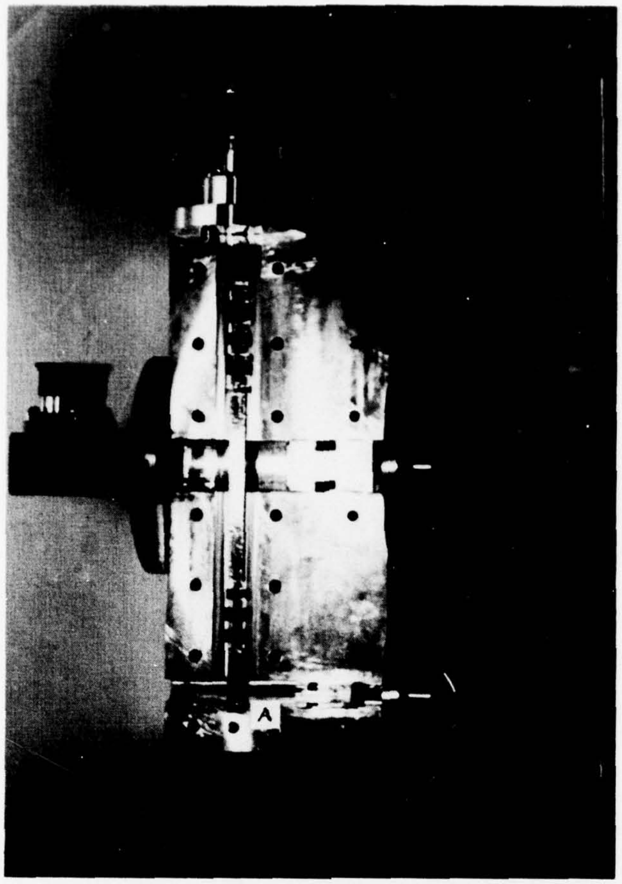

Fig. 2a : 10/5 GHz model of subharmonically pumped mixer.
The diodes are mounted with opposite polarity across a gap in the strip line at position A .

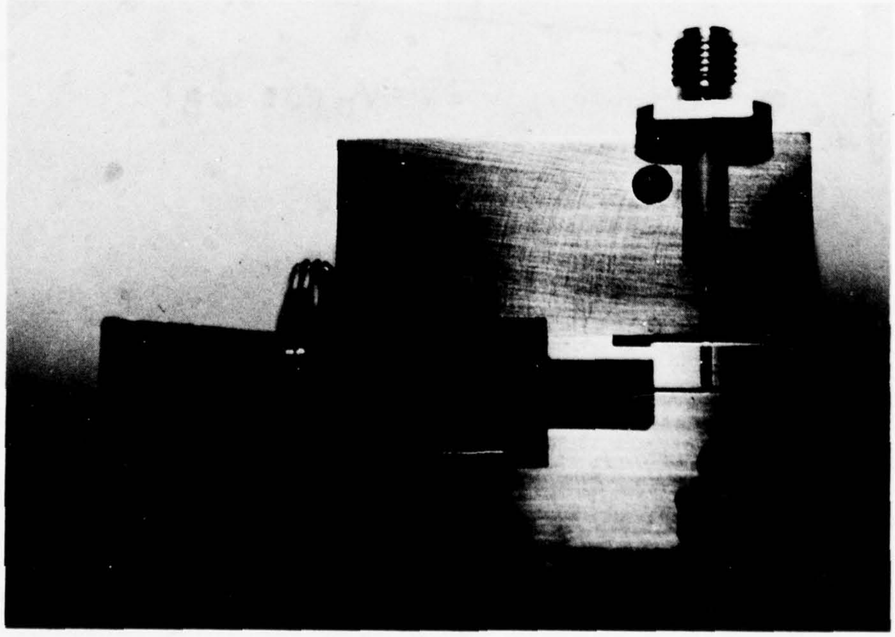

Fig. 2b : 230/115 GHz mixer
with integral horn antenna.

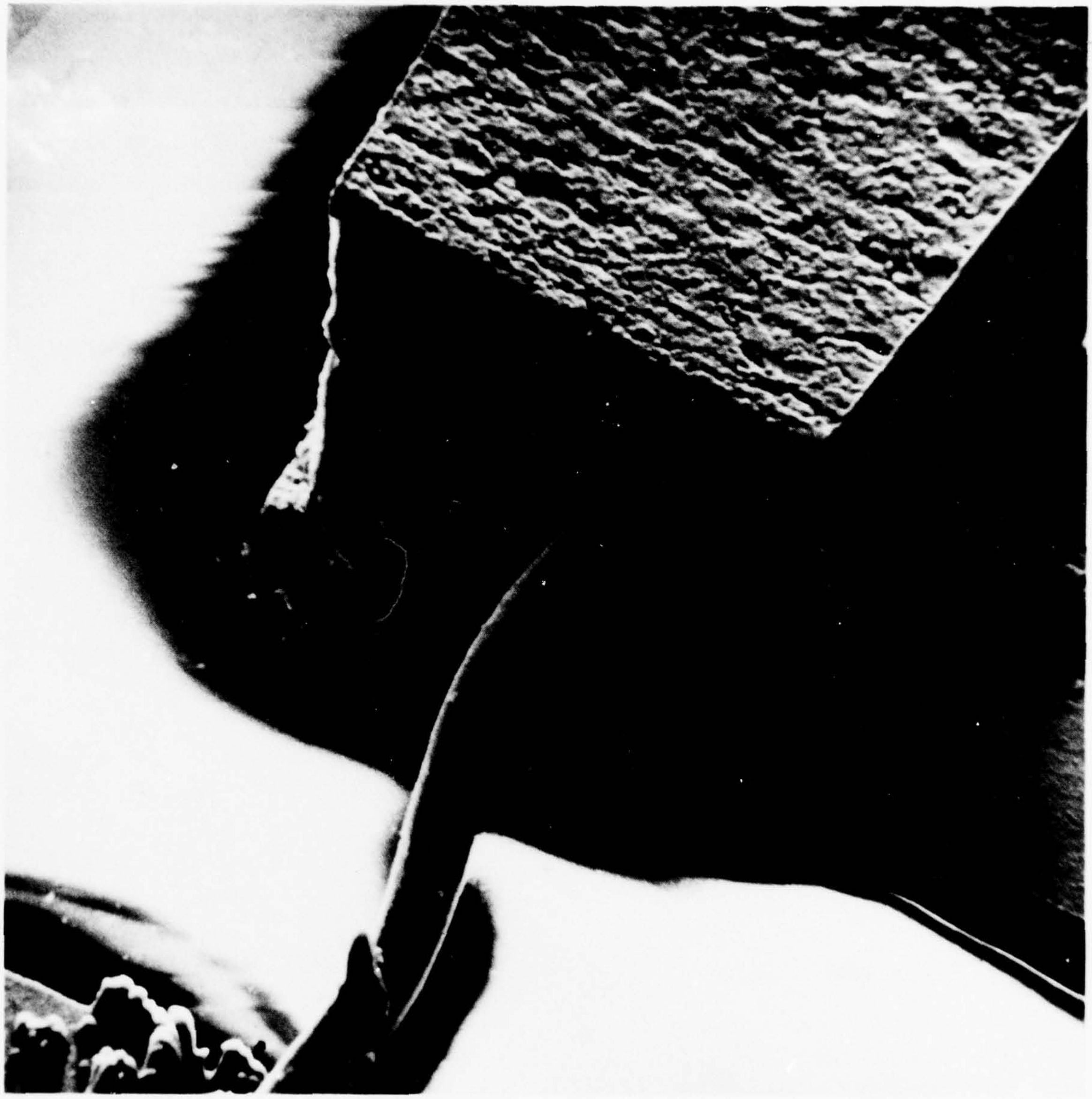

Fig. 3 : SEM-picture of contacted Notch-Front Diode mounted on a 50 μ quartz strip. The diameter of the contacting wire is 12 μ with a point etched to a radius of ~ 1μ.

SUBMILLIMETRIC RECEIVERS : LOCAL OSCILLATORS AND MIXERS

J. J. JIMENEZ, P. PLAINCHAMP, A. COMERON and A. CLAIRON

Laboratoire Primaire du Temps et des Fréquences (LPTF)

Observatoire de Paris et Bureau National de Métrologie
61, avenue de l'Observatoire
75014 PARIS (France)

ABSTRACT

With submillimetric (SUBMM) devices, lasers and mixers, the classical microwave techniques may be extended up to the SUBMM range.

The best choice for the local oscillator seems to be the optically pumped FIR laser because of the high number of active lines, output power and frequency stability. For the last one, values as low as $\sigma_y(\tau) = 2 \times 10^{-13}\tau^{-1/2}$ for $\tau \leqslant 20$ ms and a minimum measured value $\sigma_y(100 \text{ ms}) = 2 \times 10^{-12}$ have been obtained for the CH_3OH pumped laser (70.5 μm).

For a high IF bandwidth, high multiplication order and high frequency operation, the classical mixers used in microwavos (Schottky diodes, Josephson jonctions and MIM diodes) may be extended to the SUBMM as well as to the IR spectrum. Some of them have sensitivities close to the quantum limit.

Since an analysis of the optical wave propagation in the atmosphere for inclement weather operation has shown the useful windows on the SUBMM range, a SUBMM receiver appears to be very promising to operate in the battlefield on fog, rain and snow as active imaging system.

I – THE OPTICALLY PUMPED FIR LASER

a) Introduction.

Since the discovery in 1964 of the first molecular discharge laser, the H_2O lasing at 28, 78, 79 and 118 μm (Crocker, A. et al, 1964), others submillimetric (SUBMM) discharge lasers such as the HCN, H_2S, SO_2 and OCS were built within six years.

In 1970 Chang and Bridges obtained SUBMM laser action in CH_3F by optical pumping with a CO_2 laser and in the last years, more than 1 000 new lines have been reported in the 13μm - 2 mm range (Yamanaka, M., 1976) that produce laser activity in about 44 polar gases.

The generation of FIR radiation arises from rotational transitions in an excited vibrational state of a low pressure polar gas, and population inversion is achieved through selective pumping involving the near-resonant absorption of radiation from a strong infrared pump laser such as CO_2 which has about 100 lines around 9.6 - and 10.4 μm (for the $^{12}C^{16}O_2$ molecule). The CO_2 laser is a suitable choice for optical pump because many molecules have strong vibrational-rotational absorption lines in the 9 - 10 μm region. One of the more important molecules is the methyl alcohol (CH_3OH), lasing in 70 lines between 37 and 1 217 μm (Hodges, D. T., 1977). The number of FIR lines is being increased by extending the pump frequency range to the CO_2 sequence lines (Weiss, C.O. et al, 1977) which would be further extended to the complete 9 - 12 μm CO_2 region using rare isotopes (Freed, C. et al, 1974).

b) Resonator and coupling.

The more common FIR pumped laser uses a waveguide resonator constructed from hollow cylindrical dielectric or metallic tube, in order to reduce the diffraction losses (Marcatili, E.A.J. and R.A. Schmeltzer, 1964 ; Abrams, R. L., 1972). Complete data on mode properties and propagation losses have been studed for different waveguides (Yamanaka, M., 1977). In general, dielectric waveguides are used for a linearly polarized mode while metallic waveguides are quasi-randomly polarized, but these are very compact and rugged for laser construction.

Injection of the CO_2 pump into the FIR cavity is normally obtained by focusing the radiation through a hole in one of the cavity end reflectors. The outcoupling of the FIR radiation is usually performed at the opposite end of the cavity.

Figure 1 shows the common resonator and coupling configurations (Yamanaka, M., 1977 ; Hodges, D. T., 1977) :

(a) is a conventional Fabry-Perot resonator, with free space propagation between the two mirrors. For a long cavity (2-3 m) the natural divergence of free space modes at FIR wavelengths results in conventional resonators with large transverse dimensions (about 100 mm) in order to support laser modes without excessive diffraction losses.

(b) is the more classical waveguide structure, with low losses for hollow dielectric waveguide and mirrors external to the waveguide. In metallic waveguide, with broad wavelength coverage, the mirrors need to be very close to the waveguide ends, in order to reduce the propagation losses.

(d) uses parallel plate waveguide, useful for Stark effect tuning, modulation and phase-lock (Stein, S. R. et al, 1977 ; Stein, S. R. and Van de Stadt, 1977 ; Inguscio, M. et al, 1978). Linearly polarized output can be obtained using rectangular waveguides.

(c) and (e) show outcoupling systems other than the simple hole. In (c) the outcoupling mirror may be a metallic mesh (inductive grid or capacitive grid) or hybrid metal-mesh dielectric mirror (Danielewicz, E. J. et al, 1975) that couple the total mode out of the laser with a minimum angular divergence for the beam. Other mirror coupling, a variation of the conventional coupling hole, uses a high reflectivity dielectric coating for the CO_2 radiation and a metallic evaporated hole for the FIR outcoupling (Hodges, D. T. et al, 1976). Increasing the pumping efficiency, FIR output powers as high as 400 mW at 119 μm and 100 mW at 70 μm have been obtained (Hodges, D. T. et al, 1976). This system is useful up about 100 μm.

(e) is a special outcoupling developed for the 70 μm line of the CH_3OH (Plainchamp, P. to be published, 1978). A salt window (s. w in figure 1e) (KCl) at the Brewster angle for the CO_2 radiation reflects the 70 μm radiation with about 89 % reflectivity. An external concave gold mirror re-injects the CO_2 beam into the FIR cavity, increasing the pump efficiency. Such system is only useful around the 70 μm wavelength since the potasium-chloride has a high reflexion factor just around this wavelength.

c) Output power.

The state of the art of millimetric and submillimetric wave sources (fig. 2) shows that the CW optically pumped FIR laser presents good performance between 42 μm and 1 222 μm (Fesenko, L. D. and S. F. Dyubko, 1976 ; Hodges, D. T. et al, 1976 ; Hodges, D. T. et al, 1977 ; Schubert, M. R. et al, 1977 ; Evenson, K. M. et al, 1977a ; Hodges, D. T., 1977a), where powers from 10 to 400 mW have been obtained using 20 - 40 W of CO_2 pump power. The stronger lines have been obtained at 70 μm (110 mW) (Evenson, K. M. et al, 1977a) and 119 μm (400 mW) (Hodges, D. T. et al, 1976) for the CH_3OH pumped laser. For the discharge FIR laser, the maximum reported output powers are at 337 μm (160 mW) (Belland, P. 1976) and at 190/195 μm (250 mW) (Veron, D. et al, 1978) for the HCN and DCN lasers respectively (fig. 2).

For $\lambda > 450$ μm only the Backward-Wave Oscillator (BWO) has higher power than the lasers (Bonnefoy, R. et al, 1977). But in the range 40 μm $< \lambda <$ 400 μm the laser output powers are one to three orders higher than the best reported values of the CW BWO (Bonnefoy, R. et al, 1977).

The values of other tubes and solid state sources (fig. 2) are from (Kaisel, S. F., 1977) and (Kuno, H. J. and T. T. Fong, 1978).

d) FM noise and stability.

One of the more important characteristics of a local oscillator is its FM intrinsic noise. A good frequency stability can be expected from such laser due to the absence of free electrons in the optical cavity (Weiss, C. O. and G. Kramer, 1975).

One method to define the oscillator FM noise is the measurement of its fractional frequency stability (Allan variance) versus the average measurement time (Rutman, J. 1978). Figure 3 shows the frequency stability of the IF signal (180 KHz) obtained beating two similar (2 m long) free running CH_3OH laser (70.5 μm, 4.25 THz) pumped by the same free running CO_2 laser (Plainchamp, P. to be published, 1978). The mixer is a metal-insulator-metal (MIM) diode. In curve C the measurement was realized through a wide-band post-detection amplifier (0.01 - 400 MHz). This curve is similar to previously published ones (Jimenez, J. J. and F. R. Petersen, 1977 ; Jimenez, J. J. et al, 1978), obtained using a 0.1 - 1 200 MHz amplifier and a 2 MHz beat note. The stability measurement is probably limited by the wide-band amplifier noise.

Curve D shows the frequency stability of the same beat note using a narrow-band amplifier (0 - 5 MHz) (Plainchamp, P. to be published, 1978). For $\tau \leqslant 20$ ms a nearly white frequency noise is obtained, $\sigma_y(\tau) = 2 \times 10^{-13} \tau^{-1/2}$, with a minimum value $\sigma_y(\tau) = 2 \times 10^{-12}$ for $20 \text{ ms} \leqslant \tau \leqslant 100$ ms. For longer times ($\tau > 100$ ms) the laser drift with a law $\sigma_y(\tau) \simeq 1.5 \times 10^{-11} \tau$ mainly due to the FIR cavity drift and CO_2 drift.

The 22W CO_2 laser (used to pump both FIR lasers) frequency stability has been measured by comparing it with a high stability free-running low-power (2 W) CO_2 laser (Jimenez, J. J. et al, 1978). Its frequency stability (fig. 4, curves A and B) is about the same order of magnitude than the high stability laser, in despite of its high output power. Curve A is obtained under conditions where the CO_2 laser is not coupled to the FIR laser, and curve B when the CO_2 is pumping the FIR laser : a slight degradation due to the back-coupling effect (optical feedback from the FIR cavity) appears only for $\tau > 30$ ms, in good agreement with (Godone, A. et al, 1978).

The CH_3OH (70 μm) stability values are about three orders of magnitude better than the obtained with free running SUBMM lasers, such as the HCN laser (337 μm, $\sigma_y(\tau) \simeq 10^{-9}$ for $10^{-4} \leqslant \tau < 20$ s) (Wells, J. S., 1973) and far enough from the equivalent values obtained with free running millimetric tubes or solid state oscillators (typical values are $\sigma_y(\tau) = 10^{-7} - 10^{-8}$ for $\tau = 1$ s). The CH_3OH (70 μm) free running laser stability is only similar to that of the best stabilized FIR laser, the phase-locked HCN laser (Wells, J. S., 1973) and may be compared, in the short term ($\tau \leqslant 0.1$ s) with other well stabilized lasers such as the CO_2 (CO_2 stabilized) (Freed, C. 1976).

e) Long term frequency stabilization.

Until now, no classical stabilization techniques, used for other lasers have been applied to ameliorate the long term stability of the FIR laser. Instead, electronic tuning techniques have been developed for FIR lasers which make it possible both, to frequency modulate the laser at very high rate, and to phase-lock it to a reference oscillator (Stein, S. R. et al, 1977 ; Stein, S. R. and H. Van de Stadt, 1977 ; Inguscio, M. et al, 1978). Tuning is achieved by applying an electric field (Stark effect) across the laser medium (fig. 1d). This method avoid the introduction of lossy materials inside the cavity and provides high speed frequency tuning, limited only by the life time of photons inside the cavity.

Stark modulation has been applied to the CH_3F (496 μm) laser as well as to the CH_3OH laser (119 - and 70 - μm). Frequency shifts versus field strength are about 5 KHz/(V/cm) for the CH_3F (Stein, S.R. et al, 1977) ; 29 KHz/(V/cm) for the 119 μm line of CH_3OH (Inguscio,M. and F. Strumia, private communication,1978) and 45 KHz/(V/cm) for the 70 μm line of CH_3OH (Inguscio, M. and F. Strumia, private communication, 1978) and we expect the best tuning range for the 70 μm line.

Using Stark effect, a bandwidth tunability of many MHz has been obtained until now in the CH_3F (496 μm) (Strumia, private communication, 1978) but higher values may be expected. Up to date, the BWO bandwidth tunability (20 %) is much better (Bonnefoy, R. et al, 1977).

f) The optically pumped FIR laser as local oscillator.

Because of its useful output power, high number of emission lines, high free running frequency stability and possibility of tunability, the optically pumped FIR laser could be the best choice for local oscillator(L. O.) in the SUBMM region. The 70.5 μm line of *the CH_3OH laser will be used in frequency synthesis as a SUBMM frequency secondary standard for further frequency multiplication to* measure to parts in 10^{12} the frequency of the helium-neon methane-stabilized laser (3.39 μm) in a very accurate laser frequency synthesis chain (Jimenez, J. J., 1978b).

2 – THE MIXER

With an appropriate choice of the nonlinear device and a source of coherent radiation, it will be possible to built low noise SUBMM receivers in a large frequency domain.

Two methods may be considered :

1) a detector with a high quantum efficiency ($\eta \simeq 1$) but with a small bandwidth (about 100 MHz) combined with a tunable or fixed L. O., and
2) *a detector with a low quantum efficiency* ($\eta << 1$) but with a large banwidth (>> 1 GHz) combined with a L. O. of different fixed frequencies, such as the FIR pumped laser.

The classical optical detectors (Keyes, R. J., 1977) may be classified in two groups that differ by the physical mechanism involved in the detection process :

a) the thermal detectors, where the heating of the incident radiation causes a change in some electrical properties of the detector, and
b) the quantum (or photon) detectors, where there is a direct interaction between the incident photons and the carriers of the detector material.

The thermal detectors respond theoretically equally to all wavelength, but practical limitations of available blackening material often modify this assumption. The more important thermal detectors are the thermocouple, the bolometer, the pneumatic (Golay detector) and the calorimeter. The time constant of a thermal detector is usually between a few milliseconds and a few seconds.

The quantum detectors have shorter time constants, inferior or equal to a few microseconds, but its reponse varies with the wavelength. The more important quantum detectors are the photoelectric (or photoemissive), the photoconductive (intrinsic, extrinsic or free carrier) *and the photovoltaic (p-n junction) detector. The photoconductive (extrinsic and hot electrons) detectors seem to be* very promising mixers in the 100 – 2000μmregion, but the higher IF bandwidths obtained are inferior to 200 MHz, and in general, only a few MHz (Mc Coll, M., 1977).

The faster detectors used in the optical region are devices that extend the classical function of the microwave mixer through the SUBMM region as well as to the IR spectrum, to wavelengths as short as 1.52 μm (Evenson, K. M. et al, 1977b). The more used are the point contact diodes (metal–semiconductor, metal–insolator–metal (MIM), superconductor–insolator–superconductor (Josephson jonction, J. J.)and the Schottkybarrier diodes. Some of them (MIM and Schottky barrier diodes) have been built in planar structure. (For a review of SUBMM and IR mixers, see Pyée, M. and J. Auvray, 1975 ; Knight, D. J. E. and P. T. Woods, 1976 ; Mc Coll, M. 1977 ; Jimenez, J. J., 1978a).

The main parameters to choice a heterodyne mixer are its sensitivity (or noise temperature), bandwidth and operating temperature. Only the JJ and the photoconductive mixers work at liquid helium temperatures. The Schottky barrier diode has been some times cooled in order to improve its noise temperature (Kerr, A.R.. 1975).

Table I summarizes the main parameters of the highest frequency nonlinear devices, used as detectors (wavelength limit) and as mixers (heterodyne detectors) in the FIR and the IR*.

In the SUBMM range, the more used are the Si-metal (PC), Ga As–metal (PC and planar Schottky barrier) and the Josephson junction (PC). All them have a cutoff frequency in the few THz range and high multiplication orders (Table 1), the higher ones (401 and 825) corresponding to the JJ. Moreover, this device and the Schottky barrier diode, have the lowest noise as heterodyne receivers.

The Ge–metal (PC) and the In As–metal (hot carrier diode) (PC) have permitted to detect the 10 μm radiation. A mixing between two CO_2 lasers has been obtained with the last one, giving a 50 GHz beat note (Aukerman, L. W. and J. W. Erler, 1977).

The Metal–Insulator–Metal (MIM) (PC) diode, first used in MIT (Hocker L. O., et al, 1978) is the main device in the complete IR range. It is realized from a whisker (tungsten wire, 10 to 25 μm diameter) electrochemically sharpened to a tip radius of 50 – 100nm.

---

* For a complete reference of the values reported on table 1 and figure 4, see(Jimenez, J. J., 1978a and Mc Coll, M. 1977).

in contact with a polished base (nickel). A natural oxide layer, 1 - 2 nm width, is between the two metals. The straight portion of the whisker from the tip to a right angle bend serves as antenna (Matarrese, L. M. and K. M. Evenson, 1970) to concentrate the focused laser field at the tip. The same type of optical coupling is used for the others PC diodes, and antenna gains of 6 - 12 dB have been obtained in the SUBMM range using some special reflector (Krautle, M. et al, 1978 ; Fetterman, H. R. et al, 1978).

The highest frequency ever mixed, 197 THz (1.52 μm) (Evenson, K. M. et al, 1977b) has been obtained with the MIM point contact diode.

Typical IF bandwidth for the PC devices are in the 1 - 100 GHz range, with sensitivities (minimum detectable powers*) comparable and even better than the values obtained with photoconductive devices. Figure 4 shows the MDP (and noise temperature) for several mixers or receivers (filled-in data points) in the millimetric, submillimetric and infrared range. Among them, the J J and the Schottky diodes seem to be the more useful devices in the MM and SUBMM range, with MDP values about one order of magnitude higher than the quantum limit for the J J, and about two to three orders higher than the quantum limit for the Schottky diodes, in the 500 μm - 10 mm range.

The planar structure diodes, Schottky barrier and MIM (Jimenez, J J , 1978a) seem also very interesting in the SUBMM range.

Table 1 . Summary of performance characteristics of the common optical frequency detectors and mixers devices. Although some of the data has been obtained by private communications, most has been reported in the literature (Jimenez, 1978a). For a given detector, values reported in the table are not necessarily from the same experiment.

DETECTOR	Detection	Harmonic generator and mixer (heterodyne)				
	Wavelength limit (μm)	Frequency limit ν_1(b) (ν_2) (c) (THz)	Multiplication order	Time response (e) $\tau=1/\nu_1$ (fs)	MDP$^{(a)}$ at frequency ν	
					MDP (WHz^{-1})	ν(THz)
1. Point contact						
1.1. Metal-Semiconductor (MS)						
Si (PC) (e)	84	3.56 (1.58)	4 23	280	*	*
Ge (PC)	10.6	*	*	*	*	*
Ga As (PC)	337	0.89	9	1120	2×10^{-14}	0.89
Ga As (SB) (f)	5 (g) 10.6 (g) 42	4.25 2.52	1 (h) 33	235	5×10^{-17} 1 to 2×10^{-19}	2.52 0.76to0.32
In As (PC)	10.6	28.3	1 (h)	35	10^{-8}	28,3
1.2 Metal-Insulator-Metal (MIM) (PC)	0.5 (g, i) 1.52 (j)	197 (88) (10)	1 (k) 3 (l) 15	5	10^{-13} 10^{-15} - 10^{-16}	28.3 0.89
1.3. Superconductor-Insulator-Superconductor Josephson Jonction (PC)	9.5 (g) 70.5	4.25 (3.8) (0.89)	43 401 825	235	10^{-17} 6×10^{-20} 3×10^{-21}	0.89 0.45 0.32
2. Planar structure						
2.1 Metal-Semiconductor (MS) Ga As (SB)	337	0.76	82	1316	*	*
2.2 Metal-Insulator-Metal (MIM)	0.45-0.6 (g) 3.39 10.6	0.89	13	1120	*	*

(a) MDP : Minimum detectable power, represents the sensitivity of a mixer (coherent or heterodyne detector) or a receiver, in a normalized bandwith B = 1 Hz. It is expressed in units of W.Hz^{-1}. MDP = kTB_{IF}, where k is the Boltzman's constant, T the mixer (or receiver) noise temperature and B_{IF} the IF bandwith. The quantum limit is hν = kT.

(b) ν_1 is the highest frequency obtained with the device.

(c) (ν_2) (many values may be reported) is the highest frequency obtained for the highest multiplication order (next column).

(d) 1 fs = 10^{-15}s.

(*) no available data

---

* See definition in table 1.

(e) PC = point contact

(f) SB = Schottky barrier

(g) rectification may be thermal

(h) two frequencies mixing without harmonic generation

(i) positive rectified voltage

(j) negative rectified voltage

(k) three frequencies mixing without harmonic generation

(l) three frequencies mixing with harmonic generation

In order to choose the best mixer, we require some display of the difference frequency between the signal and the known reference frequency of the L. O., radiating in the same spectral region. There are two main possibilities :

a) the simplest technique would be to heterodyne the signal with an harmonic of an electronically measurable L. O. frequency, directly generated in the nonlinear device. Such devices should be capable of high-order harmonic generation and need to have high cutoff frequencies. The metal-semiconductor PC, Schottky barrier diode and J J seem to be the best choice up to a few THz.

b) we may mix the signal with a spectrally adjacent known L. O. in a wideband device. If necessary this difference is down-converted to a frequency within the response band of the device by mixing it with other radiation (usually microwaves). In this case the PC and Schottky barrier diodes may be the best choice, specially if the difference between signal and L. O. is large.

Optical frequency mixing is a new subject, but commercial development of SUBMM devices is limited to photodiodes and Schottky diodes. Other devices (JJ, MIM and in general PC diodes) are very delicate and need to be used in special laboratories. For frequencies higher than a few THz, the MIM diode is up to day the best choice.

3 – FIR WAVE PROPAGATION

Two cases need to be considered : a) the optical beam propagation at the top of the earth's atmosphere, and b) the optical beam propagation at the earth atmosphere. The first case apply to the space research, specially interstellar astronomical observations ; the second case concern the earth communications, civil or military.

The molecular line astronomy can be used as a diagnostic tool for the study of the physical conditions, such as mass, density and temperature of the interstellar gas. Rotational transitions of many molecules(H_2O, HCN, OCS, NH_3, HCOOH, CH_3OH, etc. . .) occur in the MM and SUBMM regions. In these cases, the receiver is over the top of the earth's atmosphere and its attenuation is not important.

In the second case, although the atmosphere is quite transparent in the visible and near infrared, attenuation is high into the SUBMM region. This is due to absorption of the radiation by the atmospheric constituents, the greatest problem arising from the water vapor.

Operation in inclement weather (rain, fog or snow), as it is founded in Europe, favors the near and intermediate IR regions (1 - 25 μm) and the SUBMM region (beyond 300 μm) (Kruse, F. W. and V. Garber, 1976 ; Hartman, R. L. and P. W. Kruse, 1976). In fact, the inclement weather is characterized by a distribution of particule size : at wavelength much smaller than the particle diameter the scattering of radiation is relatively independant of wavelength. In fog conditions, the more useful windows are at 337, 750, 850 and 1 300 μm (Kruse, P. W. and V. Garber, 1976), where FIR lasers are available. Experiments at 850 μm have showed the advantages of a such receiver compared with a 3 mm receiver (Hartman, R. L. and P. W. Kruse, 1976). In these conditions, a SUBMM receiver appears to be very promising to operate in the battlefield on inclement weather as active imaging system.

However, greater receiver sensitivity and/or power output of the laser sources, and more experimental studies on SUBMM propagation are needed in this wavelength region.

REFERENCES

ABRAMS, R. L. (1972) "Coupling losses in hollow waveguide laser resonators" IEEE J. Quant. Electr., QE-8, 11, pp. 838-843.

AUKERMAN, L. W. and J. W. ERLER, (1977) "Infrared hot carrier diode mixers", Optics Lett., 1, 5, pp. 178-180.

BELLAND, P., (1976) "Lois d'échelle pour la conception optimale des lasers HCN (337 μm) continus utilisant l'effet de guide d'onde." Thesis, University of Paris, January, 259 pages.

BONNEFOY, R., G. KANTOROWICZ and P. PALLUEL, (1977) "Broadbanding of a submillimetre - wave Backward - wave oscillator" Proc. 7th European Microwave Conf., Kopenhagen Danemark, Sept. pp.

CHANG, T. Y. and T. J. BRIDGES (1970) "Laser action at 452, 496 and 541 μm in optically pumped CH_3F". Optics Comm. 1, 9 pp. 423-426.

CROCKER, A. ; H. A. GEBBIE, M. F. KIMMITT and L. E. S. MATIAS. (1964) "Stimulated emission in the far-infrared". Nature, 201, pp. 250-251

DANIELEWICZ, E. J. ; T. K. PLANT and T. A. DETEMPLE (1975) "Hybrid output mirror for optically pumped far infrared lasers". Opt. comm., 13, pp. 366-369.

EVENSON, K. M., D. A. JENNINGS, F. R. PETERSEN, J. A. MUCHA, J. J. JIMENEZ, R. M. CHARLTON and C. J. HOWARD (1977a). "Optically pumped FIR lasers : frequency and power measurement and laser magnetic resonance spectroscopy" IEEE Jour. Quant. Electr., QE-13, 6, pp. 442-444

EVENSON, K. M., D. A. JENNINGS, F. R. PETERSEN and J. S. WELLS (1977 b)"Laser frequency measurements : a review, limitations, extension to 197 THz (1.5 μm)," Laser Spectroscopy III, editor J. L. Hall and J. L. Carlsten, Springer-Verlag, Berlin, pp pp. 56-68.

FESENKO, L. D. and S. F. DYUBKO (1976) "Optimization of the parameters of optically pumped submillimetric lasers" Sov. Jour. Quant. Electr., 6, 7, pp. 839-843.

FETTERMAN, H..R. ; P. E. TANNENWALD, B. J. CLIFTON, C. D. PARKER, W. D. FITZGERALD and N. R. ERICKSON, (1978) "Far IR heterodyne radiometric measurements with quasi-optical Schottky diode mixers". To be published IEEE Trans. Microwave Theory and Techniques.

FREED, C. ; A. H. M. ROSS and R. G. O'DONNELL, (1974) "Determination of laser line frequencies and vibrational-rotational constants of the $^{12}C^{18}O_2$, $^{13}C^{16}O_2$ and $^{13}C^{18}O_2$ isotopes from measurements of CW beat frequencies with fast HgCdTe photodiodes and microwave frequency counters". Jour. Molecular Spectroscopy, 49, pp. 439-453.

FREED, C and R. G. O'DONNELL, (1976) "Advances in CO_2 laser stabilization using the 4.3μm fluorescence technique". 2nd Frequency Standards and Metrology Symposium, Copper Mountains, Co USA, 5-7 July.

GODONE, A. C. O. WEISS and G. KRAMER, (1978) "FM-noise measurements on an optically pumped FIR laser". IEEE Jour. Quant. Electr., QE-14, 5, pp. 339-342.

HARTMAN, R. L. and P. W. KRUSE, (1976) "Submillimeter system for imaging through inclement weather". Proc. 2nd International Conf. and Winter School on Submillimeter waves and their applications, San Juan, Puerto Rico, 6-11 December, pp. 229-230.

HOCKER, L. O., D. R. SOKOLOFF, V. DANEU, A. SZOKE and A. JAVAN, (1968) "Frequency mixing in the infrared and far-infrared using a metal-to-metal point contact diode". Appl . Phys. Lett., 12, 12, pp. 401-402.

HODGES, D. T. ; F. B. FOOTE and R. D. REEL, (1976) "Efficient high-power operation of the CW far-infrared waveguide laser" Appl . Phys. Lett., 29, 10, pp. 662-664.

HODGES, D. T. ; F. B. FOOTE and R. D. REEL, (1977) "High-power operation and scaling behavior of CW optically pumped FIR waveguide lasers" IEEE Jour. Quant. Electr., QE-13, 6, pp. 491-494.

HODGES, D. T. , (1977) "CW (continous wave) optically pumped FIR (far infrared) lasers". Proc. of the Soc. Photo-optical Instrumentation Engrs.(SPIE), Vol 105, Far infrared/Submillimeter wave. Technology/Applications, pp. 6-10.

INGUSCIO, M. ; P. MINGUZZI, F. STRUMIA and M. TONELLI, (1978) "The Stark effect as a means for frequency tuning optically pumped FIR lasers". Proc. 3rd International Conf. on Submillimetre Waves and their applications, University of Surrey, Guildford, U.K., 29 March-1 April, pp. 144-145.

KAISEL, S. F., (1977) "Microwave tube technology review", Microwave Jour. 20, 7, pp. 23-42.

KERR, A. R. (1975) "Low-noise room-temperature and cryogenic mixers for 80 -120 GHz" IEEE Trans. Microw. Theory Techn. MTT-23, 10, pp. 781-787.

KEYES, R. J. (1977) "Optical and Infrared Detectors" 7 review papers. Edited by R. J. Keyes, Springer-Verlag, Berlin 304 pages.

KNIGH, D. J. E and P. T. WOODS, (1976) "Application of nonlinear devices to optical frequency measurements" Jour. Phys. E., 9, pp. 898-916.

KRAUTLE, H., ; E. SAUTER and G. V. SCHULTZ, (1978) "Properties of a submillimeter mixer in a open structure configuration." To be published. Also, 1977, "Antenna characteristics of whisker diodes used as submillimeter receivers" Infrared Phys. 17, 6, pp. 477-483.

KRUSE, P. W. and V. GARBER, (1976) "Technology for battlefield target recognition in inclement weather" Proc. IRIS (23).

KUNO, H. J. and T. T. FONG, (1978). "Solid-state millimeter-wave sources". EASCON Conf., Washington, D. C.

JIMENEZ, J.J. and F. R. PETERSEN, (1977) "Recent progress in laser frequency synthesis" Infrared Physics, 17, 6, pp. 541-546.

JIMENEZ, J. J. ; F. R. PETERSEN, P. PLAINCHAMP, C. SALLOT and X. DRAGO, (1978). "Mesure des fréquences optiques au LPTF" Bull. d'Information BNM (France), 9, 31, pp. 19-27.

JIMENEZ, J. J., (1978a). "Synthèse et mesure des fréquences optiques" Revue Phys. Appl. (France). To be published.

JIMENEZ, J. J., (1978b). "Microwave to visible frequency synthesis" URSI Open Symposium on Time and Frequency, Session OS1/1.2, Helsinki, Finland, 1-4 August.

MARCATILI, E. A. J. and R. A. SCHMELTZER, (1964) "Hollow metallic and dielectric waveguides for long distance optical transmission and lasers" Bell. System Tech. Jour. 43, pp. 1783-1809.

MATARRESE, L.M. and K. M. EVENSON, (1970) "Improved coupling to infrared whisker diode by use of antenna theory" Appl. Phys. Lett., 17, 1, pp. 8-10.

Mc COLL, M.(1977) "Review of submillimeter wave mixers" Proc. Soc. Photo-Optical Instruments Engrs (SPIE), Vol. 105, Far Infrared/ Submillimeter wave. Technology/Applications, pp. 24-34.

PLAINCHAMP, P. (1978) "Frequency instability measurements of the CH_3OH (70.5 μm) optically pumped laser" To be published.

PYEE, M. and J. AUVRAY, (1975) "Generation et comparaison des fréquences dans le domaine submillimétrique et infrarouge" Bull. Information BNM (France), 6, 19, pp. 11-22.

RUTMAN, J., (1978) "Characterisation of phase and frequency instabilities in precision frequency sources : fifteen years of progress" Proc. IEEE, 66, 9 , pp.

SCHUBERT, M. R. ; M. DURSCHLAG and T. A. De TEMPLE, (1977) "Diffraction limited CW optically pumped lasers" IEEE Jour. Quant. Electr., QE-13, 6, pp. 455-459.

STEIN, S. R. ; A. S. RISLEY, H. Van de STADT and F. STRUMIA, (1977) "High speed frequency modulation of far infrared lasers using the Stark effect" Applied Optics, 16, 7, pp. 1893-1896.

STEIN, S. R. and H. Van de STADT, (1977) "Electronic tuning and phase-lock technique for optically pumped far infrared lasers Proc. 31st Annual Symp. Frequency Control, editor Electronic Industries Assoc., Washington, D. C., pp. 601-604.

VERON, D., P. BELLAND and M. J. BECCARIA, (1978), *"Continuous 250 mW gas discharge DCN laser at 190/195 μm"* Proc. 3rd International Conf. on Submillimetre Waves and their applications, University of Surrey, Guildford (U. K.), 29 March-1 April, pp. 182-183.

WEISS, C. O. and G. KRAMER, (1975), "Optically pumped far-infrared laser for infrared frequency measurements" Proc. 5th International Conf. on Atomic Masses and Fundamental Constants, Paris (France) June. Edited by J. H. Sanders and A. W. Wapstra, Plenum Press, New-York, 1976, pp. 383-389.

WEISS, C. O. ; M. GRINDA and K. SIEMSEN, (1977), "FIR laser lines of CH_3OH pumped by CO_2 laser sequency lines" IEEE Jour. Quant. Electr., QE-13, 11, p. 892.

WELLS, J. S. , (1973) "A stabilized HCN laser for infrared frequency synthesis" IEEE Trans. Instrum. Meas., IM-22, 2, pp. 113-118.

YAMANAKA, M. (1976) "Optically pumped gas lasers. A wavelength table of laser lines" Rev. Laser Engr(Japan) 3, 1976, pp.57-98.

YAMANAKA, M. (1977) "Optically pumped waveguide lasers" Jour. Opt. Soc. Am., 67, 7, pp. 952-958.

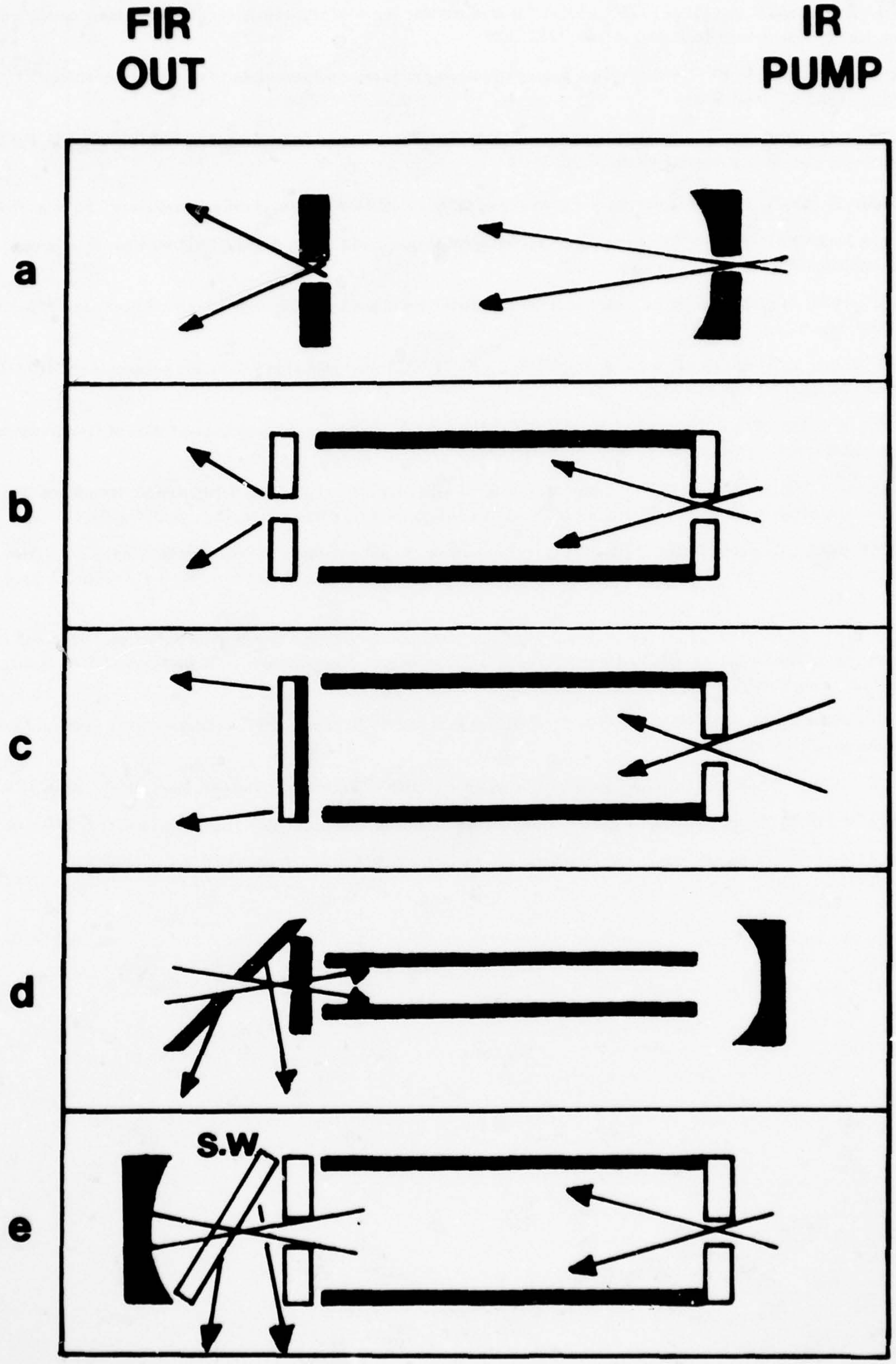
FIR
OUT
IR
PUMP
a
b
c
d
e
S.W.

Fig.1 Power vs. wavelength and frequency for various resonator and coupling configurations

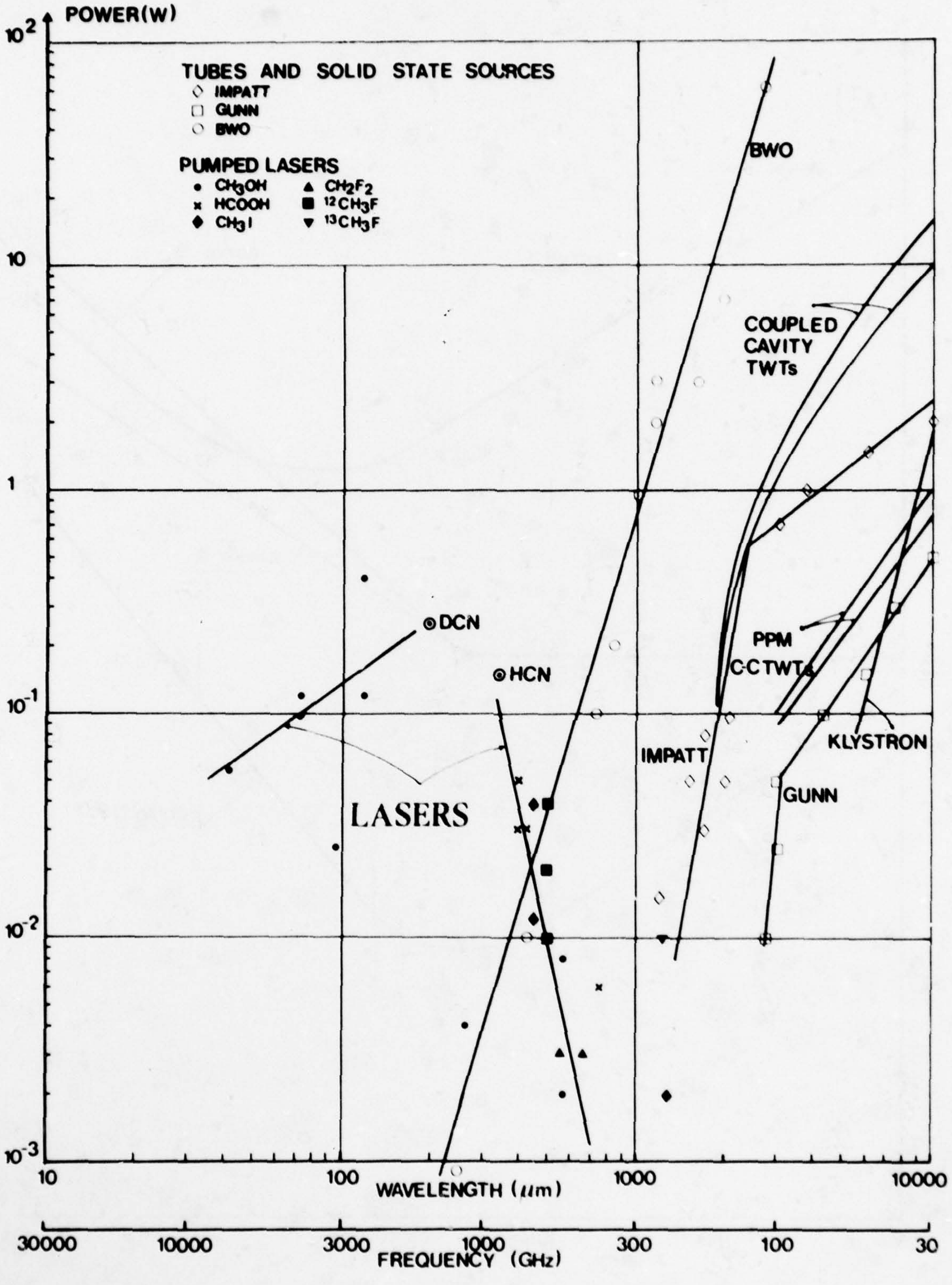

Fig.2 Millimetric and submillimetric wave sources

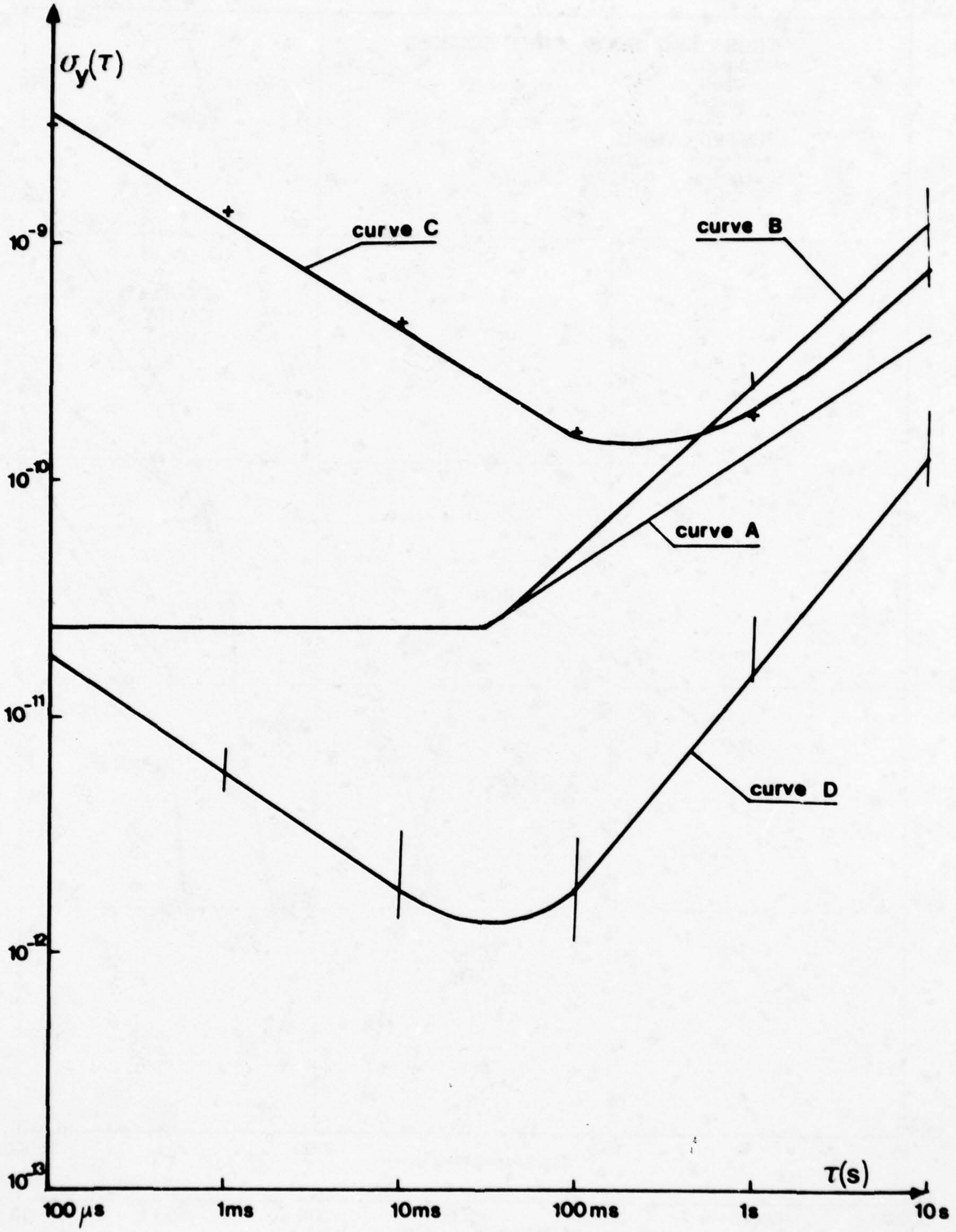

Fig.3 Frequency stability of the IF signal

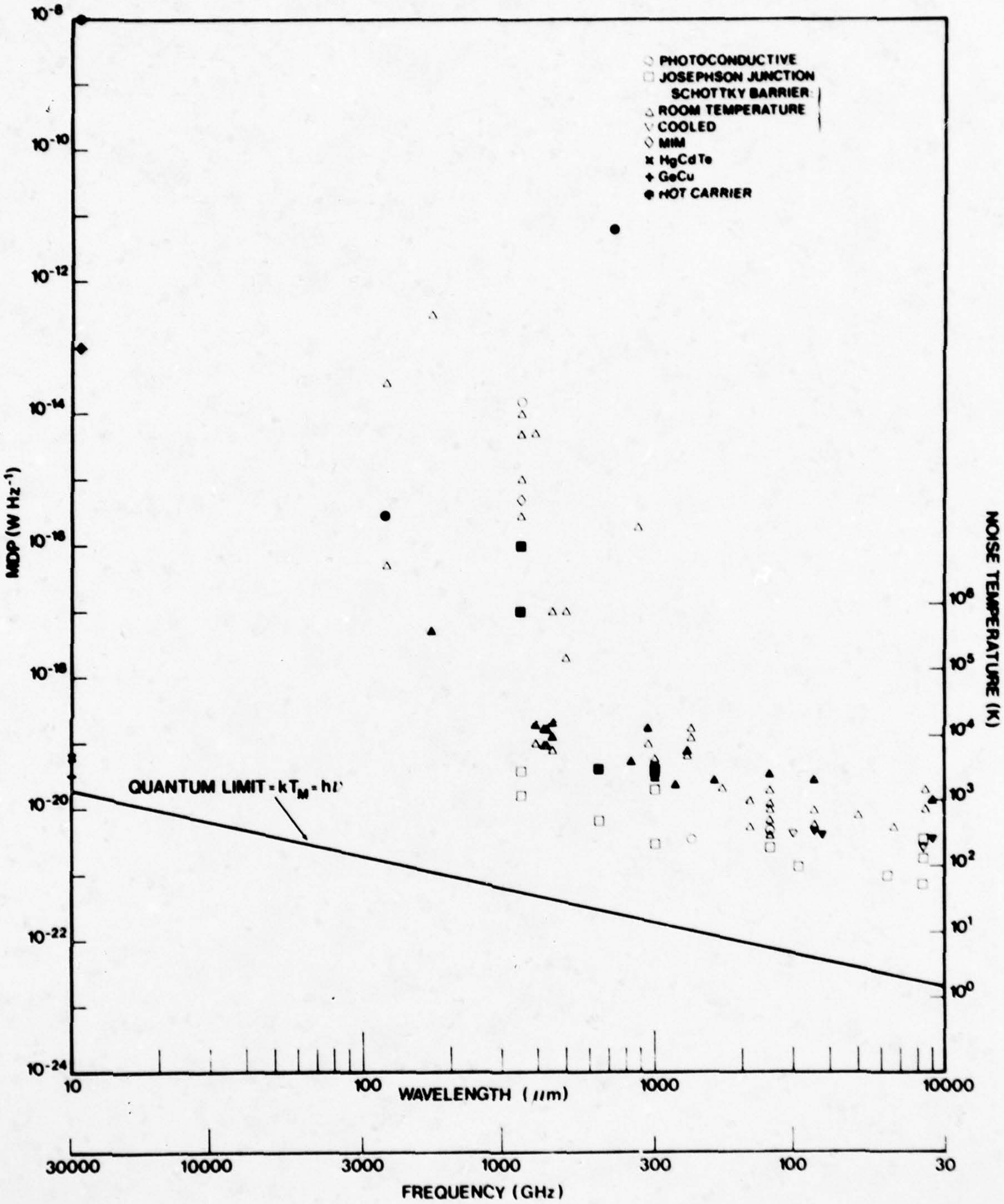

Filled-in data points refer to receivers

Fig.4 MDP for several mixers or receivers

INTEGRATED-CIRCUIT MEDIA FOR MILLIMETER-WAVE APPLICATIONS

Barry E. Spielman
Naval Research Laboratory
Washington, D.C. 20375

SUMMARY

This paper provides an overview and assessment of the principal transmission media which are being considered for integrated-circuit millimeter-wave applications. The paper starts by describing the important problems which are encountered in circuit integration at millimeter wave frequencies, including high transmission line loss, dispersion and higher-order moding, insufficient availability of design data, factors affecting cost, and suitability of transmission lines for component implementation. The principal transmission lines are compared with respect to: unloaded Q; the range of impedance levels which are offered; the anticipated useful frequency range; compatibility with solid state devices; demonstrated utility for critical components like hybrids and filters; availability of transitions to metal waveguide, need for mode suppression techniques; availability of design data; and other general considerations. The paper concludes with a summary of the outstanding features of these transmission media with particular attention to cost considerations and application areas (e.g., suitability for wideband or narrowband system applications).

1. BACKGROUND

There is considerable interest in investigating and exploiting new transmission lines for use in integrated circuits operating at higher microwave and millimeter-wave frequencies. This interest has been spurred by the success in effecting reductions in circuit cost, size, and weight through the application of microstrip at lower to intermediate microwave frequencies. Unfortunately, microstrip is discouragingly lossy and more difficult to fabricate at higher microwave and millimeter-wave frequencies. These considerations have prompted the search for transmission lines that are amenable to integrated-circuit fabrication methods and which have improved loss characteristics.

The search for transmission lines which are suitable for use in circuit integration at millimeter-wave frequencies is paced by the following problems. As frequency increases dissipation losses increase due to both conductor and dielectric loss effects. As frequency increases dispersion becomes more significant in quasi-TEM transmission lines and more caution must be used to either prevent or suppress higher-order moding in the circuits. A deficiency of information existed to assess the fundamental propagation characteristics (e.g. impedance, phase velocity, dissipation loss, and dispersion) of several new transmission line configurations and even to design practical circuits using previously conceived line configurations.

In addition to determining transmission lines with attractive fundamental characteristics, these transmission lines must also be suitable for millimeter-wave circuit applications with respect to other performance facets, compatibility with fabrication constraints, and cost. Consideration must be given to the capability for incorporation of solid-state devices, compatibility with thin film and photolithographic fabrication tolerances, and surface finish requirements. Finally, the ultimate circuits must be cost effective for the intended application.

The next two sections of this paper describe research efforts performed in the Microwave Technology Branch of the Naval Research Laboratory to provide fundamental data for dissipation losses and dispersion, respectively, for a variety of transmission media. The efforts also provided design data and tools to augment the component technology base. The results derived from these research efforts helped to augment the available information provided in the overview of millimeter-wave integrated-circuit media presented in section 4. of this paper.

2. DISSIPATION LOSSES

A computer-aided analysis for determining fundamental propagation characteristics in quasi-TEM transmission structures was formulated and implemented for use on digital computers. This analysis employs a method-of-moments boundary value problem solution using the equivalent charge principle (pulse expansion functions with point matching of boundary conditions). The analysis is capable of analyzing virtually any uniform, isolated or coupled transmission lines having cross sections composed of conductors and inhomogeneous (or homogeneous) dielectrics. For a specified isolated line configuration the analysis provides evaluations of: conductor and dielectric loss coefficients, their sum, as well as impedance and phase velocity. Similar evaluations are provided for even- and odd-mode characteristics in coupled-line structures. Some of the isolated transmission line structures analyzed are portrayed in Figure 1. Figure 2 shows a photograph of a two-section directional coupler which employs edge-coupled microstrip with dielectric overlay configurations in the two-coupled line sections. Complete details of the analysis, design curves for losses, and documentation for five, user-oriented computer programs (each program applicable to a configuration depicted in Figure 1 or 2) have been documented (SPIELMAN, B.E.., 1976 and SPIELMAN, B.E.., 1977). The accuracy of this analysis has been found to be within 0.01 dB/λ for conductor loss coefficients and within 1-2 percent for dielectric loss coefficients, these determined from tests on microstrip.

3. DISPERSION AND HIGHER-ORDER MODING

In order to provide a design tool and information on dispersion for a broad class of transmission media, a method-of-moments analysis was formulated using an equivalent current (electric and magnetic) representation. The moment solution applies pulse expansion functions together with point matching of the boundary conditions.

The solution has been programmed or use on a digital computer and has the following attributes:

1. It is capable of evaluating fundamental and higher-order mode propagation coefficients and cutoff frequencies.
2. Virtually any isolated or coupled-guide structure cross sections can be analyzed.
3. It treats inhomogeneously loaded guiding structures including packaging effects.

The correlation of results determined by this analysis for microstrip in a box with those of (MITTRA, R. and ITOH, T.., 1971) for the fundamental mode and (YAMASHITA, E. and ATSUKI, K.., 1976) for higher-order modes is seen in the dispersion plot shown in Figure 3. Figure 4 shows a dispersion plot for the transmission line cross section depicted in Figure 1d. Here, W represents the width of the strip and H represents the distance from the strip to the channel "bottom." This represents the first such design information produced for this relatively new transmission line. The dimensions of the configuration which was analyzed to provide the results in Figure 4 were purposely chosen to be compatible with microwave frequency circuit dimensions. It is to be observed that the higher-order mode cutoff frequencies (17.5 GHz and 23 GHz) fall well below the low end of the millimeter-wave frequency band. The analysis described here has been documented (GANGULY, A. and SPIELMAN, B.E.., August 1977 and December 1977).

4. OVERVIEW

Figure 5 shows generic cross sections for planar oriented transmission lines which offer some attractive features for circuit integration at millimeter-wave frequencies. Image line (and other dielectric-based guiding structures), fin line, and slot line are inherently non-TEM structures. Microstrip, coplanar waveguide, inverted microstrip, trapped inverted microstrip, and suspended strip line are quasi-TEM in nature.

Image line consists of a strip-like dielectric slab affixed to a metal ground plane. The dielectric materials commonly employed include: boron nitride, alumina, and high-resistivity silicon. Most efforts to date have employed machining processes to shape the dielectric slab.

Fin line is composed of a dielectric substrate affixed in a rectangular waveguide-like package with the substrate in the E-field plane of the "metal waveguide." Circuits are fabricated by photolithographically defining slots in metal which is deposited on the substrate. Slot line is akin to fin line, but conceptually has no surrounding metal guide or package. Dielectric materials employed are duroid, fused silica, quartz, alumina, and sapphire.

Microstrip is well-known and included for completeness. Materials commonly used at millimeter-wave frequencies include fused silica, quartz, and duroid.

Coplanar waveguide consists of a metal strip and two symmetric ground planes photolithographically fabricated on a common dielectric substrate side. Dielectrics employed have included sapphire and duroid.

Inverted microstrip employs a metal strip fabricated photolithographically on a dielectric substrate with an air region between the strip and ground plane. Since this line has a greater percentage of total energy in air than microstrip, by comparison a broader line width is possible for a prescribed impedance. Hence, fabrication constraints are relaxed and conductor dissipation losses can be diminished.

Trapped inverted microstrip is similar to inverted microstrip, but has the ground plane turned up to each side of the strip. This ground plane "channel" affords the additional feature of inherent suppression of certain higher-order modes.

Suspended strip line is akin to trapped inverted microstrip but has a completely shielding ground structure.

4.1. Unloaded Q

Figure 6 depicts representative values of unloaded Q for the transmission lines portrayed in Figure 5. The dielectric constants for the substrate materials used for this portrayal were selected to be those of commonly used materials. It is to be noted that these lines fall into roughly three categories:

1. Those having Q's ranging from approximately 100-200.
2. Those having Q's ranging from 400-700.
3. Image line having a theoretical Q of about 2500.

It is to be noted that the theoretical unloaded Q for image line has not yet been realized routinely in practice, due to problems which will be discussed in section 4.3(d). Furthermore, in practice it is the loaded Q for specific applications which is of primary importance.

4.2. Impedance Levels

Table I shows the anticipated ranges of impedance levels available for millimeter-wave circuit applications for the candidate transmission lines shown in Figure 5. These impedance ranges have been determined for commonly used materials at frequencies up through approximately 100 GHz. For the following reason only a single value (approximate) for image line is presented. Presume that fundamental mode operation is desired. As the operating frequency decreases toward the fundamental mode cutoff frequency the energy becomes less confined to the slab and impractical "cross-talk" effects can result. As the operating frequency increases from the fundamental mode cutoff operation is eventually limited by the cutoff frequency of the first, higher-order mode. It is not precisely known how close operation may be to the currently known estimated values for this frequency. The value of 26 ohms shown in Table I corresponds to operation about midway between these two cutoff frequency values.

TABLE I. - IMPEDANCE LEVELS

	(OHMS)
Image Line	∿ 26
Fin Line	10-400
Slot Line	60-200
Microstrip	20-125
Coplanar Waveguide	40-150
Inverted Microstrip	25-130
Trapped Inverted Microstrip	30-140
Suspended Stripline	40-150

4.3. General Comments

Sections 4.3(a) through 4.3(d), highlight what are deemed to be significant technological facets of the circuit technologies employing: microstrip, trapped inverted microstrip, fin line, and image line, respectively.

(a) It is anticipated that approximately 60 GHz is the upper frequency limit for extensive utility of microstrip in system applications. This limitation results from the combination of techniques required for moding suppression, fabrication tolerances, and handling fragility. The compatibility of this line with solid-state device (e.g. Gunn and IMPATT diodes) incorporation requriements is judged to be fair to good. The compatibility of microstrip for incorporation of packaged devices is somewhat poorer than for chip or beam devices due to problems associated with parasitic effects. Quadrature hybrids implemented in microstrip have been primarily the branch line and coupled comb-like type (GUNTON, D.J. and PAIGE, E.G.S.., 1975). Due to the relatively low-value of unloaded Q for microstrip, bandpass (approximately 10 percent bandwidth) are relatively difficult to achieve. Transitions from standard waveguide to microstrip (for equipment interfacing) have been developed using: probe-like feeds, ridge-like tapers and steps, and photolithographically fabricated baluns (LAVEDAN, L.., 1977). Some channelization is necessary in microstrip to suppress higher-order moding. Design information is fairly readily available for most circuit requirements using microstrip, however a deficiency exists in accurate characterizations for discontinuities (e.g. T-junctions).

(b) Trapped inverted microstrip may well have utility for applications up through 95 GHz. There has currently been little exploitation of the line for millimeter-wave applications due to the previous unavailability of fundamental design information. The compatibility of this line with solid-state devices is not yet known. However, trapped inverted microstrip may have better compatibility than microstrip by virtue of its "built-in" capability for mode suppression and better facility for incorporating shunt, as well as series, mounted devices. Preliminary transitions to standard waveguide have been developed using probe-like launchers. Some design information is available for circuit applications (SPIELMAN, B.E.., 1976) and (GANGULY, A.K. and SPIELMAN, B.E.., August and December 1977).

(c) Fin line appears to be useful in the range from about 30 through 100 GHz. The compatibility of fin line with solid-state devices is judged to be fair for packaged and chip devices and somewhat better for beam-lead devices. Some complications arise in biasing multi-function circuits and in heat-sinking techniques. Quadrature hybrids of the branch line type (DE RONDE, F.C.., 1970) using slot line appears to be feasible in this line. Bandpass filters (approximately 10 percent bandwidth) are reasonably good in this line. Transitions to waveguide have been developed using ridge-like transitions. It is to be noted that the fin line package is operationally a part of the waveguide structure and must be considered for circuit design purposes. Some design information is available for this structure (HOFMANN, H.., 1977).

(d) Image line seems likely to be especially useful at frequencies above 100 GHz. The compatibility of this line with solid-state devices is deemed poor to fair. Problems arise in developing repeatable, cost-effect device mounts. This guiding structure tends to radiate at discontinuities and offers complications for heat sinking due to the lack of metal proximity at the circuit surface. Quadrature hybrids to date are the proximity, optical-type couplers (BARNOSKI, M.K. [ed.], 1974), which are dispersive and inherently narrowband. Theoretically filters are good, but difficulties have been encountered in practice. Techniques for precisely aligning circuit patterns have not yet been completely developed. Adhesives used to affix the dielectric slab patterns to the ground plane are currently excessively lossy, thereby lowering the circuit Q. Additional problems to be addressed include the reduction of radiation and mutual coupling from device mounts and line bends. Transitions to waveguide employ tapering of the dielectric slab as it proceeds into the waveguide. Some design information is available (TOULIOS, P.P. and KNOX, R.M.., 1970).

5. CONCLUSIONS

It is of interest to assess the prospects of various circuit-integration media for applications. For perspective, this is done also for the more well-established metal waveguide technology. Metal waveguide technology is relatively expensive (in part due to low volume of system applications), generally high performance, and is particularly useful for high-performance components and systems, high-power applications, and test equipment.

Microstrip offers a high degree of potential for integration. It is relatively inexpensive and small, however the losses are relatively high. The anticipated application area for microstrip is in moderately wide to wideband components and systems.

Fin line offers a moderate degree of potential for integration. It combines printed circuit techniques with good performance and offers some reduction in cost and size. Its application appears to be reasonable in narrowband to moderately wideband components and systems. Similar remarks seem appropriate for inverted microstrip, trapped inverted microstrip, and suspended strip line.

Image line offers potentially low losses. However, problems related to radiation must be addressed. The need to gradually bend image line to minimize radiation leads to relatively large circuits. To date, the cost effectiveness of this technology is unconfirmed except for a limited number of components (e.g. hybrids). This technology seems most suitable for use in narrowband to moderately narrowband systems and components.

Finally, it is anticipated that the integration of multi-function circuits at millimeter-wave frequencies is likely to require the use of more than one type of circuit technology to achieve high-performance.

ACKNOWLEDGEMENTS

The author expresses his to Dr. Ulrich Geysel for the information he contributed. Thanks also go to Dr. Achintya Ganguly for his contributions to the work on dispersion.

REFERENCES

BARNOSKI, M.K. [ed.], 1974), "Introduction to Integrated Optics," Plenum Press.

DE RONDE, F.C., 1970, "A New Class of Microstrip Directional Couplers," 1970 IEEE G-MTT Symposium Digest, pp. 184-189.

GANGULY, A.K. and SPIELMAN, B.E., August 1977, "A Method-of-Moments Solution for Dispersion Characteristics of Arbitrarily Configured Transmission Media," NRL Memorandum Report #3581.

GANGULY, A.K. and SPIELMAN, B.E., December 1977, "Dispersion Characteristics for Arbitrarily Configured Transmission Media," pp. 1138-1141.

GUNTON, D.J. and PAIGE, E.G.S., 1975, "Directional Coupler for Gigahertz Frequencies Based on the Coupling Properties of Two Planar Comb Transmission Lines," Electron. Lett., pp. 406-408.

HOFMANN, H., 1977, "Calculation of Quasi-Planar Lines for Mm-Wave Application," 1977 IEEE MTT-5 International Microwave Symposium Digest," pp. 381-384.

LAVEDAN, L., 1977, "Design of Waveguide to Microstrip Transitions Specially Suited to Millimeter Wave Applications," Electron. Lett., pp. 604-605.

MITTRA, R. and ITOH, T., 1971, "A New Technique for the Analysis of the Dispersion Characteristics of Microstrip Lines," IEEE Trans. Micr. Th. Techs., pp. 47-55.

SPIELMAN, B.E., 1976, "Computer-Aided Analysis of Dissipation Losses in Isolated and Coupled Transmission Lines for Microwave and Millimeter-Wave Applications," NRL Formal Report #8009.

SPIELMAN, B.E., 1977, "Dissipation Loss Effects in Isolated and Coupled Transmission Lines," IEEE Trans. Micr. Th. Techs, pp. 648-656.

TOULIOS, P.P. and KNOX, R.M., 1970, "Rectangular Dielectric Image Lines for Millimeter Wave Integrated Circuits," Western Electronic Show and Convention, Los Angeles, CA.

YAMASHITA, E. and ATSUKI, K., 1976, "Analysis of Microstrip-Like Transmission Lines by Nonuniform Discretization of the Integral Equation," IEEE Trans. Micr. Th. Techs, pp. 195-200.

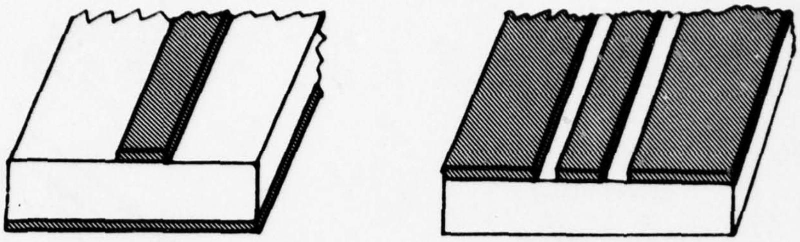

STANDARD MICROSTRIP

1a

COPLANAR WAVE GUIDE

1b

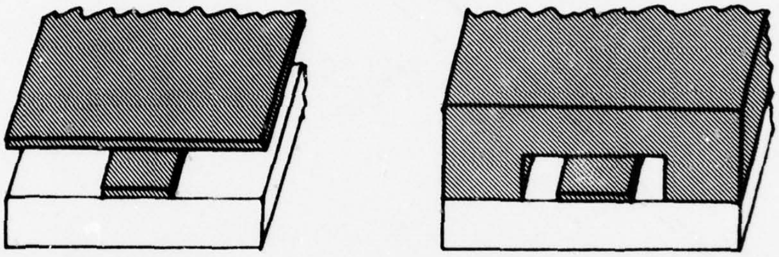

INVERTED MICROSTRIP

1c

TRAPPED INVERTED MICROSTRIP

1d

Figure 1. Four isolated transmission lines analyzed using loss analysis.

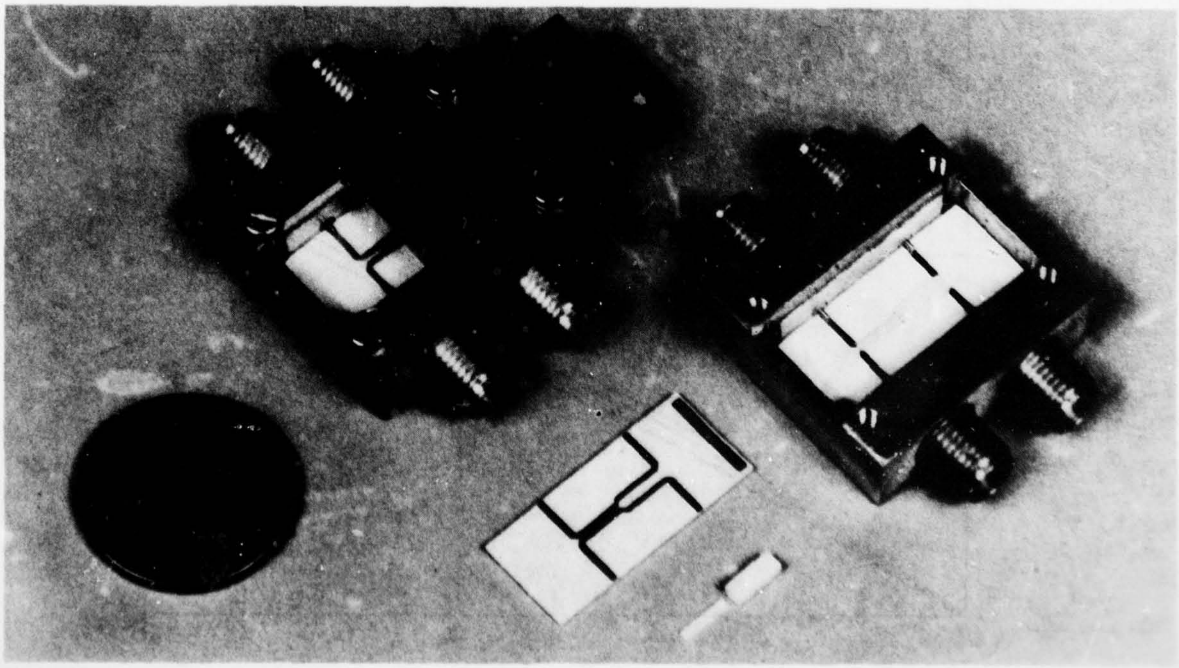

Figure 2. Three partial assemblies of a two-section coupler employing edge-coupled microstrip with a dielectric overlay

AD-A069 015　ADVISORY GROUP FOR AEROSPACE RESEARCH AND DEVELOPMENT--ETC　F/G 17/2.1
MILLIMETER AND SUBMILLIMETER WAVE PROPAGATION AND CIRCUITS.(U)
FEB 79　E SPITZ, G CACHIER
UNCLASSIFIED　AGARD-CP-245　NL

3 OF 6
AD
A069015

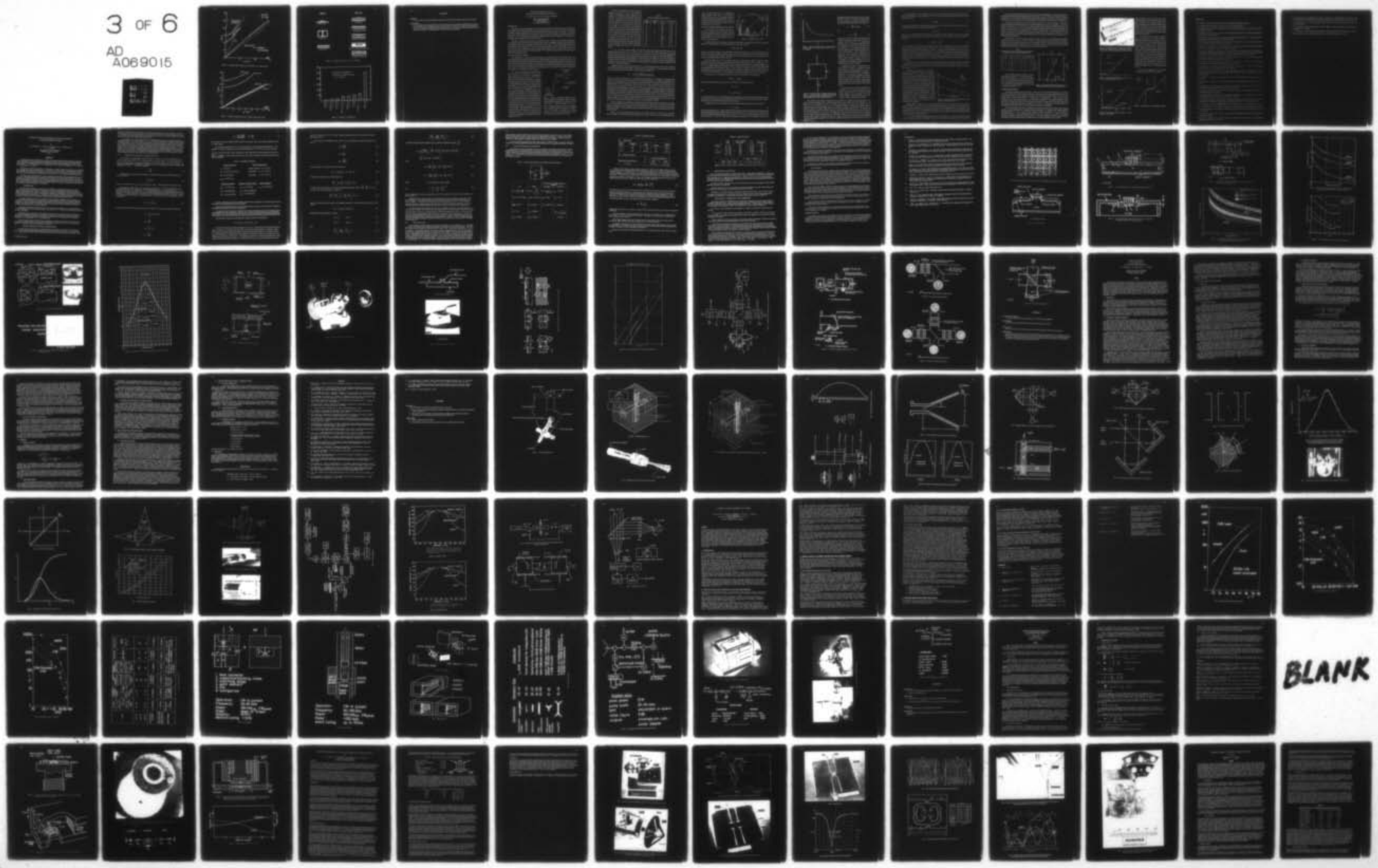

BLANK

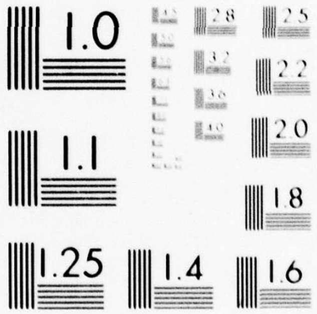
1.0
2.8
2.5
3.2
2.2
3.6
4.0
2.0
1.1
1.8
1.25
1.4
1.6

MICROCOPY RESOLUTION TEST CHART
NATIONAL BUREAU OF STANDARDS 1963 A

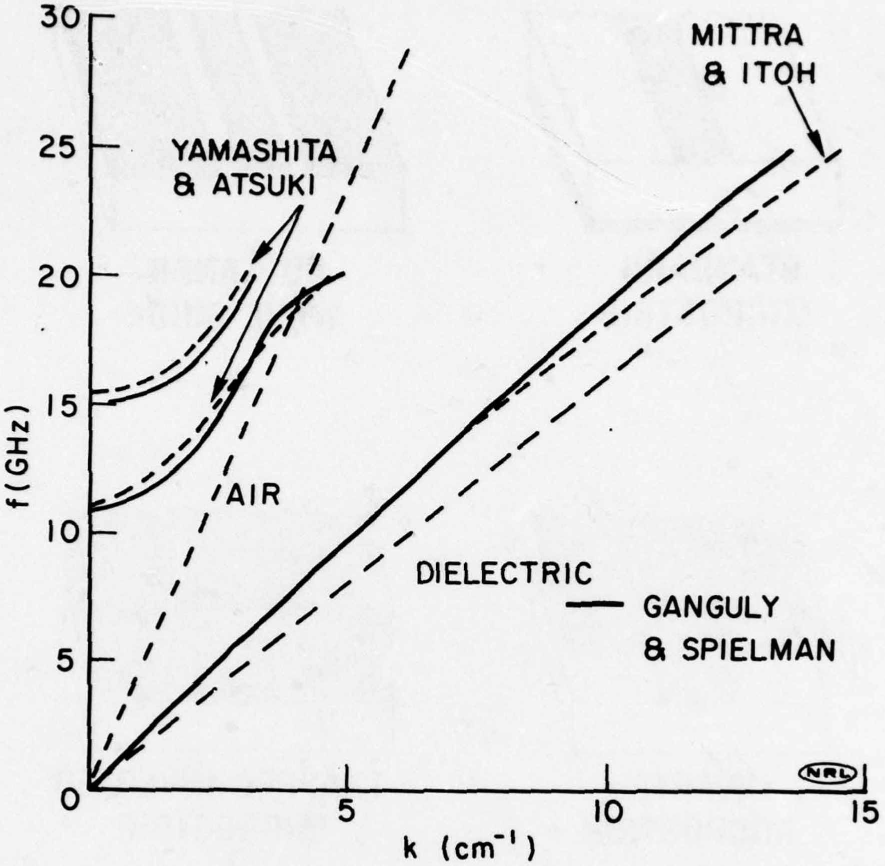

Figure 3. Dispersion characteristics for microstrip in a conducting box.

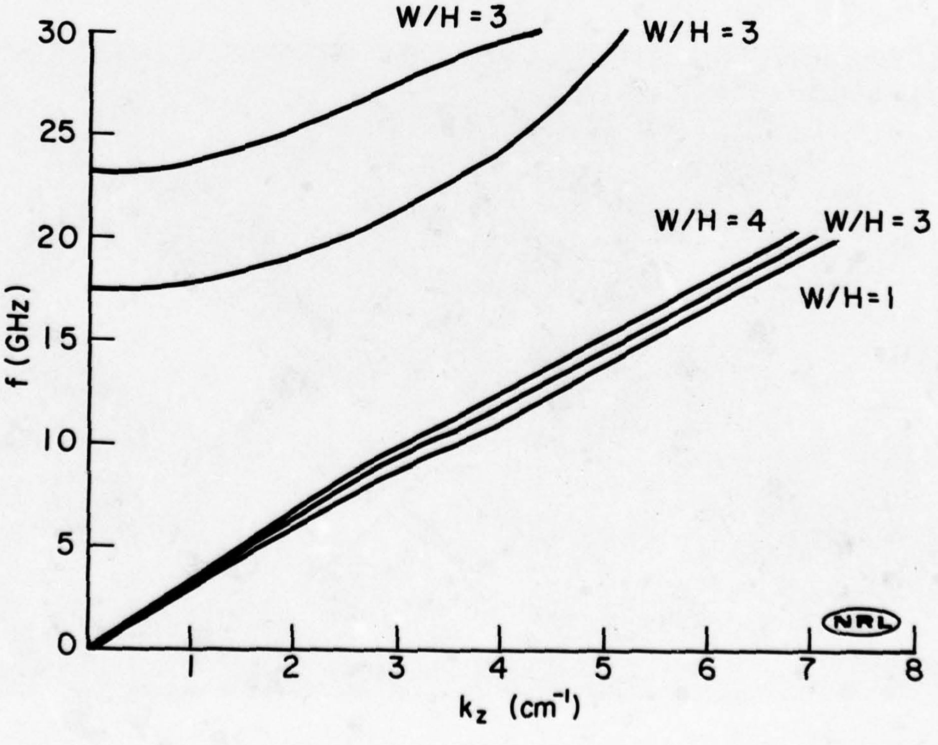

Figure 4. Dispersion characteristics for trapped inverted microstrip.

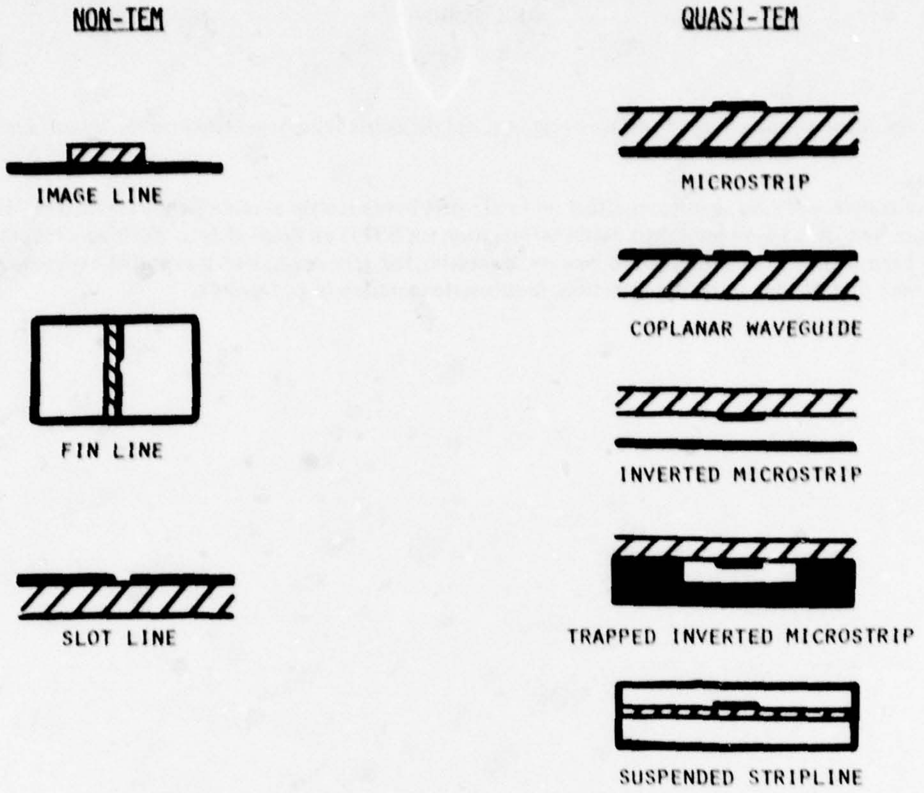
NON-TEM
QUASI-TEM
IMAGE LINE
FIN LINE
SLOT LINE
MICROSTRIP
COPLANAR WAVEGUIDE
INVERTED MICROSTRIP
TRAPPED INVERTED MICROSTRIP
SUSPENDED STRIPLINE

Figure 5. Transmission lines for circuit integration.

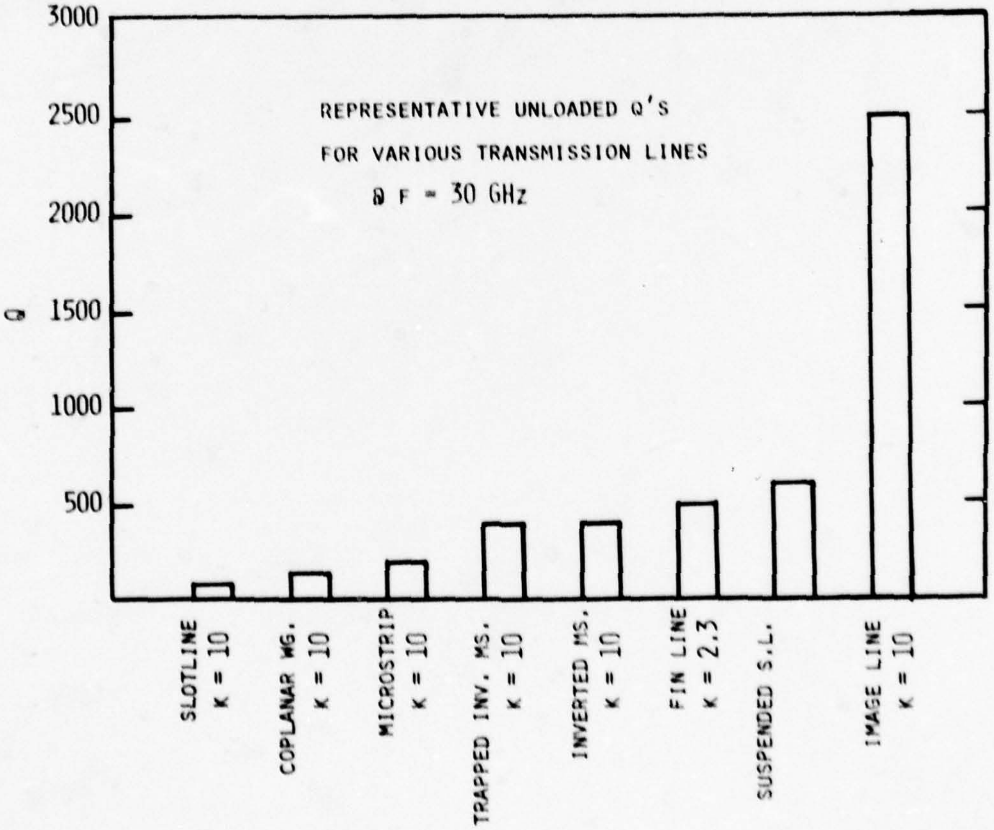

Figure 6. Comparison of unloaded Q's.

DISCUSSION

P.S.Hall, UK

Can you comment on the effect of surface roughness and dielectric inhomogeneities on the losses in microstrip?

Author's Reply

Surface roughness can have significant effect on total losses in microstrip at millimeter wavelengths, M.V.Schneider, et al. (from Bell Labs.) have published useful information (in BSTJ) on these effects. Dielectric inhomogeneities have not been treated as extensively. Microwave Associates, Inc. (for example) has reported experiencing deleterious effects above 40 GHz due to inhomogeneities, in substrate materials (e.g., Duroid).

ADVANCED TECHNOLOGY FOR THE MILLIMETER AND SUBMILLIMETER WAVE REGION

D. T. Hodges, M. McColl, A. H. Silver and T. S. Hartwick

Ivan A. Getting Laboratories
The Aerospace Corporation
P.O. Box 92957
Los Angeles, California 90009

INTRODUCTION

There has been an increasing interest in new systems that will utilize the submillimeter or near millimeter wave spectral region, which includes wavelengths between approximately 100 μm and 2 mm. This interest is stimulated by the steadily improving technology base for sources, receivers, and other components in this band. For example, hundreds of new laser sources have been discovered in the past several years with powers of 10-100 mW cw and 0.1-1.0 MW pulsed.[1] Also, several groups are successfully extending low noise receiver technology into the submillimeter wavelength region using junction type detectors and mixers.[2]

This paper summarizes recent research at our laboratory related to millimeter and submillimeter applications. The emphasis has been on laser sources and wideband junction detectors, and highlights of our work will be presented on (1) developing cw laser sources that operate between 100 μm and 1.5 μm,[1,3-5] (2) extending Schottky barrier mixer diode operation to THz frequencies,[2,6-8] and (3) developing a new cryogenic variation of the Schottky diode.[9-12] This latter device, called the super-Schottky diode, employs a superconducting contact to a heavily doped semiconductor, and is the most sensitive detector of microwave radiation.[11,12] Prospects for extending this record performance to NMMW frequencies are discussed.

OPTICALLY PUMPED CW LASERS

The development of the submillimeter spectral region has been hampered by the lack of coherent sources. This region typically utilizes a blend of technology from the optical-infrared and microwave-millimeter wave regions. The small dimensions and subsequently strict tolerances required for conventional waveguide cavity structures have slowed the extension of microwave cavity oscillators to these frequencies. The availability of good sources improved markedly with the successful development of quantum electronic techniques[13] for generating submillimeter and millimeter wave laser emissions. Our efforts have concentrated on developing cw sources, at the $10-10^3$ mW level, that are suitable as transmitters or as local oscillators in receiver systems.

The problem of generating laser radiation stems from the small energy separation between the lasing levels, typically much less than kT. Wavelengths of 100 μm-1000 μm correspond to energies of 10^{-2} - 10^{-3} eV. Electrical discharge and chemical excitation of the upper laser state are not feasible because of the poor selectivity of the pumping process. However, a very useful approach was invented in 1970[13] that consists of optically pumping polar molecules with an efficient infrared laser such as CO_2. The basic process is illustrated in Fig. 1. The accidental near-coincidence (< 100 MHz) between a vibrational-rotational absorption line of a polar molecule and the infrared laser line leads to selective population of a particular rotational sublevel in an excited vibrational state. The subsequent population inversion between adjacent rotational states and the large transition matrix element provided by the permanent moment of the molecule produces high gain (0.1 - 1.0 m^{-1}) and laser emission on pure rotational transitions throughout the 40 μm - 2 mm spectral band. This specific and selective excitation technique overcomes the difficulty of creating an inversion between closely spaced levels and the technique has proven to be very universal with approximately 1000 lines cataloged to date.[14,15]

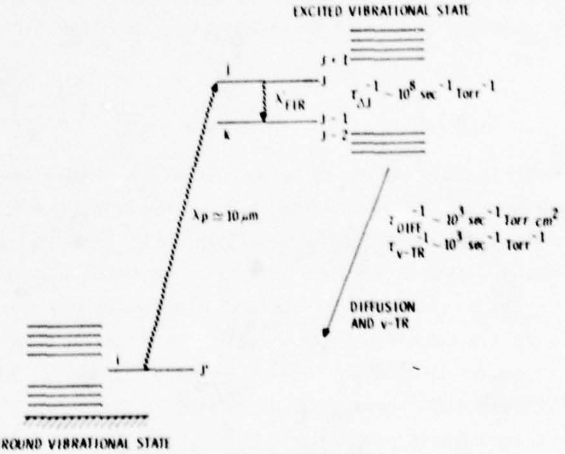
EXCITED VIBRATIONAL STATE
J + 1
J
J - 1
J - 2
λ_{FIR}
$\tau_{\Delta J}^{-1} \sim 10^8$ sec^{-1} Torr^{-1}
$\lambda_p \simeq 10$ μm
$\tau_{DIFF}^{-1} \sim 10^3$ sec^{-1} Torr cm^2
$\tau_{V-TR}^{-1} \sim 10^3$ sec^{-1} Torr^{-1}
DIFFUSION AND V-TR
J'
GROUND VIBRATIONAL STATE

Figure 1. Schematic energy level diagram of polar molecule showing laser pumping at 10 μm with subsequent submillimeter lasing between adjacent rotational states J and J-1. Collisions occurring at a rate $\tau_{\Delta J}^{-1}$ tend to thermalize population among the rotational levels. Vibrational relaxation occurring by either diffusion or V-TR processes is relatively slow. Pressure dependence of these rates limits steady state inversion and cw operation to pressures of only 0.1 Torr.

Besides the development of a fundamental understanding of the laser dynamics[16,17] our research has stressed the development of laser structures that are optimal for the optically pumped submillimeter laser process[3-5]. The laser takes on a relatively simple structural form, consisting of a cell with mirrors at each end. The pump radiation is admitted through a small hole in one of the end mirrors, and the second mirror can also be a "hole coupler" or a more sophisticated hybrid coupler which permits a fraction of the laser mode energy to be coupled out while confining the pump-radiation within the cell. The cavity must be low loss and mode selective at the near millimeter laser wavelengths and also low loss for the injected pump radiation. The typical absorption coefficients of the polar gases are 10%/m at the laser operating pressure and thus the pump must make several passes inside the laser resonator for efficient absorption. The best performance has been obtained using hollow dielectric waveguides and this work is summarized in Table 1.

TABLE 1

Summary of Strong cw Laser Transitions

WAVELENGTH (μm)	OUTPUT POWER (mW)	MOLECULE	CO_2 LASER PUMP LINE
119	400	CH_3OH	9.6 P(36)
265	3.6	CH_3OH	9.6 P(34)
306	3	CH_3OD	9.3 R(8)
372	1	CH_3CN	10.6 P(20)
393	50	HCOOH	9.3 R(18)
420	30	HCOOH	9.3 R(18)
433	35	HCOOH	9.3 R(20)
447	40	CH_3I	10.6 P(18)
496	10	CH_3F	9.6 P(20)
554	3	CH_2CF_2	10.6 P(14)
570	8	CH_3OH	9.6 P(16)
662	.3	CH_2CF_2	10.6 P(24)
744	6	HCOOH	9.3 R(20)
890	4	CH_2CF_2	10.6 P(22)
1020	0.1	CH_2CF_2	10.6 P(14)
1222	10	$^{13}CH_3F$	9.6 P(32)
1253	2	CH_3I	10.6 P(32)

It is clear from Table 1 that performance is significantly worse for wavelengths longer than 500 μm with the notable exception of the 1222 μm line in $C^{13}H_3F$. There is no theoretical basis to expect efficiency to decline with wavelength, but our efforts to improve the millimeter wave performance of these lasers have been disappointing.[18] Only a few lines are observed in laser structures optimized for millimeter wave operation. Since the percentage of the cataloged transitions that exhibit strong performance (as defined by the list in Table 1) is very small, it is reasonable to continue the search for millimeter wavelength lasers. Certainly a collection of millimeter laser lines with performance comparable to the 1222 μm line would be valuable, since the availability of these sources would be widespread and this would spur the technology development.

Significantly, even the best reported performance[1,4,5] for optically pumped lasers is still an order of magnitude less than the maximum allowed theoretically. In mathematical form, the efficiency of converting infrared pump power P_p into near millimeter power P is determined from rate equation modeling to be[17]

$$\frac{P}{V} = 1/2\left(\frac{h\nu}{h\nu_p}\right)\left(\frac{P_p}{V}\right)\left(\frac{T}{A+T}\right)\left(\frac{\gamma L}{\gamma L + a_p}\right) \tag{1}$$

where V is the volume of active medium, ν_p the frequency of pump radiation, ν the frequency of the generated laser radiation, T the mirror transmission, A the cavity loss for submillimeter radiation, γ the absorption coefficient for the pump, L the cavity length, and a_p the cavity losses at the pump wavelength. The meaning of the parenthetical terms is straightforward: the first term expresses the Manley-Rowe limit or maximum power conversion; the second term is simply the pump power injected into the cavity; and the next two terms express the cavity efficiency at the submillimeter and pump wavelengths, respectively. Most of the improvement in cw laser performance is attributable to increasing the cavity efficiency at the pump and far infrared wavelengths. For example, significant fruitful efforts have resulted in developing output coupling mirrors that efficiently reflect the pump radiation but allow a fraction of the far infrared laser mode to be transmitted. With few exceptions, typical values of α at the laser operating pressure are 0.1 m^{-1} so that the cavity losses at the pump wavelength, a_p, must be kept low for efficient conversion. This is the stringent condition on cavity design, especially when low loss is required simultaneously for two wavelengths whose ratio is 10 - 100. Further work is necessary to account for the present efficiency limitations.

If true cw operation is not essential, one can increase the submillimeter output power by pulsing the CO_2 pump laser. For example, pulses 200 μsec FWHM have been generated at the 1-2 Watt level for several lines in the 100-500 μm region. This quasi-cw mode of operation is useful for studying transient phenomena or to increase peak-power for nonlinear experiments. It is also possible to actively or passively Q-switch the CO_2 laser and generate 0.5 μsec pulses at the 0.1 kW level.

Finally, it is worth comparing cw laser sources to other sources in the band. As seen from Fig. 2, the laser source is dominant at the short submillimeter wavelengths, but probably over-matched at wavelengths longer than

1 mm. The laser suffers from lack of tunability, but exhibits excellent spectral purity. Free-running laser linewidths are less than 1 kHz and phase-locking can provide very precise frequency stabilization. The number of available strong laser transitions should increase and eventually provide a rich spectrum of discrete frequencies with power near the 100 mW level.

SCHOTTKY-BARRIER SUBMILLIMETER WAVE MIXERS

Of the various devices explored as mixers at submillimeter wavelengths, the Schottky-barrier diode has received the greatest attention. Its inherent sensitivity, wide bandwidth, room temperature operation, and mechanical stability make it an attractive choice for a variety of system applications.

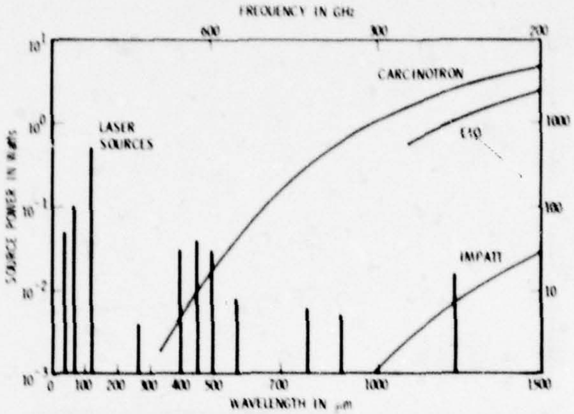

Figure 2. Comparison of cw sources.

The Schottky-barrier diode developed in this laboratory consists of a metal contact deposited on a semiconductor substrate. Its current-voltage (I-V) characteristic is given to a good approximation by

$$I = i_o \left(\exp \frac{qV}{nkT} - 1\right) \tag{2}$$

where q is the elecronic charge, T is the temperature, k is Boltzman's constant, i_o is the saturation current which is determined by the area and material parameters of the diode, and n is the ideality factor which is approximately unity for low- to moderately-doped materials. This highly non-linear relationship between I and V is responsible for the success of the Schottky diode as a detector and mixer.

This diode operates as a mixer in a fashion typical of the rectifying type of diode.[19] A large LO voltage is impressed on the diode to obtain a time-dependent conductance g(t) which is periodic in the LO frequency f_1. In the presence of a signal voltage at frequency f_s, currents and voltages are generated at the intermediate frequency $f_{IF} = f_1 - f_s$. [For example, analytically a sinusoidal IF current is produced from the product of the sinusoidal signal voltage and the fundamental Fourier component of g(t).] For low LO powers, the efficiency of this conversion process is a strong function of qV_1/nkT, where V_1 is the amplitude of the impressed LO voltage. At large LO power the conversion efficiency of the device saturates at a value determined by the impedance terminations at its input and output ports.

The sensitivity of a mixer (receiver) expressed as the minimum detectable power $MDP_M(MDP_R)$ is

$$MDP_{M,R} = kT_{M,R}B_{IF} \tag{3}$$

where B_{IF} is the IF bandwidth, and $T_M(T_R)$ is the mixer (receiver) noise temperature given by

$$T_M = L_cT_d \tag{4}$$

and

$$T_R = L_c(T_d + T_{IF}). \tag{5}$$

L_c is the conversion loss of the mixer, defined as the ratio of available power from the RF source to the power absorbed in the IF load. T_d and T_{IF} are the noise temperatures of the mixer diode and IF amplifier, respectively. Hence in fabricating a mixer, utmost attention must be paid to minimizing L_c.

Conversion loss of a mixer in a tunable mount is conveniently expressed as the product of three terms[7,20]

$$L_c = L_0L_1L_2. \tag{6}$$

The intrinsic conversion loss L_0 is that loss arising from the conversion process within the nonlinear resistance of the diode and includes the impedance mismatch losses at the RF and IF ports. L_0 as a function of qV_1/nkT for a properly-terminated sinusoidally-pumped broadband mixer is shown in Fig. 3. The L_0 of a Schottky-barrier mixer has been recently analyzed as a function of diode diameter, impedance, temperature and the Richardson constant of the

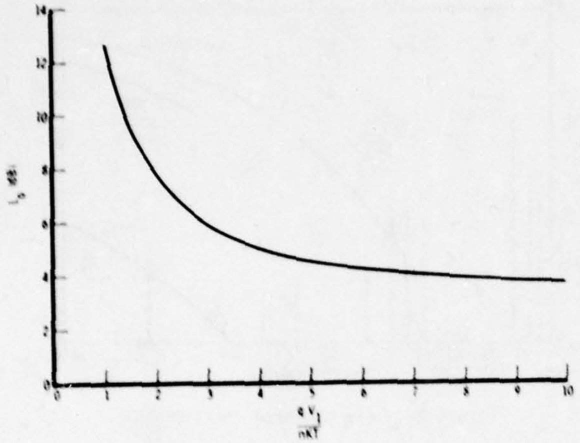

Figure 3. Intrinsic conversion loss as a function of local oscillator drive for a Schottky-barrier mixer with optimum coupling.

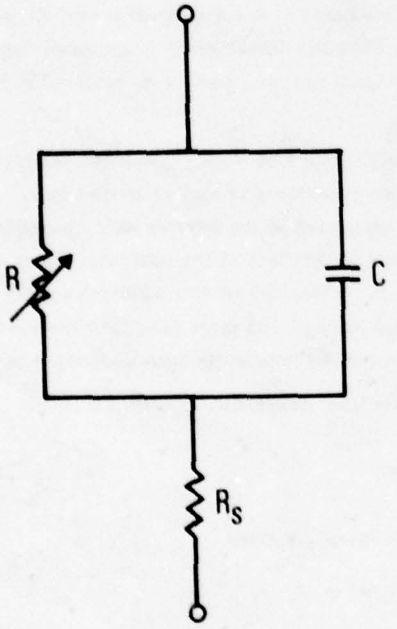

Figure 4. Equivalent circuit of a Schottky barrier diode. R_s and C are the parasitic spreading resistance and junction capacitance and R is the signal input impedance of the local oscillator pumped nonlinear resistance.

semiconductor and found to increase as any one of these quantities is reduced.[21] The RF and IF parasitic losses, L_1 and L_2, respectively, are those losses associated with the parasitic elements of the diode. These are given by

$$L_1 = 1 + \frac{R_s}{R} + \omega^2 C^2 R\, R_s \qquad (7)$$

and

$$L_2 = 1 + \frac{R_s}{R_2}\ , \qquad (8)$$

where R_s and C are the parasitic spreading resistance and junction capacitance, respectively, as shown in the equivalent circuit in Fig. 4, ω is the signal angular frequency, and R_s is the resistance which results from the crowding of the current in the semiconductor near the metal contact. R is the signal input impedance of the local oscillator pumped nonlinear resistance, and R_2 is the IF load impedance. The ω^2 dependence of the third term in Eq. (7) is principally responsible for the degradation in the performance of Schottky-barrier mixers at high frequencies. However, both L_1 and L_2 are geometry and material dependent, and it is by manipulation of these factors in the design of the diode that one reduces L_c at high frequencies.

A straightforward method for minimizing the third term in Eq. (7) is to reduce C. Capacitance is proportional to area, and contact diameters of 1 to 2 μm are commonly obtained by photolithographic techniques. A dimension of 1 μm, however, is near the photolithographic limit. Using electron lithography, diameters as small as 0.1 μm have been obtained.[7] Submicron-size diodes are useful in open or nontunable mounts as single contact diodes and in tunable mounts as multiple contact (contact array) diodes. This latter geometry is discussed below.

The loss terms in Eqs. (7) and (8) are proportional to R_s, which in turn is inversely proportional to the mobility of the semiconductor. N-type GaAs has a large mobility, operates at room temperature, and is commercially available. Nearly all millimeter and submillimeter wave Schottky diodes utilize this material.

The optimized mixer includes a Schottky-barrier diode situated in a structural mount whose functions are to provide the proper imbedding circuit to efficiently couple radiation to the diode, tune out the capacitance, C, and couple the IF and dc signals to the diode. The single-mode waveguide mixer-mount is the standard method at microwave and millimeter wavelengths, but the small dimensions required for submillimeter operation make the fabrication difficult at frequencies higher than 300 GHz and nearly impossible beyond 600 GHz. The fabrication and assembly difficulties encountered during our studies with a single-mode mount at 600 GHz have provided the incentive to try alternate approaches. It is clear that a reconfiguration of the point contact antenna geometry is necessary in order to provide optimal coupling between the submillimeter radiation field and the mixer. Since dimensional tolerances inhibit traditional microwave fabrication, it is natural to consider using "integrated optical" techniques and fabricating monolithically integrated mixer-diode/micro-antenna structures and work toward this goal is now in progress in our lab.

The performance of the super-Schottky mixer, like a conventional Schottky mixer diode, is directly related to the degree of nonlinearity of its I-V characteristic. The I-V curve of either diode can be represented over the voltage range of interest by[25]

$$I = i_o \exp(SV) \tag{9}$$

where i_o is determined by the geometrical and material parameters of the diode. The parameter S, a measure of the nonlinearity of the diode, can be expressed approximately as[25]

$$S = q/k(T + T_o) \tag{10}$$

where T_o is an empirical constant which measures the deviation from ideal behavior, and, as such, is of central importance in the determination of the sensitivity of the diode as either a video detector or mixer. Numerically, Eq. (10) becomes

$$S = 11{,}600/(T + T_o)\ \text{volt.}^{-1} \tag{11}$$

Both experimentally and theoretically for super-Schottky diodes reported by our group, $T_o \ll 1$ K if $kT \ll q\Delta$ where Δ is the superconducting energy gap parameter. Therefore, $S = q/kT$ is a good approximation. The value of T_o for Schottky barriers on n-type GaAs is greater than 40 K.[26,27] Comparing a conventional Schottky mixer with a super-Schottky, both operating at 1 K, implies greater than a 40 to 1 improvement in diode noise temperature. This reduction in noise will produce a corresponding improvement in sensitivity, if the conversion loss of the super-Schottky is equivalent to that of the conventional Schottky. As discussed below, conversion loss is a major problem for the super-Schottky. Because of the relatively limited LO voltage range, the design criteria for obtaining low conversion losses are stringent.

At the present time the super-Schottky diode has been established as the most sensitive detector of microwaves in both the video and mixing modes of operation. Measurements at X-band have yielded a video NEP of 5×10^{-16} $\text{WHz}^{-1/2}$ and a mixer noise temperature of 6 K for Pb/5×10^{19} p-GaAs. The conversion loss, 7.5 dB, is composed of $L_0 = 6$ dB and $L_1 = 1.5$ dB.

The prospects for improving the frequency response of the super-Schottky diode rely on reducing L_1 without degrading L_o or T_D, essentially minimizing parasitic losses. To achieve this goal a multiple contact diode array is being developed. The required diode impedance is obtained by making many diodes in parallel with the same total active area. Fig. 6 shows the predicted L_1 for Pb/$5 \times 10^{19}/\text{cm}^3$ p-GaAs based on the fabrication technology used in the measurements reported earlier.[10,11] Because of the very large peripheral area and the small dimensions involved, new problems are encountered and techniques for overcoming them are still being developed. A linear diode array under development is shown in Fig. 7 with the insulating layer removed for inspection.[7] The ohmic contact will be made to metal strips plated between the "string of pearls" diode. Contact along the chain is accomplished by overplating.

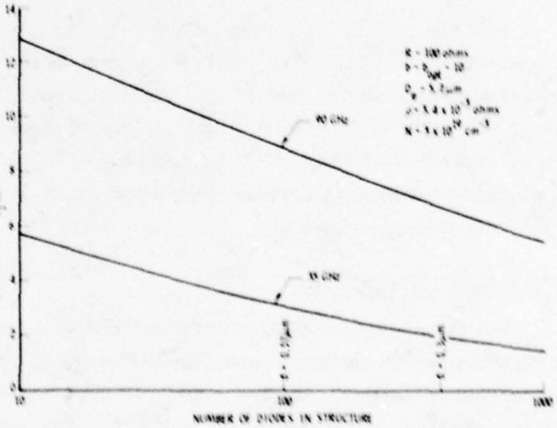

Figure 6. Predicted parasitic conversion loss for multi-contact diode array of Pb/p-GaAs.

Parallel efforts to reduce R_s and to modify the tunneling barrier are also in progress. We have been able to reduce the barrier on p-GaAs by 150 mV by chemical treatment of the surfaces to lower the Ga/As ratio and increase the As-As surface cross-linking. This treatment is consistent with our electroplating chemistry thus producing a lower impedance diode. (For n-GaAs this technique raises the barrier 150 mV). Therefore we can expect a single Pb/p-GaAs diode to perform as well at 35 GHz as did the previous device at 9 GHz. Similar improvement in the multi-contact array can be expected at higher frequencies.

For 100 GHz and higher frequency application, n-InSb is considered to be an ideal semiconductor substrate because of its high mobility and small bandgap. Predicted L_1 values extend the operating range to several hundred

As a first step toward realizing sensitive receivers at submillimeter frequencies, we measured the sensitivity of submicron diameter Schottky barrier diodes in open untuned mounts. In this configuration, the diode performance is dominated by $C \sim d^2$ and thus submicrodimensional structures appeared favorable. It is implicit in the above statement that R_s and $(\omega c)^{-1}$ are much less than the antenna impedance and this assumption is consistent with our measurements.

The radiation was focused onto the whisker contact which served as a long wire antenna. This work has compared the video and heterodyne sensitivities of diodes approximately 0.25 and 0.5 μm in diameter. The 0.25 μm diodes were fabricated on 4×10^{-17}cm^{-3} n-GaAs using a new high field pulse plating (HFPP)[22] technique which we developed in order to achieve extremely uniform electro-deposition of plated contacts to semiconductor surfaces. The method of diode formation is by electroplating the small diodes through "windows" in a protective overlayer on the surface. The uniformity of conventional dc plating is poor, and results in values of R_s well above theoretical. With the high field-pulsed plating technique,[22] however, theoretical values of R_s and uniform deposition for contacts as small as 1200 A diameter were achieved.

The performance of these new diodes is contrasted in Table 2 and Fig. 5 to our previously published measurements[6,7] on 0.5 μm dia. diodes on 5×10^{18}cm^{-3}n-GaAs. The relative video response versus frequency is difficult to interpret because the long wire antenna gain was not held constant. However, it is obvious that the short wavelength response is much improved with the 0.25 μm diode. For wavelengths shorter than 100 μm, the response of both diodes drops sharply and the mechanisms responsible for this are still the subject of study.

TABLE 2

Summary Of Video and Mixer Performance For Submicron Schottkys at 119 μm in an Open (untuned) Mount.

DIODE		VIDEO		HETERODYNE (SSB)	
d (μm)	N (cm^{-3})	R_V (V/W)	NEP (W/H$_z^{1/2}$)	L_c (dB)	MDP (W/Hz)
0.5	5×10^{18}	0.8	6×10^{-8}	69	3×10^{-14}
0.25	4×10^{17}	30	1×10^{-9}	41	5×10^{-17}

With the addition of a back reflector to improve the coupling to the diode,[23, 24] it should be possible to improve the sensitivity by one or two orders of magnitude. Thus relatively simple structures employing submicron dimensional Schottkys should provide low-noise room temperature receivers throughout the submillimeter to frequencies approaching 3 THz.

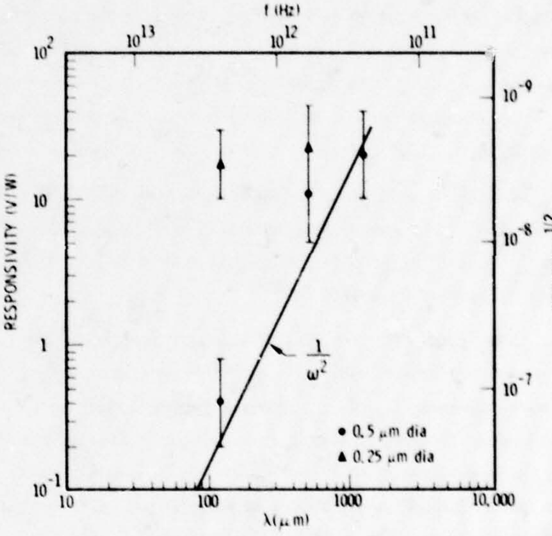

Figure 5. Summary of video data for 0.5 and 0.25 μm dia. Schottky-barrier diodes in an open (untuned) mount.

SUPER-SCHOTTKY MIXERS

For situations demanding extreme sensitivity, a cooled receiver can offer superior performance. One type of cooled device which has been successfully demonstrated in our laboratory and which has great potential for both video and heterodyne detection at near millimeter wavelengths is the super-Schottky tunnel diode,[9-12] a variant of the Schottky diode in which the metal contact to the semiconductor is a superconductor. Current flows via electron tunneling across the natural surface barrier in a heavily doped semiconductor. The principal advantages of these devices are the control and stability of the surface barrier, particularly in the high conductance regime required for high frequency applications, high intrinsic efficiency, and low noise. Disadvantages are parasitic losses in the semiconductor and incomplete control of the surface properties of certain semiconductors.

In the conventional Schottky diode, it is desirable to have thermionic emission and thermally activated tunneling dominate over pure tunneling in order to realize the greatest nonlinearity. The resulting forward biased exponential electrical behavior, Eq. (2), is a result of these thermally stimulated mechanisms. On the other hand, the super-Schottky diode is a pure tunneling-dominated device which also obeys Eq. (2) as a result of the thermal distribution of electrons in the heavily doped semiconductor. In order for tunneling to dominate the diode conductance and provide an efficient impedance match to microwave networks, the space charge barrier must be small.

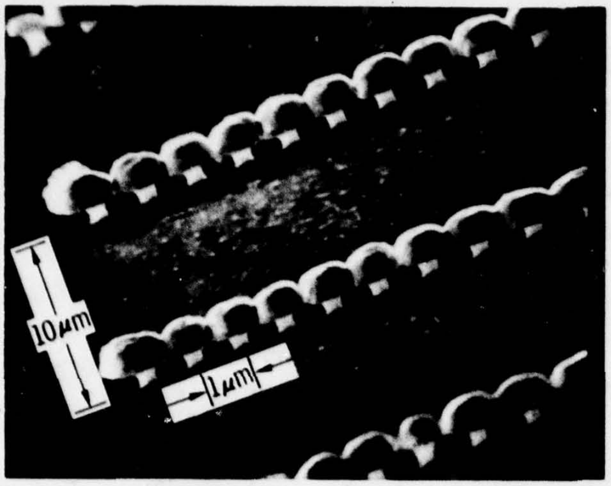

Figure 7. Photograph of linear contact array Schottky barrier diode. Insulating layer nominally present has been stripped away for accurate observation of diode structure.

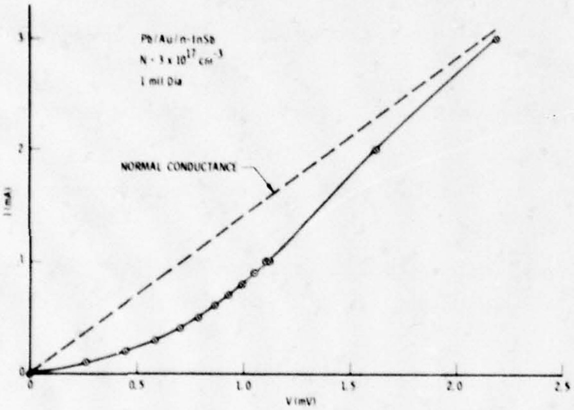

Figure 8. Superconducting energy gap effect on I-V curve of Pb/Au/n-InSb junction at 1.4 K.

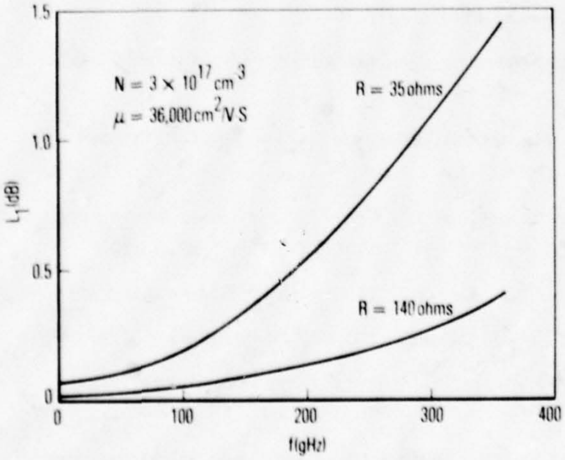

Figure 10. RF Parasitic loss vs frequency for a Pb/n-InSb Super-Schottky diode.

GHz, essentially to the limits imposed by the superconducting energy gap and the quantum limits at cryogenic temperatures. The problems encountered with InSb are barrier formation and surface leakage. Barrier heights are generally of the order of the bandgap. Therefore we expect to utilize this small barrier in InSb to make wide, low impedance junctions. The very high mobility at helium temperatures would essentially eliminate the series resistance.

Most metals make ohmic contacts to n-InSb.[29] Gold is an exception. We have been successful in fabricating a super-Schottky diode using a thin interface of Au between the Pb electrode and n-InSb (Fig. 8). However, we consider this to be a difficult and low yield technique for obvious reasons. Using chemical surface manipulation along the lines mentioned above for p-GaAs, we have fabricated super-Schottky tunneling diodes on n-InSb. In this case we want an Sb rich surface and must be careful to avoid destroying the Sb-Sb cross-linking. Fig. 9 shows the Pb energy gap observed by tunneling through a Schottky barrier on n-InSb. We believe that this type of diode will completely satisfy the requirements for millimeter and submillimeter wave low noise detectors. Fig. 10 projects the parasitic loss term for Pb/n-InSb operating at 1 K.

This work was supported by The Aerospace Corporation and under DOE and ONR Contracts.

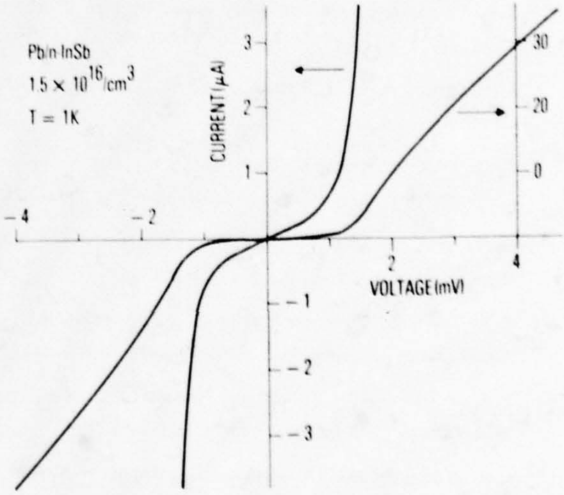

Figure 9. Super-Schottky I-V characteristic for n-InSb.

REFERENCES

[1] D. T. Hodges, "A Review of Advances in Optically Pumped Lasers," Infrared Physics (in press).

[2] M. McColl, Review of submillimeter Wave Mixers," Proc. S.P.I.E. 105, p. 24 (1977).

[3] D. T. Hodges, and T. S. Hartwick, "Waveguide Laser for the far infrared (FIR) pumped by a CO_2 laser," Appl. Phys. Letters 23, p. 252 (1973).

[4] D. T. Hodges, F. B. Foote, and R. D. Reel," Efficient high-power operation of the cw far-infrared waveguide laser," Appl. Phys. Letters 29, p. 662 (1976).

[5] D. T. Hodges, F. B. Foote, and R. D. Reel, "High-power operation and scaling behavior of cw optically pumped FIR waveguide lasers," IEEE J. Quant. Electr. QE-13, p. 491 (1977).

[6] D. T. Hodges and M. McColl, "Extension of the Schottky barrier detector to 70 μm (4.3 THz) using submicron-dimensional contacts," Appl. Phys. Letters 30, p. 5 (1977).

[7] M. McColl, D. T. Hodges, and W. A. Garber, "Submillimeter-Wave Detection with Submicron-size Schottky-Barrier Diodes," IEEE Trans. Microwave Theory Tech. MTT-25, p. 463 (1977).

[8] M. McColl, D. T. Hodges, A. B. Chase, and W. A. Garber, "Detection and mixing at submillimeter wavelengths using Schottky diodes with low junction capacitance," Conference Digest, Third International Conference on Submillimeter Waves and Their Applications, Univ. of Surrey, Guildford, England, March 1978 (to be published).

[9] M. McColl, R. J. Pedersen, M. F. Bottjer, M. F. Millea, A. H. Silver, and F. L. Vernon, Jr., "The Super-Schottky diode microwave mixer," Appl. Phys. Letters 28, p. 159 (1976).

[10] M. McColl, M. F. Millea, A. H. Silver, M. F. Bottjer, R. J. Pedersen, and F. L. Vernon, Jr., "The super-Schottky Microwave Mixer," IEEE Transactions on Magnetics, MAG-13, p. 221 (1977).

[11] F. L. Vernon, Jr., M. F. Millea, M. F. Bottjer, A. H. Silver, R. J. Pedersen, and M. McColl, "The super-Schottky diode," IEEE Trans. Microwave Theory Tech. MTT-25, p. 286 (1977).

[12] A. H. Silver, A. B. Chase, M. McColl, and M. F. Millea, "Superconductor-semiconductor Device Research," Conf. on Future Trends in Superconductive Electronics, March 1978 Charlottsville, Va., to be published in A.I.P. Conf. Proceedings Series.

[13] T.Y. Chang and T. J. Bridges, "Laser Action at 452, 496, and 541 μm in optically pumped CH_3F," Opt. Comm. 1, p. 423 (1970).

[14] M. Rosenbluh, R. J. Temkin, and K. J. Button, "Submillimeter laser wavelength tables," Appl. Optics. 15, p. 2635 (1976).

[15] J. J. Gallagher, M. D. Blue, B. Bean, and S. Perkowitz, "Tabulation of optically pumped far infrared lines and applications to atmospheric transmission," Infrared Phys. 17, p. 43 (1976).

[16] D. T. Hodges, J. R. Tucker, and T. S. Hartwick, "Basic Physical Mechanisms Determining Performance of the CH_3F Laser," Infrared Phys. 16, p. 175 (1976).

[17] J. R. Tucker,"Theory of an FIR gas laser," Conf. Digest, International Conf. on Submillimeter Waves and Their Applications, Atlanta, Ga. IEEE Cat. No. 74CH 0856-5MTT, p. 17 (1974).

[18] F. B. Foote and D. T. Hodges, "cw performance of optically-pumped lasers in the millimeter-wave spectral region," Proceedings 1977 International Microwave Symposium, San Diego, IEEE Cat. No. 77 CH 1219-5 MTT, p. 73.

[19] H. C. Torrey and C. A. Witmer, Crystal Rectifiers, M.I.T. Rad. Lab. Ser., Vol. 15 (McGraw Hill, New York, 1948).

[20] G. C. Messenger and C. T. McCoy, "Theory and Operation of Crystal Diodes as Mixers," Proc. IRE 45, p. 1269 (1957).

[21] M. McColl, "Conversion Loss Limitations on Schottky Barrier Mixers," IEEE Trans. Microwave Theory Tech. MTT-25, p. 54 (1977).

[22] M. McColl, A. B. Chase, and W. A. Garber, "Extremely uniform electrodeposition of submicron Schottky contacts," J. Appl. Phys. (in press).

[23] H. Krautle, E. Sauter, and G. V. Schultz, "Antenna Characteristics of Whisker Diodes Used as Submillimeter Receivers," Infr. Phys. 17, p. 477 (1977).

[24] H. R. Fetterman, P. E. Tannenwald, B. J. Clifton, C. D. Parker, W. D. Fitzgerald and N. R. Erickson, "Far-ir heterodyne radiometric measurements with quasi-optical Schottky diode mixers," Appl. Phys. Letters 33, 151 (1978).

[25] F. A. Padovani and G. G. Sumner, "Experimental Study of gold-gallium arsenide SChottky barriers," J. Appl. Phys. 36, p. 3744 (1964).

[26] F. A. Padovani, "Graphical determination of the barrier height and excess temperature of a Schottky barrier," J. Appl. Phys. 37, p. 921 (1966).

[27] T. J. Viola, Jr. and R. J. Mattauch, "High-frequency noise in Schottky-barrier diodes," Proc. IEEE 61, p. 393 (1973).

[28] M. McColl and M. F. Millea, "Schottky barriers on InSb," J. Electronic Materials 5, p. 191 (1976).

ADVANCED DEVICES AND COMPONENTS FOR THE MILLIMETER AND SUBMILLIMETER SYSTEMS

by

J. A. Calviello, J. J. Taub, D. I. Brietzer, E. H. Kraemer, and
J. L. Wallace

AIL Division of Cutler-Hammer
Melville, New York 11746
U.S.A.

ABSTRACT

The purpose of this presentation is to discuss key topics related to low noise mixers, high efficiency multipliers, the use of quasi-optical techniques to reduce circuit losses, and the development of very high-Q devices applicable to the millimeter and submillimeter wavelengths (Calviello, J. A. and Wallace, J. L., 1976; Calviello, J. A. and Wallace, J. L., June 1977; Calviello, J. A., Wallace, J. L., and Bie, P. R., 1974).

In particular, we plan to describe the development of a highly reliable metalized GaAs Ta-Schottky barrier diode with native-oxide passivation. The zero bias cutoff frequency of these diodes is greater than 1000 GHz when measured accurately near 60 GHz with a zero bias junction capacitance near 0.1 pF. This zero bias cutoff frequency is approximately twice the value for a comparable nonmetalized device.

Using these very high-Q devices, we have achieved RF performance that has advanced prior state of the art. In frequency multipliers, doublers (100-200 GHz), and triplers (100-300 GHz),* we have realized conversion efficiencies of 12 and 2 percent, respectively. The CW output power of the doubler was 18 mW and that of the tripler 2 mW. In an image enhanced mixer at 35 GHz with an IF of 1 GHz, we have realized conversion loss below 3 dB including 0.6 dB circuit losses, and less than 5.9 dB noise figure including a 2-dB IF noise figure contribution.

1. INTRODUCTION

The ultimate high frequency performance of components in which Schottky diodes are used is limited by the quality of the devices. For example, the noise temperature and conversion loss in a mixer, detector sensitivity, conversion efficiencies in frequency multipliers, and the pump power necessary to fully pump the varactors in a parametric amplifier are all dependent on the quality of zero volt bias cutoff frequency of these devices. In particular, the dependence of performance upon device quality becomes quite noticeable as the operating frequency approaches and goes beyond 40 GHz.

The GaAs Schottky barrier, to be described, features tantalum Schottky, with an overlayer of gold, and GaAs native oxide junction passivation for high reliability and high power handling capability. In addition, a novel metalization technique is described which minimizes the substrate skin effect contribution thus making it able to almost double the Q of these devices and thereby improve system performance when operating at very high frequencies.

The design and fabrication of such devices, its reliability and techniques to accurately measure the cutoff frequency near the operating frequency (De Loach, B. C., 1964), and RF performance achieved to date is described.

Using this device technology, the development of novel and more advanced device structures, in a beam lead configuration with minimum parasitic capacitance and comprised of multiple junctions on the same semi-insulating substrates, also adaptable to monolithic circuit integration, is presented (Calviello, J. A. and Wallace, J. L., November 1977).

The use of quasi-optical millimeter wave components, to achieve low loss and to overcome the small size and high tolerances of conventional millimeter-waveguides that restrict the design and performance of ordinary waveguide components is summarized.

2. THE METALIZED QUASI-PLANAR CONFIGURATION

The very high-Q of these devices, approximately twice the Q of a conventional unmetalized device, was achieved by minimizing the substrate resistance contribution (Calviello, J. A. and Wallace, J. L., 1976) arising from skin effect which plays a dominant role at these very high frequencies. The skin effect contribution was reduced by metalizing the total substrate N+ surface (Figure 1) to within 10 to 20 microns of the junction periphery. The metalization involves the evaporation and sinter alloying of a 700Å Ge-Au layer followed by the evaporation of a gold overlayer whose thickness was greater than the skin depth at the intended operating frequency.

---

* Patent #4,075,650.

The reliable Ta-Schottky junction and native oxide passivation in a quasi-planar (QUANAR) configuration (Calviello, J. A. and Wallace, J. L., June 1977) has been used. The ability of the tantalum to withstand ohmic contact sinter alloying temperatures has made possible the successful development of the metalized structure. This was a necessary and sufficient condition to achieve a low resistivity ohmic contact near the junction periphery without detrimental interdiffusion effects between the tantalum and GaAs active eiplayer. In addition, the native oxide junction passivation (Calviello, J. A. and Wallace, J. L., June 1977) further facilitated the fabrication of a highly reliable structure thus drastically reducing the need for photolithographic processing and costly instrumentation. Also using the quasi-planar configuration, it is possible to minimize high fields near the junction periphery and thus becomes capable to achieve near ideal devices' characteristics.

2.1 Background and Analysis of the Metalized Structure

The resistivity of n-type GaAs is limited to about 1×10^{-4} Ω-cm, which corresponds to an impurity concentration of $10^{20}(\mathrm{cm}^{-3})$. This doping level, on the other hand, is not easily realizable in practice. Typical values of resistivity, achieved to date, lie in the range of 8 to 10×10^{-4}(Ω-cm). An approximate relationship relating material resistivity to carrier concentration, electronic charge, and mobility (Sze, S. M.,) is given by equation 1.

$$\rho = \frac{1}{q\mu N} \tag{1}$$

Skin effect is well known and its dependence on material resistivity and operating frequency is given by equation 2.

$$\delta = \frac{1}{2\pi}\sqrt{\frac{\rho}{f}} \tag{2}$$

where ρ is resistivity in Ω-cm, and f is the frequency in GHz. The skin depth δ is then given in cm.

Using epitaxial GaAs material with a substrate resistivity of 1×10^{-3} Ω-cm, high quality GaAs Schottky barrier devices have previously been fabricated (Calviello, J. A. and Wallace, J. L., June 1977; Calviello, J. A. and Wallace, J. L., 1974) and achieved zero bias cutoff frequencies within 90 percent of the calculated values. For this calculation the high frequency model (Calviello, J. A. and Wallace, J. L., 1974) of Figure 2, showing the current distribution within the chip, was used. The current distribution within the N-layer is assumed uniform. The total device series resistance R_s is given by equation 3.

$$R_s = R_N + \sum_{m=1}^{5} R_m \tag{3}$$

The various resistive terms including the skin effect (equation 1) are given by equations 4 through 8.

$$R_1 = \frac{\rho_{N+}}{2\pi a} \text{ arc Tan } \frac{\delta}{a} \tag{4}$$

$$R_2 = \frac{\rho_{N+}}{4\pi\delta} \tag{5}$$

$$R_3 = \frac{\rho_{N+}}{2\pi\delta} \ln \frac{b}{a} \tag{6}$$

$$R_4 = \frac{\rho_{N+} h}{2\pi b\delta} \tag{7}$$

$$R_5 = \frac{i\beta \rho_c \, J_0(i\beta b)}{2\pi b \, J_1(i\beta b)} \quad ; \quad \beta^2 = \frac{\rho_{N+}}{r_c \delta} \tag{8}$$

where $J_0(x)$, $J_1(x)$ are the Bessel function of order zero and one, and r_c is the contact resistivity of the N+ ohmic contact.

For a junction capacitance of 0.1 pF, an N-layer carrier concentration and thickness of 1×10^{17} and about 0.4 micron, respectively, and a substrate resistivity of 1×10^{-3} Ω-cm, we get for R_N and $\sum_{m=1}^{5} R_m$ a value of 0.5Ω and 1.34Ω, respectively. Other parameters for this calculation are given in Table I. In addition, it is found that the sum of R_3, R_4, and R_5 contribute almost 50 percent of the total series resistance.

Table I. Calculation Parameters

N-layer properties	Device dimensions for
$1 \times 10^{17} (\text{cm}^{-3})$	Junction radius $a = 6.4 \times 10^{-4}$ cm
$N_t = 0.4$ to 0.5 μm (varactor)	Chip radius $b = 7.6 \times 10^{-3}$ cm
$N_t = 0.2$ μm (mixer)	Chip height $h = 7.6 \times 10^{-3}$ cm
$\rho_N = 2 \times 10^{-2}$ Ω-cm	

Substrate properties	Metal layer property (gold)	Contact resistance
$\rho_{N+} = 1 \times 10^{-3}$ Ω-cm	$\rho_m = 5 \times 10^{-5}$ Ω-cm	$r_c = 2 \times 10^{-6}$ Ω-cm^2
$\delta_{N+} = 3$ μm @ 280 GHz	$\delta_m = 0.22$ μm @ 280 GHz	
$\delta_{N+} = 6.5$ μm @ 60 GHz	$\delta m = 1.4$ μm @ 60 GHz	

In order to effectively reduce the substrate parasitic series resistance, and in particular R_3 and R_4, the metalized chip configuration has been developed.

Figure 3 shows the distribution of current at high frequencies and the various resistive components associated with the metalized varactor configuration.

The current in the N layer is again assumed to be uniformly distributed and to flow radially outward in a skin depth (δ) of the N+ substrate. However, due to the low resistance metalization just outside the mesa cylinder, the current initially will flow within the substrate skin depth (δ) and gradually through the metal contact, thus drastically reducing the value of R_3 and totally eliminating R_4 and R_5 resistive terms.

The total series resistance of the metalized varactor structure is then given by:

$$R_s = R_N + R_1 + R_2 + R_0 + R_{N+} + R_6 \tag{9}$$

The first three terms are given by equations 3, 4, and 5. The term R_0 is derived using the model shown in Figure 4. The resistive term R_0 is due to the current flowing from the N+ submesa, within a skin depth δ_s through the metal-semiconductor interface and into the metal layer. The last two terms R_{N+} and R_6 express the resistance due to the submesa N+ cylinder and a disk in the N+ substrate of wall thickness C and height δ_s, respectively. The magnitudes of the latter are directly dependent on the fabrication procedures being used. Ideally, in a well processed wafer R_{N+} should easily approach zero and

R_6 can be in the range of 0.05 to 0.1 ohm. Using the model and its electrical equivalent of Figure 4, R_0 is now derived.

For a given d_r, the resistance due to contact, metal, and substrate is given by equations 10, 11, and 12.

$$R_s = \frac{\rho_s dr}{2\pi r \delta_s} \tag{10}$$

$$R_c = \frac{r_c}{2\pi r dr} \tag{11}$$

$$R_m = \frac{\rho_m dr}{2\pi r \delta_m} \tag{12}$$

The currents I_0, I_1, and I_2 are related by equation 13.

$$I_0 = I_1 + I_2 \text{ and } dI_0 = -dI_1 = dI_2 = \frac{V}{r_c} \tag{13}$$

Writing the loop equations, we obtain equation 14

$$\frac{dV}{dr} = \left[I_2(r) \frac{\rho_m}{\delta_m} - I_1(r) \frac{\rho_s}{\delta_s} \right] \frac{1}{2\pi r} \tag{14}$$

by taking the second derivative of equation 14 and using the following relation $-\frac{dI_1}{dr} = \frac{dI_2}{dr} = V(r)\, 2\pi \frac{r}{r_c}$, we obtain, after some manipulation, equation 15.

$$\frac{d^2V}{dr^2} + \frac{1}{r}\frac{dV}{dr} - \left[\frac{1}{r_c} \left(\frac{\rho_m}{\delta_m} + \frac{\rho_s}{\delta_s} \right) \right] V(r) = 0 \tag{15}$$

Thus V is a solution of Bessel equation with imaginary argument. The general solution is given by equation 16.

$$V(r) = A_1 J_0 (i\beta r) + B_1 N_0 (i\beta r) \tag{16}$$

Applying the following boundary conditions

$$I_1(a) = I_0 \qquad I_2(b) = 0 \tag{17}$$

$$I_1(b) = 0 \qquad I_2(b) = I_0 \tag{18}$$

and

$$\left.\frac{dV_1}{dr}\right|_a = \frac{\rho_s I_0}{2\pi a \delta_s} ; \quad \left.\frac{dV_2}{dr}\right|_a = 0 \tag{19}$$

$$\left.\frac{dV_2}{dr}\right|_b = \frac{\rho_m I_0}{2\pi b \delta_m} \; ; \; \left.\frac{dV_1}{dr}\right|_b = 0 \tag{20}$$

we obtain the desired equation relating V_0 to I_0 as shown in equation 21 and $R_0 = \frac{V_0}{I_0}$

$$V_0 = \frac{\rho_s \rho_m}{\rho_s \delta_m + \delta_s \rho_m} \left\{ \frac{I_0}{2\pi} \ln \frac{b}{a} + \frac{\delta_s}{\rho_s} \left[A_1 J_0(i\beta b) + B_1 N_0(i\beta b) \right] + \frac{\delta_m}{\rho_m} \left[A_1 J_0(i\beta a) - B_1 N_0(i\beta a) \right] \right\} \tag{21}$$

where

$$A_1 = \frac{I_0}{2\pi i\beta\Delta} \left[\frac{\rho_s}{a\delta_s} N_1(i\beta b) + \frac{\rho_m}{b\delta_m} N_1(i\beta a) \right] \tag{22}$$

$$B_1 = -\frac{I_0}{2\pi i\beta\Delta} \left[\frac{\rho_m}{b\delta_m} J_1(i\beta a) + \frac{\rho_s}{a\delta_s} J_1(i\beta b) \right] \tag{23}$$

where

$$\Delta = J_1(i\beta a)\, N_1(i\beta b) - N_1(i\beta a)\, J_1(i\beta b)$$

and

$$\beta = \left[\frac{1}{\rho_c} \left(\frac{\rho_m}{\delta_m} - \frac{\rho_s}{\delta_s} \right) \right]^{1/2} \tag{24}$$

Typical semiconductor material parameters used for the calculation of the device series resistance are given in Table I.

Applying the given values in Table I, the calculated and the experimentally achieved device total series resistance for the quasi-planar conventional structure and for the metalized configuration is given in Figure 5. A graph of the theoretical zero bias cutoff frequency [$C_j(0) = 0.1$ pF] versus the operating frequency, ranging from 30 to 300 GHz and as a function of junction capacitance for the conventional and the ideal metalized varactors and mixers is shown in Figures 6 and 7, respectively.

For the metalized diode structure the total series resistance in Figure 5, given by equation 9, is calculated for two cases: (1) the ideal case, R_{N+} and R_6 equal zero and (2) using the values of the actually realized structure where R_{N+} was approximately 0.05Ω and R_6 approached 0.15Ω. For these calculations the submesa cylinder height was about 0.5 micron and the N+ disc wall thickness C, as shown in Figure 3, was approximately 6 microns. As shown in Figure 5, a very good agreement has been realized between the theory and the experimental measured series resistance. We are presently improving the device processing techniques to further minimize $R_6 + R_{N+}$ and thus are able to achieve even higher cutoff frequencies.

2.2 Device Fabrication

After necessary chemical lapping of the epilayer (Calviello, J. A. and Wallace, J. L., June 1977) an array of Ta-Schottky contact with a gold overlayer is evaporated through a bimetal mask. The tantalum and gold film thickness was 1500 and 10,000 Å, respectively. SiO_2 is sputter deposited over the entire surface. Using photolithographic techniques, grids are chemically defined and etched into GaAs to facilitate the chip separation process. A Ge-Au layer 700 to 1000 Å, and an overlayer of about 3000 Å of gold, is then deposited and sinter alloyed at 440°C for a few seconds to achieve a low resistivity ohmic contact. Depending on the frequency for which the device will be used, an additional gold layer ranging in thickness from 30,000 to 70,000 Å is deposited. The total gold thickness should be equal or greater than the skin depth at the operating frequency. Finally the junction is defined and passivated (Calviello, J. A. and Wallace, J. L., June 1977). Other metalization schemes such as Al, Ag, and Cu could be used, however for high reliability devices and for easy fabrication, gold is preferred. The resultant batch processed wafer and the cross-section of the chips is shown in Figure 1. These chips are then bonded to a copper pin, having a quartz dielectric in the shape of a horseshoe or standoff, and additional gold is electroplated to complete the gold low resistivity electrical path.

A pre-etched and preshaped gold ribbon, approximately 0.0002 inch thick, is thermocompression bonded to the metalized quartz land and to the junction using various configurations as shown in Figure 8.

2.3 Device Characteristics and Performance

Device parameters such as quality factor, barrier height, and parasitic element values including package capacitance, fringing capacitance, and series inductance are summarized in Table II. The characteristics of the Ta-Schottky junction including the novel native oxide passivation, reliability tests to date, and RF performance of unmetalized devices have already been described (Calviello, J. A. and Wallace, J. L., June 1977) and will only be briefly summarized at the present time. Table III shows the reliability results.

Table II. Varactor Equivalent Circuit and Typical Element Values

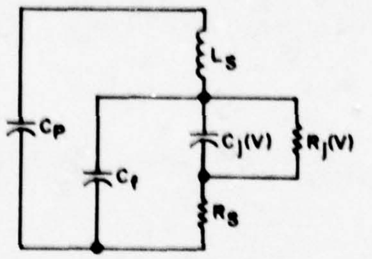

		Cutoff Frequency Measurement at 60 GHz	
Dc	1 MHz	Calculated	De Loach
$I_f = I_0 \left(\exp \frac{-qV}{nkT} - 1\right)$	$C_j(V) = \frac{C_j(0)}{\sqrt{1 + \frac{V}{\phi}}}$	$f_c(0) = \frac{1}{2\pi R_s C_j(0)}$	$L_s = 0.08$ nH
$I_0 \approx 8 \times 10^{-15}$ amp	$C_j(0) \approx 0.100$ pF	$R_s = 1.27\Omega$	$R_s < 1.5\ \Omega$
$\frac{q}{nkT} = 39\ V^{-1}$	$\phi = 0.85$ volt	$f_c(0) = 1250$ GHz	$f_c > 1000$ GHz
$n < 1.05$	$C_p = 0.020$ pF		$f_{SR} = \frac{1}{2\pi \sqrt{L_s Cj(0)}}$
$V_B \approx 14$ volts	$C_f < 0.002$ pF		> 55 GHz

Table III. Reliability Results

(a) Diode Chips

Chips (qty)	Temperature (°C)	Time (hour)	Ambient	Failure (qty)
40	300	500	Air	None
40	200	20,000	Air	None

(b) Predicted Lifetime

	Junction Temperature	
Assumed Activation Energy	100°C	200°C
1.8 to 2 eV	>10^8 hours	>10^5 hours

Typical I vs V characteristics are shown in Figure 9. The zero bias cutoff frequency was measured at about 60 GHz using the transmission technique (De Loach, B. C., 1964). An improved procedure (Calviello, J. A. and Wallace, J. L., June 1977) to characterize these devices by this technique has been employed in order to correct for the usually observed optimistic 2 to 1 discrepancy in the series resistance. Transmission loss measurements of a varactor with a $C_j(0) = 0.1$ pF are shown in Figure 10. Equation 25 was used to calculate the zero bias cutoff frequency and subsequently the product $R_s C_j(0)$. Knowing the value of $C_j(0)$ at 1 MHz, the value of R_s was then calculated.

$$f_c(0) = \frac{1}{2\pi R_s C_j(0)} = \frac{f_o^2}{\Delta f} = \frac{f_1 f_2}{f_2 - f_1} \tag{25}$$

In equation 25, f_1 and f_2 are the frequencies at the 3-dB half power point and f_o is device resonant frequency as designated in Figure 10. Using equation 25 to calculate the devices cutoff frequency has constantly yielded results in agreement with other measurements techniques (Houlding, N., 1960; Sard, E. W., 1968) and with realized RF performance. The zero bias cutoff frequency is found to be 1050 GHz and R_s is 1.5 ohms. Otherwise, straightforward use of the transmission method, by first evaluating R_s using the value of the transmission loss T and the waveguide

$$R_s = \frac{Z_o}{2} \frac{1}{\sqrt{T} - 1} \tag{26}$$

characteristic capacitance Z_o, as shown in equation 26 would have resulted in a zero bias cutoff frequency of 2050 GHz.

The RF performance in image enhanced mixers (Breitzer, D. and Sard, E. W.) frequency multipliers (Cohen, L.; 1975) is summarized in Table IV. This performance represents an improvement over the present state of the art.

In the image enhanced mixer the conversion loss of 3 dB includes 1-dB circuit losses and the 5.9 dB noise figure includes 2-dB noise contribution of the 1 GHz IF amplifier.

As doublers and triplers, the realized efficiencies and CW output power represents a state-of-the-art improvement. Circuit losses at these very high frequencies (200 and 300 GHz) are being minimized to achieve even better efficiency and higher output power.

Figures 11 and 12 show the assembled doubler (100 - 200 GHz) and tripler (100 - 300 GHz), respectively.

Table IV. Diode Performance

	Freq (GHz)	Varactor Cutoff Freq (GHz)	P_{out}	Efficiency
Doubler	50 - 100	650	20 mW	>25%
	100 - 200	650	10 mW	> 9%
	100 - 200	1000	18 mW	12%
Tripler	35 - 105	650	18 mW	>25%
	100 - 300	1000	2 mW	2%

	f_{sig} (GHz)	$f_{\ell o}$ (GHz)	$f_{i\text{-}f}$ (GHz)	$P_{\ell o}$	Mixer		Mixer + i-f		t
					Lc	NF	Lc	NF	
Mixer	34.17	35.12	0.95	10 mW	2.4	3.7	3.0	5.9	1.3

2.4 Metalized Beam-Lead Structure

We are presently developing a metalized beam lead in a quasi-planar configuration. Unlike conventional planar beam-lead devices using SiO_2 and/or Si_3N_4 to passivate the junction and to support the beam lead (giving rise to undesirable large parasitic capacitance and non-uniform field distribution across the junction), our metalized beam-lead structure will use the well proven tantalum Schottky and native oxide and the mesa configuration.

As shown in Figure 13A and B, the device's beam leads can be easily preshaped to reduce further parasitic capacitance contributions.

This type of structure is most desirable to achieve the necessary very high cutoff frequency and low parasitic elemental values [$C_j(0)$ in the range of 0.08 to 0.12 pF].

In addition, to meet future system requirements and more specifically $C_j(0) \leq 0.05$ pF, we are developing the necessary device technology that can be adapted to many circuit configurations (MIC, waveguide, and monolithic). Typical device structures under study are shown in Figure 14.

3. QUASI-OPTICAL MILLIMETER-WAVE COMPONENTS

An alternate approach to wideband low-loss millimeter components is the use of quasi-optical techniques pioneered at AIL. These techniques employ oversized waveguide which offers a practical, low-loss transmission line for millimeter and submillimeter wave. The advantage of this technique to reduce losses is more dramatic in the 1-mm region than at 10 mm as shown in Figure 15.

By contrast, oversized guides free the designer to consider more practical and efficient components.

The TE_{10} mode in 10X oversize waveguide has a wavelength, λ_g equal to 1.002 λ_o (λ_o is the free-space wavelength). Propagation is thus approximately planar and suggests the use of optical techniques as applied in free space.

Prisms, dielectric slabs, and gratings can be placed inside the waveguide to construct components. Their basic operation can be analyzed using free-space optical principles.

If these internal elements are designed to act uniformly on the entire plane-wave front, higher order modes will not be generated. Discontinuities such as screws and irises can be used if they are located in a symmetrical manner so as not to generate higher order modes which can freely propagate. This is accomplished in practice by dividing the oversized guide into repetitive half-wavelength "domains" in which the tuning elements are repeated in a symmetric fashion.

While conventional techniques can be "pushed" to operate at 100 GHz, they suffer limitations due to loss and difficulty in maintaining tolerances at operating frequencies exceeding 140 GHz. A line of quasi-optical components can, therefore, be developed to meet the long-range objectives of providing the best possible performance to 300 GHz. These components are based on basic theoretical and experimental work done at AIL from 30 to 300 GHz (Taub, J. J., 1963; Taub, J. J. and Cohen, J., 1966; Taub, J. J. et al, 1964; Kraemer, E. et al, 1970; Taub, J. J., 1970).

By use of suitable transitions, these components can be used with standard waveguide components. However, for ultimate performance, it is desirable to build up an entire system using cascaded quasi-optical components with a possible arrangement shown in Figure 14. In this way, a second source tuned to a different frequency can be switched to the mixer. Local oscillator's level can be controlled by quasi-optical attenuators, if required (Taub, J. J., 1963). An injection-locking signal is also fed through the circulator from a high-order varactor multiplier to phase lock the source. Electronically controlled ferrite phase shifters are located between the circulator and each quasi-optical source to phase shift the local oscillator as may be required in certain applications.

By using all quasi-optical components, except at the required interfaces with standard guide, the number of transitions and associated losses are minimized and full advantage of the lower-loss capability of oversized waveguide can be realized.

As can be seen from Figure 16, the advantages of oversized guide become even more pronounced when components may need to be physically separated (that is, antenna feed and receiver) which would lead to intolerable losses with regular guide but pose no major problem with oversized waveguide. AIL has carried out the basic development of most of the components described.

In Figures 17 through 20, we show possible configurations of discrete quasi-optical components that can be developed for the millimeter and submillimeter application.

4. CONCLUSIONS

A reliable and high performance metalized GaAs Ta-Schottky and native oxide passivated junction with very low parasitic device-series-resistance has been developed. The use of a novel metalization over the semiconductor N+ substrate has made it possible to minimize skin effect contribution in the frequency range of 30 to 300 GHz and thus make it able to realize, for the first time, zero bias cutoff frequency in excess of 1000 GHz, when measured near 60 GHz, for a junction capacitance near 0.1 pF. The Q of these devices is in the range of 1.5 to 2 times the Q achievable in conventional AIL high performance quasi-planar structure and greater than 2 when compared to a commercially available planar device. The metalized devices have been successfully used in parametric amplifiers, frequency multipliers to 300 GHz, and image enhanced mixers at 34 GHz, and realized a decisive improvement in RF performance that advanced prior state of the art.

The successful development of these very high-Q devices will make possible the development of lower noise, particularly above 10 GHz, parametric amplifiers in the 90 to 300 GHz region, frequency multipliers in the frequency range of 200 to 600 GHz with application as pump sources and low noise LO, image enhanced mixer to realize low conversion losses and noise figure for possible application in front-end receivers, and as efficient detectors at millimeter wavelengths.

Device fabrication improvements are being developed to realize even higher cutoff frequency. In particular our goal is to achieve zero bias cutoff frequency near 1500 GHz in mixer devices [$C_j(0) \leq 0.05$ pF] and greater than 1200 GHz for varactor applications.

A novel and more advanced metalized beam-lead device was described. In addition, to meet future system requirements such as monolithic circuit configuration, a novel configuration on semi-insulating substrate was described.

The use of oversize waveguide to overcome undesirable circuit loss at high frequencies was briefly described. Various quasi-optical components were presented, and a possible quasi-optical receiver configuration was proposed.

ACKNOWLEDGMENT

The authors wish to thank all the members of the Central Research Group Semiconductor Manufacturing staff who assisted in the fabrication of the devices, especially P. R. Bie. Special thanks are extended to D. Breitzer of AIL Central Research Laboratory staff and E. Sard of Applied Electronics Division for providing the mixer performance. We also would like to express our appreciation to E. Kraemer and L. Cohen of Applied Electronics for the frequency multiplier performance data.

REFERENCES

1. Breitzer, D. (Image Enhanced Theory) and Sard, E. W. (Mixer Design and Measurements). This technical material is being prepared for possible publication.

2. Calviello, J. A. and Wallace, J. L., November 1976, "Novel GaAs Metalized Diode Configuration to Reduce Skin Effect Contributions at High Frequencies," Electron Letters, Vol 12, No. 24, p 648-650.

3. Calviello, J. A. and Wallace, J. L., June 1977, "Performance and Reliability of a High Temperature GaAs Schottky Junction and Native Oxide Passivation," IEEE Trans on Electron Devices, ED-24, p 698-704.

4. Calviello, J. A. and Wallace, J. L., November 1977, "A Novel GaAs Schottky Diode for High Performance Millimeter-Wave Application," Sixth ARPA/TRI-Service Millimeter-Wave Conference.

5. Calviello, J. A., Wallace, J. L., and Bie, P. R., 1974, "High Performance Quasi-planar Varactors for Millimeter Waves," IEEE Trans on Electron Devices, ED-21, No. 10, p 624.

6. Cohen, L. et al, May 1975, "Varactor Frequency Doublers and Triplers for the 200 and 300 GHz Range," presented at the 1975 International Microwave Symposium, Palo Alto, Calif.

7. De Loach, B. C., January 1964 (A Modified Transmission Measurement), "A New Microwave Measurement Technique to Characterize Diodes and an 800-GHz Cutoff Frequency Varactor at Zero Volt Bias," IEEE Trans, Microwave Theory Tech, Vol MTT-12, p 15-70.

8. Houlding, N., January 1960, "Measurement of Varactor Quality," Microwave Journal, Vol 3, p 40.

9. Kraemer, E., Kurpis, G., Taub, J., and Grayzel, A., "Quasi-Optical Circuits Relating to Frequency Multipliers," Proceedings of the 1970 Submillimeter Symposium, published by the Polytechnic Press, Brooklyn, New York.

10. Sard, E. W., October 1968, "A New Procedure for Calculating Varactor Q from Impedance versus Bias Measurements," IEEE Trans Microwave Theory and Techniques, Vol MTT-16, No. 10, p 849.

11. Sze, S. M., "Physics of Semiconductor Devices."

12. Taub, J. J., November 1970, "The Status of Quasi-Optical Waveguide Components," The Microwave Journal.

13. Taub, J. J. et al, September 1963, "Submillimeter Components Using Oversized Quasi-Optical Waveguide," IEEE Trans, Vol MTT-11, p 338-345.

14. Taub, J. J. and Cohen, J., April 1966, "Quasi-Optical Waveguide Filters for Millimeter and Submillimeter Wavelengths," Proc IEEE, Vol 54, p 647-656.

15. Taub, J. J., Hindin, H. J., and Kurpis, G. P., November 1964, "Quasi-Optical Waveguide Filters," IEEE Trans on MTT, No. 6, Vol 12.

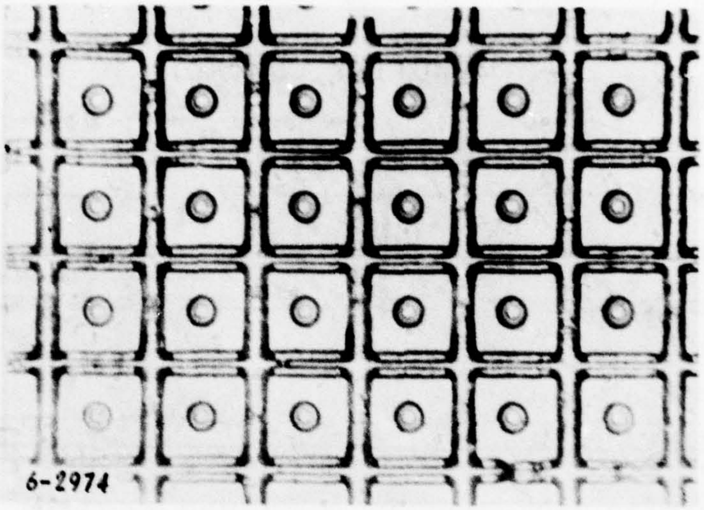

A. BATCH PROCESSED METALIZED DEVICES PRIOR TO DICING INTO CHIPS

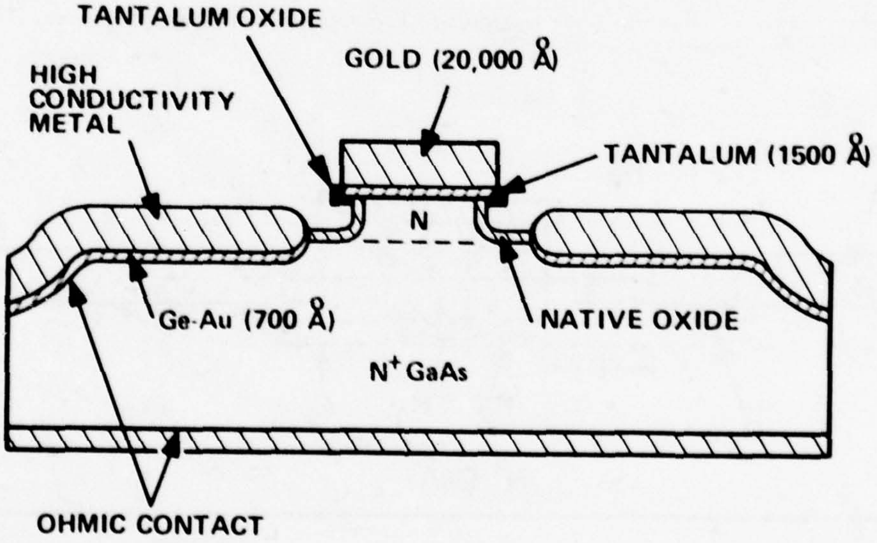
TANTALUM OXIDE
GOLD (20,000 Å)
HIGH CONDUCTIVITY METAL
TANTALUM (1500 Å)
N
Ge-Au (700 Å)
NATIVE OXIDE
N^+ GaAs
OHMIC CONTACT

B. CROSS SECTION

Figure 1. Metalized Diode

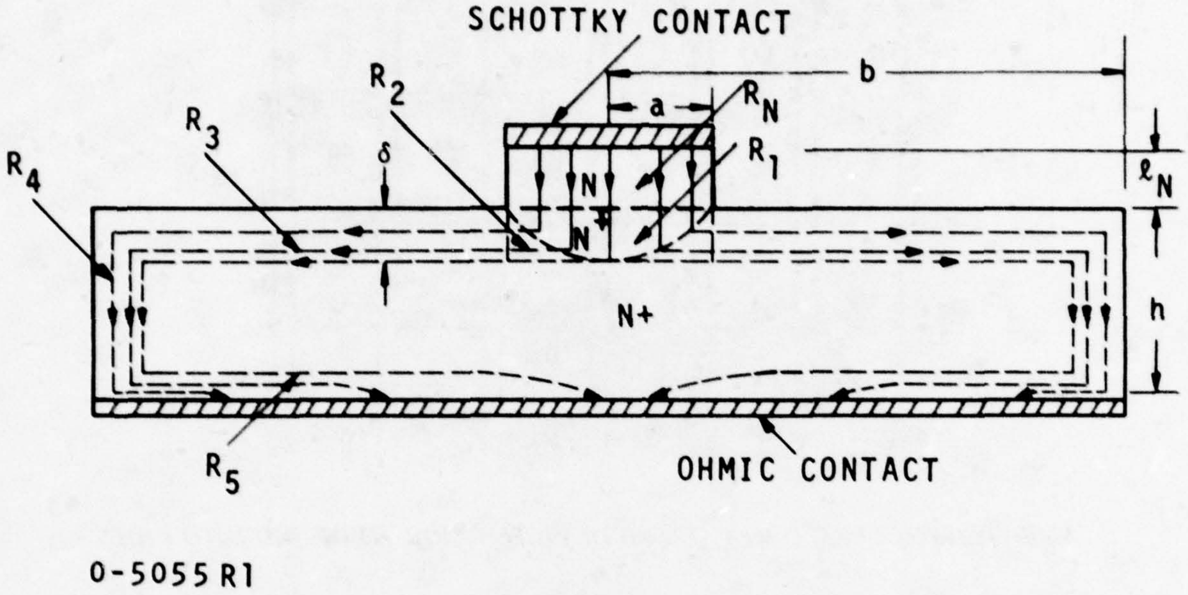
SCHOTTKY CONTACT
b
a
R_2
R_N
R_3
R_1
R_4
δ
ℓ_N
N
N+
N+
h
R_5
OHMIC CONTACT
0-5055 R1

Figure 2. Current Redistribution of Epitaxial Nonmetalized Varactor

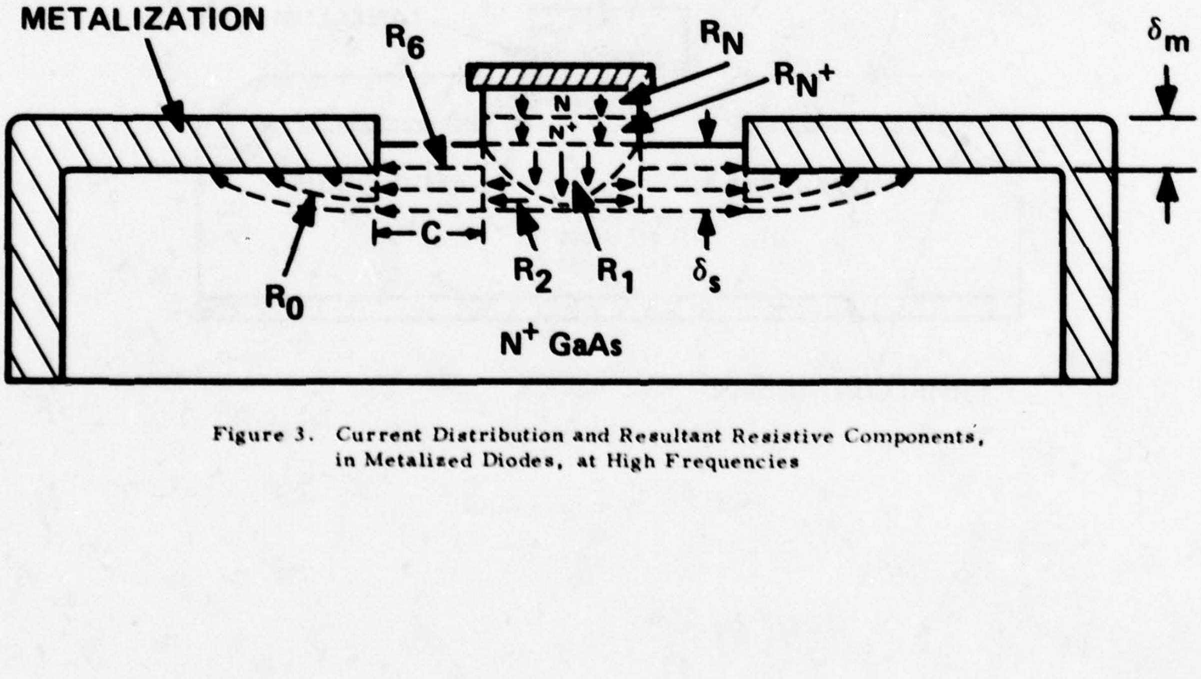
METALIZATION
R_6
R_N
R_N+
δ_m
N
N+
C
R_0
R_2
R_1
δ_s
N+ GaAs

Figure 3. Current Distribution and Resultant Resistive Components, in Metalized Diodes, at High Frequencies

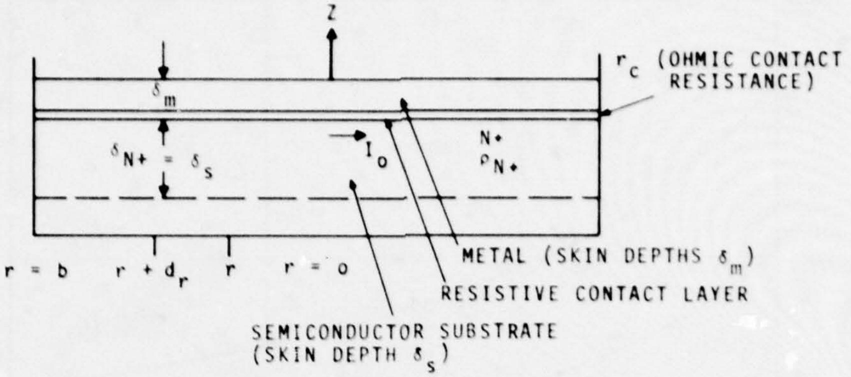
Z
r_c (OHMIC CONTACT RESISTANCE)
δ_m
$\delta_{N+} = \delta_s$
I_o
N+
ρ_{N+}
METAL (SKIN DEPTHS δ_m)
RESISTIVE CONTACT LAYER
SEMICONDUCTOR SUBSTRATE (SKIN DEPTH δ_s)
r = b
r + d_r
r
r = o

A. PHYSICAL MODEL

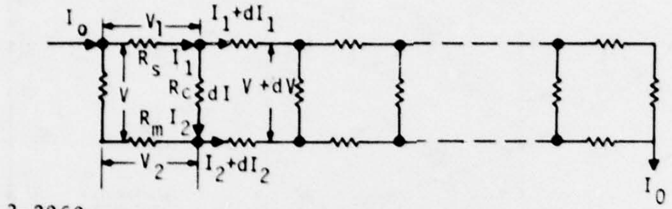
I_o
V_1
I_1+dI_1
R_s
I_1
V
R_c
dI
V + dV
R_m
I_2
V_2
I_2+dI_2
I_0
3-2960

B. EQUIVALENT CIRCUIT

Figure 4. Physical and Equivalent Circuit Model for Calculating R_o of the Metalized Diode Structure

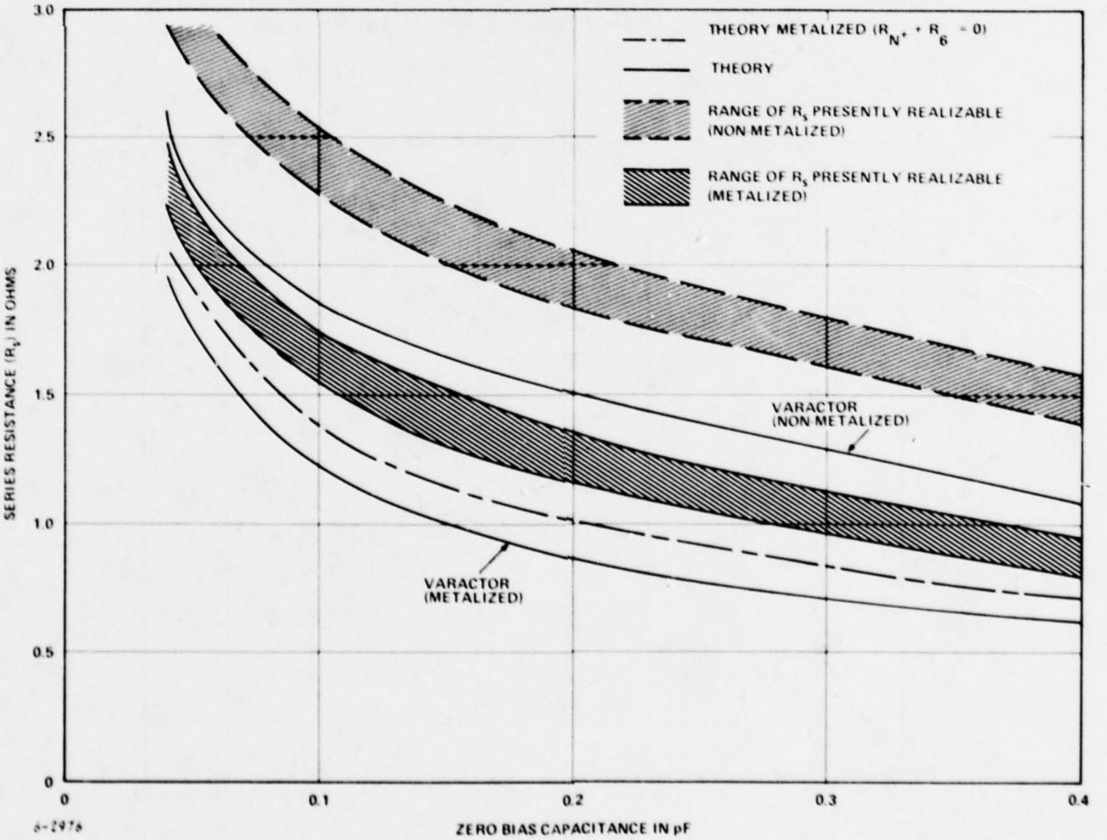

Figure 5. Total Series Resistance as a Function of Zero Bias Junction Capacitance Measured at 60 GHz

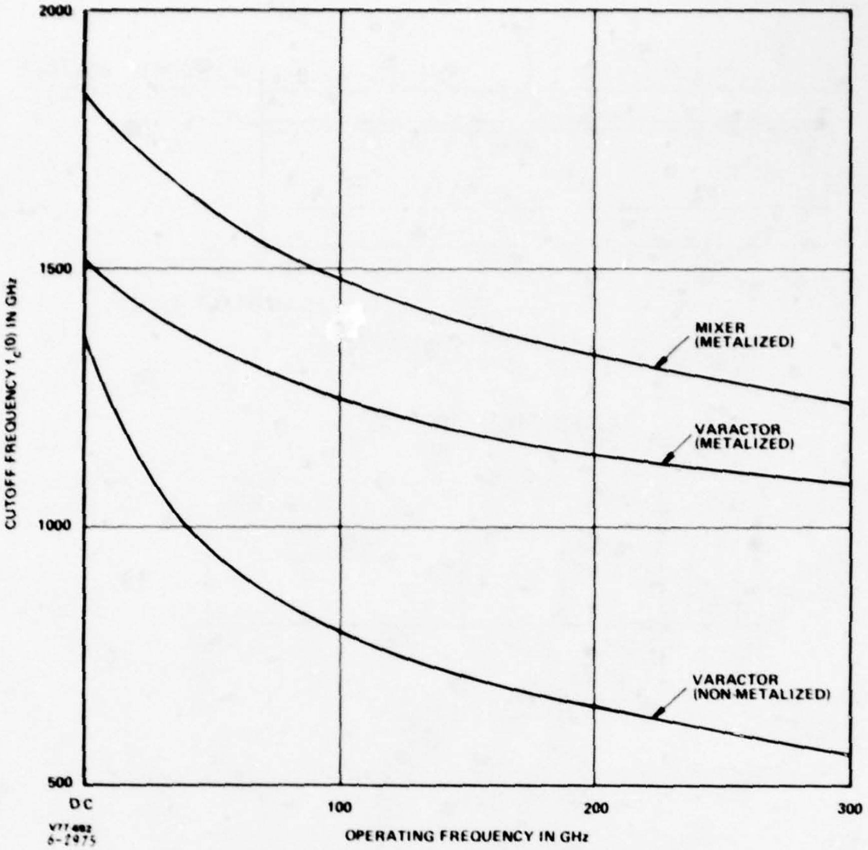

V77-482
6-1975

Figure 6. Theoretical Zero Bias Cutoff Frequency of Metalized and Non-metalized Diode Structures for $C_j(0) = 0.1$ pF

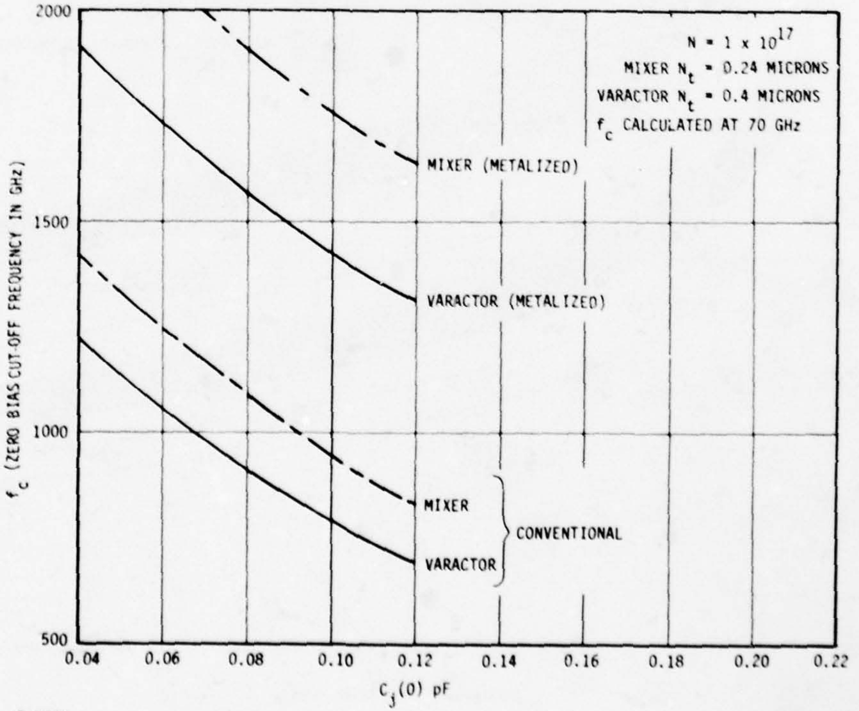

5-1320

Figure 7. Cutoff Frequency Versus Junction Capacitance

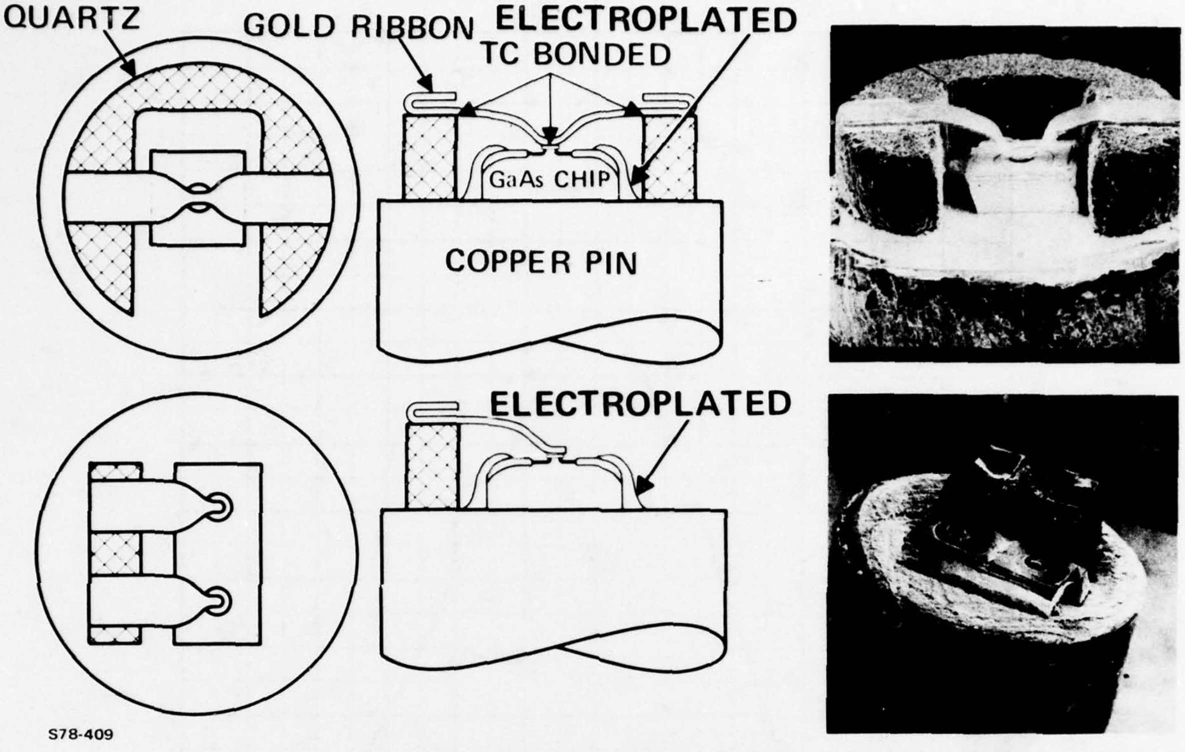
QUARTZ
GOLD RIBBON
ELECTROPLATED
TC BONDED
GaAs CHIP
COPPER PIN
ELECTROPLATED
S78-409

Figure 8. Various Device Configurations

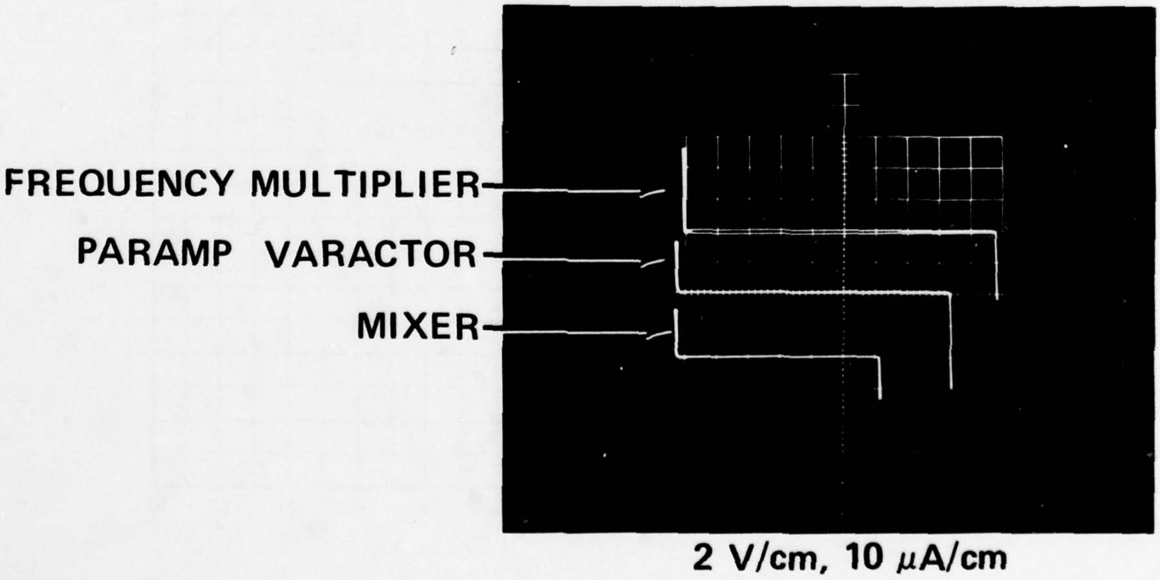

Figure 9. Typical I Versus V Characteristics for Various Metalized Devices

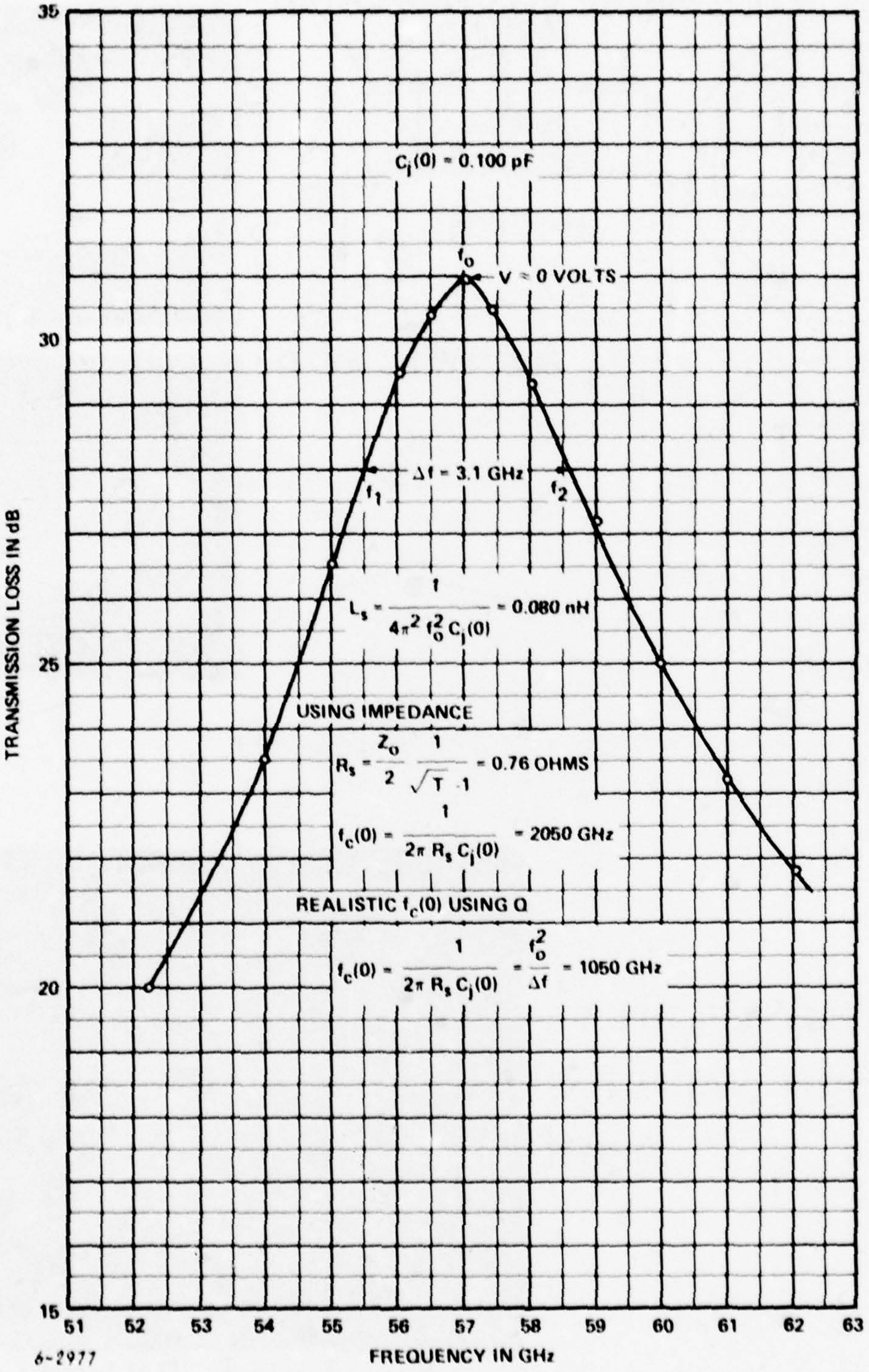

Figure 10. Results of the DeLoach Transmission Method at 57 GHz

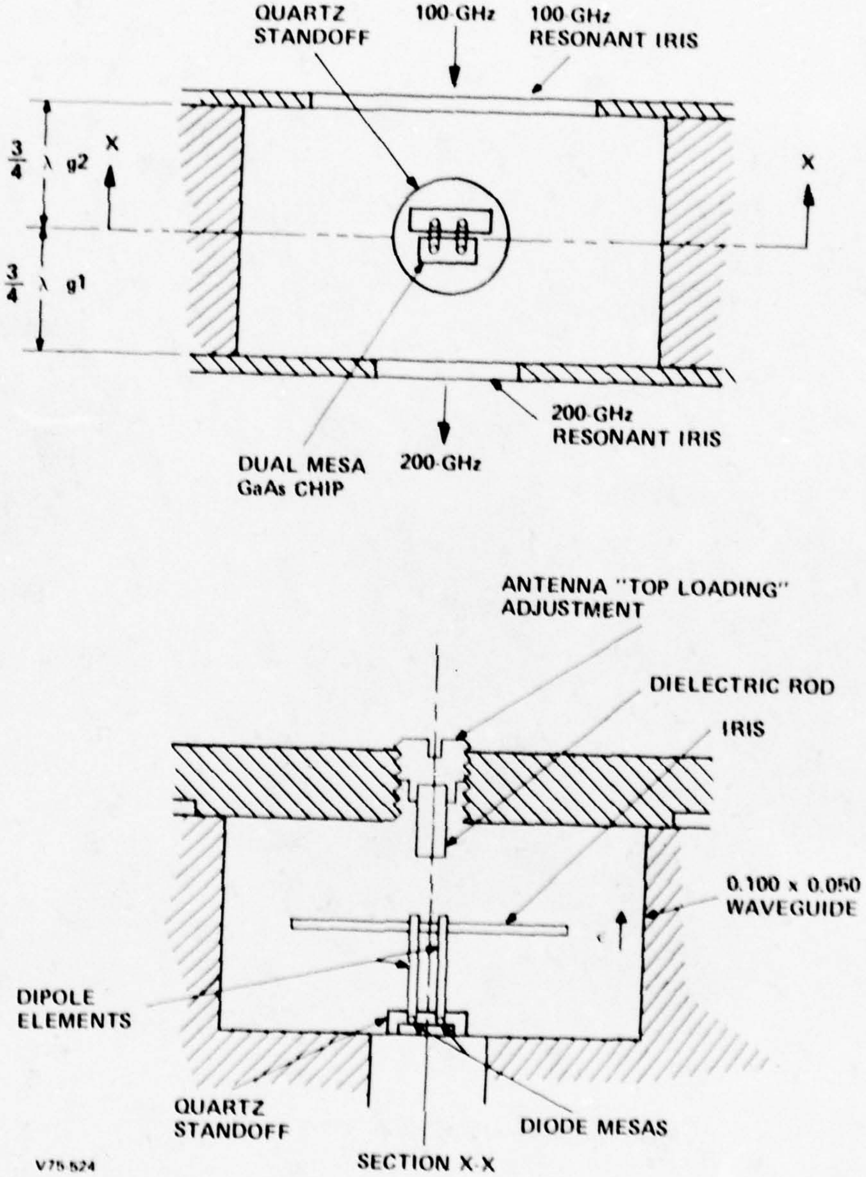
QUARTZ STANDOFF
100 GHz
100 GHz RESONANT IRIS
$\frac{3}{4}$ λ g2
X
X
$\frac{3}{4}$ λ g1
200 GHz RESONANT IRIS
DUAL MESA GaAs CHIP
200 GHz
ANTENNA "TOP LOADING" ADJUSTMENT
DIELECTRIC ROD
IRIS
0.100 x 0.050 WAVEGUIDE
DIPOLE ELEMENTS
QUARTZ STANDOFF
DIODE MESAS
SECTION X-X
V75 524

Figure 11. Monopole Quasi-Optical Doubler

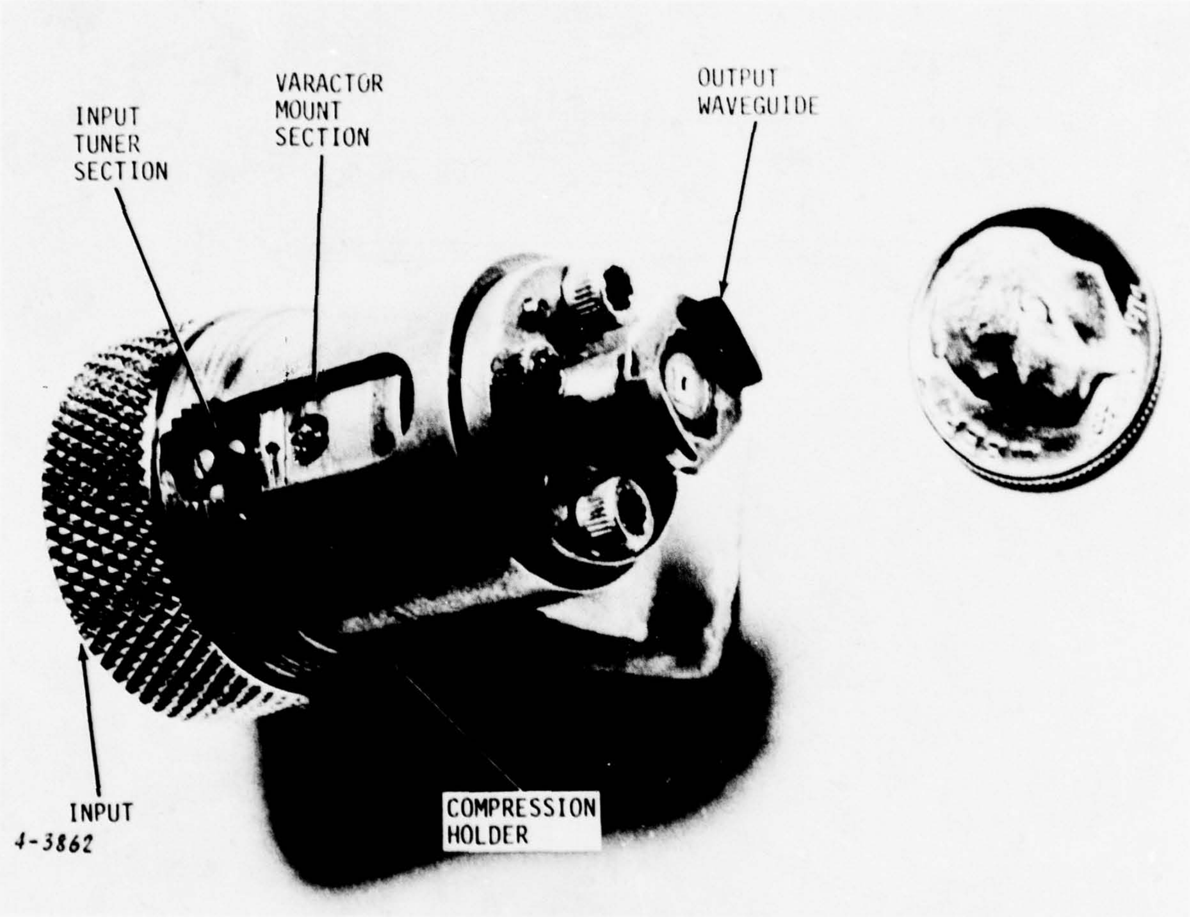
INPUT
TUNER
SECTION
VARACTOR
MOUNT
SECTION
OUTPUT
WAVEGUIDE
INPUT
4-3862
COMPRESSION
HOLDER

Figure 12. Assembled 100 to 300 GHz Tripler

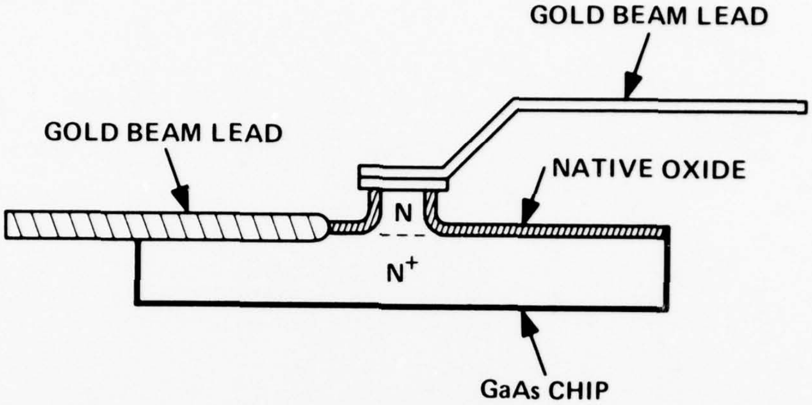
GOLD BEAM LEAD
GOLD BEAM LEAD
NATIVE OXIDE
N
N+
GaAs CHIP

A. MIC APPLICATIONS

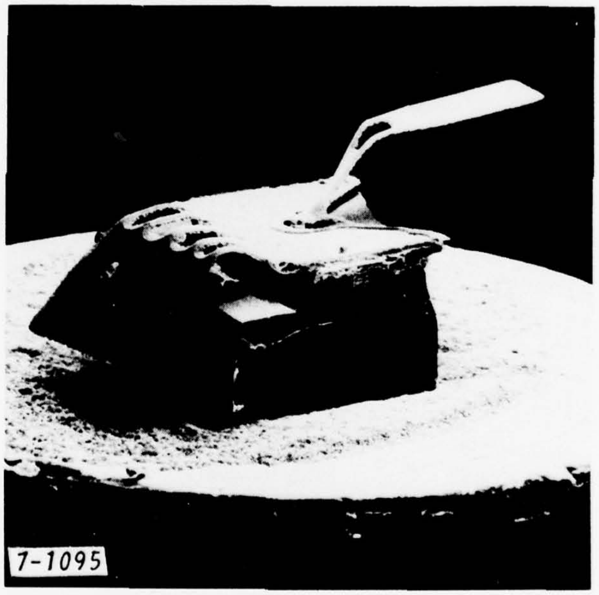

B. SEM PHOTO

Figure 13. Metalized Beam-Lead Diode

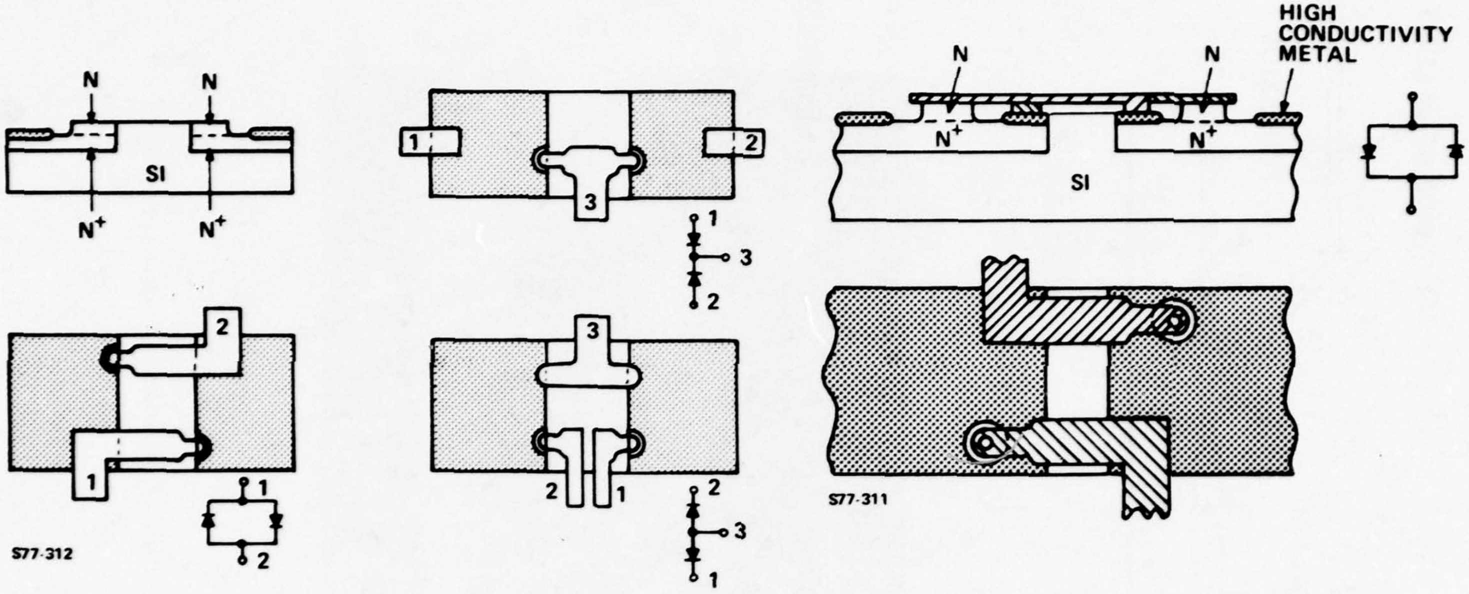
N
N
SI
N+
N+
2
1
1
2
S77-312
1
2
3
1
3
2
3
2
1
2
3
1
HIGH
CONDUCTIVITY
METAL
N
N
N+
N+
SI
S77-311

Figure 14. Schottky Barrier Devices on Semi-Insulating Substrate

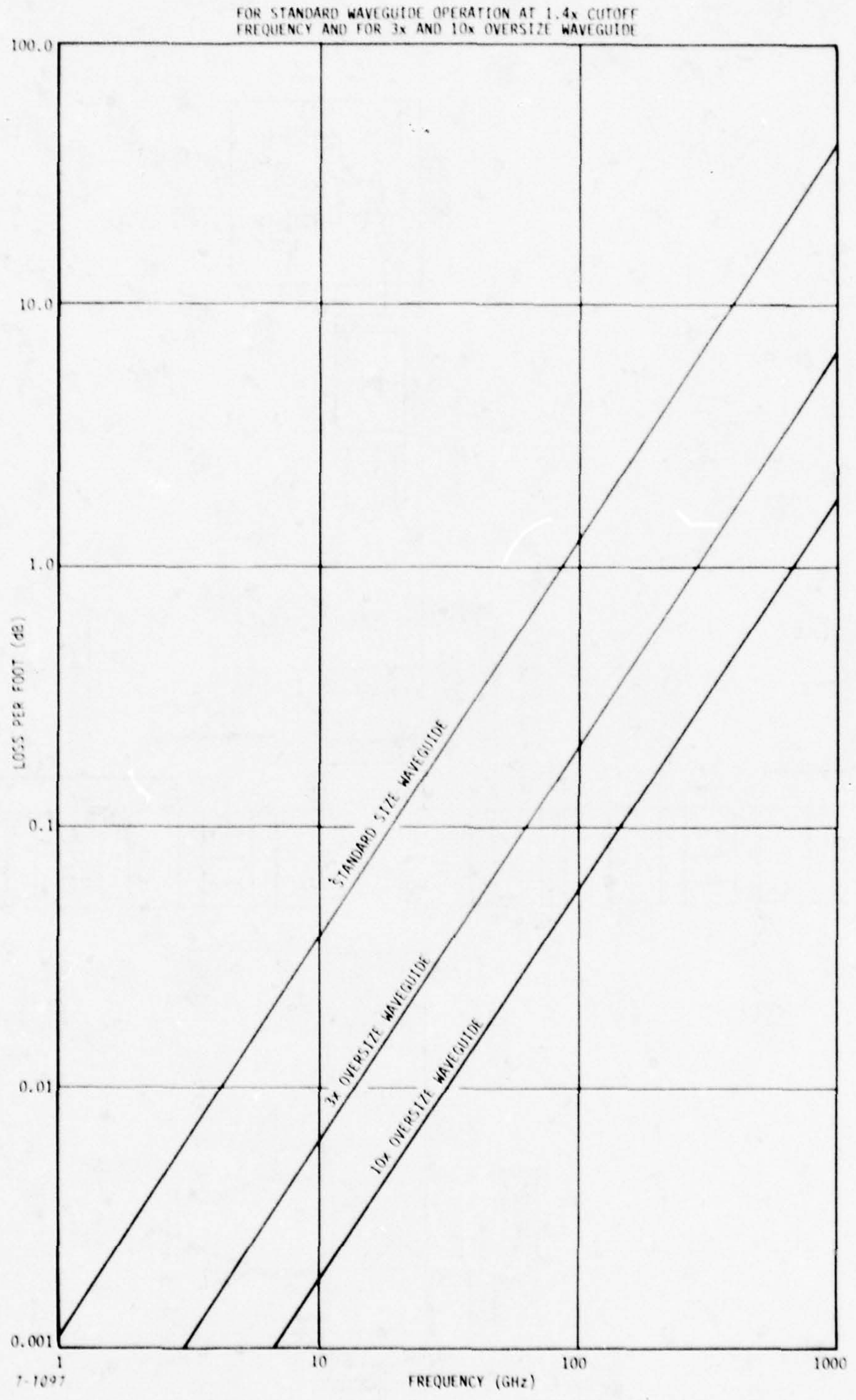

Figure 15. Loss Comparison for Various Waveguide Sizes

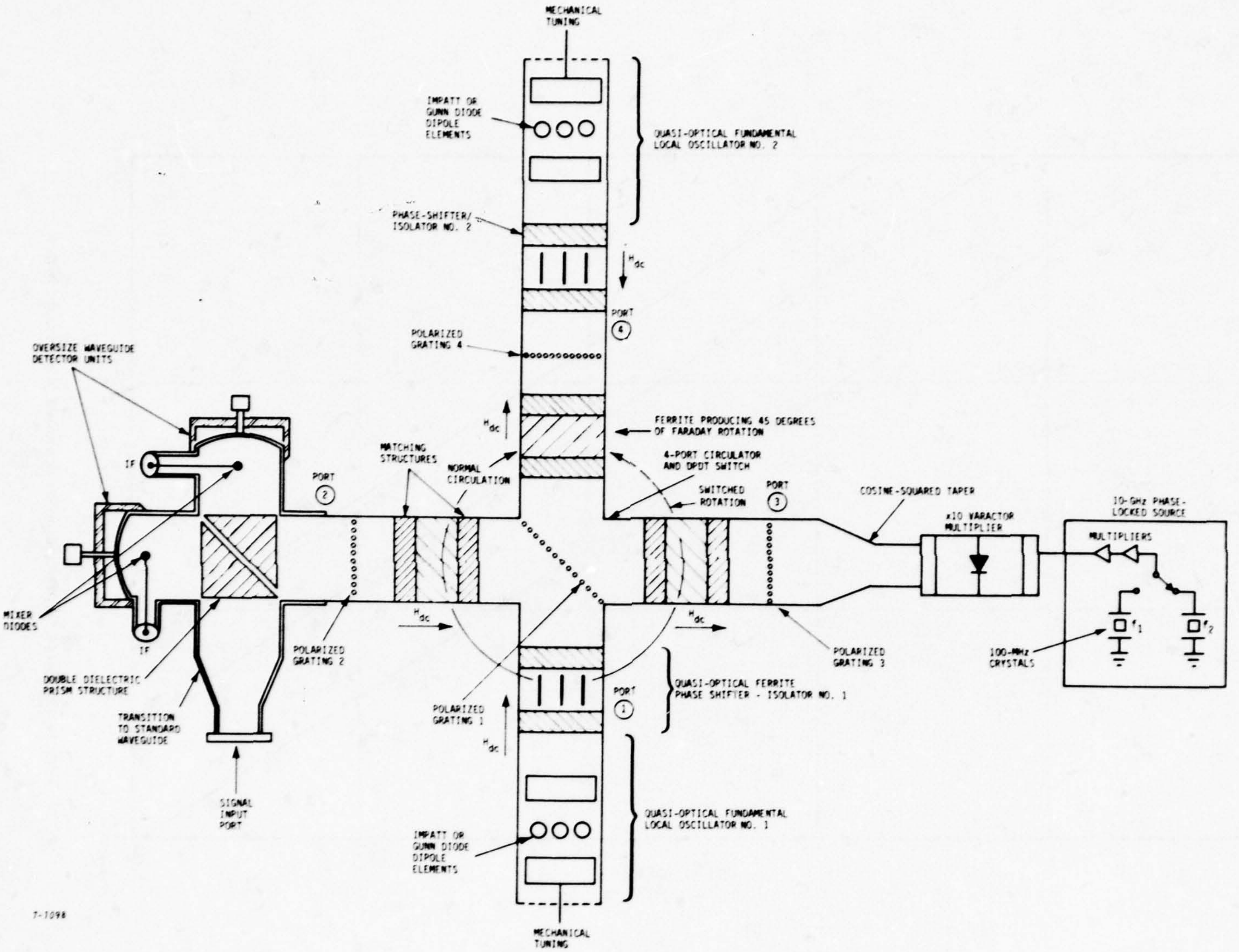
MECHANICAL TUNING
IMPATT OR GUNN DIODE DIPOLE ELEMENTS
QUASI-OPTICAL FUNDAMENTAL LOCAL OSCILLATOR NO. 2
PHASE-SHIFTER/ ISOLATOR NO. 2
H_{dc}
PORT ④
POLARIZED GRATING 4
OVERSIZE WAVEGUIDE DETECTOR UNITS
H_{dc}
FERRITE PRODUCING 45 DEGREES OF FARADAY ROTATION
MATCHING STRUCTURES
NORMAL CIRCULATION
4-PORT CIRCULATOR AND DPDT SWITCH
IF
PORT ②
SWITCHED ROTATION
PORT ③
COSINE-SQUARED TAPER
10-GHz PHASE-LOCKED SOURCE
x10 VARACTOR MULTIPLIER
MULTIPLIERS
MIXER DIODES
H_{dc}
H_{dc}
f_1
f_2
IF
POLARIZED GRATING 2
POLARIZED GRATING 3
100-MHz CRYSTALS
DOUBLE DIELECTRIC PRISM STRUCTURE
QUASI-OPTICAL FERRITE PHASE SHIFTER - ISOLATOR NO. 1
PORT ①
POLARIZED GRATING 1
TRANSITION TO STANDARD WAVEGUIDE
H_{dc}
SIGNAL INPUT PORT
QUASI-OPTICAL FUNDAMENTAL LOCAL OSCILLATOR NO. 1
IMPATT OR GUNN DIODE DIPOLE ELEMENTS
7-1098
MECHANICAL TUNING

Figure 16. Possible Quasi-Optical Receiver Configuration

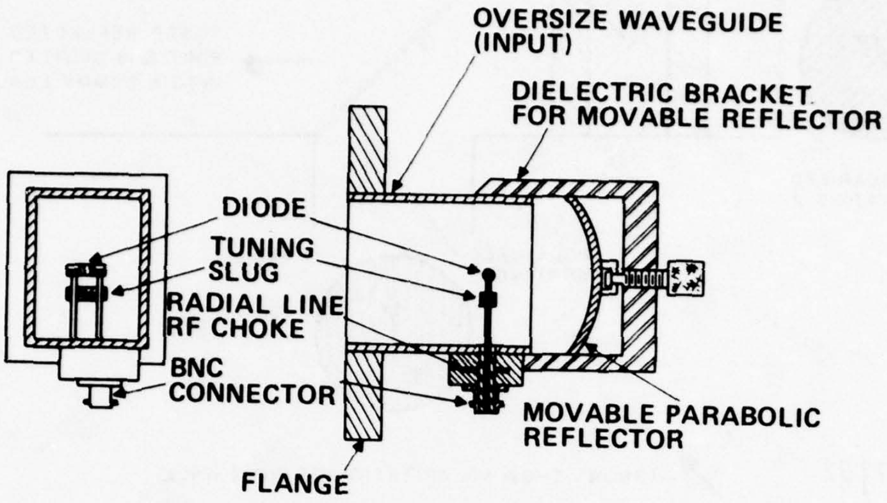
OVERSIZE WAVEGUIDE (INPUT)
DIELECTRIC BRACKET FOR MOVABLE REFLECTOR
DIODE
TUNING SLUG
RADIAL LINE RF CHOKE
BNC CONNECTOR
MOVABLE PARABOLIC REFLECTOR
FLANGE

A. FOCUSED MOUNT MODEL

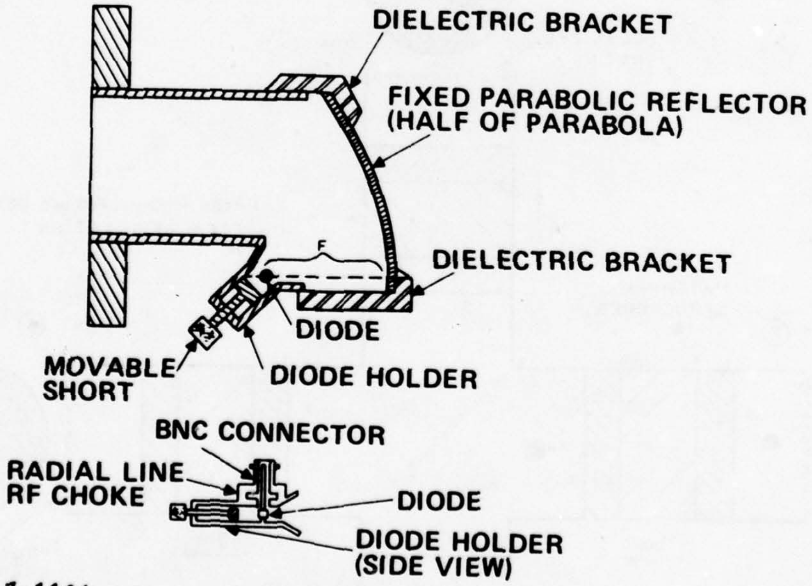
DIELECTRIC BRACKET
FIXED PARABOLIC REFLECTOR (HALF OF PARABOLA)
F
DIELECTRIC BRACKET
DIODE
MOVABLE SHORT
DIODE HOLDER
BNC CONNECTOR
RADIAL LINE RF CHOKE
DIODE
DIODE HOLDER (SIDE VIEW)

7-1106

B. FOCUSED MOUNT MODEL

Figure 17. Oversize Waveguide Mixer/Detector Mounts

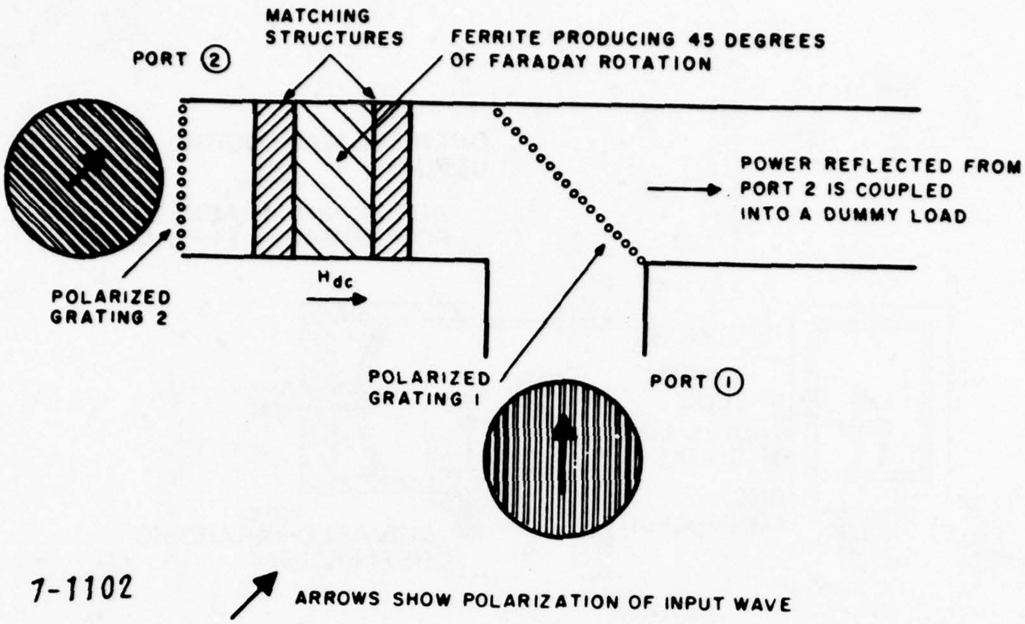
MATCHING STRUCTURES
FERRITE PRODUCING 45 DEGREES OF FARADAY ROTATION
PORT ②
POWER REFLECTED FROM PORT 2 IS COUPLED INTO A DUMMY LOAD
POLARIZED GRATING 2
H_{dc}
POLARIZED GRATING 1
PORT ①
7-1102
ARROWS SHOW POLARIZATION OF INPUT WAVE

Figure 18. Oversize Waveguide Isolator

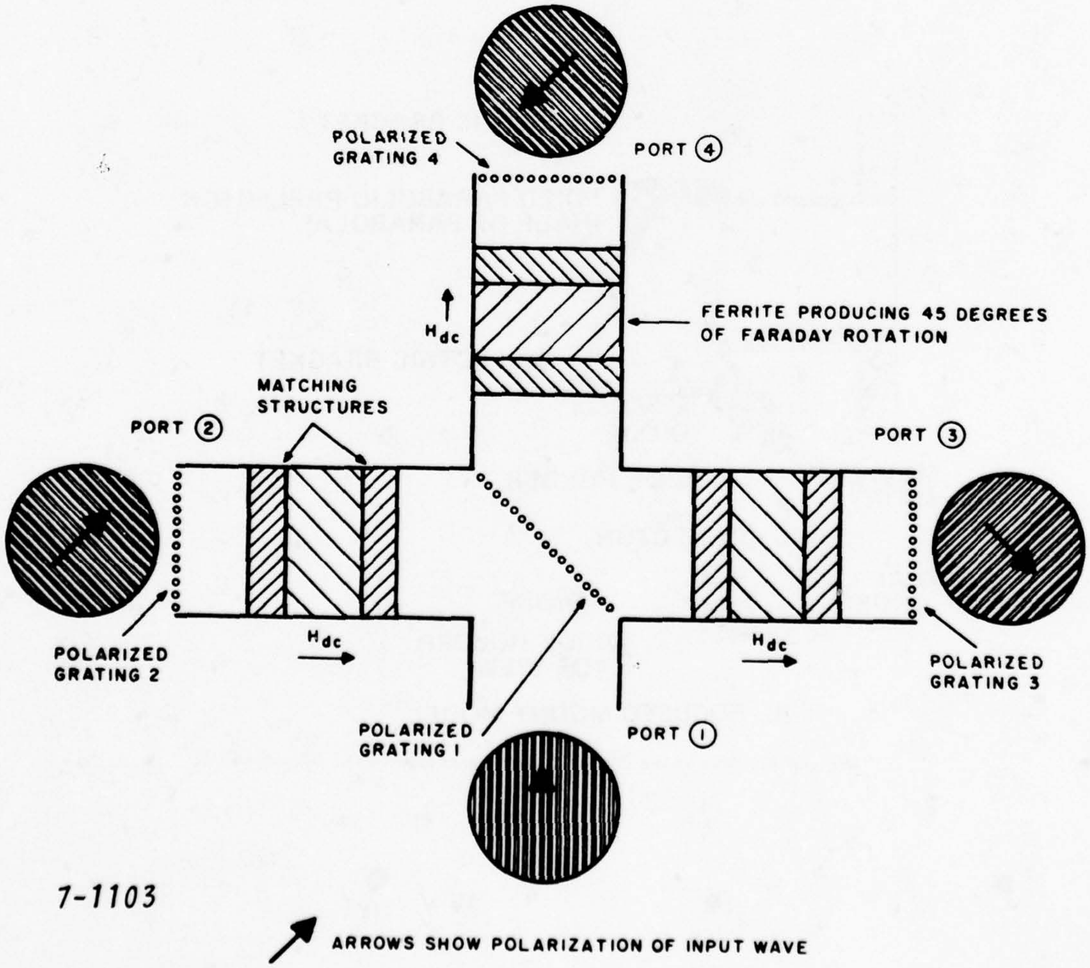
POLARIZED GRATING 4
PORT ④
H_{dc}
FERRITE PRODUCING 45 DEGREES OF FARADAY ROTATION
MATCHING STRUCTURES
PORT ②
PORT ③
POLARIZED GRATING 2
H_{dc}
H_{dc}
POLARIZED GRATING 3
POLARIZED GRATING 1
PORT ①
7-1103
ARROWS SHOW POLARIZATION OF INPUT WAVE

Figure 19. Oversize Waveguide Circulator

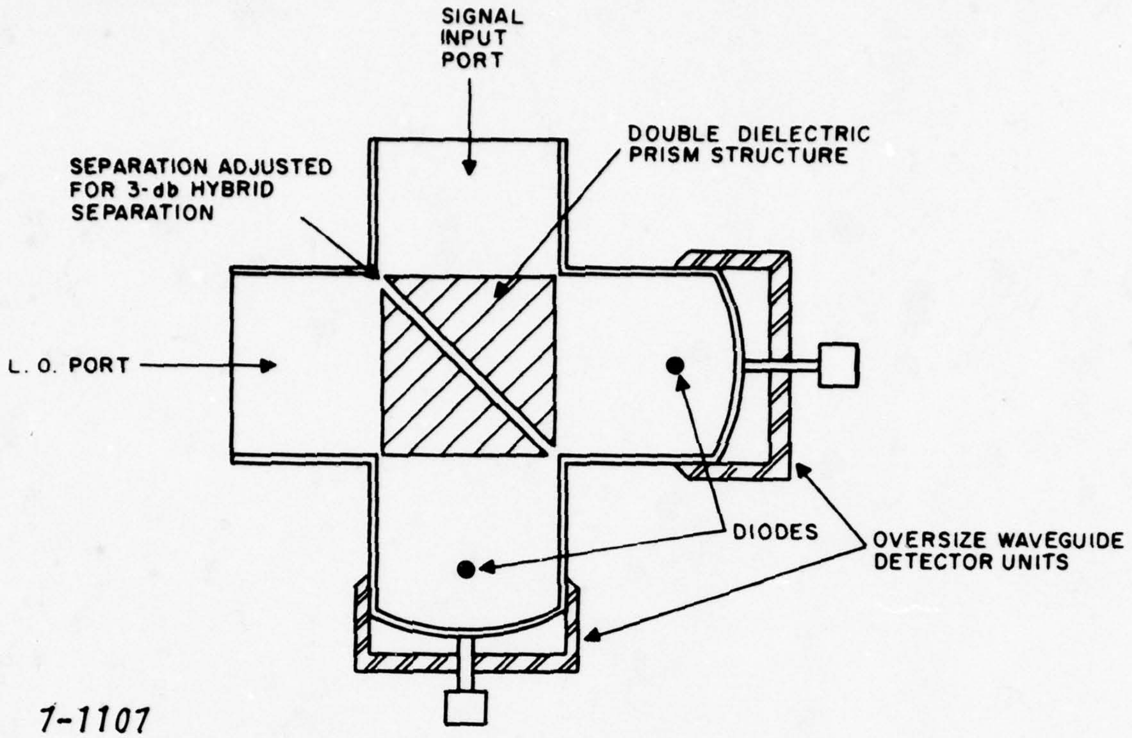
SIGNAL
INPUT
PORT
DOUBLE DIELECTRIC
PRISM STRUCTURE
SEPARATION ADJUSTED
FOR 3-db HYBRID
SEPARATION
L. O. PORT
DIODES
OVERSIZE WAVEGUIDE
DETECTOR UNITS
7-1107

Figure 20. Oversize Waveguide Mixers

DISCUSSION

A.S. Vander Vorst, Belgium

Do you use packaged diodes at those frequencies? or are they always unpackaged?

Author's Reply

All our devices use quartz packages in the form of either horseshoe or a standoff.

M.C.Carter, UK

Are there any problems with reflections when one or more quasi-optical components are put in series.

Author's Reply

AIL has developed techniques to minimize undesirable reflections, that can also give rise to multimoding. However, much work yet remains to be done in this area. We can certainly conclude that, given time, novel techniques can be developed to accurately control and solve to multimode and reflection problems. Therefore I do not anticipate any problems by integrating multi-quasi-optical components.

CONCEPTS AND TECHNIQUES
IN THE UTILIZATION OF
MILLIMETER AND SUBMILLIMETER WAVES

J. H. Rainwater, R. W. McMillan and J. J. Gallagher

Georgia Institute of Technology
Engineering Experiment Station
Atlanta, Georgia 30332

SUMMARY

Extended microwave techniques have resulted in the cross-waveguide and ridged-waveguide harmonic mixers for the higher millimeter wave frequencies in addition to single-ended fundamental mixers, all employing Schottky-barrier diodes. The newly developing technique of subharmonic pumping of an anti-parallel diode pair promises to ease the problem of insufficient local oscillator power. Quasi-optical techniques are being developed to provide more efficient energy coupling, filtering and directing components to replace the poorly performing waveguide devices above 100 GHz. Radiometry as a remote sensing tool is revealing properties of the atmosphere which are not characterized adequately by theory. Propagation measurements in the submillimeter show attenuation to be somewhat greater than previously believed. A millimeter-submillimeter transmitter and receiver system for propagation studies has been constructed at Georgia Tech with an optically pumped laser as a source and a quasi-optical superheterodyne receiver.

1.0 INTRODUCTION

The attractiveness of millimeter and submillimeter waves for remote sensing, weapon guidance and other applications has given impetus to research and development of millimeter and submillimeter devices and systems and has necessitated characterization of atmospheric propagation effects in the atmosphere. The evolution of quasi-optical devices and techniques from a synthesis of microwave and optical practices has proceeded along with the extension of more familiar microwave devices into the millimeter and submillimeter regions.

Georgia Tech is conducting extensive research and development programs aimed at the goal of full utilization of millimeter and submillimeter waves (sometimes collectively referred to as near-millimeter waves, 100 - 1000 GHz). In the sections to follow, programs and topics are discussed in the areas of extended microwave techniques, quasi-optical devices and methods, radiometry, and measurements of importance to spectroscopy and propagation. Measurements obtained with operational systems will be highlighted and their significance to physical questions and future system applications discussed.

2.0 EXTENSIONS OF MICROWAVE TECHNIQUES

Following the impetus to research and development of centimeter radar that World War II provided, physicists in various laboratories began extending the techniques of microwave radar into the near-millimeter region of the spectrum. While the generation of coherent radiation found realization in extended klystron and traveling wave tube principles, masers, optically and electrically pumped lasers and relativistic electron beam devices; non-thermal detector and mixer technology followed another path. This path paralleled the growth in knowledge of semiconductor physics and technology: the "cat-whisker" diode emerged into a new era of applicability. Current research at Georgia Tech is directed toward developing structures and techniques to utilize the recontactable Schottky-barrier diode, a descendant of the "cat-whisker" diode, as a near-millimeter detector or superheterodyne mixer.

Harmonic superheterodyne mixers, which require local oscillator (LO) pumping at one-half the signal frequency, have been constructed for the near-millimeter in both crossed-waveguide and single-ended configurations. Figure 1 illustrates two mixer structures which are in operation at Georgia Tech. The crossed-waveguide mixer (1(a)) couples LO energy to the diode through a coupling hole in the LO waveguide, to the signal waveguide. The diode mixes harmonics of the local oscillator with the signal, heterodyning spectral information to a convenient intermediate frequency (IF) for amplification and further processing. IF filtering and matching are accomplished within the barrel part of the mixer using appropriately machined impedance transforming materials. Fibure 1(b) shows a ridged-waveguide, single-ended mixer designed by G. T. Wrixon of University College, Cork Ireland. This mixer was constructed to operate near 230 GHz and couples both LO and signal frequencies in the same port, in this case a ridged-waveguide which allows simultaneous transmission of the fundamental signal and LO modes to the diode throughout a bandwidth larger than typical rectangular waveguide would provide. IF matching and filtering is achieved within the block by a precision machined stripline, five element, low pass Tchebyscheff filter. By way of comparison, the best noise figures obtained with a crossed-waveguide mixer at 183 GHz have been 16 dB while the ridged-waveguide mixer is expected to yield noise figures below 15 dB at 230 GHz.

Fundamental mixing in the near-millimeter has been achieved at Georgia Tech with two mixer structures illustrated in Figure 2. Figure 2 shows a conventional single-ended mixer with replaceable Sharpless-wafer mounted diodes. This type of mixer is convenient for systems where a field replaceable diode capability is desired. Noise figures of 12 dB have been obtained at 183 GHz with these devices at Georgia Tech. Figure 3 shows another single-ended configuration, designed to ease the difficulty of contacting typical 4 μ diameter diodes with etched, pointed 12 μ diameter whiskers. The mixer block can be partially disassembled for diode contacting in the laboratory and then quickly reassembled for operational use. This mixer, often called a split block mixer, contains an integral IF matching and filter network in stripline design. Noise figures of 14 dB have been demonstrated at 183 GHz with the split block mixer to date.

Both fundamental and harmonic mixing schemes for the near-millimeter require reliable, stable, LO sources which are always expensive and sometimes unavailable for the higher frequencies. To overcome these disadvantages a new harmonic mixing technique, referred to as subharmonic mixing, is being developed at Georgia Tech. Typically, subharmonic mixing is the process of pumping an anti-parallel diode pair [1] with a LO frequency one-half or one-fourth the signal frequency. The anti-parallel diode configuration, illustrated in Figure 4, has the advantages of reducing conversion loss by suppressing fundamental mixing products and lowering the mixer noise figure through suppression of LO noise sidebands. In addition, a mixer with such an anti-parallel diode pair requires less LO power than its single diode equivalent.

Future mixing schemes at higher near-millimeter wave frequencies will, of necessity, be of an open structure design because fundamental mode waveguide dimensions approach diode crystal dimensions near 400 GHz. The reader is referred to Gallagher and Blue (reference 2), for examples and discussion of open structure type mixers.

3.0 QUASI-OPTICAL DEVICES AND TECHNIQUES

3.1 Background

The continuing extension of microwave source and detector technology further into the near-millimeter portion of the electromagnetic spectrum has created a need for low-loss components suitable for use at these shorter wavelengths. In particular, the availability of optically pumped lasers [3], extended interaction oscillators, and relativistic electron beam devices [4], as near-millimeter sources, and the development of quasi-optical mixers have contributed to this need.

In the region of frequencies above about 100 GHz, losses in waveguides become significant, and this limitation is further aggravated by poorer performance of couplers, attenuators, wavemeters, and other passive components at higher frequencies. Fortunately, since wavelengths in the submillimeter are small compared to practical optical component dimensions, and excellent transmitting and reflecting materials are available in this frequency region, it is possible to overcome most of these limitations by using quasi-optical techniques.

3.2 Quasi-Optical Antennas

Antennas used in the near-millimeter spectrum are essentially identical in form to those used in the optical portion of the electromagnetic spectrum, consisting of lenses and mirrors; but the materials used for fabrication of these elements may be different. Lenses are generally made of plastics such as rexolite, TPX or teflon, and mirrors are made of high-conductivity metals such as are used for optical mirrors. Antenna feeds are usually conical or pyramidal horns, except at the shorter wavelengths where direct focussing of radiation is a practical approach to avoiding waveguide losses.

Diffraction losses in a near-millimeter wave antenna system will be higher than for a corresponding optical system because the full-width Fraunhofer diffraction limited beamwidth is approximately $2.4 \lambda/d$, where d is aperture diameter, at the 90% power points. Although diffraction limited output is easy to achieve in these systems, the above expression shows that near millimeter beamwidths will be several orders of magnitude greater than corresponding beamwidths for optical and near infrared systems. Furthermore, geometrical or ray optics descriptions of quasi-optical devices will require significant corrections for the effects of diffraction [5] since the aperture diameters involved are on the order of one hundred wavelengths instead of several thousands of wavelengths as for the case of visible light.

Microwave lenses are usually machined from a block of rexolite, teflon, polyetheylene, or other suitable low-loss material. Because of the comparatively long wavelengths, and corresponding immunity to slight surface defects, it is possible to machine lenses directly with a hyperbolic shape, thus eliminating spherical aberration. Machine tool cutters can be fashioned from aluminum or other easy-to-work material, and polishing can be done with fine sandpaper.

Fresnel reflection from lens surfaces is a difficult problem to solve in the design of microwave quasi-optics. Lenses are usually made in the plano-convex configuration, and are anti-reflection "coated" by bonding a quarter wavelength thick layer of a dielectric material with a refractive index equal to $n^{1/2}$, where n is the refractive index of the lens, to the surfaces. Unfortunately, such materials are not generally easy to find. Alternatively, quarter wave deep grooves may be machined into the surface with a spacing such that the average index of the grooved volume is equal to $n^{1/2}$. This machining is difficult on the curved surface of the lens, so that this surface is generally left uncorrected. Figure 5 shows the details of the matching of lenses to air by slotting.

Reflecting antennas for near-millimeter systems may take the same variety of configurations as has been devised for optical telescopes including Newtonian, Cassegrain, Gregorian, and variations of these types. The secondary mirror of such a reflecting telescope is usually driven with a feed horn. Because of the comparatively large beamwidth of near-millimeter systems, both primary and secondary mirrors must be made large to minimize spillover power. Reflective optics have the advantage of not requiring the matching layer required in refractive systems, and may be made from commonly used reflecting metals, such as gold and aluminum, which have excellent reflectivity in the near-millimeter spectrum.

Horn antennas may be used as feeds for both lens and mirror antenna systems up to a frequency of about 300 GHz. Corrugated horns have been devised which have minimum side lobes in this range of frequencies. Beyond 300 GHz, sources consist mainly of optically pumped or electric discharge pumped lasers, which use partially reflecting mirrors for output coupling. Figure 6 shows a corrugated horn antenna designed for 30.0 GHz with its associated radiation pattern. Computer programs have been devised to aid in the design of such horns.

3.3 Quasi-Optical Diplexers

The design of diplexers used for coupling both local oscillator and signal power to a single mixer is a difficult problem in the near-millimeter wavelength region that has received some attention during the last few years. This problem is especially important because of the low output power of available local oscillators in the near-millimeter region. Successful diplexer designs must be configured so as not to waste any of this scarce LO power.

A diplexer designed by Martin and Puplett [6] is shown in Figure 7. A signal beam plane polarized at 45° to the normal to the page is incident from the left. This beam is divided into components polarized parallel and perpendicular to the page by wire grid D1. The component perpendicular to the page is reflected from the wire grid and the mirrors A and is recombined at the output of grid D2 with the component polarized parallel to the page. A local oscillator input incident from above, also polarized at 45°, follows essentially the same path, and is combined with the signal in the mixer as shown. The diplexer is tuned by varying the distance of the plane reflectors from the wire grids so as to give constructive interference of signal and local oscillator at the output. Diplexers based on similar interferometric principles have been designed by Wrixon [7], Gustincic [8], and Erickson [9]. Schematic drawings of these devices are shown in Figures 8, 9, and 10.

3.4 Quasi-Optical Filters and Interferometers

Several different types of quasi-optical filters have been devised using Fabry-Perot interferometers in plane, confocal and semiconfocal configurations. Confocal and semiconfocal devices use solid metal mirrors with small coupling holes for input and output radiation. These devices have extremely high Q's, sometimes reaching 10^6, but these higher Q devices generally have higher losses. Plane-mirror Fabry-Perot interferometers may use solid mirrors, wire grids, or perforated metal plates for reflectors. The Q's of these devices depend upon coupling hole size, grid spacing and orientation, and the size of the perforations, respectively.

The four-grid Fabry-Perot interferometer has been analyzed by McMillan and Langley [10] and by McMillan, Branch, and Lamb [11], who have found that this filter is bandpass tunable by either varying the relative grid orientation or by varying the spacing between elements of the two grid pairs. Furthermore, this filter can be made to rotate the plane of polarization of an incident signal on reflection, and there is some indication that this rotation can be carried out on transmission also.

The transmitted power τ for the four-grid array shown in Figure 11(a) is given by

$$\tau = T^4 \cos^2(\theta-\beta) \left\{ \left[1 + \frac{\sin^2\gamma(1-R^2 \cos^2\gamma - RT \sin^2\gamma)}{\cos^2\gamma(1-2R \cos 2\phi_1 + R^2)} \right]^2 + 4RT \sin^4\gamma \left[\frac{\sin\delta + R \cos^2\gamma \sin(2\phi_1-\delta)}{\cos^2\gamma(1-2R \cos 2\phi_1 + R^2)} \right]^2 \right\}^{-1} . \tag{1}$$

where R and T are reflectivity and transmissivity of a single grid for radiation polarized parallel and perpendicular to the wires, respectively, β is the angle of input polarization, γ is the angle between the grids, ϕ_1 is the phase shift between elements of a grid pair, and δ is the total phase shift through the grid. The grid angles θ and α are defined as shown in Figure 11(b). Using this equation, tunable grid filters have been constructed which have performances which agree well with theory. Figure 12 shows measured and calculated results for a filter of this type.

A very useful three-grid quasi-optical filter has been designed by Saleh [12, 13], who has achieved excellent agreement of measured transmission with theory based on measurements made at 50 GHz. The bandpass characteristics of this filter are similar to those of the four-grid filter discussed above, and it is also tunable by varying the angle of the interior grid of the three-grid array.

One of the most effective quasi-optical devices which is used in the near-millimeter wave region is the interferometer. The device has taken many forms in the applications which have been addressed so far, and their use can be seen in many future system applications. Both Fabry-Perot and Michelson interferometers have been employed, and for the Fabry-Perot interferometer, high-Q and low-Q devices exist depending upon the application for the apparatus. The devices can be parallel plate, semi-confocal or confocal interferometers and can be employed as either waveguide coupled or horn/lens coupled resonators. Figure 13 shows an example of the use of one of these interferometers in a molecular beam spectrometer [14].

3.5 Miscellaneous Components

Submillimeter analogs for many optical devices have been devised, including polarizers, beam splitters, quarter wave plates, attenuators, and the Fresnel rhomb. Each of these component types will be discussed briefly in this section.

Wire grids are extensively used as polarizers and beam splitters in the submillimeter, and recent advances in fabrication techniques have extended the usefulness of these devices into the near infrared. When used as a polarizer, the component polarized parallel to the wires is reflected and the component perpendicular to the wires is transmitted. Beam splitter applications use these same properties, with the result that the wire grid is a polarizing beam splitter.

A beam splitter based on frustrated total internal reflection (FTIR) has been described by Baker and Valenzuela [16], which uses two identical low-loss dielectric prisms which form a cube when joined together. The prisms are separated on a face diagonal of the cube, and the attenuation and resultant off-axis coupling can be varied by changing the spacing along this diagonal. These devices are described analytically by Fellers [17]. This beam splitter consists of two 90° prisms with a small gap between them. If no gap exists, an incident beam would be transmitted without change of direction, whereas in the absence of one prism, the incident beam would be totally internally reflected, emerging at an angle of 90° to the incident beam. With a gap between the prisms, the beam is partially transmitted and partially reflected. Figure 14 shows the configuration of the double-prism while the transmittance as a function of wavelength is shown in Figure 15. The reflected signal is R = 1-T.

The double-prism can be employed for several applications. Figure 16 shows it employed as an attenuator [18]. The attenuation as a function of the prism separation is given in Figure 17 for both parallel and perpendicular polarization, relative to the plane of incidence. The curves were obtained by using $\varepsilon = 2.54$ for the dielectric constant of rexolite. Figure 18 shows the double-prism as a directional coupler, the coupling of which can be varied as a function of the prism separation. Figure 19 shows the prisms fed by a 300 GHz carcinotron with a horn/lens system. The detector is shown at the left of this figure. A micrometer adjusts the separation of the prisms for use as an attenuator and/or a directional coupler.

Wave plates may be fabricated from biregringent materials in a manner similar to that used for optical retarders. Because of its good transparency throughout much of the submillimeter region [19], crystalline quartz is a good choice for this application, but practical quartz wave plates may be prohibitively thick at the longer wavelengths because of its low biregringency. For generating circular polarization, a Fresnel rhomb has been devised by Strauch et al [20]. This device was used to analyze Zeeman components in submillimeter spectroscopy, and is shown in Figure 20.

3.6 Uses and Limitations of Quasi-Optics

It appears likely that optical techniques will provide many of the methods required to extend the usefulness of the wavelength region between 10 and 1000 microns for remote sensing, spectroscopic and military applications. Submillimeter analogs of many optical and microwave components are available, and concentrated effort by many workers is resulting in the discovery of new techniques at a rapid pace.

The availability of sources such as optically pumped lasers, relativistic electron beam devices, and extended interaction oscillators, will surely stimulate the development of quasi-optical techniques in the near-millimeter spectral region. This development may not be as fast as that associated with the evolution of the laser in the visible and near infrared, because lasers are readily available and have reached a high level of development; and because most of the optical techniques used with lasers were well known before the laser was invented.

Of the areas that should be pushed to speed up development, the availability of a reliable duplexer for the near millimeter spectrum would appear to be important. The development of suitable matching techniques, such antireflection coatings; and the design of quasi-optical microwave devices, such as isolators and circulators would also be helpful.

4.0 RADIOMETRY

4.1 Theoretical Aspects

The properties of the atmosphere, as they affect the propagation of near-millimeter radiation, can be characterized by the remote sensing technique of radiometry. In radiometric terminology the effective brightness temperature of the sensed medium, called the antenna temperature, is determined by a radiometer. The effective background sky brightness temperature T_b, measured by a radiometer at altitude h with an infinitesimally narrow beamwidth looking upward at zenith angle θ, is

$$T_b = \int_h^{\infty} \alpha(Z)T(Z) \cdot \exp\left(-\int_h^{Z} \alpha(Z')\sec\theta \, dZ'\right)\sec\theta \, dZ, \qquad (2)$$

in which T(Z) is the temperature of a stratum of atmosphere of thickness dZ located at altitude Z. The parameter $\alpha(Z)$ is the atmospheric absorption coefficient which depends on several factors in addition to the line shape factor. There is also a strong dependence on altitude because the density of water vapor molecules decreases rapidly with increasing altitude. These dependences are discussed in detail by McMillan, et al [21].

Equation (2) must in general be solved numerically because of the complex nature of the absorption coefficient $\alpha(Z)$. A computer was programmed to solve this equation using the Gross analytical line shape [22], an empirical modification to the Gross line shape proposed by Gaut and Reifenstein [23], and the Schulze-Tolbert empirical line shape [24]. The water vapor density and temperature variables used in the calculations were obtained from ground level measurements at the time radiometric measurements were made.

4.2 Experimental Aspects

A Dicke superheterodyne radiometer has been developed to measure the emission spectrum of atmospheric water vapor from 160 to 210 GHz. The radiometer, as shown in Figure 21, employs a crossed waveguide harmonic mixer containing a recontactable Schottky-barrier diode. The diode junction is made by a 12.7 μ diameter gold plated phosphor-bronze whisker etched into a 1 μ tip. Water cooled millimeter wave reflex klystrons, operating at one-half the signal frequency, are used as local oscillators to provide the radiometer a tuning range spanning the 183.3 GHz emission line. The IF output of the harmonic mixer is amplified by two Avantek AM2020-M FET amplifiers centered at 1.6 GHz in a bandwidth of 1.4 GHz. An Aertech 4-diode Schottky-barrier square law second detector provides a DC signal for snychronous detection.

A Fabry-Perot wire grid interferometer has been constructed to function as a tunable bandpass filter in order to effectively eliminate detecting signals at the third harmonic of the local oscillator. The output of the interferometer is focused into a conical, corrugated horn through a 77 mm focal length rexolite lens. The horn feeds the harmonic mixer through WR-5 waveguide.

The chart-recorded output of the radiometer is calibrated at each measurement frequency by observing the DC output change as an ambient load (300°K) is replaced by a calibration load (98°K). The temperature difference between the ambient reference load and a calibration load determines a scale factor from which the antenna temperature of the sky can be determined. The Georgia Tech radiometer has demonstrated total system noise figures as low as 14 dB which corresponds to 0.22°K minimum detectable temperature.

4.3 Comparison of Experimental with Theoretical Data

The calculations discussed in Section 4.1 were made under the conditions measured at the ground based radiometer site at the time the radiometer measurements were made. Figure 22 shows typical results obtained in this way. The three curves are the calculated results using the Gross, modified Gross, and Schulze-Tolbert line shapes; and the points represent measured values of antenna temperature obtained during the late mornings and early afternoons of 7 July and 25 August, 1977, respectively. Since the skirts of the water vapor absorption lines extend to frequencies far removed from their center frequencies, a total of six of the stronger lines extending in frequency up to 556.7 GHz were considered in the calculations.

Figure 22 shows that none of the line shapes considered give good agreement with experiment, although the Schulze-Tolbert expression comes closest. The measurements of antenna temperature away from the absorption line peak, which show disagreement with theory, are given more credibility by the fact that the radiometer consistently measures ambient temperature at frequencies near the line peak, in agreement with theory. Measurements near the line peak therefore provide another method of calibrating the radiometer and serve to confirm data in the wings. This type disagreement has also been observed in propagation experiments in this frequency region, especially under conditions of high humidity. For a time, this excess attenuation was thought to be due to water vapor dimers, but it has been shown that dimers will not account for the magnitude of the observed attenuation. H. A. Gebbie [25] has characterized this disagreement as "anomalous absorption". The continued generation of experimental data is needed to improve the analytical models of atmospheric absorption so that attenuation can be calculated with some degree of certainty in the near-millimeter region.

5.0 NEAR-MILLIMETER WAVE PROPAGATION STUDIES

The measurement of atmospheric parameters can be performed by a combination of techniques, which include laboratory spectroscopic measurements, propagation of monochromatic signals and broadband incoherent source propagation. Each of these processes contribute significant information toward the understanding of the atmosphere. In performing laboratory experiments, care must be taken in both the experimental techniques and the interpretation of the data.

5.1 Laboratory Measurements

Spectroscopy of the millimeter-submillimeter wavelength region is closely related to the molecular constituents of the atmosphere. Currently, at Georgia Tech, an extensive program on water vapor absorption is being performed. The water molecule, despite the long history of its spectroscopic observation, is still a difficult molecule to understand with respect to its contribution to atmospheric attenuation. Clustering, difficulties of accurately determining densities, adequacy of line shape theory and interaction of the molecule with the measurement apparatus can seriously affect the analysis of the data. As a result, several laboratory techniques are being employed at Georgia Tech to provide a broad spectral coverage, permit observations in the transmission windows and on the spectral lines, and provide redundancy of results by a variety of techniques. Both coherent and incoherent spectroscopic methods are being employed. Spectrometric apparatus includes large Fabry-Perot spectrometers (for non-resonant absorption measurements), waveguide cells for line width and line shape measurements at reduced pressures, parallel plate Stark cells for dipole moments and Fourier spectrometers for broad band measurements.

Propagation through long cells with optically pumped lasers and a carcinotron complement the absorption measurements being made with the above apparatus. The optically pumped lasers provide a large number of emission lines across the submillimeter wavelength region. The technique shown schematically in Figure 23 has been employed to utilize a TEA laser-pumped submillimeter laser for observations at discrete wavelengths throughout the spectral region of interest. Because of the amplitude instability of the TEA laser, it is necessary to provide a monitor of the emission before transmission through the absorption cell. The reference channel and signal channel outputs are averaged over several pulses and compared with the gas in and out of the cell. Detection is achieved by either pyroelectric detectors or Schottky-barrier diodes.

The many techniques which are available for providing data on atmospheric absorption should contribute significantly to an understanding of the absorption mechanism. However, the results continue to produce values which are higher than the theoretical values based upon a monomer water molecule. The suggestion has been made by Derek Martin [26] to perform measurements in the spectral region between absorption lines of molecules that do not contain hydrogen. This would allow the checking of line width/shape theory for molecules without hydrogen bonding. It would give an indication if the theory is correct and the hydrogen bonding in water is causing the difficulties or if further theoretical work is required. Currently, Georgia Tech is initiating a program of measurements on non-hydrogen molecules, OCS, CO, ICN, SO_2, N_2O, NO and PF_3. These measurements will be extended to hydrogen - containing molecules, $CH_3C\ell$, NH , CH_3CN, HCN, CH_3F, CHF_3 and H_2S, before continuing the H_2O measurements.

5.2 A Near-Millimeter Wave System For Propagation Studies

5.2.1 Optically Pumped Source

The optically pumped laser used for propagation studies is a pulsed device pumped by a Lumonics CO_2 TEA laser. The pump laser has an output of 2-10 joules depending on the transition, and outputs ranging from 35W to 25kW have been obtained with the far infrared laser, also depending on the transition being excited.

Figure 24 is a sketch of the far infrared laser. The end boxes are machined from a single piece of aluminum to minimize leaks. The waveguide is a section of 38 mm glass pipe which may be chosen to be any convenient length up to 2 m by using standard glass pipe lengths. A zinc selenide window couples in the CO_2 radiation, and the laser mirrors are made from tightly stretched square nickel meshes. For most applications, the input mesh has a period of .0625 mm and the output mesh is 0.125 mm. The mirrors have x--y adjustments and the output mirror has a translation adjustment in addition. Invar rods are used between the end boxes for good stability.

In testing this laser, a total of 27 lines were seen in 4 gases. No attempt was made to observe a large number of lines, since the primary interest in propagation measurements lies in the atmospheric window regions. However, previously unreported lines were observed in $C_2H_2F_2$ and CH_3I. For most gases a pressure of 1 to 5 torr produced good output.

5.2.2 Superheterodyne Receiver

The receiver used in conjunction with the transmitter described in the previous section is shown in block form in Figure 25. The receiver is of quasi-optical design, a Fabry-Perot interferometer being used to diplex signal and local oscillator radiation into a single-ended ridged waveguide mixer. The Fabry-Perot grid spacing is adjusted to reflect the local oscillator frequency (110 - 115 GHz) while transmitting the signal (220 - 230 GHz). The IF frequency, 6.75 - 7.25 GHz, is amplified with 60 dB of gain and then detected with a square law detector for video presentation of the transmitter pulse.

5.2.3 Propagation Facility

A meteorologically instrumented propagation range is being assembled at Georgia Tech to provide comparative measurements for wavelengths from the visible through the millimeter wavelength region. The following sources are being made available with appropriate receivers:

An Argon laser at 0.5 μm;

A YAG:Nd laser at 1.06 μm;

A 10.6 μm CO_2 laser;

An optically pumped laser (outputs at several wavelengths across the submillimeter region);

A 1 mm carcinotron

A 2.1 mm klystron

A 3 mm klystron

An 8 mm klystron

simultaneous operation of all systems is planned.

6.0 CONCLUSIONS

The instrumentation and measurements described in this paper are designed to contribute to an understanding of the atmospheric characteristics relevant to applications in the near-millimeter wavelength region. Among these applications, for which further discussion can be given, are radiometric work for airborne applications for Project Storm Fury and ground mapping, theoretical studies of satellite radiometric observations of millimeter/submillimeter water lineshapes as a means of determining water vapor distribution, a transportable propagation facility and trends in military applications of near millimeter wave technology.

ACKNOWLEDGEMENTS

The research activities described within this paper are sponsored by the following U. S. Government grants and contracts:

NASA/Goddard Space Flight Center - Grant No. NSG-5012

U. S. Army Research Office (ARO) - Grant No. DAAG29-76-G-0280

U. S. Army, Contract No. DAAK40-77-C-0047

REFERENCES

1. M. Cohn, et al, "Harmonic Mixing With An Antiparallel Diode Pair", IEEE Trans. MTT, Vol. 23, No. 8, (Aug. 1975).

2. J. J. Gallagher and M. D. Blue, "Submillimeter Wave Spectroscopy and Technology Second Semi-Annual Technical Report", U. S. Army Research Office, Grant No. DAAG29-76-G-0280, Engineering Experiment Station, Georgia Institute of Technology, (Sept. 1977).

3. J. J. Gallagher, M. D. Blue, B. Bean and S. Perkowitz, "Tabulation of Optically Pumped Far Infrared Laser Lines and Applications to Atmospheric Transmission", Infrared Phys., Vol. 17, pp. 43-55, (1977).

4. J. J. Gallagher, H. A. Ecker, M. D. Blue and R. G. Shackelford, "Applications at Submillimeter Wave Gigawatt Sources", ARPA Order Number 2840, Contract N00014-75-C-1011, (Sept. 1975).

5. R. H. Garnham, "Quasi-Optical Components", in Millimeter and Submillimeter Waves, F. H. Benson, Ed., London, Fliffe Bucks, Ltd., 1969, Chapter 21.

6. D. H. Martin and E. Puplett, "Polarized Interferometric Spectrometry For the Millimetre and Submillimetre Spectrum", Infrared Physics 10. 105 (1969).

7. G. T. Wrixon, University College, Cork, Ireland, private communication, (1977).

8. J. J. Gustincic, "A Quasi-Optical Radiometer", Second International Conference on Submillimeter Waves and Their Applications, San Juan, Puerto Rico, (1976).

9. N. R. Erickson, "A Directional Filter Diplexer Using Optical Techniques for Millimeter to Submillimeter Wave Lengths", IEEE Trans. Microwave Theory Tech., to be published.

10. R. W. McMillan and J. B. Langley, "Analysis of Submillimeter Wave Fabry-Perot Interferometers Made of Four Wire Grids", Second International Conference on Submillimeter Waves and Their Applications, San Juan, Puerto Rico, (1976).

11. R. W. McMillan, C. H. Branch, and G. M. Lamb, "Polarization Twisting, Bandpass Tunable Fabry-Perot Filters for Submillimeter Applications", Third International Conference on Submillimeter Waves and Their Applications, Guildford, England, (March, 1978).

12. A. A. M. Saleh, "An Adjustable Quasi-Optical Bandpass Filter - Part I: Theory and Design Formulas", IEEE Trans. Microwave Theory Tech., Vol. MTT-22, No. 7, pp. 728-734, (July, 1974).

13. _____________, "An Adjustable Quasi-Optical Bandpass Filter - Part II: Practical Considerations", IEEE Trans, Microwave Theory Tech., Vol. MTT-22, No. 7, pp. 734-739, (July, 1974).

14. R. E. Cupp, R. A. Kempf, and J. J. Gallagher, "Hyperfine Structure in the Millimeter Spectrum of Hydrogen Sulfide: Electric Resonance Spectroscopy on Asymmetric-Top Molecules", Phys. Rev. 171, 60, (1968).

15. A. E. Costley, K. H. Hursey, G. F. Neill and J. M. Ward, "Free-standing fine-wire grids: Their manufacture, performance, and use at millimeter and submillimeter wavelengths", J. Opt. Soc. Amer. 67, No. 7, pp. 979, (July, 1977).

16. H. D. Baker and G. R. Valenzuela, "A Double Prism Attenuator for Millimeter Waves", IRE Trans. Microwave Theory Tech., Vol. MTT-10, pp. 392-393, (Sept. 1962).

17. R. G. Fellers, "Measurements in the Millimeter to Micron Range", Proceedings IEEE, Vol. 55, No. 6, pp. 1003-18, (June, 1967).

18. B. H. Garnham, "Optical and Quasi-Optical Transmission Techniques and Components Systems for Millimeter Waves", RRE Report 3020.

19. A. M. Frank, "A Birefringent Polarization-Independent Beam Splitter for the Submillimeter", Third International Conference on Submillimeter Waves and Their Applications", Guildford, England, (March, 1978).

20. R. G. Strauch, R. E. Cupp, M. Lichtenstein and J. J. Gallagher, "Quasi-Optical Techniques in Millimeter Spectroscopy", Symposium on Quasi-Optics, Polytechnic Institute of Brooklyn, (June 8-10, 1964).

21. R. W. McMillan, J. J. Gallagher, and A. M. Cook, "Calculations of Antenna Temperature, Horizontal Path Attenuation, and Zenith Attenuation Due to Water Vapor in the Frequency Band 150-700 GHz", IEEE Trans. Microwave Theory Tech., Vol. MTT-25, No. 6, pp. 484-488, (June, 1977).

22. E. P. Gross, "Shape of Collision-broadened Spectral Lines", Phys. Rev., Vol. 97, pp. 394-403, (Jan. 1955).

23. N. E. Gaut and E. C. Reifenstein, III, Environmental Research and Technology Report No. 13, NASA Contract NAS8-26275, Waltham, Mass., (Feb. 1971).

24. A. E. Schulze and C. W. Tolbert, "Shape, Intensity, and Pressure Broadening of the 2.53 - Millimeter Wave-Length Oxygen Absorption Line", Nature, Vol. 200, No. 4908, pp. 474-740, (Nov. 23, 1963).

25. H. A. Gebbie, "New Molecular Absorbers in the Earth's Atmosphere and Their Submillimeter Spectra", Second International Conference on Submillimeter Waves and Their Applications, San Juan, Puerto Rico, (Dec. 1976).

26. D. H. Martin, Private Communication, (1978).

DISCUSSION

R.J.Emery, UK

I have two questions concerned with the propagation aspects of your work:

(1) Did you include a water dimer component in making the comparison between your radiometric measurements of the sky and theory?

(2) Have you come to any conclusion about the transmission of millimeter waves through water vapour/atmosphere, based on the laboratory measurements you have made so far?

Author's Reply

(1) A dimer component was not included.

(2) Only preliminary measurements have been made so far, and no conclusions have been drawn.

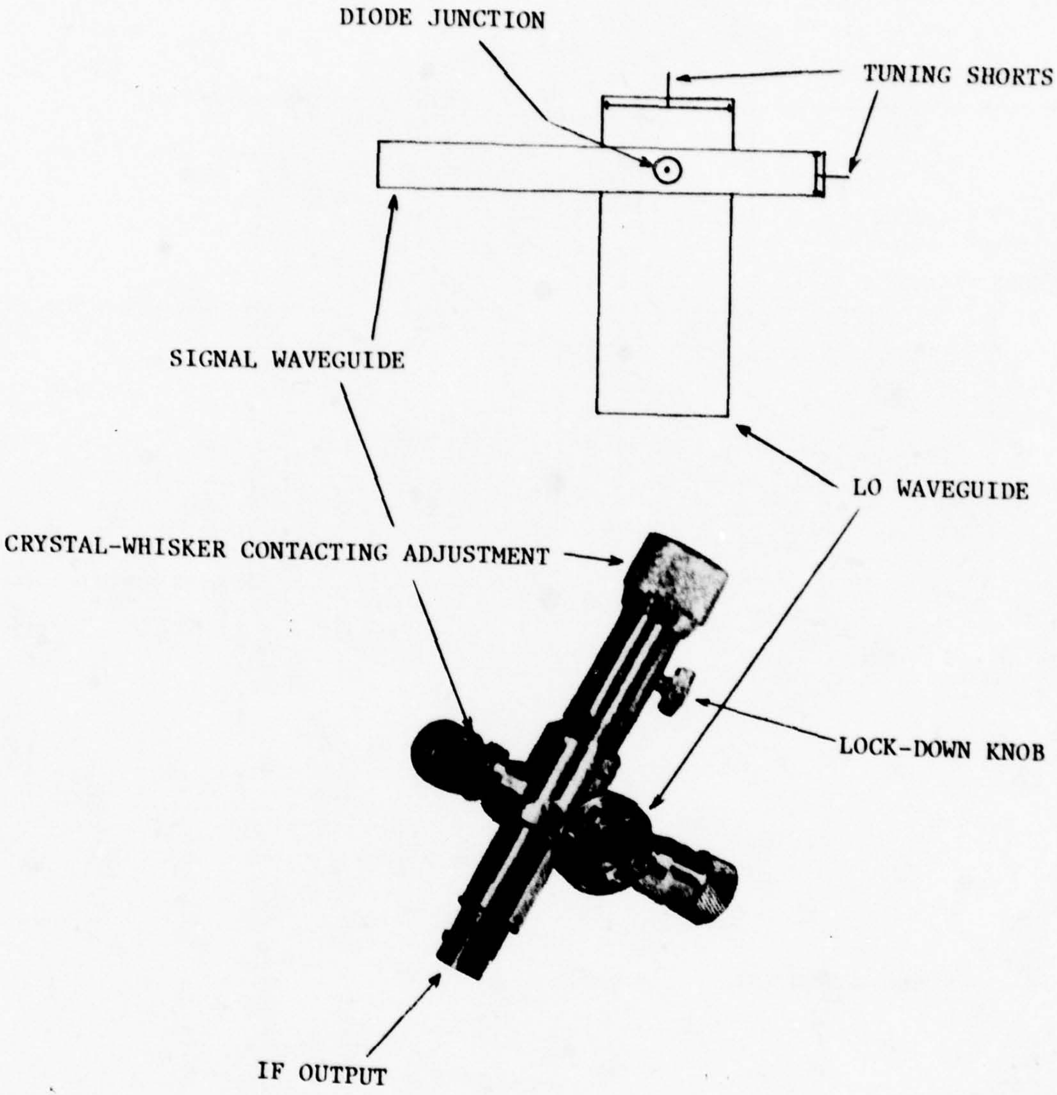
DIODE JUNCTION
TUNING SHORTS
SIGNAL WAVEGUIDE
LO WAVEGUIDE
CRYSTAL-WHISKER CONTACTING ADJUSTMENT
LOCK-DOWN KNOB
IF OUTPUT

Fig.1(a) Crossed-waveguide mixer

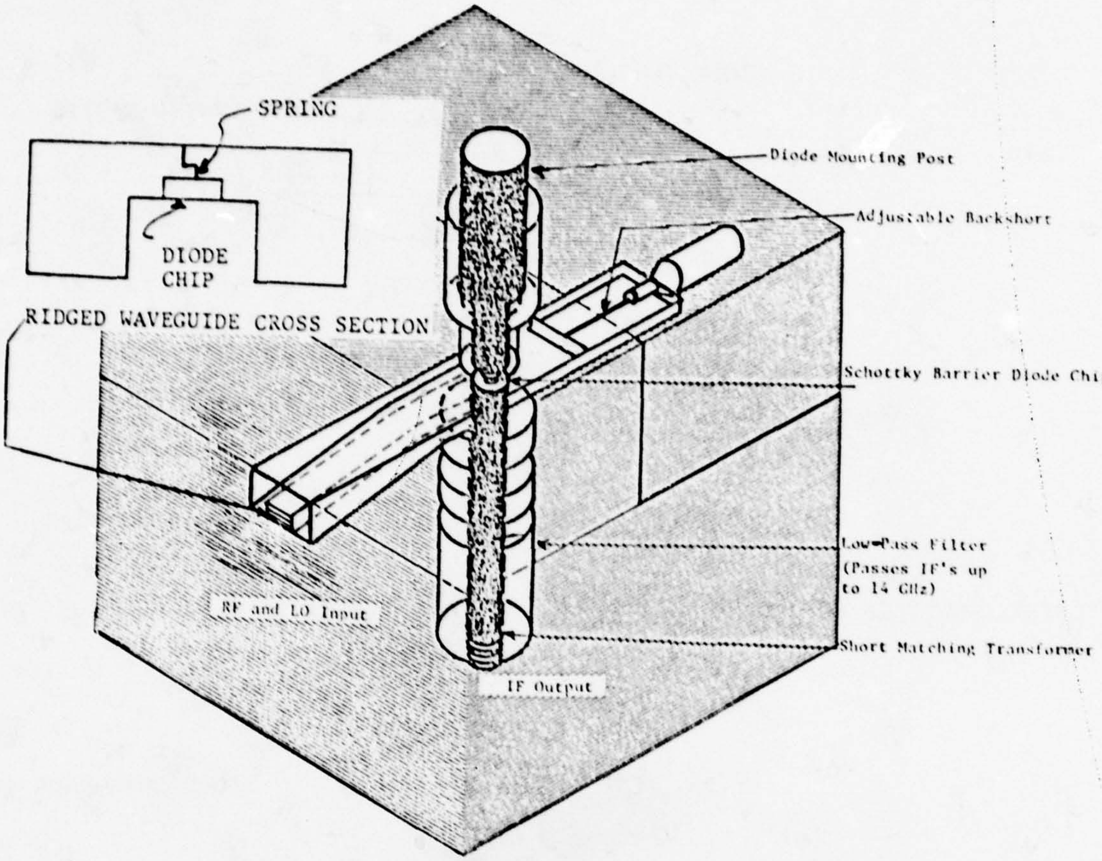
SPRING
DIODE CHIP
RIDGED WAVEGUIDE CROSS SECTION
Diode Mounting Post
Adjustable Backshort
Schottky Barrier Diode Chip
Low-Pass Filter (Passes IF's up to 14 GHz)
RF and LO Input
Short Matching Transformer
IF Output

Fig.1(b) Ridged-waveguide mixer

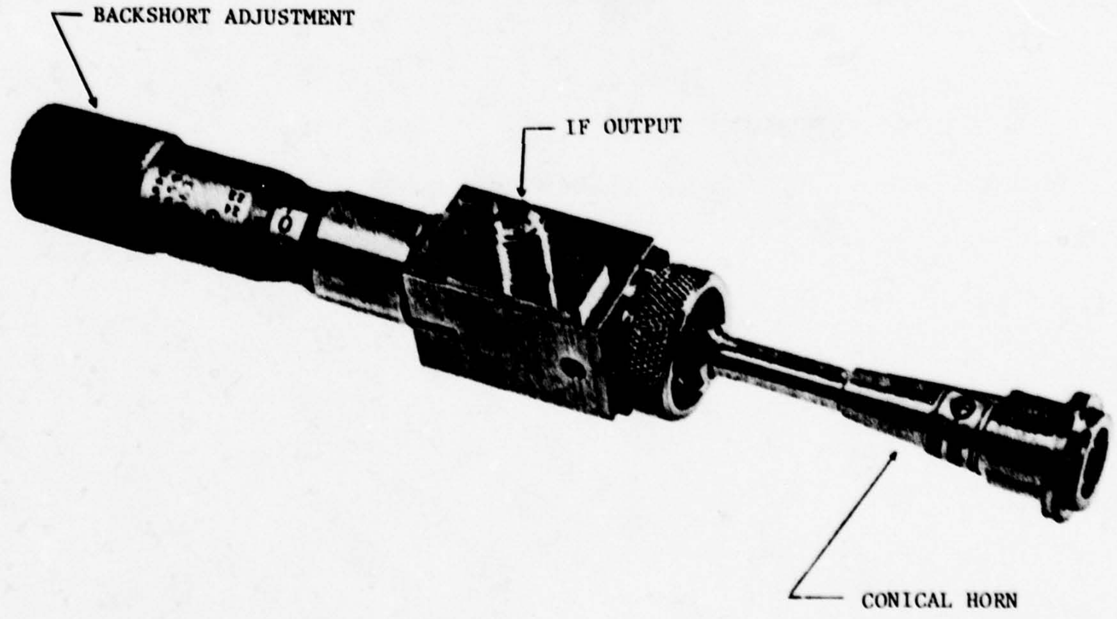
BACKSHORT ADJUSTMENT
IF OUTPUT
CONICAL HORN

Fig.2 Sharpless-wafer mixer, shown without diode wafer

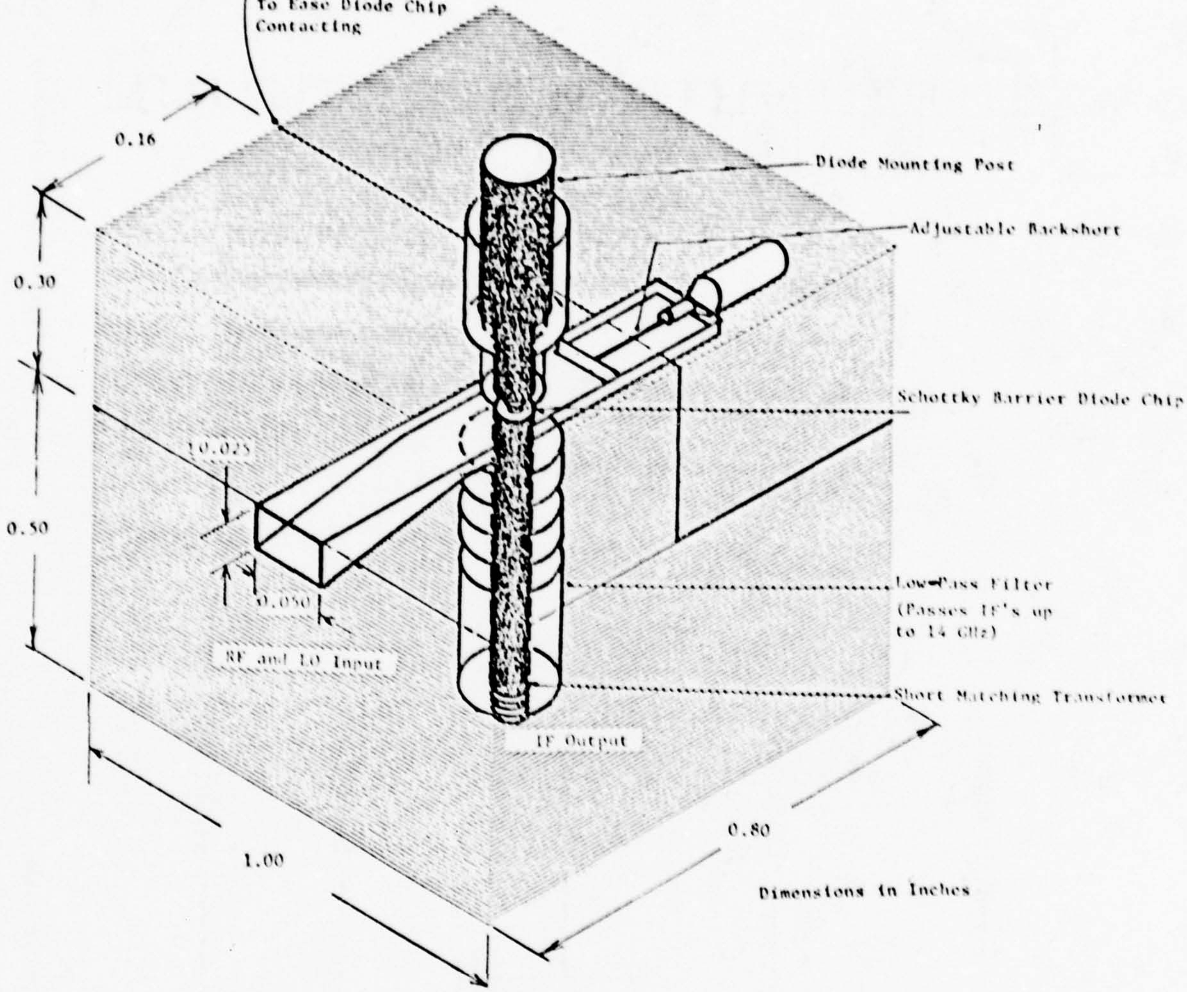
Split Block Construction To Ease Diode Chip Contacting
0.16
Diode Mounting Post
Adjustable Backshort
0.30
Schottky Barrier Diode Chip
0.025
0.50
0.050
Low-Pass Filter (Passes IF's up to 14 GHz)
RF and LO Input
Short Matching Transformer
IF Output
0.80
1.00
Dimensions in Inches

Fig.3 Split block mixer (dimensions shown are for WR-5 waveguide band, 140–220 GHz)

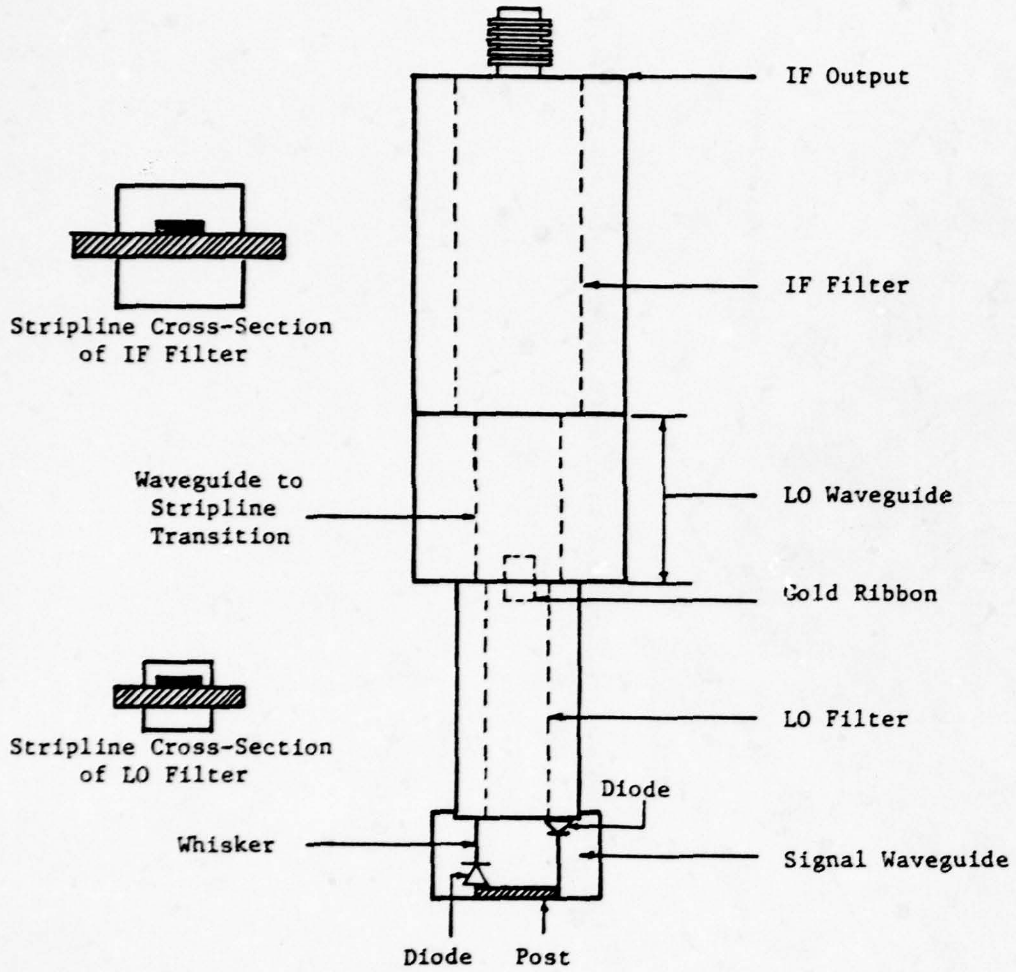
IF Output
IF Filter
LO Waveguide
Gold Ribbon
LO Filter
Diode
Signal Waveguide
Stripline Cross-Section of IF Filter
Waveguide to Stripline Transition
Stripline Cross-Section of LO Filter
Whisker
Diode
Post

Fig.4 Subharmonic mixer showing anti-parallel diodes

TYPICAL
PARAMETERS
FOR
REXOLITE
AT 168 GHz

ℓ = 0.36 mm
d = 0.13 mm
y = 0.28 mm

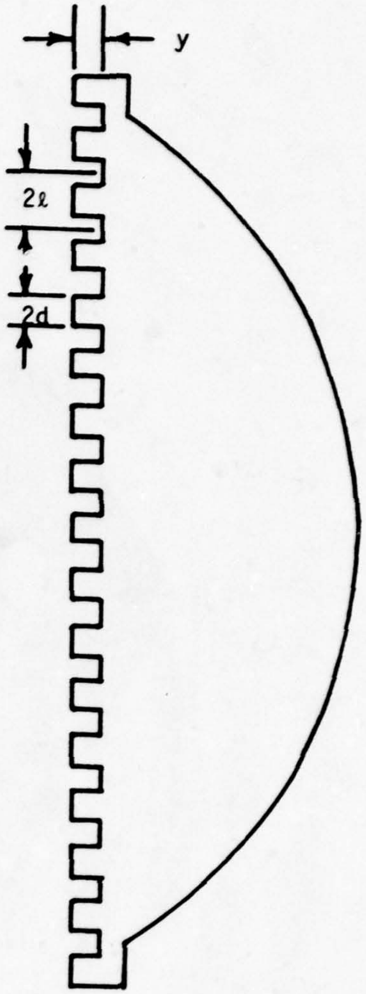

Fig.5 Detail of matching lens to air by slotting

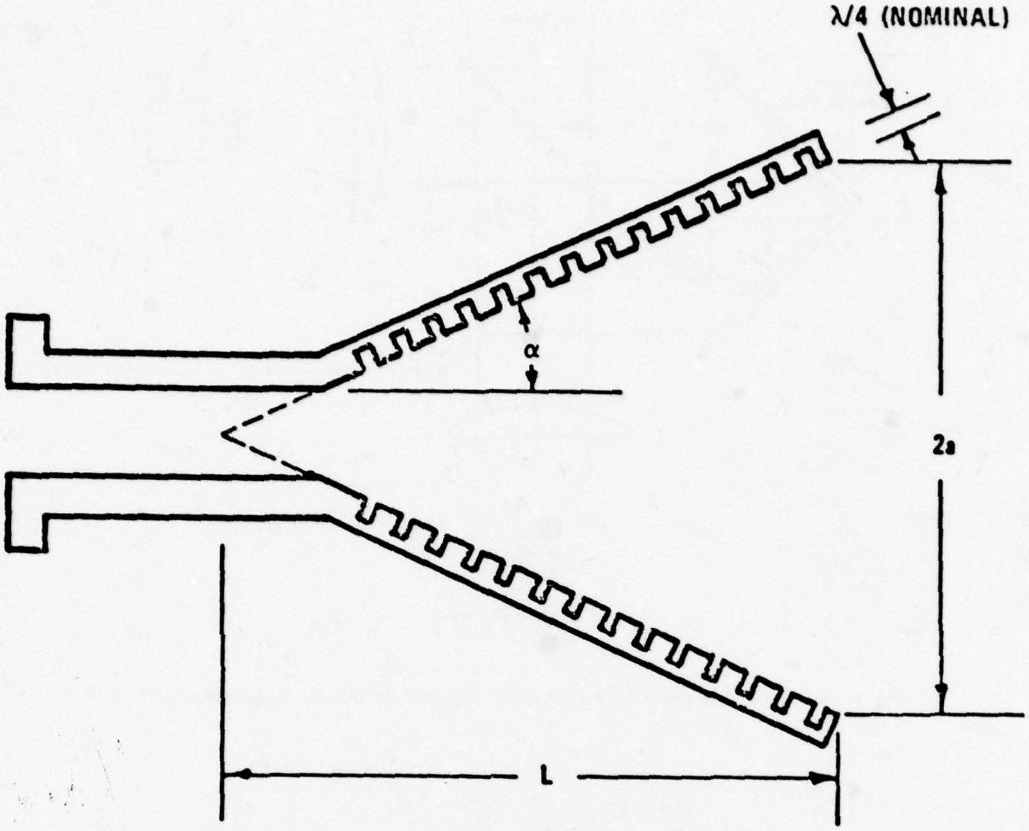

Fig.6(a) Conical corrugated horn geometry used in calculations

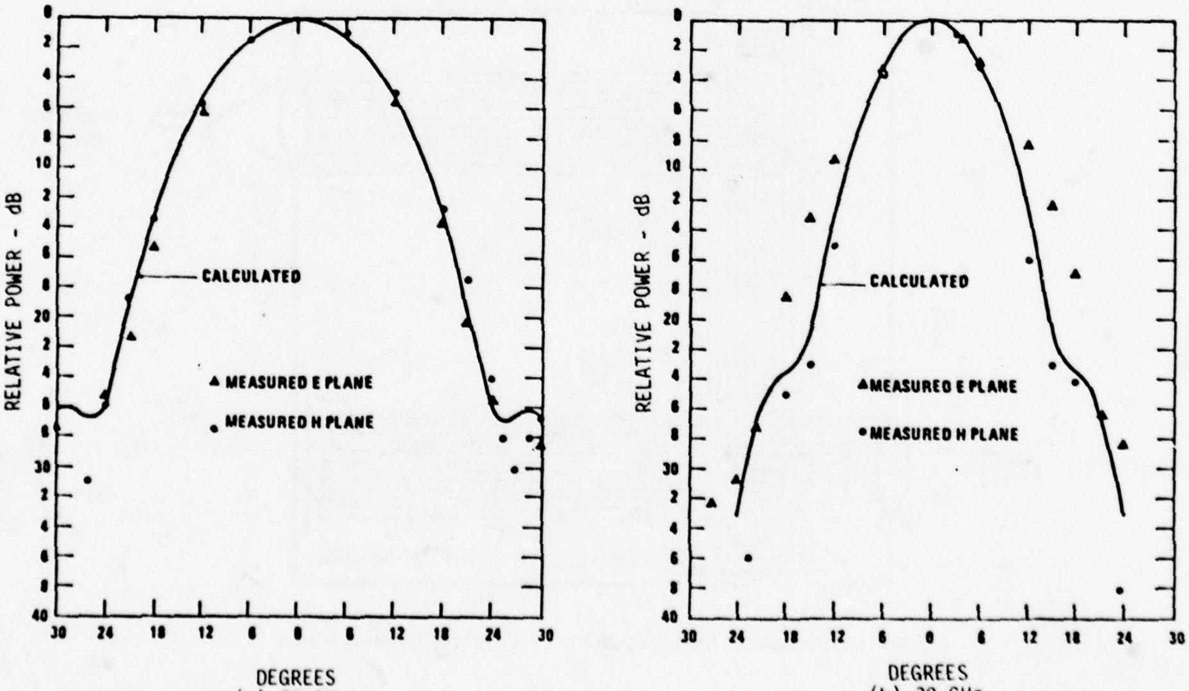

(a) 20 GHz

(b) 30 GHz

Fig.6(b) Comparison of calculated and measured antenna patterns

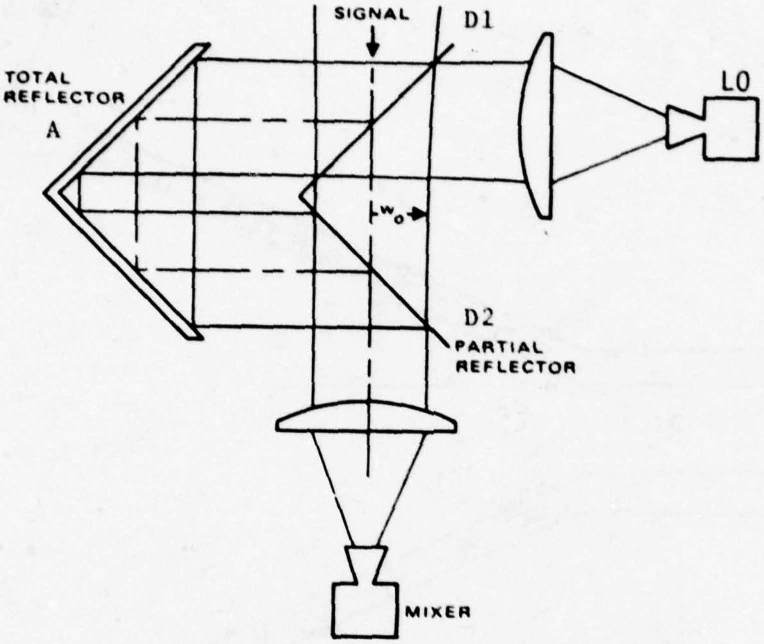
SIGNAL
D1
TOTAL
REFLECTOR
A
LO
w_o
D2
PARTIAL
REFLECTOR
MIXER

Fig.7 Schematic diagram of the diplexer designed by Martin and Puplett [6]

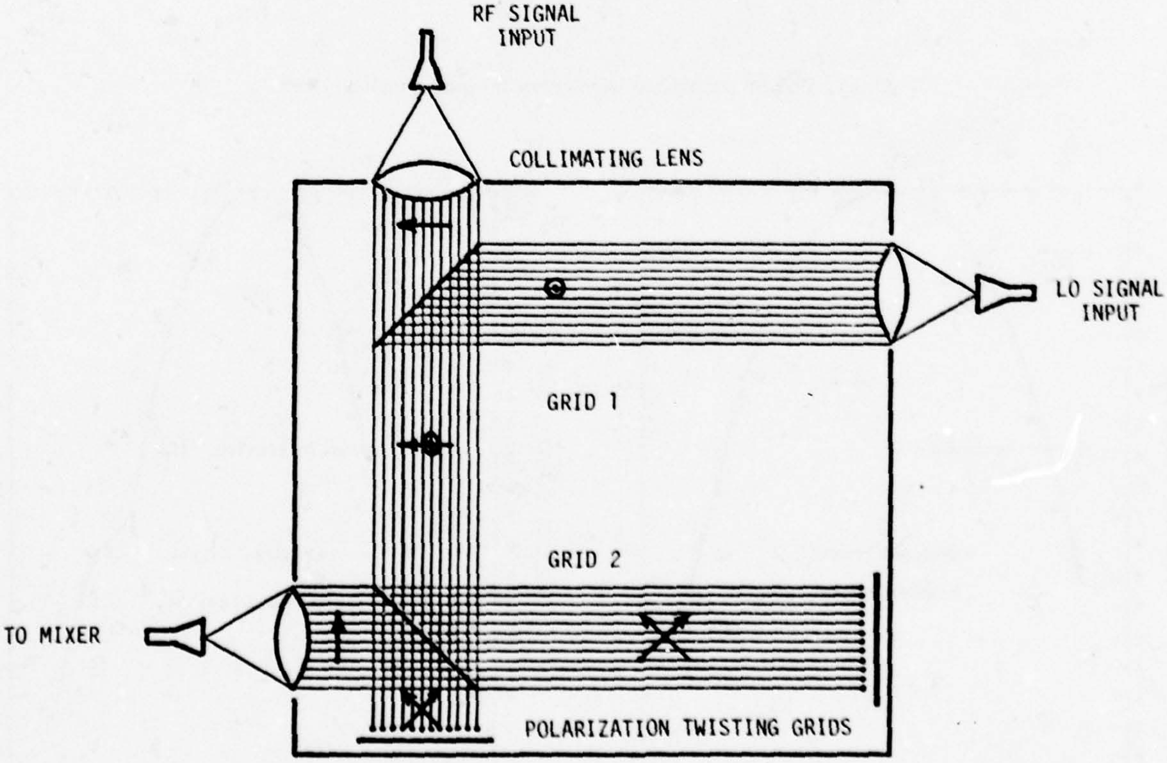
RF SIGNAL
INPUT
COLLIMATING LENS
LO SIGNAL
INPUT
GRID 1
GRID 2
TO MIXER
POLARIZATION TWISTING GRIDS

Fig.8 Quasi-optical LO injection diplexer with collimating lenses

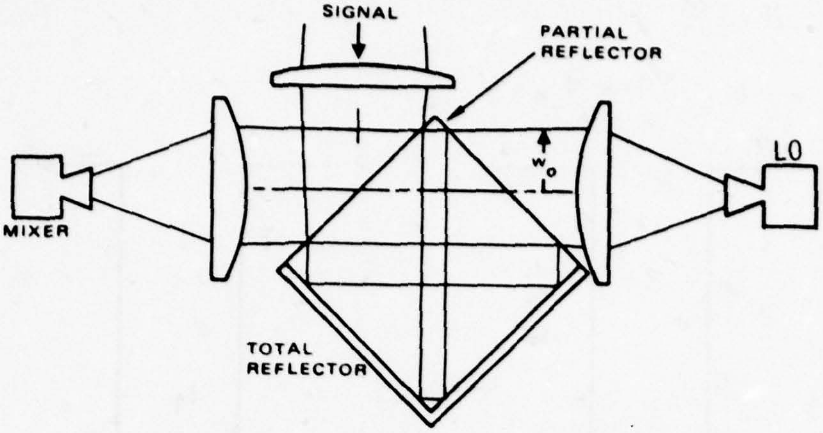
SIGNAL
PARTIAL REFLECTOR
w_o
LO
MIXER
TOTAL REFLECTOR

Fig.9 Quasi-optical diplexer using a square resonator. After Gustincic

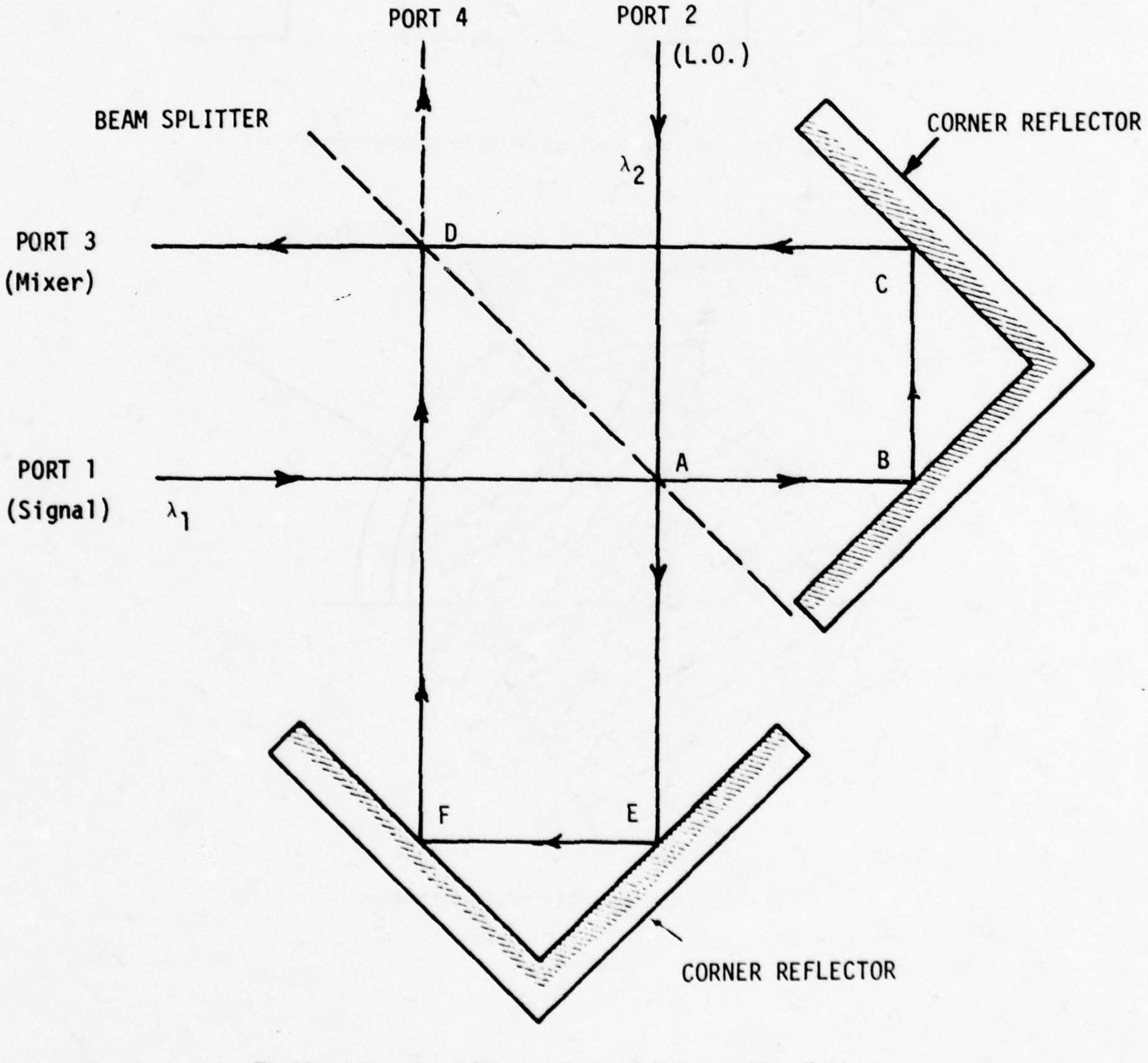
PORT 4
PORT 2
(L.O.)
BEAM SPLITTER
CORNER REFLECTOR
λ_2
PORT 3
(Mixer)
D
C
PORT 1
(Signal)
λ_1
A
B
F
E
CORNER REFLECTOR

Fig.10 A directional filter quasi-optical diplexer. After Erickson

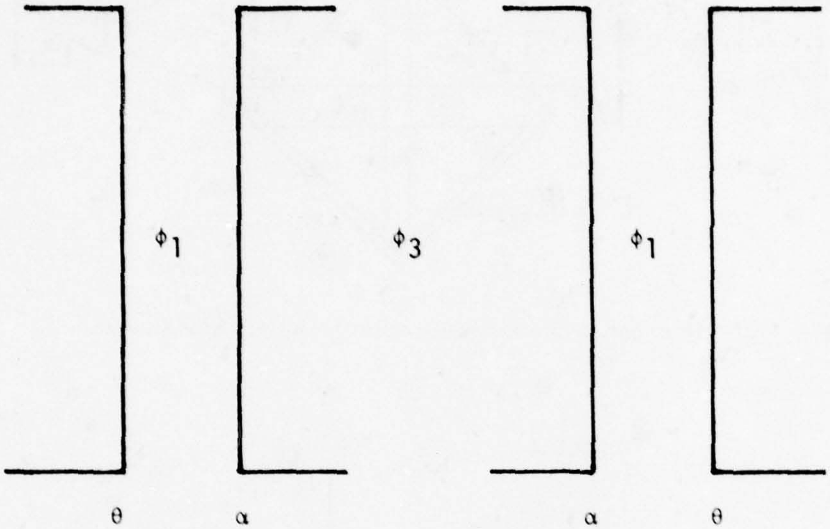

ϕ_1
ϕ_3
ϕ_1
θ
α
α
θ

Fig.11(a) Two pairs of grids forming an interferometer

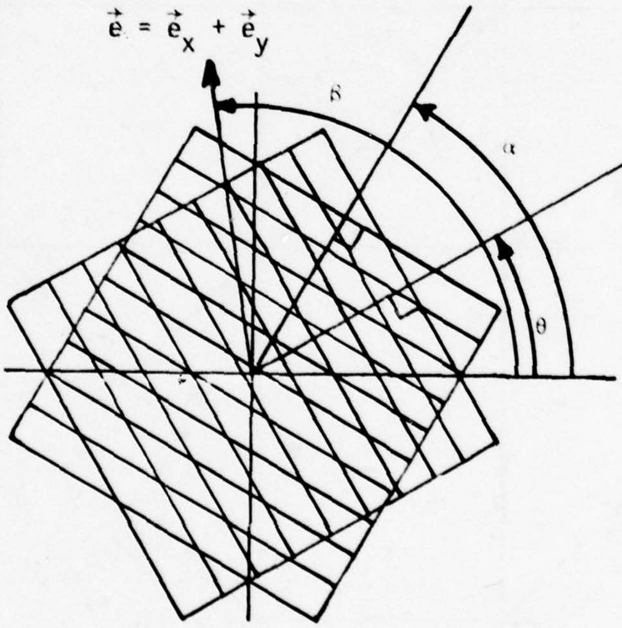

$\vec{e} = \vec{e}_x + \vec{e}_y$
β
α
θ

Fig.11(b) Definition of wire grid parameters

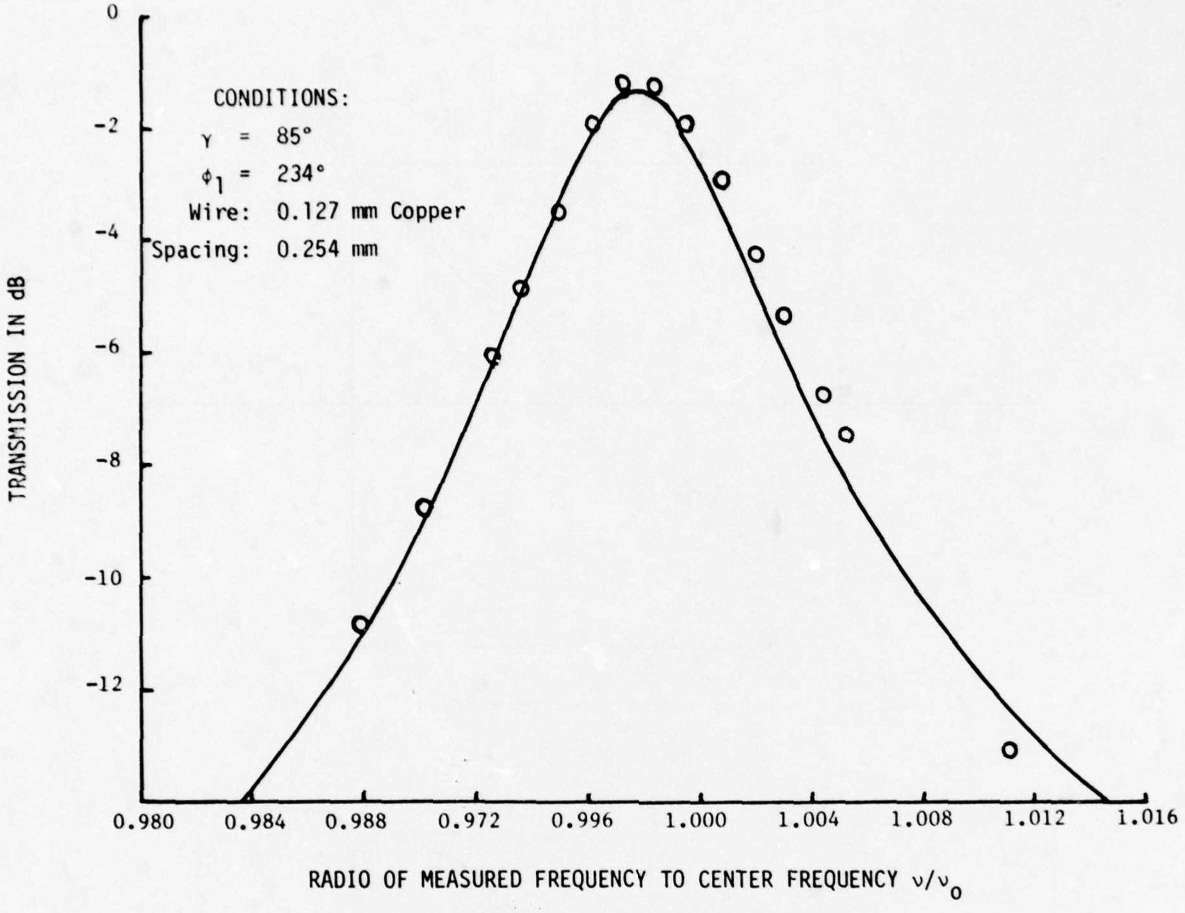

Fig.12 Grid interferometer transmission as a function of frequency. The center frequency appears to be offset because of the presence of a frequency dependent factor in the transmission loss term

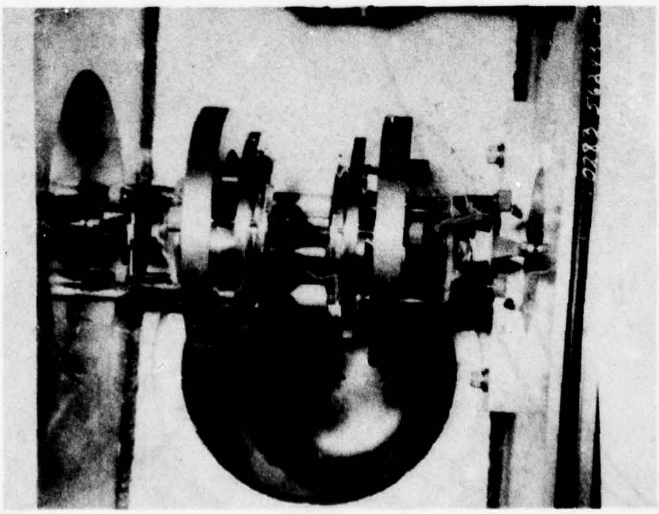

Fig.13 Parallel plate Fabry-Perot interferometer used in molecular beam studies [14]

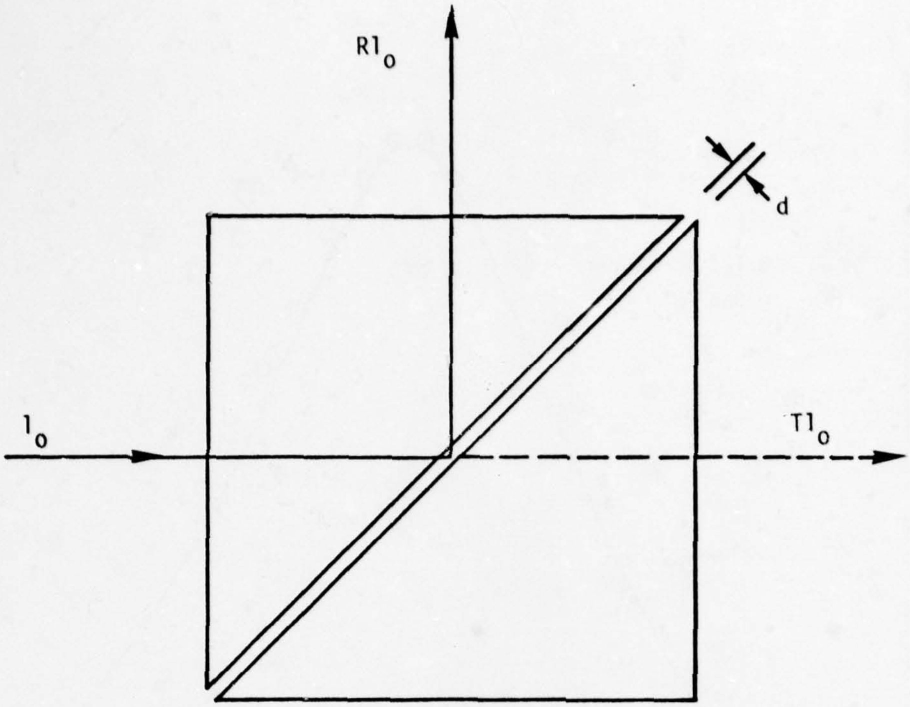

Fig.14 Double prism configuration

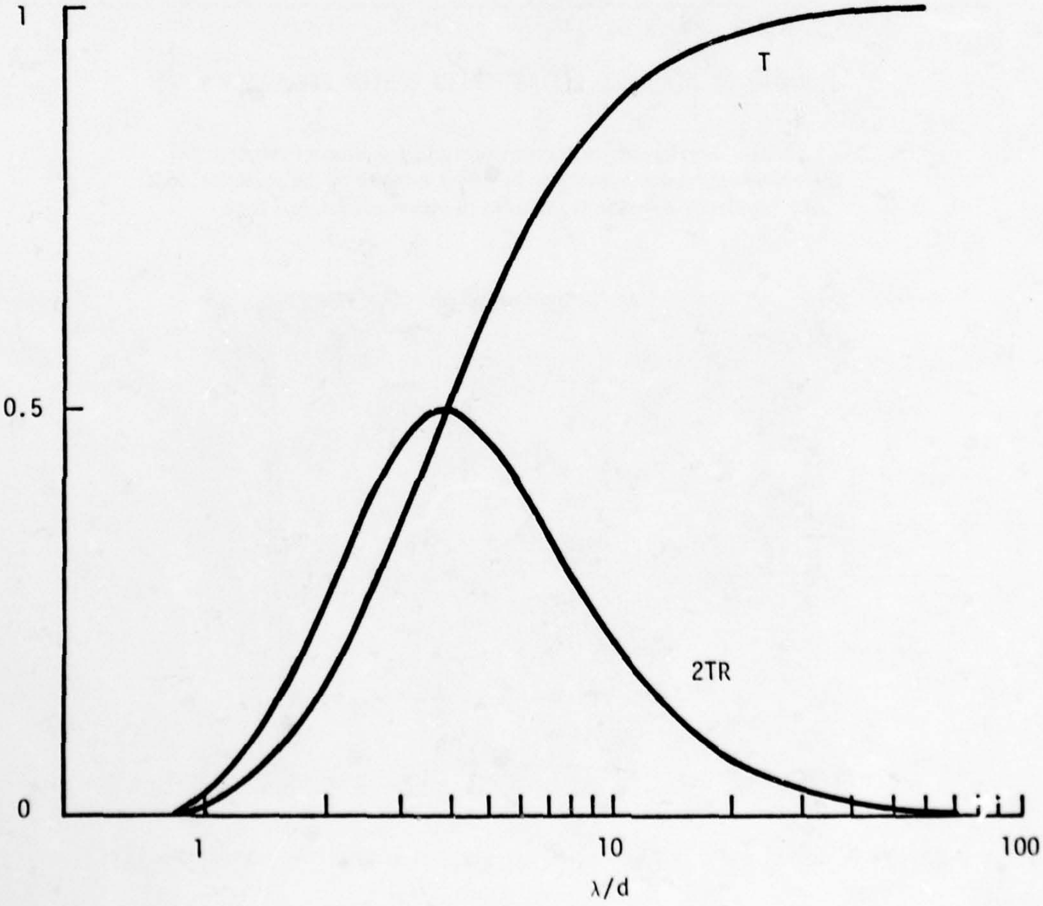

Fig.15 Transmittance of double prism as function of λ/d

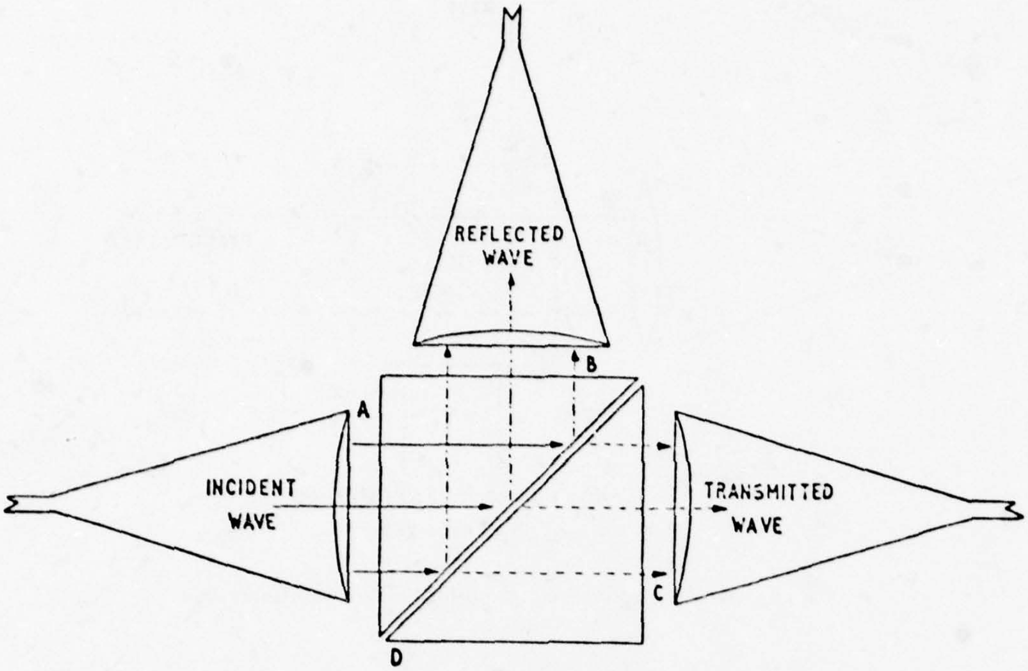
REFLECTED
WAVE
B
A
INCIDENT
WAVE
TRANSMITTED
WAVE
C
D

Fig.16 The double-prism attenuator as used at millimeter wavelengths

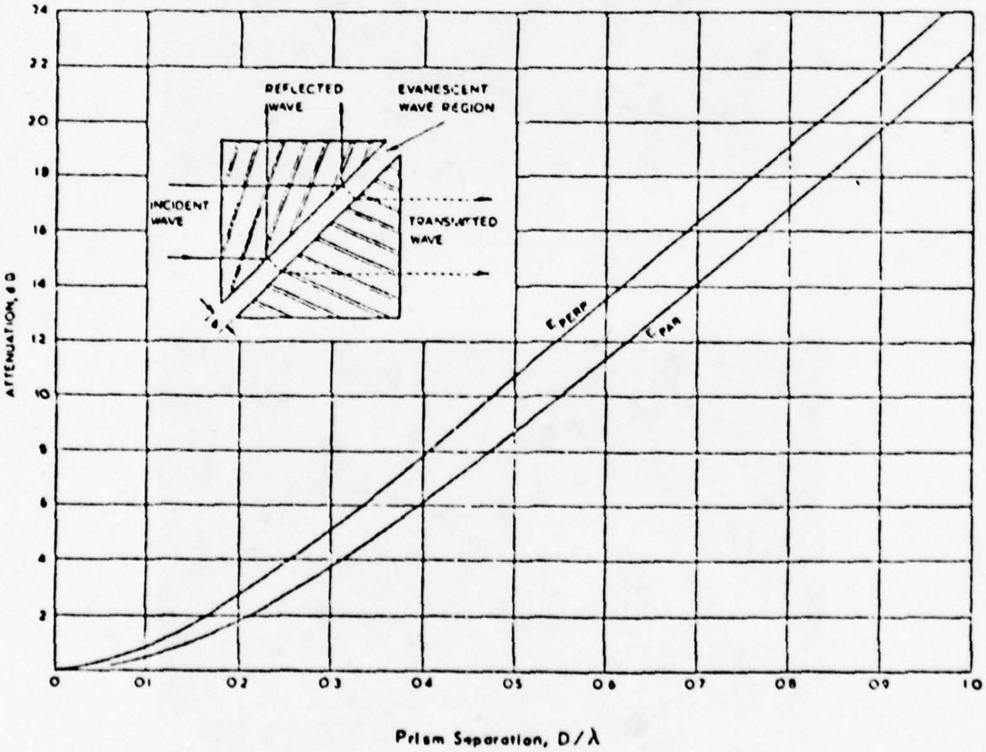

Fig.17 Graph of attenuation vs air gap

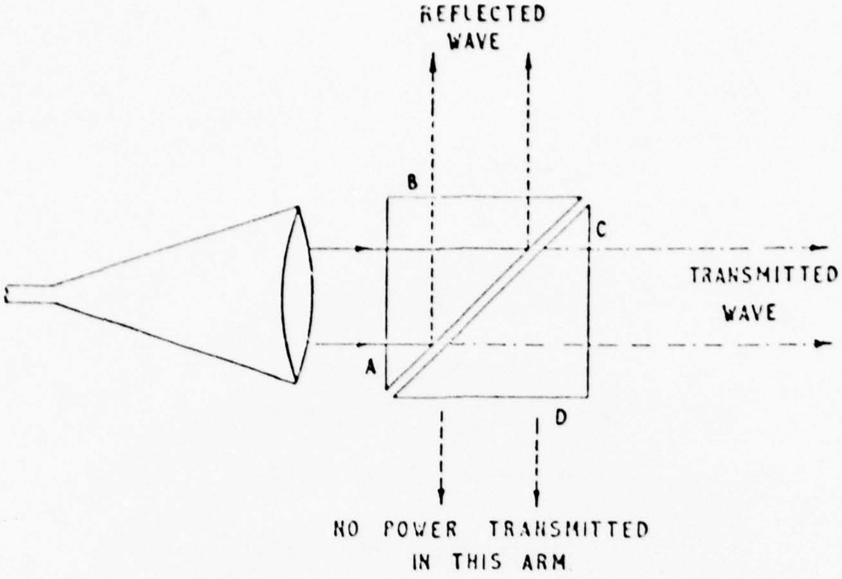
REFLECTED
WAVE
B
C
A
D
TRANSMITTED
WAVE
NO POWER
IN THIS ARM
TRANSMITTED

Fig.18 Optical directional coupler using the double-prism system

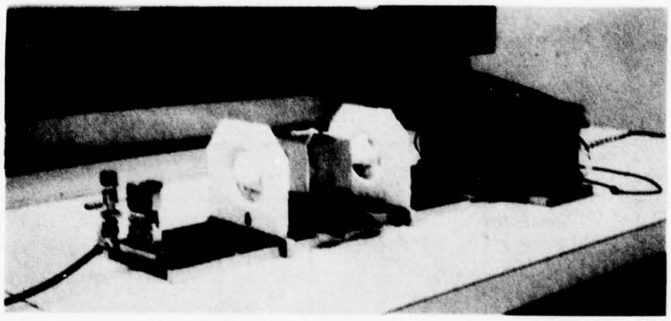

Fig.19 Double-prism used with 300 GHz Carcinotron

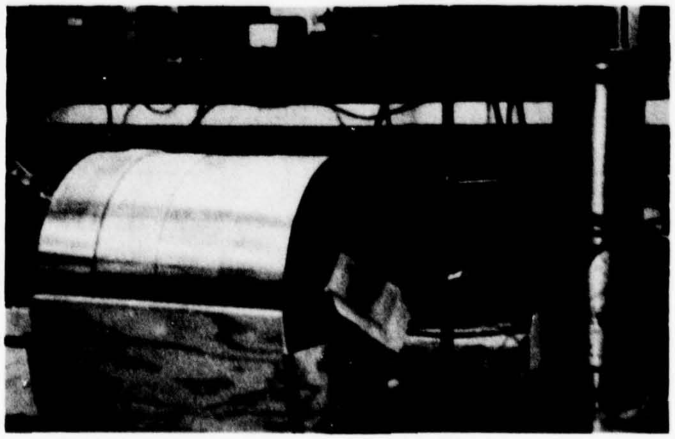

Fig.20 Side view of Fresnel Rhomb used as circular polarizer in Zeeman effect experiment

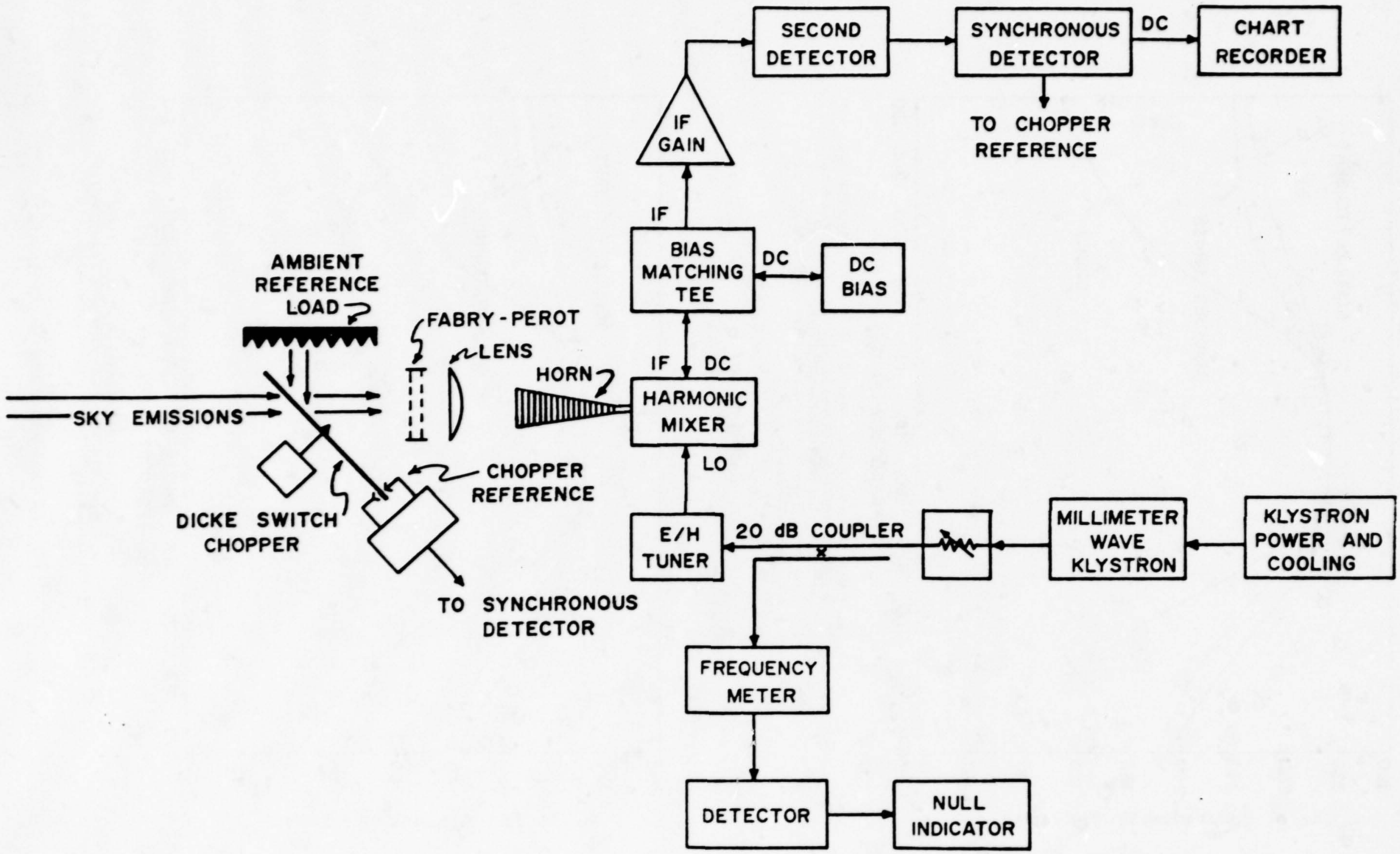
SECOND DETECTOR
SYNCHRONOUS DETECTOR
DC
CHART RECORDER
TO CHOPPER REFERENCE
IF GAIN
IF
BIAS MATCHING TEE
DC
DC BIAS
AMBIENT REFERENCE LOAD
FABRY-PEROT
LENS
HORN
IF
DC
HARMONIC MIXER
SKY EMISSIONS
LO
CHOPPER REFERENCE
DICKE SWITCH CHOPPER
E/H TUNER
20 dB COUPLER
MILLIMETER WAVE KLYSTRON
KLYSTRON POWER AND COOLING
TO SYNCHRONOUS DETECTOR
FREQUENCY METER
DETECTOR
NULL INDICATOR

Fig.21 Tunable radiometer

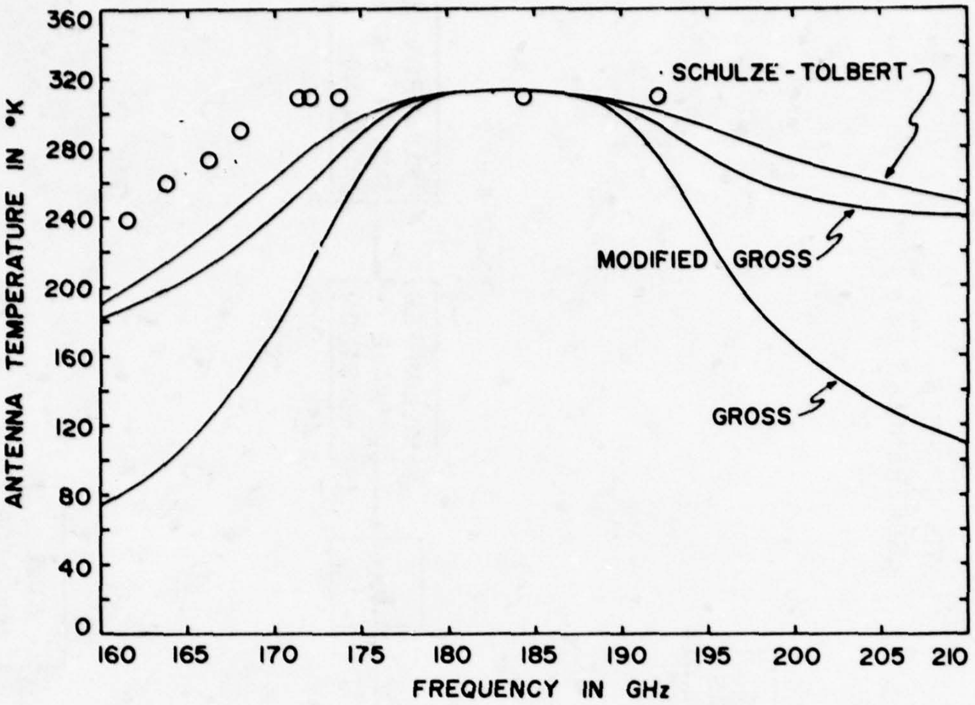

Antenna Temperatures measured on 7 July 1977. The solid lines are calculated curves using the various line shape factors, and the circles are experimental points. The surface water vapor density was 20.2 g/m^3 and the temperature was 311.0°K for these measurements.

Fig.22(a) Radiometric data

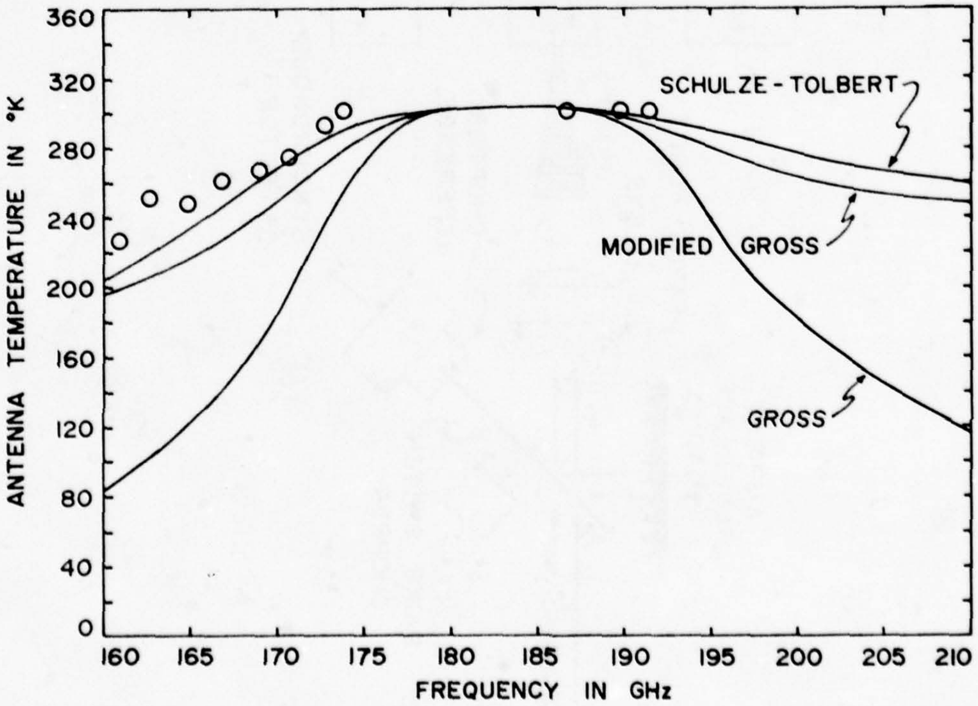

Antenna temperatures measured on 25 August 1977. The surface water vapor density was 22.9 g/m^3 and the temperature was 301.3°K for these measurements.

Fig.22(b) Radiometric data

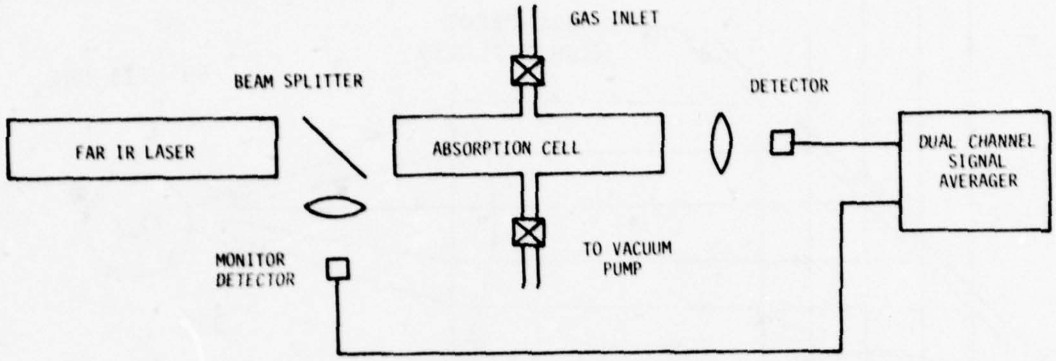
GAS INLET
BEAM SPLITTER
DETECTOR
FAR IR LASER
ABSORPTION CELL
DUAL CHANNEL SIGNAL AVERAGER
TO VACUUM PUMP
MONITOR DETECTOR

Fig.23 Apparatus used for Far infrared absorption measurements using a pulsed Far infrared laser

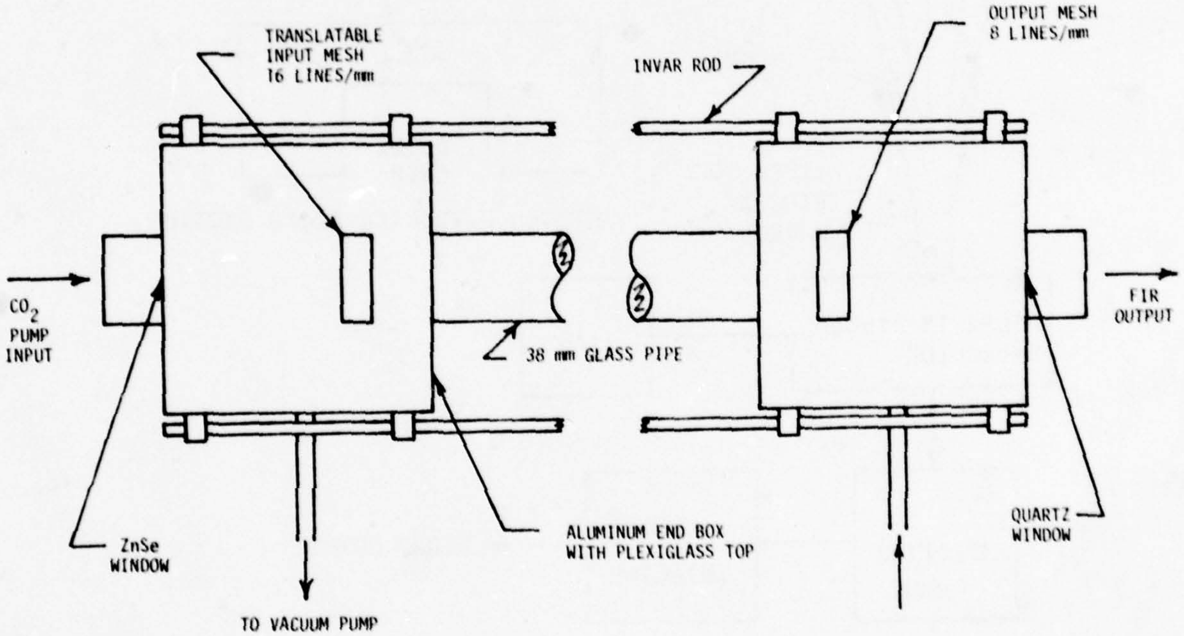
TRANSLATABLE INPUT MESH 16 LINES/mm
OUTPUT MESH 8 LINES/mm
INVAR ROD
CO_2 PUMP INPUT
FIR OUTPUT
38 mm GLASS PIPE
ZnSe WINDOW
ALUMINUM END BOX WITH PLEXIGLASS TOP
QUARTZ WINDOW
TO VACUUM PUMP

Fig.24 Schematic of far infrared pulsed laser

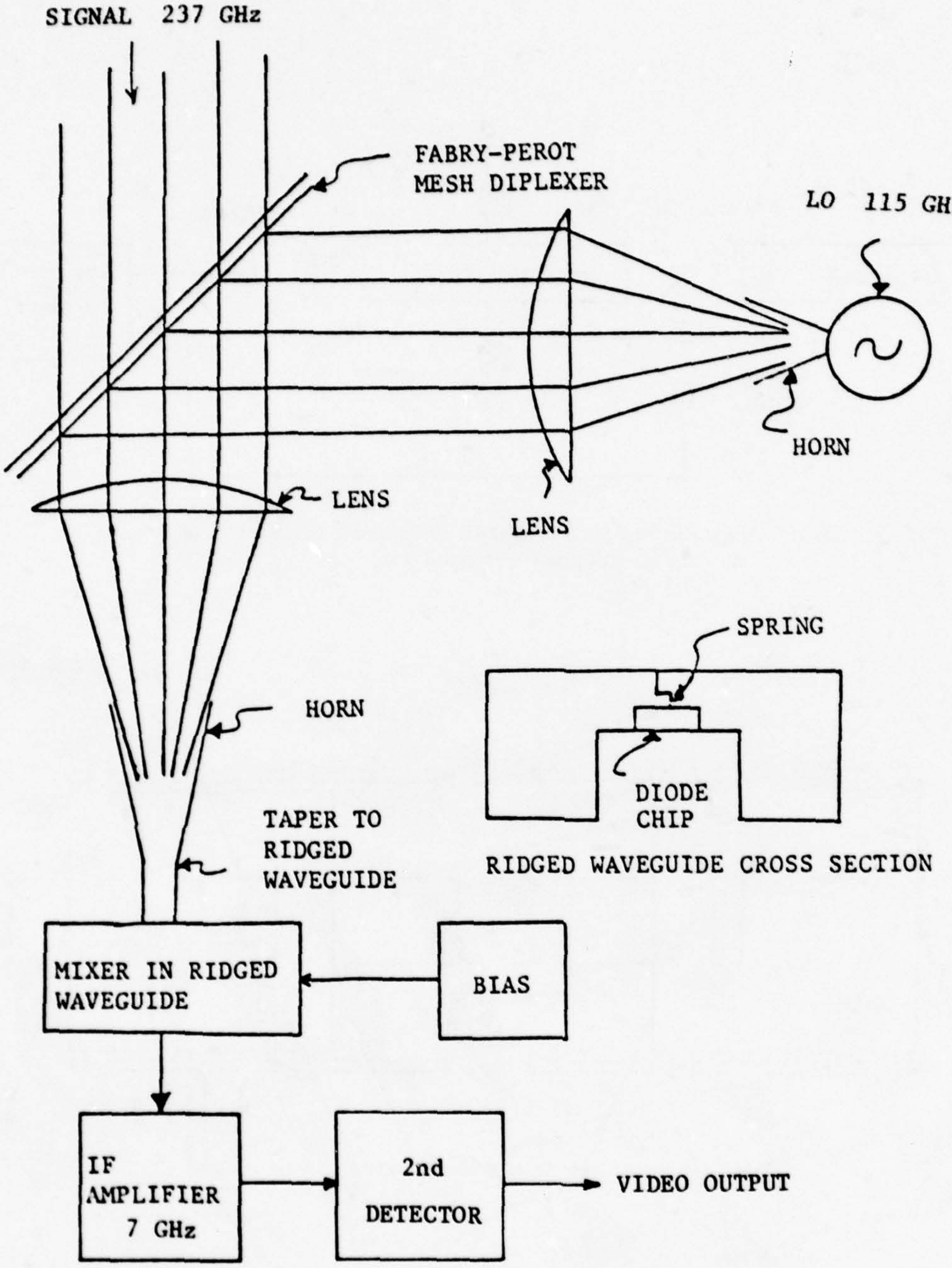
SIGNAL 237 GHz
FABRY-PEROT MESH DIPLEXER
LO 115 GHz
HORN
LENS
LENS
SPRING
HORN
DIODE CHIP
TAPER TO RIDGED WAVEGUIDE
RIDGED WAVEGUIDE CROSS SECTION
MIXER IN RIDGED WAVEGUIDE
BIAS
IF AMPLIFIER 7 GHz
2nd DETECTOR
VIDEO OUTPUT

Fig.25 Superheterodyne receiver

ADVANCES IN MM-WAVE COMPONENTS AND SYSTEMS

B. Adelseck, H. Barth, H. Hofmann, H. Meinel, B. Rembold
AEG-TELEFUNKEN
Geschäftsbereich Hochfrequenztechnik
7900 Ulm/Do.
Federal Republic of Germany

SUMMARY

In the first part this paper gives an overview on state-of-the-art and availability of mm-wave semiconductors. Laboratory results are compared with the data of commercially available diodes. The second part is dealing with new active and passive mm-wave components. Because of different applications, very distinguished problems have to be solved leading to different technologies. While for high Q and high performance rectangular waveguide devices are in use, in recent time new combinations of waveguide and planar structures (fin-lines) has been developed to reduce cost and weight and to increase reliability and reproductivity. Typical examples of components will be demonstrated: High Q and high stable Gunn oscillators as well as swept Impatt sources up to 90 GHz, frequency converters as parametric up converters at 64 GHz, mixers at 35, 60 and 90 GHz and doublers at 90 GHz. In addition, fin-line components, for instance detectors, PIN-attenuators and double-throw-switches will be shown. Using these components some mm-wave-appliances have been developed and will be presented.

1. INTRODUCTION

The rise in mm-wave development observed in recent years is caused by the availability of semiconductors like Gunn devices, Impatt- and Schottky-diodes as well as by the increasing activities on mm-wave circuit design. Both trends are at least promoted by the broad spectrum of applications on civil market and by military employments like radar, radiometry, and communications.

Though well known since many years, the breakthrough in mm-wave radarsystems at 8 mm wavelength came only recently as now the system dimensions can be minimized using exclusively semiconductors. Mm-wave radars operate at frequencies determined by the atmospheric attenuation minima about 35 and 90 GHz. Due to the small dimensions mm-wave radars mounted on mobil carriers are well suited for short distance applications ($<$ 10 km). Typical radar employments are terrain surveillance, defence against low-flying aircrafts, signification of aircrafts, helicopter radar, and active terminal guidance. Coherent as well as incoherent-puls devices and FM-CW-radars find their application in these tasks.

Radiometer receivers used for military purposes in general are established at frequencies about 35 and 90 GHz. Radiometers are utilized for terrain observation, terminal homing and radiomapping. Main topics of research are to decrease the noise figure of the front ends and to improve the computer interpretation of the measured contrast.

Using mm-wave frequencies mobile radio links with small demensions can be established which almost are not sensitive against jamming. Making use of the narrow antenna beams and the high atmospheric attenuation for instance at 60 GHz these links have a likewise low probability of intercept (LPI). Typical applications are battle field communications, datalink between radarstations, and microwave ampling employments in a convoy.

2. STATE OF THE ART AND AVAILABILITY OF MM-WAVE SEMICONDUCTORS

Because of the rapid development of semiconductor technologies mm-wave techniques today mostly use diodes for power generation, signal detection, and frequency conversion.

Fig. 1 shows a graph of the power increase of Impatt- and Gunn oscillators respectively at the example of 35 GHz diodes. The data are the highest catalogue specifications which has been available in recent years. The annual increase of power observed up to now is about 3 dB/year.

Impatt diodes mainly are used as transmitter diodes in radar or communication systems. Compared with Gunn oscillators, Impatt devices are easier to sweep by changing the current. Sweep ranges up to 10 GHz at 90 GHz center frequency are achievable. In the question of available power, the silicon technology today delivers up to 10 watt peak power at 90 GHz using double drift Impatts on diamond heat sink, fig. 2. These values are the best reported data /1/. The best commercially available data, today are about 5 W peak power and 200 mW CW-power. Because of the price, however, these diodes are not suited for massproduction up to now.

Gunn devices today are available up to 100 GHz, fig. 3. The well known advantage of these elements is the better noise measure as compared to Impatt diodes. Therefore Gunn elements are used for local oscillators and for transmitters of self-mixing doppler systems for instance. Furthermore Gunn-elements are appropriate for puls-oscillators especially at frequencies in Ka-band. The disadvantage of Gunn-elements, however, is the smaller obtainable power which today is about 10 mW at 90 GHz. Standard material of Gunn devices is GaAs. The InP-technology, theoretically promising better efficiency, recently renders better results /2/.

The package of Gunn- or Impatt diodes in most cases consists of a quartz or ceramic ring surrounding the chip, which is soldered on a copper or diamond heatsink. The chip-top is contacted with a metal coverdisk using a small ribbon in a single or crossover version.

Schottky-Barrier-diodes on GaAs today are the standard semiconductors used for down-converting mm-wave signals in the lower IF-bands below X-band. Compared to Impatt- or Gunn-diodes the variety of commonly used package types is obvious, which is caused by different problems to be solved. Some examples of typical mixer diodes are shown in fig. 4.

Best results in question of noise figure can be obtained using honeycomb-whisker-diodes. The diode chip containing thousands of single Schottky-diodes is contacted by a whisker. The disadvantage of poor mechanical stability can be avoided using planar structures (slot-line or fin-line on quartz-substrat). Experiences concerning with this technique have shown similar noisefigures compared to the conventional whisker method /3/.

Whisker-diodes encapsulated in a ceramic package deliver quite good electrical values as well as good mechanical performance /4/. The built-in procedure is easier compared to the pure whisker-technologie, but the price of these diodes is very high. For lower frequency application, bonded diodes incorporated in a similar package give good results. For lower frequencies also beam-lead diodes or "chip+wire"-devices are well suited again. Beam-lead devices - Schottky as well as PIN - become more and more important at all especially in mm wave integrated circuits (MMIC). These devices are less expensive than whisker contacted diodes. The mechanical performance is better. The electrical properties though somewhat worse compared to whisker diodes are sufficient for many applications.

3. MM-WAVE CIRCUITS, DIFFERENT TECHNOLOGIES FOR DIFFERENT DEMANDS

Mm-wave circuits are not only an accumulation of semiconductors. Circuit and technology are rather more important if thermic, mechanic or low cost requirements must be observed. Concerning a mm-wave mass production fin-line structures obviously are the most sucessfull alternative to rectangular wave-guide. Nearly all microwave components can be realised using fin-lines unless high Q-factors are required. For high Q and high frequency devices about 90 GHz and above, however, today conventionally tooled block mounts using rectangular waveguides still give better results.

3.1 Oscillators and mixers up to 90 GHz

Gunn- or Impatt-oscillators as well as Schottky mixers are the most important components for mm-wave-equipments at all. Concerning oscillators results can be predicted very well. Using a test oscillator-mount unknown values of diode parameters, e.g. negative resistance, junction capacitance, and post reactance are derived from measured behaviour of oscillator frequency and power depending of iris-diameter /5/. In conjunction with producer data of package capacitance and ribbon inductance the oscillator performance can be calculated including power output, frequency, temperatur stability, quality-factor, pushing, and pulling.

Fig. 5 shows an approved oscillator device well suited for cw- or pulse applications up to 60 GHz. The oscillator does not need a reduced hight waveguide, thus for mass production a short piece of a commonly used waveguide embedded in a roughly tooled block mount can establish the cavity /6/. The power obtained is in general higher than that noted on the producer's diode data sheet. Temperatur stability as well as mechanical tuning range are sufficient for most applications in radar, radiometry, and communications.

For frequencies above 60 GHz oscillators containing a coaxial low pass filter as shown in fig. 6 are easier to fabricate. Due to the higher frequency this mount is mainly used for Impatt diodes. To obtain good results the low pass filter ("choke") must be designed and tooled very carefully to achieve reproductivity and to avoid rf-leakage. Depending on the employed diodes cw-power of more than 100 mW at 90 GHz is a typical value.

Mixer devices at mm-wavelength in general exhibit more variety compared with oscillators. This is caused by different diode packages as well as by different mixer applications. Fig. 7 shows a very simple but rugged mixer device, which exhibit excellent low conversion loss and noise figure at frequencies up to 60 GHz /7/. Similar to the oscillator as described above the mixer's cavity is not more than a piece of the related rectangular waveguide incorporating a quartz-substrat in cross plane. A slot resonator carries a beam-lead diode on it's backside thus separating IF and RF circuits. The diode's IF-circuit is floating in respect to ground so that diode polarities can be chosen arbitrarily. This is important for combining units to balanced mixers. A tuning screw enables to compensate deviations of diode parameters or to change the center frequency up to 500 MHz. Depending on diodes, best mixer data are 4.6 dB conversion loss at 7 dB SSB noise figure including 2 dB IF amplifier noise contribution.

At frequencies about 60 GHz good results have been obtained using encapsulated whisker diodes. To achieve the right diode position a small collet is used to pick up the diode /8/. This important detail is responsible for a reliable mixer operation at good electric values: Conversion losses of 4.5 dB at 60 GHz and 6.5 dB at 90 GHz can be reproduced.

3.2 Fin-line structures

As mentioned above, the fin-line is a very successfull alternative to the commonly used rectangular waveguide. The most important fin-line cross sections are shown in fig. 8. The simplest type of line is the wellknown unilateral fin-line which is best suited for almost all fin-line components /9/. The bilateral fin-line carries a metalisation on both substrate sides. This provides a lower transmission loss as well as more freedom in biasing active components, for instance matched PIN-attenuators or mixers with antiparallel switched diodes. The smallest wave impedance this line is delivering is about 100 Ω. Lower wave-impedances down to 10 Ω, however, can be realized using antipodal fin-lines, which are best suited for wave transformers with very high transformation factors ($>$ 20:1). Therefore the antipodal fin-line is a good transition medium between rectangular waveguide and microstrip. Nevertheless great care must be taken to design a well matched broadband transition from rectangular waveguide to fin-line. Extensive experiments testing a lot of transition contours lead to an unstepped device incorperating a curved shape similar to a parabola /10/. As a result transitions with better than 20 dB return loss covering entire waveguide bands have been realized. In addition, because of no broadband demands for most applications, narrow band return losses better than 40 dB are possible. This of cause only can be carried out using computer aided design and automatic plotted layout generation. Fig. 9 gives a summary of realized passive components. Regarding fin-line mixers, detectors and PIN-diode-components the inherent broadband characteristics overcome all conventional waveguide devices. In most cases the band limits are not given by the circuit but by the measurement equipment. The conversion loss of balanced mixers can be reduced down to 7,5 dB broadband using a tuned LO. Otherwise losses do not exceed 11 dB over the entire Ka-band incorporating a fixed LO in midband as an integrated part of the front end. These oscillators can quite easily be built up by heatsinking the diode at the waveguide wall.

PIN-attenuators and switches are developed in manyfold versions: Broadband-devices with insertion loss less than 1 dB and isolation better 25 dB over the entire Ka-band have been realized. Narrow band resonator-typ attenuators only need one diode to achieve similar values as the broadband attenuators. Even at 90 GHz 2 dB loss and 13 dB isolation have been obtained using only one low cost beam-lead PIN-diode.

For some applications, in the turned-off case no power should be reflected. Providing a seperately biased matching PIN-diode in front of the others 15 dB return loss at all transmission values has been realized.

PIN-attenuators furthermore can be expanded to multi-port-pin-switch-components using fin-lines. These devices in general exhibit the same data as compared to PIN-attenuators. Designing power dividers, the choice of impedance relation between outgoing arms determins the power division.

Fin-line couplers have shown good results. Remarkable properties are high coupling factors up to cross-over operation as well as excellent broadband directivity. Finally the main advantages of fin-lines compared with the rectangular waveguide, should be summarised:

- concentration of field and waves on small diode dimensions
- multiband devices are possible
- almost all components can be realized
- a high integration level is possible
- more flexible than monolithic devices
- suited also for small size mass production
- low cost circuit design and development

4. MM-WAVE SYSTEMS FOR MILITARY APPLICATIONS

As mentioned in the introduction the most important applications of mm-wave components are radar, communications and radiometry. In the following some examples recently developed at AEG-TELEFUNKEN are given.

4.1 A coherent pulse-radar at 35 GHz

In fig. 10 a block diagramm of a coherent 35 GHz pulse-radar is shown /11/. The heart of the system is a 34.5 GHz CW Gunn-oscillator which is locking a 500 MHz amplitude-modulated Gunn source by means of the lower sideband. This delivers a quartz stabilized IF-reference to provide a coherent down conversion. In addition the overlayed pulse modulation avoids spurious signals at 35 GHz which may decrease mixer's sensitivity. After passing a 35 GHz bandpass the pulse is amplified using a pulsed synchronised Gunn-oscillator. The antennas output power is about 1.5 W.

The received signal is attenuated by means of a PIN-STC using fin-lines. The insertion loss is 0.4 dB, the isolation 28 dB. Noise figure of the mixer is about 6 dB including 1.4 dB IF amplifier contribution.

Fig. 11 shows the radar without cover. The microwave circuit is embedded in the upper part. The right and left sides contain the transmitter- and receiver electronic circuits. Inputs and outputs as well as controll equipment is situated on the backside.

4.2 A 64 GHz radio-link using a parametric up-converter

Another example of mm-wave applications is a broadband radio-link at 64 GHz which is under construction at present, fig. 12. Most important part of the transmitter (on left) is a parametric up-converter, which renders a broadband modulation up to 500 MHz bandwidth at a conversion gain of 7 dB, /12/. The mixer's SSB noise figure is less than 6 dB. Fig. 13 shows on left the parametric up-converter containing two waveguide-filters for signal- and pump-power respectively and the varactor doubletee-mount in between. On the right, the down - converter is shown, containing the directional filter, the LO, the mixer mount, and an adjustable high precision tunable backshort.

4.3 A 90 GHz radiometer receiver frontend

A well known application of mm-wave components at higher frequencies are radiometer receivers. A typical block diagram of a frontend is shown in fig. 14. Although today sufficient Gunn-LO power at 90 GHz is available, varactor doubled sources at 45 GHz are less expensive and deliver more power. This is usefull if encapsulated mixer diodes are utilized requiring somewhat more power than whisker contacted diodes without package. The LO decoupling of the signal input considerably can be increased by compensating the input circulator by means of a sliding load. More than 40 dB is reproducible. The total system DSB-noise figure which can be reproduced including circulator loss and IF-noise contribution is about 9 dB.

REFERENCES

/1/ Kramer, N.B. — Solid State Technology for Millimeter Waves. **Microwave Journal 8 (21) (1978) S. 57-61.**

/2/ Kennedy, J.K.; Lessoff, H.; Lile, D.L. — InP - An Assessment of United States Activities. Symposium on Micr. Comp. for the Frequ. Range above 6 GHz, Bruxelles (1978). Symp. Digest.

/3/ McMaster, T.F.; Carlson, E.R.; Schneider, M.V. — Subharmonically pumped mm-wave mixers built with notch-front and beam-lead diodes. IEEE MTT-S Conf. (1977) Symp. Digest pp 389-392.

/4/ Texas Instruments Diode data sheet MDX 623.

/5/ **Barth, H.; Bischoff, M.; Schroth, H.:** — 64/4-GHz-Empfangsmischer für ein 60 GHz-Transpondersystem. Abschlußbericht Vertr. Nr. 01 TI 077A-AK/RT/WRT 2077 AEG-TELEFUNKEN, Ulm (1978).

/6/ Lindner, K.; Wiesbeck, W. — Die Mikrowellenbaugruppen eines 35 GHz Abstandswarnradars für Kraftfahrzeuge. Mikrowellenmagazin 5 (1977) pp 398-403.

/7/ Meinel, H. — Aufbau eines Ka-Band-Mischers in hybrider Hohlleitertechnik. Interner Bericht AEG-TELEFUNKEN, Ulm (1978).

/8/ Barth, H.; Rembold, D. — 90 GHz Radiometrie-Empfänger. Interner Bericht AEG-TELEFUNKEN, Ulm (1978).

/9/ Hofmann, H.; Meinel, H.; Adelseck, B.
New integrated mm-wave components using fin-lines.
IEEE MTT-S (1978). Symp. Digest pp 21-23.

/10/ Adelseck, B. e.a.
Neue Wellenleiter und Schaltkreise für mm-Wellensysteme. 2. Zwischenbericht zum Vertrag T/RF 31/60007/61010.
AEG-TELEFUNKEN, Ulm (1977).

/11/ Lindner, K.
Ka-Band Radar (Gera). Abschlußbericht zum Vertrag T/RF 31/71418/71310.
AEG-TELEFUNKEN, Ulm (1978).

/12/ Barth, H.; Meinel H.
Design of a 4 GHz to 64 GHz parametric upper-sideband up-converter.
Symp. on Microwave Components for the Frequency Range above 6 GHz, Bruxelles (1978) Symp. Digest.

/13/ Barth, H.; Rembold, B.
Design and performance of 90 GHz radiometer front ends.
AGARD-Symposium on Millimetre and Submillimetre wave propagation. Munich (1978).

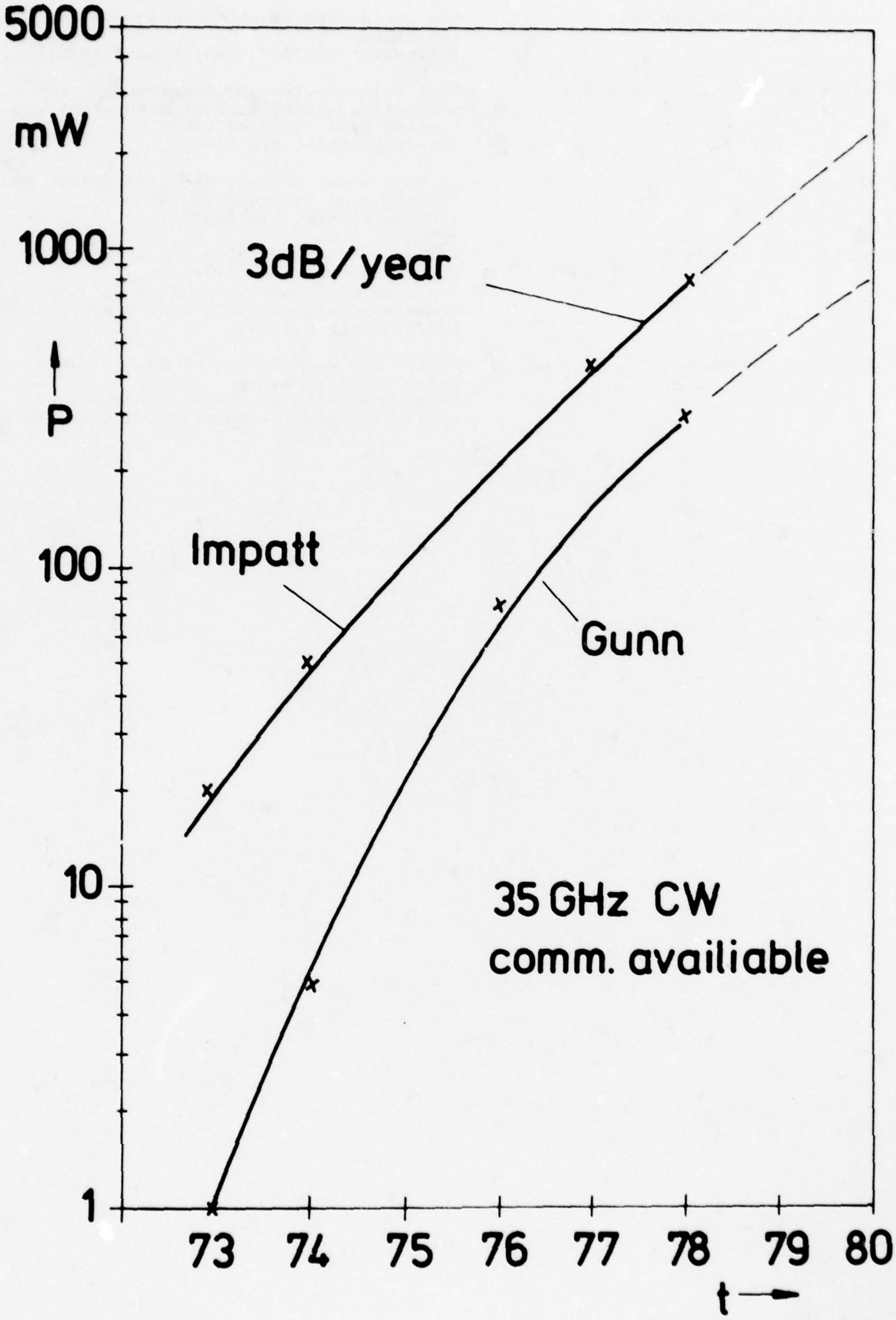

Fig. 1 Power increase of Impatt and Gunn diodes

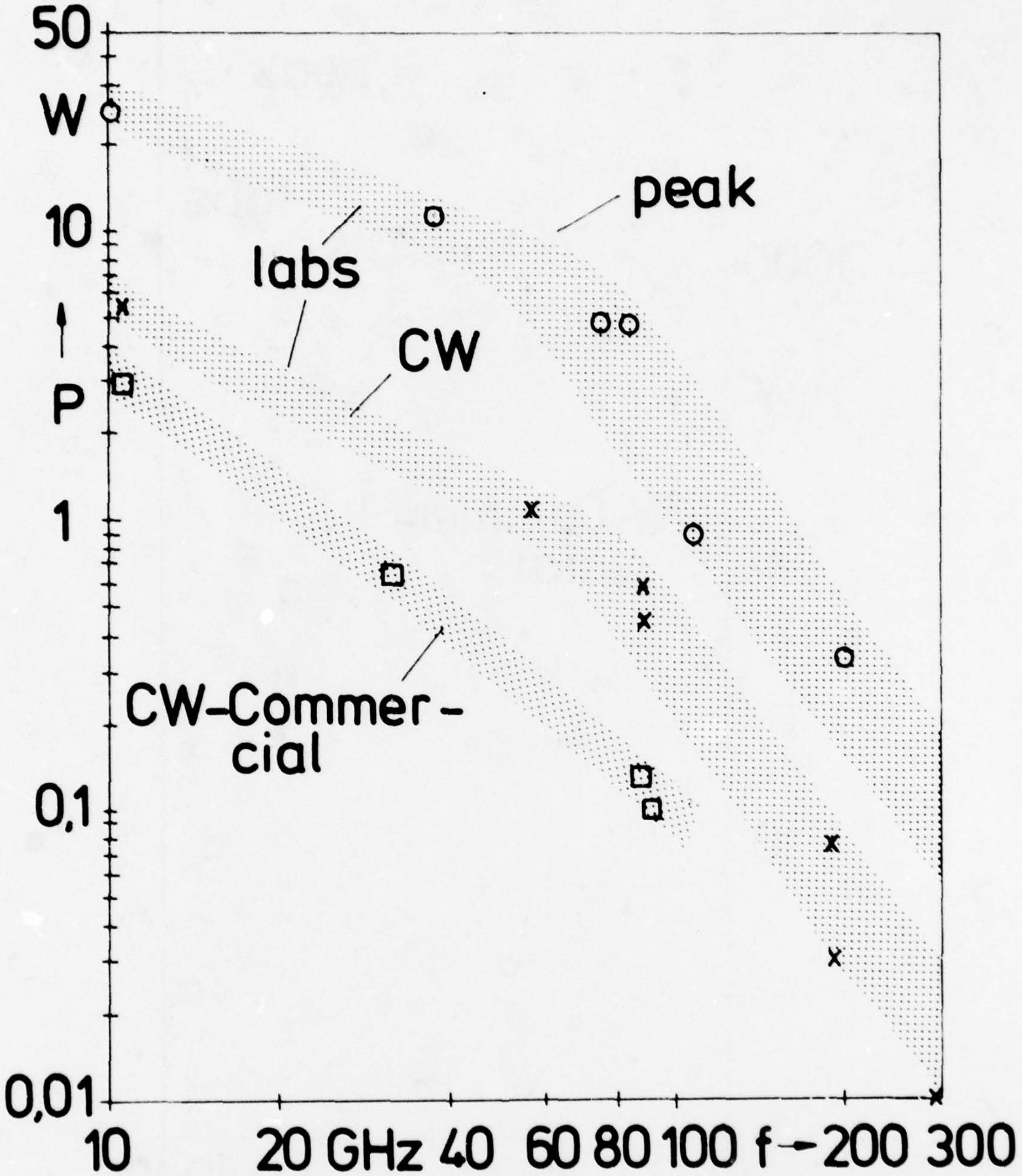

Fig.2 Impatt-diode power vs. frequency

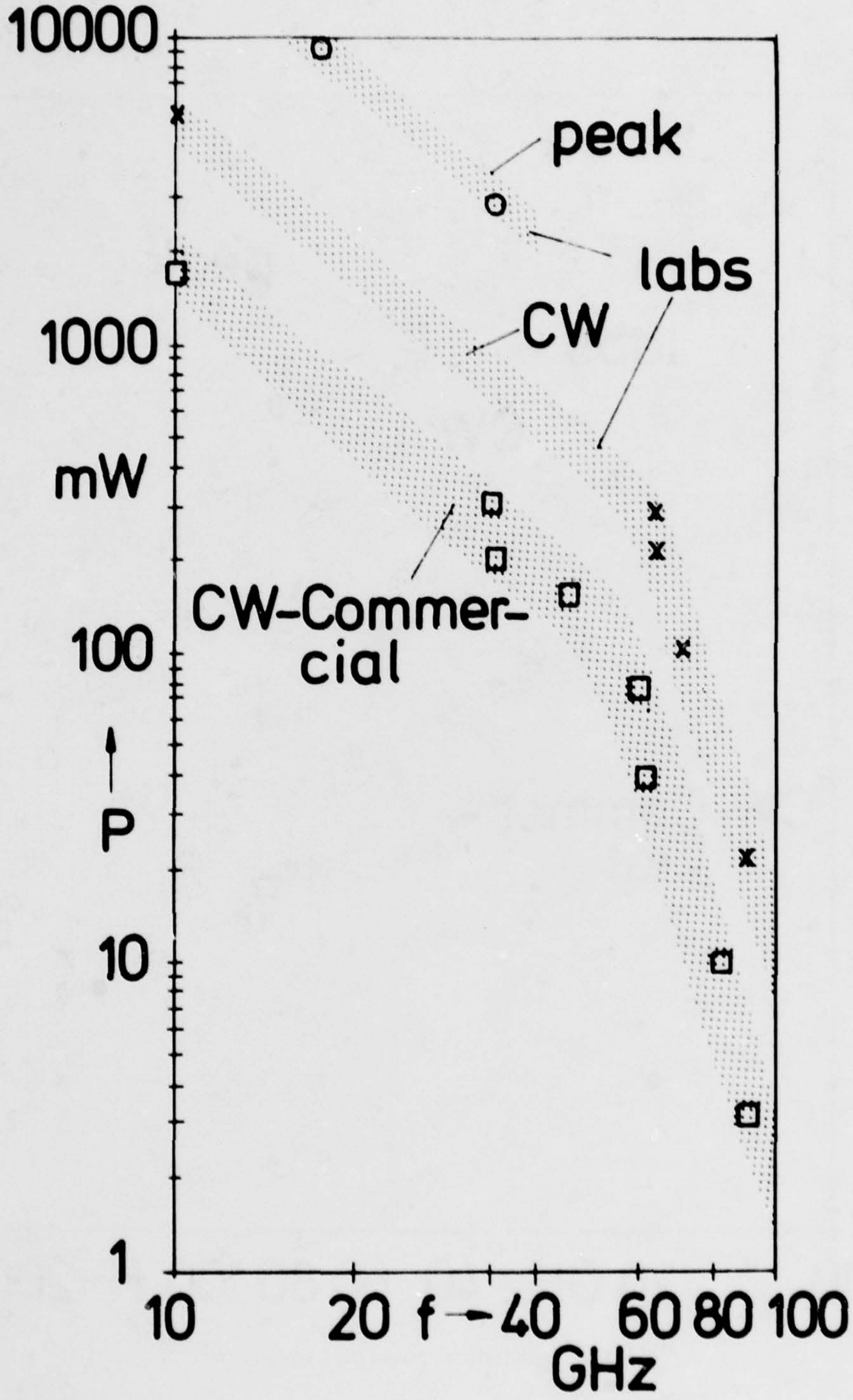

Fig.3 Gunn-element power vs. frequency

	whisker	notchfront + whisker	ceramic package + whisker	gold ribbon	beamlead	chip + wire
diode	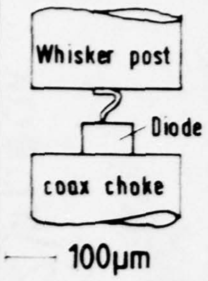 Whisker post Diode coax choke 100µm	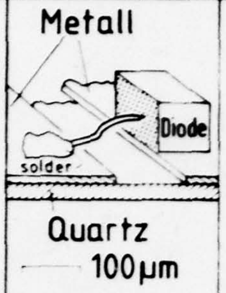 Metall Diode solder Quartz 100µm	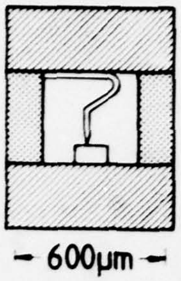	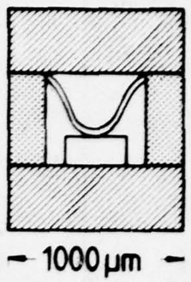	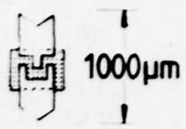	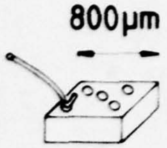
Cj / fF	6 - 12	6 - 12	30	150	50 15	60
Cp / fF	-	-	60			
Rs / Ω	5 - 15	5 - 15	10	10	5 10	25
conversion - loss/dB	5-6 (90 GHz)	8 (90 GHz)	5 (60 GHz) 7,5(90 GHz)	5 (35 GHz)	5 (35 GHz) 8 (90 GHz)	6 (35 GHz)
noise figure/dB SSB, without IF	4 (90 GHz)	4,6 (98 GHz)	5-6 (90 GHz)	5-6 (35 GHz)	8 (98 GHz)	6-7 (35 GHz)
advantages	best values at f > 60 GHz	good values and rugged performance	good values and easy to build in	low cost, high reliable, suited up to 60 GHz	suited for planar structures up to 100 GHz	low cost suited up to 40 GHz

Fig.4 mm-wave mixer diodes

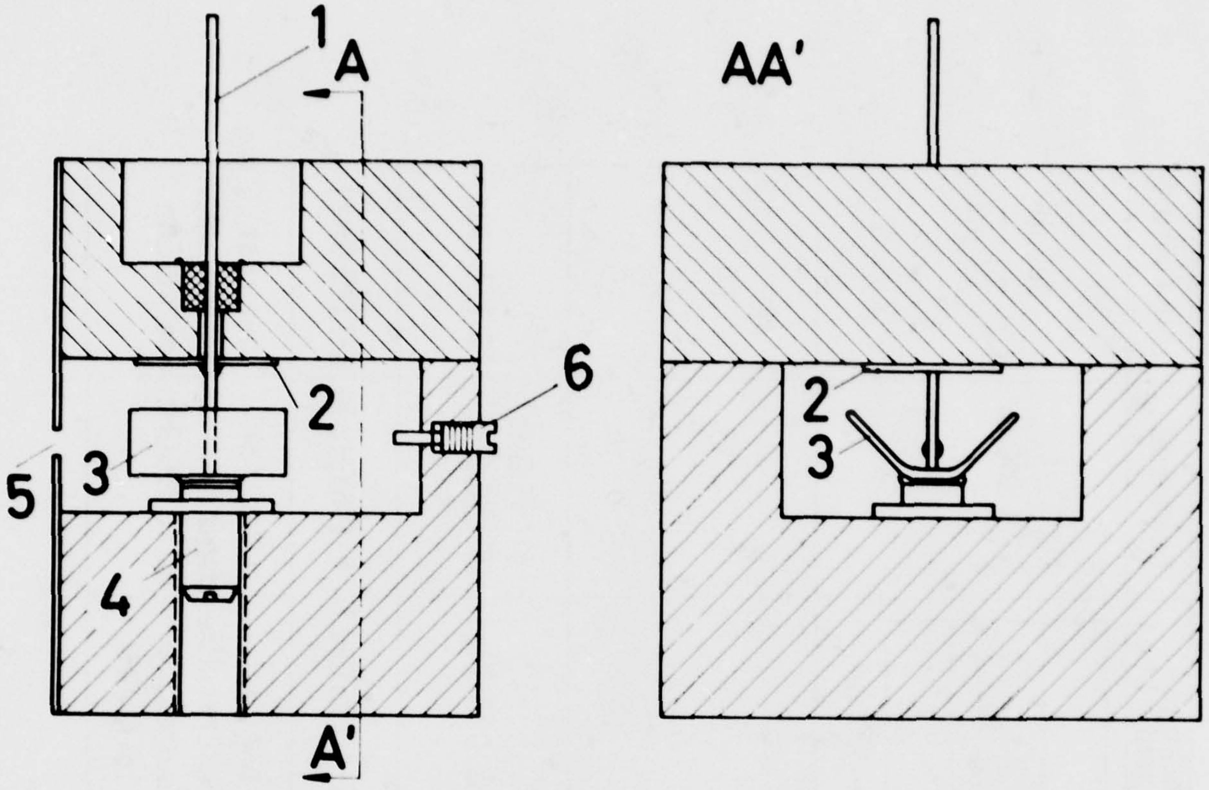

1 bias connector
2 capacitive blocking choke
3 matching wings
4 gunn element
5 iris
6 tuningscrew

Operation: CW or pulsed
Frequency: 26-60 GHz
Power: 100 mW_{cw}, 2 W_{peak}
Pulse: down to 5 nsec
Stability: $10^{-6}/°C$
Mechan. tuning: >1 GHz

Fig.5 Gunn-oscillator

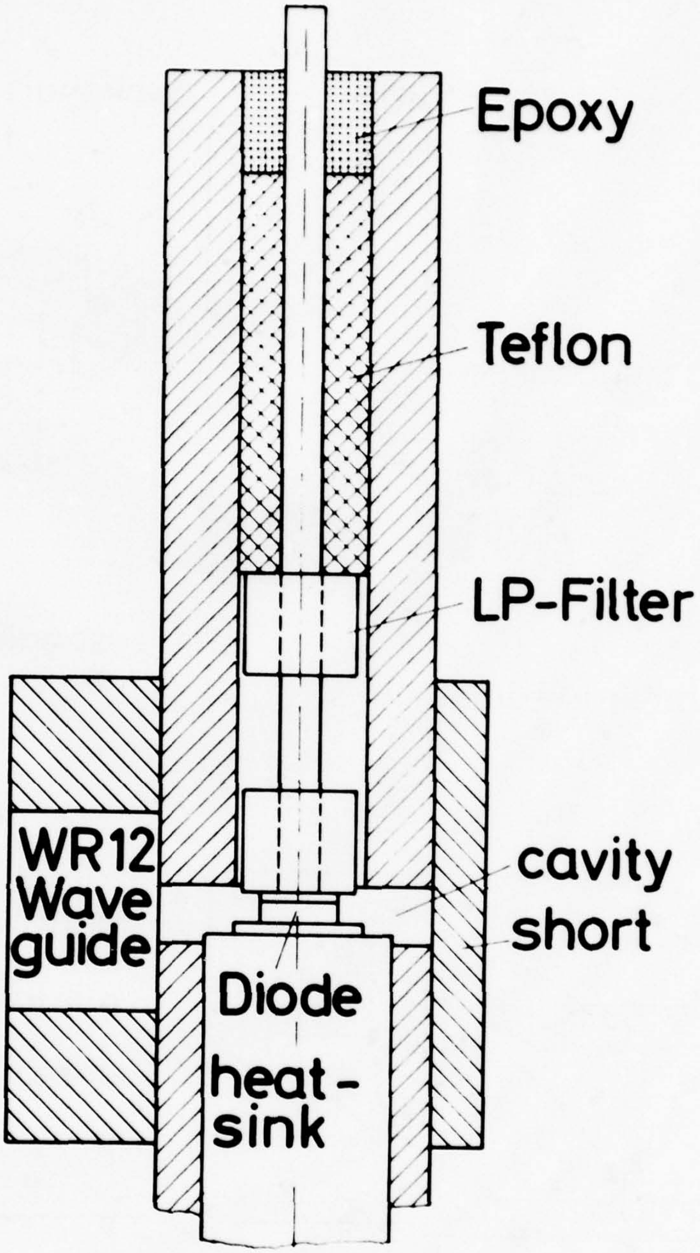
Epoxy
Teflon
LP-Filter
WR12 Wave guide
cavity
short
Diode
heat-sink

Operation: CW or pulsed
Frequency: 60-100 GHz
Power: 100 mW_{cw}, 2 W_{peak}
Pulse: $\geq$100 nsec
electr. tuning: up to 10 GHz

Fig.6 Impatt-oscillator

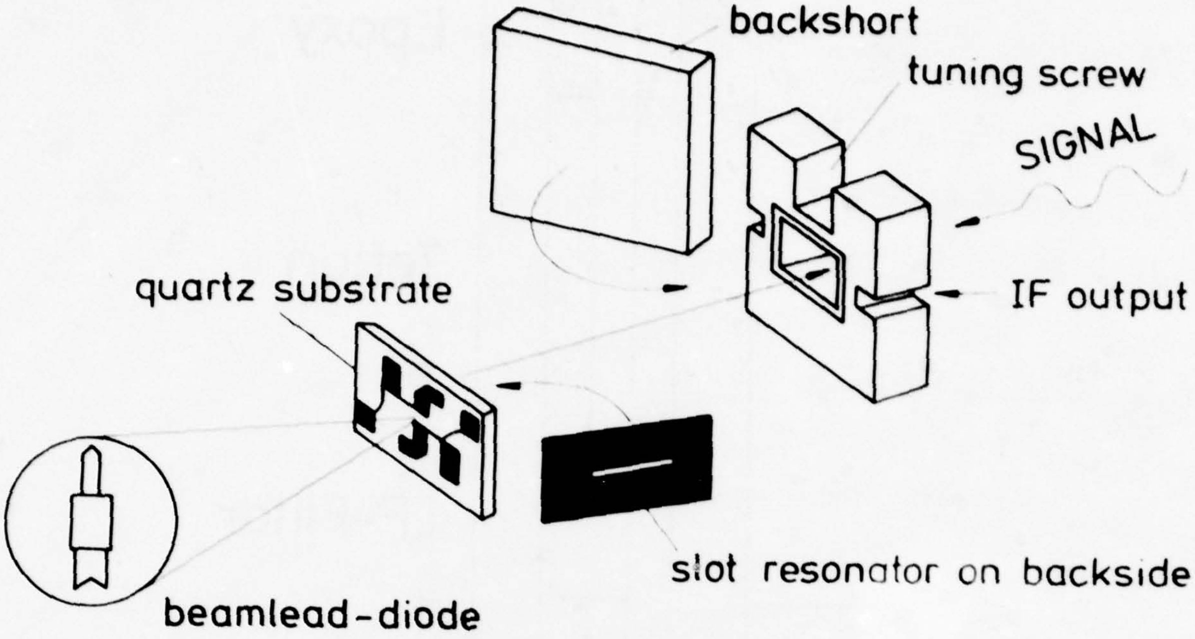
backshort
tuning screw
SIGNAL
quartz substrate
IF output
slot resonator on backside
beamlead-diode

Fig. 7 mm-wave-mixer

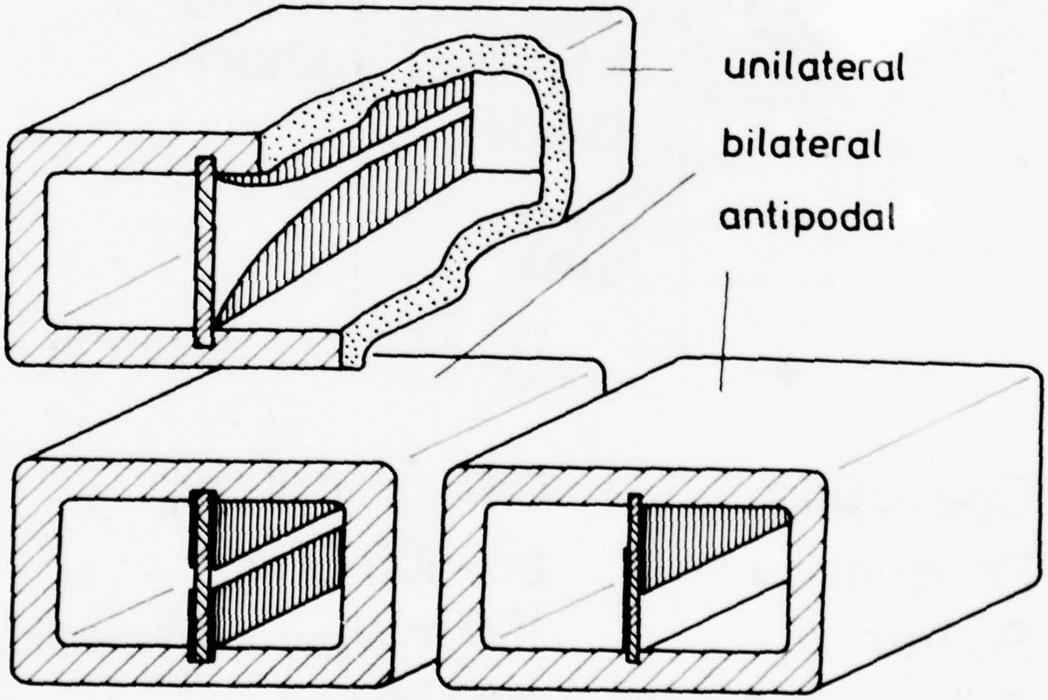
unilateral
bilateral
antipodal

Fig. 8 Finline-structures

component		frequency, GHz	properties
balanced mixer	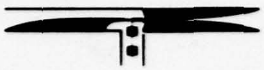	26-40	L_c<8dB broadband
oscillator		26-40	Gunn devices for integrated LO's
detector		26-40	Sensitivity >.5mV/μW broadband
PIN-attenuator		18-60	loss <1dB, isol.>30dB entire band
		60-90	loss <2dB, isol.>13dB/diode 90GHz
PIN-switch power divider	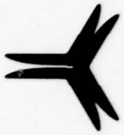	18-60	loss <2dB, isol.>20dB broadband power division adjustable, ripple ±.2dB broadb.
coupler	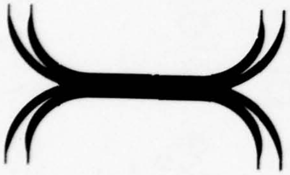	26-40	k down to 0dB (crossover) directivity: >15dB entire band; >40dB narrowband

Fig.9 Finline components

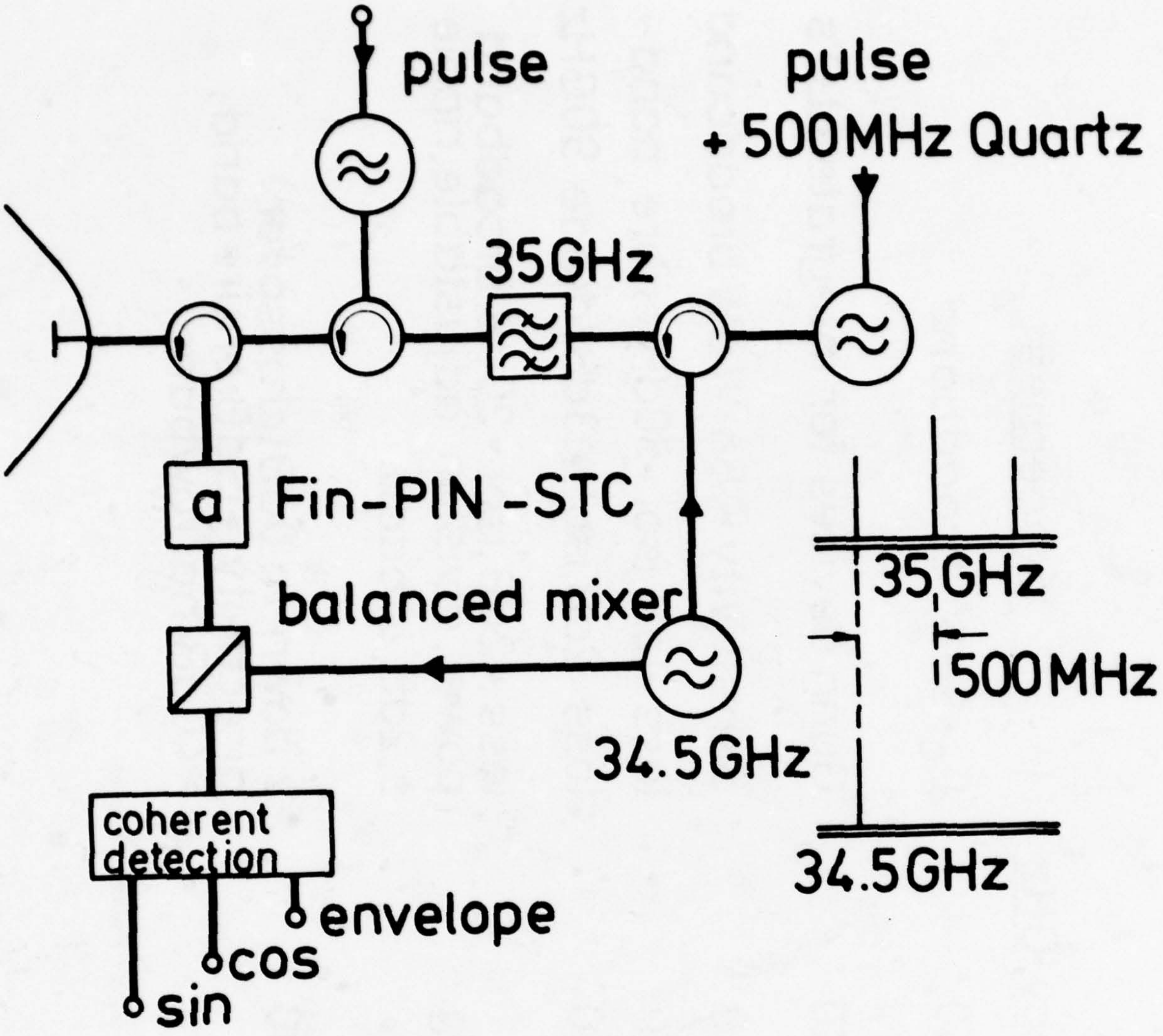
pulse
pulse
+ 500MHz Quartz
35GHz
a
Fin-PIN-STC
balanced mixer
34.5GHz
35 GHz
500MHz
34.5GHz
coherent detection
envelope
cos
sin

System data

peak power	1,5 W
pulse width	20-40 nsec
RPF	adjustable or extern
noise figure	6 dB
outputs	envelope, sin-, cos- pulse doppler

Fig.10 35 GHz pulse doppler radar principle block diagram

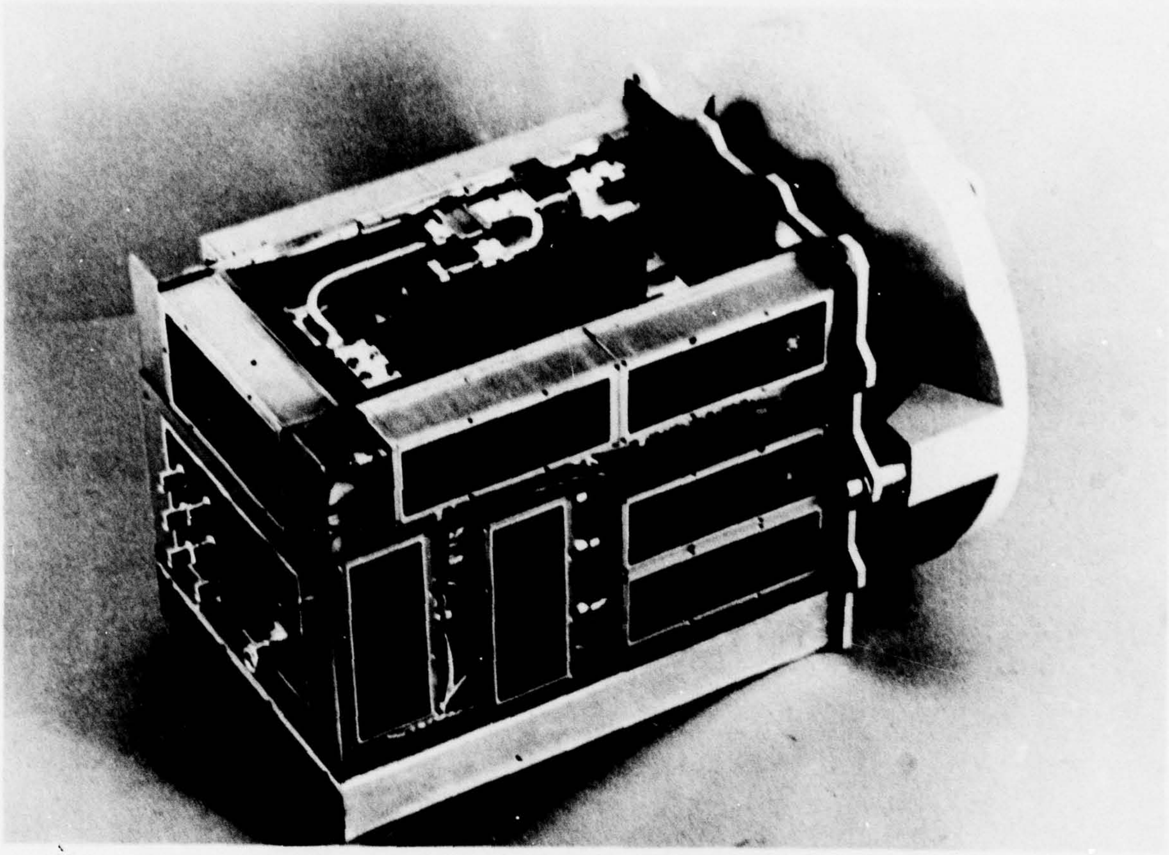

Fig. 11 A coherent 35 GHz pulse radar

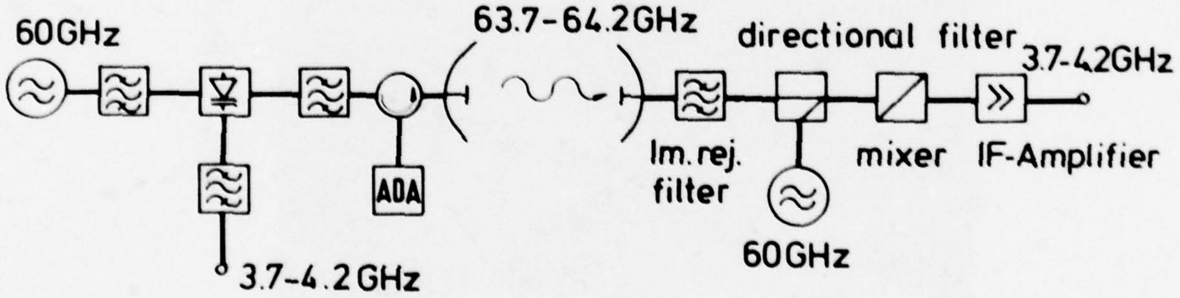
60GHz
63.7-64.2GHz
directional filter
3.7-4.2GHz
ADA
Im. rej. filter
mixer
IF-Amplifier
60GHz
3.7-4.2GHz

System data

transmitter

power	10 mW (100 mW)
bandwidth	500 MHz
ripple	± 0.2 dB
gain	7 dB

receiver

noise figure	6 dB
LO decoupling	> 30 dB
gain	30 dB

Fig. 12 Broadband radio-link at 64 GHz

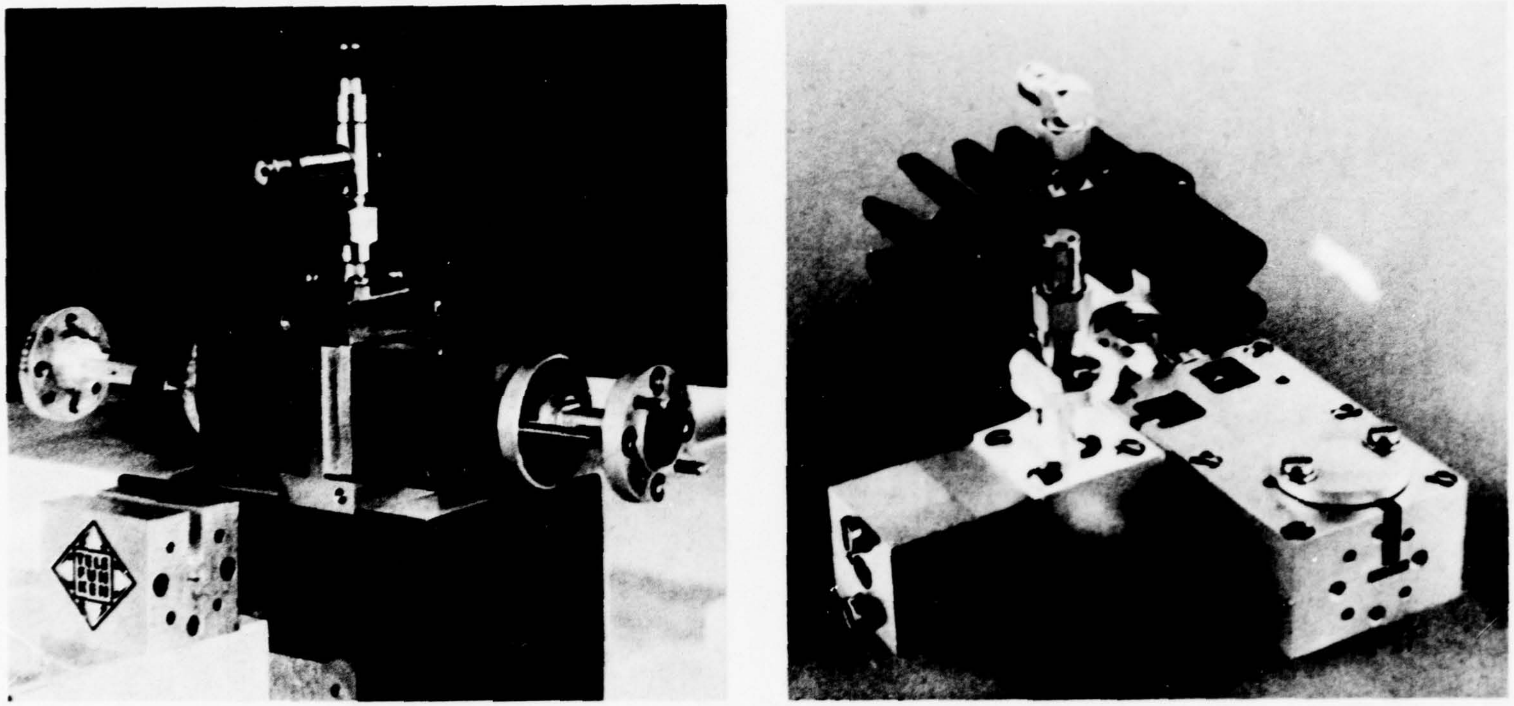

Fig.13 Up- and down-converter of a 64 GHz radio link

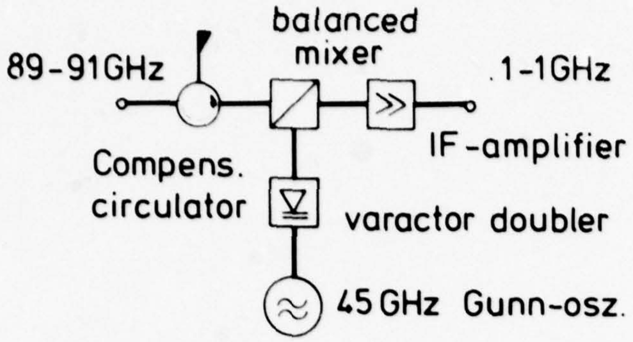
balanced mixer
89-91GHz
.1-1GHz
IF-amplifier
Compens. circulator
varactor doubler
45GHz Gunn-osz.

Systemdata

noise figure (dsb)	9 dB
LO decoupling of signal input	>40 dB
input matching	18 dB
RF/IF-gain	54dB
IF-bandwith	0.9 GHz
ripple	±0.8 dB

Fig.14 A 90 GHz radiometer receiver front end

DISCUSSION

H.G.Oltmam, US

(1) What was the instantaneous and tunable bandwidth of your example 35 GHz coherent radar?

(2) Is the local oscillator tunable?

Author's Reply

(1) Bandwidth is about $\frac{1}{10 \times 10^{-9}}$ Hz, given by the transmitter pulse.

(2) The local oscillator is not tunable, but may be replaced by another at a different frequency.

M.C.Carter, UK

Were there any problems due to leakage through the circulator.

Author's Reply

The attenuation of the isolated circulator path combined with the PIN-STC-attenuation is sufficient for our application.

VARACTOR TUNED MILLIMETER WAVE OSCILLATOR
IN THE PRETUNED MODULE TECHNOLOGY

Gerard Cachier, Jean Stevance
THOMSON-CSF
Domaine de Corbeville
91401 Orsay - France

SUMMARY

The pretuned module (PTM) is a new millimeter oscillator, which has been first described at the 1977 ISSCC. It is a rugged device wich integrates, together with an IMPATT diode, all the elements for both internal matching and external radiation towards the utilization. It makes the control of the oscillator really easy.

In this paper we show that it also lends itself quite well to electronic tuning with a varactor diode. This is done by inserting two identical modules in each broad wall of a retangular waveguide, one of them being polarized below the breakdown. A few percent tuning bandwidth can thus be obtained.

1. INTRODUCTION

Many applications of the millimeter waves require electronic frequency tuning. Examples of this are automatic frequency control of local oscillators, FM transmitter oscillators for communication applications, transmitters for FM radars, and phase locked oscillators for a wide variety of applications.

In the millimeter range, oscillators are Gunn or IMPATT diodes. These diodes can be frequency modulated by the modulation of the bias current, as it was shown by CHAO and by CHANG for IMPATTS, by LAZARUS for Gunns. This method necessitates only one diode. It has been used especially in the case of IMPATT oscillators. A better technique for achieving this modulation consists of controling the oscillator frequency with a separate varactor diode. This method necessitates more refined circuit techniques, which have been achieved successfully both in a conventional waveguide by CHANG and on a microstrip by GLANCE and by RUBIN.

If we consider now the problem of millimeter circuits, it turns out that a careful choice has to be done as one selects a given technique. In addition to the performance , the simplicity of the design and the cost are important factors. The reason is that, in many of the applications considered up to now - and particularly for military applications - these techniques are in competition with both lower frequency microwaves and higher frequency infrared techniques. Our approach, which was presented at the 1977 ISSCC, is to realize the millimeter oscillators as integrated modules, which will be described in the first part of this paper. It will then been shown that these modules lend themselves quite well to the realization of varactor tuned oscillators by simply combining two separate modules in a standard waveguide.

2. THE PRETUNED MODULE

2.1 Description of the module

The device (fig. 1) has the shape of a flat dielectric cylinder attached to a copper holder, and metallized on the top. It incorporates a silicon IMPATT diode in its center and a radial circuit around it, which matches the diode to the outside world. The whole structure is a pretuned oscillator, which can be used in a wide variety of millimeter circuits.

As it has been explained at the Cornell conference, the principle of the matching radial line is similar to the well known cap circuit described by MISAWA wich usually gives the best results at millimeter frequencies. The radial line has a radius of about $\lambda/4$ (the wavelength is computed within the dielectric material constituting the module). This brings to the diode a selfic reactance which tunes it to the desired frequency. The rim of the module is the open end of the line. It acts as an antenna which couples the module either to the free space, or to a standard rectangular waveguide. This also brings to the diode the proper value of circuit resistance, wich is necessary for the diode to operate with maximum output power.

In design, a silicon IMPATT diode is initially thermocompression bonded to the holder, junction down for best thermal dissipation. Then a quartz ring is attached to the holder, around the diode. This ring is made by truncating a capillary tube. The diode is then passivated with a polyimid resin. The structure is polished to bring the diode, the resin and the quartz to the same height above the holder. It is metallized, both for making an ohmic contact to the back of the diode and forming a radial waveguide between the metallization and the holder. Typical dimensions are a height of $0{,}03\lambda$ (λ = free space wavelength), and a diameter of $0{,}3\lambda$ for fused quartz as a constituting material ($\varepsilon = 4$). We can see therefore that the module has a low profile and a large metallized top surface. This will ensure both mechanical ruggedness and easy handling.

2.2 Mounting and performance

This module can be used in simple millimeter circuits. One of mounting techniques consists of inserting the module horizontally in a standard rectangular waveguide as indicated on fig. 2. The large metallized top surface allow easy bias with a thin wire wich crosses the walls of the waveguide through alumina rings. This wire is used to control the insertion of the module in the waveguide, so that the surface of the thermal holder lies in the plane of the bottom wall. The output power has been up to 400 mW at 45 GHz. The behaviour as a function of the bias current is smooth : the frequency pulling is less than 100 MHz over the whole oscillation range, without frequency jumps.

Another alternative consists of making a small (about 1 cm^3) holder, with the bias feed incorporated to it. The d.c. bias is applied through an insulated wire crossing the thermal heatsink attached to the holder. A thin (∿ 30µm) gold wire is then T.C. bonded on the top of the PTM as shown on fig. 3. This wire is soldered to the bias feed. Then this holder is inserted horizontally in the waveguide as in the previous technique.

3. VARACTOR TUNED OSCILLATOR

3.1 Varactor tuning

Varactor tuning of negative resistance oscillators has been described theoretically by CAWSEY. We will assume here a series tuning-that is the varactor is mounted in series with the oscillator (fig. 4). This corresponds to the mounting scheme wich will be described later. The transformer represents the amount of coupling to the oscillator.

In this circuit, the frequency tuning $\frac{\Delta f}{f}$ obtained when the capacitance of the varactor is changed between C_{MAX} and C_{MIN} is :

$$\frac{\Delta f}{f} = \frac{1}{2}\frac{Q_e}{Q_d} C_d n^2 \left[\frac{1}{C_{min}} - \frac{1}{C_{max}} \right]$$

where $Q_e = \frac{1}{2}\frac{f}{R_c}\frac{dX_c}{df}$ (external Q of the circuit)

$Q_d = \left| \frac{X_d}{R_d} \right|$ (Q of the diode)

It is often more convenient to introduce

$$S = 2\frac{Q_e}{Q_d} = \frac{f}{X}\frac{dX}{df}$$

which represents the logarithmic derivative of the reactance vs. the frequency. S can be computed, and also measured on a model scaled down at a lower frequency. Usually, $2 < S < 10$. The frequency tuning is now :

$$\frac{\Delta f}{f} = \frac{1}{S} C_d n^2 \left[\frac{1}{C_{min}} - \frac{1}{C_{max}} \right]$$

This formula shows that :

- the resistive component of the circuit impedance does not affect the frequency tuning
- there are two independant factors which are of importance. One is the sensitivity S of the reactance to the frequency. The other is the relative change of the varactor capacitance as it is seen by the IMPATT diode. The tuning is higher with small varactor diodes, closely coupled to the IMPATT.

It is important to have the two diodes as close as possible, in order for the microwave circuit which does the coupling between them to be as constant as possible. The PTM lends itself quite well to that constraint.

3.2 PTM with a varactor diode

The varactor diode is an IMPATT diode polarized below its breakdown voltage. It is therefore straightforward to make a tuning module, which looks identical to the oscillator. Its electrical description is now a small length of radial transmission line, fed from its periphery, and terminated by the varactor diode.

Assuming that the radial line is low loss, and that it is fed by a matched transmission line, one finds, after YOULA, that the reflection coefficient on the varactor diode is :

$$\rho = e^{j\theta} \frac{Z_r^* - Z_v}{Z_r + Z_v}$$

where $Z_v = R_v + \frac{j}{\omega C_v}$ (impedance of the varactor)

Z_r = impedance of the matched radial line as seen from the varactor

θ = phase (independant of Z_v)

Z_r can be calculated by the method described at the Cornell Conference.

However, a simple result is obtained by observing that the maximum influence happens when the reactances of Z_r and Z_v are equal. This is exactly the case of an oscillator. It therefore follows that the design of a tuning module with maximum coupling and the design of an oscillator are quite similar. We will actually use identical modules for either oscillators or tuning elements.

3.3 Varactor tuned oscillator

The oscillator module and the tuning module are capacitively coupled by bringing together at a close distance the top surface of each module. This is done easily by inserting each of them horizontally in the waveguide through each broad wall, as shown on fig. 5. Each module is biased separately : the oscillator by a wire crossing the waveguide, the varactor by using a mount with an incorporated bias feed (both techniques described in § 2-2). This design allows enough flexibility by changing the distance between the two modules.

We have observed experimentally that the coupling is higher if the two modules are closer. This shows that the coupling is due to the proximity of the metallized surfaces of the modules.

We have obtained with that technique 500 MHz of smooth tuning at 45 GHz, as shown on fig. 6. Power variation over 500 MHz tuning was 3 dB. The Q_e of the oscillator, measured by the tuning bandwidth, was between 60 and 90. By changing the coupling, we have obtained in the same range 1020 MHz smooth tuning with somewhat less power, and also 2000 MHz tuning, but with a 300 MHz frequency jump. With a slightly different cavity 900 MHz tuning was obtained in the 30 GHz range.

As a conclusion, an electronic tuning bandwidth of a few percent can be obtained by varactor tuning of a pretuned module. This looks sufficient for some of the typical applications already considered.

References

CACHIER, G., ESPAIGNOL, J., 1977 "The pretuned module : an integrated millimeter wave oscillator". 1977 International Solid State Circuits Conference Digest, p. 126

CACHIER, G., DEL GIUDICE, M., DERYCKE, A.C., DUPONT, L., ESPAIGNOL, J., STEVANCE, J., SFIKOPOULOS, T., 1977, "Circuit modeling of the millimeter wave modular oscillators". 6th biennial conference on active microwave semiconductors and circuits, Cornell University

CAWSEY, D., 1970, "Wide range tuning of solid state microwave oscillators" IEEE Journal of Solid State Circuits Vol. SC5, p. 82

CHANG, Y., HELLUM, J.M., PAUL, J.A., WELLER, K.P., 1977 "Millimeter wave IMPATT sources for communication applications", 1977 IEEE MTT symposium digest, p. 216

CHAO, C., HADDAD, G.I., 1973, "Nonlinear behaviour and bias modulation of an IMPATT diode oscillator", IEEE Transactions on M.T.T., Vol. 21, p. 619.

GLANCE, B.S., 1976 "Microstrip varactor tuned millimeter wave transmitter" IEEE Transactions on MTT, Vol. 24, p. 156.

LAZARUS, M.J., CHEUNG, K.Y., NOVAK, S., SOKULLU, A.M., 1975 "Bias Frequency Modulation of Ga As Millimeter Wave Diode Oscillators", IEEE Transactions on M.T.T., Vol 23, p. 700

MISAWA, T., KENYON, N.D., 1970, "An oscillator circuit with cap structures for millimeter wave IMPATT diodes " IEEE Transactions M.T.T., Vol. 18, p. 969

RUBIN, D., 1976 "Varactor tuned MIC oscillator" IEEE Transactions on M.T.T., Vol. 24, p. 866

YOULA, D.C., (1964) "A new theory for broadband matching" IEEE Transactions on circuit theory, Vol. CT 11, p. 30

BLA

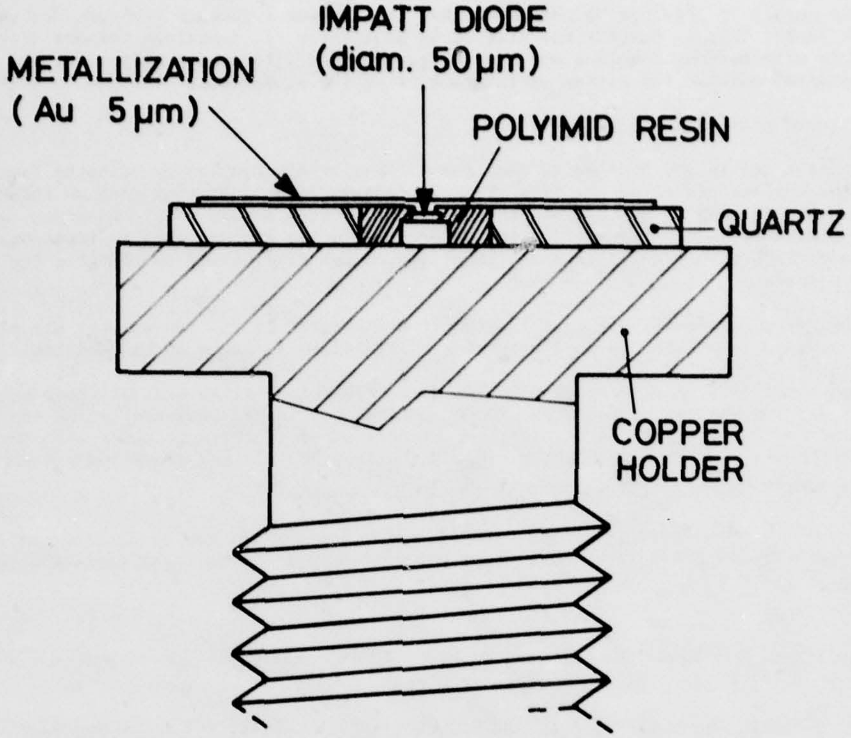
IMPATT DIODE
(diam. 50µm)
METALLIZATION
(Au 5µm)
POLYIMID RESIN
QUARTZ
COPPER
HOLDER

FIGURE 1 Schematic cross section of the PTM, emphazing the position of the IMPATT diode in the center of the module

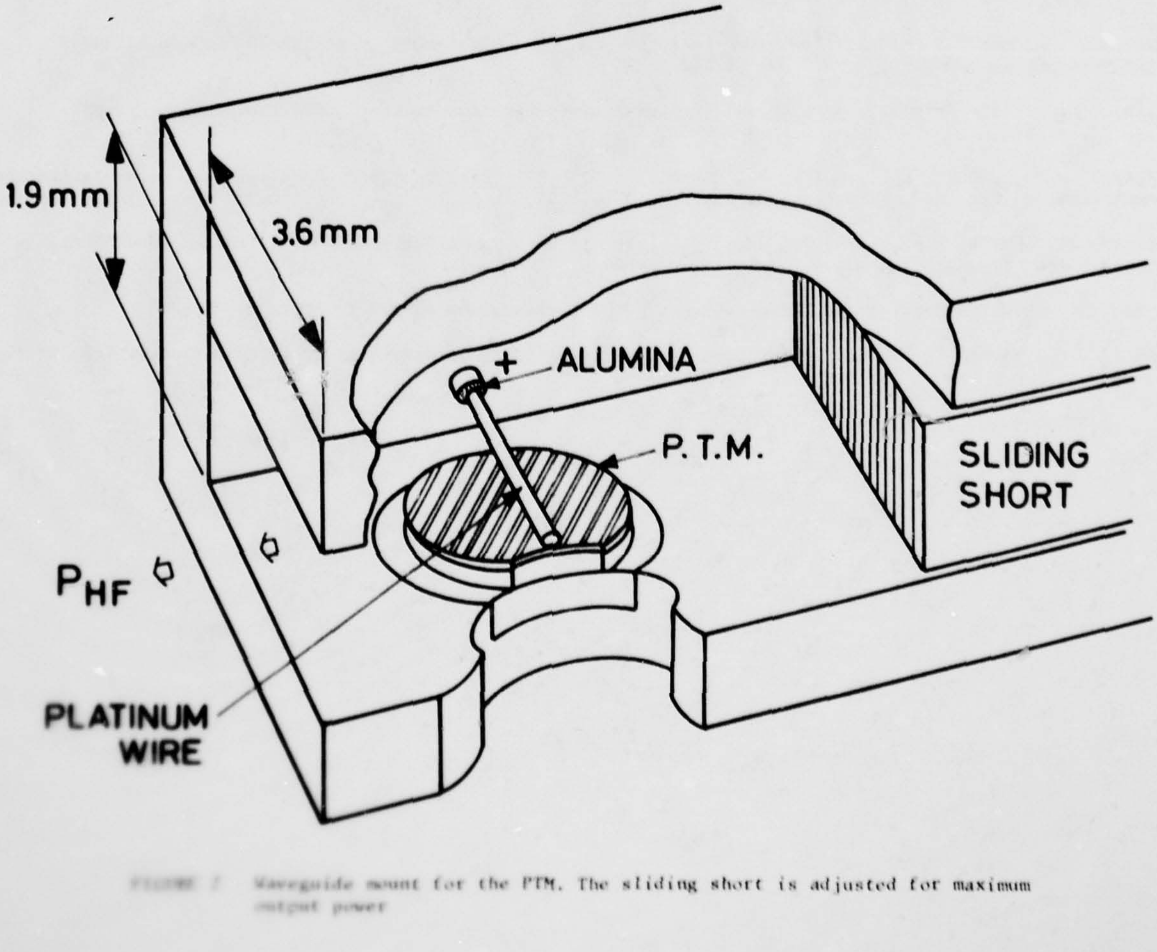
1.9mm
3.6mm
ALUMINA
+
P. T. M.
SLIDING
SHORT
P_{HF}
PLATINUM
WIRE

FIGURE 2 Waveguide mount for the PTM. The sliding short is adjusted for maximum output power

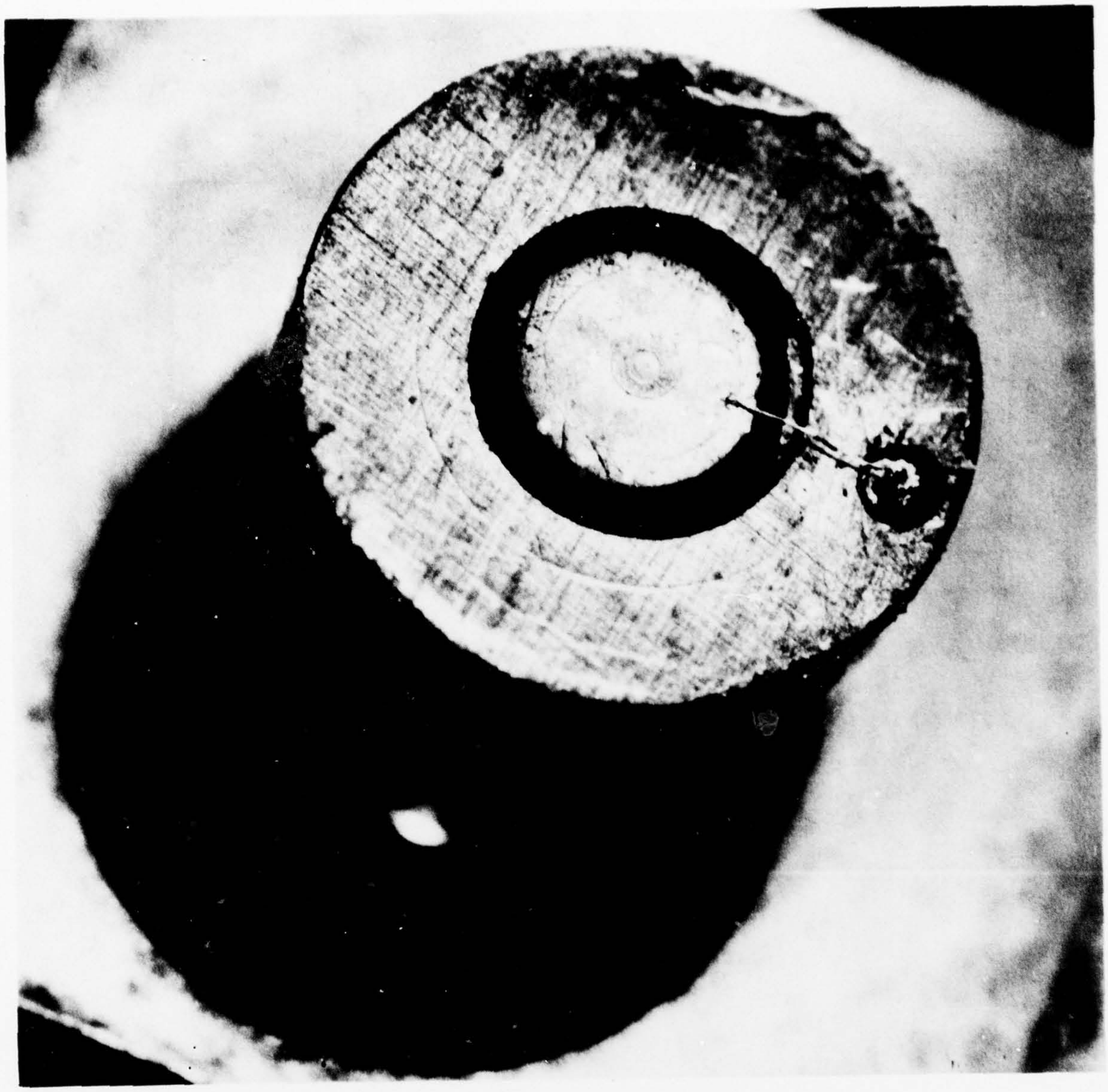

FIGURE 3 Photomicrograph of a PTM mount with an incorporated bias feed. The quartz ring is 2,5 mm in diameter, and the T.C. bonded gold wire on the right is 25 μm thick.

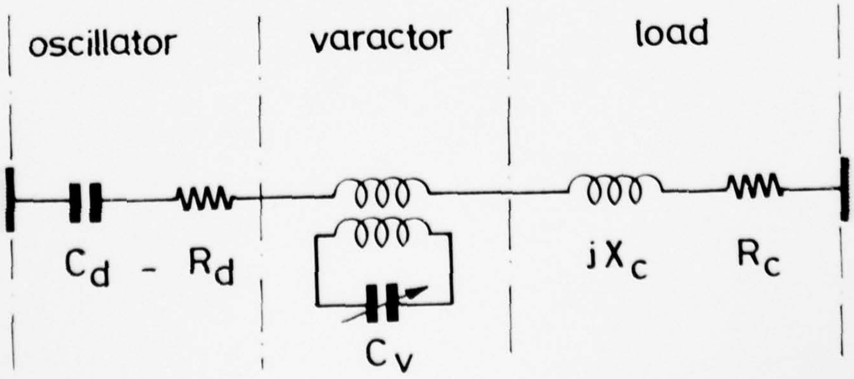
oscillator
varactor
load
C_d - R_d
C_v
jX_c
R_c

FIGURE 4 Equivalent circuit for a series-varactor tuned oscillator

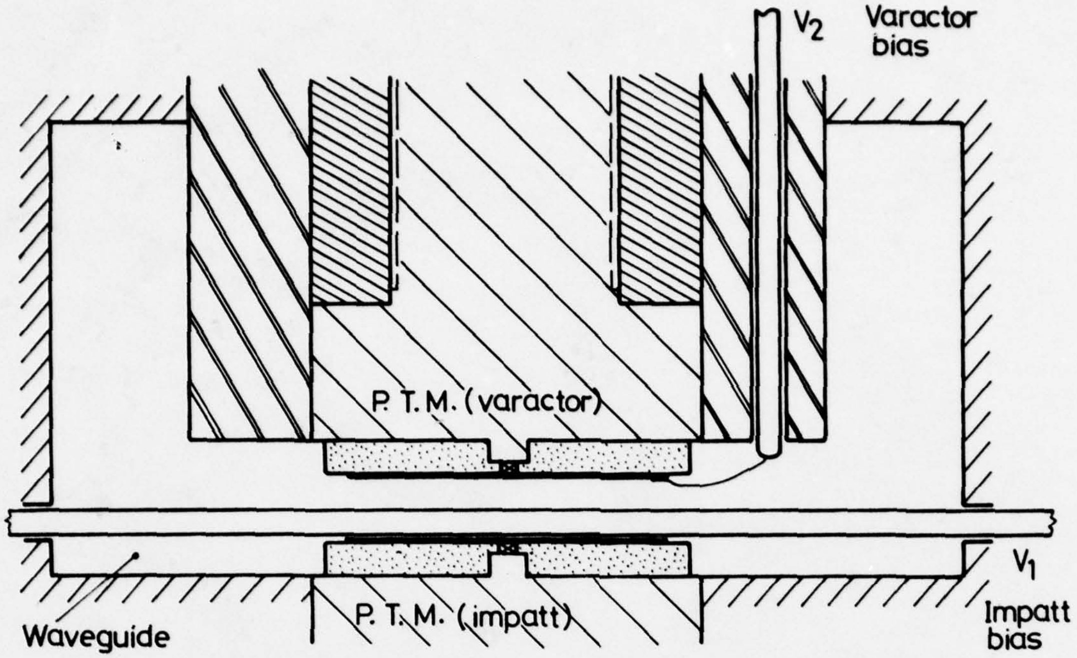
V2
Varactor bias
P. T. M. (varactor)
V1
Impatt bias
Waveguide
P. T. M. (impatt)

FIGURE 5 Cross section of the waveguide with the IMPATT module in the bottom part, and the varactor module in the upper part. The distance between the two modules can be easily adjusted for optimum coupling.

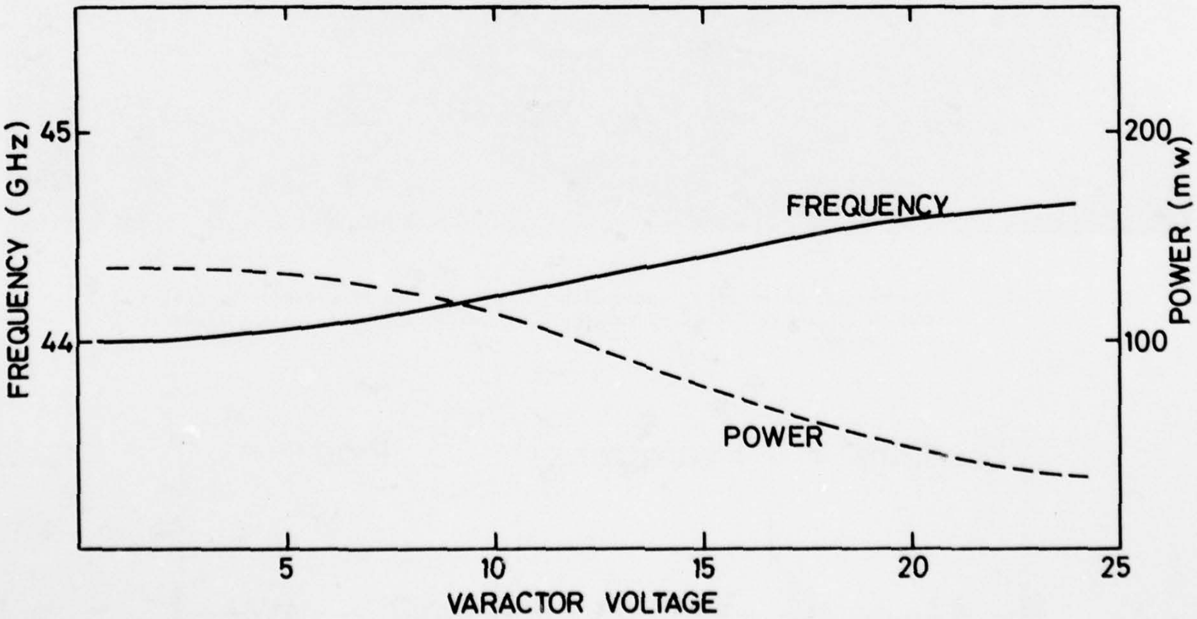

FIGURE 6 Tuning curves of a 45 GHz oscillator.

MICROSTRIP COMPONENTS FOR LOW COST MILIMETER WAVE MISSILE SEEKERS

BY

H. G. OLTMAN, D. M. WEEMS, G. M. LINDGREN, F. D. WALTON
Hughes Aircraft Company
Canoga Park, California, USA

Abstract

For adverse weather applications short millimeter wavelengths offer needed high resolution to the smallest of missiles. In the past, the high cost of millimeter wave (MMW) components has all but precluded its application to systems of any kind. Missiles in particular need inexpensive components in order to be cost effective. The paper addresses the development of low cost photo-etched microstrip components and integrated circuits for such applications.

Described are an antenna, hybrid and mixer suitable for incorporation into a single integrated circuit for either monopulse or sequential lobing seekers. Incorporation of all components onto a single substrate offers advantages of direct incident radiation to IF conversion, no troublesome connectors between components, and accurate reproduction of the optimized circuit in production. The cost of developing the optimized circuit for the MMW band is substantially reduced by scaling the circuit in all details to a lower frequency and hence, larger size. Components for the MMW circuit described were first designed and optimized and then integrated and optimized at a 28:1 scale. The final MMW circuit was a photo-reduction of a photograph of the optimized integrated low frequency circuit.

Introduction

Although milimeter waves have been actively studied for nearly thirty years, their widespread application to terrestrial communication or weapon systems has been long coming. Primary reasons for the slow utilization have been the small waveguide dimensions requiring close tolerances which imply high costs; the small, fragile connectors between components which are difficult to align and have poor reliability; atmospheric propagation loss; and until recently, the relative poor performance of components. Component performance has been improving with better semi-conductors and with better design concepts — applications are now much more practical. It remains, however, to achieve low-cost components and eliminate connections between components.

This paper describes microstrip integrated circuit (MIC) work oriented toward the realization of as many microwave components fabricated on a single substrate as practical. In this manner, it is expected to achieve low-cost components, elimination of connectors between components, and properly done to still achieve high performance. The work is being done at 94 GHz.

Why choose 94 GHz? The 94 GHz band offers several advantages over other frequency bands. Higher directivity is realized from small, missile-sized antenna apertures than from 35 or 10 GHz seekers systems; good adverse weather operation can be realized; back scatter data taken in rain shows a distinct advantage at 94 GHz over 35 GHz; small targets can be more readily picked out of cluttered backgrounds; in the past few years, components have become readily available.

In the recent past, antenna and component techniques have been demonstrated which suggest that most of the components of an active missile seeker, including the antenna feed, can be integrated on to a single substrate. The work to be described illustrates the progress that has been made toward this goal. Figure 1 illustrates the work accomplished thus far. Shown is a monopulse antenna feed integrated with a monopulse comparitor. To use it effectively, the circuit would be located in the focus of a reflector or lens antenna such as those illustrated in Figures 2 and 3. The objective is to demonstrate signal conversion from incident RF radiation to signal outputs at the IF frequency, and to do this on a single MIC substrate.

Scaled Frequency Tests

Working with circuits as small as those illustrated in Figure 2 is difficult, and instead, the designs were first fabricated and tested at a scaled frequency of 3.3 GHz. To scale properly, all dimensions are increased by the chosen scale factor, here 28.4:1. The scaled circuit maintains constant the impedance, the wave velocity, and the dimensions relative to the wave length.[1] Only losses cannot be scaled. Losses are not a problem so long as there are no high Q resonances in the circuit.

Figure 4 shows the scaled antenna feed circuit composed of four offset dipole elements, and Figure 5 shows the scaled quadrature hybrid. Each of these circuits were fabricated using copper tape which facilitated easy trimming, and were then optimized in performance. Following optimization, the circuits were photographed, photo-reduced to make a mask, and then MIC were fabricated at 94 GHz. Also shown in Figures 4 and 5 are the eccentric coax-to-microstrip launchers necessary to minimize radiation from the large coax/microstrip interface. These launchers improve the match between the coax and microstrip electromagnetic fields by slowly concentrating the coax fields onto one side of the center conductor. Minimizing spurious radiation is important on circuits containing antennas.

The measured performance of the antenna feed at 3.3 GHz is shown in Figures 6 and 7. The bandwidth of the offset dipoles is 2 GHz for a VSWR less than 2:1. This is more than adequate for the required system bandwidth, but does require precision photolithography at 94 GHz. The dipole lengths must be held within ±5 microns (±0.0002") in order to hold the dipole frequency within ±.5 GHz. This precision is being accomplished with the fabrication procedures that have been developed. Figure 7 shows the sum and difference patterns of the scaled circuits. An excellent 30 dB difference null was obtained A slight amount of tilt can be observed which is due to an error in the line lengths of the comparitor network.

---

1. M. V. Schneider, "Millimeter Wave Integrated Circuits", 1973 IEEE-G-MTT International Symposium, Boulder Colorado, June 4-6, 1973, p. 16-18.

The measured hybrid performance is described in Table 1. The measured bandwidth was greater than that expected on a theoretical basis and is probably due to forward coupling in the hybrid arms.

TABLE 1. BRANCHLINE COUPLER PERFORMANCE

Center Frequency	3.31 GHz
Input VSWR (7% Bandwidth)	1.12:1
Insertion Loss	0.10 dB
Balance	0.10 dB
Isolation (7% Bandwidth)	25.0 dB
Bandwidth (Ret. Loss of 19 dB)	
Experimental	16%
Theoretical	12%

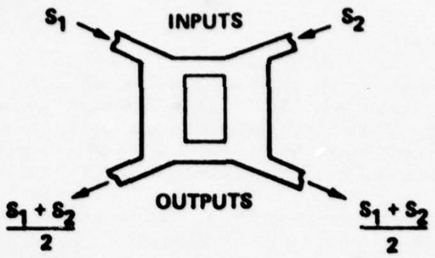

Arranging the scaled antenna feed and hybrids into an antenna/microwave comparator network results in the circuit shown in Figure 8. The impedance level of the microstrip circuit was chosen 80 ohms in order to realize adequately proportioned hybrids. Too low an impedance level would cause the rectangular aperture to close because the hybrid linewidths are inversely proportional to the circuit impedance level. The tapered microstrip lines alter the circuit impedance level from 80 to 50 ohms, and are only needed in these test circuits to interface with standard measuring equipment. The generous curves in the microstrip layout were used to minimize radiation from the narrow 80 ohm lines. Radiation not only degrades the antenna patterns, but would result in circuit loss and, hence, degraded performance. The performance of this circuit is listed in Table 2.

TABLE 2. SCALED ANTENNA/COMPARITOR PERFORMANCE

VSWR	(X. XX;1)	ISOLATION (dB)	
SUM	1.19	ΔAz – SUM	26.2
ΔAz	1.55	ΔAz – EL	22.8
ΔEl	1.06	ΔAz – ΔΔ	17.5
ΔΔ	1.51	ΔEl – SUM	22.4
		ΔEl – ΔΔ	26.6
		SUM – ΔΔ	41.3

94 GHz Circuits and Measurements

Figure 9 is a photograph of the antenna feed-microwave comparator MIC that, as previously mentioned, was fabricated by photographing the scaled circuit, photo-reducing it and photo-etching it on a fused silica substrate. All substrates were 0.11 mm (0.0044 in.) thick, and the photographed substrate is 13 by 15 mm (0.50 by 0.57 in.). The circuit is mounted on a replaceable carrier that interfaces with the two waveguide-to-microstrip launchers shown in Figure 9. Circuits have been fabricated using both gold and copper metalizations.

The waveguide-to-microstrip adapters use a ridged waveguide transformer to transform waveguide signals onto the microstrip circuit. The transformer is a five-step Chebyshev design with a theoretical VSWR of 1.02:1. Over a 25% bandwidth, a scaled version of the adapter achieved a maximum VSWR of 1.09:1. The 94 GHz version showed a maximum VSWR of 1.23:1 in the measured band from 90 to 100 GHz. The source of the mismatch was found to be the ridge transformer — a not unexpected result upon considering the tolerances. Metal to metal contact is made between the ridge and microstrip circuit. To achieve this contact without restrictive tolerances, the top wall of the waveguide is made flexible so that it may be deformed, and thereby press the ridge onto the microstrip circuit.

The measured return loss of the three major channels of the 94 GHz antenna/comparator MIC is shown in Figure 10. Note that the best match is obtained at approximately 93.5 GHz. With this circuit, the best match should be obtained at the resonant frequency of the dipoles. The latter were designed for a best match at 94 GHz. Hence, these measurements imply that the etched circuit is slightly oversized, which accounts for the 0.5 GHz reduction in frequency. Precision measurements of the dipole lengths confirm they are oversized by 1/2%, which accounts for the error in resonant frequency.

The impedance matches seen at the three terminals are not equally good. This is to be expected. Due to mutual coupling between the closely spaced dipoles, it is not possible for each terminal to see the same match. Mutual coupling effects differ in each channel due to the fact that the dipoles' signals are added and subtracted in different ways to form each channel signal.

Microstrip Circuit Losses

Of critical importance is measurement of microstrip losses at 94 GHz. It is well known that microstrip is a relatively lossy transmission line medium when compared with waveguide. On a per-unit-length basis, microstrip has an order of magnitude greater loss. Hence, microstrip can only be a useful circuit medium if the total circuit size can be kept small, thereby keeping losses small. To verify that microstrip losses could be kept small, it was considered important to measure these losses.

The losses due to the microstrip lines can be obtained by a differential measurement using U-shaped circuits like that shown in Figure 11. By measuring the loss from waveguide port to waveguide port of two U-shaped circuits of different length and then subtracting, the loss due to the length difference is obtained. The latter is the only variable in the test.

The measurements show that the 50 ohm microstrip has 1.1 db/in. loss. This implies that the antenna/comparator circuit will have a total insertion loss of 0.8 db — a reasonable value for this type of circuit.

Conclusion

The fabrication processes and tests conducted thus far on the 94 GHz MIC show the feasibility for integrating microstrip/dipole antenna on the same substrate with other RF circuitry. Scaled frequency tests showed good results which were generally confirmed at 94 GHz. Although microstrip line losses are higher than waveguide when compared on a basis of equivalent lengths, such is not true when compared on a basis of equivalent circuits. Losses for equivalent circuits are essentially the same — about 0.8 dB for the described circuit. The ability to fabricate seeker circuits using photoreplicating techniques promises to yield low cost, reproducible circuits. It remains to integrate mixers and other seeker components to determine performance limits. This work is continuing.

Acknowledgement

We wish to recognize the excellent work and support of Dr. Hugh L. Garvin who fabricated the 94 GHz circuits, and Messrs. Irving Baker, Dan Agan, and E. A. Eyraud, who ably assisted in the laboratory.

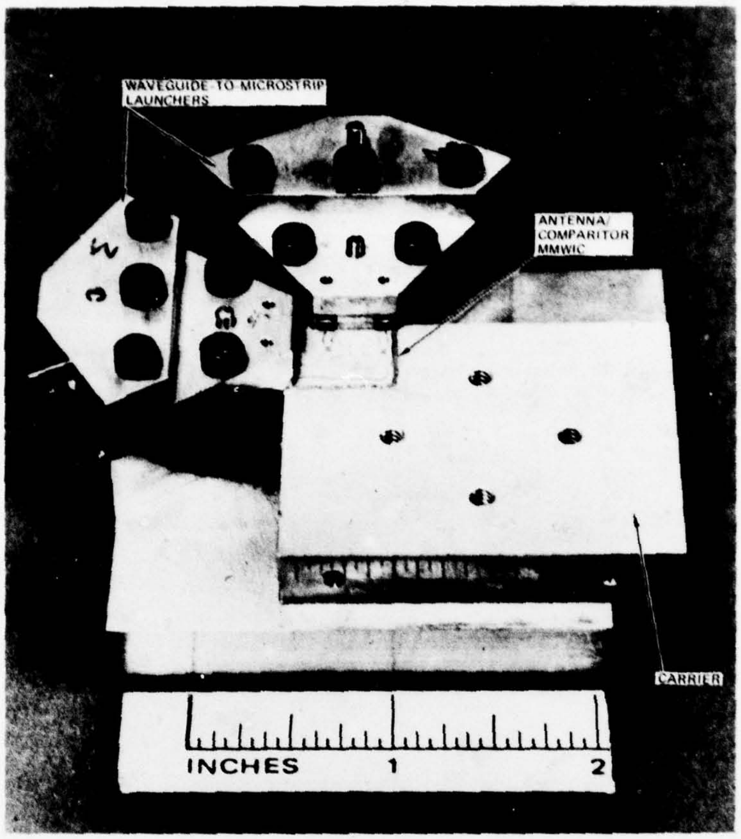
WAVEGUIDE TO MICROSTRIP LAUNCHERS
ANTENNA/ COMPARITOR MMWIC
CARRIER
INCHES 1 2

Fig. 1 Antenna/comparitor (MMWIC) mounted in its waveguide adapting test fixture

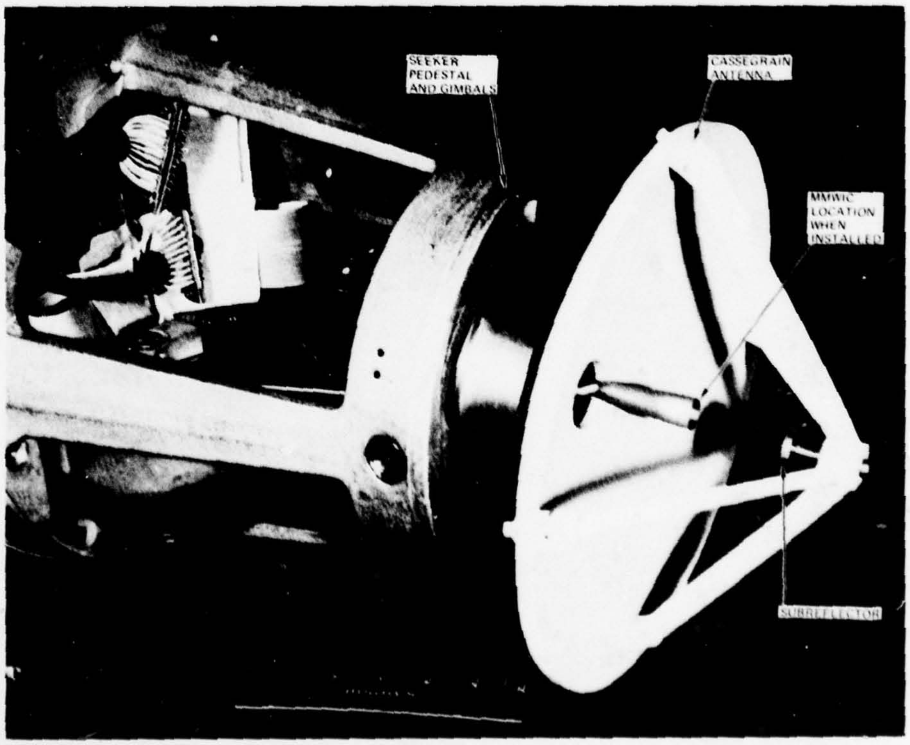
SEEKER PEDESTAL AND GIMBALS
CASSEGRAIN ANTENNA
MMWIC LOCATION WHEN INSTALLED
SUBREFLECTOR

Fig. 2 In reflector applications, the MMWIC would replace the MMW hardware shown and would be located at the prime focus (horn aperture)

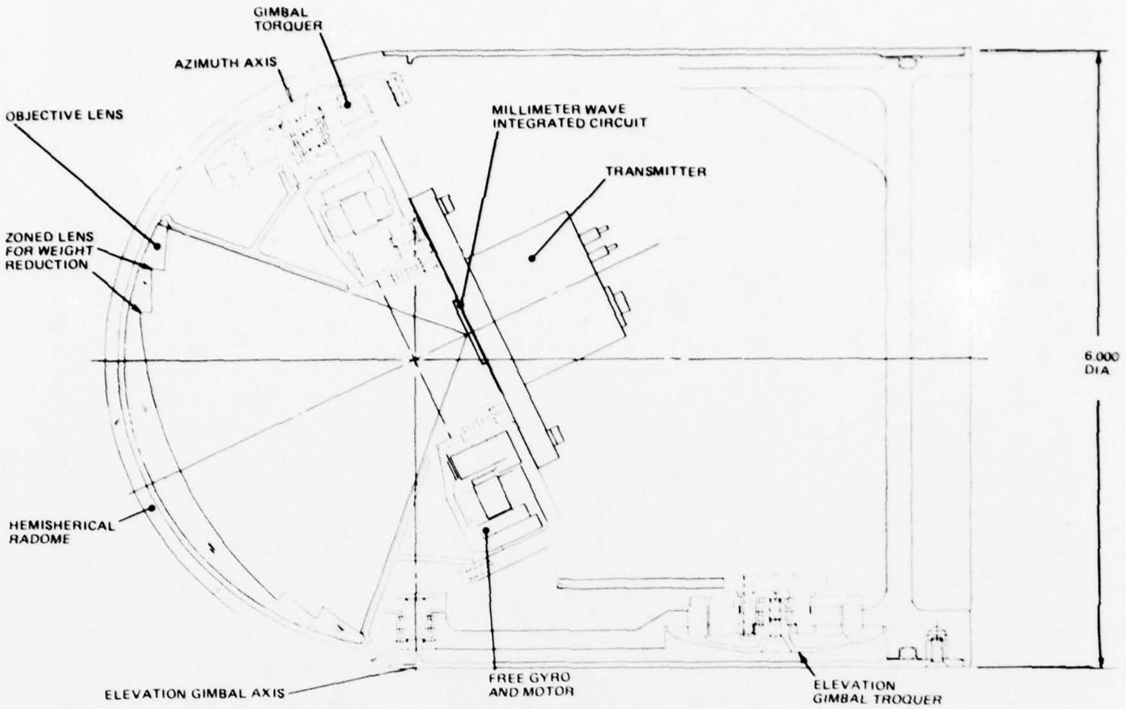
GIMBAL TORQUER
AZIMUTH AXIS
OBJECTIVE LENS
MILLIMETER WAVE INTEGRATED CIRCUIT
TRANSMITTER
ZONED LENS FOR WEIGHT REDUCTION
6.000 DIA
HEMISHERICAL RADOME
ELEVATION GIMBAL AXIS
FREE GYRO AND MOTOR
ELEVATION GIMBAL TROQUER

Fig.3 Incorporation of an MMWIC in an example small diameter missile

COAX-TO-MICROSTRIP LAUNCHER
FUSED SILICA SUBSTRATE
DIPOLES
IMPEDANCE TAPER
HUGHES

Fig.4 Scaled monopulse feed antenna in process of dipole trimming

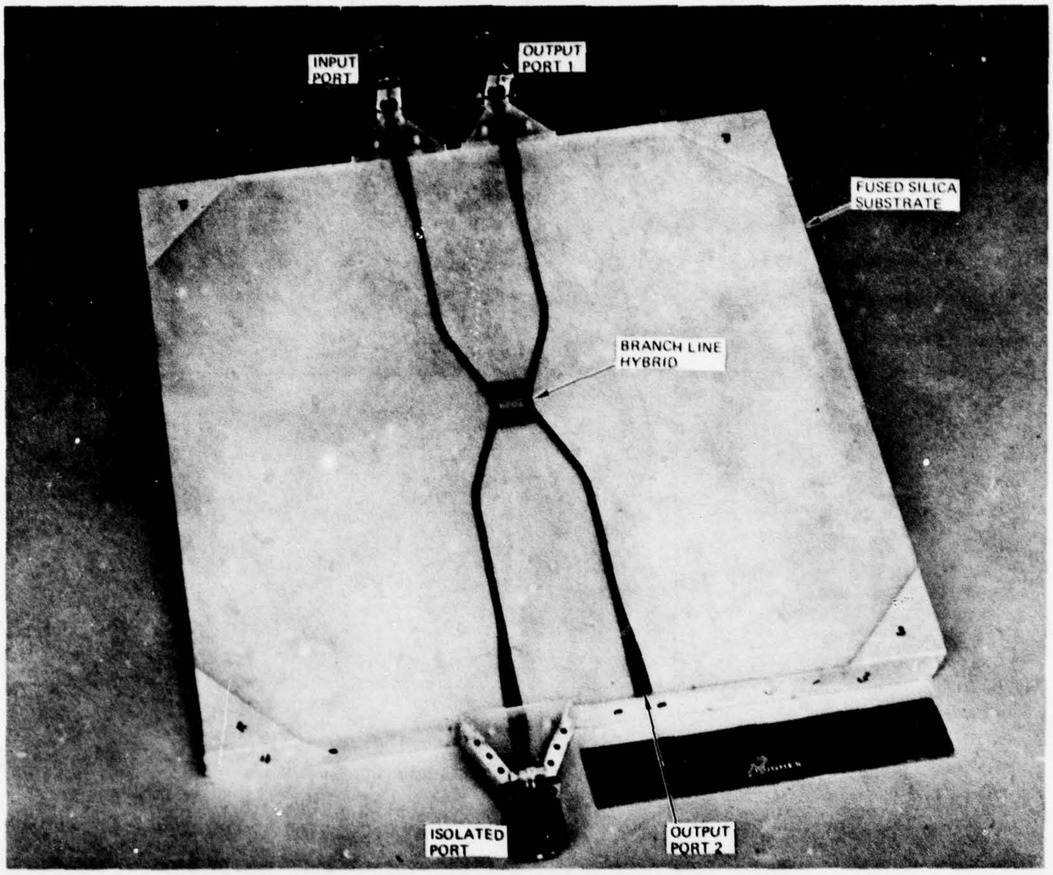
INPUT PORT
OUTPUT PORT 1
FUSED SILICA SUBSTRATE
BRANCH LINE HYBRID
ISOLATED PORT
OUTPUT PORT 2

Fig.5 Scaled hybrid

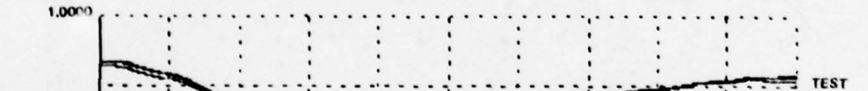

Fig.6 Overlay of resonance curves of four offset dipoles

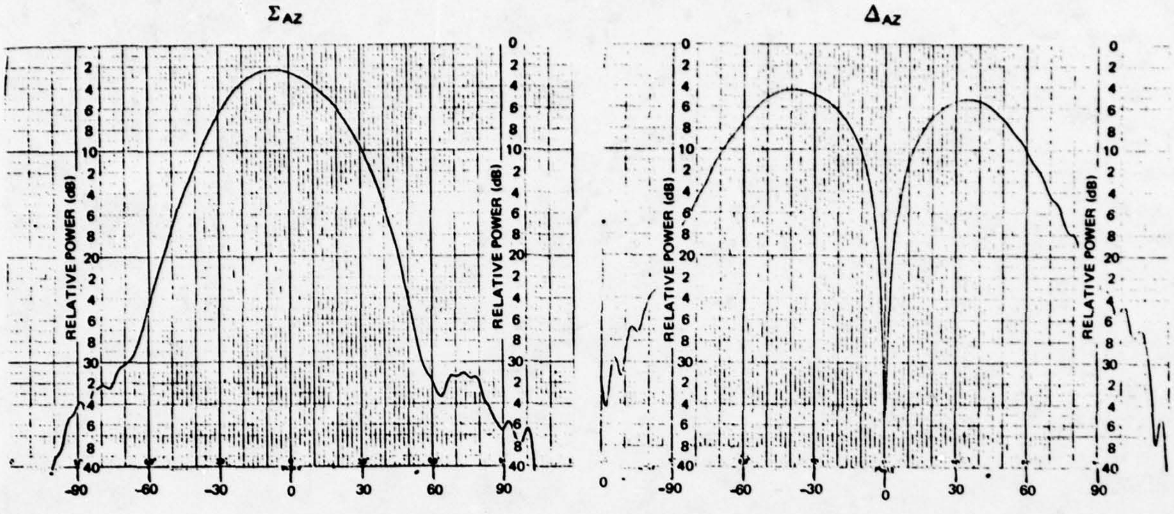

Fig.7 Sum and azimuth difference patterns at scaled frequency

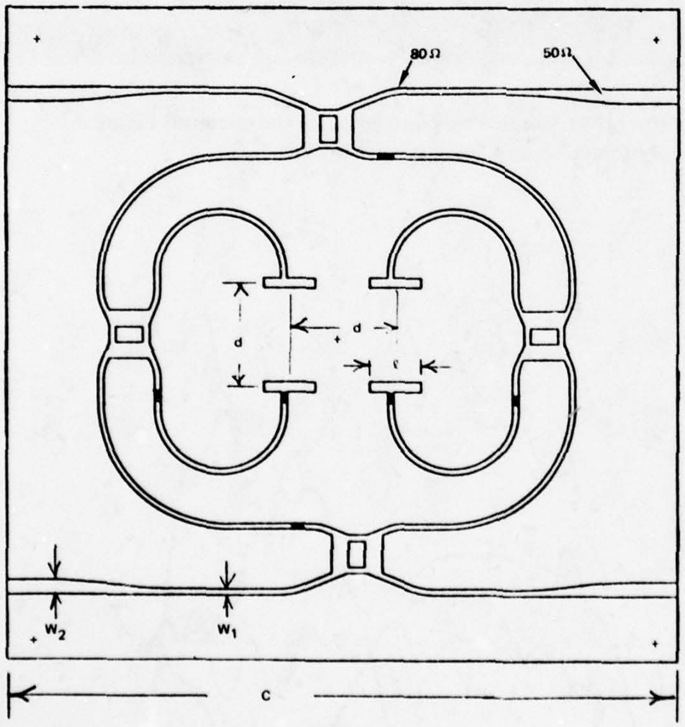

DIMENSIONS

DIMENSION	3.31 GHz	94.0 GHz
C	12.4	0.4366
D	1.96	0.0690
ℓ	0.951	0.0335
W1	0.110	0.0039
W2	0.266	0.0094
SUBSTRATE THICKNESS	0.125	0.0044
METAL THICKNESS	0.0017	0.00008

SUBSTRATE:	FUSED SILICA
DIEL CONST:	3.83

Fig.8 Comparitor layout and dimensions at 3.31 and 94 GHz

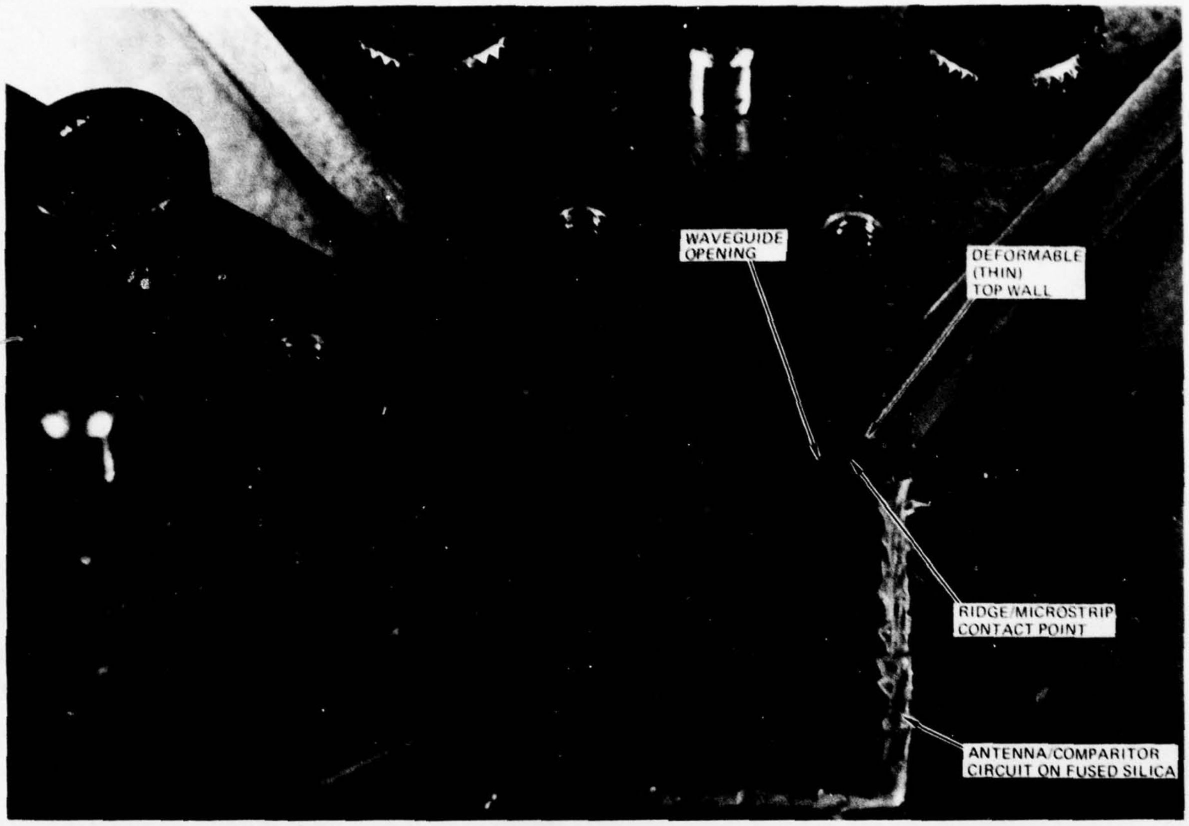
WAVEGUIDE OPENING
DEFORMABLE (THIN) TOP WALL
RIDGE/MICROSTRIP CONTACT POINT
ANTENNA/COMPARITOR CIRCUIT ON FUSED SILICA

Fig.9 Antenna feed/microwave comparitor MIC fabricated by photographing the circuit of Figure 9, photoreducing and photoetching on a fused silica substrate

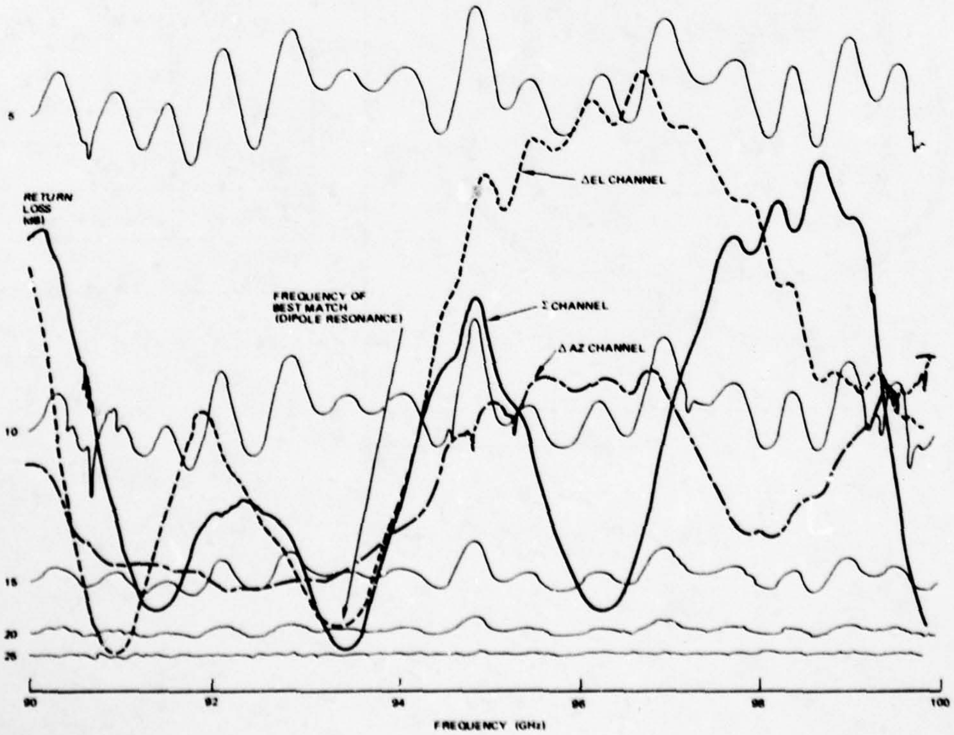

Fig.10 Measured return loss of the three major channels, sum and azimuth and elevation difference, of the 94 GHz antenna/Comparitor MIC

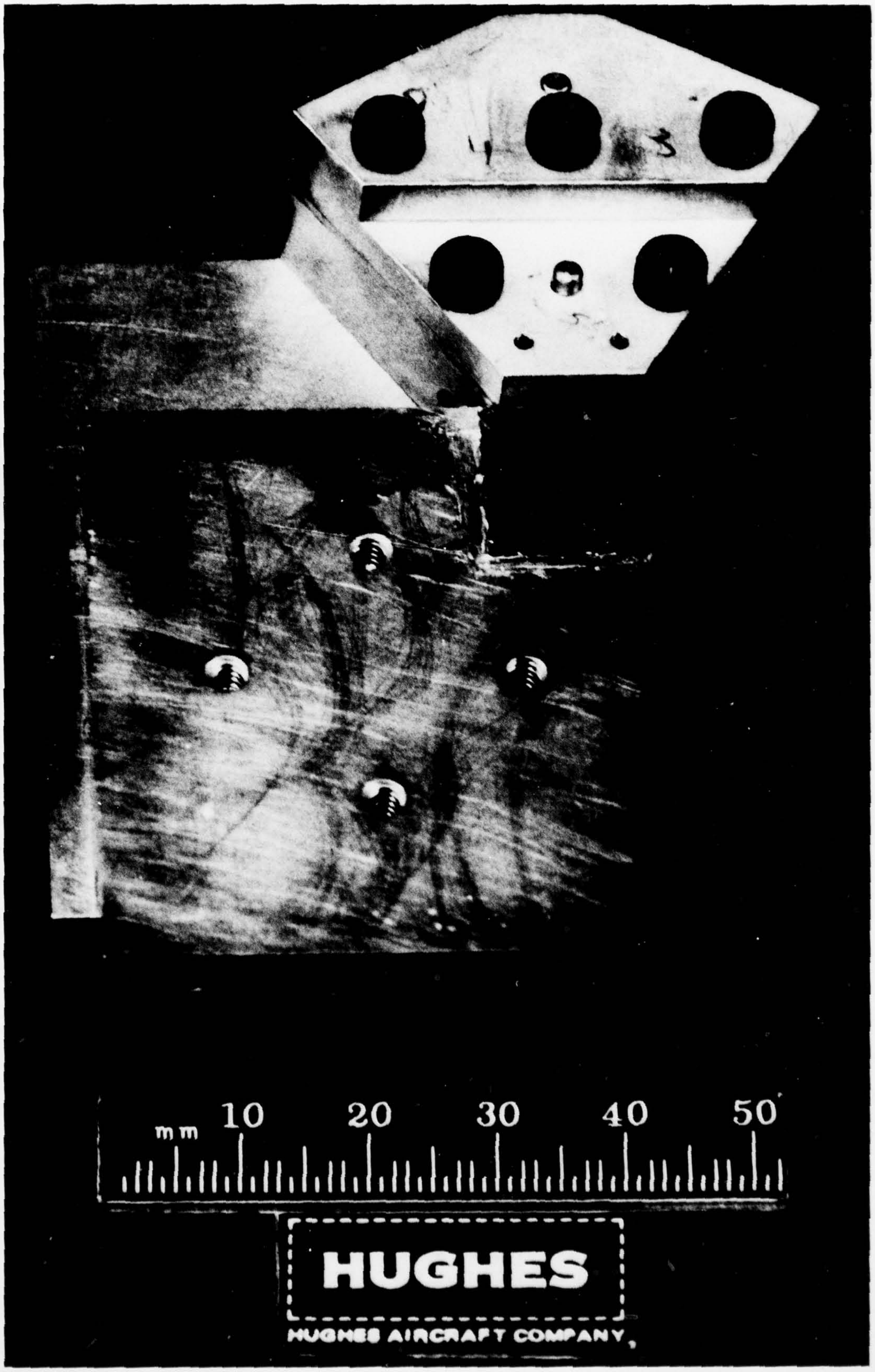
mm
10
20
30
40
50
HUGHES
HUGHES AIRCRAFT COMPANY

Fig.11 One of the three U-shaped microstrip lines differing in length used for determining microstrip loss factors at 94 GHz

HYBRID-OPEN MICROSTRIP MIC TECHNOLOGY AT MILLIMETER WAVELENGTHS

T.H. Oxley

GEC Hirst Research Centre
Wembley England

SUMMARY

The technological, fabrication and performance features of the hybrid-open microstrip MIC design approach are discussed when applied to the superheterodyne type of receiver in the frequency range of 26 to 90 GHz. Gold microstrip circuits formed by thin film techniques, broadband waveguide feeders, non-reciprocal devices formed by embedding the ferrite disk in the dielectric substrate, and improved rugged construction gallium arsenide beam lead diodes provide the basis for the design of mixers and receivers in this frequency range. Special packaging techniques to provide a rugged construction to meet the requirements of military environments are described. A balanced mixer designed for the frequency range of 65 to 85 GHz with an overall noise figure of about 10 dB (F_{if} = 1.5 dB) and an operation temperature range of at least -55°C to +85°C provides a good example of the techniques employed and is discussed in detail. Finally, the application of these features to provide rugged multi-circuit receivers operating at about 35 GHz is described. Such receivers combine several circuit functions on a single substrate including isocirculators, and provide an overall noise figure of about 8.0 dB.

1. INTRODUCTION

The increasing system interest at millimeter wavelengths is stimulating the need for compact-rugged receiver circuits based on the superheterodyne principle of operation, and many forms of transmission line are being explored by the circuit designer to meet these requirements.

It may be claimed that open-microstrip, air-spaced triplate, fin line, dielectric guide in the form of image and insular line, and conventional waveguide all have particular merits. However, the ultimate objective of the transmission medium must be to provide application and integration versatility. This implies the capability of active and passive circuit function integration, to enable many circuit functions to be combined in compact structures, by the use of technologies which realise the reliability and environmental aims of military type systems.

The open-microstrip transmission medium in conjunction with hybrid techniques has found wide acceptance for MIC applications up to at least 18 GHz, and the design and reliability aspects are now well proven for system requirements. The main advantages of the hybrid-microstrip design approach are : circuit fabrication by well known thin film techniques, easy inclusion of active devices due to the open configuration, and versatility provided by the capability to combine circuit functions of active and passive form. The main disadvantages may result from the radiation and low Q characteristics. In general therefore, it is a potentially easy fabrication - low cost circuit structure, provided that it is not overdesigned for a particular application. However, as with many microwave components, high costs can be involved when considering the packaging and test aspects, particularly for the small volume requirements of the specialised product.

It is the intention of this paper to indicate that, although the application of hybrid-microstrip techniques to millimeter wavelengths may involve specialised and high technology features, it is still a very competitive design approach up to at least 90 GHz for applications to mixer and associated receiver circuits.

2. OPEN MICROSTRIP

The open-microstrip line consists essentially of a strip conductor deposited on to a flat dielectric substate, the reverse side of which is metallized to provide a ground plane. Conventionally, high purity alumina is used as the substrate material up to about 20 GHz, but above this frequency the propagation characteristics of microstrip suggest that there is every advantage in reducing the relative permittivity of the substrate material together with reducing the substrate thickness. Briefly, this reduces problems associated with dispersion and over-moding, and the lower permittivity enlarges the circuit pattern. Quartz (silica) and some forms of plastic laminate substrates provide a more suitable permittivity than alumina (e.g. 2.5 to 4.0 compared with about 9.5). Quartz however has the advantage of a rigid material which can be machined to provide a smooth surface finish, is drillable and can be made thin enough for use up to 100 GHz. The most undesirable features of thin quartz however, is the potential handling fragility before being incorporated into the final product.

The preferred maximum microstrip structure dimensions for acceptable transmission propagation with the use of quartz are : 500 μm wide lines on 250 μm thick substrate for 50 ohm characteristic impedance in the frequency range 26 to 40 GHz; and 250 μm wide lines on 125 μm thick substrate for 50 ohm characteristic impedance in the frequency range 60 to 90 GHz. The resulting transmission line losses are about 0.25 dB and 0.5 dB per cm for the 26-40 GHz and 60-90 GHz frequency bands respectively; these are obviously undesirable from the point of view of long general purpose transmission feeders, but are considered acceptable for the short line lengths associated with compact circuit assemblies.

3. WAVEGUIDE FEEDER

The waveguide feeder to the microstrip line can be more problematical for millimeter-wave applications, in terms of design, construction and hermeticity compared with microwave frequencies where coaxial feeders are commonly used. The transition from waveguide may employ stepped or smooth taper ridge impedance transformers, or coupling probes.

The coupling probe design is usually based on the formation of a length of a microstrip line with the ground plane removed, which is inserted through an E-plane slot in a length of short-circuited waveguide.

The design is potentially simple and low cost, but has the disadvantage of limited bandwidth (about 5%), critical position tolerancing, additional substrate machining, and is difficult to seal against the ingress of moisture.

Similar broadband performance, covering the waveguide frequency band, may be achieved with smooth taper or four to six step ridge transition designs. For example vswr < 1.3:1 up to 50 GHz and < 1.5:1 up to 90 GHz, with an insertion loss of about 0.25 dB and 0.5 dB respectively.

The advantage of the stepped ridge structure is the provision of a more compact structure; the length of the tapered ridge requiring about three guide wavelengths compared with about one guide wavelength for the multi-step ridge. In addition, however, the broadband performance of the multi-step ridge transformer is unnecessary for many practical system applications, and the needs of extreme compact assemblies may be met by the design of narrower band types with reduced number of steps, such that they may be incorporated in the box wall of the final product. For example, a single step transition can provide a vswr of < 1.2:1 with an insertion loss of < 0.25 dB for a 10% bandwidth in the 26 to 40 GHz frequency range, and can be accommodated in a box wall thickness of about 5 mm.

4. ACTIVE DEVICES

The heart of the mixer circuit (or superheterodyne receiver) is the mixer diode, and Schottky barrier metal-semiconductor techniques are commonly used to produce the requisite rectifying junction. As the result of its high electron mobility and associated material technology, gallium arsenide is generally accepted as the best semiconductor material for application at millimeter wavelengths. Two main diode configurations are normally considered; the so-called multi-dot and the beam lead.

The multi-dot consists essentially of an array of rectifying junctions produced on a semiconductor chip, with a wire pressure contacting one of the junctions and the ohmic contact formed on the base or the side of the chip. The beam lead consists essentially of a semiconductor chip with two co-planar beams, one contacting the rectifying junction and the other providing the ohmic contact. Although each structure has particular merits, the beam lead provides a low-controlled inductance, and easy series mounting into open microstrip by thermo-compression bonding techniques, with the essential feature of a very rugged structure after incorporation into the circuit.

Gallium arsenide beam lead diodes, originally developed at the GEC Hirst Research Centre (OXLEY, T.H. and SWALLOW, G.H., 1970), are now available commercially from AEI Semiconductors Ltd., for operation up to about 40 GHz. Special low capacitance versions will also provide operation up to 100 GHz, as indicated in Table 1. The small junction areas of about 3 μm dia. can readily be produced in beam lead technology (as for the multi-dot structure), the difficult technology in the beam lead approach is minimising the overlay capacitance associated with the beam contacting the rectifying junction. This affects the performance adversely as it effectively shunts the junction capacitance and series resistance. The diode requirements are thus to minimise the series resistance, the junction capacitance and the stray capacitance, consistent with a reproducible rugged structure.

TABLE 1

Typical Characteristics of GaAs Schottky-barrier Beam Lead Diodes

Design Frequency		12 to 20 GHz	26 to 50 GHz	60 to 90 GHz
Contact diameter		8 μm	5 μm	3 μm
Total capacitance	C_T	0.1 pF	0.055 pF	0.045 pF
Junction capacitance	C_j	0.05 pF	0.025 pF	0.015 pF
Stray capacitance	C_S	0.05 pF	0.03 pF	0.03 pF
Series resistance	R_S	4 Ω	7 Ω	12 Ω
Series inductance	L_S	0.25 nH	0.25 nH	0.25 nH
Series resonant frequency	f_{res}	15 GHz	38 GHz	70 GHz
Cut-off frequency	f_{co}	∿800 GHz	∿1000 GHz	∿1000 GHz

A diode design for operation above 26 GHz is shown in figure 1. It can be seen that the stray capacitance resulting from the overlay area of junction contacting beam has been minimised by setting the junction close to the edge of the chip and contacting it by two 10 μm wide fingers. Although these devices function well and provide rugged structures once the diode is incorporated in the circuit, the small beam to chip attachment area can lead to poor mechanical strength during handling, particularly in the case of diodes aimed at the highest frequency operation. Further development, however, has now resulted in a mechanically stronger device with equivalent electrical parameters to the device designed for the 26 to 40 GHz range (Table 1). The key to this improvement is the incorporation of a thick dielectric layer of glass beneath the beam, thus enabling the contact area to be increased. This improved structure is shown in Figure 2. Briefly, a trough is chemically etched in the gallium arsenide which is then filled with a glass frit; windows are defined for the ohmic and rectifying contacts; the gold beams are defined and plated up; the devices are finally separated on the parent slice by chemical back etching. It is considered that ultimately this basic technology could realise devices for operation up to 300 GHz.

5. NON-RECIPROCAL DEVICES

Circulators and isolators form important features of microwave receivers to provide high levels of isolation together with maintaining good circuit vswr characteristics. In the interest of compactness there is every advantage in incorporating these devices with the other receiver circuit functions.

AD-A069 015 ADVISORY GROUP FOR AEROSPACE RESEARCH AND DEVELOPMENT--ETC F/G 17/2.1
MILLIMETER AND SUBMILLIMETER WAVE PROPAGATION AND CIRCUITS.(U)
FEB 79 E SPITZ, G CACHIER
UNCLASSIFIED AGARD-CP-245 NL

4 OF 6
AD
A069015

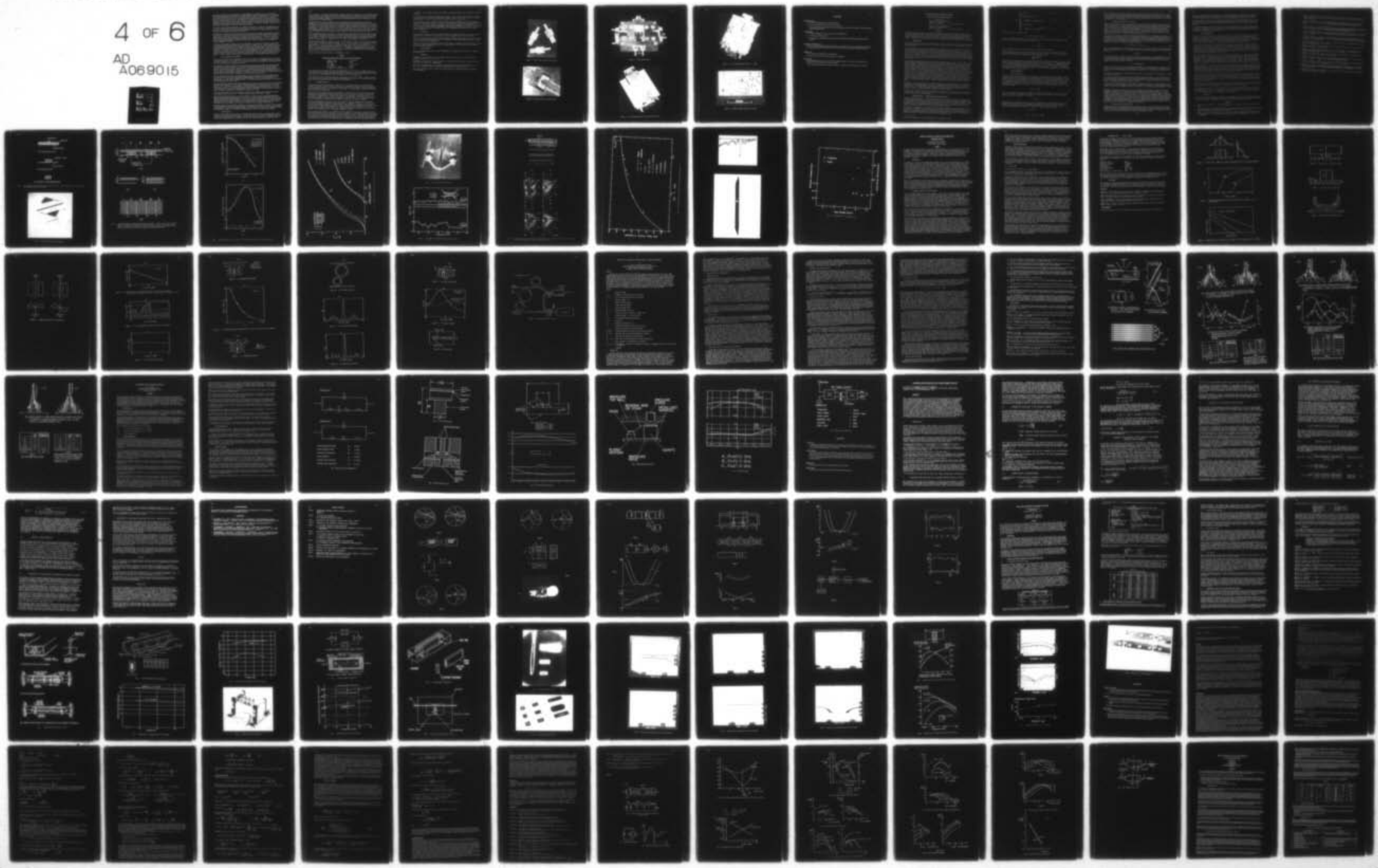

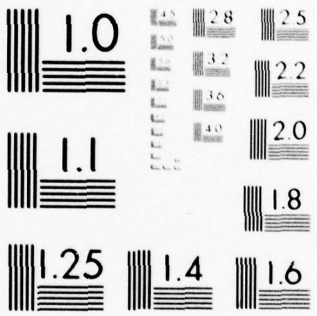
1.0
1.1
1.25
1.4
1.6
1.8
2.0
2.2
2.5
2.8
3.2
3.6
4.0
4.5
5.0
5.6

MICROCOPY RESOLUTION TEST CHART
NATIONAL BUREAU OF STANDARDS-1963-A

Techniques developed at microwave frequencies (BRIGGINSHAW, P.M. and RICHES, E.E., 1975) in which a ferrite disk is embedded in the dielectric substrate have been applied at frequencies up to 40 GHz, and are considered applicable up to 90 GHz. As already indicated quartz (silica) provides a rigid substrate which is drillable. Single crystal z-cut quartz provides a good thermal match to ferrite and this material is thus preferred to silica. The diameter of the ferrite disk is about 2 mm and the substrate thickness is about 250 μm at about 35 GHz. The circuit process involves high precision machining: the appropriate hole is drilled in the substrate which is oversize on thickness; the ferrite disk is attached in position with an epoxy adhesive, and the substrate is ground to the final thickness; the circuit is defined on the substrate by conventional thin film techniques.

A three-port circulator may be converted to a two-port non-reciprocal isolator by terminating the third port with a matched load, and this technique is applied to form an isocirculator; a matched load consisting of a 50 ohm thin film resistor is thermo-compression bonded across a gap between the circulator third port and a broadband short-circuit termination.

Satisfactory non-reciprocal characteristics at millimeter wavelengths require a high value of saturation magnetisation (4π Ms) for the ferrite material and the highest 4π Ms commercially available material is used, that is a nickel-zinc ferrite with 4π Ms about 0.5 T (5000 gauss). This value of 4π Ms is a limiting design factor for all millimeter wavelength non-reciprocal devices; 1.0 T and 2.0 T would be preferred for optimum bandwidth performance at 40 GHz and 75 GHz respectively. Due to its high energy product (BH_{max}) and thus weight and space advantage, samarium cobalt is preferred as the material to provide the magnetic field bias.

At frequencies above about 20 GHz, the effective impedance of the circulator Y junction is greater than 50 ohms and the matching transformers take a different form compared with the lower frequencies. The triangular geometry, shown for the isocirculator in figure 6, illustrates one form of matching transformer which has recently been developed. This employs full-wave linear matching tapers : the centre frequency of operation is related to the diameter of the junction triangle while the three areas of the triangle outside the circle form the on-ferrite part of the matching/coupling circuit. Isolation/return loss and insertion loss characteristics of > 20 dB and about 0.5 dB respectively are typically achieved for a 20% bandwidth at about 35 GHz. A broadband isolation characteristic of about 15 dB for an insertion loss of about 1.5 dB may be obtained by curving the triangular geometry to the edge-mode guided wave contour.

6. BASIC CONSTRUCTIONAL TECHNIQUES

Constructional techniques for the application of the circuit design are an important aspect of the final product for system use. These involve the inclusion in the circuit of active/passive devices and fitting the circuit substrate into a suitable box. The techniques evolved must be compatible with long-term high reliability under adverse environmental conditions.

Many techniques already established for MICs at microwave frequencies may be applied to millimeter-wave hybrid-microstrip integrated circuits. For example, although thermo-compression bonding is generally favoured, particularly for bonding connections to the gold thin film circuit when fitting beam lead diodes, thin film loads, tapes for transitions etc., conducting epoxy and solder techniques may still be used in particular circumstances. Non-reciprocal devices, as already mentioned in the previous section, are also based on lower frequency experience. Incorporation of the thin, potentially fragile quartz (silica) substrate into a base may however necessitate the use of specialised techniques.

There are mechanical and electrical disadvantages, which can be apparent in extreme environments, with structures produced by the more conventional assembly approach of clamping the quartz substrate into a milled dural box. The thermal expansions are widely different and there is the possibility of r.f. leakage under the ground plane at high frequencies. The following constructional methods can be applied to overcome these potential deficiencies.

One method provides a means of attaching the substrate to the base of the box by the use of a non-conductive adhesive (Patent Application, 1975). The evaporated ground plane is omitted from the substrate and the floor of the box provides this requirement. A suitable adhesive is a cyanocrylate glue. The relative permittivity is about 3.3 and the small associated changes in impedance and phase velocity, for a thin layer of about 10 μm thick, can be compensated for in the circuit design, if found necessary. Temperature tests show adequate strength over the temperature range -100 to +125°C.

A further method adopts the use of a controlled conducting epoxy adhesive layer between the substrate ground plane and the floor of the box. Thermal shock tests again show adequate strength.

Both construction approaches allow the circuit inclusion of active devices etc by thermo-compression bonding techniques after incorporation of the substrate, and result in very rugged assemblies capable of meeting severe military type environments. It has not been found necessary to reduce the thermal mismatch between the quartz and the dural box by the use of lower expansion materials, such as titanium or nickel-iron alloys, either as substrate carriers or as the box material. These materials would in any case be undesirable as the box material in the interest of weight, corrosion, magnetic properties etc.

Hermeticity may also be an important requirement of some system applications. The use of sealing techniques already established for MICs to provide hermetically sealed units at the lower frequencies are in general also applicable to millimeter wavelength packages. The main additional feature is the requirement to seal the waveguide apertures; this may readily be accomplished by the use of suitable glass windows.

7. MIXER CIRCUITS

There are two main forms of mixer circuit, the single-ended and the balanced. The single-ended consists essentially of a single diode using one port for both local oscillator and signal frequencies, which are combined by circuitry external to the mixer : this provides simplicity and wide r.f. bandwidth capability but has the disadvantage of loss of signal power due to the circuit required to couple in the local oscillator power. The balanced mixer normally consists of two diodes (effectively two single-ended mixers), fed by a four port 3 dB coupler : this provides the characteristics of cancellation of a.m. noise generated by the local oscillator, isolation of the local oscillator from the antenna and the possibility of lower local oscillator power requirement, but the overall performance does depend on the characteristics of the coupler as well as the mixer diodes.

The balanced mixer is the more acceptable version and exhibits the greater application versatility. Integration of the coupler and diode circuits is obviously desirable to provide the mixer circuit in compact form, and, as at microwave frequencies, the hybrid-microstrip design approach provides the versatility for this aim. Both the 'branch arm' and the 'rat race' coupler configuration are applicable to millimeter-wave design : the 'branch arm' is basically a 90° coupler compared with 180° for the 'rat race', but it can be converted to 180° by the addition of a $\lambda/4$ length of line on one of the two output arms. The 'branch arm', although slightly inferior to the 'rat race' on bandwidth performance, has a circuit layout advantage as the two coupled arms, being adjacent, provide a common i.f. output in the plane of the circuit.

These design approaches have been applied to millimeter-wave balanced mixers covering the frequency range of 26 to 90 GHz, and commercial products are available from AEI Semiconductors Ltd in the frequency range 26 to 40 GHz. In general the circuits are produced on 250 μm thick substrates using the GaAs beam lead diodes of Table 1. Typically these provide a S.S.B. (image matched) overall noise figure performance of about 8.0 dB including an i.f. contribution of 1.5 dB, for an r.f. bandwidth of about 10%.

A balanced mixer designed for a frequency of about 75 GHz is shown in figure 3. The overall size is about 48 × 48 × 20 mm including the waveguide flanges; the r.f. ports are in WG26; the i.f. output is designed for the range 1 to 1.5 GHz and is via a 3 mm SMA connector; two solder pins are provided for the application of d.c. bias and to monitor the diode rectified current. The circuit is produced on a 125 μm thick, 10 × 10 mm, quartz substrate, and consists of a 3 dB coupler in branch arm 180° form. The mixer diodes are GaAs beam lead devices indicated in Table 1. Appropriate isolating capacitors and chokes for the 1 to 1.5 GHz r.f. are incorporated in the unit. The construction techniques employ the non-conductive adhesive method; broadband transitions are employed.

The typical performance characteristics are summarised in Table 2.

TABLE 2

Typical Performance Characteristics of 75 GHz Balanced Mixer

Frequency range	65 to 85 GHz
Conversion loss	8.5 dB
Input vswr	2.0:1
I.F. range	1 to 1.5 GHz
I.F. impedance	50 ohms
Isolation (l.o. to signal)	20 dB
L.O. power (0.5 v fwd d.c. bias)	10 mW

The conversion loss is obtained from direct power measurement at the r.f. and i.f. terminals, thus the S.S.B. (image matched) overall noise figure performance including a 1.5 dB i.f. contribution may be expected to be about 10 dB. Actual measurement using the hot and cold load technique, has indicated a S.S.B. noise figure of about 12 dB including a 1.25 GHz i.f. amplifier with a 3 dB contribution.

The storage and potential operating temperatures are rated as at least -55°C to +85°C. However, the waveguide apertures are not sealed so the low operating temperature is restricted to 0°C unless precautions are taken to avoid condensation forming on the surface of the substrate.

8. INTEGRATED RECEIVERS

The design aim to derive the benefits of integration is to incorporate as many circuit functions as is feasible in as small a volume as possible. The concept is illustrated by figure 3, which clearly shows that the limiting size factor for the millimeter-wave single circuit function unit can be the package, and thus the greater the number of circuits which can be provided in a single package, the greater the volume, weight and reliability advantages.

MIC techniques can be adopted at millimeter wavelengths to combine several circuit functions in a single package by the use of separate substrates, either butt joined or screened by inclusion in separate box compartments. Experience at the lower frequencies however has shown that such techniques are not in the best interest of compactness or reliability, and there is every advantage in producing as many circuit functions as possible on a single substrate (LANCASTER, M. and OXLEY, T.H., 1975). This is the aim which has also been adopted for hybrid-microstrip integration techniques at millimeter wavelengths.

An additional consideration, which must not be overlooked for an overall integrated receiver package is that of the associated low frequency circuits, such as the i.f. amplifier, monitors etc. There are for instance several benefits derived from incorporating the first stages of i.f. amplification arising from the electrical interfacing between the mixer and the i.f. amplifier and the elimination of connectors. Thus the realisation of compact, high reliability i.f. amplifiers can also form an important feature of the overall receiver package, and thick film circuit techniques in place of conventional p.c.b.'s can play an important role in this concept for the MHz range intermediate frequency.

Figure 4 shows the next stage of r.f. integration from the single circuit functions. Two balanced mixers are combined with signals fed in phase and l.o. power in quadrature to provide image suppression characteristics at about 35 GHz. The quartz substrate is 250 μm thick and 25 mm square. The output from the two mixers is 90° out of phase and thus a further 90° phase shift is required at i.f.. The thick film i.f. stages are shown in figure 5. To minimise noise figure, the 90° i.f. phase shift is provided after amplification and two balanced head amplifiers (one following each mixer) are incorporated, with the output combined by the

3 dB hybrid. The i.f. stages provide a good example of the high packaging density achieved by thick film techniques.

The overall size of the particular package shown is about 70 × 40 × 20 mm, but the unit does not include all the design features discussed to minimise the volume. An overall noise figure of about 9.0 dB and image suppressions > 20 dB is obtained for an 8% bandwidth centred at about 35 GHz.

The more complex receiver could include non-reciprocal circuits. An example of the single substrate technology is illustrated in figure 6. The size of the 250 μm thick z-cut single crystal quartz substrate is about 35 × 20 mm. This type of circuit may be fabricated and packaged by the techniques already discussed, to form compact, rugged, lightweight, high reliability, hermetically sealed structures, suitable for a wide range of applications and environments. The technology can provide a receiver S.S.B. noise figure performance of about 8.0 dB at about 35 GHz, with a degradation of less than 1.0 dB at high elevated temperatures.

9. CONCLUSIONS

The application of hybrid-open microstrip MIC techniques to millimeter wavelengths can provide compact, rugged and high reliability circuit structures for receiver applications up to at least 90 GHz.

Mixer circuits of this type can either provide individual components with competitive performance to more conventional waveguide techniques, but with the advantage of the MIC compact-rugged structure or they can form the basis for further integration.

Complex receivers may be produced which derive the full benefit of integration by combining several circuit functions, including non-reciprocal devices, on a single substrate. Such receivers may be packaged to meet military type environments.

10. ACKNOWLEDGEMENT

Part of this work has been carried out with the support of Procurement Executive, Ministry of Defence, sponsored by DCVD.

11. REFERENCES

BRIGGINSHAW, P.M. and RICHES, E.E.: "Development of MIC circulators from 1 to 40 GHz", IEEE Trans. on Magnetics, MAG-11, No. 5, pp. 1273-5.

LANCASTER, M. and OXLEY, T.H.: 1975, "Production of a high reliability J(Ku)-band transmit-receive unit using hybrid MIC technology", INTERNEPCON UK.

OXLEY, T.H. and SWALLOW, G.H.: 1970, "Beam lead mixer and detector diodes for MIC applications", 8th Int. Conf. on Microwave and Optical Generation and Amplification (MOGA), Amsterdam.

Patent Application No: 41624/75, October 1975, "Improvements in or relating to microwave integrated circuit assemblies".

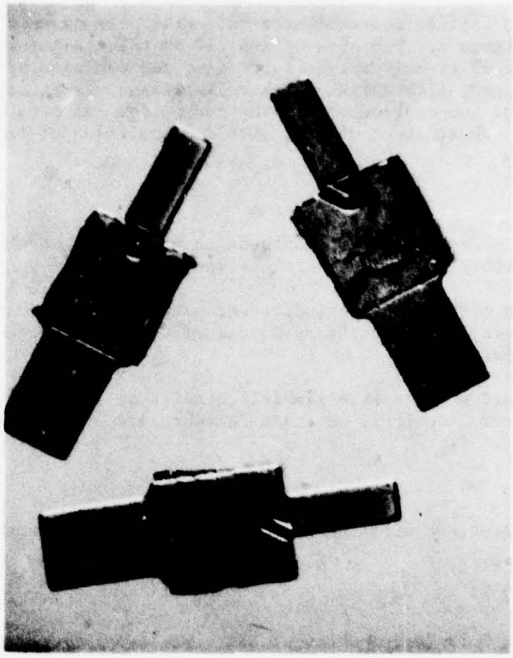

Figure 1. Earlier beam lead diode configuration.

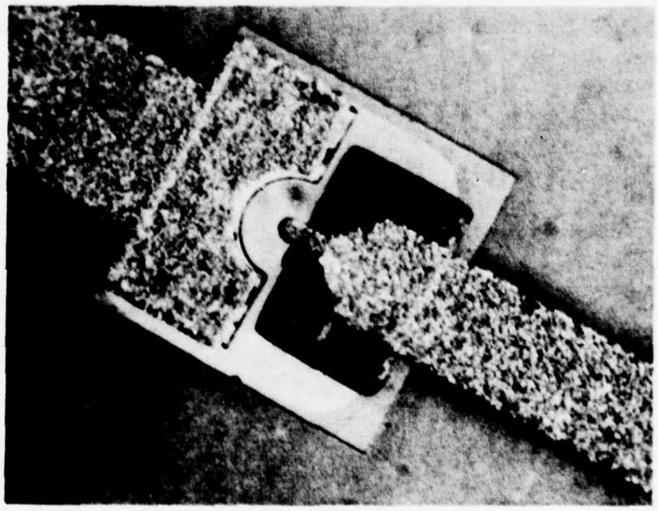

Figure 2. Improved structure beam lead diode.

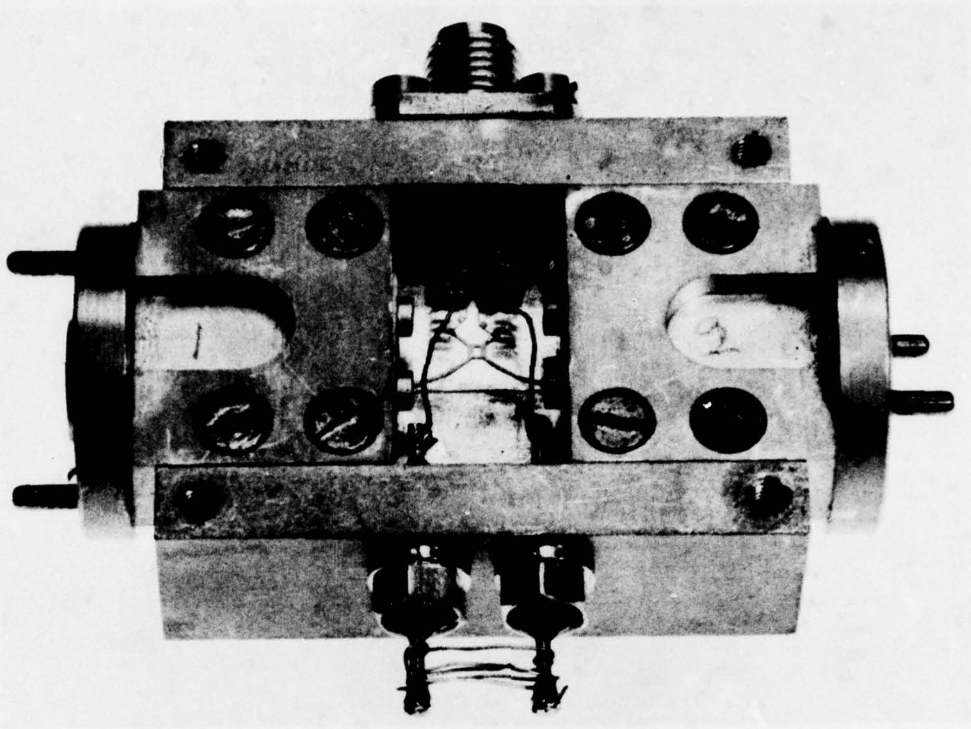

Figure 3. 75 GHz balanced mixer.

Figure 4. 35 GHz image suppression mixer microstrip circuit.

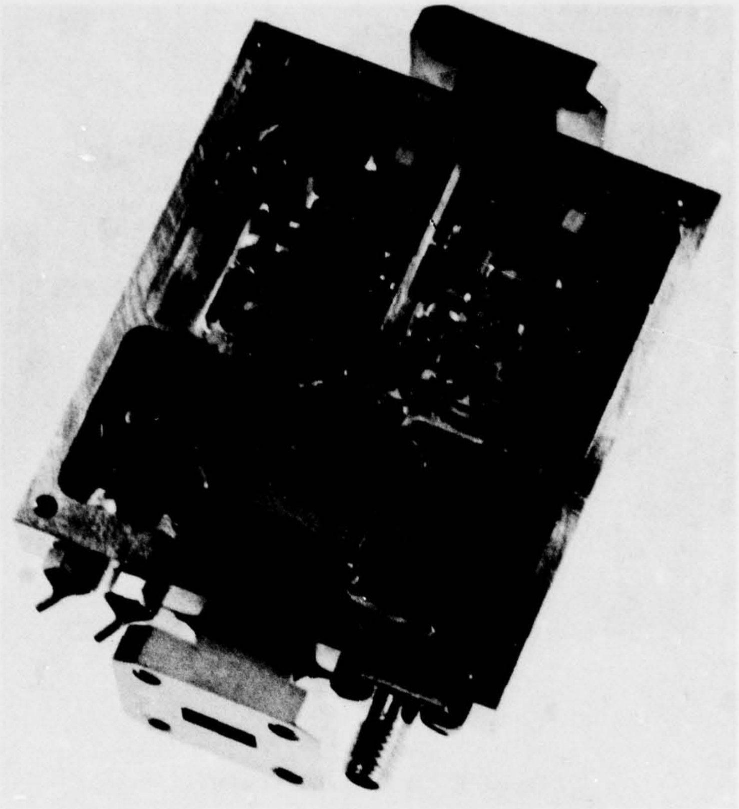

Figure 5. 35 GHz image suppression mixer i.f. stages.

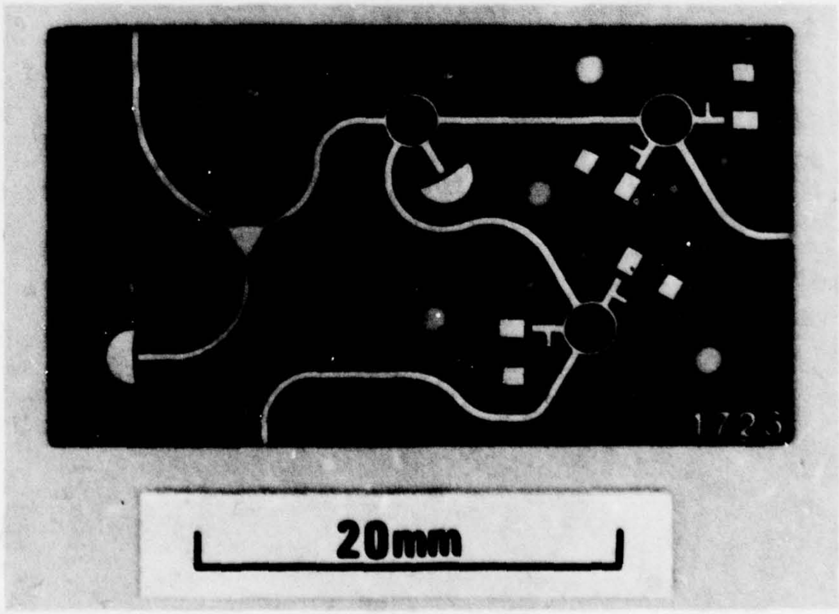

Figure 6. Example of single substrate technology.

DISCUSSION

J.R.Mahieu, France

(1) What is the highest frequency you made circulator?

(2) What are the insertion losses of your 40 GHz circulator?

(3) Can you make some comments about the DC field magnetic circuitry for the circulator? (The DC field being large and junction small.)

Author's Reply

(1) 40 GHz, although this is not considered to be the frequency limit.

(2) 0.5 dB for the substrate circuit.

(3) the circulators are magnetically biased by open-circuit Samarium Cobalt magnet positioned beneath the substrate.

Comment by H.G.Oltman, USA

It has been our observation that coupling between lines on a microstrip circuit are no problem as long as the lines are not parallel for appreciable lengths. If the lines are curving there is no appreciable coupling between lines.

W.Hauth, FRG

Did you measure the coupling between adjacent lines?

(Lines are close to each other due to the high degree of integration.)

Author's Reply

About 30 dB isolation between circuit functions is generally experienced. Coupling is not considered to be a problem when the line-gaps are in excess of a line width.

Comment from another listener (from Hughes Company): coupling is only significant between curved lines.

QUASI-PLANAR DIELECTRIC WAVEGUIDE APPROACH FOR MILLIMETER-WAVE INTEGRATED CIRCUITS

Tatsuo Itoh
Dept. of Electrical Engineering
University of Kentucky
Lexington, KY 40506, USA (Until June 30, 1978)

Dept. of Electrical Engineering
University of Texas at Austin
Austin, TX 78712, USA (After July 1, 1978)

ABSTRACT

This paper describes a number of quasi-planar techniques for millimeter-wave integrated circuits which become increasingly more attractive at higher frequencies. Many of these techniques resemble those used in optical integrated circuits. Operating principles of the quasi-planar waveguides employed in the present techniques are first described. Some passive components made of these waveguides are then presented. Current efforts toward developing novel active components and associated problems are discussed.

1. INTRODUCTION

This paper describes a new approach to millimeter-wave integrated circuits. The first half reviews some works reported previously and the latter half discusses current development and some problems associated with the technique.

There are two types of approaches in millimeter-wave integrated circuits. One of them is based on so-called printed-line structures such as microstrips, suspended striplines and fin-lines.[5,11,16] They are essentially extensions of well-established microwave integrated circuit (MIC) technology. Another type is, in principle, a millimeter-wave replica of optical integrated circuits. The basic building block of this type is a dielectric waveguide. A number of components and subsystems have been developed by several workers.[7,9,10] In these works, however, they used either rectangular dielectric waveguide, image guide or their variants (see Fig. 1). Unlike in integrated optics where the dielectric constants in the waveguide and the surrounding media are only slightly different, high permittivity materials are used in millimeter-wave schemes.

The quasi-planar waveguides described in this paper, although belonging to the second type, differ both in structures and operating principle from conventional rectangular and image guides. One of these quasi-planar waveguides, called the inverted strip (IS) dielectric waveguide, consists of dielectric strip(s) sandwiched between a ground plane and a guiding dielectric layer. Since the layered medium has a dielectric constant larger than that of the strip medium, most of the energy propagates in that portion of the layer immediately above the strip. Hence, the conductor loss is minimized and yet the ground plane can be conveniently used, when necessary, as a heat sink and dc bias return of solid-state devices implemented in the IC. A typical IS waveguide made for 60-90 GHz operation is shown in Fig. 2. The guiding layer is a fused silica with dielectric constant 3.75 and the strip is made of teflon whose dielectric constant is 2.1. A number of advantages and characteristics have been reported on the IS guide.[2] Two of them are noted here, low radiation loss and ease of adjustment. They are mainly caused by the quasi-planar structure of the waveguide. As the major portion of the energy propagates in the layered region, the wall irregularity of the strip causes less radiation loss than that in conventional dielectric waveguide with a similar dielectric constant. However, radiation at the bend in the IS guide is stronger than in the conventional guide because the field is "weakly" guided, unless some special provision is made.

In prototype component development, the IS guide is attractive because adjustment of, say, coupling between guides or a guide and a device can be done by changing the location of the strip. At higher frequencies, such as at submillimeter spectrum, the quasi-planar nature of the IS guide may reduce the fabrication cost if an appropriate planar technology is adapted. Conventional mechanical process may no longer be available or may be prohibitively expensive at such frequencies.

In what follows, we first briefly review the operating principle of the IS guide followed by description of some passive components. More recent development and proposed novel devices will then be discussed, and some problems to be attacked summarized.

2. GUIDED WAVES IN THE INVERTED STRIP DIELECTRIC WAVEGUIDE

Since the detailed analysis of the IS guide has been reported previously,[2] only the key steps necessary for understanding will be listed. Figure 3(a) shows the cross section of the coupled IS waveguide. When the separation of two strips becomes infinite, we can recover the uncoupled (isolated) IS guide. Although an exact analysis of the present structure is extremely difficult, very accurate solutions have been obtained by the use of the effective dielectric constant (EDC) method. This method is the first step of transverse resonance approach[12] which is exact when carried out correctly.

To this end, we subdivide the cross section in Fig. 3(a) into five regions. The EDC of regions I, III and V and that of regions II and IV may be obtained from the surface wave solutions of Figs. 3(b) and (c), respectively. For instance, the EDC of regions II and IV may be obtained in the following manner. Assuming the sinusoidal field variation in the layer with highest dielectric constant ε_2 and decaying field expressions outside this layer, we can derive the field distributions from

---

This work was supported by U.S. Army Research Office Grant DAAG29-77-G-0220.

$$\phi(y) = \begin{cases} \cosh \eta_1 y & 0 < y < h \\ \cosh \eta_1 h \cos [k_y(y - h)] & \\ \quad + \dfrac{\eta_1 \varepsilon_2}{k_y \varepsilon_1} \sinh \eta_1 h \sin[k_y(y - h)] & h < y < h + d \\ [\cosh \eta_1 h \cos k_y d & \\ \quad + \dfrac{\eta_1 \varepsilon_2}{k_y \varepsilon_1} \sinh \eta_1 h \sin k_y d] e^{-\eta_3(y-h-d)} & y > h + d \end{cases} \tag{1}$$

where η_1, k_y and η_3 are related via

$$k_o^2 + \eta_3^2 = \varepsilon_2 k_o^2 - k_y^2 = \varepsilon_1 k_o^2 + \eta_1^2 \tag{2}$$

When all the boundary conditions at dielectric interfaces are imposed, we obtain an eigenvalue equation for k_y. Now, the EDC of this structure is defined by

$$\varepsilon_{eII} = \varepsilon_2 - \frac{k_y^2}{k_o^2} \tag{3}$$

The corresponding quantity ε_{eI} for regions I, III and V may be similarly derived.

Now the original structure in Fig. 3(a) is modeled by the one in Fig. 3(d). Once again an eigenvalue equation for this hypothetical structure is derived. When such is solved for the field variable k_x in the x direction, we obtain the propagation constant of the IS waveguide

$$\beta = \sqrt{\varepsilon_{eII} k_o^2 - k_x^2} \tag{4}$$

The accuracy of the EDC method has been checked by comparing the computed and measured field distributions.[2] Typical field distributions in the transverse directions are plotted in Fig. 4. The measurement was done at 81.7 GHz and the agreement with theoretical prediction is seen to be quite good. Dispersion characteristics for the two lowest order modes are provided in Fig. 5 for an IS guide with typical dimensions. The curves for uncoupled guide have been computed by letting the separation s be infinity. These dispersion curves will be the basis for designing a number of passive and active components, some of which will be described in the following sections.

3. PASSIVE COMPONENTS

3.1 Directional Couplers

From the knowledge of field distributions and propagation constants in the IS guide, a number of passive components can be developed. Examples are 3 dB directional couplers and 20 dB cross couplers.[15] Fig. 6 shows a typical 3 dB coupler designed for 75-80 GHz operation. Fig. 7 shows computed and measured results for the coupler. In the so-called coupling section with length ℓ as shown in the inset of Fig. 7, the even and odd modes interact with each other. Hence, this type of coupler is often called distributed coupling type. The analysis and design can be done based on the coupled mode analysis as long as the coupling per unit length is not too strong. From this analysis, the ratio of the power outputs at terminals 2 and 3 becomes

$$\frac{P_3}{P_2} = \tan^2 \left(\frac{\pi \ell}{2L}\right) \tag{5}$$

when all the terminals 1 through 4 are terminated with loads with negligible reflections. The quantity L in (5) is called the total coupling length and is the length needed to completely transfer energy incident at terminal 1 to terminal 3. L is given by

$$L = \frac{\pi}{\beta_e - \beta_o} \tag{6}$$

where β_e and β_o are propagation constants of even and odd modes such as those presented in Fig. 5. The foregoing analysis is valid only if no coupling exists between four connecting guides. However, in practice this coupling may not be trivial and hence must be included in a more accurate analysis. This effect can be incorporated if we replace ℓ in (5) with an effective length $\bar{\ell}$ defined by

$$\bar{\ell} = \ell + \frac{\Delta\phi}{\pi} L \tag{7}$$

$$\Delta\phi = 2 \int_{z_o}^{z'} [\beta_e(z) - \beta_o(z)]dz \tag{8}$$

where the integration is carried out along the axial (z) direction of the directional coupler. z_o corresponds to the junction between the coupler and the connection arm, whereas z' is chosen to be some value of z beyond which the coupling between arms is negligible. The factor of 2 occurs because of the symmetry of the coupler. As shown in Fig. 7, agreement between computed and measured data is better if the effective length $\bar{\ell}$ is used in computation.

3.2 Integrated Scannable Planar Antennas

In many millimeter-wave systems, antennas and RF front ends are designed separately and the overall performance is considered only in the system design phase. However, as the operating frequency gets higher, such a "luxury" may not be allowed and more efficient antennas need to be integrated in the close vicinity of the RF front end. In the printed-type millimeter-wave IC's, the logical choice may be microstrip antennas for such purposes. However, microstrip antennas are usually of low gain, unstable and narrow-banded. A leaky-wave antenna described in this section, on the other hand, is quite attractive to integrate with RF front ends of the quasi-planar dielectric IC's. In addition to being of high gain, the antenna presented below has a scannable radiation characteristic.

Fig. 8 shows the side and top views of the leaky-wave antenna made in the IS waveguide. This structure is essentially a millimeter-wave replica of the grating beam coupler used in optical integrated circuits. In the dielectric strip, periodical grooves are created which modulate the propagation characteristics of the IS guide periodically, resulting in a grating mechanism. It is well-known that the field associated with a grating in a dielectric waveguide can be expressed in terms of infinitely many space harmonics. The propagation constant of the p-th space harmonic is given by

$$\beta_p = \beta_o + \frac{2p\pi}{\ell} \ , \quad p = 0, \pm 1, \pm 2, \ldots \tag{9}$$

where β_o is closely related to the propagation constant of the IS waveguide without perturbation (gratings), and ℓ is the grating period. If the propagation constant of one of space harmonics is in the radiation region, viz,

$$|\beta_p/k_o| < 1 \tag{10}$$

then the grating section supports a leaky-wave and all β_p become complex. Their imaginary parts account for the energy loss due to leakage (radiation) as the wave propagates along the grating section. Now the grating section becomes a leaky-wave antenna. The direction of main beam measured from the broadside (normal to the IS guide surface) is given by[10]

$$\theta_p = \sin^{-1}[\mathrm{Re}\beta_p/k_o] \tag{11}$$

One way to scan the beam is to change the operating frequency. This is because β_p is a function of frequency. This frequency scanning is demonstrated in Fig. 9 which shows both measured and computed radiation patterns from the grating leaky-wave antenna at 15 and 17 GHz.[3] The main beam is steered from -27° to -10°.

This antenna may be useful for airborne application because it is conformable and no metal part is exposed to external environment.

It is often required to scan the beam without changing the operating frequency. Such requirement can be satisfied if an electronic phase shifter is directly incorporated in the grating section of the IS guide. Such a device changes the dielectric constant of the medium, thus causing the propagation constant β_p to shift. Accordingly, the beam direction θ_p is altered.

A study has been made which simulates such a phase shift mechanism by means of a small mechanical motion.[4] An additional layer with thickness t and dielectric constant ε_4 is placed on top of the guiding layer (ε_2) in Fig. 8. This layer is maintained parallel to the surface of the guiding layer and separated by air gap δ.

Depending on the value of the air gap δ, the field distribution in the IS guide changes and hence the propagation constant β_p in the grating section also changes, causing the beam direction θ_p to change. Therefore, the change in δ is equivalent to varying the dielectric constant in the IS guide. Fig. 10 shows the main beam direction versus the gap size δ. It is seen that a considerable amount of scanning is possible by modest change in δ. This study is useful in its own right as a mechanism to adjust the beam direction or even to scan the beam if the speed is not of primary concern. However, more importantly, the findings obtained in the simulation study can be used to estimate how much change in dielectric constant is needed for a given amount of scan angle. Thereby, the requirement to the electronic phase shifter is established. Before concluding this section, it is noted that the experiments have been done in the Ku-band, mainly due to availability of the measurement equipments.

3.3 Band-Reject and Bandpass Filters

Another application of grating structures is the band-reject filter. It is well-known when the grating period ℓ in Fig. 8 is made sufficiently small so that none of space harmonics is in the radiation region, the grating section of the IS guide suyports only the surface waves.[1] Under such circumstances, wave interaction in the grating section creates a stopband at frequencies for which

$$\beta\ell = \pi \tag{12}$$

holds. The center frequency, band width and Q of the stopband depend on the grating profile, and may be calculated by using a coupled mode analysis. A typical swept frequency response from such a grating section is shown in Fig. 11. A strong reflection at the stopband around 15.5 GHz is clearly seen.[11]

When an electronic phase shifter or its mechanical simulation by means of an additional dielectric layer is incorporated as in 3.2, the center frequency of the band-reject filter may be altered. Also, a bandpass filter may be fabricated by combining a 3-dB hybrid reported in 3.1 with two grating band-reject filters.

The stopband phenomenon is often referred to as the Bragg scattering in optics. In optical integrated circuit, such phenomena are used for realizing distributed feedback (DFB) and distributed Bragg reflector (DBR) lasers. In the next section, we will propose a novel active component resembling a DBR laser and some initial investigation will be reported.

4. ACTIVE COMPONENTS

In conventional dielectric waveguide technique, an oscillator is created by either a Gunn or IMPATT diode mounted in a dielectric cavity. The latter is usually a finite section of the rectangular or image guide.[15] The end surfaces of the cavity provide reflection which leads to an oscillation. Since such reflection is of Fresnel type, it is desirable that the dielectric constant of the cavity is high. In the present IS waveguide, the dielectric constants involved are relatively small, and the finite section of the IS guide is not appropriate as a cavity because the end reflection is rather small.

In the previous section, however, we established that a grating section provides a strong reflection at frequencies in the stopband. This suggests that such a grating may be used as a frequency-selective reflector. Hence, when two grating sections are created in the IS guide with some distance apart and a diode is placed at the center, an oscillator may be realized. As this is a millimeter-wave counterpart of the DBR laser, it may be called DBR solid-state oscillator. The major difference between the DBR oscillator in millimeter-waves and DBR laser is that the gain is provided by a discrete device in the former whereas it is given by a distributed active region.

This oscillator may potentially be useful for increasing the output power by multiple diode implementation without degrading the coherence. When a number of diodes are implemented in a conventional cavity in order to increase the output power, the separation of diodes cannot be made too small due to heat consideration. Then the cavity becomes longer, and the oscillator may oscillate at more than one longitudinal mode. In the cavity with grating reflectors, it is possible to obtain a single mode oscillation in which only one longitudinal mode is selected by designing the center frequency of the stopband of the gratings to coincide with this mode, and making Q's of the resonator at all other modes sufficiently low.

To date, development of the proposed DBR Gunn or IMPATT oscillator was not successful. Some initial investigations, however, have been done by fabricating an oscillator made of an image guide on which grating reflectors (DBR's) are created. Figure 12 shows such an oscillator.[6] A Gunn diode is implemented in the cylindrical hole and grating reflectors are created on both sides of the diode. The tapers at both ends of the cavity prevent unwanted reflection there. Some results on oscillation characteristics are shown in Fig. 13. Relatively stable oscillation frequencies have been reported.[6]

The reason why we were unable to develop a DBR oscillator in the IS guide may be conjectured that the diode cannot couple the RF energy into the IS guide efficiently. The diode could emit the radiation in all directions and since the IS guide is a weakly guiding structure, most of the energy is radiated. The IS guide can guide the RF energy well if it is injected along the guide axis. On the other hand, the image guide uses a high permittivity material and hence a large portion of the energy emitted by the diode may be captured inside the guide.

Recently, new propagation phenomena in the IS guide have been investigated.[13] It is reported that the IS guide can sometimes support leaky-waves that radiate energy in the sideward direction. If this situation is encountered, the structure becomes quite lossy and no oscillator can be created.

One approach, if possible at all, to create DBR oscillator in the IS guide may be the use of continuous gain medium similar to the one in the optical laser. It was reported that such a gain medium tends to increase the guiding ability of the waveguide.[14] However, realization of such device requires effort in solid-state materials and devices at millimeter-wave frequencies.

5. CONCLUSIONS

In this paper, we first reviewed a novel quasi-planar waveguide structure for millimeter-wave integrated circuits. Several passive components developed to date are described. An effort toward developing solid-state active components is presented and a number of problems to be solved are discussed.

REFERENCES

1. COLLIN, R.E. and ZUCKER, F.J., 1969, Antenna Theory, Part II, Chapters 19 and 20, McGraw-Hill, New York.

2. ITOH, T., November 1976, "Inverted Strip Dielectric Waveguide for Millimeter-Wave Integrated Circuits," IEEE Transactions on Microwave Theory and Techniques, vol. MTT-24, no. 11, pp. 821-827.

3. ITOH, T., December 1977, "Application of Gratings in a Dielectric Waveguide for Leaky-Wave Antennas and Band-Reject Filters," IEEE Transactions on Microwave Theory and Techniques, vol. MTT-25, no. 12, pp. 1134-1138.

4. ITOH, T. and HEBERT, A.S., June 1978, "Simulation Study of Electronically Scannable Antennas and Tunable Filters Integrated in a Quasi-Planar Dielectric Waveguide," Ottawa, Canada, International Microwave Symposium.

5. ITOH, T. and HEBERT, A.S., 1978, "A Generalized Spectral Domain Analysis for Coupled Suspended Microstrip Lines with Tuning Septums," IEEE Transactions on Microwave Theory and Techniques, vol. MTT-26.

6. ITOH, T. and HSU, F.J., "Distributed Bragg Reflector Gunn Oscillators for Dielectric Millimeter-Wave Integrated Circuits," submitted to IEEE Transactions on Microwave Theory and Techniques (Special Issue on Microwave/Millimeter-Wave Power Generation, Amplification and Modulation).

7. JACOBS, H. and CHREPTA, M.M., April 1974, "Electronic Phase Shifter for Millimeter-Wave Semiconductor Dielectric Integrated Circuits," IEEE Transactions on Microwave Theory and Techniques, vol. MTT-22, no. 4, pp. 411-417.

8. JACOBS, H., NOVICK, G., LOCASCIO, C.M. and CHREPTA, M.M., November 1976, "Measurement of Guide Wavelength in Rectangular Dielectric Waveguide," IEEE Transactions on Microwave Theory and Techniques, vol. MTT-24, no. 11, pp. 815-820.

9. KNOX, R.M. and TOULIOS, P.P., 1974, "A V-Band Receiver Using Image Line Integrated Circuits," Proc. National Electronics Conf., 29, pp. 489-492.

10. KUNO, H.J. and CHANG, Y., June 1974, "Millimeter-Wave Integrated Circuits," U.S. Army Electronics Command, Final Report No. ECOM-73-0279-F.

11. MEIER, P.J., December 1974, "Integrated Fin-Line Millimeter Components," IEEE Transactions on Microwave Theory and Techniques, vol. MTT-22, no. 12, pp. 1209-1216.

12. OLINER, A.A. and PENG, S.T., September 1976, "Waveguides for Integrated Optics Formed by Metal Platings," Rome, Italy, European Microwave Conference.

13. OLINER, A.A., PENG, S.T. and HSU, J.P., June 1978, "New Propagation Effects for the Inverted Strip Dielectric Waveguides," Ottawa, Canada, International Microwave Symposium.

14. ROZZI, T.E., ITOH, T. and GRUN, L., June-August 1977, "Two Dimensional Analysis of the GaAs Double-Hetero Stripe Geometry Laser," Radio Science, vol. 12, no. 4, pp. 543-549.

15. RUDOKAS, R. and ITOH, T., December 1976, "Passive Millimeter-Wave IC Components Made of Inverted Strip Dielectric Waveguides," IEEE Transactions on Microwave Theory and Techniques, vol. MTT-24, no. 12, pp. 978-981

16. SCHNEIDER, M.V., June 1973, "Millimeter-Wave Integrated Circuits," Chicago, Illinois, International Microwave Symposium Digest, pp. 16-18.

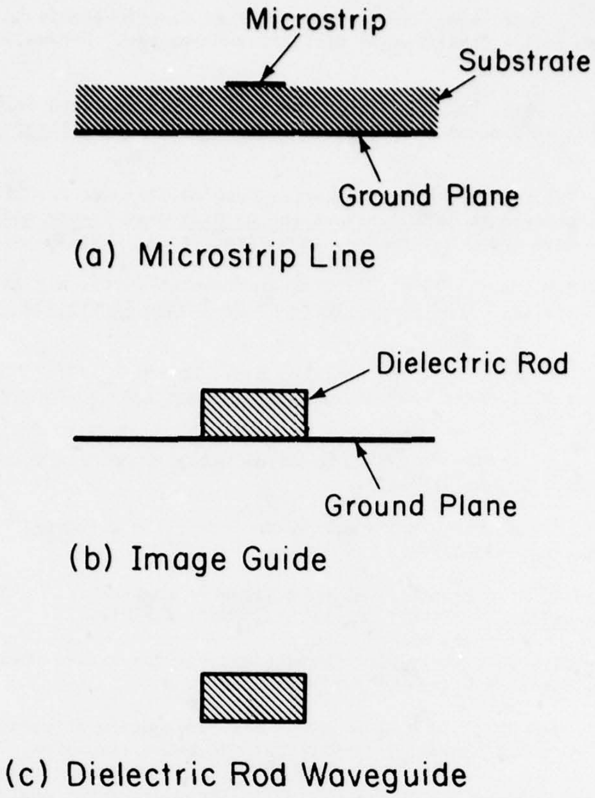
Microstrip
Substrate
Ground Plane
(a) Microstrip Line
Dielectric Rod
Ground Plane
(b) Image Guide
(c) Dielectric Rod Waveguide

Fig. 1 Some waveguides for millimeter-wave integrated circuits: (a) Microstrip line; (b) Image guide; (c) Rectangular dielectric waveguide.

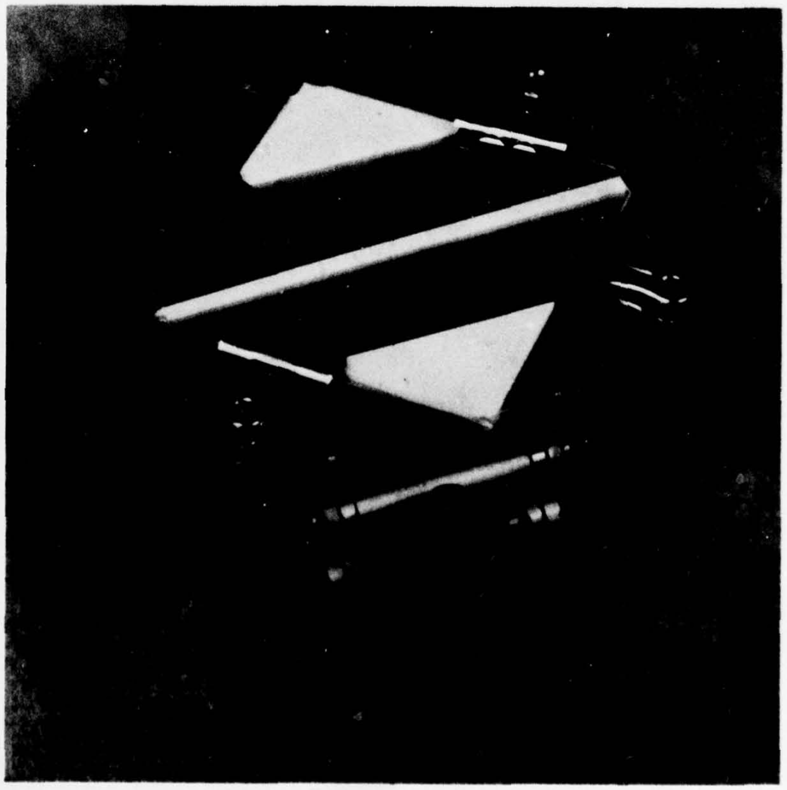

Fig. 2 Inverted strip dielectric waveguide.

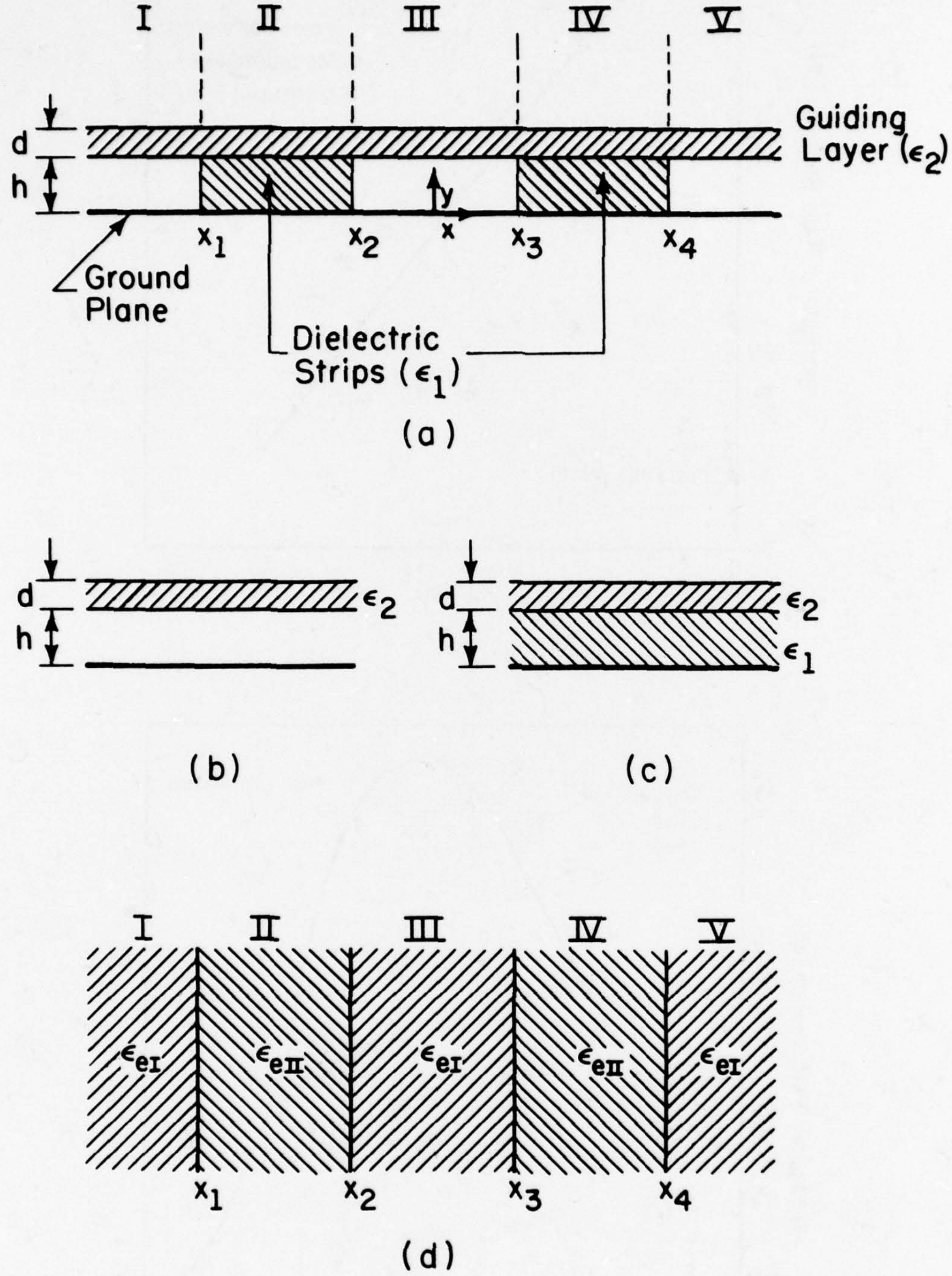
I
II
III
IV
V
d
h
Guiding Layer (ϵ_2)
y
x
x_1
x_2
x_3
x_4
Ground Plane
Dielectric Strips (ϵ_1)
(a)
d
h
ϵ_2
d
h
ϵ_2
ϵ_1
(b)
(c)
I
II
III
IV
V
ϵ_{eI}
ϵ_{eII}
ϵ_{eI}
ϵ_{eII}
ϵ_{eI}
x_1
x_2
x_3
x_4
(d)

Fig. 3 Analysis procedure of inverted strip dielectric waveguide: (a) Cross section of a coupled IS guide; (b) Structure for deriving the effective dielectric constant for the single layered region; (c) Structure for deriving the effective dielectric constant for the double layered region; (d) Hypothetical structure for computing the propagation constant.

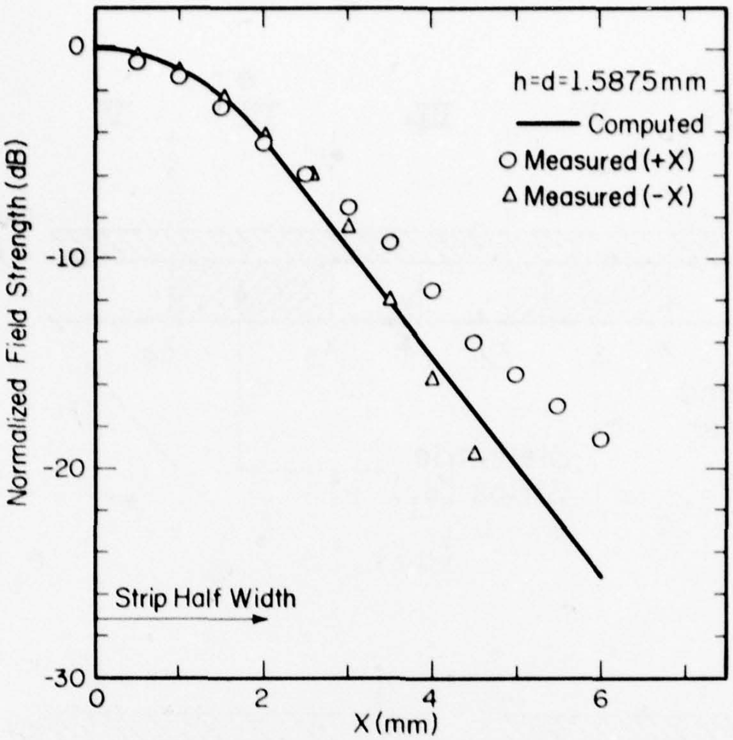

(a)

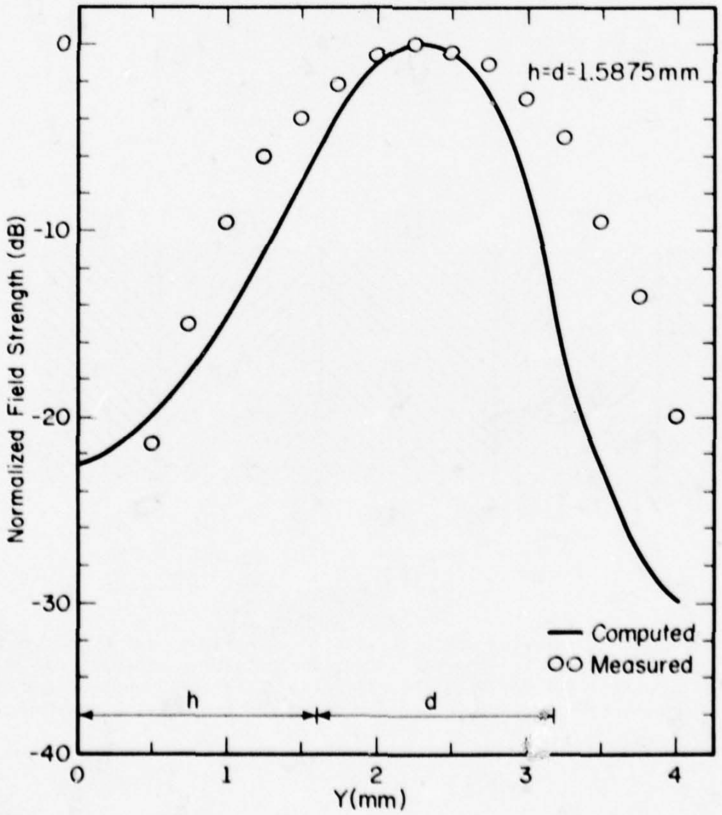

(b)

Fig. 4 Field distribution in an IS guide: (a) Horizontal direction; (b) Vertical direction.

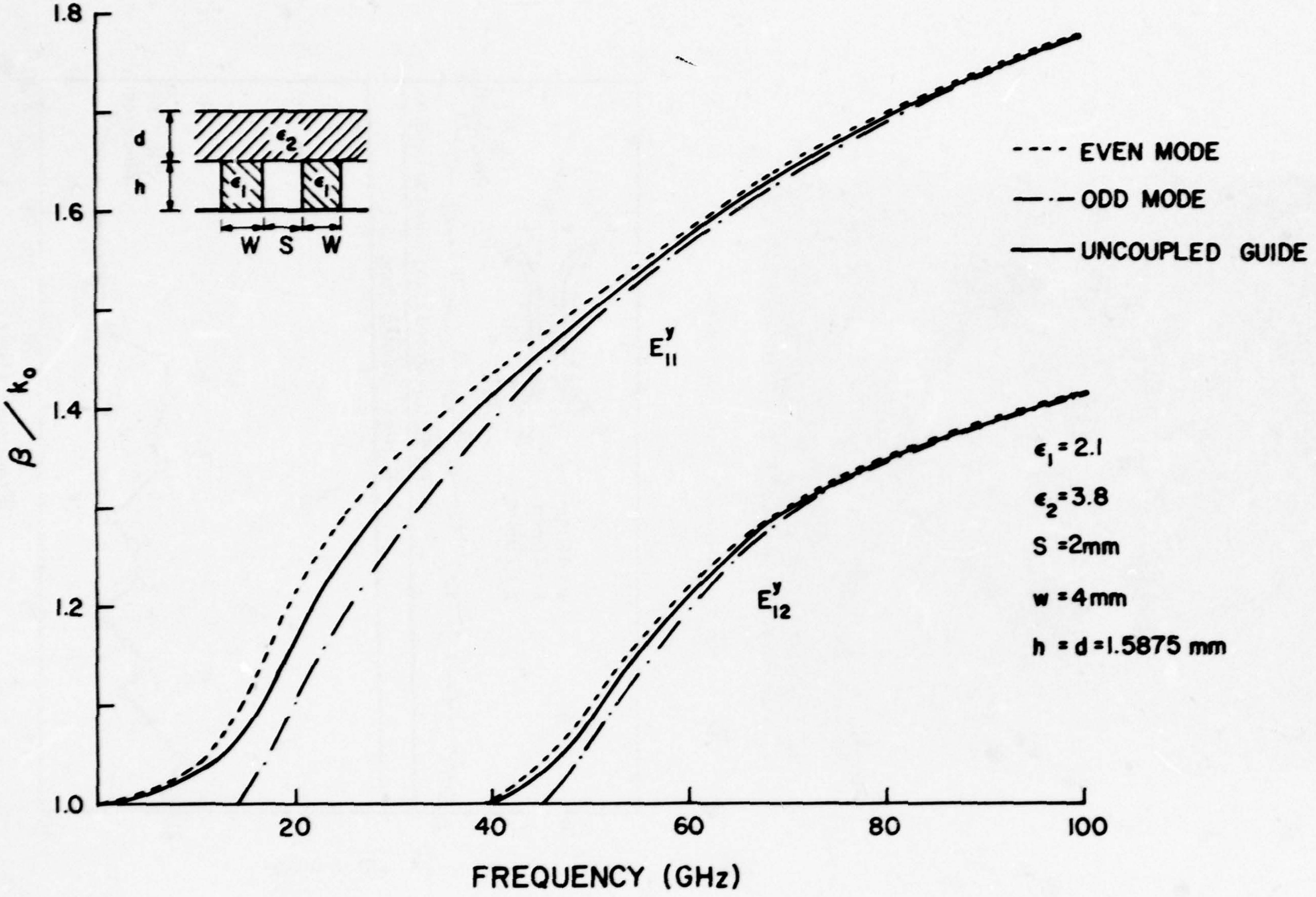

Fig. 5 Dispersion characteristics of IS guide structures.

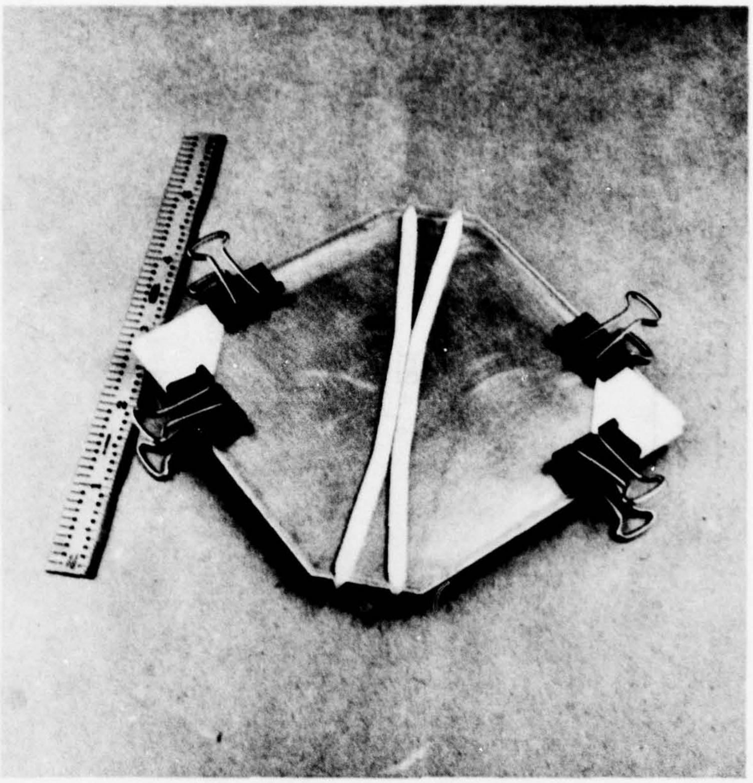

Fig. 6 Distributed directional coupler.

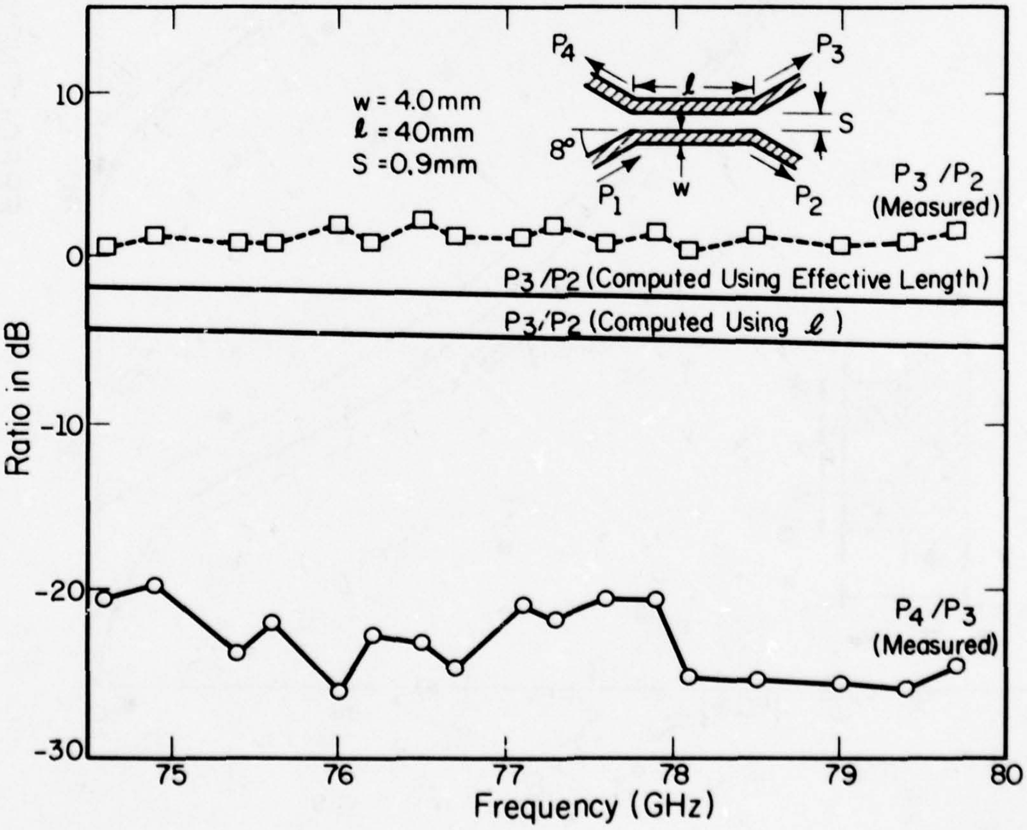

Fig. 7 Performance of the distributed directional coupler.

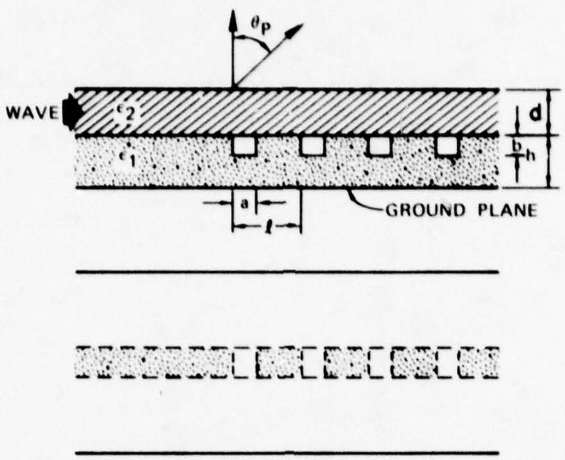
θp
WAVE
ε2
ε1
d
b
h
a
ℓ
GROUND PLANE

Fig. 8 Grating structure in an IS guide.

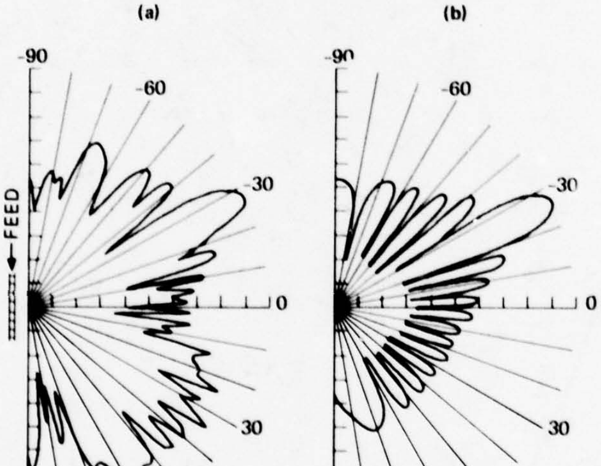

Fig. 9 Radiation patterns of the integrated leaky-wave antenna: (a) Measured at 15 GHz; (b) Computed at 15 GHz; (c) Measured at 17 GHz; (d) Computed at 17 GHz.

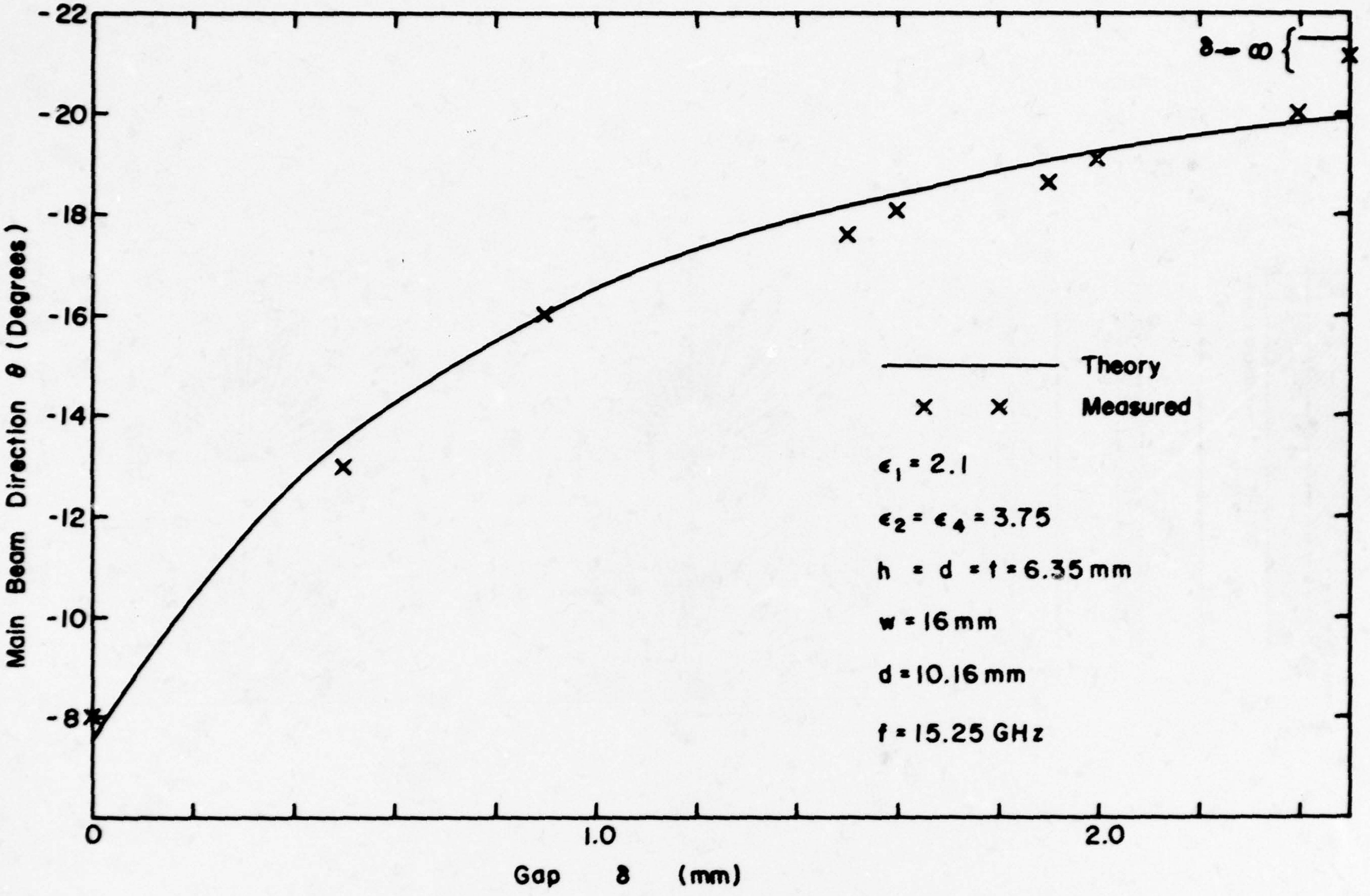

Fig. 10 Main beam direction vs. gap size for mechanically scanned antenna.

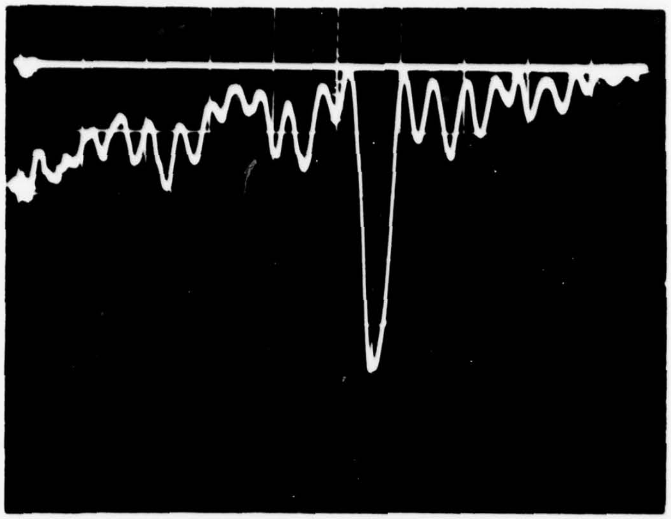

Fig. 11 Swept frequency response from the grating band-reject filter: 12.4-18 GHz, 20 mV/div.

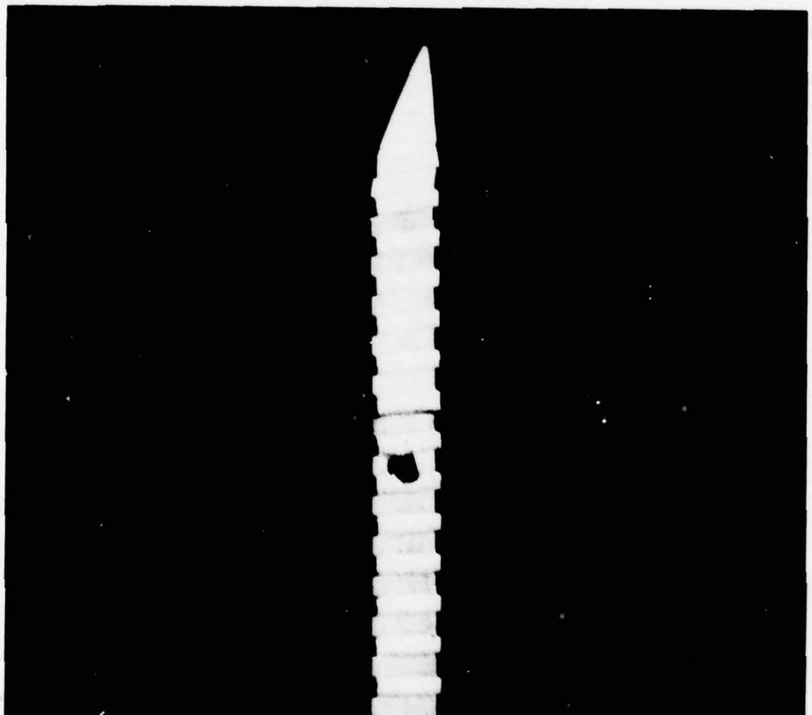

Fig. 12 Distributed Bragg reflector oscillator cavity.

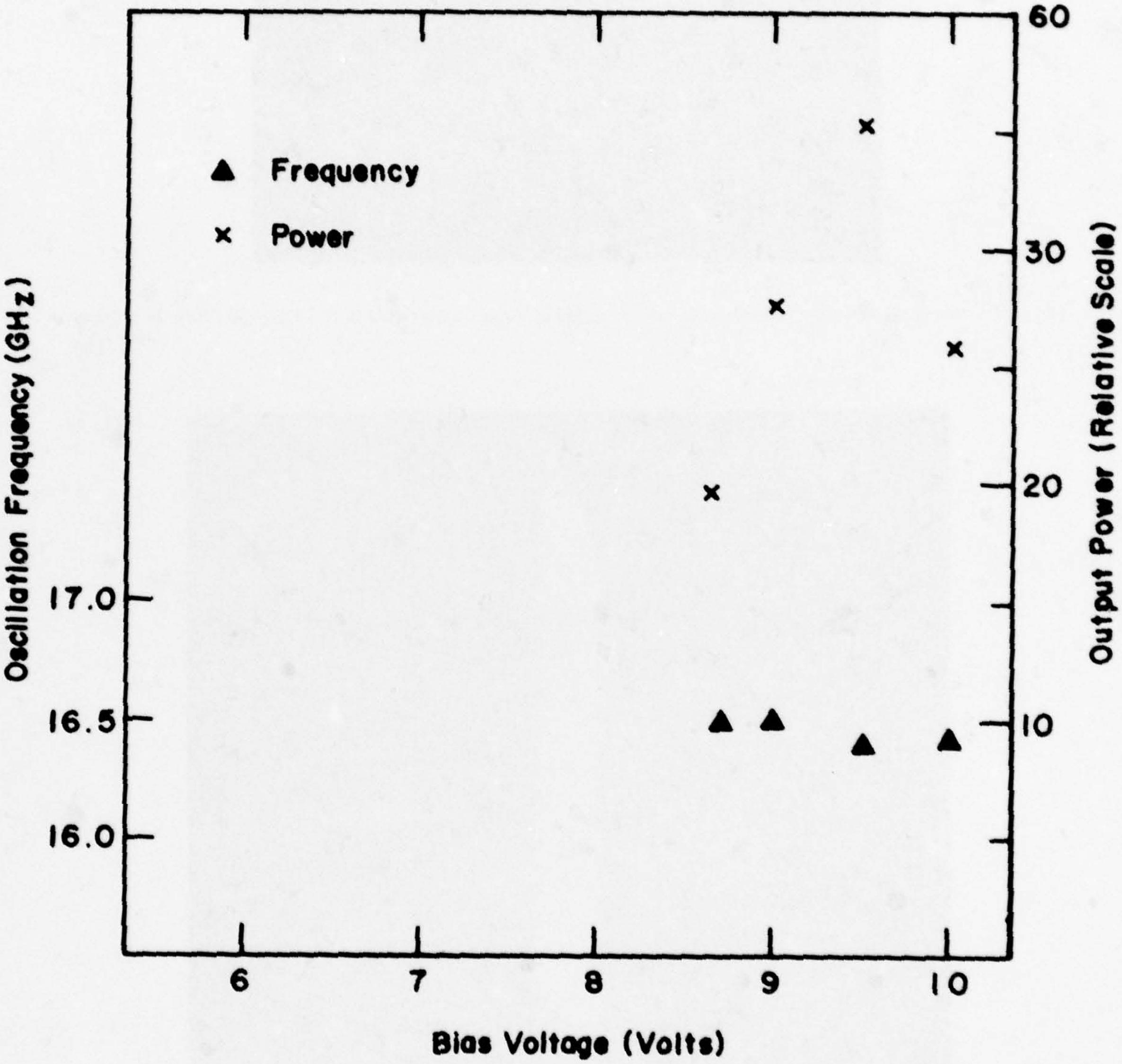

Fig. 13 Characteristics of a DBR oscillator.

FEASIBILITY STUDIES OF INSULAR GUIDE MILLIMETRE WAVE INTEGRATED CIRCUITS

M J Aylward and N Williams
RF Technology Centre, ERA Ltd.
Leatherhead, Surrey, England

SUMMARY

The paper considers the realisation of millimetre wave integrated circuits using a dielectric waveguide technology. The characteristics of image line and related structures are described and their applicability to integrated circuits discussed. The structure chosen for these studies, insular guide, is a variant of image line and allows a relaxation in tolerances so that conventional laboratory fabrication techniques can be employed. The design of a range of components is reviewed and the development of a prototype integrated circuit, aimed at fully establishing the feasibility of the approach, is described.

1. INTRODUCTION

The congestion of lower frequency bands and the demands for ever increasing bandwidths are forcing the system designer to consider utilising millimetre waves for applications which are particularly suited to their peculiar properties. The advantages of millimetre waves are well known (GIBBS, 1977) and include improved angular resolution, resistance to jamming and covertness of operation at frequencies within the atmospheric absorption bands. In addition, their penetration in adverse weather conditions is better than that in the IR and visible portions of the spectrum and they are thus being examined for systems operating at these higher frequencies. The viability of many of these systems relies heavily upon achieving the reduced weight and lower costs afforded by integrated circuit techniques. It is unlikely, however, that scaling microwave circuits in microstrip will provide a cost effective solution: it is difficult to achieve the necessary print definition and, with the problems of spurious modes, accurately machined boxes are needed for repeatable results. A further disadvantage of the medium is the high transmission losses which tend to preclude its use in large scale circuits at frequencies above 40GHz.

Against this background, alternative transmission line technologies, including dielectric image line, which offer the potential of lower losses, relaxed tolerances and reduced unit costs are under investigation. They are, however, insufficiently developed for immediate exploitation and the literature has concentrated mainly on establishing theoretical models and investigating some individual components. This paper describes some results obtained during a research programme aimed at developing a complete range of practical components in a variant of image line, termed insular guide, and establishing the feasibility of integrating these into complete circuits.

2. DIELECTRIC IMAGE LINE AND ITS VARIANTS

The cross section of image line is shown in Figure 1. The structure supports hybrid modes with transverse field distributions which are of a standing wave type within the line and decaying exponentially outside. The distribution of the dominant mode, designated the E^y_{11}, is shown in Figure 1. The propagation constant is computed using an approximate analysis which makes use of the concept of effective dielectric constants and a partial solution of the boundary value problem (MARCATILI, 1961, KNOX and TOULIOS, 1970). The predictions have been found adequate for the design of most components and can be employed in efficient computer models for parameter optimisations. The dispersion characteristics of the lower order modes are shown in Figure 2. As the frequency is raised from cut-on, the dispersion increases until it approaches the bulk medium value, when the energy is almost totally contained within the line. The bandwidth is, however, limited at high frequencies by the onset of the asymmetric E^y_{21} mode which may be excited in curved sections of the line.

Of particular interest for integrated circuit applications is the guidability in curved sections of line and it is obviously important to ensure that radiation losses are kept to a minimum. The radiation losses in curved lines have been estimated using a perturbation analysis. Some sample results are plotted in Figure 3 with the same line parameters as for Figure 2. It is apparent that the radiation is very frequency sensitive but, provided the mode is well guided, may be kept to acceptable levels with a bend radius approximately 4 x 1 (guide width).

Alternative dielectric structures have been proposed which have some advantages from a mechanical viewpoint. The cross section of inverted strip guide (ITOH and MITTRA, 1975) is shown in Figure 4. It consists of a slab of dielectric material separated from the ground plane by a strip which has a lower dielectric constant. Then, most of the energy is contained within the top slab and concentrated above the strip. Although this configuration may be easier to fabricate, its application to integrated circuits appears to be limited by its poor guidability in curved sections. Insular guide, shown in Figure 5, is similar to image line but includes a thin "insulating" film of low dielectric constant material between the line and the ground plane. The field decays exponentially in the layer and this reduces conductor losses in the ground plane and also relaxes fabrication tolerances such that components may be assembled using standard laboratory facilities. One disadvantage of the structure is that the dominant orthogonal E^x_{11} mode is no longer suppressed; however, no evidence of coupling to this mode has been found in the circuits so far tested, even at frequencies where it is able to propagate.

With the use of high quality dielectrics, the losses in insular guide approach those of copper waveguide and are significantly less than microstrip. Thus high Q resonant elements can be realised. The open structure may be exploited in adjustable components and directional couplers and is convenient for the integration of components into complete circuits. The presence of the ground plane is required for mechanical support and as a heat sink for active devices. The development of these components is described in the following section.

3. COMPONENT DEVELOPMENT

A number of components have been developed and constructed at a modelling frequency of 30GHz. In this band alumina, with a dielectric constant of 9.8, has been chosen to provide reasonably compact circuits without significant radiation from curved sections. For the prototype work, a machinable ceramic loaded plastic material is employed; although the dielectric constant is nominally the same as that of alumina, its loss target is approximately an order higher and the line losses (made up of dielectric and conductor losses) are approximately 0.04dB/guide wavelength at 30GHz. The corresponding loss using alumina is calculated to be approximately 0.01dB/guide wavelength. The insulating film is of polythene which also serves to adhere the line to the ground plane without introducing any significant additional losses.

Directional couplers consist simply of two lines in close proximity as shown in Figure 6. The structure is most conveniently analysed in terms of symmetric and asymmetric modes. Their propagation constants, K_{ZS} and K_{ZA} respectively, are computed by modifying the boundary value problem of the isolated line to include electric and magnetic walls at the symmetry plane as shown in Figure 7. The coupled voltage, V_c, is given by

$$V_c = j \sin CZe^{-jKZ}$$

where the coupling coefficient, C, = $(K_{ZS} - K_{ZA})/2$

K is the propagation constant of the isolated line and Z is the distance along the coupler. Either the line spacing or the length can be adjusted to give a particular coupling value. It is apparent that when $CZ = \pi/2$, complete power transfer takes place.

A typical coupling response is shown in Figure 8(a). The measurement of directivity reproduced in Figure 8(b) is limited by the vswr of the loads which consist of diamond shaped sections of lossy material placed directly on the line. However, it is seen that, with the absence of discontinuities in the coupling region, the directivity is at least better than 30dB. The coupling is a monotonic function of frequency. A flatter response can be achieved by modifying the structure to make the propagation constants different for the two lines. In Figure 8(c) a variation of ± .25dB has been achieved over a 20% bandwidth.

The open structure of insular guide has been exploited in the design of the adjustable phase changer and attenuator shown in Figure 9. In the phase changer, the transverse fields are distorted by the presence of the metallic wall to produce a modification in the propagation constant. The variation in phase as the position of the metallic plate is moved relative to the line is plotted in Figure 9(b). Good agreement is obtained between the experimental and predicted behaviour. The adjustable attenuator is realised by replacing the metallic plate with a resistive card. With the card length shown in Figure 9(c), an attenuation range of 20dB was obtained.

Filters are realised using resonant rings with proximity lines to couple in and out of the structure. Q's of 700 have been obtained with the plastic material but values of at least 3000 should be achievable using pure ceramics. The circumference must be a multiple number of wavelengths to prevent excessive radiation. It is then necessary to use a number of coupled rings with differing diameters to suppress the unwanted resonances adjacent to the pass-band. Tuning elements, similar in principle to the adjustable phase shifter, are required to align the responses of the individual rings. A two pole band pass filter is shown in Figure 10(a). The predicted and measured responses, reproduced in Figures 10 (b) and (c), are well correlated and the filter has a bandwidth of 150MHz, a loss of 2.5dB and a pass band ripple of .25dB. It should be noted that since the rings are essentially reflectionless, filters can be cascaded without the interaction problems usually encountered.

Active devices are generally considered to be difficult to integrate with dielectric waveguide structures because they represent an abrupt discontinuity in the line and result in radiation which is difficult to suppress. However, detector and mixer diodes have been successfully mounted using the arrangement shown in Figure 11(a). For convenience, coaxial diodes were used, mounted in the baseplate. A transition from coaxial line to the dielectric waveguide is then formed by a vertical pin positioned centrally in the line, approximately $\lambda g/4$ from its end. The top face and end wall of the line is metallised to reduce radiation and provide a good match. The sensitivity of the arrangement with a IN53 diode when operated as a detector is shown in Figure 11(b). The performance was comparable to that measured with the same diode mounted in a metallic waveguide mount.

With oscillators, the difficulty lies in realising a suitable high-Q cavity. As with MIC systems, it is considered that the most satisfactory solution is to employ conventional metallic waveguide cavities and provide a transition to the dielectric line. A gunn oscillator using this approach is shown in Figure 12. The output waveguide is of the same dimension as the dielectric line and is cut off in the air-filled section. The cavity coupling is then conveniently optimised by adjusting the position of the dielectric line. Using this arrangement, the rated output power of the gunn diode has been achieved with a cavity Q of approximately 1000.

4. INTEGRATED CIRCUIT ASIBILITY STUDIES

A large range of standard rf components have been realised in insular guide and reasonable performances have been achieved. Further work is being carried out on additional components such as ferrite non-reciprocal devices and PIN diode modulators. To investigate integration problems, the components so far developed have been included in a demonstration transceiver circuit, again operating at a modelling frequency of 30GHz. A similar circuit in metallic waveguide is currently under development for a 60GHz covert communications link terminal. The insular guide technology is being considered to reduce the unit cost and improve the system viability.

The prototype circuit is shown in Figure 13. A fraction of the transmitter power is extracted by a directional coupler to provide the local oscillator signal for the balanced mixer, (the transmit and receive signal frequencies being separated by the IF frequency). The received signal is extracted by the two-pole band pass filter. In the final system, a polyrod antenna would be integrated with the circuit to illuminate the high gain offset reflector developed for the terminal.

Target figures for the principal circuit parameters are listed below; the figures in brackets indicate the improvement in performance to be expected when the ceramic loaded plastic material is replaced by alumina.

Transmitter power	50mW	
Transmitter frequency	30.000 GHz	
Receiver frequency	29.750 GHz	
IF frequency	250 MHz	
Filter bandwidth	200 MHz	
Filter insertion loss	3dB	(1dB)
Line losses	2dB	(.5dB)
Mixer conversion loss (IN53 diode)	8dB	

The mixer conversion loss is limited at present by the characteristics of available mixer diodes. Initial results show that the desired performance can, in the most part, be achieved although difficulties have been encountered in optimising the mixer arrangement. This resulted in a higher mixer conversion loss of 10dB and improvements are currently being made in the design of the IF matching circuit.

5. CONCLUSIONS

The feasibility of insular guide integrated circuits has been established. Further work is required in the development of additional components, such as modulators and non-reciprocal devices. However, it is considered that emphasis should now be given to improving techniques for fabricating circuits with pure ceramics. This area is being explored so that the technology can be applied to practical systems.

REFERENCES

GIBBS, S E. 1977, "Potential for millimetre waves in radar and telecommunications", IEE Colloquium on Millimetre wave antennas and associated components. (London) October 4.

KNOX, R M and TOULIOS, PP. 1970, "Integrated circuits for the millimetre through optical frequency range". Proc Syp Sub-millimetre waves (New York) March 31-April 2.

ITOH, T and MITTRA, R. 1975, "New waveguide structures for millimetre wave integrated circuits", International Microwave Symposium Digest. (Palo Alto, Ca) May 12-14.

MARCATILI, E A J. 1969, "Dielectric rectangular waveguide and directional couplers for integrated optics", Bell System Tech. J. 48 (10).

ACKNOWLEDGEMENT

This work has been carried out with the support of Procurement Executive, Ministry of Defence, UK.

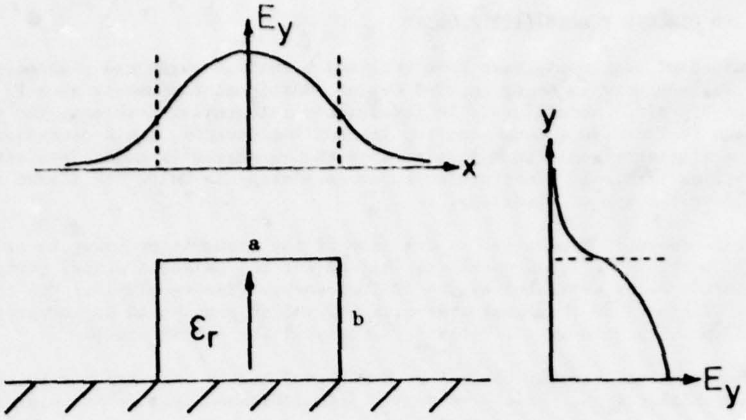

Figure 1: Cross section of image line and typical field distribution of the dominant E_{11}^{y} mode.

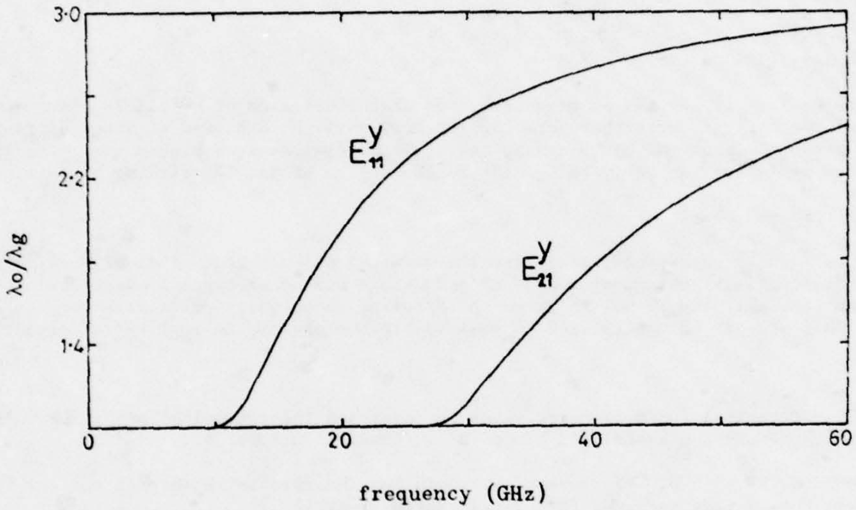

Figure 2: Propagation characteristics of the lower order modes in image line. $E_r = 9.8$, $a = b = 2.0$mm

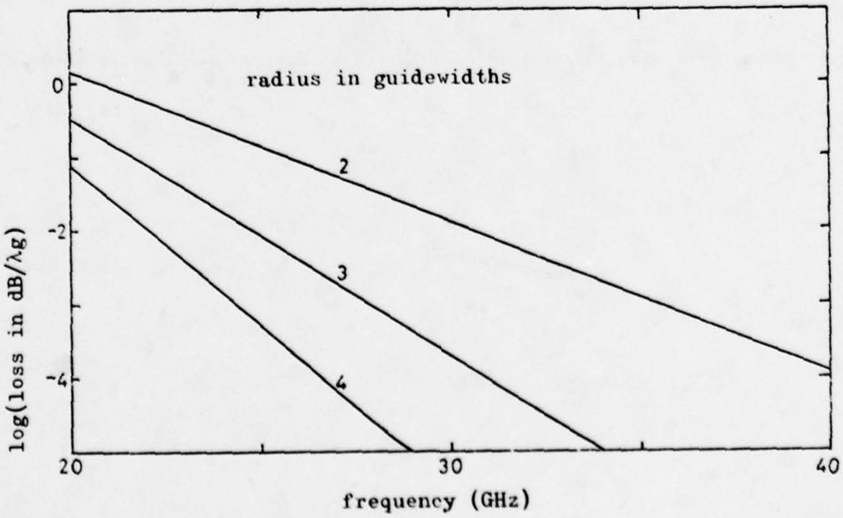

Figure 3: Radiation losses in curved sections of image line. Line parameters are as for Figure 2.

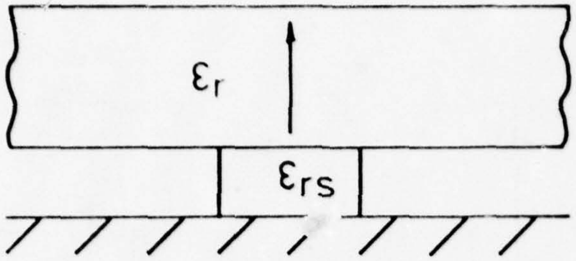

ε_r
ε_{rs}

Figure 4: Cross section of inverted strip guide

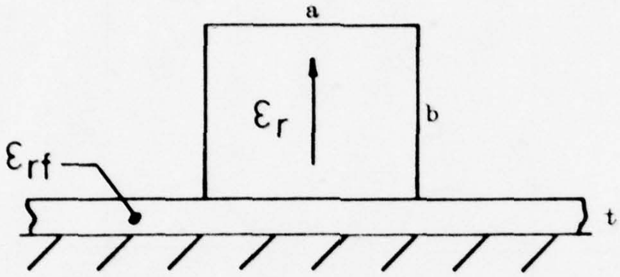

a
ε_r
b
ε_{rf}
t

Figure 5: Cross section of insular guide

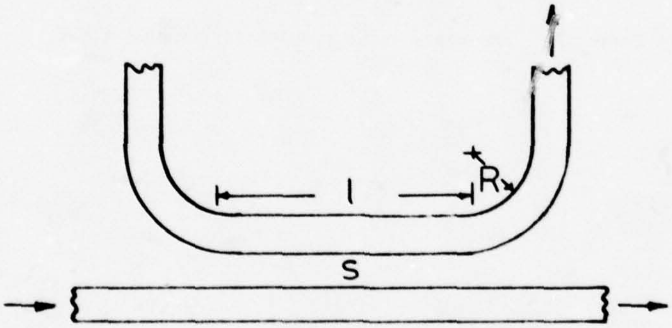

Figure 6: Proximity line directional coupler

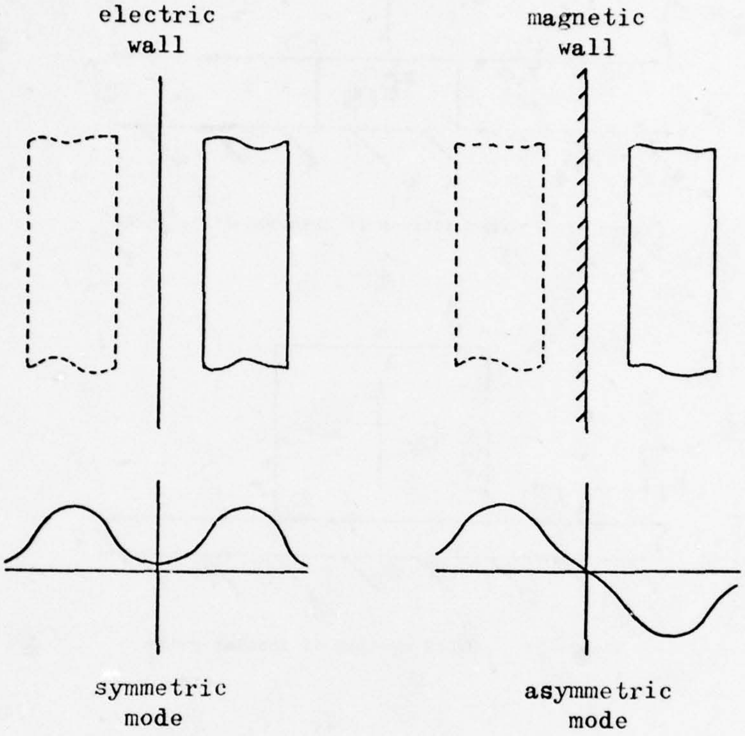
electric
wall
magnetic
wall
symmetric
mode
asymmetric
mode

Figure 7: Boundary value problem for coupled lines

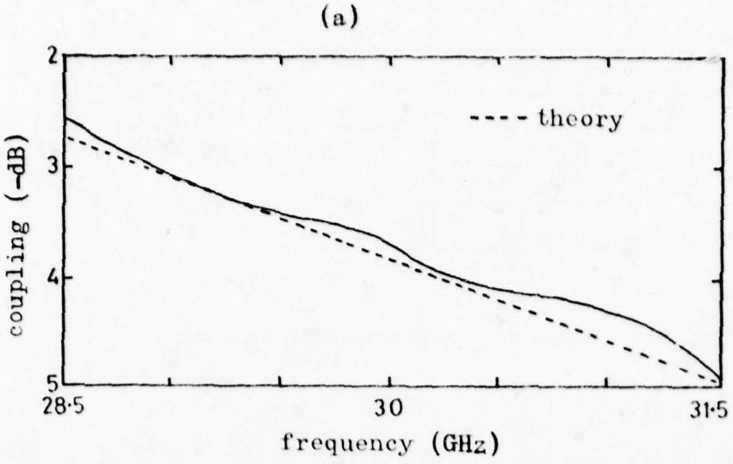

Figure 8: **(a) Measured and predicted coupling response as a function of frequency.** $\varepsilon_r = 9.8$, a = b = 2.00mm, t = .25mm, s = .91mm, l = 0mm, R = 25.4mm, $\varepsilon_{rf} = 2.25$.

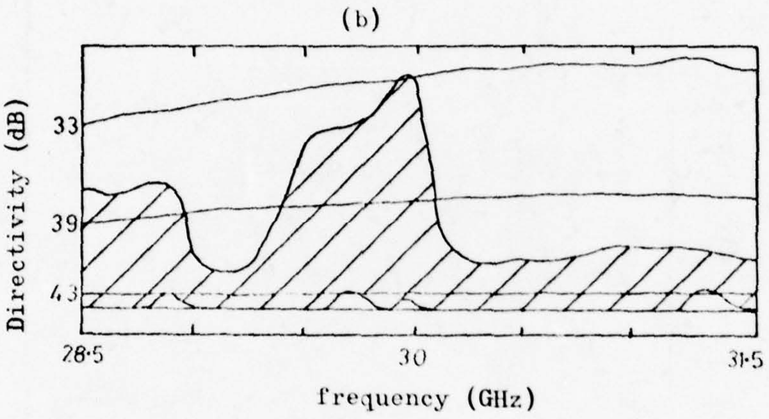

Figure 8: **(b) Corresponding directivity as a function of frequency**

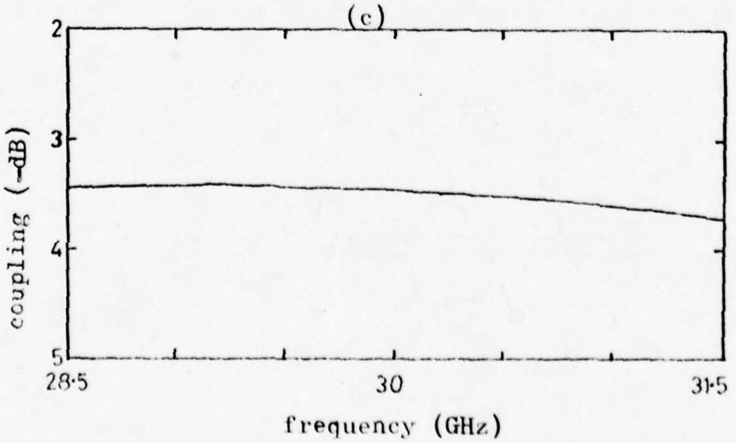

Figure 8: **(c) Optimised coupler response**

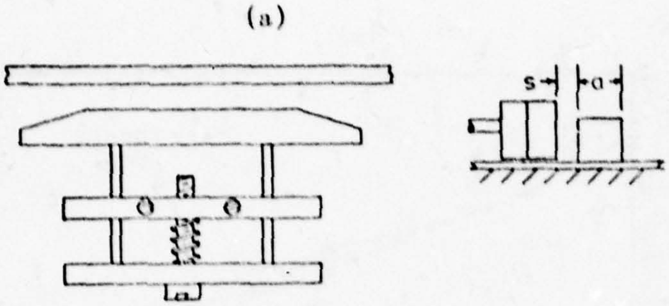

Figure 9: (a) Adjustable phase changer

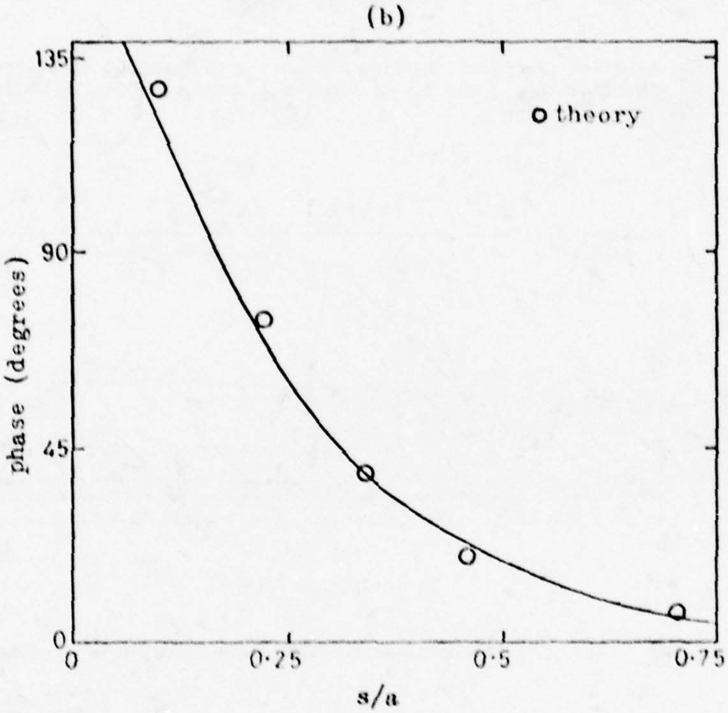

Figure 9: (b) Measured and predicted phase shift as a function of the plate-to-line spacing.

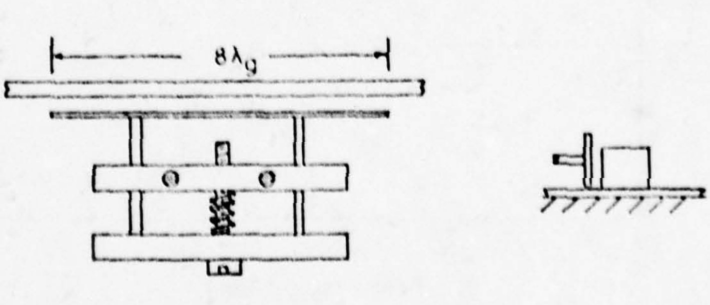

Figure 9: (c) Adjustable attenuator

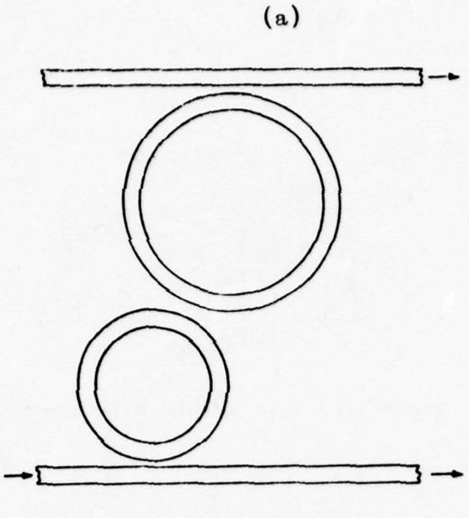

Figure 10: (a) Two-pole ring filter

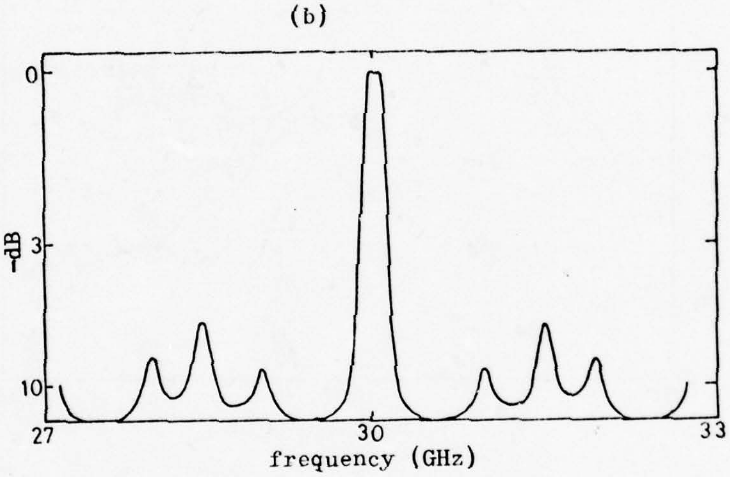

Figure 10: (b) Predicted filter response

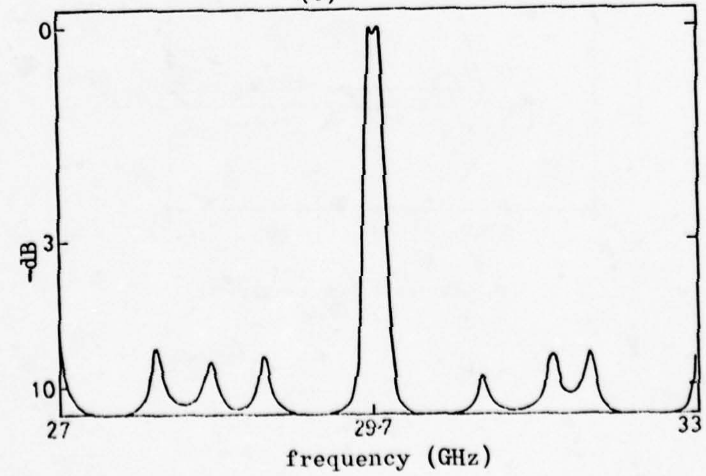

Figure 10: (*c*) Measured filter response

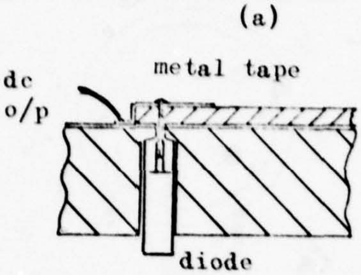
(a)
metal tape
dc
o/p
diode

Figure 11: (a) Detector/mixer mount

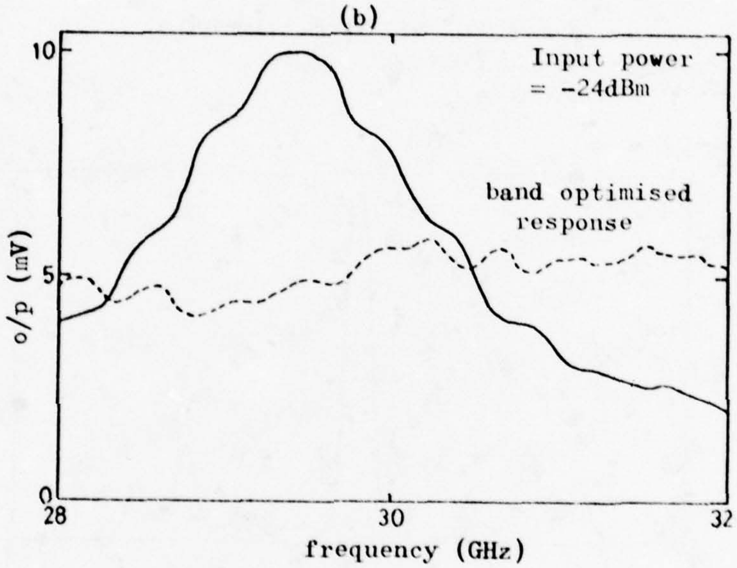

Figure 11: (b) Detector response

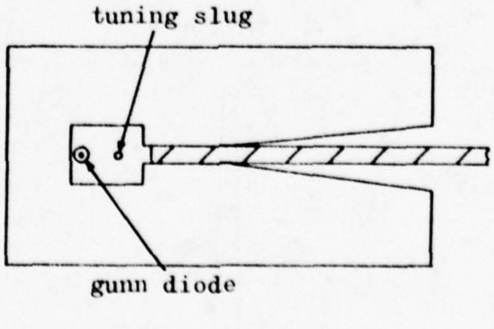
tuning slug
gunn diode

Figure 12: Gunn oscillator

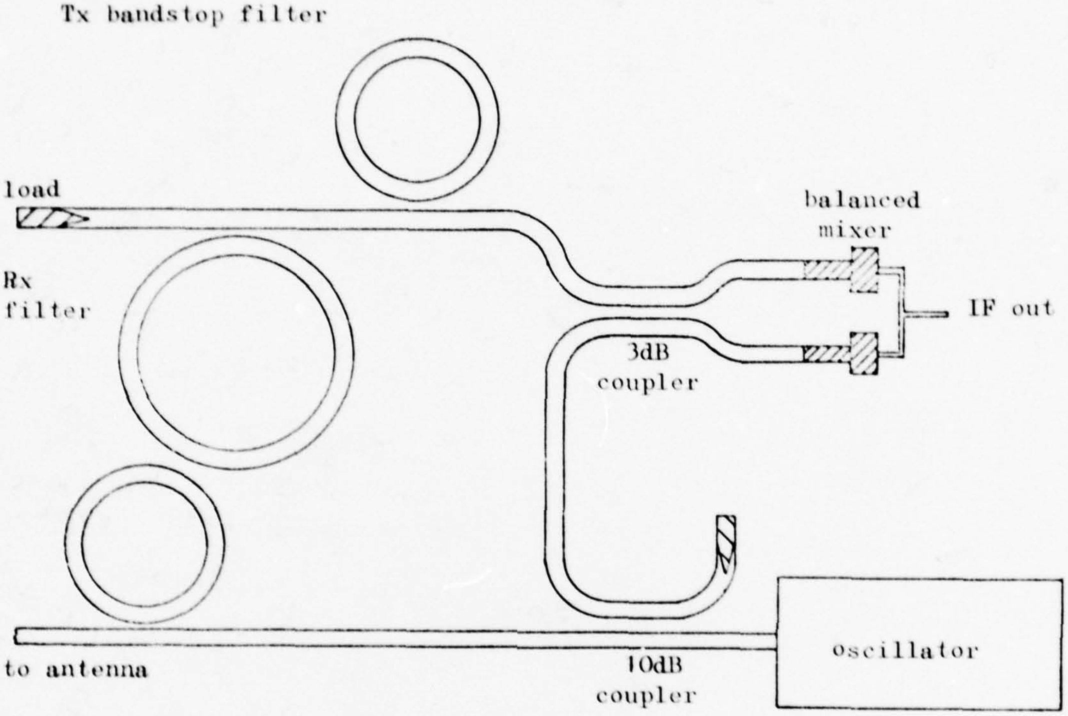
Tx bandstop filter
load
balanced mixer
Rx filter
IF out
3dB coupler
oscillator
to antenna
10dB coupler

Figure 13: Prototype transceiver circuit.

FEASIBILITY OF DESIGNING MILLIMETRE MICROSTRIP PLANAR ANTENNA ARRAYS

by

P.S. Hall, C. Garrett and J.R. James,
Department of Electrical and Electronic Engineering,
Royal Military College of Science,
Shrivenham, Swindon, Wilts, SN6 8LA, England.

SUMMARY

New types of low cost microstrip millimetre wave antennas having flat profiles which can be made conformal with the surface of missiles etc, are investigated. The antenna design is carried out using a computer design technique that has recently proved successful up to 17 GHz; this process computes antenna gain, sidelobes, efficiency, etc prior to drawing the photographic mask, and the fundamental aspects of the technique are briefly noted. The design and subsequent performance of planar arrays using RT Duroid and alumina substrates at both 36 and 70 GHz is then described and critically examined. The mechanical and electrical control of tolerances are obvious sources of difficulty which reflect in the results but the outcome is far less problematical than expected. It is concluded that microstrip antennas can be designed at millimetre wavelengths to achieve comparable performance to that obtained at lower frequencies; but that the precision with which the substrate can be manufactured and processed determines the actual performance obtained. No fundamental upper frequency limitation has yet been established.

SYMBOLS

h = substrate height

μ_o, ϵ_o = permeability and permittivity of free space

ϵ_r, ϵ_e = rel. and effective permittivity of substrate

i = positive integer $< N$

N = number of stubs on feeder

m = higher order mode number

w = microstrip feeder width

w_i, ℓ_i = width and length of ith stub

w_e = effective width of microstrip or triplate line

d_i = distance between $(i - 1)$ and ith stubs

ℓ, d = stub length and spacing when identical

$\Delta\ell/h$ = end-effect

Z_m = impedance of microstrip line

α = attenuation constant of microstrip line (dB/λ_g)

λ_o, λ_g = free space and microstrip line wavelength

$G_r + jB_r$ = radiation admittance of open-circuit termination aperture

$G_s + jB_s$ = admittance due to surface wave generation in aperture

P_G = power gain of antenna array above isotropic

η_L, η_s, η_f = power losses in load, microstrip lines and corporate feed

η_r = power radiated at triplate/microstrip interface

k_o, k_z, k_y = wave numbers in free space, in substrate in direction of propagation and across the stripline respectively

f = frequency

1. INTRODUCTION

The recent progress in the generation and transmission of millimetre waves together with the upsurge of commercial and military interest highlights the need to design new types of antennas to suit the various constraints imposed by these systems. A common requirement is for antennas with flat profiles since these are compatible with modern integrated circuits and can be made conformal with the surfaces of missiles, aircraft, vehicles etc; antennas with low manufacturing costs as well are additionally advantageous. A recent survey (HALL, P.S. and JAMES, J.R., 1978) has indicated that little work has been done on the problem of creating flat profile antennas at millimetre wave frequencies and only one example, a very narrow band antenna at 36 GHz, has been presented, (WILLIAMS, J.C. 1978). At lower frequencies new types of low cost flat profile antennas have been successfully designed using printed microstrip technology (JAMES, J.R. and WILSON, G.J., 1977) (JAMES, J.R. and HALL, P.S., 1977) and many innovative ideas are emerging on basic array design (JAMES, J.R. and WILSON, G.J., 1975), on frequency swept array design (AITKEN, J.E., HALL, P.S. and JAMES, J.R., 1978) and on circularly polarised array design (HALL, P.S., 1978). The potential usefulness of microstrip antennas, as judged by recent discussions (FLAT PLATE ANTENNA SYMPOSIUM, RSRE MALVERN, ENGLAND, 1978), is likely to be considerable and the question arises as to how high in frequency the microstrip antenna concept can be usefully extended. The purpose of this paper is to investigate the feasibility of designing travelling wave millimetre wave microstrip antennas and the frequency range of immediate interest is up to 70 GHz. A brief outline of the fundamental action of microstrip antennas and the computer design technique is given prior to discussing the application of the latter at millimetre wave frequencies. The findings are then critically reviewed, conclusions drawn and recommendations for both further research and development made.

2. DESIGN OF MICROSTRIP ANTENNA ARRAYS

2.1 Fundamental Action

A detailed description of the fundamental action of microstrip antennas and a new design technique for microstrip antenna arrays are given in the literature (JAMES, J.R. and WILSON, G.J., 1977), (JAMES, J.R. and HALL, P.S., 1977). The main points of the design process are now summarised and updated in the light of our on-going research programme.

An open-circuit microstrip stub Fig 1(a) has in the past been regarded as an ideal open-circuit termination in conjunction with a line extension $\Delta\ell$, the latter being the end-effect $\Delta\ell/h$ where h is the substrate height; the strip width is denoted by w and the relative and effective permittivity of the substrate are ϵ_r and ϵ_e respectively. It has now been shown that a significant loss of radiation can occur in the region of the termination and the open-circuit stub can in fact be utilised as a radiating element. The radiation conductance G_r has been measured and the radiation pattern is essentially that of a magnetic Hertzian dipole. Another effect taking place is the launching of surface waves into the substrate and if these waves are not reflected back to the termination by obstacles or discontinuities in the substrate, the additional loss of power is represented by a conductance G_s; there is also some susceptive contribution B_s but in practice it is difficult to separate B_r and B_s. More recent estimates and an analysis of these parameters have been given (WOOD, C., HALL, P.S., and JAMES, J.R., 1978), (HENDERSON, A. and JAMES, J.R., 1978). These parameters, Fig 1(b), form the basis of the design process to be used and are valid for arrays of open-circuit terminations, provided the distance of separation of the latter is sufficiently large not to create significant coupling of the evanescent fields of the apertures.

Some recent data for G_r and G_s for both RT Duroid and alumina substrates is given in Fig 2. A linear array can be formed by attaching several open-circuit stubs to a microstrip feeder line and by printing such linear arrays side-by-side, a two dimensional array can be designed; a corporate feed system is then required. The aperture distributions of the linear arrays can be controlled to a high degree by varying the width of the stubs and both resonant and travelling wave antennas have been designed on this basis.

2.2 Computer Design

Given the desired antenna specification, the entire array can be designed and a photographic mask drawn by computer. In addition to the G_r data, quasi-static estimations (HAMMERSTAD, E.O. and BEKKADAL, F., 1975) have been used to correct for the end-effect $\Delta\ell/h$ and also the behaviour of the T-junctions where the stubs are attached to the feeder lines. We now find it necessary to supplement these estimates with our own empirical data to improve the design accuracy.

The computer programme calculates the radiation pattern (H plane) of a linear array and when several linear arrays form a two dimensional array then the E-plane pattern is also given. The phase and amplitude of the aperture distribution, the antenna power gain P_G above isotropic, the power loss, η_L, in the load for the travelling wave antenna case only, the power loss, η_s, in the microstrip lines and stubs and finally the input VSWR of a linear array are also calculated. The total line loss, η_F, of the corporate feed, when applicable, is also computed. The design process has been extensively tested up to 17 GHz. Linear arrays with sidelobe levels of -23dB can be realised but surface waves and particularly mechanical and electrical tolerance problems at present prevent the attainment of lower sidelobe levels. We have subsequently found that radiation from microstrip corporate feeds is intolerable and triplate feeds are now used; some power, η_R, is lost due to radiation from the triplate to microstrip transition. Further improvements in the corporate feed design will probably depend on mechanical and electrical tolerances and a computer assisted study of this problem is currently in progress; recent results indicate that an E-plane sidelobe level of -25dB can be achieved using improved design methods. Microstrip arrays have lower bandwidths and efficiencies and higher cross-polarisation levels than conventional antennas but the cost and system advantages of this new antenna concept are likely to outweigh the disadvantages for numerous applications.

2.3 Design Implications of Millimetre Wave Frequencies

If the same substrate material and height is used at millimetre wave frequencies as at lower frequencies then it follows from Fig 2 that the G_s/G_r ratio increase at higher frequency and more power is injected into the substrate. Experience has shown that the radiation of this surface wave power at a substrate discontinuity is most likely to create problems at the periphery of the array where the substrate regions are free of printed conductors. Evanescent higher order modes are also more important at higher frequencies, producing phase errors at junctions in the corporate feed and antenna structure and when allowed to propagate severe amplitude errors. Propagation can be prevented and phase errors reduced by a correct choice of line width and substrate height; this is an important design constraint and is discussed more fully in section 3.2. These factors indicate that where possible the substrate height should also be scaled with frequency. The increased importance of manufacturing and material tolerances and the expected increase in the microstrip line attenuation at higher frequencies are further problems that must be considered.

Apart from these factors the computer programme will model the antenna behaviour at these high frequencies to an accuracy comparable with lower frequency operation. The direct use of this computer programme at millimetre wave frequencies therefore provides a definitive test of the validity of scaling the microstrip dimensions down as the frequency is increased, thus obviating the need to redesign at each new frequency. This then is the main aim of this paper.

3. EXPERIMENTAL AND COMPUTED RESULTS

The general form of the microstrip antenna arrays to be considered here is illustrated in Fig 3. The array is composed of eight identical linear comb line arrays which are fed by a corporate feed. All the cases considered are travelling wave arrays and each linear array is terminated in a DAG painted-on matched load. The H-plane sidelobe level is determined by the distribution of stub widths along the linear arrays while the corporate feed is designed to create the desired E-plane distribution. Radiation from the corporate feeds can be prevented by constructing the feed in triplate and this is readily achieved using conventional techniques for the RT Duroid substrates. The design concepts are given in the literature (JAMES, J.R. and HALL, P.S., 1977) and it is sufficient here to identify the parameters to be quoted in addition to P_G, η_L, η_S, η_r and η_r which have been defined in section 2.2 and h, ϵ_r and ϵ_e in section 2.1

The attenuation of a microstrip line, α, in dB per microstrip wavelength is calculated from PUCEL, MASSE and HARTWIG, 1968 with the resistivity of copper increased to account for surface roughness effects at high frequency (BENSON and STEVEN, 1963) to be $\alpha = 0.07$ dB/λ_g for 0.79 mm thick RT Duroid substrate at 36 and 70GHz, $\alpha = 0.11$ dB/λ_g for 0.25mm RT Duroid substrate at 70GHz and 0.08 dB/λ_g for the alumina substrate used at 36 and 70GHz.

d_i = separation between adjacent stubs, w_i = stub width, ℓ_i = stub length, w = feeder width for the linear array; i is a positive integer $1 < i < N$, where N is the number of stubs on the linear array.

3.1 Array Design At 36GHz

Previous experience has shown that arrays made on 0.79mm RT Duroid substrates gives better results than the thicker 1.58mm substrates at 17GHz and the difficulties with the latter substrate at that frequency are attributed to the increased surface wave contribution. At 36GHz even the 0.79mm substrate may be too thick but no evidence of this is apparent in the first example Figs 4 and 5. The array was designed to have both uniform E and H-plane aperture distributions. A large amount of power was dumped in the load as shown in Table 1; η_L is determined by the finger width which was arbitrarily chosen to be 0.3mm; η_L can be reduced by increasing w although additional phase and amplitude errors are introduced if excessively wide fingers are used. The H-plane squint is due mainly to inaccuracies in the value of ϵ_e used together with small phase errors due to the T junctions and open circuit ends.

No precise measurements of these effects were made at 36 or 70GHz during this work; in practice such measurements would have to be made, to allow this squint to be removed. The sidelobe levels of the radiation patterns are consistent with a uniform illumination. A usable bandwidth of about 1GHz is indicated by the VSWR curves centred at 36.5GHz but the bandwidth for -13dB sidelobe levels is somewhat less. The power gain P_G is calculated from the area of the array which is 69mm x 57mm and produces an actual antenna system of 24.0dB. Table 1 substantiates the aggregate of the various loss factors η_L, η_S, η_r and η_f. The measured gain, which corresponds to an efficiency of 29%, does not include the 3dB loss in the coax to triplate transition and thus represents the gain of the array and corporate feed only. In practice a low loss transition should be used. The antenna system gain could be substantially increased by using wider stubs thus reducing η_L and it would appear that no significant problems with surface waves or overmoding are apparent at this sidelobe level.

At 17GHz alumina substrates can be used as radiators although, as shown in Fig 2, the radiation conductances are low; in consequence losses in the lines and loads become more significant and low efficiency antennas result. Low radiation conductance is to be expected as alumina substrates are used up to this frequency for circuits in which it is required to keep radiation to a minimum.

Our measurements on alumina antennas at 36GHz clearly indicate that the radiation conductances are still too low and the stub widths cannot be made wide enough to release the guided power. This is summarised for one example in Table 2. This antenna had overall dimensions of 31mm x 26mm and was again designed to be a uniform aperture distribution but for the stub widths required (w_i = 0.1mm) most of the power was dumped in the loads. This antenna had a low system gain and could not be measured properly. Furthermore no simple triplate arrangement for the corporate feed was available and a further power loss of probably 2dB was attributed to radiation from the feed alone. Sidelobe levels in the H-plane are generally around -9dB due to the unwanted feed radiation. It is concluded that alumina of this thickness is unsuitable for antenna array applications at 36GHz but the construction of simpler antennas such as patch radiators may be possible. Construction of a triplate feed network is an important requirement for these antennas and we have not yet solved this problem in alumina.

The final experiment at 36GHz was to investigate the extent to which the aperture distribution of an array on RT Duroid can be tapered to reduce the sidelobe levels. The sidelobe levels aimed at in the H and E-planes are -18dB and -23dB respectively and the actual physical layout is that of the example used in Fig 3; the results are given in Figs 6 and 7 and Table 3. The H-plane squint at 36GHz was not corrected at this stage and apart from this departure the computed and measured sidelobe levels show reasonable agreement within 2dB. As with the uniform array there is considerable low level radiation away from boresight which is attributed to spurious surface effects and aperture distribution errors. The sidelobe level in the E-plane is not lower than for the uniform array due mainly to errors in the distribution produced by the corporate feed. The asymmetrical power splitters used in the tapered corporate feed will tend to excite the first higher order mode which gives rise to severe amplitude and phase errors at these junctions. This problem can be alleviated by using a higher impedance level throughout the feed or a thinner substrate, although this limits the available aperture taper due to printing limitations. The VSWR Fig 7 is not quite as good as in the uniform feed case Fig 5 due to the errors in the tapered corporate feed but is otherwise reasonable giving much the same bandwidth performance. This array occupies an area 57mm x 125mm and the stubs widths w_i ranges from 0.1mm to 1.12mm. The non-uniform stub widths lead to non-uniform stub separation, d_i, and length, ℓ_i, with average values similar to d and ℓ quoted in Fig 4. Less power was dumped in the loads than in the uniform array case as a comparison of Table 3 and Table 1 shows; the array was also longer producing an increased P_G and η_s. The computed system gain is of the same order as that measured; the measured value does not include the loss in the coax to microstrip transition mentioned earlier. The measured efficiency of 30% is lower than obtained at 17GHz due to increased line loss η_c and radiation loss η_r from the microstrip to triplate transition. The uncertainty in the measured gain is due to the difficulty of accurately characterising the transitions used in the measurement. It is concluded that surface wave effects do not materially affect the H-plane performance at the sidelobe level achieved and the E-plane problems are entirely due to the difficulties introduced by the corporate feed. As such the antenna part itself appears to behave in much the same way as comparable designs at 17GHz.

3.2 Array Design At 70GHz

To examine the performance of microstrip arrays on RT Duroid substrates 0.79mm thick at 70GHz an array having a uniform aperture distribution in both planes was designed having a stub width of 0.1mm and 50Ω feed lines in the array and a minimum impedance level of 30Ω in the triplate corporate feed. However the line widths used allowed higher order modes to propagate. The cut-off condition for these modes occurs when the wave number in the direction of propagation, k_z, becomes zero. k_z is given by

$$k_z^{\,2} = k_o^{\,2} - k_y^{\,2} = (2\pi f)^2\, \mu_o \epsilon_o \epsilon_r - \left(\frac{\pi m}{w_e}\right)^2$$

where k_o and k_y are the wave numbers in free space and in the direction across the microstrip or triplate lines respectively; f is the frequency, μ_o and ϵ_o are the permeability and permittivity of free space, ϵ_r is the relative permittivity of the substrate, m is the higher order mode number and w_e is the equivalent width of the microstrip or triplate line and is defined as the width of a section of parallel plate line of equal impedance. In the microstrip 50Ω line, the cut-off frequency for $m = 1$ is 38.6GHz while for $m = 2$ is above 70GHz. For triplate 30Ω line the cut-off frequencies are 30 and 60GHz for $m = 1$ and 2 respectively. The array E-plane radiation pattern was severely degraded due to overmoding in the corporate feed and when the minimum impedance was raised to 50 , cutting off the $m = 2$ mode, sidelobe levels of about -10dB were obtained. However acceptable patterns in the H-plane were obtainedwith 50Ω line impedance which were degraded when a thinner 80Ω feed line was used. The precise explanation for this is unclear; from Fig 2 it can be seen that the surface wave excitation is only 10dB down on radiation and this together with the looser trapping and hence higher spurious radiation from the junctions of the 80Ω line will reduce the effective control of the aperture distribution. The conclusion is then that 0.79mm RT Duroid substrate is too thick at this frequency due to overmoding, spurious radiation and surface wave generation.

An array was then made on 0.25mm thick RT Duroid substrate which was the closest to a scale substrate height that was readily available. The array has uniform distributions in both planes and used impedance levels that ensured that all higher order modes were cut-off. Due to the narrow bandwidth of the signal source at 70GHz measurements were only made at that frequency. Fig 8 shows the H and E-plane radiation patterns. Good agreement with theory is noted while the squint in the H-plane is again due largely to the inaccuracy in the value of ϵ_e used. The power gain, Table 5, is computed from the array area which is 43.5 x 28.5mm and produces an antenna system gain of 24.1dB. The measured gain corresponds to an efficiency of 23%. The uncertainty in the measured gain figure is due to the difficulty in accurately defining the transmission characteristics of the transitions used in the measurement. The measured gain does not include about 5dB loss in the coax to triplate transition and is therefore the gain of the array and triplate corporate feed only. The commercial coax to triplate transition used was intended for 1.58mm triplate and in practice a properly designed low loss transition should be used. The measured VSWR of the array and transition was found to be 1.7:1. These results show that performance close to that of equivalent arrays at 17GHz can be obtained at 70GHz by use of scaled substrates.

Fig 2 shows that at 70GHz, the radiation conductance of alumina is such as to allow efficient antennas to be constructed. This is borne out by comparison of the gain budget of Table 5 with that at 36GHz in Table 2. The power lost in the load is now significantly reduced. However line losses are increased as is the power lost by radiation from the microstrip corporate feed and the uncertainty of this figure reflects the difficulties in measuring this loss. 6dBs of gain is unaccounted for and is possibly due to further losses in the microstrip to coax transition used to feed the array and power lost in the sidelobes of the radiation pattern. The power radiated from the feed was responsible for severely degrading the radiation patterns which in the H-plane had a -3dB sidelobe level and in the E-plane showed no sensible directional properties.

Similar radiation patterns were obtained from an array with a uniform aperture distributions made on a 0.82mm thick substrate of ordinary photographic slide glass. However the measured gain of this array was about 3dB down on the alumina array due probably to losses in the substrate. No effort was made here to obtain high purity glass and the inhomogeneities in the material would further degrade the radiation patterns. The use of a quartz substrate would improve the loss and inhomogeneity problem. These results show that antenna arrays could be made from higher dielectric constant materials but that feed radiation must be suppressed if useful sidelobe levels are to be obtained. Circuit dimensional tolerances on these substrates are inherently better than on low dielectric constant substrates due to the use of evaporation techniques, but this is largely offset by the smaller circuit element size.

4. DISCUSSION AND CONCLUSIONS

Starting from a knowledge of a previous research program at 17GHz in which an RT Duroid substrate 0.79mm thick was found to give best results and that arrays on alumina substrates were possible the present work has shown that for RT Duroid substrates up to 70GHz:-

a. Use of a 0.79mm thick substrate results in reduced aperture distribution control due to an increased surface wave to radiation ratio and generation of higher order modes.

b. Reduction of higher order moding by increased impedance levels for 0.79mm substrate results in improved corporate feed performance but severely degraded linear array performance.

c. Use of 0.25mm substrate height allows arrays to be made with radiation patterns that can be controlled at 70GHz as well as at 17GHz within the limits set by manufacturing and material tolerances.

d. The measured antenna gain was generally more uncertain than at lower frequencies and we attribute this to the difficulty of completely defining the transmission characteristics of the connectors used in the measurements. Allowing for this the computed antenna efficiencies are somewhat lower than at 17GHz due mainly to increased line losses.

For alumina and glass substrates we conclude that:

a. At 36GHz alumina substrates 0.5mm thick do not radiate strongly enough to allow efficient antennas to be made.

b. At 70GHz radiation is increased and computed results show that useful efficiencies can be obtained.

c. The use of ordinary glass substrates as a cheap substitute for quartz is not possible due to considerably increased losses.

d. Radiation patterns and gain are severely degraded by radiation from the corporate feed and unless a closed form of feed structure, such as triplate, is made alumina, glass or quartz substrates are unsuitable for this type of antenna.

This investigation therefore confirms that the design and construction of microstrip arrays is feasible up to 70GHz on low dielectric constant substrates and that if the substrate height is scaled only manufacturing and material tolerances limit the performance. Although no tests have been carried out at higher frequencies it seems apparent that the upper frequency limit of operation of microstrip arrays is determined only by tolerance control and the availability of the very thin substrates required.

5. ACKNOWLEDGEMENT

We thank Dr G.N. Taylor, RSRE, for helpful discussions and Mr P. Harris for fabrication of the antennas. One of us (P.S.H.) is financially supported by the Procurement Executive, Ministry of Defence. Copyright Controller HMSO, London, 1978.

6. REFERENCES

AITKEN, J.E., HALL, P.S. and JAMES, J.R., 1978, British provisional patent application extension of 6691/75.

BENSON, F.A. and STEVEN, D.H., "Rectangular Waveguide Attenuation at Millimetre Wavelengths", Proc IEE, Vol 110, No 6, pp 1008-1014, June 1963.

FLAT PLATE ANTENNA SYMPOSIUM, May 23 1978, RSRE, Malvern, England.

HALL, P.S. and JAMES, J.R., 1978 "Survey of design techniques for flat profile microwave antennas and arrays". The Radio and Electronic Engineer, Vol 48, No 10, October.

HALL, P.S. 1978, British provisional patent application, No 29460/78, 11 July.

HAMMERSTAD, E.O. and BEKKADAL, F., 1975 "Microstrip handbook", ELAB report STF 44A74169, University of Trondheim, pp 87-90.

HENDERSON, A. and JAMES, J.R., 1978 "Continuous eigenvalue mode spectrum analysis of microstrip open-circuit terminations". Proceedings of the 8th European Microwave Conference, Paris.

JAMES, J.R. and WILSON, G.J., 1977 "Microstrip antennas and arrays, Pt 1 Fundamental action and limitations", IEE Jour Microwaves, Optics and Acoustics, Sept, Vol 1, No 5, pp 165-174.

JAMES, J.R. and HALL, P.S., 1977 "Microstrip antennas and arrays, Pt 2 New array-design technique", IEE Jour Microwaves, Optics and Acoustics, Sept, Vol 1, No 5, pp 175-181.

JAMES, J.R. and WILSON, G.J., 1975, British provisional patent application 6691/75.

PUCEL, R.A., MASSE, D.J. and HARTWIG, C.P., "Losses in Microstrip", IEEE Trans Vol MTT-16, No 6, pp 342-350, June 1968; plus Vol MTT-16, No 12, p 1064, Dec 1968.

WILLIAMS, J.C. 1978, "A 38GHz Printed Planar Array", Electron Lett., Vol 14, No 5, pp 136-137.

WOOD, C., HALL, P.S., and JAMES, J.R., 1978 "Radiation conductance of open-circuit low dielectric constant microstrip" Electron Lett., Vol 14, No 4, pp 121-123.

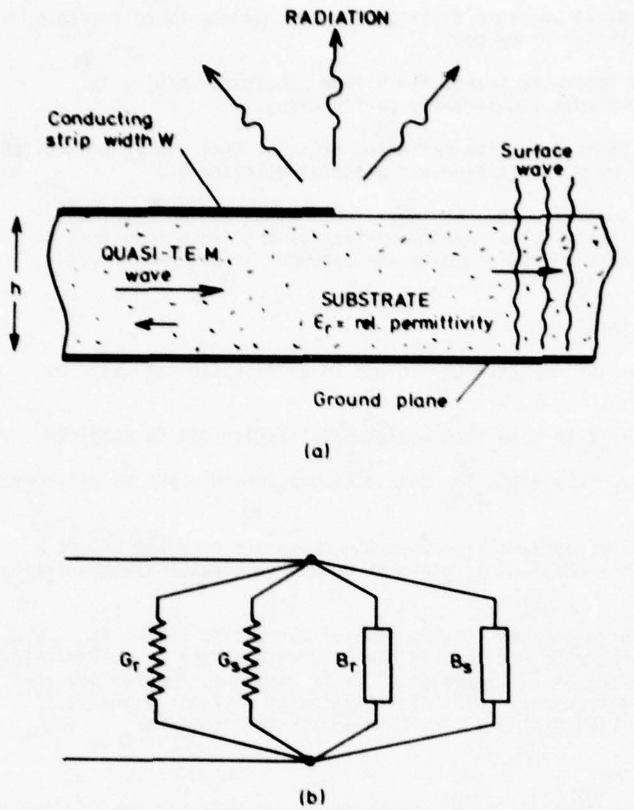
RADIATION
Conducting strip width W
Surface wave
QUASI-T.E.M. wave
h
SUBSTRATE
ϵ_r = rel. permittivity
Ground plane
G_r
G_s
B_r
B_s

(a)

(b)

Fig.1 Admittance Parameters of Microstrip Open-Circuit Termination ; r and s subscripts denote Radiation and Surface wave effects respectively

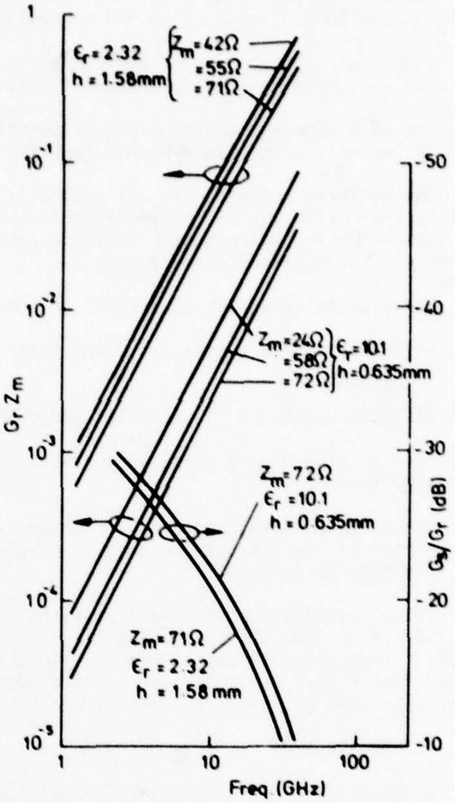

Fig.2 Computed G_r and G_s values.

Z_m is the Microstrip Line Impedance

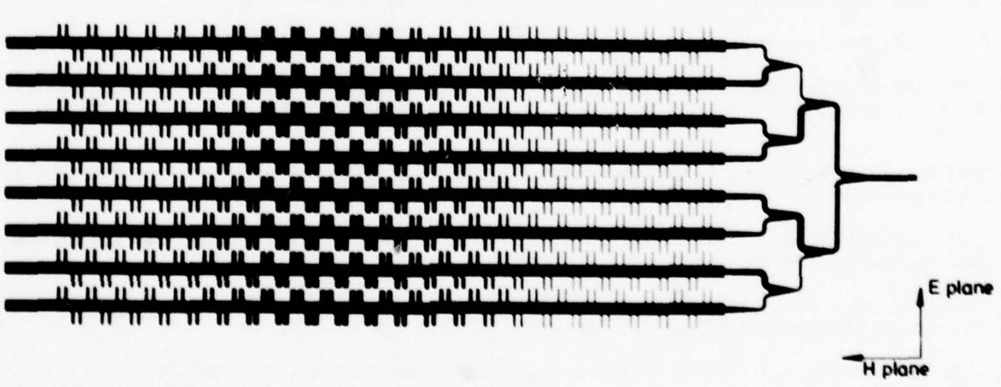
E plane
H plane

Fig.3 Computer Drawn Photographic Mask of Microstrip Antenna Array

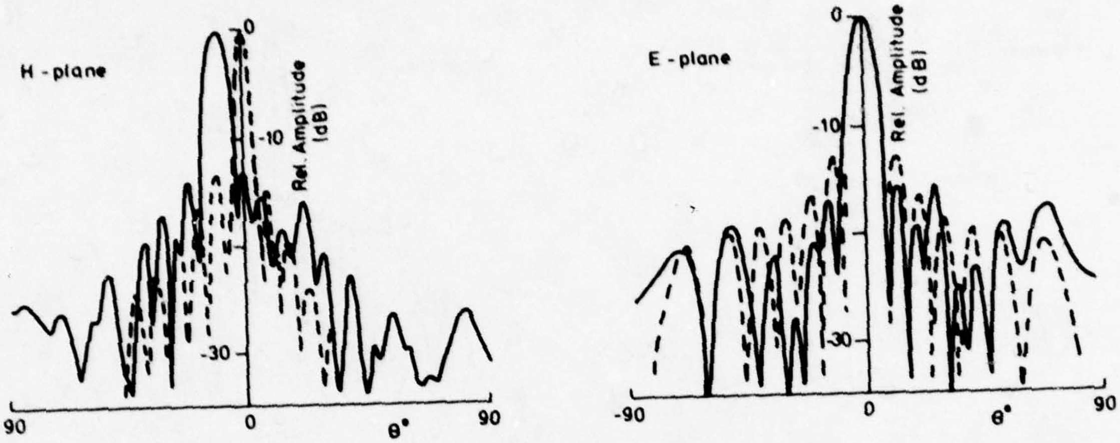

Fig. 4 Radiation Patterns of Uniform Aperture Distribution RT Duroid Array at 36 GHz

—— Measured - - - - Computed, h = 0.79 mm, w = 2.32 mm, ϵ_r = 2.32, l = 2.67 mm

d = 1.4 mm, α = 0.07 dB/strip wavelength, N = 50

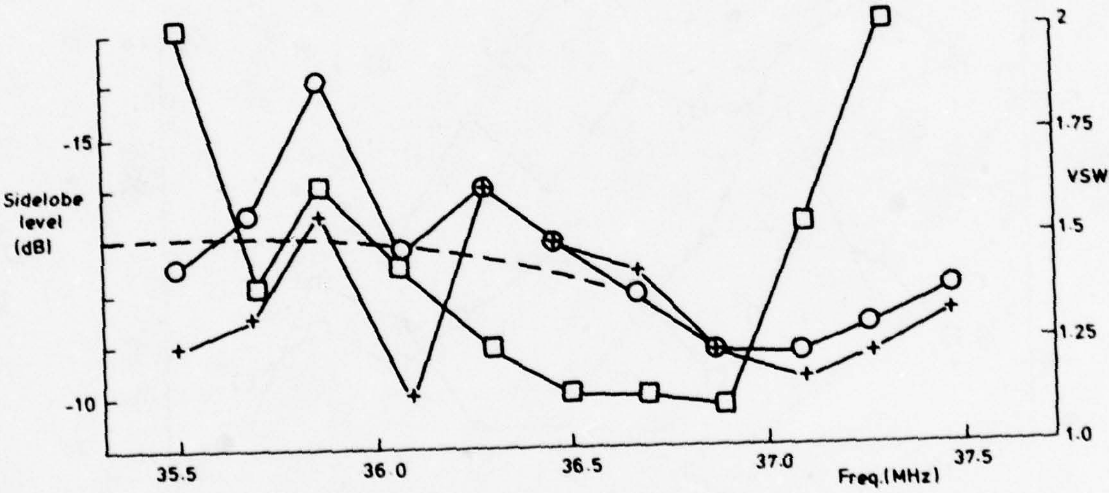

Fig. 5 Behaviour of Array of Fig. 4 as a Function of Frequency

Measured Sidelobe Levels, H-plane +, E-plane ○

Computed Sidelobe Levels, H-plane – – – –

□ VSWR

	Computed (dB)	Measured (dB) (NOT INCLUDING COAX TO TRIPLATE TRANSITION)
P_0	29.7	
η_L	3.1	
η_s	1.0	
$\eta_f + \eta_r$	0.6 + 1.0	
$P_0 - (\eta_L + \eta_s + \eta_f + \eta_r)$	24.0	25.0 ± 2.0
Efficiency		29 %

Table 1

Power Loss and Gain of Array of Fig. 4 at 36 GHz

	Computed (dB)
P_0	27.9
η_L	11.0
η_s	1.5
η_f + radiation	0.6 + >1.0
$P_0 - (\eta_L + \eta_s + \eta_f$ + rad)	< 13.9

Table 2

Power Loss and Gain of Uniform Aperture Alumina Array at 36 GHz; h = 0.5 mm, w = 0.516 mm, ϵ_r = 9.8, l = 1.38 mm, N = 50 d = 0.73 mm, α = 0.08 dB/strip wavelength

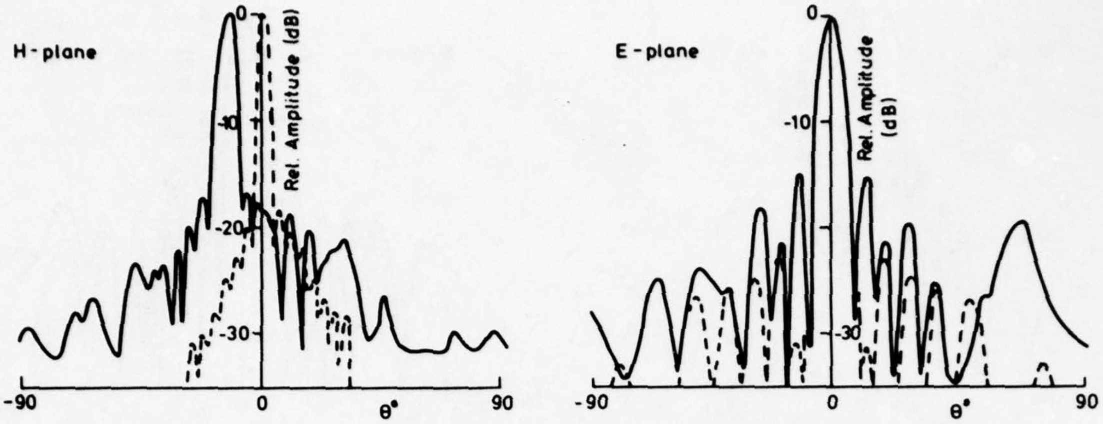

Fig.6. Radiation Patterns of Tapered Aperture Distribution RT Duroid Array at 36 GHz

—— Measured -----Computed h = 0.79 mm, w = 2.32 mm, ϵ_r = 2.32, α = 0.07 dB/strip wavelength

N = 90

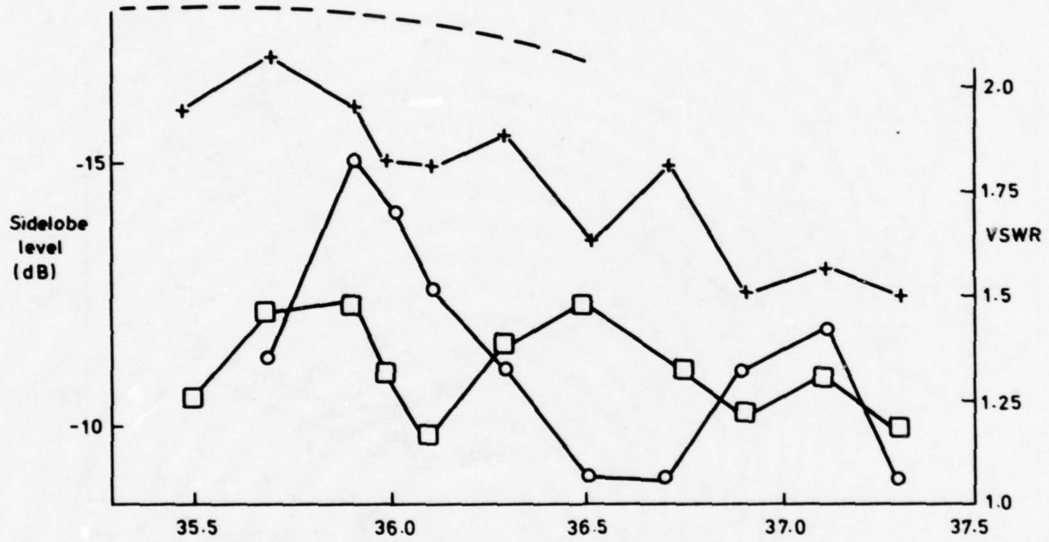

Fig.7 Behaviour of Array of Fig.6 as a Function of Frequency

Measured Sidelobe Levels, H-plane +, E-plane ○

Computed Sidelobe Levels, H-plane - - - -

□ VSWR

	Computed (dB)	Measured (dB) (NOT INCLUDING COAX TO TRIPLATE TRANSITION)
P_G	31.7	
η_L	1.3	
η_s	1.6	
$\eta_f + \eta_r$	0.6 + 1.0	
$P_G - (\eta_L + \eta_s + \eta_f + \eta_r)$	27.2	26.5 ± 2.0
Efficiency		30%

Table 3

Power Loss and Gain of Array of Fig. 6 at 36 GHz

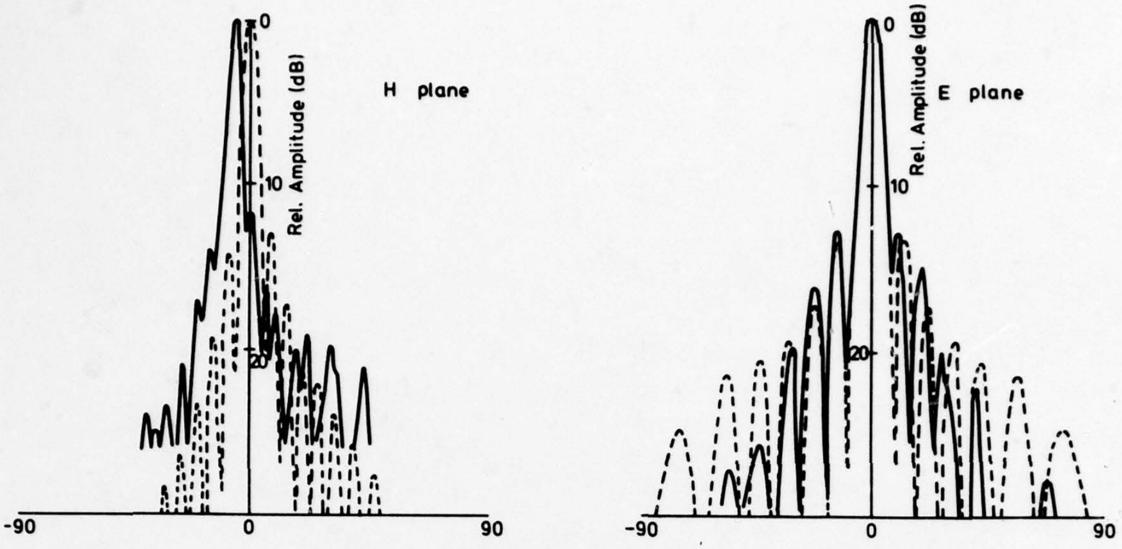

Fig. 8 Radiation Patterns of Uniform Aperture Distribution RT Duroid Array at 70 GHz

——— Measured, – – – Computed, h = 0.25 mm, w = 0.75 mm, $\epsilon_r = 2.32$, l = 1.41 mm

d = 0.73 mm, α = 0.11 dB/strip wavelength, N = 60

	Computed (dB)	Measured (dB) (NOT INCLUDING COAX TO TRIPLATE TRANSITION)
P_G	29.4	
η_L	2.2	
η_s	1.7	
$\eta_f + \eta_r$	0.9+0.5	
$P_G - (\eta_L + \eta_s + \eta_f + \eta_r)$	24.1	23.1 ±2.0
Efficiency		23%

Table 5

Power Loss and Gain of Fig. 8 at 70 GHz

	Computed (dB)	Measured (dB)
P_G	30.6	
η_L	1.2	
η_s	2.4	
$\eta_f + \eta_r$	0.7+ >0.5	
$P_G - (\eta_L + \eta_s + \eta_f + \eta_r)$	< 25.8	17.6 ±2

Table 6

Power Loss and Gain of Uniform Aperture Alumina Array at 70 GHz, h = 0.5 mm, w = 0.514 mm, $\epsilon_r = 9.8$, l = 0.6 mm, N = 110, d = 0.5 mm, α = 0.08 dB/strip wavelength, w_i = 0.1 mm

MILLIMETRE PIN DIODE CONTROL DEVICES

M. L. Nyss
Microwave Associates Ltd.,
Woodside Estate, Humphreys Road,
Dunstable, U.K.

SUMMARY

This paper covers work carried out at Microwave Associates Limited with the support of the Procurement Executive, DCVD, The Ministry of Defence on millimetre wave PIN diode control devices, and will encompass circuit techniques that have been developed to overcome the problem of stray parasitics limiting the performance of high frequency components. The components described operate in the 'reverse tuned' mode in which low loss is achieved when the diode is forward biassed and isolation is achieved when the diode is reverse biassed. Packaged PIN diodes have been used for frequencies up to 38 GHz and unpackaged devices for frequencies up to 70 GHz.

1. INTRODUCTION

Systems operating at millimetre wave frequencies require solid state control components such as switches, attenuators, modulators, duplexers etc. Two types of active device can be employed in these components, PIN diodes and Schottky diodes, but in either case it is important to keep the stray parasitics of the device to a minimum.

Schottky diodes have the advantage of fast switching, making them suitable for fast switches and modulators, but they have a severe limitation with regard to power handling. PIN diodes with a very low minority carrier lifetime can be used in fast switching applications with an increase in power handling over Schottky diodes. In addition, PIN diodes with a large I region thickness can be used in applications where high peak or mean power handling capability is required.

Three components are described in this paper:

(i) A fast Q-band modulator (26 - 40) GHz

(ii) A fast O-band modulator (50 - 70) GHz

(iii) A Q-band Duplexer

2. Q-BAND MODULATOR

The initial objectives were to produce a fast PIN modulator operating over a 3% band at 30 GHz for use in a high speed digital data link. However, techniques were developed which demonstrated that waveguide switches and modulators using packaged PIN diodes can operate over a 20% band. The main problem encountered in components operating at these frequencies using packaged diodes is the limitation in performance due to the package parasitics. The method used to overcome this problem is to utilise these parasitics in conjunction with the diode capacitance and bonding inductance to carry out the switching function.

Fig. 1 shows the simplified equivalent circuit of a packaged PIN diode. Under forward bias, the package capacitance, if correctly chosen, can be made to resonate with the package and bonding inductance at the desired operating frequency. The resultant high impedance, if placed across a transmission line of suitable characteristic impedance, results in a low loss condition. Under reverse bias, the junction capacitance forms a resonant structure with the bonding and package inductance resulting in a low impedance across the transmission line.

This gives an isolation condition. Clearly there exists a compromise between the isolation and insertion loss of the device, depending upon the impedance of the transmission line.

The first decision that had to be made, was the choice of a suitable diode package; one with a package capacitance that could be resonated with the stray inductance, and in addition, having physical dimensions considerably smaller than a quarter wave length at the operating frequency.

To this end, the Microwave Associates ODS 33 package was selected as meeting these requirements (Fig. 2)

The next problem was how to physically mount the package across the transmission line, and how to apply bias to the diode. The method chosen is shown in Fig. 3.

The packaged diode is mounted between the top wall of the waveguide, and a section of ridged guide with 75 ohm characteristic impedance. This is matched to the waveguide impedance by a 4-step Tchebyshev transformer at each end. The ridge is DC isolated from the base of the waveguide by a mylar shim .05mm thick and held in place by two nylon screws. It is important to keep the mylar shim as thin as possible in order to prevent the propogation of other modes under the ridge.

Bias is applied to the diode via this ridge, obviating the necessity for any bias filter, and earth contact is achieved by deforming the waveguide above the diode. The deformation is of the order of only .05mm, and does not impair the RF performance. The maximum width of the ridge is determined by the Te$_{20}$ cut off frequency, which must be maintained higher than the maximum operating frequency.

This construction for the modulator has proven both mechanically and electrically sound in addition to being very reproducible.

Fig. 4 shows the construction of the PIN diode used in the fast modulator. It consists of a mesa diode utilising an inverse PIN structure mounted on an integral copper plate heat sink, similar to that used in Impatt diodes.

The N$^+$ layer is thinned using a spin etch process after the heat sink has been plated. The main advantage of this construction is the reduction of the R$_s$, and consequently the insertion loss of the diode by reducing the spreading resistance of the N$^+$ layer.

It has been proven that the insertion loss of a diode manufactured in this way has a 1dB improvement at 30 GHz over that of a conventional PIN diode of the same capacitance and I region thickness.

The performance of a modulator incorporating two diodes spaced $3\lambda_g/4$ apart and using the techniques just described is shown in Fig. 5.

The switching speed from 10% to 90% of the detected RF pulse is less than 1 nS, although there is a delay of about 6 nS from 50% of the TTL input to 10% of the RF pulse.

This modulator was incorporated in an ASK digital data link operating in excess of 120 m.bits/second with a transmit power of 500 m.watts. To date, no problems have been encountered with reliability.

It is possible to vary the centre frequency of the operating band by using packages with a different stray capacitance, and a modulator operating up to 38 GHz has been built.

3. O-BAND MODULATOR

The techniques employed in the Q-band modulator have also been used for an O-band modulator operating at 60 GHz. However, in this case, it was not possible to use packaged diodes because of the constraints of physical size.

To overcome this problem, an unpackaged diode was mounted on top of the ridge adjacent to a quartz stand-off, as shown in Fig. 6. A wide bonding strap, tapered at one end, was used to achieve the inductance necessary to resonate the capacitance of the stand-off at 60 GHz.

Mylar windows were incorporated at each end of the waveguide in order to hermetically seal the unit. Fig. 7 shows the performance of the modulator, which had less than 1½ dB insertion loss, and greater than 20 dB isolation over a 6 GHz band. The switching speed of the device was less than 1 nS.

4. Q-BAND DUPLEXER

Fig. 8 shows a block schematic of the duplexer which is of a balanced configuration. Two reflective PIN switches are mounted between two 3 dB hybrid couplers. During the transmit period, the switches are isolating and the power reflected from them appears at the antenna. During the receive period, the switches are in their low loss state, and the transmitted power is recombined by the 3 dB hybrid and appears at the receiver port.

Clearly, since the transmitter is turned off during the receive period, the switches only have to handle the transmitter power in the isolation state. Tapered transformers are used in place of stepped transformers in order to avoid the possibility of breakdown on high peak powers. In addition to this, the waveguide is pressurised at 2 atmospheres.

The diode in this application is a conventional PIN mesa structure, with an I region thickness of 120 microns. The surface of the junction is passivated with a thermally grown layer of silicon dioxide. An insertion loss of less than 1½ dB's and an isolation greater than 20 dB's over a 4 GHz band at 35 GHz was achieved for the switch.

This switch has been tested up to power levels of 20 kilowatts peak, and 100 nS pulse width in its isolation state, after which no apparent degradation of the DC characteristics of the diode occurred.

An active duplexer, incorporating two of these switches, has yet to be built, but work is continuing.

REVERSE BIAS

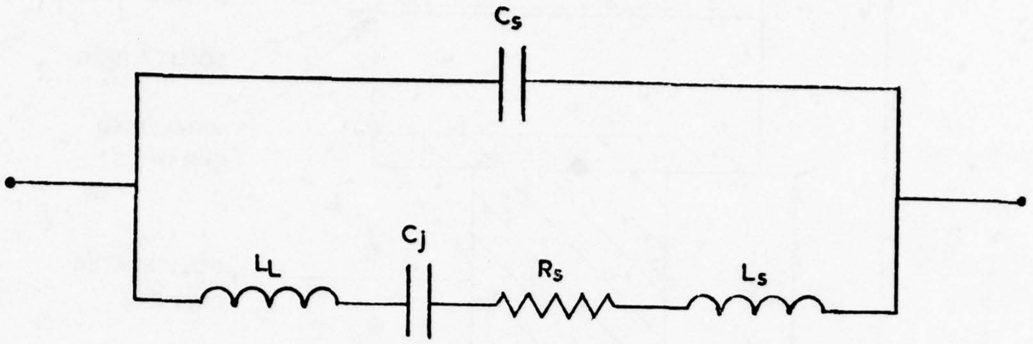

FORWARD BIAS

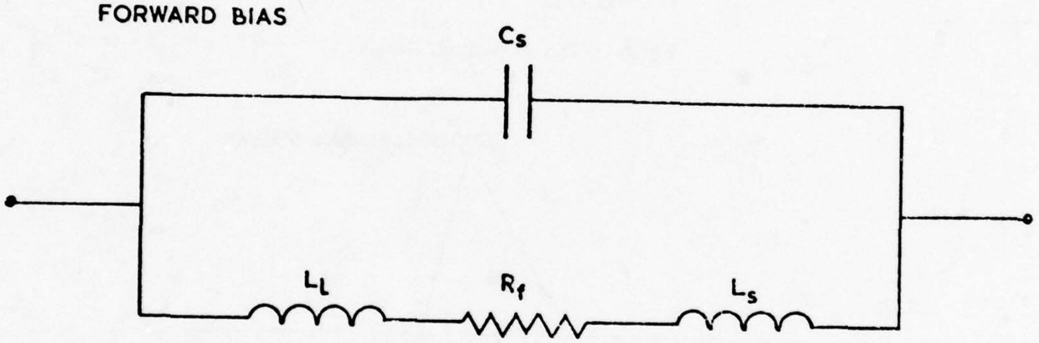

Junction Capacitance Diode	C_j	0.15 pf
Series Resistance Diode	R_s	2.5 ohm
Forward Bias Resistance	R_f	1.0ohm
Lead Inductance	L_L	0.08nH
Package Stray Inductance	L_s	0.10nH
Package Stray Capacitance	C_s	0.17 pf

Fig.1 Equivalent circuit of packaged diode

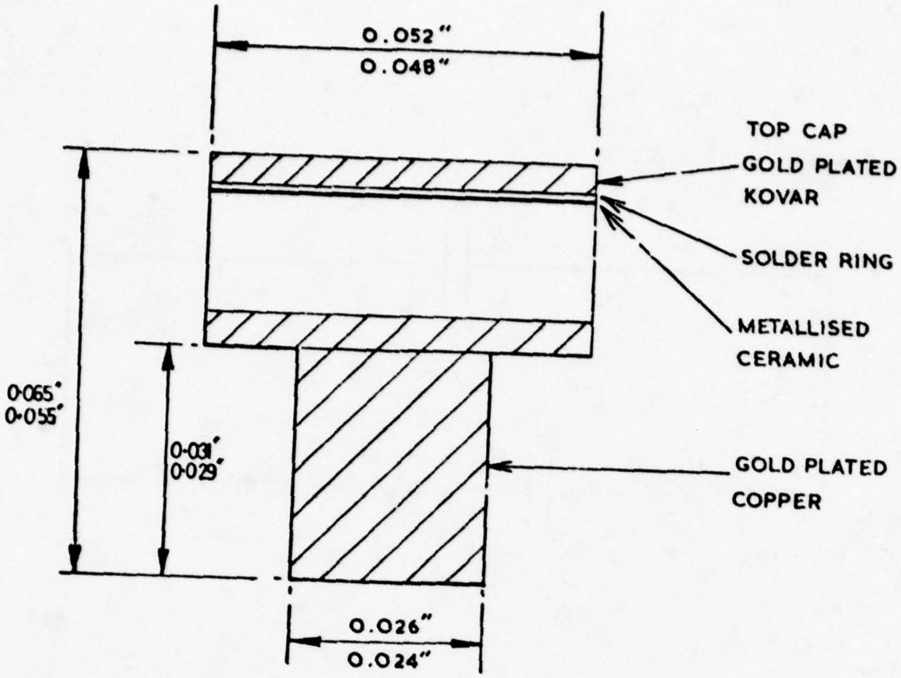
0.052"
0.048"
TOP CAP
GOLD PLATED
KOVAR
SOLDER RING
METALLISED
CERAMIC
0·065"
0·055"
0·031"
0·029"
GOLD PLATED
COPPER
0.026"
0.024"

Fig.2 O.D.S 33 without flange

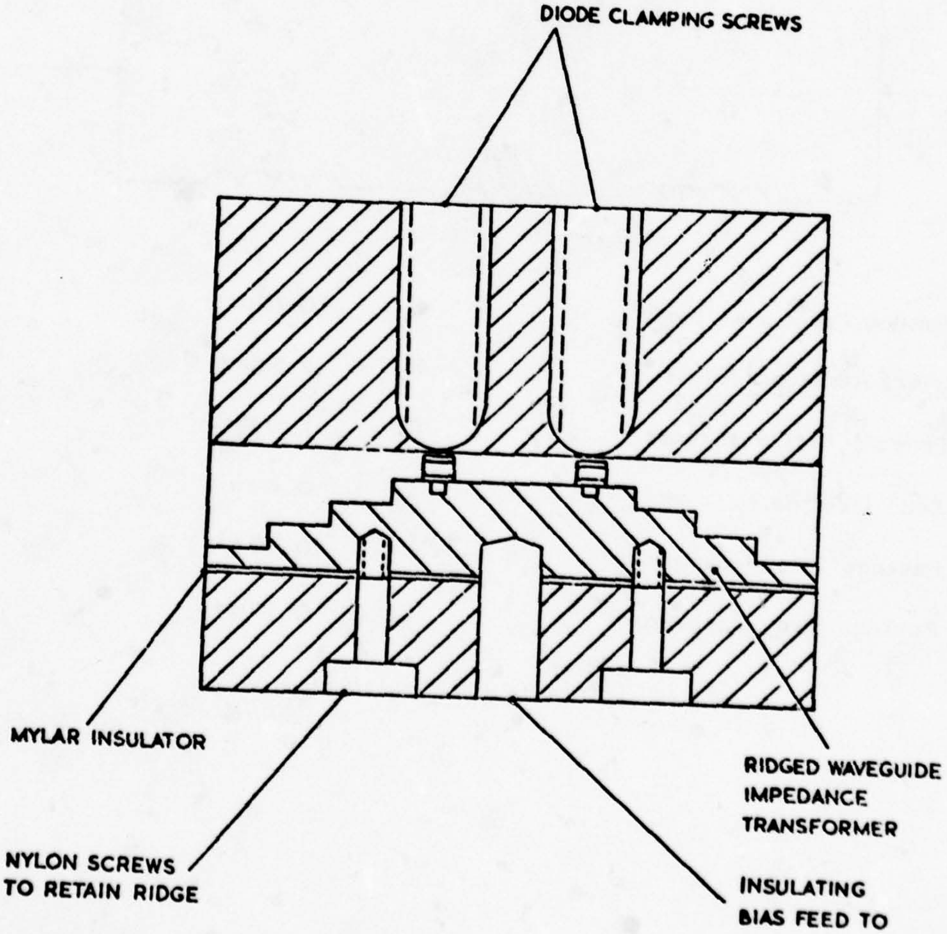
DIODE CLAMPING SCREWS
MYLAR INSULATOR
RIDGED WAVEGUIDE
IMPEDANCE
TRANSFORMER
NYLON SCREWS
TO RETAIN RIDGE
INSULATING
BIAS FEED TO
RIDGE

Fig.3 Section through R.F circuit

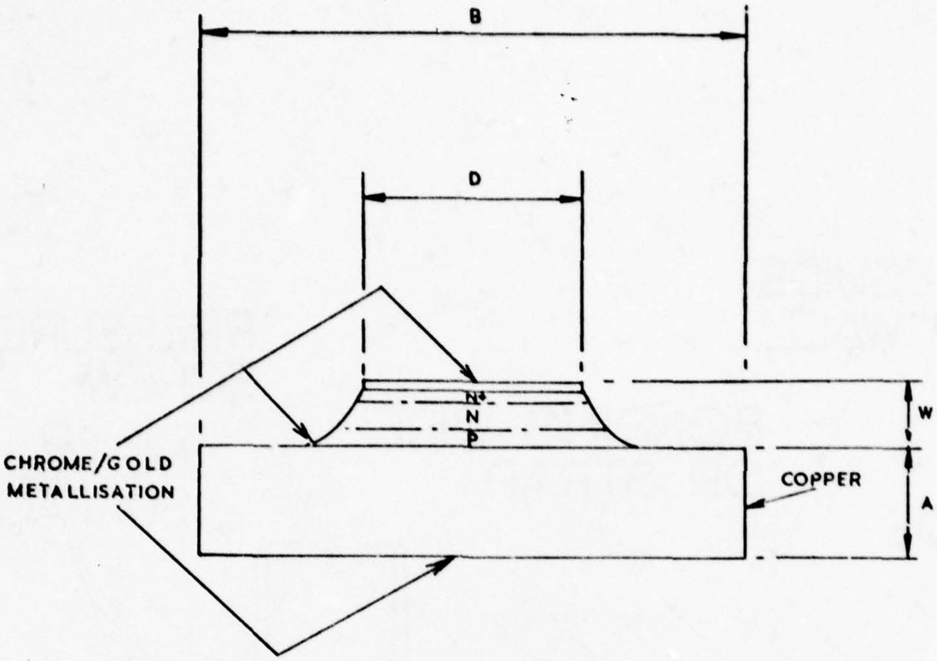
B
D
N+
N
P
W
A
CHROME/GOLD METALLISATION
COPPER

Fig.4 Inverse P.I.N. diode

Mesa diameter	D	0.0017"
Diode thickness	W	0.0008"
Heatsink thickness	A	0.005"
Heatsink width	B	0.020"

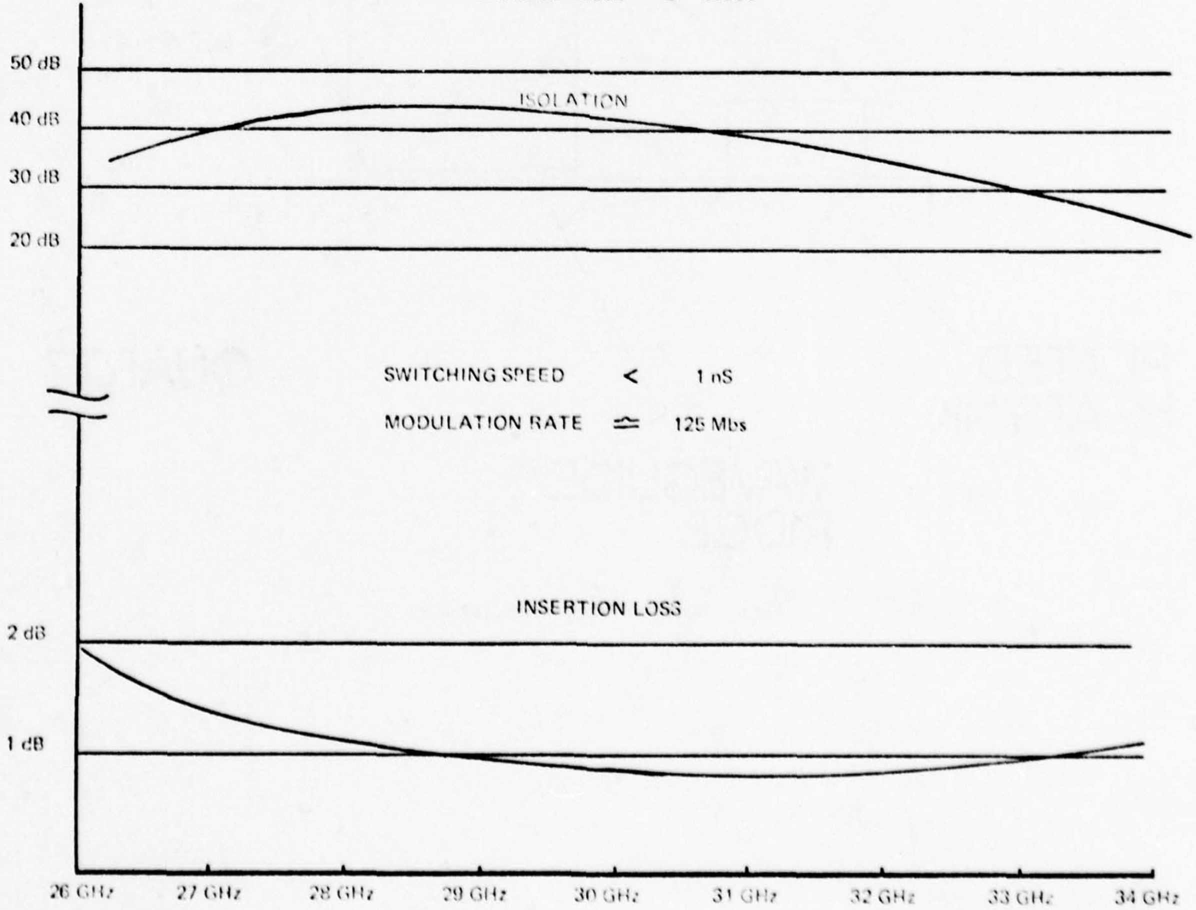

Fig.5 Q-band modulator performance

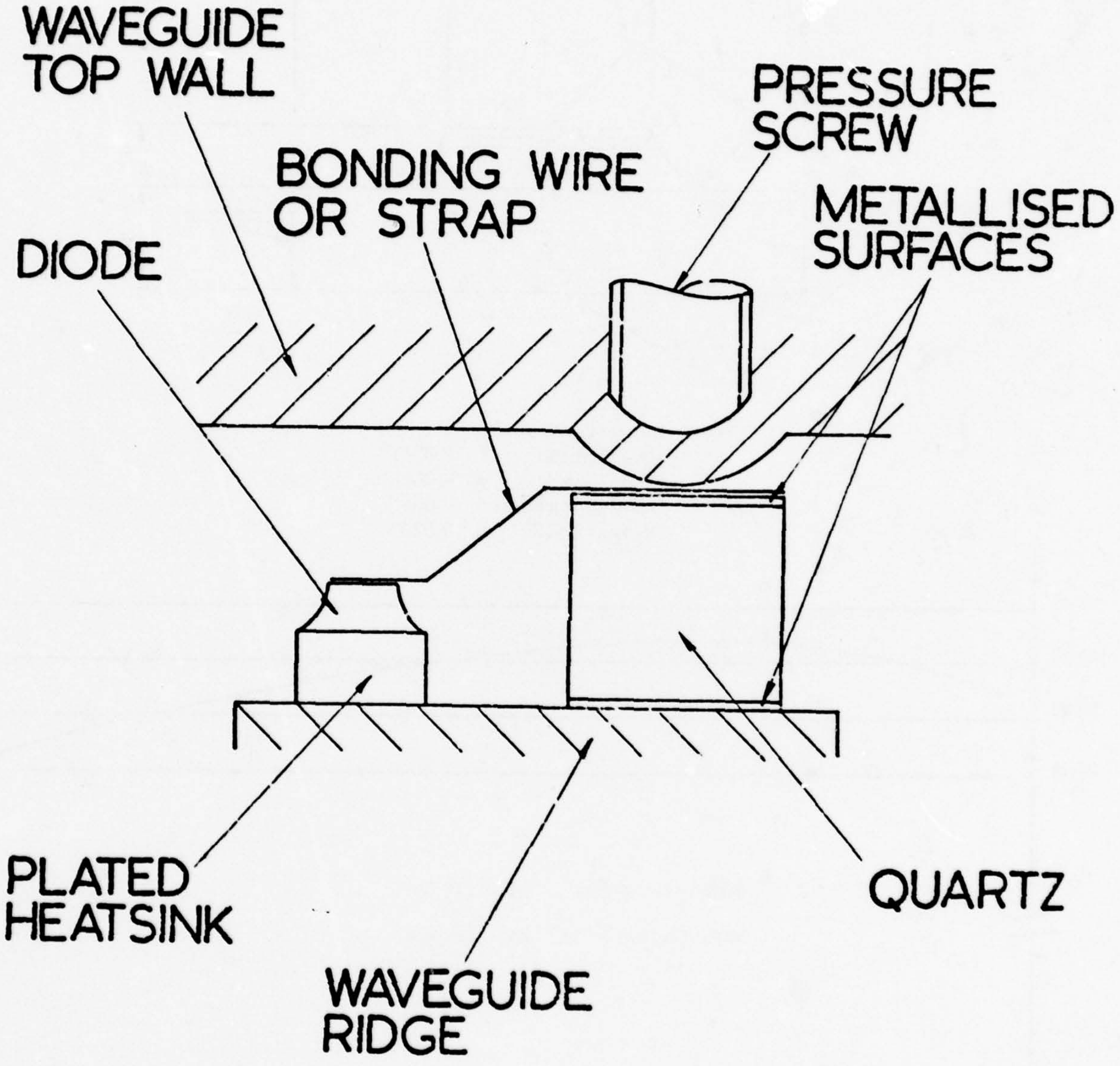
WAVEGUIDE TOP WALL
PRESSURE SCREW
BONDING WIRE OR STRAP
METALLISED SURFACES
DIODE
PLATED HEATSINK
QUARTZ
WAVEGUIDE RIDGE

Fig.6 Detail of diode resonant circuit

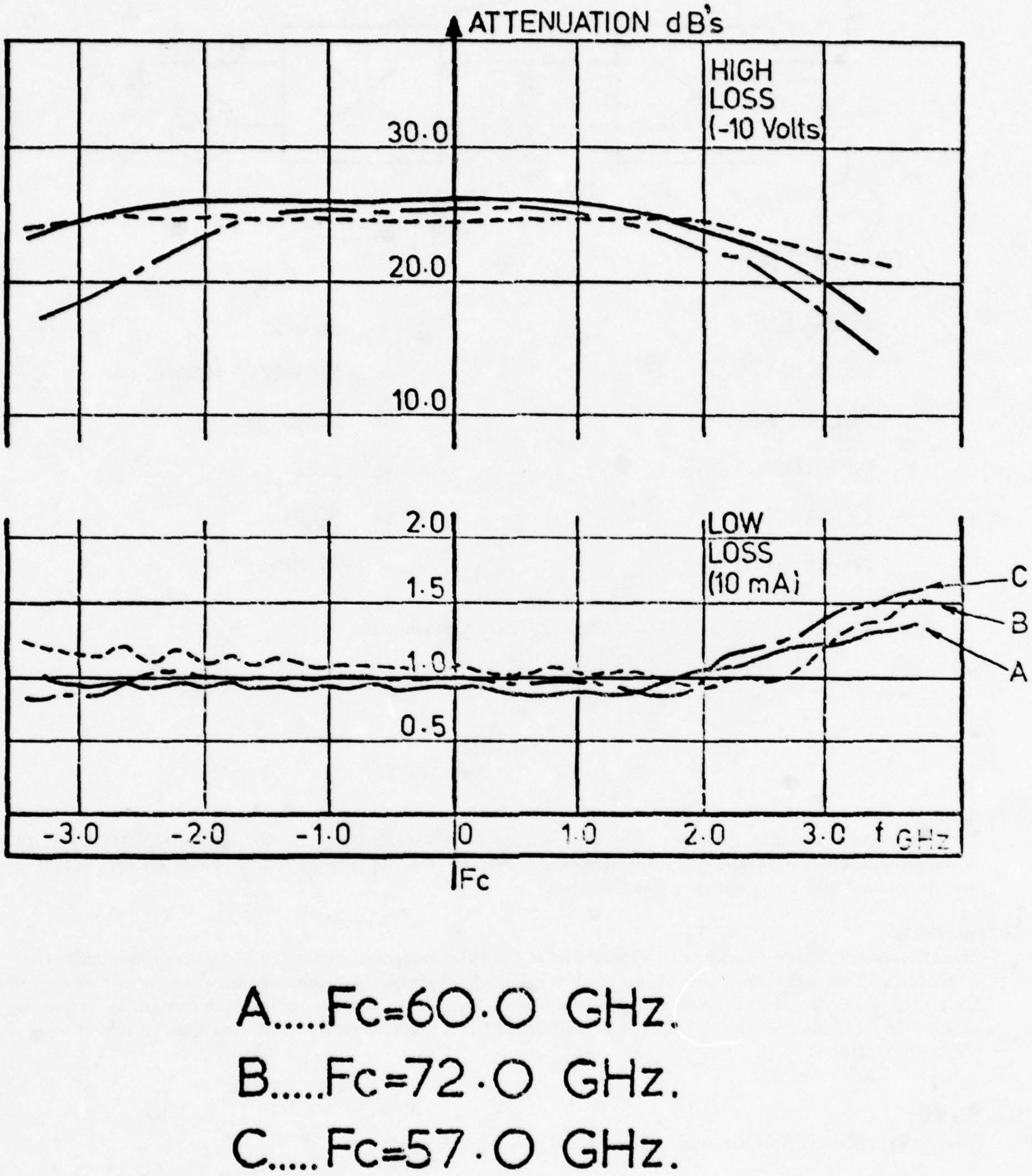

Fig.7 Switch performance

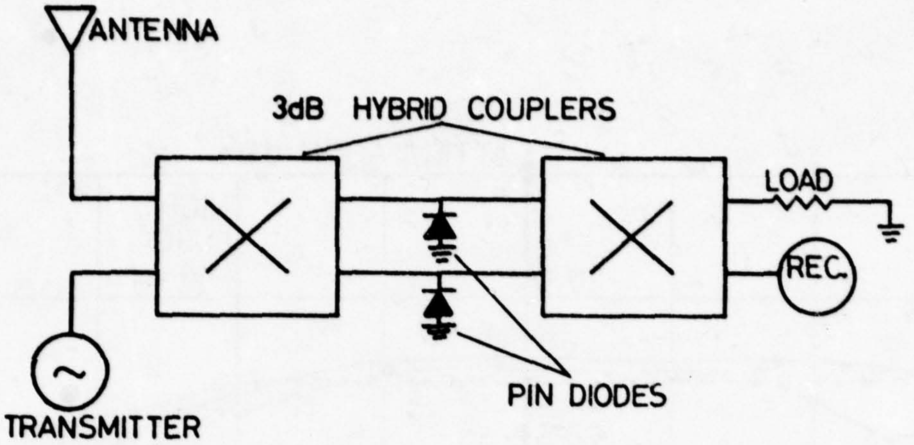

FREQUENCY = 35GHz
PEAK POWER = 15Kw(2w mean)
PULSE WIDTH = 35nS
INSERTION LOSS < 2dB
ISOLATION > 30dB
BAND WIDTH > 2GHz

Fig.8 Basic duplexer requirements

DISCUSSION

F.Fedi, Italy

I understand your pin diode modulator may work around 30 or 60 GHz with a bit rate of about 125 Mbit/sec. As in communication digital systems at these frequencies 140 Mbit/sec is usually used, do you envisage that this bit rate may be reached with the modulation you described?

Author's Reply

These modulators can be operated at 140 Mbits/sec with further improvements in the driver unit to overcome the driver delay. This delay is made up of two parts, the delay through the driver and the delay due to the carrier lifetime of the diode. The delay due to the carrier lifetime only occurs when watching from forward to reverse bias on the diode thus making the total delay non-symmetrical. It is this asymmetry which limits the bit rate of the present modulations.

H.Brand, FRG

How long is the delay time between logic pulse and f-power envelope?

Author's Reply

5 ns, due to bias capacitance, carrier life time and a delay through the driver.

MILLIMETER PULSE MODULATION WITH LUMPED ELEMENT CIRCUITRY

E. Kpodzo, G. Begemann, and K. Schuenemann
Institut für Hochfrequenztechnik, Technische Universität Braunschweig,
Postfach 3329, D-3300 Braunschweig, FRG

ABSTRACT

This contribution deals with both AM and PM pulse modulators for millimeter waves using lumped element circuits. A circuit technique will be described which utilizes evanescent mode resonators. In this technique, inductance is represented by short sections of rectangular waveguide below cutoff, capacitance by obstacles in the waveguide, such as capacitive screw or a thin sheet of dielectric. The diode imbedding is assumed to be a matching network. By applying a new mathematical technique known as matching of the hyperbolic middle point of the pin-diode impedances a broader band performance has been achieved compared to typical bandwidths of phase modulators in the Q-band region. The 180° reflection modulator shows 12 o/o bandwidth and an insertion loss below 0.7 dB. The AM-modulator has a bandwidth exceeding 3 o/o, while its reflection factor in the foward state remains below 0.5 dB, for the reverse state a factor above 20 dB has been realized. A new type of transmission modulator with a phase shift of 45° has also been developed with two diodes switching elements having an insertion loss below 0.5 dB.

1. INTRODUCTION

Modern radio links, satellite, radar, phased arrays and communication systems in the millimeter wave region make extensive use of fast digital phase modulators and switches. As has widely been accepted the modulation should be performed in an extra modulator rather than in the oscillator itself. Phase modulators can be divided into two main categories: the reflection type and the transmission type. Both types are going to be described in this paper and practical examples of the reflection type utilizing pin-diodes will be thoroughly elaborated.

For phased arrays applications pin-diode phase modulators pocess important advantages over other types of similar millimeter wave devices; these are light weight, temperature sensitivity, repeatable insertion loss and phase characteristics, simple driver requirements and high switching speed.

The basic requirements to a phase modulator can be summarized as follows (SCHUENEMANN, K., MUELLER, J., DORSCHNER, T.A., SPORLEDER, F., 1975):

a) The amplitude error (i.e. the imbalance in the reflection coefficients for the two states) must notexceed 5 o/o in order not to degrade the demodulated signal amplitude by more than 0.3 dB.

b) The phase error must not exceed ±4° for the same reason.

c) The switching times must be short as compared to the pulse width. Here again a switching time to pulse width ratio 1:4 limits the degradation of the demodulator output signal to 0.3 dB as compared to the case of abrupt switching.

d) The insertion loss should be kept as low as possible.

e) The modulator bandwidth (i. e. the frequency range in which a given maximum phase and amplitude error will not be exceeded) must have a particular value normally given by system considerations.

f) The transient input reflection coefficient trace of the modulator should go through the matching point of the Smith-chart in order not to degrade the system signal-to-noise ratio. In the case of a transient reflection coefficient, whose magnitude stays constant, some extra components in the output spectrum of the modulator will be generated which can lead to unwanted portions in the demodulator output signal.

It is however not an easy task to fulfil all these requirements simultaneously.

2. REFLECTION PHASE MODULATOR AS AN IMPEDANCE MATCHING NETWORK PROBLEM

The compromise which has to be undergone to fulfil the requirements on a phase modulator in a PCM communication system can be explained by thorough examination of the relations between the pin-diode (nonlinear element) and its imbedding. Due to certain nonideal qualities such as diode losses, finite switching times and package parasitics the impedances of a pin-diode in foward and reversed state differ in magnitude and an 180 degrees phase difference between the two states will not be achieved. Therefore the diode imbedding must simultaneously transform the two diode states so as to give the modulator input equal magnitudes of reflection coefficients and the desired phase difference (usually 180 degrees for a two level DCPSK, Differentially Coherent Phase Shift Keying). In a case of a 180 degrees modulator it will be shown that the imbedding network has just to match the hyperbolic middle point of the diode impedances (DORSCHNER, T.A., 1973) making use of the guidelines of hyperbolic geometry.

To carry out the transformation successfully the modulator will be assumed to be a lossless linear imbedding of a nonideal, two-state switching element. Let the two diode states be represented by the impedances Z_1 and Z_2 or the reflection coefficients ϱ_1 and ϱ_2. For a lossless imbedding the insertion loss of the modulator can be assumed to be diode losses. These losses will be described in this context by the quality factor Q introduced by Kurokawa and Schlosser.

2.1. MATHEMATICAL DEFINITIONS OF THE HYPERBOLIC GEOMETRY

The euclidian geometry and the hyperbolic geometry differ from one another only through the axiom of parallels. Let us assume a straight line with a point outside it. In the euclidian geometry there can be only one line through this point parallel to the already existing straight line. In the hyperbolic geometry on the other hand there is an infinite number of such parallel lines. These complicated axioms are illustrated in Fig. 1. The hyperbolic plane lies completely within the unit circle and coinsides therefore with the plane of the Smith-chart. The relationship between the euclidian length and the hyperbolic length of a distance between $\varrho = 0$ and $\varrho = \varrho_1$ can be expressed in the following equation:

$$\left[0,\varrho_1\right] = k\cdot\ln\frac{1+\overline{0,\varrho_1}}{1-\overline{0,\varrho_1}} \qquad (2.1)$$

$\left[0,\varrho_1\right]$: hyperbolic length between the two points

$\overline{0,\varrho_1}$: euclidian length between the same two points as above.

k : a constant

For a special case when $\overline{0,\varrho_1}$ becomes ±1, $\left[0,\varrho_1\right]$ takes the values of ± infinity. This means that the borders of the Smith-chart coincide with infinite points of the hyperbolic geometry. The influence of the constant k is shown for two special cases in Fig. 1.:

Case 1: $k = 1/2$

a) a hyperbolic straight line appears here also as a straight line in the euclidian sense.

b) Lengths and angles can be measured with a protractor (of course through measurements and calculations).

c) the angles are not euclidian.

Case 2: $k = 1$

a) a hyperbolic straight line is part of an euclidian circle.

b) the hyperbolic straight line meets the euclidian unit circle at right angle.

c) the angles can be considered euclidian.

One important aspect of the hyperbolic geometry being applied by this network matching theory is the congruency of two triangles when the corresponding angles are equal in magnitude.

2.2. QUALITY FACTOR OF SWITCHING DIODES

A quality factor of switching diodes (KUROKAWA, K., SCHLOSSER, W.O., 1970) is defined by

$$Q = \sqrt{\frac{(r_1+r_2)^2+(x_1-x_2)^2}{r_1\cdot r_2}} \qquad (2.2)$$

where $Z_1 = r_1+jx_1$

and $Z_2 = r_2+jx_2$

are the diode impedances in the two states.

Taking the reflection coefficients into consideration the same quality factor can be redefined as

$$Q = \frac{2\cdot|\varrho_1-\varrho_2|}{\sqrt{\left[(1-|\varrho_1|^2)\ (1-|\varrho_2|^2)\right]}} \tag{2.3}$$

where $\varrho_1 = |\varrho_1|\cdot e^{j\varphi 1}$

and $\varrho_2 = |\varrho_2|\cdot e^{j\varphi 2}$

are the reflection coefficients in the two states.
The introduction of this quality factor has various advantages. Q is invariant to lossless imbeddings (see Fig. 2) and express the relationship between the losses in the two switching states of the diode in a way which shows what tradeoff exists between the two states for a particular diode configuration. Assuming equal losses in both states one can write:

$$1-|\varrho_1|^2 = 1-|\varrho_2|^2 = 4(\sin \tfrac{\phi}{2}/Q)^2\ \left(\sqrt{Q/\sin \phi/2)^2+4}-2\right) \tag{2.4}$$

where ϕ is the phase shift between the two states.
The transformed quality factor Q' which is the quality factor at the input of the matching network (Fig.2a.) can be easily determined through network analyzer measurements in form of the reflection coefficients in the millimeter wave range. Therefore making use of the simplified diode model in Fig. 2b.

Q has the Form $$Q = \frac{1}{\omega r_1 C} \tag{2.5}$$

which gives a simple handy formular for the description of pin-diode losses. C is the pin-diode capacitance.

2.3. MATCHING OF THE HYPERBOLIC MIDDLE POINT FOR A 180 DEGREES REFLECTION PHASE MODULATOR

Z_M and ϱ_M are the hyperbolic middle point of the diode for impedance and reflection coefficient matching respectively. Important for the middle point matching are the relationships $\varrho_M = f(\varrho_1,\varrho_2)$ and $Z_M = f(Z_1,Z_2)$. The figures 3 and 4 show the process of the transformation. ϱ_1', ϱ_2' and ϱ_M' or Z_1', Z_2' and Z_M' are transformed hyperbolic values respectively. Segments $[\varrho_1,\varrho_M]$ and $[\varrho_2,\varrho_M]$ (e.g. refl. coeff.case) have equal hyperbolic lengths and subtend an angle of 180 degrees relative to ϱ_M or Z_M. Since lossless bilinear transformations are congruent and at the same time preserving the angle and distance relationships, any lossless network which matches $\varrho_M(Z_M)$ is also a 180 degrees modulator. It is also correct to say the matching of $\varrho_M(Z_M)$ is a condition for the network to be a 180 degrees modulator. Making use of the euclidian law of displacement the values $\varrho_M = f(\varrho_1,\varrho_2)$ and $Z_M = f(Z_1,Z_2)$ can finally be determined mathematically to be:

$$\varrho_M = \frac{1}{\varrho_1^*(1-|\varrho_2|^2)+\varrho_2^*(1-|\varrho_1|^2)}\cdot\left(1-|\varrho_1\varrho_2|^2-\sqrt{(1-|\varrho_1.\varrho_2|^2-|\varrho_1(1-|\varrho_2|^2)+\varrho_2(1-|\varrho_1|^2)|^2}\right) \tag{2.6}$$

$$r_M = \sqrt{r_1r_2\left(1+\left(\frac{x_1-x_2}{r_1+r_2}\right)^2\right)} \tag{2.7}$$

$$x_M = \frac{x_1r_2+x_2r_1}{r_1+r_2} \tag{2.8}$$

ρ_1^* and ρ_2^* are the congugate complex values of ρ_1 and ρ_2 respectively.

The hyperbolic middle point impedance of a pin-diode is known to be a low one having values in the region of 10-30Ω for millimeter wave applications. It is therefore easier to match the middle point impedance to a 50Ω tranmission line than to a 500Ω transmission line. This means that to achieve a reasonable standing wave ratio the impedance seen by the diode has to be in the region of 10Ω to 30Ω.

Based on the hyperbolic theory it has herewith been shown that, for a reflection type phase modulator the network between the diode and the waveguide can be considered as a matching network facilitating a more optimal design criteria for reflection type modulators.

4. DESCRIPTION OF THE REFLECTION PHASE MODULATOR

Many versions of phase modulators have been designed, but none of these designs have exploited the full bandwidth possibilities of these circuits. Most designs have a maximum bandwidth of barely 1o/o, although most of the circuits have greater bandwidth potential.

The bandwidths and maximum phase shifts of phase modulators have been limited by resonance effects which cause notches in the amplitude response and large errors in the phase response. By eliminating these resonance effects, ultra-broad-band phase modulators with large amounts of phase shifts can be realized. The contribution to be presented in this paper deals with a new type of reflection modulator with broadband performance in the millimeter wave region utilizing lumped element circuit. This type of modulator has also good AM qualities achieved by practical tuning facilities which will also be discussed in the later part of this contribution.

The modulator to be discussed utilizes evanescent mode technique for the Q band range. Fig.5a. shows the reflection type modulator. The pin-diode D is imbedded in a below cutoff waveguide. The cutoff frequency of the evanescent mode waveguide W_2 lies above the operating frequency of the modulator. The input and output coupling over a circulator is performed through the propagating waveguide W_1. The two waveguides W_1 and W_2 are coupled to each other by a narrow slot in their common walls. The characteristic features of the circuit which is being presented here is not a passive resonance circuit in the conventional sense, since the TE_{10}-mode stores more magnetic than electric energy by operation below the cutoff frequency of the evanescent mode waveguide. Resonance is achieved by introduction of a nonlinear device which is designed to store mainly electric energy and thereby establishing the necessary balance between the time averageamounts of electric and magnetic stored energies. The resonance structure can be assumed to be in the immediate surroundings of the active element (e.g. pin-diode) being used.

To ease the complications involved in the tuning of the modulators, additional resonators have to be introduced in the below cutoff waveguide by means of tuning screws. Creation of additional resonators enlarges the bandwidth of the modulator in a way, which is similar to the method of reactance compensation well known from injection locked amplifiers for FM signals. The resonant frequencies for the realisation of this network have to be chosen in such a way that one is above and the other below the resonant frequency of the diode imbedding.

As shown in Fig.5a. the resonator is just a thin slice of waveguide below cutoff with a capacitive tuning element imbedded in it. Fig.5b. shows a photograph of this device. The modulator network can therefore be modeled by the equivalent circuit of Fig.6. The network consists of three resonant circuits: the pin-diode itself and the two tuning screws S_1 and S_2. The resonators are inductively coupled to one another, which can be explained by well known inductive characteristic of cutoff waveguides. The coupling strength between the resonators can be controlled by suitably choosing the distance between a screw and a diode. The coupling slot in the common wall between the cutoff waveguide and the propagating waveguide is modelledby a coupling reactance Z_R and an ideal transformer . Measurements with a network analyzer confirm the equivalent circuit of Fig.6. The screws have a capacitive behaviour until their ends touch the opposite wall of the cutoff waveguide. If so they then become inductive.

The equivalent circuit of the reflection modulator is herewith successfully modelled for practical realization of the modulator.

5. BASIC FEATURES OF THE REFLECTION MODULATOR

An evanescent mode modulator has a significant feature of broadband performance, due to the peculiar character of this network. The individual elements approximate lumped elements in a large frequency range. One can practically assume the absence of capacitive parasitic elements in networks realized below cutoff. There is no periodic relationship between reactance and frequency as in distributed networks, for progressive waves are not supported in such a structure. In order to see the relevance of these features, one has to consider a 180 degrees reflection phase modulator as a circuit, which has to match the hyperbolic middle point of the two impedance states of the pin-diode to the line impedance as has already been explained in chapter 3. Because of the lumped element character of the circuit any impedance transformation, which must be performed is hence a broadband one.

Another advantage of the technique is that a given equivalent circuit can be realized without introducing parasitic elements of capacitive character into the set up, because generally in an evanescent mode structure, all types of discontinuities with the exception of screws and thin sheets of dielectric behave like inductances (SCHUENEMANN,K., KNOECHEL,R., BEGEMANN,G., 1977). The only parasitic elements present are of inductive character. Hence their effect can entirely be included in the resultant inductance of the cutoff waveguide. The situation is quite different in normal waveguide technique. Here a circuit realization introduces a lot of inductive and capacitive parasitic elements, which strongly limit the electrical performance.

Based on the facts that the structure has lumped element character and the lack of parasitic elements, the modulator can adequately be described by the equivalent circuit shown in Fig.6. underlining its broadband performance. Further advantages of the technique are small circuit losses and a substantial reduction in size, weight and cost of both passive and active components.

6. FILTER TRANSMISSION TYPE PHASE MODULATOR

The types of transmission phase modulators so far known are the loaded line, the high-low pass and the switched line phase shifters. The one now going to be described is a new type making use of the typical qualities of a bandpass filter. While the phase shifters mentioned above can be limited to low impedance networks for large phase shifts, the filter type can be applied for any line impedance values.

6.1. QUALITIES OF A FILTER

It is generally known that every filter has got not only insertion loss but also a phase shift of the output signal relative to the input signal. Making use of the [ABCD]-Matrix and values based on Fig.7. the insertion loss and the phase shift of a bandpass filter consisting of two resonators are expressed by the following equations:

$$a_{ins}\ \mathrm{dB} = 10.\log \left\{ \frac{\left[X_1R_L + R_0(X_1+X_2)\right]^2 + \left[X_1X_2 - R_0R_L\right]^2}{X_1^2\left[R_0 + R_L\right]^2} \right\} \quad \text{insertion loss} \quad (6.1)$$

$$\phi = \mathrm{arc\ tan}\left[\frac{X_1X_2 - R_0R_L}{X_1R_L + R_0(X_1+X_2)}\right] \quad \text{phase} \quad (6.2)$$

$$S_{12} = 2X_1\sqrt{R_0R_L}\left\{\frac{\left[X_1R_L + R_0(X_1+X_2)\right] - j(X_1X_2 - R_0R_L)}{\left[X_1R_L + R_0(X_1+X_2)\right]^2 + \left[X_1X_2 - R_0R_L\right]^2}\right\} \quad \text{transmission coefficient} \quad (6.3)$$

$$\left|S_{12}\right| = \sqrt{\frac{4X_1{}^2R_0R_L}{\left[X_1R_L + R_0(X_1+X_2)\right]^2 + \left[X_1X_2 - R_0R_L\right]^2}} \tag{6.3}$$

Within the 3dB-bandwidth for example of a maximally flat bandpass filter the phase is directly proportional to the frequency. At greater distances of the frequency from the center frequency of the filter the phase takes the value of $\pm n\pi/2$, whereby n is the number of resonators of the filter. So long as operation is within the passband of the filter, the phase-frequency relationship can be assumed to be linear. This important quality of a bandpass filter is made use of to realize a transmission type phase modulator. Fig. 7b,c. show the insertion loss and phase of a bandpass filter. A maximally flat filter has been taken here as example because calculations have shown that for our purpose and frequency range and taking evanescent mode technique into consideration only such type of filter can be theoretically realized with two resonators as in Fig.7a .

6.2. FILTER AS A PHASE MODULATOR

One shall assume the curves a_1 to be the original characteristics of the bandpass filter (Fig.7b,c.). The capacitances of the resonators jX_1 and jX_2 are then multiplied by a common factor α (switching factor) meaning C_1 becomes αC_1 while C_2 becomes αC_2. f_0 is the center frequency of the curves a_1. Due to the switching factor α the center frequency changes giving the new curves a_2. For certain values of α the phase relationship to the frequency within the 3dB-bandwidth of a_1 remains linear. This switching between (C_1, C_2) and $(\alpha C_1, \alpha C_2)$ creates the phase shift $\Delta\phi$ which remains constant over a reasonable range, in other words we then have a type of transmission modulator with the phase shift $\Delta\phi$ as shown in Fig.7b,c.

In the case of the maximally flat bandpass behaviour the center frequency of the phase modulator can be calculated by equating the insertion loss for the two states a_1 and a_2. In the case of a Tchebyscheff filter the relationships are somewhat more complicated. Anyway the phase shift $\Delta\phi$ is directly proportional to n and also to the frequency within the passband. This means that, to realize phase shifts of 45 degrees and more with broadband performance , n should be made greater than 2.

6.3. DESCRIPTION OF THE MODULATOR AND THEORETICAL AND PRACTICAL RESULTS

The outline of the 45 degrees transmission phase modulator which is now going to be described consists of two evanescent mode resonators, utilizing varactors or pin-diodes as switching elements. The transmission modulator and its equivalent network is illustrated in Fig.8. D_1 and D_2 are diodes imbedded in a cutoff waveguide W_2 and coupled to one another by a piece of waveguide with the length l_2. From the propagating waveguide W_1 the signal is coupled in and out of the modulator. The junctions between the cutoff and the propagating waveguides can be described by ideal transformers with parallel inductances (Fig.8a,b.). Fig.8c. shows the equivalent circuit of the transmission modulator in evanescent mode technique after a straight forward reduction of the network of Fig.8b.

The modulator has theoretically a phase shift of 45 degrees by a switching factor $\alpha=1.112$. Fig.9. shows the input reflection coefficient and the phase shift $\Delta\phi$ of the modulator at Q-band. Within the phase bandwidth B_ϕ of 3o/o is the phase deviation from $\Delta\phi=45$ degrees less than ± 1 degree. The reflection coefficient of the modulator within B_ϕ is less than 0.3, which means an insertion loss of less than 0.4 dB.

For a practical check of the modulator a filter has been realized in evanescent mode technique with a center frequency of 30 GHz with screws instead of diodes as tuning elements. The results are shown in Fig.10. The curves b_1 and b_2 represent the insertion loss and the phase for two different tuned states of the screws. Fig.10. shows the insertion loss and the phase of the simulated modulator to be similar to the theoretically predicted values of Fig.9., except that the insertion loss is about 0.4 dB over a frequency range where the phase shift is about 45 degrees.

Work is in progress to replace the screws by varactors and pin-diodes respectively. First measurements show encouraging results.

7. MEASUREMENTS OF REFLECTION COEFFICIENTS UTILIZING A NETWORK ANALYZER

Measurements of the reflection coefficients and the phase shift of a modulator have been a tedious task. The method so far used in practice, which is a laborious one, utilizes an impedance normal in connection with a magic T. There is no means of observing the curves during the tuning process. It is therefore a time spending factor to get a reflection modulator tuned and its bandwidth properly accessed. The method to be described now eases the whole tuning process. The measuring technique is more accurate and much quicker than the former method, because here the desired values can be seen displayed on a screen all through the tuning process.

Fig.11. shows the set up for the reflection measurements. The reflection modulator is driven by a low frequency sinus or square wave generator, while the sweep oscillator is swept over the required frequency range at a speed which is much slower than the speed at which the modulator switches. In so doing the amplitudes and phases of the reflection coefficient for the two states of the modulator are simultaneously displayed on the screen of a two trace oscilloscope, connected to the network analyzer. These values can also be recorded on paper utilizing an X-Y recorder. This tuning method makes it possible to examine the broadband behaviour of the modulator.

By the method discussed above , the reflection coefficients and the phase shift of the reflection phase modulator have been conveniently and successfully measured. The same method has been used to tune the reflection type modulator for AM applications. To this purpose one of the states of the reflection phase modulator has to be matched to the impedance of the input line.

8. RESULTS

Utilizing the theory of evanescent mode resonators and the measuring method described above, a reflection type phase modulator for both AM and PM transmission techniques has been developed.

The 180 degrees reflection modulator shows broadband performance: the bandwidth amounted to 12o/o for an insertion loss of 0.5 dB at a midband frequency of 34 GHz. Phase shift error $\Delta\phi$ and imbalance ΔR of the reflection coefficients are illustrated in Fig.12.

In the case of the AM modulator a bandwidth of 3o/o by a midband frequency of 32.5 GHz has been achieved. In the forward state the losses lie below 0.5 dB while in the reversed state a value above 20 dB has been realized (see Fig.13.).

The switching time for both the reflection phase modulator and the AM modulator is about 1 ns for pin-diodes made in the Institut für Hochfrequenztechnik of the Technische Universität Braunschweig.

9. CONCLUSIONS

The modulators presented in this paper utilize evanescent mode resonators. In this technique, inductance is represented by short sections of rectangular waveguide below cutoff and capacirance by obstacles in the waveguide. The individual elements approximate lumped elements in a large frequency range. Any impedance transformation has a broadband performance. Both AM and PM modulators have been realized in waveguide below cutofftechnique working at Q band frequencies. Varactors and pin-diodes have been used as switching elements. Design criteria and performance data have been given for an AM modulator, a 180 degrees reflection type and a 45 degrees transmission type phase modulator. The bandwidth of the reflection modulators have been generally limited to 1o/o till now. The one described here presents a broader band performance namely up to 12o/o compared to hitherto known modulators.

Summarizing therefore evanescent mode technique is well qualified for integrated circuit application in the millimeter wave range. Finally the technique described in this paper involves small circuit losses and substantial reduction in size, weight and costs.

10. ACKNOWLEDGEMENTS

The authors wish to express their appreciation and gratitude for the financial support of the Deutsche Forschungsgemeinschaft.

11. REFERENCES

1. DORSCHNER,T.A., 1973, "Characterization of Reflection Phase Modulators Using Hyperbolic Geometry" , Brussel, Proc. of the European Microwave Conference,pp.A.9.1.

2. KUROKAWA,K., SCHLOSSER,W.O., 1970, "Quality Factor of Switching Diodes for Digital Modulation ", Proc. IEEE vol.58, pp. 180-181 .

3. SCHUENEMANN,K., KNOECHEL,R., BEGEMANN,G., 1977, "Components for Microwave Integrated Circuits With Evanescent Mode Resonators" , San Diego, Cal., 1977 IEEE MTT-S International Microwave Symposium Digest, pp. 377-380 .

4. SCHUENEMANN,K., MUELLER,J., DORSCHNER,T.A., SPORLEDER,F., 1975, " A Reflection Type Phase Modulator With Fast Switching Pin-Diodes " , TU Braunschweig, Communication from the Institut für Hochfrequenztechnik, NTZ(1975)H.9, pp. 319-322 .

12. FIGURE CAPTIONS

Fig.1. Hyperbolic straight lines for various values of k
a) k= 1/2
b) k= 1

Fig.2. a) Diode and imbedding
b) A simplified pin-diode model

Fig.3. Matching of the hyperbolic middle point (refl. coeff.)

Fig.4. Matching of the hyperbolic middle point (impedances)

Fig.5. a) Prototype reflection phase modulator
b) Prototype reflection phase modulator compared to the size of a five mark piece

Fig.6. Equivalent network of the prototype reflection modulator

Fig.7. a) Prototype bandpass filter with two resonators jX_1 and jX_2
b) Insertion loss of a bandpass filter
c) Phase of a bandpass filter

Fig.8. a) Prototype filter transmission type modulator
b,c) Equivalent network of the transmission type modulator

Fig.9. Filter transmission modulator

Fig.10. Insertion loss and phase of a simulated transmission type modulator at 30 GHz

Fig.11. Schematic for reflection measurements

Fig.12. Phase shift error $\Delta\phi$ and imbalance ΔR of the reflection coefficients of a reflection phase modulator with a pin-diode

Fig.13. Reflection coefficients of an AM modulator

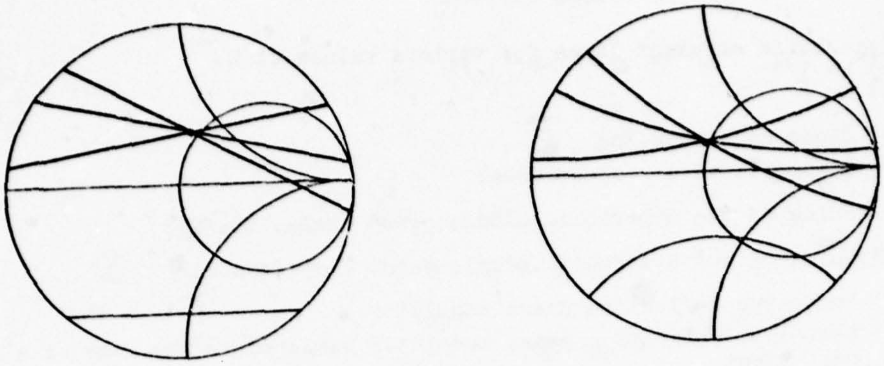

Fig.1.

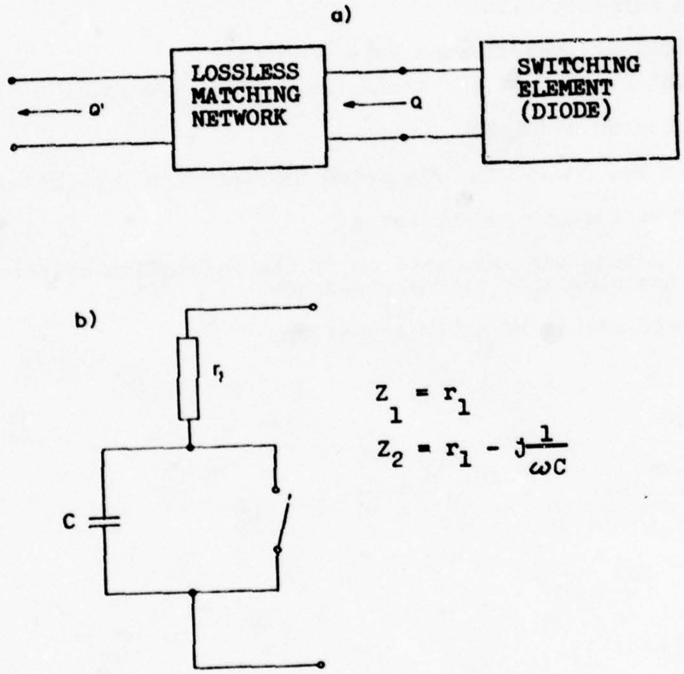
a)
LOSSLESS MATCHING NETWORK
SWITCHING ELEMENT (DIODE)
ρ'
ρ
b)
r_1
C

$$Z_1 = r_1$$
$$Z_2 = r_1 - j\frac{1}{\omega C}$$

Fig.2.

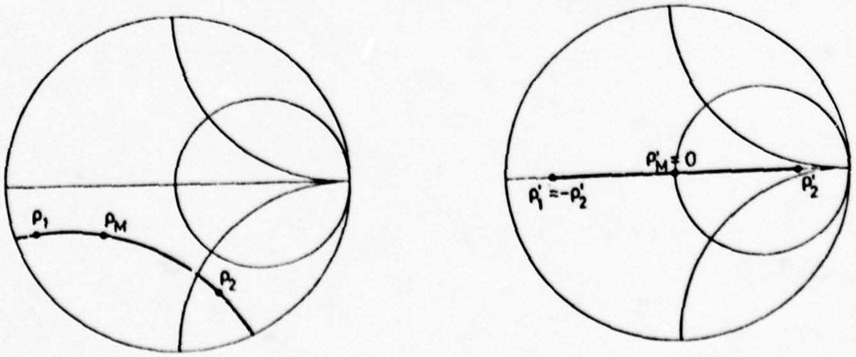
ρ_1
ρ_M
ρ_2
$\rho'_M = 0$
$\rho'_1 = -\rho'_2$
ρ'_2

Fig.3.

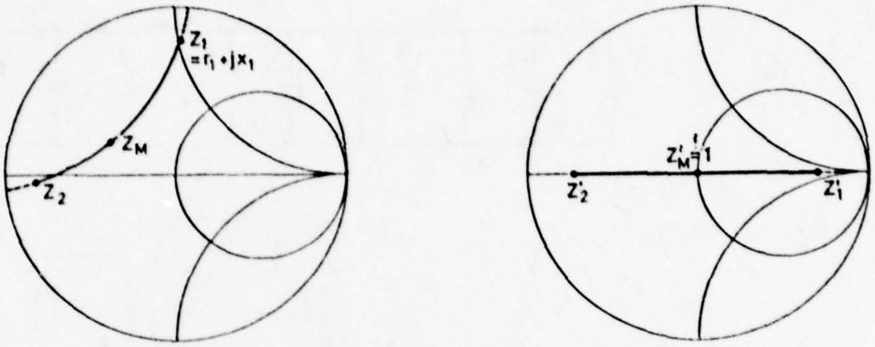
Z1
= r1 + jx1
ZM
Z2
Z'M = 1
Z'2
Z'1

Fig.4.

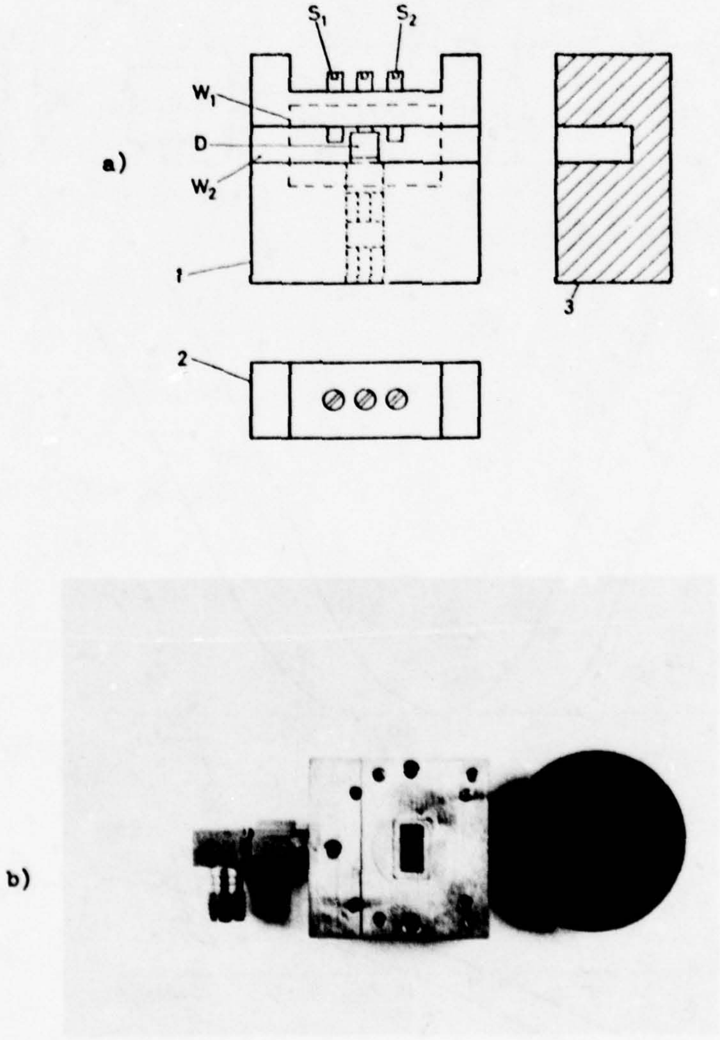
S1
S2
W1
D
W2
a)
1
3
2
b)

Fig.5.

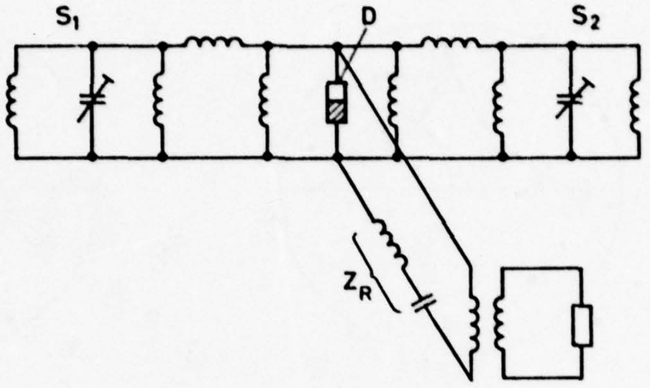
S$_1$
D
S$_2$
Z$_R$

Fig.6.

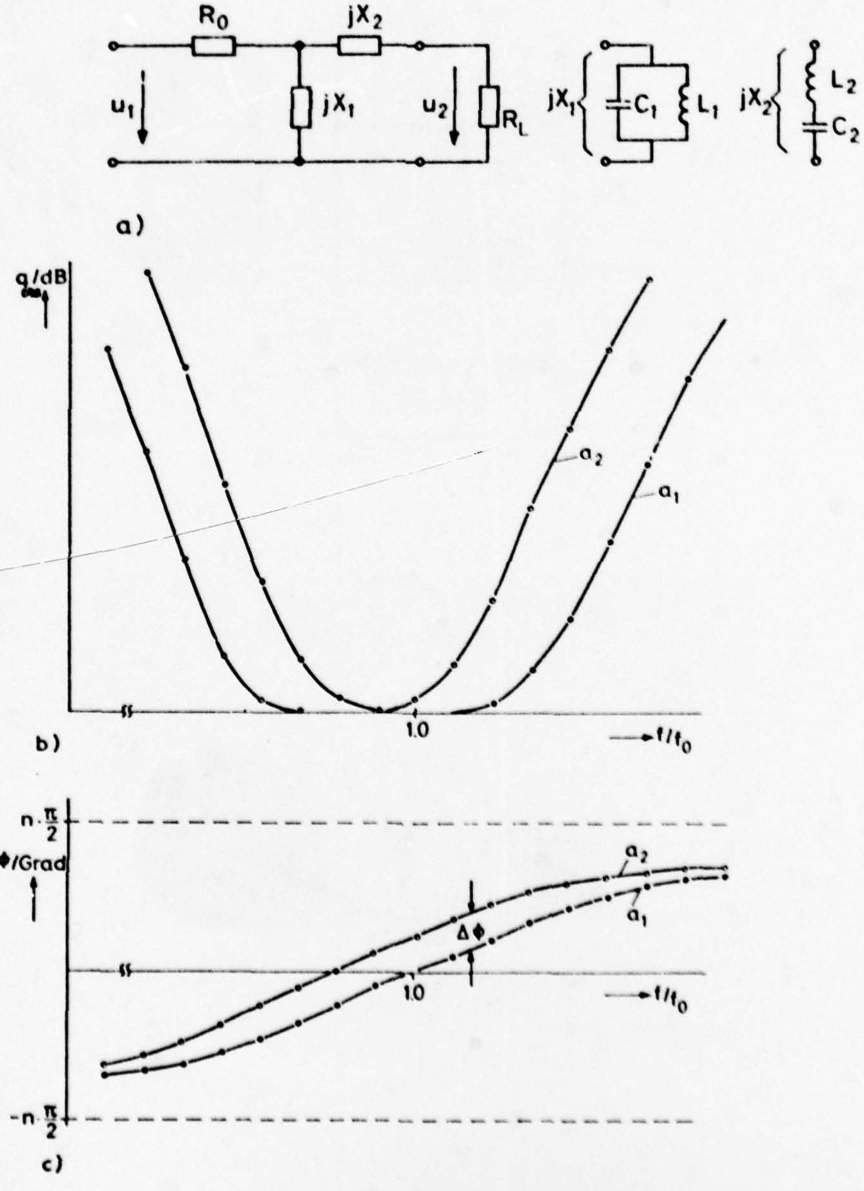
R$_0$
jX$_2$
u$_1$
jX$_1$
u$_2$
R$_L$
jX$_1$
C$_1$
L$_1$
jX$_2$
L$_2$
C$_2$
a)
a/dB
a$_2$
a$_1$
1.0
f/f$_0$
b)
n·π/2
Φ/Grad
a$_2$
a$_1$
ΔΦ
1.0
f/f$_0$
-n·π/2
c)

Fig.7.

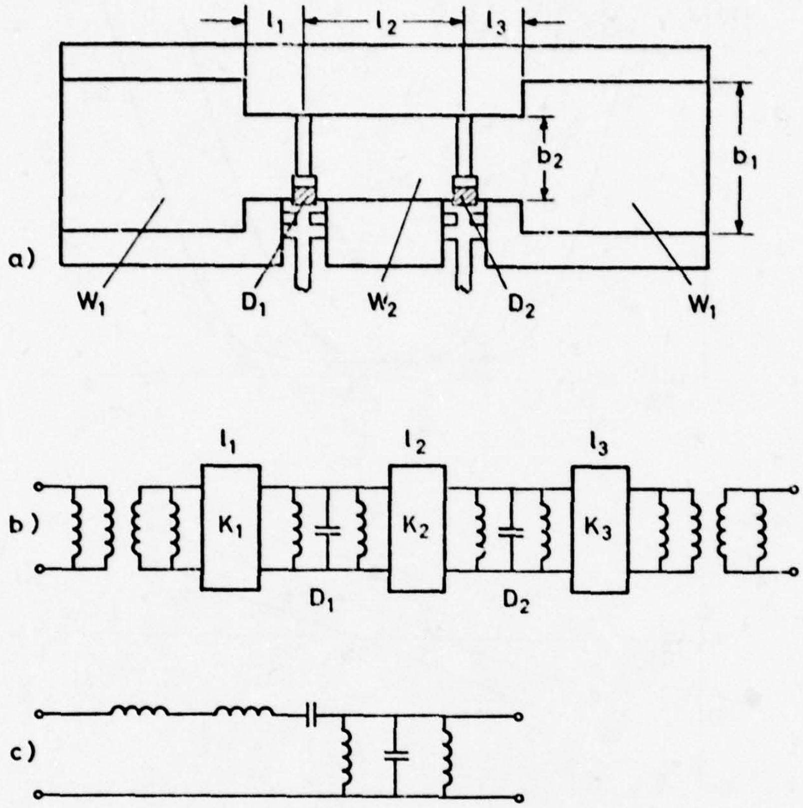
l1
l2
l3
b2
b1
a)
W1
D1
W2
D2
W1
l1
l2
l3
b)
K1
K2
K3
D1
D2
c)

Fig.8.

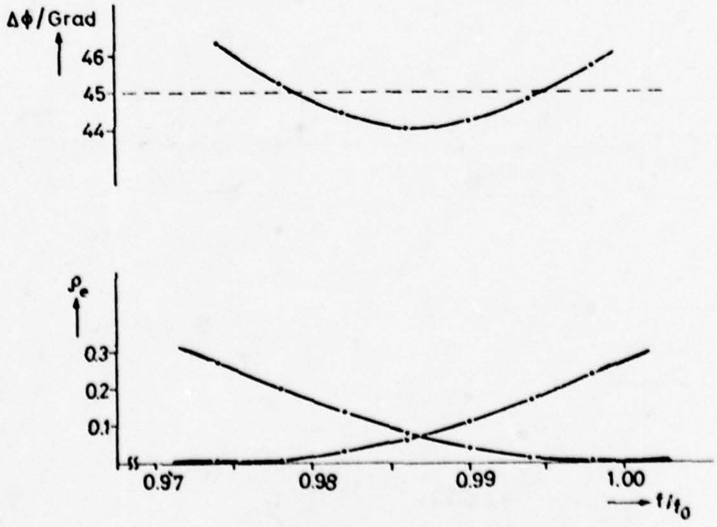
ΔΦ/Grad
46
45
44
ρe
0.3
0.2
0.1
0.97
0.98
0.99
1.00
f/f0

Fig.9.

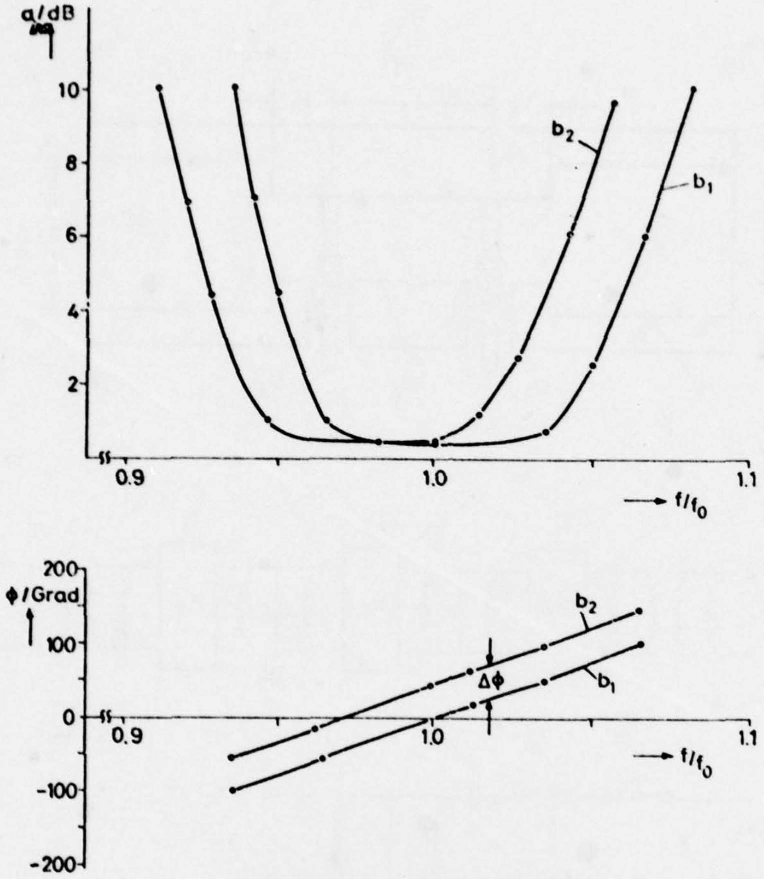
a/dB
10
8
6
4
2
0.9
1.0
1.1
→ f/f0
b2
b1
200
φ/Grad
100
0
-100
-200
0.9
1.0
1.1
→ f/f0
b2
b1
Δφ

Fig.10.

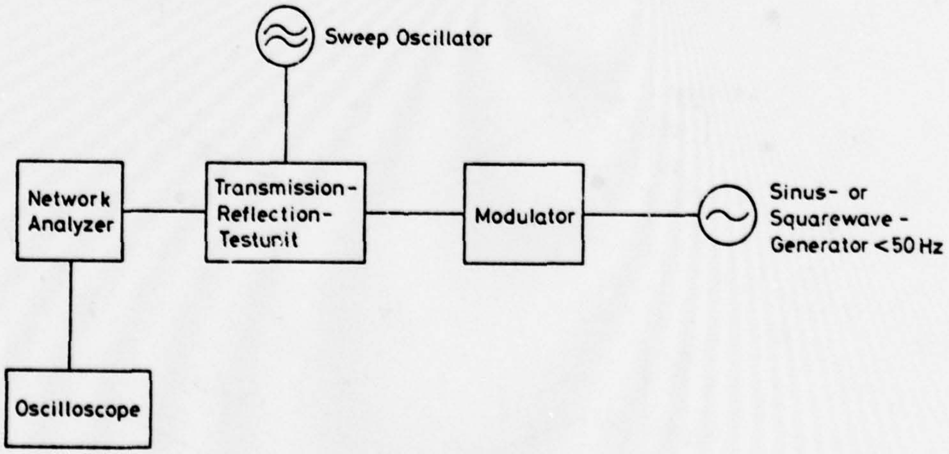
Sweep Oscillator
Network Analyzer
Transmission-Reflection-Testunit
Modulator
Sinus- or Squarewave - Generator <50 Hz
Oscilloscope

Fig.11.

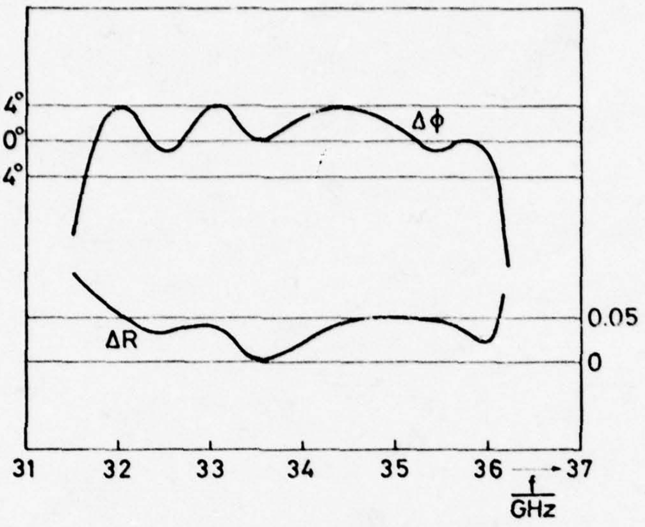
4°
0°
-4°
Δφ
ΔR
0.05
0
31
32
33
34
35
36
37
f
GHz

Fig.12.

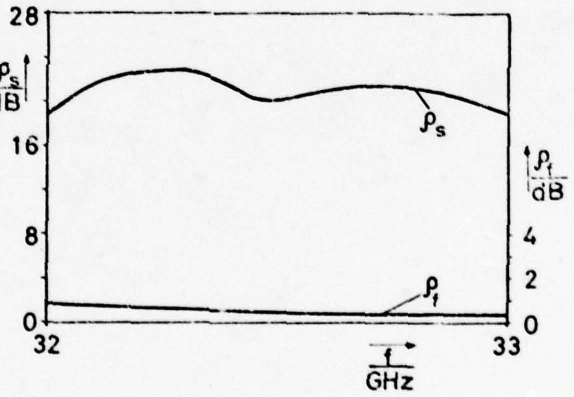
28
ρ_s
dB
16
8
0
32
33
ρ_s
ρ_f
dB
4
2
0
ρ_f
f
GHz

Fig.13.

PHASE CONTROL ELEMENTS FOR MILLIMETER WAVE SYSTEMS

R.W.Babbitt, R.A.Stern
ERADCOM-ETD
Ft.Monmouth, NJ 07703, U.S.A.

and

L.R.Whicker, C.W.Young, Jr.
Naval Research Laboratory
Washington, DC 20375, U.S.A.

SUMMARY

Future millimeter wavelength radar and communication systems will require phase control components. Many will require the use of phased array antennas. In this paper, the state-of-the-art for two classes of ferrite phase shifters is discussed. Two development efforts are described which promise to improve the performance and reduce the cost of millimeter wavelength phase shifters. One program is concerned with the arc plasma spray (APS) process for fabricating ferrite toroids. Data for experiments at 35 GHz, 65 GHz, and 94 GHz are presented. The second program describes efforts to obtain nonreciprocal phase control elements which exhibit full waveguide bandwidths. Design and test data for a 26.5-40 GHz phase shifter is presented.

1. INTRODUCTION

High performance millimeter wavelength phase shifters are needed in switching and control circuitry for future millimeter wave systems. Many applications require electronically scanned phased array antennas utilizing a phase shifter for each radiating element. At frequencies above 20 GHz, diode phase shifters become quite lossy. Thus, fast switching latching, reciprocal or latching nonreciprocal phase shifters (phasers) represent the present candidate phase control element. In this paper, the state-of-the-art for these two classes of phase shifters is discussed. (BABBITT, R.W., 1978), (WHICKER, L.R., 1974), (WHICKER, L.R., 1973) The relative characteristics of both classes are compared for use in the 30-300 GHz frequency region.

In addition to the discussion of the present state-of-the-art for millimeter phase shifters, two new developments are described which promise to improve the performance and reduce the cost of millimeter wavelength phase shifters. The first program is being conducted at the U.S.Army Electronics Technology Laboratory and is concerned with fabrication techniques of millimeter wavelength phase shifters. The second program is being conducted at the Naval Research Laboratory. Here, emphasis is being placed on obtaining broadband operation of millimeter phase shifters.

2. STATE OF THE PHASE SHIFTER ART AT MILLIMETER WAVELENGTHS

2.1 The Toroidal Nonreciprocal Phaser

Work on the toroidal, nonreciprocal phaser has been underway in the United States since early in 1963. (TREUHAFT, M.A., 1958), (KEMPIC, J.A., 1965), (WHICKER, L.R., 1966) The basic operating mechanism of this type of phaser is reviewed in Figure 1. Figure 1(a) shows the ferrimagnetic toroid centered in either a standard or reduced width waveguide. Figures 1(b) and 1(c) review the two types of construction which are normally utilized. Computer programs are utilized to optimize the phaser designs at center frequencies ranging from about 3 to 35 GH. In designing such phasers, it is desirable to select a ferrimagnetic material such that a fixed ratio of remanent flux density to operating frequency is maintained. However, at frequencies above about 35 GHz, this cannot be done. The choice then is to use materials having the largest possible saturation magnetization while maintaining a good squareness ratio. Nickel zinc ferrites and lithium zinc ferrites offer the highest available saturation moment of about 5,000 gauss.

In 1966, Stern and Agrios (STERN, R.A., 1966) reported on a 35 GHz high power switch using 90° phase shifter elements. A similar geometry was used in 1967 by Whicker, Degenford and Wantuch (WHICKER, L.R., 1967) (WANTUCH, E., 1969) in investigating phase shifters in the 35-94 GHz region. The geometries used in 35 GHz and 75 GHz designs are shown in Figure 2. Phase shift data obtained using two Nickel Zinc materials are shown in Figures 3-4. Several 35 GHz phasers were subsequently fabricated. Phase shifter properties for 35 GHz units and for a 75 GHz experimental unit are listed in Table I. It should be noted that because of severe tolerances and machining capability, the data listed in Figure 4 is not for a truly optimized 75 GHz phaser. In following sections of this paper, new methods to eliminate these fabrications using the Arc Plasma Spray Technique will be described.

TABLE I
NONRECIPROCAL PHASE SHIFTER PERFORMANCE

f_c BANDWIDTH	34.5 GHz 34 - 35 GHz	75.5 GHz 74 - 77 GHz
Insertion Loss:	1.5 dB	3.5 - 4.0 dB
VSWR:	< 1.25	< 1.25
Switching:	3 Bit or Flux Transfer	3 Bit or Flux Transfer
Length:	3 inches	4 inches

Since 1967 some improvement in materials and fabrication techniques have been made. Figure 5 is a photograph of a state-of-the-art nonreciprocal phaser which operates over the 43-45 GHz band. Data for this unit is given in Table II. The photograph and data have been furnished courtesy of Electromagnetic Sciences, Inc.

TABLE II
DATA FOR STATE OF THE ART MILLIMETER WAVE NONRECIPROCAL PHASE SHIFTER
(EMS MODEL 339A-1)

FREQUENCY RANGE:	43-45 GHz
INSERTION LOSS:	1.25 dB max. (1.1 dB typical)
INPUT VSWR:	1.20:1 Max.
PHASE SHIFT AVAILABLE:	0° - 360° in continuous steps
PHASE CONTROL:	Either analogue (variable pulse width or variable pulse height) or digital (series or parallel) inputs available.
SWITCHING TIME:	2 microseconds max.
AMBIENT TEMPERATURE RANGE:	0° - +40°C
DIMENSIONS	
MICROWAVE HOUSING:	0.75" x 0.75" x 1.5" long
ELECTRONIC CIRCUITRY:	1-3/4" x 2" x 1/2" (approximate depending upon driver interface)
WEIGHT:	2.5 oz.

2.2 The Dual Mode Reciprocal Phaser

In looking for a phaser geometry which might be less tolerance sensitive than the toroidal type, the dual mode reciprocal phaser is considered to be a good candidate. A test phaser has been fabricated (WHICKER, L.R., 1971) with a center frequency of 35 GHz. The phaser design is shown in Figure 6. The basic concept is shown schematically in Figure 6(a). Here, linearly polarized energy in rectangular waveguide is passed through nonreciprocal polarizers and is converted to either left or right circular polarized energy in quadrantally symmetric waveguide, phase shifted and reconverted to linear polarization in rectangular waveguide. As indicated in the figure, a metal fixture-housing is used which provides access to the phaser for tuning of the nonreciprocal polarizers.

Phase shift data for the 35 GHz unit are given in Figure 7. The other performance parameters for the phaser unit are as follows:

Bandwidth	34 - 36 GHz
Insertion Loss	< 2.2 dB
VSWR	< 1.3
Length	< 2 inches

Other than precision grinding of the ferrite rod which forms the body of the phaser element, only standard tolerance parts have been used. Computer computational techniques have been used in designing and predicting the performance of this unit.

In addition to the 35 GHz phaser design, computer designs for phasers centered at 55 and 95 GHz have been prepared. The predicted loss characteristics for these phasers are summarized in Table III. It is interesting to note that for the material used in the calculations dielectric losses predominate at the higher frequencies. In general, the dual mode phaser appears well suited for use above 35 GHz. Loss restrictions rather than tolerance problems are expected to provide an upper frequency bound for use of this phaser. Further calculations and evaluations are required to find ferrimagnetic materials with lower dielectric loss tangents.

TABLE III
CALCULATED LOSS FOR DUAL-MODE PHASERS

	FREQ. (GHz)	COND. LOSS (dB)	DIEL. LOSS (dB)	MAG. LOSS (dB)	TOTAL LOSS (dB)
35 GHz PHASER	33.0	.647742	.671986	.455419	1.775147
	34.0	.617772	.680227	.422221	1.720220
	35.0	.591495	.689347	.392912	1.673754
	36.0	.568277	.699191	.366848	1.616875
	37.0	.547628	.715052	.332770	1.585960
55 GHz PHASER	50.0	1.010916	.996375	.224717	2.232006
	52.0	.946206	1.010553	.202189	2.158951
	54.0	.892059	1.027143	.183219	2.102711
	56.0	.846123	1.046387	.167035	2.059543
	58.0	.806698	1.066971	.153073	2.026749
	60.0	.772529	1.088862	.140919	2.002315
95 GHz PHASER	90.0	1.583211	1.749832	.066403	3.399442
	92.0	1.531693	1.766884	.062749	3.361328
	94.0	1.484813	1.785147	.059417	3.329370
	96.0	1.441991	1.804462	.056367	3.302827
	98.0	1.402732	1.824697	.053565	3.280996
	100.0	1.366624	1.845743	.050983	3.263345

3.0 A NEW TECHNIQUE FOR FABRICATING MILLIMETER WAVELENGTH PHASERS

In order to alleviate many of the fabrication problems associated with the nonreciprocal phaser at millimeter wavelengths a novel arc plasma spray (APS) process has been developed at the U.S.Army Electronic

Technology Laboratory. This technique offers great potential for cost-effective, high performance components at frequencies up to 94 GHz or higher. (BABBITT, R.W., 1978). Moreover, this technique may be suitable for fabricating integrated array structures containing several phaser elements.

3.1 APS Fabrication Procedure

Figure 8 repeats the sketch of the basic structure of a nonreciprocal latching ferrite phase shifter. As indicated earlier the ferrite toroid geometry with dielectric loading presents a serious fabrication problem for operating frequencies above 35 GHz. To obtain good electrical performance air voids both at the ferrite-dielectric interface and at the ferrite-waveguide wall must be minimized. Air gaps or voids tend to launch unwanted waveguide modes and/or surface wave modes which result in poor electrical performance. For frequencies above 35 GHz the toroid's small size and critical tolerances lead to high costs.

The APS process eliminates many of these problems. In this process a ferrite powder is deposited around a dielectric insert. The desired dielectrically loaded toroid is formed in this manner. The process yields a toroid with intimate contact between the ferrite and the dielectric. The outer dimensions of the toroid are machined to the required tolerance.

3.2 Experimental Phasers

A lithium zinc ferrite powder has been selected for spraying millimeter phaser toroids. This material has been selected since the material composition can be tailored to exhibit saturation magnetizations up to 5000 gauss. The hysteresis loops of these materials exhibit good squareness ratios. In preparing the toroids, a lithium titanate ($\epsilon_r = 26$) core material is used about which the lithium zinc ferrite powder is arc plasma sprayed. This particular dielectric material has been used since its relatively high dielectric constant concentrates the rf energy in the toroid leading to large differential phase shifts. Secondly, the thermal coefficient of expansion of this dielectric matches that of the ferrite thereby minimizing stresses and cracks in the prepared toroid.

Figure 9 gives the cross-sectional schematic of the basic phaser-test fixture configuration used at 35, 65, and 94 GHz. Each waveguide housing has been designed to be slightly undersized [~ 0.001 inch (.003 cm)] and fitted with a spring-loaded top wall to ensure a secure toroid fit in the housing. Figure 10 is a photograph of the toroids. The small hole, for the latching conductor in the toroids has been formed by bonding a strip of boron nitride to the dielectric core material. The boron nitride remains intact during the APS operation but sublimes during the toroid anneal cycle, leaving a hole for inserting the switching conductor.

3.3 Test Results

Phase shifters operating in each of the three frequency bands of interest have been evaluated. The internal structure of each of these phasers is shown in Figure 11.

Figure 12 indicates the insertion loss and reflection loss of a 35 GHz unit utilizing a 1.35 inch (3.43 cm) APS toroid sample. This unit yields less than 0.7 dB insertion loss over a 0.6 GHz bandwidth exhibiting 422° of differential phase shift (i.e., figure of merit = 649°/dB). Data on a 65 GHz phaser [APS toroid length = 0.31 inch (0.8 cm)] is shown in Figure 13. The insertion loss as shown is less than 0.9 dB over a 1 GHz bandwidth while the differential phase shift is 87° (i.e., figure of merit = 97°/dB). Both of these units exhibit reflection loss > 18 dB (i.e., VSWR < 1.3:1) over the designated bandwidths. Preliminary data on a 94 GHz phaser indicates a nominal insertion loss of 1.5 dB over a 1 GHz bandwidth as shown in Figure 14 when using a 0.25 inch (.64 cm) length APS toroid. The reflection loss of this unit is > 16 dB and the differential phase shift measured was found to be 38°. Switching time less than 1μsec are possible with each of these three devices.

A computer program has been used to predict the theoretical phase shift which could be expected for various phaser design parameters. The test results agree reasonably well with that of the theoretical predictions.

The insertion loss of each of these phasers could be further reduced through the use of a lower loss dielectric loading material. The lithium zinc presently being used exhibits a dielectric loss tangent of < .0025. Loss measurements made at millimeter wavelengths indicate a significant amount of loss contributed by this dielectric, particularly at the higher frequencies (65 GHz and 94 GHz) where the dielectric material represents a greater proportion of the phaser cross-section. Further improvement in lithium zinc ferrite powders and APS techniques will result in improved figures of merit for these millimeter phasers.

4.0 BROADBANDING STUDIES ON MILLIMETER WAVELENGTH PHASERS

While efforts at the U.S.Army Electronics Technology Laboratory have been addressing fabrication problems for millimeter wavelength phasers, efforts at the Naval Research Laboratory have centered on obtaining full waveguide bandwidth operation of the basic nonreciprocal toroidal phaser. Present experiments have centered on the realization of a fast switching phaser to operate over the 26-40 GHz band.

Computer computational techniques have been utilized to investigate the bandwidth characteristics for candidate geometries. Figure 15 gives typical plots of phase shift activity as a function of dielectric loading within the toroid slot for a particular geometry. Figure 16 shows typical phase shift variation which may be obtained using a fixed dielectric loading and slot width ($\epsilon_r = 16$, T = 0.015 inches (0.04 cm)). Similar calculations have been performed for several waveguide widths (A).

In general, large waveguide widths result in low insertion loss but allow for propagation of some higher order modes with corresponding insertion loss spikes. Using a reduced waveguide width results in higher nominal insertion loss but tends to eliminate or minimize moding effects. As a design compromise the following dimensions for the phaser cross section have been utilized:

WAVEGUIDE HEIGHT (B)	....	0.140 inches (0.36 cm)
WAVEGUIDE WIDTH (A)	....	0.160 inches (0.41 cm)
TOROID WIDTH (W)	....	0.054 inches (0.14 cm)
TOROID SLOT WIDTH (T)	....	0.015 inches (0.04 cm)
CENTER LOADING	....	$\epsilon_r = 16$

Data measured for the experimental phaser are shown in Figure 17. Figure 17(a) shows insertion loss measured across the 26.5-40 GHz frequency range. Some insertion loss spikes are present at the higher frequencies. Figure 17(b) gives the measured return loss of 12 dB or better across the frequency band. Three step matching transformers are used. Figure 17(c) indicates the rather flat phase shift characteristics which have been obtained. A photograph of the experimental phaser is shown in Figure 18.

The work thus far conducted has utilized conventional fabrication techniques. Further experiments are required to combine the demonstrated broadbanding techniques with the APS fabrication process. The APS fabrication will be essential to the realization of broadband phasers in higher frequency bands.

5. CONCLUSIONS

In this paper the present state-of-the-art for ferrite phasers to operate at millimeter wavelengths have been reviewed. Two programs--one dealing with the Arc Plasma Spraying technique for fabricating phasers and one dealing with broadbanding studies have been described.

It is believed that the Arc Plasma Spray Technique can be a valuable tool in realizing millimeter wavelength control components. Some areas which require additional experiments include:

- fabrication of broadband nonreciprocal phasers.
- fabrication of reciprocal dual mode phasers.
- fabrication of other phaser geometries such as the two toroid design (STERN, R.A.,1968).
- fabrication of integrated assemblies containing several phase shifter elements.
- tradeoff studies and experiments to evaluate the reciprocal versus nonreciprocal phaser geometries at 60 and 94 GHz.

REFERENCES

BABBITT, R.W., STERN, E., June 1978,"Non-Reciprocal Ferrite Phase Shifters for Millimeter Applications," 1978 IEEE International Microwave Symposium.

KEMPIC, J.A., JONES, R.R., 1965, "A Temperature Stable High Power C-Band Digital Phase Shifter," NEREM Record, pp.12-13.

STERN, R.A., AGRIOS, J.P., May 1966, "A Fast Millimeter Ferrite Latching Switch," IEEE International Microwave Symposium Digest, pp.219-223.

STERN, R.A., AGRIOS, J.P., 1968, "A 500 K-W X-Band Air Cooled Ferrite Latching Switch," IEEE International Microwave Symposium Digest, pp.264-283.

TREUHAFT, M.A., SILBER, L.M., August 1958, "Use of Microwave Ferrite Toroids to Eliminate External Magnets and Reduce Switching Power," Proceedings IRE, Vol.46, pp.15-38.

WANTUCH, E., DEGENFORD, J.E., WHICKER, L.R., February 1969, "Modified Nickel Zinc Ferrites with High Saturation Magnetization and Improved Hysteresis Properties," Journal of Applied Physics, Vol.39, No.2, Part 1, pp.723-725.

WHICKER, L.R., 1966, "Recent Advances in Digital Ferrite Devices," IEEE International Convention Record, Vol.14, Part 5, pp.49-57.

WHICKER, L.R., DEGENFORD, J.E., WANTUCH, E., 1967, "Millimeter Wavelength Latching Ferrite Phase Shifters," NEREM Record, pp.60-61.

WHICKER, L.R., BOYD, C.R., JR., December 1971, "A New Reciprocal Phaser for Use at Millimeter Wavelengths," IEEE Transactions, MTT-19, pp.944-945.

WHICKER, L.R., 1973, "The Present Status of Ferrite Phase Shifter Technology in U.S.A., "Proceedings European Microwave Conference, B.10.4.

WHICKER, L.R., 1974, Ferrite Control Components, Vol.2, Artech House, Inc.

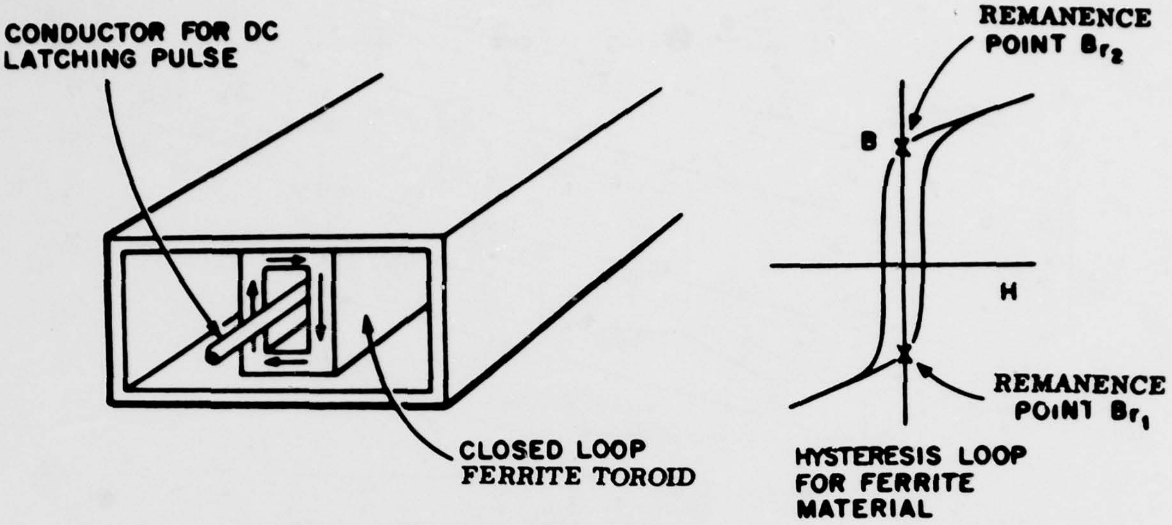
CONDUCTOR FOR DC LATCHING PULSE
CLOSED LOOP FERRITE TOROID
REMANENCE POINT B_{r_2}
B
H
REMANENCE POINT B_{r_1}
HYSTERESIS LOOP FOR FERRITE MATERIAL

(a) Switching of ferrite toroid waveguide

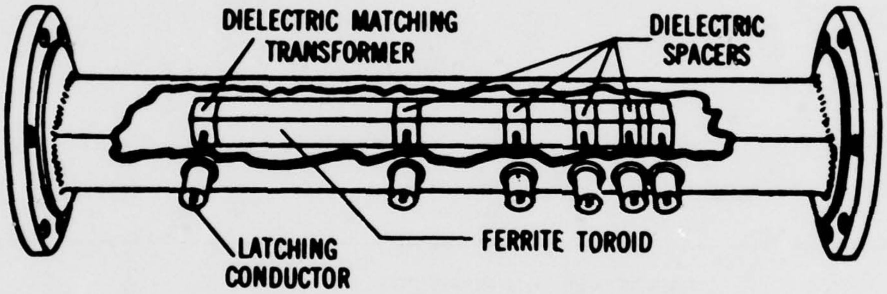
DIELECTRIC MATCHING TRANSFORMER
DIELECTRIC SPACERS
LATCHING CONDUCTOR
FERRITE TOROID

(b) Five bit nonreciprocal phaser

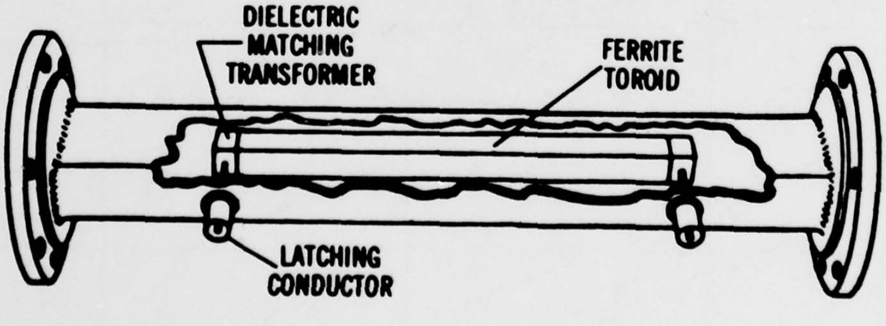
DIELECTRIC MATCHING TRANSFORMER
FERRITE TOROID
LATCHING CONDUCTOR

(c) Single Toroid Phaser--To Be Switched By Flux Transfer Techniques

Fig.1 Nonreciprocal Toroidal Ferrite Phaser

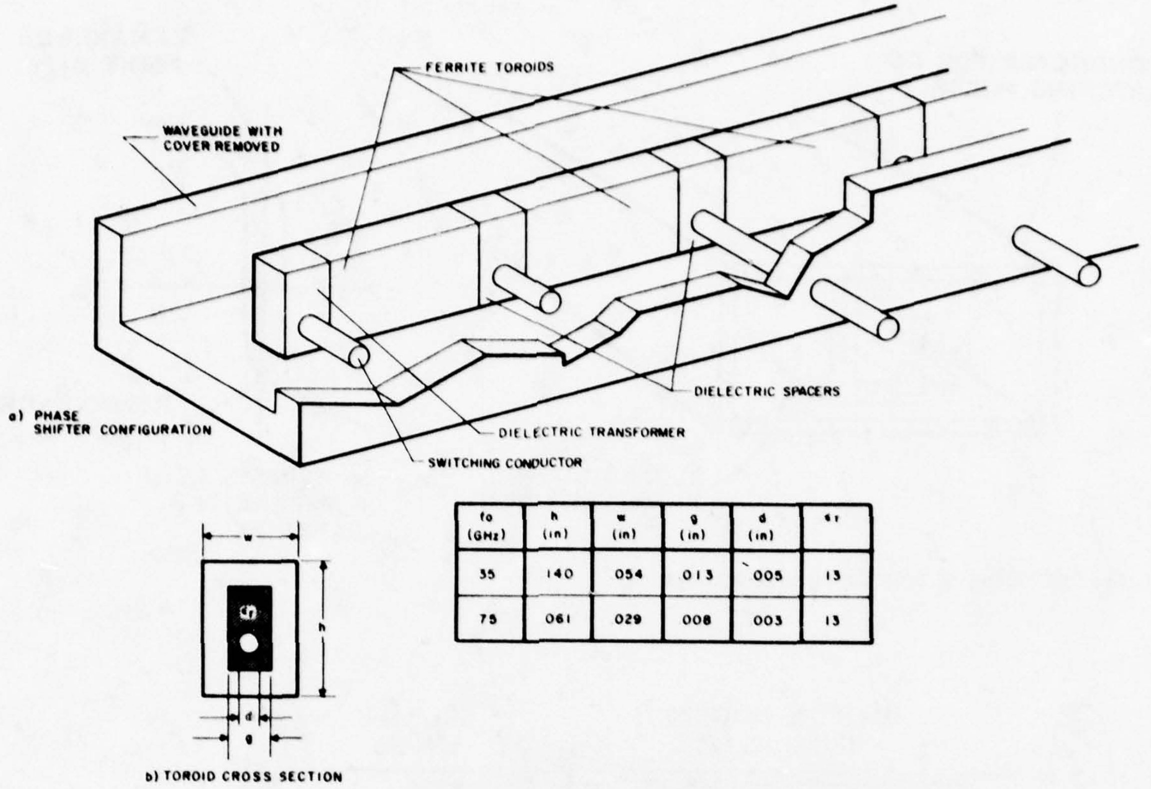
FERRITE TOROIDS
WAVEGUIDE WITH COVER REMOVED
DIELECTRIC SPACERS
DIELECTRIC TRANSFORMER
SWITCHING CONDUCTOR
a) PHASE SHIFTER CONFIGURATION
w
h
d
g
b) TOROID CROSS SECTION

f_o (GHz)	h (in)	w (in)	g (in)	d (in)	ϵ_r
35	140	054	013	005	13
75	061	029	008	003	13

Fig.2 Millimeter Phase Shifter Configuration

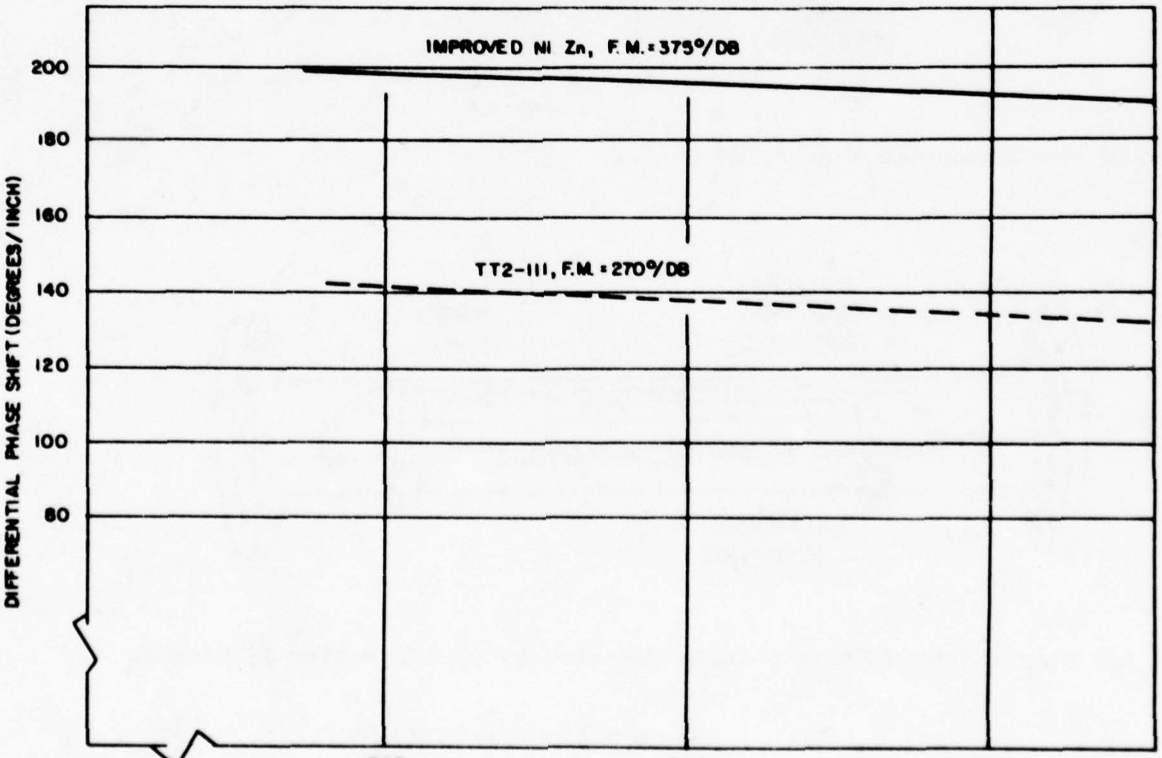

Fig.3 Phase Shift vs. Frequency Data for 35 GHz Phaser

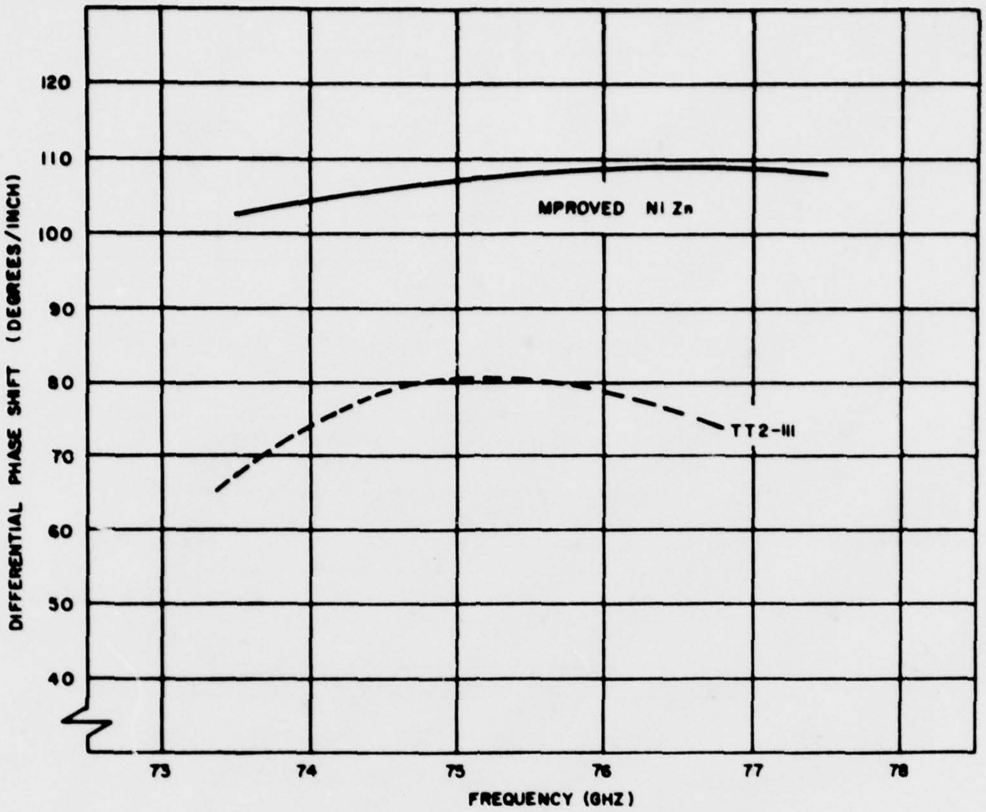

Fig.4 Phase Shift vs. Frequency Data for 75 GHz Phaser

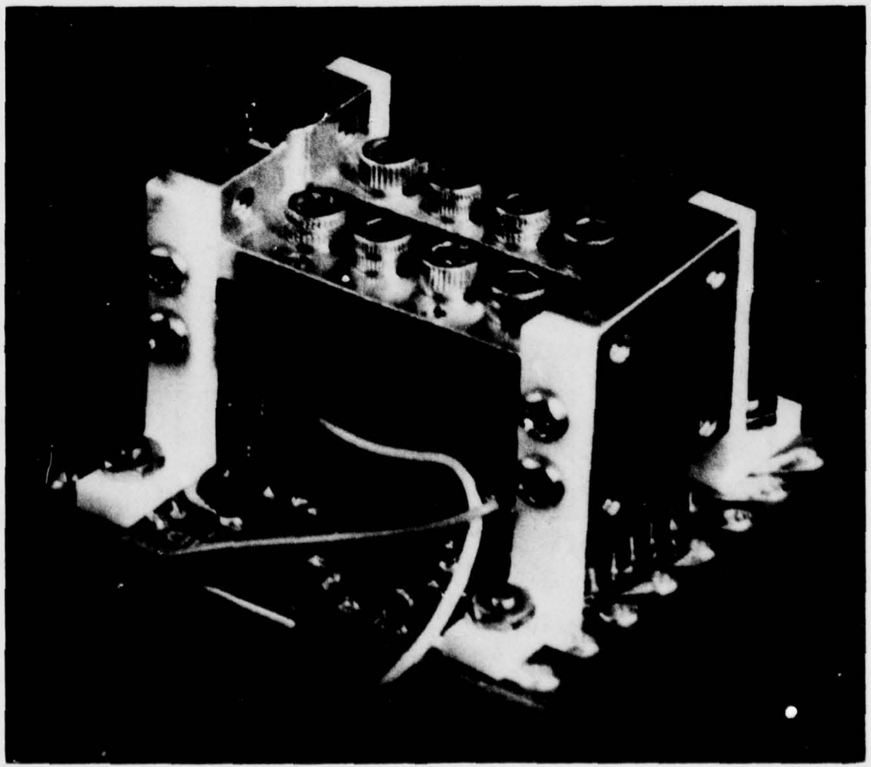

Fig.5 State-of-the-Art 44 GHz Phaser

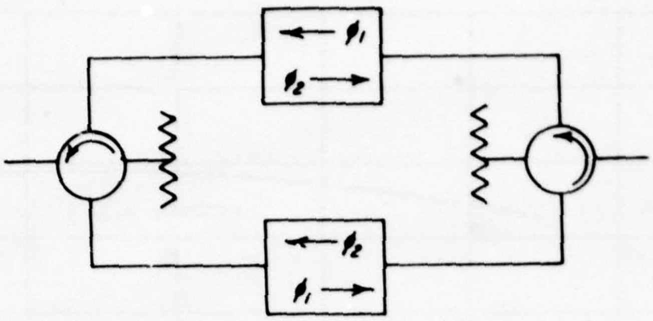
ϕ_1
ϕ_2
ϕ_2
ϕ_1

(a) BASIC CONCEPT OF DUAL MODE PHASER

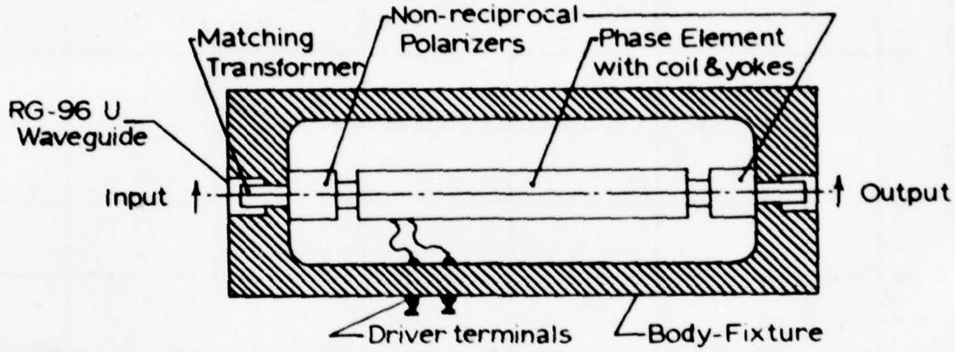
Non-reciprocal Polarizers
Matching Transformer
Phase Element with coil & yokes
RG-96 U Waveguide
Input
Output
Driver terminals
Body-Fixture

(b) DUAL MODE PHASER CONFIGURATION

Fig.6 Dual Mode Phaser Configuration

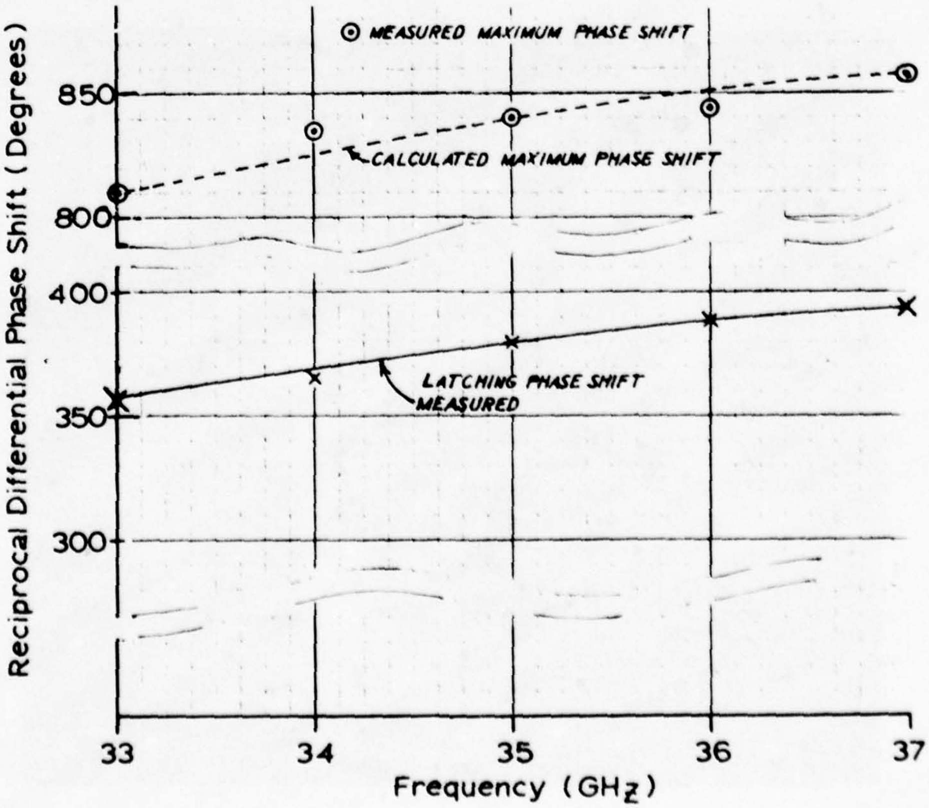

Fig.7 Phase Shift Data for Dual Mode Phaser

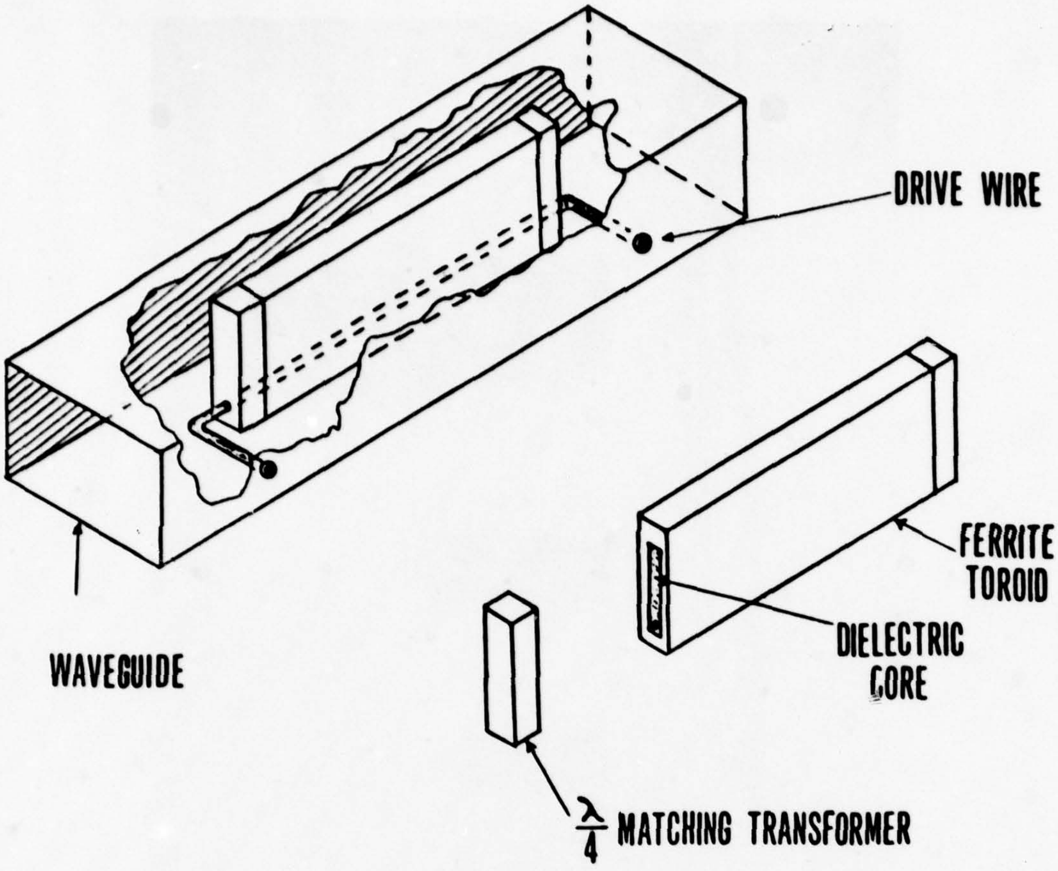
DRIVE WIRE
FERRITE TOROID
DIELECTRIC CORE
WAVEGUIDE
$\frac{\lambda}{4}$ MATCHING TRANSFORMER

Fig.8 Toroidal Phaser Configuration

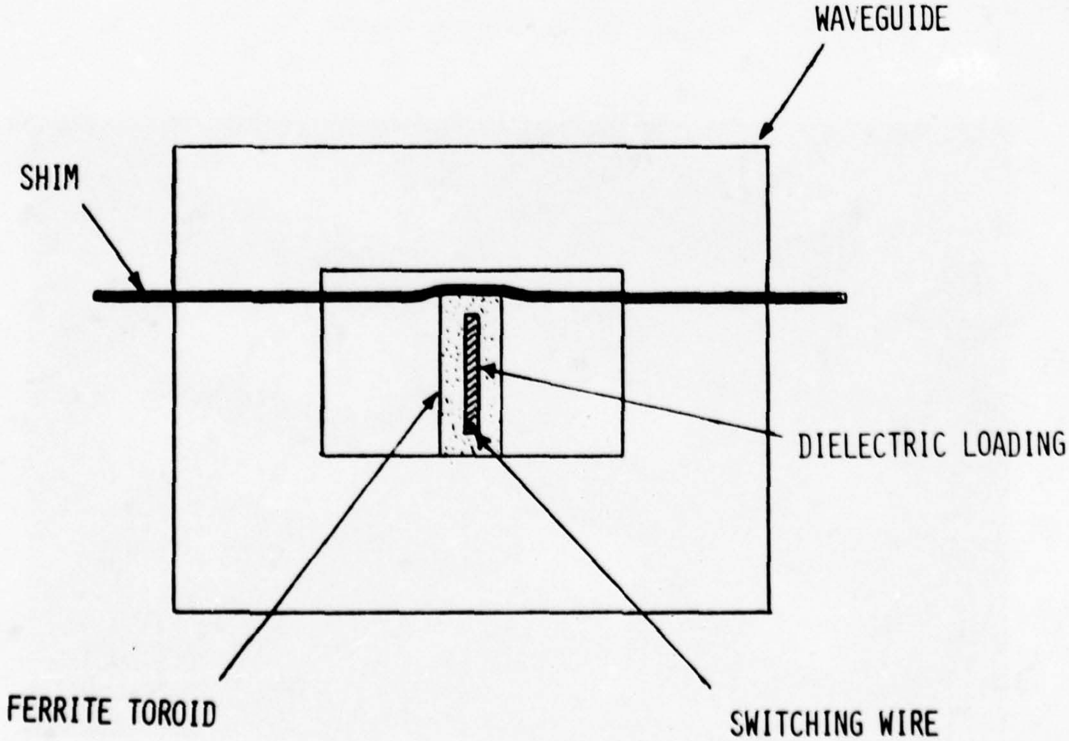
WAVEGUIDE
SHIM
DIELECTRIC LOADING
FERRITE TOROID
SWITCHING WIRE

Fig.9 Cross Section of Phaser Test Fixture

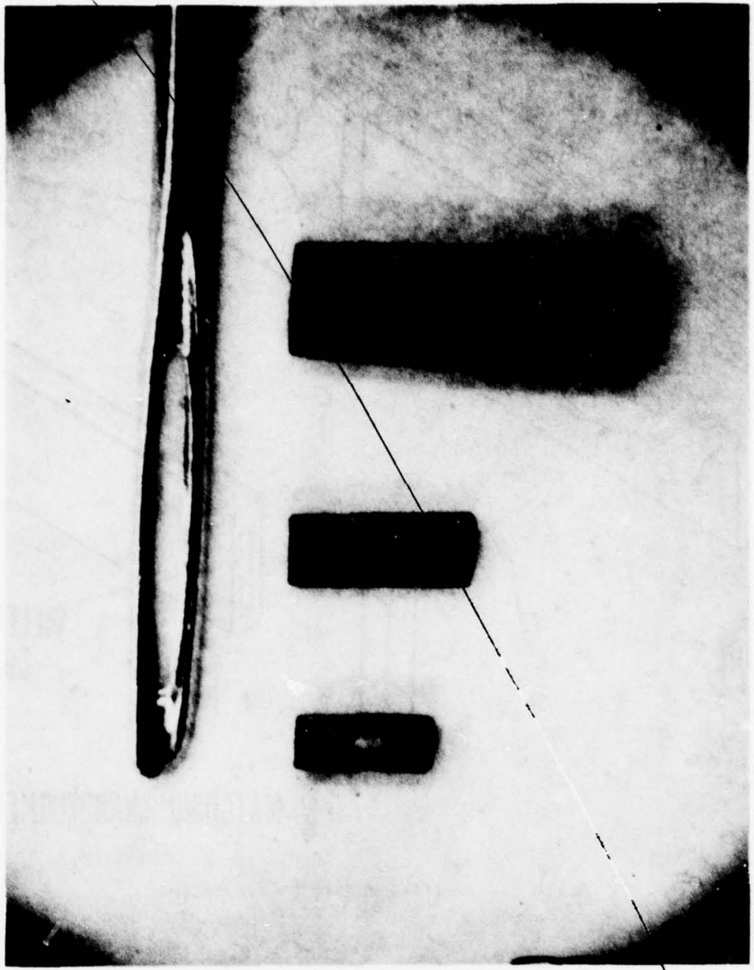

Fig.10 Millimeter Phaser Toroids

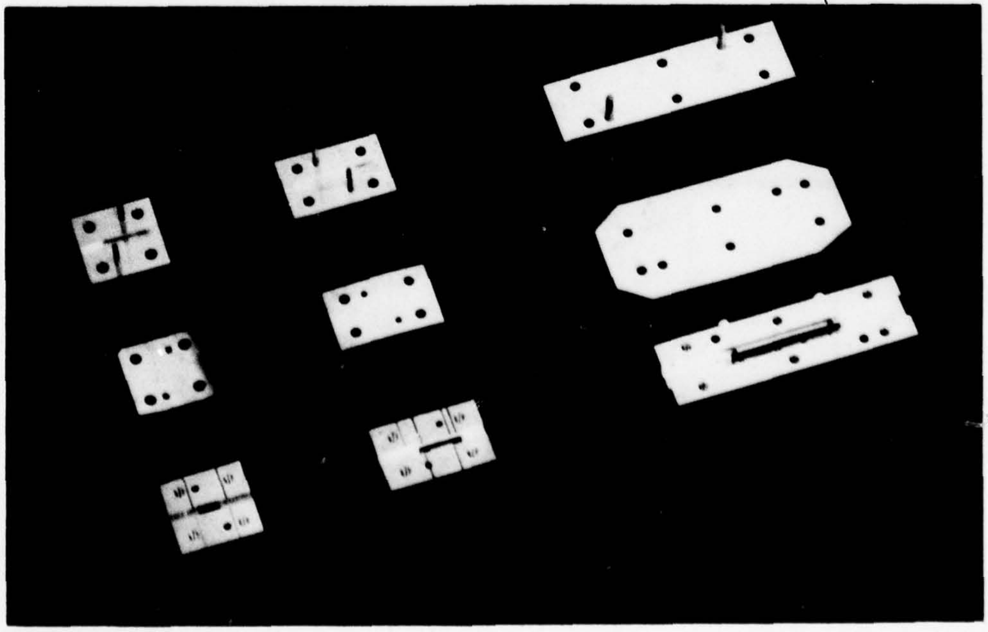

Fig.11 Millimeter Phaser Structures

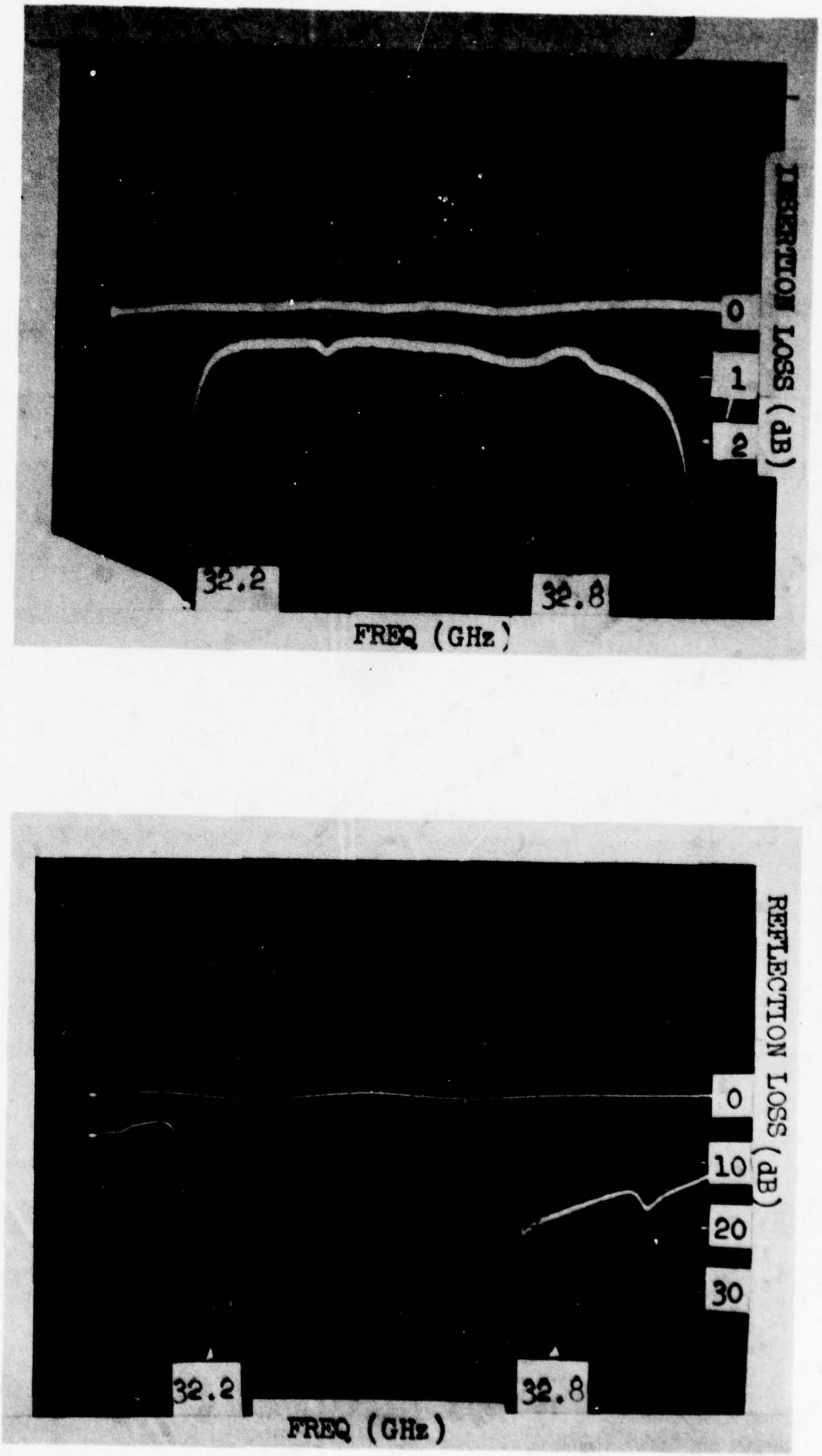

Fig.12 Insertion Loss and Return Loss for 35 GHz Phaser

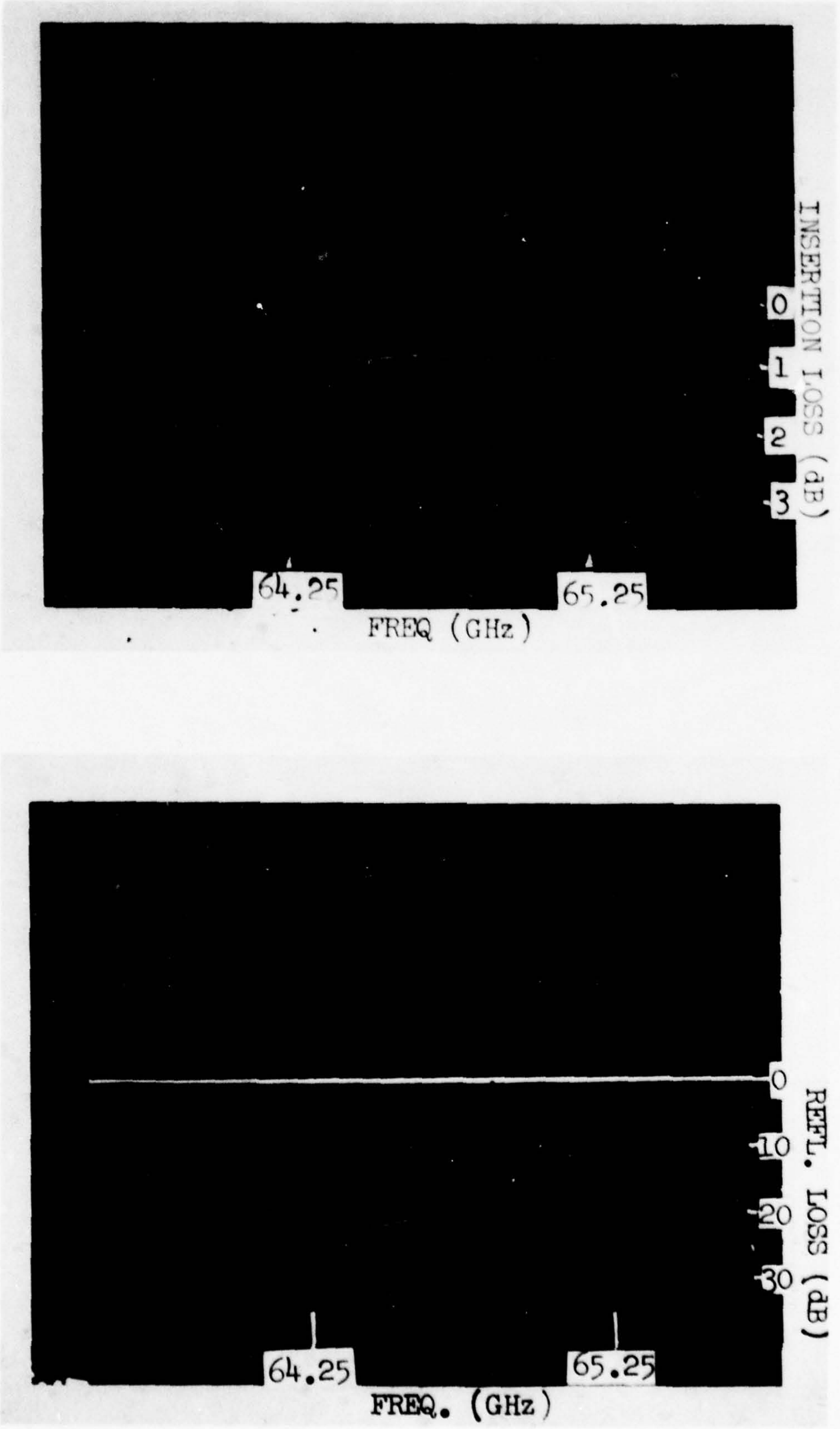

Fig.13 Insertion Loss and Return Loss for 65 GHz Phaser

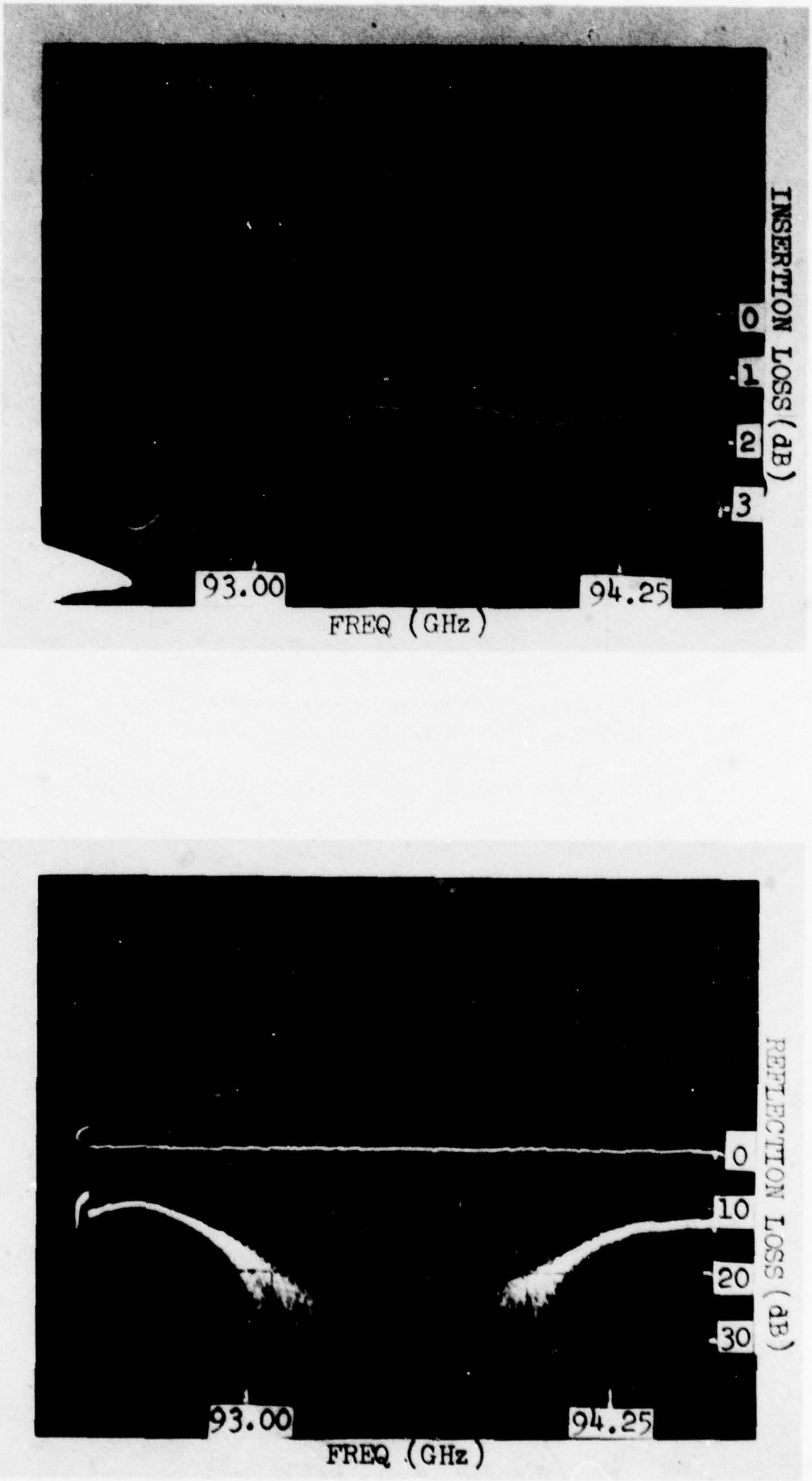

Fig.14 Insertion Loss and Return Loss for 94 GHz Phaser

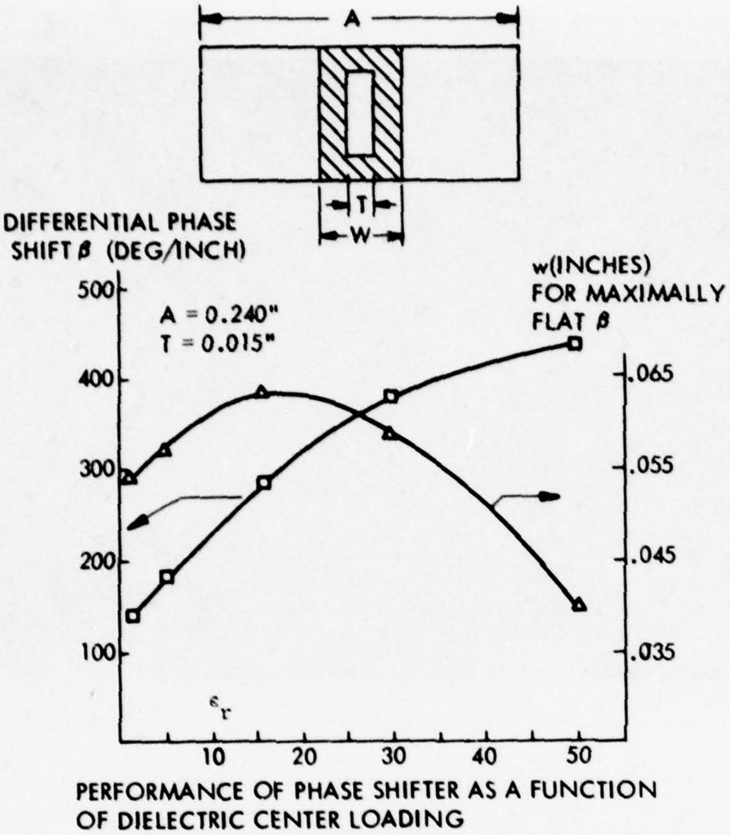

Fig.15 Phase Shift Activity vs. Dielectric Center Loading

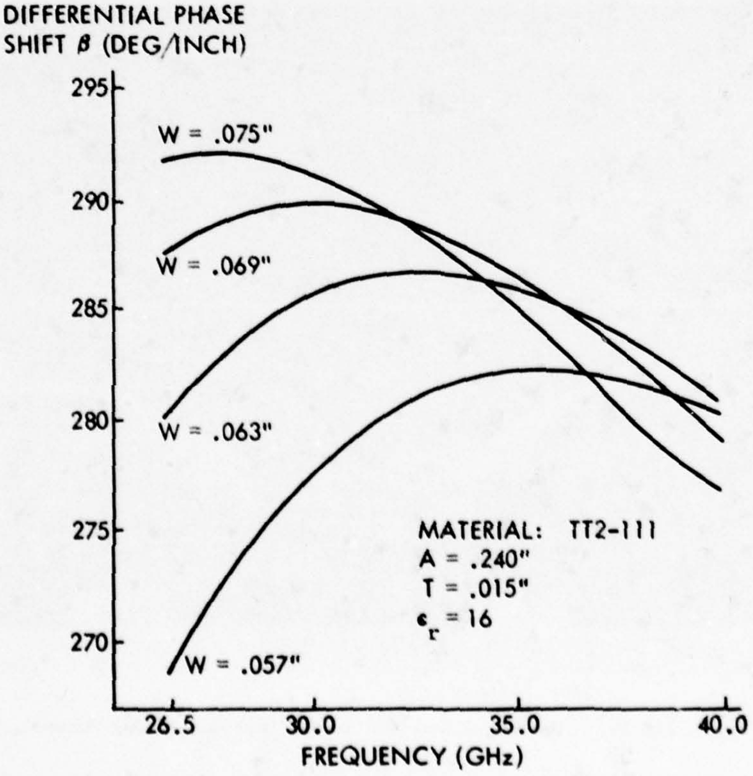

Fig.16 Phase Shift vs. Frequency for Various Toroid Widths

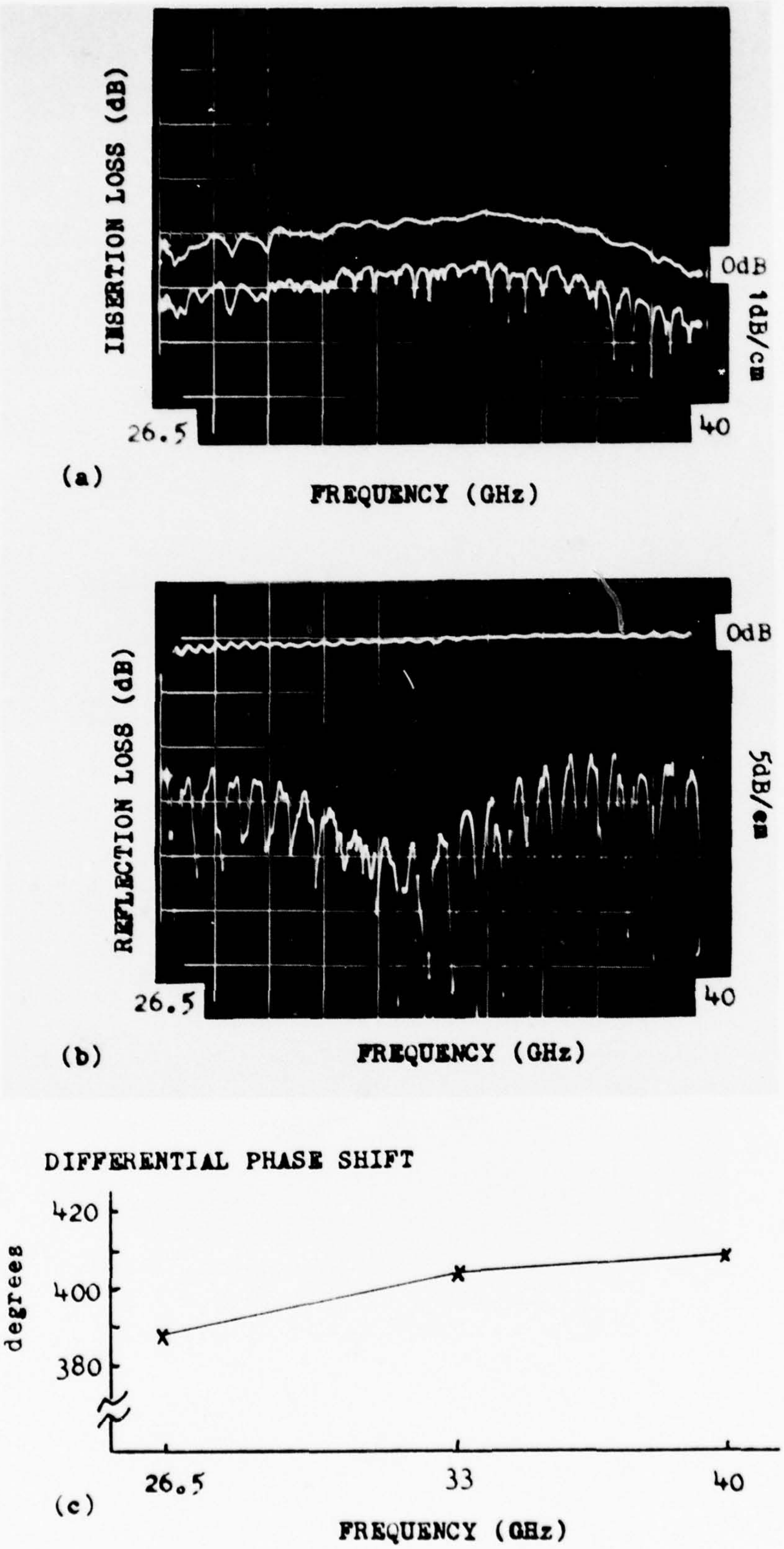

Fig.17 Performance Data for 26.5-40 GHz Phaser

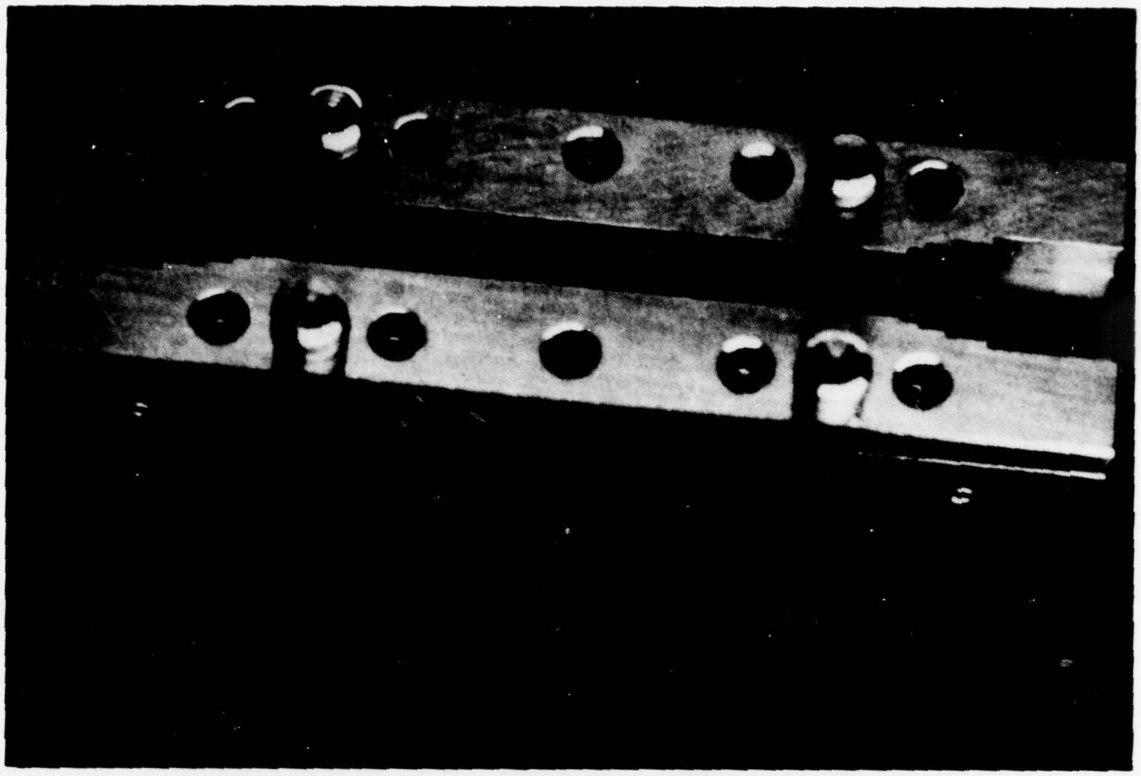

Fig.18 Open View of 26.5-40 GHz Phaser

DISCUSSION

J.Snieder, Netherlands

(1) Is mentioned switching time of 1 μsec valid for complete phase shifter or for the examined piece of ferrite with much less phase shift than 360° (360° at 94 GHz)?

(2) Can you mention the peak power capability of the described phase shifters?

Comment:

(1) Cylindrical toroids, extensively examined at the Physics Laboratory TNO, do not show moding problems as shown in your 26, 5–40 GHz ferrite phase shifters.

(2) Reggia-Spencer type of phase shifters look very promising at mm wavelength, as our first experiments have shown.

The production of these rectangular slabs is easy. Only the waveguide wall is an extra item to look at.

Author's Reply

(1) This phase can be suitable as fast as 200 nsec and most likely less since small amount of ferrite is involved (< 200 ns for 1 switching operation). This would be valid for a 360° complete phasor.

(2) Peak power capability should be at least several kilowatts, possibly up to 50 kW (see 1968 MIT Symposium Digest, Stern). These phasors should operate under peak power similar to that of low-frequency phasors with appropriate power capability reduction due to decreasing size at mm waveguides.

AN OSCILLATOR-MULTIPLIER CIRCUIT FOR THE GENERATION OF MILLIMETER WAVES

L. Szabo, K. Schünemann

Institut für Hochfrequenztechnik, Technische Universität Braunschweig,
D-33 Braunschweig, PF 3329, W-Germany

ABSTRACT

This contribution deals with theoretical and experimental investigations on a solid-state millimeter wave source, which combines a negative-resistance device (Impatt diode or Gunn element) with a varactor diode in a common imbedding. Frequency generation and multiplication are thus performed in one circuit. The oscillator can be regarded as a two-frequency device, because the imbedding is designed to support only two frequencies: the fundamental and the desired harmonic wave. In comparison with an ordinary oscillator followed by a frequency multiplier, the new circuit shows no isolator between these two components.

This feature must, however, be thought of as of minor importance. The aim of the compound oscillator-multiplier structure is to establish a two-frequency device, which shows some advantagous properties. The first is obviously, that the ouput power is transferred to a higher frequency. We will show both theoretically and experimentally the effectiveness of a frequency doubling device, which simultaneously operates at Ku-band and Q-band frequencies. The FM-noise favourable compares with that of an oscillator, which directly generates the higher frequency.

Another characteristic of the compound oscillator is, that its "idler" circuit (i.e. that circuit at which no output power is extracted) may be utilized to stabilized the oscillator against frequency drifts due to both temperature changes (long-term stability) and noise sources (short-term stability). This can be performed by establishing an idler circuit with high Q-factor. The attainable frequency stability surely depends on the amount of power dissipated in the high-Q resonator. It could be shown, however, that a reduction in ouput FM-noise of 20 dB is possible at the sacrifice of only 10% of ouput power.

Another possible application is an oscillator, which is synchronized at its harmonic frequency. It thus acts as a frequency dividing circuit of high efficiency and large bandwidth. This is due to the rich harmonic content of the compound oscillator. Thus frequency division by a factor of 4 would be observed in a 3% bandwidth. The system showed a power gain of 6 dB. Such a frequency dividing oscillator is useful, when an indirect amplification scheme shall be established. In this case amplification takes place at a lower frequency, what is attractive especially for signals in the millimeter wave range.

As a last application an oscillator shall be mentioned, which is capable of delivering ouput power at two frequencies (preferably at the fundamental and its first harmonic). This oscillator can be used as local oscillator in both resistive frequency downconverters and parametric amplifiers or frequency upconverters. It enables a more efficient pumping of the mixing devices, thus leading to a higher conversion gain. Work is now in progress towards an oscillator configuration, which allows adjusting the power distribution on the two frequencies.

INTRODUCTION

The combination of two-terminal active elements, such as Gunn and IMPATT diodes, and a varactor frequency multiplier will make it possible to construct new compact RF power sources for microwave integrated circuits in the millimetric wave region too. However, no adequate design theories for integrated multiplying oscillators have been proposed. This paper presents a simplified general exact disign theory of the integrated multiplying oscillator, by considering the large-signed nonlinearities of the active element and the varactor that are strongly mutually coupled. Figure 1 shows the general circuit representations for the frequency multiplier in the microwave oscillators. The ideal filters are short circuits for Fig. 1a and open circuits for Fig. 1b at all frequencies except the one specified. The varactor series resistance is considered to be represented by equivalent shunt conductances at the input and output frequencies. Such a transformation is valid for high Q varactors. For sake of simplicity the package and mount elements are not considered here, however the introduction of these elements cannot fundamental limit the circuit performance.

Since this circuit contains nonlinear elements, a computer optimization would be necessary for the exact design of a circuit. But computer optimization requires much time and lacks generality. In order to simplify the design procedure, we assume that the optimum overall performance will be achieved when the multiplier is matched to the oscillator, acting as the optimum load for the active element, and at the same time operates under the maximum efficiency condition. We take into account the nonlinear dynamic property of the active element in the form of a dynamic admittance $Y_D=G_D+jB_D$, which is in general dependent to the oscillation voltage amplitude.

The optimum load condition for the oscillator is first obtained by using the dynamic conductance G_D. Then the parameters of the multiplier are chosen so that the input conductance and the RF voltage of the fundamental frequency coincide with those of the active element under the maximum efficiency condition of the multiplier. The matching of the susceptance component is met by adding the stub (B_s) in the fundamental frequency circuit. To facilitate the design, the design charts are given for the case of a doubler operating in the charge controlled mode.

The idea of the dynamic conductance was confirmed by experiments on the oscillators employing a Gunn-diode. A multiplying oscillator with an output frequency in the Q-band was constructed by using the Gunn-diode as the active element. The experimental results of its power performance were consistent with those predicted by the design theory. It was found that this design theory gives almost the same optimum values as those obtained by computer optimization.

THEORETICAL STUDY

Oscillator

In general we represent the oscillator section by the equivalent circuit shown in Fig. 2. in which G_D and G_L are conductances of the active element and the load, respectively.

The characterisation of negative-resistance diodes, however is very difficult since these diodes have complicated nonlinear characteristics and can operate in several different modes according to operating conditions:Pence (1970) and Getsinger (1966). Therefore, special emphasis is given here to a simple model involving a cubic nonlinearity, and the idealized LSA mode operation of a Gunn-effect device.

In general a negative resistance diode has a V-I characteristic shown in Fig.3. When the diode is biased at a dc voltage and draws a dc current of I_B at this point, the following relationship can be used:

$$I_a=a_1V_a+a_2V_a^2+a_3V_a^3+\ldots=\sum_{n=1}^{\infty}a_nV_a^n \quad \text{where} \quad V_a=V-V_B \quad \text{and} \quad I_a=I-I_B$$

If the diode is biased at a point of negative conductance, a_1 will be negative. Because the device contains no energy source, a valid finite series must terminate in an odd order term with a positive coefficient. We will assume that the device is to be excited by a purely sinusoidal voltage wave at a frequency ω and with a peak amplitude of V_1 volts. Because of the capacitance involved, we also assume that current flow in the generator is not inhibited by significant impedance at the harmonic frequencies, and that no significant harmonic voltages appear except the fundamental $V_1 \cos \omega t$. It is preferable to use Fig. 1a for a device that is biased through a constant voltage source while it is convenient to work with Fig. 1b for a device that in biased by a constant current source.

We first assume that the V-I law is a simple cubic relationship. The power generated by the diode is (Hines 1970): $P_{Dgen}=\frac{1}{2}a_1V_1^2+\frac{3}{8}V_1^4$

The effective conductance $G_{D1}=a_1+\frac{3}{4}a_3V_1^2$ as seem by the fundamental wave.

This approach can also be used for a Gunn device which operates in the LSA mode under certain conditions (Copeland, Mircea). In this case the V-1 characteristic can easily be obtained from the velocity field relationship. The following analysis is used for our analysis (Camp, Johnston).

$$I=K\frac{\mu_1E+V_s(E/E_N)^4}{1+(E/E_N)^4}$$

μ_1	low field mobility $\vert cm^2/Vs \vert$
V_s	saturated velocity $\vert cm/s \vert$
E	electric field $\vert V/cm \vert$
E_N	4000 V/cm
K	= $f(R_0)$
R_0	low field resistance

Applied a sinusoidal voltage drive with various amplitude to the bias point, we obtained data for the fundamental conductance and the generated power using the Fourier analysis - in a computer. The Fig. 4 shows these relationships calculated using normalized voltage and current in terms of their values at the peak or critical point of the curve. Bias is assumed to be three times the critical field value. These curves agree with the data obtained by Hines feeding in a large number of points from the curve. In the Fig. 5 only the region for $V \geq 2.235$ is the idealized LSA condition. For lower drive, space charge accumulation (domain formation) would be expected according to the theory of Copeland and the validity of the curve is highly questionable.

Analysis of varactor harmonic generation

For harmonic generation provide the Manley-Rowe relations the fundamental limits. In reality the achievement of high conversion efficiency is dependent upon the provision of proper circuits, and upon an appropriate degree of nonlinearities of the reactive element. Leeson and Weinreb (1959) analyzed frequency multiplication using a varactor diode as a nonlinear capacitance. They considered a circuit that contained only an input and the required output circuits, and showed that the efficiency is even worse than Page's limit for higher order frequency multipliers when the circuit losses and small varactor resistance are included. Later it was shown that this efficiency can be improved significantly by adding idler circuits at intermediate harmonics (Utsunomiya).

Several authors carried out large signal analysis of a varactor harmonic generator using Taylor series expansion (Machard, Roulston) or a Fourier series representation (Scanlan) for the varactor voltage-charge relationship. However this analysis are usually limited to the case in which the diode is arranged in shunt with input and output circuits. This avoids complexity when the exponent of the voltage-charge relationship is not an integer.

General analysis

We have obtained the following relationship between the stored charge and the junction voltage across the varactor diode

$$Q=-\frac{c_1(\phi-V)^{(1-\gamma)}}{1-\gamma}$$

Considering the circuit of Fig. 1a if we let the voltages across the diode at the fundamental frequency and the required harmonic be given by $V_1\cos\omega t$ and $V_N\cos(N\omega t+\phi_N)$ we become

$$q=\left\{1-V_1\cos\omega t+V_N\cos(N\omega t+\phi_N)\right\}^{(1-\gamma)}$$

The lower case letters indicate the normalized value

$v_1 = V_1/V_B \qquad v_N = V_N/V'_B \qquad q = Q/Q_B$

$V'_B = \phi - V_B \qquad Q_B = -C_B V'_B/(1-\gamma) \qquad C_B = C_1/V'_B\gamma$

Expanding as a Fourier series

$$q = a_0/2 + \sum_{n=1}^{\infty} (a_n \cos n\omega t + b_n \sin n\omega t)$$

$$a_n = \frac{1}{\pi}\int_{-\pi}^{\pi} \left\{1 - v_1\cos\omega t + v_N\cos(N\omega t + \phi_N)\right\}^{(1-\gamma)} \cos n\omega t \; d(\omega t)$$

$$b_n = \frac{1}{\pi}\int_{-\pi}^{\pi} \left\{1 - v_1\cos\omega t + v_N\cos(N\omega t + \phi_N)\right\}^{(1-\gamma)} \sin n\omega t \; d(\omega t)$$

If the output circuit is resonated, we have $\phi_N = \frac{\pi}{2}$ and the circuit equations are (Scanlan).
From Kirchhoffs I equation

$$\left\{G_{D_1}\right\} V_1\cos\omega t = m^2\left\{G_{l_1} V_1\cos\omega t + \frac{V_1}{\omega L_1}\sin\omega t + Q_B\omega b_1\cos\omega t - Q_B\omega a_1\sin\omega t\right\}$$

and

$$Q_B N\omega b_N\cos N\omega t - Q_B N\omega a_N \sin N\omega t = -(G_{LN} + G_{lN})V_N\sin N\omega t + \frac{V_N}{N\omega L_N}\cos N\omega t$$

G_{l_1} and G_{lN} represents the input and ouput circuit losses including the equivalent varactor conductances at input and output frequencies. The device reactance is not considered here, for convenience; however it could easily be included in input equation. To get oscillation at fundamental frequency f we need

$$L_1 = \frac{V_1}{Q_B\omega^2 a_1} \qquad \text{from} \qquad \frac{1}{\omega^2 L_1 C_1} = 2\frac{V'_B}{V_1}a_1$$

and

$$|G_D(V_1)| = m^2\left(G_{l_1} + \frac{Q_B\omega b_1}{V_1}\right)$$

Output resonance requires

$$L_N = \frac{V_N}{Q_B(N\omega)^2 b_N} \qquad \text{and} \qquad G_{LN} = \frac{Q_B N\omega a_N}{V_N} - G_{lN}$$

In this case the Fourier coefficients a_N and b_N are

$$a_N = \frac{1}{\pi}\int_{-\pi}^{\pi} (1 - v_1\cos\omega t - v_N\sin N\omega t)^{(1-\gamma)}\cos n\omega t \; d(\omega t) \qquad \text{and} \qquad b_N = \frac{1}{\pi}\int_{-\pi}^{\pi} (1 - v_1\cos\omega t - v_N\sin N\omega t)^{(1-\gamma)}\sin n\omega t \; d(\omega t)$$

Now the solutions, v_1 and v_N can be found in terms of other circuit parameters and the output power at the required harmonic can be calculated

$$P_N = \frac{1}{2} G_{LN} V_N^2$$

In the case represented on Fig. 1b. the voltage-charge relationship is

$$\Phi - V = V'_B\left(\frac{Q}{Q_B}\right)^{\Gamma} \qquad \text{where} \qquad \Gamma = \frac{1}{1-\gamma}$$

Again biasing of the diode must be done with a voltage source and the constraint on the charge is given by the bias voltage. Let $Q = Q_{AV} + Q(t)$ where
$Q(t) = Q_1\cos\omega t + Q_N\cos(N\omega t + Q_N)$ such that $I(t) = I_1\sin\omega t + I_N\sin(N\omega t + \Phi_N) = -\omega Q_1\sin\omega t - N\omega Q_N\sin(N\omega t + \Theta_N)$

Here $Q_{AV} = Q_B + Q_t$ where Q_t is the component of the average charge value due to the presence of the time varying elements. Fortunately for the case of greatest practical interest of $\Gamma = 2$, all the higher order terms become zero and the equation for Q_t reduces to a quadratic form. The equation clearly shows that when both Q_1 and Q_N are zero, then $Q_t = 0$, and there is no average charge.

$V = V_B + V(t)$ however $V(t)$ now will have components at the fundamental and all the harmonic frequencies. Therefore can be written as

$$\Psi - V = \{1 + q'_1\cos\omega t + q'_N\cos(N\omega t + \Theta_N)\}^{\Gamma} = \frac{C_o}{2} + \sum_{n=1}^{\infty} (c_n\cos n\omega t + d_n\sin n\omega t)$$

where

$$c_n = \frac{1}{\pi}\int_{-\pi}^{\pi}\{1 + q'_1\cos\omega t + q'_N\cos(N\omega t + \Theta_N)\}^{\Gamma}\cos n\omega t \; d(\omega t), \quad d_n = \frac{1}{\pi}\int_{-\pi}^{\pi}\{1 + q'_1\cos\omega t + q'_N\cos(N\omega t + \Theta_N)\}^{\Gamma}\sin n\omega t \; d(\omega t)$$

The normalizations are the same as before and $q'_1 = \frac{Q_1}{Q_{AV}} \qquad q'_N = \frac{Q_N}{Q_{AV}}$

Similarly if the output circuit is resonated, $\Theta_N = \pm\frac{\pi}{2}$ depending on the value of Γ as well as the harmonic number N. The following equation can be obtained

$$R_D(I_1) = \frac{1}{m^2}\left(R_{l_1} - \frac{V'_B d_1}{I_1}\right) \qquad L_1 = -\frac{V'_B C_1}{\omega I_1} \qquad \text{and}$$

$$\beta_k = \frac{Q_B^k}{v_B'k!} \frac{d^k v}{dQ^k}\bigg|_{Q=Q_B} .$$

The normalized power output at the Nth harmonics.

$$p_N = \frac{1}{2} r_{LN} |i_N|^2 = \frac{1}{2} r_{LN} N^2\omega^2(q_{Nr}^2 + q_{Ni}^2) = 2N^2\omega^2\beta_N^2(\frac{q_1}{2})^{2N} \frac{r_{LN}}{(\beta_1 - N\omega x_N)^2 + (N\omega r_N)^2}$$

for resonant $\beta_1 = N\omega x_N$ we becomes

$$z_i = \frac{\beta_N^2}{\omega^2 r_N} (\frac{q_1}{2})^{2N-2} - j\frac{\beta_1}{\omega} = \frac{\beta_N^2}{\omega^{2N} r_N}(\frac{i_1}{2})^{2N-2} - j\frac{\beta_1}{\omega} \qquad p_N = \frac{2\,{}^2_N r_{LN}}{r_N^2} (\frac{q_1}{2})^{2N} = \frac{2\beta_N^2 r_{LN}}{\omega^{2N} r_N^2} (\frac{i_1}{2})^{2N} .$$

This analysis applied to a varactor diode the Taylor series coefficients becomes (Leeson)

$$a_k = (-1)^k \frac{(1-\gamma)!}{k!((1-\gamma)-k)!} \qquad \beta_k = \frac{(\frac{1}{1-\gamma})!}{k!(\frac{1}{1-\gamma} - k)!} \qquad \gamma \text{ doping constant } 0 < \gamma < 1$$

denormalized the expressions became

$$v_N = \frac{V_N}{V_B'} \qquad q_n = \frac{Q_n}{Q_B} = - \frac{Q_n(1-\gamma)}{C_B V_B'} = - \frac{In(1-\gamma)}{n\omega C_B V_B'} \qquad z_n = \frac{v_n}{i_n} = \frac{C_B}{(1-\gamma)} Z_n \qquad y_n = \frac{i_n}{v_n} = \frac{(1-\gamma)}{C_B} Y_n .$$

V_B' is the total bias voltage, Q_B and C_B the values for the bias. Using the factors

$$y_1 = \frac{N^2\omega^2 C_B^2 \alpha_N}{(1-\gamma)^2 V_B'^{2N-2}(G_{LN} + G_{1N})} (\frac{V_1}{2})^{2N-2} + j\omega\alpha_1 \qquad P_N = \frac{2N^2\omega^2 C_B^2 \alpha_N^2}{(1-\gamma)^2 V_B'^{2N-2}(G_{LN} + G_{1N})^2} (\frac{V_1}{2})^{2N} \quad \text{and for 1b.}$$

$$z_1 = \frac{(1-\gamma)^{2N}\beta_N^2}{\omega^{2N} C_B^{2N} V_B'^{2N-2}(R_{LN} + R_{1N})} (\frac{I_1}{2})^{2N-2} \qquad P_N = \frac{2(1-\gamma)^{2N}\beta_N^2 R_{LN}}{\omega^{2N} C_B^{2N} V_B'^{2N-2}(R_{LN} + R_{1N})} (\frac{I_1}{2})^{2N}$$

Self excited frequency multiplying oscillator

When the conditions for 1a.

$$L_1 = \frac{V_1}{Q_B\omega^2 a_1} \qquad |G_D(V_1)| = \omega^2(G_{11} + \frac{Q_B\omega b_1}{V_1}) \qquad L_N = \frac{V_N}{Q_B(N\omega)^2 b_N} \qquad G_{LN} = \frac{Q_B N\omega a_N}{V_N} - G_{1N}$$

or those for case 1b.

$$|R_D(I_1)| = \frac{1}{\omega^2} (R_{11} - \frac{V_B' d_1}{I_1}) \qquad L_1 = - \frac{V_B' c_1}{\omega I_1} \qquad R_{LN} = \pm \frac{V_B' c_N}{I_N} - R_{1N} \qquad L_N = \mp \frac{V_B' d_N}{N\omega I_N}$$

are satisfied, harmonics of the input oscillation frequency can be obtained at the output circuit of the self exited frequency multiplying oscillator. The oscillation frequency ω is determined from the susceptance condition and the amplitude of this signal wave V_1 can be found from the conductance condition of the input circuit. Due to the complexity of those equations, solutions are generally obtained using numerical methods. Here we will consider only the case of Fig. 1a using the previously developed model of a Gunn device operating in the LSA mode. The Fig. 1b can be solved similarly.

Assuming that both input and output circuits are resonated, the calculation procedure is as follows:

Specify an output signal amplitude V_N
Find the Fourier coefficients a_n and b_n for different V_1
Determine V_1 and G_{LN}
Using the value from above find the generated power P_{DGEN}
Determine the output power at a specified harmonic
Compute the efficiency which is defined $\eta = \left| \frac{P_N}{P_{DGEN}} \right|$

This procedure is then repeated for different values of V_N. However it should be realized that this analysis is valid only for those values of V_1 which satisfy the conductions of LSA mode operation. The Fourier coefficients a_n and b_1 are calculated using a computer as we did for the characterization of the Gunn-device based on the describing before. Then L_1 and L_N can easily be found to satisfy the assumed resonance conditions of input and output circuits.

Figure 5. shows the variation of input conductance G_1 and input signal amplitude V_1 with output amplitude V_2 for a frequency doubler.

For this computation typical values are used for both the Gunn device and varactor diode. The Gunn-device is assumed to have a thresold voltage of 3,6V and a maximum current of about 800mA. The maximum negative conductance obtained from this Gunn device is about -25 mmhos and the maximum generated power is about 750mW. An abrupt junction varactor of 0,6 V contact potential is considered. This varactor is assumed to

$$R_{LN} = \pm \frac{V_B' C_N}{I_N} - R_{1N} \qquad L_N = \mp \frac{V_B' d_N}{N\omega I_N} \qquad \text{where}$$

$$c_n = \frac{1}{\pi}\int_{-\pi}^{\pi} 1+q_1'\cos\omega t \mp q_N'\sin N\omega t^{\,\Gamma} \cos n\omega t \; d(\omega t)$$

$$d_n = \frac{1}{\pi}\int_{-\pi}^{\pi} 1+q_1'\cos\omega t \mp q_N'\sin N\omega t^{\,\Gamma} \sin n\omega t \; d(\omega t) \; .$$

The sign choice again depends on Γ and the harmonic number N. In this case the output power can be obtained from

$$p_N = \frac{1}{2} R_{LN} I_N^2 \; .$$

Small signal analysis

For small signal operation for Fig.1.a) following relationship can be found (Leeson)

$$q_1 = a_1 V_1 + a_n \frac{N}{2^{N-1}} V^{N-1} V^N \qquad q_N = a_1 V_N + a_N \frac{1}{2^{N-1}} V_1^N \qquad a_k = \frac{V_B'^{\,k}}{Q_B k!} \left.\frac{d^k Q}{dv^k}\right|_{V=V_B'}$$

Q_B and U_B' are the dc operating points of the charge and voltage, respectively. Here we have used the following equation forms of complex Fourier series for the normalized values

$$q = \sum_{\substack{n=-\infty \\ n\neq 0}}^{\infty} \frac{q_N}{2} e^{jn\omega t} \qquad i = \sum_{\substack{n=-\infty \\ n\neq 0}}^{\infty} \frac{i_n}{2} e^{jn\omega t} = \sum_{\substack{n=-\infty \\ n\neq 0}}^{\infty} jn\omega \frac{q_N}{2} e^{jn\omega t} \qquad v = \sum_{\substack{n=-\infty \\ n\neq 0}}^{\infty} \frac{v_n}{2} e^{jn\omega t}$$

where $v_n = v_{-n}^{*} = |v_n| e^{j\Phi_n}$ $\qquad q_n = q_{-n} = |q_n| \, e^{j\Phi_n}$

Letting $v_1 = v_{-1}$ for convenience and then separating q_1 and q_N into real and imaginary parts

$$q_{1r} = a_1 v_1 + a_N \frac{N}{2^{N-1}} v_1^{N-1} v_{Nr} \, , \qquad q_{1i} = a_N \frac{N}{2^{N-1}} v_1^{N-1} v_{Ni} \, , \qquad q_{Nr} = a_1 v_{Nr} + a_N \frac{1}{2^{N-1}} v_1^N \, , \qquad q_{Ni} = a_1 v_{Ni}$$

For the load

$$q_N = -\frac{v_N Y_N}{jN\omega} \, , \qquad q_{Nr} = -\frac{1}{N\omega}(b_N v_{Nr} + q_N v_{Ni}) \, , \qquad q_{Ni} = \frac{1}{N\omega}(q_N v_{Nr} - b_N v_{Ni})$$

q_N represents combination of load conductance q_{LN} and circuit loss q_{iN} at the output circuit. We can now solve v_{Nr} and v_{Ni}

$$v_{Nr} = -\frac{a_N v_1^N}{2^{N-1}} \frac{\left(a_1 + \frac{b_N}{N\omega}\right)}{\left(a_1 + \frac{b_N}{N\omega}\right)^2 + \left(\frac{q_N}{N\omega}\right)^2} \qquad v_{Ni} = -\frac{a_N v_1^N}{2^{N-1}} \frac{\left(\frac{q_N}{N\omega}\right)}{\left(a_1 + \frac{b_N}{N\omega}\right)^2 + \left(\frac{q_N}{N\omega}\right)^2}$$

The normalized admittance of the varactor diode from the input terminal is

$$y_1 = \frac{i_1}{v_1} = -\frac{q_{1i}\omega}{v_1} + j\frac{q_{1r}\omega}{v_1} = N\omega a_N^2 \left(\frac{v_1}{2}\right)^{2N-2} \frac{\frac{q_N}{N\omega}}{\left(a_1 + \frac{b_N}{N\omega}\right)^2 + \left(\frac{q_N}{N\omega}\right)^2} + j\left\{\omega a_1 - N\omega a_N^2 \left(\frac{v_1}{2}\right)^{2N-2} \frac{\left(a_1 + \frac{b_N}{N\omega}\right)}{\left(a_1 + \frac{b_N}{N\omega}\right)^2 + \left(\frac{q_N}{N\omega}\right)^2}\right\}$$

The normalized power output at the N-th harmonics

$$p_N = \frac{1}{2} q_{LN} |v_N|^2 = \frac{1}{2} q_{LN}(v_{Nr}^2 + v_{Ni}^2) = 2a_N^2 \left(\frac{v_1}{2}\right)^{2N} \frac{q_{LN}}{\left(a_1 + \frac{b_N}{N\omega}\right)^2 + \left(\frac{q_N}{\omega N}\right)^2}$$

If the output circuit is resonated $a_1 + \frac{b_N}{N\omega} = 0$ and so

$$y_1 = \frac{N^2\omega^2 a_N^2}{\varepsilon_N} \left(\frac{V_1}{2}\right)^{2N-2} + j\omega a_1 \qquad p_N = \frac{2N^2\omega^2 a_N \varepsilon_{LN}}{\varepsilon_N^2} \left(\frac{V_1}{2}\right)^{2N} \; .$$

A similar analysis can also be applied to the dual circuit of Fig.1b. In this case the normalized impedance from the circuit terminal is

$$z_1 = \frac{v_1}{i_1} = \frac{v_{1i}}{q_1\omega} - j\frac{v_{1r}}{q_1\omega} = \frac{N\beta_N^2}{\omega}\left(\frac{q_1}{2}\right)^{2N-2} \frac{N\omega r_N}{(\beta_1 - N\omega x_N)^2 + (N\omega r_N)^2} - j\,\frac{\beta_1}{\omega} - \frac{N\beta_N^2}{\omega}\left(\frac{q_1}{2}\right)^{2N-2} \frac{(\beta_1 - N\omega x_N)}{(\beta_1 - N\omega x_N)^2 + (N\omega r_N)^2}$$

be biased at 25V and to have a capacitance of 2 pF when Φ-V= 1V. The terms ratio m of the transformer in the input circuit is assumed to be 1 and circuit losses are included by considering a circuit Q of 25 at the fundamental frequency of 10 GHz.

Additional output power versus output signal amplitude curves are shown on the next Fig.6. with the varactor nonlinearity factor γ and capacitance C_1 as parameters. Some points are missed for large values of V_2 simplify became the circuit conditions cannot be satisfied at these values. From the Fig.4. can observe that both the varactor nonlinearity factor and the capacitance value affect the power output at harmonics, because C_1 as well γ affects the input conductance G_1 which determines the power generation from the device. For higher power generation, the circuit element values must be adjusted to give higher (G_1+G_{11}), however this cannot be greather than $|G_{D1}|/m^2$. Variyng the bias voltage changes the voltage normalizing factor, and the significance of this effect is also shown.

On the next Fig.7. is the power output plotted as a function of the output resistance, which may be readily adjusted for circuit design-again with γ and C_1 as parameters. It is clearly see that the maximum output is obtained at different loading conditions according to the particular varactor characteristic. In general a varactor of higher nonlinearity or of larger capacitance yields higher power output as long as (G_1+G_{11}) is less than $|G_{D1}|/m^2$.

On the Fig.8. shows the efficiency variation with load resistance. The maximum efficiency changes quite significantly for different γ values but changes little for different C_1 values. Obviously efficiency increases with increasing circuit Q as denoted

$$\eta = \frac{G_1}{G_1+G_{11}}\,\frac{G_{LN}}{G_{LN}+G_{1N}}$$

For higher order harmonic generation, the output power decreases very rapidly since both the input conductance G_1 and the output signal amplitude V_N decrease rapidly to satisfy the conductance conditions.

It is interesting to compare the results of the small signal analysis with those of the above derived large signal analysis. Therefore the same typical values used a general analysis are again used for both diodes. Fig.9. represent the power output versus load resistance curves with C_1 as the parameter for different circuit Q values. The efficiences of these circuits are shown in Fig.10. As mentioned previously, the efficiency increases as the circuit Q increases. In general, calculated values from the small-signal analysis are slightly smaller then those from the large-signal analysis. However, excellent agreement can be observed in comparing the curves of Fig.7. and Fig.8. with those of Fig.9. and Fig.10., thus verifying these analyses.

The power output at different harmonics is also considered, and is shown in Fig.11 for two different load resistances. The rapid decrease of output power with harmonic number N again indicates that this circuit is not suitable for higher harmonic generation.

Combining the equations from the cubic relationship of the Gunn-device with those from the small-signal analysis of varactor multiplication, we will consider the available maximum power output.

Again assuming both input and output circuits are resonated, the conductance condition of the input circuit is given by:

$$\frac{m^2N^2C_B^2\,\omega^2\,\alpha_N^2}{(1-\gamma)^2\,(G_{LN}+G_{1N})}\left(\frac{V_1}{2V_B'}\right)^{2N-2}+\frac{3}{4}a_3v_1^{\,2}+m^2G_{11}-a_1'=0$$

where a_1 is now positive: $a_1' = |a_1|$

Differentiation of this equation with respect to G_{LN} yields:

$$\frac{dV_1}{dG_{LN}}=\frac{\dfrac{m^2N^2\omega^2C_B^2\,\alpha_N^2V_1^{\,2N-3}}{(1-\gamma)^2G_{LN}(1-\xi)^2\;2V_B'^{\;2N-2}}}{\dfrac{3}{2}a_3+\dfrac{m^2(2N-2)N^2\omega^2C_B^2\alpha_N^2\;V_1^{\,2N-4}}{(1-\gamma)^2\;G_{LN}(1+\xi)\;(2V_B')^{2N-2}}}\qquad\qquad \xi=\frac{G_{1N}}{G_{LN}}$$

The load conductance which yields maximum power output can be found by differentiating P_N with respect to G_{LN} and equating this to zero. Then using the equation before we obtain

$$G_{LNm}=\frac{1+(N-1)\xi}{(1+\xi)(1-\xi)}\;\frac{4m^2N^2C_B^2\;\alpha_N^2}{3a_3(1-\gamma)^2(2V_B')^{2N-2}}\left\{\frac{/1+(N-1)\xi/}{/2+(N-2)\xi/}\;\frac{4(a_1'-m^2G_{11})}{3a_3}\right\}^{(N-2)}$$

Substituting G_{LNm} into the condition equation gives us the signal amplitude which yields maximum power output at the harmonic frequency.

$$V_{1m}=\sqrt{\frac{1+(N-1)\xi}{2+(N-2)\xi}\;\frac{4(a_1'-m^2G_{11})}{3a_3}}$$

Finally using the above values we obtain the maximum power output

$$P_{Nmax} = \frac{/1+(N-1)\xi/\ (1-\xi)}{/2+(N-2)\xi/^2\ (1+\xi)} \frac{2(a_1'-m^2G_{11})^2}{3a_3m^2}$$

With this signal amplitude the generated power from the device is:

$$P_{DGEN} = -\frac{1+(N-1)\xi}{2+(N-2)\xi} \frac{2(a_1'-m^2G_{11})}{3a_3} \{a_1' - \frac{/1+(N-1)\xi/\ (a_1'-m^2G_{11})}{2+(N-2)\xi}\}$$

and the negative conductance becomes

$$G_{D1} = -\{a_1' - \frac{1+(N-1)\xi}{2+(N-2)\xi} (a_1' - m^2G_{11})\}$$

The efficiency is now calculated from P_{Nmax} and P_{DGEN}

$$\eta_m = \frac{(1-\xi)}{(1+\xi)m^2} \frac{(a_1' - m^2G_{11})}{|2+(N-2)\xi|a_1' - |1+(N-1)\xi|(a_1'-m^2G_{11})}$$

In this analysis if G_{1N} is specified G_{LN} should be chosen so that ξ satisfies

$$G_{1N} = \frac{1+(N-1)\xi}{(1+\xi)(1-\xi)} \frac{4m^2N^2\omega^2C_B{}^2\alpha_N{}^2}{3a_3(1-\gamma)^2(2V_B')^{2N-2}} \frac{1+(N-1)\xi}{2+(N-2)\xi} \left(\frac{4(a_1'-m^2G_{11})}{3a_3}\right)^{(N-2)}$$

If the circuit losses are neglected, the input conductance equation becomes

$$\frac{m^2N^2\omega^2C_B^2\alpha_N^2}{(1-\gamma)^2G_{LN}} \left(\frac{V_1}{2V_B'}\right)^{2N-2} + \frac{3}{4}a_3V_1^2 - a_1' = 0$$

Similarly the maximum power output at the harmonic frequency is obtained

$$P_{Nmax} = \frac{a_1'^2}{6a_3}$$

at the following values

$$G_{LN_m} = \frac{m^2N^2\omega^2C_B^2\alpha_N^2}{3a_3(1-\gamma)^2V_B'^{2N-2}} \left(\frac{V_1}{2}\right)^{2N-4}$$

and $$V_{1m} = \sqrt{\frac{2a'}{3a}}$$

If the load is properly adjusted, the maximum power output is $a_1'^2/6a_3$ regardless of the harmonic number N with the signal amplitude of $\sqrt{2a_1'/3a_3}$. Note here that the maximum power generated by the device is also $a_1'^2/3a_3$ with the same signal amplitude, thus verifying that all the power generated must be converted into power at harmonics in lossless case. In this case the fundamental negative conductance has fallen to half of its small-signal value.

EXPERIMENTAL WORK:

The above analysis has been carried out using several assumptions. Since it is extremely difficult to satisfy all the conditions in our waveguide mounting structure, only those that are basic to our investigation are studied in our experiments.

To measure the effects of input power level and varactor bias voltage on the output of the second harmonic. The post mounted element was optimized for their optimal position, based on our previous investigations. We can determine the oscillation frequency by adjusting the distance between post and a sliding short and can vary the input power into a varactor multiplier using an attenuator. The input circuit of the varactor multiplier tuned mainly by adjusting the sitance between the varactor post and isolator - placed between the oscillator and varactor mount - and the output circuit is tunde using a slide screw tuner.

Rapid increases of output power are observed as the input power increases or as the varactor bias decreases. However, only show the proportional change in the output power with change in the input power level or the varactor bias voltage, because part of the generated power is obsorbed by the isolator.

If the input level increases too much, or the varactor bias decreases to a value close to zero, a forward conduction current is observed in the bias circuit, decreasing the output power. Under special conditions, however, anomalous reverse current is notized, as reportet by Siegel (1960)

Combined the Gunn and varactor diodes, we may consider two different cases plotted in Fig.13 . An X-band E-H-tuner is used for tuning the input circuit at the fundamental frequency while the Ku-band slide screw tuner is introduced to tune the output circuit at the second harmonic. Usually the oscillation frequency changes while the circuits are being tuned.

For the case of Fig13a. when the circuit is tuned for an oscillation frequency at aboat 10 GHz, the maximum power output of the second harmonic obtainable from port is about 15 mW. However, when we changed the varactor bias, we observed almost no change in either output power on the oscillation frequency - as well as the second harmonic. The power measured from port A increases slightly as the varactor bias decreases, possibly due to the changing of tuning conditions resulting from varactor capacitance variation. In this case, the oscillation frequency appears to be controlled by the cavity between the Gunn post and Ku-band slide-screw tuner. The distance between the two posts determines the oscillation frequency.
For the second case Fig.13b.the oscillation frequency was mainly dependent on the setting of the X-band E-H-tuner, and therefore we adjusted the oscillation frequency so that the carity between the two posts was also at resonance. Indeed, the power output of the second harmonic varies as the varactor bias changes, and large forward conduction current in the bias circuit is observed, when the varactor bias decreases below 5 V. However in this case the whole circuit condition changes, since the oscillation frequency also depends on the varactor bias voltage.

CONCLUSION:

A design theory of a multiplying oscillator was presented. The method of oscillator optimization using the dynamic conductance concept (Furukawa 1970) was applied. The design is basically the determination of the circuit parameters to realize the optimum matching of the fundamental frequency circuit f.e. the condition

$$G_D + jB_S + G_{in} = 0$$

where Y_{in} is the input admittance of the multiplier. To avoid the tedious calculations, the design have been made by using the equations, describing the varactor in the charge controlled made. It is to be noted that the same method presented in this paper can be applied to higher order multipliers and other modes of operation of the varactor. If there is more than one frequency that satisfies the basic condition at the same bias condition, then spurious oscillations will occur. However, this is a very strict condition that requires the matching of conductance, susceptance, and voltage of the active element to the multiplier at the same frequency. Spurious oscillations were not observed in the experiment in this paper.

The band-width of this circuit is determined mainly by the freqeuncy range in which the matching conditions is satisfied. Thus it is dependant on G_D and the characteristics of the active element.
The system aspects of our contribution are described in the abstact. Some of them are considerated and found as realizable.

REFERENCES

CAMP W.O., High-Efficiency GaAs Transferred Electron Device Operation and Circuit Design
IEEE Trans. Electron Devices, Vol ED-18, December 1971, pp.1175-84.

COPELAND J.A., LSA Oscilator-Diode Theory,
J.Appl. Phys., Vol 38, July 1967, pp. 3096-101.

COPELAND J.A. Characterization of Bulk Negative Resistance Diode Behavior,
IEEE Trans.Electron Devices, Vol. ED-14, September 1967, pp.461-3.

FURUKAWA S. NAKAGAMI T. Design Theory of a Self-Excited Frequency-Multiplying Oscillator
IEEE Journal of Solid-State Circuits, Vol. SC-5, June 1970, pp. 87-94.

GETŚINGER W.J. The Packaged and Mounted Diode as a Microwave Circuit
IEEE Trans. Microwave Theory and Techniques, Vol. MTT-14, February 1966, pp. 58-69.

GETSINGER W.J. Mounted Diode Equivalent Circuits
IEEE Trans. Microwave Theory and Techniques, Vol. MTT-15,November 1967,pp. 650-1.

HINES M.E. Negative Resistance Diode Power Amplification
IEEE Trans.Electron Devices, Vol.ED-17, January 1970, pp.1-8.

JOHNSTON R.H., KIDDLE E.R. Harmonic Tuning for High-Efficiency GaAs Oscillators
Proc.IEEE, Vol.60, November 1972, pp.1449-51.

LEESON D.B. WEINREB S. Frequency Multiplication with Nonlinear Capacitors-A Circuit Analysis
Proc. IRE, Vol.47, December 1959, pp.2076-84.

MACKARD E. YUAN S. High Efficiency, High Order, Idler-less Frequency Multipliers using Hyperabrupt Varactors
RCA Review, Vol.26, September 1965, pp. 400-23.

MANLEY J.M. ROWE H.E. Some General Properties of Nonlinear Elements
Proc. IRE, Vol44, July 1956, pp904-13.

MIRCEA A. A simple Criteria for LSA Oscillation
IEEE Trans.Electron Devices, Vol.ED-18, July 1971, p449.

PENCE I.W. KHAN P.J. Broad-Band Equivalent-Circuit Determination of Gunn Diodes
IEEE Trans. Microwave Theory and Techniques, Vol.MZZ-18, November 1970,pp. 784-90.

ROULSTON D.J. BOOTHROYD A.R. A Large Signal Analysis and Design Approach for Frequency Multipliers Using Varactor Diodes
IEEE Trans.Circuit Theory, Vol.CT-12,June 1965, pp.194-205.

SCANLAN J.O. LAYBOURN P.J.R. Large Signal Analysis of Varactor Harmonic Generators without Idlers
Proc.IEE, Vol.112, August 1965, pp.1515-22.

SCHÜNEMANNK. SCHIEK B. Optimaler Wirkungsgrad von Frequenzverfielfachern mit Speicherdiode
AEÜ Vol.22. 1968, pp. 186-96, 293-302.

UTSUNOMIYA T. YUAN S. Theory, Design and Performance Frequency Multipliers
Proc.IRE, Vol.50, January 1962, pp.57-65.

FIGURES

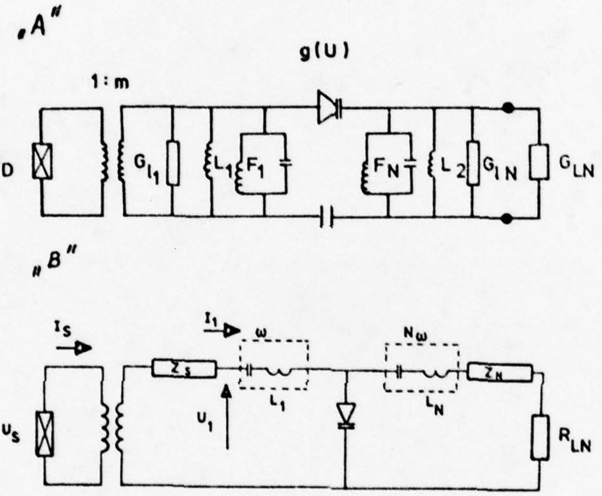

Fig.1 Equivalent circuits for self-excited frequency-multiplying microwave oscillators

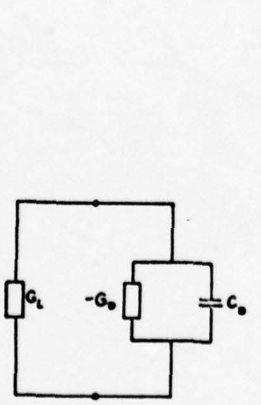

Fig.2 Oscillator equivalent circuit

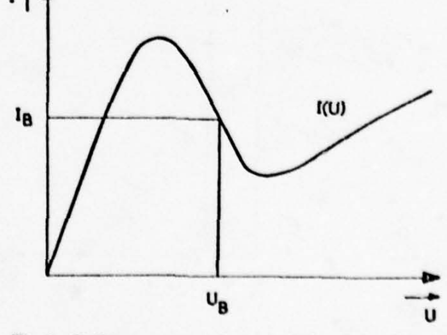

Fig.3 Voltage-current characteristic of the Gunn-device

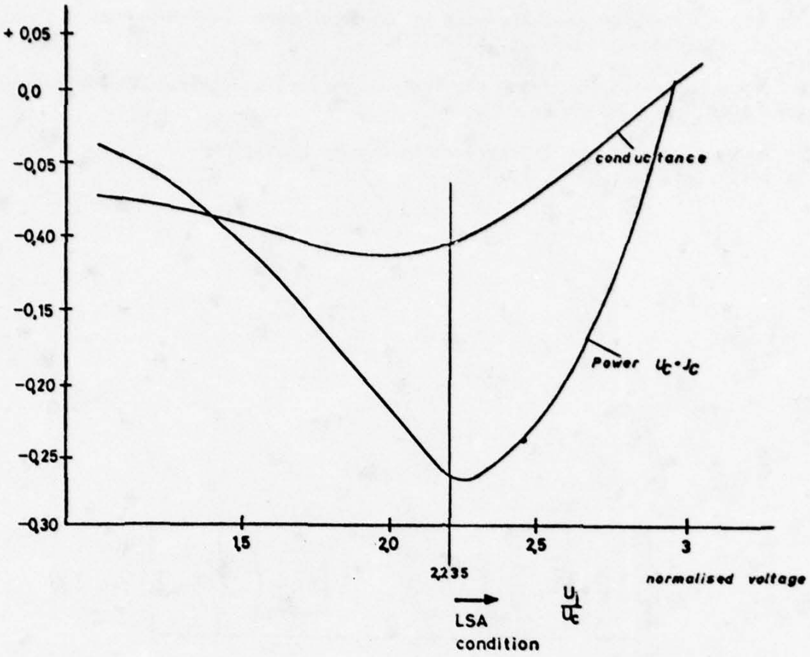

Fig.4 Input conductance and generated power variations with the drive of the Gunn-device

$m = 1$ $\gamma = 0,5$ $f_1 = 10$ Ghz
$N = 2$ $C_1 = 2$ pF $Q_1 = 25$
$\varphi = 0,6$ V $V_B = -25$ V

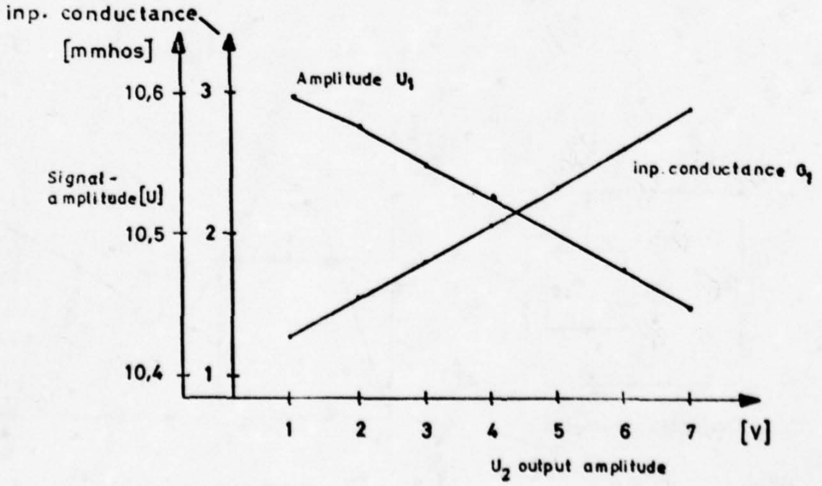

Fig.5 Input characteristics versus output amplitude

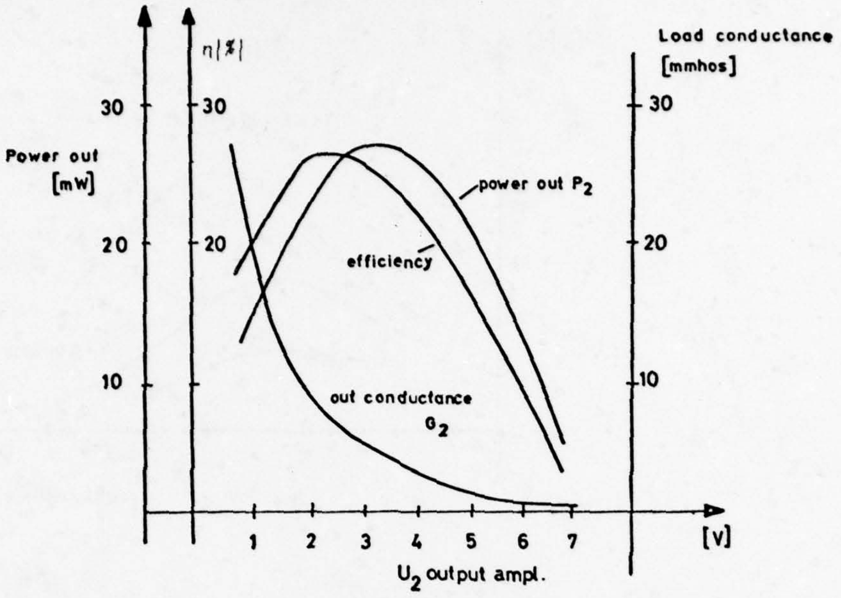

$m = 1$ $\quad \gamma = 0{,}5$ $\quad f_1 = 10$ GHz

$N = 2$ $\quad C_1 = 2$ pF $\quad Q_1 = 25$

$\varphi = 0{,}6$ V $\quad V_B = -25$ V

Fig.6 Power output and efficiency versus output amplitude

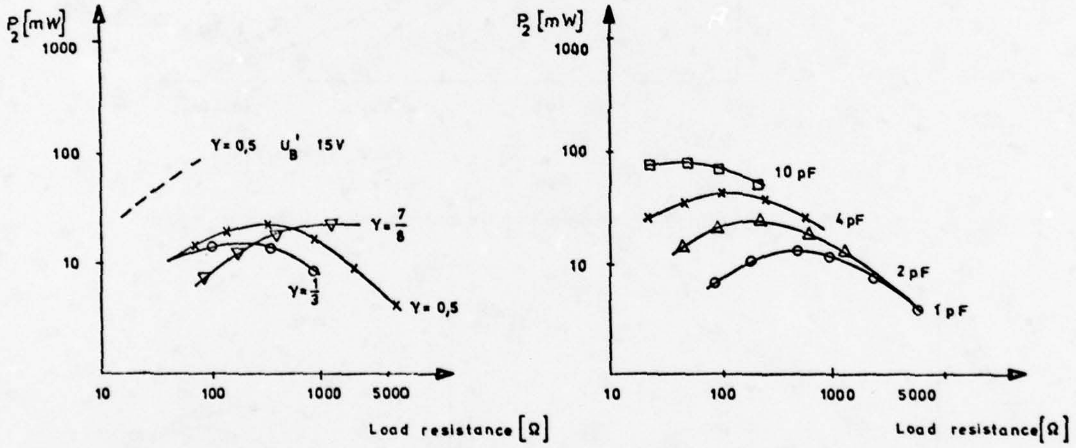

Fig.7 Power output variation with output amplitude

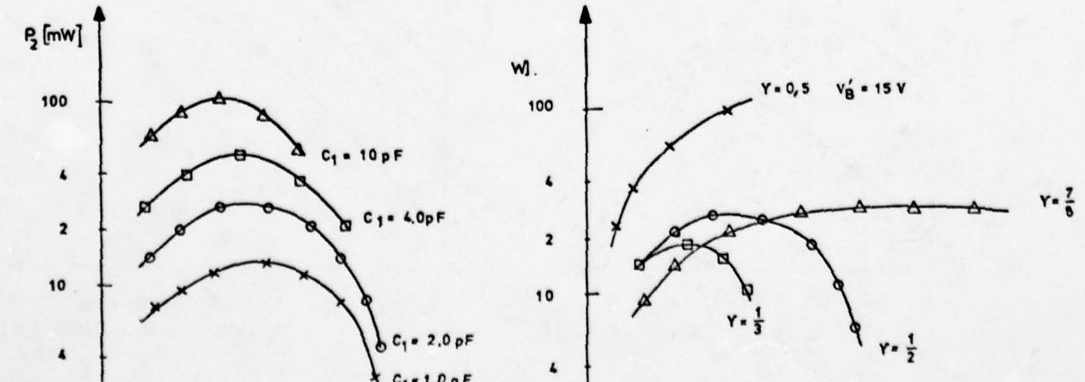

Fig.8 Power output versus load resistance – large signal analysis

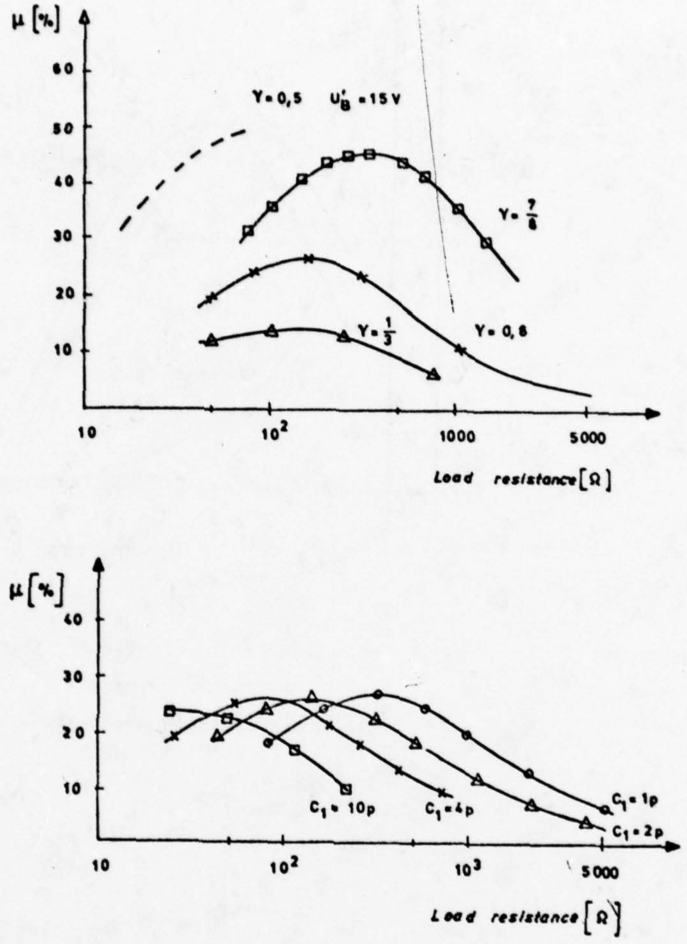

Fig.9 Efficiency variations with the load resistance – large signal analysis

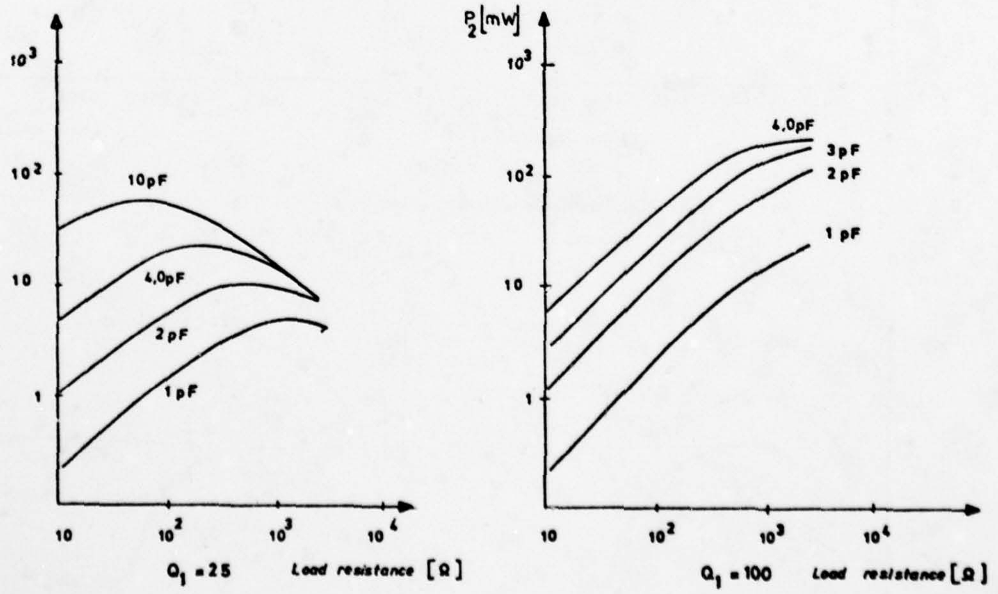

small signal

Fig.10 Power output versus load resistance

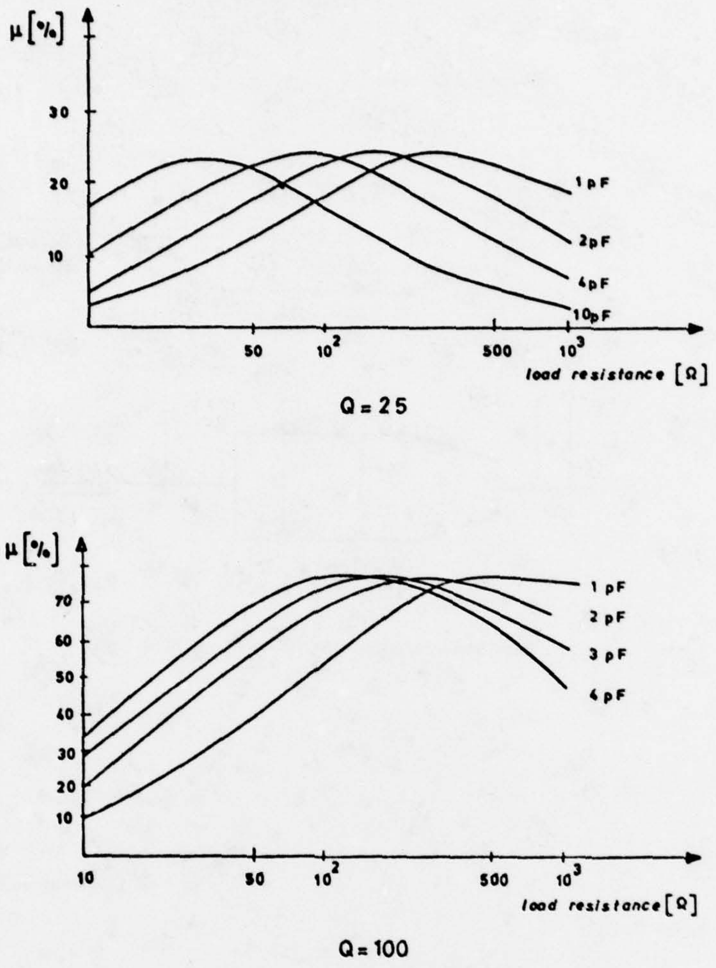

Fig.11 Efficiency variations with the load resistance – small signal

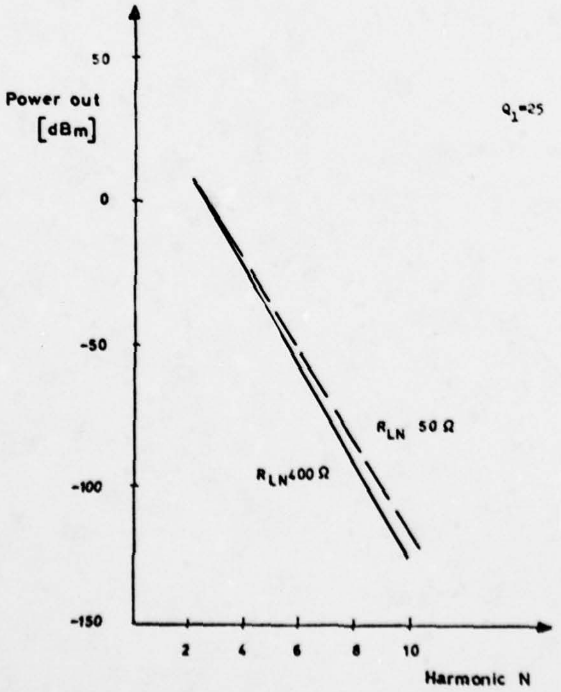

Fig.12 Power output by various harmonic numbers

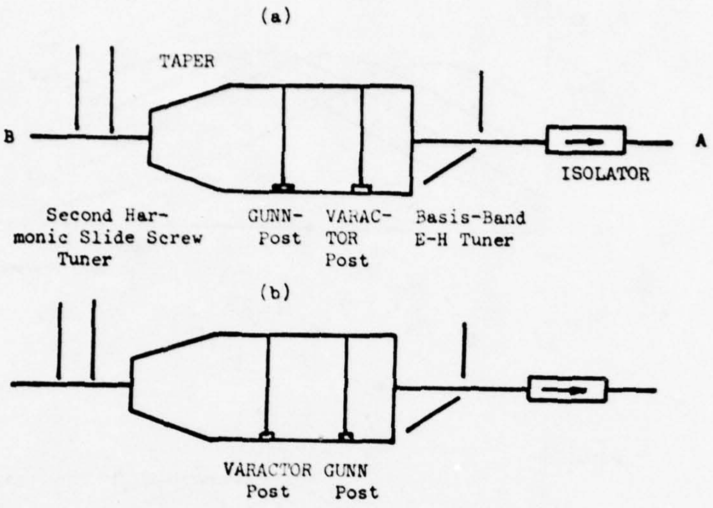
(a)
TAPER
B
A
ISOLATOR
Second Harmonic Slide Screw Tuner
GUNN-Post
VARACTOR Post
Basis-Band E-H Tuner
(b)
VARACTOR Post
GUNN Post

Fig.13 Basic combinations of the diodes

RECENT PROGRESS AND FUTURE PERFORMANCES OF MILLIMETER-WAVE BWO's

B. EPSZTEIN

THOMSON-CSF
38, rue Vauthier
92100 BOULOGNE-BILLANCOURT
FRANCE

SUMMARY

Up to now, backward-wave oscillators have been the most powerful and reliable millimeter wave generators. Among microwave tubes, they have also reached the highest frequencies (840 GHz for a CSF tube, 1200 - 1300 GHz for a Russian tube).

The present communication will be devoted to the recent progress achieved on these tubes.

- A modification of the slow-wave structure has resulted in a considerable increase in the electronic tuning range : having initially a few percent bandwidth, a tube operates now between 325 and 390 GHz, delivering more than 50 mW over most of the band and more than 10 mW over the whole band.*
- A narrow-band tube delivers more than 5 W at 280 GHz.
- Improvements are under way to reduce the weight and improve focusing.*

I. INTRODUCTION

As evidenced by this meeting, the millimeter-wave area, after a long period of low-level activity, is again becoming very much alive, since a number of new applications are coming up.

New military applications have already been described during this conference and will not be touched upon here. But new scientific applications have also recently appeared, among which one may mention far-infrared spectroscopy. This method of analysis constitutes a new approach to the study of molecular structure and promises to yield basic information on the structure and composition of the universe and, perhaps, the origin of life, since molecules can now be detected and identified at extra-galactic distances. Beside their use as a diagnostic tool, either in interferometry or in radiometry, millimeter waves are also now under serious consideration for heating of plasmas in thermonuclear fusion reactors.

Most applications, if not all, require millimeter-wave sources, whether it is for transmission or for reception. Some of the needs at low power levels and at the lower frequencies in the millimetric range are beginning to be filled by solid-state oscillators, but for high powers and high frequencies, millimeter-wave tubes are still without competition and will remain so for some time.

Among these tubes, the backward-wave oscillator (BWO), otherwise known as the "O" type carcinotron, is particularly outstanding for several reasons :

Created in 1951 at CSF and independently at Bell Labs, this tube has reached the highest frequencies ever obtained with a microwave tube : 850 GHz at CSF in 1963 [1] and 1300 GHz by a Russian team led by Golant in 1969 [2]. Thus it has closed the far infrared gap in coherent generation between low-frequency devices such as microwave tubes and the optical frequencies obtained by lasers. For example, the HCN laser delivers its power at a frequency of 890 GHz. Figure 1 shows a plot of power versus frequency for most millimeter-wave sources described in the literature.

On the other hand, this tube is continuously voltage tunable over a wide frequency range, which can reach one octave in the UHF region and is still greater than 20 % in the millimeter wave region.

Backward-wave oscillators are the only commercially available sources at frequencies above 150 GHz. Up to now, tubes in current production are available at up to 300 GHz, but it is to be expected that the available frequency range will be extended far beyond that value.

And last but not least, these tubes have shown a surprising long life, the average being 4000 hours for 70-GHz tubes and 1000 hours for 300 GHz tubes, when one takes into account the very difficult conditions under which they operate, such as the small size of the tube parts as well as the very large current densities which are required.

II. PRINCIPLE OF OPERATION AND STRUCTURE OF THE BWO

Since BWO's have been mostly replaced in the UHF frequency band by solid-state devices, such as varactor-tuned or YIG - tuned solid-state oscillators, and have therefore fallen somewhat out of fashion, it is perhaps useful to give a brief reminder of their principle of operation.

Basically, a BWO (Figure 2) is a traveling-wave tube, the beam of which interacts with an electromagnetic wave supported by a periodic slow-wave structure[4]. The main difference with ordinary traveling-wave tubes lies in the fact that the electron beam and the electromagnetic wave propagate in opposite directions, cumulative interaction still taking place due to a stroboscopic effect. Thus a continuous feedback process is set up, the beam current modulated by the wave giving up energy to the wave which flows toward the electron gun [1,2], thus enhancing the beam modulation. The RF power is extracted by means of a coaxial or waveguide output section [5] located near the gun.

The spent beam strikes a collector [6]. The slow-wave structure is usually attenuated toward the collector to prevent unwanted extra feedback due to multiple reflections.

The electron beam is part of the feedback loop described above. Thus, by modifying its velocity, it is possible to continuously change the feedback delay, so that the tube's oscillating frequency can be continuously varied as a function of the beam voltage.

---

*Studies supported by ESTEC, a division of ESA.

There principles have been applied, in particular at THOMSON-CSF, to the generation of millimeter-wave power. For this application, three difficult conditions have to be met :

- First, a very high current density in the beam is required in order to achieve acceptable efficiency.
- Second, the slow-wave structure, which includes a number of very minute parts, has to be machined extremely accurately, with tolerances of one micrometer.
- Third, this structure should have excellent thermal properties, in particular a high thermal conductibility and a large thermal capacitance.

The first condition is fulfilled by using a highly converging Pierce-type electron gun (area convergence on the order of 100), including an impregnated cathode operating at very high current densities (15 A/cm² for the 1 millimeter wavelength tube).

The second and third conditions are satisfied by using a vane-type slow-wave structure (Figure 3), whose transverse dimensions are on the order of a quarter of the free-space wavelength. Its pitch, which is twice the vane thickness, is about half this value. This structure is obtained by milling a solid copper block. Each vane includes a hole (the diameter being 1/10 of the wavelength) to allow the passage of the beam in a region where the high-frequency electric field is strong and fairly uniform.

III. TUBES IN PRODUCTION

Several carcinotrons operating at wavelengths in the range of 1 cm to 1 mm have been developed at THOMSON-CSF. At the time of their development, the primary goal was to obtain as much power as possible, even at the expense of bandwidth. There is a trade-off between these characteristics due to the fact that the higher the coupling impedance of the slow-wave structure, the higher the efficiency but the smaller the bandwidth.

Table I gives the performances of the millimeter-wave carcinotrons presently in production at THOMSON-CSF.

TABLE I

Tube type	Center Frequency (GHz)	Bandwidth (GHz)	Power out (W)	Voltage (V)	Current (mA)	Average life (hours)
CO. 80	40	1	min. 10 max. 40	3000 6900	60 80	5000
CO. 40	70 or 74	3	min. 3 max. 15	3000 6000	60	4000
CO. 20	136 or 154	2 to 4	min. 1.5 max. 3	3000 6000	max. 60	2000
CO. 10	282	15	min. 0.2 max. 1	5000 11000	max. 30	1000

IV NEW DEVELOPMENTS

As new requirements have recently appeared, a development effort has been made and is still in progress to respond to them. This effort is oriented toward several directions and includes :

- Increase of the bandwidth by redesign of the slow-wave strucure.
- Increase of the efficiency and output power as well as bandwidth by redesign of the electron optics and beam transmission improvement.
- Reduction in size and weight by use of samarium-cobalt magnets.
- Increase of life by use of new cathodes.

IV. 1 Wideband Tubes

Recently, the European Space Agency has initiated a program of research and development of components required for space borne submillimeter-wave spectroscopy. As a part of this program, a general study of submillimeter-wave sources tunable over a wide band for use as a local oscillator in heterodyne detection has been launched.

The general requirements for such sources are listed in Table II.

TABLE II - Requirements for the Submillimeter-Wave Local Oscillator

REQUIREMENTS	REASONS FOR
. Extended frequency range (wavelengths between 0. 5 and 1 mm) . Frequency stability	Heterodyne detection with high spectral resolution
. Broadband tunability	As few models as possible to cover the spectral range of interest
. Sufficient output power	Not to restrict the choice of the detector
. Reduced mass, volume and power consumption	Space-borne equipment
. Continuous tunability . Limited operational constraints	Easier use on board a space platform

AD-A069 015   ADVISORY GROUP FOR AEROSPACE RESEARCH AND DEVELOPMENT--ETC   F/G 17/2.1
MILLIMETER AND SUBMILLIMETER WAVE PROPAGATION AND CIRCUITS.(U)
FEB 79   E SPITZ, G CACHIER
UNCLASSIFIED   AGARD-CP-245   NL

5 OF 6
AD
A069015

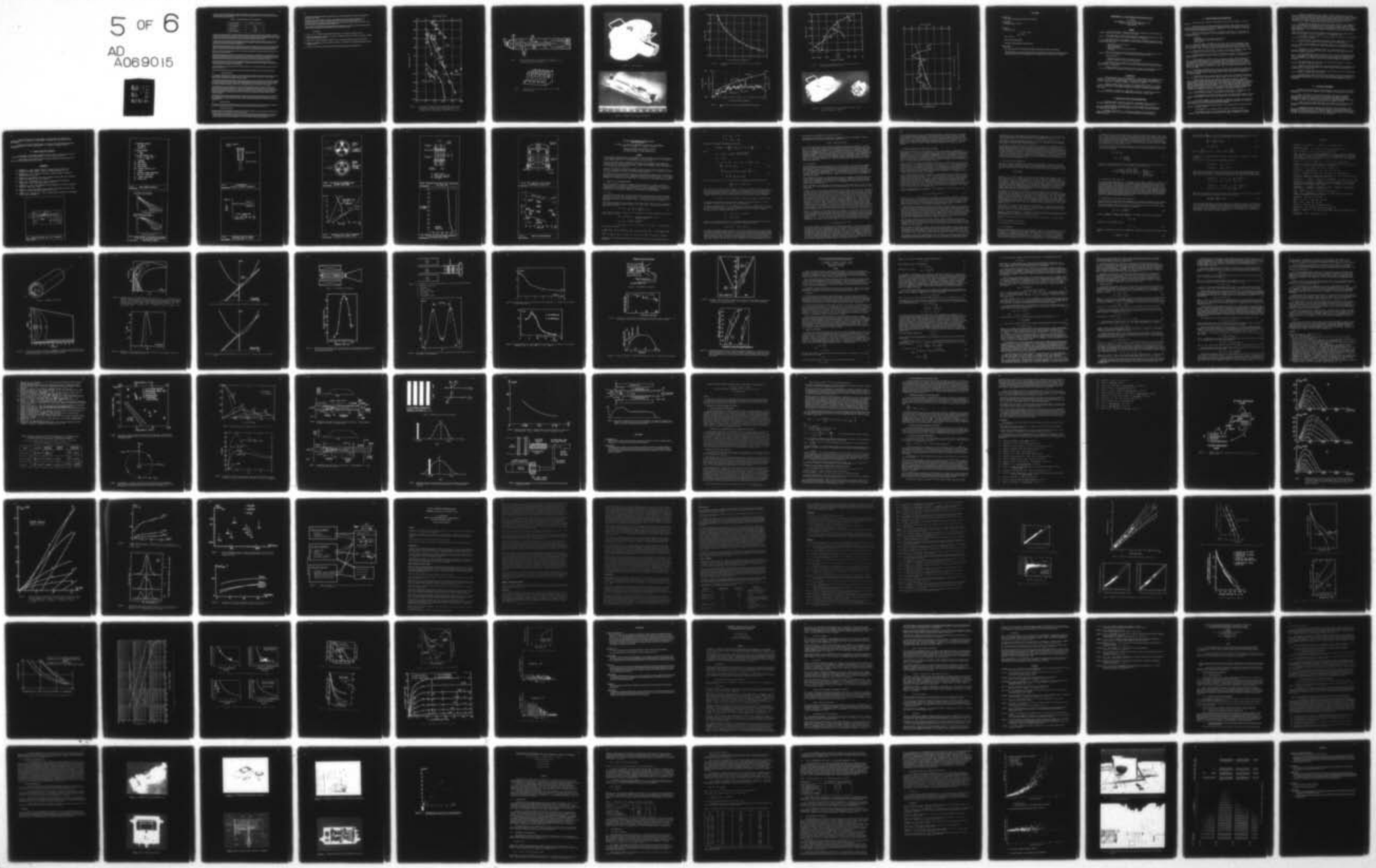

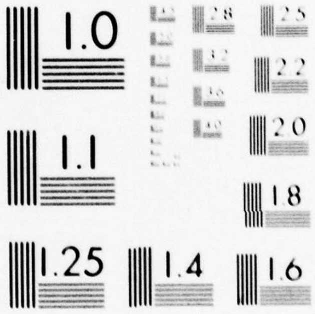
1.0
2.8
2.5
3.2
2.2
3.6
4.0
2.0
1.1
1.8
1.25
1.4
1.6

MICROCOPY RESOLUTION TEST CHART
NATIONAL BUREAU OF STANDARDS-1963-A

To meet there requirements, ESA decided to support the development by THOMSON-CSF's Electron Tube Division of a new carcinotron model, with extended bandwidth together with sufficient output power in the 0.75-1 mm range [3]. The specifications for this carcinotron are listed in Table III.

TABLE III - Extended-Bandwidth Carcinotron Specifications

Central wavelength	$0.8\ \text{mm} < \lambda_o < 0.9\ \text{mm}$
Tunable bandwidth	20 %
Output power	>10 mW
Power consumption	< 150 W

In order to meet these specifications, an extensive computer evaluation of the interaction was first made, followed by a completely new design of the slow-wave circuit. Its dimensions were chosen so that, compared to the circuit of a regular production tube, it would operate in a region allowing much wider frequency tuning, at the expense of a reduced coupling impedance, which results in a decrease of output power. In view of the requirements, this reduction could well be afforded in this particular case.

A tube was built whose wavelength versus voltage characteristics are shown in Figure 6. The measurement accuracy is ± 0.5 %. The tube covers a continuous spectrum from 0.95 mm at 4000 V to 0.75 mm at 9000 V. Depending on the operating frequency, the voltage frequency sensitivity varies between 8 and 40 MHz/volt.

Figure 7 shows output power, beam power and frequency versus voltage. The main result is that more than 10 mW are obtained above 330 GHz. The ripples exhibited by the power curve are explained by combined reflections at the line terminals, output window and output load. They never exceed a slope of 0.01 dB/MHz, characteristic value for a well designed and well matched X-band TWT.

As shown in Figure 8, the efficiency is about 0.07 %, of the same order of magnitude as for previous narrow-band carcinotrons. The beam power is always less than 100 W.

Voltage tunability might seem to preclude the use of a BWO when a stable frequency is needed. However, experiments conducted at ESA [4] on this tube have shown that it can be frequency-locked to an external stable reference source of lower frequency. It has thus been possible to phase-lock a carcinotron operating at 244 GHz with the 24th harmonic of a frequency synthesizer. The measured linewidth is 750 Hz at 40 dB below the peak value and is determined by the resolving power of the spectrum analyser.

The same studies were also concerned with the noise properties of the carcinotron. Experimental results show that the noise temperatures measured on three carcinotrons between 230 GHz and 380 GHz lie between 1000 K and 3000 K, which corresponds to a signal-to-noise ratio approximately equal to 120 dB/MHz.

In 1977, radiometers using carcinotrons were flown on NASA's CV-990 and C-141 aircraft . System performance was as good as in laboratory conditions [4].

These results show that carcinotrons are particularly well suited as tunable local oscillators for low-noise heterodyne detection.

IV. 2 Further Improvements

For the spaceborne application planned by ESA, it is important that the bulk and weight of the tube plus its impedimenta, that is its power supply and cooling system, be as limited as possible. In order to achieve this goal, one approach is to use new magnetic materials in order to reduce the size and weight of the focusing magnet.

A study to achieve this, sponsored by ESA, has been initiated, leading to the results shown in Figure 9. Shown on the left is the new magnet, made of samarium-cobalt (SmCo5). On the right, the usual magnet made of Ticonal 600 (this material is similar to Alnico) is shown for comparison. Both magnets produce an induction of 0.6 tesla (6 kilogauss) over a focusing length of 30 mm. The total weight of the tube plus its magnets is thus reduced to 8.5 kg. This is to be compared to 30 kg for the tube with a Ticonal magnet.

Another approach to reduce size and weight is to try to improve the beam transmission which would allow, for the some output power, having reduced power consumption, hence a smaller mass for the power supply and the cooling circuit. Furthermore, an improvement in beam transmission should result in a widening of the bandwidth, since it is the factor which limits the tube operation toward lower frequencies, at low voltages. For these reasons, a new gun structure has been designed with the help of computer programs, the main difficulty, beside the sheer size of its elements, being that it should be able to operate correctly with widely varying beam voltages.

Preliminary experiments made on a beam tester have shown a large increase in total as well as in relative current transmission at lower beam voltages, below 6 kV, while the transmission at higher voltages is correspondingly decreased. The comparison is, however, somewhat pessimistic since the drift sections are different. A valid conclusion will be reached when these improvements are tested on an operating tube.

IV. 3 Higher-Power Tube

As a result of the know-how acquired during these studies and the improvements achieved in the accuracy of carcinotron fabrication, a narrow-band production tube has been built that delivers 5 watts CW at a frequency of 280 GHz (Figure 10).

V FUTURE EVOLUTION

The achievement just mentioned shows that the evolution of the millimeter-wave BWO is by no means terminated. Among others, the following objectives for further development of this tube can be defined :

- Increase in power output and efficiency, a goal of 10 watts CW at 1 mm wavelength appearing perhaps feasible. This, of course, is well below what one could expect from the gyrotron, but it should be remembered that a gyrotron operating at this frequency would unavoidably require superconducting magnetic coils and the liquid helium equipment that goes with them.

- Development of tubes capable of being put into production, either narrow band, high power, or wideband, in the submillimetric region, down to 0.5 - 0.3 mm.
- Increase of life by use of new cathodes : for instance, it should be possible to obtain the same current density as with an impregnated tungsten matrix cathode at a temperature 100 °C lower by using an osmium-coated tungsten matrix.

  Even better results may be obtainable with barium-scandate cathodes, for which current densities of *100 A/cm² at 1050 °C with a* life of many thousands of hours have recently been mentioned [5].
- Last but not least, more widespread use of these tubes, which are now produced in very small quantities and are therefore expensive, should result in an improvement of the production efficiency and a reduction in their cost.

REFERENCES

[1] Convert, G., Yeou, T. (1964) "Millimeter and submillimeter waves" - Chap. 4. Benson Ed., Iliffe Books, London.

[2] Golant, M.B.; Alekceenko, Z.I.; Korotkova, Z.S.; Lunkind, L.A.; Negerev A.A.; Petrova, O.P.; Rebrova, T.B.; Saveleva, V.S. (1969). Pribory i Tekhnika Eksperimenta p. 231.

[3] Kantorowicz, G.; Palluel, P.; Pontvianne, M. (1978) 3ᵈ Int. Conf. on Submillimeter Waves, University of Surrey, Guilford.

[4] de Graauw, Th.; Anderegg, M.; Fitton, B.; Bonnefoy, R.; Gustencic, J.J., (1978) 3ᵈ Int. Conf. on Submillimeter Waves, University of Surrey, Guilford.

[5] Van Ostrom, A. (1978) 1978 Tri-Service Cathode Workshop, Naval Research Laboratory, Washington (D.C.).

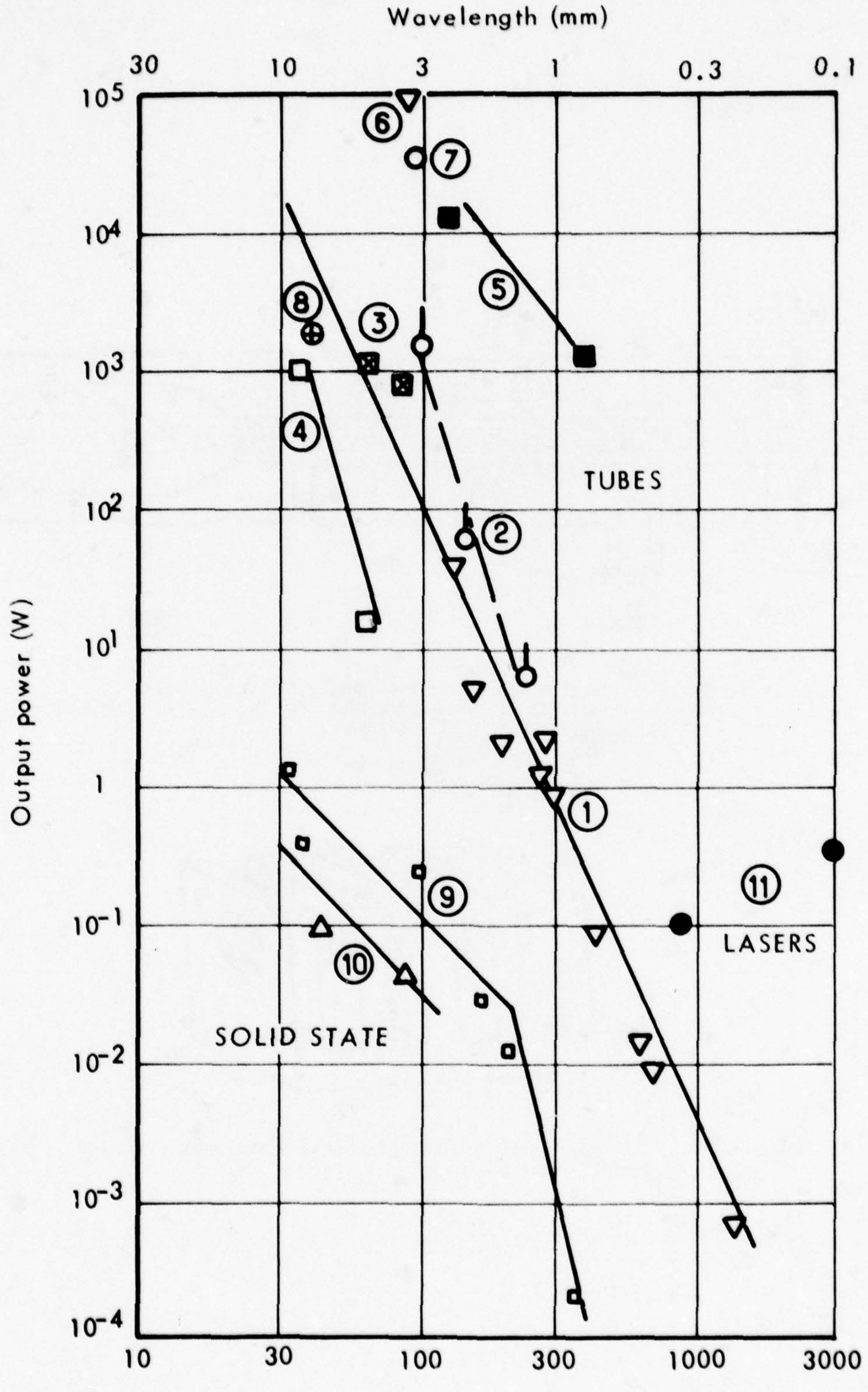

Figure 1. Output power of millimeter-wave and submillimeter-wave sources : (1) CW BWO, (2) pulsed EIO, (3) CW solenoid TWT, (4) CW ppm TWT, (5) CW gyrotron, (6) pulsed BWO, (7) pulsed magnetron, (8) CW klystron, (9) IMPATT diodes, (10) TEO, (11) CW FIR lasers.

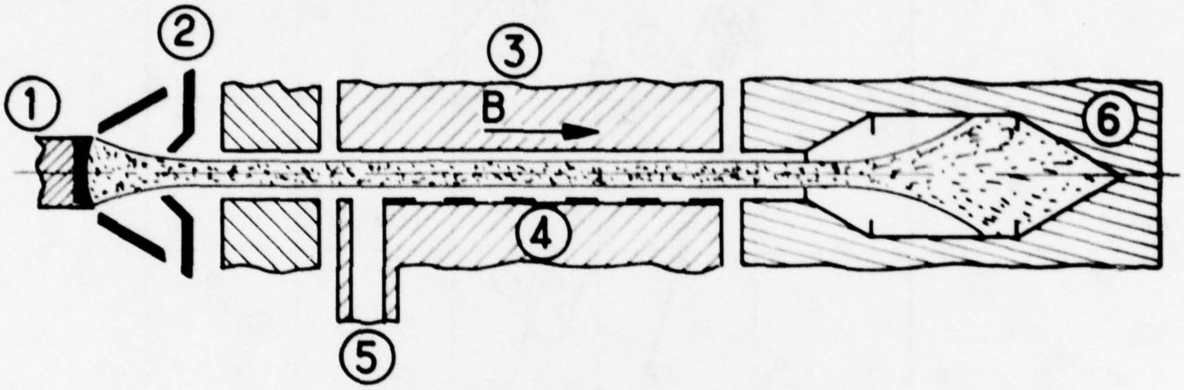

Figure 2. Cross-sectional diagram of a BWO showing (1) the cathode, (2) the anode, (3) the focusing magnet, (4) the slow-wave structure, (5) the RF output and (6) the collector.

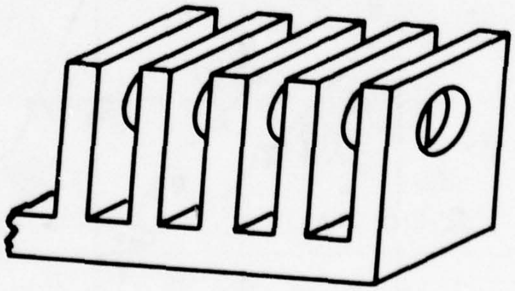

Figure 3. Construction of a vane-type slow-wave structure for a BWO (greatly enlarged).

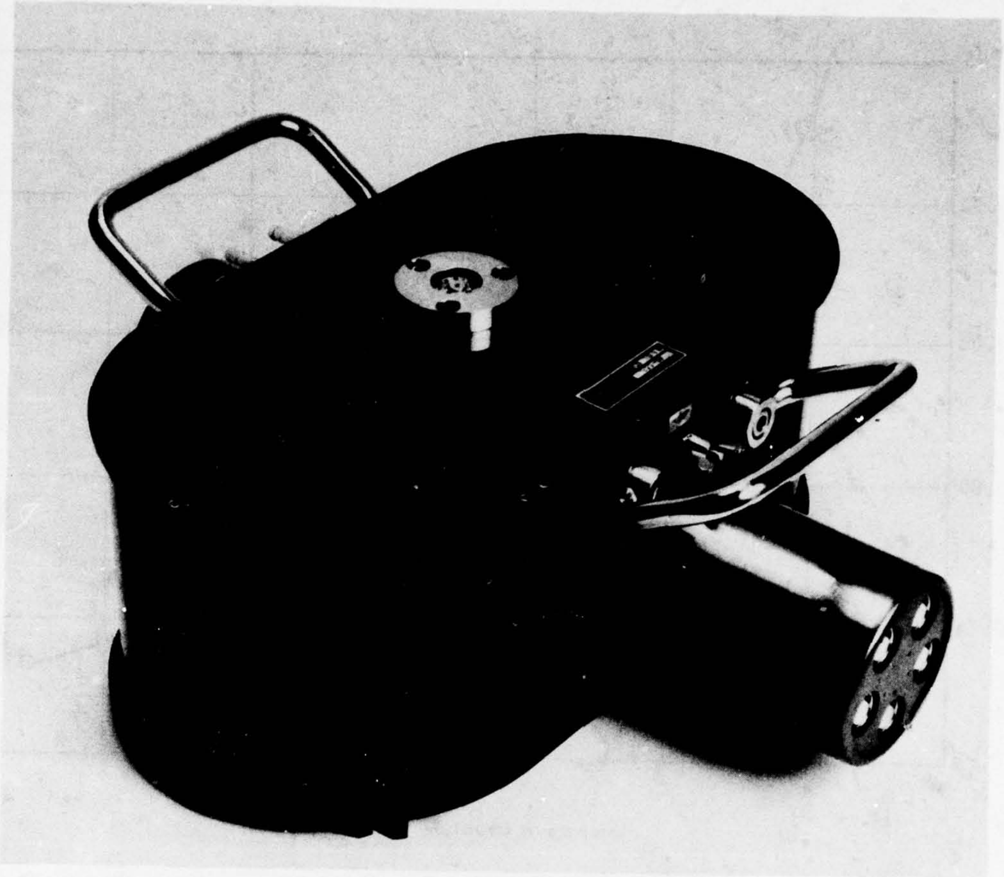

Figure 4. CO.10 carcinotron.

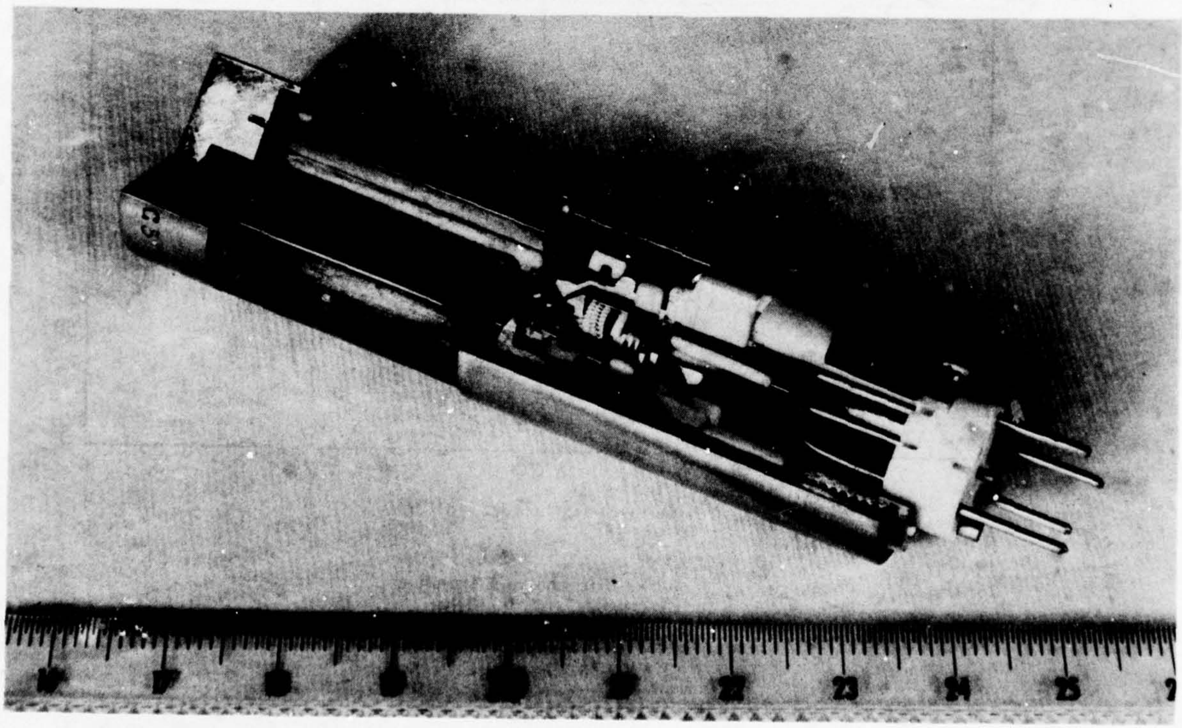

Figure 5. Cutaway view of a production Carcinotron.

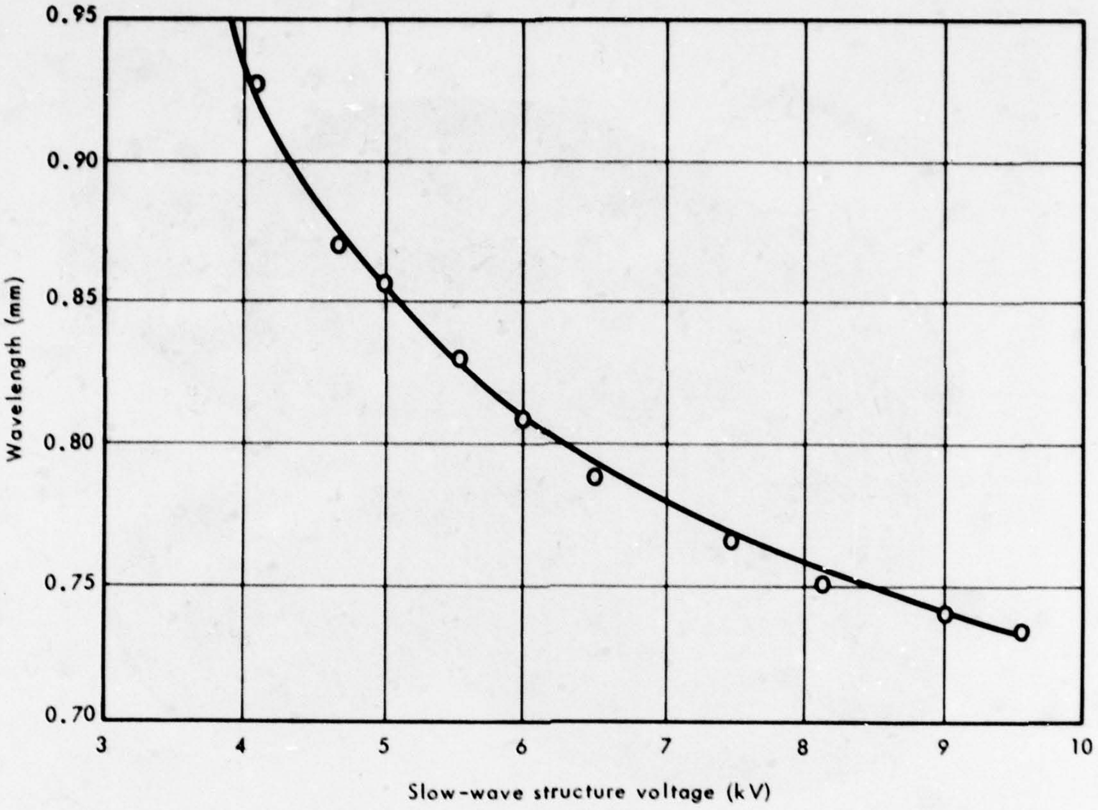

Figure 6. Wavelength versus voltage characteristics for the new broadband carcinotron.

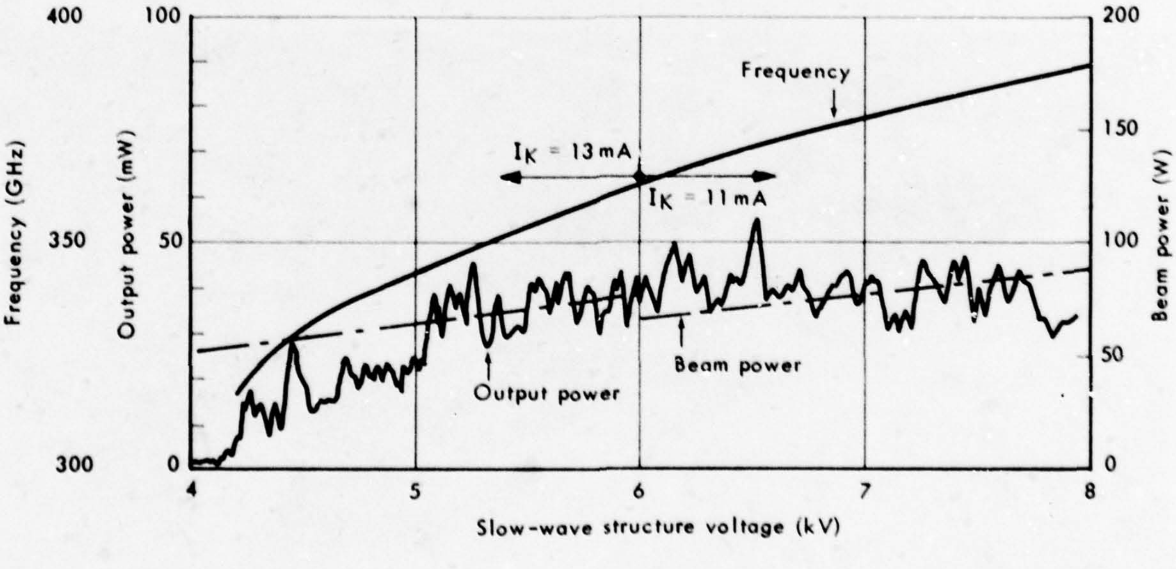

Figure 7. Characteristic curves for the new broadband submillimeter-wave BWO.

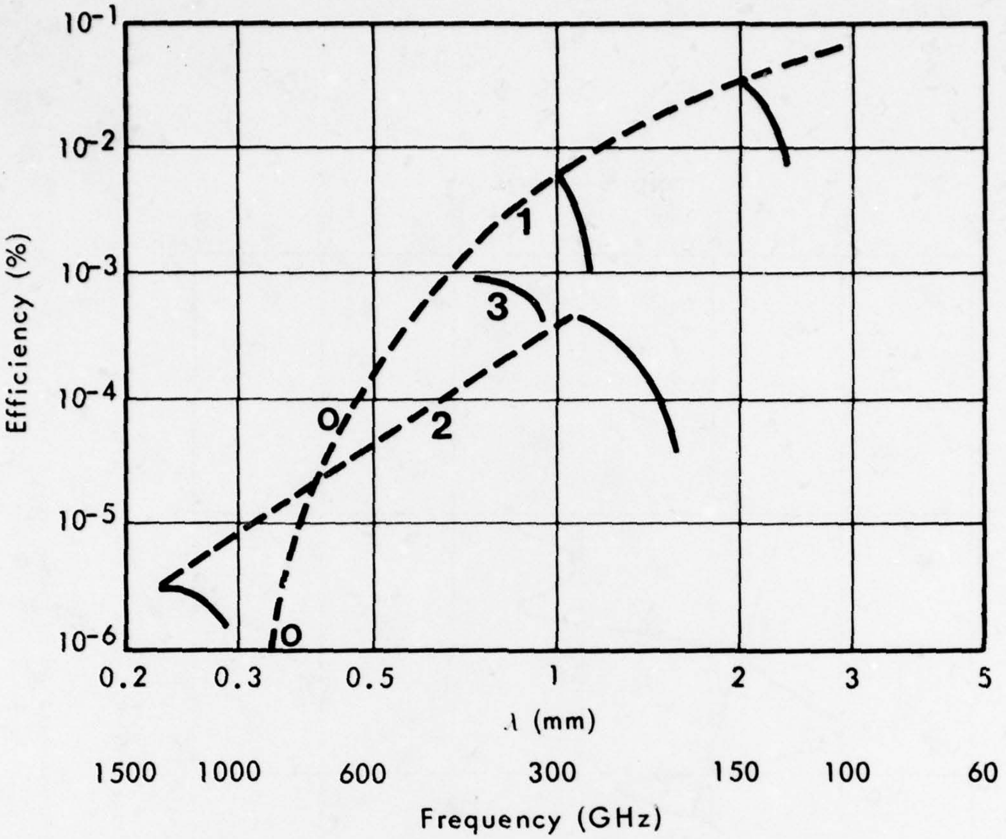

Figure 8. Efficiency of the new broadband carcinotron (3) as compared to earlier narrow-band models (1 and 2).

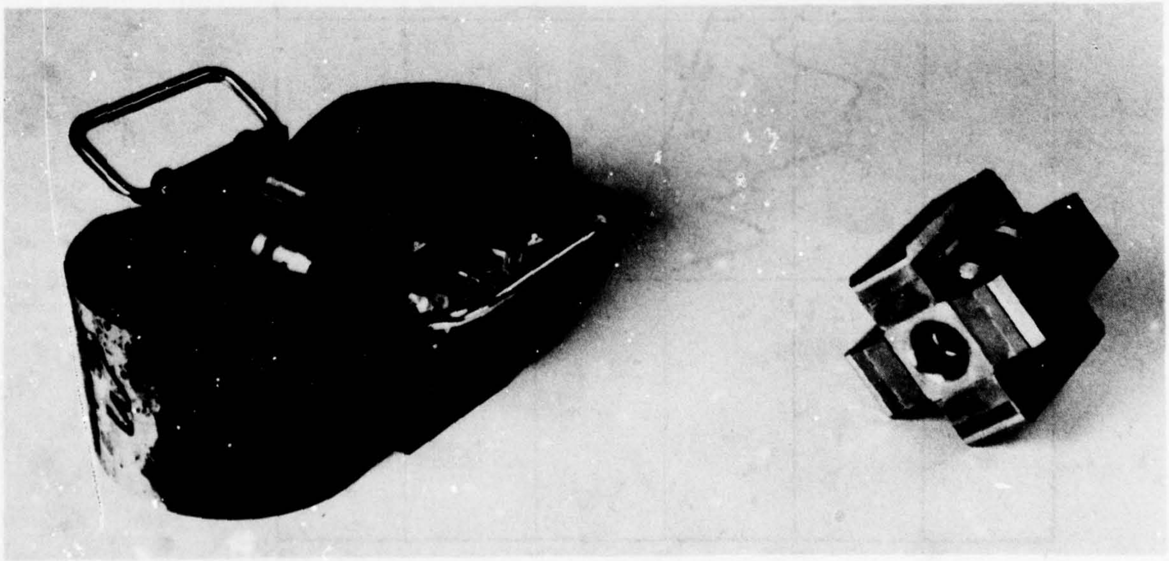

Figure 9. The new lightweight $SmCo_5$ focusing magnet (left) and a standard Ticonal® 600 magnet, for comparison.

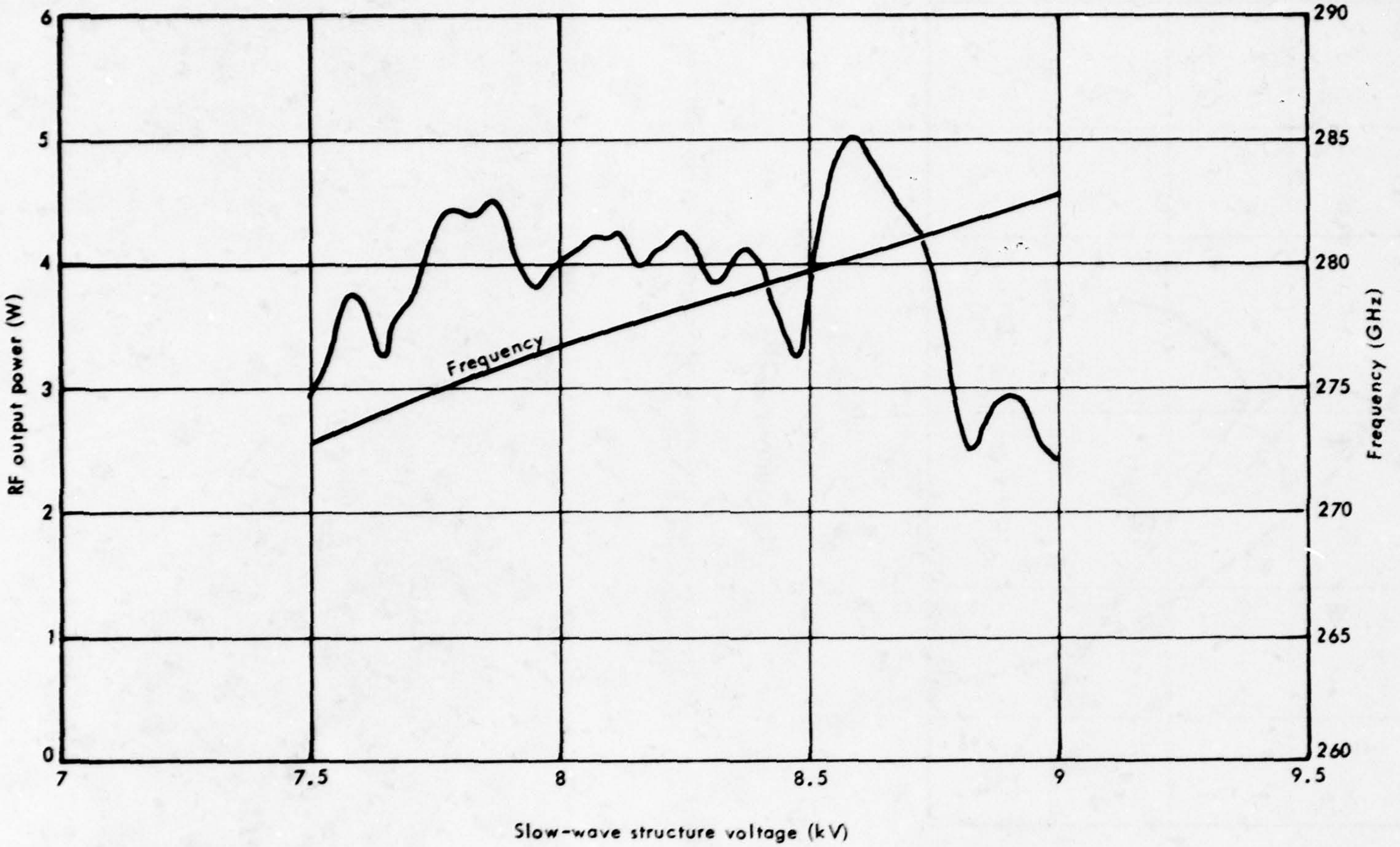

Figure 1C. Characteristics of an improved narrow-band BWO in production.

DISCUSSION

N.Pranter, FRG

How high is the cathode emission density of your BOW's?

Author's Reply

Emission density is 15 A/cm².

S.Kulpa, US

For the tube with

$$\lambda = 0.80 - 0.9 \text{ mm}$$

$$\Delta f/f \sim 20\%$$

For > 10 mm.

What are the anticipated $\frac{\Delta f}{\Delta v}$?

How stable a power supply can Thomson provide?

Author's Reply

$\frac{\Delta f}{\Delta v}$ is larger than 8 MHz/V and smaller than 40 MHz/V depending on the frequency of operation.

Thomson-CSF does not, for the time being, manufacture the power supply for this tube but can help to obtain it at given specifications. Usual power supplies have a 10^{-4} stability but 10^{-5} and even 10^{-6} can be obtained

DEVELOPMENT OF A 5 WATT TRAVELLING WAVE TUBE FOR 60 GHz

N. PRANTER

AEG-TELEFUNKEN, Tubes and Subassemblies Division
Soeflinger Strasse 100, 7900 Ulm
West Germany

SUMMARY

For data transmission between geostationary communication satellites the frequency range from 54 GHz ... 64 GHz will be used.

The communication system design demands a transmitter output power of some watts. This can be achieved with a travelling wave tube amplifier.

This paper shows, how frequency, output power, bandwidth, high efficiency and extremely long tube life determine the following main design parameters for such a travelling wave tube,

- perveance of the electron gun
- beam compression
- slow wave structure
- dimensions of the slow wave structure
- collector.

Due to the required electrical parameters,distortion effects must be considered which are negligible for the design of lower frequency TWT's.

These effects are:

- thermal velocity spread of the beam electrons
- undesired modes of the slow wave structure.

The thermal velocity spread of the beam electrons has great influence on the performance of the electron gun and the beam focusing system. A method to reduce this influence is described.

Undesired modes of the slow wave sturcture impair the gain characteristics of the tube. Methods of preventing such modes are being further developed.

INTRODUCTION

This paper deals with the development of a ppm-focused double-stage-collector 60 GHz / 5 W helix TWT for space applications with a design goal of an operating efficiency of 10 % and a saturated gain of 30 dB within a frequency range of 54 GHz - 64 GHz. In addition, a general treatment of "mm TWT's" is given.

Firstly, a short review is given of the applications for TWT's in the mm-frequency range. Then, main design problems and considerations based on the development of the 60 GHz / 5 W TWT are outlined and solutions to overcome these problems are shown.

Furthermore, an efficiency improvement technique is described and finally, the state of the art of mm-TWT's is summarised showing upper design limits.

I - APPLICATION OF TWT'S FOR MILLIMETRE WAVES

Millimetre waves, defined as waves with a wavelength from 1 to 10 mm or a frequency range from 300 - 30 GHz, are used in a wide field of applications.

In this frequency range TWT's may act as power amplifiers both for ground and space applications. Main ground applications are for radar, electronic warfare and communication systems.

Frequencies from 54 GHz ... 64 GHz are envisaged for intersatellite communication where TWT's will be used as high-efficiency and high-reliability power amplifiers.

II - DESIGN PROBLEMS AND CONSIDERATIONS

Before going into details a three-stage-collector-TWT schematic is shown in Figure 1:

The tube sections for beam generating and shaping, beam interaction with the delay line structure and beam collecting, together with their associated voltages can be seen. Multistage beam collectors will be described in a later chapter of this paper as an efficiency improvement technique.

The most frequently used delay line system for mm-TWT's are either helix or coupled cavity chain. In general, the choice between these is made by considering the following factors:

- bandwidth
- dispersion, gain and phase fine structure
- heat transfer to the vacuum envelope
- fabrication.

In view of these considerations, the helix with excellent broadband performance and simple fabrication is used for small power tubes. The coupled cavity chain with its better heat transfer to the vacuum envelope than the helix is normally used for high power tubes. Its disadvantages are small bandwidth and complicated machining.

Beam focusing in most mm-TWT's is done with a periodic-permanent magnet stack using $SmCo_5$-magnets. These reduce size and weight of the focusing system.

Design relations for the delay line propagation constant, the beam perveance and the focusing magnetic field are listed in Figure 2 to explain the fundamental design theory.

The propagation constant is one of the most important design parameters. To achieve optimum tube operation in the mm-range the beam voltage must be very high, which means low beam perveance and very small delay line diameter. This fact leads to high density electron beams for the helix and coupled cavity structure and limits the manufacture with respect to frequency. On the other hand some restrictions have to be made to the beam voltage especially for space tubes to achieve good reliability of the tube power supply.

Due to the requirements for long tube life and high reliability the emission density of cathodes used may not exceed certain values. The beam area compression, i.e. the ratio of cathode area to beam area inside the delay line, will be determined by the cathode design.

From these points it can be seen that electron guns for mm-wave TWT's are of the low perveance type, producing high density beams with a high beam area compression.

Under these conditions the commonly used laminar theory for designing electron guns and beam focusing systems is not valid, as the thermal spread of the beam electrons leaving the cathode is no longer negligible. The influence of transverse thermal electron velocities on the design of electron guns and the beam focusing field has been investigated by several authors [1, 2, 3, 4]. Results achieved there have been used for the design of the 60 GHz / 5 W TWT electron gun and beam focusing field. Formula (3) from Figure 2 derived in [1] shows the influence of cathode temperature, cathode field, beam radius and area compression on the beam focusing field.

An estimation of the effect of thermal spread based on considerations described in [4] is shown in Figure 3, calculated for the 60 GHz / 5 W TWT:

The percentage of electrons inside an ideal equilibrium beam diameter, called the Brillouin-diameter, versus beam area compression for a beam power of 250 W can be seen.

From these figures it is evident that in general a low beam area compression will avoid a lot of problems caused by thermal electron beam spread for the electron gun design and also for the beam focusing field design.

The upper limit of emission density of the tungsten matrix cathode used for mm-TWT's is about 1 A/cm^2.

The schematic of the tungsten matrix cathode is shown in Figure 4:

The cathode consists of a porous tungsten body impregnated with Ba-Ca-Aluminate. This body is held by a moly-sleeve. The heater is embedded in alumina.

During the development of the 60 GHz / 5 W TWT, cathodes with very high emission density to reduce the beam area compression were also tested. Figure 5 shows the first accelerated life test results achieved under high emission density conditions for various new cathode designs. The change of current density versus life time beginning with a density of 6 A/cm^2 can be seen by 1 000 h. This is equivalent to a cathode life of 30 000 h minimum under normal operating conditions.

Another problem concerning slow wave structures is seen in the propagation of the electromagnetic waves along the structure. Resulting from an exact analysis, there exists not only the fundamental mode of propagation, commonly used for interaction with the electron beam, but also an infinite number of so-called space harmonics. These harmonics all have the same frequency and the same group velocity but different phase velocities.

These cause undesired effects such as backward wave oscillations and under certain conditions they impair the helix impedance for the fundamental wave.

Two possible configurations of the helix delay line structure of the 60 GHz / 5 W TWT can be seen in Figure 6:

Figure 6a shows a configuration using heat shrink techniques to fix the helix inside the vacuum envelope, Figure 6b shows the use of moly-springs.

Based on the assumption of a tape helix model [5, 6, 7] a space harmonic analysis of the 60 GHz / 5 W TWT helix delay line system has been made and is shown in Figure 7:

Helix waves of the fundamental order ($m = 0$) and the order $m = \pm 1$ in a frequency-propagation constant plane have been computed for the dimensions of the delay line system of Figure 6b.

It can be seen that waves of the order $m = \pm 1$ have a cutoff frequency of about 30 GHz. These waves may be explained up to about 70 GHz as the dominant transverse electromagnetic or TEM-mode of a coaxial line having an inner conductor with the helix diameter and an outer conductor with the inner diameter of the vacuum envelope.

Hot measurements have shown that this mode seriously impairs the helix impedance and hence the gain of the tube.

Methods are under development to optimize the boundary value conditions for the helix waves in such a manner that the cutoff frequency of undesired modes of propagation will be shifted up.

Similar problems, especially backward wave problems, are to be solved under the development of coupled cavity structures.

A coupled cavity delay line structure is shown in Figure 8. The dimensions in millimetres are typical for a tube with a centre frequency of about 50 GHz. It is evident that machining will be also a serious problem for mm-coupled cavity tube development.

III - EFFICIENCY IMPROVEMENT

Methods frequently used are velocity tapering of the delay line structure, multistage collectors or both together. The multistage collector method will be described here:

Due to the modulation of the electron beam a wide range of electron velocities will occur and it is possible to collect several velocity groups on corresponding collector stages with the lowest possible voltages allowing all electrons of a group to be collected. It is possible to improve the basic efficiency of mm-TWT's by two to four times, using double to five stage collectors.

Figure 9 shows the spent beam energy distribution of the 60 GHz / 5 W TWT computed for saturated output power. For this tube a double stage collector is provided.

To demonstrate a more sophosticated multistage collector design, a five stage self-radiating collector can be seen in Figure 10. This collector has been developed for space application. The collector stages are insulated from the collector envelope, the collector envelope is bolted by a flange to the satellite and radiates the heat, conducted from each stage to it, into deep space.

Results achieved in the development of the 60 GHz / 5 W TWT will be published later with reference to high emission cathodes and mode shifting under development.

The tube is being developed under a contract of the "Deutsche Forschungs- und Versuchsanstalt für Luft- und Raumfahrt e.V." (German Aerospace Research Institute).

IV - STATE OF THE ART OF MM-TWT'S

At the end of this paper a general review is given of the state of the art of mm-TWT's developed or under development. It can be seen in Figure 11:

Upper design limits based on tube design and manufacturing techniques are shown for helix and coupled cavity tubes.

REFERENCES

[1] HERRMANN, G., 1958, "Optical Theory of Thermal Velocity Effects in Cylindrical Electron Beams". Journal of Applied Physics, Vol. 29.

[2] HERRMANN, G., 1957, "Transverse Scaling of Electron Beams". Journal of Applied Physics, Vol. 28.

[3] CUTLER, C.C., and HINES, M.E., 1955, "Thermal Velocity Effects in Electron Guns". Proceedings of the I.R.E., March.

[4] PIERCE, I.R., and WALKER, L.R., 1953, "Brillouin Flow with Thermal Velocities". Journal of Applied Physics, Vol. 10.

[5] SENSIPER, S., 1951, "Electromagnetic Wave Propagation on Helical Conductors (Thesis)". Mass. Inst. Techn.

[6] STARK, L., 1954, "Lower Modes of a Concentric Line Having a Helical Inner Conductor". Journal of Applied Physics, Vol. 25.

[7] PIERCE, I.R., and TIEN, P.K., 1954, "Coupling Modes in Helixes". Proceedings of the I.R.E., September.

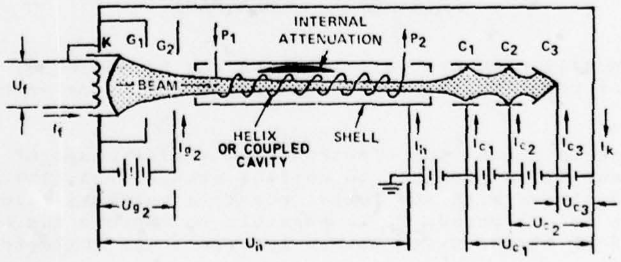

FIG 1 THREE-ELECTRODE COLL. TWT SCHEMATIC

AEG-TELEFUNKEN

(1) PROPAGATION CONSTANT

$$\gamma \cdot B_R \sim \frac{F}{\sqrt{U_0}} \cdot B_R$$

$$(\gamma \cdot B_R)_{OPT} \sim 0{,}6$$

(2) BEAM PERVEANCE

$$P = \frac{I_0}{U_0^{3/2}}$$

(3) FOCUSING MAGNETIC FIELD

$$B^2 = B_B^2 + A \cdot T_C \cdot \left(\frac{V}{R_0^2}\right) + B_C^2 \cdot V^2$$

F... FREQUENCY
B_R... BEAM RADIUS
U_0... BEAM VOLTAGE
I_0... BEAM CURRENT
B_B... "THERMAL" BRILLOUIN - FIELD
A... CONSTANT
T_C... ABSOLUTE CATHODE TEMPERATURE
V... BEAM AREA COMPRESSION
R_0... "THERMAL" BEAM RADIUS
B_C... CATHODE FIELD

FIG. 2 MAIN DESIGN FORMULAE

AEG-TELEFUNKEN

PERCENTAGE OF ELECTRONS INSIDE BRILLOUIN DIAMETER

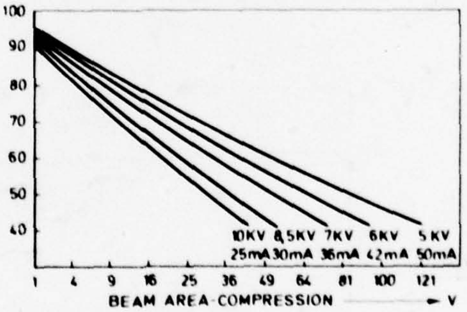

PERCENTAGE OF ELECTRONS INSIDE $\sqrt{2}$ BRILLOUIN DIAMETER

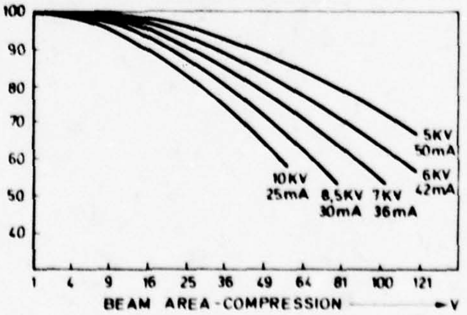

FIG. 3 60 GHZ/5W-TWT FRACTION OF ELECTRON FLOW INSIDE BRILLOUIN DIAMETER FOR 250W BEAM POWER

AEG-TELEFUNKEN

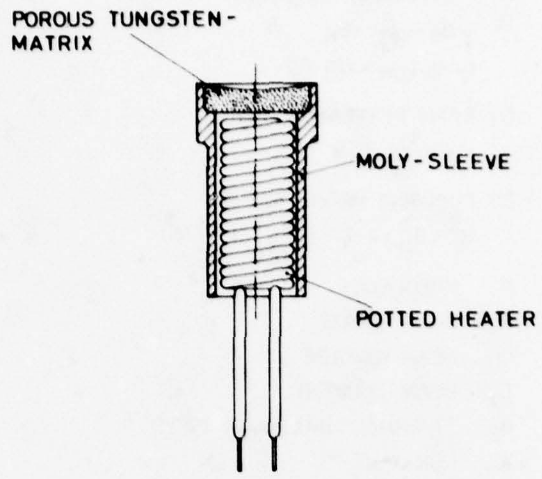
POROUS TUNGSTEN-
MATRIX
MOLY-SLEEVE
POTTED HEATER

FIG. 4 IMPREGNATED MATRIX - CATHODE SCHEMATIC

AEG-TELEFUNKEN

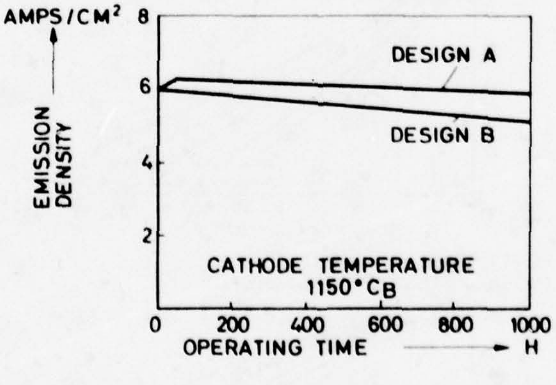

FIG. 5 EMISSION DENSITY DURING ACCELERATED LIFE - TEST

AEG-TELEFUNKEN

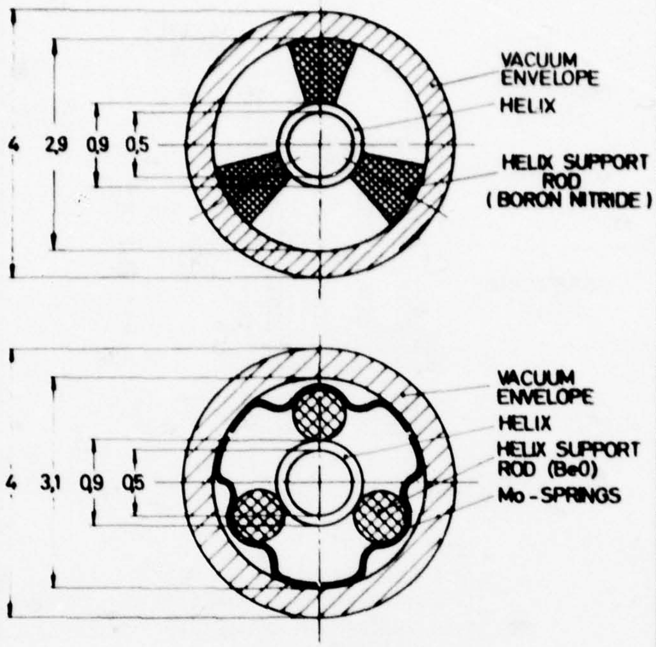
4
2,9
0,9
0,5
VACUUM ENVELOPE
HELIX
HELIX SUPPORT ROD (BORON NITRIDE)
4
3,1
0,9
0,5
VACUUM ENVELOPE
HELIX
HELIX SUPPORT ROD (BeO)
Mo - SPRINGS

FIG. 6 60 GHZ/5W TWT POSSIBLE HELIX SUPPORT STRUCTURES

AEG-TELEFUNKEN

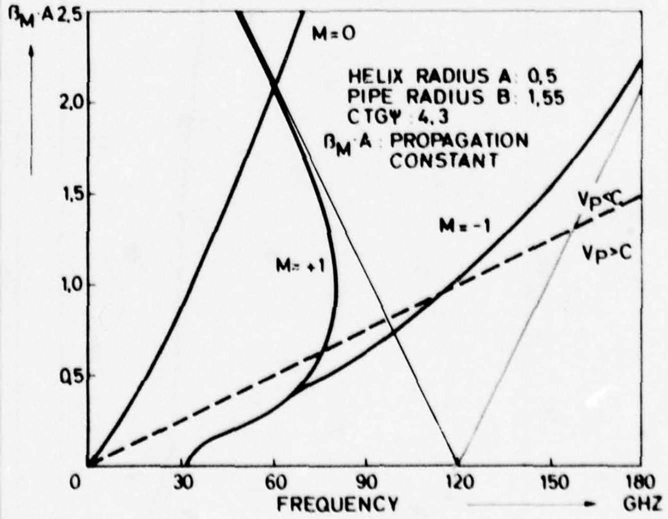

FIG. 7 60 GHZ/5W TWT SPACE HARMONIC ANALYSIS OF DELAY LINE

AEG-TELEFUNKEN

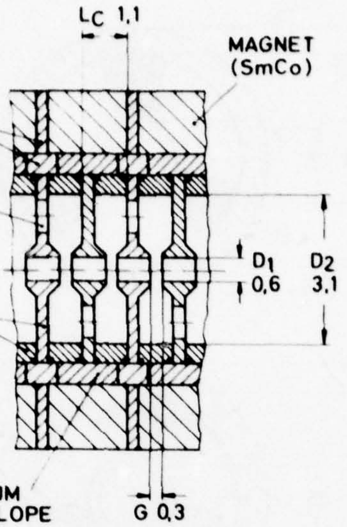
LC 1,1
MAGNET (SmCo)
POLE PIECE (Fe)
COUPLING SLOT
D1 0,6
D2 3,1
RESONATOR (Cu)
VACUUM ENVELOPE
G 0,3

LC = CAVITY LENGTH
D1 = BEAM HOLE DIAMETER
D2 = RESONATOR DIAMETER
G = GAP WIDTH

FIG. 8 COUPLED-CAVITY DELAY LINE STRUCTURE FOR MM-TWT

AEG-TELEFUNKEN

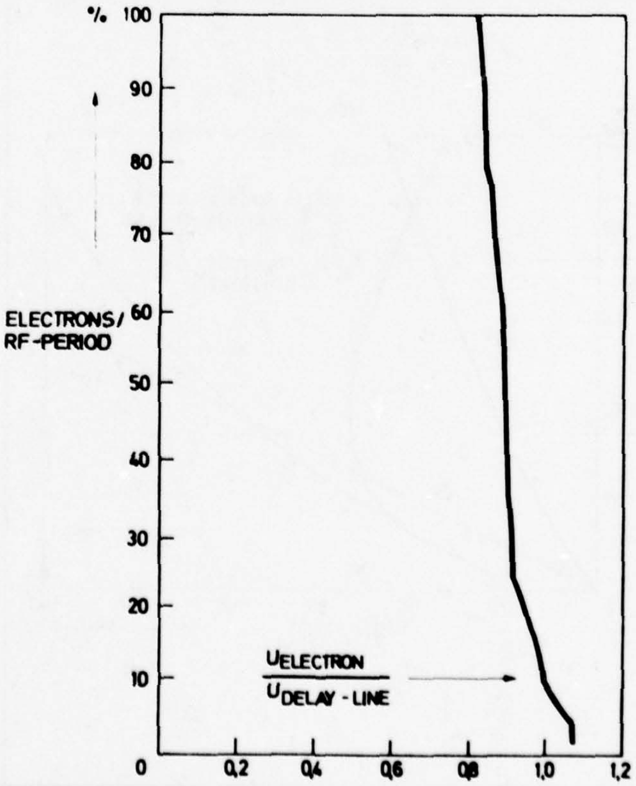

FIG. 9 60 GHZ/5W TWT SPENT BEAM ENERGY DISTRIBUTION FOR SATURATED OUTPUT POWER

AEG-TELEFUNKEN

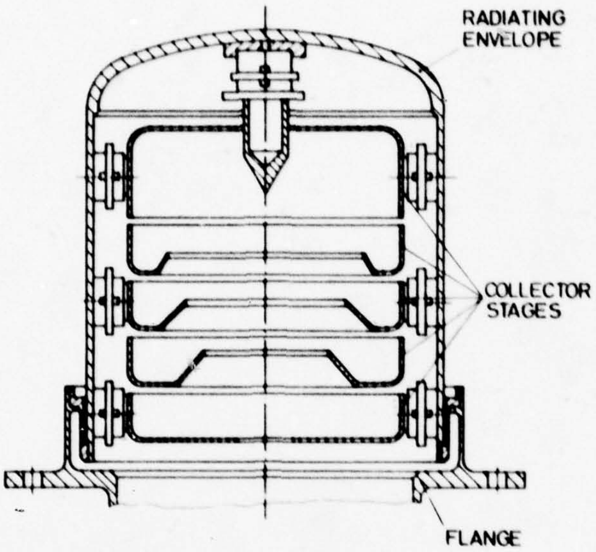
RADIATING ENVELOPE
COLLECTOR STAGES
FLANGE

FIG. 10 SELF RADIATING MULTISTAGE DEPRESSED COLLECTOR

AEG-TELEFUNKEN

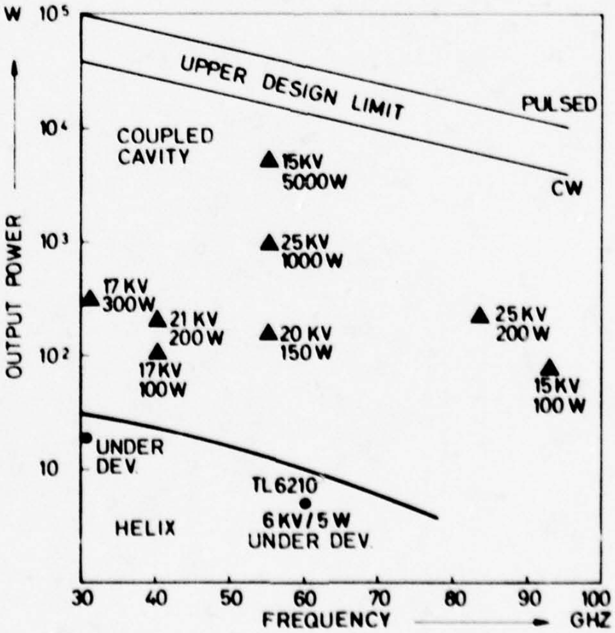

FIG. 11 MM-TWT DESIGN REVIEW

AEG-TELEFUNKEN

NEW HIGH POWER MICROWAVE SOURCES IN THE MILLIMETRIC RANGE

J.M. BUZZI, H.J. DOUCET, P. DROSSART, B. ETLICHER, P. HALDENWANG
H. LAMAIN, X. MAUCHANT, J.P. MARQUE, C. ROUILLE

Laboratoire de Physique des Milieux Ionisés
Groupe de Recherche N° 29 du C.N.R.S.
Ecole Polytechnique, 91128 Palaiseau Cedex

SUMMARY

In this paper, three process of electromagnetic wave generation by intense pulsed relativistic electron beams (REB) are investigated : a) The synchrotron maser b) The relativistic Doppler shift and c) the collective free electron laser.

For the synchrotron maser instability, theoretical linear growth rate and threshold conditions are derived for annular beams in cylindrical waveguides. Experiments where the efficiency of the microwave generation reaches 10 % with REB current of the order of 1 kA are presented and discussed.

Frequency conversion of microwaves by Doppler shift using a relativistic beam front as a mirror is a possibility for the conversion of X-band radiation in the millimetric range. Conversion frequency from 9 GHz to 30 GHz has been observed.

The collective free electron laser also uses the relativistic Doppler shift for frequency conversion but the mirror effect is obtained by Raman backscattering of the incident wave. Moreover the incident wave in the laboratory frame can be of zero frequency, i.e. a simple modulation of a static B field. Results of our preliminary investigations are presented.

1. STUDIES OF THE SYNCHROTRON MASER.

First the stability of circular waveguide modes perturbed by an annular relativistic electron beam is investigated. The model can describe the situation for low current operating devices of the gyratron type (FLYAGIN, V.A., 1977) or experiments using cold cathode devices with intense relativistic electron beams (GRANATSTEIN, V.L., 1975). The second part of the section is devoted to a description of the experiments.

1.1 Theory.

In the model we assume that : (a) the electron beam flows through a circular waveguide immersed in a constant axial magnetic field. (b) The electrons all have the same energy and Larmor radius r_L. (c) Their guiding center is located on a circle of radius r_b centered on the waveguide axis as shown in Fig. 1. (d) The self-fields of the beam are neglected.

Under these assumptions it is possible to use a perturbation theory for the description of the beam-waveguide interaction (BUZZI, J.M., 1977). Then, the dispersion relation for $TE_{\ell n}$ modes is given by

$$\omega^2 - k^2c^2 - \omega_{\ell n}^2 = \omega_p^2 \, \tau_{\ell n} \sum_{p=-\infty}^{p=+\infty} J_{\ell-p}^2 (\mu) \, S_p \tag{1}$$

where $\omega_{\ell n}$ is the cut-off frequency of the $TE_{\ell n}$ mode in the empty waveguide ($\omega_{\ell n} = \beta_{\ell n}c/a$ with $J'_\ell(\beta_{\ell n}) = 0$) and

$$\omega_p^2 = N_o \, e^2/\varepsilon_o \, m_o \gamma$$ (N_o mean electron density in the waveguide section)

$$\tau_{\ell n} = \left[(1 - \ell^2/\beta^2_{\ell n}) \, J_\ell^2 (\beta_{\ell n}) \right]^{-1}$$

$\mu = \beta_{\ell n} \, r_b/a$, $\gamma = (1 - \beta)^{-\frac{1}{2}}$ and $\beta = v/c$ where v is the speed of the electrons. Moreover

$$S_p = \left\{ J_p^2 (\lambda) \pi_p^2 + J_p'^2 (\lambda) \omega'^2 \right\} / (\Psi_p^2 - \omega_b^2) - 2J_p' (\lambda) \, \pi_p/\Psi_p(\Psi_p^2 - \omega_b^2) - (\omega^2 - k^2c^2)\beta_\perp^2 J_p'^2 (\lambda)/\Psi_p^2$$

with : $\lambda = \beta_{\ell n} r_L/a$, $\Psi_p = \omega' - p\omega_b$, $\omega' = \omega - kv_{//}$, $\pi_p = p\omega'/\lambda - \lambda\omega_b$ and $\omega_b = eB_o/m_o\gamma$.

On looking for solutions of equation (1) arround the points $(\omega_\pm, k_\pm)$ solutions of the equations

$$\begin{cases} \omega^2 = \omega_{\ell n}^2 + k^2 c^2 \\ \omega = m\,\omega_b + k v_{//o} \end{cases}$$

One obtains the simplified dispersion relation :

$$(\delta\omega/\omega_{\ell n})^3 - 3\,q\,\frac{\omega_p^2}{\omega_{\ell n}^2}\,(\delta\omega/\omega_{\ell n})\,F_{\pm}^{-1} + 2\,\beta_{\perp}\,F_{\pm}^{-1}\,\frac{\omega_p^2}{\omega_{\ell n}^2}\,r = 0 \qquad (2)$$

where :

$$F_{\pm} = \gamma_{//}^{\,2}\left\{1 \pm \beta_{//}\sqrt{1 - \omega_{\ell n}^2/m^2\,\gamma_{//}^2\,\omega_b^2}\right\}$$

$$\omega_{\pm} = m\,\omega_b\,F_{\pm}$$

$$\omega = \omega_{\pm} + \delta\omega\,,\ \beta_{//} = v_{//}/c,\quad \gamma_{//} = (1 - \beta_{//}^{\,2})^{-1/2} \text{ and :}$$

$$r = \frac{\tau_{\ell n}}{4m}\,\lambda\,J_{\ell-m}^2(\mu)\,J_m'^{\,2}(\lambda) \qquad (3)$$

$$q = \frac{\tau_{\ell n}}{3}\,J_{\ell-m}(\mu)\,J_m'(\lambda)\left[J_{\ell-m}(\mu)\,J_m(\mu)\,\lambda\left(\frac{m^2}{\lambda^2} - 1\right) \dots\right.$$

$$\left.\dots - \frac{\lambda^2}{m}\,\frac{\ell-m}{\mu}\,J_{\ell-m}'(\mu)\,J_m'(\lambda)\right] \qquad (4)$$

From the cubic equation (2) it is clear that the instability condition is given by :

$$-\frac{\omega_p^{\,2}}{\omega_{\ell n}^{\,2}}\,q^3 / F_{\pm} + \beta_{\perp}^2\,r^2 > 0 \qquad (5)$$

Expression (5) is useful because the terms q and r are functions only of the Larmor radius r_L and of the guiding center radius r_b. Evaluating Eq. (5) in the beam frame gives the instability region in the r_L, r_b diagram as a function of ω_p. As an example, Fig. 2 gives the instability domains for the TE_{01} mode interacting with the first synchrotron harmonic. Note that r_b can vary from 0 to a, but r_L must satisfy the two conditions :

$$r_L + r_b \leqslant a \quad \text{and} \quad r_L < m\,a/\beta_{\ell n} \quad (\beta_{\perp} < 1 \text{ and } m\,\omega_b > \omega_{\ell n} \text{ in the beam frame}).$$

A more detailed discussion of the threshold condition (5) has been given by one of us (ETLICHER, B., 1978) for others modes and various harmonics.

By solving numerically Eq. 1 one can compute for any real k the complex roots ω^*. Thus one obtains the groth rate $\omega_i = \mathrm{Im}\,(\omega^*)$ where ω^* is a function of k, B_o, $\beta_{//}$, $\beta_{\perp}$ and ω_p^2 for the interaction between a particular waveguide mode and a synchrotron harmonic. Fixing B_o, $\beta_{//}$, $\beta_{\perp}$ and ω_p^2 one can define :

$$\overline{\omega_i} = \mathrm{Sup}\,(\omega_i(k)) = \mathrm{Im}\,(\omega(\bar{k}))$$

$$\overline{\omega_r} = \mathrm{Real}\,(\omega(\bar{k}))$$

where $\bar{k}$ is a particular value of k for which we have the maximum groth rate. Now by varying the external field B_o one can compute the amplification rate :

$$A\,(B_o, \overline{\omega_r}) = \exp\left[2\,\overline{\omega_i}\,\tau\right]$$

An example of numerical results is given on Fig. 3a for a particular set of beam parameters. This calculation predicts the value of the magnetic field for wich emission occurs and the value of the emitted frequency. It should be pointed out that the maximum growth rate in the case of Fig. 3a is not as usually assumed at the grazing intersection of the waveguide mode with the synchrotron resonance but very close to the cut-off frequency. This can be explained by the fact that the perpendicular energy is well above the threshold value. In this case, the term r in Eq. 2 dominates the term proportionnal to q and the growth rate is maximized for small values of ω.

The fact that the emission is maximum for a particular value of the magnetic field is illustrated by Fig. 3b where we plot $\bar{A}(B_o)$ defined by :

$$\bar{A}(B_o) = \mathrm{Sup}\left[A(B_o, \omega_r)\right]$$

It is also interesting to investigate the synchrotron maser as an amplifier by solving Eq. (1) for real ω and complex k. The dispersion diagramm differs from the usual case where k is real and ω complex because as shown on Fig. 4a, for a magnetic field close to that corresponding to the onset of the instability we have two branches of complex k. Branch 1 corresponds obviously to an evanescent wave and branch 2 to an amplifying wave. But when the magnetic field increases the situation is described by Fig. 4b where the two branches collapse. In this case, application of the Bers and Briggs criteria (BRIGGS, R.J., 1964) shows that we have an absolute instability with a large growth rate. This would appear to be a serious problem for an amplifier. However the finite length of the amplifier is not taken into account in this calculation and should limit the effect of this dangerous instability.

1.2 Experiments.

The experimental set up is described on Fig. 5. The cathode is a 4 cm diameter graphite disk and the anode a thin titanium foil (tickness 20 μ). The waveguide is a circular copper pipe (5 cm inner diam.) terminated by a Teflon window and a conical microwave horn. The air pressure in both the diode and the waveguide are always less than 10^{-4} torr. A B field parallel to the waveguide axis is produced by external coils. In contrast to previous experiments (GRANATSTEIN, V.L., 1975 for example), the B field is homogeneous in the diode as well as in the waveguide, except for the fringing field in the vicinity of the microwave window.

A Marx generator connected to a 40 Ω Blumlein delivers a voltage of 700 keV during 20 ns to the diode. During that time electrons flow through the diode and a fraction of the diode current propagates in the waveguide. The microwave emission occuring during that short time is detected by a microwave horn and propagates in a delay line for a time of flight frequency measurement.

Behind the anode a 2 mm stainless steel plate stops the electrons except around the axis where there is a 20 mm diameter hole. This diaphragm appears to be essential for microwave generation.

As shown on Fig. 6, without the diaphragm the microwave power is very low. The interesting result is that with the diaphragm the microwave power reaches large values for a particular magnetic field. This resonance of the microwave emission with the magnetic field suggests that the synchrotron maser process is a possible explanation of the emission. Moreover the frequency (8,6 GHz) of the emission is slightly above the cut-off frequency of the TE_{01} mode (7,3 GHz) predicted from the theory. In order to check the polarization of the radiation we have been using a photographic method (EFFEMEY, H.G., 1959) as illustrated in Fig. 7. The microwave power enters a circular chamber of 2,6 cm length where a pressure of 400 torr in Argon is maintained. Microwave breakdown occurs in this chamber and because of the very short lifetime of the radiation one can expect that the light emitted by the gas is a picture of the electric field intensity. A photographic picture is there taken of the chamber. An example of a densitimetric measurement of these pictures is given in Fig. 8. The interesting conclusion is that the shape of the light emission is in good agreement with the electric field distribution of the TE_{01} mode. The points of maximum brigthness are also at the positions of maximum electric field for the TE_{01} mode.

Now it is interesting to investigate the beam parameters. Longitudinal and radial current density measurements have been performed using Faraday cups. As shown in Fig. 9a, except for few centimeters behind the anode, the beam current is homogeneous along the magnetic field direction z. Fig. 9b shows a radial current profile which has been found to be independent of z for $z > 3$ cm. From these measurements, the beam appears to be annular and homogeneous in z. Since we know the voltage (0.7 MeV) and the current (810 A) in the waveguide we can compute the electrical power and the microwave generation efficiency :

$$\eta = P_{wave}/P_{electrical} \approx 10\ \%$$

This result appears very interesting for a device working with a large current. However in order to scale the possibilities of such a high power device we have to understand how the electrons can have a perpendicular energy inversion in this experimental situation. As shown by the current measurements along the z axis, a virtual cathode is propably present behind the anode. Electrons flowing through this virtual cathode can increase their perpendicular energy. Moreover because the beam is limited by the diaphragm, electrons outside the geometrical shadow of the diaphragm hole should have a minimum Larmor radius in order to reache their positions. Therefore population inversion could occur in an annular region arround the beam edge. However, we should point out that at present we do not have clear experimental evidence that this explanation is correct.

From a pratical point of view, one should note that only a small fraction of the diode current flows through the waveguide. (The diode current is 15 kA). Therefore the practical efficiency is much less than 10 %. The solution to this problem is to match the diode current to the maximum current that one can propagate in the waveguide. This can be done by the use of much smaller Marx generators. In the future the aim of our research program is to understand the population inversion mechanism with currents in the kiloampere range. This will be done using small Marx generators with higher duty rates (10 Hz).

2. FREQUENCY CONVERSION BY BEAM FRONT SCATTERING.

Beam front scattering of an electromagnetic wave has been suggested (GRANATSTEIN, V.L., 1975, DOUCET, H.J., 1975) as a useful process, based upon the relativistic Doppler effect (LANDECKER, K., 1962), for shifting the frequency of a short and intense microwave pulse towards infrared. In recent experiments (GRANATSTEIN, V.L., 1976, PASOUR, J.A., 1977), microwave reflection on a relativistic electron beam has been observed and attributed to beam-front scattering. The associated relativistic Doppler shift found experimentally was in agreement with a theoretical beam front velocity calculated using a free-streaming model for the description of the electron motion.

In the present work, microwave reflection is observed on a relativistic beam front propagating in a gas. The experimental configuration is shown in Fig. 10. The electron beam is produced by a P.I. Pulserad 110 A device. The cathode is a 4 cm diam graphite disk located 1 cm from a 50 μm thick titanium foil. The diode impedance is 40 Ω and the diode voltage 750 kV. The electron beam propagates in an evacuated circular waveguide (42 mm diam) terminated by a Teflon window. The diode and the waveguide are immersed in an uniform static magnetic field. The waveguide is then connected to a rectangular circular T shape coupler and to a large conical horn.

The incident microwave signal is provided by a pulsed magnetron (50 kW, 800 ns pulse duration, tunable between 8.6 and 9.6 GHz). The microwaves are injected into the circular waveguide through the rectangular - to - circular transition, which is a bidirectionnal 3 dB coupler, exciting each side of the circular waveguide with opposite-phase electric fields. Therefore, half of the magnetron power leaves the device through the conical antenna and is monitored by an X-band detector at the end of a 50 m delay line. The radiation pattern of the antenna has been measured an it agrees with the theoretical prediction for the TE_{01} mode. The second half of the magnetron power propagates towards the electron beam, mainly in the TE_{01} mode. The reflected signal is measured in the K_a-band with crystal detectors and a 13 m delay line.

Frequency conversion from the reflection in a waveguide by a mirror moving at speed v is given by (GRANATSTEIN, V.L., 1976)

$$f_1 = f_o(1 + 2\,\beta\beta_g + \beta^2)\,\gamma^2 \qquad (6)$$

with $\beta = v/c$, $\gamma = (1 - \beta^2)^{-\frac{1}{2}}$ and $\beta_g = v_g/c$ where v_g is the group velocity of the incident wave. Since in our experiment, the incident wave lies in the X-band and the expected reflected wave lies in the K_a band, we see from eq. (6) that we need a value of β close to 0.7. We have chosen to adjust the value of the beam front velocity by changing the background gas pressure in the waveguide, holding constant all other parameters : the diode voltage, the current rise time and the magnetic field (5 kG).

In order to measure the beam front velocity, two B_θ probes were located on the surface of the waveguide with a spacing of 68 cm between probes. Time-of-flight measurements between the two probes allows the determination of an average beam front velocity. Fig. 11 shows the variation of this beam front velocity as a function of the air pressure. Taking into account the delay in the cables, we have determined the beam current while measuring the beam front velocity with two B_θ probes. As shown in Fig. 12, this velocity measurement is made when the beam current in the drift tubes is half of the peak value and we can thus measure the beam front velocity. Moreover in Fig. 11 we see that we reach the value $\beta \approx 0.7$, needed for the reflection, with about 400 μ of air.

Working with a background pressure of about 400 μ, without incident microwave power from the magnetron, we observe an emission in the K_a band. Accurate measurements of the propagation delay in the cables and in the waveguides give us the time evolution of this emission with respect to the current (see Fig. 12). This emission occurs when the current is maximum in the waveguide.

When the magnetron signal is applied, other stronger spikes appear in the K_a band and as shown in Fig. 12, before the emission of the beam, when the current reaches about 2/3 of its maximum value. This signal is attributed to the reflection on the beam front. Since the β values for the reflection in the K_a band are very limited around 0.7, from the results given in Fig. 13, one should expect that the pressure is a very critical parameter.

As a matter of fact, the K_a band detectors do not indicate any reflected signal when the pressure lies outside the range 350-450 μ. We have also varied the magnetron frequency f_0 and measured the reflected frequency f_1 with a K_a-band delay line. The results are presented in Fig. 16 and compared to the theoretical curves given by eq. (6) for the TE_{01} and TE_{31} modes. Fairly good agreement is found for β close to 0.7. Therefore, the corresponding velocity of the mirror is close to the beam front velocity.

Note that for one given magnetron frequency one observes very short reflected pulses with slightly different frequencies for about 3 ns. This suggests that the reflecting beam front is the result of a transient phenomena.

In conclusion, we have observed the reflection of microwaves on a relativistic electron beam front propagating in a gas. The mirror velocity deduced from the relativistic Doppler shift for various incident frequencies agrees with the beam front velocity measured with B_θ probes. we have also shown that the reflection occurs during the rise time of the beam current. However, the reflected power has not yet been measured and the reflection coefficient is unknown. The specific mechanism for the change of the waveguide cut off due to the beam front in a gas has not been determined. These two points, particularly the importance of the ionization front, are presently under investigation. If ionization processes participate in the reflection mechanism, the reflection coefficient could be rather small (LAMPE, M., 1977).

3. COLLECTIVE FREE ELECTRON LASER.

The basic idea that propagation of an electron beam through a rippled static magnetic field could produce microwave radiation is due to Motz (Motz, H., 1951). Devices like the Ubitron (Philips, R.M., 1960) have first been working with low current and non relativistic electron beams. However, since the wavelength of the output radiation is given by :

$$\lambda_s \approx \lambda_o / 2\gamma^2 \tag{7}$$

where $\gamma = (1 - v^2/c^2)^{-1/2}$ and λ_o is the period of the rippled static magnetic field, it is more interesting to use relativistic beams. The work of Madey et al. (Madey, J.M.J., 1971 ; Elias, L.R. et al., 1976 ; Deacon, D.A.G., et al., 1977) has shown the practical possibilities of producing radiation in the infrared (10 µm and 3.4 µm) using the electron beam of a LINAC with energies in the 20 - 50 MeV range. This device is now called a free electron laser and the production of radiation is interpreted as a single particle phenomena, the induced Compton scattering. However this interpretation has been criticized by Bernstein and Hirshifield (Bernstein, I.B. and Hirshfield, J.L.) because a simple linear analysis of beam/rippled magnetic field equilibrium can yield also to instabilities which are of kinetic origin.

Nevertheless, another kind of free electron laser was suggested by Schlesinger et al. (Efthimion, P.E., Schlesinger, S.P., 1977). The basic idea is that if one use an intense relativistic electron beam, collective emission of radiation will occur. Now the rippled magnetic field is considered as a "pump wave". As a matter of fact, this "zero frequency pump" in the Laboratory frame appears after Lorentz transformation, as a slow electromagnetic wave in the beam frame. If the wave power in the beam frame is large enough, Raman scattering can occur and a backscattered wave appears in the Laboratory frame with a wavelength given approximately by Eq. 7. Therefore, the "collective free electron laser" appears as the reflection by a non linear phenomena (Raman scattering) of a "zero pump frequency wave".

Dawson et al. have given a good theoretical description of a "collective free electron laser" (Kwan, T. ; Dawson, J.M. ; Lin, A.T., 1977). However the model is not realistic because the beam is infinite and there is no magnetic field (except the helical field of the pump wave) to assure the beam propagation.

Recently, Sprangle (Sprangle, P. ; Dobrot, A.T., 1978) have taken into account the guiding magnetic field. Their theory (as the model of Dawson et al.) predicts good theoretical efficiencies for the "collective free electron laser".

In the work presented here, we have studied two important aspects of a possible experiment :

a) The finite geometry effects and

b) The excitation of the "pump wave".

3.1 Finite geometry.

The first problem one has to look is the dispersion diagram in finite geometry. The model we consider is an homogeneous cold beam, propagating with an axial external magnetic field B_o, in a circular waveguide. In the beam frame, the linear dispersion relation can be obtained by standard techniques (Bevc, V. ; Everhart, T.E., 1962). The calculations are tedious but the dispersion diagram and the polarization of the modes are obtained using a computer. Because the nonlinear wave coupling theory in finite geometry for a cold plasma with magnetic field is a very challanging task, it is more straightforward to consider the cases in which the infinite linear beam theory gives results very close to the finite geometry case. Therefore, the solution of the linear problem in finite geometry allows us to predict the wave satisfying the selection rules for the nonlinear three waves coupling process, but estimation of the nonlinear growth rate is made from well known results of the infinite magnetized plasma nonlinear plasma theory. Generally when the wave number is not too small, for the fundamental modes of the waveguide, the dispersion diagram and the polarization are close to the well known results in infinite plasma for propagation along the magnetic field.

When this is the case, the "pump wave" (ω'_o, k'_o) in the beam frame can be a R.H.C. polarized wave, the scattered wave a plasma wave (ω'_p, k'_p) and the backscattered wave (ω'_s, k'_s) a R.H.C. polarized wave :

$$\omega'_s = \omega'_o - \omega'_p$$

$$k'^2_s c^2 = \omega'^2_s - \frac{\omega'_s \omega'^2_p}{\omega'_s - \omega'_b} \qquad (8)$$

Moreover, using classical results from plasma theory (Wilhehmson, H., 1969) one can evaluate the nonlinear growth rate of the instability in the beam frame :

$$\nu^2 \approx \frac{1}{2}\left(\frac{eE_o}{m}\right)^2 \left\{\frac{k'_p - \omega'_b\left(\frac{k'_o}{\omega'_o} - \frac{k'_s}{\omega'_s}\right)}{(\omega'_s - \omega'_b)\ (\omega'_o - \omega'_b)}\right\}^2 \frac{\omega'_s \omega'_p}{\left(1 - \frac{\omega'_b \omega'^2_p}{2\omega'_s\ (\omega'_s - \omega'_b)}\right)} \qquad (9)$$

3.2 Excitation of the "pump wave".

In previous works (Efthimion, P.E. ; Schlesinger, S.P., 1977 ; Sprangle, P. ; Dobrot, A.T.) it is assumed that the beam does not screen the rippled magnetic field. However, if the modulated magnetic field satisfies the linear dispersion relation the excitation of the "pump wave" will be much stronger and this is a useful circumstance for the study of a nonlinear phenomena. Therefore we plan to excite the primary wave (ω'_o, k'_o) with a helical static magnetic field of period λ_o. This zero frequency "wave" in the laboratory frame becomes an infra-luminous wave in the beam frame and can match for ω'_o below ω'_b the dispersion diagram and the polarization for a R.H.C.P.W. In these conditions, this last wave is resonantly excited and the induced field can reach much larger values than the external field alone. Matching the helical field with the dispersion diagram of the beam will be made by tuning the longitudinal magnetic field.

3.3 Determination of the experiment parameters.

At this point we can define the main parameters of a possible experiment. In our research program we plane to work first at 0,75 MeV (Experiment A) and at 8 MeV (Experiment B).

The first condition one has to satisfy is that the "pumpe wave" has to match the dispersion curve on the R.H.C.P.W. This yields the relation :

$$x_p^2 = \eta\ (1 - \eta)/\beta^2\gamma^2 \qquad (10)$$

where $x_p = \omega'_p/\omega'_b$, $\eta = \omega'_o/\omega'_b$ and $\omega'_o = \beta\gamma\, 2\pi c/\lambda_o$. One should also satisfie the condition :

$$\omega'_o > \omega'_p$$

This gives a new limitation on η :

$$\eta > x_p \qquad (11)$$

Moreover, assuming that the beam is homogeneous in density we can express the beam current by :

$$I = I_A \pi^2 \xi^2\ (1 - \eta)/\eta \qquad (12)$$

where I_A (kA) = $17\beta\gamma$, $\mu = a/\lambda_o$ and a is the radius of the waveguide. Finally, the frequency conversion factor and the resonant magnetic field B_o are given by :

$$\frac{\lambda_o}{\lambda_s} = \frac{U}{c} \frac{\gamma}{2\pi x_p} (\alpha + \beta K_s) \tag{13}$$

$$B_o = \frac{U}{\lambda_o x_p} \frac{m}{e} \tag{14}$$

where $U = \sqrt{\frac{I}{I_A}}\, 2c/\mu$, $\alpha = \eta - x_p$ and $K_s^2 = (\alpha^2 - \frac{x_p^2\alpha}{1-\alpha})$.

Equations 10 - 12 show that there is an upper current limit : This limit is a function of γ only.

Assuming that $a = 0,5\,\lambda_o$ for both experiments we found :

Experiment A $I_{max} = 132$ kA

Experiment B $I_{max} = 204$ MA

These values are much larger than the currents one can reach with diode impedances around 40Ω. Therefore the actual current limit is given by the diode current and by the limit current one can transport in a magnetized waveguide. One can make the following estimates

Experiment A : $I \approx 7$ kA $\eta = 0,96$ and $\frac{\lambda_o}{\lambda_s} = 9,6$
for $\lambda_o = 2$ cm $B_o = 13$ kGauss $\Delta\gamma_o = 0,8$

Experiment B : $I \approx 50$ kA $\eta = 0,93$ and $\frac{\lambda_o}{\lambda_s} = 567$
for $\lambda_o = 6,5$ cm $B_o = 30$ kGauss $\Delta\gamma_o = 0,8$

$\Delta\gamma_o$ is the maximum energy spread of the beam. This limitation results from the requirement that the Laudau damping of the plasma wave has to be small :

$$\Delta\gamma < \Delta\gamma_o = \lambda_o \beta \omega_p' / (1 + \beta)\, c \tag{15}$$

These estimates show that the frequency shift one can obtain are close to the theoretical value Eq. 7. The longitudinal beam spread limitation for both experiments is not too strong, but difficulties are probably to be expected from the cyclotron damping of the pump wave (η is close to one). As shown by Eq. 12, the only way of reducing η is to increase the beam current, and the main problem of the experiments will probably be the difficulty of propagating a high current of small brigthness.

REFERENCES

BERNSTEIN I.B., HIRSHFIELD J.L., 1978, Phys. Rev. Letters, 40, 761.

BRIGGS R.J., 1974,
Research Monograph no. 29, the MIT Press, Cambridge, Massachusetts, p. 8.

BEVC V. EVERHART T.E., 1962, J. Electron. Control 13, 185

BUZZI J.M., DOUCET H.J., ETLICHER B.,HALDENWANG P., HUETZ A., LAMAIN H., ROUILLE C., CABE J.,DELVAUX J., JOUYS J.C.and PEUGNET C. 1977, Proceedings of the 2nd International Topical Conference on High Power Electron and Ion Beam Research and Technology, Laboratory of Plasma Studies, Cornell University, Ithaca N.Y., J.A. Nation and R.N. Sudan Editors, Vol. II, p. 663.

DEACON D.A.G., ELIAS L.R., MADEY J.M.J., 1977, Phys. Rev. Letters 38, 892.

DOUCET H.J., 1975, Advisory Group Meeting on Experimental Aspect of Laser and Electron Beam produced Thermonuclear Plasmas, Trieste, Italy.

EFFEMEY H.G., 1959, Proceedings IEE, paper no. 2837R, p. 75.

EFTHIMION P.E., SCHLESINGER S.P., 1977, Phys. Rev. A, 15, 1633.

ELIAS R.L., FAIRBANK W.M., MADEY J.M.J., 1977, Phys. Rev. Letters 38, 892.

FLYAGIN V.A., GAPONOV A.V., PETELIN M.I. and YULPATOV V.K., 1977, IEEE Transanctions on Microwave Theory and Technique, Vol. MTT-25, 6.

GRANATSTEIN V.L., SPRANGLE P., PARKER R.K. and HERNDON M., 1975, JAP vol. 46, p. 2021

GRANATSTEIN V.L., PARKER R.K., SPRANGLE P., 1975, in Proceedings of the International Topical Conference on Electron Beam Research and Technology, vol. II, Sandia Laboratories, report SAND76 - 5122, p. 401.

GRANATSTEIN V.L., SPRANGLE P., PARKER R.K., PASOUR J., HERNDON M., SCHLESINGER S.P. and SEFTOR J.L., 1976, Phys. Rev. A14, 1194.

KWAN T., DAWSON J.M., LIU A.T., 1977, Phys. Fluids 20, 581.

LAMPE M. OTT E., MANHEIMER W.M., KAINER S., 1977, IEEE Transactions on Microwave Theory and Techniques, Vol. MTT-25, 6, 556.

LANDECKER K., 1952, Phys. Rev. 86, 852.

MADEY J.M.J., 1971, J. Appl. Phys., 42, 1906.

MOTZ H., 1951, J. Appl. Phys. 22, 527.

PASOUR J.A., 1977, Ph D Thesis, Raleigh University.

PHILLIPS R.M., 1960, IRE Trans. Elect. Devices, ED-7, 231.

SPRANGLE P., DOBROT A.T., 1978, NRL Memorandum Report 3581 (to be published in Phys. Rev.).

WILHELMSON H., 1969, J. Plasma Phys. 3, 215.

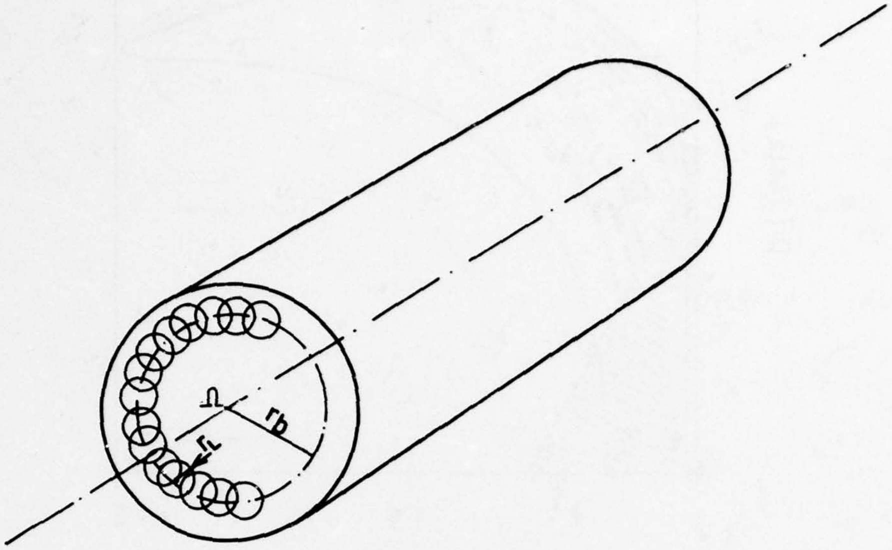

Figure 1. Geometry of the beam.

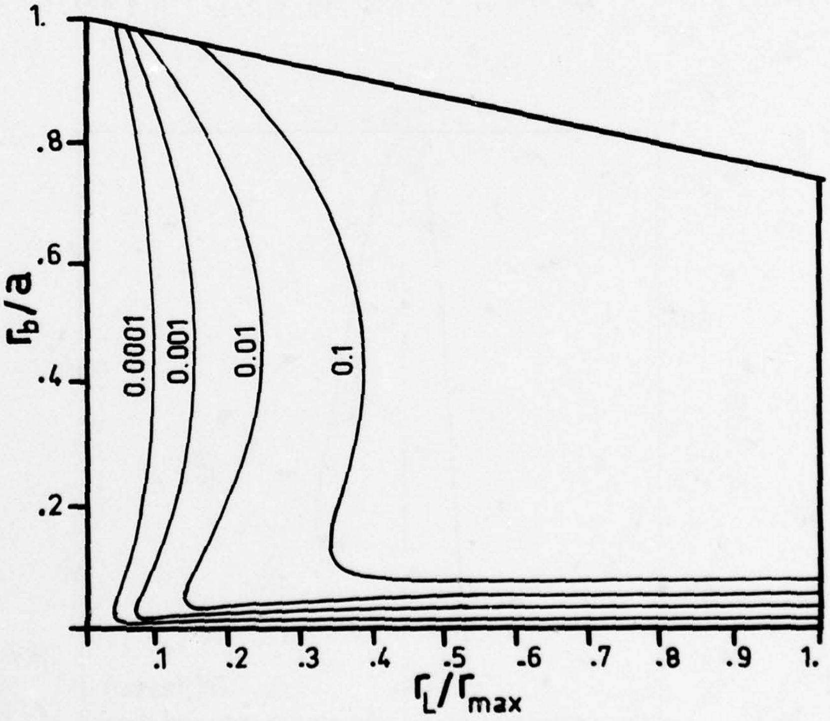

Figure 2. Threshold condition in the r_b, r_L diagram for various plasma densities. The numerical parameter of the curve is ω_p^2/ω_{01}^2 where ω_{01} is the cut-off frequency of the TE_{01} mode for an empty circular waveguide.

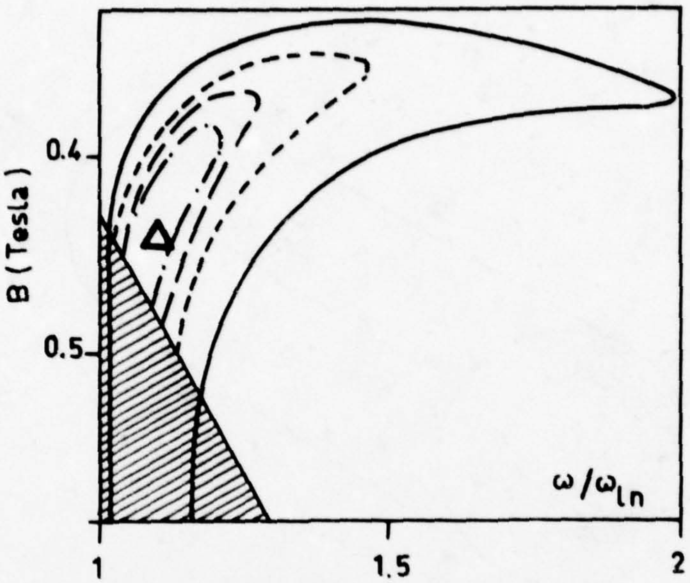

Figure 3a. Altitude chart of the amplification rate A for $\tau = 5$ ns as a function of the magnetic field and frequency for the TE_{01} mode interacting with the first synchrotron harmonic. ω_{ln} is the cut-off frequency of the TE_{01} mode. The waveguide radius is 2.5 cm. The triangle indicates the maximum amplification A_{max}. The beam parameters are $\gamma = 2$, $\beta_{\parallel} = 0,757$, $\beta_{\perp} = 0,42$ and I = 650 A.
— $A/A_{max} = 0,05$; --- $A/A_{max} = 0,25$; -- $A/A_{max} = 0,5$ and -.- $A/A_{max} = 0,75$.
$A_{max} = 5,46 \times 10^8$.

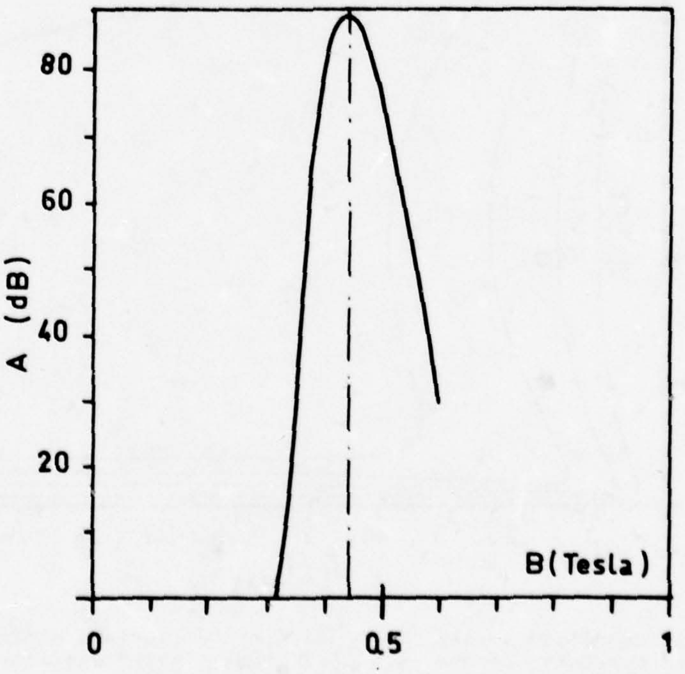

Figure 3b. Resonance of the amplification rate as a function of the magnetic field. The conditions are the same as in Fig. 3a.

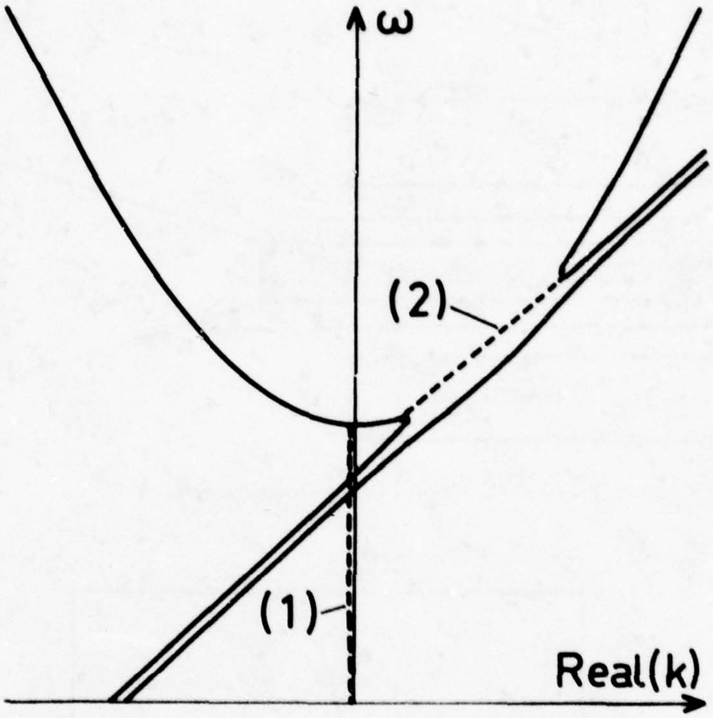

Figure 4a. Dispersion diagram for real ω. The dotted curves indicate complex k.

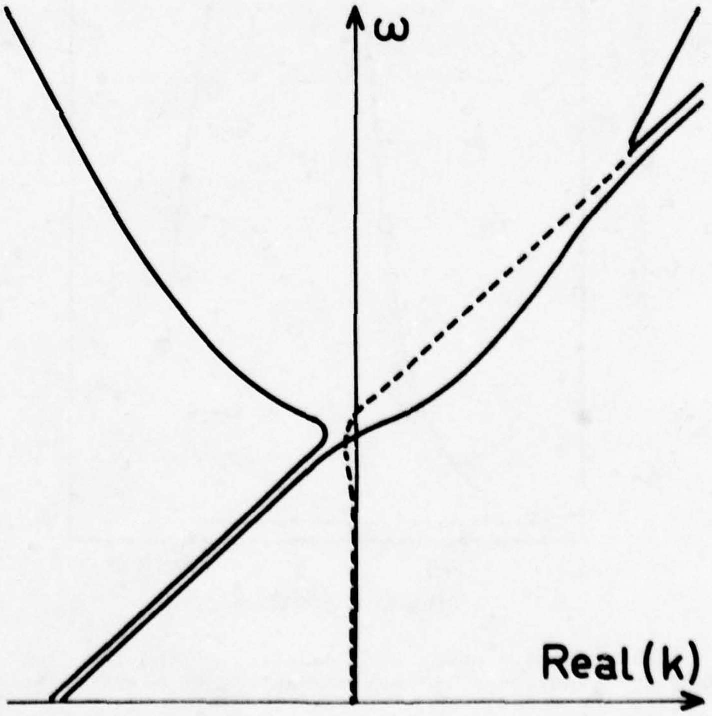

Figure 4b. Same dispersion diagram than in Fig. 4a, but for a larger value of the magnetic field.

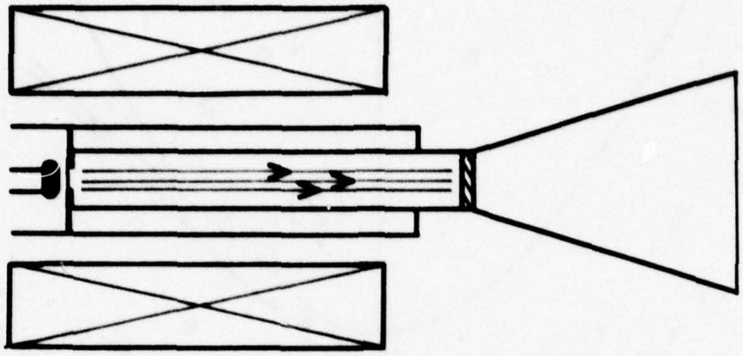

Figure 5. Experimental arrangement.

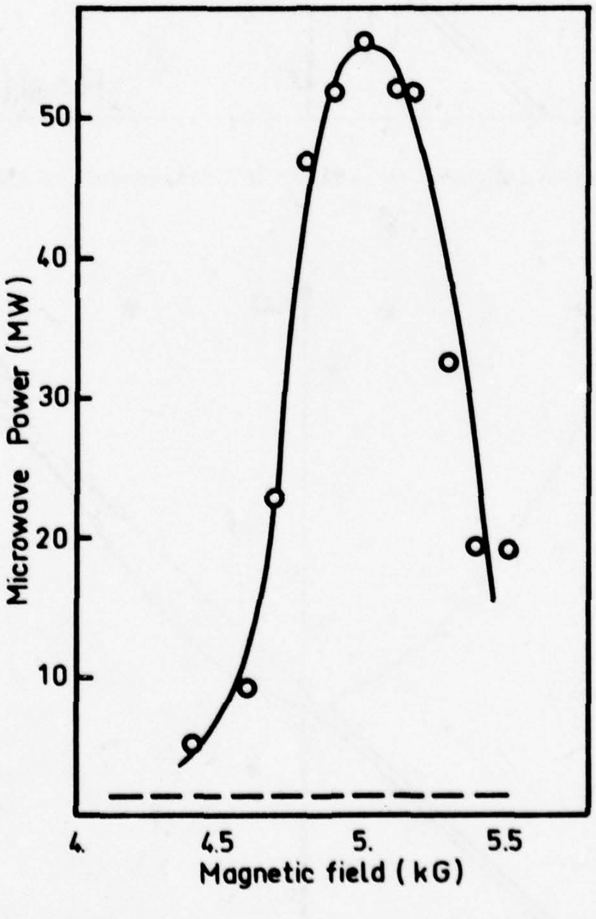

Figure 6. Measured microwave peak power as a function of the longitudinal magnetic field. The dotted line indicates the maximum microwave power detected without diaphragm behind the anode.

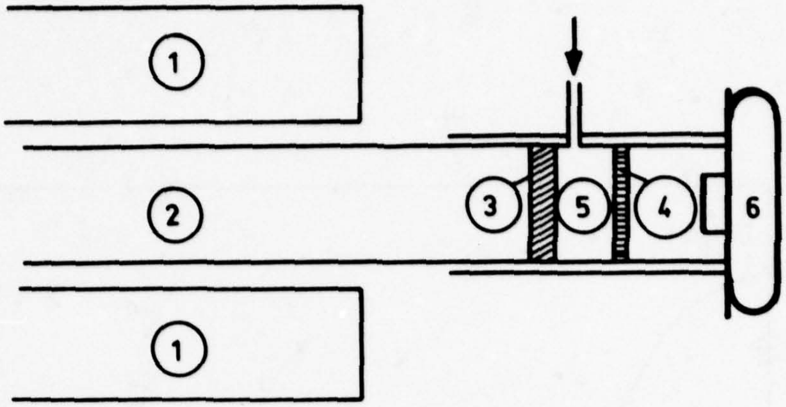

Figure 7. Experimental set-up for the measurement of the microwave polarization.

1. Magnetic field coils.
2. Waveguide.
3. Opaque window.
4. Transparent window.
5. Gaz chamber.
6. Photographic camera.

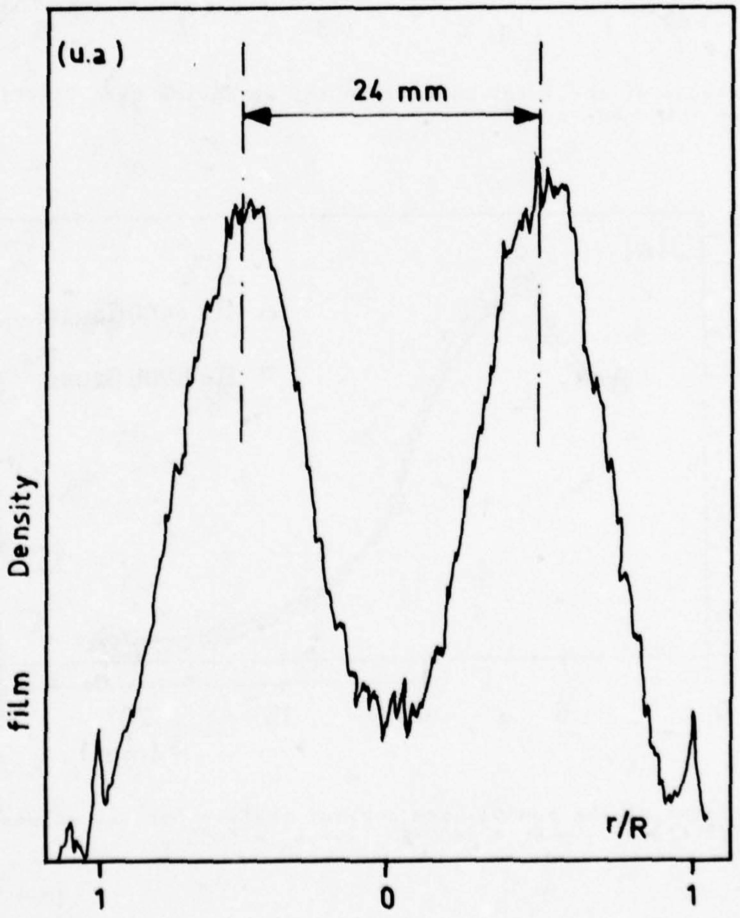

Figure 8. Densitometry measurement of a picture indicating the mode polarization. R is the radius of the waveguide.

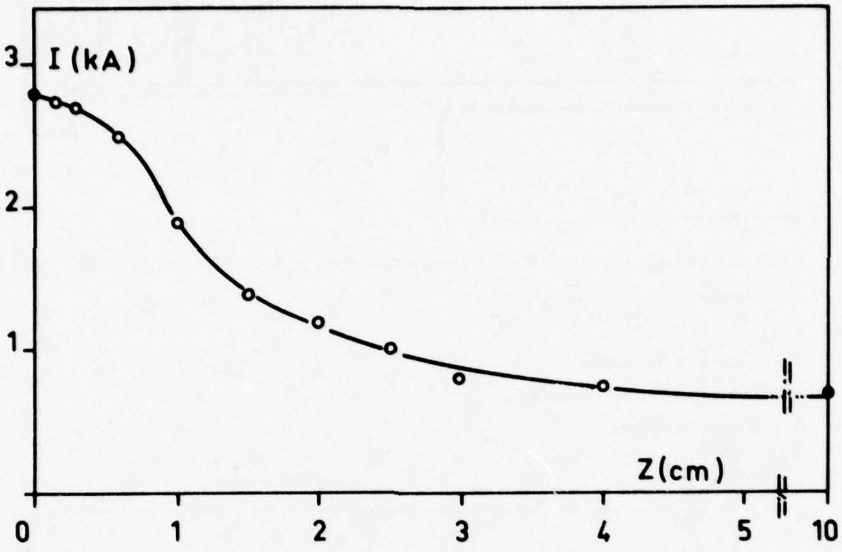

Figure 9a. Measurement of the total current in the waveguide as a function of the distance from the anode z.

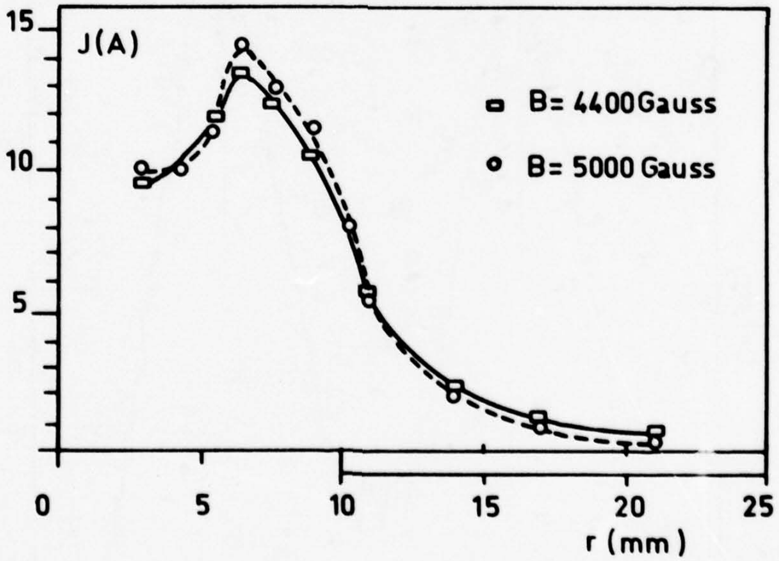

Figure 9b. Measurement of the radial beam current profile for two values of the external magnetic field. —— B_o = 4400 G ; --- B_o = 5000 G.

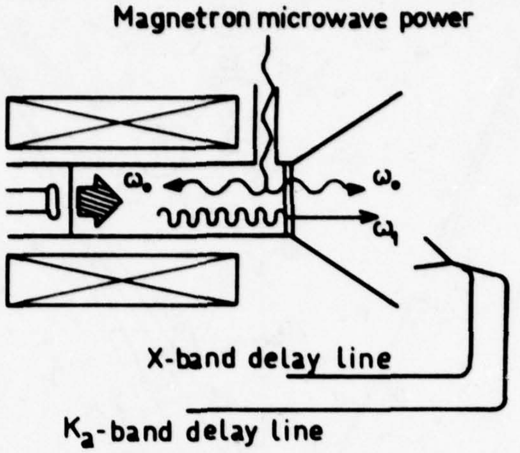
Magnetron microwave power
ω_o
ω_o
ω_1
X-band delay line
K_a-band delay line

Figure 10. Experimental arrangement.

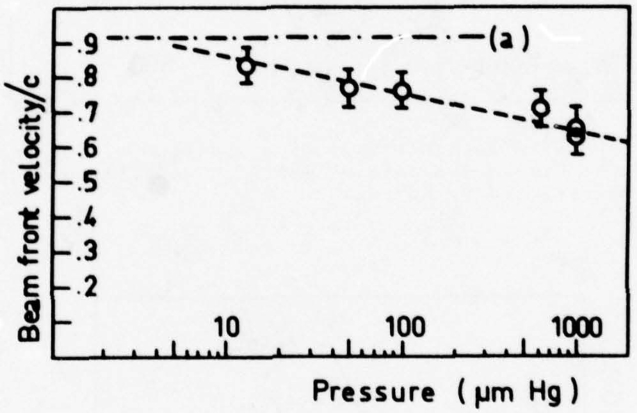

Figure 11. Variation of the beam front velocity as a function of the air pressure. The dotted line (a) gives the value of β deduced from the diode voltage.

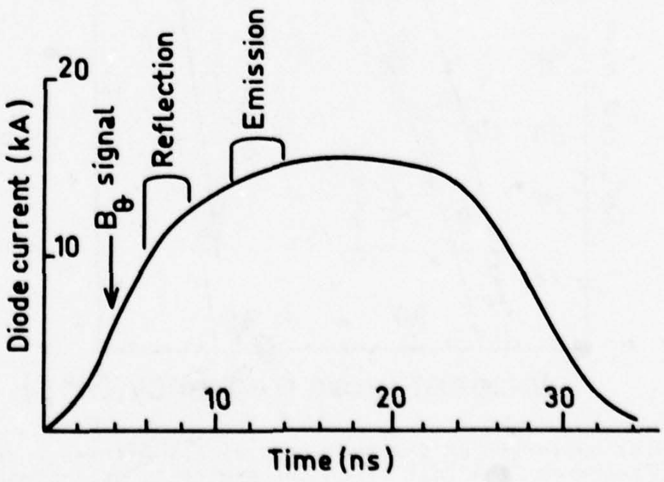

Figure 12. Timing of emission, reflection, diode current and B signal in the waveguide.

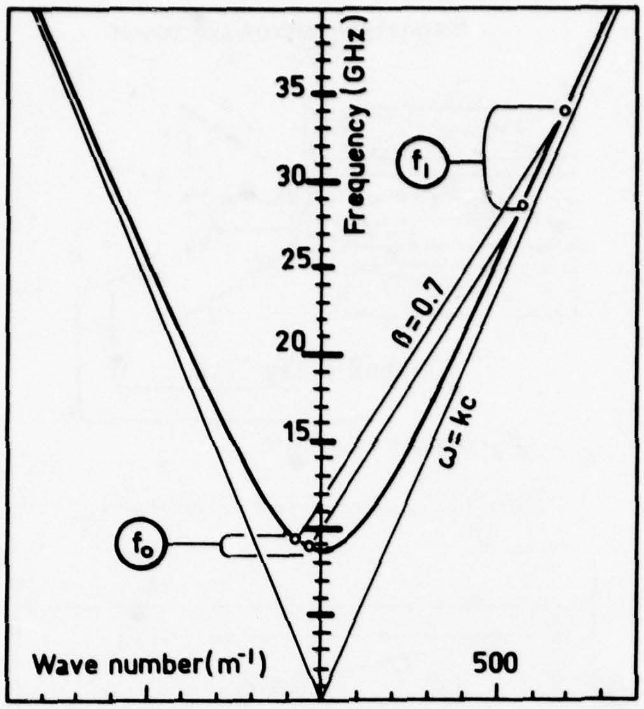

Figure 13. Frequency of the reflected signal as a function of the incident frequency predicted for β = 0,7 in the case of the TE_{01} mode for a 42 mm diam waveguide. f_o and f_1 are related by Eq. 6.

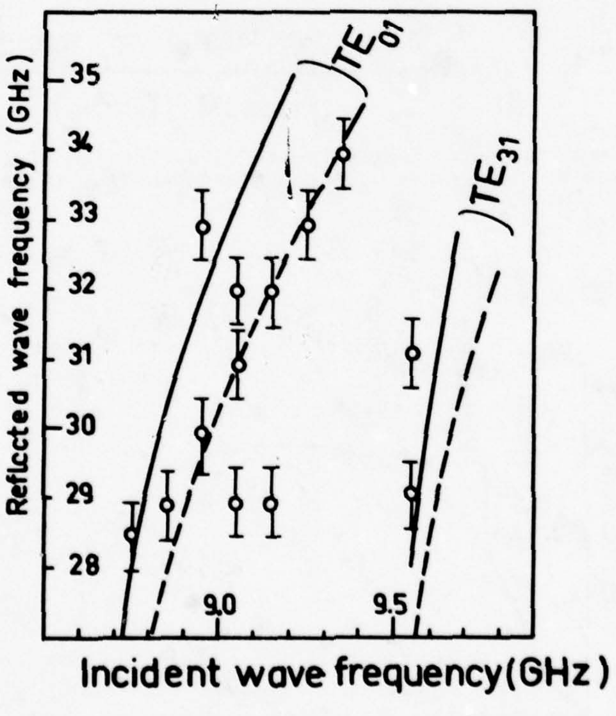

Figure 14. Experimental variation of the reflected signal frequency as a function of the incident frequency. The full lines correspond to predicted variation for β = 0,7 and the dotted lines for β = 0,68 for the TE_{01} and TE_{31} modes. Error bars indicate uncertainities du to finite delay-line length and duration of the microwave pulse.

RELATIVISTIC ELECTRON BEAM INTERACTIONS FOR GENERATION OF HIGH POWER MILLIMETER AND SUBMILLIMETER WAVES

V. L. Granatstein, P. Sprangle, R. Parker, K. R. Chu,
A. T. Drobot*, L. Seftor, M. Read† and T. Coffey
Naval Research Laboratory
Washington, D. C. 20375

SUMMARY

Several coherent emission processes operative within high power, relativistic electron beams have been studied. The spectral range of interest extends from centimeter to submillimeter wavelengths. Effort is presently concentrated in two areas: (1) exploratory development of the electron cyclotron maser (gyrotron) for millimeter wave sources, and (2) a basic study of coherent scattering mechanisms whereby incident microwave radiation is Doppler shifted to higher frequencies.

The cyclotron masers (gyrotrons) under development include a gyro-travelling wave amplifier designed to operate with 280 kw output power at 35 GHz. This amplifier is expected to have a wide bandwidth (~ 10%). Also under development are gyro-monotron oscillators of widely ranging characteristics; (1) 200 kw at 35 GHz; and (2) 1 - 10 kw at 250 GHz. An extensive nonlinear theory of the cyclotron maser has been carried out; and, phase trapping is found to be the most important saturation mechanism and efficiencies in excess of 50% have been calculated.

The coherent scattering studies employ intense relativistic electron beams. Results to date include backscattering of an input wave of 500 kw at 10 GHz to produce an output wave of 5 MW at 50 GHz, and backscattering of an input wave of 10 MW at 15 GHz to produce an output of 1 MW at 750 GHz.

I. INTRODUCTION:

In recent years there has been considerable renewed interest in the development of novel electron devices for the production of high power coherent electromagnetic radiation. This renewed interest has been motivated largely by the realization that certain processes in non neutral plasmas can, using existing technology, produce coherent, electromagnetic radiation at power levels far in excess of those achievable by conventional electron devices. In the present paper an attempt will be made to present a brief review of work which has been performed at the Naval Research Laboratory during the past several years.

The work which will be discussed involves the use of relativistic processes in non neutralized electron beams. The electron beams themselves may be highly relativistic or only weakly relativistic, depending upon the mechanism and the objective (e.g., desired power level, efficiency, pulse length, etc.). Two basic processes have been considered: the electron cyclotron maser and coherent scattering of electromagnetic radiation from relativistic electron beams. The first process exploits the fact that the electron cyclotron frequency is a function of the relativistic factor γ of an electron beam. The second process (coherent scattering) is primarily an exploitation of the Lorentz transformations which come into play during the interaction of electromagnetic radiation with relativistic particles.

Figure 1 presents a very simplistic summary of the experimental data (peak power vs frequency) obtained from the above mentioned processes and other processes using intense relativistic electron beams. The data points are identified as to the responsible mechanism. The state-of-the-art in conventional technology (e.g., klystrons, magnetron, ubitron) is also indicated in Figure 1 by the shaded area. Although Figure 1 does not tell the whole story for either conventional devices or the present work, it is clear that significant advances have been made in terms of power available and in frequency range. In the remaining sections, a brief review of the theoretical and experimental understanding of the new devices will be presented. Section II discusses the work on electron cyclotron masers, Section III discusses the work on coherent scattering, and Section IV concludes the paper.

II. ELECTRON CYCLOTRON MASER

In this section a brief review will be given of the theory and the experimental status of the electron cyclotron maser. For historical background one should refer to Hirshfield and Granatstein (1977). The cyclotron maser process is derived from a negative mass instability which occurs in a system of electrons gyrating in a magnetic field. The instability is due to the dependence of the electron mass on the relativistic factor γ for the electrons. A simple physical picture of the instability mechanism can be developed by considering the relativistic particle orbits of electrons gyrating in a magnetic field in the presence of an applied electromagnetic wave. This situation is schematically illustrated in Figure 2 for two particles. In the absence of the electromagnetic wave, it is well known that the particles execute simple circular motion about the applied magnetic field with a cyclotron frequency.

$$\Omega_0 = \frac{eB_0}{\gamma mc} \tag{1}$$

where

$$\gamma = \left(1 - \frac{v^2}{c^2}\right)^{-\frac{1}{2}} \tag{2}$$

One knows from the theory of relativity that a particle with rest mass m and velocity $\bar{v}$ (in a given reference frame) has an energy

$$\epsilon = \gamma mc^2 \tag{3}$$

If one considers the motion of a particle for a short time Δt, then we can write

$$\Delta\epsilon = \Delta\gamma mc^2 \tag{4}$$

Similarly, if a particle is acted upon for a short time by a force

$$\bar{F} = -e\bar{E} \tag{5}$$

then the change in energy of that particle is

$$\Delta\varepsilon = -e\bar{E} \cdot \bar{v}\,\Delta t \tag{6}$$

Equating (4) and (6) gives

$$\Delta\gamma = -\frac{e\bar{E} \cdot \bar{v}\,\Delta t}{mc^2} \tag{7}$$

For the situation shown in Figure 2, one sees that $\Delta\gamma > 0$ for particle 1 while $\Delta\gamma < 0$ for particle 2. From equation (1), it follows that $\Delta\Omega < 0$ for particle 1 while $\Delta\Omega > 0$ for particle 2. Hence, particle 1 slows down in its cyclotron motion while particle 2 speeds up. If now the time dependence of the electric field E(t) is chosen such that the electric field is fully reversed when particle 2 reaches the original position (as shown in figure 2) of particle 1, the process will continue, i.e., particle 2 will continue to gain phase while particle 1 will continue to lose phase. If the situation is arranged so that more particles gain phase (lose energy since $\Delta\gamma < 0$) than lose phase (gain energy) then by conservation of energy the electromagnetic field must increase. This requires that the wave frequency ω slightly exceed the cyclotron frequency Ω_0. Detailed numerical studies of this process of phase bunching have been reported by Sprangle and Drobot (1977). From the above discussion, one sees that the cyclotron maser process is inherently relativistic.

A more sophisticated treatment of the cyclotron maser requires examination of the plasma dispersion relation. This is obtained by examing the linear solutions of the coupled Vlasov-Maxwell equations. The simplest dispersion relation is obtained for a cold electron distribution

$$F_0 = \delta\,(p_\perp - p_{\perp 0})\,\delta(p_z)/2\pi p_\perp \tag{8}$$

where $p_\perp$ and p_z are the transverse and axial momenta respectively, $p_{\perp 0}$ is a constant and $\delta(x)$ is the Dirac delta function. Such a distribution is an approximation to the electron beam frame representation of electron distributions used for cyclotron maser research. In this special case, the dispersion relation for an unbounded plasma becomes

$$\omega^2 - k_z^2 c^2 = \frac{\omega_p^2}{\gamma}\left[\frac{\omega}{\omega - \Omega_0} - \frac{\beta_{0\perp}^2\,\omega^2}{2(\omega - \Omega_0)^2} + \frac{v_{\perp 0}^2 k_z^2}{2(\omega - \Omega_0)^2}\right], \tag{9}$$

$$\beta_{0\perp} = v_{\perp 0}/c\ ,\ v_{\perp 0} = p_{\perp 0}/\gamma\,m.$$

This dispersion relation is, of course, appropriate for an electromagnetic wave propagating in the z direction along the applied magnetic field B_0. The left hand side (LHS) of (9) is simply the dispersion of light in vacuum. The right hand side (RHS) represents the presence of the electron plasma. The first term on the RHS is simply the usual plasma dispersion for a right hand circularly polarized wave in a magnetized electron plasma. The second term on the RHS is clearly of relativistic origin and is indeed the term which leads to the cyclotron maser process described earlier. The last term on the RHS is a term which leads to bunching in the direction of propagation of the electron beam, i.e., along the applied magnetic field. This so called axial bunching is distinct from the azimuthal (perpendicular to the applied magnetic field) bunching described above. It should be noted from (9) that both azimuthal bunching and axial bunching are present simultaneously and enter the dispersion relation with different signs. A discussion of the relative importance of azimuthal bunching as opposed to axial bunching has been given by Chu and Hirshfield (1978). They find that, from a practical standpoint, azimuthal bunching dominates when

$$\omega^2/k_z^2 > c^2$$

while axial bunching dominates when

$$\omega^2/k_z^2 < c^2\ .$$

In the case where axial bunching dominates, one is dealing with an instability akin to those studied by Weibel (1959).

Consider the case $\omega^2 \gg k_z^2\, c^2$ (i.e., $k_z \sim 0$ in the beam frame) and recall that the cyclotron maser requires $\omega \approx \Omega_0$. If we set $\omega = \Omega_0 + \delta\omega$ then, retaining only the dominant terms, the dispersion relation (9) becomes

$$\delta\omega^2\,\Omega_0^2 = \frac{\omega_p^2}{\gamma}\left(\Omega_0\,\delta\omega - \frac{\beta_{0\perp}^2}{2}\,\Omega_0^2\,\frac{\omega_p^2}{\gamma}\right) \tag{10}$$

The solution of (10) is

$$\delta\omega = \Omega_0\,\beta_{\perp\mathrm{crit}} \pm \Omega_0\,\beta_{\perp\mathrm{crit}}\sqrt{1 - \beta_{0\perp}^2/\beta_{\perp\mathrm{crit}}^2} \tag{11}$$

where

$$\beta_{\perp\mathrm{crit}}^2 = \frac{\omega_p^2}{2\gamma\,\Omega_0^2}\ . \tag{12}$$

It is clear from (11) that instability exists for this case ($k_z = 0$ in the beam frame) only when

$$\beta_{0\perp} > \beta_{\perp crit}.$$

The existence of a critical value of $\beta_{0\perp}$ is found to occur in more complex situations also. The value of $\beta_{\perp crit}$ derived here refers to the rest frame of the electron beam. To obtain the criterion in the laboratory frame, one must make the appropriate Lorentz transformation.

For cases of interest for the laboratory production of cyclotron maser radiation, one wishes to produce the radiation in a waveguide or cavity. In this case the radiation is restricted to those modes which can propagate in the waveguide. The dispersion relation given in (9) is modified to account for the conducting walls. Discussion of the dispersion relation in this case has been given by Friedman, et al (1973) and Ott and Manheimer (1975) as well as others. The discussion of this dispersion relation will not be treated here.

Studies of the non linear behavior of the cyclotron maser have been carried out by a number of authors (Jory, H., 1968; Zhurakovskiiy, 1964; Rapoport, et al, 1967; Nusinovich and Erm, 1972; Demidovich, et al, 1973; Sprangle and Manheimer, 1975; Sprangle and Drobot, 1977). Sprangle and Drobot have performed the most complete study. They find, as in the discussion of (9), that there is a critical value $\beta_{\perp crit}$ which $\beta_{0\perp}$ ($= v_{\perp 0}/c$) must exceed for the cyclotron maser to be operative (the value of $\beta_{\perp crit}$ is, of course, obtained from linear theory). The expression for the critical value of β_0 is (in the case of parallel plate geometry)

$$\beta_{\perp crit} = \ell\Omega_b (Q_{n\ell}/W_{n\ell})^{\frac{1}{2}} \cdot \left[(2/27)\delta_{n\ell}\omega_b^2 Q_{n\ell}/(\gamma\, \omega_b \ell\, \Omega_b)\right]^{\frac{1}{4}}/ck_n \tag{13}$$

where k_n is the perpendicular wave number, n = 1, 2, 3,..., ℓ = 1, 2, 3,... is the magnetic harmonic number, ω_b is the modified plasma frequency, $\delta_{n\ell} = (1 + -1)^{n+\ell})$. Plots of $Q_{n\ell}(x_n)$ and $W_{n\ell}(xn)$ are given in Figure 3. It can be seen from Figure 3 that for $x_n \ll 1$ $Q_{11} \rightarrow .5$ while $W_{11} \rightarrow .25$. One typically works in this parameter range.

Sprangle and Drobot show that the saturation mechanisms for the cyclotron instability depends upon the value of $\beta_{0\perp}$ relative to $\beta_{\perp crit}$. For $\beta_{0\perp} > \beta_{\perp crit}$ saturation occurs by depletion of the free energy in the electron beam. For $\beta_{0\perp} \gg \beta_{\perp crit}$ saturation occurs by phase trapping of the electron beam. In other words, the electric field grows to such an amplitude that the electrons become trapped.

For a given saturation mechanism, one can estimate the efficiency of the cyclotron maser process. It has been pointed out that there is a critical value which $\beta_{0\perp}$ must exceed. Therefore, the free energy per particle available for the electromagnetic wave is

$$\epsilon_{free} = (\gamma_{0\perp} - \gamma_{\perp crit})mc^2, \tag{14}$$

where $\gamma_{\perp crit} = (1 - \beta_{\perp}^2{}_{crit})^{-\frac{1}{2}}$.

If the particles were to lose all of their available free energy, then the efficiency η is

$$\eta = \frac{(\gamma_{0\perp} - \gamma_{\perp crit})}{(\gamma_{0\perp} - 1)} \tag{15}$$

In the case where saturation occurs by phase trapping, Sprangle and Drobot estimate the efficiency to be

$$\eta = 2(\Delta\,\omega/\omega)\,\gamma_{0\perp}/(\gamma_{0\perp} - 1) \tag{16}$$

where $\Delta\omega$ is the frequency shift obtained from the linear dispersion relation. Figure 4 shows the comparison among the efficiencies predicted by (15) and (16) and that obtained from computer simuation of the non linear particle dynamics (Sprangle and Drobot, 1977). This calculation is for the case when $\omega_b/(\sqrt{\gamma_{0\perp}}\Omega_b) = .1$. Other cases may be found in Sprangle and Drobot, 1977. In general, design for a specific gyrotron tube requires a detailed design study. One such study has been reported by Chu, et al (1977) for the case of a gyrotron travelling wave amplifier. This study resulted in the design of an electron cyclotron maser amplifier with predicted operating parameters of 35 GHz with an output power of 340 kw, a power gain of 2 db/cm and an efficiency of 51%. A schematic of the resulting amplifier is shown in Figure 5 along with the required magnetic field.

The experiments on the cyclotron maser process at NRL began with fundamental experiments employing single intense pulses of electrons at energies in the megavolt range. These experiments produced record peak power levels over a range of wavelengths 3 cm > λ > 4 mm (Hirshfield and Granatstein, 1977) and yielded considerable insight into the nature of the cyclotron maser process (Sprangle and Drobot, 1977). Currently, the work has progressed to the stage of building experimental models of practical devices. These employ hot cathodes so that they may be operated either repetitively pulsed or with very long single pulses; voltages are moderate, V < 100 kV; and the devices employ carefully designed electron guns of the magnetron-injection type to optimize device efficiency.

A 35 GHz gyrotron oscillator has been designed to operate with a 70 kV, 8 A electron beam at 30% efficiency. The configuration is shown in Figure 6. In initial laboratory tests output peak powers up to 100 kW have been achieved. The device operates at the fundamental of the cyclotron frequency (B_0 = 13.7 kG) and generates a wave with azimuthal electric field in TE^0_{01} mode. Mode conversion from TE^0_{01} to the linearly polarized fundamental mode in rectangular waveguide with a loss of only 0.5 dB has been successfully demonstrated. The pulse length of the 35 GHz radiation is 1.3 μsec with a PRF of 10 pps. Increasing PRF and achieving average powers up to 10 kW requires improvement in the beam collector but is considered to be a straightforward task. There are plans to drive this gyrotron from a single pulse 10 millisecond modulator; in this mode of operation the gyrotron will be used in electron cyclotron resonance heating (ECRH) experiments on Tokamak plasmas.

In addition to the gyrotron oscillator work, an experimental 35 GHz gyrotron travelling wave amplifier is being fabricated. The feasibility of such an amplifier has been demonstrated (Granatstein, et al, 1975) in an experiment employing an intense relativistic electron beam. The device currently under construction is shown in Figure 5. It will employ the same electron gun and superconducting magnet used with the oscillator described above. The amplifier will operate repetitively pulsed with 1 μsecond long pulses. Theoretical design (Sprangle and Drobot, 1977; Chu, et al, 1977) values predict an output peak power of 280 kW, an efficiency of 51% and a small-signal bandwidth of 10%.

Experiments are being prepared to examine gyrotron oscillators and amplifiers operating at the second harmonic of the cyclotron frequency. Experimental devices resulting from this work should be operational in 1979 and will exhibit power levels of ~ 100 kW at 90 GHz and ~ 10 kW at 250 GHz. Investigations are also starting into optimizing gyrotron efficiency by axially contouring the device radius and the applied magnetic field strength. Modified gyrotron travelling wave amplifier designs allowing for ultra-wideband operation ($\Delta f/f \sim 40\%$) are also being considered. The theory of cyclotron maser operation at harmonic frequencies has been discussed by Chu (1978).

III. COHERENT SCATTERING

A low-frequency electromagnetic pump wave can be backscattered from an electron stream producing a high-frequency electromagnetic wave if the pump wave vector is antiparallel to the electron velocity. The frequency upshift can be seen by noting that in the reference frame where the electron streaming velocity is zero (i.e., the beam frame in which quantities will be primed) the frequency and wave number of the pump wave are given by

$$\omega_o' = \gamma_{11}(\omega_o + \langle v_z\rangle k_o) \tag{17a}$$

$$k_o' = \gamma_{11}(k_o + \langle v_z\rangle \omega_o/c^2) \tag{17b}$$

where $\gamma_{11} = (1 - \langle v_z\rangle^2/c^2)^{-\frac{1}{2}}$, $\langle v_z\rangle$ is the mean axial velocity of the electron stream in the laboratory frame and (ω_o, k_o) are the frequency and wave number magnitude of the pump wave in the laboratory frame. The direction of the pump wave has been taken to be antiparallel to the direction of the of the electron stream in the laboratory frame; i.e., $k_o \cdot \langle v_z\rangle < 0$. The frequency of the scattered wave in the laboratory frame is

$$\omega_s = \gamma_{11}(\omega_s' + \langle v_z\rangle k_s') \tag{18}$$

where (ω_s', k_s') are the frequency and wave number of the scattered wave in the electron rest frame.

Typically in the electron rest frame the frequency of the scattered wave is nearly equal to the frequency of the incident pump wave, while the scattered wave vector is opposite in direction but nearly equal in magnitude to the incident wave vector; i.e.,

$$\omega_s' \approx \omega_o' \quad \text{and} \quad k_o' \approx k_s' . \tag{19}$$

Then combining (17) through (19) gives

$$\omega_s \approx \gamma_{11}^2((1 + \langle v_z\rangle^2/c^2)\omega_o + 2\langle v_z\rangle k_o). \tag{20}$$

If the pump frequency in the laboratory frame is much larger than the characteristic frequencies of the system, the free space dispersion relation $\omega_o = ck_o$ holds for the pump wave and (20) becomes

$$\omega_s \approx (1 + \langle v_z\rangle/c)^2 \gamma_{11}^2 \omega_o . \tag{21}$$

It should be appreciated that the frequency conversion factor in (21) $(1 + \langle v_z\rangle/c)^2\gamma_{11}^2$ can be large. For example, if the electron streaming energy is 2MeV, $\gamma_{11} = 5$ and $\langle v_z\rangle/c \approx 1$ so that $\omega_s/\omega_o \approx 100$. Thus a 3-cm pump wave would produce a 300-μm scattered wave.

Stimulated scattering of photons by an electron ensemble was first predicted by Kapitza and Dirac (1933). Consider the details of this process in the beam frame depicted in Figure 7. The incident pump electromagnetic wave $(\omega_o' k_o')$ has a transverse electric field E_{oy}' which excites a zero-order transverse oscillation of the electrons with velocity

$$v_o' = \hat{e}_y (e/m) E_{oy}'/\gamma' \omega_o' \tag{22}$$

where $\gamma' = [1 - (v_o'/c)^2]^{-\frac{1}{2}}$. In the presence of an incipient backscattered wave (ω_s', k_s') with magnetic field $B_s' \hat{e}_x$, an axial force $ev_o' B_s \hat{e}_z$ is exerted on the electrons. The coupling between the scattered electromagnetic wave and the incident wave thus produces a pondermotive force (radiation pressure force) which leads to a low-frequency density modulation of the electrons $(\omega' K')$ and a grouping of the electrons into bunches distributed along the z axis. The complete expression for the pondermotive force is given by $\bar{F} = -e(\bar{v}_o' \times \bar{B}_s' + \bar{v}_s' \times \bar{B}_o')$. The frequency and wave number of the electron density modulation satisfies the following conservation laws:

$$\omega' = \omega_o' - \omega_s' \qquad K' = k_o' + k_s' \tag{23}$$

where K', k_o', and k_s' are positive real quantities denoting wave number magnitudes. [It should be noted that typically $\omega' \ll \omega_o'$ and $K' \approx 2k_o'$ so that the approximate equalities of (19) are satisfied.]

The growth of the density modulation gives increasing coherence to the scattering process, resulting in a growing scattered wave which in turn increases the density modulation still further. Thus, there is a feedback mechanism in this process which may result in an instability and exponential growth of the scattered wave.

The growth rate for the stimulated scattering instability depends on a number of factors, viz. the strength of the pump wave, the wavelengths of the incident and scattered waves, the electron density, and the electron temperature. It is useful to distinguish between two regions of parameter space, one in which the Debye length of the electron ensemble is small compared to the electromagnetic wavelengths (stimulated Raman scattering), and the other in which the Debye length to wavelength ratio is not small (stimulated Compton scattering).

The relations between the electron distribution in axial velocity $f(v_z')$ and the phase velocity of the density wave are shown in Figure 8. For the case of stimulated Raman scattering, as depicted in Figure 8(a), the magnitude of the density wave phase velocity is much larger than the thermal velocity, i.e.,

$$\frac{\omega'}{k'} \gg v_{TH}' . \tag{24}$$

In such a situation, the entire electron distribution participates in the density wave which takes the form of a collective plasma oscillation; i.e.,

$$\omega' = \omega_p \tag{25}$$

where ω_p is the invariant plasma frequency. Upon substituting (23) and (25) into (24), one finds that the following inequality is implied for the Debye wave number $k_D' = \omega_p / v_{th}'$:

$$k_D' \gg k_o' + k_s' . \tag{26}$$

Thus, in the case of stimulated Raman scattering, Figure 8 (a), the Debye length of the electron ensemble $(\lambda_D' = 2\pi / k_D')$ must be smaller than the wavelength of either the incident or scattered waves.

Stimulated Raman scattering has been analyzed in connection with laser pellet interactions (Manheimer and Ott, 1974) and ionospheric effects (Perkins and Kaw, 1971), as well as the production of submillimeter waves (Sprangle and Granatstein, 1974; Sprangle, et al, 1975) The expression for the Raman growth rate in an unmagnetized electron stream may be extracted from the literature (Sprangle and Granatstein, 1974) and takes the form

$$\Gamma_R' \approx .5 \; (v_o'/c)(\omega_s' \omega_p)^{\frac{1}{2}} \tag{27}$$

where v_o' is given by (22). Equation (27) is the Raman growth rate in the beam frame under the condition that $\omega_p \ll \omega_s'$. The growth rate of (27) depends linearly on the oscillation velocity excited by the pump wave, and in order to have a reasonably large growth rate in a laboratory device, one requires a very strong pump wave source.

In order to satisfy the Raman scattering condition of (26), a dense and cold electron distribution is required. When the electron distribution is tenuous or warm, it becomes difficult to achieve the condition in (26). In that case, the phase velocity of the density disturbance overlays the electron distribution function as shown in Figure 8(b), and only those electrons in the vicinity of $v_z' \approx \omega'/k'$ participate in the stimulated scattering process. This type of scattering is known as stimulated Compton scattering. Its potential for generating submillimeter waves was first investigated theoretically by Pantell, et al (1968). Elaboration was subsequently furnished by Sukhatme and Wolff, 1973 (1974) who considered boundary effects and magnetization.

The following expression has been derived for the Compton growth rate (Hasegawa et al, 1976)

$$\Gamma_c' \approx (\omega_p^2/\omega_s')|v_o'/v_{th}'|^2 . \tag{28}$$

Unlike the Raman growth rate in (27), the Compton growth rate of (28) depends strongly on the electron thermal velocity and decreases rapidly as the electron stream becomes warmer.

Recently, Sprangle and Granatstein (1974) and Sprangle, et al (1975) have extended the analyses of Raman scattering to produce results which are directly applicable to the production of submillimeter radiation. In this work the growth rate of the backscattered wave was shown to increase when an external constant magnetic field $B_o e_z$ was applied and its strength adjusted so that $\omega_o' \approx \Omega_o'$, where $\Omega_o' = |e| B_o / m_o c$ is the electron cyclotron frequency. The transverse electron velocity in the beam frame then becomes

$$v_o' = \frac{|e|}{\gamma m_o} E_{oy}' \frac{\omega_o'}{\omega_o' - \Omega_o'} \hat{e}_y . \tag{29}$$

In (29), the pump frequency ω_o' must satisfy a dispersion relation. The dispersion relation of the pump wave in the magnetized electron stream in the beam frame is

$$\omega_o'^2 - c^2 k_o'^2 - \omega_p^2 \omega_o' / (\omega_o' - \Omega_o') = 0. \tag{30}$$

Hence $\omega_o' - \Omega_o'$ cannot be made arbitrarily small and is determined by the dispersion relation in (30).

The temporal growth rate for the stimulated magnetoresonant scattering process has been derived in the beam frame as (Sprangle and Granatstein, 1974)

$$\Gamma_M' \approx \frac{v_o'}{c} \omega_s' \left(\frac{\omega_p'}{\omega_s' + \Omega_o'/2} \right)^{\frac{1}{2}} . \tag{31}$$

The laboratory frame growth rate for the stimulated scattering instability may be found from the beam frame growth rate through the relationship $\Gamma = \gamma_{\parallel}^{-1} (1 + v_g' \langle v_z \rangle / c^2)^{-1} \Gamma'$ where v_g' is the group velocity of the pump wave in the beam frame. Results for parameters characteristic of an intense relativistic electron beam (2 MV, 30 kA) are presented in Figure 9 as a plot of c/Γ versus v_o/c. It will be noted that when the oscillation velocity induced by the pump wave is one-tenth the speed of light ($v_o/c = 0.1$), the e-folding length for the instability is on the order of a few centimeters, short enough to be of practical interest. The pump wave field required to achieve the condition $v_o/c = 0.1$ is of order $E_o \sim 10^5$ V/cm, corresponding to a power density in the pump wave of tens of megawatts per square centimeter.

A number of mechanisms may be responsible for saturating the backscattered wave. For example, in the case of stimulated Raman scattering, thermalization of the electron stream to the point where $v_{TH}' \approx \omega'/k'$ will result in the trapping of the electrons in the potential well of the density wave, thus stopping the scattering process.

In the stimulated Compton regime, saturation occurs when the electrons fall to the bottom of the potential well associated with the density fluctuation. Therefore, for an instability to occur in the Compton region, the Compton growth rate must be much greater than the frequency of oscillation (bounce frequency) of the electrons in the potential well. Since the bounce frequency is proportional to the square root of the amplitude of the longitudinal fluctuation, an estimate for the maximum amplitude can be obtained.

Finally, depletion of the energy in the pump wave may also place limits on the energy in the backscattered wave. A discussion of saturation mechanisms has been given by Sprangle and Drobot (1978). The results of this study are summarized in Table I.

In an initial experiment at NRL (Granatstein, et al, 1977a), a single intense electron beam ($\gamma = 5$, I - 30 kA) was split into two regions and used both to generate the pump wave ($\lambda_o = 2$ cm, $P_o \sim 100$ MW) and subsequently, to wiggle the beam in this wave to produce a superradiant oscillator at a wavelength $\lambda_s = \lambda_o/2\gamma_\parallel^2 = 400$ μm. Output power was ~ 1 MW. In this arrangement, it was difficult to simultaneously optimize both for pump wave generation and stimulated scattering, and to carefully study each process individually.

An improved experiment is now underway which employs two intense electron beam accelerators which are synchronized in time. The arrangement is shown in Figure 10. A smaller 600 kV, 6 kA pulser injects a beam into a relativistic magnetron structure of unique design (Granatstein, et al, 1977b). The magnetron is designed to operate with 50% efficiency producing a pump wave at $\lambda_o = 10$ cm and $P_o = 1.8$ GW.

The magnetron wave will also be used as the "wiggler" field in a stimulated Raman scattering experiment on a 2 MeV, 100 KA electron beam. The scattered output radiation will be at $\lambda_s \sim 2$ mm. Using a recent non linear analysis of the scattering process (Sprangle and Drobot, 1978) one calculates that ~ 10% of the electron beam energy may be converted into radiation at $\lambda_s = 2$ mm. This would correspond to an output power of $P_s \sim 10^{10}$ watts; realization of even a fraction of this theoretical value would represent phenomenally large power at millimeter wavelengths.

A second set of experiments is also underway at NRL in collaboration with researchers from Columbia University. These experiments employ a static spatially periodic magnetic field to "wiggle" the intense relativistic electron beam. Preliminary experiments (Marshall, et al, 1977) have produced a superradiant oscillator at $\lambda_s = 2$ mm $\Delta\lambda_s/\lambda_s = 7\%$, and $P_s = 8$ MW. The thrust of the work at NRL is to employ a quasi-optical cavity to improve coherence of the output radiation. The configuration is shown in Figure 11.

IV. CONCLUSION

A brief review has been given of the experimental and theoretical work underway at NRL on the use of relativistic processes in electron beams for the production of coherent microwave, millimeter wave, and submillimeter wave radiation. It is clear that the processes discussed have considerable potential for producing dramatic increases in the available power in the wavelength range discussed. The devices discussed are tunable and have significant bandwidth capability. This new technology is expected to have broad application in a number of fields of physics and engineering.

REFERENCES

*Science Applications, Inc., McLean, Virginia 22101
†JAYCOR, Inc., Alexandria, Virginia

1. Chu, K. R., 1978, "Theory of Electron Cyclotron Maser Interactions in a Cavity at the Harmonic Frequencies", NRL Memorandum Report 3672.
2. Chu, K.R., Drobot, A.T., Granatstein, V.L. and Seftor, J.L., 1977, "Calculation of Optimum Operating Parameters for a Gyrotron Travelling Wave Amplifier", NRL Memorandum Report 3553.
3. Chu, K.R. and Hirshfield, J.L., 1978, "Comparative Study of the Axial and Azimuthal Bunching Mechanisms in Electromagnetic Cyclotron Instabilities", Phys. Fluids 21 (3).
4. Demidovich, E.M., Kovalev, I.L., Kurayev, A.A. and Shevchenko, F.C., 1973, "Efficiency optimized cascaded circuits utilizing the cyclotron resonance", Radiotekhnika i Electronika 18, p. 2097.
5. Friedman, M., Hammer, D.A., Manheimer, W.M. and Sprangle, P., 1973, "Enhanced microwave emission due to the transverse energy of a relativistic electron beam", Phys. Rev. Lett., 31, p. 752-755.
6. Granatstein, V.L., Parker, R.K., Pasour, J.A., Sprangle, P. and Drobot, A.T., 1977b, "Coherent Microwave Scattering from Intense Relativistic Electron Beams-A Powerful Tunable Source of Millimeter and Submillimeter Radiation", Proc. of 2nd International Topical Conference on High Power Electron and Ion Beam Research and Technology, Cornell University, Ithaca, New York, p. 675-690.
7. Granatstein, V.L., Schlesinger, S.P., Herndon, M., Parker, R.K. and Pasour, J.A., 1977a, "Production of Megawatt Submillimeter Pulses by Stimulated Magneto Raman Scattering", Appl. Phys. Lett. 30, p. 384.
8. Granatstein, V.L., Sprangle, P., Herndon, M., Parker, R.K. and Schlesigner, S.P., 1975, "Microwave Amplification with an Intense Relativistic Electron Beam", J. Appl. Phys. 46, p. 3800.
9. Hasegawa, A., Mina, K., Sprangle, P., Szu, H.H. and Granatstein, V.L., 1976, "Limitation in Growth Time of Stimulated Compton Scattering in X-ray Regime", Appl. Phys. Lett. 29, p. 542.

10. Hirshfield, J.L. and Granatstein, V.L., 1977, "The Electron Cyclotron Maser-An Historical Survey", IEEE Trans. MTT-25, p. 522-527.
11. Jory, H., 1968, "Investigation of electronic interaction with optical resonators for microwave generation and amplification", Research and Development Technical Report, ECOM-01873-F, Varian Associates.
12. Kapitza, P.L., and Dirac, P.A.M., 1933, Proc. Cambridge Phil. Soc., Vol 29, p. 297.
13. Manheimer, W.M. and Ott, E., 1974, "Theory of Microwave Generation by an Intense Relativistic Beam in a Rippled Magnetic Field", Phys. Fluids 17, p. 463.
14. Marshall, T.C., Talmadge, S., and Efthimion, P., 1977, "High-Power Millimeter Radiation from an Intense Relativistic Electron-Beam Device", Appl. Phys. Lett. 31, p. 320.
15. Nusinovich, G.S. and Erm, R.E., 1972, Elektronnaya Tekhnika, Sec. 1, Elektronika SVCH, No. 2, p. 55.
16. Ott, E. and Manheimer, W.M., 1975, "Theory of microwave emission by velocity-space instabilities of an intense relativistic electron beam", IEEE Trans. Plasma SC., Vol. PS-3, p. 1-5.
17. Pantell, R.H., Soncini, G., and Puthoff, H.E., 1968, IEEE J. Quantum Electron, QE-4, p. 905.
18. Perkins, F. W., and Kaw, P.K., 1971, J. Geophys. Res. 76, p. 282.
19. Rapoport, G.N., Nemak, A.K. and Zhurakovskiy, V.A., 1967, "Interaction between helical electron beams and strong electromagnetic cavity fields at cyclotron frequency harmonics", Radiotekhnika i. Electronika Vol. 12, p. 587.
20. Sprangle, P. and Drobot, A.T., 1977, "The Linear and Self-Consistent Nonlinear Theory of the Electron Cyclotron Maser Instability", IEEE Trans. Microwave Theory and Techniques, MTT-25, 6.
21. Sprangle, P. and Drobot, A.T., 1978, "Stimulated Backscattering from Relativistic Unmagnetized Electron Beams", NRL Memorandum Report 3587.
22. Sprangle, P. and Granatstein, V.L., 1974, "Stimulated cyclotron resonance scattering and production of powerful submillimeter radiation", Appl. Phys. Lett. 25, p. 377.
23. Sprangle, P., Granatstein, V.L. and Baker, L., 1975, "Stimulated Collective Scattering from a Magnetized Relativistic Electron Beam", Phy. Rev. A 12, p. 1697.
24. Sprangle, P. and Manheimer, W.M., 1975, "Coherent nonlinear theory of a cyclotron instability", Phys. of Fluids 18, p. 224-230.
25. Sukhatme, V.P. and Wolf, P.E., 1973-1974, J. Appl. Phys. 44, p. 2331 and IEEE J. Quantum Electron, QE-10, p. 870.
26. Weibel, E.S., 1959, Phys. Rev. Lett. 2, p. 83.
27. Zhurakovskiy, V.A., 1964, "Using an averaging method to integrate nonlinear equations for phase-synchronous instruments", Radiotekhnika i. Electronika, Vol 9, p. 1527.

Table I. Summary of Collective Wave-Wave Scattering Results in the Laboratory Frame for a Highly Relativistic Electron Beam. The parameters are defined as

$$\beta_o \approx 1,\ \beta_{os} = |e| E_o/(\gamma_o m_o \omega_o c),\ \beta_1 = (32)^{-1/2}\gamma_o^{-5/2}\xi^{3/2},\ \beta_{crit} = \gamma_o^{-3/2}\xi^{1/2},$$

$$\xi = (\omega_p/\gamma_o^{1/2})/\omega_o \text{ and } \Delta\epsilon_{th}/\epsilon_o = 2\gamma_o^3 (v_{th}/c)/(\gamma_o - 1).$$

Regime	Growth Rate	Saturation Mechanism	Saturation Efficiency	Energy Spread Requirements
$0 < \beta_{cs} < \beta_1$	$\Gamma = \frac{\beta_{os}}{\sqrt{2}} \gamma_o^{1/2} \omega_o \xi^{1/2}$	pump depletion		$\frac{\Delta\epsilon_{th}}{\epsilon_o} << \frac{\xi}{2(\gamma_o - 1)}$
$\beta_1 < \beta_{os} < \beta_{crit}$	$\Gamma = \frac{\beta_{os}}{\sqrt{2}} \gamma_o^{1/2} \omega_o \xi^{1/2}$	trapping	$\eta = \frac{\xi}{4(\gamma_o - 1)}$	$\frac{\Delta\epsilon_{th}}{\epsilon_o} << \frac{\xi}{2(\gamma_o - 1)}$
$\beta_{crit} < \beta_{os}$	$\Gamma = \frac{\sqrt{3}}{2} \omega_o (\beta_{os}\xi)^{2/3}$	trapping	$\eta = \frac{1}{8} \frac{\gamma_o}{\gamma_o - 1} (\beta_{os}\xi)^{2/3}$	$\frac{\Delta\epsilon_{th}}{\epsilon_o} << \frac{\gamma_o (\beta_{os}\xi)^{2/3}}{4(\gamma_o - 1)}$

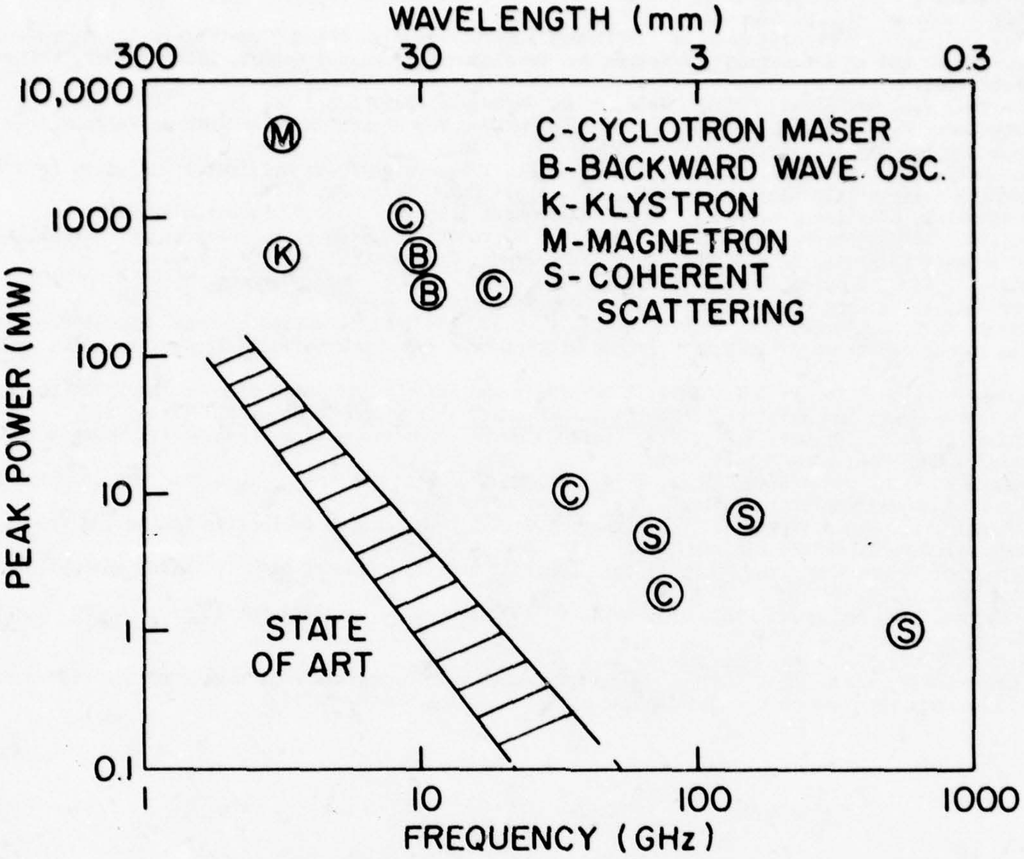

FIGURE 1. Peak power vs frequency obtained using relativistic electron beams. The appropriate mechanisms are identified. The state-of-the-art using conventional tubes is indicated by the shaded region.

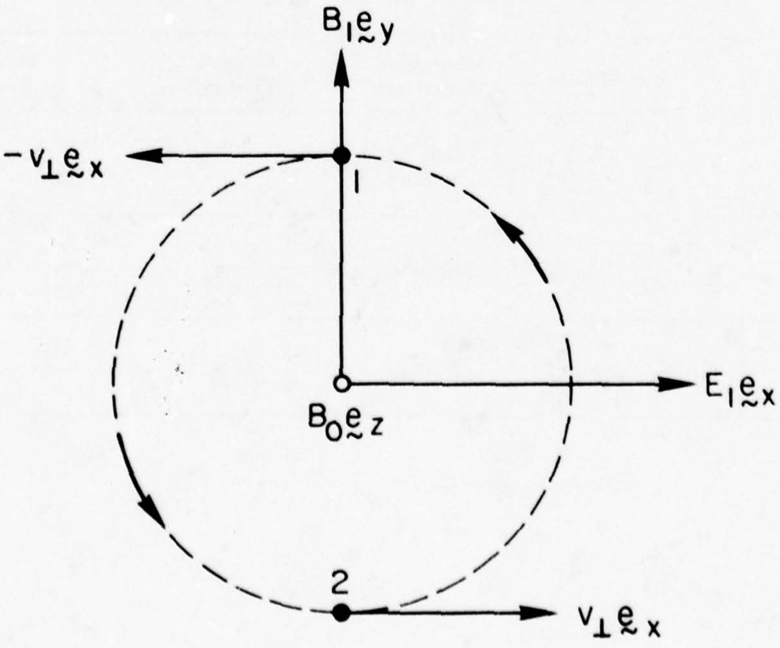
$B_1 \underset{\sim}{e}_y$
$-v_\perp \underset{\sim}{e}_x$
1
$E_1 \underset{\sim}{e}_x$
$B_0 \underset{\sim}{e}_z$
2
$v_\perp \underset{\sim}{e}_x$

FIGURE 2. Instantaneous (t = 0) vector relationships of the wave fields, the external magnetic field, the positions (points 1 and 2), and the perpendicular velocities of two electrons. The projection of the unperturbed electron orbit is shown by the dashed circle.

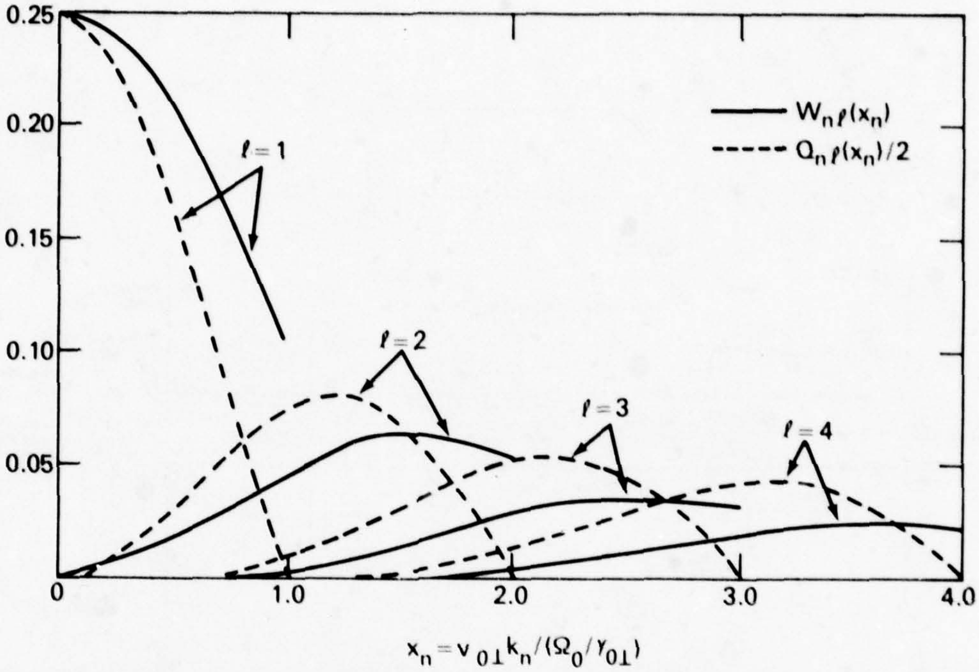

FIGURE 3. The functions $Q_{n\ell}(x_n)$ and $W_{n\ell}(x_n)$ versus x_n for ℓ = 1, 2, 3, 4.

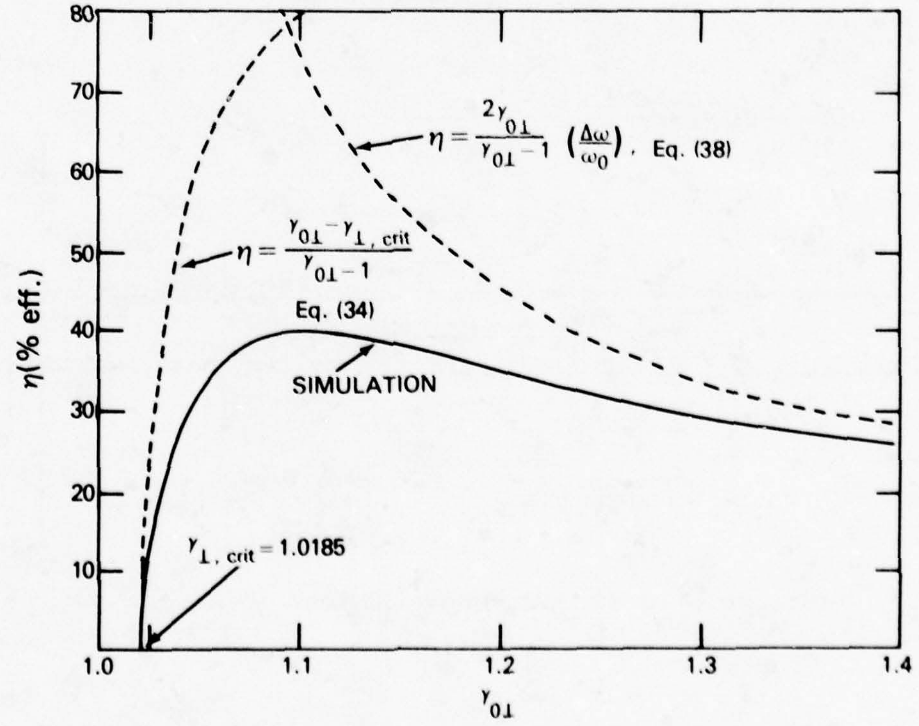

FIGURE 4. The efficiency of the cyclotron maser as a function of energy found from the two mechanisms of saturation and from computer simulation. For this case $\omega_b/\sqrt{\gamma_{0\perp}\omega_0} = .1$.

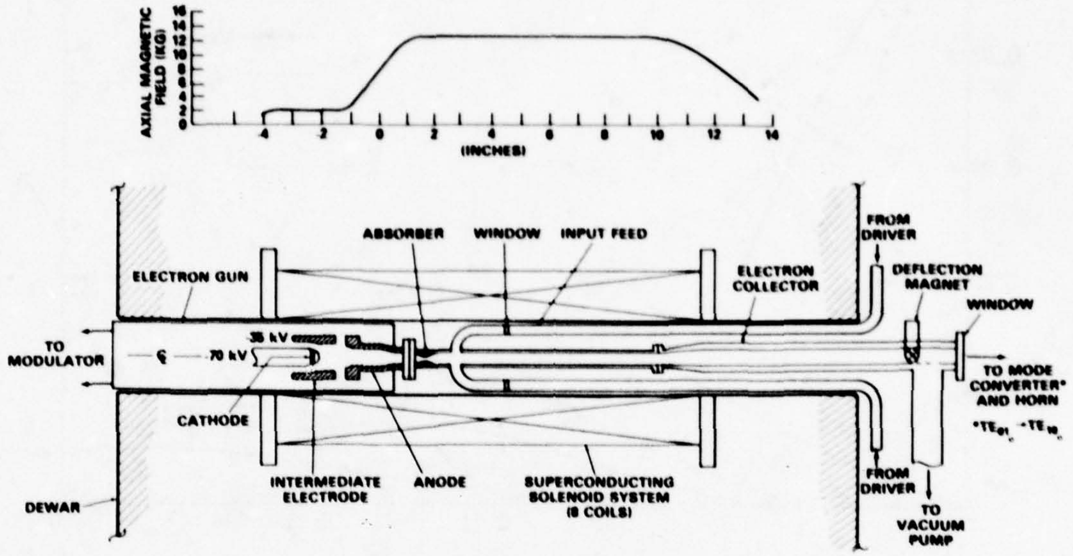
AXIAL MAGNETIC FIELD (KG)
0
2
4
6
8
10
12
14
16
4
2
0
2
4
6
8
10
12
14
(INCHES)
ABSORBER
WINDOW
INPUT FEED
FROM DRIVER
DEFLECTION MAGNET
WINDOW
ELECTRON GUN
ELECTRON COLLECTOR
TO MODULATOR
35 kV
70 kV
℄
TO MODE CONVERTER* AND HORN
*TE01 -TE10
CATHODE
INTERMEDIATE ELECTRODE
ANODE
SUPERCONDUCTING SOLENOID SYSTEM (8 COILS)
FROM DRIVER
TO VACUUM PUMP
DEWAR

FIGURE 5. Configuration of the NRL 35 GHz gyro travelling wave amplifier. (Design parameters: 20 dB gain, 280 kw, Eff = 51%, bandwith 10%)

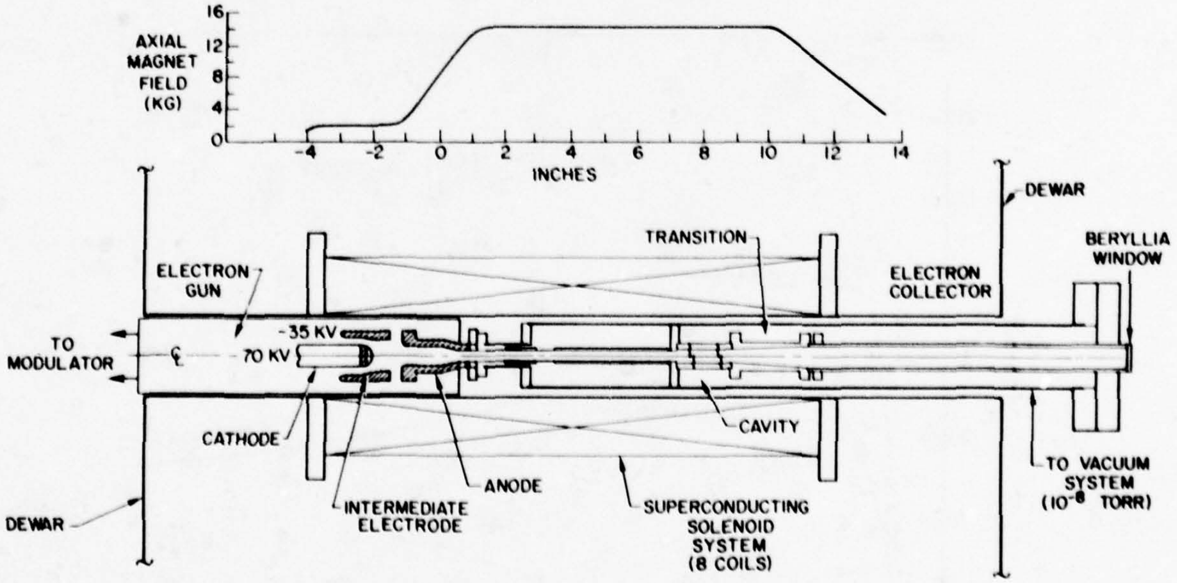
AXIAL MAGNET FIELD (KG)
0
4
8
12
16
-4
-2
0
2
4
6
8
10
12
14
INCHES
DEWAR
TRANSITION
BERYLLIA WINDOW
ELECTRON GUN
ELECTRON COLLECTOR
TO MODULATOR
-35 KV
70 KV
℄
CATHODE
CAVITY
ANODE
TO VACUUM SYSTEM (10^{-8} TORR)
INTERMEDIATE ELECTRODE
SUPERCONDUCTING SOLENOID SYSTEM (8 COILS)
DEWAR

FIGURE 6. Configuration of the NRL 35 GHz gyrotron oscillator. (Design parameters: v = 70 kv, I = 8 A, Eff = 30%, p = 170 kw)

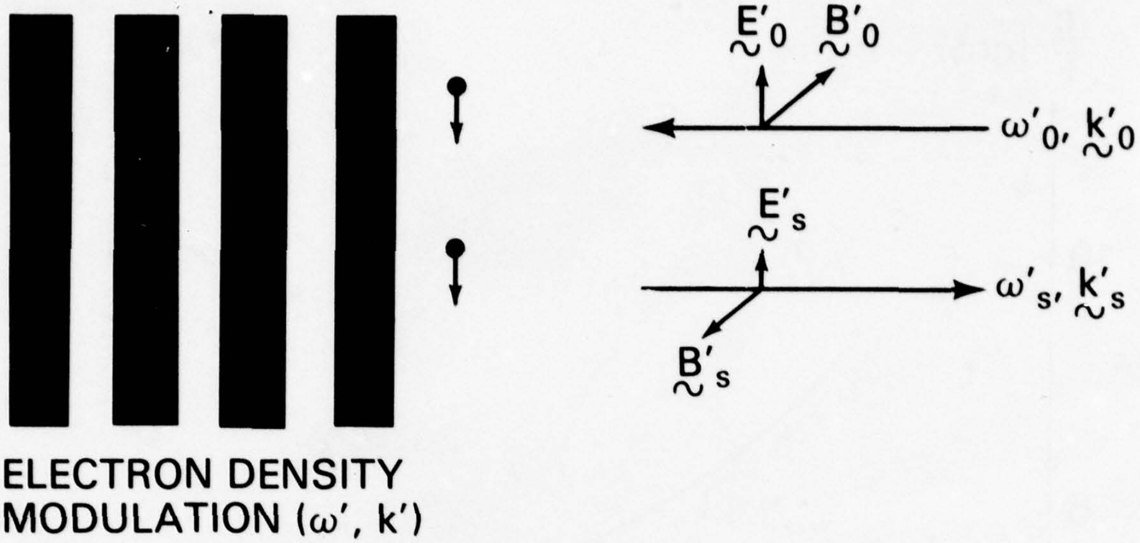
$\underset{\sim}{E}'_0$
$\underset{\sim}{B}'_0$
$\omega'_0, \underset{\sim}{k}'_0$
$\underset{\sim}{E}'_s$
$\omega'_s, \underset{\sim}{k}'_s$
$\underset{\sim}{B}'_s$
ELECTRON DENSITY MODULATION (ω′, k′)

FIGURE 7. Stimulated scattering in the beam frame.

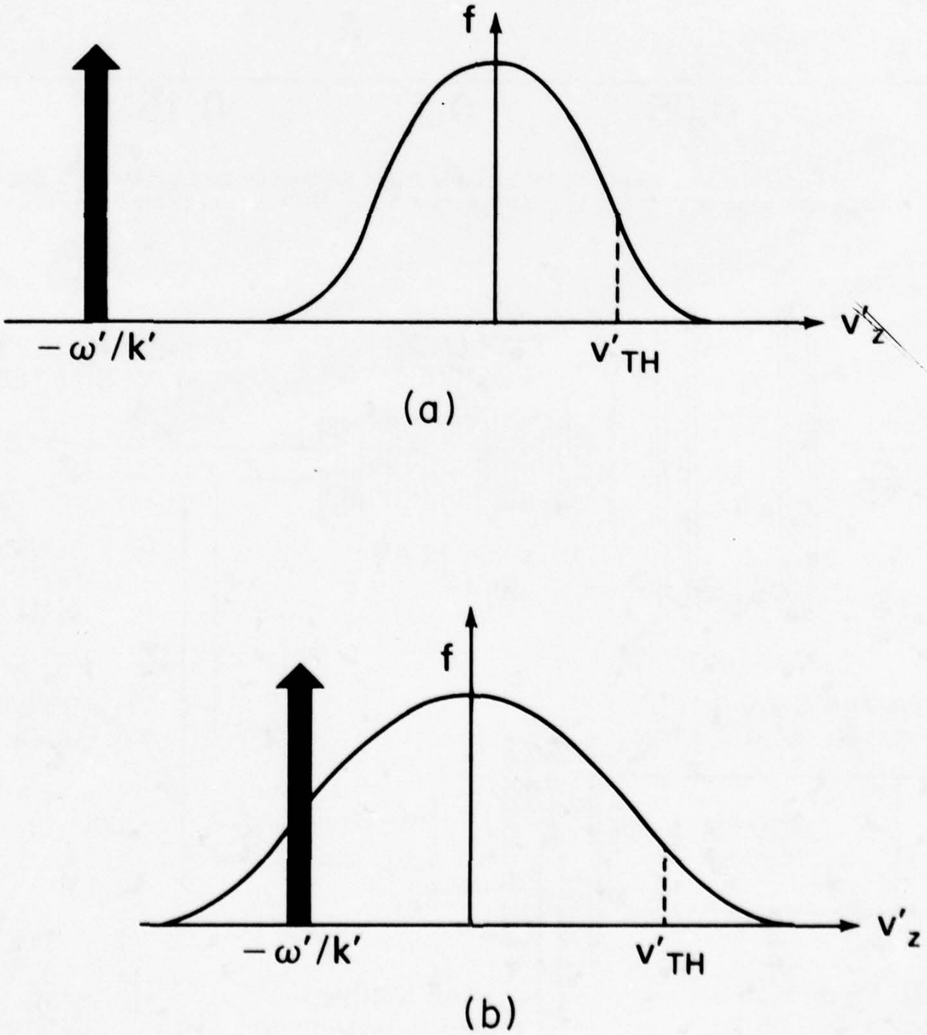
f
$-\omega'/k'$
v'_{TH}
v'_z
(a)
f
$-\omega'/k'$
v'_{TH}
v'_z
(b)

FIGURE 8. Relationship between the phase velocity of the density disturbance and the electron distribution function. (a) Stimulated Raman scattering. (b) Stimulated Compton scattering.

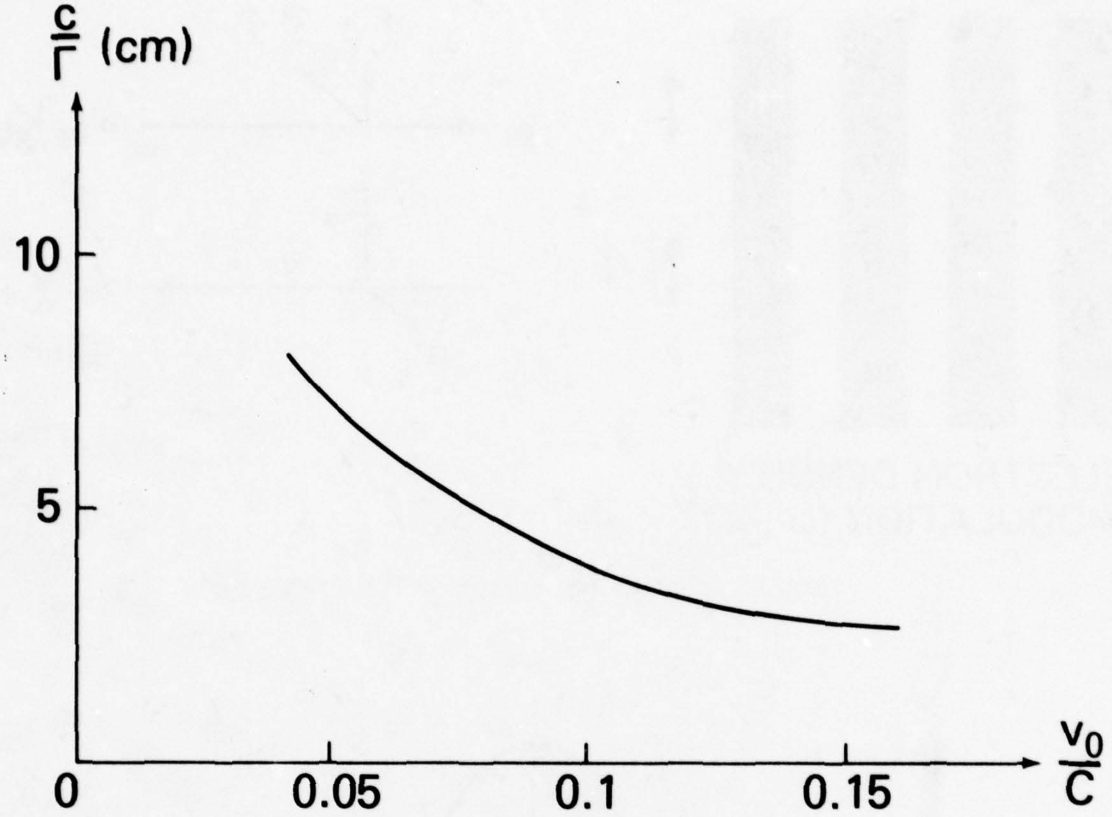

FIGURE 9. Exponential growth length for stimulated Raman scattering instability in a magnetized electron beam (λ_o = 2 cm, λ_s = 440 μm, γ = 5, $\omega_p/2\pi$ = 3 GHz, $\Omega/2\pi\gamma$ = 9 GHz).

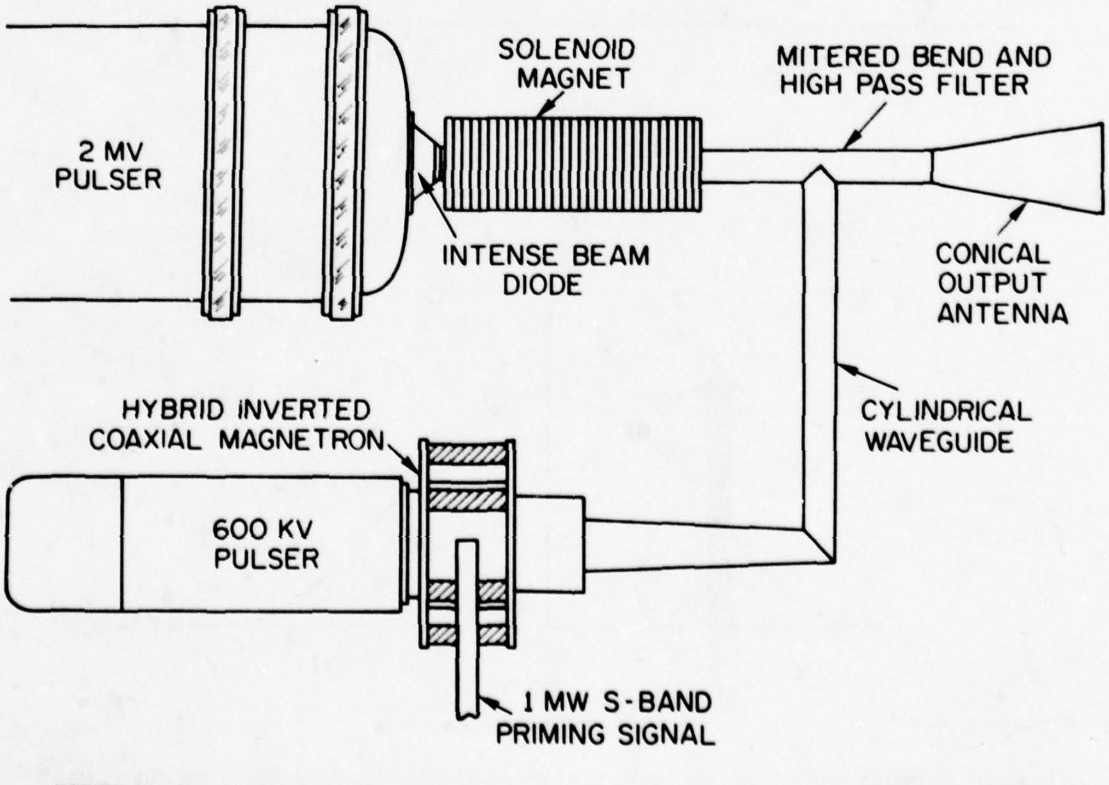

SOLENOID MAGNET
MITERED BEND AND HIGH PASS FILTER
2 MV PULSER
INTENSE BEAM DIODE
CONICAL OUTPUT ANTENNA
CYLINDRICAL WAVEGUIDE
HYBRID INVERTED COAXIAL MAGNETRON
600 KV PULSER
1 MW S-BAND PRIMING SIGNAL

FIGURE 10. Experimental configuration for ultra high power millimeter wave stimulated Raman scattering experiment.

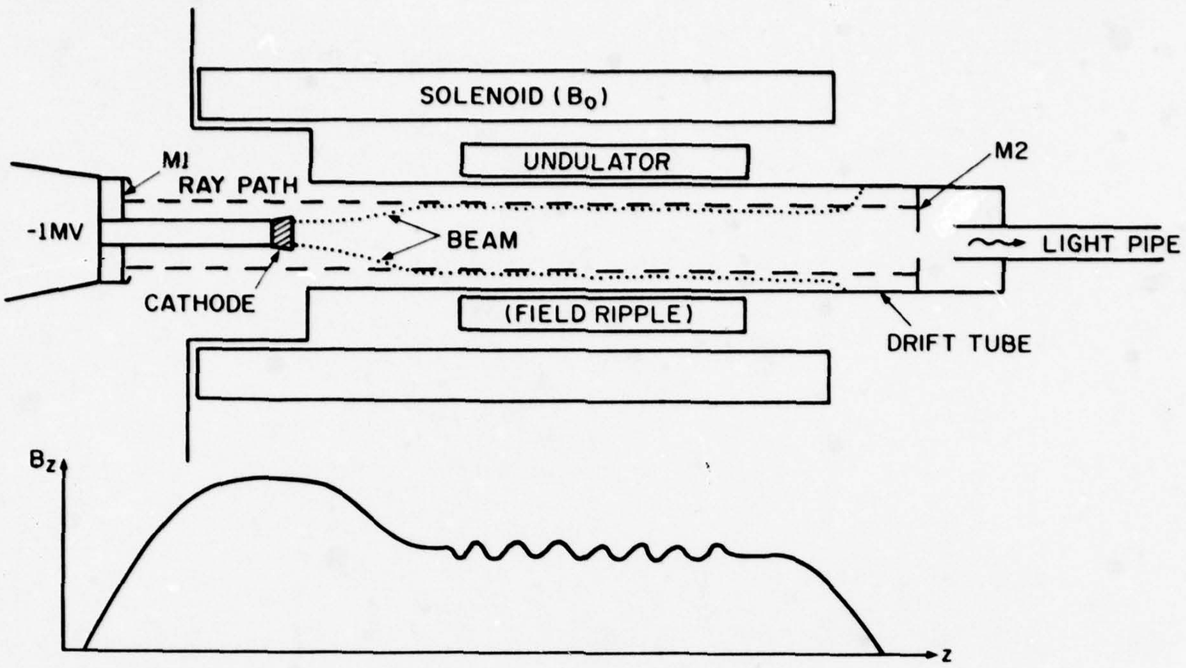

FIGURE 11. Experimental configuration for optical cavity experiment. M_1 and M_2 are adjustable plane mirrors. The initial expansion of the electron beam decreases transverse temperature thus improving conditions for stimulated Raman scattering.

DISCUSSION

K.G.Hambleton, UK

Figure 4 indicates a maximum practical efficiency on simulation of about 40%, yet Figure 5 indicates a practical design aim of 51%. How are these two values of efficiency reconciled?

Author's Reply

The simulation shown in Figure 3 was for particular beam conditions. The results were useful in pointing the way towards more optimum conditions. Hence efficiencies greater than 50% can be contemplated in optimised structures. Figure 3 was presented to illustrate the effects of the physical constraints, not to show the optimum result of the simulation.

ANALYSIS OF OPTICALLY PUMPED CW (CONTINUOUS WAVE) FIR (FAR INFRARED) LASER EFFICIENCY * *

J-M. Lourtioz, R. Adde, J. Pontnau
Institut d'Electronique Fondamentale, Bât. 220, Université de Paris XI
91405 ORSAY (France) .

Summary :

Multitude of CW laser lines providing stable output at the mW level are now available between 40 µm and 2 mm since the advent of optically pumped CW FIR lasers (1). In this paper we concentrate essentially on the different aspects of the FIR power optimization and start the discussion from a simplified analytical expression of the FIR power.

1. Introduction to the optically pumped CW FIR lasers :

1.1. Basic principles and pumping schemes :

The basic pumping scheme of a CW optically pumped FIR laser is represented in Figure 1. The optical pumping of the polar molecule is associated with a vibrational rotational transition in near coincidence with an infrared emission line of the pump laser (CO_2, N_2O...). Since the thermal population in the upper vibrational state is very small, an inversion of population is readily established between the pumped level and the subjacent rotational levels and the FIR laser emission arises from a rotational transition. The short rotational lifetime ($\tau_R \sim 10^{-8}$ sec Torr^{-1}) due to collisions between the molecules which tends to thermalize the population of the vibrational manifold is responsible of the low operating gas pressure of these lasers. The vibrational relaxation ($\tau_v \sim 10^{-3}$ sec.Torr$^{(4)}$)to the ground state occurs mainly through diffusion to the walls or vibration-translation/rotation processes. The energy level diagramm of Figure 1 is typical of symetric - top molecules (1). Assymetric top molecules (e.g. CH_3OH) have a more dense spectrum (2) which explains the abundance of their FIR transitions but the pumping cycle scheme of Figure 1 to consider in the evaluation of the FIR power efficiency remains a good approximation at least for not too short FIR wavelength ($\gtrsim$ 40 µm).

1.2. Description of an experimental set-up for high FIR power efficiency (3) :

The experimental set-up used in our experiments consists of a grating tuned CO_2 laser and an oversized FIR waveguide resonator (see 3.4). The CO_2 laser is 1.70 m long and has a discharge length of 1.20 m. Both Brewster windows and output mirror are made of zinc selenide. The output mirror is mounted on a piezoceramic translator which allows a fine frequency tuning over a 60 MHz range. About 30 watts are obtained on the strongest lines and up to 20 watts on the weaker ones in single mode operation. The FIR resonator is mounted on an invar support structure for thermal and mechanical stability. The cavity is composed of a standard pyrex tube (2m long and 25 mm inner diameter) and of two gold-coated flat mirrors. Injection of the CO_2 pump into the FIR cavity is accomplished by focussing the radiation through a 2 mm hole. The FIR is essentially coupled at the opposite end with a 4 mm or 5 mm coupling hole. The stabilization system is quite simple : the CO_2 laser is frequency locked by maximizing the FIR amplitude and the error signal is obtained through a weak frequency modulation of the CO_2 cavity. On the 70 µm and 118 µm CH_3OH "test lines", this optimized set-up has provided respective powers of 40mW and 70 mW with a long term amplitude stability better than 10% on time intervals of at least 3-5 hours.

2. Modeling of the CW FIR lasers processes :

The understanding and even more the prediction of the influences of the laser parameters upon the power efficiency require to model the laser processes. The two main directions of development of models of optically pumped CW FIR lasers are :

1/ Quantomechanic models (4)-(6) which have been developed recently and consider a limited three level system interacting with both pump and FIR fields. Calculations of the FIR gain are made using the density matrix formalism. Such treatments can take into account the two photon processes and have successfully predicted their influences on the FIR gain lineshape (dynamical Stark splitting, gain anisotropy). However there are some difficulties in order to include relaxation mechanisms such as the vibrational ones. A complete model combining both quantum effects and dynamical processes is underway in a few groups. This requires computer methods and analytical solutions are excluded.

2/ Rate equation models (7)-(14) which have been the first ones to be developed. The pumping scheme is a simplified version of the diagram of Fig. 1. Five levels are involved in the laser processes: the three levels system directly related to the IR and FIR transitions is completed by the set of exchange rotational sublevels in the upper and lower vibrational manifolds. The result of rate equation models is contained in two basic sets of equations. The first is related to the evolution of the different populations, the second is related to the evolution of the photon densities inside the FIR cavity. And the steady state solution is obtained by setting the time derivatives equal to zero. The main advantage of these models is they allow a semi-quantitative analysis of the FIR power efficiency as relaxation effects may be introduced in a relatively simple way. The fundamental molecular relaxation mechanisms are the rotational relaxation which tends to restore the Boltzmann distribution over the rotational sublevels and the vibrational relaxation which favorably competes with this thermal effect (11).

This work was supported in part by the Groupement de Recherches Coordonnées du CNRS n° 11 (Greco Microondes).

We have developed recently (13),(14) a rate equation model where :

- The parameters are measurable quantities (absorption coefficient and saturation intensity of the pump transition, infrared and far infrared cavity loss per pass...)
- The velocity distribution of the molecules is introduced due to the Doppler broadening of the absorption transition at the low operating pressure of CW FIR lasers ($\simeq$ 100 mTorr). In effect the two traveling pump waves in the FIR cavity excite two groups of molecule of opposite velocity. This selective pumping and the thermalization of the molecules over the rotational levels lead to the FIR excited state absorption which is treated explicitly.
- Moreover the nature of the FIR line broadening (Doppler or homogeneous), the "on" or "off" resonance of the IR pumping with the absorption line are taken into account. For a large majority of the FIR molecules the pump can only approach the IR absorption line center within the frequency range 20 MHz - 60 MHz. The two traveling pump waves inside the FIR cavity excite two separated velocity groups of molecules, and at short wavelengths, the FIR gain curve as a function of the FIR frequency exhibits two quite distinct peaks. At long FIR wavelengths, the Doppler effect is quite reduced and the FIR lineshape just exhibits a smooth dip. For the best FIR lines, the pump can be tuned close to the absorption line center and the velocity distributions of the active pumped molecules overlap. Then, at any wavelength, the FIR lineshape just exhibits a peak close to the FIR line center. However, the "hole burning effect" related to the pump transition is expected to favour the longest wavelengths.

The different situations above give rise to different laser gain expressions and we have calculated the corresponding forms of the FIR output power at the gain maximum value. The formulas (13),(14) giving P_{FIR} approach the standard expression for saturated homogeneously broadened transitions and may be written in a closed form :

$$P_{FIR} = \frac{1}{2} \cdot I_{SAT} \cdot (tS) \left[\frac{(2)}{(tS)} \times P_{IR} \times \eta_{th} \times f_{abs} \times f_{trans} \times \frac{1}{I_{SAT}} - 1 \right] \qquad (1)$$

where :

- P_{IR} is the pump power
- t is the FIR transmission coefficient per pass
- S is the FIR resonator cross-section
- $\eta_{th} = \frac{1}{1 + g_2/g_3} \times \frac{\nu_{FIR}}{\nu_{IR}} \simeq \frac{1}{2} \times \frac{\nu_{FIR}}{\nu_{IR}}$ is the theoretical photonic conversion efficiency.
- I_{sat} is the saturation intensity of the FIR transition and varies as the square of the gas pressure and the inverse of oscillator strength related to the transition.
- $f_{abs} = \frac{\alpha L}{\alpha L + \beta_{IR}} (\xi)$ is the fractional absorption of the pump power, α is the saturated IR absorption coefficient, L, the cavity length and β_{IR} is the FIR cavity loss coefficient per pass for the pump. ξ represents the possibility for the pump to fall in coincidence with another absorption line.
- $f_{trans} = \frac{t(1-h-\delta)}{t+a}$ is the fractional transmission loss of the FIR radiation,a is the FIR cavity loss coefficient per pass at the FIR wavelength (absorption loss at the mirrors of the cavity + propagation loss in waveguide structures or diffraction loss in conventional Fabry-Perot resonators). δ is the fractional self absorption of the FIR in the excited states (due to the vibration bottleneck, it strongly increases with pressure when the vibrational relaxation is diffusion dominated : $\delta \sim p^n$ with $n \simeq 2$). h represent the hole burning effect at short wavelengths.

All of the physics of the model is contained in the term η_{th}, f_{abs}, f_{trans} and I_{SAT} which we discuss in part 3 owing both to our experiments and recently published works.

3. Influence of the experimental parameters upon the FIR power efficiency :

The laser parameters may be classified in three categories (see also Fig. 6 in Ref. 14) :

- pumped gas parameters : pressure, temperature and buffer gas addition.
- FIR cavity parameters : cavity type, length, section, output and input coupling method.
- Injected pump beam parameters : IR power, frequency matching to the absorption frequency of the pumped gas, spatial extension of the injected beam inside the FIR cavity.

We will specially emphasize in the following on the influences of the FIR gas pressure, the IR pump power and the frequency offset $\delta\nu_{IR}$ of the pump radiation from the absorption line center of the FIR gas which may be considered as the main parameters. Our diagnostic experiments have been performed on the strong CW FIR lines of CH_3OH at 570 µm, 118 µm and 70 µm.

3.1. Pressure dependence of the FIR output power :

Figure 2 represents the variation of P_{FIR} recorded continuously as a function of the FIR gas pressure for different values of the pump power P_{IR}. It shows the strong similitude of the results at the three wavelengths studied. At low pressure the saturation intensity and the self absorption of the FIR are weak and the increasing output power with pressure simply reflects the increasing pump absorption . On the other hand, above some FIR gas pressure the decreasing output level corresponds to the increase of I_{SAT} and δ , while the fractional absorption term approaches more slowly its limit value and finally a cut-off pressure is reached. Therefore at a given pump power, there is a relatively low optimum pressure which value increases slowly with pump power. Furthermore the largest wavelength transitions reach their maximum at lower pressure and in the same range of wavelength, the optimum pressure is lower for the strongest pump absorption coefficient.

3.2. Pump power dependence of the FIR output power :

Figure 3 shows the FIR power at 118 µm monitored continuously as a function of the pump power, the pressure being a controlled parameter. The situation is quite similar for the 70 µm and 570 µm wavelengths. At a given pressure, the pump power must exceed a threshold value for laser action. Due to the FIR oscillation, the left term in the bracket of Eq. 1 must be superior to 1. Beyond this threshold value P_{FIR} increases with P_{IR}. At low pressures (curves 1 → 5), *the increase of* $P_{FIR} = f(P_{IR})$ given by the slope :

$$\frac{dP_{FIR}}{dP_{IR}} = \eta_{th} \times f_{abs} \times f_{trans} \qquad (2)$$

is essentially governed by f_{abs} since f_{trans} remains nearly constant as a consequence of the low FIR excited state absorption. The curvature of the graphs indicates the strong saturation of the absorption at high values of P_{IR}. For a further increase of pressure the slope reaches a maximum (pressure value between curve 5 and curve 6), then decreases (curves 6→9) near the cut-off region (see part 3.1 and Fig. 2) when the decrease of f_{trans} is dominant in dP_{FIR}/dP_{IR}. Figure 4 represents the evolution of $(\eta_{exp}^{opt} / \eta_{th})$ as a function of P_{IR}, where η_{exp}^{opt} is the experimental photonic conversion efficiency at the optimum pressure. The zero limit is related to the threshold condition. In the domain of standard pump powers, the efficiency increases slowly. A further increase of the pump power with more powerful CO_2 lasers is expected to increase the FIR power in the same ratio.

3.3. Influence of the pump detuning on the FIR power :

Figure 5 shows the influence of the pump detuning. The tuning curves for the 118 µm CH_3OH laser have been recorded with different frequency offsets of the pump from the absorption line center. The decrease of the FIR peaks with increasing detuning is approximately related to the Doppler factor contained in the absorption coefficient $\alpha(\delta\nu_{IR}) = \alpha(0) \times \exp(-\delta\nu_{IR}^2/4\,\delta\nu_D^2)$, where $\delta\nu_D$ is *the full Doppler* width of the absorption transition. α is explicitly included in the term f_{abs} (see section 2).

3.4. Techniques for FIR power optimization :

We discuss now the influence of the other parameters in the favorable case of a strong FIR line. In this case, at the optimum pressure, the right term in the bracket of P_{FIR} (Eq. 1) may be neglected and the experimental efficiency may be written simply :

$$P_{FIR}/P_{IR} = \eta_{exp}^{opt} = \eta_{th} \times (f_{abs} \times f_{trans})_{\text{optimum pressure}} \qquad (3)$$

Using available data in the litterature (15), we have represented in Figure 6. $(\eta_{exp}^{opt} / \eta_{th})$ which shows how far experiments are from the theoretical limit. We have plotted in Figure 7 the fractional absorption versus pump power in the optimized conditions of our experiments. It clearly proves that the low values of $(f_{abs})_{\text{optimum pressure}}$ achieved are responsible of the poor FIR laser efficiency. However f_{abs} and f_{trans} are strongly correlated through the many laser parameters and must be optimized simultaneously.

The enhancement of the optical pumping efficiency during the past few years has been essentially achieved in two steps :

- The first decisive progress has been the result of *waveguide operation* (16)-(19) allowed by materials with low loss in the FIR. Waveguide cavities are constructed with smaller cross-sections as compared to the conventional and bulky resonators. This facilitates the vibrational relaxation of the molecules due to desexcitations on the walls, and the self absorption is strongly reduced at a given pressure . In the same way, at a given pump power, the optimum pressure is increased and the fractional absorption too. Metallic waveguide resonators have the smallest cross-sections, but the mode outcoupling optimization is difficult and the diffraction losses at the mirrors are important, which explains the better performances of the dielectric waveguides (3). Besides, in some cases, the buffer gas addition has the same beneficial influence on f_{trans} (20).

- The second and more recent progress is due to hybrid couplers. As compared to the simple hole couplers, they allow both to optimize the FIR transmission coefficient t and to reduce the losses of the pump radiation at the output mirror. Here we give the main types of hybrid couplers. They are mainly based on a silicon substrate due to its low absorption losses in the IR and FIR region (21)-(26)

The hybrid metal dielectric hole coupler (21) gives actually the highest P_{FIR}. The integrated metal mesh dielectric coupler (23) is the convenient element for frequency selectivity and a weak divergence of the output beam. A third alternative consists of silicon Fabry-Perot type couplers (24),(26). Calculations of a two silicon plates coupler have been performed in our group (25) which show that, due to the high refractive index of silicon, FIR transmission coefficients of a few percent may be achieved in a rather large frequency range with a simultaneous high reflection coefficient ($\simeq$ 90%) at 10 µm. Therefore such couplers combine all the qualities expected from the hybrid coupling and moreover they are suitable at short wavelengths. However they are only convenient for strong lines.

Besides the improvement brought by FIR laser waveguide structures and hybrid couplers, we may finally propose the following direction for a further increase of f_{abs} owing to our previous discussion (3.1 to 3.3). Figure 8 summarizes the overall influences of the laser parameters on f_{abs} and its analysis indicates that there are three main directions to improve this factor.

- We have previously underlined the dramatic influence of the frequency offset of the pump from the absorption line center (section 3.3). The tunable waveguide CO_2 laser is the convenient tool(27) to improve the line coïncidence in many cases and this may increase the power efficiency, provided the CO_2 laser is followed by a CO_2 waveguide amplifier to reach high enough pump power.
- Increasing the FIR cavity length, i.e, the IR absorption path has beneficial effect for molecules with low absorption coefficient as far as the cavity finesse at pump and FIR wavelengths can be maintained. Cavity lengths of 2m-3m are generally good experimental solutions.
- However, the main source of improvement is a further decrease of the FIR cavity losses at pump radiation. Due to the IR focussing and the small injection hole, the pump beam reaches the waveguide walls at a too weak incidence and the propagation losses of the IR radiation generally exceed 0.15 m^{-1}. Owing to the hybrid outcoupling method, larger injection holes have been used and have allowed the injection of a collimated pump beam (3). This intermediate solution is beneficial. But the best solution would be to enter the pump beam without any focussing systems. This requires appropriate otpical set-up to match the IR transmission and FIR reflection conditions.

4. Conclusion :

In conclusion, we have briefly analyzed the different aspects of the FIR power optimization and the results show that :

- output powers exceeding the milliwatt level are obtained over the whole FIR spectrum with simple devices and not too expensive materials.
- a further increase in power efficiency may be expected with improved FIR resonator designs, a better frequency coincidence of the pump and, of course, with more *powerful CO_2 lasers.*

The versatility of the optical pumping technique is not to be demonstrated.Although it results essentially from the versatility of the CO_2 laser, the relative independence of the operating conditions with the pumped gas nature and the simple stabilization systems (28) which may be used contribute to the same result.

(1) Chang T.Y. and Bridges T.J., Opt. Commun. 1 (1970) 423

(2) Henningsen J.O., IEEE J. Quant. Electron. QE.13 (1977) 435

(3) Hodges D.T., Foote F.B. and Reel R.D., IEEE J. Quant. Electron. QE.13 (1977) 491

(4) Panock R.L. and Temkin, IEEE J. Quant. Electron. QE.13 (1977) 425

(5) Temkin R.J., IEEE J. Quant. Electron. QE-13 (1977) 450

(6) Selingson D. et al., IEEE J. Quant. Electron. QE-13 (1977) 468

(7) De Temple T.A. and Danielewicz E.J., IEEE J. Quant. Electron. QE-12 (1976) 40

(8) Koepf C.A. and Smith K., IEEE J. Quant. Electron. QE-14 (1978) 333

(9) Hodges D.T., Tucker J.R. and Hartwick T.S., Infrared Physics 16 (1976) 175

(10) Yamanaka M. et al., Jap. Journ. Appl. Phys. 13 (1974) 843

(11) Tucker J.R., Intern. Conf. Submillimeter Waves and their Applications, Atlanta, GA (1974) Conference Digest, p. 17

(12) Henningsen J.O. and Jensen H.G., IEEE J. Quant. Electron. QE-11 (1975) 248

(13) Lourtioz J-M., Adde R. and Pontnau J., Intern. Conf. Submillimeter Waves and their applications Guilford (1978) Conference Digest p. 188.

(14) Lourtioz J-M. and Adde R., *submitted* for publication.

(15) Hodges D.T., Proc. Soc. Phot. Opt. Instrum. Engineers, 105 (1977) 6.

(16) Hodges D.T. and Hartwick T.S., App. Phys. Lett. 23 (1973) 252

(17) Yamanaka M., J. Opt. Soc. Am. 7 (1977) 52.

(18) Degnan J.J., Appl. Phys. 11 (1976) 1

(19) Marcatili E.A.J. and Schmeltzer, Bell. Syst. Tech. J. 43 (1964) 1783.

(20) Chang T.Y. and Lin C., J. Opt. Soc. Am. 66 (1976) 362

(21) Hodges D.T., Foote F.B. and Reel R.D. Appl. Phys. Lett. 29 (1976) 662.

(22) Wood R.A., Brignall N., Pidgeon C.R. and Al-Berkdar F., Infrared Physics 16 (1976) 201.

(23) Danielewicz E.J., Plant T.K. and De Temple T.A., Opt. Commun. 13 (1975) 366.

(24) Evenson K.M. et al., IEEE J. Quant. Electron. QE-13 (1977) 442

(25) Julien F. and Lourtioz J-M. Private Communication.

(26) Weiss C.O., Appl. Phys. Lett. 13 (1977) 383

(27) Abrams R.L., Appl. Phys. Lett. 25 (1974) 304)

(28) Busse G., Basel E. and Pfaller A., Appl. Phys. 12 (1977) 387.

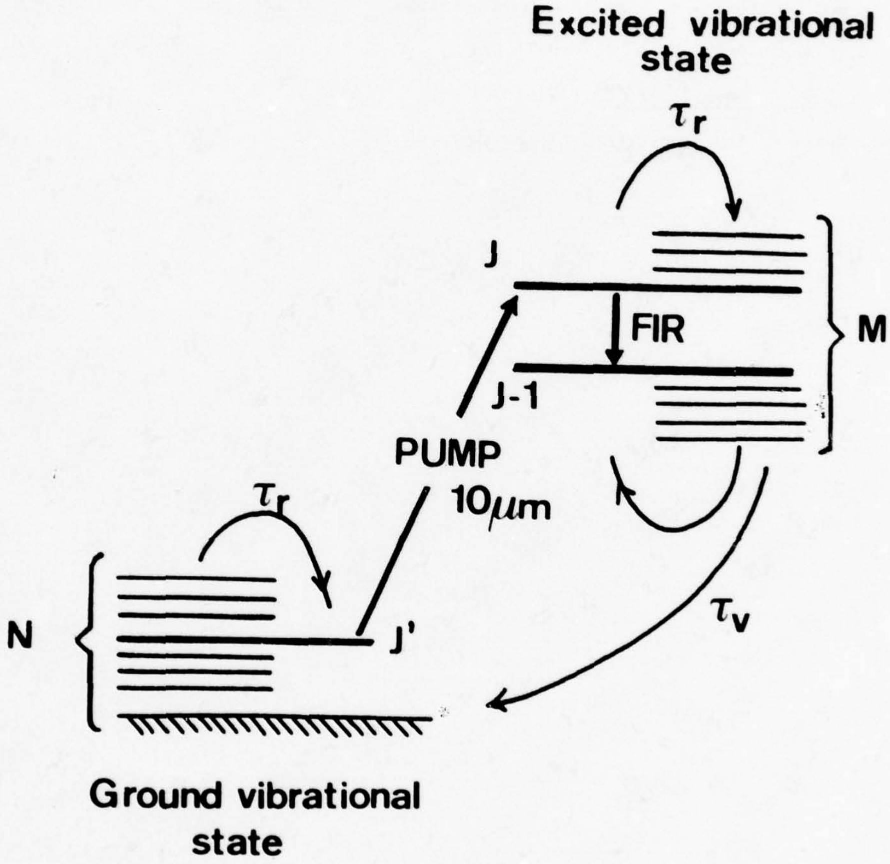
Excited vibrational state
τ_r
J
FIR
M
J-1
PUMP
10μm
τ_r
N
J'
τ_v
Ground vibrational state

Figure 1 : Schematic energy level diagramm showing the transitions involved in optically pumped FIR laser.

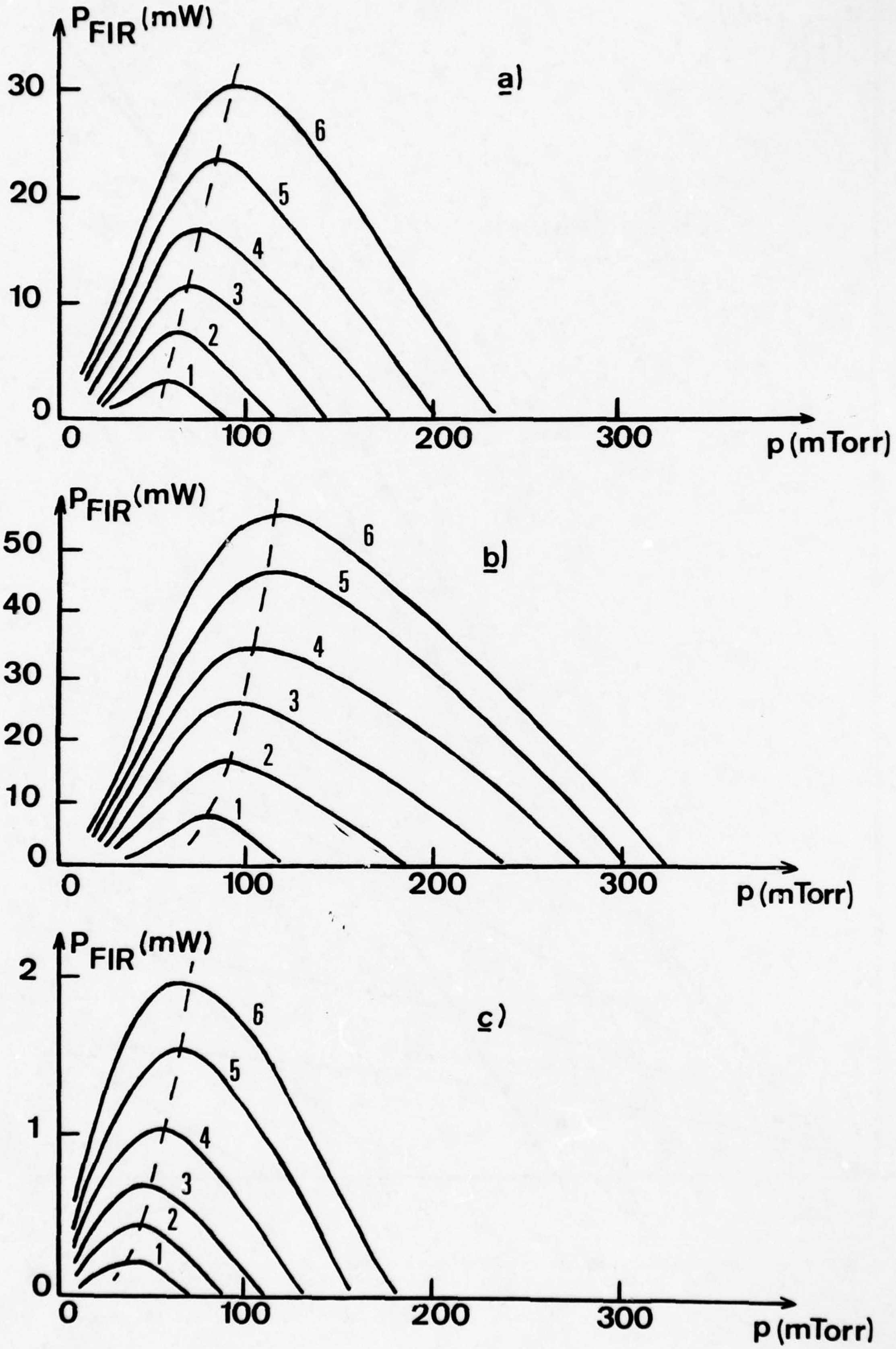

Figure 2 : CH_3OH laser powers at 70 µm (2.a), 118 µm (2.b) and 570 µm (2.c) monitored continuously as functions of the CH_3OH gas pressure, the pump power P_{IR} being a controlled parameter. The different values of P_{IR} are : 1) 3 W, 2) 5,5 W, 3) 8 W, 4) 11 W, 5) 13 W, 6) 15 W. The FIR power is measured with a calibrated thermopile.

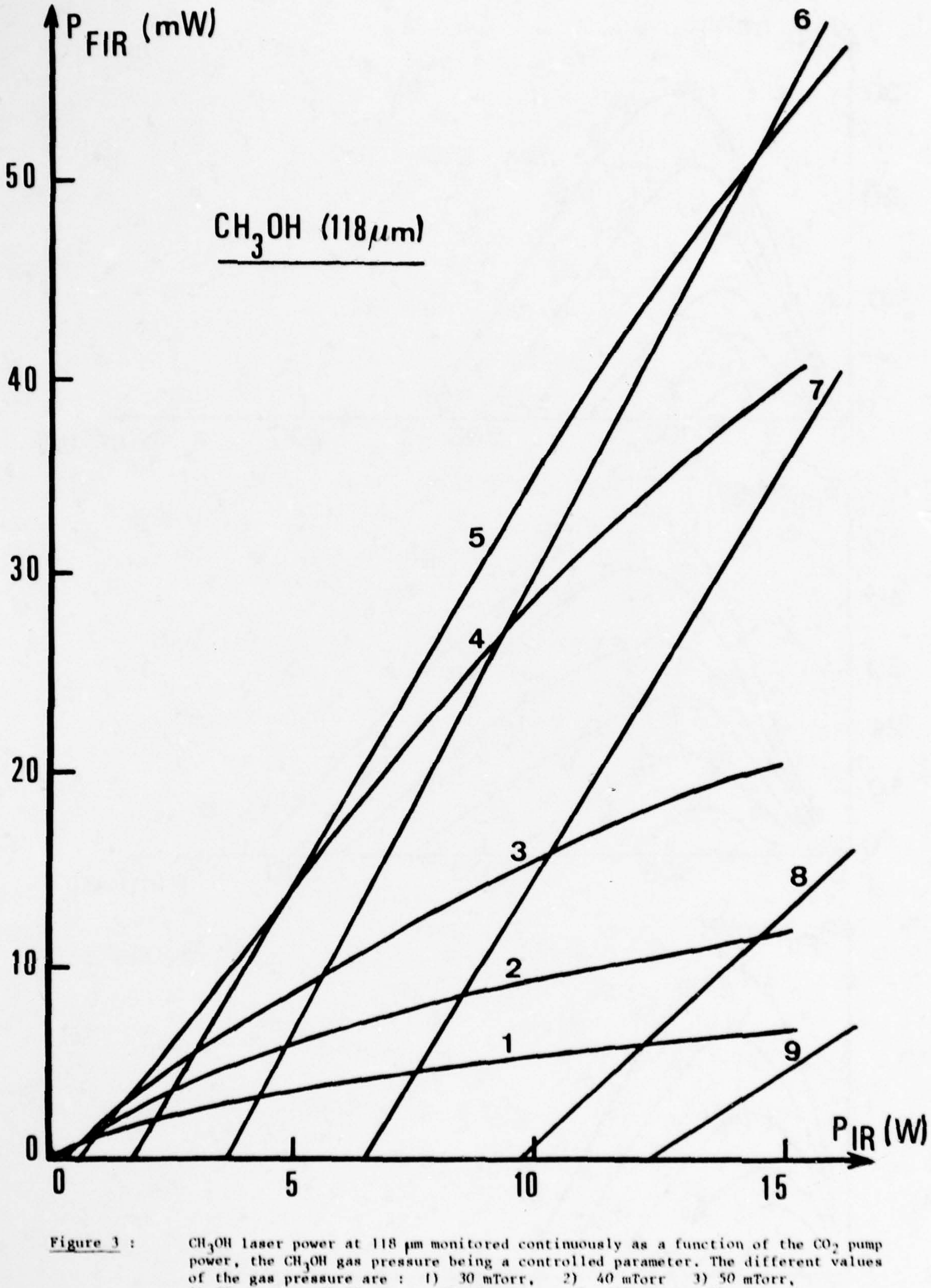

Figure 3 : CH_3OH laser power at 118 μm monitored continuously as a function of the CO_2 pump power, the CH_3OH gas pressure being a controlled parameter. The different values of the gas pressure are : 1) 30 mTorr, 2) 40 mTorr 3) 50 mTorr, 4) 77 mTorr , 5) 95 mTorr, 6) 160 mTorr, 7) 230 mTorr, 8) 270 mTorr, 9) 290 mTorr.

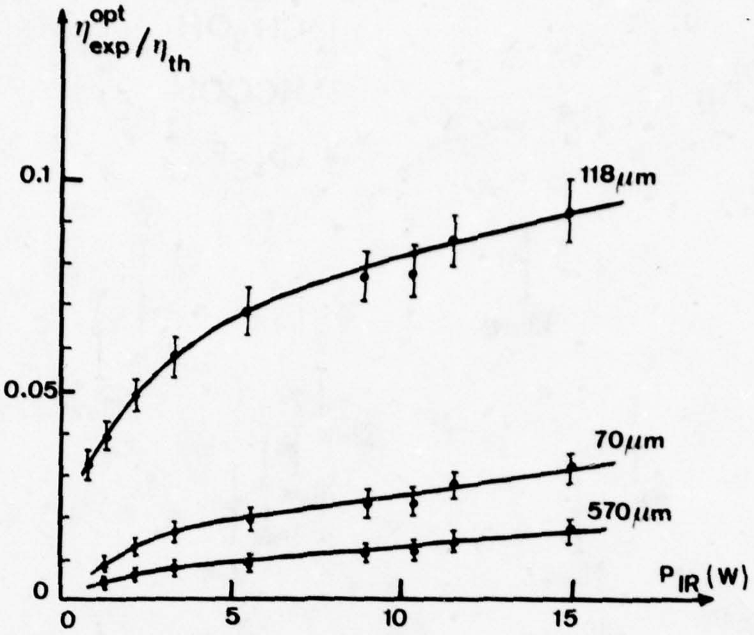

Figure 4 : Relative experimental photonic conversion efficiency at the optimum pressure ($\eta^{opt}_{exp}/\eta_{th}$) as a function of the CO_2 power for the CH_3OH FIR lines at 70 μm, 118 μm and 570 μm.

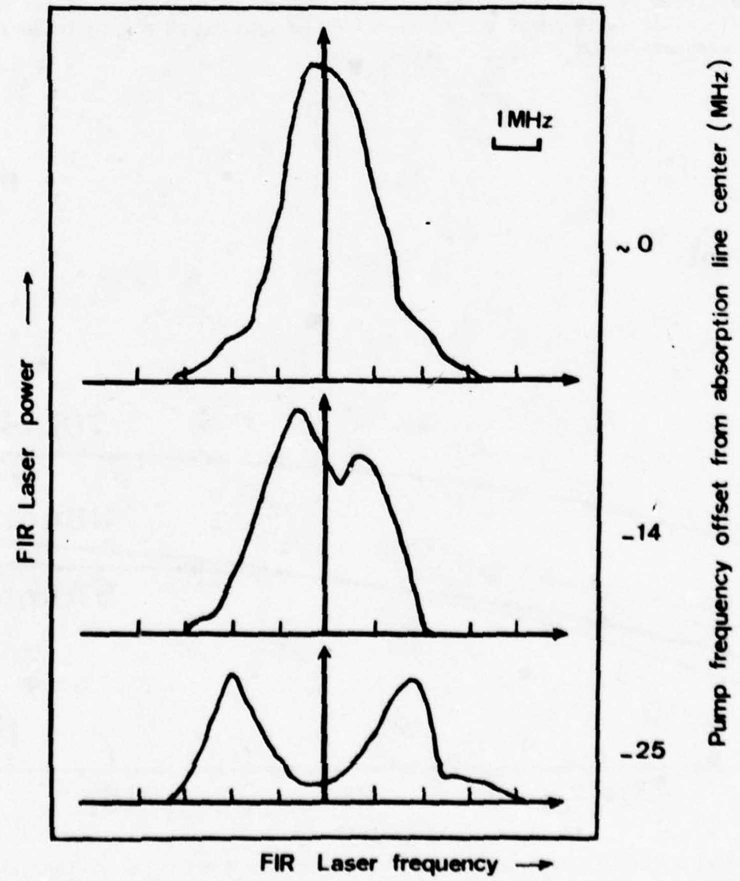

Figure 5 : Tuning curves (output power versus FIR frequency) for the 118 μm CH_3OH laser recorded with different pump frequency offsets from absorption line center. (pump power ≃ 3 W, CH_3OH gas pressure ≃ 60 mTorr).

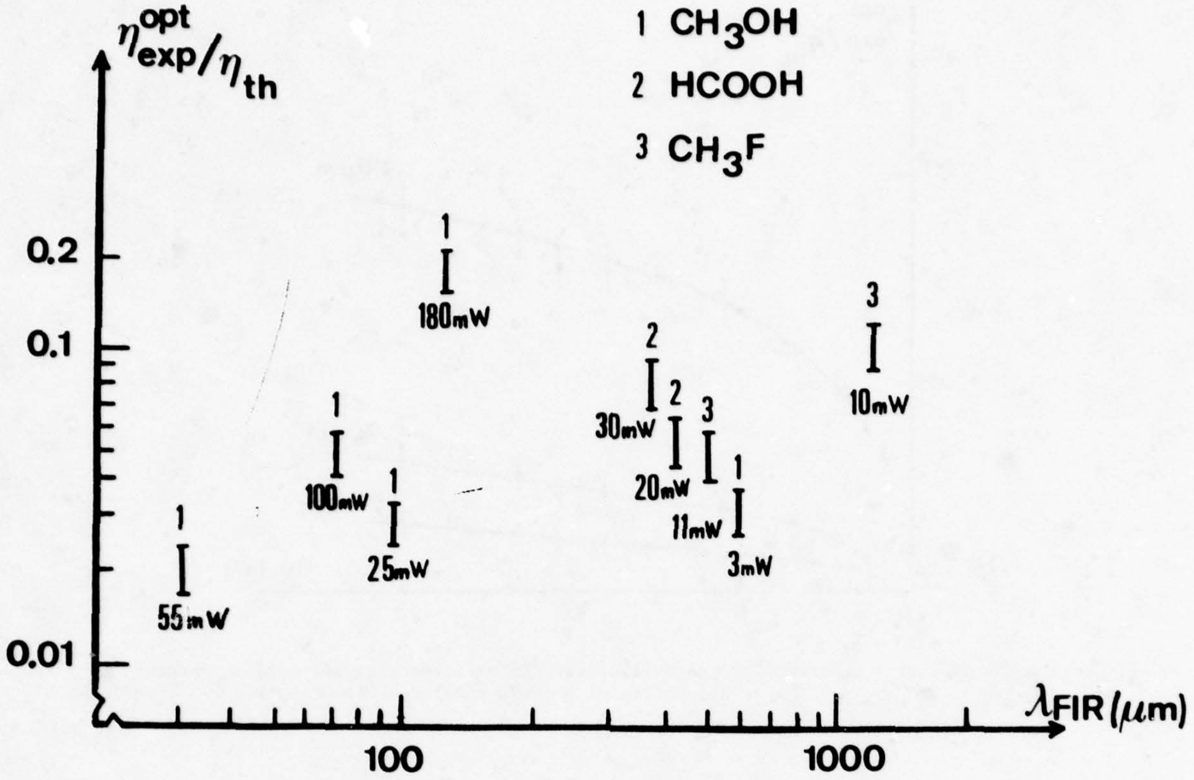

Figure 6 : Relative experimental photonic conversion efficiency obtained for the "best" FIR lines (15) throughout the 40 μm - 1200 μm wavelength region (uncertainty of power measurements ≃ 20%).

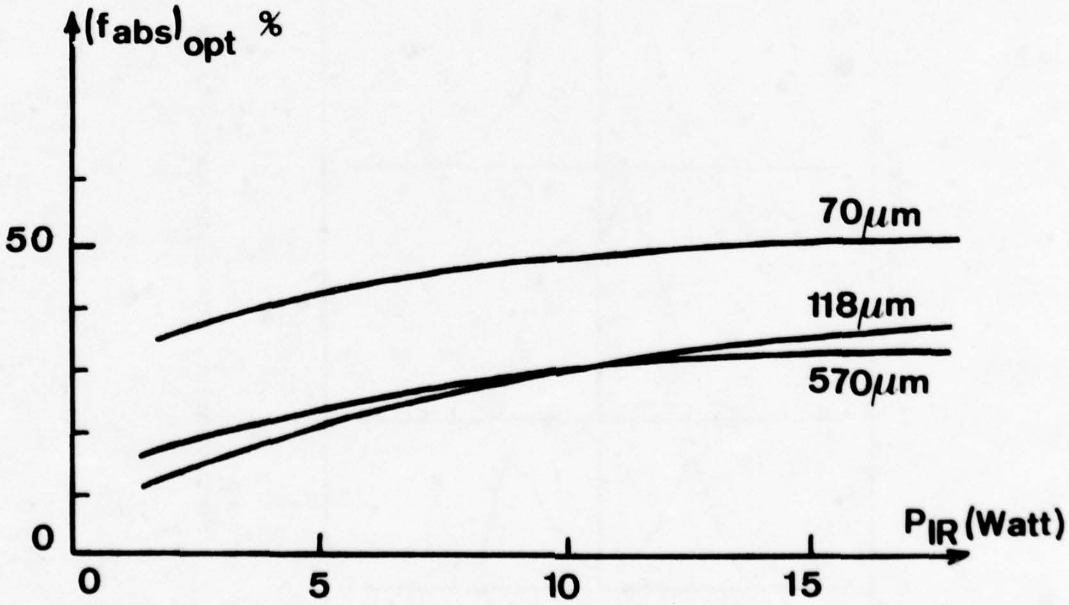

Figure 7 : Evaluation of the fraction of pump power absorbed in the lasing gas at the optimum pressure for the CH_3OH transitions at 70 μm, 118 μm and 570 μm.

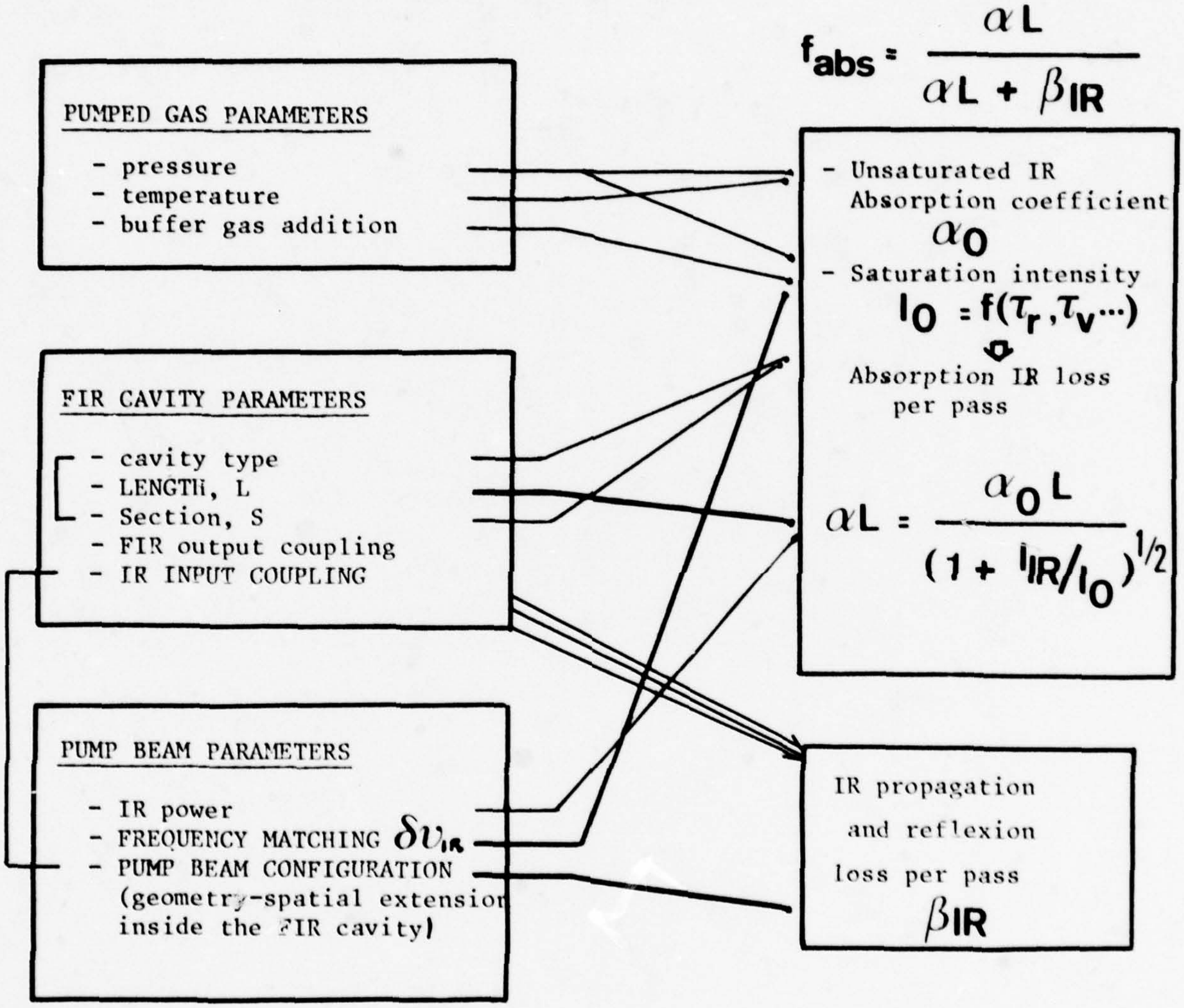
$f_{abs} = \frac{\alpha L}{\alpha L + \beta_{IR}}$
PUMPED GAS PARAMETERS
- pressure
- temperature
- buffer gas addition
FIR CAVITY PARAMETERS
- cavity type
- LENGTH, L
- Section, S
- FIR output coupling
- IR INPUT COUPLING
PUMP BEAM PARAMETERS
- IR power
- FREQUENCY MATCHING $\delta\nu_{IR}$
- PUMP BEAM CONFIGURATION (geometry-spatial extension inside the FIR cavity)
- Unsaturated IR Absorption coefficient α_0
- Saturation intensity $I_0 = f(\tau_r, \tau_v \cdots)$
Absorption IR loss per pass
$\alpha L = \frac{\alpha_0 L}{(1 + I_{IR}/I_0)^{1/2}}$
IR propagation and reflexion loss per pass β_{IR}

Figure 8 : Overall influences of the laser parameters upon f_{abs} (fractional pump power absorbed in the pumped gas).

A SURVEY OF ATMOSPHERIC PROPAGATION RESEARCH
EXPERIMENTS ON SLANT PATHS, IN THE BAND 15-40 GHz

A.S. VANDER VORST
Laboratoire de Télécommunications et d'Hyperfréquences
Université Catholique de Louvain
Louvain-la-Neuve, BELGIUM

ABSTRACT

A study of the available literature is presented, resulting in a review of the present knowledge with respect to 15 to 40 GHz slant path propagation.

Experiments are presented first by location in a decreasing order of complexity, then by subject : attenuation, depolarisation, space diversity, and signal fluctuation. They are illustrated by key diagrams.

A short compilation of sixteen survey papers is also presented.

This bibliographic study has retained about one hundred references out of several hundred papers.

INTRODUCTION

A study of the available literature has been carried out, resulting in a review of the present knowledge with respect to slant path propagation, in the frequency band 15 to 40 GHz. American and European experiments are pretty well covered in this survey. Some Japanese results are also covered.

The accent is put on results and not on theory or on models. The first part of the paper is devoted to a short compilation of sixteen survey papers, published in the open literature. It was felt that such a compilation is useful to introduce the subject.

The second part is devoted to a survey of experiments, ranked by decreasing order of complexity and summarized by location. This gives a compact view of what has been done and what is being done. It gives a summary of representative results, including key diagrams.

SHORT COMPILATION OF SURVEY PAPERS

Medhurst (1965, 30 references) publishes numerical calculations based on the original G.E.C. Report by Ryde, with corrections and improvements. The results apply to wavelengths from 15 cm to 3 mm, taking into account droplets diameters from 0.5 to 7 mm. He compares the calculations to American, Japanese and Russian measurements at frequencies between 11 and 31 GHz and obtains a theoretical attenuation smaller than the measured one.

Altschuler (1968) presents the general problems, with not many details.

Hogg (1972) shows, on a theoretical basis, that depolarisation is more significant for circular than for linear polarisation.

Dougherty et al. (1973, 31 references) describe a model for estimating the expected performance degradation of satellite-to-ground microwave systems due to atmospheric gases, clouds and rain as well as local and regional rainfall statistics. Composite predictions are given for 15 GHz.

Wiley et al. (1973, 31 references) review the literature : Mie, Ryde, Medhurst, Oguchi. They mainly discuss a theoretical model.

Fedi (1973, 43 references) reviews physical phenomena, but with terrestrial links as main application. He discusses scintillation and absorption through various causes (atmosphere, precipitations, multipaths), polarisation and depolarisation. He also points out the use of precipitation statistics.

Blevis (1974, 62 references) synthesizes problems of attenuation, radar backscatter, emission, forward scatter and polarisation effects as well as measurement methods (airborne beacons, satellite beacon ATS-5, radiometry and radar). Diffusion is one of the main topics handled in this paper.

Dudzinsky (1974) concentrates on terrestrial links. He recapitulates measurements from 8 to 70 GHz as a function of rain, giving the "world" maximum and minimum. He investigates the effect of snow and fog at frequencies above 100 GHz, as well as the length of the path. This publication is a summary of RAND report R-1335-ARPA, March 1974.

Straiton (1975), in a short review paper, treats the absorption by oxygen and water vapor. The effect of rain is not looked at.

This work was supported by a contract from the European Space Agency.

Watson (1975, 88 references) reports the most recent measurements at microwave and millimetric frequencies, in a very comprehensive paper, trying to cover the interest in cumulative distribution of fade depth and fade duration as well as the relation between attenuation and meteorological parameters. He first covers direct attenuation measurements, polarisation effects, and attenuation of snow, and discusses the use of dystrometers. This part, however, is related to terrestrial propagation. He then covers indirect attenuation measurements : radiometry, including the diffusion effect calculated by Zavody (1974), comparison between radiometry and ATS-5 measurements, pointing out a discrepancy during certain deep fades, and radar methods. He then discusses attenuation statistics. Several pages are devoted to terrestrial paths. Only a small part is devoted to attenuation statistics for satellite radio paths (the amount of available data was of course too small in 1975 to provide useful statistics).

Hogg et al. (1975, 119 references) discuss almost all the aspects. The title seems to indicate that they concentrate on satellite-earth paths, but this is not true : Part II is devoted to theory and experiments for terrestrial paths. The authors discuss the methods of measurement of rain attenuation on earth-space paths : suntrackers at 19 and cumulative distributions at 19 and 30 GHz, passive radiometers, among others at 15.5, 16 and 30 GHz, as well as the comparison with the ATS-5 beacon at 15.3 GHz. Part IV is devoted to path diversity in earth-space transmission : the three-radiometer experiments of Bell Laboratories at 16 GHz with separation of 3, 11 and 14 km, as well as separation of 11, 19 and 30 km, and the 35 GHz suntrackers experiment. They also discuss depolarisation effects, and the frequency dependance of attenuation by rain on earth-space paths.

Crane (1975) publishes a mini-review, mainly on the comparison between theory and measurement of attenuation due to rain. The only earth-to-space path mentioned is of course ATS-5.

Dudzinsky (1975, 31 references) is an extended version of Dudzinsky, 1974. He reviews the available data : attenuation due to rain from 3 to 300 GHz and maximum and minimum limits. He points out that the attenuation due to fog, hail and snow is much smaller than that due to rain below 100 GHz. Furthermore, he relates time-averaging to length-averaging for terrestrial paths.

Oguchi (1975, 96 references) is a main paper on depolarisation. He first reviews the literature. Starting from droplets photographs and related calculations, he develops a theory for depolarisation : diffusion effects, effective constants of propagation, differential attenuation with a maximum at 30 GHz, relative differential attenuation with a maximum at 5 and 20 GHz, differential phase shift with a maximum at 20 GHz going to negative values above 30 GHz. He reviews the measurements published in the literature on linear and circular polarisation, gives a histogram of canting angles, and recalls measurements on differential attenuation and phase shifts. Radar measurements at 3 and 16.5 GHz are also given.

Rogers (1976, 59 references) concentrates on rainstorm models. He recognizes that there are no models as yet with wide and proven applicability for generating attenuation statistics from climatological data, but that a number of empirical relations are emerging which are providing a rather consistent picture of the relevant structural details of rain. Much of the work he reviews was reported at the IUCRM Colloquium in Nice, 1973. Attenuation by rain is covered : rainfall rate, radar reflectivity, and precipitation noise temperature. He also covers fine-scale structure aspects of rain : point-rainfall statistics and path-averaged rainfall statistics. Part IV is related to terrestrial paths. Part V, however, is devoted to attenuation statistics for earth-space paths. About statistics of actual propagation experiments, he mentions that fading distributions are available for only a small number of locations, elevation angles and frequencies, and are usually based on data from short time periods : suntrackers at Bell Laboratories and a few other experiments. From indirect measurements, he mentions slant-path attenuation statistics based on radar observations, at various frequencies, usually on the low side of the band. He finally compares three rainstorm models : Zintsmaster-Hodge, McGill, and Strickland.

Gaudissart et al. (1977, 117 references) give a rather complete coverage of the whole subject, in a brochure of 120 pages. They put the accent, however, more on the physical phenomena than on statistics. They concentrate on the observed effects : refraction, scintillation, multipaths, attenuation by absorption and diffraction, depolarisation, and thermal noise. Measurement methods are also compared : terrestrial links, slant path including diversity, radiometry and radar, as well as meteorological measurements.

SUMMARY OF REPRESENTATIVE RESULTS

This section is illustrated by diagrams summarizing key results. It is divided into the following paragraphs : attenuation, comparing measurements on beacons, radiometers and radars, depolarisation, space diversity, and signal fluctuation.

Attenuation

ATS-6 and COMSTAR measurements lead to essentially the same ratio of attenuation at 30 and 20 GHz; it is of the order of 2. Figure 1 shows the two results obtained one at the British Post Office on ATS-6 (Howell et al., 1977), for twenty rain events (1318 minutes of data), the other one by Bell Labs on COMSTAR (Muller, 1977) at Palmetto, Georgia, for six months of operation. Figure 2 compares the value of the ratio of the attenuation at the two frequencies : scattergram of the same twenty rain events on ATS-6, instantaneous measurements on COMSTAR, statistical correlation of the cumulative fading at the two frequencies for the same purcentage of time, and empirical equation (Howell et al. 1977; Muller, 1977; Drufuca, 1973)

$$A\ (\mathrm{dB})\ /\ A_o(\mathrm{dB}) = (f\ /\ f_o)^{1.72}$$

Satellite beacons have been used to calibrate radiometers. Figure 3 shows the result of a calibration at 15.3 GHz (Strickland, 1973). An equivalent mean temperature has of course to be assumed. The calibration shown is based on an assumed value of 278°K. The two sets of bounding curves show how the relationship changes when temperature changes of ± 10 and ± 20°K are introduced with respect to 278°K. It should be noticed that when the sky temperature approaches the assumed temperature of the medium, errors in either temperature tend to introduce large errors into the derived attenuation : at a 10 dB attenuation, a 5° error in the temperature leads to a 0.8 dB error in the attenuation. Figure 4 shows the same agreement for calibrations made respectively at 20 and 30 GHz on ATS-6 (Bell et al., 1977). Of course, a fade distribution obtained from measurements made on beacon receivers indicates the effect of both absorption and scattering by hydrometeors, while radiometric measurements are insensitive to scattering and indicate the effect of absorption only. The difference has been evaluated (Zavody, 1974). Hence, the calibration of a radiometer on beacon measurements is valid only for the average structure of precipitations which occured during the calibration, it may be completely wrong to calibrate a radiometer in one location and put it afterwards in another location.

Statistics have been obtained both on beacons and by radiometry. The time duration of measurements on beacons however is rather small and does not lead to a representative data sample for statistical purposes. European Space Agency radiometer data (Brussaard, 1977) represent a total data base of 31 years (Watson, 1977). Figure 5 compares curves of cumulative attenuation, calculated at 20 and 30 GHz from the radiometric data, with actual measurements made in Europe on ATS-6, at the same frequencies. The agreement is very good. The same figure also shows measurements made in the United States. The agreement here is not excellent. This is to be attributed to the difference in meteorological climate, hence in rain distribution.

To be useful, such cumulative diagrams should be compared to cumulative diagrams on rain statistics, as the one illustrated by Figure 6 (Muller, 1977). Such rain statistics, however are not available in Europe yet. They will be published in the near future, since they are included in the final report of the COST Action 25/4, "Influence of atmospheric conditions on electromagnetic wave propagation at frequencies above 10 GHz".

Radars have been used in conjunction with radiometers. Figure 7 compares statistics obtained from a radar and a radiometer at 13 GHz. A 390 minutes calibration period accured. There is no doubt that radar has brought and may still bring valuable information in atmospheric research. Any use of radar, however, also has limitations. Figure 8, for instance, shows a comparison between theoretical and experimental specific attenuation - reflectivity relationships (Hodge et al., 1977). Especially, the two curves at 13 GHz, marked respectively "Theory" and "Data", are quite different. The difference is due to the difference between the distribution during which measurements were actually made and the one on which the theoretical calculation is based.

Radiometric data, also, have to be used with care. Figure 9 compares statistical data obtained with the same radiometer at 35 GHz, during different time intervals (Funakawa et al., 1973). There may be a ten dB difference between the various results at 0.1 % of time. This discrepancy is, of course, more apparent on the low-percent-of-time side, since the existence of one particular event may be of very much importance there, while not affecting the statistics at the high-percent-of-time side. When using sun-trackers, one has to take into account the variation of the elevation angle during the measurements. Hence, the statistics have to be corrected for the periods of time corresponding to the various elevation angles. Measurements made at 20 GHz have been corrected that way which makes the interpretation of the results much easier (Fimbel et al., 1975). A correction also has to be used to compare measurements made at different elevation angles. Down to 5°, a simple cosecant correction may be applied. Figure 10 compares the value of attenuation, calculated at 20° elevation from measurements made at 5° elevation, with actual measurements made at 20°; the frequency is 17 GHz; the agreement is very good (Watson, 1975). On the other hand, not enough attention has been paid to the limitations of accuracy (Van Vyve et al., 1974).

Depolarisation

Meteorological events are pretty well analyzed. Fiugre 11 shows scattergrams of the cross-polar discrimination versus the co-polar attenuation (Howell et al., 1977), at 20 and 30 GHz. Actual results are compared with a theoretical curve based on the drop-size distribution determined by Marshall and Palmer (1948) and on the calculation of rain depolarisation (Uzunoglu et al., 1977) with a correction for clouds, assuming a liquid water content of 1.5 g/m^3 extending over a vertical height of 1 km. The agreement is good.

Measurements on satellite beacons showed for the first time the "anomalous" depolarisation, attributed to ice particles, statistically aligned under the influence of an electric field. Figure 12 makes the phenomenon quite apparent : there is a strong decrease in corss-polar discrimination with almost no attenuation (Howell et al., 1977). Those results may well have been dismissed as "bad data" had it not been for the radar evidence obtained on other occasions by the Appleton and Bradford radars (Watson, 1978). Hence, the role of radars in the ATS-6 study should not be lightly dismissed.

There are presently not many cumulative diagrams on cross-polar discrimination : the time duration of measurements is small which does not lead to a representative data sample for statistical purposes. Figure 13 shows the presently available results at 20 and 30 GHz (Dijk et al., 1977; Howell et al., 1977; Watson et al., 1977). Obtaining such statistics in the future, however, is important. Depolarisation due to ice particles, indeed, may reach a maximum of - 20 dB with a co-polarised signal attenuation smaller than 1 dB, before and after a rain attenuation event, and may be of long duration, of the order of 10 minutes to more than an hour (Cox et al., 1977). Cumulative diagrams on depolarisation may hence be quite different from attenuation statistics.

Space diversity

Two main questions with regard to path diversity improvement are the separation and the orientation of the baseline with respect to the earth-satellite path, taking into account the direction of persistent weather fronts at the particular location.

The influence of the separation is shown on Figure 14, for three radiometers operating by 11, 19 and 30 km (Wilson et al., 1973).

The influence of the baseline orientation is shown to some extent on Figure 15 for three radiometers in a L configuration (Wilson et al., 1973). It is presently believed that baselines normal to the path and, secondarily, to the direction of convective weather fronts, are most efficient for path diversity. A theoretical study (Austin et al., 1975) has simulated path diversity systems and shown that diversity pair orientation perpendicular to the elongation of the precipitation lines yields the best diversity performance.

It is not too easy to define the most appropriate criterion for evaluating diversity performance. Some authors use conditional probability, for instance for simultaneously exceeding the same attenuation over two parallel slant paths. Wilson (1973) has defined the diversity advantage as the ratio of the percent of time level for a diversity combination to that of a single path. This leads to diagrams showing the advantage plotted versus separation, with the attenuation as a parameter. As an example, at 15.5 GHz, for a pair separated by 30 km and an attenuation level of 9 dB, the diversity improvement factor is about one hundred which, on a yearly basis, means that the outage of a system with a 9 dB fade margin is reduced from eight hours to less than 5 minutes. The diversity gain, defined by Hodge (1973) is an appropriate criterion. It is the difference between the path attenuations associated with a single terminal and diversity modes of operation for a given probability level. The optimum diversity gain for a dual-path system is obtained by squaring the single-terminal probabilities, which amounts to assuming statistical independance of the alternate paths. Figure 16 shows diversity gain versus separation distance at various frequencies, with the attenuation as a parameter (Hodge et al., 1976). The data for separation distances of 8 km or more fall within 1.5 dB of the optimum two-terminal diversity gain. Moreover, little is gained by increasing the separation beyond 10 km. The diversity gain in dB, for an 11 km separation distance, is approximately equal to 0.7 times the single path attenuation in dB. Diversity gain versus single location attenuation is independent of frequency, as shown on Figure 17 (Vogel et al., 1976).

It should be noticed that all this concerns space diversity effects on the co-polar signal. It would be interesting to set up space diversity experiments on the cross-polar signals. Because of the long duration of the ice particles depolarisation, it may be expected that the variation of the diversity gain versus separation distance will be quite different.

Signal fluctuation

This is not to be confused with scintillation. Strictly speaking, indeed, scintillation is related to variations of the index of refraction. Calculations of scintillation have been made for terrestrial links, for instance at 35 and 100 GHz (Lane, 1968). The conclusion was that amplitude scintillations of up to 10 dB may be expected on terrestrial links in the frequency range 35-100 GHz. For earth-space links near the vertical, the maximum value is unlikely to exceed 3 to 4 dB.

Another study on scintillation (Millman, 1970) summarizes various results : fluctuations of less than 1.5 dB at 15.3 GHz along a 20 km clear air path with periods of less than one minute, except during the passage of a cold front with rapid variations up to 5 dB, as well as long term fades up to 6 dB presuarise periods when a strong ground moisture layer is present. It also mentions rms phase jitter at near vertical incidence at 10 GHz, between 2.5 and 25°, decreasing linearly with frequency. The deviations in both phase and range are directly proportional to the size if the turbulent eddies while the angular jitter decreases with an increase in eddy size.

Variations in transit time have been investigated at 36 GHz (Vilar et al., 1973 and 1974). These variations induce changes in the instantaneous frequency, hence a broadening of the carrier frequency spectrum. Actual measurements were compared with the results obtained from the theoretical model.

On the other hand, measurements of signal fluctuation were made on ATS-6, as well at medium as at low elevation angle. The following table summarizes results.

Reference	Frequency (GHz)	Elevation (°)	Measurements
Vogel et al., 1977	30	17.3 to 1.5	standard-deviation from 0.2 to 6 dB, without precipitation
Stutzman et al., 1975	20	9 to 0	from 2 to 7 dB fluctuation
Hodge et al., 1977	30	0.38	20 dB ptp
Howell et al., 1977	20,30	23	0.7 dB ptp at 30 GHz with bursts of up to 6 dB ptp, associated with clouds; ratio of amplitudes 30/20 GHz is 1.6
Browning et al., 1977	30	21	1 to 3 dB ptp
		0	10 dB ptp during rain
Dijk et al., 1977	30	25	3 dB ptp on co-polar, 12 dB on cross-polar

It can be seen that even at 23° elevation, the fluctuation may be of more than 5 dB ptp on the co-polar signal. Fluctuation on the cross-polar signal may even be much more important. Fluctuations are usually associated with the presence of clouds; they can be important in the absence of precipitations. Figure 18 compares the power spectrum of the signal at a 42° elevation with a 2° elevation, at 20 GHz (Hodge et al., 1976). Results at 30 GHz are very similar.

CONCLUSIONS

From this survey, the following conclusions can be drawn.

1. There are not enough coordinated data on the co-polar signal to establish reliable cumulative diagrams.
2. XPD information is important on particular events; cumulative data are almost completely lacking.
3. Scintillation is only in an early stage of study. Spectrum analysis is necessary.
4. Anomalous depolarisation is only in an early stage of study.
5. A lot of radiometric data are available. They should be normalized for comparison.
6. Normalized space diversity measurements are not available.
7. Data show that radar may be very useful. At the present time, data are available from 2.8 to 95 GHz. A unified approach is necessary.
8. There are almost no data on the influence of the involved phenomena on composite digital signals.
9. Among all the experiments, there is almost always a confusion between the two main purposes : analysis of physical phenomena on one hand, acquisition of data in a statistical purpose on the other hand.

REFERENCES

ALTSCHULER, E.A., "Tropospheric effects on earth-to-space propagation at millimeter wavelengths", Tropospheric wave propagation, I.E.E., Conf. Publ. n° 48, 1968, pp 151-158.

AUSTIN, L.B., AUSTIN, G.I., "Techniques for the calculation of attenuation from precipitation for single station and path diversity satellite communication systems from digital radar data", Radio Science, vol. 10, December 1975, pp 1019-1024.

BELL, R.R., "The calibration of 20 and 30 GHz radiometers using the ATS-6 satellite beacons", U.R.S.I., La Baule, May 1977, pp 351-356.

BELL, R.R. et al., "The calibration of 20 and 30 GHz radiometers using the ATS-6 satellite beacons", ESA-SP-131, September 1977, pp 135-148.

BLEVIS, B.C., "Microwave attenuation and scatter. Theory and measurement", Journal de Rech. Atmosph., vol. 8, Jan-June 1974, pp 5-21.

BROWNING, D.J., PRATT, T., "Low-angle propagation from ATS-6 at 30 GHz", ESA-SP-131, September 1977, pp 149-154.

BRUSSAARD, G., "Rain attenuation on satellite-earth paths at 11.4 and 14 GHz", U.R.S.I, La Baule, May 1977, pp 393-398.

COX, D.C., ARNOLD, H.W., RUSTAKO, A.J., "Some observations of anomalous depolarisation on 10 and 12 GHz earth-space propagation paths", Radio Science, bol. 12, n° 3, May-June 1977, pp 435-440.

CRANE, R.K., "Attenuation due to rain. A mini review", I.E.E.E., AP-23, September 1975, pp 750-752.

DIJK, J., MAANDERS,E.J., DE WINTER, P.J., "Scintillation effects receiving ATS-6 at 30 GHz", U.R.S.I., La Baule, May 1977, pp 381-386.

DIJK, J., et al., "ATS-6 experiments at Eindhoven University", ESA-SP-131, September 1977, pp 37-54.

DOUGHERTY, H.T., DUTTON, E.J., "Estimating attenuation, scintillation and scattering due to rainfall for satellite/ground systems", Propagation effects on frequency sharing, AGARD-CP-127, 1973, pp 9-1 to 9-13.

DUDZINSKY, S.J., "Atmospheric effects on terrestrial millimeter-wave communications", E.M.C., Montreux, 1974, pp 197-201.

DUDZINSKY, S.J., "Atmospheric effects on terrestrial millimeter-wave communications", Micr. Jl., vol. 18, December 1975, pp 39-42.

FEDI, F., "Atmospheric effects on electromagnetic-wave free propagation at frequencies above 10 GHz", E.M.C., Brussels, 1973, pp B-11-1 to B-11-16.

FIMBEL, J., MISME, P., "Introduction de la notion de distance équivalente dans le calcul des affaiblissements sur une liaison oblique", ESA-SP-113, Graz, April 1975, pp 129-134.

FUNAKAWA, K., OTSU, Y., "Characteristics of the slant path rain attenuation at 35 GHz obtained by solar radiation and atmospheric emission observations", I.U.C.R.M., Nice, 1973, pp III.9.1 to III.9.5.

GAUDISSART, E., SOBIESKI, P., VAN VYVE, J., "Propagation aux fréquences supérieures à 10 GHz", Univ. Louvain, Labo. Télécom. Hyperf., January 1977, 120 pages.

HODGE, D.B., "The characteristics of millimeter wavelength satellite-to-ground space diversity links", Prop. rad. waves at freq. above 10 GHz, I.E.E. 98, 1973, pp 28-32 plus addendum.

HODGE, D.B., THEOBOLD, D.M., TAYLOR, R.C., "ATS-6 millimeter wavelength propagation experiment", O.S. Univ. Final Report, January 1976.

HODGE, D.B., THEOBOLD, D.M., DEVASIRVATHAM, D.M., "Amplitude sincitllation at 2 and 30 GHz on earth-space paths", U.R.S.I., La Baule, May 1977, pp 421-425.

HODGE, D.B., AUSTIN, G.L., "The comparison between radar - and radiometer - derived rain attenuation for earth-space links", Radio Science, vol. 12, n° 5, September-October 1977, pp 733-740.

HOGG, D.C., "Depolarization of microwaves in transmission through rain", AGARD-CP-107, 1972, pp 6-1 to 6-5.

HOGG, D.C., CHU, T.S., "The role of rain in satellite communications", I.E.E.E. Proc., vol. 63, n° 9, September 1975, pp 1308-1331.

HOWELL, R.G., THIRLWELL, J., "20 GHz cross-polarisation and dual frequency attenuation and scintillation measurements using the ATS-6 satellite", U.R.S.I., La Baule, May 1977, pp 339-344.

HOWELL, R.G., et al., "20 and 30 GHz attenuation measurements using the ATS-6 satellite", ESA-SP-131, September 1977, pp 55-68.

HOWELL, R.G., et al., "20 and 30 GHz cross-polarisation measurements using the ATS-6 satellite", ESA-SP-131, September 1977, pp 85-102.

LANE, J.A., "Scintillation and absorption fading on line-of-sight links at 35 and 100 GHz", I.E.E. 48, 1968, pp 166-174.

MARSHALL, J.S., PALMER, W., "The distribution of raindrops with size", J. Meteorol., 1948, 5, pp 165-166.

MEDHURST, R.G., "Rainfall attenuation of centimeter waves : comparison of theory and measurement", I.E.E.E., AP-13, n° 4, July 1965, pp 550-564.

MILLMAN, G.H., "Tropospheric effects on space communications", AGARD-CP-70, 1970, Düsseldorf, pp 4.1 to 4.29.

MULLER, E.E., "Long-term rain attenuation observations at 13, 19 and 28 GHz", Symp. Adv. Sat. Comm. Syst. 20-30 GHz, Genova, December 1977, preprint pp 81-83.

OGUCHI, T., "Rain depolarisation studies at centimeter and millimeter wavelenghts. Theory and measurement", U.R.S.I., Lima, August 1975, 46 pages.

ROGERS, R.R., "Statistical rainstorm models. Their theoretical and physical foundations for performance prediction of single-path and path diversity systems in microwave transmission", I.E.E.E., AP-24, July 1976, pp 547-566.

STRAITON, A.W., "The absorption and reradiation of radio waves by oxygen and water vaport in the atmosphere. Microwave transmission characteristics", I.E.E.E., AP-23, July 1975, pp 595-597.

STRICKLAND, J.I., "Comparison of direct and indirect measurements of precipitation attenuation at 15.3 GHz", AGARD-CP-107, 1973, pp 21-1 to 21-8.

STUTZMAN, W.L., et al., "ATS-6 satellite 20 GHz propagation measurements at low elevation angle", Electr. Letters, vol. 11, December 11, 1975, pp 635-636.

UZUNOGLU, N.K., EVANS, B.G., HOLT, A.R., "Scattering of electromagnetic radiation by precipitation particles and propagation characteristics of terrestrial and space communication systems", Proc. I.E.E., May 1977, vol. 124, pp 417-424.

VAN VYVE, J., VANDER VORST, A., "A complete sutdy of the accuracy of the computed atmospheric attenuation by radiometric measurements", E.M.C., Montreux, September 1974, pp 217-221.

VILAR, E., MATTHEWS, P.A., "Propagation noise and frequency stability at 36 GHz", I.E.E. 98, 1973, pp 83-89.

VILAR, E., MATTHEWS, P.A., "Importance of amplitude sinctillations in millimetric radio links", E.M.C., Montreux, 1974, pp 202-206.

VOGEL, M.J., STRAITON, A.W., FANNIN, B.M., WAGNER, N.K., "Attenuation diversity measurements at 20 and 30 GHz", Radio Science, vol. 11, March 1976, pp 167-174.

VOGEL, M.J., STRAITON, A.W., FANNIN, B.M., "ATS-6 ascending : near horizon measurements over water at 30 GHz", Radio Science, vol. 12, September-October 1977, pp 757-765.

WATSON, P.A., "Results of measurements of attenuation by rain and other hydrometeors", U.R.S.I., Lima, August 1975, 35 pages.

WATSON, P.A., et al., "Attenuation and crosspolarisation measurements at 20 GHz using the ATS-6 satellite with simultaneous radar observations", ESA-SP-131, September 1977, pp 119-126.

WATSON, P.A., private communication, February 1978.

WILEY, P.H., BOSTIAN, C.W., STUTZMAN, W.L., "The influence of polarization on millimeter wave propagation through rain", Ph.D. Thesis, Interim Report, Virginia Pol., June 1973, 89 p., 31 references.

WILSON, R.W., MAMMEL, W.L., "Results from a three radiometer path-diversity experiment", I.E.E. 98, April 1973, pp 23-27 and addendum.

ZAVODY, A.M., "Effect of scattering by rain on radiometer measurements at millimetric wavelengths", Proc. I.E.E., vol. 121, n° 4, April 1974, pp 257-263.

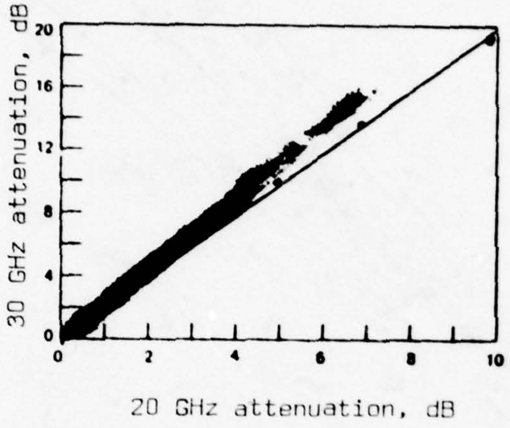

Figure 1. Comparison of attenuation at 30 and 20 GHz (two experiments).

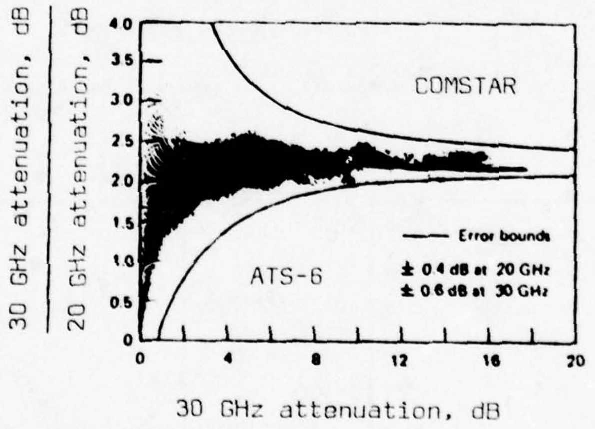

Figure 2. Ratio of attenuation at 30 and 20 GHz.

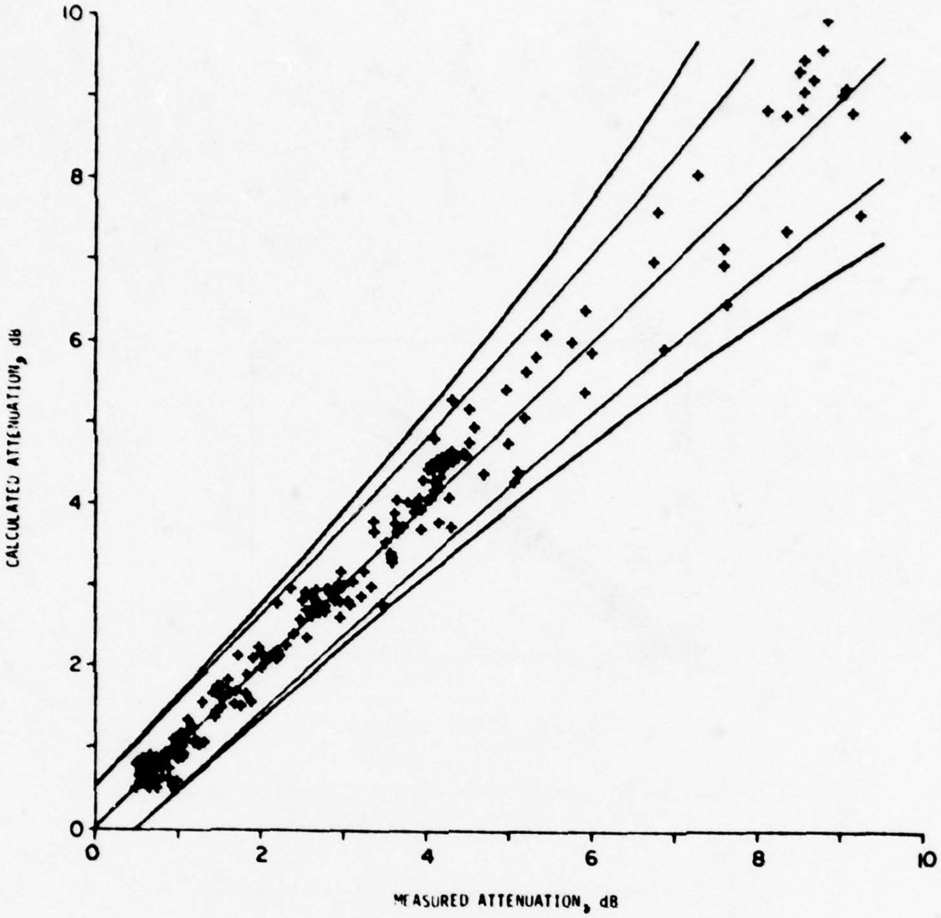

Figure 4. 20 GHz and 30 GHz predicted versus measured attenuation.

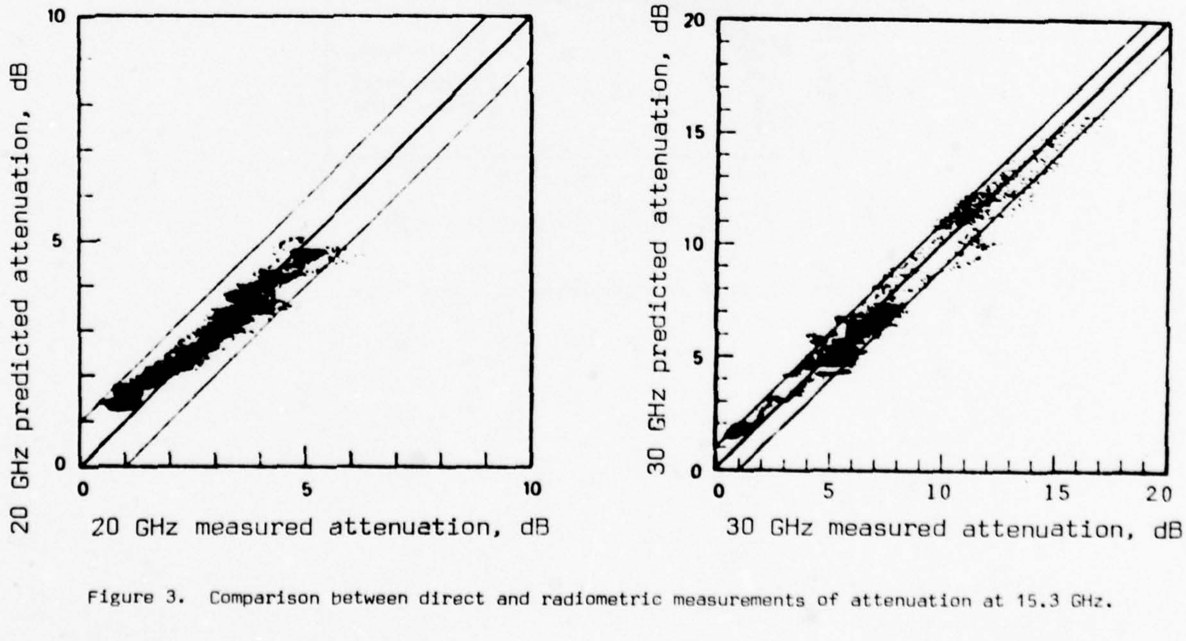

Figure 3. Comparison between direct and radiometric measurements of attenuation at 15.3 GHz.

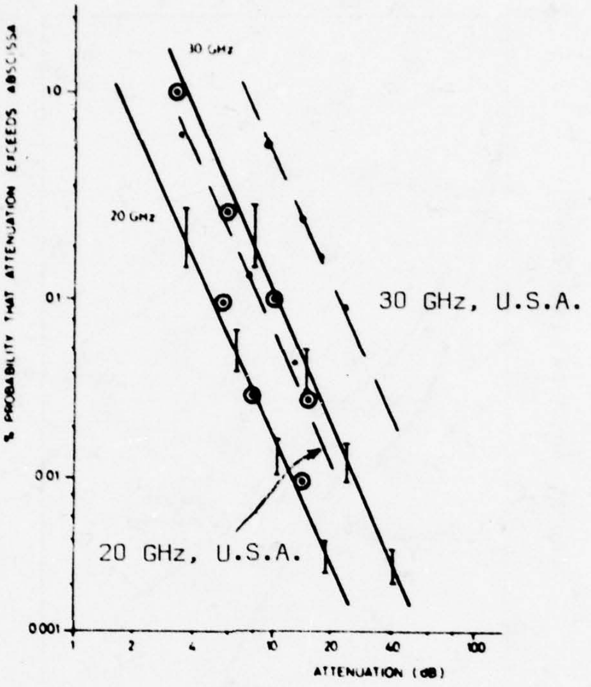

Figure 5. Statistics of attenuation with comparison between beacon and radiometer, at 20 and 30 GHz.

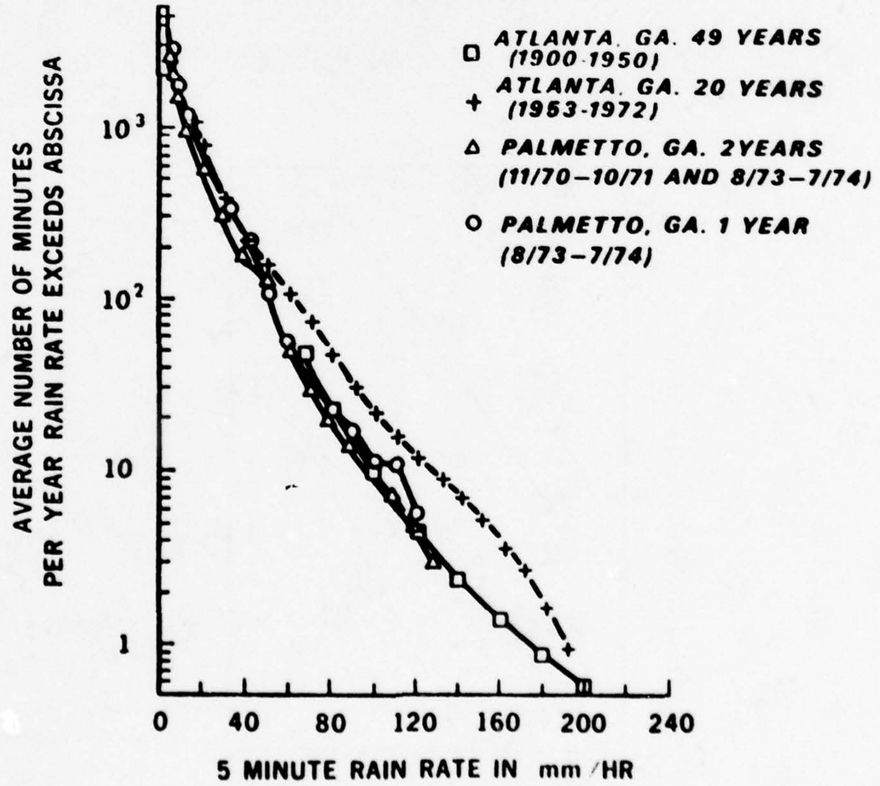

Figure 6. Cumulative rain statistics.

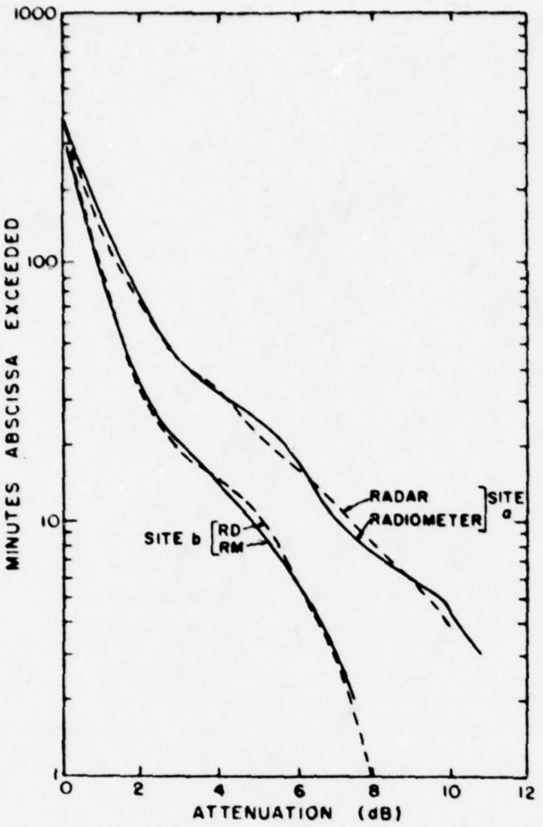

Figure 7. Radar and radiometer derived attenuation statistics at 13 GHz.

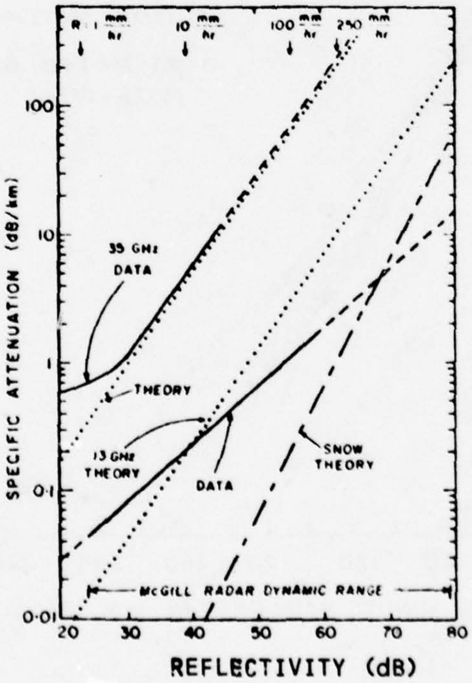

Figure 8. Comparison of theoretical and experimental attenuation-reflectivity relationships.

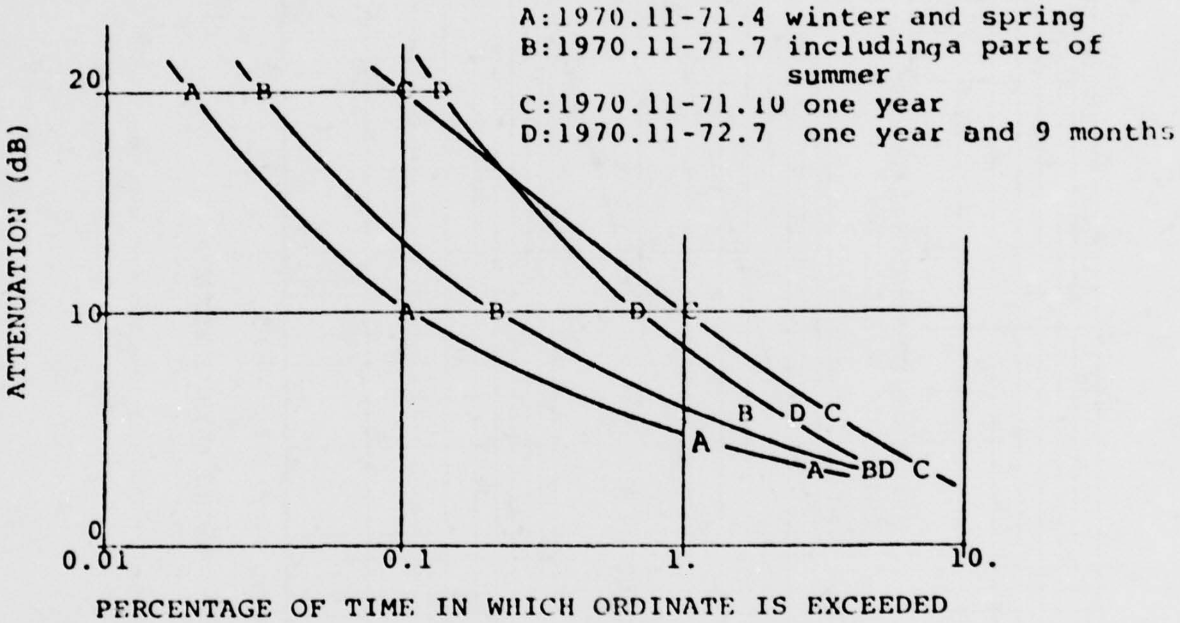

Figure 9. Influence of time interval on 35 GHz radiometer statistics.

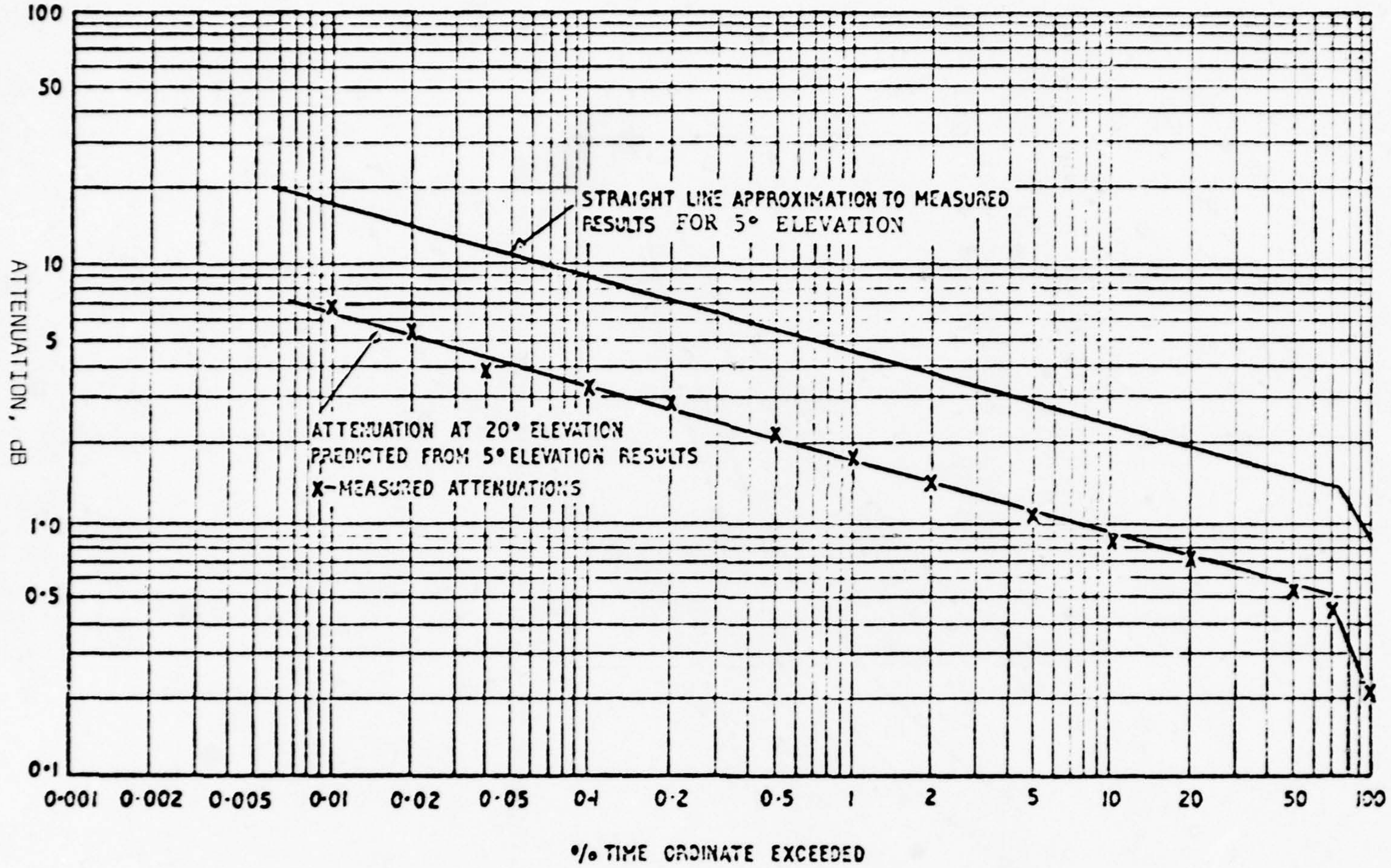

Figure 10. Comparison of 20° attenuation statistics predicted from measurements at 5° with actual measurements.

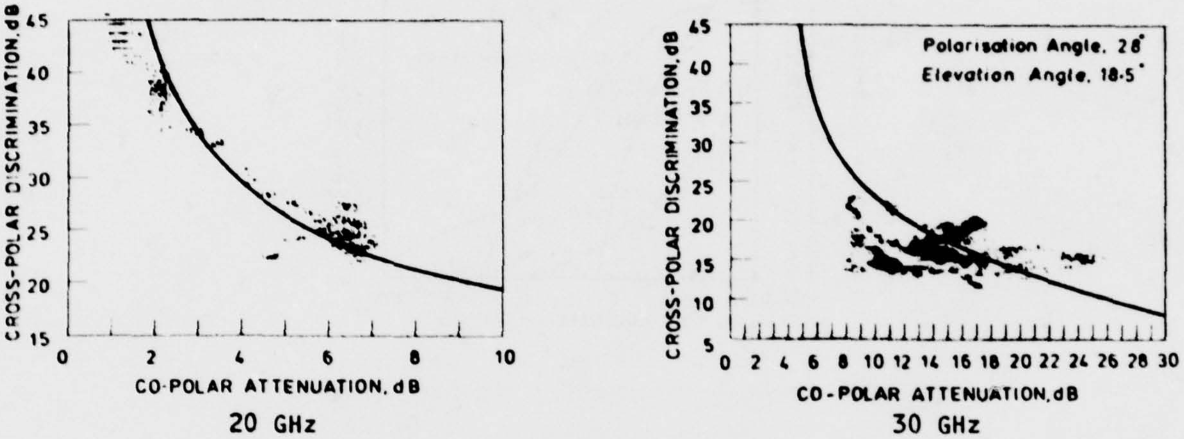

Figure 11. Scattergrams of cross-polar discrimination versus co-polar attenuation.

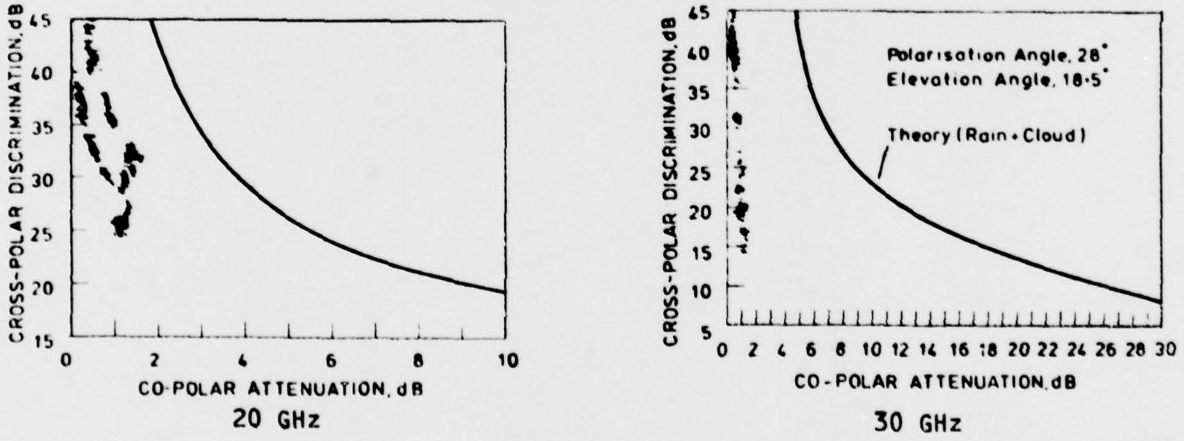

Figure 12. Scattergrams of "anomalous" cross-polar discrimination versus co-polar attenuation.

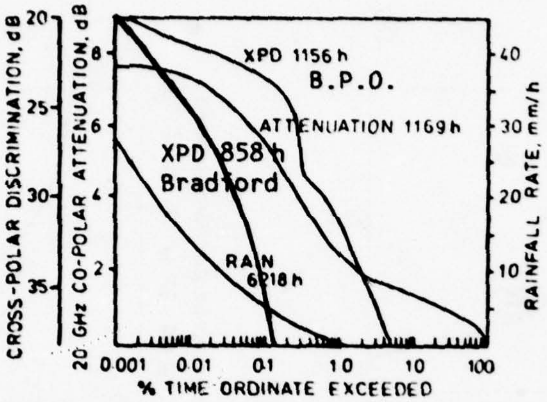

Figure 13. Cumulative statistics on cross-polar discrimination.

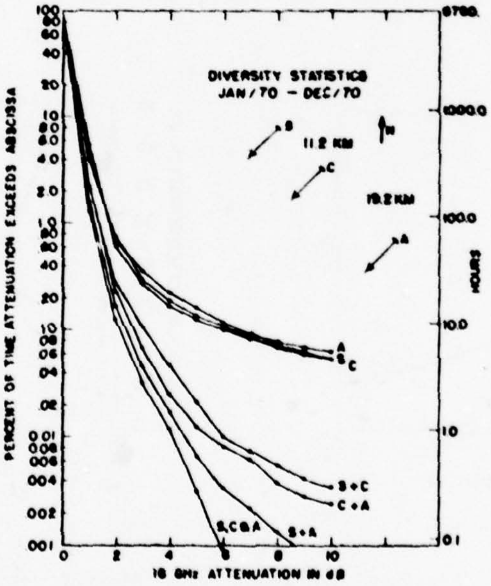

Figure 14. Influence of separation distance in space diversity.

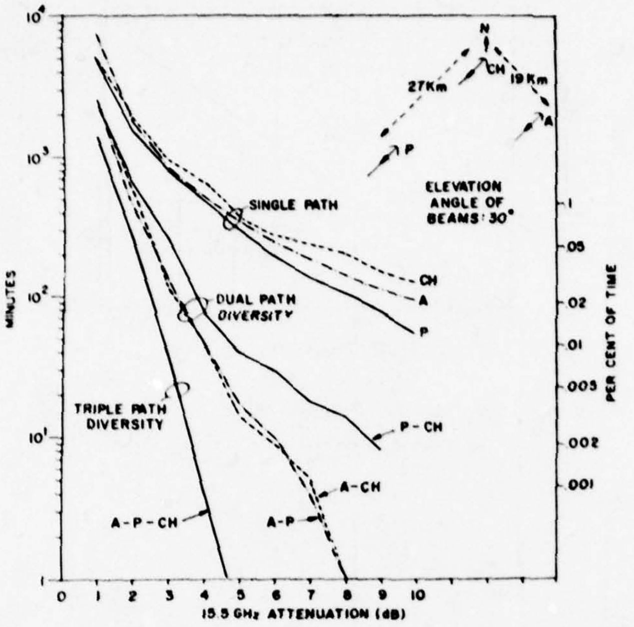

Figure 15. Influence of baseline orientation in space diversity.

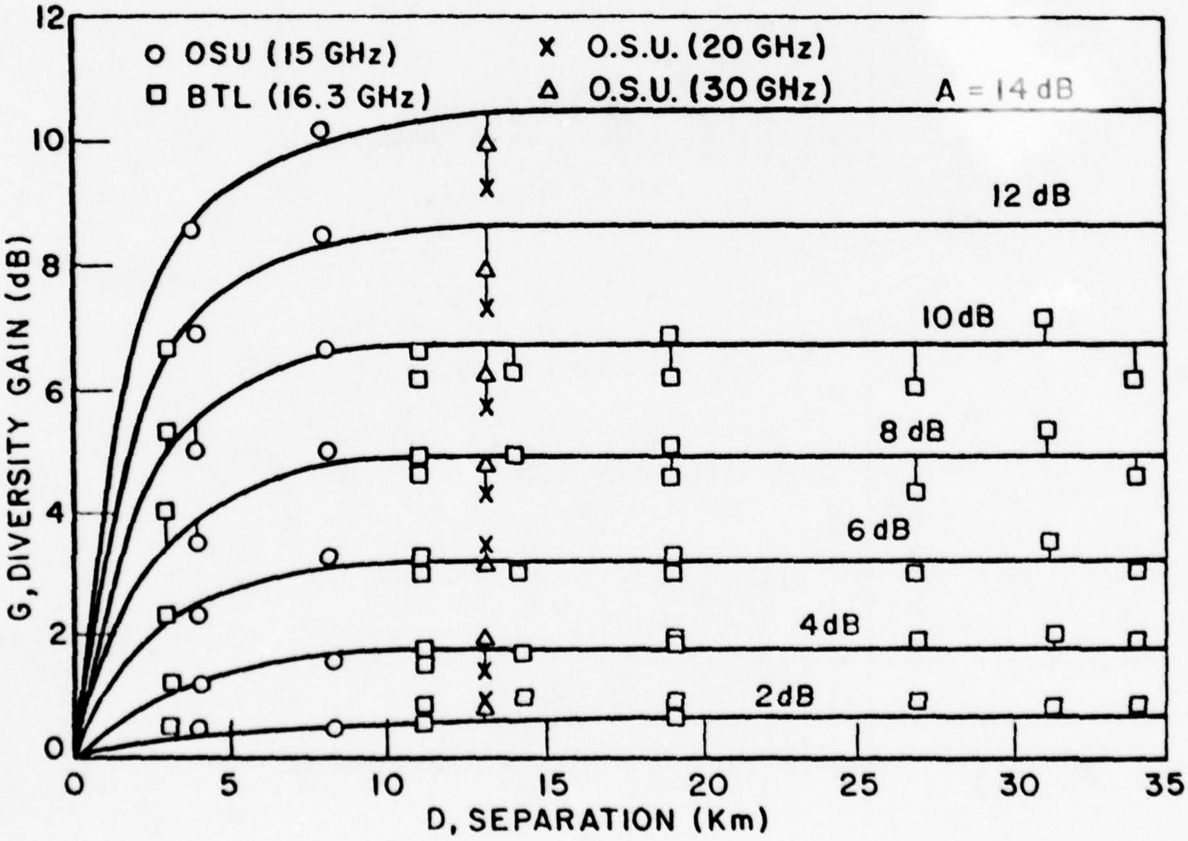

Figure 16. Diversity gain versus separation distance.

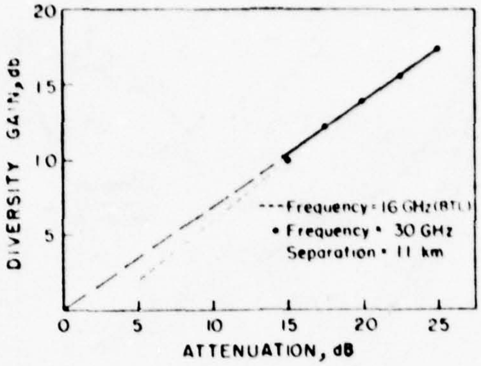

Figure 17. Influence of frequency on diversity gain.

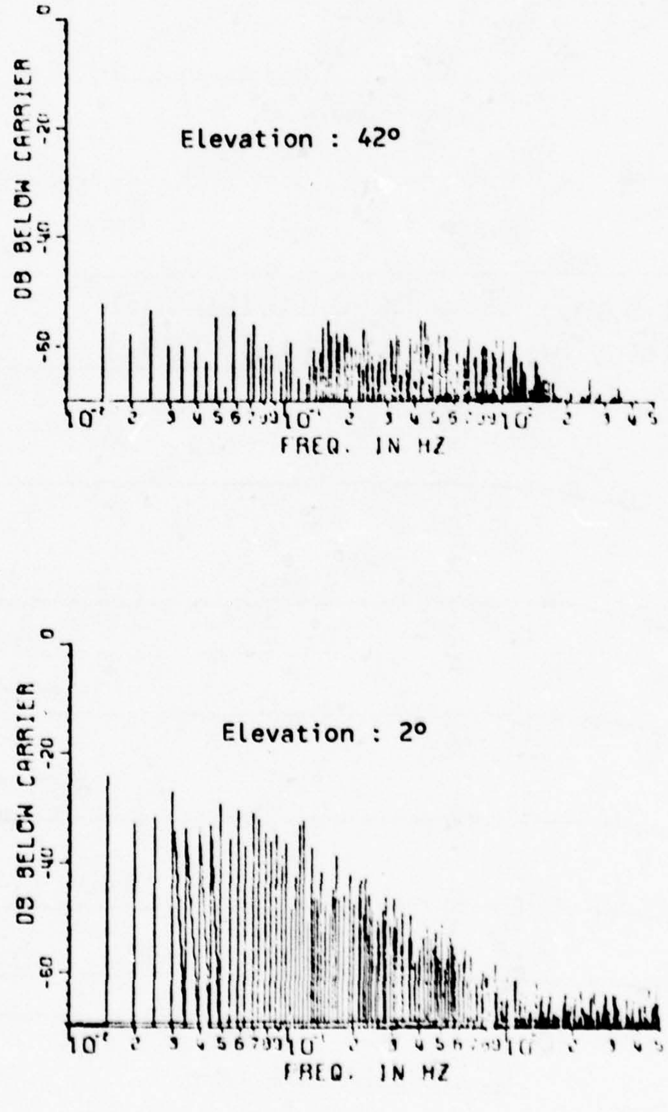

Figure 18. Power spectrum at 42 and 2° elevation, at 20 GHz

DISCUSSION

Comment by E.Altshuler, US

I would like to comment on the advantages and disadvantages of using a radiometer for estimating atmospheric attenuation. The main advantage is that long term statistical data can be obtained continually at any elevation angle at very low cost. The disadvantage is that rain attenuations above approximately 10 dB which are estimated from atmospheric emission measurements become less accurate since scattering losses which are not included in the emission become appreciable and must be taken into account. Methods for estimating the scattering losses have been published. A limitation of using a radiometer for propagation measurements is that no information on depolarization on bandwidth can be obtained.

C.P.Fischer, FRG

(1) Are the reported values to the enormous depolarisation referred to linear or circular polarisation?

(2) Is there any difference in the depolarisation at circular or linear polarised waves?

Author's Reply

The reported values are obtained for linear polarisation. There is a difference between results obtained in circular and in linear polarisation, on attenuation, depolarisation and fluctuation measurements. The proceedings, on the E.S.A. symposium at Genoa (20–30 GHz bands, ESA-SP-138, 1977) offer quite a lot of information on this subjec

F.Feds, Italy

In your excellent review you have shown advantages and disadvantages of direct (beacon measurements) and indire methods (passive radiometer and radar) to obtain attenuation statistics for earth satellite radiolinks. On the basis of the data collected so far, what method would you suggest to obtain reliable statistical information on attenuation at these frequencies on slant paths?

Author's Reply

It seems that radiometry during several years (3 or 4) may be sufficient for obtaining reliable statistical informatior if the radiometry is calibrated on a satellite beacon at that particular location, which takes into account the "average" rain distributions at that place.

S.Kulpa, US

What do you expect to be the effects of including near-field patterns when interpreting the various slant path measurements?

Author's Reply

A paper has been published by Watson (Electr. Letters, 1978) showing that rain attenuation measurements do not depend on the near field. When using radar however, Nicobeck (A.E.V. 1974 and 1976) has shown that there is an influence from the difference between the near field and the far field.

ATMOSPHERIC INFLUENCES ON THE MILLIMETER AND SUBMILLIMETER WAVE PROPAGATION

Karl-Erdmann Fischer

Amt für Wehrgeophysik
5580 Traben - Trarbach, Germany

SUMMARY

The paper is a review of the millimeter and submillimeter wave propagation in the atmosphere emphasizing the problems arising at the attempt of parameterisation and numerical prediction of the interference with radio systems in the above-mentioned frequency range from the influence exerted by the atmosphere.
The first main part deals with the various types of interaction of the millimeter and submillimeter wave propagation with the influence of the atmosphere as well as with their mathematical approach. The second part begins with the supply of meteorological input data for computing the effect caused by hydrometeors, by molecular absorption and mere refraction. Furthermore, an account is given of the applicability of meteorological routine measurements to radio techniques as well as of special measurements of drop size distributions and precipitation intensities.

1. INTRODUCTION

Due to an increasing shortage of radio frequencies, it is necessary to use millimeter and submillimeter waves for radio communication links. Here, however, the atmosphere produces disturbing effects which cannot be controlled by technical means. So, an unrestrained use of this frequency range or an application of frequency reuse techniques is not secured in any case.

The first part of this review paper deals with the influence of the atmosphere on millimeter and submillimeter wave propagation. In the second part, methods for analysis and prediction of propagation conditions in actual weather situations and for planning are discussed.

2. TRANSMISSION PROPERTIES OF THE ATMOSPHERE

First, the main influences of the atmosphere on millimeter and submillimeter wave propagation are summed up briefly.

2.1. Hydrometeors

Disturbances caused by hydrometeors constitute one of the main difficulties in using the millimeter and submillimeter band. These effects undergo strong space and time fluctuations, and a quantitative analysis suffers from a lack of input data.

Hydrometeors are defined as condensation products of water vapour which are suspended in the atmosphere. They can be fluid (e.g. rain, fog) or solid (e.g. snow, ice crystals). Sometimes, there exists a mixed form (e.g. melting hail, wet snow). The influence of hydrometeors can be described by solutions of the vectorial wave equation. The choice of appropriate dielectric constants of the precipitation particles is part of the boundary conditions. Suitable theories have been set up, for example, by Mie and - in the case of very small particles compared with the wavelength - by Rayleigh (Lammers, 1965). There are expressions for the total attenuation cross-section which is composed of a back scattering cross-section and an absorption cross-section.

Attenuation caused by hydrometeors can be calculated if the rain drop size distribution between transmitter and receiver is known. Directional radio systems operating in the same frequency - especially - satellite communications - may suffer from severe cross talking caused by scattering on hydrometeors even when using strong beaming antennas (e.g. Crane, 1977; Chu, 1977; Li at al., 1977). In this case, too, the magnitude of the effect can be estimated by Mie's theory, for example, if the rain drop size distribution is given. (Scattering due to inhomogeneities of the atmospheric refractive index is of a smaller order of magnitude and is not concerned here.)

Beyond this, hydrometeors will turn the plane of polarisation of electromagnetic waves more or less (e.g. Crane, 1977; Neves, Watson 1977; Hogler et al., 1977). So, synchroneous communication between parallel radio links using the same frequency but cross-polarized antennas will be disturbed by cross talking due to depolarisation. Finally, the effectiveness of polarisation diversity will be reduced by depolarisation.

A more subtile analysis of Mie's theory shows that depolarisation is mainly due to deviations of the shape of the scattering particles from spherical form (e.g. Crane 1977). In the case of liquid hydrometeors, this effect is brought about by variations of the wind gradient (Brussaard 1976). Enhanced depolarisation is observed in connection with solid particles, especially if strong electrical fields are present - e.g. in shower and thunderstorm clouds (Mc Cormick, Hendry 1977; Evans et al. 1977). Strong field strength changes due to lightning discharges will lead to sudden changes of depolarisation (Shutie et al., 1977). A quantitative analysis of depolarisation requires not only the size distribution of hydrometeors but also informations concerning their shape. Because, normally, the latter is not available, there are attempts for looking for empirical relations between depolarisation and attenuation which can be determined in an easier way (Nowland et al., 1977; Strichland et al., 1977). These correlations, however, sometimes yield biased results, so that their practicability is reduced.

2.2. Molecular absorption

The reliability of a millimeter or submillimeter radio link is not only impaired by hydrometeors but also by molecular absorption in the atmosphere mainly due to water vapour and oxygen. In certain frequency ranges, communication will break down even on very short links (e.g. several 100 m) - especially in the submillimeter range.

Molecular absorption is caused by interactions between electromagnetic waves and gases. It results in selective attenuation. Atomic and molecular physics provide the tool for computing central frequencies, band widths and intensities of absorption bands. So, attenuation coefficients which strongly depend on the frequency can be derived if the distribution of water vapour and oxygen along the propagation path is known (Liebe 1977). These computations usually agree well with laboratory tests (Liebe, et al., 1977).

According to Kirchhoff's law, a medium penetrated by electromagnetic radiation will re-radiate in those frequency ranges where absorption occurs. So, the signal to noise ratio is reduced when using frequencies in the centre or in the vicinity of absorption bands (Albrecht 1972; Hall, 1977).

2.3. Refraction

In the millimeter and submillimeter range, the influence of mere refraction - that is the actual deviation of the path of an electromagnetic wave compared to vacuum conditions - is exceeded by the effects caused by hydrometeors and by molecular absorption. A consequent analysis based on simple ray theory is cumbersome or impossible, resp., because of dispersion and the existence of numerous absorption lines and bands. A complex refractive index combines the influences of refraction (real part) and absorption (imaginary part).

In the case of specific vertical distributions of the (real) refractive index - mainly given by the vertical profiles of atmospheric humidity and temperature - multi-path conditions between transmitter and receiver are possible. (Cartwright, Tattersall 1977). Especially on line-of-sight paths, deep interference fading will occur (Hartmann, Smith 1977). Diversity techniques and tilting the antennas, for example, are used for corrective measures.

Short small scale fluctuations of the (real) refractive index of the atmosphere caused by atmospheric turbulence will sometimes lead to marked scintillation fading (Ho et al., 1977). Even man made turbulence produced by chimneys or exhausters of air condition devices, for example, gives rise to scintillation fading (Mavrokouloulakis at al., 1977). Antenna or frequency diversity can be used for remedy. Refraction effects can be estimated if the refractive index distribution and its fluctuations are known.

3. ANALYSIS AND FORECASTING OF ATMOSPHERIC INFLUENCES

In the case of millimeter and submillimeter propagation, the theoretical approach to estimating the influence of hydrometeors, molecular absorption, and refraction is available. An appropriate analysis and forecasting of propagation conditions suitable for practical use is mainly a problem of sampling meteorological data. Forecasts, weather charts, statistics, etc, supplied by the weather services can be used only with caution. Therefore, often, special measurements are necessary, especially if qualitative results are not sufficient.

3.1. Effects caused by hydrometeors

A consequent analysis of disturbances caused by hydrometeors is often not feasible because of the lacking information on the actual and the expected size distribution within the common volume covered by the patterns of the antennas. Moreover, calculations of depolarisation require information about the shape of the hydrometeors and - in some special cases - about the electrical fields in shower and thunderstorm clouds.

3.1.1. Meteorological routine measurements

For radiocommunication purposes, the informations supplied by the weather services can often be used only in a qualitative way. Precipitation totals (e.g. 12 or 24 hourly) are of no use because actual intensities cannot be derived from them.

Only few meteorological observation sites are equipped with devices for measuring precipitation intensities. But usually, the integration time of the instruments in use (some minutes) is too long compared with the disintegration required for propagation purposes (some seconds). Moreover, there is a considerable lack of accuracy in the range of small and medium precipitation intensities - a disadvantage with respect especially to the submillimeter range. A satisfactory regional break-down cannot be achieved because of the above mentioned small number of stations.

A general analysis or detailed forecast of the meteorological situation (e.g. no precipitation at all, locally light rain, heavy shower with thunderstorm) is helpful for qualitative conclusions on the occurrence of disturbances due to hydrometeors.

Weather radar (operational frequency in the cm-band) is a very useful tool to determine location, speed and direction of movement of precipitation fields and their horizontal and vertical structure within an area of about 100 km in radius and more around the station.

Backscattering, attenuation, and depolarisation can be estimated when using the measured echo intensities and empirical relations (iso-echo-techniques).

In spite of shortcomings due to inadequacies of radar equipment, in the above mentioned relations, and in organisation of the observation network, the weather radar is an appropriate instrument for analysis and short term forecasts of propagation conditions (up to some hours) in the millimeter and submillimeter range. It is also suitable for operation at sea where conventional methods of measuring precipitation sometimes yield biased results.

3.1.2. Special meteorological measurements

Exact modelling of hydrometeor effects on millimeter and submillimeter radio links requires information on drop size distribution within the common volume covered by the pattern of transmitting and receiving antennas. Distrometer measurements are very helpful to reach this aim. A disintegration time down to few seconds can be achieved, and the size classes to be determined cover a range from 0.3 to 5 mm in 20 steps (Breuer, 1973; Kreuels, 1977). The measured time dependent drop size distribution can easily be transformed into rain intensities.

The principle of a distrometer is based upon an electrodynamical receptor which changes the impulse of a falling rain drop into an electric signal so that electronical data processing and evaluation can be employed.

Unfortunately, distrometers are rather expensive and complicated in operating so that, today, routine measurements at a sufficient number of observation sites are not achievable. So, for example, distrometer measurements are used to derive drop size distributions in dependence of different weather situations. By this means, relations with meteorological measurements (to achieve with less expenditure) could be established.

3.1.3. Planning of millimeter and submillimeter radio links

Precipitation statistics supplied by the climat departments of the meteorological services should carefully be interpreted to avoid severe misinterpretations when planning millimeter or submillimeter radio links. Figures concerning monthly or daily mean values of precipitation or even hourly mean values do not answer the question for frequency and duration of precipitation of a given intensity. Generally, only self-recordings during at least several years provide results usable for planning millimeter and submillimeter links. Moreover, a regular analysis of weather radar observations will contribute to a "radio climatology".

Climatological statistics of frequency and duration of fog, however, are advantageous for planning purposes because there are empirical relationships between visibility in fog and drop size distribution. So, for example, attenuation concerning the smaller wavelengths of the discussed frequency range can be estimated.

3.2. Molecular absorption

Molecular absorption caused by the atmosphere usually does not necessitate daily analysis or forecasting because its variations are not so large as in the case of hydrometeor effects.

Vertical soundings af atmospheric humidity and temperature run by the weather services every 12 hours with spacings of about 200 - 300 km will supply informations on the vertical distribution of the water vapour content of the atmosphere. Near the surface, however, radiosonde data are not reliable. Special soundings, e.g. with tethered balloons, will lead to better results - especially in mountainous areas.

The actual profile of oxygen has to be determined by special soundings because there are no routine measurements by the meteorological service.

3.3. Refraction

Vertical soundings of the atmosphere as mentioned above can be used to compute effects due to mere refraction, e.g. multipath fading or extremely long ranging. There are well established formulas correlating the (real) refractive index and air pressure, humidity, and temperature (Kruspe, 1965).

Measurements of actual refractive index fluctuations caused by atmospheric turbulence with respect to scintillation fading need much expenditure. As a rule, they are taken up only within the scope of special research programmes. Appropriate statistics are available, today (e.g. Kruspe 1972).

For practical use in the millimeter and submillimeter range, it is often sufficient to use some empirical rules to estimate and forecast disturbances due to mere refraction. Multipath fading and extremely long ranging, for example, is to be expected if the antennas are located near atmospheric layers where the air humidity undergoes sharp discontinuities, e.g. over vast, damp areas during clear, calm nights with strong upward thermal radiation. Enhanced scintillation fading may occur near the (humid) ground during strong solar radiation and windy weather.

4. CONCLUSIONS

Effects caused by hydrometeors - e.g. attenuation, cross talking due to scattering or depolarisation - will sometimes lead to severe restrictions in using millimeter or submillimeter waves. An analysis and forecast of these effects is necessary because of their considerable inhomogeneity and variability with respect to time and space.

The consequence of molecular absorption by water vapour and oxygen is a strong frequency dependent attenuation. Especially, the use of the submillimeter band is hampered by this effect.

Mere refraction leads to multipath and scintillation fading and to extremely long ranging. But, as a rule, these effects are considerably exceeded by the foregoing influences.

The effects mentioned above can be evaluated by existing mathematical methods. For practical use, meteorological input data are necessary. Among the routine measurements carried out by the weather services, weather radar data provide an analysis and a short term forecast of millimeter and submillimeter propagation conditions. On the other hand, conventional routine weather analysis, forecasts, and statistics will give only qualitative hints. They have to be interpreted carefully, especially in the case of planning radio links.

Special measurements, e.g. by distrometers, are suitable for providing the desired input data on precipitation. But as a rule, they are very expensive. So parametrisation techniques based on meteorological routine measurements may give approximative solutions.

REFERENCES

ALBRECHT, H.J., 1972, "The Identification of Military Utilisation of Frequency Bands above 10 GHz"
AGARD Advisory Report No. 42 (NATO RESTRICTED)

BREUER, L. and R. KREUELS, 1973, "Rainfall intensity distribution, drop size spectra and attenuation measurements at Bonn, Germany"
I.U.C.R.M. Colloq. Nice, Tome 2, IV-16

BRUSSAARD, G., 1976,"A Meteorological Model for Rain-Induced Cross Polarisation"
IEEE Transactions on Antennas and Propagation, Vol AP-24, No. 1

CARTWRIGHT, N.E. and R.L. TATTERSALL, 1977,"Simultaneous Measurements of Radio Refractivity and Multipath Fading on 2 July 1975 at 11, 19 and 36 GHz on a 7.5 km Path"
Electronics Letters, Vol. 13, No. 7

CRANE, T.S., 1977, "Rain-Scatter Interference on an Earth-Space Path"
IEEE Transactions on Antennas and Propagation, March 1977

HALL, M.P.M., 1977,"Variability of Atmospheric Water-Vapour Concentration and its Implications for Microwave-Radio-Link Planning"
Electronics Letters, Vol. 13, No. 21

HARTMAN, W.J. and D. SMITH, 1977, "Tilting Antennas to Reduce Line-of-Sight Microwave Link Fading"
IEEE Transactions on Antennas and Propagation, Vol. AP-25, No. 5

HO, K.L. et al., 1977, "Wavelength Dependence of Scintillation Fading at 110 and 36 GHz"
Electronics Letters, Vol. 13,No. 7

HOGLER, J.L. et al., 1975, "Statistical Variations in Forward Propagation Rain Depolarisation due to Drop Size Fluctuations"
IEEE Transactions on Antennas and Propagation, May 1975

KREUELS, R., 1977,"Strukturanalysen und Statistik des Niederschlages auf einminütiger Kurzzeitmeßbasis und das Problem der indirekten Niederschlagsbestimmung mittels Radar"
Dissertation, Bonn

KRUSPE, G., 1965, "Der atmosphärische Brechungsindex und seine Messung mit Mikrowellenrefraktometern"
Technische Mitteilungen aus dem Institut für Radiometeorologie und Maritime Meteorologie an der Universität Hamburg - Institut der Fraunhofer-Gesellschaft

KRUSPE, G., 1972 "Autospectra of radio-refractive index, vertical wind, temperature, and humidity, cospectra of vertical turbulent fluxes of heat and moisture above the sea"
Berichte des Institutes für Radiometeorologie und Maritime Meteorologie an der Universität Hamburg - Institut der Fraunhofer-Gesellschaft

LAMMERS, U., 1965 "Untersuchungen der Niederschlagseinflüsse auf die mm-Wellenausbreitung"
Dissertation, Bonn

LI, Z. et al., 1977, "Forward Scattering due to Rain at 11 GHz"
IEEE Transactions on Antennas and Propagation, Vol. AP-25, No. 5

LIEBE, H.J., 1977,"EHF Properties of Air"
Nachrichtentechnische Zeitschrift (NTZ) , Vol. 30, No. 1

LIEBE, H.J. and J.D. HOPPONEN, 1977, "Variability of EHF Air Refractivity with Respect to Temperature, Pressure, and Frequency"
IEEE Transactions on Antennas and Propagation, Vol. AP-25, No. 3

LIEBE, H.J. et al., 1977, "Atmospheric Oxygen Microwave Spectrum - Experiment versus Theory"
IEEE Transactions on Antennas and Propagation, Vol. AP-25, No. 3

MAVROKOUKOULAKIS, N.D. et al., 1977 "Observation of Millimetre-Wave Amplitude Scintillations in a Town Environment"
Electronics Letters, Vol. 13, No. 14

MCCORMICK, G.C. and A. HENDRY, 1977, "Depolarisation by Solid Hydrometeors"
Electronics Letters, Vol. 13, No. 3

NEVES, J. and P.A. WATSON, 1977, "Propagation Coefficients for Vertically and Horizontally Polarized Waves at 36.5 GHz"
Electronics Letters, Vol.13, No. 21

NOWLAND, W.L. et al., 1977, "Theoretical Relationship between Rain Depolarisation and Attenuation"
Electronics Letters, Vol. 13, No. 22

SHUTIE, P.F. et al., 1977, "Satellite-Ground Signal Depolarisation at Millimetre Wavelengths Through Thunderstorms"
Electronics Letters, Vol. 13, No. 19

STRICKLAND, J.I. et al., 1977, "Measurements of Depolarisation and Attenuation at 11.7 GHz by Using the Communications Technology Satellite"
Electronics Letters, Vol. 13, No. 24

REALISATION D'EQUIPEMENTS EMISSION RECEPTION POUR SYSTEMES DE TRANSMISSION AUX LONGUEURS D'ONDES MILLIMETRIQUES ET APPLICATION A L'ETUDE DES CARACTERISTIQUES RADIOELECTRIQUES DANS LA REGION PARISIENNE

J.R. MAHIEU
R. DEVINNE
S.A. LIGNES TELEGRAPHIQUES ET TELEPHONIQUES
Département Hyperfréquence
B.P. N° 5
78702 - CONFLANS-STE-HONORINE
France

RESUME

Dans la première partie de l'exposé nous décrirons des équipements hyperfréquence constituant les étages haute fréquence et fréquence intermédiaire de divers systèmes de transmission fonctionnant aux longueurs d'ondes millimétriques dans la gamme de fréquences comprises entre 30 et 110 GHz.

Dans la deuxième partie une liaison radioélectrique constituée en particulier à l'aide des équipements étudiés dans la première partie sera décrite, et les caractéristiques de propagation radioélectrique à 31 GHz suivant différentes conditions de propagation seront données.

1 - ETUDE D'EQUIPEMENTS EMISSION RECEPTION POUR SYSTEMES DE TRANSMISSION AUX LONGUEURS D'ONDES MILLIMETRIQUES

Notre effort a porté particulièrement au niveau des sous-ensembles fonctionnels tant au point de vue des circuits mis en oeuvre que de celui des technologies, et dans tous les cas, les meilleurs compromis technico-économiques ont été recherchés.

1.1 - Etude des sous-ensembles modulateurs

1.1.1. - Modulation directe

Des modulateurs de phase $0, \pi$ utilisant respectivement des diodes PIN et des diodes Schottky ont été réalisés dans la gamme de fréquences de 30 à 45 GHz. (Fig.1).

Le modulateur est constitué d'un circulateur qui sépare l'énergie entrante de l'énergie sortante, associé à une structure à diode. Celle-ci constitue un court-circuit ou un circuit ouvert, selon qu'elle est saturée ou bloquée, et commute une longueur de guide d'onde réglable par un court-circuit, qui permet d'obtenir un écart de phase de 180°. Le signal modulant est appliqué à la diode par l'intermédiaire d'un système de piège assurant un découplage entre les accès "modulateur" et signal millimétrique.

Dans le cas du modulateur à diode PIN, les puissances modulables peuvent être importantes ($\geq$ 23 dbm), les pertes inférieures à 2,5 dB mais le rythme de modulation est limité à 20 Mbit/s. Par contre, pour les modulateurs à diode Schottky, les rythmes peuvent atteindre 400 Mbit/s. Les diodes utilisées sont des puces, polarisées à l'aide d'un fil épointé à faible self. Les pertes otenues sont inférieures à 5 dB, mais la puissance incidente est limitée ($\leq$ 5 mW). L'emploi d'un amplificateur est alors nécessaire.

1.1.2. - Modulation en fréquence intermédiaire

Des modulateurs de phase $0, \pi$ ont été réalisés en bande L (1,2 à 1,8 GHz) en technologie microélectronique utilisant deux coupleurs 3 dB.

Des diodes PIN ou Schottky sont employées selon le débit numérique du système de transmission concerné.

Des pertes d'insertion inférieures à 0,5 dB, pour des variations de phase de 180°, ont été obtenues avec ces dispositifs.

1.2 - Etude des transposeurs de fréquences d'émission aux longueurs d'ondes millimétriques

1.2.1. - Transposeurs de fréquences haut niveau à varactor AsGa

Divers dispositifs permettant la transposition de fréquences intermédiaires bande L à des fréquences supérieures à 30 GHz ont été réalisés. Les diodes utilisées sont des varactors montés dans des structures guide d'ondes apériodiques associées à des circulateurs très faibles pertes. (Fig. 2). Ces mélangeurs comportent en outre un filtre de réjection et d'élimination de bande latérale inférieure. De tels transposeurs de fréquences présentant d'excellentes caractéristiques de conversion amplitude phase (inférieure à 1° par dB) et des pertes de conversion inférieures à 6,5 dB dans de très larges bandes passantes ($>$ 1 GHz) pour des puissances de sortie supérieures à 17 dbm, ont été obtenus.

1.2.2. - Transposeurs de fréquences bas niveau à diodes Schottky associés à des amplificateurs à diode à avalanche

Des essais en émission d'utilisation de mélangeurs à diodes Schottky utilisés habituellement en réception ont été effectués.

Il a été possible, par une simple modification de certains filtres utilisés dans la structure, de réaliser des transposeurs de fréquences à diodes Schottky fonctionnant à l'émission qui présentent des pertes de conversion inférieures à 10 dB jusqu'à des fréquences de 50 GHz. Cependant, le niveau de sortie de tels mélangeurs reste limité à des puissances relativement faibles, inférieures à 7 dbm, de telle sorte qu'il est souvent nécessaire d'y associer des amplificateurs à état solide.

Une association comprenant un transposeur de fréquences à diode Schottky associé à un amplificateur à diode à avalanche a été réalisée. L'amplificateur fonctionne en réflexion par l'intermédiaire d'un circulateur. La diode Impatt est polarisée à travers un filtre passe-bas éliminant les oscillations parasites. Un adaptateur d'impédance est inséré entre le circulateur et la diode. Le niveau de sortie de l'association transposeur-amplificateur présente un niveau de sortie comparable à celui du mélangeur haut niveau à varactor.

Il faut cependant noter que dans le cas du transposeur à diodes Schottky, la puissance de l'oscillateur local est de 10 mW alors que dans le cas du transposeur à varactor, elle est de 200 mW.

1.3 - Etude des transposeurs de fréquences de réception aux longueurs d'ondes millimétriques

1.3.1. - Transposeurs de fréquences faible bruit

Une gamme importante de mélangeurs faible bruit réalisés en technologie microélectronique couvrant la bande de 30 à 120 GHz a été developpée dans nos laboratoires.

Les technologies mises en oeuvre pour la réalisation de ces mélangeurs ont permis d'obtenir des fréquences intermédiaires pouvant varier entre 50 MHz et 5 GHz.

La réalisation de tels mélangeurs n'a été rendue possible que grâce au développement de transition guide-circuit microélectronique large bande: ces transitions ont été réalisées sur substrat quartz. Elles présentent un T.O.S. inférieur à 1,20 jusqu'à la fréquence de 50 GHz et un affaiblissement inférieur à 0,1 dB. De 50 à 70 GHz, le T.O.S. reste inférieur à 1,40 et les pertes à 0,3 dB.

Les mélangeurs sont du type à une diode; l'entrée de l'oscillateur local et du signal s'effectuant par l'intermédiaire d'un circulateur. Un filtre associé au circulateur réfléchi le signal sur le mélangeur. (Fig.3).

Les diodes utilisées sont des beam-lead AsGa. Les pertes de conversion restent inférieures à 5,5 dB de 31 à 45 GHz et inférieures à 7 dB jusqu'à 70 GHz. Dans la gamme de fréquences de 70 à 110 GHz une technologie différente a été employée. Les diodes utilisées sont des diodes en puce Schottky AsGa raccordées par fil épointé sur la structure microélectronique. Cette technologie permet d'obtenir des pertes de conversion inférieures à 6 dB jusqu'à 110 GHz. Ce type de mélangeur est utilisable sans aucune modification à température cryogénique pour des applications en radioastronomie par exemple.

1.3.2. - Dispositifs amplificateurs à fréquence intermédiaire

Des amplificateurs large bande ont été réalisés à L.T.T. en technologie microélectronique.

Certains de ces amplificateurs ont été associés à des dispositifs générateurs de bruit à diodes Schottky et developpés dans la bande 1,2 à 1,7 GHz. (Fig. 4).

Le générateur de bruit est composé d'une diode Schottky polarisée en inverse, d'un amplificateur de bruit et d'un coupleur 3 dB. L'excès de bruit produit par la diode (18 à 28 dB) est gaussien pour un courant de polarisation de 0,2 à 2 mA. Le circuit complet est réalisé en technologie microélectronique et permet de tester l'augmentation du taux d'erreur en fonction de la dégradation du rapport signal à bruit d'une liaison.

2 - ETUDE DES CARACTERISTIQUES DE PROPAGATION RADIOELECTRIQUE A 31 GHz DANS LA REGION PARISIENNE

Les variations de l'affaiblissement de propagation des transmissions radioélectriques aux longueurs d'ondes millimétriques dépendent exclusivement des fluctuations des conditions atmosphériques. De nombreuses études théoriques et expérimentales ont été publiées par de nombreux auteurs ([1] [2] [3] [4]). Les gaz atmosphériques, la vapeur d'eau et les différentes précipitations (pluie, neige, grêle...) sont les principaux responsables des variations d'absorption. En théorie, l'absorption des gaz et des molécules d'eau se fait à des fréquences discrètes, mais différents phénomènes, en particulier la pression atmosphérique, font que le spectre d'absorption s'étend sur toute la gamme des longueurs d'ondes millimétriques. L'absorption engendrée par les molécules d'oxygène est assez bien connue et pratiquement constante, sa densité variant très peu. Sa variation peut être considérée comme nulle sur une liaison de faible distance. Les évanouissements les plus importants sont dus à la variation de la masse d'eau par une unité de volume d'air humide (humidité absolue en g/m^3) brouillard et aux précipitations.

---

[1] J.W. Ryde and D. Ryde, "Attenuation of centimetre and millimetre waves by rain, hail, fogs, and clouds", RES.Labs. of the General Electric Company, Wembley, England, Rep.8670,1945.

[2] J.R. Norbury and W.J.K. White, "Microwave attenuation at 35,8 GHz due to rainfall", Electron. Lett. Vol.8 pp. 91-92, 24 Feb.1972.

[3] J.O. Laws and D.A. Parsons, "The relation of raindrop-size to intensity", Trans.Amer.Geophys. Union Vol.24, pp.452-460, 1943.

[4] R.L. Olsen, D.V. Rogers, D.B. Hodge, "The aR^b Relation in the calculation of rain attenuation" IEEE Trans.Ant.and Propag., Vol.A.P.26, N°2, March 1978.

Des études systématiques ont été entreprises afin de relever les différentes perturbations apportées par ces différents éléments sur le niveau de réception d'une liaison et d'en déduire un certain nombre d'éléments essentiels à l'établissement d'un projet industriel. (Dynamique des CAG, pourcentage du temps pendant lequel la liaison est inexploitable,...).

2.1 - Equipements et système de mesure

A l'aide des matériels décrits précédemment, une liaison radioélectrique à 31 GHz sur une distance de 500 m a été installée dans la région parisienne, à Conflans-Ste-Honorine. Les aériens utilisés sont des antennes paraboliques munies de radômes de gain de 30 dB, installés à une hauteur suffisante pour éviter les évanouissements importants et assurer une propagation pratiquement libre. Les oscillateurs locaux utilisés sont des oscillateurs à état solide, stabilisés en température et délivrant pour l'oscillateur local d'émission une puissance CW de 23 dbm. A cet oscillateur local d'émission est associé un enregistreur permettant de relever les fluctuations occasionnelles en fonction de la température. A la réception, un système sensible et stable a été developpé dans la plage de dérive des oscillateurs locaux pour une gamme de température de - 10° C à + 50° C. Ce système de réception est du type superhétérodyne comportant un mélangeur en structure microélectronique décrit précédemment. Le facteur de bruit de l'ensemble de la chaine de réception à l'entrée du mélangeur a été mesuré et est égal à 7 dB. La sensibilité de la chaine de réception, pour une bande de bruit de 40 MHz, est meilleure que 90 dbm. Des systèmes d'enregistrements automatiques des résultats ont été mis au point de telle sorte qu'il a été possible de réaliser tout au long de l'année des enregistrements significatifs des conditions climatiques qui prévalent en région parisienne. Des pluviomètres, des sondes de température et d'humidité ainsi que des enregistreurs continus de la puissance de réception ont été notamment installés sur la liaison.

2.2 - Résultats expérimentaux

Dès le mois d'avril 1977, une observation systématique et continue de cette liaison a été entreprise. Des mesures de l'affaiblissement de propagation par temps clair ont été effectuées et les résultats obtenus sont en bon accord avec la théorie. (116,2 dB d'affaiblissement pour 500 m).

Grâce au système d'enregistrement automatique des conditions atmosphériques et des variations de l'affaiblissement mis en place, il a été possible de constater que sur une liaison aussi courte, la variation du taux d'humidité absolue qui a oscillé durant toute cette période entre $3g/m^3$ d'air humide et $15g/m^3$, n'a eu aucune influence mesurable sur l'affaiblissement de propagation.

Les relevés du coefficient d'atténuation en fonction de l'intensité de la pluie sont représentés sur la figure 5. L'on peut remarquer que l'intensité maximale des précipitations relevée durant toute cette période a atteint l'équivalent de 64 mm/heure pendant 4 minutes. La variation d'affaiblissement correspondant à cet orage a été de 6,2 dB pour les 500 m de la liaison.

Depuis le mois d'avril 1977, la dégradation des pertes de propagation provoquée par les précipitations n'a excédé 3 dB que pendant une durée totale de 45 minutes.

3 - CONCLUSION

Dans le cas d'une transmission radioélectrique à 31 GHz, l'augmentation des pertes due aux précipitations peut être compensée sur des distances de l'ordre de 5 km. Nous pensons aussi, grâce également aux progrès réalisés dans le domaine des composants et sous-ensembles, qu'il est possible désormais de réaliser des équipements fonctionnant aux longueurs d'ondes millimétriques présentant des performances électriques très satisfaisantes avec des coûts de fabrication très acceptables.

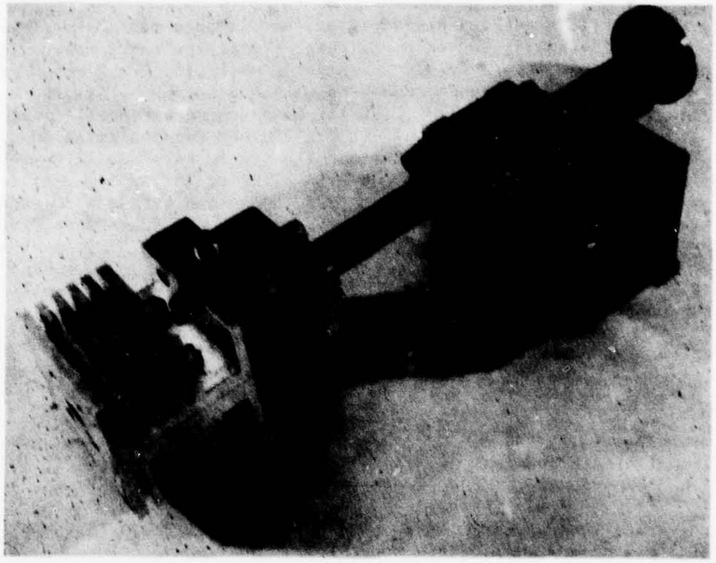

Figure 1 : Ensemble Source-Modulateur PIN

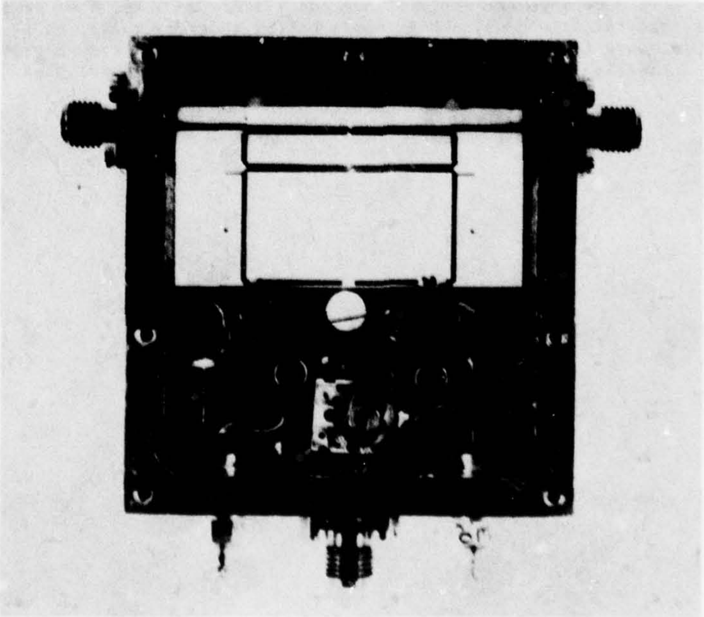

Figure 1 bis : Modulateur bande L

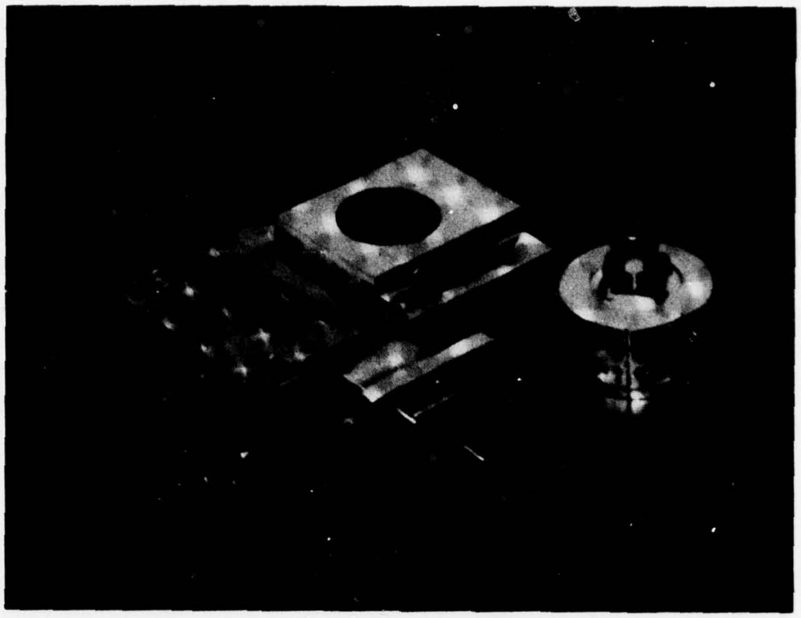

Figure 2 : Transposeur Haut-Niveau à varactor

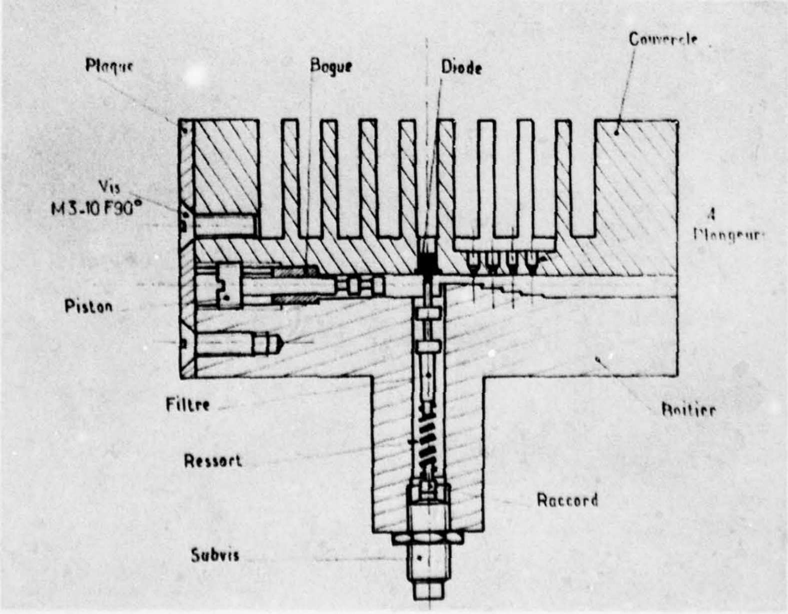
Plaque
Bogue
Diode
Couvercle
Vis
M3-10 F90°
4
Plongeurs
Piston
Filtre
Boitier
Ressort
Raccord
Subvis

Figure 2 Bis : Amplificateur à diode à avalanche

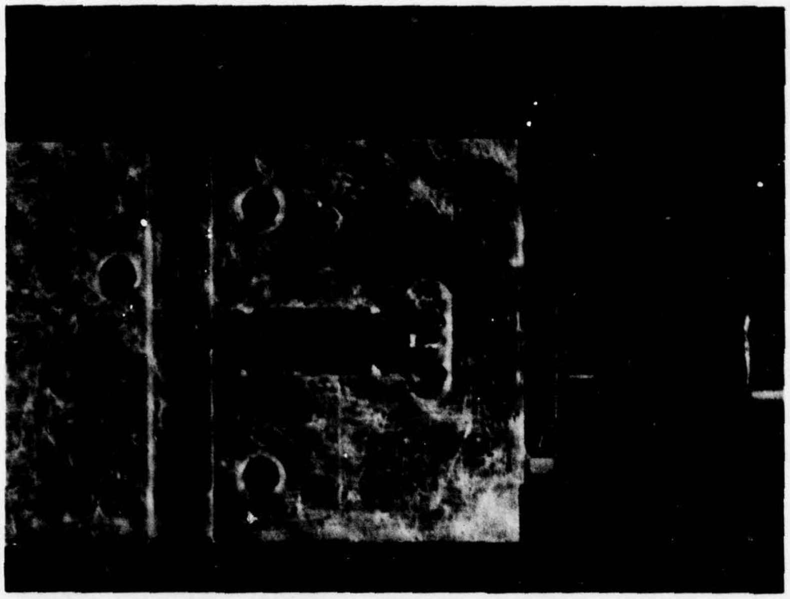

Figure 3 : Transposeur de Fréquence de réception Schottky

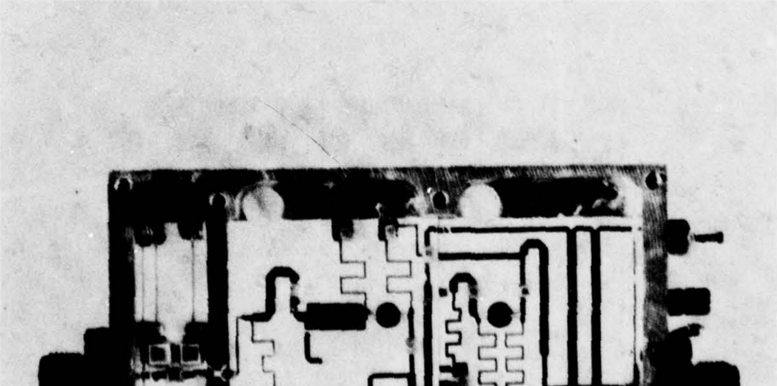

Figure 4 : Ensemble Amplificateur-Générateur de bruit

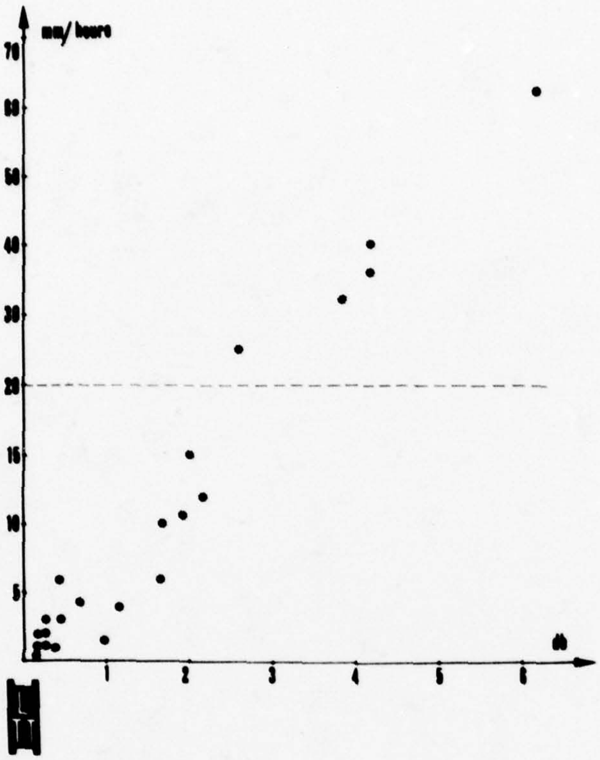

Figure 5 : Atténuation en fonction de l'intensité des précipitations pour une liaison de 500 m

RAIN ATTENUATION MEASUREMENTS AT 94 GHz: COMPARISON OF THEORY AND EXPERIMENT

W.P.M.N. Keizer, J. Snieder and C.D. de Haan

Physics Laboratory TNO

P.O.Box 96864

2509 JG The Hague

The Netherlands

SUMMARY

Measurements have been made of attenuation at 94 GHz caused by rain on a 935 m terrestial path since October 1977. Simultaneously the raindrop size distribution has been measured with a distrometer, together with the rainfall intensity recorded with three rapid response rain gauges spaced about 500 m apart along the propagation path.

Using the actually measured raindrop size distribution and assuming spherical raindrops, the attenuation caused by rain has been calculated with the aid of Mie's scattering theory for water spheres. The result is compared with the measured data. In case of uniform rainfall along the path a good agreement has been observed between the measured and the calculated attenuation.

This paper deals with the description of the propagation link, the experimental results and the comparison between theory and measurement. The paper describes also the decrease of antenna gain at 94 GHz due to water on a 1.2 m Cassegrain antenna. It will be shown that for accurate propagation measurements it is absolutely necessary to equip the antennas with protective shelters.

1.0 INTRODUCTION

Crowding of the microwave frequencies and the readily availability of solid-state and other millimeter wave components has stimulated the use of millimeter wave frequencies for radar and communication. The attenuation due to rain has only a small influence on systems operating in the microwave region, but at millimeter wave frequencies rain attenuation becomes a dominant factor. Hence the knowledge of rain attenuation statistics is of particular interest for reliable system design.

Due to the lack of sufficient reliable rain attenuation data for frequencies around 100 GHz, a propagation experiment at 94 GHz has been set up in the Netherlands in order to supplement these data. At present only two publications (Sander, J., 1975; Zavody, A.M. et al, 1976) are available in which propagation measurements are reported for the frequency range 90-110 GHz. A second objective of this propagation experiment is to make a comparison between the measured rain attenuation and the attenuation calculated from the actually measured dropsize distribution using Mie's scattering theory. It will be shown that the comparison obtained by this approach reveals a much better agreement between theory and experiment than the comparisons where the calculated attenuation is based on one of the commonly used dropsize distributions, such as the Laws-Parsons distribution, Marshall-Palmer one etc.

The measurements of the attenuation due to rain at 94 GHz on a 935 m propagation path have been started in October 1977. Along this propagation path the rainfall rate and the dropsize distribution are recorded simultaneously.

2.0 THEORETICAL CONSIDERATIONS

The attenuation of electromagnetic radiation caused by rain along a propagation path is dependent on the rainfall intensity. For a path of extent L, the attenuation A(dB) through rain at wavelength λ may be written by

$$A = \int_0^L Y(\lambda,z)\,dz$$

where $Y(\lambda,z)$ (dB/km) is the specific attenuation due to rain at wavelength λ. On the assumption that the raindrops are spherical, randomly situated and no multiple scattering occurs, Y may be related to the raindrop size distribution

$$Y(\lambda,z) = 4.343 \times 10^{-3} \int_0^\infty N(z,D)\,Q_T(\lambda,D)\,dD$$

where D(mm) is the raindrop diameter, $N(z,D)dD$ (m^{-3}) the number of drops per unit volume with a diameter between D and D + dD, and Q_T(mm^2) the extinction-cross section of a spherical water drop with diameter D at wavelength λ. The extinction-cross section Q_T can be calculated using Mie's scattering theory (Kerker, M.,1969) for spheres. The permittivity of water which is used in the calculation can be taken from the publication of Ray (Ray, P.S., 1972). The relation between the rainfall rate R(mm/h) and the dropsize distribution is given by

$$R(z) = 1.885 \times 10^{-3} \int_{0}^{\infty} N(z,D)v(D)D^3 dD$$

where v(D) (m/s) is the fall velocity of a drop with diameter D.

In order to determine the specific attenuation Υ as a function of rainfall rate R, knowledge is required of the fall velocity of raindrops as a function of dropsize and of the dropsize distribution as a function of rainfall rate. For the fall velocities of the drops the values experimentally determined by Gunn-Kinzer (Gunn, R. et al, 1949) are generally taken. One of the most commonly used dropsize distributions for the calculation of the rain attenuation is that proposed by Laws-Parsons (Laws, J.O. et al, 1943). Laws-Parsons derived their dropsize distribution from ground-based pellet measurements and published their results in tabulated form.

Subsequently Marshall-Palmer (Marshall, J.S. et al, 1948) and later Joss et al (Joss, J. et al, 1968) proposed distributions of a negative exponential type that give N(D) directly. All these distributions are identical in expression

$$N(D) = N_o e^{-qD}$$

$$q = \alpha R^{-0.21}$$

where N_o and α are constants depending on the type of rain. Instead of a single dropsize distribution, as proposed by Marshall-Palmer, Joss et al proposed three distributions applicable to three types of rain: drizzle, widespread and thunderstorm. The constants N_o and α for evaluating the Marshall-Palmer and the Joss et al distributions are listed in Table 1.

Table 1. Constants for the evaluating dropsize distributions

Type of dropsize distribution / Constants	N_o $m^{-3} mm^{-1}$	α mm^{-1}
Marshall-Palmer	8000	4.1
Joss et al drizzle	30000	5.7
Joss et al widespread	7000	4.1
Joss et al thunderstorm	1400	3.0

The attenuation due to rain at 94 GHz has been calculated for the five above mentioned dropsize distributions. The results of these calculations are shown in Fig. 1A by the solid curves. It can be seen that the attenuation due to rain at 94 GHz is strongly influenced by the type of dropsize distribution. Since the measurements of raindrop spectra have shown large variations for the same location, rain type and rain rate, a comparison between theory and experiment can hardly be successfull if the calculated attenuation due to rain is not based on the actually measured dropsize distribution.

3.0 INSTRUMENTATION

3.1 Millimeter equipment

The propagation tests have been made on a terrestial propagation link situated near The Hague. The path length of the link is 935 meters and the transmitting and receiving antennas are 1.2 m Cassegrain dishes. The two antennas have a gain of 58 dB and a halfpower beamwidth of 0.19 degrees. The transmitting antenna is placed 0.8 m above ground level at one end of the link, the receiving antenna is located on a tower at the other end at a height of 3.6 m. Because of the very small beamwidth, no ground reflections are picked up by the receiving antenna.

At present the transmitted signal is vertically polarised and is provided by a 40 mW CW Impatt oscillator. During reception this signal is modulated at 1 kHz rate by a ferrite switch in the receiving antenna and after RF detection by a 1N53 diode fed to a synchronous detector. Drift problems in the receiver are minimized by means of temperature stabilization.

The measuring system has a dynamic range of 30 dB, an accuracy of 5 percent and a long term stability of ± 0.15 dB.

3.2 Meteorological equipment

The meteorological measurements along the link consist of rainfall rate, drop size distribution, wind speed and direction in the horizontal plane and atmospheric temperature, pressure and humidity.

The rainfall rate is measured with three rapid response rain gauges located about 500 m apart along the propagation path. The two rain gauges placed at the endpoints of the link, are commercially available instruments, tradename Ombrometer. The Ombrometer is provided with a standard-drop counter for measuring rain intensities less than 72 mm/h and a tipping-bucket system for measuring higher intensities. The third rapid response rain gauge, located at midpoint along the propagation path, is of the standard-drop counting type and is made at the Physics Laboratory TNO. Near the receiver site a second TNO made rapid response rain gauge is installed. This instrument is used for checking purposes.

Information on raindrop size distribution is obtained with a distrometer which measures the moments of drops falling on an electromagnetical sensor of 50^2 cm area. This instrument distinguishes between drops with a time spacing of about 1 msec and can measure diameters between 0.3 and 5 mm. The measured drops are catalogued into 20 size classes with a resolution varying from 0.1 mm for small drops to 0.5 mm for large drops.

If N_i indicates the number of drops with diameters (mm) between $D_i - 0.5\Delta D_i$ and $D_i + 0.5\Delta D_i$ striking the surface S (cm^2) of the distrometer in time T_s (sec), then the corresponding number of drops per unit volume (m^{-3}) is given by

$$N(D_i)\Delta D_i = 10^4 \frac{N_i}{ST_s v(D_i)}$$

where $v(D_i)$ (m/sec) is the fall velocity of a drop with diameter D_i.

The rainfall rate (mm/h) averaged over T_s follows from

$$\overline{R} = \frac{6\pi}{ST_s} \sum_{i=1}^{20} N_i (D_i^3 + 0.25 D_i \Delta D_i^2)$$

in case of uniform distribution for D in each class.

Information on the 20 size classes as distinguished by the distrometer and on the fall velocities of the drops is given by Table 2.

Table 2. Diameters and fall velocities for the 20 size classes of the distrometer.

D (mm)	ΔD_i (mm)	D_i (mm)	$v(D_i)$ (m/s)
0.3 - 0.4	0.1	0.35	1.40
0.4 - 0.5	0.1	0.45	1.84
0.5 - 0.6	0.1	0.55	2.27
0.6 - 0.7	0.1	0.65	2.67
0.7 - 0.8	0.1	0.75	3.07
0.8 - 1.0	0.2	0.9	3.67
1.0 - 1.2	0.2	1.1	4.34
1.2 - 1.4	0.2	1.3	4.91
1.4 - 1.6	0.2	1.5	5.41
1.6 - 1.8	0.2	1.7	5.87
1.8 - 2.1	0.3	1.95	6.39
2.1 - 2.4	0.3	2.25	6.99
2.4 - 2.7	0.3	2.55	7.50
2.7 - 3.0	0.3	2.85	7.88
3.0 - 3.3	0.3	3.15	8.21
3.3 - 3.7	0.4	3.5	8.52
3.7 - 4.1	0.4	3.9	8.78
4.1 - 4.5	0.4	4.3	8.95
4.5 - 5.0	0.5	4.75	9.06
5.0 -	0.5	5.25	9.13

The distrometer is located near the receiver site close to the Ombrometer and the TNO made rain gauge.

A single anemometer measures wind speed and direction in the horizontal plane. Atmospheric pressure, temperature and relative humidity are measured with a barometer, a thermometer and a hydrometer respectively. The location of these instruments is in the neighbourhood of the receiver site.

4.0 LOSS IN ANTENNA GAIN FOR A WET 1.2 M CASSEGRAIN ANTENNA AT 94 GHz

From the beginning of the 94 GHz propagation experiment it was recognized that rain on uncovered antennas could introduce unpredictable additional attenuation beside the attenuation due to rain along the path. In order to see to which extent water on antennas and randomes can degrade the accuracy of rain attenuation measurements at 94 GHz, a series of artificial wetting tests have been carried out on one of the 1.2 m Cassegrain antennas. Beside the whole antenna also the various parts were separately sprayed with water and every time the loss in antenna gain has been measured. Also the loss due to a wetted reinforced teflon sheet placed in front of the antenna has been measured. During all these wetting tests, large fluctuations in antenna loss have been observed and the results in terms of minimum and maximum loss values are presented in Table 3.

Table 3. Wetting tests on a 1.2 m Cassegrain antenna at 94 GHz.

Condition	decrease in antenna gain (dB)
whole antenna wet	3.0 - 5.8
only radome on feedhorn wet	1.8 - 3.5
only subreflector wet	1.4 - 2.1
only main reflector wet	0.3 - 0.9
only teflon sheet in front of antenna wet	0.6 - 1.0
10 seconds after stopping to spray water in sheet	0.25

This table clearly shows that water on reflector antennas and radomes can cause considerable losses. Since the decrease in antenna gain occurs in an unpredictable manner accurate rain attenuation measurements are hardly possible with uncovered antennas.

A wet teflon radome introduces much less degradation in antenna gain as is shown in Table 3. Therefore, radomes can be a useful solution for long propagation links where high rain attenuations will be encountered. However, for short propagation links the fluctuations in antenna gain due to a wet radome are still unacceptably high.

In our propagation experiment each Cassegrain antenna has been placed behind a teflon sheet at the end of a 4 m long tunnel. Precautions have been taken also to prevent condensation of water on the teflon sheets. The photographs in Figs 2-3 show the tunnels in which the transmitting and receiving Cassegrain antennas have been placed.

5.0 DATA RECORDING AND HANDLING

The registration of the data is done in digital form on cassette tape under control of a 8 K memory minicomputer. The data of each instrument, except the data of the distrometer, are recorded with an accuracy of 11 bits together with an instrument label. Each registered data quantity occupies 3 characters of 8 bits on cassette tape.
The drops, observed by the distrometer, are not individually registered on cassette tape, but are first sorted according to size by the minicomputer. The minicomputer counts also the number of drops in each size category and once per 83 seconds a histogram for registration on cassette tape is formed. Only when drops are counted in a size category, 3 characters of 8 bits are recorded on cassette tape containing the number of counted drops, the size category and the instrument label of the distrometer.
The sampling period is for all instruments equal to 83 seconds except for the 94 GHz propagation for which the sampling period is 16 2/3 seconds. Data from the instruments are collected on a semi-continuous basis, the measurements are performed during 37 minutes per hour, night and day. The remaining 23 minutes per hour data recording does not take place because of use of the minicomputer in an optical propagation experiment. During the hourly 37 minute recording period data and time labels are recorded twice on cassette tape.

To ensure rational use of cassette tape, the measured data of all rain instruments are only recorded in case of positive non-zero values. The output of data of the propagation experiment amounts to less than one cassette tape per week.

The numerical treatment of data is made with a CDC 6400 computer. The data from the cassette tape is converted into CDC 6400 format, processed and subsequently placed in library files. In order to facilitate data handling and processing, extracts are made from the original files, which only contain data taken during rainfall. These extracts are also placed in library files.

The listing of the computer printout in Fig. 4 illustrates the processed data of a file containing only data taken during rainfall. The first column of this listing with the heading DAY/TIME gives the date and time of the recording. The first data-time label in the listing 134/0112 corresponds with 15 April 1978/1 hr 12 min. The second column with the heading MPROP gives the measured specific attenuation and the third column with the heading CPROP gives the calculated specific attenuation derived from the dropsize distribution measured with the distrometer. The number of drops observed by the distrometer and the distribution over the 20 size classes are shown in the next 20 columns. The next 3 columns with the headings DISTR, RAIN1 and OMBR1 give the rainfall rates determined by the distrometer, the first TNO made rapid response rain gauge and the first Ombrometer, respectively. These three instruments are grouped together at the receiver site. The last two columns with the headings RAIN2 and OMBR2 give the rainfall rate determined by the second TNO made rain gauge, located at midpoint along the propagation path, and the second Ombrometer, located at the transmitter site, respectively. At the time of recording the second TNO made rain gauge was out of use. Each row in the listing corresponds with a 83 second sampling period.

6.0 EXPERIMENTAL RESULTS AND COMPARISON WITH THEORY

Fig.1A shows the measured attenuations for vertical polarisation (denoted by triangles Δ) and the calculated attenuations based on the actually measured dropsize distribution (denoted by crosses +) as a function of the measured rainfall rates. The measured attenuation and rainfall rate values are averaged over 83 seconds. All the displayed measured attenuation points represent measurements with almost uniform rainfall along the whole propagation path. Fig.1B expresses in detail the agreement between the measured attenuation and that calculated from the actually measured dropsize distribution. The points denoted by circles (o) give the difference of the measured attenuation with the calculated attenuation. It can be seen that the agreement between theory and measurement is very satisfactory. Only for low rainfall rates the measured attenuations are in most cases slightly higher than the calculated ones. Possible cause is that the distrometer is not able to measure drop diameters smaller than 0.3 mm.

7.0 CONCLUSION

For vertically polarised transmissions on a 935 m path a very satisfactory agreement has been obtained between experimental and theoretical attenuation in case of uniform rainfall rates along the whole path. The reasons for this good agreement are: calculation of theoretical attenuation using actually measured dropsize distributions and the use of antennas placed in protective shelters.

REFERENCES

Gun, R., and Kinzer, G.D., 1949,"The Terminal Velocity of Fall for Water Droplets in Stagnant Air", J. Meteorol., Vol. 6, pp. 243-248.

Joss, J., Thams, J.C., and Waldvogel, A., 1968,"The Variation of Raindrop Size Distribution at Locarno", Proceedings of the International Conference on Cloud Physics, Toronto, Canada, pp. 369-373.

Kerker, M., 1969, "The Scattering of Light and other Electromagnetic Radiation", New York, Academic Press.

Laws, J.O. and Parsons, D.A., 1943,"The Relation of Rain-Drop Size to Intensity", Trans. Amer. Geophys. Union, Vol. 24, pp. 453-460.

Marshall, J.S. and Palmer, W. Mck., 1948, "The Distribution of Rain Drops with Size" J. Meteorol., Vol. 5, pp. 165-166.

Ray, P.S., 1972, "Broadband Complex Refractive Indices of Ice and Water", Applied Optics, Vol. 11, pp. 1836-1844.

Sander, J., 1975, "Rain Attenuation of Millimeter Waves at λ = 5.77, 3.3 and 2 mm", IEEE Trans. on Ant. and Prop., Vol. AP-23, pp. 213-220.

Zavody, A.M. and Harden, B.N., 1976, "Attenuation/Rain-Rate Relationships at 36 and 110 GHz", Electronic Letters, Vol. 12, pp. 422-424.

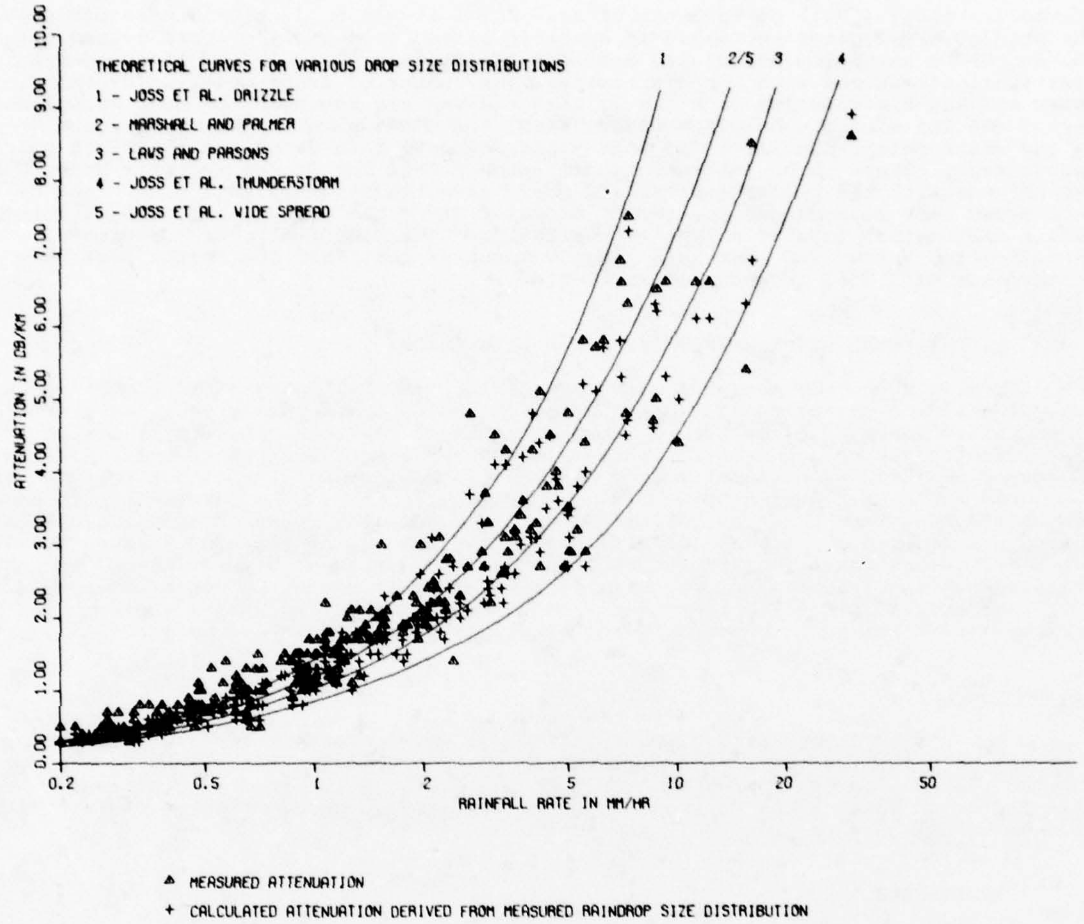

FIG. 1A MEASURED AND CALCULATED ATTENUATION VERSUS RAINFALL RATE AT 94 GHZ

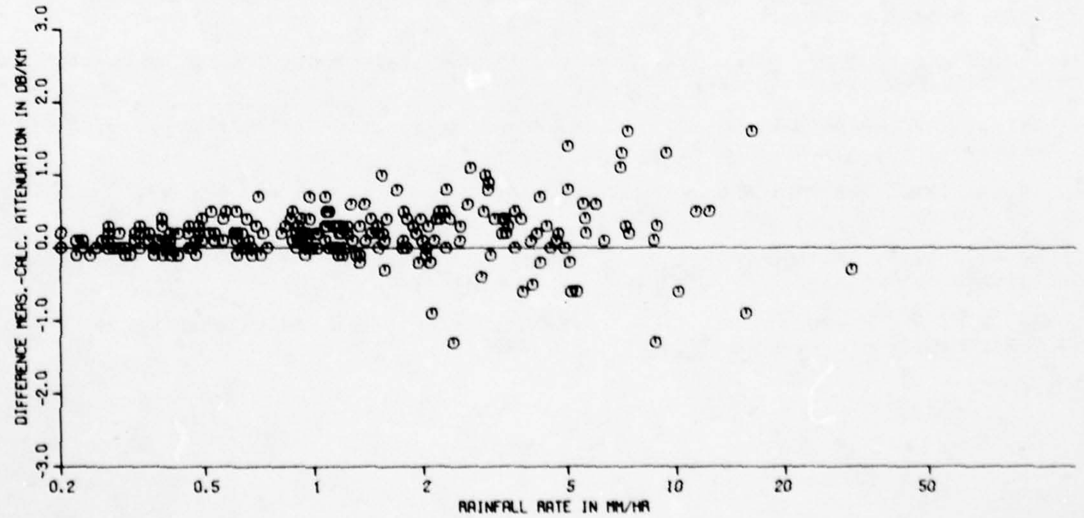

FIG. 1B DIFFERENCE OF MEASURED AND CALCULATED ATTENUATION

FIG. 1 RAINFALL ATTENUATION AT 94 GHZ: COMPARISON OF THEORY AND MEASUREMENT

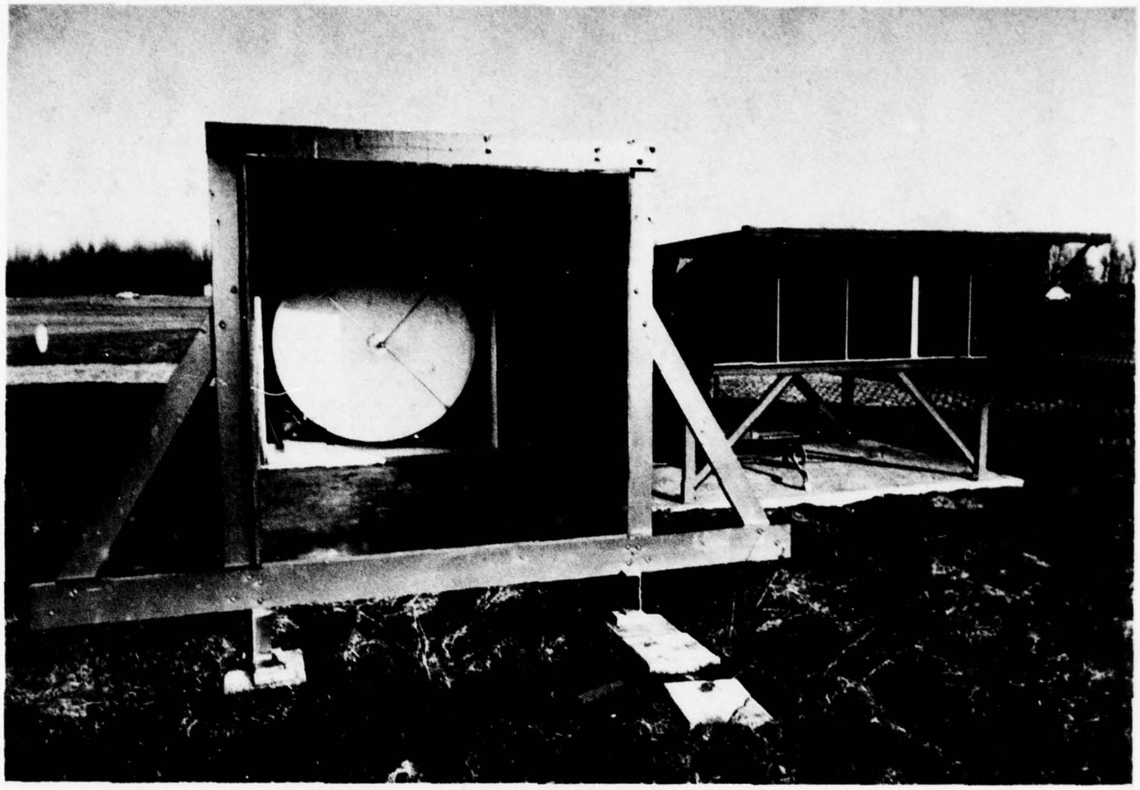

Fig. 2. View of the inside of the 4 m long tunnel housing the transmitting 1.2 m Cassegrain antenna.

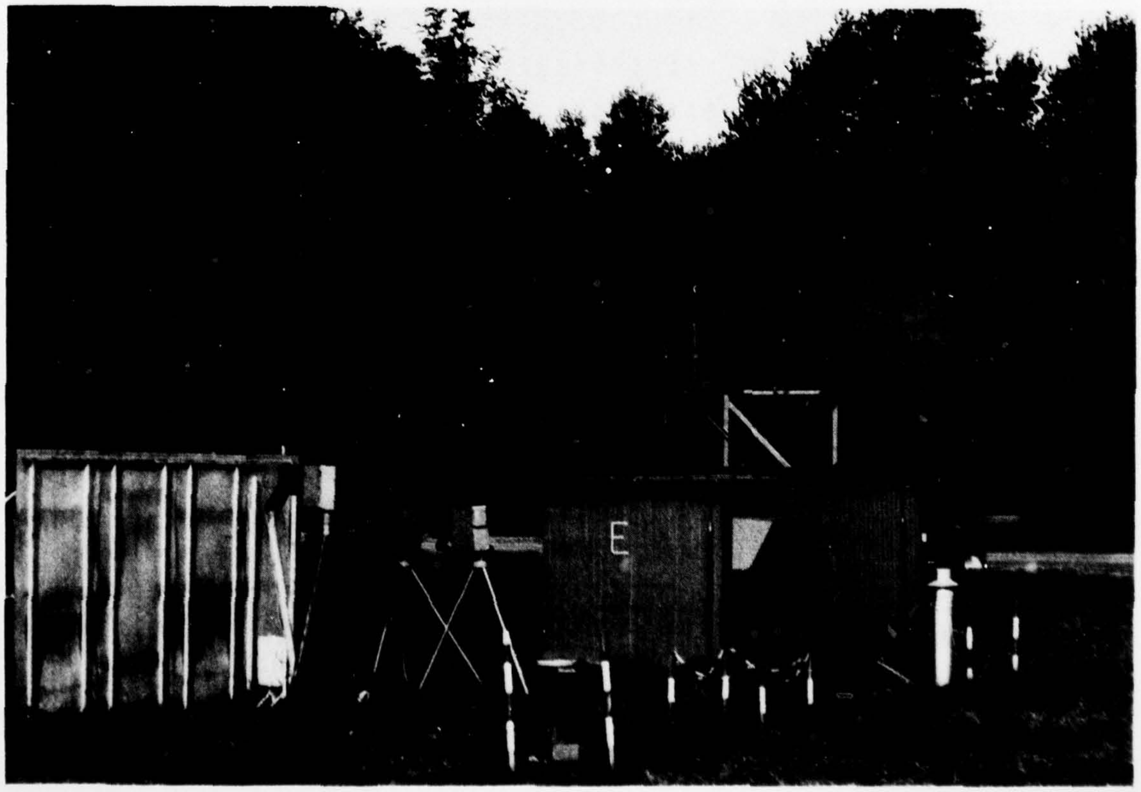

Fig. 3. Sideview of the 4 m long tunnel housing the receiving 1.2 m Cassegrain antenna.

```
DAY/TIME MPROP CPROP                             DISTROMETER                                     DISTR   RAIN1   OMBR1   RAIN2   OMBR2
         DB/KM DB/KM                        RAINDROP SIZE DISTRIBUTION                           MM/HR   MM/HR   MM/HR   MM/HR   MM/HR

                           1   2   3   4   5   6   7   8   9  10  11  12  13  14  15  16  17  18  19  20


134/0112
              -.0          0
              -.1    -.0   0           2   1                                                               .00     .05
              -.0    -.0   0   1   3   8   1   2                                                           .02     .01
              -.1    -.0   3   8  10   6                                                                   .02
              -.1    -.1   6  16  18   6   6                                                               .04
              -.2    -.1  24  11  11   4   2   2   2                                                       .05
              -.1    -.1  32  12  19  15  10   6   1                                                       .09
              -.2    -.3  54  62  61  34  17   9   3                                                       .21
              -.2    -.4  43  79  47  31  21  16   7                                                       .25
              -.4    -.3  40  92  41  28  12  15   1                                                       .19     .09
              -.3    -.2 101  65  24  17   5   6   1                                                       .12     .06
              -.3    -.4 221  93  33  40  24   9   1                                                       .24     .36     .22
              -.2    -.6 205 251 102  67  15  14   5                                                       .41     .18

134/0154

             -1.8   -2.9  72 196 177 137  93 111  83  32  19  10  11   1                                  2.72    2.66    2.39            1.08
             -2.6   -4.5  31 157 171 185 102 123 104  62  33  36  26  13   6                              5.62    5.06    5.42            1.73
             -3.7   -4.8  23 115 162 148  91 131 111  68  29  27  49  18   5   1       1                  6.66    7.68    7.16            1.08
             -4.4   -5.8   4  73  94 112 101 108 118  74  55  33  57  31   8  12   6   1                 10.31    9.85    8.89            1.08
             -4.8   -4.5  17  90  89 129  93  98 112  55  34  15  37  19   9   7   3   1                  7.15    8.95    8.24            2.17
             -4.7   -4.6  15  93 138 151  65  81  70  54  33  28  42  30  15   7   5   1                  8.60    8.85    8.67            3.69
             -4.4   -5.1   7 104 133 138  60  81  84  57  43  37  57  26  13   8   5   2   1              9.76    9.26    9.11            5.20
             -4.4   -5.1   8  86   1 135  68  78 103  59  37  36  68  25  12   8   3   1                  9.17    9.30    9.98            4.99
             -5.0   -6.3  14 105 159 174 141 182 166  94  47  34  44  18   9   1   1   2   1              8.72    9.32   10.19            5.20
             -5.8   -5.2  27 142 189 217 122 168 183  70  31  22  23   9   1   1                          5.50    6.35    6.72            6.94
             -5.7   -5.1  32 130 142 166  98 151 152  82  46  29  34   5   5                              5.97    6.00    6.07            7.59
             -5.5   -4.7  37 145 161 204 124 169 144  59  35  20  20   6   1   1                          4.88    4.97    4.99            7.37
             -5.4   -3.8  47 143 155 172  97 145 121  57  25  10  16   1       1                          3.69    3.69    4.12            6.94

134/0213

             -5.1   -3.8  37 169 138 162 105 158 123  55  22   7   9   5                                  3.48    4.00    3.90            5.42
             -5.1   -3.8  57 133 154 161 127 155 137  48  20  10  10   1                                  3.39    3.22    3.47            6.51
             -4.4   -3.5  44 135 138 195 135 155 126  32  17   6   4                                      2.80    3.12    3.47            6.07
             -4.3   -4.1  60 109 148 164 144 205 140  63  17  11   7                                      3.37    3.12    3.47            3.47
             -4.5   -4.2  57 118 155 254 170 204 147  53   4   5   1                                      3.14    3.12    3.47            2.60
             -4.8   -3.7  95 206 274 301 165 166  99  26  16                                              2.68    3.12    3.47            3.25
             -4.5   -2.5 159 334 297 258 118  99  44   6   1   1                                          1.65    2.07    2.17            3.47
             -3.7   -2.4 167 344 341 291 133  89  18   3       1                                          1.52    1.55    1.73            4.34
             -2.7   -2.3 146 320 252 244 117 108  36   4   2                                              1.54    1.73    1.73            4.12
             -2.0   -2.3 170 262 239 205 103 112  53   5   2                                              1.56    1.75    1.73            3.25
             -1.4   -1.6 176 213 147 123  76  82  30   6   1                                              1.07    1.22    1.30            2.82
             -1.2   -1.3 113 135 138  98  66  45  30   9   5                                               .94    1.17    1.08            1.30
             -1.0   -1.3 121 127 103 106  59  58  29  10   2   1                                           .93    1.06    1.08             .65

134/0254

              -.4    -.4  84  58  60  48  20  11   6   2                                                   .28     .27     .22             .43
              -.4    -.4  76  73  51  39  25  11   4                                                       .24     .37     .22             .43
              -.4    -.3  73  78  45  40  15   8                                                           .19     .33     .43             .43
              -.1    -.2 117  70  48  26   8   6   1                                                       .16     .28     .22             .22
              -.1    -.2  78  58  37  20   4   3   1                                                       .12     .12     .22             .43
              -.1    -.2  52  62  44  19   3   1                                                           .10     .11
```

Fig. 4. Listing of computer printout of processed data.

DISCUSSION

Comment by A.S.Vander Vorst, Belgium

About the question by Valentin on the near field of antenna.

Two different results have been published. One, by Watson (Electr. Letters, 1978) shows that rain attenuation measurements do not depend on the near field of the antenna. The other one, by Wiesbeck (A.E.V., 1974 and 1976) relates to radar and shows that the coherent echo is proportional to the inverse of the gain which makes the result depending on the near field.

M.C.Carter, UK

Could you tell me if the 4 m long tunnel in front of the aerial affects the polar diagram? And does the polar diagram change in wet and dry conditions of the tunnel?

Author's Reply

The cross-section of the tunnel has been varied from very large to the actual size and all the time and antenna radiation pattern has been observed. No deviation from the uncovered situation has been observed, even not for the case that the wooden walls have been covered with metal sheets. From these experiments we concluded that water on the walls of the tunnel will not have any influence on the antenna radiation pattern.

G.Tricoles, US

Would you describe the checks on multipath?

Why did you choose vertical polarization?

Author's Reply

(1) Due to the very small beamwidth of both antennas of 0.18 degrees and the low sidelobe levels and due to the slanted path no multipath effects will occur.

(2) The first experiments have been performed with vertical polarization, horizontal polarization will be used in the near future.

AD-A069 015 ADVISORY GROUP FOR AEROSPACE RESEARCH AND DEVELOPMENT--ETC F/G 17/2.1
MILLIMETER AND SUBMILLIMETER WAVE PROPAGATION AND CIRCUITS.(U)
FEB 79 E SPITZ, G CACHIER
UNCLASSIFIED AGARD-CP-245 NL

6 OF 6
AD
A069015

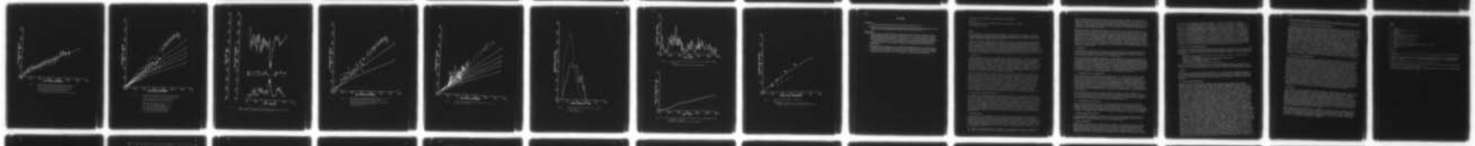

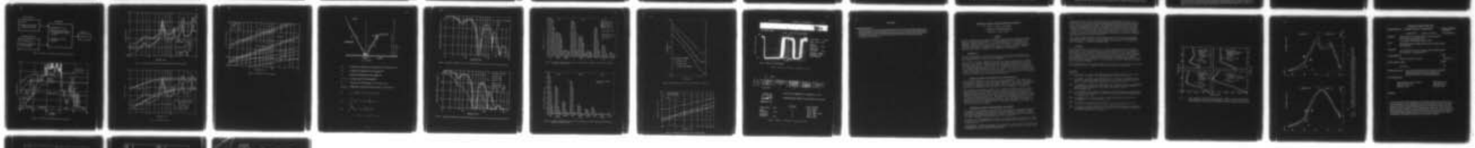

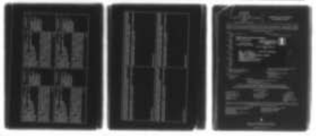

END
DATE
FILMED
6-79
DDC

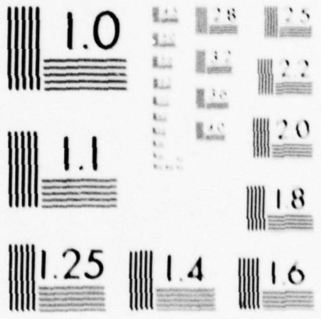
1.0
2.8
2.5
3.2
2.2
3.6
4.0
2.0
1.1
1.8
1.25
1.4
1.6

MICROCOPY RESOLUTION TEST CHART
NATIONAL BUREAU OF STANDARDS-1963-A

MEASUREMENTS OF EFFECTIVE SEA REFLECTIVITY AND ATTENUATION DUE TO RAIN AT 81 GHz

R J Sherwell

Admiralty Surface Weapons Establishment, Portsmouth, UK.

SUMMARY

The performance of millimetre-wave radars in a maritime environment is critically dependent on the absorption characteristics of the atmosphere close to the sea and on the effective reflectivity of the sea surface. Many theoretical predictions have been made, but little experimental data has been published. This paper describes results obtained with a link at 81 GHz established over a 5.6 km path close to the sea surface in S. England. It concludes that the probability of observing large values of specular reflection coefficient is very small and highlights the need for better data on which to predict the statistical behaviour of attenuation at millimetre wavelengths with rainfall over maritime paths.

1. INTRODUCTION

Conventional X-band tracking radars provide inadequate performance when the target is close to the sea because of multipath; that is the tracker is unable to distinguish between the target and its image in the sea. One solution to this problem is to use a higher radar frequency. For a given aperture, the antenna beam width is inversely proportional to frequency and so if the operating frequency of the radar is increased the gain of the antenna in the direction of the image of the target in the sea is less and the effect of multipath is reduced. In addition the sea appears rougher as frequency increases so, for a given sea state, the effective reflectivity of the sea is reduced. A preliminary study has shown that the choice of optimum frequency lies in one of the two so-called atmospheric windows at 30-35 GHz and 75-95 GHz. The lower frequency band has the advantage of better component availability and less rain attenuation and clutter, whereas the use of a higher frequency gives a significantly narrower antenna beam width for a given aperture. The final choice depends on the availability of more reliable measurements of certain critical parameters such as atmospheric attenuation close to the sea, the magnitude of sea and rain backscatter coefficients and the effective sea reflectivity, particularly at the higher frequencies of interest. This paper describes measurements which have been made to provide this data at 81 GHz.

2. EFFECTIVE SEA REFLECTIVITY

The effective reflectivity of the sea at low angles of incidence was measured at 81 GHz using a one-way propagation link, 5.6 km long, established at low level over the sea near Portsmouth. The site plan is shown in Figure 1. The transmitter was a cw Varian klystron modulated at 1 kHz and the receiver used a Plessey IMPATT local oscillator, a GEC balanced mixer and a narrow-band, post-detection filter centred at 1 kHz. The dynamic range of the system was 40 dB. The gains of the transmitting and receiving antenna (46 and 53 dB respectively) were not chosen to give narrow beams but were deliberately picked to give appreciable gain in the direction of the sea. Both antennas were mounted 10 m above mean sea level, but the path difference between direct and reflected signals was allowed to vary as the tide state changed. Thus at certain tide states appreciable cancellation occurred and the total received signal went through a series of maxima and minima as can be seen in Figure 2, which shows a typical 14 hour period in a calm sea. This graph was produced by sampling and recording the received signal every 2 seconds. The site geometry is such that a tide change of only 0.5 metres is required for the received signal to move from a maximum, through a minimum to the next maximum, giving the 8 peaks shown for a tide change of 4 metres. From the peak to trough ratios of the received signal and a knowledge of antenna gains the effective specular reflectivity of the sea can be calculated and from the width of the trace the diffuse reflection coefficient can be estimated. The results are summarised in Figure 3. On this graph are shown the effective specular and diffuse coefficients as a function of rms surface roughness $\frac{\sigma \sin \beta}{\lambda}$, where σ is the rms wave height. β is the grazing angle and λ the radar wavelength. The two solid curves are from Beckmann and Spizzichino (1963) and represent well the behaviour of specular (ρ_S) and diffuse (ρ_D) reflectivities at lower radar frequencies. The experimental points for ρ_S agree well with the curve for sea state 2 and above (corresponding to an rms surface roughness of about 0.12) but at lower sea states the agreement is less good and high values of ρ_S are not often seen. The reason for this descrepancy is believed to be that the macroscopic description of the sea surface in terms of rms wave height is not sufficiently accurate at very short wavelengths. It was observed that values of ρ_S approaching unity occurred only when the sea was mirror-calm and that the presence of small wind-generated capillary waves was sufficient to reduce ρ_S significantly. Measured values of ρ_D agree reasonably well with the Beckmann and Spizzichino curve, but no values were measured in high sea states. No difference in ρ_S or ρ_D was observed between vertically and horizontally polarised beams. The important conclusions to be drawn from these results are that the probability of observing values of ρ_S in excess of about 0.65 is very low since mirror-calm seas are very rare and that in sea state 2 and above the effective specular coefficient will be less than 0.4. This result represents an important advantage for the use of such high radar frequencies.

3. EFFECT OF RAINFALL

3.1 The absorption coefficient as a function of rainfall rate, drop size distribution and frequency is well known (see, for example, Lin, S.H. 1975). But rainfall rate is seldom uniform along path lengths of interest in radar systems. This is illustrated in Figure 4, which shows a comparison of the rates (integrated over 1 minute intervals) measured at each end of the link during a typical shower. The standard requirement for military systems to work in rainfall rates of up to 4 mm per hour is thus somewhat meaningless since uniform rain at such a rate over ranges of practical interest is unlikely. This has long been appreciated by users of land-based communications systems and models exist (eg Harden, Norbury and White 1978) which predict the percentage of time during which attenuation across a given range will exceed given levels. This is a much more meaningful criterion. Such models are unlikely to be valid at sea and unfortunately no adequate statistics appear to exist on which a sea-based model could be constructed. The British Meteorological Office is currently examining this situation with a view to providing such data. The provision of an adequate model is considered important, since the use of the 4 mm per hour criterion may give an unduly pessimistic view of the potentialities of millimetre wave systems. Our present link is unsuitable for the generation of data since rainfall statistics would be dominated by the presence of land, but the effect of spatial non-uniformity of rainfall can be seen in Figure 5 in which measured attenuations are plotted as a function of rainfall rate measured at the receiving end only (integrated over a 1 minute period). Insufficient data was collected for the results to be statistically valid, but the solid curve on the graph which is a least-squares fit to the data, shows clearly the effect of spatial non-uniformity of rainfall rate above about 2.5 mm per hour. At low rates the slope of the line corresponds to an absorption coefficient of 0.9 dB/km, in reasonable agreement with other published data from short links.

3.2 A possible source of error in the measurement of absorption coefficients over short links is the effect of water on the radomes or antennas of the measurement facility. In a preliminary investigation, a garden spray was used to wet the radome of the receiver in a 500 m land-based link at 81 GHz. It was not possible to quantify the spray rate in terms of rainfall rate, but in what could qualitatively be called heavy rain additional losses of up to 3 dB were observed, falling to less than 0.25 dB about 30 seconds after spraying had ceased. Unless special steps are taken to protect radomes, then serious anomalies can result in the measurement of absorption coefficients using short ranges. It is obvious, too, that this effect needs further investigation in practical radar systems, especially where the antenna is to be mounted on-board ship and be subject to sea spray.

4. CONCLUSIONS

Measurements of the effective reflectivity of the sea have shown that the probability of observing strong specular multipath at 81 GHz is very low. The need for a statistical model to predict the effect of rainfall on the System performance of millimetre wave radars at sea has been highlighted by preliminary measurements of rainfall attenuation across a 5.6 km link. Many other measurements, especially of backscatter from rain and sea, need to be made before the choice of optimum operating frequency can be made and to this end a prototype tracker at 81 GHz is currently being commissioned at ASWE.

References

BECKMANN P and SPIZZICHINO A, 1963 "The Scattering of EM Waves from Rough Surfaces", Pergamon Press.

HARDEN S H, NORBURY J R and WHITE W J K 1978. To be published in Journal of Microwaves, Optics and Acoustics.

LIN S H 1975, Bell System Technical Journal Volume 54 p 1051

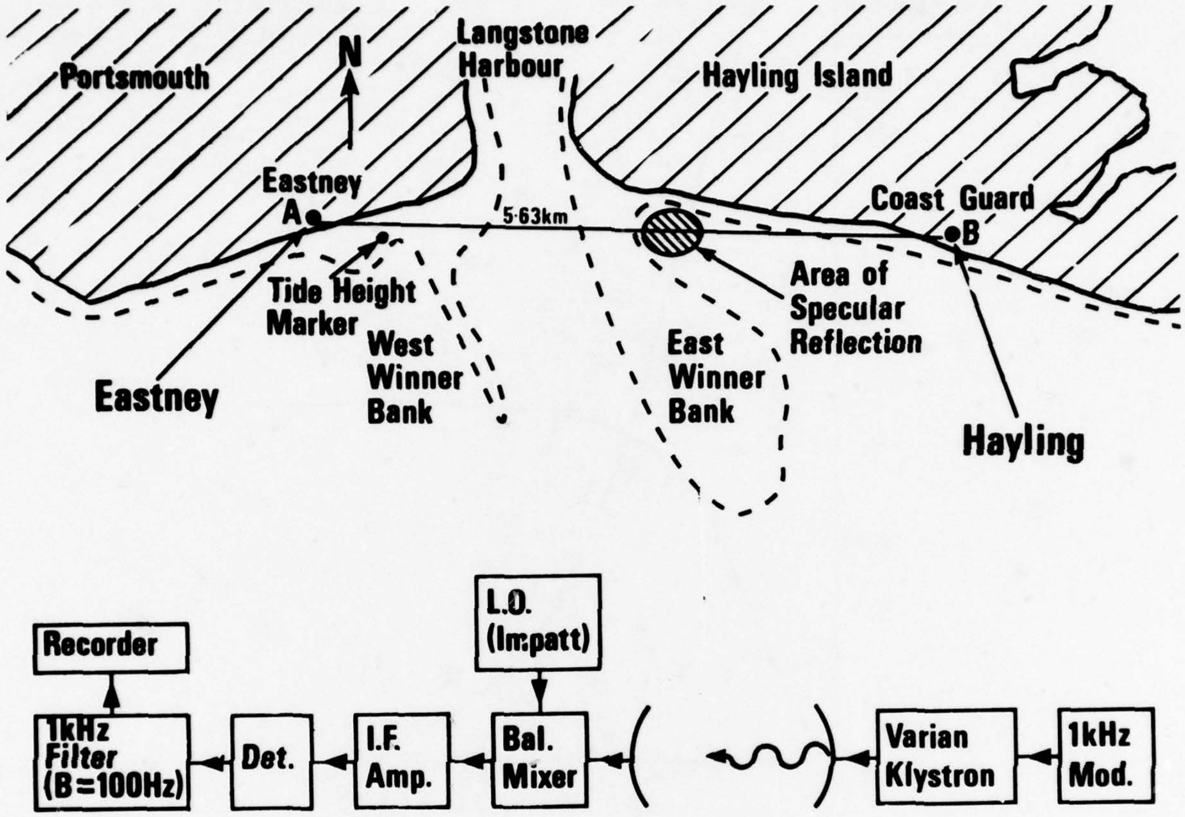
Portsmouth
N
Langstone Harbour
Hayling Island
Eastney
A
5·63km
Coast Guard
B
Tide Height Marker
West Winner Bank
East Winner Bank
Area of Specular Reflection
Eastney
Hayling
Recorder
L.O. (Impatt)
1kHz Filter (B=100Hz)
Det.
I.F. Amp.
Bal. Mixer
Varian Klystron
1kHz Mod.

Fig.1 80 GHz propagation experiment

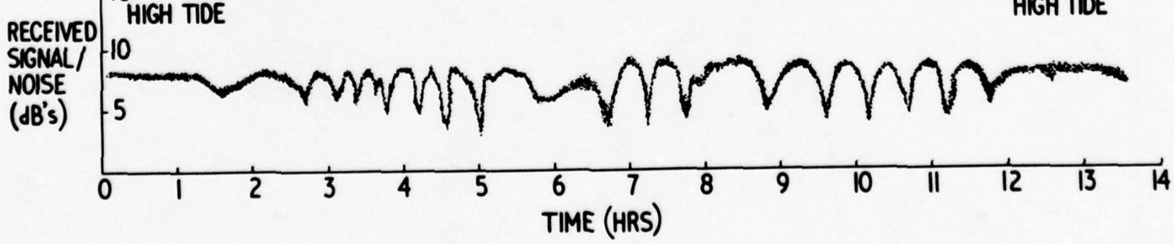

Fig.2 Variation of received signal level with time

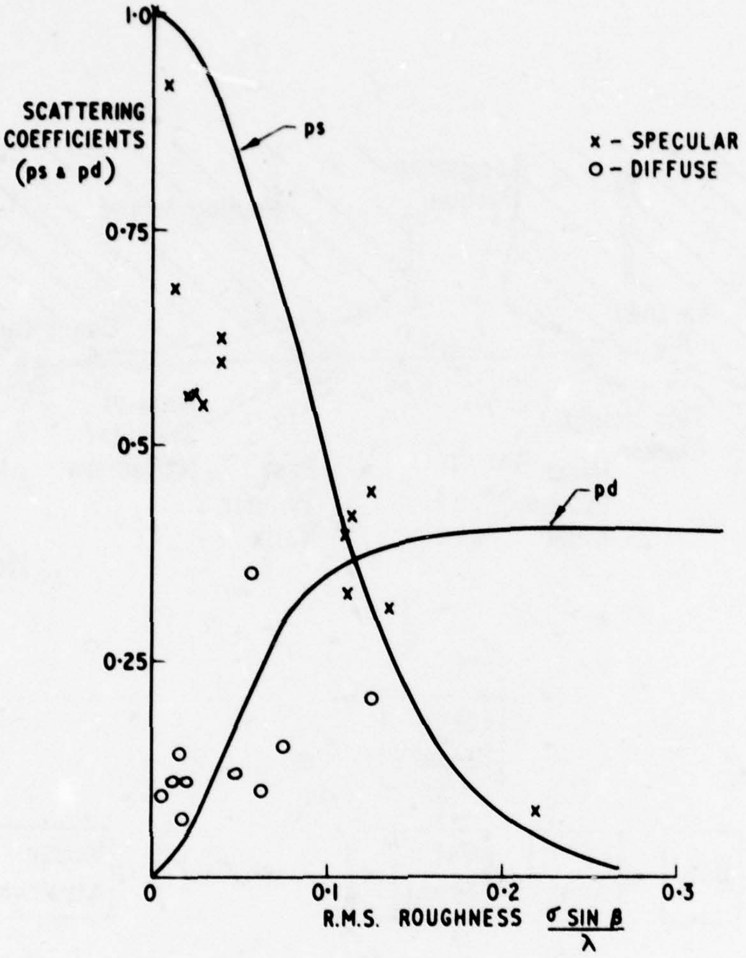

Fig.3 Specular and diffuse scattering coefficients versus roughness

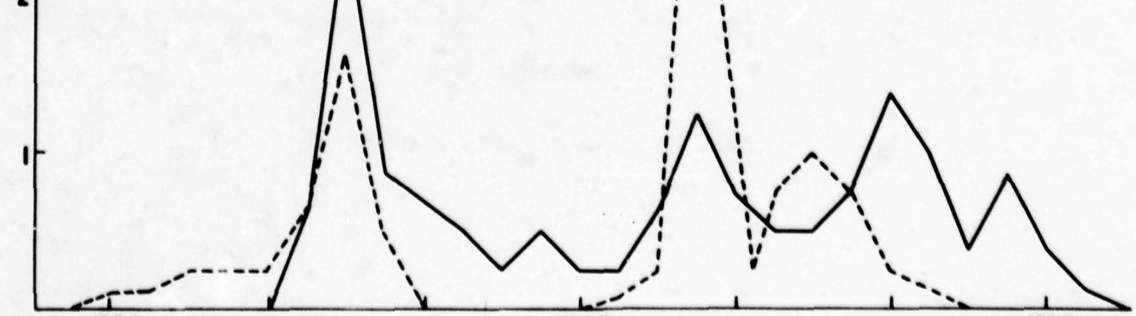

Fig.4 Graph showing rainfall variation at Hayling and Eastney

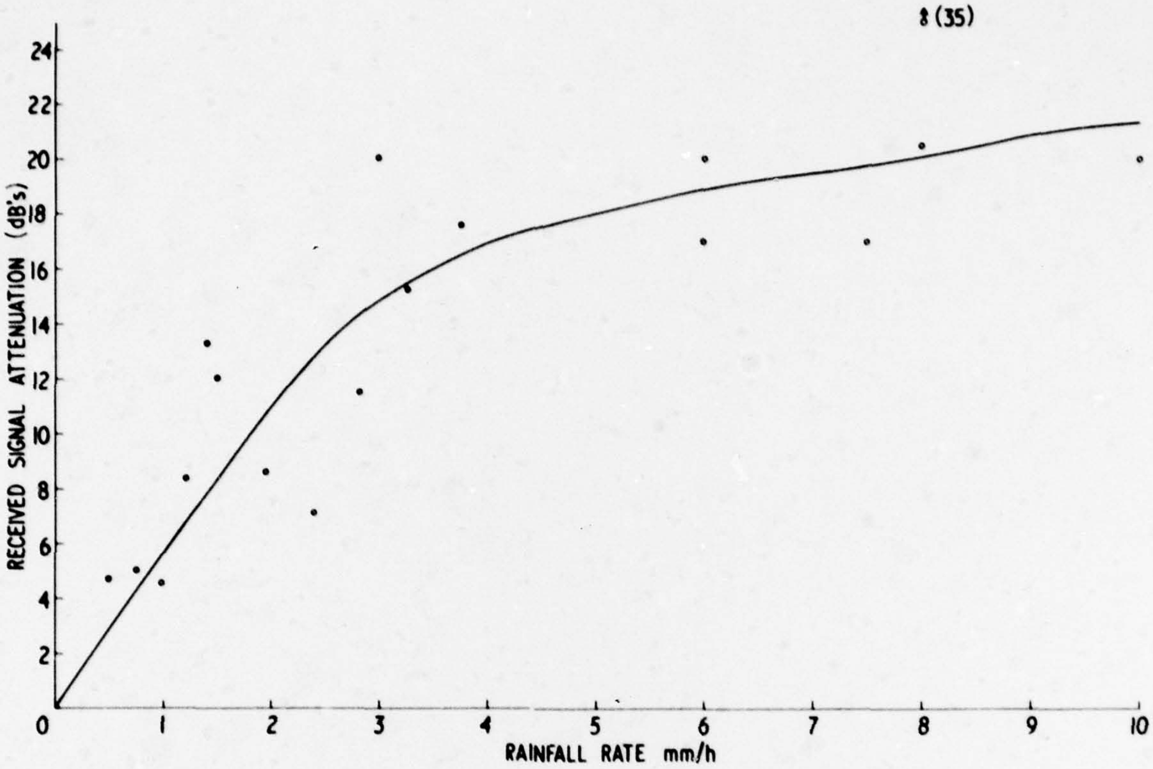

Fig.5 Attenuation of received signal at different rainfall rates

MEASUREMENT OF ATTENUATION DUE TO RAIN AT 74 GHZ

M.M. Kharadly, J.D. McNicol and J.B. Peters
Department of Electrical Engineering, University
of British Columbia, Vancouver, B.C. Canada V6T 1W5

SUMMARY

This paper describes and presents the results of an experiment designed primarily to measure attenuation due to rain at 74 GHz. Emphasis is placed on comparisons between measured and theoretically predicted attenuation. The latter is based on measured as well as some widely-used drop-size distributions.

1. INTRODUCTION

Increasing interest in higher frequencies has created a need for more knowledge about atmospheric propagation of millimetre waves. Of major concern is attenuation due to rain. Unlike the situation at lower frequencies, it is not possible to accurately predict the attenuation from knowledge of rain rates alone because, at mm-wave frequencies, the drop-size distribution is far more important in the calculation of attenuation (Olsen et al., 1978). In addition, the measurement of rain rates in most previous experiments has not been done with sufficient temporal and spatial resolution to allow accurate determination of "instantaneous" path-average rain rates to be made (See Medhurst, 1965 and Watson, 1976 for a survey of experiments). As a result of the above two factors, it has not been possible to make accurate correlations between measured and theoretically-predicted attenuation values at these frequencies.

The present experiment, in a similar way to some recent experiments (e.g. Fedi, 1973 and Zavody and Harden, 1976), has been designed with the above in mind. Our observations indicate that, even within relatively short periods of time, attenuation due to rain over the same path can vary within a wide margin at any particular rain rate, especially at low and moderate rain rates. Thus, a system to measure drop-size distribution has been constructed in an attempt to more fully explain the behaviour of the observed attenuation. The drop-size measuring system appears to function correctly but a satisfactory comparison between calculated attenuation based on drop-size measurements and measured values has not yet been achieved with the limited data recorded.

2. THE EXPERIMENT

2.1 General Description

The transmission path is of the radar type, almost horizontal and has a total (return) length of approximately 1.8 km. The layout of the path is shown in Fig. 1. With this arrangement, at 74 GHz, no multipath fading is likely to take place and any excess attenuation is considered to be entirely due to precipitation.

The transmitting and receiving equipment and the data logging system are located at the Electrical Engineering building on the extreme right of Fig. 1 and a passive plane reflector, 1 m x 1 m, is located on the roof of the building on the extreme left.

The antennas used are parabolic reflectors of approximately 1 m diameter and have measured gains of 49.5 db and 48. db for the transmitting antenna and receiving antenna, respectively. Air is continuously pumped through the entire waveguide system, including antenna feeds, to keep the system dry and to make sure that no moisture accumulates at the feed apertures.

The microwave source is a 500 mW klystron. The receiver is a narrow-band phase/amplitude receiver with a dynamic range of 60 db and 0.25 db linearity. Horizontal polarization is used and a clear-weather fade margin of about 40 db is obtained.

Five identical specially-constructed tipping-bucket rain gauges, relatively closely spaced at 220 m along the path, are placed on the roofs of certain buildings, as indicated by the circles in Fig. 1. The tip size of the gauges is 0.05 mm, which is 1/5 that of standard gauges and therefore gives a much shorter integration time (18 seconds at 10mm/hr.). It has proved important to have at least this number of gauges along the transmission path because, at times, the rain rates measured by the individual gauges differ considerably, especially at the edge of an approaching or departing rain cell. Temperature and wind velocity are also measured and recorded on a continuous basis.

2.2 Drop-size Apparatus

An electrostatic transducer, similar to the one described by Lammers, 1969, has been constructed. Its basic elements are two fine nichrome wire grids. The two grids are placed in a horizontal position one above the other with a spacing of 4 cm between them, as shown in Fig. 2. The top grid is maintained at a potential of 300 V above ground and the bottom grid is connected to ground through a very high resistance. As a rain drop falls through the first grid it picks up a charge related to its diameter. Part of this charge is deposited on the second grid as the drop passes through it. The flow of this charge through the high resistance to ground produces a voltage pulse whose amplitude, after amplification and filtering is used to categorize the drops according to diameter into sixteen size categories.

A microprocessor system (RCA 1802) is used to sort the drops and compute the number of drops in each category every second. The amplified, filtered pulse due to each drop is rapidly (25 μsec) sampled and digitized by a 12 bit A/D converter. The microprocessor determines the peak pulse voltage by comparing successive digitization results. The peak value is then compared to stored category boundary constants to determine the diameter category in which the drop belongs. Once per second the main data-acquisition minicomputer interrogates the microprocessor and the total number of drops in each of the 16 categories is transferred for recording on magnetic tape. With the 25 cm^2 collecting area of the transducer, there is a negligible probability that a drop will be missed by the microprocessor during a sorting or data-transfer routine, even during heavy rain.

The apparatus was calibrated in the laboratory with drops of various known sizes. Large- and medium-sized drops were formed by gravity and surface tension through orifices of different diameters, geometries and materials. Drops under 1 mm diameter were formed by guiding a uniform flow of air around the orifice of a very small diameter nozzle. The calibration of this transducer yielded the relation:

$$\text{Voltage pulse amplitude} = \text{Constant} \times D^{1.97},$$

where D is the drop diameter. This is similar to Lammers' result, where the output voltage was proportional to $D^{2.32}$.

2.3 Data-acquisition System

The main component in this system is a NOVA minicomputer. A block diagram is shown in Fig. 3. Information already in digital form (24 channels) is fed directly to the computer, while information in analog form reaches the computer via an A/D converter (16 channels). Calculation of rain rates is also performed in this computer (8 channels). The information in the 48 words is recorded on 1/2", 9 track magnetic tape compatible with IBM computers. Further processing is done at the University Computing Centre and the processed data are finally recorded on tape as part of a permanent data base.

All measured quantities are sampled once a second except for the state of the rain gauges where sampling is done at the rate of 16 times per second.

3. EXAMPLES OF THE RESULTS

A useful description of a rain/attenuation activity is the graphical representation of Fig. 4. In this figure, the upper plot gives the relative amplitude of the received signal in decibels versus time in hours, while the lower plot shows path-average rain rate in mm/hr. For the above activity, the mean specific attenuation is plotted against path-average rain rate in Fig. 5. The latter is grouped in classes differing by 0.5 mm/hr. The attenuation values thus calculated agree quite well with those predicted theoretically by employing Laws and Parsons drop-size distribution (Medhurst, 1965).

Although several other storms yielded similar results, many others did not. As an example of the latter, Fig. 6 shows the specific attenuation versus path-average rain rate for a rain activity that extended for a period of about 23 hours (on and off). The solid curves 1-5 give theoretically predicted values based on some widely-used drop-size distributions*. For this activity, it is clear that there exists a definite and significant discrepancy between measured and theoretically predicted values at certain rates. In this case, the attenuation was considerably higher than the values predicted from the drop-size distributions considered.

A more detailed examination of the various periods of rain activity in the above storm revealed that, while the measured attenuation was generally on the higher side, a certain 1½ hour period was primarily responsible for the observed discrepancy. Fig. 7 shows a graphical representation of the rain activity at that time, where this 1½ hour period is indicated by the interval T_1. By inspection of Fig. 7, it is evident that the received signal level during, say, the interval T_2, dips to significantly lower values than during the interval T_3, the corresponding peak rain rates being comparable. The overall averages and 10-second averages for the period T_1 are shown in Fig. 8 and Fig. 9, respectively. It is also interesting to note that the vertical component of wind velocity during T_2, measured at the transmitter/receiver location, was generally upward (with peak values up to 2 m/s), while, during T_3, it was generally downward (with peak values up to 1 m/s). This could have an effect on the instantaneous concentration of the smaller rain drops in the signal path.

At present only a few hours of data which include measured drop-size distributions have been recorded. This is because the prototype drop-size instrument has only recently been constructed and calibrated. Some preliminary data are presented to illustrate the operation of the system.

Fig. 10 shows the measured drop-size distribution at a rain rate of 1.25 mm/hr, obtained from data during a period of two hours of light rain. Laws and Parsons distribution for the same rain rate and diameter categories is shown for comparison. One-minute average rain rates have been calculated from the drop-size histogram during those two hours and are compared with those measured directly by an adjacent tipping-bucket rain gauge in Fig. 11(a). The corresponding total rain fall is shown in Fig. 11(b). There is a reasonably good agreement between the graphs of the latter figure.

---

* Calculations were performed by D.V. Rogers and R.L. Olsen of C.R.C., Ottawa and are based on Mie's scattering theory and single scattering approximation. Curves 1,3 and 5 are normalized on the basis of rain-rate integral equation (Olsen et al., 1978)

The specific attenuation at certain rain rates, computed from the measured drop-size distribution during the whole two hour period, is indicated by the crosses in Fig. 12. The asterisks indicate measured mean values of attenuation. Agreement here is not satisfactory*. But one must keep in mind two factors: the first is that the computed attenuation values are based on drop-size measurements only at one point along the transmission path, while the measured attenuation values apply to the whole path. The second is that relatively large errors are more likely to occur in the measurement of low rain rates because of the relatively long integration time of the tipping-bucket rain gauges and in the measurement of low values of attenuation because of the small amplitude fluctuations that exist even in a clear atmosphere. The measurements cited above involve both low rain rates and small values of attenuation.

4. CONCLUDING REMARKS

Based on the data obtained in the experiment described above, over a period of more than a hundred hours, it would be reasonable to conclude that attenuation due to rain at 74 GHz cannot be accurately predicted only from measured path-average rain rates and "standard" drop-size distributions, even when closely-spaced, short-integration-time rain gauges are used. In this experiment, however, while spatial resolution of rain rate measurements is considered adequate, temporal resolution is still unsatisfactory, partiuclarly at low rain rates.

It has also been shown that attenuation due to rain can be significantly greater than predicted using Mie's scattering theory, single-scattering approximation and Joss et al. drizzle distribution. Our observations suggest that the vertical component of wind velocity may be partially responsible for this result in some cases.

The measurement of the drop-size distribution of rain should provide further clarification concerning the observed attenuation and probably resolve the difficulty concerning temporal resolution of rain rate measurement. So far, in this experiment, measured drop-size data are limited and available only at one point on the transmission path. Thus, it has not yet been possible to make accurate and decisive comparisons between measured and calculated values of attenuation based on drop-size distribution. Further improvements in the drop-size measuring system are under way.

REFERENCES

Fedi, F., 1973, "Criteria and expected accuracy of the measurements envisaged in the research programme under way in Italy", NATO/AGARD Conference Proceedings No. 107, pp 8-1 - 8-23.

Keizer, W.P.M.N., Sneider, J. and de Haan, C.D., 1978, "Rain attenuation measurements at 94 GHz: Comparison of theory and experiment", Paper No. 44 of this volume.

Lammars, U.H.W., 1969, "Electrostatic analysis of raindrop distributions", J. App. Metero., vol. 8, pp 330-334.

Medhurst, R.G., 1965, "Rainfall attanuation of centimeter waves; Comparison of theory and measurement", IEEE Trans. Antennas Propagat., vol. AP-13, pp 560-564.

Olsen, R.L., Rogers, D.V. and Hodge, D.B., 1978, "The aR^b relation in the calculation of rain attenuation", IEEE Trans. Antennas Propagat., vol. AP-26, pp 318-329.

Watson, P.A., 1976, "Survey of measurements of attenuation by rain and other hydrometeors", Proc. IEE, vol. 123, pp 863-871.

Zavody, A.M. and Harden, B.N., 1976, "Attenuation/rain-rate relationships at 36 and 110 GHz", Electron. Lett., vol. 12, pp 422-424.

---

* The discrepancy is similar to that observed in a recent investigation (Keizer et al. 1978).

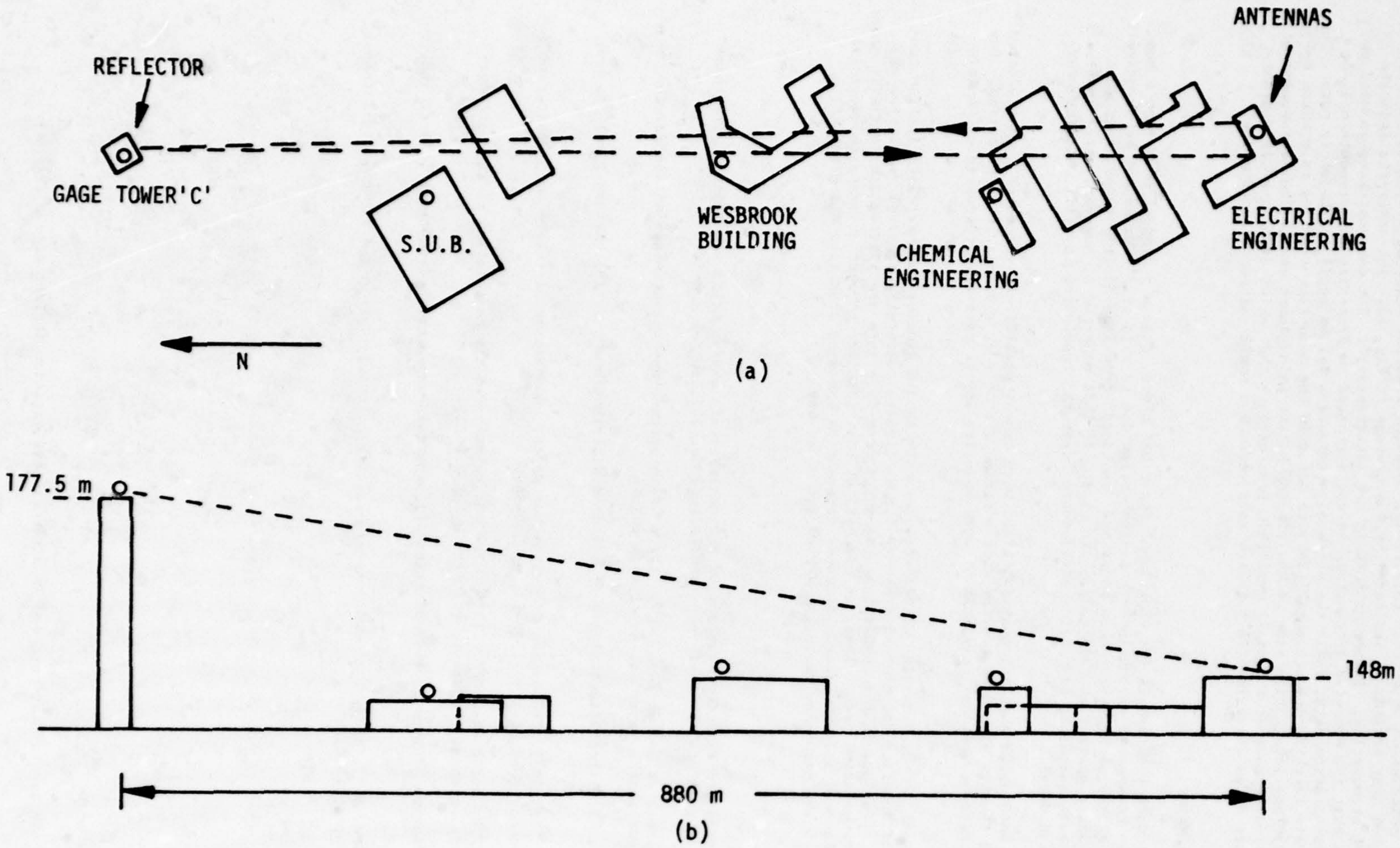
REFLECTOR
GAGE TOWER'C'
S.U.B.
WESBROOK BUILDING
CHEMICAL ENGINEERING
ELECTRICAL ENGINEERING
ANTENNAS
N
(a)
177.5 m
148m
880 m
(b)

Fig. 1 Transmission path

(a) Aerial view
(b) Side view

circles mark rain gauge positions

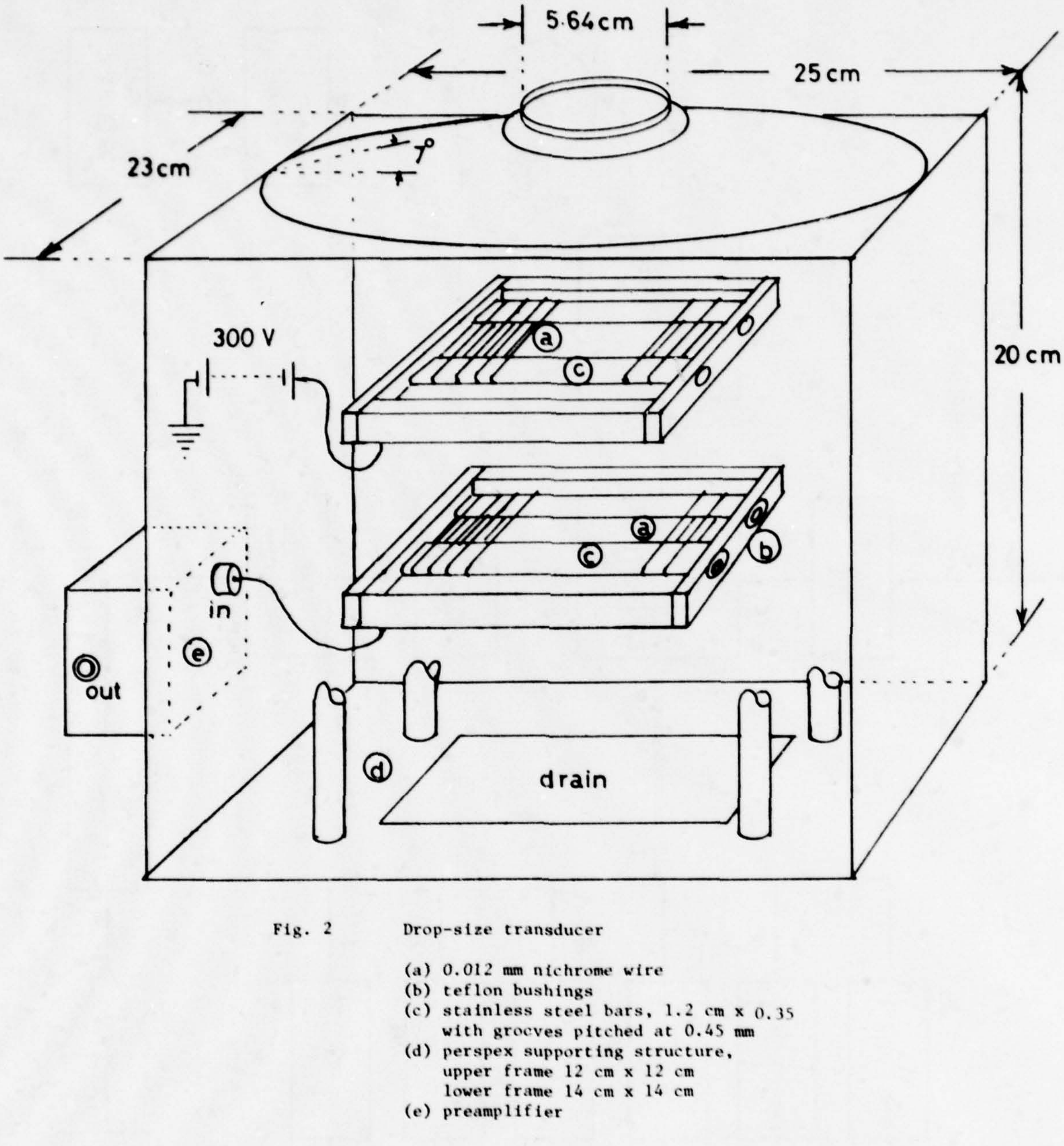
5.64cm
25 cm
23cm
7°
20 cm
300 V
a
c
a
c
b
in
e
out
d
drain

Fig. 2 Drop-size transducer

(a) 0.012 mm nichrome wire
(b) teflon bushings
(c) stainless steel bars, 1.2 cm x 0.35
with grooves pitched at 0.45 mm
(d) perspex supporting structure,
upper frame 12 cm x 12 cm
lower frame 14 cm x 14 cm
(e) preamplifier

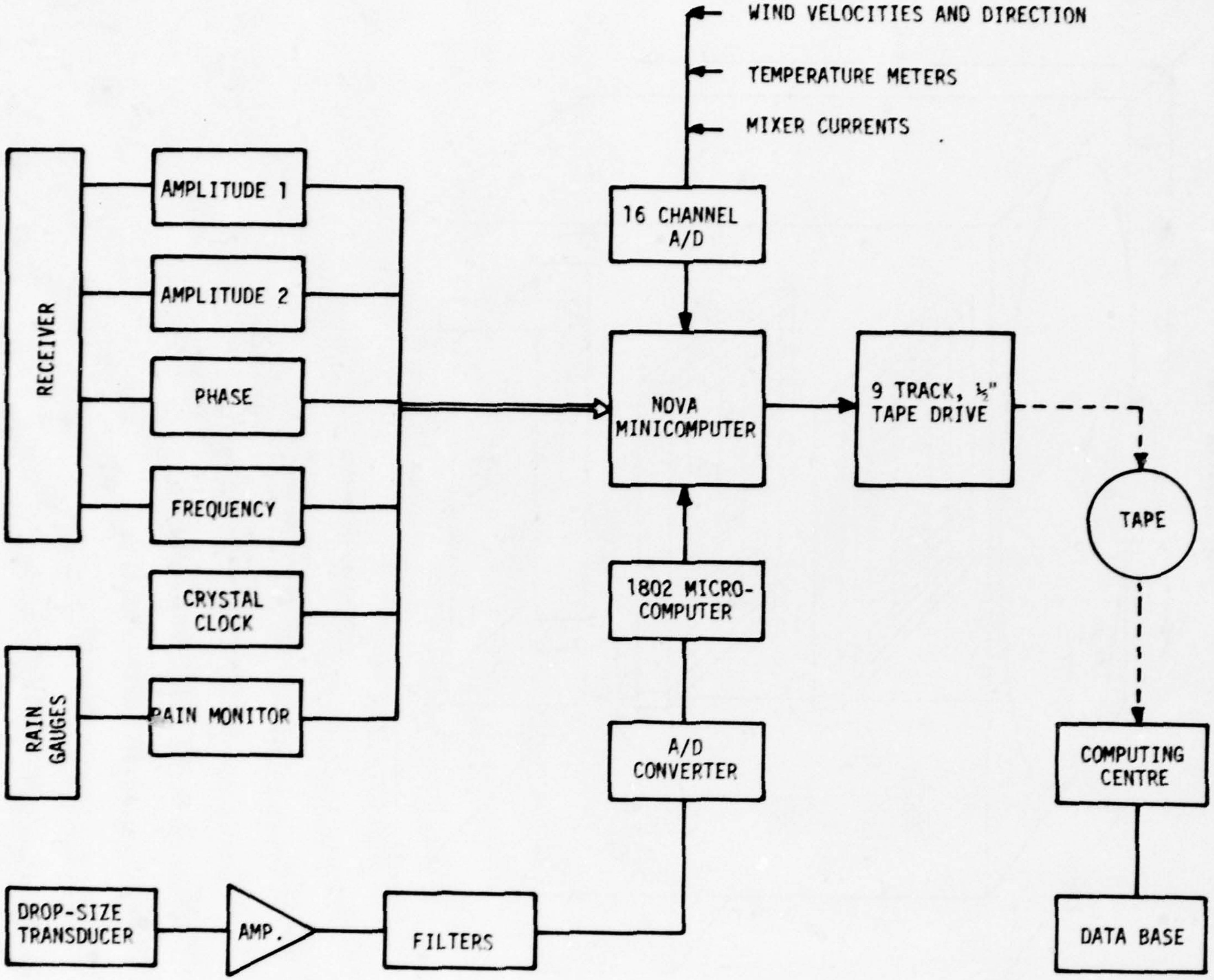
WIND VELOCITIES AND DIRECTION
TEMPERATURE METERS
MIXER CURRENTS
RECEIVER
AMPLITUDE 1
AMPLITUDE 2
PHASE
FREQUENCY
CRYSTAL CLOCK
RAIN GAUGES
RAIN MONITOR
16 CHANNEL A/D
NOVA MINICOMPUTER
9 TRACK, ½" TAPE DRIVE
TAPE
1802 MICRO-COMPUTER
A/D CONVERTER
COMPUTING CENTRE
DATA BASE
DROP-SIZE TRANSDUCER
AMP.
FILTERS

Fig. 3 Block diagram of data-acquisitions system

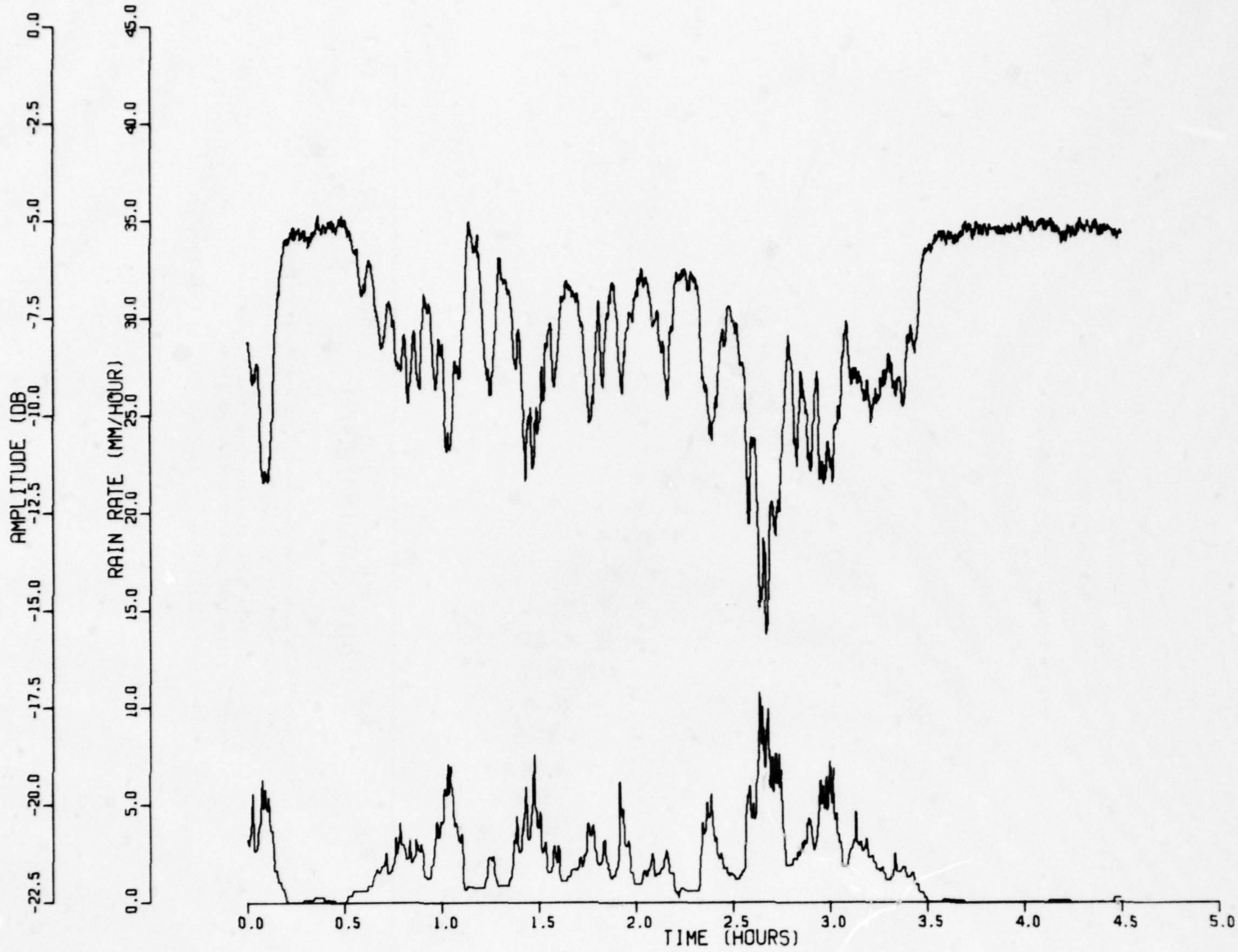

Fig. 4 Relative signal level (upper plot) and path-average rain rate (lower plot) versus time for the period 00:13 to 05:13 h, February 12, 1977

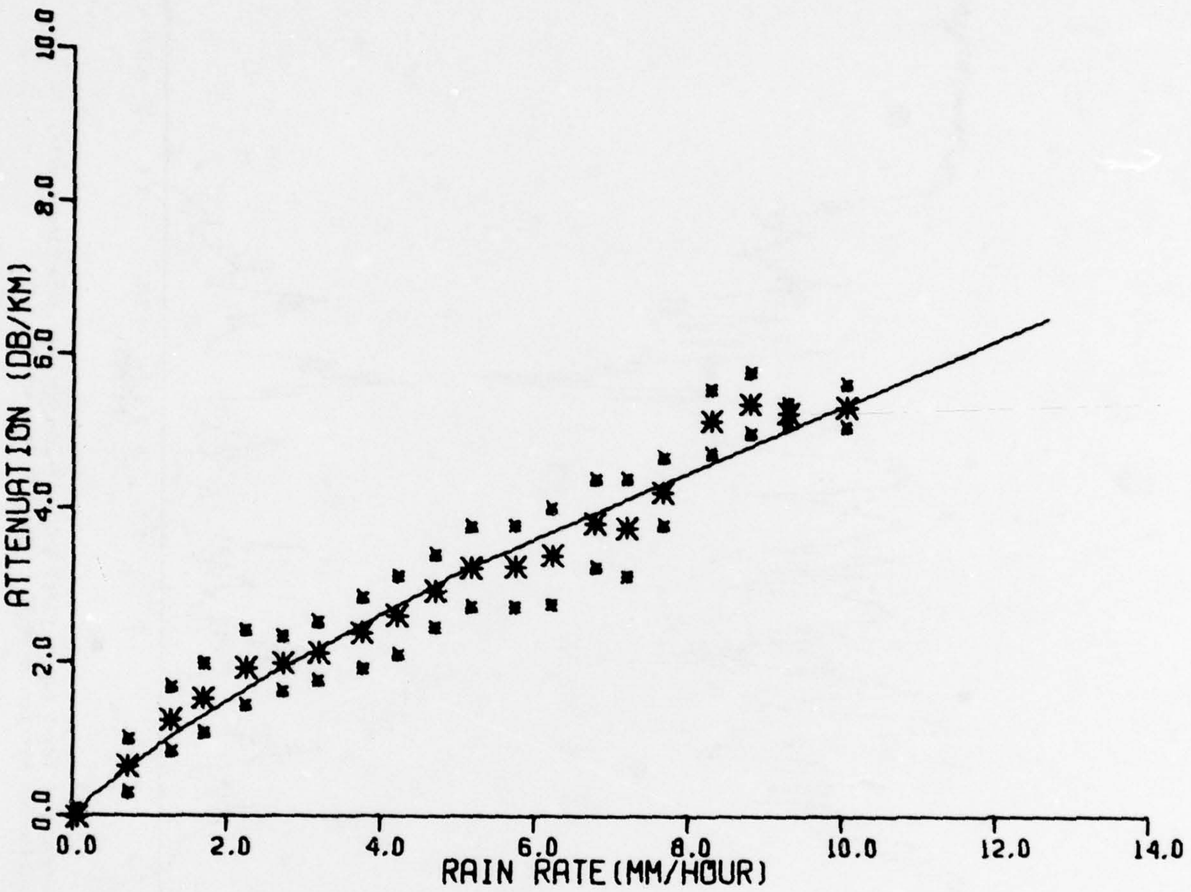

Fig. 5 Mean specific attenuation versus path-average rain rate for the period 00:42 to 05:12 h, February 12, 1977

Large asterisks mark the means and small asterisks mark one standard deviation about the mean

—— Theoretical, based on Laws and Parsons distribution

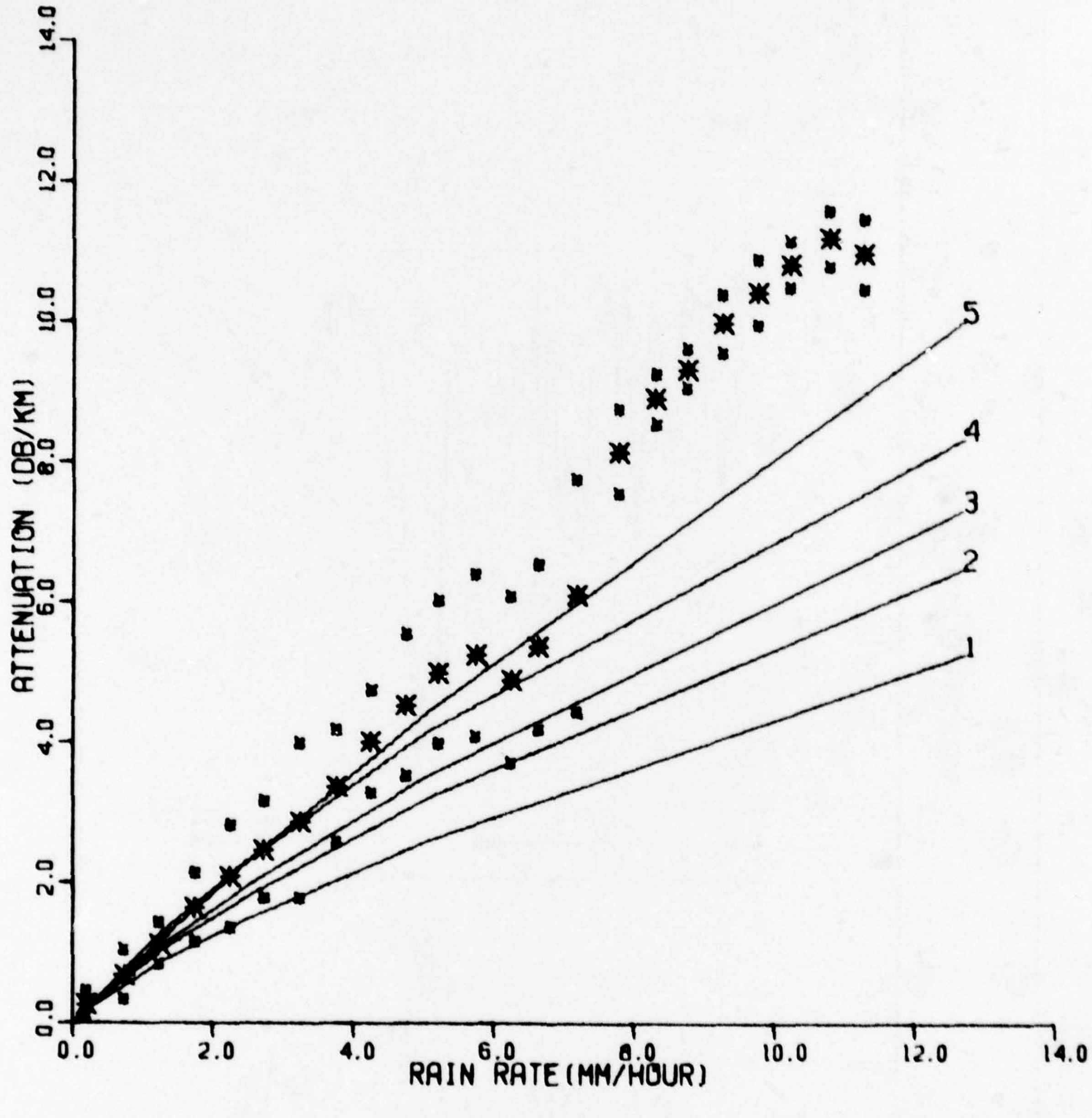

Fig. 6 Mean specific attenuation versus path-average rain rate for the period 23:43 h, May 30 to 22:43 h, May 31, 1977

Large asterisks mark the means and small asterisks mark one standard deviation about the mean

For theoretical curves 1-5, f=74 GHz, T=20°C, refractive index $M=3.698-j2.181$

(1) Joss et al. thunderstorm distribution
(2) Laws and Parsons distribution
(3) Joss et al. widespread distribution
(4) Marshall and Palmer distribution
(5) Joss et al. drizzle distribution

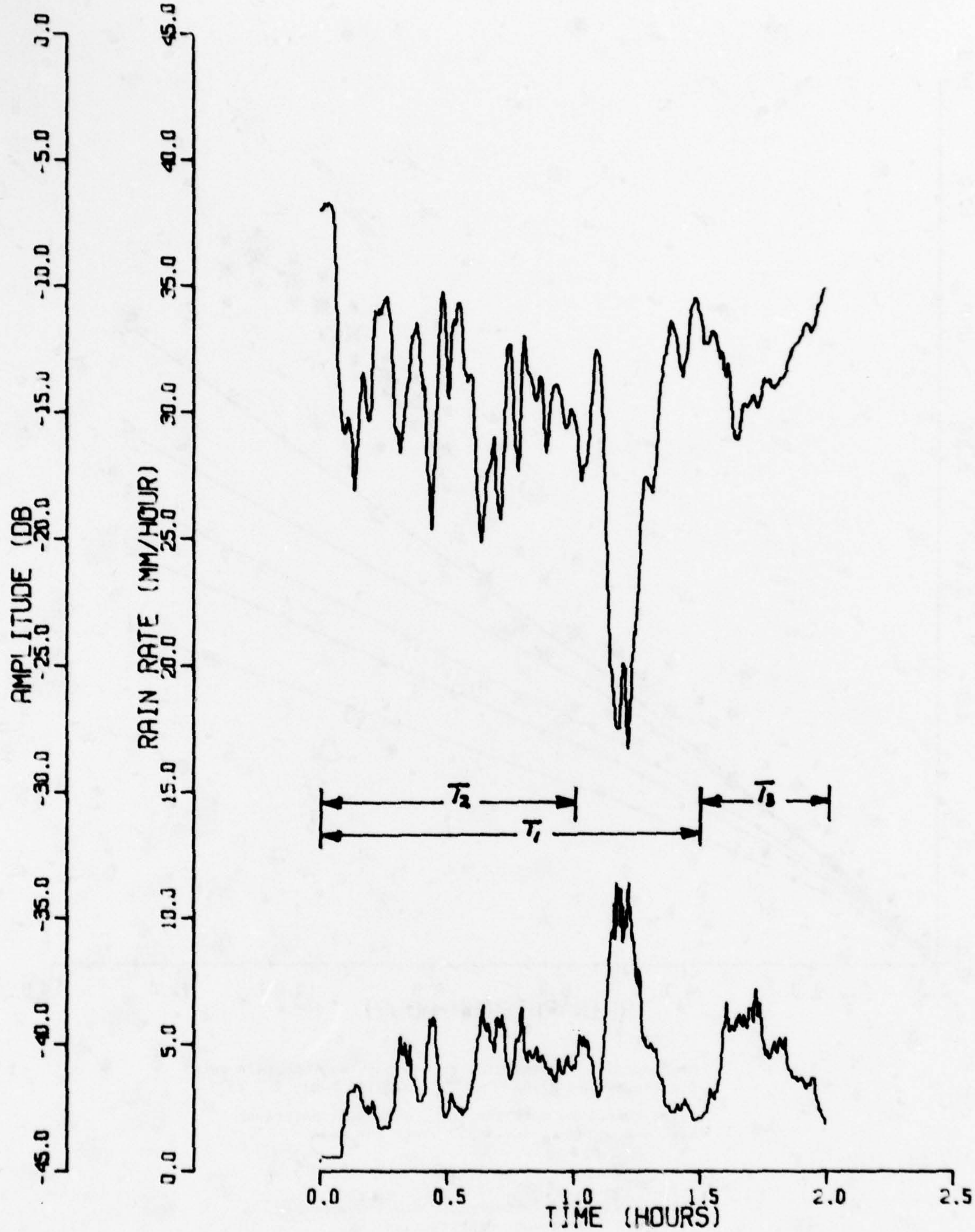

Fig. 7 Relative signal level (upper plot) and path-average rain rate (lower plot) versus time for the period 18:43 to 20:43 h, May 31, 1977

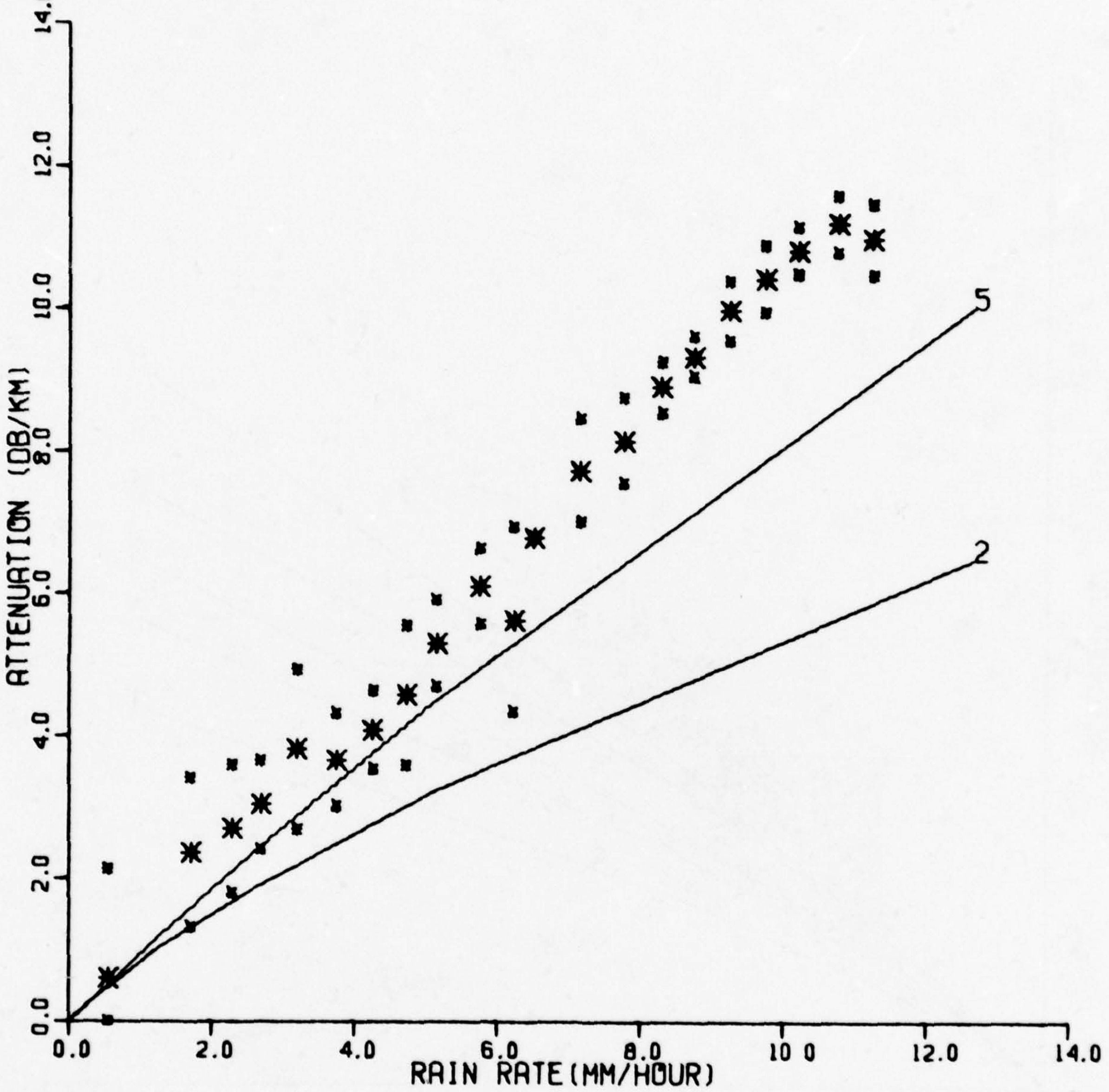

Fig. 8 Mean specific attenuation versus path-average rain rate for the period 18:43 to 20:12 h, May 31, 1977

Large asterisks mark the means and small asterisks mark one standard deviation about the mean

Curves 2,5 as in Fig. 6

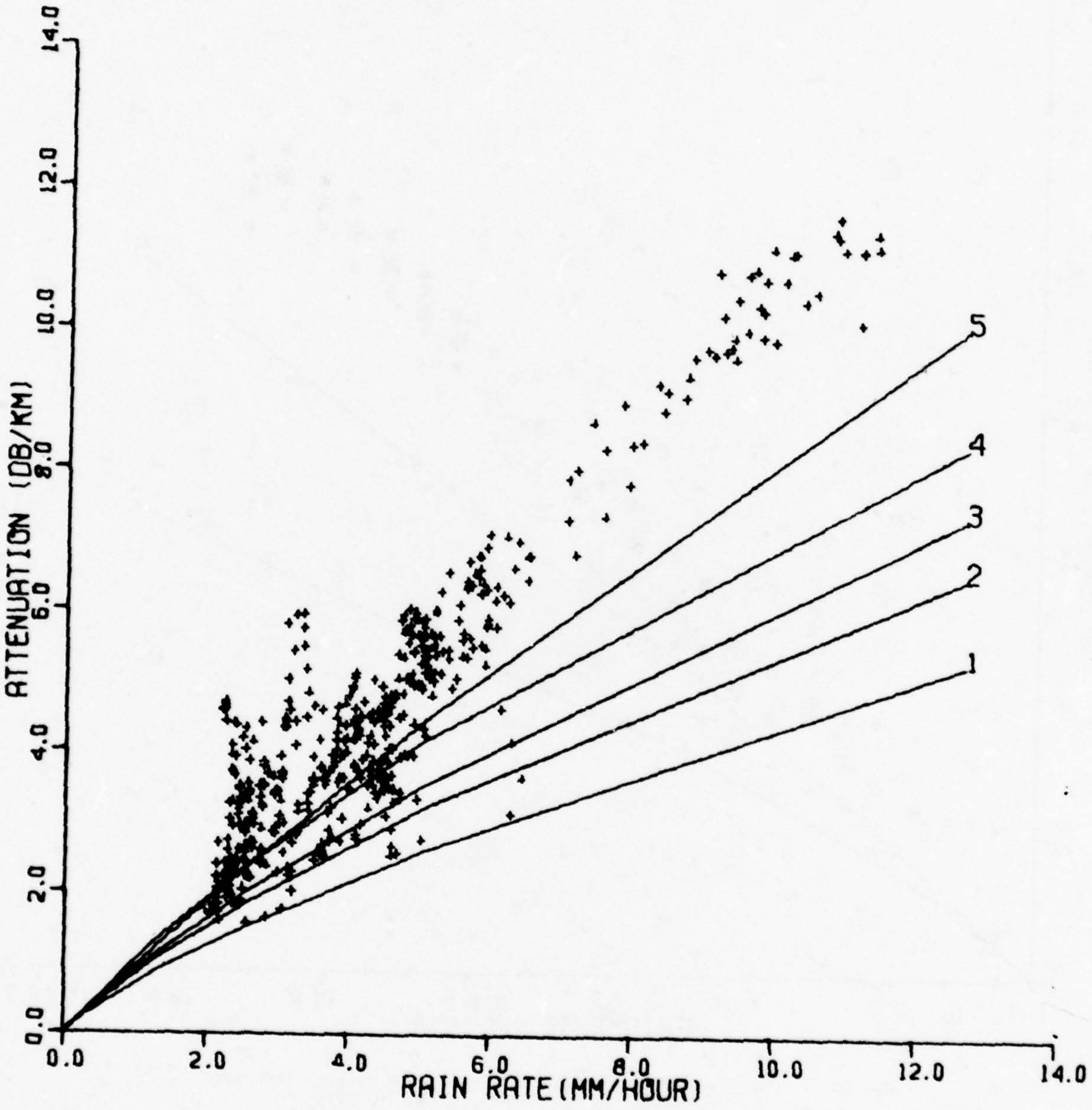

Fig. 9 10-second average scatter plot for the period of Fig. 8
Curves 1-5 as in Fig. 6

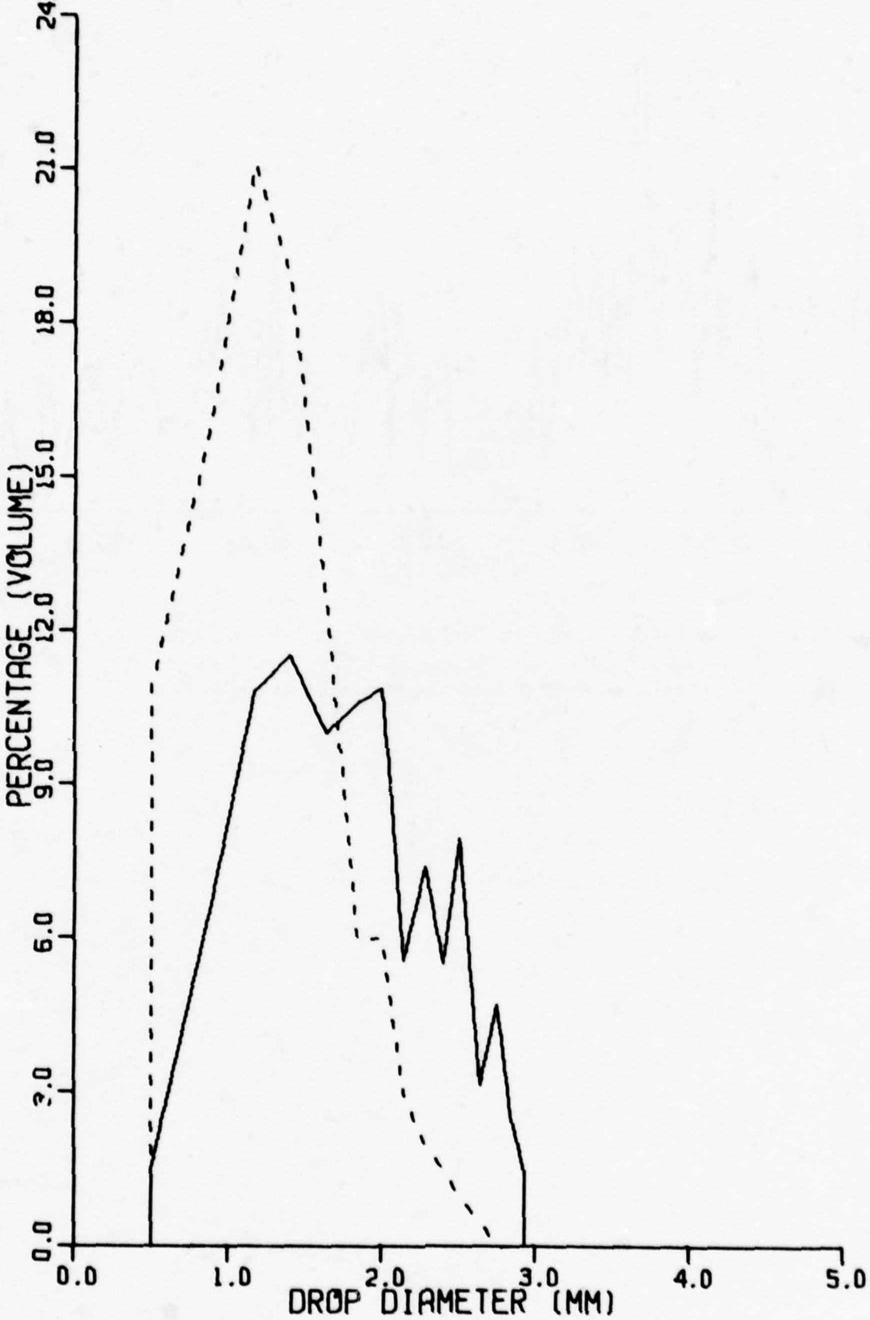

Fig. 10 Drop-size distributions at rain-rate of 1.25 mm/h

—— measured

-----Laws and Parsons

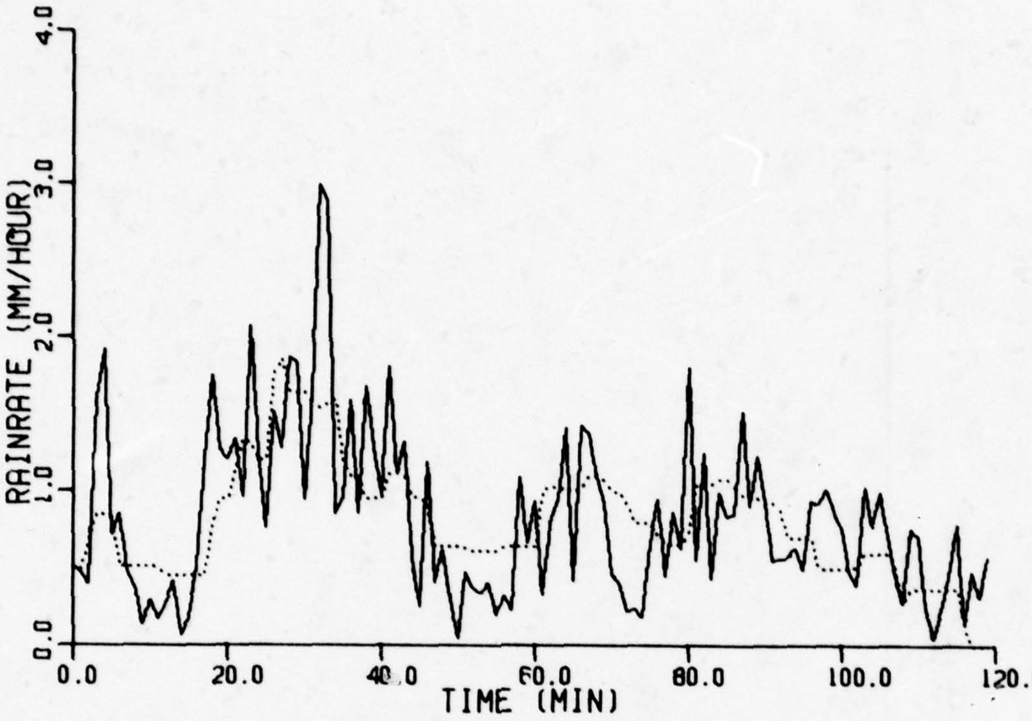

Fig. 11(a) Rain rates versus time for the period 13:46 to 15:46 h, May 26, 1978

·····measured

—— calculated from measured drop-size distribution

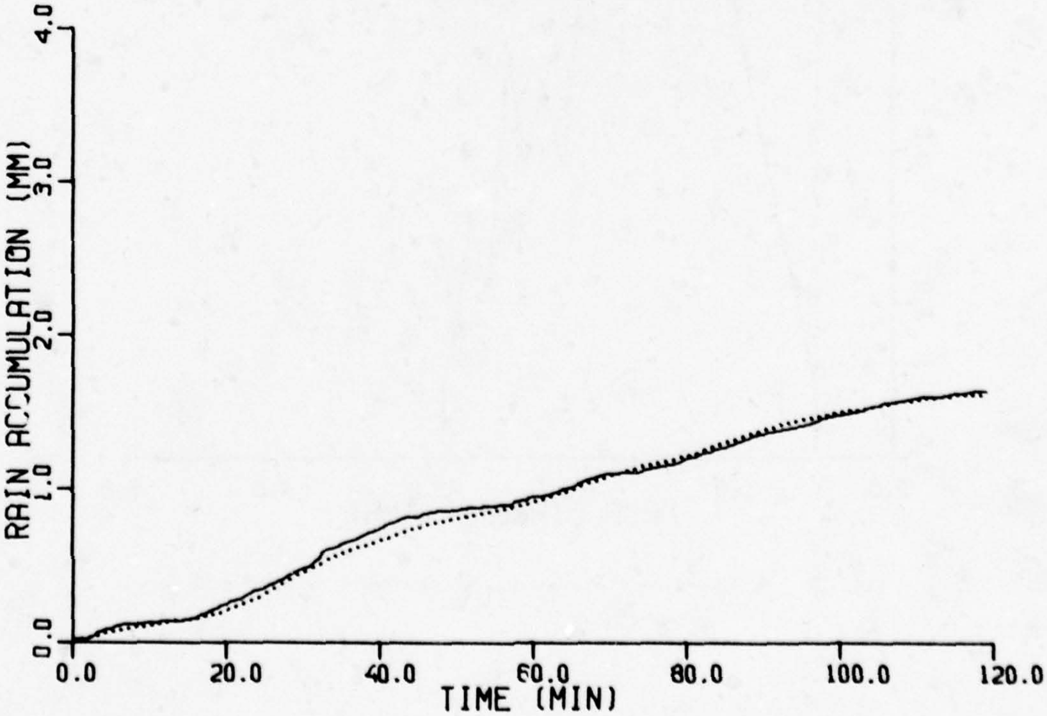

Fig. 11(b) Rain accumulation versus time for the period 13:36 to 15:46 h, May 26, 1978

·····measured by rain gauge

—— calculated from measured drop-size distribution

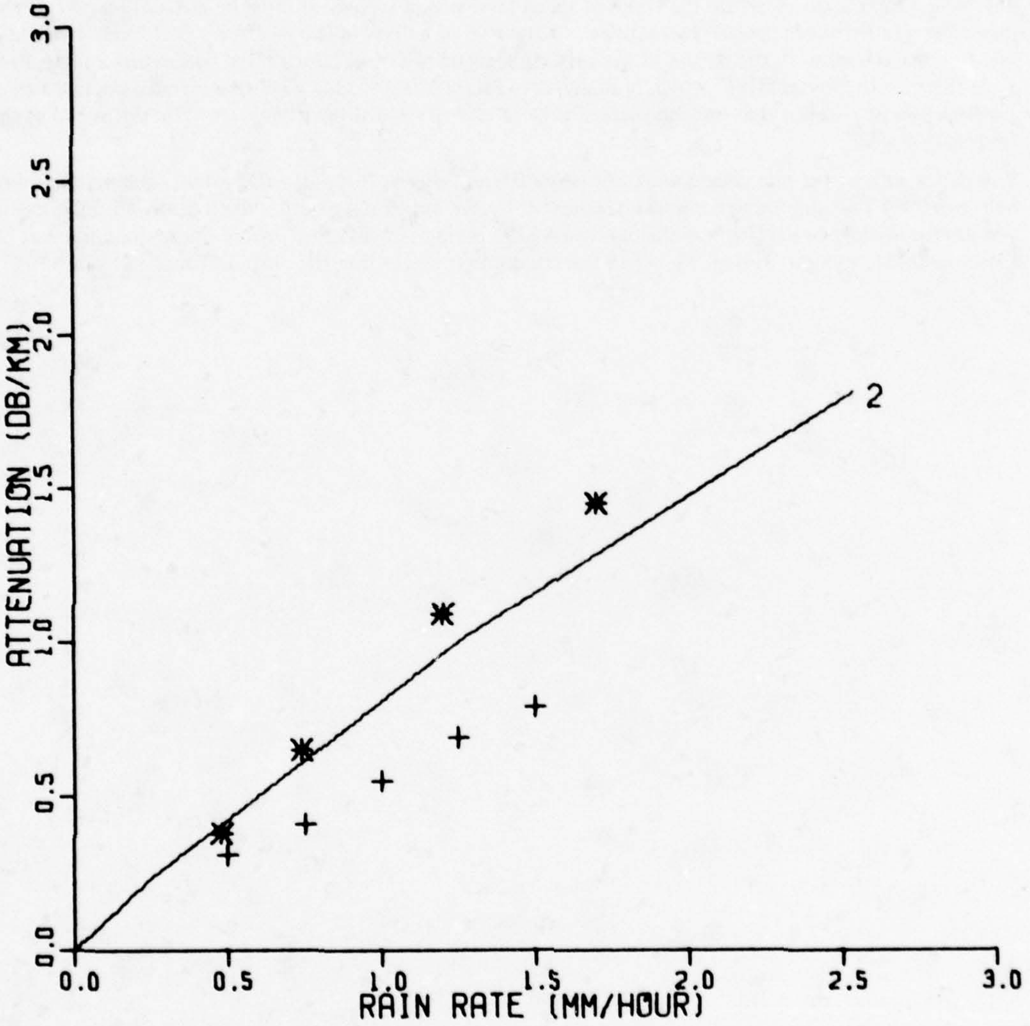

Fig. 12 Comparison between values of attenuation

* measured

+ calculated from measured drop-size distribution

—— predicted on the basis of Laws and Parsons distribution

DISCUSSION

F.Fedi, Italy

(1) Could you give us an idea on what was the effect of rain on the reflector you used?

(2) During the event you showed during which attenuation data were higher than those predicted (Fig.8) were the indications of the various raingauges along the path very different one from the other?

Author's Reply

(1) Very little if any. During the initial stages of the experiment, water was sprayed on the reflector on a clear day but no significant effect on the received signal level was observed. It must be noted, however, that even on a clear day there exist small fluctuations – a fraction of a db – in the received signal level. I would also like to draw attention to the nature of the reflecting surface. It was constructed by coating a plate glass sheet, 1 cm thick, with 'Scotch Tint" which is an adhesive plastic sheet loaded with fine metallic particles. This construction provided a very smooth surface with reflectivity indistinguishable from that of metal at the frequency used.

(2) The indications of the rain gauges were not very different during this particular event. The maximum ratio between the 10-second average rain-rates indicated by the individual gauges, which occurred only occasionally, was approximately two. This was the case during the period T_1, Figure 7, when the attenuation was higher than predicted, and also during T_3, when the attenuation was within the range of predicted values.

The Influence of the Atmosphere on Passive Radiometric Measurements

Preissner, J.

Deutsche Forschungs- und Versuchsanstalt für Luft- und Raumfahrt e.V. (DFVLR),

8031 Wessling, West Germany

Summary

This investigation is an attempt to describe completely the influence of the atmosphere on sensing the earth's surface by microwave radiometers in the frequency range from 10 GHz to 1000 GHz. The dominant influences (atmospheric gases, hydrometeors) are described. Primary attention is given to the so-called window frequencies in the range from 10 GHz to 400 GHz.

A computer program was developed which determines, for any object on the ground, the brightness temperature as it is seen from an airborne sensor. The input required are the object parameters (physical temperature, reflectivity), parameters of the atmosphere (e.g. temperature, pressure, humidity) and parameters of hydrometeors, flight height and sensor parameters (viewing angle, polarization, frequency). Statistical information about the atmospheric variables and the weather conditions, valid for the area of West Germany is incorporated in the program in order to compute probabilities that at a given flight height and for certain regions and times of the year objects (like woods, fields, roads, cars) can be detected. Some results of computation will be given and compared qualitatively with some actual airborne measurements at 11 GHz, 32 GHz and 90 GHz which were carried out at the DFVLR in the last few years.

1. Introduction

An airborne radiometer receives radiation from sources on the earth's surface. It is common to express the intensity of radiation in brightness temperature. This brightness temperature of an oject is influenced by many parameters, for instance by interfering sources (sun, moon, galaxy), background, parameters of the radiometer (antenna sidelobes, losses of the receiver) and by the atmospheric scene (figure 1). In order to get knowledge of the real nature of the object all these influences must be known to correct the radiometric signal. Some influences can be regarded as constants (e.g. receiver parameters), others vary with locality and time (e.g. atmospheric parameters). This study describes the atmospheric effects which can cause great changes in the radiometric signal. The brightness temperature of objects is increased or decreased by the atmosphere whereas the contrast between two objects is decreased in all cases. The strength of this effect in general increases at higher frequencies.

For applications in the field of radiometry, which are both civil and military, it is desirable to use frequencies as high as possible in order to get the best possible spatial resolution at a given size of antenna. To improve the contrast, however, a lower frequency may be necessary. The calculation of the brightness temperature and brightness temperature contrast makes it possible to decide which frequency shall be used in order to detect certain objects in a certain surrounding at a given weather condition, flight height and temperature resolution of the sensor. The most uncertain parameter is the weather condition. Therefore - if you want to investigate a certain region - it is useful to have some statistical information about the weather parameters in dependence of the daytime and the season of the year. It was not possible for us to get these informations by measurements. It is a common difficulty to get all atmospheric parameters as a function of height and therefore an exact description of the actual weather status is nearly impossible. It was also not possible to do flights at all weather conditions because of flight limitations at certain weather conditions for the available aircraft. Therefore comparison of theory with actual measurements is given only for some cases (fog, cloud cover).

2. Attenuation by atmospheric constituents

The attenuation of microwaves through the atmosphere, called extinction, is the sum of absorption and scattering. Absorption (and emission) is caused by gaseous molecules, whereas particles in the atmosphere (hydrometeors, dust, smoke) are responsible for absorption and scattering. The influence of dust and smoke as well as refraction and turbulent and ionospheric effects are not regarded in this paper, because they are of minor importance for the radiometry. The attenuation by atmospheric gases and by hydrometeors (rain and fog) is shown in figure 2 as a function of frequency (radio frequency up to visible region). The attenuation of the clear atmosphere rises with frequency, has a maximum of about 10,000 dB/km at wavelengths around 100 μ and decreases beyond this point. This main tendency is disturbed by many individual maxima of attenuation which are mainly caused by resonances of the gases O_2, H_2O and CO_2. The attenuation by rain increases with frequency; above 200 GHz the attenuation is nearly constant. The attenuation by fog also increases with frequency, has weak maxima and minima in the infrared region and is constant at wavelength below 3 μ.

2.1 Atmospheric gases

In the microwave (cm, mm wavelengths) and far infrared region (sub-mm wavelengths) only oxygen and water vapour produce significant absorption. Other constituents of the atmosphere as CO, N_2O, O_3 have only negligibly small influence. Oxygen is distributed homogenously in the atmosphere. Its amount depends on the pressure and therefore decreases exponentially with height. The absorption by oxygen is caused through its permament magnetic moment. There are 46 significant resonant lines, most of them (39) are centered around 60 GHz and pressure broadened into a continuous band. At 118.75 GHz there is a single resonant line. The six lines between 300 GHz and 900 GHz are of little influence. The weak nonresonant spectrum can be neglected (Liebe, H.J., 1977).

Water vapor is not uniformly spread in the atmosphere; its amount depends on the balance between evaporation, condensation and precipitation processes and in general decreases with height. The values for absolute humidity at ground level vary from 1 g/m^3 in winter to 20 g/m^3 in summer. Its amount above 10 km can be neglected. Water vapour is a polar molecule and the attenuation is caused by the electric dipole moment. For frequencies up to 1000 GHz 15 resonant lines must be considered. At 22.2 GHz and 183.3 GHz only rotational excitations occur. Above 300 GHz in addition to the rotational also vibrational transitions occur resulting in a strong absorption throughout the sub-millimetre and far infrared region. Water vapour has a nonresonant spectrum whose origin is not yet satisfactory understood and cannot be neglected and must be taken into account by an empirical formula.

The attenuation caused by oxygen and water vapour can be calculated for any frequency between 10 GHz and 1000 GHz. Five spectroscopic parameters (strength-, width- and interference factors) for each of the 46 O_2 and 15 H_2O lines plus a nonresonant H_2O absorption spectrum are required as well as the pressure, temperature and water vapour content. The spectroscopic parameters are taken from investigations and recent measurements of H.J. Liebe. The values for pressure, temperature and water vapour which are a function of the height are taken from the standard atmosphere distribution. Figure 3 shows the attenuation by oxygen and water vapour for horizontal propagation for the heights 0 km and 4 km in the frequency range from 10 GHz to 400 GHz. The curves are given by Rosenbaum (1961), the dashed lines are calculated from the values and formulae given by H.J. Liebe (1977), the single points are results from a computer program written by Fluess (1977). There are some differences in the absolute values mainly in the window frequencies which, however, compared to the effects caused by hydrometeors, are of little influence. For the computer program the values given by H.J. Liebe were used.

2.2 Hydrometeors

Absorption and scattering by solids and liquids are very different from that of gaseous molecules. There are no sharp spectral resonances but a monotonic variation with frequency. Rain causes an increase of attenuation with frequency up to 200 GHz; at higher frequencies the attenuation is nearly constant. Fog and clouds show an increase in attenuation up to the infrared region.

For the calculation of the attenuation (absorption and scattering) as a function of frequency the size of the particles is essential. When the particle size is small compared to the wavelength, Rayleigh's theory is valid and attenuation is mainly caused by scattering which is inversely proportional to the fourth power of wavelength. If the particle size is very small compared to the wavelength the absorption dominates and the attenuation then varies with aproximately the first or second power of wavelength. At the other extreme, when the particle size is considerably greater than the wavelength, scattering is independent of the wavelength and the attenuation is nearly a constant and is derived from geometrical optics. For particles which are comparable in size to the wavelength the analysis of scattering processes becomes more complex. The theory was developed by Mie. It containes expressions for scattering and absorption by spherical particles. In practice the assumption of spherical shape instead of the drop shape is satisfactory.

2.2.1 Attenuation due to rain, hail and snow

Rain causes the most severe attenuation in the microwave region. Its amount can be calculated from the rainfall rate which can vary from less than 1 mm/h (drizzle) over 3 - 10 mm/h (moderate rain) to values above 30 mm/h (excessive rain), from the drop size distribution (100 μ to more than 1 mm), terminal velocity and scattering properties of spheres of a given size, which are temperature dependent because the complex refractive index is a function of temperature. Figure 4 shows the attenuation caused by rain in the frequency range from 10 GHz to 1000 GHz for two different rain rates. The values are taken from three different authors, namely Joss et al., Laws and Parsons, Marshall-Palmer. The differences are caused by different assumptions for the standard drop size distribution (Olsen, R.L., 1977). In practice these deviations are of little importance compared to the inaccuracies in the calculations of the attenuation along a path, resulting from the ignorance of the exact rainfall rate and the variation in the horizontal and vertical extension.

The attenuation by hail and snow is much smaller than by rain (about two orders of magnitude). The reason is the difference of dielectric properties between the two phases frozen and liquid. If the snow or hail is melting the attenuation will be higher than for rain because the fractional volume is higher than for a rain drop with the same water content. While the attenuation by rain decreases with rising temperature, the attenuation by snow and ice is increasing with higher temperature.

2.2.2 Attenuation due to fog and clouds

The size of the particles in fog and clouds is considerably smaller than in precipitation (less than 100 μ). Therefore the attenuation mainly is caused by absorption and not by scattering effects and is dependent on the total water content and not on the particle size distribution. Fog and clouds are similar in nature, differing only in location and particle size distribution. Ice clouds cause only little attenuation and are in general negligible. Figure 5 shows the attenuation for ice clouds and for fog and waterclouds as a function of frequency (Fluess, H. 1975). The dependence on temperature is also shown in the diagram.

3. Brightness temperature calculation

To get the brightness temperature of objects on the earth's surface the radiative transfer equation must be used because emission and absorption occurs at all layers within the atmosphere. First the physical fundamentals will be given and then some details of the computer program.

3.1 Physical fundamentals

Figure 6 shows the individual terms of radiation which contribute to the radiometric signal. The radiometer receives by the main beam of the antenna (the sidelobes are neglected here) three kinds of radiation. The first term is the emitted energy of the object expressed in brightness temperature. This is the physical temperature of the object multiplied by the emissivity (1-R) (R = reflectivity, (1-R) = emissivity in the case of specular reflection) and multiplied by the transmissivity t, of the atmosphere between object and sensor. The second term is the energy which is reflected by the object. This are again two components. One of them is the brightness temperature of the space T_s multiplied by the transmissivity t_1 of the atmosphere between object and space. The amount of the brightness temperature is very low (less than 3 K) and can be neglected in most cases except when T_s is the brightness temperature of the sun, moon or an artificial transmitter. The other part of radiation which incidents onto the object is the radiation caused by the atmosphere itself. Its brightness temperature between space and earth (T_1) is calculated in the following way: The physical temperature of each layer is multiplied by its emissivity ($1-t_{(h)}$) and by the transmissivity between the height (h) of this layer and the ground level. This expression must be integrated between the height h_s of the space and the height of the ground level. Both the brightness temperature of the space ($T_s \cdot t_1$) as well as the brightness temperature of the atmosphere between space and earth (T_1) are multiplied with the reflectivity of the object (R) and the transmissivity of the atmosphere between earth and sensor (t_2). The third term of radiation which is received by the radiometer is the brightness temperature of the atmosphere between earth and sensor (T_2). It is calculated in the same manner as described above. In practice instead of an integration between the heights a summation over layers with constant parameters is carried out. For this purpose the atmosphere up to a height of 20 km is devided into spherical layers of varying thickness. Near the earth more layers are needed (distance between two layers 20 m) than in heights above 10 km (distance between two layers 500 m).

3.2 Some details of the computer program

The computer program first calculates the attenuations for each height level, which are the sum of the single contributions by atmospheric gases and hydrometeors. Then by aid of the radiometric transfer equation, described above, the values for transmission, emission and the brightness temperature (in K) are computed. The input needed is

- parameters of the object (physical temperature, reflectivity as a function of frequency, polarization and incident angle)
- parameters of the atmosphere (temperature, pressure, water vapour content)
- parameters of the hydrometeors rain, clouds, fog, snow
- flight parameters (height over ground)
- sensor parameters (frequency, polarization, viewing angle)

The values of the brightness temperature were calculated for 38 different frequencies in the range from 10 GHz to 400 GHz, for 2 viewing angles (0°, 60°), for 6 flight heights between 100 m and 8000 m, for 41 reflectivities of the object (steps of 0.025 in the range from 0 to 1) and for 19 different weather conditions.

4. Results

The results of the computation get the most practical use if - instead of absolute brightness temperature - the brightness temperature contrast between two objects is shown as a function of frequency, weather condition or other parameters. This is done in the first part of the discussion of the results; in the second part some statistical information about the weather conditions in West Germany will be related to the computed data.

4.1 Brightness temperature contrasts

Figure 7 shows the brightness temperature contrast between the two objects vegetation-concrete as a function of frequency. The values were computed for three different flight heights and for standard atmosphere condition. The reflectivity was assumed to be frequency independent for vegetation (R = 0.025) and for concrete (R = 0.175). The figure is similar to figure 3, but with inverse amplitudes. This is evident because high attenuation (fig. 3) must correspond to low contrast (fig. 7). The absolute values of the contrast are only of interest when the temperature resolution of the radiometer is known. Radiometers exist up to 220 GHz and have a temperature resolution of about 1 K to 5 K at 10 ms integration time. This integration time is necessary to produce radiometric images from an aircraft with usual antenna sizes (~ 30 cm Ø), flight heights (several hundred m) and flight velocities (100 - 200 kn). Radiometers at higher frequencies (up to 300 GHz) will be built with similar performance in future. The quality of the received signal can be determined by regarding the ratio of the brightness temperature contrast to the temperature resolution of the receiver. For recognition of objects this ratio must be greater than 1. This is fulfilled - as can be seen in fig. 7 - for all flight heights and frequencies up to 250 GHz, with the exception of the 60 GHz region and the 180 GHz region. If low error probabilities for the detection of contrasts are demanded (< 1 %) this ratio should be at least 10. In this case one can see from the diagram that at flight heights of about 3 km radiometers above about 160 GHz cannot be used. The detection will be possible at higher frequencies if more contrasting object combinations are considered like vegetation-water or vegetation-metal. If the weather conditions are worse, lower frequencies must be used. This effect is shown in figure 8. The brightness temperature contrast as a function of the frequency is shown for five different weather conditions. The diagram shows that for detection of the objects concrete-vegetation frequencies up to 30 GHz are suitable for all weather conditions, 80 GHz - 90 GHz frequencies are not suitable for heavy rainfall, 130 GHz - 140 GHz is only suitable for standard atmosphere condition and fog (or clouds) and 220 GHz is only suitable for standard atmosphere and light fog (or cloud). The data are valid for a flight height of 3 km and for a viewing angle of 0°. At lower flight heights the contrast will be improved; for viewing angles greater than 0° the contrast - according to the greater path length through the atmosphere - will be decreased. Figure 9a, b shows the temperature contrast for 3 object combinations and for the same 5 weather conditions as in fig. 8 for the most important window frequencies (11 GHz, 32 GHz, 90 GHz, 140 GHz, 220 GHz, 300 GHz). The reflectivities for metal and concrete were assumed to be frequency independent (R = 1 for metal and R = 0.175 for concrete), whereas water, because of its polar character, has a strong frequency dependence up to about 1000 GHz. The values are taken from the empirical formula given by Stogryn and Hasted. The reflectivity decreases from about 0.6 at 11 GHz to about 0.3 at 220 GHz. The flight height was assumed to be 500 m and the viewing angle 0°. The diagram shows not only the absolute value of the brightness temperature contrast but additionally demonstrates how to distinguish different objects at various and even unknown weather conditions. If the columns of a certain object shown in figure 9 representing the different weather conditions are all distinct from the columns of the other object - as it is the case at 11 GHz - the objects metal, water and concrete can be detected in a surrounding of vegetation uniquely without the knowledge of the weather conditions. At 32 GHz this is only true in the absence of heavy rainfall. At 90 GHz this is only possible for standard atmosphere and fog (or clouds). At 140 GHz and 220 GHz a clear detection and distinction of the objects is only possible for standard atmosphere and light fog. With the aid of such diagrams for different flight heights one can predict at what frequencies and at what weather conditions certain objects can be distinguished.

4.2 Relation of the detectibility of objects to weather statistic

For a radiometric system in action it is necessary to know for how many hours (e.g. per month) the system can operate without being disturbed by the weather conditions when the detection of certain objects is demanded. This information should be known for each region. For the area of West Germany there exist a lot of detailed measurements for some regions. A complete survey of all weather conditions for all regions including the occurance in % time per year or month does not exist. Therefore only few examples of the use of statistical information can be shown. A very rough weather statistic model is given by Fluess for two large districts of West Germany. Continuous measurements were done in summer and winter 1973. The values for pressure, temperature and humidity as a function of height (up to 12 km) are given. They are listed as averaged values, minimum values and maximum values each for summer and winter. Thus there were obtained 12 model atmospheres. The frequency of occurance of these model conditions, however, is not given; also hydrometeors, fog and clouds are not included in the investigation. Figure 10 shows the vertical temperature distribution for the area of Munich in summer 1973 in comparision with the values of US-midlatitude summer. For the area of Munich the extreme values are also shown in the diagram. Figure 11 shows the visibility in fog for W. Germany. The results are based on the data of 35 meteorological stations and have been collected in a period of ten years. The data are separated for North- and South-Germany and for day and night. Fog is defined to begin at a visibility of 1000 m; the measurements were carried out down to 200 m visibility. It is seen from the diagram that fog will occur in South Germany at night much more often than at day or at day and night in North Germany. Similar observations exist for rain or for temperature inversions in the atmosphere. A complete weather statistic model which takes into account all weather conditions and a great number of climatological areas of West Germany (at least 10 or more) is in preparation.

4.3 Some results of actual measurements

Airborne measurements with radiometers were carried out at the three frequencies 11 GHz, 32 GHz and 90 GHz. The weather conditions during the flights were clear weather, fog, cloud cover, light rain. Although the exact weather conditions (temperature, humidity) were registrated in no case, some interesting results were obtained by comparison of the weather situation, described by the crew of the aircraft during the flight, and the measured brightness temperature of objects on the earth. At 11 GHz there was no noticable reduction of contrast between the observed objects at the various weather conditions. At 32 GHz a flight was done over two lakes one of which was covered with a layer of fog with a thickness of about 200 m, whereas the other was free of fog. The brightness temperature difference between the two lakes is about 5 K and can be seen from figure 12. Figure 12 also shows that the brightness temperature of the first lake, which is free of fog, is not constant, but increases along the flight path up to the value of the brightness temperature of the lake, which is covered with fog. The reason is supposed to be the continuous increase of air humidity which results in an increase of brightness temperature as well as fog. It was tried to compare the measured brightness temperature contrast between the two lakes with theoretical calculations. From observation it is known that the visibility in the fog layer was less than 200 m. If a visibility of 100 m is assumed the calculation of contrast will result in a value of about 5 K which agrees with measurement. Figure 13 shows the brightness temperatures of a lake at 90 GHz for five different flights. The fraction of cloud cover and the height of the clouds during the flights was described by the crew of the aircraft. The brightness temperature varies from about 225 K to 260 K. In general the brightness temperature increases with an increase of cloud cover. It is seen from figure 12 that there are some exceptions which are supposed to be due to different water content of the clouds during the different flights.

5. Conclusions

The possibility to calculate the probable brightness temperature contrast between two objects on the ground as it is seen by an airborne radiometer at a given flight height, viewing angle and receiver frequency is an essential tool for system designers. In combination with statistic weather information it is possible to predict at what times of the year and in which regions radiometers can usefully operate. In order to get complete information about the actual brightness temperature measured by a radiometer a survey of the parameters of the most common natural objects as a function of frequency and angle must be done. These parameters (conductivity, dielectric properties) provide the reflectivity which is needed for the calculation. Further parameters which are needed to correct the brightness temperature are the properties of the receiver (noise figure, antenna diagram). Essential preliminary results of this study were among others that above 250 GHz radiometers for ground observations are not useful (unless one is satisfied with the detection of just water or metal) and that observation above 90 GHz is not possible at rainfall-rates above about 5 mm/h (unless the flight height is essentially lower than 300 m).

Future investigations will be efforts to get - in reverse to the above calculations - information about the actual weather conditions and thus to have the possibility to calculate the real brightness temperature of the object. This could be done by at least two or more simultaneous measurements. Some of these possibilities would be the measurement of the brightness temperature of the object and of the sky, measurement at two angles (e.g. 0^{o} and 45^{o}), measurement at two polarizations at an angle greater than 20^{o}, or measurement at two or more frequencies (multispectral radiometry).

Contents

Summary

1. Introduction
2. Attenuation by atmospheric constituents
2.1 Atmospheric gases
2.2 Hydrometeors
2.2.1 Attenuation due to rain, hail and snow
2.2.2 Attenuation due to fog and clouds
3. Brightness temperature calculations
3.1 Physical fundamentals
3.2 Some details of the computer program
4. Results
4.1 Brightness temperature contrasts
4.2 Relation of the detectibility of objects to weather statistic
4.3 Some results of actual measurements
5. Conclusions
References

References

1. Amt für Wehrgeophysik 1977, "Gebietsmäßige Sichtkurven für die Bundesrepublik Deutschland", Porz-Wahn, W. Germany.

2. Fluess, H. 1975, "Beschreibung des Einflusses der Atmosphäre und der Reflexions- und Emissionseigenschaften der Erdoberfläche auf die Leistung von Mikrowellen-Aufklärungssystemen", MBB, Ottobrunn b. München, W. Germany.

3. Liebe, H.J., 1977, "EHF Properties of Air", NTZ Bd. 30 (1977) Heft 1.

4. Olsen, R.L., Rogers, D.V., Hodge, D.B., 1977, "The aR^b Relation in the Calculation of Rain Attenuation" To be submitted for publication in the IEEE.

5. Preißner, J., 1975, "Mikrowellenradiometrische Messungen vom Flugzeug aus bei zum Teil fehlender Bodensicht", DFVLR, Oberpfaffenhofen, W. Germany.

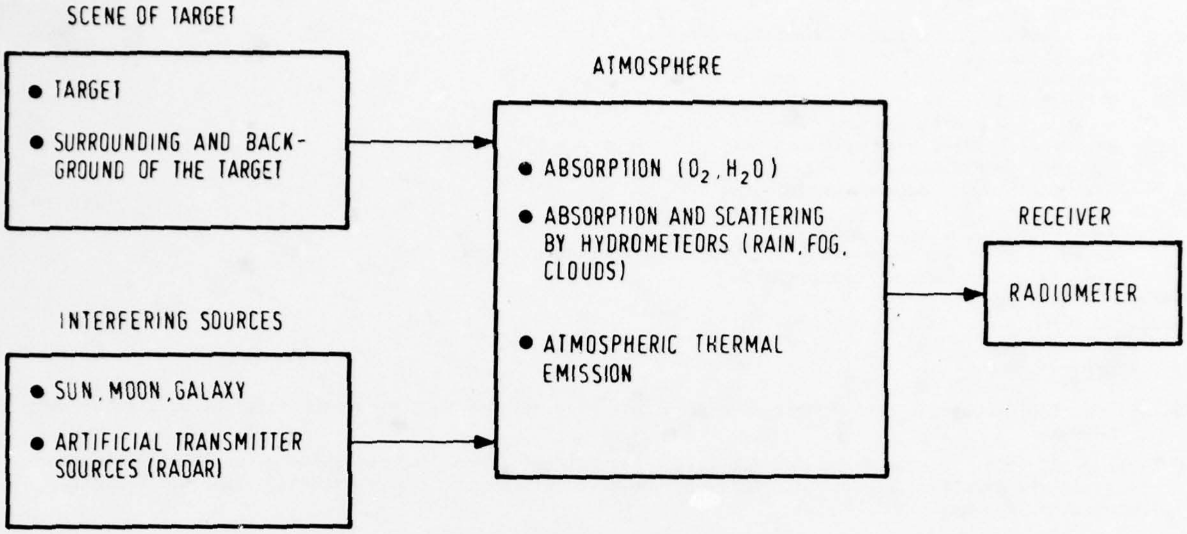
SCENE OF TARGET
TARGET
SURROUNDING AND BACKGROUND OF THE TARGET
INTERFERING SOURCES
SUN, MOON, GALAXY
ARTIFICIAL TRANSMITTER SOURCES (RADAR)
ATMOSPHERE
ABSORPTION (O_2, H_2O)
ABSORPTION AND SCATTERING BY HYDROMETEORS (RAIN, FOG, CLOUDS)
ATMOSPHERIC THERMAL EMISSION
RECEIVER
RADIOMETER

Figure 1 Parameters influencing the radiometer input signal

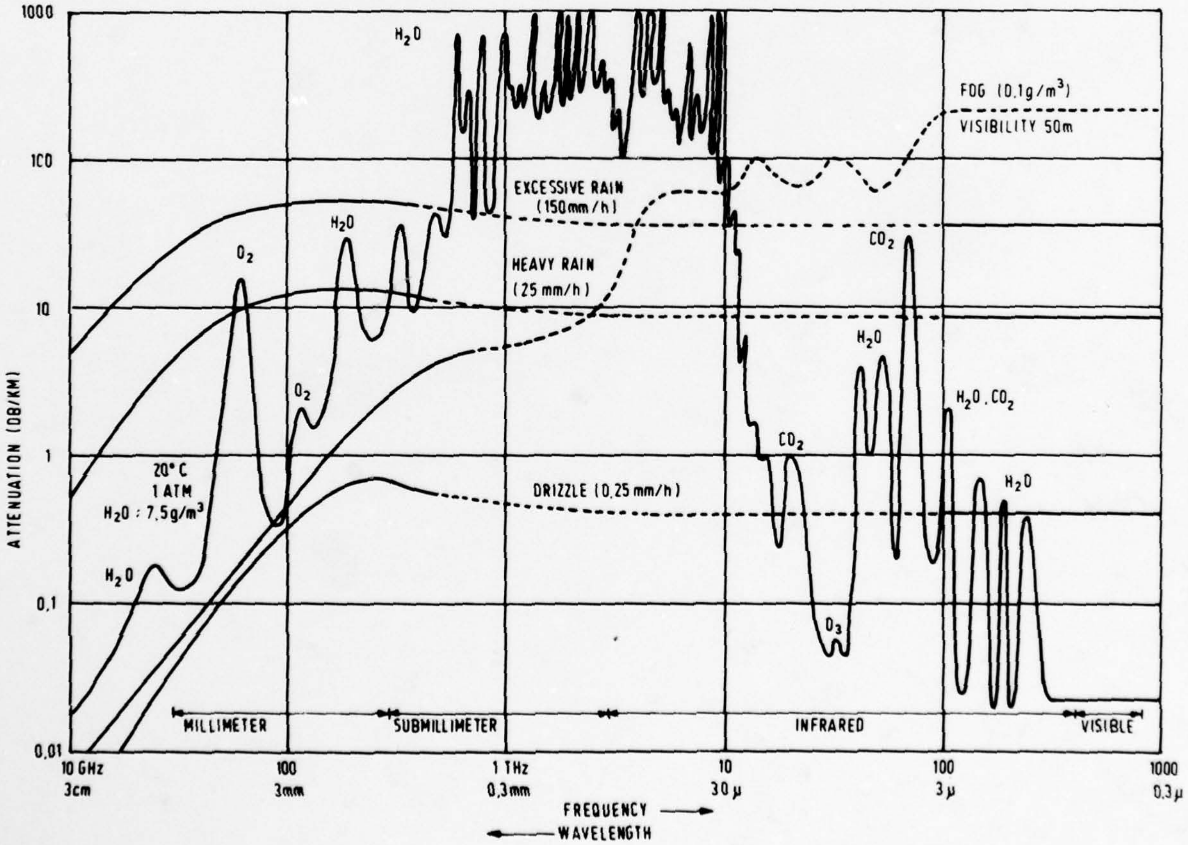

Figure 2 Attenuation by atmospheric gases, rain and fog

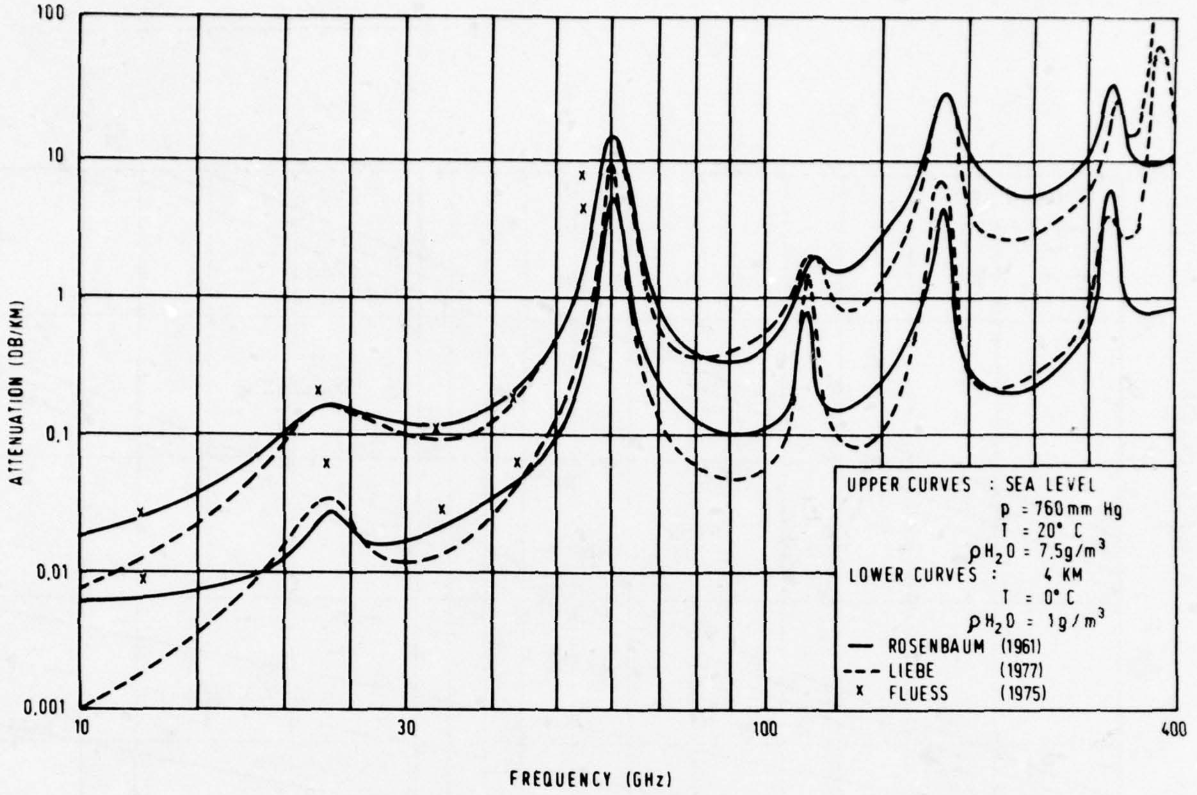

Figure 3 Attenuation by atmospheric gases (References by different authors)

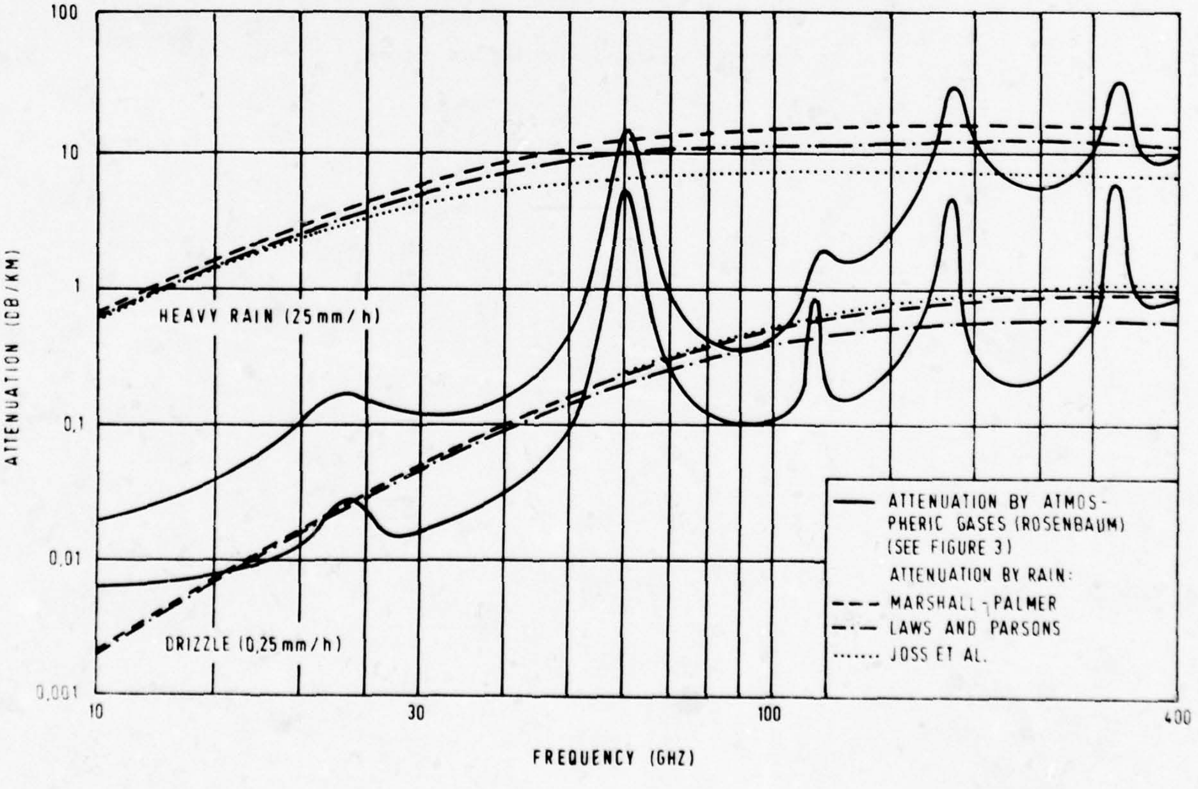

Figure 4 Attenuation by rain

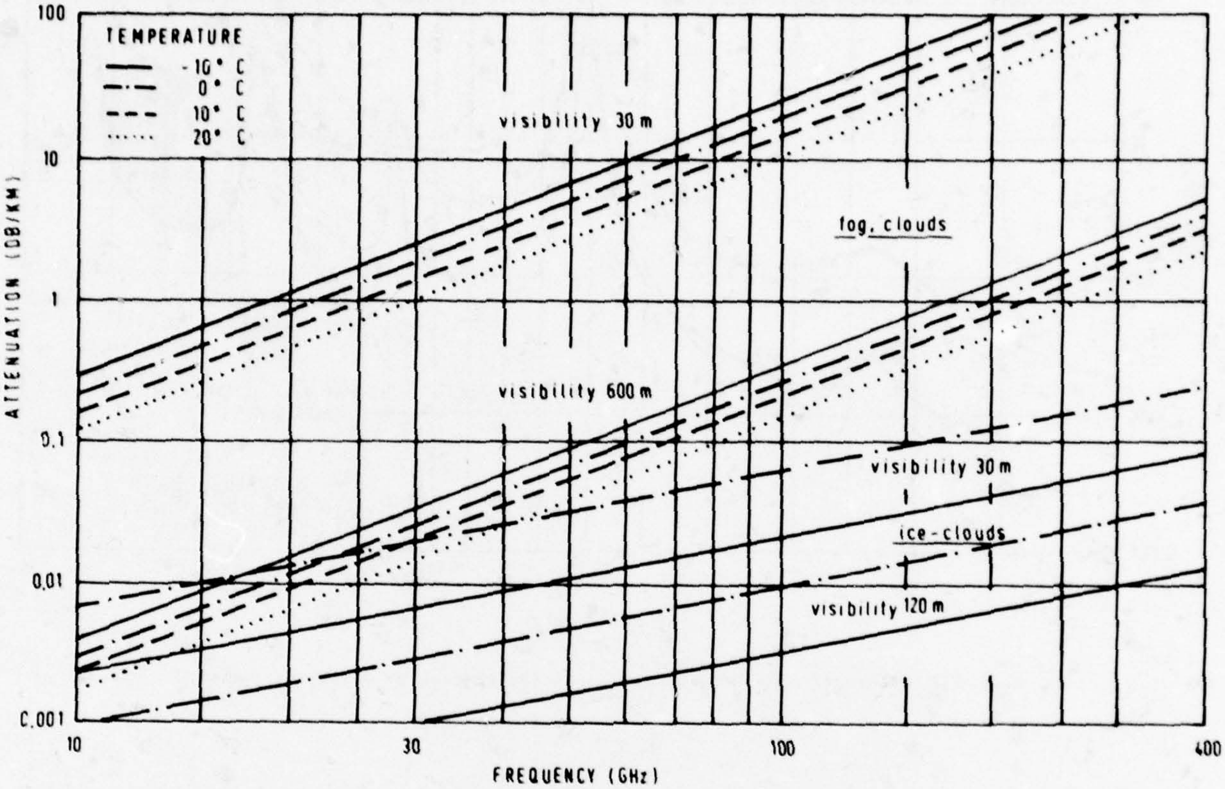

Figure 5 Attenuation by fog and clouds

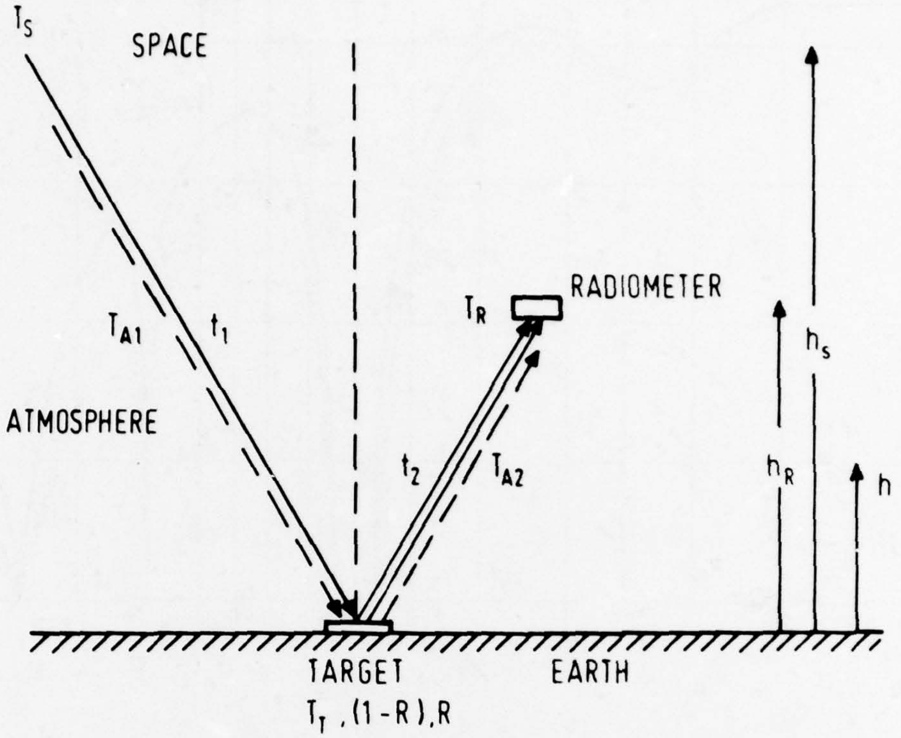
T_S
SPACE
T_{A1}
t_1
ATMOSPHERE
T_R
RADIOMETER
t_2
T_{A2}
h_S
h_R
h
TARGET
T_T, (1 - R), R
EARTH

T_R = brightness temperature received by the radiometer (K)

T_S = brightness temperature of the space (K)

T_T = physical temperature of the target (K)

t_1, t_2 = transmission of the atmosphere

R = reflectivity of the target, $(1 - R)$ = emissivity

T_{A1}, T_{A2} = brightness temperature contributed by atmosphere (K)

$$T_R = t_2 \cdot ((1-R) \cdot T_T + R\,(t_1 \cdot T_S + T_{A1})) + T_{A2}$$

$$T_{A1} = \int_{h_S}^{0} T_{(h)} \cdot (1 - t_{(h)}) \cdot \left(\overset{0}{\underset{h}{\pi}}\, t_{(h)}\right) dh$$

$$T_{A2} = \int_{0}^{h_R} T_{(h)} \cdot (1 - t_{(h)}) \cdot \left(\overset{h_R}{\underset{h}{\pi}}\, t_{(h)}\right) dh$$

Figure 6 The radiometric equation

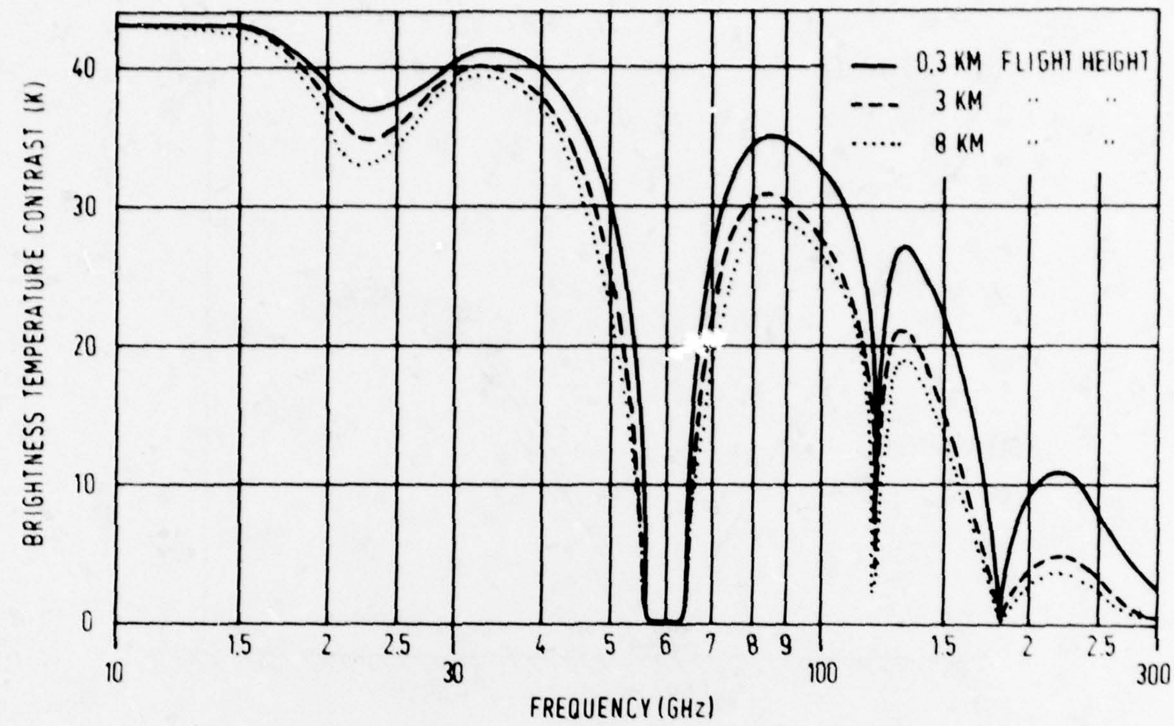

Figure 7 Brightness temperature contrast between vegetation and concrete for three different heights

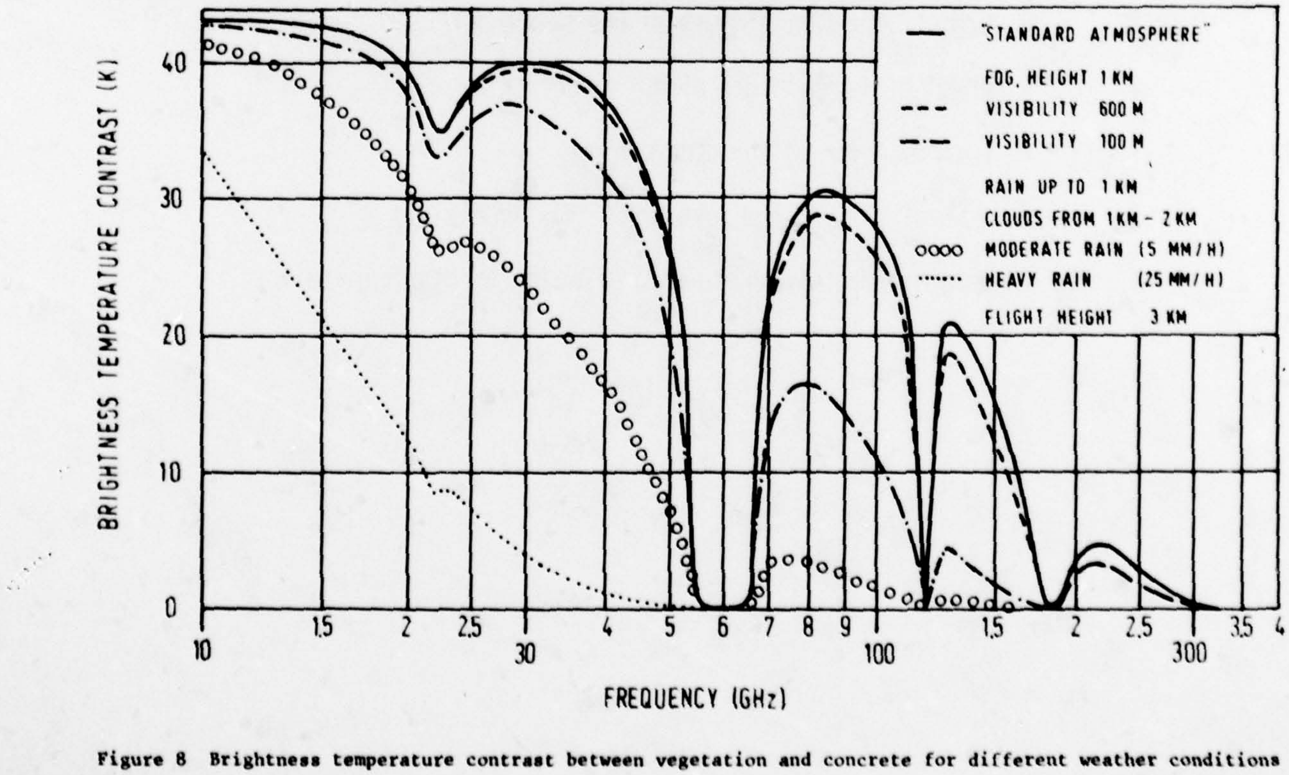

Figure 8 Brightness temperature contrast between vegetation and concrete for different weather conditions

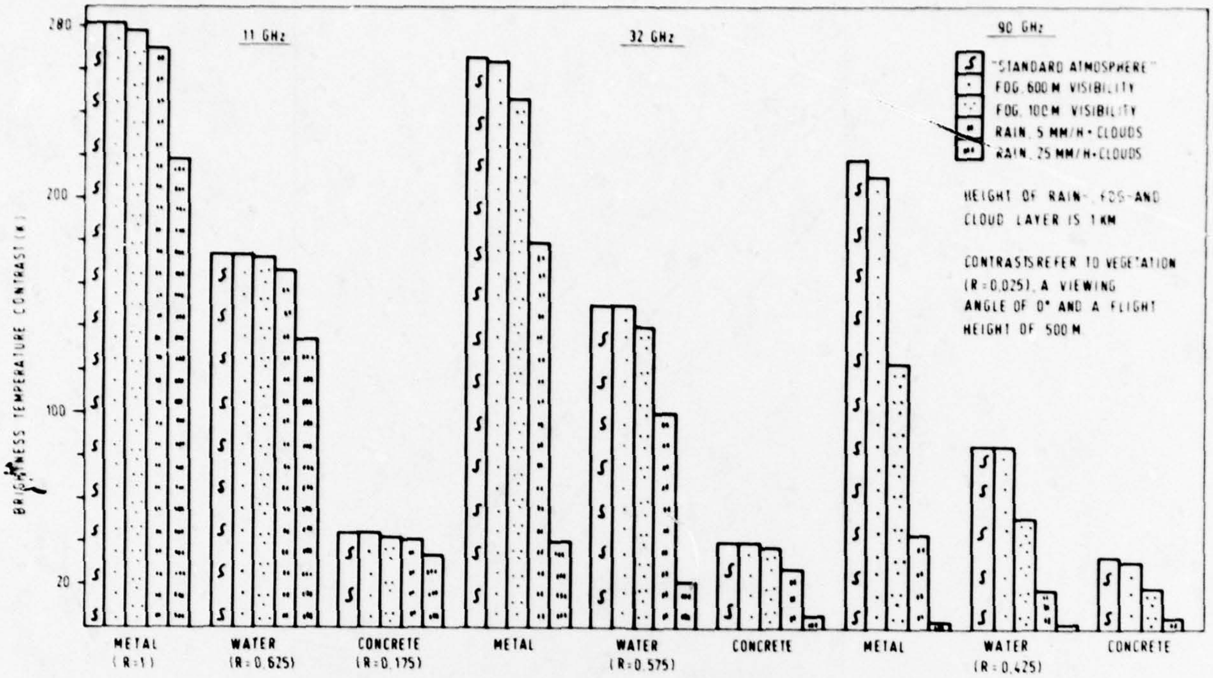

Figure 9a Brightness temperature contrast for different objects, weather conditions and frequencies (11 GHz, 140 GHz, 90 GHz)

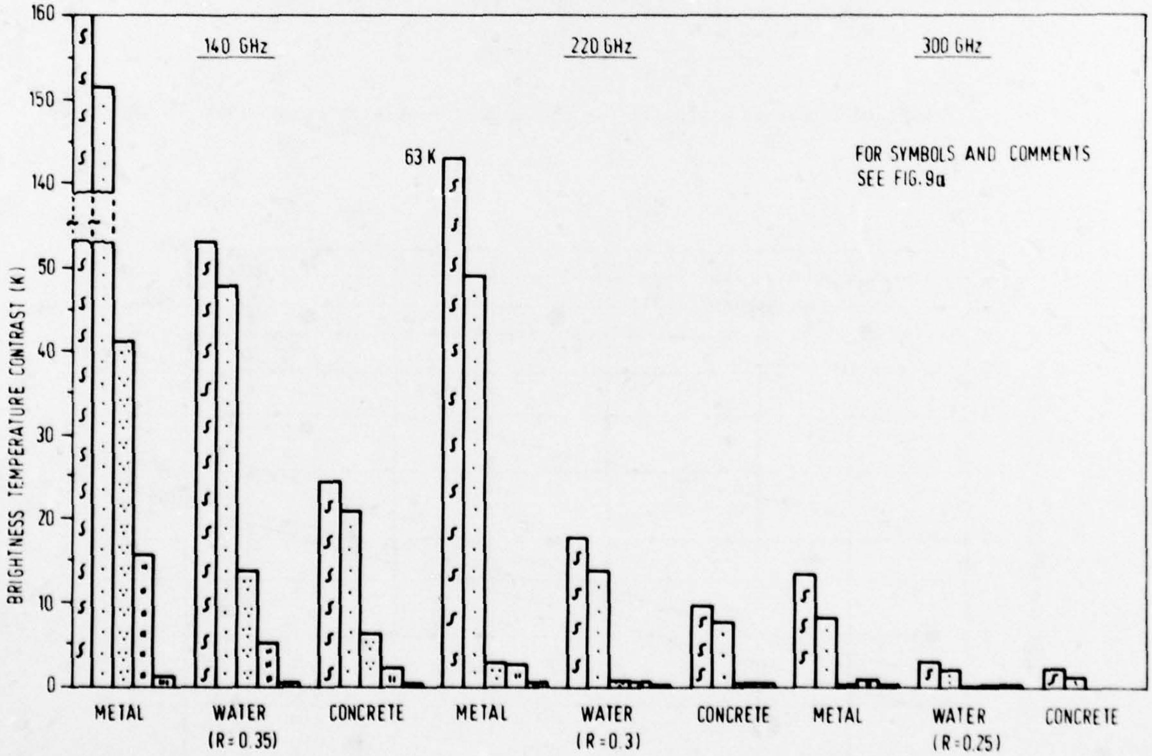

Figure 9b Brightness temperature contrast for different objects, weather conditions and frequencies (140 GHz, 220 GHz, 300 GHz)

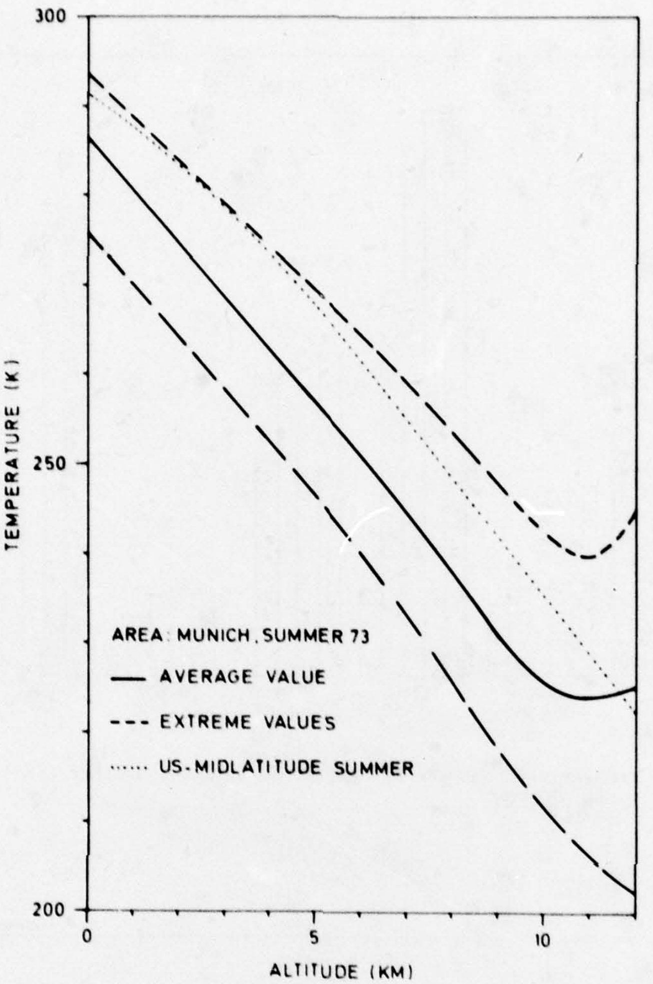

Figure 10 Temperature profils for the area of Munich in summer 1973

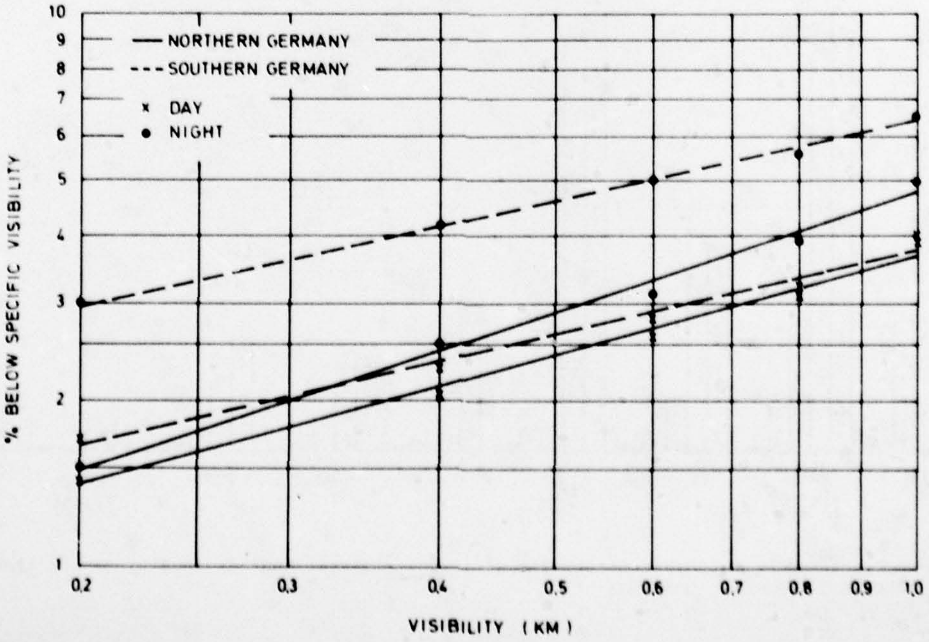

Figure 11 Visibility in percent of time for West Germany

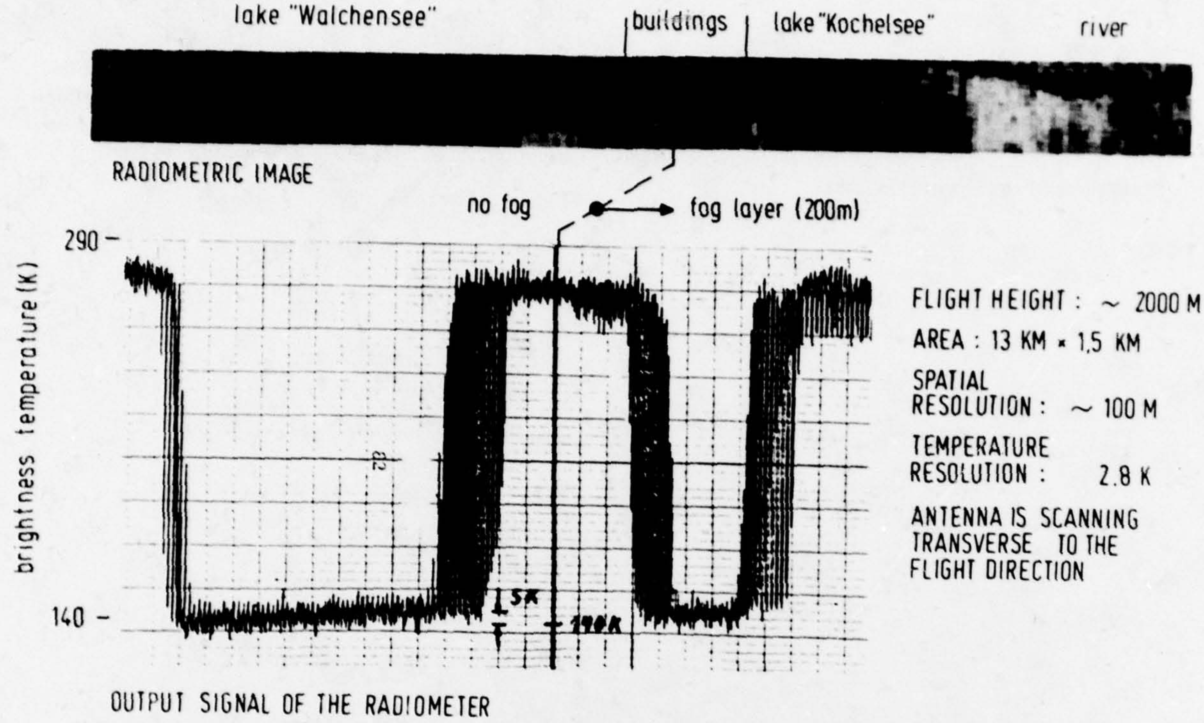

Figure 12 Example of a radiometric measurement at 32 GHz

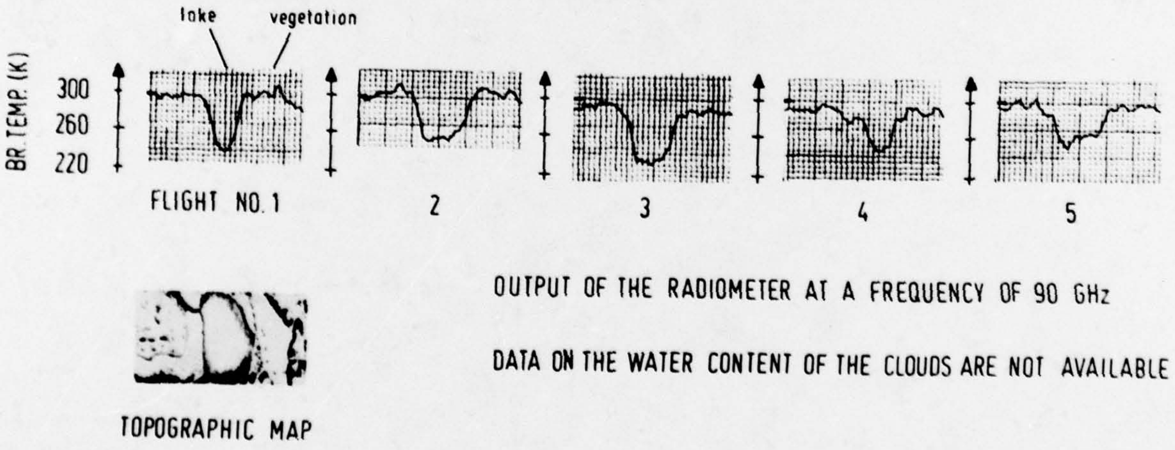

FLIGHT HEIGHT : 400 M
SPATIAL RESOLUTION : 6 M
TEMPERATURE RESOLUTION : 10 K

FLIGHT NO.	CLOUD SITUATION
1	3/8 IN 1200 M
2	4/8 IN 1200 M
3	4/8 IN 600 M - 1500 M
4	8/8 IN 400 M
5	8/8 IN 350 M

Figure 13 Example of a radiometric measurement at 90 GHz

DISCUSSION

Comment by R.J.Emery, UK

I should like to point out to the speaker that there is confusion in the data used for calculating molecular absorption in the atmosphere, as well as in defining fog conditions. Figure 2 is not realistic for the molecular absorption measured in the window regions at submillimetre and infrared wavelengths, and disagreed with the figure given by Dr L.Whicker in the first paper. For radiometric measurements, the calculations must include atmosphere broadening of the absorption lines.

ATMOSPHERIC SOUNDING USING MILLIMETER WAVE RADIOMETRY

K.F. Künzi, D. Meier, A. Randegger

Institute of Applied Physics
University of Berne, Switzerland
Sidlerstr.5, CH-3012 Berne

SUMMARY

Microwave radiometry can be used to investigate the atmosphere by measuring thermal emission from molecular resonances. These measurements provide information on atmospheric temperature and composition. A major advantage of this technique over comparable infrared methods is the capability of microwaves to penetrate clouds. Microwave instruments are presently being used in satellites, aircrafts and ground based for investigations in meteorology (temperature, atmospheric water content), and atmospheric physics (composition of stratosphere and mesosphere).

1. INTRODUCTION

The fast progress made in recent years in the field of low noise millimeter wave receivers is making this portion of the spectrum very attractive for passive microwave radiometry (PMR) to study the earth atmosphere.

The atmospheric microwave spectrum is dominated by resonant absorption of the oxygen molecules (O_2), the water vapor molecule (H_2O) and non-resonant absorption by water vapor and liquid water. In addition many minor atmospheric constituents show microwave resonances such as O_3, N_2O, CO, SO_2, etc. Atmospheric pressure is the dominant line broadening mechanism up to altitudes of ∿ 80 km, therefore by measuring accurately the pressure broadened absorption line of a molecule, it is possible to determine the height distributions of this particular constituent. Or in the case the height distribution is well known (e.g., O_2 has a constant mixing ratio up to 80 km), it is possible to infer the height profile of atmospheric temperature.

2. MICROWAVE SPECTROMETER EXPERIMENTS ON THE NIMBUS SATELLITES

The microwave experiments on the weather satellites NIMBUS-5, 6, and G are used to produce global atmospheric temperature maps independent of cloud cover and to determine the atmospheric water vapor and liquid water content over ocean. These instruments also provide information on the earth surface such as ice coverage over ocean and snow cover over land [1], this later data is of great importance in climatology.

The microwave spectrometers on NIMBUS-5 and -6 (NEMS and SCAMS) are measuring atmospheric emission at 5 frequencies, on the weak water vapor resonance at 22.2 GHz, in the atmospheric window at 31.2 GHz, and at 3 frequencies on the O_2 absorption line complex at 60 GHz. The two lower frequencies provide information on atmospheric water vapor and liquid water content over ocean and on surface parameters such as snow and ice cover over land and ocean areas. The atmospheric temperature profile up to 25 km altitude can be retrieved with an rms accuracy of 2 K. Fig.1 shows four examples of NEMS temperature profiles compared with data from radio sondes [2]. Water vapor retrievals are accurate to about 0.4 gr/cm^2. Liquid water estimates are believed to be accurate to about 0.01 g/cm^2 [3].

3. EXPERIMENTS TO MEASURE MINOR ATMOSPHERIC CONSTITUENTS

More recently the technique of observing the thermal emission of microwave resonances of atmospheric constituents has been applied to investigate the atmospheric composition in the stratosphere and mesosphere. Because the absorption coefficients tend to be higher for higher frequencies, only the frequency range above 100 GHz is of interest for sensing atmospheric constituents such as O_3, CO, N_2O, etc.

Experiments, both groundbased and airborne, have been conducted by GOLDSMITH et.al. [4], and WATERS et.al. [5] among others to detect stratospheric trace gases such as O_3, H_2O, CO, N_2O, and ClO.

For application in atmospheric physics the mixing ratio profile has to be retrieved from the measurement. For our groundbased ozone sounder we have developed an inversion algorithm based on Chahine's relaxation method [6].

Figures 2a and 2b show ozone profiles (measured with radiosondes up to 35 km) and corresponding ozone profiles retrieved from calculated microwave brightness temperatures. For this test of the iteration method noiseless radiometric data was assumed and an infinite frequency resolution. The inversion accuracy with this iteration technique is approximately 0.5 ppm. The accuracy of the determined profiles remain virtually unchanged for data with an rms-noise in the order ∿ 0.1 K and a frequency resolution of ∿ 0.1 MHz near line center. The height resolution is in the order of ∿ 10-12 km, given by the width of the weighting function in the radiative transfer equation. The width of the weighting function is essentially the same for groundbased and spaceborne (nadir-looking) observation.

A much better height resolution can be obtained with limb sounding from spacecraft. This observing mode requires a very narrow antenna beam. A microwave limb-sounding experiment has been proposed for spacelab with a 1m antenna for a 250 km altitude orbit, providing ∿ 3 km height resolution [7].

4. CONCLUSION

Microwave spectrometers are presently being used on experimental weather satellites, and are going to be used operationally on the TIROS-weather-satellites. Groundbased and airborne microwave sensing provide important information on trace constituents in the atmosphere. The advantage of microwave remote sensing over other remote techniques such as infrared sensors is the ability of microwaves to penetrate clouds (important for groundbased and all tropospheric measurements) and the possibility to perform measurements which are not possible with other remote sensing techniques such as determining the kinetic temperature up to ∿ 90 km altitude or to obtain information on atmospheric liquid water content.

With the availability of low noise millimeter wave receivers, this technique will become a very important tool in atmospheric physics, meteorology and climatology.

REFERENCES

[1] K.F. KUNZI, A.D. FISHER, D.H. STAELIN, and J.W. WATERS, "Snow and Ice Surfaces Measured by the Nimbus 5 Microwave Spectrometer", JGR, Sept.20, 1976.

[2] J.W. WATERS, K.F. KUNZI, R.L. PETTYJOHN, R.K.L. POON, and D.H. STAELIN, "Remote Sensing of Atmospheric Temperature Profiles with the Nimbus-5 Microwave Spectrometer", Journal of Atmospheric Sciences, Vol.32, No.10, Oct.1975.

[3] D.H. STAELIN, K.F. KUNZI, R.L. PETTYJOHN, R.K.L. POON, R.W. WILCOX, and J.W.WATERS, "Remote Sensing of Atmospheric Water Vapor and Liquid Water with the Nimbus-5 Microwave Spectrometer", Journal of Applied Meteorology, Vol.15, No.11, November 1976.

[4] P.F. GOLDSMITH, M.M. LITVAK, R.L. PLAMBECK, and D.R.W. WILLIAMS, "Carbon Monoxide Mixing Ratio in the Mesosphere Derived from Ground-Based Microwave Measurements", to be published in JGR.

[5] J.W. WATERS et.al., "Aircraft Search for Millimeter-Wavelength Emission by Stratospheric ClO", to be published in JGR.

[6] M.T. CHAHINE, "A general relaxation method for inverse solution of the full radiative transfer equation", J.Atmos.Sci., 29, (4), 741-747, 1972.

[7] E. SCHANDA, K. KUENZI, R.HOFER, "Microwave Experiments for Spacelab and Nimbus-6", Proceedings from "Colloque du GDTA sur l'utilisation des Satellites en Teledetection" Saint-Mande/Paris, 21-23 Sept. 1977.

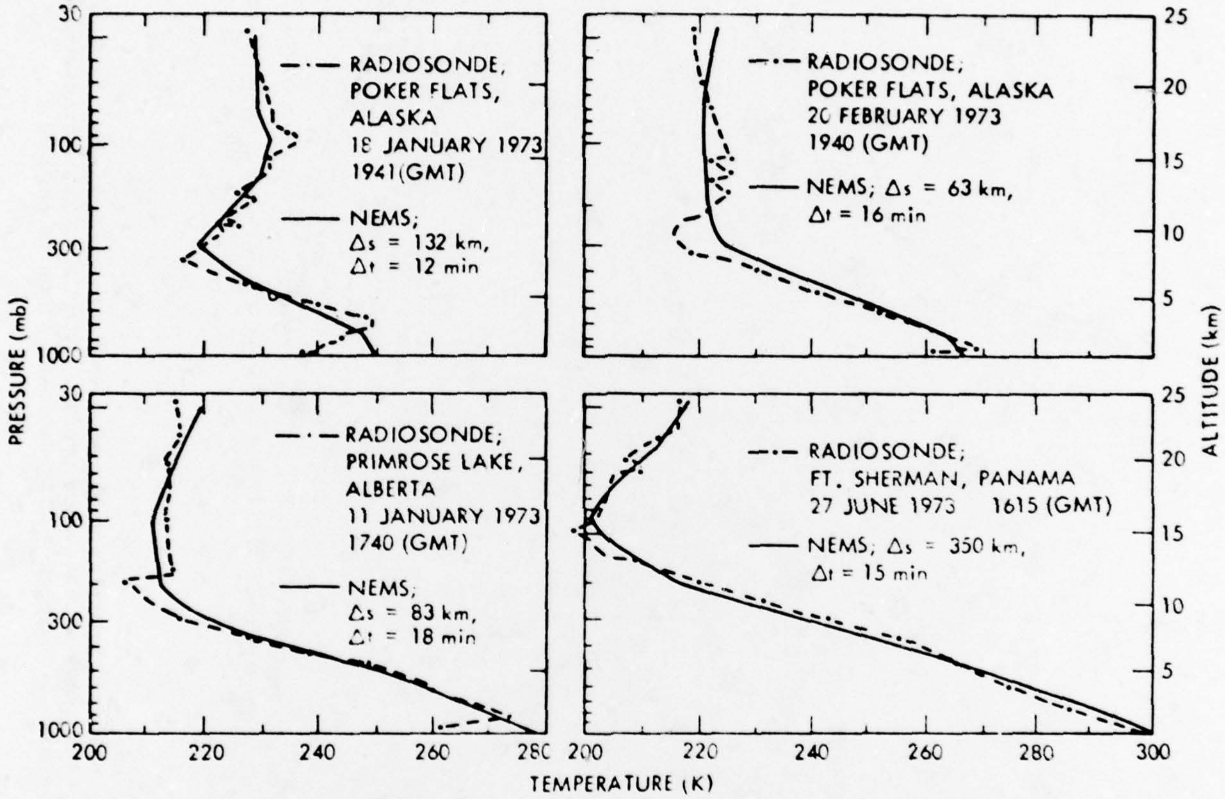

Fig. 1 : Four temperature profiles measured with the NIMBUS-5 microwave spectrometer (NEMS) compared with data from radiosondes; Δs and Δt are the spatial and time differences respectively between NEMS sounding and radiosonde launch[2].

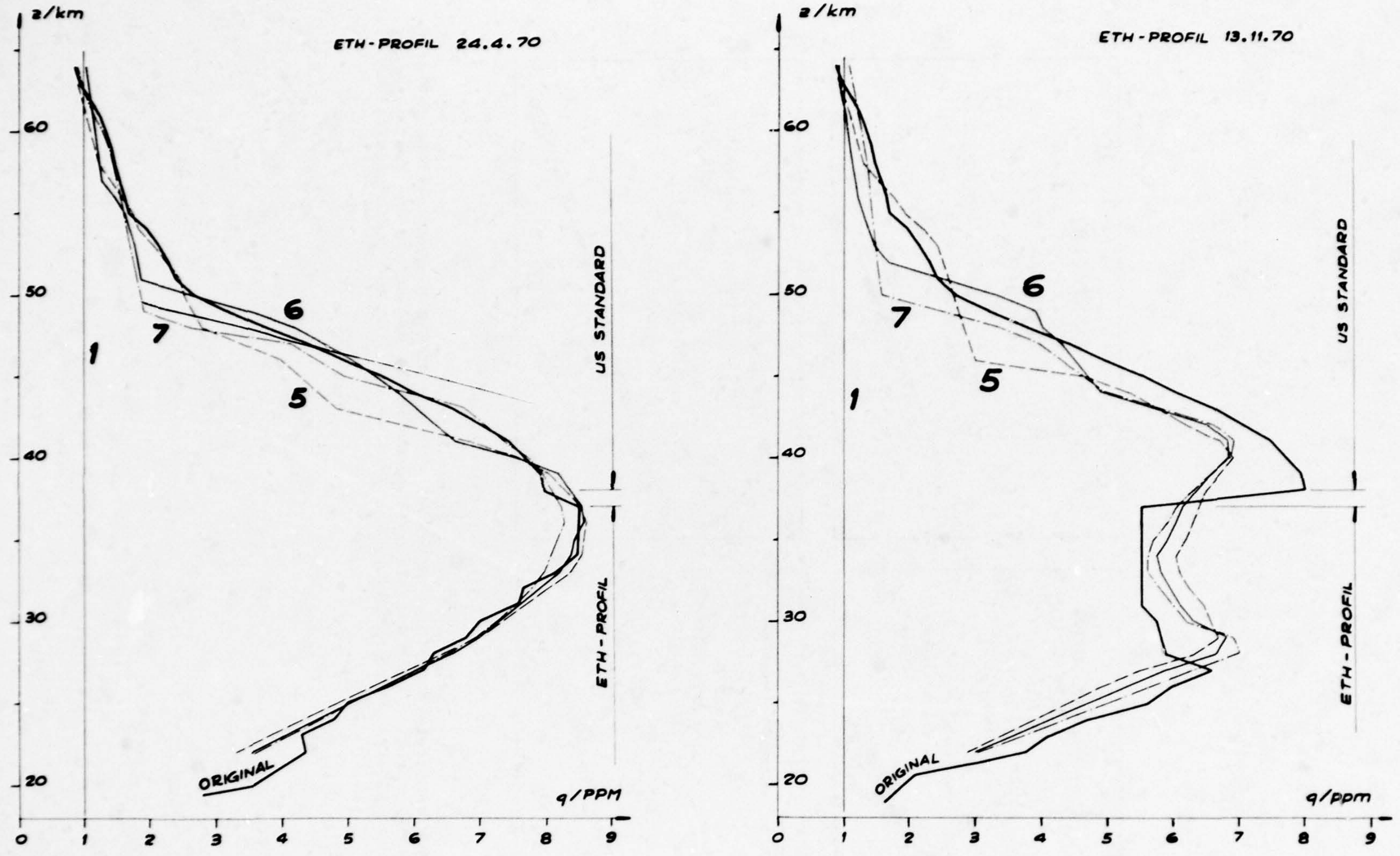

(a)

(b)

Fig.2a and Fig.2b : Two examples of ozone profiles measured with radio-sondes up to 35 km and iterations 5 through 7 of the ozone profile using simulated microwave data. A first guess with a constant mixing ratio of 1 ppm is assumed.

REPORT DOCUMENTATION PAGE

1. Recipient's Reference	2. Originator's Reference	3. Further Reference	4. Security Classification of Document
	AGARD-CP-245	ISBN 92-835-0231-0	UNCLASSIFIED

5. Originator Advisory Group for Aerospace Research and Development
North Atlantic Treaty Organization
7 rue Ancelle, 92200 Neuilly sur Seine, France

6. Title MILLIMETER AND SUBMILLIMETER WAVE PROPAGATION AND CIRCUITS

7. Presented at the 25th Meeting of the Electromagnetic Wave Propagation Panel held in Munich, 4–8 September 1978.

8. Author(s)/Editor(s)	9. Date
Edited by E.Spitz and G.Cachier	February 1979

10. Author's/Editor's Address	11. Pages
See Fly Leaf	546

12. Distribution Statement This document is distributed in accordance with AGARD policies and regulations, which are outlined on the Outside Back Covers of all AGARD publications.

13. Keywords/Descriptors

Electromagnetic wave transmission
Microwave frequencies
Millimeter waves
Submillimeter waves
Solid state devices
Solid state lasers

14. Abstract

The Proceedings deal with the millimeter and submillimeter ranges in the upper part of the microwave spectrum. Some applications are derived from optial techniques. Technology progress in the last few years, particularly that due to development of passive and active solid state devices, is reviewed. The proceedings present a broad view of state-of-the-art in solid-state sources and detectors and deal with progress in power tubes, laser techniques and high-power techniques. System aspects are covered. Future developments are assessed as to desirability and feasibility, particularly from the military viewpoint.

AGARD Conference Proceedings No.245
Advisory Group for Aerospace Research and Development, NATO
MILLIMETER AND SUBMILLIMETER WAVE PROPAGATION AND CIRCUITS
Edited by E.Spitz and G.Cachier
Published February 1979
546 pages

The Proceedings deal with the millimeter and submillimeter ranges in the upper part of the microwave spectrum. Some applications are derived from optical techniques. Technology progress in the last few years, particularly that due to development of passive and active solid state devices, is reviewed. The proceedings present a broad view of state-of-the-art in solid-state

P.T.O.

AGARD-CP-245

Electromagnetic wave transmission
Microwave frequencies
Millimeter waves
Submillimeter waves
Solid state devices
Solid state lasers

AGARD Conference Proceedings No.245
Advisory Group for Aerospace Research and Development, NATO
MILLIMETER AND SUBMILLIMETER WAVE PROPAGATION AND CIRCUITS
Edited by E.Spitz and G.Cachier
Published February 1979
546 pages

The Proceedings deal with the millimeter and submillimeter ranges in the upper part of the microwave spectrum. Some applications are derived from optical techniques. Technology progress in the last few years, particularly that due to development of passive and active solid state devices, is reviewed. The proceedings present a broad view of state-of-the-art in solid-state

P.T.O.

AGARD-CP-245

Electromagnetic wave transmission
Microwave frequencies
Millimeter waves
Submillimeter waves
Solid state devices
Solid state lasers

AGARD Conference Proceedings No.245
Advisory Group for Aerospace Research and Development, NATO
MILLIMETER AND SUBMILLIMETER WAVE PROPAGATION AND CIRCUITS
Edited by E.Spitz and G.Cachier
Published February 1979
546 pages

The Proceedings deal with the millimeter and submillimeter ranges in the upper part of the microwave spectrum. Some applications are derived from optical techniques. Technology progress in the last few years, particularly that due to development of passive and active solid state devices, is reviewed. The proceedings present a broad view of state-of-the-art in solid-state

P.T.O.

AGARD-CP-245

Electromagnetic wave transmission
Microwave frequencies
Millimeter waves
Submillimeter waves
Solid state devices
Solid state lasers

AGARD Conference Proceedings No.245
Advisory Group for Aerospace Research and Development, NATO
MILLIMETER AND SUBMILLIMETER WAVE PROPAGATION AND CIRCUITS
Edited by E.Spitz and G.Cachier
Published February 1979
546 pages

The Proceedings deal with the millimeter and submillimeter ranges in the upper part of the microwave spectrum. Some applications are derived from optical techniques. Technology progress in the last few years, particularly that due to development of passive and active solid state devices, is reviewed. The proceedings present a broad view of state-of-the-art in solid-state

P.T.O.

AGARD-CP-245

Electromagnetic wave transmission
Microwave frequencies
Millimeter waves
Submillimeter waves
Solid state devices
Solid state lasers

sources and detectors and deal with progress in power tubes, laser techniques and high-power techniques. System aspects are covered. Future developments are assessed as to desirability and feasibility, particularly from the military viewpoint.

Papers and discussion presented at the 25th Meeting of the Electromagnetic Wave Propagation Panel held in Munich, 4–8 September 1978.

ISBN 92-835-0231-0

sources and detectors and deal with progress in power tubes, laser techniques and high-power techniques. System aspects are covered. Future developments are assessed as to desirability and feasibility, particularly from the military viewpoint.

Papers and discussion presented at the 25th Meeting of the Electromagnetic Wave Propagation Panel held in Munich, 4–8 September 1978.

ISBN 92-835-0231-0

sources and detectors and deal with progress in power tubes, laser techniques and high-power techniques. System aspects are covered. Future developments are assessed as to desirability and feasibility, particularly from the military viewpoint.

Papers and discussion presented at the 25th Meeting of the Electromagnetic Wave Propagation Panel held in Munich, 4–8 September 1978.

ISBN 92-835-0231-0

sources and detectors and deal with progress in power tubes, laser techniques and high-power techniques. System aspects are covered. Future developments are assessed as to desirability and feasibility, particularly from the military viewpoint.

Papers and discussion presented at the 25th Meeting of the Electromagnetic Wave Propagation Panel held in Munich, 4–8 September 1978.

ISBN 92-835-0231-0

AGARD

NATO OTAN

7 RUE ANCELLE · 92200 NEUILLY-SUR-SEINE

FRANCE

Telephone 745.08.10 · Telex 610176

DISTRIBUTION OF UNCLASSIFIED AGARD PUBLICATIONS

AGARD does NOT hold stocks of AGARD publications at the above address for general distribution. Initial distribution of AGARD publications is made to AGARD Member Nations through the following National Distribution Centres. Further copies are sometimes available from these Centres, but if not may be purchased in Microfiche or Photocopy form from the Purchase Agencies listed below.

NATIONAL DISTRIBUTION CENTRES

BELGIUM
Coordonnateur AGARD – VSL
Etat-M
Quartie
Rue d'I

CANADA
Defenc
Depart
Ottawa

DENMARK
Danish
Østerb
Copenl

FRANCE
O.N.E.
29 Ave
92 Chá

GERMANY
Zentra
dokum
c/o Fa
Physik
Kernf
7514 I

GREECE
Hellenic Air Force General Staff
Research and Development Directorate
Holargos, Athens, Greece

ICELAND
Director of Aviation
c/o Flugrad
Reykjavik

ITALY
Aeronautica Militare
Ufficio del Delegato Nazionale all'AGARD

nment

Department of Research and Development (ARGE)
Ministry of National Defence, Ankara

UNITED KINGDOM
Defence Research Information Centre
Station Square House
St. Mary Cray
Orpington, Kent BR5 3RE

National Aeronautics and Space Administration
WASHINGTON, D.C. 20546

OFFICIAL BUSINESS
Penalty For Private Use, $300.00

POSTAGE AND FEES PAID
NATIONAL AERONAUTICS AND
SPACE ADMINISTRATION
NASA-451

SPECIAL FOURTH CLASS MAIL
BOOK

12 2 4B,9, 051179 S02672DU
DEPT OF DEFENSE
DEFENSE DOCUMENTATION CENTER
ATTN: DDC-DDA-2
CAMERON STATION BLDG 5
ALEXANDRIA VA 22314

UNITED STATES
National Aeronautics and Space Administration (NASA)
Langley Field, Virginia 23365
Attn: Report Distribution and Storage Unit

THE UNITED STATES NATIONAL DISTRIBUTION CENTRE (NASA) DOES NOT HOLD STOCKS OF AGARD PUBLICATIONS, AND APPLICATIONS FOR COPIES SHOULD BE MADE DIRECT TO THE NATIONAL TECHNICAL INFORMATION SERVICE (NTIS) AT THE ADDRESS BELOW.

PURCHASE AGENCIES

Microfiche or Photocopy
National Technical
Information Service (NTIS)
5285 Port Royal Road
Springfield
Virginia 22161, USA

Microfiche
Space Documentation Service
European Space Agency
10, rue Mario Nikis
75015 Paris, France

Microfiche
Technology Reports
Centre (DTI)
Station Square House
St. Mary Cray
Orpington Kent BR5 3RF
England

Requests for microfiche or photocopies of AGARD documents should include the AGARD serial number, title, author or editor, and publication date. Requests to NTIS should include the NASA accession report number. Full bibliographical references and abstracts of AGARD publications are given in the following journals:

Scientific and Technical Aerospace Reports (STAR)
published by NASA Scientific and Technical
Information Facility
Post Office Box 8757
Baltimore/Washington International Airport
Maryland 21240, USA

Government Reports Announcements (GRA)
published by the National Technical
Information Services, Springfield
Virginia 22161, USA

Printed by Technical Editing and Reproduction Ltd
Harford House, 7–9 Charlotte St, London W1P 1HD

ISBN 92-835-0231-0